

# AGARD

ADVISORY GROUP FOR AEROSPACE RESEARCH & DEVELOPMENT

7 RUE ANCELLE, 92200 NEUILLY-SUR-SEINE, FRANCE

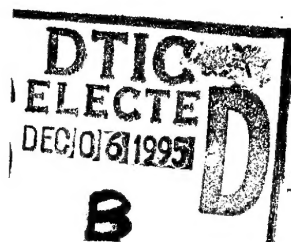
DISTRIBUTION STATEMENT A

Approved for public release  
Distribution Unlimited

AGARD ADVISORY REPORT NO. 318

## Aerodynamics of 3-D Aircraft Afterbodies

(l'Aérodynamique des arrière-corps tridimensionnels)



19951205 020



NORTH ATLANTIC TREATY ORGANIZATION

Published September 1995

Distribution and Availability on Back Cover

# AGARD

ADVISORY GROUP FOR AEROSPACE RESEARCH & DEVELOPMENT

7 RUE ANCELLE, 92200 NEUILLY-SUR-SEINE, FRANCE

---

**AGARD ADVISORY REPORT NO. 318**

## **Aerodynamics of 3-D Aircraft Afterbodies**

(l'Aérodynamique des arrière-corps tridimensionnels)

DTIC QUALITY INSPECTED 8



North Atlantic Treaty Organization  
*Organisation du Traité de l'Atlantique Nord*

---

# The Mission of AGARD

According to its Charter, the mission of AGARD is to bring together the leading personalities of the NATO nations in the fields of science and technology relating to aerospace for the following purposes:

- Recommending effective ways for the member nations to use their research and development capabilities for the common benefit of the NATO community;
- Providing scientific and technical advice and assistance to the Military Committee in the field of aerospace research and development (with particular regard to its military application);
- Continuously stimulating advances in the aerospace sciences relevant to strengthening the common defence posture;
- Improving the co-operation among member nations in aerospace research and development;
- Exchange of scientific and technical information;
- Providing assistance to member nations for the purpose of increasing their scientific and technical potential;
- Rendering scientific and technical assistance, as requested, to other NATO bodies and to member nations in connection with research and development problems in the aerospace field.

The highest authority within AGARD is the National Delegates Board consisting of officially appointed senior representatives from each member nation. The mission of AGARD is carried out through the Panels which are composed of experts appointed by the National Delegates, the Consultant and Exchange Programme and the Aerospace Applications Studies Programme. The results of AGARD work are reported to the member nations and the NATO Authorities through the AGARD series of publications of which this is one.

Participation in AGARD activities is by invitation only and is normally limited to citizens of the NATO nations.

The content of this publication has been reproduced  
directly from material supplied by AGARD or the authors.

Published September 1995

Copyright © AGARD 1995  
All Rights Reserved

ISBN 92-836-1023-7



Printed by Canada Communication Group  
45 Sacré-Cœur Blvd., Hull (Québec), Canada K1A 0S7

# Contents

	Page
Preface	ix
Recent Publications	xi
General Nomenclature	xiii
<b>SECTION 1 — INTRODUCTION</b>	
by A. Wood and D. Bowers	
1.1 BACKGROUND, OBJECTIVES AND SCOPE OF WORK	1
1.2 CONTRIBUTORS	1
1.2.1 Group Members and Meetings	1
1.2.2 CFD Contributors	2
1.3 REPORT ORGANISATION	2
1.3.1 Fundamental Flow Phenomena	3
1.3.2 Design	3
1.4 REVIEW OF WG-08 (1986)	3
1.5 REFERENCES	4
1.6 ACKNOWLEDGEMENTS	5
<b>SECTION 2 — FUNDAMENTAL FLOW PHENOMENA</b>	
2.1 FUNDAMENTAL FLOW PHENOMENA RELATED TO 3-D AFTERBODIES	7
by R. Jouty	
2.1.1 DESCRIPTION OF THE FLOW FUNDAMENTALS	7
2.1.1.1 Boundary layer separation	7
2.1.1.2 Effect of wall temperature on boundary layer separation	8
2.1.1.3 Effect of jet temperature	8
2.1.1.4 Jet Structure	8
2.1.1.5 Waves/shear layers interactions	8
2.1.1.6 Compressibility effect on shear layer expansion	9
2.1.1.7 Aeroacoustic — screech	9
2.1.2 COMPLEX GEOMETRIES AND 3-D PHENOMENA	9
2.1.2.1 Double-flux nozzles	10
2.1.2.2 Two-dimensional versus three-dimensional separation and vortical flows	11
2.1.2.3 Jet structures and shear layers in 3D	23
2.1.2.4 Twin supersonic plume resonance — screech	23
2.1.3 CONCLUSIONS — RECOMMENDATIONS	23
REFERENCES	23

<b>Accession For</b>	
NTIS GRA&I	<input checked="" type="checkbox"/>
DTIC TAB	<input type="checkbox"/>
Unannounced	<input type="checkbox"/>
Justification	
By	
Distribution/	
Availability Codes	
Dist	Avail and/or Special
A-1	



2.2	EXPERIMENTAL TECHNIQUES FOR THE STUDY OF COMPLEX FLOWS	25
	by J.M. Delery	
2.2.1	INTRODUCTION	25
2.2.2	SURFACE PROPERTIES CHARACTERIZATION	26
2.2.2.1	General Remarks	26
2.2.2.2	Surface Pressure Measurements	26
2.2.2.3	Skin Friction Measurements	27
2.2.2.4	Surface Heat Transfer Measurements	28
2.2.2.5	Surface Flow Visualizations	30
2.2.3	CLASSICAL INTRUSIVE TECHNIQUES FOR FIELD MEASUREMENTS	30
2.2.3.1	General Remarks	30
2.2.3.2	Pressure Probes	30
2.2.3.3	Temperature Probes	32
2.2.3.4	Anemometric Measurements	33
2.2.4	NON-INTRUSIVE TECHNIQUES FOR FIELD MEASUREMENTS	33
2.2.4.1	Introductory Remarks	33
2.2.4.2	Optical Visualization Techniques	34
2.2.4.3	Interferometry	34
2.2.4.4	Laser Doppler Velocimetry	37
2.2.5	LASER SPECTROSCOPIC FLOW DIAGNOSTICS	41
2.2.5.1	General remarks	41
2.2.5.2	Laser Absorption	42
2.2.5.3	Rayleigh Scattering	42
2.2.5.4	Raman Scattering	42
2.2.5.5	Stimulated Raman Scattering	43
2.2.5.6	Laser-Induced Fluorescence	43
2.2.6	EXPERIMENTAL SET-UP AND JET SIMULATION	44
2.2.6.1	General Remarks	44
2.2.6.2	Model Support	44
2.2.6.3	Jet Simulation	45
2.2.7	CONCLUDING REMARKS	46
2.2.8	REFERENCES	46
2.3	APPLICATION OF CFD TECHNIQUES TO MODEL 3-D AFTERBODY FLOW PHENOMENA	51
	by R. Cosner	
2.3.1	INTRODUCTION	51
2.3.2	PERTINENT FLOW PHYSICS ISSUES	51
2.3.2.1	Geometry Issues	51
2.3.2.2	Boundary Layer Properties	51
2.3.2.3	Plume Issues	52
2.3.2.5	Tail Interactions	54
2.3.3	ELEMENTS OF CFD ANALYSIS	54
2.3.3.1	Geometry Definition	54
2.3.3.2	Grid Generation	55
2.3.3.3	Flow Solver Algorithms	56
2.3.3.4	Turbulence Models	57
2.3.3.5	Unsteady Flows	58
2.3.3.6	Implementation	58
2.3.3.7	Usage Practices	60
2.3.3.8	Post-Processing	60
2.3.4	SUMMARY	61
	REFERENCES	61

2.4	REVIEW OF COMPUTATIONAL METHODS	63
	by <b>R. Cosner</b>	
2.4.1	SEMI-EMPIRICAL METHOD	63
	2.4.1.1 Method Description	63
2.4.2	CFD METHODS (EULER AND NAVIER-STOKES)	64
	2.4.2.1 Grid Generation Impact	64
	2.4.2.2 Turbulence Model Impact	64
	2.4.2.3 Performance Issues	68
2.4.3	CONTRIBUTED PREDICTIONS	68
	2.4.3.1 Grid Generators	68
	2.4.3.2 Flow Solvers	69
2.4.4	NUMBERING SYSTEM (To identify Codes used for Computations)	72
	REFERENCES	74
2.5	DESCRIPTION OF TEST CASES A	77
	by <b>J.-M. Delery</b>	
2.5.1	INTRODUCTORY REMARKS	77
2.5.2	ACCURACY OF TEST RESULTS	77
2.5.3	TEST CASES	77
	2.5.3.1 Test Case A.1.1 : Axisymmetric Body Without Jet at Incidence	77
	2.5.3.2 Test Cases A.2.1 and A.2.2 : Axisymmetric Body with Jet Cold/Hot Flow	79
	2.5.3.3 Test Cases A.3.1 and A.3.2 : Twin Jet Cold Flow	82
2.5.4	REFERENCES	90
2.6	COMPUTATIONAL RESULTS AND EVALUATION	93
	by <b>G. Rollin and J.-D. Marion</b>	
2.6.1	PRELIMINARY REMARKS	93
2.6.2	CASE A.2	93
	2.6.2.1 Description of the flow features	93
	2.6.2.2 Presentation of different numerical approaches	94
	2.6.2.3 Evaluation of results	98
2.6.3	CONCLUSIONS OF A.2 TEST CASES	105
2.7	RECOMMENDATION FOR FUTURE WORK	141
	by <b>G. Rollin</b>	

### SECTION 3 — DESIGN

3.1	DESIGN OF COMPLEX 3-D AIRCRAFT AFTERBODIES — GENERAL CONSIDERATIONS	143
	by <b>C. Lee</b>	
3.1.1	INTRODUCTION	143
3.1.2	AFTERBODY AERODYNAMICS WITHIN THE OVERALL DESIGN PROCESS	143
3.1.3	FACTORS INFLUENCING 3-D AFTERBODY DESIGN	145
	3.1.3.1 Performance	145
	3.1.3.2 Flow Characteristics	146
	3.1.3.3 Stability and Control	147
	3.1.3.4 Buffet, Vibration and Acoustics	147
	3.1.3.5 Configuration Integration	147
	3.1.3.6 Engine Installation Requirements	147
	3.1.3.7 Structural Considerations	148
	3.1.3.8 Equipment Installations	148
	3.1.3.9 Other Considerations	148
3.1.4	TOOLS AND TECHNIQUES	148
3.1.5	CONCLUDING REMARKS	149
3.1.6	REFERENCES	149

3.2	THE ROLE OF EMPIRICAL, ANALYTICAL AND CFD METHODS IN THE DESIGN PROCESS	151
	by E. Merlo	
3.2.1	DESCRIPTION	151
3.2.1.1	Integral Mean Slope	152
3.2.1.2	Integral Mean Slope Truncated, IMST	152
3.2.1.3	Engine/Airframe Integration Methods	152
3.2.1.4	Empirical Supercirculation Effect Correlations	153
3.2.1.5	CFD Design Methods	153
3.2.2	USE	155
3.2.3	NEEDS	155
3.2.4	REFERENCE	156
3.3	STATE OF THE ART ASSESSMENT OF TESTING TECHNIQUES FOR AIRCRAFT AFTERBODIES	169
	by P.R. Kern	
3.3.1	INTRODUCTION	169
3.3.2	THRUST-DRAG BOOKKEEPING	169
3.3.3	CURRENT TEST METHODS	170
3.3.3.1	Support Methods	171
3.3.3.2	Metric break	172
3.3.3.3	Balances	173
3.3.3.4	Surface pressures	173
3.3.3.5	Pressure Indicating Paint (PIP)	174
3.3.4	FUTURE NEEDS	175
3.3.4.1	Balance development	175
3.3.4.2	Test Techniques	175
3.3.4.3	Experimental Investigations Required	176
3.3.4.4	Synergistic Optimization	177
3.3.4.5	Data Manipulation Development	177
3.3.4.6	Model design challenge	178
3.3.5	REFERENCES	178
3.4	DESCRIPTION OF GROUP B TEST CASES	181
	by B. Berrier	
3.4.1	INTRODUCTION	181
3.4.2	GROUP B TEST CASE SELECTION	181
3.4.3	ACCURACY OF TEST RESULTS	181
3.4.4	TEST CASES	182
3.4.4.1	Test Cases B.1. and B.2 — NASA Langley Single Engine Afterbody with (B.1) and without (B.2) tails	182
3.4.4.2	Test Case B.3 — NASA Langley Twin Engine Afterbody with tails	182
3.4.4.3	Test Case B.4 — NASA Langley 2-D C-D Single Isolated Nozzle	183
3.4.5	REFERENCES	183

3.5	COMPUTATIONAL RESULTS FOR ENGINEERING CASES by R. Cosner	199
3.5.1	CASE B.1	200
3.5.1.1	Case B.1.1	201
3.5.1.2	Case B.1.2	207
3.5.1.3	Sensitivity to Trailing Edge Modeling Technique	213
3.5.1.4	Discussion of Results	214
3.5.2	CASE B.2	224
3.5.2.1	Case B.2.1	225
3.5.2.2	Case B.2.2	239
3.5.2.3	Case B.2.3	249
3.5.2.4	Discussion of Results	254
3.5.3	CASE B.3	261
3.5.3.1	Case B.3.1	263
3.5.3.2	Case B.3.2	282
3.5.3.3	Case B.3.3	285
3.5.3.4	Discussion of Results	301
3.5.4	CASE B.4	304
3.5.4.1	Case B.4.1	304
3.5.4.2	Case B.4.2	344
3.5.4.3	Discussion of Results	369
	REFERENCES	369
3.6	RECOMMENDATION FOR FUTURE WORK by N.C. Bissinger and R. Cosner	379
SECTION 4	— CONCLUDING REMARKS by P. Martin	381
4.1	FUNDAMENTAL FLOW PHENOMENA	381
4.2	DESIGN	381
4.3	GENERAL	382

## APPENDICES

<b>APPENDIX A: EXPERIMENTAL RESULTS FOR GROUP A TEST CASES</b>			A-1
by J.M. Delery			
A.1	A.1.1	TEST CASE (AXISYMMETRIC BODY WITHOUT JET AT INCIDENCE)	A-1
A.2	A.2	TEST CASES (AXISYMMETRIC BODY WITH JET)	A-10
	A.2.1	TEST CASE A.2.1 (COLD JET FLOW)	A-10
	A.2.2	TEST CASE A.2.2 (HOT JET FLOW)	A-10
A.3	A.3	TEST CASES (TWIN JET AFTERBODY)	A-17
	A.3.1	TEST CASE A.3.1 ( $M_\infty = 0.85$ )	A-17
	A.3.2	TEST CASE A.3.2 ( $M_\infty = 0.8$ )	A-22
<b>APPENDIX B: EXPERIMENTAL DATA FOR GROUP B TEST CASES</b>			B-1
by B. Berrier			
B.1	B.1	TEST CASES — AXISYMMETRIC, SINGLE-ENGINE BODY WITH NO TAILS	B-1
	B.1.1	TEST CASE B.1.1 ( $M_\infty = 0.901$ , NPR = 2.033)	B-1
	B.1.2	TEST CASE B.1.2 ( $M_\infty = 0.901$ , NPR = 4.991)	B-3
B.2	B.2	TEST CASES — AXISYMMETRIC, SINGLE ENGINE BODY WITH STAGGERED TAILS	B-5
	B.2.1	TEST CASE B.2.1 ( $M_\infty = 0.900$ , NPR = 2.027)	B-5
	B.2.2	TEST CASE B.2.2 ( $M_\infty = 0.900$ , NPR = 2.997)	B-9
	B.2.3	TEST CASE B.2.3 ( $M_\infty = 0.900$ NPR = 5.033)	B13
B.3	B.3	TEST CASES — TWIN-JET BODY, $M_\infty = 0.90$ , NPR = 3.4	B-17
	B.3.1	TEST CASE B.3.1 (MID HORIZONTAL TAILS, MID VERTICAL TAILS, $M_\infty = 0.901$ , NPR = 3.407)	B-17
	B.3.2	TEST CASE B.3.2 (MID HORIZONTAL TAILS, AFT VERTICAL TAILS, $M_\infty = 0.899$ , NPR = 3.400)	B-21
	B.3.3	TEST CASE B.3.3 (MID HORIZONTAL TAILS, FWD. VERTICAL TAILS, $M_\infty = 0.899$ , NPR = 3.402)	B-22
B.4	B.4	TEST CASES (SINGLE JET, NONAXISYMMETRIC 2-D C-D NOZZLE WITH NO TAILS)	B-25
	B.4.1	TEST CASE B.4.1 ( $M_\infty = 0.600$ , NPR = 4.00)	B-25
	B.4.2	TEST CASE B.4.2 ( $M_\infty = 0.938$ , NPR = 4.02)	B-40
<b>APPENDIX C: CFD USAGE NOTES</b>			C-1
Compiled by R. Cosner			
C.1	TEST CASE SERIES A		C-1
	C.1.1	TEST CASE SERIES A.2	C-1
	C.1.2	TEST CASE SERIES A.3	C-3
C.2	TEST CASE SERIES B		C-4
	C.2.1	TEST CASE SERIES B.1	C-4
	C.2.2	TEST CASE SERIES B.2	C-7
	C.2.3	TEST CASE SERIES B.3	C-10
	C.2.4	TEST CASE SERIES B.4	C-12
C.3	POST-PROCESSING TECHNIQUES		C-20
	REFERENCES		C-21

# Preface

This report presents the findings of a study performed by AGARD Working Group 17 into the current understanding of the aerodynamics of complex 3-D aircraft afterbodies and the status of the methods now available to aid in their design optimisation. Assembled by a group of computational, experimental and application specialists selected from industry, government agencies and universities and bringing together material gathered over the two years between the autumns of 1992 and 1994, the work fulfils one of the main recommendations of the preceding working Group, WG08 (1986), namely — to provide an update on the state-of-the-art with particular consideration of the progress made on the computational simulation of three-dimensional viscous flow.

The major part of the report is given over to the results obtained and lessons learned from the application of current CFD procedures to a selection of test cases ranging in complexity from a simple axisymmetric body with jet to a twin-jet body complete with wings and empennage. Comprehensive descriptions of the selected test cases with their experimental data bases are appended to the report in the hope that these will continue to serve other researchers in the field. Other sections of the report review the developments made in empirical/semi-empirical procedures and in the experimental techniques applicable to support both future computational developments and aid directly in the task of aircraft design optimisation.

Comparing the current scene with that in 1986 the group found:

- Major advances have been made in the capabilities of CFD which, provided great care is taken, can now be usefully applied to some of the most highly complex geometries and flow situations with growing confidence in the quality of the prediction of the general flowfield and incremental performance trends. Reliable prediction of absolute performance remains elusive, however. Ease, consistency and quality of mesh generation, accurate representation of geometric detail and turbulence modelling rank high amongst the issues seen as setting the pace of further improvements.
- Semi-empirical procedures retain an important position in the design development process offering a highly cost effective means of using available experimental data to yield performance predictions to an accuracy that is still hard to match using CFD. Further expansion of the experimental data base to support these methods continues to be justified.
- Among the most influential developments in the experimental field are those laser and paint based techniques that enable non-intrusive global flow-field sampling and near complete mapping of the model surface pressures and viscous forces. As well as greatly extending the scope for understanding general flow field behaviour these techniques now allow measurement of the detailed information needed for the validation of developing computational techniques, and notably turbulence models. Wider and more practised use of these new techniques, more careful experimental conditioning to minimise model support interference on balance force measurements and further exploration of the effects of hot jets are highlighted as areas deserving future research attention.

# Préface

Ce rapport présente les conclusions d'une étude réalisée par le groupe de travail No. 17 de l'AGARD, sur l'état actuel des connaissances dans le domaine de l'aérodynamique des arrière-corps complexes tridimensionnels, ainsi que sur les méthodes actuellement disponibles pour l'optimisation de leur conception. Un groupe de spécialistes en informatique, en expérimentation et en applications venant de l'industrie, des agences gouvernementales et des universités a rassemblé des éléments d'information collectés entre l'automne 1992 et l'automne 1994. L'ouvrage répond à l'une des principales recommandations du groupe de travail précédent (WG08) (1986), c'est-à-dire: présenter une mise à jour de l'état de l'art, en apportant une attention particulière aux progrès réalisés dans le domaine de la simulation par ordinateur des écoulements visqueux tridimensionnels.

La majeure partie du rapport est consacrée aux résultats obtenus et aux enseignements tirés des procédures courantes en aérodynamique numérique appliquées à une série de cas d'essais allant du simple module axisymétrique simple avec réacteur jusqu'à l'ensemble complet biréacteur avec voilure et empennage. Des descriptions très complètes des cas d'essais retenus, avec leurs bases de données expérimentales, sont annexées au rapport, à l'intention d'autres chercheurs travaillant dans le même domaine. D'autres sections du rapport examinent les développements intervenus dans les procédures empiriques/semi-empiriques, ainsi que dans les techniques expérimentales applicables au soutien des futurs développements informatiques et à l'optimisation de la conception des aéronefs.

Le groupe a comparé la situation actuelle à celle existant en 1986 et ses conclusions ont été les suivantes:

- des progrès considérables ont été réalisés en ce qui concerne les possibilités de l'aérodynamique numérique, lesquels, sous réserve des précautions qui s'imposent, peuvent désormais être appliqués profitablement à certaines des géométries et aux cas d'écoulement les plus complexes en faisant de plus en plus de confiance à la qualité de la modélisation du champ d'écoulement global et aux tendances d'accroissement des performances. La prévision absolue des performances reste, cependant, encore intangible.  
La facilité, la cohérence et la qualité de la génération des maillages, ainsi que la représentation fidèle du détail géométrique et de la modélisation de la turbulence figurent parmi les questions les plus importantes pour ce qui concerne les améliorations futures.
- les procédures semi-empiriques occupent une position importante dans le processus d'évolution de la conception puisqu'elles offrent un moyen extrêmement rentable d'utiliser des données expérimentales existantes, et sont susceptibles de donner des prévisions d'une précision qui serait encore difficile à atteindre par les méthodes CFD. Un accroissement permanent de la base de données expérimentales, demandé pour le soutien de ces méthodes, continue à être justifié.
- parmi les développements qui ont eu le plus d'impact dans le domaine expérimental figurent les techniques à base de lasers et de peintures permettant l'échantillonnage non perturbateur du champ d'écoulement global et la cartographie quasi-complète des pressions superficielles et des forces visqueuses du modèle. Ces techniques permettent à la fois de mieux comprendre le comportement général du champ d'écoulement et d'établir les paramètres des informations détaillées demandées pour la validation des techniques de calcul en cours de développement et notamment les modèles de la turbulence. La mise en œuvre plus généralisée et plus experte des ces nouvelles techniques, le conditionnement expérimental plus soigné afin de réduire au minimum la perturbation induite par le support du modèle lors des mesures des forces par balance, ainsi que d'autres explorations des effets des gaz chauds, sont les domaines qui mériteraient une attention particulière lors des futurs travaux de recherche.

# Recent Publications of the Fluid Dynamics Panel

## AGARDOGRAPHS (AG)

**Computational Aerodynamics Based on the Euler Equations**  
AGARD AG-325, September 1994

**Scale Effects on Aircraft and Weapon Aerodynamics**  
AGARD AG-323, July 1994

**Design and Testing of High-Performance Parachutes**  
AGARD AG-319, November 1991

**Experimental Techniques in the Field of Low Density Aerodynamics**  
AGARD AG-318 (E), April 1991

**Techniques Expérimentales Liées à l'Aérodynamique à Basse Densité**  
AGARD AG-318 (FR), April 1990

**A Survey of Measurements and Measuring Techniques in Rapidly Distorted Compressible Turbulent Boundary Layers**  
AGARD AG-315, May 1989

**Reynolds Number Effects in Transonic Flows**  
AGARD AG-303, December 1988

## REPORTS (R)

**Optimum Design Methods for Aerodynamics**  
AGARD R-803, Special Course Notes, November 1994

**Missile Aerodynamics**  
AGARD R-804, Special Course Notes, May 1994

**Progress in Transition Modelling**  
AGARD R-793, Special Course Notes, April 1994

**Shock-Wave/Boundary-Layer Interactions in Supersonic and Hypersonic Flows**  
AGARD R-792, Special Course Notes, August 1993

**Unstructured Grid Methods for Advection Dominated Flows**  
AGARD R-787, Special Course Notes, May 1992

**Skin Friction Drag Reduction**  
AGARD R-786, Special Course Notes, March 1992

**Engineering Methods in Aerodynamic Analysis and Design of Aircraft**  
AGARD R-783, Special Course Notes, January 1992

**Aircraft Dynamics at High Angles of Attack: Experiments and Modelling**  
AGARD R-776, Special Course Notes, March 1991

## ADVISORY REPORTS (AR)

**A Selection of Experimental Test Cases for the Validation of CFD Codes**  
AGARD AR-303, Vols I and II, Report of WG-14, August 1994

**Quality Assessment for Wind Tunnel Testing**  
AGARD AR-304, Report of WG-15, July 1994

**Air Intakes for High Speed Vehicles**  
AGARD AR-270, Report of WG13, September 1991

**Appraisal of the Suitability of Turbulence Models in Flow Calculations**  
AGARD AR-291, Technical Status Review, July 1991



**Rotary-Balance Testing for Aircraft Dynamics**

AGARD AR-265, Report of WG11, December 1990

**Calculation of 3D Separated Turbulent Flows in Boundary Layer Limit**

AGARD AR-255, Report of WG10, May 1990

**Adaptive Wind Tunnel Walls: Technology and Applications**

AGARD AR-269, Report of WG12, April 1990

**CONFERENCE PROCEEDINGS (CP)**

**Aerodynamics and Aeroacoustics of Rotorcraft**

AGARD CP-552, August 1995

**Application of Direct and Large Eddy Simulation to Transition and Turbulence**

AGARD CP-551, December 1994

**Wall Interference, Support Interference and Flow Field Measurements**

AGARD CP-535, July 1994

**Computational and Experimental Assessment of Jets in Cross Flow**

AGARD CP-534, November 1993

**High-Lift System Aerodynamics**

AGARD CP-515, September 1993

**Theoretical and Experimental Methods in Hypersonic Flows**

AGARD CP-514, April 1993

**Aerodynamic Engine/Airframe Integration for High Performance Aircraft and Missiles**

AGARD CP-498, September 1992

**Effects of Adverse Weather on Aerodynamics**

AGARD CP-496, December 1991

**Manoeuvring Aerodynamics**

AGARD CP-497, November 1991

**Vortex Flow Aerodynamics**

AGARD CP-494, July 1991

**Missile Aerodynamics**

AGARD CP-493, October 1990

**Aerodynamics of Combat Aircraft Controls and of Ground Effects**

AGARD CP-465, April 1990

**Computational Methods for Aerodynamic Design (Inverse) and Optimization**

AGARD CP-463, March 1990

**Applications of Mesh Generation to Complex 3-D Configurations**

AGARD CP-464, March 1990

**Fluid Dynamics of Three-Dimensional Turbulent Shear Flows and Transition**

AGARD CP-438, April 1989

**Validation of Computational Fluid Dynamics**

AGARD CP-437, December 1988

**Aerodynamic Data Accuracy and Quality: Requirements and Capabilities in Wind Tunnel Testing**

AGARD CP-429, July 1988

**Aerodynamics of Hypersonic Lifting Vehicles**

AGARD CP-428, November 1987

**Aerodynamic and Related Hydrodynamic Studies Using Water Facilities**

AGARD CP-413, June 1987

**Applications of Computational Fluid Dynamics in Aeronautics**

AGARD CP-412, November 1986

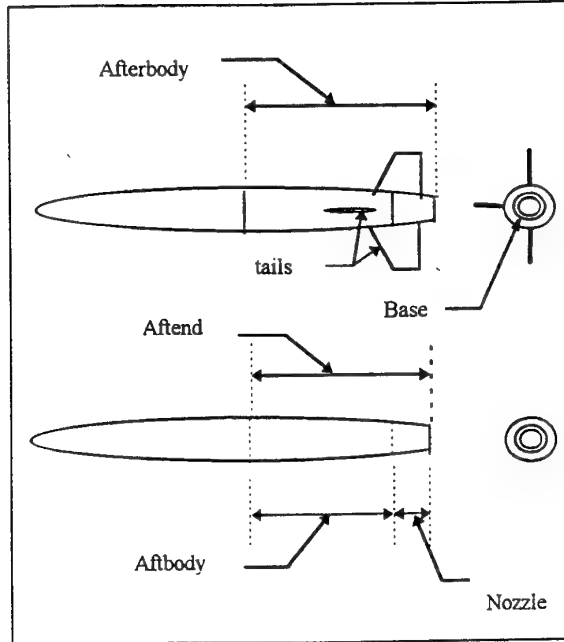
## General Nomenclature

Unless otherwise noted in the text the following nomenclature applies throughout this report. Many of the terms used for the more specialised discussions are left to be introduced where used. The aim of this list is to cover the more general terms which are used often or within more than one section.

A	cross-sectional area
A <sub>MAX</sub>	maximum cross-sectional area of body
A <sub>MB</sub>	area of afterbody at metric break
AR <sub>W</sub>	wing aspect ratio, $b^2 / A_{wing}$
A <sub>Wing</sub>	wing area
AR <sub>N</sub>	nozzle aspect ratio, width/height
b	wing span
b <sub>t</sub>	tail span
c	local airfoil chord
c <sub>m</sub>	Specific heat
$\bar{c}$	mean aerodynamic chord
C <sub>A</sub>	afterbody axial force coefficient, $C_A = \frac{\text{axial force}}{q_\infty A_{\max}}$
C <sub>A</sub> <sup>+</sup>	afterbody axial force coefficient, $C_A^+ = \frac{\text{axial force}}{q_\infty A_{wing}}$
C <sub>L</sub>	lift coefficient, $C_L = \frac{\text{lift force}}{q_\infty A_{wing}}$
C <sub>m</sub>	pitching moment coefficient, $C_m = \frac{\text{pitching moment}}{q_\infty A_{wing}}$
C <sub>f</sub>	skin friction coefficient $C_f = (\text{local wall shear stress}) / q_\infty$
C <sub>D</sub>	drag coefficient, $C_D = \frac{\text{drag}}{q_\infty A_{MAX}}$
C <sub>D</sub> <sup>+</sup>	drag coefficient, $C_D^+ = \frac{\text{drag}}{q_\infty A_{wing}}$
C <sub>DF</sub>	friction drag coefficient, $C_{DF} = \frac{\text{friction drag}}{q_\infty A_{MAX}}$
C <sub>DP</sub>	pressure drag coefficient, $C_{DP} = \frac{\text{pressure drag}}{q_\infty A_{MAX}}$
C <sub>DT</sub>	total drag coefficient, $C_{DT} = \frac{\text{pressure drag} - \text{friction drag}}{q_\infty A_{MAX}}$

$$\text{drag build up} = \frac{1}{A_{MAX}} \int_{X_{START}}^{X_{END}} C_p (\Delta A) dx$$

## Naming convention for body forces



Aftbody	rear fuselage region from start of closure to the beginning of the nozzle
Nozzle	outer surface from end of aftbody to the nozzle exit (excludes nozzle base)
Nozzle base	vertical rearward facing area generated by mismatch in nozzle external and internal dimensions at nozzle exit.
Aftend	aft fuselage region extending from start of closure to nozzle exit = aftbody + nozzle+ base
Afterbody	aft fuselage region including empennage = aftend + tails

## Subscripts used

B	base
A	aftbody
N	nozzle
HT	horizontal tail
VT	vertical tail
T	total(Afterbody) = A + N - HT + VT + B

$C_{DPB}$	base pressure drag coefficient	$p_j$	jet static pressure
$C_{DPT}$	pressure drag coefficient for afterbody $= C_{DPB} + C_{DPA} + C_{DPN} + C_{DPHT} + C_{DPVT}$	$P_{tj}$	jet total pressure
$C_{DTA}$	Total Drag Coefficient (pressure+skin friction) for aftbody $= C_{DPB} + C_{DPA} + C_{DPN}$	$q$	dynamic pressure, for perfect gas $q = \frac{\gamma}{2} p_{\infty} M_{\infty}^2$
$C_p$	pressure coefficient, $C_p = \frac{p - p_{\infty}}{q_{\infty}} = \frac{p - p_{\infty}}{\frac{\gamma}{2} p_{\infty} M_{\infty}^2}$	$q_{\infty}$	free-stream dynamic pressure
$C_v$	velocity coefficient	$r$	radius
$D$	drag	$r_{max}$	maximum radius
$d_{th}$	nozzle throat diameter	$Re$	Reynolds number, $Re = \frac{\rho_{\infty} U_{\infty} L}{\mu}$ where $L$ = body length unless otherwise stated
$d_{max}$	maximum diameter of afterbody	$S/D$	nozzle spacing ratio of distance between nozzle centrelines to the nozzle diameter at junction with afterbody
$Deq$	equivalent diameter	$T$	local temperature (absolute)
$\theta$	Oswald factor, $\theta = \frac{C L^2}{\pi A R_w} \frac{1}{(C_D - C_{D_0})}$	$T_{\infty}$	free-stream static temperature (absolute)
$F$	gross thrust	$T_t$	local total temperature (absolute)
$F_i$	isentropic fully expanded gross thrust	$T_{t\infty}$	free-stream total temperature (absolute)
$F_N$	net thrust ( $F$ or $F_i$ minus free stream inlet momentum)	$T_{tj}$	jet total temperature (absolute)
$F_R$	resultant gross thrust	$u, v, w$	velocity components in x-, y-, z- direction
$h$	2-D nozzle height	$U_{\infty}$	free-stream velocity
$k$	turbulent kinetic energy, $k = \frac{1}{2} (\overline{u'^2} + \overline{v'^2} + \overline{w'^2})$ approximation $\overline{v'^2} = \frac{\overline{u'^2} + \overline{w'^2}}{2}$ is used in the calculation of this quantity	$-\overline{u'w'}$	Reynolds shear stress correlation ( $\tau = -\rho \overline{u'w'}$ )
$K_{L,D,or M}$	empirically derived correlation constants	$w_{dh}$	2-D nozzle width
$L$	length, reference length, model length	$x, y, z$	cartesian coordinates
$M$	Mach number	$x$	streamwise coordinate + $_{ve}$ in flow direction
$M_{\infty}$	free-stream Mach number	$y$	spanwise coordinate
$M_j$	jet exit Mach number	$z$	normal coordinate
$M_{DD}$	drag divergence Mach number	$x_t$	Cartesian coordinate with origin at tail leading edge (measured along local chord)
$NPR$	nozzle pressure ratio, $P_{tj} / p_{\infty}$	$y_t, z_t$	Cartesian coordinate with origin at tail root leading edge
$p$ & $P_{s loc}$	local static pressure	$x_{sep}, z_{sep}$	separation location on boattail surface
$P_{\infty}$ & $P_{s_{\infty}}$	free-stream static pressure	$y+$	non dimensional distance from wall $= \frac{y \rho \sqrt{\tau_w / \rho_l}}{\mu_l}$ where : $y$ normal distance from wall $\tau$ wall shear stress $\rho_l \mu_l$ local density and viscosity
$P_t$	local total pressure, $P_t = p \left( 1 + \frac{\gamma - 1}{\gamma} M^2 \right)^{\frac{\gamma}{\gamma - 1}}$	$\alpha$	angle of attack
$P_{t\infty}$	free stream total pressure	$\beta$	boattail angle

$\delta_v$	nozzle vector angle
$\mu$	dynamic viscosity
$\rho$	density
$\rho_\infty$	free-stream density
$\tau_w$	wall skin friction
$\tau$	thrust vector induced aerodynamic force or moment increments referred to unvectored, jet-on conditions
$\phi$	meridian angle about nozzle/model axis. origin at model top. positive counterclockwise looking upstream
$\phi'$	roll angle of survey rake - 0 deg. when rake is horizontal in +y direction, positive in counterclockwise direction
$\lambda$	leading edge sweep angle else wavelength
$\sigma(u)$	rms of fluctuating velocity component u
$\sigma(w)$	rms of fluctuation velocity component w
$\delta$	boundary layer thickness
$\delta^*$	boundary layer displacement thickness
$\theta$	boundary layer momentum thickness

#### Abbreviations

AIAA	American Institute of Aeronautics and Astronautics
AEDC	Arnold Engineering Development Centre
AEM	Aermacchi SpA
AFWL	Airforce Wright Laboratory
ARA	Aircraft Research Association
AS&M	Analytical Services & Materials Inc.
ASME	American Society of Mechanical Engineers
AVA	Aerodynamische Versuchsanstalt
B-B	Baldwin-Barth
BMVg	Bunderminster der Verteidigung,
BL	Model Butline
B-L	Baldwin-Lomax
CAD	Computer-Aided Design
CFD	Computational Fluid Dynamics
C-D	Convergent-Divergent
CPU	Central Processing Unit
C-S	Cebeci-Smith
DASA	Daimler-Benz Aerospace.
DEI	Dynamic Engineering Incorporated.

DRA	(UK) Defence Research Agency
Fs, Sta	fuselage station measured from model nose
HAI	Hellenic Aerospace Ind.
IMS	Integral Mean Slope
IMS <sub>T</sub>	Integral Mean Slope Truncated
ISL	Institute of Saint Louis
ITU	Intanbul Technical University
J-L	Jones-Lauder
LaRC	Langley Research Center
LDV	Laser Doppler Velocimetry
MDC	Mc Donnell Douglas Corporation
NACA	National Advisory Committee for Aeronautics
NASA	National Aeronautics and Space Administration
N-R	Noris-Reynolds
ONERA	Office National d'Etudes et de Recherches Aérospatiales.
PDA	Partial Differential Equations
R-R	Rolls-Royce
RSTM	Reynolds Stress Transport Model
S-A	Spalding-Allmaras
STOVL	Short-Take-Off and Vertical Landing
STPA	Service Technique Des Programmes Aéronautiques
2-D	two dimensional
3-D	three-dimensional

Units of variables are in SI units m, kg, sec, kPa, K unless otherwise specified.

## 1. INTRODUCTION

### 1.1 BACKGROUND, OBJECTIVES AND SCOPE OF WORK

AGARD's support in furthering the subject of aftbody/nozzle integration and, specifically, the computational and experimental tools used to design and test new installation concepts, has prompted the activities of two earlier working groups who reported their work in 1974 and 1982.

The first of these, AGARD Working Group 04, "Improved Nozzle Testing Techniques in Transonic Flow" (reference 1.5.1), experimented on a series of three reference aftbody boattails in an investigation of the influence of test facilities and model support systems on the resultant data. When boattail pressure distributions were compared alternative model installation techniques applied in a variety of tunnel types were found to produce varying results. Early analytical procedures were then used to help interpretation of the experimental data and found to be valuable only for the restricted case of flow fields where there were no extensive flow separations. Recommendations followed for continued efforts to be directed towards refining the analytical approaches and extend them to flow situations which included strong shock-boundary layer interactions.

AGARD Working Group 08, "Aerodynamics of Aircraft Afterbody" (references 1.5.2, 1.5.3), was formed eight years later with the brief to critically review the State-Of-the-Art (SOA) in computational and experimental tools for afterbody/nozzle aerodynamics, nozzle integration and jet/airframe interference. The assessment that followed included an examination of the applicability and accuracy of the range of inviscid and viscous computational codes then available for afterbody drag prediction. WG 08's earlier interest in experimental techniques was followed-up by an extensive review of new developments, with particular emphasis on the requirements for force measurement accuracy. Attention was also paid to the growing use of afterbody nozzle testing techniques to investigate nozzle external/internal flow instabilities and unsteadiness, boundary layer separation effects and buffeting. The final report (reference 1.5.4) included a substantial section on wind tunnel correction methods and made many recommendations on the future direction of experimental developments and the role of CFD within the vehicle performance definition process. These selections from the concluding remarks of the study report are an indication of the foresight gained through the project.

*"In the ten years since the publication of AGARDograph 208, much progress has been made on both experimental and numerical methods. Because of the tremendous progress which can be expected from the use of Vector-Computers within the next years, the report may be considered to be only a "snapshot" from 'Status 1984.' the present WG08 report should be revised in time, considering especially the progress of computational methods for three-dimensional viscous flow. Experimental techniques have reached a very high level of reliability if proper correction procedures are applied and error analysis is performed as recommended."*

*"It can be definitely stated that numerical analysis will not replace the wind tunnel test, but as an outcome of the*

*Working Group, it may be stated that numerical analysis will play a more and more important role as a supplement to the experiment in the future."*

The WG08 final report, which is further reviewed in section 1.4, thus stood as a good point of departure for a new assessment of the state-of-the-art in exhaust nozzle integration. As we shall see, while many of the areas identified for future work have now been addressed, many are still wanting. Meanwhile, exhaust nozzles and their installations have evolved into even more complex shapes making both the CFD and experimental analysis tasks all the more necessary and difficult.

The third and latest working group was organised by the AGARD Fluid Dynamics Panel in the autumn of 1991. Its main goal, like its predecessor, was to critically review advances made since 1984 on the understanding of complex 3D aircraft afterbodies, and in particular the developments made in computational and experimental techniques available to both understand the flow phenomenon and to design optimum aircraft installations. Specific Working Group aims were to :

- study 3D aspects of aircraft afterbody integration, that is, at angle of attack, and non-axisymmetric afterbodies, and twin jets.
- evaluate present experimental methods and recommend additional techniques as appropriate.
- collect data cases:
  - to understand the flowfield
  - to validate the computational tools
- calculate 3-D afterbody flows :
  - to establish the SOA
  - to recommend needed advancements

In a departure from WG08 practice, the latest group met as a whole, computational, experimental and application specialists together. The differing perspectives of those involved in method development and method application were accommodated by dividing the attentions of the group, like its report, into two parts - the first focused on the fundamental flow phenomena the latter addressing wider application and design centred issues. The developments in CFD and test techniques were reviewed in relation to both.

### 1.2 CONTRIBUTORS

#### 1.2.1 GROUP MEMBERS AND MEETINGS

To complete the assignment, a number of highly qualified specialists were nominated by the national delegates of AGARD. Representing both panel and non-panel members, industry, government agencies, and universities these individuals were:

Jean-Denis Marion	Dassault	France
Jean Delery	ONERA	France
Christian Thery	ONERA	France
Gilles Rollin	SNECMA	France
Remi Jouty	STPA	France
Norbert Bissinger	DASA	Germany
George Sideridis	HAI	Greece
Emanuele Merlo	AERMACCHI	Italy
Veysel Atli	ITU	Turkey
Chris Lee	BAe	United Kingdom
Peter Martin	DRA	United Kingdom

Andy Wood	RR	United Kingdom
Richard Kern	Boeing	United States
Bobby Berrier	NASA	United States
Ray Cosner	McDonnell-Douglas	United States
Doug Bowers	USAF	United States

On formation the group was chaired by Christian Thery assisted by Doug Bowers. After Mr Thery's retirement from the Fluid Dynamics Panel at the end of 1994 Remi Jouty assumed Mr Thery's role.

### 1.2.2 CFD CONTRIBUTORS

CFD contributions were provided by the most of the organisations represented by group members. Other organisations who also contributed solutions, either on their own behalf or in support of others, were :

Rockwell  
Lockheed  
Dynamic Engineering Inc.(DEI)  
Analytical Services & Materials Inc. (AS&M)  
Aircraft Research Association. (ARA)

The individuals within the participating organisations who are acknowledged for their part in the generation of the solutions evaluated by the group are :

#### CFD CONTRIBUTORS

Individual	Organisation	Test Case
John R Carlson	NASA LaRC	A.2.1,A.2.2
William B Compton III	NASA LaRC	B.4.1,B.4.2
William T Jones Khalid S Abdol-Hamid	DEI AS&M	B.1.1, B.1.2, B.2.1, B.2.2, B.2.3, B.3.1, B.3.3
James A Rhodes Philip Wang Paul G Willhite	Mc Donnell Douglas	A.2.1,A.2.2, A.3.1, A.3.2,B1.1, B.1.1, B.1.2, B.2.1, B.3.1, B.3.3 ,B.4.1, B.4.2
Michell Crose Richard Semmes	Lockheed	B.4.1
Skip Gridley Mary K Lockwood	Wright AFWL	B.1.1, B.1.2, B.2.1,B.2.2, B.2.3, B.4.1, B.4.2
John Kingsley	Rolls-Royce Inc.	A.2.1,A.2.2, B.4.1, B.4.2
Amrik S Bahamra	Rolls-Royce plc	A.3.1
Y K Ho Richard Bailey	Rolls-Royce plc	A.3.1
R Behan	Rolls-Royce plc	B.4.1, B.4.2
Frederic Schenher	SNECMA	A.2.1
Gilles Rollin	SNECMA	A.2.2
Piere-Yves Bourquin	SNECMA	B.4.1,B.4.2
Jean-Denis Marion	Dassault	A.2.1, A.2.2, A.2.3, B.4.1,B.4.2
Richard Benay	ONERA	A.2.1, A.2.2
Xavier Bousquet	Aerospatiale	A.2.1, A.2.2

Livio Visintini Srefaus Sibilla Georgio Travostino	Aermacchi	B.1.1, B.1.2 B.2.1, B.2.2, B.2.3
Emauele Merlo <sup>1</sup>	Aermacchi	B.1.1, B.1.2, B.2.1, B.2.2, B.2.3, B.3.1, B.3.2, B.3.3,
Mark Pocock Andrew Peace	ARA	B4.1,B4.2

Five meetings were arranged to co-ordinate the work of the group :

1-2 October 1992, Banff, Alberta, Canada to:

- organise, review, clarify objectives
- summarise results of WG-08
- review SOA in participating countries
- establish experimental test cases
- structure final report

15-16 April 1993, Winchester, UK to:

- assess availability/distribution of test cases
- establish data format
- review/approve nomenclature
- assign responsibility for final report sections
- develop schedule for remainder of effort

11-12 October 1993, Paris, France to:

- status of test case computations
- review/status of final report sections
- update schedule for remainder of efforts

14-15 April 1994, Crete, Greece to:

- review all CFD contributions
- review 1st draft of final report

10-11 October 1994, Berlin, Germany to:

- agree recommendations/ conclusions
- review/approve final report

### 1.3 REPORT ORGANISATION

In reviewing progress since WG 08 the group consensus at the outset was that the most significant developments since 1986 had been in the increased capability and widespread application of computational methods. In support of this it was claimed that Navier Stokes codes, as now used in industry, had reached the standard where they could be applied, almost routinely, to complex 3-D aftbody geometries establishing trends and substantially aiding the design optimisation process. Furthermore, such codes and the computational machines to run them on were developing so fast that the point was near where usable predictions of absolute performance would also be possible.

On the basis that the greatest scope for effecting future changes in the vehicle design process lay in this direction and less-so on improvements in experimental techniques, which by comparison are more mature, it was accepted that WG17 would concentrate its efforts on gauging the capabilities of the current generation of computational tools. Recognising the nonetheless undiminished importance of the experimental process, both for the acquisition of data to support further improvement in the computational techniques and as the

<sup>1</sup> Responsible for application of a semi-empirical method

current ultimate arbitrator within the design definition process, 'State of the art' SOA test techniques updates covering both roles would also be performed. These are to be found in report sub-sections 2.2 and 3.3, respectively.

As previously stated the activities of the group were divided into two parts :- the first concentrating on the understanding and numerical simulation of the detailed flow physics, termed "the fundamental flow phenomena" and the second addressing the wider practicalities of applying such simulations to the highly complex real geometries typical of advanced fighter aircraft and, moreover, doing so within real-world cost, time scale and human resource constraints, termed the "design" or "engineering" aspects.

The report has been arranged accordingly into two sections which are introduced below.

### 1.3.1 FUNDAMENTAL FLOW PHENOMENA

This section concentrates on the fundamental understanding of the flow phenomena that occur within the complex flow fields that surround the afterbody/nozzle installations of modern military fighter aircraft. The initial discussions within sub-sections 2.1 and 2.3 concern the description of the micro-physics involved and the experimental techniques available to measure the pertinent dynamic flow quantities. Subsequent sub-sections discuss the issues involved in the quest to computationally simulate these phenomena and then go on to review the CFD methods employed.

There then follows an account of efforts to apply existing computational tools to the simulation of the detailed flow field measured around one test cases from a selection introduced in section 2.5. Known as "Group A" these test cases were picked-out for the quality and detail of the available flowfield measurements but, as a consequence of difficulty of obtaining such data are restricted to comparatively simple geometries. Computational results obtained for test case A.2, a single isolated axisymmetric body with cold and hot jet exhaust, are reported and discussed in section 2.6. The experimental data for the remaining test cases, for which no computations were submitted, are provided in Appendix A. These include an un-blown axisymmetric body at angle-of-attack (A1) and a closely spaced axisymmetric twin jet installation without empennage (A.3).

Recommendations for future experimental and computational work arising from the evaluation of test case A.2 are recorded within sub-section 2.7

### 1.3.2 DESIGN

Beyond an understanding of the fundamental processes and the means to reproduce basic flowfield phenomena on simple geometries, the aircraft designer must have at his or her disposal practical tools that can instruct on changes in the important measures of drag, thrust and steady or unsteady structural loads that result from the myriad of complex flow interactions generated around three-dimensional afterbody geometries of the highest complexity. Moreover, these tools must be robust, reliable and capable of being applied in reasonable time and cost. Whilst progress on the computational algorithms and the machines available to run them is rapid, it is increasingly appreciated that it will be a long time, if ever, before CFD can, meet these demands

alone.

In the meantime the inventory of tools that must be maintained to support the design process remains wide. The second half of this report begins with an overview of the wider practicalities of the design process. This is then followed by a review of semi-empirical drag prediction methods and a "State of The Art" update on developments in supporting experimental techniques.

Sub-section 3.4 then introduces a second set of test cases, "Group B", chosen this time to more closely represent the true complexity of modern military fighter nozzle/afterbody installations. Included are single and twin axisymmetric nozzle aftbodies tested with and without tails (B1 B2 and B3), a twin-jet configuration (B3) and a two-dimensional nozzle installation (B4). All cases feature blown jet simulation. Other variables represented are nozzle pressure ratio, tail position and Mach number.

Results from the application of a range of CFD methods and where possible one empirical technique to these test cases are presented and discussed in section 3.5. Recommendations for future work which stem from the evaluations are presented in section 3.6

Recommendation and conclusions formed from both the "fundamental" and "design" focused group activities are brought together in section 4

Finally, following the example of WG 08, appendices A and B supply the experimental data for all test cases assembled by the group. The purpose is to make this information available to others involved in this field for assessing current or future CFD developments against the benchmarks established by this review. Appendix C is used to collect together statistics and observations collected from the organisations who contributed predictions for both sets of test cases.

## 1.4 REVIEW OF WG-08 (1986)

In 1982, the Fluid Dynamics Panel of AGARD formed a working group to critically review recent activities on afterbody/nozzle aerodynamics, nozzle integration, and jet/airframe interference effects. The working group was to address both theoretical and experimental developments.

In its assessment of theoretical capabilities, the working group was to (1) review the status of inviscid flow methods; (2) assess the status of inviscid/viscous interaction methods for predicting the flow over nozzle afterbodies with jet exhaust; (3) assess the status of Navier-Stokes solutions of such flows; and (4) evaluate the critical range and accuracy of the available methods with respect to afterbody drag prediction. The working group chose to limit its assessment to axisymmetric nozzle configurations at zero angle-of-attack with jet exhaust flow. Thirteen test cases were identified. The prime criteria for selection was the availability of extensive experimental measurements of surface pressure and flow field characteristics. Eight of the test cases were typical aeroplane-type nozzle configurations and the remaining five were typical missile afterbody configurations. In all cases, the jet exhaust was simulated with high-pressure air. Cases were selected to show the effects of nozzle geometry, nozzle pressure ratio, freestream Mach number, jet exhaust temperature, and tunnel blockage.

The WG 08 test cases used for the CFD comparisons were limited to axisymmetric configurations at zero degrees angle-of-attack. The thirteen test cases included external pressure distributions, and some boundary layer and flowfield measurements. Eighteen contributors submitted solutions to one or more test cases. At that time, the solutions consisted of a few full Navier-Stokes methods, many mixed or patched methods with inviscid solvers and a viscous displacement, and a few Euler solvers. The problem of turbulence models for Navier-Stokes solvers and artificial viscosity in the numerical scheme of Euler solvers was identified. For subsonic cases, some of the coupled inviscid-plus boundary layer approaches predicted the surface pressure distributions, the boundary layer separation point and the drag coefficients very well. The Navier Stokes solutions were found in good agreement with the experimental surface pressure distributions up to the point of flow separation. Quoting the final report.

*"Today's Navier Stokes calculations generally cost 5 to 20 times as much as an inviscid/viscous interaction calculation on the same super computer. The rapid increases in hardware technology and improvements in numerical techniques may soon make Navier Stokes codes inexpensive enough for production calculations."*

The conclusions and recommendations of the CFD subgroup were as follows:

- "Computational research should improve two-dimensional modelling of the separation region for inviscid/viscous interaction methods."
- "Navier Stokes code development should continue with concentration on grid generation, solution algorithms, turbulence modelling and user friendliness."
- "Detailed studies of the effect of turbulence modelling should be undertaken".
- "Three-D methods should be developed."
- "Zonal approaches plus full 3-D Navier Stokes solutions should be pursued."
- "Careful 'test case' experiments should be undertaken to provide flow field details for the development of turbulence models".
- "Results indicate the potential of Navier Stokes analysis to predict many features of the flow correctly"
- "The rapid growth and improvements of computers and in theoretical methods should in the future provide significantly better methods for predicting the effects of engine installations on the aeroplane aerodynamics."

Please note that the WG included this comment in their report:

*"Because of the rapid changes occurring in the computational fluid dynamics, the assessment conducted by the working group provides only a 'snapshot' of the capabilities of theoretical methods at about the middle of 1984. The rapid growth and improvements of computers and in theoretical procedures should, in the future, provide significantly better methods for predicting the effects of engine installation on aeroplane and missile aerodynamics."*

The experimental techniques subcommittee reviewed and evaluated experimental testing procedures and investigations to improve these procedures. The group concentrated on jet simulation, wind tunnel testing techniques, afterbody nozzle flow instability, and sources of error in wind tunnel and flight measurements. These elements were further broken down into hot versus cold exhaust gas simulation, turbine and ejector powered simulators, and annular blowing stings. Force balances, surface pressures and integration, wind tunnel model support systems, testing uncertainties, and recommended testing practices were also considered. Specific flight examples of afterbody/nozzle flow instabilities, their impact on aircraft performance, and the resolution of the problem were discussed as were errors in measurement of forces and pressures, and the influence of blockage and wall effects on these errors.

The conclusions as a result of this study were as follows:-

- *"The choice of wind tunnel testing techniques for aircraft aftbodies must include consideration of many factors with the test objective, available facilities and model hardware the most important."*
- *"Force balances must be used with great care to minimise and account for all tares and corrections, and an assessment should be made of the predicted levels of accuracy and repeatability versus levels required to meet the test objectives."*
- *"Wind tunnel model support must be chosen with great care"*
- *"The key to utilisation of both computations and experiments is understanding the flow physics involved in the aftbody area."*
- *"Special advanced and more complex testing techniques should be emphasised for future development."*

And finally :

- *"Experiment techniques have reached a very high level of reliability if proper corrections are applied and error analysis is performed as recommended."*

The complete WG 08 report is reference 1.5.4.

## 1.5 REFERENCES

- 1.5.1 Ferri, A., "Improved Nozzle Testing Techniques in Transonic Flow," AG-208, Oct. 1975.
- 1.5.2 Bowers, D., Laughrey, J. "A Summary of an AGARD Assessment of Testing Techniques for Aircraft Afterbody Flows," AIAA 85-1465, Jul 1985.
- 1.5.3 Putnam, L., "Results of AGARD Assessment of Prediction Capabilities for Nozzle Afterbody Flows," AIAA 85-1462, Jul 1985.
- 1.5.4 Sacher, P., "Aerodynamics of Aircraft Afterbody," AR-226, Jun. 1986.



## **1.6 ACKNOWLEDGEMENTS**

The chairman of this Working Group is pleased to acknowledge the support of the agencies involved and of the management of different institutions which have allowed their members to participate in this activity.

We also thank the host countries for the local arrangements and meeting and organisation.

Finally, we express our thanks to our panel executives, Dr. Winston Goodrich and Jack Molloy, and the FDP secretary Ms. Anne Marie Rivault for their help and patience as we accomplished our tasks.

## 2. FUNDAMENTAL FLOW PHENOMENA

### 2.1. Fundamental Flow Phenomena Related to 3D Afterbodies

#### 2.1.1. Description of the flow fundamentals:

A good understanding of the flow physics involved at the back end of a fighter aircraft is necessary to develop suitable computational models and to provide a proper interpretation of both computational and experimental results. New afterbody geometries are being developed, in response to new requirements such as thrust vectoring, stealthiness and acoustics. This may increase the need of a better understanding and modelling of some flow features such as : mixing shear layers, vortical flows...

A description of some of the most important flow phenomena occurring on typical aircraft afterbodies is presented in this section. The qualitative effect of some flow parameters is briefly discussed.

The following figure provides a schematic description of the complex physics of the flowfield surrounding an axisymmetric subsonic or transonic single flux nozzle :

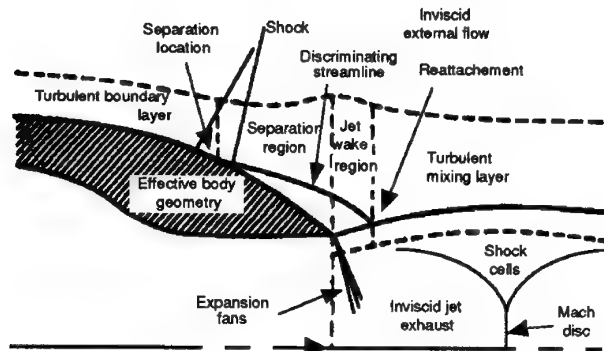


Fig. 2.1-1

This relatively simple geometry exhibits already many complex flow features :

- expansion/shocks
- turbulent boundary layer separation
- recirculation
- mixing layers
- shock/mixing layer interaction
- shock/boundary layer interaction

The prediction of the performance of this afterbody relies crucially on a correct prediction of the external boundary layer separation on the boat-tail and its associated recirculation region.

This separation is induced by the adverse pressure gradient created by the boat-tail and the jet plume. The extent of the separation region is dependent on the boat-tail and jet plume geometry (seen as a solid body) -displacement effect-, and on the entrainment of the outer flow by the jet flow -entrainment effect-.

In the case the nozzle is not adapted, expansion fans and shocks can be observed. The boundary layer may be separated either inside the nozzle (over-expanded jet) or

outside on the fuselage (under-expanded jet). The external and internal boundary layers join in the confluence region, forming a mixing layer with vortical structures surrounding a separated recirculation region. From a design point of view this separated region where the dynamic pressure is weak increases the drag and can lower the control surface efficiency.

In addition to that, important thermal phenomena take place around afterbodies. Actually confluent flows not only have different velocities, Mach numbers and temperatures but also different chemical composition. So a lot of transfer processes exist like dynamic and energetic transfers and diffusion with high turbulence rate.

All these phenomena are observed experimentally (Ph. Reijasse and J. Delery [2.1-1]), and numerically (S. M. Dash and D. E. Wolf [2.1-2]).

Thus it is also necessary to predict accurately the jet expansion, and its boundary with the outer flow (*free shear layer*) in order to achieve a good prediction of the separated recirculation region and the associated pressure distribution.

#### 2.1.1.1 Boundary layer separation

Simpson [2.1-3] made a review of many different flow cases with two dimensional separation. The intermittent behaviour of separation (induced by adverse pressure gradient) and reattachment is described. This unsteadiness can be linked to the passage of large scale turbulent structures in the boundary layer.

Experimental data show that the velocity fluctuations in the recirculation region can be comparable to the maximum mean back flow velocities.

In our case of an afterbody with jet, the intermittent behaviour of the separation may be expected to interact with the jet and mixing layer. This should be taken into account for the prediction of acoustic effects (see screech phenomenon described below).

In the transonic flight regime, the flow often accelerates to supersonic speeds before the nozzle, and part of the subsequent recompression occurs through a shock wave. Different kinds of shock wave / boundary layer interactions can exist (Delery [2.1-4]) :

In the case no separation occurs, two different configurations can exist :

- if the shock wave is weak, it penetrates deeply inside the boundary layer
- when the shock wave is stronger, compression waves form inside the boundary layer, originating from a region close to the wall and converging to a point from which a quasi-normal shock seems to emanate.

The rise in pressure produced by the shock propagates upstream through the subsonic part of the boundary layer. The subsequent deceleration entails a thickening in this subsonic layer.

On the other side, a transonic interaction strong enough to cause a sizeable separation (when the Mach number immediately upstream of the shock exceeds 1.3) is

characterized by the existence in the outer flow of a lambda shock pattern (there are no compression waves). It is very important to take into consideration this interaction phenomena since it influences the boundary layer characteristics downstream and thus may introduce changes in the whole flow picture.

#### 2.1.1.2 Effect of wall temperature on boundary layer separation

One important characteristic of the problem of predicting afterbody flows, lies in the fact that the surface temperatures in these areas are high due to the proximity of hot gases from the nozzle (Cousteix [2.1-5]). So it is necessary to determine the importance of the fluid-heated wall interaction on the formation and extension of separated areas around an afterbody.

Delery [2.1-6] and Benay [2.1-7] have investigated a shock/boundary layer interaction on a heated flat plate. The experimental results show that, although the turbulent boundary layer mean and fluctuating velocity profiles ahead of the interaction region are not affected by the temperature except in the immediate vicinity of the surface, the wall heating strongly influences the shock-boundary layer interaction, by causing a strong dilatation of the interaction area especially in the presence of separation. However, the limit for shock induced separation did not seem affected by wall heating.

#### 2.1.1.3 Effect of jet temperature

The effect of jet temperature on the afterbody flow (assuming the geometry and NPR are kept constant) is twofold :

##### 1 - Inviscid flow - displacement effect :

For typical aircraft jet temperature, that can reach 1000°K in dry conditions and 1700°K during afterburning at the nozzle exit, the specific heat ratio  $\gamma$  usually can not be assumed to be constant and equal to 1,4 ( $\gamma \# 1,35-1,25$ ). This may influence the jet structure (plume expansion angle, shock cells, etc...), especially at high NPR.

##### 2 - Viscous flow - entrainment effect :

Increasing the jet temperature increases the jet velocity (for the same Mach number) and thus increases the shear stresses and the entrainment effect. This may be significant in case of incipient separation.

The structure of the turbulence in the mixing layer may also be affected by the temperature.

In addition to that, an increase in the jet temperature induces an increase of the temperature of the nozzle's external surfaces and of the interaction domain (see § above on wall temperature).

A numerical study of the effect of jet temperature on the afterbody flow can be found in reference [2.1-8].

#### 2.1.1.4 Jet structure

It is necessary to accurately predict the initial plume shape, since this shape will influence the pressure distribution on the boat tail and, consequently, all the viscous effects on the afterbody flow (and particularly the boundary layer separation and the extent of the recirculation region).

Under-expanded supersonic jets have a shock cell structure formed by oblique shocks and expansion fans generated at the nozzle lip region where there is a mismatch of the static pressure inside and outside the jet.

These shock cells are quasi-periodic because when the oblique shocks and expansion fans impinge on the jet boundary, they are reflected into the jet ; they are trapped inside the plume bouncing from one side to the other forming a standing wave pattern. Embedded zones of subsonic flow can occur behind Mach disks, while a significant portion of the plume mixing layer will be subsonic for jets exhausting into subsonic external stream.

A transitional region joins the predominantly inviscid near field with the fully viscous, pressure-equilibrated far field. Here, the mixing layers come to engulf the entire jet and shock cells formation occurs in a strongly turbulent environment. In this region, wave fronts are curved by the flow rotationality and wave intensity are diminished by turbulent dissipative effects. In the jet far field, wave processes have been totally dissipated and constant pressure mixing prevails.

Since the working group decided to concentrate their efforts on afterbody performance prediction and not on plume characteristics, we will not discuss here the transitional region and far field of the jet.

#### 2.1.1.5 Waves / shear layers interactions

There are interactive phenomena between the wave structures of a supersonic jet and the shear layers : expansion fans and shock waves are reflected by the shear layers, and the mean flow and turbulent variables in the shear layer are altered by the waves.

Dash and al. [2.1-9] have studied numerically the interactions existing between an under-expanded jet and the external stream, and their dependence on Mach numbers of both flows. They found for example that in a supersonic jet/supersonic stream mixing region interactive effects are fairly weak in the first cell, and thus that the inviscid solution is close to the viscous flow. These interactive effects then increase as the width of the mixing region becomes substantial. They also studied the interaction between a supersonic jet and a subsonic stream and successfully compared their analysis results with experimental results of Seiner and al. [2.1-10].

### 2.1.1.6 Compressibility effect on shear layer expansion

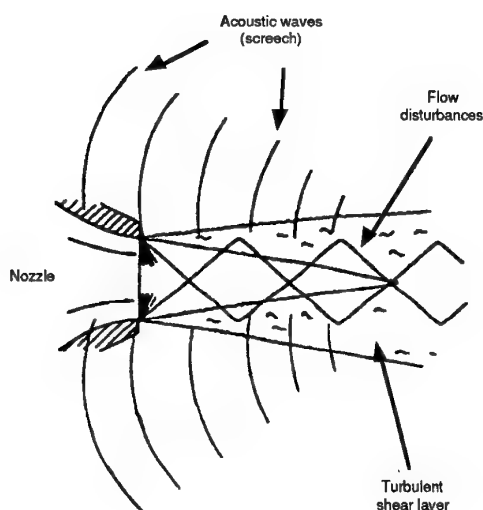
It has been shown that a turbulent mixing layer can be affected by compressibility (Bogdanoff [2.1-11], Samimy and Elliot [2.1-12], Papamoschou and Roshko, [2.1-13]). The *convective Mach number*  $Mc$ , a Mach number based on a frame of reference travelling with the large scale structures in the mixing layers, seems to be the most significant parameter. A simplified definition of  $Mc$ , valid when  $\gamma$  is the same on both sides of the mixing layer, is :

$$Mc = \frac{V_1 - V_2}{a_1 + a_2}$$

where  $V_1$  and  $V_2$  are the mean flow velocities on both sides of the mixing layer, and  $a_1$  and  $a_2$  the respective sound velocities.

Compressibility effects appear for  $Mc$  greater than about 0.6, and thus may be encountered on real aircraft applications. Experimental results on plane mixing layers show that, as  $Mc$  is increased, the mixing layer growth rate, the spatial correlation levels, the Reynolds stress and the extent of the turbulent mixing region are drastically reduced, and the turbulent structures become spanwise-oblique. Recent experimental results [2.1-14] show an asymmetry between the subsonic and supersonic side of the mixing layer.

### 2.1.1.7 Aeroacoustic - screech :



*Powell's screech feedback mechanism*

Fig. 2.1-2

Sonic fatigue on nozzle flaps (for example on F-15 and B-1 aircraft) has been observed on many occasions and has motivated increased research in aeroacoustics (cf. Walker S.H. [2.1-15]). This fatigue is due to acoustic wave instabilities originating in the supersonic plume; as a matter of fact, the shock wave structure inside the exhaust jet generate narrowband and broadband shock-associated noise (Davis [2.1-16]). Powell [2.1-17] investigated this noise and isolated tones of discrete frequencies referred to as *screech tones*. According to him some flow disturbances initiated at the nozzle lip region propagate downstream, in the shear layer, and strongly interact with the shock cells. As it can be seen on fig 2.1-2, acoustic waves (called screech) are thus created and a part of them propagate upstream in the subsonic region outside the jet flow. Then these waves reach the nozzle lip and generate downstream propagating flow disturbances that close a cycle or *feedback-loop*.

Under certain conditions in underexpanded jet flow, the concomitant sound production accelerates the spreading of the jet and enhances mixing (Krothapalli and al.[2.1-18]). A list of references on the sound field of an underexpanded jet can be found in a paper by Yu and Seiner [2.1-19].

### 2.1.2. Complex geometries and 3D phenomena

After these general considerations on phenomena that may occur around a 2D or 3D afterbodies we have to look at some specific flow field features around complex three-dimensional configurations.

We should, first of all, remember that the flow arriving on the afterbody has been affected by the full length of the fuselage. This implies that it usually can not be assumed to be axisymmetric even for a single engine configuration, and that the boundary layers are very thick and strongly three-dimensionnal. Obstacles like antennas and lifting surfaces leave the marks of low total pressure areas, and longitudinal vortices.

In addition to that, the nozzles we have to deal with in real aircraft applications have complex and various geometries :

Convergent-divergent axisymmetric exhaust nozzles may present considerable loss of thrust if they operate in over-expansion (Carrière P. [2.1-20]). Thus different nozzle shapes like *double-flux nozzles* or *blow-in doors* have been studied in order to avoid this drawback.

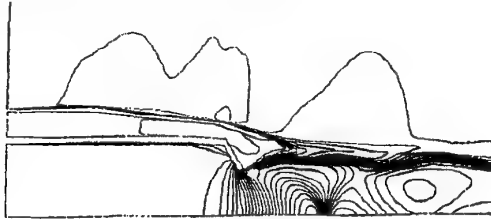
Increasing interest in V/STOL or highly maneuverable aircraft has caused a great deal of attention to be focused on jet flows exiting from *rectangular vectoring nozzles*. The mixing characteristics of an underexpanded jet coming from a converging rectangular nozzle is of great interest, and has been studied by Krothapalli and al.[2.1-18]. Specific aircraft like tactical military aircraft designed for high performance in all mission segments may require integration of highly three-dimensional advanced exhaust

nozzles, featuring *thrust vectoring* (TV) and/or *thrust reversing* (TR) capabilities.

In addition to that, while considering problems of weight and bulk, it is interesting to examine *unsymmetrical* nozzles (shorter walls on the lower surface) for hypersonic applications.

### 2.1.2.1 Double-flux nozzles

The flow complexity is increased in the case of the *double flux ventilated nozzle* below :



Double-flux nozzle

Fig.2.1-3

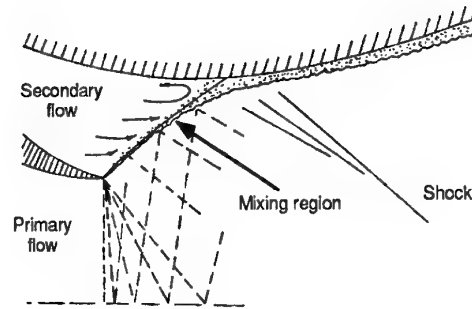
All the flow features discussed above are present on this configuration. The increased complexity comes from the interactions of the primary, secondary, and external flows. Problems of confluence and mixing may then appear in the divergent part of the nozzle. Iso-Mach number lines from a calculation made at the SNECMA company are represented to help to visualize the flow behaviour. The stagnation pressure of the secondary flow is here a critical parameter as it affects the primary flow expansion -and the nozzle thrust efficiency-, and the base drag. The base pressure is dependent on the secondary mass flow and NPR.

Here again, an accurate modeling of the entrainment effect of the mixing layer between the primary and secondary flows is necessary to predict the whole flow field.

Two main flow regimes may be encountered :

#### 1 - Low secondary mass flow :

The secondary flow is weak enough so that its velocity can be neglected except in the region where it mixes with the primary flow. A reattachment of this primary flow on the secondary divergent wall can be observed and induce a shock. Along the primary jet frontier, and separating the jet from a "dead water" region, a mixing region is developing, where diffusion and energetic exchanges exist. A certain amount of secondary airflow is extracted by an *entrainment* process.

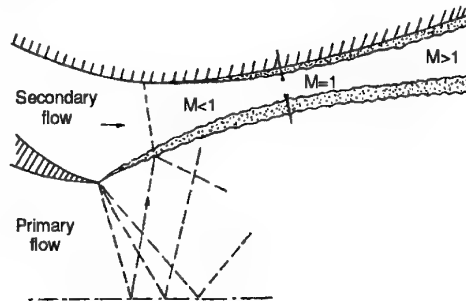


Weak secondary flow

Fig. 2.1-4

#### 2 - Higher secondary mass flow

In that case the velocity of the secondary flow being more important, the entrainment process can be neglected, as a first approximation, and the two flows keep their individuality on each side of the fluid frontier. Along this frontier a non-isobaric mixing region is developing. Then the following phenomenon appears : the secondary flow is accelerated in the convergent formed by the secondary flow and the fluid frontier, and under certain conditions may become sonic and even supersonic (as in the supersonic transport aircraft Concorde).

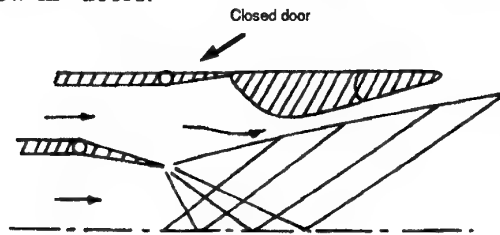


Strong secondary flow

Fig. 2.1-5

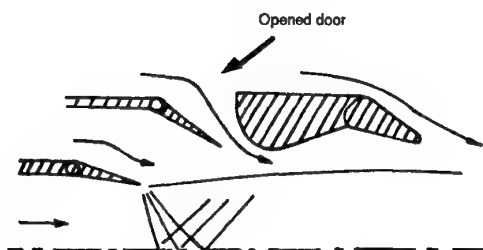
It is also interesting to note that the secondary air jet generally decreases the noise waves, with the greatest noise reduction occurring for the highest secondary air jet pressure.

In order to improve the performance of a convergent-divergent exhaust nozzle by avoiding the overexpansion in the divergent part, another solution may be chosen : the **blow-in doors**.



Cruising conditions

Fig. 2.1-6



Low speed conditions

Fig. 2.1-7

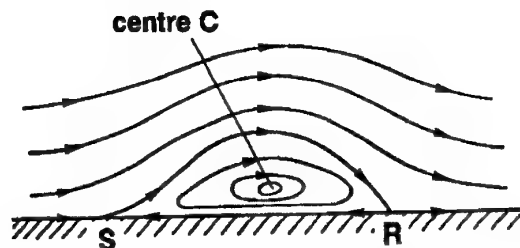
This ventilation system shown on the figures above consists in articulated doors opening on the external stream, and placed around the nozzle throat. The interactions of primary, secondary and external flows are then very complex since four different flows and several mixing regions are at stake.

#### 2.1.2.2 Two-dimensional versus three-dimensional separation and vortical flows

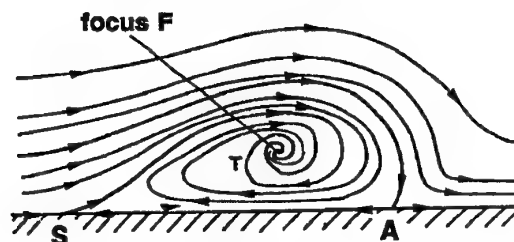
The considerations which follow are applied to *steady flows*, which means that the flow in the boundary layers, mixing zones and wakes being turbulent, we consider a mean flow according to Reynolds or Favre averaging. This is a strong simplification, since real flows are fluctuating, especially when separation occurs. However, this description is consistent with flow modelling based on the time averaged Navier-Stokes equations. Furthermore, it corresponds to measurements performed by classical devices which always perform an averaging of the flow quantities.

In *two-dimensional flows*, it is usual to consider that separation occurs when the skin friction  $\tau_w$  goes to zero at a separation point S. Downstream of this point, a

region exists where  $\tau_w$  is negative. Thus, the velocity distribution along a normal to the body surface includes, near the wall, a portion where the longitudinal component is opposite to the main flow direction. The flow frequently reattaches at some distance downstream of S at a point R, where the skin friction passes through zero to become positive again. As shown in Fig. 2.1-8, the only way the flow can be organized is a recirculation bubble, often called a vortex. Further features are that the boundary layer thickness grows rapidly at and downstream of the separation point and that the interaction between the viscous and inviscid flow becomes large (there is a change from a weak interaction to a strong interaction process).



a - Two-dimensional flow



b - Three-dimensional flow

Simple conceptions of separation

Fig. 2.1-8

In *three-dimensional flows*, separation entails the formation of vortical structures, or vortices, formed by the rolling up of the viscous flow "sheet", previously confined in a thin layer attached to the wall, which suddenly springs into the outer non dissipative flow (Délery [2.1-21], Van den Berg [2.1-22]).

In three-dimensional flows, the definition of separation as the zero-crossing of the skin friction (now, the skin friction acts as a vector) is inadequate and two-dimensional concepts are no longer appropriate to describe separated three-dimensional flows. A rational definition of three-dimensional separation can be made by resorting to the *Critical Point Theory* of Poincaré [2.1-23], applied to fluid mechanics problems by Legendre [2.1-24]. Here, we will restrict ourselves to a rapid presentation of this theory which provides a very

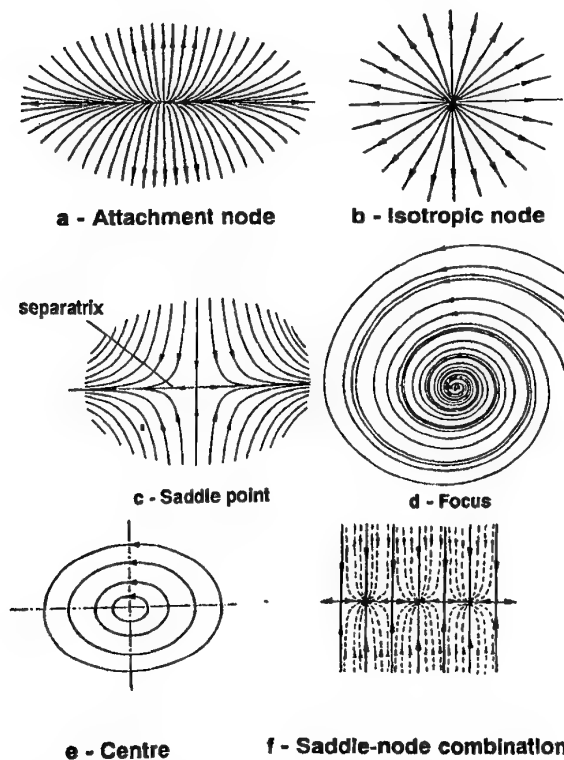
powerful tool to interpret the structure of three-dimensional separated flows.

The most important concepts are introduced by considering the vector field made of the skin friction vectors on the body. In general, it is possible to determine the lines of force of this vector field, the *skin friction lines*, except at point (most often isolated) where the skin friction vector vanishes. Such points are called *critical points*. The behaviour of the skin friction line pattern in the vicinity of a critical point is studied by performing a Taylor series expansion of the skin friction vector components of the form:

$$\tau_{wx} = a_{xx} \cdot x + a_{xy} \cdot y$$

$$\tau_{wy} = a_{yx} \cdot x + a_{yy} \cdot y$$

where  $x$  and  $y$  designate coordinates on the body (for sake of simplicity, metric coefficients are omitted, which does not change the conclusions),  $\tau_{wx}$  and  $\tau_{wy}$  being the corresponding skin friction vector components.



Skin friction line pattern in the vicinity of the critical points

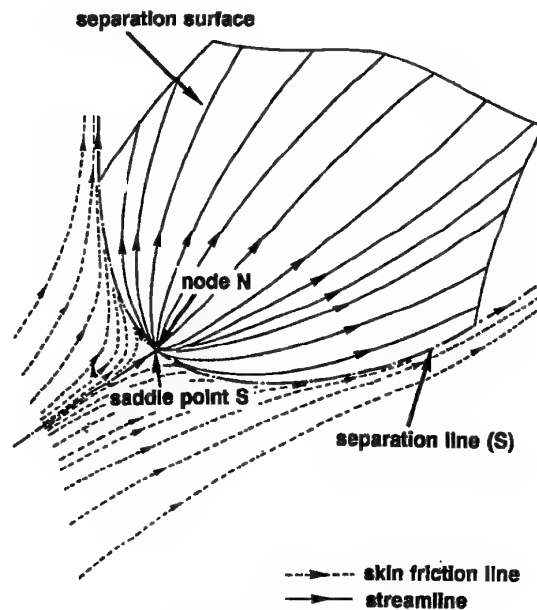
Fig. 2.1-9

Depending of the sign and magnitude of the coefficients  $a_{xx}$ ,  $a_{xy}$ ,  $a_{yx}$ ,  $a_{yy}$ , different types of critical points are

obtained: *nodal points* (nodes and foci) and *saddle points*. The behaviour of the skin friction lines in the vicinity of these critical points are illustrated in Fig. 2.1-9. In some circumstances, a node can degenerate into an isotropic node (see Fig. 2.1-9.b) and a focus into a centre as shown in Fig. 2.1-9.e (case of the two-dimensional vortex, see above). A focus is associated with a vortex springing out from the surface. A special situation corresponding to a succession of saddle points and nodes, infinitely close to each other, is sketched in Fig. 2.1-9.f.

Thus, the skin friction is everywhere non zero in three-dimensional flows, except at isolated critical points. As a matter of fact, in such flows, there are no privileged directions along which the sign of the skin friction has a well defined physical meaning. Furthermore, contrary to a two-dimensional flow in which the motion is confined within a plane, a three-dimensional flow has the capability to develop transverse components, allowing the fluid to escape laterally. This capability gives three-dimensional separated flows their essential features.

The above analysis, generalized to three dimensions, can be extended to the outer flow velocity field, since it applies to any vector field. Then, skin friction lines are streamlines. Thus, critical points, and their associated patterns, can also be found in the flow field.

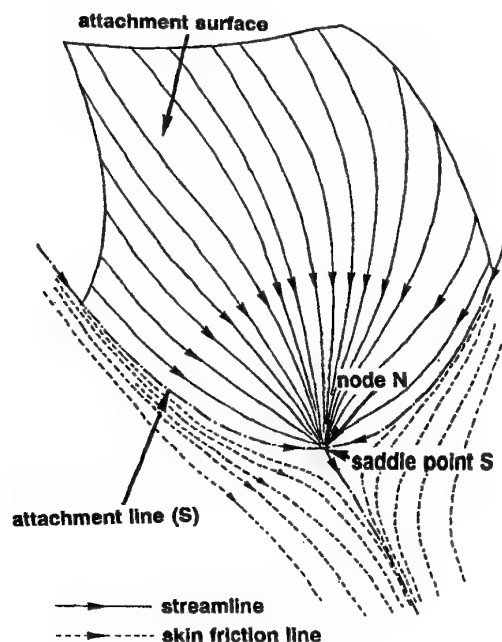


Flow structure during a separation process

Fig. 2.1-10

Through a saddle point pass two special skin friction lines (or streamlines) which are called *separatrices*, in the sense that they separate the above lines into well distinct families. Depending of the skin friction line behaviour on

approaching the saddle point and the associated separatrices, the physical situation corresponds either to effective separation, or to attachment. The flow organization during a separation process is shown in Fig. 2.1-10. Then, the skin friction lines are flowing towards the saddle point  $S$  and are diverted, on approaching  $S$ , into two families streaming along the *separation line* ( $S$ ) going through  $S$ . The line ( $S$ ) sustains a *separation surface* which is constituted of the streamlines emanating from the node  $N$  (in fact a half-node) coincident with  $S$  on the body. The attachment process is sketched in Fig. 2.1-11.

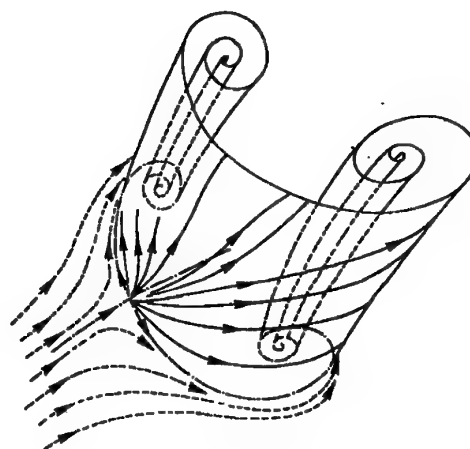


*Flow structure during an attachment process*

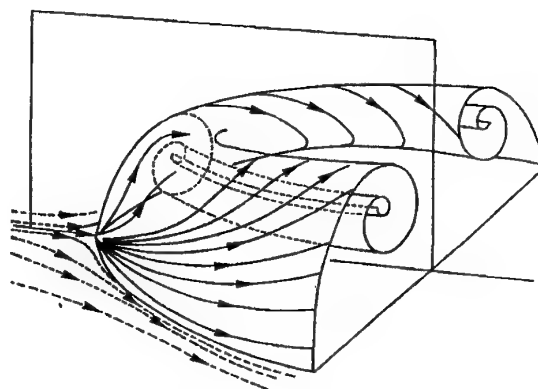
Fig. 2.1-11

One also finds the saddle point and the associated separatrices, but now the skin friction lines stream away from  $S$  and move off the separatrix ( $S$ ) which is an *attachment line*. In a similar way, ( $S$ ) sustains an *attachment surface* made of streamlines ending at the attachment node  $N$  coincident with  $S$ .

In most situations, the separation line ( $S$ ) ends at a focus around which it spirals. This focus is the trace on the body of the vortical structure ("vortex") which results from the rolling up of the separation surface. Such a situation with two foci is depicted in Fig. 2.1-12.a. This type of structure is called a *tornado like vortex*. The focus sustaining the vortex can also be in a plane of symmetry, leading to the formation of a *horseshoe vortex*, as the one forming in front of a blunt obstacle (see Fig. 2.1-12.b).



**a - Tornado-like vortex**



**b - Horseshoe vortex**

*Vortex formation*

Fig. 2.1-12

Such a topological analysis is usual to help achieving a good understanding of three-dimensional separated flows. It is clear that the Critical Point Theory can be applied to viscous as well as to inviscid flows (in fact, it deals only with a vector field). The concept of vortex sheet pertains to perfect fluid model of the separated flow where it is defined as a surface bearing velocity tangential discontinuities, represented by a concentrated distribution of vorticity. Such a sheet has no physical existence and has not to be confused with the separation surface. If the flow effective vorticity is initially confined within thin boundary layers then, during the separation process, this vorticity tends to migrate in regions of small thickness close to the separation surface. In this case, there is a fair similarity between the vortex sheet model and reality. However, in the case of aircraft afterbodies, the incoming boundary layers are usually very thick and it might be



difficult to define without ambiguity such vortex sheets in a separated three-dimensional afterbody flow.

#### *Application to the description of some typical afterbody flows*

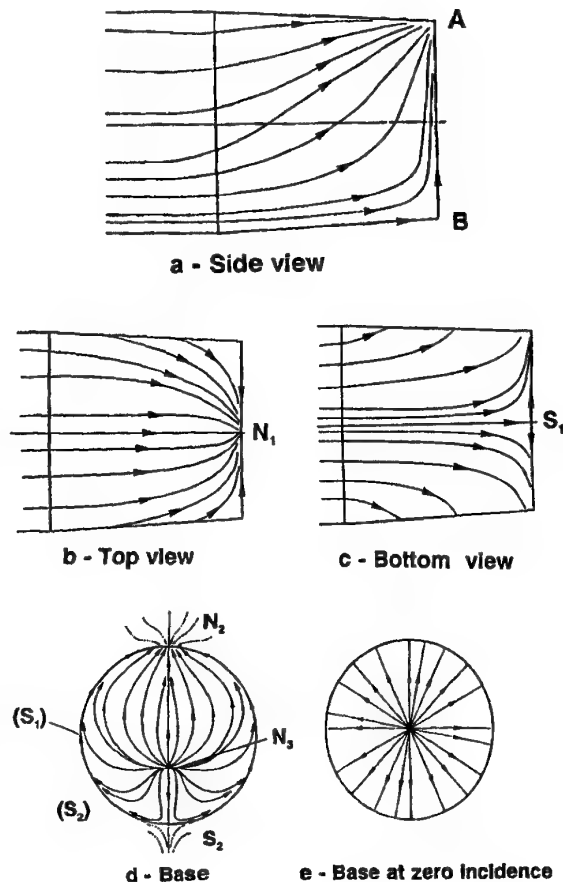
In the discussion which follows, the topology - or more simply the organization - of the flow will be commented by considering an assembling of the skin friction line pattern on the afterbody, the streamlines in planes of symmetry (most of the flow analyzed have only one plane of symmetry) and on the surface constituting the boundary of the jet, if any. The picture will be completed by the drawing of some streamsurfaces playing a special role in the flow field (namely, separation and attachment surfaces). This assembling is necessary to arrive at a consistent representation of the three-dimensional field. It is clear that the proposed organizations are not unique (and some of them hypothetical), since other flow structures can be conceived with a similar degree of topological consistency. Only experiment, or calculation, can give information on the effective organization which establishes itself for given geometrical and flow conditions. However, the following flow descriptions are very likely to occur in reality since they correspond to the simplest topologies. In the presentation which follows, flows of increasing complexity will be examined, some of them corresponding to Test Cases A or B for which measurements are available to substantiate the proposed organizations.

##### *2.1.2.2.1 Unpowered axisymmetric afterbody at incidence*

The present flow description is made by considering the axisymmetric boattailed afterbody constituting Test Case A.1.1 (see Section 2.5). In this case, detailed flow field measurements have been executed, so that we have a rather firm basis to describe the outer flow structure. However, no surface flow visualizations having been made, the given skin friction line pattern is partly speculative, although probably not far from the reality since it is compatible with the outer flow structure.

If we consider first this pattern, represented in Fig. 2.1-13, a half-node  $N_1$  must exist at the base edge A located on the lee side. Diametrically opposite to A, one must have at point B on the windward side, a half-saddle point  $S_1$ . A separatrix ( $S_1$ ), passing through  $S_1$ , runs along the base edge and terminates at  $N_1$ . The skin friction lines coming from upstream "infinity" all stream from the windward side towards the lee side on approaching the base edge. Then, they end into the separation node (or half-node)  $N_1$ . Another attachment node  $N_3$  must exist on the base (see Fig. 2.1-13.d). The skin friction lines originating at  $N_3$  first stream in the direction of the base edge which is, as we already know, a separatrix ( $S_1$ ). Then, they are diverted towards the half-node  $N_2$ , the

combination  $N_1+N_2$  forming a node. Diametrically opposite to  $N_2$ , is the half-saddle point  $S_2$  forming with  $S_1$  a complete saddle point. The line ( $S_2$ ) passing through  $S_2$ ,  $N_3$  and  $N_2$  plays the role of a separatrix.

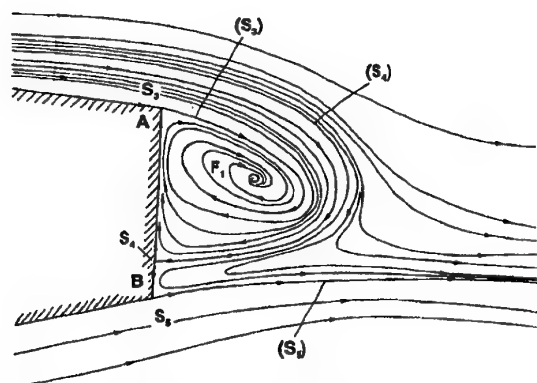


*Unpowered afterbody at incidence. Skin friction line pattern.*

Fig.2.1-13

Let us now consider the flow in the vertical symmetry plane containing points A and B (see Fig. 2.1-14). At the base corner A, is located a half-saddle point  $S_3$  which is the origin of a separatrix ( $S_3$ ) spiralling around the focus  $F_1$ . A second half-saddle point  $S_4$  is located on the base, coincident with the node  $N_3$  belonging to the skin friction line pattern. The separatrix ( $S_4$ ) ending at  $S_4$  separates the streamlines coming from upstream "infinity" to downstream "infinity", from those spiralling around the focus  $F_1$ . A third half-saddle point  $S_5$  is present at the base edge B. It is the origin of the

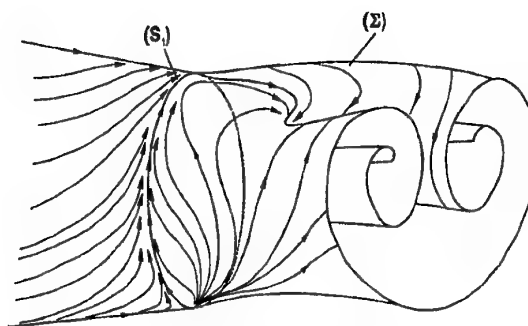
separatrix ( $S_5$ ) which separates the lee side flow from the windward flow.



Unpowered afterbody at incidence. Flow organization in the symmetry plane

Fig. 2.1-14

As shown in Fig. 2.1-15, the separation line ( $S_1$ ) sustains a separation surface ( $\Sigma$ ) which, in a rather complex motion, rolls up to form a hem distorted into two branches bending in the downstream direction. The trace of ( $\Sigma$ ) in the vertical plane of symmetry is the focus  $F_1$ . Cutting ( $\Sigma$ ) by a vertical plane gives two foci which are clearly visible in the measured velocity field (see Appendix A.1). The streamlines constituting the separation surface ( $\Sigma$ ) emanate from a node located on its windward side and coincident with the half-saddle point  $S_2$  of the skin friction line pattern. These streamlines run from the windward side towards the lee side where they are separated into two families by a separatrix emanating from a half-saddle point coincident with the node  $N_1$ . The combination saddle point on the body/node on the separation surface - and vice versa - is a common feature of the topology of separating three-dimensional flows. The rolling up of the separation surface ( $\Sigma$ ) forms a horseshoe-like vortex, similar to the vortex forming ahead of a blunt body. Similar vortical structures will be found in the flow field analyzed hereunder.



Unpowered afterbody at incidence. Main separation surface

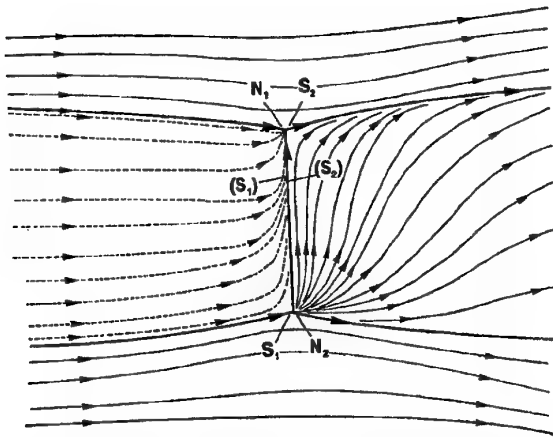
Fig. 2.1-15

#### 2.1.2.2.2 Powered axisymmetric afterbody without base

##### Unseparated outer flow

Let-us first consider the case of an axisymmetric afterbody with jet and no base placed at a small incidence. We assume that the thickness of the afterbody trailing edge is zero (or sufficiently thin to have no effect on the flow structure, except at a microscopic scale at the trailing edge itself). If the nozzle expansion ratio is not too high, jet pluming at the nozzle exit is moderate so that the jet does not induce separation on the afterbody. This configuration could correspond to Test Case A.2.1 (see Section 2.5).

The corresponding flow topology is shown in Fig. 2.1-16. Because of the driving pressure forces due to the incidence effect, the afterbody skin friction lines tend to converge towards a separation node  $N_1$  located in the afterbody plane of symmetry, on its lee side (in fact  $N_1$  is a half-node). On the windward side, a saddle point  $S_1$  forms (in fact a half-saddle), opposite to  $N_1$ , a separatrix contained in the plane of symmetry passing through  $S_1$ . This line separates the skin friction lines into two families which are flowing, on each side of the afterbody, towards the separation node  $N_1$ .



*Powered afterbody without base. Low jet expansion ratio. Skin friction line pattern and flow organization in the symmetry plane and on jet boundary*

Fig. 2.1-16

The second separatrix going through  $S_1$  coincides with the afterbody extremity. It constitutes a separation line ( $S_1$ ). The skin friction lines coming from the upstream part of the flow, without being much affected beforehand, are rapidly bent on approaching ( $S_1$ ). Then, they follow closely this line before ending into the separation node  $N_1$ .

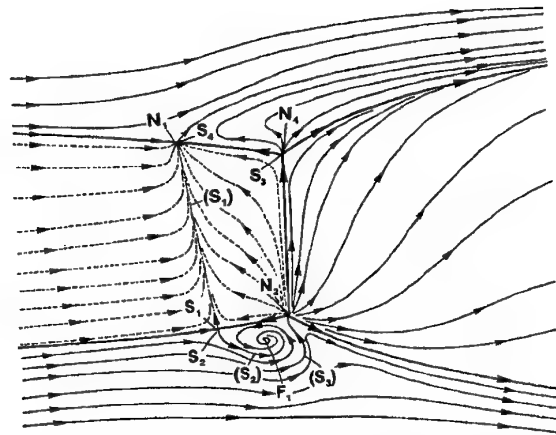
The figure also represents the separation surface, the trace of which on the afterbody, is the separation line ( $S_1$ ). This surface, which is the boundary of the jet, is constituted by the streamlines coming from a half-node  $N_2$  coincident with the half-saddle  $S_1$ , but located in the flow, whereas  $S_1$  is on the body and belongs to the skin friction line pattern. On the lee side, a half-saddle  $S_2$  exists on the separation surface. It coincides with the separation node  $N_1$  of the skin friction line pattern.

In the immediate vicinity of the afterbody trailing edge, the streamlines coming from  $N_2$  follow the separation line ( $S_2$ ), coincident with ( $S_1$ ). A separatrix passing through  $N_2$  is located in the flow plane of symmetry. It plays a role similar to the separatrix of the skin friction line pattern going through  $S_1$ . All the streamlines emanating from  $N_2$  flow towards another separatrix, of the separation type, contained in the plane of symmetry and coming from the half-saddle  $S_2$ . Thus, the streamlines of the jet boundary tend to flow from the windward side to the lee side. This flow organization is rather simple and corresponds the normal afterbody flow situation, even at the so-called zero incidence case, since a

purely axisymmetric flow is extremely unlikely. However, it is clear that the unavoidable three-dimensional situation associated with nominally zero incidence does not entail noticeable differences with the purely axisymmetric case, as far as pressure distributions and drag are concerned. This is the case of Test Case A.1.2 (see Section 2.5). Hence, an axisymmetric mathematical model gives a precise prediction of the flow, even if its intimate structure is not respected.

#### *Separated outer flow*

Let us now consider the more complex situation which would result from a stronger expansion of the under-expanded jet at the nozzle exit. Beyond a certain limit, the jet expansion causes an obstacle effect which separates the outer flow upstream of the afterbody trailing edge. If at the same time the afterbody is at incidence, a possible flow organization is the one represented in Fig. 2.1-17.



*Powered afterbody without base. High jet expansion ratio. Skin friction line pattern and flow organization in the symmetry plane and on jet boundary*

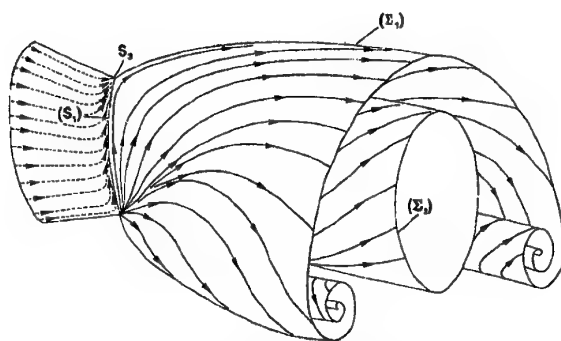
Fig. 2.1-17

Considering first the skin friction line pattern, there exists a saddle-point  $S_1$  located upstream of the afterbody trailing edge, in the plane of symmetry, on the windward side. From  $S_1$  emanates a separation line ( $S_1$ ) going from the windward side to the lee side where it terminates in the separation node  $N_1$ . The separation line ( $S_1$ ) separates the skin friction line into two families: one made of the skin friction lines coming from the upstream part of the afterbody (upstream "infinity"), the other of the skin friction lines emanating from the node  $N_2$  located at the trailing edge. These two families terminate into the node  $N_1$ .

The flow in the plane of symmetry contains now a focus  $F_1$ , around which spirals the separatrix ( $S_2$ ) coming from the half-saddle  $S_2$ , coincident with  $S_1$  on the surface. A second separatrix of the outer flow - ( $S_3$ ) - terminates at the attachment node  $N_2$  located at the trailing edge. The streamlines streaming between the surface and ( $S_3$ ), and then between ( $S_2$ ) and ( $S_3$ ), all spiral into the focus  $F_1$ .

On the lee side of the flow, there are a half saddle point  $S_4$ , coincident with  $N_1$  on the surface, and a node  $N_4$  located at the trailing edge.

As sketched in Fig. 2.1-18, the outer flow structure contains two main separation surfaces. The first one - ( $\Sigma_1$ ) - emanates from the separation line ( $S_1$ ) located on the afterbody, upstream of the trailing edge. It is made of the streamlines originating at a node coincident with  $S_2$ . These streamlines stream from the lee side to the windward side where a saddle point  $S_3$ , coincident with  $N_1$ , is the origin of a separatrix separating the streamlines flowing on each side of the plane of symmetry. This separation surface rolls up to constitute a vortex, the trace of which in the symmetry plane is the focus  $F_1$ . As the flow is streaming in the downstream direction, this vortex is bent and constitute the familiar horseshoe vortex. The second separation surface - ( $\Sigma_2$ ) - is the jet boundary, its origin on the afterbody being the separation line coinciding with the trailing edge.



*Powered afterbody without base. High jet expansion ratio. Main separation surfaces*

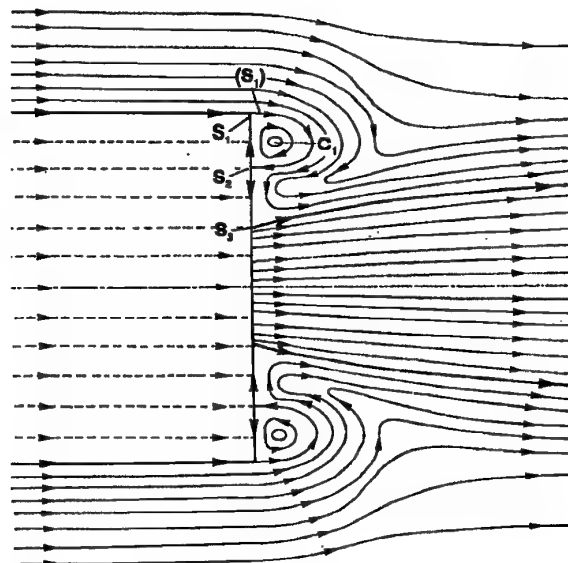
Fig. 2.1-18

#### 2.1.2.2.3 Powered axisymmetric afterbody with base

##### *The purely axisymmetric case*

We consider now the case of an afterbody with a base at zero incidence, the configuration being assumed perfectly axisymmetric. As shown in Fig. 2.1-19, the skin friction

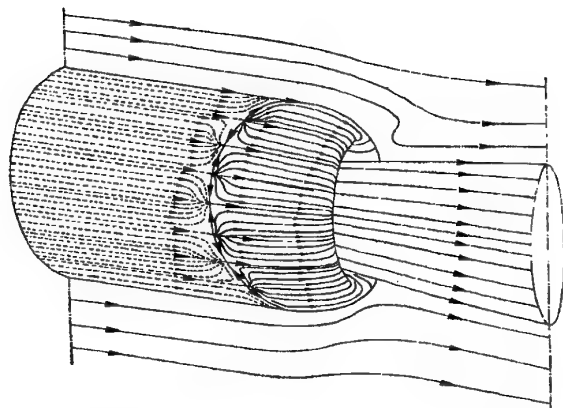
line pattern is made of parallel lines ending at the afterbody extremity. In the outer flow plane of symmetry, a separatrix ( $S_1$ ) emanates from the half-saddle  $S_1$ , at the base shoulder, and terminates at a second half-saddle  $S_2$ , located on the base. The separatrix ( $S_1$ ) isolates the recirculation flow, swirling around the centre  $C_1$ , from the flow streaming from upstream to downstream "infinity". A third half-saddle -  $S_3$  - coincides with the nozzle exit. It is the origin of a second separatrix which is in fact the jet boundary. The same description can be made for the lower half part of the figure. Thus, the main feature of the flow is the existence of a toroidal vortex whose trace in any meridian plane is a centre.



*Powered afterbody with base. Purely axisymmetric case. Skin friction line pattern and flow organization in the symmetry plane and on jet boundary*

Fig.2.1-19

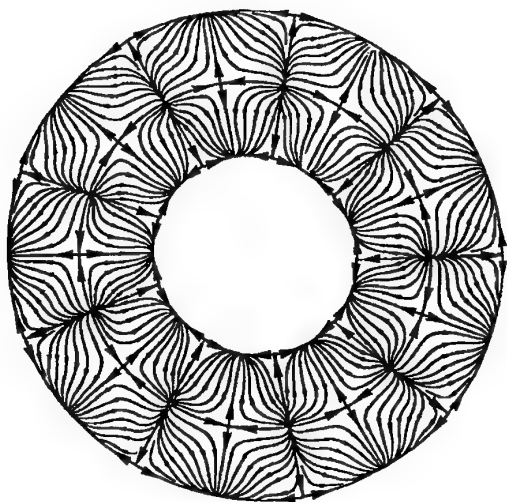
The above topology is very unlikely to occur in the real world since it contains highly singular features. For example, in this case the base shoulder, where all the afterbody skin friction lines terminate, must be the locus of an infinite number of node - saddle point combinations, as shown in Fig. 2.1-9.f. In the reality, in a nominally axisymmetric configuration, the flow adopts a three-dimensional pattern by avoiding these singular situations. Based on experimental results obtained in an axisymmetric reattachment, we can propose the effective axisymmetric topology shown in Fig. 2.1-20.



*Powered afterbody with base. Purely axisymmetric case.  
Main separation surfaces*

Fig. 2.1-20

Now, the base shoulder bears a finite number of critical points, which are in succession half-nodes and half-saddle points. To this pattern corresponds, in the flow field, a similar succession of critical points, with nodes corresponding to saddle points and saddle points to nodes. The skin friction line pattern on the base must have the structure shown in Fig. 2.1-21 with three separatrices: one coinciding with the base shoulder, another with the nozzle exit and the third one located somewhere on the base. This last line bears a succession of complete nodes and saddle points.



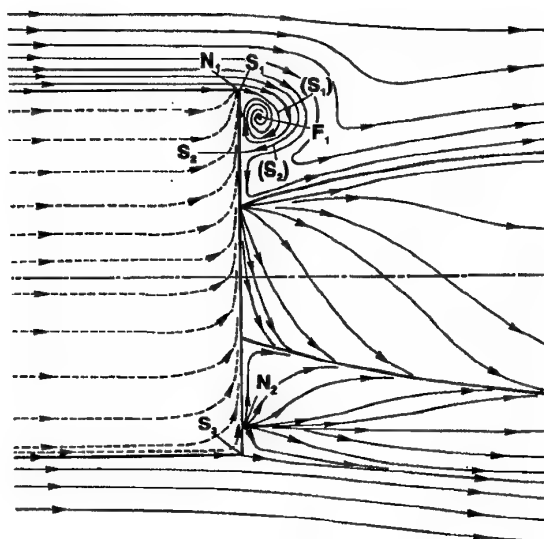
*Powered afterbody with base. Purely axisymmetric case.  
Skin friction line pattern on the base*

Fig. 2.1-21

It is clear that the topological organization of such a flow is extremely complex so that we have not tried to represent it in more detail. However, in spite of this complexity, this organization is more likely to occur than the fully axisymmetric case since it does not contain highly singular features.

#### *Non-axisymmetric case*

Now, a true - or macroscopic - three-dimensional effect is introduced by setting the afterbody at incidence. The flow organization which may result is represented in Fig. 2.1-22.

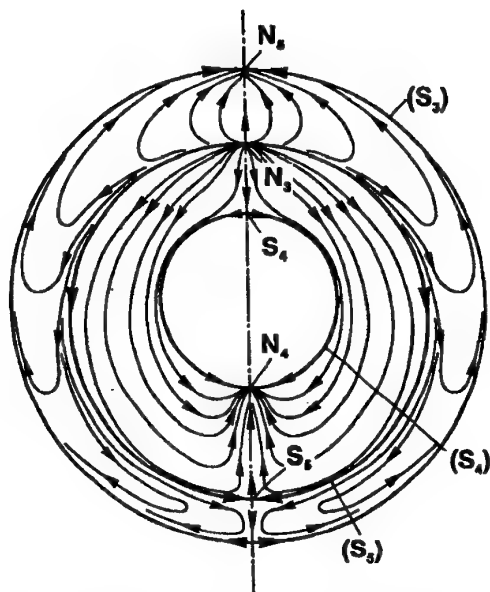


*Powered afterbody with base. Non axisymmetric case.  
Skin friction line pattern and flow organization in the  
symmetry plane and on jet boundary*

Fig. 2.1-22

All the skin friction lines coming from upstream "infinity" terminate into the node  $N_1$ , the situation on the afterbody being similar to that of Fig. 2.1-13. In the present case, the separatrix  $(S_1)$  emanating from the base shoulder spirals into the foci  $F_1$ . A second separatrix  $(S_2)$  terminates on the base at the saddle point  $S_2$ , the streamlines flowing between  $(S_1)$  and  $(S_2)$  spiralling into the focus  $F_1$ . On the windward side, the situation is different, with the existence of a node  $N_2$  on the base and a half-saddle point  $S_3$  on the base shoulder. The skin friction line pattern on the base itself is shown in Fig. 2.1-23. To the half-saddle point  $S_2$  corresponds the attachment node  $N_3$  and to the node  $N_2$ , the saddle point  $S_4$ . The pattern includes three separatrices:  $(S_3)$

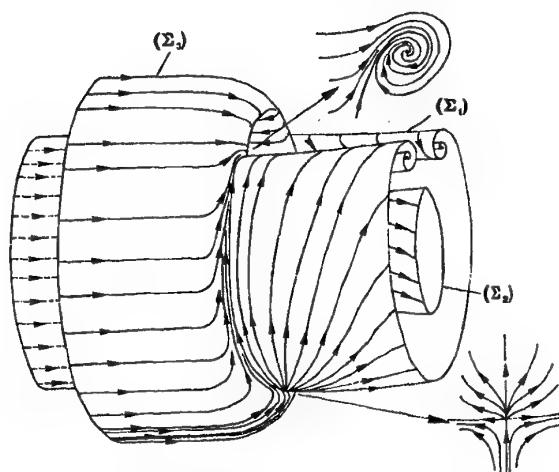
coinciding with the base shoulder, ( $S_4$ ) with the nozzle lip and ( $S_5$ ) between these two lines. The separatrix ( $S_5$ ) separates the skin friction lines coming from the attachment node  $N_3$  into one family terminating into the separation node  $N_5$  and one family ending in the node  $N_4$ .



*Powered afterbody with base. Non axisymmetric case.  
Skin friction line pattern on the base*

Fig. 2.1-23

The main streamsurfaces are drawn in Fig. 2.1-24.



*Powered afterbody with base. Non axisymmetric case.  
Main separation surfaces*

Fig. 2.1-24

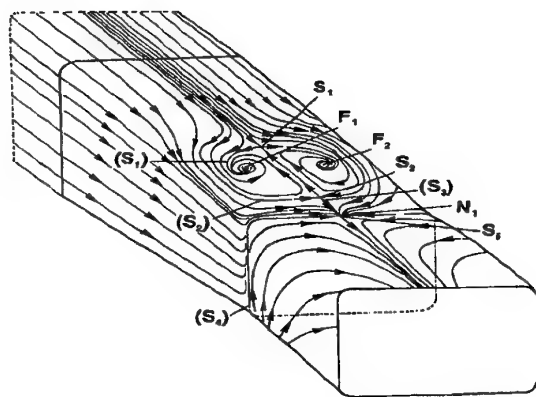
The separation surface ( $\Sigma_1$ ), emanating from the separation line ( $S_3$ ) at the base shoulder, rolls up to form a horseshoe vortex, as in the case of Fig. 2.1-18. A second separation surface - ( $\Sigma_2$ ) - is the jet boundary. The third surface represented - ( $\Sigma_3$ ) - is an attachment surface which hits the base along the separatrix ( $S_4$ ). The reader will interpret by himself the other features represented in the figure.

#### 2.1.2.2.4 Powered non-axisymmetric afterbody

##### Single-jet rectangular afterbody

The following case corresponds to Test Case B.4 (Single jet, 2-D, C-D nozzle, see Section 3.4) for which computed skin friction lines are available. The afterbody has a rectangular cross section, with rounded corners, and presents a boattail. It is equipped with a converging-diverging nozzle whose exit section is equal to the terminal cross section of the afterbody (no base). Here, we consider only Test Case B.4.2, for which the outer flow is transonic and who leads to the most interesting topological features. In the drawings presented below, the proportions of the tested model have not been respected, for reasons of convenience. However, the proposed flow organization is topologically equivalent to what it would be for the real model.

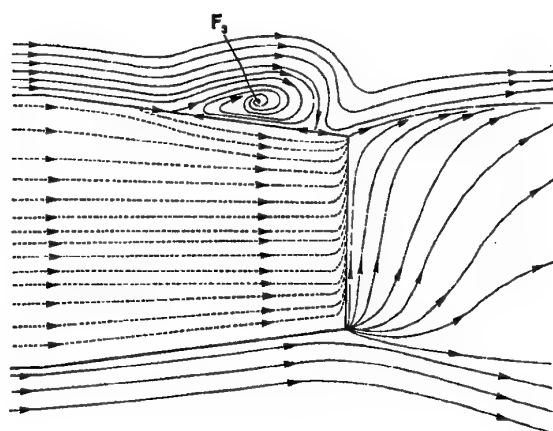
Let us first examine the skin friction line pattern represented in Fig. 2.1-25. We examine only the pattern on the lee side since it shows the most interesting features. Two saddle points  $S_1$  and  $S_2$ , and two foci  $F_1$  and  $F_2$ , are clearly identified on this part of the model. To  $S_1$  is associated the separatrix ( $S_1$ ) which is made of two branches winding, respectively, around the foci  $F_1$  and  $F_2$ . This line constitutes a barrier for the skin friction lines coming from upstream "infinity", which are first deflected on approaching the saddle point  $S_1$  and then turned in the upstream direction, before disappearing into the foci  $F_1$  and  $F_2$ . The second separatrix ( $S_2$ ), going through  $S_2$ , separates the skin friction lines into one family which is spiralling around  $F_1$  and  $F_2$  and one family which continues in the downstream direction to reach, in this case, the separation node  $N_1$  located on the afterbody trailing edge, slightly downstream of the saddle point  $S_2$ . This pattern is classically associated with shock induced separation in three-dimensional transonic flow, as it occurs in the present experiment. Some authors object that a pattern in which two saddle points are located on the same separatrix - here ( $S_3$ ) - would be unstable. It is an easy matter to slightly modify the picture in Fig. 2.1-25 to get a stable situation.



*Powered non axisymmetric afterbody. Skin friction line pattern and flow on the jet boundary*

Fig. 2.1-25

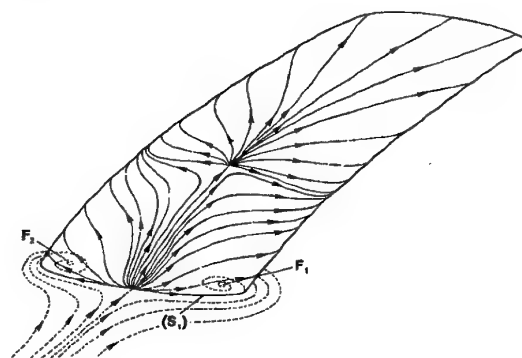
The pattern on the windward side (not represented) must present a saddle point, opposite to the node  $N_1$ , through which passes a separatrix of the attachment type. This line separates the skin friction lines which stream towards the left hand part of the model, from those which flow towards the right hand part. All the skin friction lines (except those reaching the foci  $F_1$  and  $F_2$ ) are bent in the vicinity of the afterbody trailing edge where they follow the separatrix ( $S_4$ ) coinciding with the trailing edge. We have also represented in Fig. 2.1-25 a part of the jet boundary where the lines drawn are streamlines constituting a separation surface. According to a classical result, the half-saddle point  $S_5$  in the separation surface coincides with the node (in fact a half-node)  $N_1$  of the surface pattern. A representation of the flow in the vertical plane of symmetry is given in Fig. 2.1-26. The pattern includes a focus  $F_3$  which is the trace of a vortex which, in other circumstances, would form a horseshoe vortex escaping downstream. However, in the present situation, is it probable that the core of this vortex - which is made of a left and a right legs - rolls up around the cores of the vortices emanating from the foci  $F_1$  and  $F_2$ , to be evacuated downstream. This point will not be discussed here.



*Powered non axisymmetric afterbody. Flow in the symmetry plane and on the jet boundary*

Fig. 2.1-26

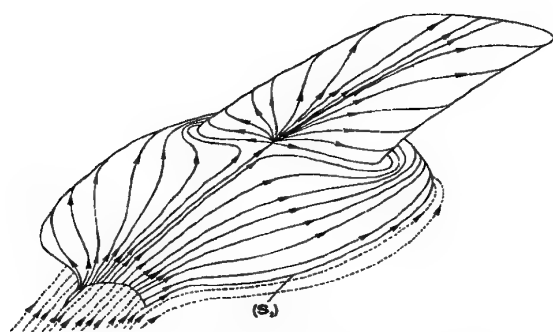
The present flow contains - at least - three separation surfaces. The trace on the afterbody of one of these surfaces is the separatrix ( $S_1$ ) which spirals around the foci  $F_1$  and  $F_2$ . The rolling up of the corresponding separation surface ( $\Sigma_1$ ) forms a pair of tornado like vortices springing up from the surface, as shown in Fig. 2.1-27.a. The second separatrix ( $S_2$ ) is the trace of the attachment surface ( $\Sigma_2$ ), represented in Fig. 2.1-27.b. The crossing of ( $\Sigma_2$ ) by ( $\Sigma_1$ ) leads to the pattern shown in Fig. 2.1-27.c.



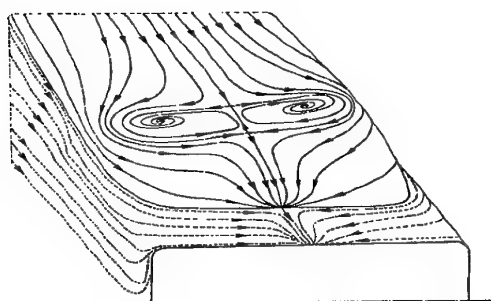
*a - First separation surface ( $S_1$ )*

*Powered non axisymmetric afterbody. Formation of the separation surfaces*

Fig. 2.1-27



*b - Second separation surface ( $S_2$ )*

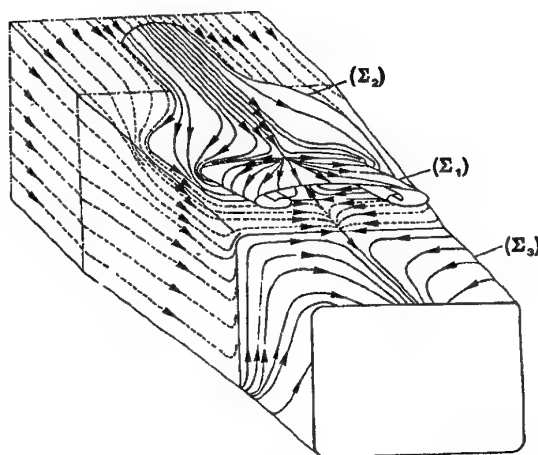


*c - Interference of separation surfaces ( $S_1$ ) and ( $S_2$ )*

*Powered non axisymmetric afterbody. Formation of the separation surfaces*

Fig. 2.1-27

This pattern, which is made of two foci, with associated separatrices, is the trace on  $(\Sigma_2)$  of the vortices springing up from  $F_1$  and  $F_2$ . This crossing gives the streamline organization shown in Figs. 2.1-27.b and 2.1-27.c with the existence on  $(\Sigma_1)$  of a half-saddle point/half-node combination. The third separation surface -  $(\Sigma_3)$  - is the jet boundary. The whole flowfield organization is shown in Fig. 2.1-28. We shall not comment any more the above pictures whose main features have already been found in previous flows.



*Powered non axisymmetric body. Main separation surfaces*

Fig. 2.1-28

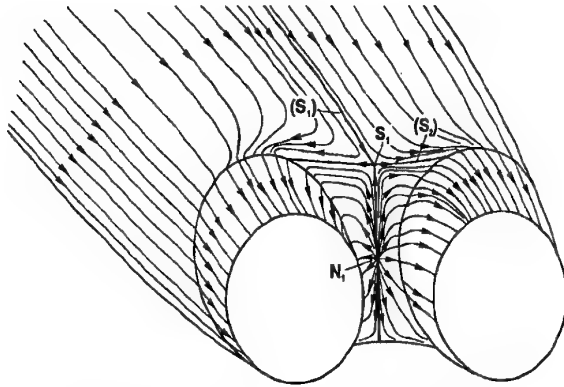
#### *Twin-jet afterbody*

The last field analyzed is the flow produced by a twin-jet afterbody, as the one constituting Test Case A.1.3 (see Section A.2.5). A precise definition of the afterbody is given in Appendix A.1. Here, we will consider that the afterbody geometry has two symmetry planes, one (horizontal) containing the nozzle axes, the other (vertical) perpendicular to the first symmetry plane (in reality, the tested afterbody has only one symmetry plane, but the asymmetry is weak so that it does not affect much the general flow structure). The angle of incidence is assumed equal to zero.

For this case, surface flow visualizations and velocity measurements have been performed, so that the flow description is founded on experimental evidences. An interpretation of the observed surface flow pattern is given in Fig. 2.1-29. The skin friction lines coming from upstream "infinity" are separated into two families by the separatrix ( $S_1$ ) passing through the saddle point  $S_1$  located at the extremity of the afterbody, in the vertical symmetry plane. On approaching the afterbody base, one family is turned towards one of the nozzle while the other family streams towards the other nozzle. The second separatrix ( $S_2$ ) passing through  $S_1$  is first running along the base shoulder and then it must be bent to continue its path on the nozzles. An attachment node  $N_1$  is clearly identified at the center of the base. The skin friction lines originating from  $N_1$  all stream towards the extremity of the nozzles. The separatrix ( $S_2$ ) separates the skin friction lines coming from upstream from those having their origin at  $N_1$ . The nozzle extremities must bear at least two separatrices on which are located critical points (most probably separation nodes) into which the



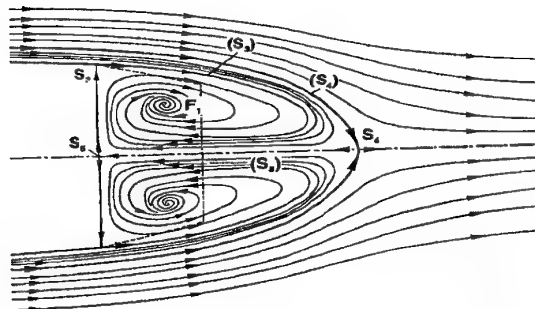
skin friction lines coming, either from upstream "infinity", or from the node  $N_1$ , terminate. However, the surface flow visualization was not fine enough to allow an identification of these points.



*Twin jet afterbody. Skin friction line pattern*

Fig. 2.1-29

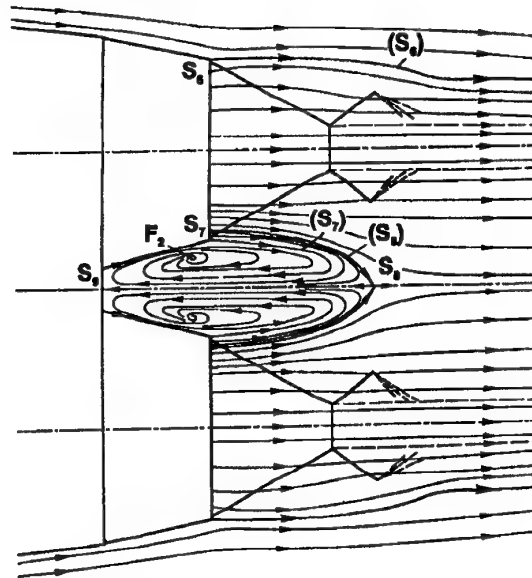
The outer flow streamlines in the vertical plane of symmetry are represented in Fig. 2.1-30. Considering only one half of the figure, it is possible to identify a half-saddle point  $S_3$  located at the base shoulder. From  $S_3$  starts the separatrix ( $S_3$ ) which spirals into the focus  $F_1$ . A complete saddle point  $S_4$  is present on the axis of the configuration. Through  $S_4$  passes a second separatrix ( $S_4$ ) which separates the streamlines streaming from upstream "infinity" to downstream "infinity" from those spiralling into the focus  $F_1$ . A third half-saddle point -  $S_5$  - exists on the base, in the symmetry plane, which contains the separatrix ( $S_5$ ).



*Twin jet afterbody. Flow organization in the vertical symmetry plane*

Fig. 2.1-30

The streamlines in the symmetry plane containing the nozzle axes are represented in Fig. 2.1-31 (on this tracing we have superimposed the shock system shown by the schlieren pictures). A first half-saddle point  $S_6$  is present at the nozzle extremity. This point is the origin of the separatrix ( $S_6$ ) which separates the outer flow from the jet issuing from the nozzle (the second skin friction line which must meet at  $S_6$  is coming from inside the nozzle). A second half-saddle point  $S_7$  exists diametrically opposite to  $S_6$ . It is the origin of the separatrix ( $S_7$ ) which spirals into the focus  $F_2$ . The axis of symmetry bears the saddle point  $S_8$  through which passes the separatrix ( $S_8$ ) coming from inside the nozzle. Thus, a part of the jet flow is diverted to constitute the "recirculation" flow which disappears into the focus  $F_2$ . Another half-saddle point  $S_9$  must be present on the base. The present flow organization is very similar to the one existing in the other symmetry plane.



*Twin jet afterbody. Flow organization in the horizontal symmetry plane*

Fig. 2.1-31

The separation surfaces will not be represented for this configuration, their shapes being very complex and difficult to establish on firm basis. A double pair of horseshoe vortices must probably exist, their traces in the two planes of symmetry being the four foci which can be identified. A drawing of such a structure has been attempted, the result being too speculative to be given here.

### 2.1.2.3 Jet structures and shear layers in 3D

Rectangular jets also have a shock cell structure, and Tam [2.1-25] found that for rectangular jets with aspect ratio greater than four the jets are essentially two dimensional as far as shock cell spacing is concerned.

Most of the work reported in the literature has been associated with the flow field of an axisymmetric jet; although the structure of a rectangular jet exhibits some features similar to those of an axisymmetric jet, there are some important differences between the two flows.

The large scale structures existing in the mixing layers of the turbulent flow are visible in both planes of the jet, but they appear at different locations on each plane. According to Krothapalli and al. [2.1-18], such structures appear just downstream from the acoustic sources in the small dimension's plane of the nozzle, but more than six times further in the long dimension's one.

Experimental studies on shear layers are usually performed on nominally two dimensional configurations (axisymmetric or 2D plane shear layers), and turbulence models used in CFD codes are calibrated on such configurations. There is a lack of experimental data to validate the use of such modelisation in more complex tridimensional viscous layers.

### 2.1.2.4 Twin supersonic plume resonance - screech

Seiner and al. [2.1-26] defined and studied the phenomenon of *twin supersonic plume resonance*. The results of this study revealed that, when two adjacent supersonic nozzles have a centerline spacing within two nozzle diameters, the axial evolution of each nozzle plume's preferred shear layer instability wave is coupled together. This coupling results in a large increase in the dynamic pressure level (screech) in the nozzle exhaust plane. It may even be a possible mechanism for engine nozzle flap failure. Among the conclusions of this study, it can be noted that rectangular twin nozzle geometry produces higher resonance amplitude levels than the axisymmetric geometry, and that higher plume temperatures can also produce higher amplitude levels.

Walker [2.1-15] also studied the effect of the lateral spacing of the two nozzles on the noise level, and realized that the highest amplitude levels occurred at the closest nozzle spacing ratio.

For twin two-dimensional vectoring nozzles, it has been observed experimentally that screech amplitude increases for a 10° pitch setting, and considerably decreases for a 20° pitch setting (Walker [2.1-15]).

### 2.1.3. Conclusions - Recommendations

Most of the articles that can be found in the literature about aircraft afterbody flow structure are dealing with the development of computational methods determining the

flow characteristics in this region. These calculations are compared to experimental results which are unfortunately in a restricted number, particularly for 3D complex configurations. It seems thus necessary to conduct detailed experimental studies on realistic 3D configurations, in order not only to validate the calculated results, but also to describe the exact topology of this kind of flow. A lot of configurations like twin nozzle flows or rectangular and/or vectoring nozzle flow structure are not well known and a topological knowledge of these flows appears to be a first-order priority.

### Références :

- [2.1-1] Reijasse, Ph. and Détery, J. - *PREPHA : Problèmes de confluence en aval d'un arrière-corps - Étude de synthèse et description du montage expérimental*, RTS ONERA, Nov. 1993
- [2.1-2] Dash, S. M. and Wolf, D. E. - *Interactive phenomena in supersonic jet mixing problems, Part I : Phenomenology and numerical modelling techniques*, AIAA Paper 83-0288, 1983
- [2.1-3] Simpson R. L. - *Two-dimensional turbulent separated flow*, : AGARD AG-287-Vol.1
- [2.1-4] Delery, J. M., Marvin, J. G. - *Shock wave boundary layer interactions*, AGARDograph n°280, 1986.
- [2.1-5] Cousteix J. - *Turbulence et couches limites*, Cours professé à l'ENSAE, CEPADUES, Toulouse, 1990.
- [2.1-6] Delery J. - *Étude expérimentale de la réflexion d'une onde de choc sur une paroi chauffée en présence d'une couche limite turbulente*, Recherche Aérospatiale n°.1992-1
- [2.1-7] Benay R. - *Assessment of three models of turbulence in a shock-boundary layer interaction on a heated wall*, Recherche Aérospatiale n°.1991 - 5
- [2.1-8] Dash, S.M. and Wolf, D.E. - *Shock-capturing parabolized Navier-Stokes model (SCIPVIS) for the analysis of turbulent underexpanded jets*, AIAA Paper 83-0704, April 1983
- [2.1-9] Dash, S.M. and Wolf, D.E. - *Interactive phenomena in supersonic jet mixing problems, Part II : Numerical studies*, AIAA Paper 83-0288, January 1983
- [2.1-10] Seiner, J. M. and Norum, T. D. - *Aerodynamic aspects of shock containing jet plumes*, AIAA Paper 80-0965, June 1980
- [2.1-11] Bogdanoff D.W. - *Compressibility Effects in Turbulent Shear Layers*, AIAA Journal, Vol. 21, pp 926-927, 1983.
- [2.1-12] Samimy M., Elliot G.S. - *Effects of Compressibility on the Characteristics of Free Shear Layers*, AIAA Journal, Vol. 28, N°3, pp 439-445, 1990.
- [2.1-13] Papamoschou, D. and Roshko, A. - *The compressible turbulent shear layer : An experimented study*, Journal of Fluid Mechanics, Vol. 197, 1988, pp.453-477.

- [2.1-14] Bonnet, J.P., Ouzaa, T., Cabrit B., and Gresillon, D. - *Density fluctuations and acoustic waves in supersonic mixing layers*, 9th Symposium on "Turbulent Shear Flows", Kyoto, Japan, August 16-18, 1993
- [2.1-15] Walker, S.H. - *Twin jet screech suppression concepts tested for 4.7% axisymmetric and two-dimensional nozzle configurations*, AIAA Paper 90-2150, July 1990
- [2.1-16] Davis, M.R. - *Identification of vortex motions in turbulent mixing of choked jets*, Experiments in Fluid 6, 1988
- [2.1-17] Powell, A. - *On the mechanism of choked jet noise*, Proc. Phys. Soc., Vol. 66, Pt. 12B, 1953
- [2.1-18] Krothapalli, A., Hsia, Y., Baganoff, D. and Karamcheti, K. - *The role of the screech tones in mixing an underexpanded rectangular jet*, J. Sound and Vibration, 106, 119-143, 1986
- [2.1-19] Yu, C. J. and Seiner, M. J. - *Near field observations of tones generated from supersonic jet flows*, AIAA Paper 83-0706, 1983
- [2.1-20] Carrière, P.- *Aérodynamique interne, 2ème partie : Tuyères et Jets - Cours ENSAE*, 1980
- [2.1-21] Délery, J. M. - *Physics of vortical flows*, Journal of Aircraft, Vol. 29, N°. 5, Sept-Oct 1992
- [2.1-22] Van den Berg, B. - *Physical aspects of 3D separated boundary layer flows*, AGARD AR-255, May 1990
- [2.1-23] Poincaré, H. - *Les points singuliers des équations différentielles*, Comptes Rendus à l'Académie des Sciences de Paris, 13 Février 1882
- [2.1-24] Legendre, R. - *Lignes de courant d'un écoulement permanent - Décollement et séparation*, La Recherche Aérospatiale, N°6, 1977, pp.327-335
- [2.1-25] Tam, C.K.W., Jackson, J.A., Seiner, J.M. - *A multiple-scales model of the shock cell structure of imperfectly expanded supersonic jets*, J. Fluid Mech., 153, 123-149, 1985
- [2.1-26] Seiner, J. M., Manning, J. C. and Ponton, M. K. - *Dynamic pressure loads associated with twin supersonic plume resonance* AIAA Paper 86-1539, 1986

## 2.2. Experimental Techniques for the Study of Complex Flows

### 2.2.1. Introduction

Formerly, validation of predictive methods, in particular those applied to afterbody flows, was made by comparison of computed results with some measured wall properties, essentially the pressure. In many situations, this kind of comparison was sufficient since "old" predictive methods, which were either fully empirical or based on a multi-component type approach, allowed only the prediction of the wall pressure and more rarely the temperature (in the dead air region of a base flow). They could also give a gross idea of the flow organization by predicting the size of a separated region and the location of a separation point, but this information was more or less considered as qualitative. Methods based on viscous-inviscid coupling were more involved and ambitious; however they were basically restricted to the prediction of surface pressure, and in some cases skin-friction and heat transfer [2.2.1].

The flow prediction landscape has completely changed with the advent of advanced theoretical models based on the solution of the full time averaged Navier-Stokes equations. It is clear that this approach is the only method suitable to compute complex flows containing shock waves, centered expansion waves, separated regions etc, the dissipative zones being turbulent in all practical applications. Then, not only wall properties are computed, but also field quantities, including the mean velocity and the turbulent fields. However, in its present state, the full Navier-Stokes approach is still far from being free of critics, since many difficulties persist both on the numerical side and in the modelling of turbulence. There is thus a strong need to validate Navier-Stokes codes before their routine use for design purposes.

Though the prediction of wall properties remains a key target for most predictive methods, since the afterbody drag/thrust and in some cases its thermal loading are the quantities of most practical and direct interest, it rapidly became obvious that a comparison restricted to wall properties was insufficient to properly validate the most advanced predictive methods. In general, Navier-Stokes codes give a faithful and sometimes impressive picture of the flowfield structure. The complex organization of the jet, with its pseudo periodic pattern of shocks and expansion waves, the separated zone forming on the afterbody with, at transonic speed, a possible induced lambda shock system, are most often well reproduced. However, a more careful analysis of the data shows that the situation is far from being entirely satisfactory.

Firstly, it is observed that a fairly good prediction of the wall pressure (the base pressure in the case of a missile type afterbody) can coexist with a poor quantitative prediction of the velocity field. Frequently, the extent of the separated regions is under-

estimated, sometimes considerably. In addition, the turbulent quantities are most often poorly predicted, especially if the flow is largely separated. Such discrepancies render suspect the validity of the code since they are indicative of some basic deficiency either in its numerical scheme or its turbulence model, or both.

On the other hand, a rather fair prediction of the flowfield can be accompanied by large errors in the calculation of surface properties, affecting mainly transfer coefficients, skin-friction and heat flux. In base flow prediction, it is common for codes to give unrealistic variations of the pressure along the base of the afterbody.

Lastly, in certain applications, the knowledge of the outer field itself is of prime interest. This is the case for problems dealing with infra red signature where a detailed description of the hot propulsive jet, with an exact localization of the Mach discs, is essential. Pollution studies necessitate a good prediction of the jet properties to allow accurate evaluation of chemical processes and species concentration. A good representation of the flow resulting from interferences between the external flow and the propulsive jet(s) also requires a faithful prediction of the flowfield.

The problem of code validation is still more stringent in three-dimensional applications where Navier-Stokes analysis is the only credible approach. Due to the complexity of such flows, it is clear that the consideration of the surface pressure alone is completely inadequate, partly because this information gives a very partial view of the flow (in three-dimensional flow, it is no longer possible to infer separation from an inspection of the wall pressure distributions), and partly because pressure measurements are nearly always too sparse due to the difficulty of properly instrumenting small scale models.

In these conditions, the validation of advanced computer codes requires well documented experiments providing detailed and reliable flow field measurements. In these experiments, the description of the flow must be as complete as possible, including - ideally - the determination of all the flow variables, including mean velocity, stagnation pressure and temperature, static pressure and temperature, density, species concentration, turbulence properties (including the components of the Reynolds tensor), power spectra ... the present list being not exhaustive. Of course, wall properties must not be forgotten such as pressure, skin friction and heat transfer, since, as already stated, they are quantities of prime interest in most applications. Also, surface flow visualizations are extremely valuable, especially in three-dimensional flows, where inspection of the surface flow pattern is the only way to detect separation.

The experimental means to perform the above measurements already exist; however, their degree of reliability, ease of use and accuracy are extremely vari-

able. In practice, it is impossible to perform all the measurements on the same model and in the same facility or laboratory. Indeed, the use of the sophisticated techniques needed to make some of the above measurements is so complex that it necessitates teams of highly specialized experimentalists working in specific facilities. Thus, for validation purposes, one has frequently to rely on fragmentary experiments in which a limited number of flow phenomena has been investigated, where the pressure and temperature fields may be from one source, mean velocity and turbulence fields from another source and density from a third source...

Nevertheless, progress accomplished in the measurement techniques in the past 30 years, mainly with the advent of laser based optical methods, has operated a true break through in our capacity to investigate complex turbulent flows, containing shock waves, strong expansions, thin shear layers and recirculation regions.

The purpose of this chapter is to give a presentation of methods now available to perform detailed investigations of afterbody flows with a view to characterizing the field properties. This knowledge is indispensable not only to validate computer codes, but also to improve our physical understanding of flows which can be extremely complex, especially past three-dimensional configurations. For the sake of completeness, classical probing techniques will be briefly considered as well as visualization methods which are of great help to comprehend the structure of the flow. Surface measurements will also be presented, since they are of prime practical interest and essential to fully understand the flow physics. However, more emphasis will be placed on non intrusive techniques, especially those based on laser instrumentation, even if some of these techniques are still difficult to implement in wind tunnels and, for this reason, not yet routinely employed in flow investigation.

There is a huge number of publications on measurement techniques, so that we had to make a rather arbitrary selection of the cited references. The interested reader will find in them other references providing more ample information on the subject.

## 2.2.2. Surface Properties Characterization

### 2.2.2.1. General Remarks

The main surface properties of interest are the pressure, the skin-friction and the heat-transfer. The knowledge of pressure - and to a lesser extent of skin-friction - is of obvious importance to determine the afterbody drag, if no direct force measurements are performed. The wall pressure distribution also gives an indication of the general flow structure revealing, by special features, the presence of a pressure plateau for example, or the existence of separated zones. This is less true in three-dimensional flows where separation is a more complex process which

cannot generally be inferred from the sole inspection of surface pressure distributions.

The knowledge of skin-friction is valuable, not only for drag determination, but also to validate computer codes. This quantity is difficult to predict accurately since its calculation depends both on the accuracy of the numerical schemes and on the quality of the physical models. Furthermore, in two-dimensional and/or axisymmetric flows, the change from positive to negative or negative to positive is the best indication of separation and the capability of codes to predict the location of this point, as well as that of the reattachment point if it exists, is a key factor of their validity. In three-dimensional flows, the definition of separation is more subtle, since the skin-friction vector does not vanish at the crossing of a separation line, except in very special situations.

As far as afterbodies are concerned, heat transfer is of prime importance for missiles and space launchers whose base is submitted to intense thermal loads at some flight conditions. The problem is apparently less severe for the aircraft afterbodies, although some part of a supersonic aircraft can be subjected to significant heat loads when the Mach number is above 2.5 (leading edges of wings or tails, external cowl of an air-intake, for example). Because it also involves transfer phenomena, heat transfer is a quantity difficult to predict accurately and thus is a good candidate for code validation.

### 2.2.2.2. Surface Pressure Measurements

The measurement of the pressure at the surface of a model is classically made through orifices of small size connected to a transducer via a tubing system. This technique is well known and there exists a great variety of transducers, whose choice is dictated by the level of pressure to be measured, the response time (case of unsteady measurements), the size and cost. Due to the large number of orifices which must equip a model to have a precise and complete information on the distribution of the pressure on its surface, several orifices are most often connected to a common transducer via a *scanning device*. In the classical method, the pressure transducer is installed in a mechanically driven scanner, each of the pressure ports of the scanner being successively connected to the transducer. These scanners offer good accuracy at relatively low cost, but they are limited to low scanning rates (a few readings per second).

The advent of *electronic pressure scanners* has permitted a considerable increase in scanning rate (up to 20,000 ports per second). The electronic pressure scanner consists of an array of transducers, each in contact with its own pressure port. The transducer is a Wheatstone bridge diffused into a single silicon crystal using semiconductor processing. The voltage outputs from the transducers are input to a digitally addressed multiplexer so that transducer's output can be selectively scanned or measured. The

scanner most often includes a calibration valve placing the transducers in contact with a known pressure before performing the test. The electronic scanners are small enough to be installed in the models, close to the orifices to minimize the response time. The number of transducers per scanner is generally in the range 20 to 50.

Recently a completely new technique has been proposed to determine the entire pressure distribution over a model. It calls upon the use of *pressure sensitive paints* [2.2.2]. This method is based on the fact that some compounds emit light when excited by a suitable source, the emitted light having a longer wave-length than the excitation light. The quantity of light emitted depends strongly on the oxygen diffused into the paint because oxygen quenches and deactivates the excited molecules. Since the internal concentration of oxygen is a linear function of the external pressure of the same gas, one can measure the pressure acting on the paint by detecting some of its luminescent parameters (for details on this technique see Section 3.3.5).

#### 2.2.2.3. Skin Friction Measurements

Accurate measurement of skin-friction is a delicate task, especially in regions of strong pressure gradient. The most direct method is to use a *floating element* made of a small independent insert, mounted flush with the model surface and isolated from it [2.2.3,4]. The element is fixed to a balance which measures the force exerted by the flow on it. This is the most straightforward method to obtain the skin-friction since it does not rely on any theoretical considerations about boundary layer properties. However, in practice the floating element technique is difficult to implement on real models because of the curvature of their surface. Also, a major source of error comes from misalignment of the sensing part with the surface and from the influence of pressure gradients. The floating element technique can be used to calibrate other techniques by considering a simple flat plate situation in which this method can be made very accurate.

A more practical technique is to use surface gages made of a *thin heated film* or wire installed on the model surface, the film being mounted to an insulating part [2.2.5,6]. The measure of the film resistance gives its temperature change due to the cooling or heating action of the flow. The skin-friction determination is based on the Reynolds analogy between heat transfer rate and skin friction. In fact, the device must be calibrated and its output can be difficult to interpret in supersonic flows [2.2.7]. Nevertheless, hot film gages have been - and are still - used with success, even in hypersonic flows, their essential advantages being their small size, which allows a local measurement, and their short response time (hence their general use in hypersonic facilities [2.2.8]). In principle, it is possible to determine the skin-friction in three-dimensional flows, when the shear stress at

the wall is a two-component vector, by placing two gages making an angle between them on the model surface [2.2.9]. Other techniques have been proposed to measure the skin-friction in two- and three-dimensional flows (buried wire, surface fences, etc) that will not be described here [2.2.10,11].

Another popular method is the so-called *Preston tube* which consists of measuring the pressure given by a Pitot type tube, flattened at its extremity, placed in contact with the surface (the sensing part is sometimes made of a razor blade attached to the surface with a static pressure orifice underneath) [2.2.12-14]. The skin-friction is then indirectly deduced from the measured pressure by relying on an assumed law for the velocity distribution in the wall region of the boundary layer. This device also requires calibration.

More recently, it has been proposed to determine the skin-friction by measuring the rate of deformation of a *thin oil film* deposited on the model surface. The shear stress at the wall is then deduced from the lubrication theory [2.2.15-18]. If the film of oil is thin compared to its length, its surface takes the shape of a small wedge which practically does not affect the flow. If  $\mu$  designates the oil viscosity,  $\tau$  the wall shear stress,  $t$  the time,  $y$  the film thickness at the distance  $x$  from the wedge apex, then one has:

$$y = \frac{\mu x}{\tau t}$$

The thickness  $y$  at any time  $t$  can be accurately measured by a classical interferometric technique. Thus, knowing the location  $x$  of the measurement point and the time  $t$ , the determination of  $\tau$  is theoretically straightforward. In fact, the time origin of the oil film is not well known since it depends on the tunnel starting transients. Also, the wedge origin can be difficult to find. A way to avoid these difficulties to measure the oil thickness at two distinct, but close, points. Then, one can determine in a simple manner the effective "time" and "origin" of the oil film and deduce the skin-friction (for details, see Ref. [2.2.18]). The method can be extended to three-dimensional flows but in this case a knowledge of the direction of the skin-friction vector is most often required [2.2.19,20].

It is also possible to consider the use of *liquid crystals* to determine the skin friction distribution on a model [2.2.21]. As their name implies, liquid crystals are substances which exhibit crystalline type properties while still remaining in a liquid state. Liquid crystals are optically active mixtures of organic compounds which have the ability to reflect light of a particular wave-length changing in response to certain physical stimuli: temperature, pressure, shear stress, magnetic and electrical fields, etc. Considering wind tunnel applications in which temperature, pressure and shear stress are of interest, it is possi-



ble to retain only one stimulus by suppressing the response to the other stimuli. Thus, one can find compounds which only respond to shear stress under certain circumstances (or to temperature for heat transfer measurements, see below). In practice, the model is covered by a thin film of the substance and illuminated by an appropriate source of white light. The liquid crystal film produces a picture in the visible wave-length range which is recorded either on a photographic plate or by a video camera

The liquid crystals technique presents several advantages: its very high sensitivity, reversible nature and capacity to provide information on a whole surface at once. Thus, liquid crystals are frequently used to locate the boundary layer transition from laminar to turbulent on a model, the transition process being well visualized by a change in colour. Quantitative measurement of shear stress by liquid crystals are, in principle, possible by determining their colour change under the action of the shear stress. An analysis of the picture by means of video digitizing techniques and the use of a suitable processing of the signal allow the determination of the wave-length  $\lambda$  of the reflected light. Then the local value of the shear stress  $\tau$  can be found by a calibration giving  $\tau$  with  $\lambda$ . However, such measurements seem to be very delicate and, to our knowledge, applications of this method to afterbody flow studies have not yet been published.

#### 2.2.2.4. Surface Heat Transfer Measurements

The local convective heat transfer between the flow and the model surface is frequently determined by using calorimetric techniques which consist of measuring the time variation  $T(t)$  of the local temperature of the surface or of a sensing element (transducer) inserted into the surface. Then, an inverse solution of the equation governing heat conduction through the model wall or transducer gives the heat supplied by the flow to the surface. In practice, simplified forms of the heat conduction equation are used by considering extreme situations leading to simple analytical solutions [2.2.22,23]. For example, if heat conduction in the material constituting the model is assumed one-dimensional and if the wall can be considered as semi-infinite in depth - the so-called thick wall technique - then one has the solution:

$$(1) \quad q(t) = \sqrt{\frac{\rho_m c_m \lambda}{\pi}} \int_0^t \frac{\frac{dT(\tau)}{d\tau}}{\sqrt{t-\tau}} d\tau$$

in which  $q(t)$  is the heat transfer rate (energy/unit time/unit surface),  $\rho_m$  the density of the material constituting the wall,  $c_m$  its specific heat,  $\lambda$  the thermal conductivity. If the heat transfer rate can be assumed constant over the time of measurement, one obtains the still simpler form:

$$(2) \quad q(t) = \frac{\sqrt{\pi \rho_m c_m \lambda}}{2} \frac{T(t)}{\sqrt{t}}$$

Another extreme situation - the so-called thin film technique - is obtained if the wall can be considered as infinitely thin; then the heat transfer rate is given

by:

$$(3) \quad q(t) = \rho_m c_m e \frac{dT(t)}{dt}$$

where  $e$  is the wall thickness. In the thin wall method, the model wall must be a metallic skin whose thickness is of the order of a few tenths of a millimeter, which makes the use of this technique difficult for models having a complex shape. Thus, knowing the material properties - its effusivity  $\sqrt{\rho_m c_m \lambda}$  - the heat transfer rate is computed by formula (1), (2) or (3) from a recording of the time history  $T(t)$  of the wall temperature. The above methods most often require a rapid establishment of the flow past the model in order that the heat flux be nearly instantaneously applied. This condition is achieved either by working in a quick starting wind tunnel or by injecting the model into the flow field after establishment of the nominal flow conditions.

The simplifying assumptions underlying the above formulae are not always satisfied; the local curvature of the wall can be large, the heat transfer is not constant with time, conduction is not one-dimensional (lateral conduction can be important), the material properties vary with temperature and the wall is neither "thick", nor "thin"... In these cases, correction terms must be introduced. A more rigorous processing technique is to solve the complete heat conduction equation by a numerical method, which now becomes possible with the advent of computerized processing methods.

There exists a variety of techniques to measure the wall temperature, the most commonly used in wind tunnel applications being thermocouples, inserted in the model wall and in contact with the surface, and surface films (frequently platinum films) similar to those used to determine the skin friction. The films are most often deposited on an insert made of thermally insulating material to minimize losses by lateral conduction.

The above techniques cannot be used if the flow is adiabatic; i. e., if the stream and the model are in thermal equilibrium which is frequently the case in transonic and supersonic continuous wind tunnels. Then, the calorimetric method must be modified by inserting a heat source - an electrical resistor - in the model wall, near the thermocouple or hot film. The convective heat transfer due to the flow is then deduced from the energy which must be supplied to maintain the surface at a certain temperature [2.2.24].

Classical calorimetric techniques have reached a high degree of sophistication and they are widely used to perform heat transfer measurements, even in extreme conditions. They are generally considered as the most reliable techniques. Their main disadvantage is that they perform local measurements, which is a guarantee of good spatial resolution, but which necessitates the installation of a large number of gages or thermocouples if the heat transfer distribution

over a complex shape is to be determined (on some models of hypersonic vehicles, several hundred thermocouples are installed).

Methods like the use of thermosensitive paint or infrared thermography do not have this disadvantage since they can provide the heat transfer distribution over the entire model, at the price of an accuracy which is not always well assessed.

In the *thermosensitive painting* technique the model, made of a thermally insulating material, is covered by a special paint whose colour depends on the surface temperature, changing from green-blue, to yellow, brown and black as its temperature rises; the colour changes take place at well defined temperature levels [2.2.25]. To determine the heat transfer, the variation in colour during the wind tunnel run is filmed. Then, an analysis of the film frame by frame allows the determination of the temperature history of the model surface by noting times where changes in colour occur. This procedure is most often calibrated by comparison with colour changes on a shape for which temperature distributions are well known (a sphere, for example). Then application of appropriate heat conduction formulae gives the local heating at any point where colour changes have been analyzed. Also, direct calibration can be used by comparing the colour changes with those occurring on a sphere on which the heat transfer distribution is known. This technique is very powerful since it can give the entire heat transfer distribution over a complex model from a single run and without having to build costly equipment. The main shortcoming of the method is its irreversible character, in the sense that the colour changes are not reversible, which renders impossible the immediate re-use of the model. Also, the processing, which is frequently done "by hand", is time-consuming and somewhat subjective (more objective and rapid methods are now developed based on processing of digitized video pictures). In addition, measurements on parts of the model having a small radius of curvature, where the heat transfer rates tend to be very high, are inaccurate.

As mentioned above, *liquid crystals* also respond to temperature by changing their colour, giving the possibility to determine the heat transfer by recording the temperature history of the model. Thus, the non reversible character of classical thermosensitive paint can be overcome. However, this promising technique seems more delicate to apply [2.2.26].

Over the past 15 years quantitative *infrared thermography* has experienced a strong development in a large number of laboratories [2.2.27-29]. As it is well known from basic physics, a body emits a radiative signal whose intensity is a strong function of its temperature  $T$ . One generally distinguishes between the total intensity radiated over the whole spectrum and the intensity radiated on a particular wave-length  $\lambda$ . For the so-called *black body*, the radiated energy is

given by the Planck law. Thus, the energy per unit of time (power) radiated in a certain direction  $OX$  by a unit surface of the black body - the radiative flux - is given by:

$$L_{\lambda}^0 = \frac{2hC^2\lambda^{-5}}{\exp\left(\frac{hc}{\lambda T}\right) - 1}$$

where  $h$  is the Planck constant,  $k$  the Boltzmann constant and  $C$  the speed of light.

The radiative property of a real body is characterized by a factor called its *emissivity*  $\epsilon_{0X}$  which is defined as the ratio between the intensity  $L_{0X}$  of the light radiated by this body to the intensity of light radiated by the black body at the same temperature. Hence:

$$L_{0X} = \epsilon_{0X} L_{\lambda}^0$$

In infra-red thermography, the model is observed by an infrared camera, containing a detector element, sensitive to infrared radiations at a certain wave-length. A sweeping mechanism, made of prisms or mirrors, operates a line by line analysis of the model optical image, the system delivering an electrical signal which is recorded for appropriate processing. Since the signal delivered by the camera is proportional to the radiative flux  $L_{0X}$ , it is necessary to convert this information into temperature in order to construct the temperature map of the model. This can be done by calibrating the system by observing a black body whose emissivity and temperature are known. One can also calibrate by placing thermocouples on the model to provide the temperature at well chosen points. Then, a thermal picture of the model is obtained in which regions at different temperatures are portrayed by different levels of grey or with different (false) colours. This qualitative aspect of thermography is very useful to detect laminar-turbulent transition, for example [2.2.30].

By processing a series of pictures taken at known time intervals, it is possible to construct the time history of the model temperature and to deduce the surface heat transfer distribution by means of the heat equation.

The method is very powerful, in the sense that it gives a complete picture of the heat transfer distribution over the entire model, it is very sensitive and reversible (the model does not have to be changed between each test). On the other hand, it requires a test section window made of a material transparent to infra-red radiations (except if the camera can be installed inside the test section). Accuracy can deteriorate unless the surface viewed by the camera is within a small angle or perpendicular to the surface and parasitic radiations due to external heat sources can perturb the measurements.



### 2.2.2.5. Surface Flow Visualizations

The aim of surface flow visualization is to reveal what are called the limit, or wall, streamlines which are defined as the limit of the flow streamlines when the distance  $y$  to the wall goes to zero. For a Newtonian fluid, it can be demonstrated that the limit of the velocity vector direction, when  $y \rightarrow 0$ , is colinear with the shear-stress vector at the wall (or skin friction vector); hence the concept of skin-friction line, defined as a line of force of the skin-friction vector field. Wall streamlines and skin-friction lines are in principle identical. However from a sounder physical point of view, it seems preferable to adopt the skin-friction line concept which is clearly and unambiguously defined from a physical and measurable quantity, rather than the concept of limit streamline which results from a passage to the limit sometimes questionable. The set of the skin-friction lines covering an obstacle is called the surface flow pattern.

To realize a surface flow visualization, the model - or part of it - is coated by a more or less viscous product before the establishment of the flow. The postulate of such visualization techniques is that the traces or streaklines resulting from the shearing action of the flow on the product can be identified with skin-friction lines. This supposes that the coating is thin enough not to influence the flow in the near wall region and has the right viscosity to be entrained, without being swept out, by the flow. Visualization products are frequently made of an oil (machine or silicone oil) or carrier liquid (water, kerosene) intimately mixed with a dying agent. Different colours may be used to visualize complex surface flows. There is not a general "recipe" to make a good product. The quality of the flow visualization produced depends on the nature and viscosity of the oil, the dye and the recording technique as well as on the velocity, pressure and temperature of the flow to be investigated. Wind tunnel operation (blow-down, continuous, etc) mode can also affect the results.

In two-dimensional or axisymmetric flows, surface visualizations are valuable, first to check the two-dimensional or axisymmetric character of the flow and secondly to detect possible separation or reattachment phenomena. For three-dimensional configurations, surface flow visualizations are more important since then the surface pattern is the imprint on the body of the outer flow structure which can be far more complex than in two-dimensional flows. In most circumstances of practical interest, the surface pattern of a three-dimensional field exhibits special and typical features revealing the existence of *critical points* and *separator lines* in the set of the skin-friction lines surrounding the model. The rational interpretation of these features call upon the Critical Point Theory whose presentation, even briefly, would be far beyond the scope of the present document [2.2.31,32]. Let us simply recall that among

the critical points, one distinguishes nodes, foci and saddle points, a separator line being a skin-friction line passing through a saddle point. Separators can be of the separation or attachment type depending on the flow behaviour in its vicinity. It is the careful inspection of the surface flow pattern, with detection and identification of its critical points and separation/attachment lines, which provides a first firm idea about the structure of the whole flowfield. Separation lines are the trace on the body of separation surfaces whose rolling-up will constitute the vortical structures of prime importance in separated three-dimensional flows. Thus, a good surface flow visualization is a prerequisite to any further investigation of the flowfield by probing techniques.

### 2.2.3. Classical Intrusive Techniques for Field Measurements

#### 2.2.3.1. General Remarks

To a large extent, flowfields are still explored by means of physical probes, like Pitot tubes, thermocouples and hot wires which give extremely instructive information about the flow structure and which are easy to handle. In spite of the existence of more sophisticated methods, their use must not be discounted and in many cases they provide reliable and accurate measurements at a relatively low cost. The main disadvantage of intrusive probes is their perturbing effect which renders their use impossible in separated flows or extremely delicate at transonic speed. Furthermore, the probes must be firmly held and displaced in the flow to execute traverses, which requires displacement systems whose size can be prohibitive in some circumstances. In addition, if a hot jet is simulated, the probe must be able to withstand high temperatures without melting or distorting itself. A stagnation temperature of 1200K is an upper limit for the use of simple probes; above this limit the probes must be cooled which complicate their fabrication and handling. In small scale facilities, the deformation and vibration of probes is a major problem since this may introduce a large uncertainty on the exact location of the measurement point.

#### 2.2.3.2. Pressure Probes

The *stagnation pressure* in a flow is classically measured by using a Pitot tube. Frequently the sensing part of the Pitot tube is flattened to allow a closer approach to the model surface which is essential to probe boundary layers (a minimum thickness of 0.2mm can be achieved). Also, flattened probes are used in thin mixing zones, like those developing at the edge of a jet. Measurement of the *static pressure* within a flowfield is more difficult since pressure is an intrinsic and local property of the fluid which cannot be directly determined. The only way to determine the static pressure - by probes - is in fact to measure a surface pressure given by an orifice. Two types of static pressure probes are commonly used:

- Conical type probes consist of a long cylindrical tube, with a conical and elongated tip. Pressure orifices are placed on the cylindrical part at some distance downstream of the tip (at least 10 diameters). It is then assumed that the pressure given by these orifices is equal to the static pressure of the flow upstream of the probe.

- Wedge type probes are made of a cylindrical tube equipped with a tip made of a small angle wedge with pressure orifices on each face, the pressure at the level of these orifices being assumed equal to the upstream static pressure.

In gently varying flows (low pressure gradients), these probes (which can be calibrated) give accurate results. However, their use in regions of rapid pressure variation becomes questionable as the pressure at the level of the orifices can be very different from the effective flow pressure. In such situations, the results given by the wedge type probe seem of better quality.

Pressure probes are also routinely used to determine the mean velocity vector in three-dimensional flows. For this purpose, *multi-hole* probes are constructed, the simplest arrangement being the three-hole pressure probe. This kind of probe is made of three orifices disposed as shown in Fig. 2.2.1 [2.2.33]. The central orifice acts as a Pitot tube; the two lateral orifices are symmetrically placed and made of slanted holes. Frequently, the probe is made of three tubes, welded together and flattened to reduce the thickness of the sensing part. The probe is sometimes curved in shape to allow the sensing element to come in contact with the surface, hence its name: "cobra probe". This kind of probe is mainly used to investigate boundary layer flows, in which the velocity vector is contained in a plane parallel to the surface of the model. The thickness of the flattened part can be as small as 0.2mm, the width being close to 1.5mm. The sensing extremity being set in such a way that the three orifices are in the plane containing the velocity vector, the magnitude of the velocity is deduced from the indication  $p_3$  of the central orifice and the local pressure measured at the surface.

The direction  $\beta$  of the velocity vector results from the pressure difference  $\Delta p = p_2 - p_1$  between the two lateral holes. The most accurate procedure is a zeroing method in which the probe is rotated until the pressure difference  $\Delta p$  cancels out. Then the direction of the probe axis can be identified with the velocity direction  $\beta$ . In fact, since this procedure is very much time consuming,  $\Delta p$  is measured and  $\beta$  as well as the true stagnation pressure are deduced from calibration curves. It is usual to introduce the following coefficients:

$$C_{p\beta} = \frac{p_2 - p_1}{\bar{Q}}, C_{p_{st}} = \frac{p_3 - p_{st}}{\bar{Q}}$$

with:  $\bar{Q} = (p_3 - p_0) - p_m$  and  $p_m = \frac{p_2 + p_1}{2}$

Calibration curves are of the form:  $C_{p\beta} = f(\beta)$  and  $C_{p_{st}} = g(\beta)$ .

Having measured  $p_1, p_2, p_3$  and the upstream reference pressure  $p_0$ , the first calibration curve gives the flow direction  $\beta$ ; the second curve allows the determination of the stagnation pressure  $p_{st}$ . The local static pressure being identified with the pressure measured at the wall (boundary layer basic assumption), the Mach number can be computed from the isentropic or Pitot formula according to the subsonic or supersonic nature of the local flow. The readings from this kind of probe can be sensitive to Reynolds number effects, proximity of the wall can also influence the measurements for distances less than 0.3mm.

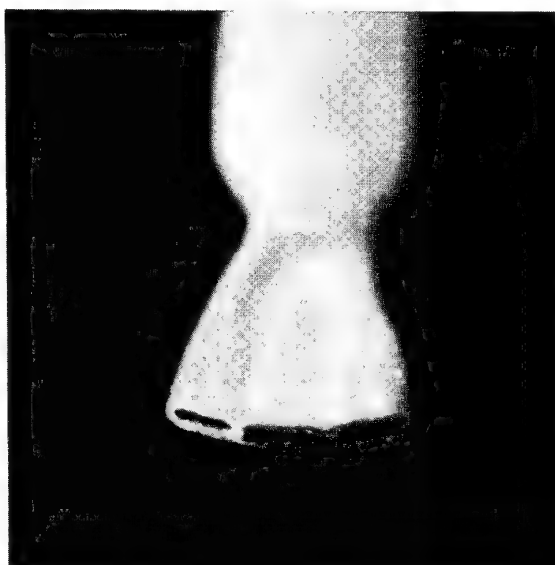
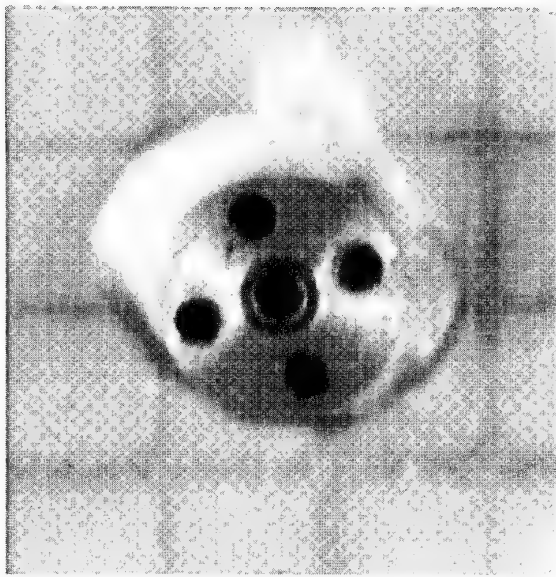
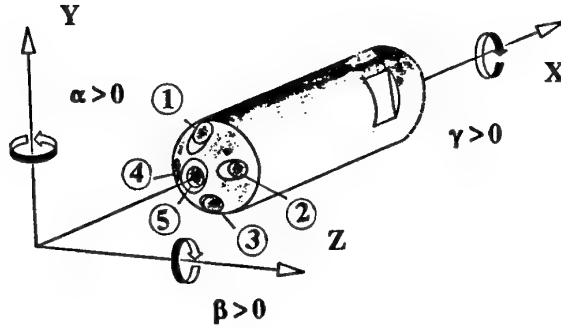


Fig. 2.2.1 - Sensing part of a three-hole pressure probe (thickness = 0.1mm)

Three-hole pressure probes give correct results as long as the velocity vector remains in the same plane and provided that the angle between the probe axis and the velocity vector is not too large, a maximum being  $40^\circ$ . If the third component of the velocity is comparable to the two other components, a truly three-dimensional probe must be used. The most common three-dimensional probe is the *five-hole* pressure probe whose arrangement is sketched in Fig. 2.2.2 [2.2.34,35]. The sensing extremity is most often made of a cone on which four independent orifices are machined, a fifth hole being placed at the cone apex. The conical part is mounted on a cylindrical tube through which pass the five pressure tubes to the transducers. The diameter of this probe can be as small as 1.5mm. Smaller diameters can be realized, but then the response time may be

come prohibitive. Numbering the orifices as shown in Fig. 2.2.2, the pressures  $p_1$ ,  $p_2$ ,  $p_3$ ,  $p_4$  and  $p_5$  are measured. Orientation of the velocity with respect to the probe axis is defined by angles  $\alpha$  and  $\beta$  shown in Fig. 2.2.2 and the probe axis is defined by angles  $\theta$  and  $\varphi$ , with respect to the "absolute" or "laboratory" system. The calibration is made by determining the following coefficients as function of the Mach number and angles  $\theta$  and  $\varphi$ :



**Fig. 2.2.2** - Sensing part of a five-hole pressure probe (diameter = 1.5mm)

$$C_{p, st} = \frac{p_5}{p_{st}}$$

where  $p_{st}$  is the stagnation pressure in subsonic flows and the Pitot pressure in supersonic flows.

$$C_{ps} = \frac{p_m}{p_5} \quad \text{with} \quad p_m = \frac{p_1 + p_2 + p_3 + p_4}{4}$$

$$K_\alpha = \frac{p_4 - p_2}{p_5 - p_m}, \quad K_\beta = \frac{p_3 - p_1}{p_5 - p_m}$$

$$K_\theta = \sqrt{K_\alpha^2 + K_\beta^2}, \quad K_\varphi = \tan^{-1} \left( \frac{K_\alpha}{K_\beta} \right)$$

In the probing of an unknown flowfield, the five pressure  $p_{i's}$  are measured and the above coefficients are computed, from which the magnitude and direction of the velocity vector, the local Mach number and static pressure are determined from calibration matrices. This kind of probe can be used in a velocity domain ranging from low subsonic to high supersonic Mach numbers and provide accurate and reliable results. The primary limitation comes from the maximum allowable angle between the probe axis and the velocity vector. In this case,  $40^\circ$  is an upper practical limit.

Probes having more than 5 holes have been developed to introduce redundancy in the measurements and to extend their domain of application, however their use seems less common than that of the five-hole probes.

### 2.2.3.3. Temperature Probes

The stagnation temperature of a stream is classically measured by means of a probe made of a thermocouple whose junction is chosen according to the temperature range to be measured. The simplest arrangement is made of a bare junction placed in the flowfield. This type of probe, whose size can be extremely small, has a short response time and gives very good results. However, its response is affected by a coefficient depending on the Mach number of the flow, which necessitates a careful calibration of the probe.

The response of the probe can be improved by using an arrangement where the thermocouple junction is placed inside a tube through which a low velocity air-flow is established by means of holes located in the downstream part of the tubing. This kind of *ventilated probe* has better operation conditions than the previous one, its disadvantage being its larger size.

Stagnation temperature measurements are delicate, and for this reason often inaccurate:

- The response of the thermocouple junction is a function of its shape and size. Short response times require extremely small junctions so that one must be cautious when making measurements in a blow-down facility.

- The indication of the sensing element can be affected by thermal losses due to convection in the stream, conduction through the thermocouple holder and radiation. These effects can differ in proportion according to the flow region which is probed, hence, their representation by means of a calibration curve may be incomplete.

#### 2.2.3.4. Anemometric Measurements

Conventional anemometric measurements are made by *hot wires*, and to a lesser extent by hot films. The principle of hot wire anemometry is well known and needs not to be repeated here in detail [2.2.36]. In practice, hot wires are mainly used to perform detailed turbulence studies at subsonic velocities. Their use has been extended to transonic and supersonic flows, at the price of more complex calibration and data processing procedures [2.2.37,38]. Typical dimensions of a hot wire are a diameter of 5 to 10  $\mu\text{m}$  and a length of 1 to 2 mm. In high speed flows, wires of diameter as small as 2.5  $\mu\text{m}$  are used. The main advantage of a hot wire is its very short response time which allows its use to make high frequency unsteady measurements (the maximum band pass can be in excess of several 100kHz).

Two different modes of operation are adopted, depending on the kind of measurements to be performed:

- In the *constant current* mode, the intensity of the electrical current traversing the wire is maintained constant and one measures the variation of voltage at its extremity resulting from the change in its resistance due to the cooling effect of the flow.

- In the *constant temperature* mode, the resistance of the wire is kept constant by varying - through an appropriate electronic circuit - the intensity traversing the wire.

A hot wire produces a signal whose processing allows the determination not only of the mean flow velocity but also of its fluctuating component. Analog or numerical treatment then permits the calculation of the various statistical moments of the fluctuating variable: RMS values, Skewness, Flatness factors, etc. Because of the fast response time, power spectra can be constructed and a vast amount of information in the temporal domain can be gathered, which gives indication on the turbulence scales. Single and multi wire probes exist: the classical X-wire probe is made of two slanted wires giving two velocity components  $U$  and  $V$ , their RMS values and the correlation (or Reynolds shear stress)  $\overline{u'v'}$ . Three-dimensional measurements can be made by means of four-wire probes which give the complete velocity vector and the full Reynolds tensor. However, because of their fragility in high speed flows hot-wire probes are essentially used for basic turbulence studies and, to our knowledge, have been rarely employed to probe

the flow induced by an afterbody with jet (although they are intensively used to investigate turbulence in jets and mixing layers). Four-wire probes lead to complex calibration and data processing procedures. In addition, hot-wire probes are ineffective in separated flows and cannot be used in high temperature jets. These reasons lead to the consideration of non-intrusive optical techniques which do not suffer from these shortcomings but which are still able to perform reliable spectrum measurements.

#### 2.2.4. Non Intrusive Techniques for Field Measurements

##### 2.2.4.1. Introductory Remarks

All non intrusive methods are based on optical techniques, which confers them spectacular advantages, but put severe limitations on their general application. Apart from the specific problems of data processing and interpretation, that we shall consider below and which are inherent to the techniques themselves, the use of optical methods imposes stringent conditions on the experimental arrangement. Thus, the zone of interest must be accessible, with a sufficiently large field, for the radiations employed by the optical system. This obvious and first condition is not always easy to satisfy in commonly used wind tunnels or test rigs. Hence, the test section must be equipped with properly sized transparent windows made of high quality glass (a condition particularly severe for classical interferometry). If non visible radiation is used - in the infra red, for example - the windows must be made of special material, like quartz or zinc seleniur. This difficulty can be circumvented by placing the apparatus in the test section or if the experiments are performed in the open atmosphere.

Correct focusing of the beams may impose a maximum admissible length for the distance between the measurement point and the optics, thus precluding the use of some of these techniques in large facilities. Mechanical vibrations or intense acoustic waves can damage delicate optical components, which can prevent measurements on engine test rigs. Good visibility through the windows is indispensable. This apparently trivial condition can be critical if pollution by the flow itself or injected particles of a tracer tend to obscure the windows.

A class of optical methods is based on the deviation of a light beam caused by variations of the refractive index occurring in regions of a compressible flow where the velocity, hence the density, is varying rapidly. For a gas, air in most applications, the refractive index  $n$  is linked to the local density  $\rho$  by the Gladstone-Dale law which is written:

$$n = B\rho + A$$

where  $A$  and  $B$  are two constants.

Thus any variation in the optical properties of the flow which can be detected by an appropriate method can be related to the variation of its density. In these conditions, we can expect that regions where  $\rho$  varies rapidly will be made visible: shock waves, centered expansion waves, mixing zones, boundary layers.

#### 2.2.4.2. Optical Visualization Techniques

Although they are classical and, for this reason, do not need explanation, it is worth to cite schlieren and shadowgraph techniques which are widely and routinely used to visualize high speed flows. Let us simply recall that the schlieren technique is sensitive to gradients in the density and the shadowgraph to the second space derivative of  $\rho$ . In two-dimensional and axisymmetric flows, these techniques allow a clear identification of the structure of the flow, showing the system of compression and expansion waves or shocks forming in a non adapted jet and also the interaction with the outer stream. For instance, schlieren / shadograph pictures can reveal the shock forming on the afterbody boattail at high subsonic speed and the separated zone caused by this shock or by the expansion of the propulsive jet.

In conventional schlieren systems, the focus extends essentially through the entire region between the two mirrors, placed on each side of the test section, to form the beam of parallel light traversing the observed flow. The result is that the system gives sharp images of all the flow features crossed by the beam. Thus, in three-dimensional flows, such schlieren pictures are difficult to interpret. In *focusing schlieren* systems, which we shall not describe here (for details see Ref. [2.2.39]), objects go out of focus in a fairly short distance. Thus focusing schlieren systems show effects of the density variation in a narrow slice of the flow normal to the optical axis. If the flow is steady, or if only averaged features are observed in a turbulent flow, the focal plane slice can be moved through the test volume to obtain a three-dimensional record made of images recorded at different times. If a three-dimensional record is required at a single time, holography can be used and the slices at different depths can be examined from the reconstructed images.

Special optical arrangements, such as *conical shadowgraphy*, have been developed to make observation in planes perpendicular to a direction along which the flow adopts a conical similarity [2.2.40].

Spark photographs, with an exposure time of  $1\mu\text{s}$  or less, are especially instructive since they give a vivid picture of the flow by enhancing discontinuities and showing turbulent structures which are frozen in their displacement. Coupled with high speed cinematography, spark photographs are invaluable to detect and qualify unsteady phenomena, more likely to occur in case of separation.

With the exception of the focusing schlieren system, the above methods can be of limited help in complex

three-dimensional flows where interpretation of the pictures is difficult. Some view of the flowfield structure can be obtained by performing what is called light screen, or light sheet or vapor screen visualization [2.2.41,42]. The basic principle of these methods is to introduce particles in the flow and to observe the light scattered by these particles when they are strongly illuminated (Mie scattering in this case). One may use droplets of water or the smoke generated by combustion of an appropriate oil as tracers. In most present applications, the light sheet is produced by a laser whose beam is expanded into a plane by a glass cylinder or a combination of lenses. Very impressive pictures can be obtained showing the traces of vortices, boundary layers or shock-waves.

We will cite among these methods: *Particle Image Velocimetry (PIV)* because its basic principle is also to illuminate particles by a laser sheet and to observe the scattered light [2.2.43]. The major difference, is that PIV is a quantitative technique performing a measurement of the flow velocity. For this purpose, two laser pulses, separated by a short and known time interval  $\Delta t$ , are emitted to provide two images recorded on the same photographic plate. During the interval  $\Delta t$  each particle has moved over a distance proportional to its velocity (assumed to be that of the flow), giving two images on the plate. Thus, by measuring the displacement of the particle, one can deduce immediately the velocity component contained in the plane of the image. The main difficulties in PIV come from the processing of the photographic plates, which must be done by automated procedures using sophisticated algorithms to identify the particles and follow them in their displacement. The most convincing applications of the method are still restricted to low speed flows.

#### 2.2.4.3. Interferometry

Interferometry has long been used to visualize compressible flows where it gives spectacular pictures of the field. However, in addition, interferometry can provide quantitative information in a straightforward - if not always easy - way, which makes it a valuable tool to investigate some basic properties of high speed flows in the transonic and supersonic ranges. It is recalled that the principle of interferometry is to record on a photographic plate the interference of two waves coming from the same monochromatic source:

- One wave, constituting the so called *study beam*, traverses the flow under investigation;
- The other beam, the *reference beam*, passes outside the test section, thus traversing an unperturbed medium.

The two waves will interfere on the plate giving interference fringes which are lines of equal optical path:  $L = \int \nu(l)dl$  where  $\nu$  is the index of refraction and  $l$  the geometrical path of the beam. If the flow is perfectly uniform, and the interferometer appropri-

ately adjusted, the plate will be covered by a unique white fringe giving a uniform illumination. If the flow is non uniform, variations  $\Delta\rho$  of its density will result in variations  $\Delta\nu$  of the index of refraction  $\nu$  (see above) leading to variations of the optical path  $L$  (the geometrical length  $l$  being kept constant by construction). Hence, the study wave will be distorted and interference fringes will form to constitute an *interferogram* of the flow.

Let us consider, to simplify, the case of a two-dimensional flow in a test section of span  $b$ . Then, the variation in optical path introduced by the flow at any point is given by:

$$\Delta L = \Delta\nu b$$

Starting from a reference fringe, the variation in optical path between two points R and M in the field can be computed from the numbering of the fringes by using the formula:

$$\Delta L = \lambda(N_M - N_R) = b(\nu_M - \nu_R)$$

in which  $\lambda$  is the light wave-length,  $N_M$  and  $N_R$  designating the fringe numbers at M and R, respectively.

If the flow is two-dimensional,  $\rho$  does not vary with the spanwise direction and the span of the test section  $b = l$  being constant and known, the value of  $\rho$  at a point located on fringe  $N_R$  is obtained by the relation:

$$\rho_M = \rho_R + \frac{\lambda}{bB} (N_M - N_R)$$

where  $\rho_R$  is the value of  $\rho$  corresponding to the reference fringe  $N_R$ . The value  $\rho_R$  is determined by considering a fringe passing in a region where the flow is uniform and where the pressure and the temperature can be measured.

In practice, each fringe - white or black - will be identified with its middle line, i. e., the location where the light intensity passes through a maximum or a minimum (in principle, it would be possible to consider fractions of fringes, but their localization would be inaccurate). Thus, the major problem in the processing of an interferogram is to determine with accuracy the middle of each fringe from the photographic plate. This determination can be made by using a microdensitometer which measures the optical density of the plate [2.2.44]. The apparatus can be linked to a computer which commands the displacement of the analyzed point along a pre-programmed path and records the values of the optical density at each point. Then, by a proper processing of the data, the middle of each fringe is determined and the value of density computed, the end product being the distribution  $\rho(X, Y)$  in the investigated field. More advanced techniques, based on video systems with CCD cameras can also be used to record and process the interferograms.

The above mode of operation, in which the plate is uniformly illuminated if the flow is perfectly uniform, is called the *infinite fringe* mode of operation. With this adjustment of the apparatus, fringes (or more exactly their middle) can be identified with lines of constant density, hence lines of constant Mach number, pressure, etc, if the flow is isentropic. However, in most cases where the density variations are moderate, the number of fringes is small, which limits the number of measurement points, since in practice only the middle of the fringes can be detected with accuracy. In order to increase the number of measurement points, the *finite fringe* mode of operation is frequently adopted. In this case, an optical part of the interferometer - a mirror for example - is adjusted in order to introduce a linear optical path variation throughout the flowfield at rest. Then, a

pattern of parallel fringes forms in the absence of flow, which is recorded on a first photographic plate. When the flow is established, it introduces density changes which cause a distortion of the reference fringe pattern. This new pattern is recorded on a second photographic plate. Density is then computed by processing and comparing the two fringe patterns. The method used, which is slightly more involved than that for the infinite fringe mode, will not be explained here [2.2.45].

Interferometry can also be used in axisymmetric flows without major changes in the mode of operation, compared to the two-dimensional case. The only differences lie in the processing method since then the relation between fringe numbers and the change in the optical path is not simple, the field being no longer uniform in the spanwise direction. For this case, the determination of  $\rho$  necessitates the inversion of an Abel integral by means of classical methods [2.2.46]. The possibility of investigating axisymmetric flows by interferometry is of great interest for afterbody applications. Thus, interferometry was extensively used to define the transonic domain of sonic nozzles and to determine their discharge coefficient [2.2.47]. An example of such a result is given in Fig. 2.2.3. Also, interferometry was valuable in measuring the expansion rate of the mixing zone of a turbulent jet at supersonic Mach numbers [2.2.48].

The classical interferometric technique usually uses Mach-Zehnder type interferometers (see Fig. 2.2.4) whose adjustment is a delicate task because of the extremely short coherence length of ordinary light. Thus, the optical paths of the study and reference beams must be made nearly equal with a tolerance corresponding to a few wave lengths. This necessitates the use of interferometric quality glass and the introduction of a pair of compensation windows in the path of the reference beam to compensate for the change in optical path caused by the test section windows.



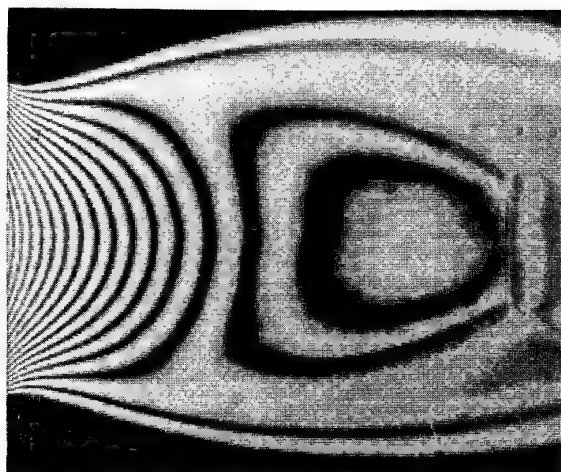


**Fig. 2.2.3** - Interferogram of the transonic flow issuing from a conical ejector

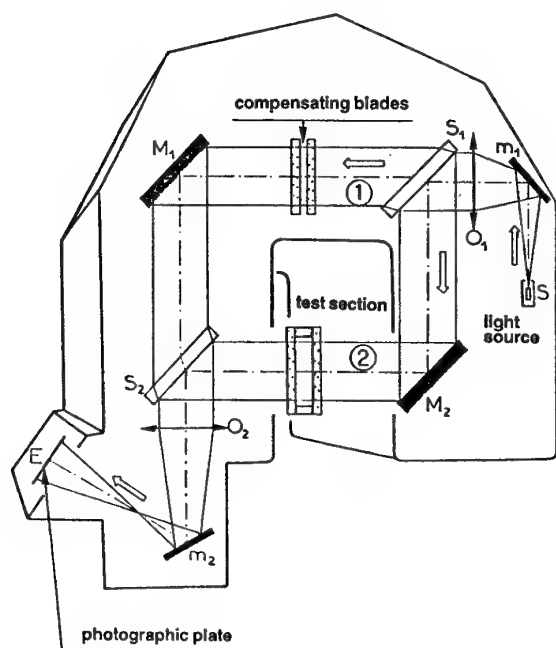


**Fig. 2.2.4** - Schematic arrangement of a Mach-Zehnder interferometer

The advent of laser sources has considerably simplified interferometry by calling upon holographic techniques to create interferometric pictures, although the essence of the method and the mode of data processing remain the same [2.2.44]. There exist several ways to obtain an interferogram by holographic imaging. Here, we will only consider the *double exposure* technique which was intensively used to investigate transonic flows [2.2.49]. With the holographic

technique, the reference and study beams are produced by a laser source, usually a Helium-Neon or Argon laser. As shown by the sketch in Fig. 2.2.5, the study beam is expanded by an appropriate lens to constitute a beam of parallel light traversing the test section and covering the field to be investigated. The reference beam, which does not need to be expanded, passes outside the test section by the most convenient path. After having traversed the test section, the study beam and the reference beam - which has been expanded - interfere at the photographic plate P to create a hologram. By illuminating the plate with a source of coherent light, the wave which has thus been recorded in the hologram is reconstructed. To obtain an interferogram, the above process is repeated twice without changing the plate. A first hologram is made in the absence of flow, a second one with the flow established. Thus, two waves are recorded on the plate: one having traversed a uniform field, a second a field perturbed by the flow. By illuminating the plate with a laser source, the two waves are simultaneously reconstructed leading to an interference pattern. This pattern is photographed to get the interferogram of the flow, which is then processed by using the usual method. For the finite fringe mode of operation, two such interferograms are made, one with the pattern of parallel fringes obtained by moving an optical component of the apparatus, the other by superimposing the disturbances produced by the flow.

Holographic interferometry is far less complicated to operate than classical interferometry. Because of the important coherence length of the laser light, the reference and the study beams need not be adjusted as precisely as with ordinary light. Furthermore, good quality glass is sufficient for the test section windows and the lens, making the system rather cheap.

Interferometry (in a general sense) is a very powerful tool to investigate complex flowfields sensitive to the perturbing effect of probes. It is an accurate technique which can provide a vast amount of results on a complete field. The fact that the whole flowfield is recorded at once on a unique picture avoids the long testing times required by other techniques.

However, interferometry suffers from shortcomings which have limited its use. The method loses its sensitivity in separated flows where the density is almost constant and it is not possible to make really usable turbulence measurements. In practice, interferometry is restricted to two-dimensional and axisymmetric flows. Its extension to three-dimensional flows is in principle possible by tomographic imaging, but the mode of operation and the processing procedures are so complex that three-dimensional interferometry has been applied to a very restricted number of cases [2.2.50]. If the investigated flow field possesses some similarity property, simplified versions of three-dimensional interferometry can be used [2.2.51-53].

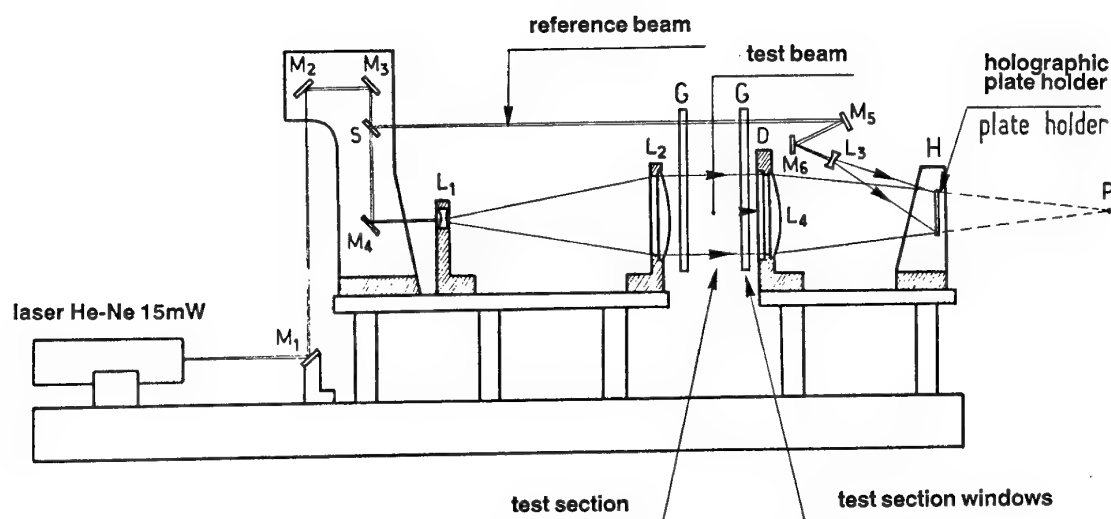


Fig. 2.2.5 - Schematic arrangement of a holographic interferometer

#### 2.2.4.4. Laser Doppler Velocimetry

**Introductory Remarks.** The advent of Laser Doppler Velocimetry (LDV) in the early 70s has considerably increased the capacity to investigate high speed flows by giving access to quantities whose determination was heretofore unreliable, if not impossible [2.2.54-56]. With LDV it has become possible to safely probe turbulent separated flows in order to determine not only their mean structure, but also their fluctuating properties [2.2.57,58]. Here, it is not relevant to develop the crucial contribution of LDV to our physical understanding of complex flows and the validation of predictive methods. Nevertheless, it is worth mentioning that the advent of LDV nearly coincided with the manufacture of large computers and the parallel progress in numerical methods which allowed the development of advanced theoretical models. Thus, the progress in flow modelling was accompanied by the development of a tool which allowed an in depth validation of the models [2.2.59].

**Basic Principles.** The basic idea underlying LDV is to measure the velocity of tiny particles which are transported by the flow. If these particles are small enough, their velocity is assumed to be that of the stream and LDV provides a measure of the local instantaneous velocity of the flow. This postulate is not always true: in highly decelerating or accelerating flows the particles cannot instantaneously adjust their velocity to that of the fluid, so that a certain distance is necessary for the particles to reach the flow velocity. The problem of particle lag is at the heart of LDV and one should be cautious in the use of results obtained in regions where the velocity undergoes a large variation over a short distance. Such a situation occurs downstream of a shock wave, in the diverging part of a supersonic nozzle or in a flow

with high frequency fluctuations. However, if one excludes these regions - whose relative extent is most often small - the results given by LDV can be considered as reliable and remarkably accurate, considering the complexity of the investigated phenomena.

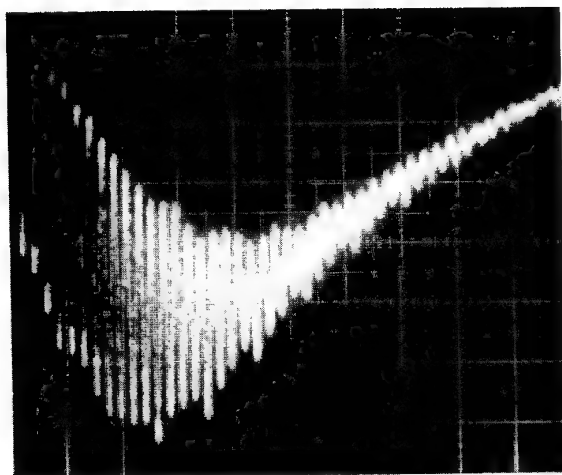
There are several types of LDV systems and different interpretations of the phenomena involved. In this chapter, only the so called *fringe velocimeter*, which is the most commonly used for high speed measurements in airflows, will be considered.

In order to measure the velocity of a moving particle, two beams from the same laser source are made to cross in the flow at what constitutes the *probe volume*. Because of the high coherence of the laser light, the two beams interfere to form a pattern of real fringes in the probe volume. When a particle crosses this fringe pattern, it is more or less illuminated, depending if it crosses a bright or a dark fringe. Hence the intensity of the light scattered by the particle will be modulated at a frequency  $f_m$  inversely proportional to the fringe spacing  $i$  and proportional to the component  $U$  of the particle velocity normal to the fringes. The fringe spacing  $i$  being known, from optical laws or from a direct calibration, and the measured frequency  $f_m$  determined by a method which will be explained below, the component  $U$  is simply given by:

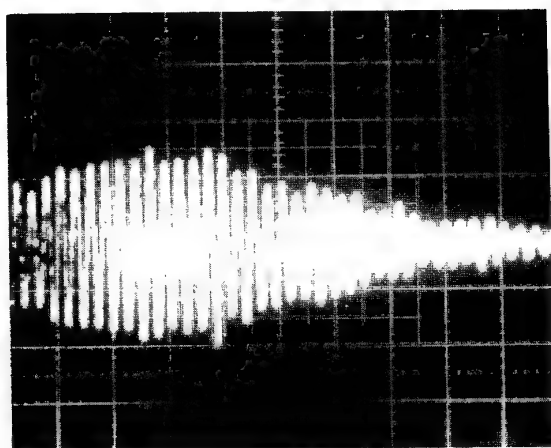
$$U = i f_m$$

**Signal Processing.** The light scattered by the particle is sent to a photomultiplier which converts it into an electrical signal. The passage of a particle in the probe volume produces a signal, or *burst*, as the one shown in Fig. 2.2.6. This signal is composed of a low frequency component, the so called pedestal,





a - Photomultiplier signal



b - Filtered signal

**Fig. 2.2.6 - Laser Doppler Velocimetry.** Burst produced by the passage of a particle through the probe volume

corresponding to the Gaussian light distribution in the laser beam, on which the Doppler signal containing the interesting information is superimposed, and high frequency noise. The problem is to extract the frequency  $f_m$  from the burst. This is a complex and very technical problem which will not be presented in detail here; only some basic principles will be discussed. To give an idea of the difficulties encountered in the determination of  $f_m$ , let us consider a flow velocity of  $300\text{ms}^{-1}$ , with a fringe spacing of  $15\mu\text{m}$  (which is a typical value). Then  $f_m$  will be equal to  $20\text{MHz}$ , the duration of the burst being of the order of  $1\mu\text{s}$ . The problem is to accurately measure a high frequency in a very brief signal which generally contains much noise.

In most circumstances, before being processed, the signal goes through high pass and low pass filters to remove the pedestal and the noise. Also, maximum and minimum thresholds are set to eliminate too strong signals, assumed to be produced by big particles which do not follow the flow, or erratic signals. Several techniques are used to treat the resulting signal and to extract  $f_m$ : bench of filters, frequency trackers (for low velocity applications), photon correlation, counters (which in fact measure the period) and frequency analyzer based on a Fourier transform of the signal. In counters, which are probably the most commonly used devices for high velocity measurements, a clock is started at a predetermined zero crossing of the filtered signal. The clock is stopped after a given number of zero crossings or periods  $N_1$  giving a value  $T_1$  for the period. A second counting is made by considering a number  $N_2$  of periods, which gives a second estimation  $T_2$  of the period. The measurement is validated if the two values  $T_1$  and  $T_2$  agree, within a certain tolerance. In most systems  $N_1 = 5$  and  $N_2 = 8$ . This validation test eliminates too short signals which could be produced by particles passing near the border of the probe volume.

*The Different Modes of Operation.* The part of the system producing the laser beams and focussing them into the probe volume is the *emitting optics*; the part observing the scattered light is the *collecting optics*.

The scattering of light by the particles used in LDV is called Mie scattering. This process involves particles which have a size comparable to the light wavelength. It is an elastic interaction between light and matter, in the sense that the scattered light has the same wave-length as the incident light (see Section 2.2.4). The light is scattered in selected directions making lobes. The most intense emission is in the direction opposite to that of the incident beam, it is called forward scattering. Two other lobes are directed towards the source, symmetrically placed with respect to the incident beam corresponding to back scattering. The light scattered in the forward mode is at least 100 times more intense than in the back scatter mode. Hence the two fundamental mode of operation of LDV systems:

- In the *forward scattering* mode, the collecting optics are opposite to the emitting optics, the two parts being installed on separate benches located on each side of the test section. This arrangement is the most advantageous as far as the optical performance of the system is concerned. It gives a much better signal-to-noise ratio and is generally adopted to perform measurements in high speed flows. Its disadvantage is the necessity to use two separate benches whose displacements must be very accurately controlled.

- In the *back scattering* mode, the emitting and collecting optical parts are on the same side with re-

spect to the test section and can be installed on the same bench, which provides a more compact system and a greater ease of use. The main disadvantage in this case, is a poor signal-to-noise ratio which may preclude measurements in high speed flows (above  $300\text{ms}^{-1}$ ).

In this basic version, a LDV system cannot detect the direction - or sign - of the measured velocity components, which is a severe shortcoming if the flow contains regions of reversed flow. To overcome this difficulty, a permanent shift of the fringes is created by making the beams pass through acoustic modulators of Bragg cells which produce a slight change of the light frequency. For a fixed observer, the fringe motion is equivalent to a shifting frequency  $f_B$  which corresponds to a uniform velocity  $U_B = if_B$ . The frequency  $f_B$ , hence the velocity  $U_B$ , are chosen such that the relative velocity  $U_r$  deduced from the frequency  $f_m$  measured in the moving fringe pattern is always positive (one always has an idea of the amplitude of the maximum reversed velocity). Then the absolute velocity  $U_a$ , in the laboratory reference frame, is given by:

$$U_a = U_m + U_r = i(f_m + f_r)$$

Bragg cells are also used, even if there are no reversed flows, to avoid the measurement of a too small velocity component and to make sure that a particle crosses a sufficient number of fringes.

**Multi-Component Systems.** To measure two components of the velocity vector, one creates two fringe systems in the probe volume, each having an orientation different from that of the other, the optimum angle between  $90^\circ$ . In this case, four beams cross in the probe volume. In order for the collecting part to distinguish the components, the two systems are produced by beams of different colours (or wave-lengths). Usually, the two set of beams are produced by the same laser working in a multi-mode type of operation. The beams of different colours are separated by filters or semi-transparent mirrors. The third velocity component can be measured in the same way by introducing a third fringe system set at an angle different from the orientation of the two other systems. Thus, the three fringe systems constitute a system of axes along which the velocity components are measured. Because of limited access to the test section in most experimental arrangements, the three axes are not orthogonal which tends to restrict the accuracy of the measurements. It is recommended that angles between fringe orientation be larger than  $40^\circ$ . Simple formulae then allow the velocity to be expressed in the most adequate system, which is in general orthogonal. Introduction of a third component necessitates the use of a third colour which is frequently provided by a second laser working in single-mode (i.e., emitting only one wave-length). The use of a second laser is

frequently mandatory to perform measurements at high speed, which requires high power for the three colours. Also, because of the bigger probe volume of a three component system, a simultaneity checking module is placed in the processing system to reject signals produced by different particles crossing the probe volume. This device ensures that the three signals come from the same particle having crossed the probe volume by retaining signals contained within a given time interval.

**Statistical Treatment.** At a given measurement point,  $N$  values of the instantaneous velocity vector - corresponding to  $3N$  values for the three components  $U_i$  - are acquired. A statistical treatment is applied to this sample to determine:

- the mean velocity:

$$\bar{U}_i = \frac{1}{N} \sum_{n=1}^{n=N} U_i^n$$

- the Reynolds tensor components which are identified to:

$$\overline{u_i u_j} = \frac{1}{(N-1)} \sum_{n=1}^{n=N} \left( U_i^n - \bar{U}_i \right) \left( U_j^n - \bar{U}_j \right)$$

To have some idea about the probability density function of a fluctuating component  $U_i$ , it can be useful to compute the skewness factor  $S_k$  and the flatness factor  $F_l$  of the sample (for a Gaussian distribution:  $S_k = 0$  and  $F_l = 3$ ), which are given by:

$$S_{k_i} = \frac{1}{N\sigma^3} \sum_{n=1}^{n=N} \left( U_i^n - \bar{U}_i \right)^3$$

$$F_{l_i} = \frac{1}{N\sigma^4} \sum_{n=1}^{n=N} \left( U_i^n - \bar{U}_i \right)^4$$

In the two last expressions,  $\sigma$  represents the R.M.S of the fluctuating quantity.

The choice of the size  $N$  of the sample results from a compromise between a small statistical uncertainty, which requires large  $N$ , and an acceptable duration of the test, which requires small values of  $N$ . A good solution is to adopt  $N = 2000$ .

Velocity and turbulence measurements by a LDV system can be affected by uncertainties coming from the optical arrangement and the electronic components but also from many other origins. In particular, the orientation of the fringe patterns with respect to the velocity vector, the statistical nature of data reduction and the particle density, introduce errors, frequently called bias, which have been the subject of many studies (for information, see Refs. [2.2.60-62]).

**Practical Arrangement.** To illustrate the LDV concept, the sketch in Fig. 2.2.7 gives a schematic representation of the three component LDV system developed at ONERA to perform measurements in high speed flows [2.2.63]. This velocimeter, which can work in the forward scattering as well as in the back scattering mode of operation, is equipped with two identical Argon lasers giving a maximum power of 15W in the all-line mode of operation. In most applications, the first laser works in the single-line mode to give a violet component (wavelength  $\lambda = 476.5\text{nm}$ ) with a power of 3W. The second laser, working in the all-line mode with a power of 6W, delivers the blue ( $\lambda = 488.0\text{nm}$ ) and green ( $\lambda = 514.5\text{nm}$ ) components. These two colours are separated by a set of dichroic mirrors. Then, each of the three beams are split into two beams by means of the beam splitters DV, DB and DG. The six resulting beams pass through Bragg cells inducing a fringe shift at an adjustable frequency (usually 10Mz). Then, each pair of beams are focused by means of appropriate optics to constitute the probe volume whose useful diameter is close to 0.5mm (a smaller size is obtained in the two-component version of the system).

In general, the green and blue radiations are emitted in a horizontal plane along a direction making an angle  $\alpha_1$  with respect to the axis OY directed along the test section spanwise direction. Their interference produces two fringe systems making angles equal to  $-45^\circ$  and  $+45^\circ$  with respect to the horizontal. The violet colour is also emitted in a horizontal plane but along a direction making an angle  $\alpha_2$  with OY. The optimum setting of the system would be to adjust  $\alpha_1$  and  $\alpha_2$  in such a way that  $\alpha_1 + \alpha_2 = 90^\circ$ . In reality, because of limited access to the test section, a value  $\alpha_1 + \alpha_2 \sim 50^\circ$  is most often adopted. The associated fringe system is vertical and located in a plane normal to this direction. The following values are typical of fringe spacings:

Blue :  $i = 14\ 500\text{nm}$

Green :  $i = 13\ 400\ \text{nm}$

Violet :  $i = 13\ 100\text{nm}$

Fringe spacings depend on the focal length of the focusing optics which, in turn, is partly determined by the distance of the optics to the probe volume. The adjustment of the system must be such that a sufficient number of fringes are formed (15 is a minimum); this conditions fixes the size of the probe volume.

The collecting part of the system comprises two Cassegrain telescopes having a diameter of 200mm in order to collect a maximum of the light scattered by the particles. The first telescope is followed by interferential filters to select and separate the blue and green components. In a similar way, the second telescope selects the violet. The radiations, thus separated, are sent to three photomultipliers whose

signal are processed by DANTEC 55L counters. The frequencies measured by the counters are acquired by a computer which manages the complete test sequence and performs a first statistical treatment of the measurements. In the forward scattering mode of operation, the emitting and collecting parts of the velocimeter are mounted on two independent benches capable of precise displacements along three perpendicular directions. These benches are computer controlled in such a way that the collecting optics follows the probe volume as it moves along the survey line.

**Flow Seeding.** In most air flow facilities, the flow must be seeded, natural particles being either too sparse to provide sufficient sampling rate or too big to follow the stream. Adequate flow seeding is a delicate problem since the validity of LDV measurements depends critically on the response of the particles to rapid changes in velocity [2.2.64]. The choice of correct seeding particles is dictated by many factors, some of them subjective, including:

- Their proper size: very small particles will follow the flow perfectly but, the scattered signal will be small.
- Their polluting action: some particles can be a hazard for health, so that their use is forbidden or precautions must be taken to avoid their dispersion outside the wind tunnel. Less dramatically, some particles have a strong tendency to deposit on the windows, obscuring them rapidly.
- Particles of good size can agglomerate during their travel with the flow, thus forming big particles incompatible with accurate measurements in rapid compression / expansion regions.
- In afterbody flow studies with hot jet simulation, the particles must withstand high temperature without burning or melting.

There is a relatively large variety of particles presently used by experimentalists, none of them being an entirely satisfactory solution: incense smoke, latex balls, silicone oil droplets, olive oil droplets, zinc oxide or alumina (to seed high temperature flows). The behaviour of the particles introduced in the flow is critical for the accuracy of the measurements. In addition to the lag problem, already mentioned, a statistical bias can be introduced by using different seedings in different parts of the flow. In afterbody studies, the outer flow and the jet are seeded independently, and frequently with different particles if the jet is hot. In intense vortical structures, the particles are most often ejected from the centre of the structure by the centrifugal force, which makes measurements in the vortex core impossible. In some circumstances, the seeding of separated regions may be insufficient because of the difficulty for the particles to enter the recirculation region.

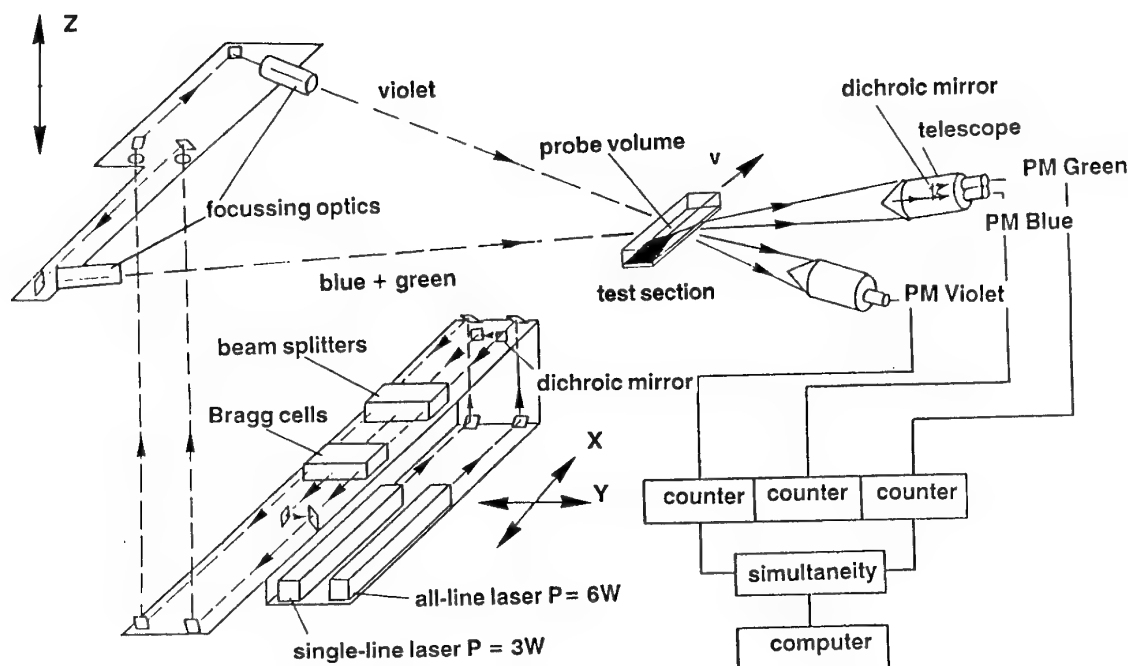


Fig. 2.2.7 - Schematic arrangement of the ONERA three-component LDV system

## 2.2.5. Laser Spectroscopic Flow Diagnostic

### 2.2.5.1. General Remarks

The advent of laser sources in the early 60s has given a dramatic impetus to the development of non intrusive methods allowing - in principle - a nearly complete and in situ determination of the properties of a gas, including its velocity. These methods are based on fundamental physical processes related to the interaction between light and matter. By analyzing the resulting phenomena, it is possible to deduce the characteristics of the atoms and/or molecules constituting the tested gas, their nature, concentration, energy levels,... Although these methods are not yet commonly used in aerodynamic applications because of their complexity, they represent extremely powerful tools to investigate complex flows. In particular, they give access to species concentration, local pressure and temperature, and therefore can be of great interest for the study of afterbody flows with propulsive jets containing chemically active combustion products.

A thorough presentation of laser diagnostic methods would be far beyond the scope of the present article. The purpose here is to simply give an overview of these techniques by briefly exposing their principle and possibilities. The interested reader will find detailed and more rigorous information in Refs. [2.2.65-67], which themselves contain a large number of references on the subject.

In general, laser spectroscopic measurements are based on the radiative interaction of a laser beam with

spectroscopic properties of the investigated flow. Depending on the interaction process, the laser light is either absorbed or scattered by those species which are radiatively active at the wave-length used.

As a general rule, the interactions between light and matter can be classified into two categories:

- In *elastic* processes, light is scattered instantaneously, without exchanging energy with the internal states of the medium molecules.
- In *inelastic* processes, the light exchanges energy with specific molecules depending of the wave-length of the incident light.

Absorption and/or scattering processes are also characterized by a *cross section* which is a measure of the amount of the radiation which is absorbed/scattered in the process: the higher the cross section, the greater the intensity of the absorbed/emitted radiation. In the two cases, the intensity of the resulting signal depends mainly on the population density of the atomic or molecular energy states responsible for the interaction. Furthermore, the radiative signal resulting from the interaction has well defined spectral properties as functions of the nature of the interacting species and its molecular energy state. Thus, measurements are made on selected populations from which it is possible to deduce the local gas temperature and density of the species from analysis of the spectrum of the radiated light.

From these primary parameters, the other thermodynamic quantities, such as bulk gas density and

pressure, can be deduced by using appropriate thermodynamic laws. Gas velocity can also be obtained by less direct methods.

As already discussed, the thermodynamic properties of a species are linked to the spectral features of the radiative signal. Hence the determination of two quantities (e.g., temperature and pressure), require the measurement of at least two spectral features. In some circumstances, the variation of a single spectral feature is sufficient to determine the thermodynamic conditions of the flow. The intensity of the radiative signal gives a measure of the species concentration (or atom/molecule number density). The temperature is most often deduced from the broadening of a spectral line due to the Doppler effect induced by the motion of the atoms or molecules (the energy contained in this motion being proportional to the square root of the translational temperature). The velocity of the flow is deduced from the shift of the central frequency of the signal coming from the Doppler effect produced by the bulk motion of the gas. Rotational and vibrational temperatures can also be deduced from an analysis of the radiative signal.

Laser spectroscopic methods present several obvious advantages: they are non intrusive, they are adapted to the measurement of specific thermodynamic parameters and selected species, most of them have a good spatial and temporal resolution for the characterization of three-dimensional flows.

On the other hand, they need optical access, they are in general complex and expensive to implement, their use is often restricted to small facilities and they require operation and data analysis by specialists in the field.

#### 2.2.5.2. Laser Absorption

In this technique, the laser beam is tuned to a wavelength which is resonant with an absorbing transition of a selected species. The attenuation of the beam passing through the test region is measured, the absorption of two or more wave-lengths being used to determine both the gas temperature and the density of the absorbing species.

This technique is simple to implement since it requires an optical access which is just sufficient to allow the laser beam to pass through the test region. Production of a detectable and usable signal does not depend on the laser power, so that small power lasers can be used. As a consequence, fiber optics may be employed to make measurements in internal flows. Laser absorption permits, in principle, the measurement of species concentration, temperature, pressure and velocity of the gas.

However, the method lacks spatial resolution. A measurement represents an integrated average along the path of the beam through the test region. This restricts its use to two-dimensional flows, which are

uniform along a transverse direction, or to axisymmetric flow, where the local properties can be extracted from Abel inversion. For three-dimensional flow probing, this shortcoming can be overcome but at the price of a complication of the technique which makes the choice of a different method preferable. Also, to have enough absorption for accurate measurements, the absorbing species must be present with a sufficient density.

#### 2.2.5.3. Rayleigh Scattering

Laser Rayleigh scattering is an elastic radiative interaction with the gas, in which light from a laser beam is scattered at nearly the same frequency as that of the incident light. The scattered light intensity is proportional primarily to the sum of the densities of all species in the gas, weighted by their respective Rayleigh cross section. Spatial resolution is obtained by observing the scattered light from a small region of the beam or by imaging the scattering from a two-dimensional light sheet.

By measuring the intensity of the scattered light and its spectral properties, it is possible to determine the density, pressure and velocity of the gas.

Rayleigh scattering is probably the simplest method giving a local measurement of flow properties, since it does not rely on any spectral resonances of a seed material (see LIF below). All species in the gas scatter the laser light, and the laser can be - in principle - at any wave-length.

On the debit side, the method lacks spectral difference between the light scattered by the gas and the background light scattered by any other objects that can illuminate the field and by the material constituting the optics. Also, the flow has to be free of solid particles whose scattering cross section is much greater than the cross section of atoms or molecules. It is thus difficult to distinguish the useful signal from parasitic light which can be of equal or greater intensity.

The intensity of the scattered light being inversely proportional to the fourth power of the laser wavelength, there is a strong advantage to work with small wave - length, in particular ultra - violet lasers which are now commercially available.

#### 2.2.5.4. Raman Scattering

Raman scattering is a radiative interaction in which light from a laser beam is scattered inelastically by the gas at wave-lengths shifted from that of the incident light. The Raman scattering cross section is much smaller than that of Rayleigh scattering, making observation of the radiative signal more difficult.

With this technique, it is possible to determine species concentration, vibrational and/or rotational temperature of the particular species and gas velocity.

When a photon strikes a molecule, it leaves a fraction of its energy to the molecule which is then raised to

a higher energy state. When deexcitation occurs, a photon is released which has a longer wave-length - or lower energy - than the incident photon. This process is called Raman Stokes scattering. The scattered light has a spectrum whose frequencies are characteristic of the molecule. In particular, the distribution of intensities between the frequencies in the radiative signal depends on the initial distribution of energy states in the tested gas. Thus, analysis of the emitted spectrum constitutes a way to measure the vibrational and rotational temperatures in this particular state. Species concentration is determined from the amount of light contained in a certain narrow spectral band.

If the photon emerges from the interaction at a shorter wave-length, hence higher energy, the process is called Raman Anti Stokes scattering. This scattering process takes place with molecules of a higher energy level whose relative number tends to be small; thus the Raman Anti Stokes signal is naturally fainter than the Stokes signal. The use of stimulated Raman scattering alleviates this drawback (see below).

The basic Raman scattering technique, called *spontaneous Raman scattering*, presents a certain number of advantages: it can be implemented with one laser with an arbitrary wave-length. However there is interest in using short wave-lengths, as for Rayleigh scattering. Frequently, pulsed lasers are used because they can deliver the highest power to a small sample volume. Raman signals are at a wave-length different from that of the laser and consequently are affected very little by background scattering. In addition, the Raman effect is an interaction driven by the radiation field and, for this reason, is not affected by collisional quenching (see below). The essential disadvantage of the technique is that the signal is very weak. Furthermore, the laser beam is scattered in all directions of space. Hence, since spatial resolution is obtained by observing the signal from a small region of the laser beam, the efficiency of spontaneous Raman scattering at visible wave-lengths is ordinarily very weak (about 1000 times less than Rayleigh scattering). In order to eliminate this serious disadvantage, *stimulated Raman spectroscopy* has been developed.

#### 2.2.5.5. Stimulated Raman Scattering

Basically, this technique is analogous to spontaneous Raman scattering, the scattering being produced by a first laser called the *pump laser*. The system now includes a second laser, the *probe laser*, whose frequency is shifted so that the differences in wave-length with the pump laser matches a resonant frequency of the molecule.

This arrangement is used in **Coherent Anti-Stokes Raman Scattering (CARS)** in which measurements are made with the Anti-Stokes radiation. In this method, the gas is illuminated by the pump laser at a frequency  $f_1$ . The Raman scattering is stimu-

lated by a tunable probe laser whose frequency  $f_2$  is adjusted in such a way that the difference  $(f_1 - f_2)$  is equal to the frequency associated with a certain energy state of the molecule. Then, the resonant interaction induces a strong Raman Anti-Stokes scatter at a frequency  $f_3$  such that:  $f_3 = f_1 + (f_1 - f_2)$ . The main advantage of CARS is that the scattering cross section is much higher than that of the spontaneous Raman effect by several orders of magnitude. Furthermore, the emitted light leaves in a preferred direction defined by the directions of the incident beams. Thus, the useful light is collected more efficiently than in ordinary Raman scattering. Analysis of the CARS signal allows the determination of the nature of the species, of their concentration, temperature, etc. Also, the gas velocity can be determined from Doppler shift. There are several variants of CARS, for example, in Dual Line CARS (DLCARS) four beams are used to excite two energy levels of the studied molecule which allows a more direct determination of the density and temperature of the gas [2.2.68].

Because of the intensity and high directivity of the emitted signal, CARS is extensively used to perform measurements in flames. It can be used with great effectiveness to probe high temperature propulsive jets.

#### 2.2.5.6. Laser Induced Fluorescence

Laser Induced Fluorescence (LIF) belongs to the same category of radiative / absorption process as those used by the other techniques, but here the measured signal is obtained from the subsequent spontaneous emission of absorbed energy - or fluorescence [2.2.69, 70]. In this process, the emission takes place after a relatively long time, several seconds in some cases, whereas in other types of interaction, emission occurs after  $10^{-8}$ secs for most molecules. Due to this long relaxation time, the signal analysis must consider the effect on some species of non-radiative energy transfers taking place through collisions between molecules (quenching). This phenomenon competes with the emission process as a path for energy relaxation, thus reducing the fluorescence signal. Quenching depends on temperature and species concentration.

To implement LIF, the laser beam is tuned to a suitable resonant wave-length of an absorbing species and excites a fraction of it to the upper state of the radiative transition. The excited species then spontaneously radiates the absorbed energy, which is not lost through other relaxation paths, at wave-lengths which are allowed by the fluorescence spectrum of the excited species.

Spatial resolution is obtained by observing the fluorescence from a small region of the laser beam or by imaging all of the fluorescence from a two - dimensional sheet of light.



By appropriate analysis of the fluorescence signal, one can determine the species concentration, the gas temperature and pressure and the flow velocity.

Proper operation of LIF requires the presence of species in the flow having the correct fluorescence properties in terms of signal intensity, spectroscopic characteristics and absorbing capacity at wave-lengths accessible by a laser. They must also be thermodynamically coupled to the flow in a well known manner. In flows with chemical reactions, many of the reaction products provide acceptable species for LIF; hence the interest in LIF for the qualification of propulsive jets. For aerodynamic research in non reacting fluids, the flow must be seeded with a small concentration of an adequate species (sodium, iodine, nitric oxide,...). Because of limitations due to the toxic and corrosive characteristics of these species, aerodynamic studies with seed materials must be executed in small facilities. Furthermore, the quenching phenomenon limits application of LIF to pressures lower than the atmospheric pressure.

Fluorescence properties are also used to obtain a picture of an entire flow region by using Planar Laser Induced Fluorescence (PLIF) [2.2.71,72]. In this technique, the zone of interest is illuminated by a laser sheet and the fluorescence picture recorded by a camera containing a two-dimensional array of photo detectors. In general, the camera records and digitizes the fluorescence intensity associated with absorption by a single spectral feature; hence the possibility to visualize the velocity, temperature, concentration...field according to the feature selected.

As explained above, the velocity of the field is deduced from the global Doppler shift of the radiative signal. Thus, to accurately determine velocity, this method requires measurement techniques sensitive to small frequency changes or sufficiently high velocities. To allow the measurement of low velocities, one may use a "flow tagging" technique in which a small volume of the fluid is marked by a laser-induced process. Due to its long relaxation time, LIF is a good candidate to locate, after a specified time interval, this volume, which is convected in the downstream direction. With this technique, velocities of almost any magnitude and direction can be measured without strong demands on the spectroscopic qualities of the signal. In this application, LIF is superior to LDV since LIF measures the velocity of atoms or molecules whereas LDV gives the velocity of particles which are much bigger than the gas constituents. However, in practice the proper operation of LIF is still delicate and complex, and for this reason it is still far from routine use. Furthermore, LIF only works in a well defined domain of pressure.

## 2.2.6. Experimental Set-up and Jet Simulation

### 2.2.6.1. General Remarks

The experimental study of afterbody flows raises, at least, two major problems which have not found fully satisfactory solutions. The first difficulty comes from the fixation of the model in the wind tunnel test section. The afterbody being in the aft part of the model, it tends naturally to be affected by disturbances produced by the support system, since these disturbances propagate mainly in the streamwise direction, even in subsonic flows.

The second major experimental difficulty is the correct simulation of the propulsive jet(s). In the reality, these jets are made of high temperature gases, with more or less complex thermodynamical properties, resulting from a combustion involving kerosene, hydrogen or liquid or solid propellants, in the case of a missile. For obvious reasons, it is extremely difficult to duplicate such jets in a wind tunnel, especially for basic experiments requiring long testing times, and one has to adopt a compromise in which the jets are simulated by a gas easier to handle than the real combustion products.

The following sections give a rapid overview of the solutions most commonly adopted to cope with these difficulties.

### 2.2.6.2. Model Support

The **lateral strut** is very commonly used in wind tunnel testing, the strut being fixed to the tunnel wall or to a table allowing the setting of the model at incidence. In this arrangement, the afterbody under study is fixed to a forebody which can schematically represent a missile or aircraft body. The strut must have a thickness sufficient to allow the passage of the fluid supplying the nozzle(s) as also the wiring system of the transducers. Thermal effects can be simulated by feeding the nozzle(s) with hot gases produced either by a combustion chamber or an electric heater, the heating device being installed either outside the wind tunnel test section or in the model itself.

The main disadvantage of this type of experimental set up comes from the disturbances generated by the strut. Early studies [2.2.73] have shown that any side fixation of the model may affect the pressure field in the base region and provoke an irregular triggering of the transition on the model body. These disturbances render highly suspect results obtained at supersonic speeds where the strut can generate shock waves. If the afterbody has a base, the low velocity flow constituting the dead-air region in contact with the base is very sensitive to even weak disturbance because of its low energy. Thus, the base pressure can be substantially altered by the presence of a strut.

Another type of support is the **rear sting** holding the model from downstream. This facilitates testing at incidence, no disturbances being created in the outer high speed flow. This type of support has been much used to investigate base flows without jet and the effect of the sting on the base pressure has been carefully investigated [2.2.74]. The rear sting can also be used to study powered afterbody. In one solution, the sting has a contour reproducing the shape of the real jet (solid jet concept). In other arrangements, the sting is made of a tube allowing the passage of the gas supplying the nozzle which in this case has an annular shape surrounding the sting [2.2.75]. It is clear that the rear sting concept prohibits any realistic simulation of the effects of the propulsive jets. It is only accepted as a way to avoid the strong disturbances produced by a strut in the testing of full aircraft where an accurate simulation of the jet(s) is not a major concern.

The best solution being the absence of any material support, important efforts have been made in the early 50s to develop the **magnetic suspension** of models [2.2.76-77]. In a solution worked out at ONERA, the model was held by intense magnetic fields produced by a V-shaped arrangement of four coils placed above the model to compensate for gravity, a fifth coil, upstream of the model and concentric to the nozzle, compensating the drag force. The location of the model was sensed by light beams falling on photo-cells activating a servo system controlling the electric current in the coils. At that time, the base pressure only could be measured by a transducer and a radio emitter installed inside the model. The magnetic suspension is of exceptional interest for base flow and wake studies since it allows results to be obtained free of any disturbance. Due to the spectacular progress accomplished since the 50s by transducer technology and with the advent of micro electronics, it would now be possible to perform a great number of measurements on a small scale model. In fact, the magnetic suspension had a very limited development, due to the difficulty of holding models of complicated shape and, in afterbody study, to simulate the propulsive jet.

In basic study, the **nose sting** support presents important advantages [2.2.78]. In this case, the afterbody is fixed at the rear of a long sting aligned with the flow direction and held by a support system located upstream of the test section in a region where the flow velocity is still low. Thus, practically no disturbances are generated, provided that the diameter of the sting is not too large. For test in supersonic flows, the sting is fixed upstream of the nozzle throat, the contour of the nozzle being computed to produce a uniform flow, the presence of the central coaxial sting being taken into account. The sting is also used for the passage of the fluid simulating the jet(s) and the wiring. This arrangement has been used extensively to perform basic studies of powered

and unpowered afterbodies [2.2.79]. The results thus obtained constitute probably the most reliable test cases to validate computer codes since they are free of major disturbances. The main disadvantage attributed to the nose sting solution is the additional boundary layer thickness which develops on the sting which is not present in real configurations. In addition, the front part of the vehicle (aircraft or missile) cannot be represented and the effect of incidence is difficult to produce.

### 2.2.6.3. Jet Simulation

The interaction between the propulsive jet(s) and the outer stream involves the following processes whose relative importance varies according to circumstances:

- Obstacle effect due to the strong expansion of an underexpanded jet.
- Heat transfers between a high temperature jet and a separated region forming on the fuselage.
- Strong entrainment effects produced by the highly turbulent mixing zone forming along the jet boundary.
- Aerothermochemical effects due the presence in the jet of incompletely burned species which can burn in a separated region by mixing with the outer fresh air (these effects mainly concern missile and launcher afterbody flows).

In general, it is not possible to simulate all these effects simultaneously, except in very complex - and costly - experiments performed on specific configurations. In basic studies, one must accept an approximate simulation of these effects, emphasis being placed on one of them according to the phenomenon to be investigated (the last effects are most often impossible to simulate because of the too short residence time of the species in the separated region forming on a small scale model).

To investigate confluence problem with risks of jet induced separation, one tries to duplicate the obstacle effect of the expanding jet. For obvious simplicity reasons, the jets are frequently simulated by high pressure air whose ratio of specific heat  $\gamma$  is largely different from the  $\gamma$  of combustion products (1.4 instead of 1.25 - 1.15). Hence, largely different expansion conditions leading to very different jet shape. To achieve with air a realistic jet shape at the nozzle exit, one frequently adopts the so-called Goethert similarity rules [2.2.80] according to which the simulated nozzle Mach number  $M_{js}$  is given by the relation:

$$\gamma_s \frac{M_{js}^2}{\sqrt{M_{js}^2 - 1}} = \gamma_r \frac{M_{jr}^2}{\sqrt{M_{jr}^2 - 1}}$$

where  $M_{jr}$  and  $\gamma_r$  are relative to the effective nozzle.

More constraining similarity rules can be adopted [2.2.81]. One can also simulate the jet by "exotic"



gases whose  $\gamma$  is close to the  $\gamma$  of combustion products ( $CO_2$  or freon) but whose handling is delicate.

The duplication of the entrainment effect requires the duplication of the jet velocity, hence a high jet stagnation temperature, close to the real stagnation temperature  $T_{ij}$ . This condition can be achieved without major difficulties if  $T_{ij}$  is not higher than 1300K. Then, a combustion chamber - using kerosene or hydrogen - or an electrical heater (see test case A.2.2) can be used to produce the hot jet. Higher values of  $T_{ij}$  are more difficult to simulate because of problems raised by material endurance at high temperature. The simulation of entrainment effects with ambient temperature gas can be made by using a gas in which the speed of sound is high, helium for example. However, then the value of  $\gamma$  is then much higher (1.667) than the effective value for air-kerosene combustion products (1.25).

If the simulation of aircraft jets does not lead to intractable problems, this is not the case of missile or launcher jets whose stagnation temperature is much higher (for more ample information on jet simulation, see [2.2.80]).

### 2.2.7. Concluding Remarks

In depth validation of advanced theoretical models based on the solution of the time-averaged Navier-Stokes equations requires detailed and careful comparison with reliable and well documented test cases providing a thorough description of the flowfield. Progress made in metrology over the past twenty years now offers the possibility to obtain a nearly complete definition of the flow past complex afterbody models. Surface pressure and heat transfer can be determined by entirely new methods using emissive properties of the model surface which gives the distribution of these quantities over the entire model without the need of transducers. The advent of laser sources has led to a spectacular development of non intrusive optical techniques. The mean velocity and Reynolds tensor components can be determined by LDV which has reached a high degree of efficiency in the probing of complex turbulent flows. Methods based on laser spectroscopy allow the definition of the fluid properties at the molecular level. Thus, its density, pressure and temperature can be directly measured. Species concentration can also be determined in reacting flows.

However, in their present development these methods still suffer from shortcomings which restrict their general use. Thermosensitive or pressure paints and infra-red thermography are delicate to use and of limited accuracy in regions where the flow properties vary rapidly. The measurement of skin friction is still a challenge if the model geometry is complex or if the wall is heated by the proximity of a hot jet. Interferometry remains a complex technique requiring a special environment and good specialists. As far as LDV is concerned, the results can be seri-

ously affected by errors due to particle lag in regions of rapid velocity variation. Also, the probing of intense vortices or separation bubbles may be difficult. Methods based on laser spectroscopy are limited to a relatively narrow range of conditions. In addition, their use remains complex, which requires special facilities and highly specialized teams. Consequently, the cost of these techniques may become prohibitive.

It is not generally possible to operate all the above methods on the same model and facility. Most of them are still in a development stage and can only be used in research facilities, especially designed for this purpose. It is clear that the complete definition of the flow past an afterbody tested in a large facility is still out of reach. In these facilities, one has to rely on conventional techniques to determine the main surface flow properties, the outer flow field being essentially characterized by visualizations. The detailed description of an afterbody flow with a view to validating Navier-Stokes codes must be made on small or medium scale facilities by considering simplified configurations. Important progress has still to be made to arrive at a routine use of advanced diagnostic techniques in industrial wind tunnel.

In addition, proper model installation in the wind tunnel remains an open question since most support systems used to date generate disturbances whose influence on the afterbody flow can be detrimental, especially when a dead-air region forms downstream of a base. Furthermore, in basic experiments, it is generally not possible to faithfully simulate the propulsive jets which are constituted by hot gases having more or less complicated properties. In most cases, the numerical codes must be validated by comparison with experiments performed with simple cold or "warm" jets; so that there is no guarantee that the code, along with the physical model, remain valid for realistic configurations.

### 2.2.8. References

- [2.2.1] Report of the Working Group O8 on Aerodynamics of Aircraft Afterbody. AGARD Advisory Report N° 226 (1986)
- [2.2.2] Crites, R. C.: Pressure sensitive paint technique. VKI Lecture Series 1993-05 on *Measurement Techniques* (April 1993)
- [2.2.3] Acharaya, M.; Bornstein, J.; Escudier, M. P. and Vokurka, V.: Development of a floating element for the measurement of surface shear-stress. *AIAA Journal*, Vol. 23, N° 3, pp. 410-415 (March 1985)
- [2.2.4] McAllistair, J. E.; Pierce, F. J. and Tennant, M. H.: Direct force wall shear measurements in pressure-driven three-dimensional turbulent boundary layers. *Journal of Fluid Engineering*, Vol. 104, pp. 150-155 (June 1982)
- [2.2.5] Leipmann, H. W. and Skinner, G. T.: Shearing - stress measurements by use of a heated element. NACA TN 3268 (1954)

- [2.2.6] Diaconis, N. S.: The calculation of wall - shearing stress from heat transfer measurements in compressible flows. J.A.S., Vol. 21, pp. 201-202 (1954)
- [2.2.7] Bellhouse, B. J. and Schultz, D. L.: The measurement of skin friction in supersonic flow by means of heated thin film gauges. A.R.C. R & M N° 3490 (1968)
- [2.2.8] Hankey, W. L. and Holden, M. S.: Two - dimensional shock wave / boundary layer interactions in high speed flows. AGARDograph N° 203 (1975)
- [2.2.9] Rubesin, M. W.; Okuno, A. F.; Mateer, G. G. and Brosh, A.: A hot-wire surface gage for skin friction and separation detection measurements. NASA TM X-62.465 (1975)
- [2.2.10] Higushi, H. and Peake, D.: Bi-directional, buried-wire skin-friction gage. NASA TM 78531 (Nov. 1978)
- [2.2.11] Higuchi, H.: A miniature, directional surface fence gage for three-dimensional turbulent boundary layer measurements. AIAA Paper 83-1722 (July 1983)
- [2.2.12] Preston, J.H.: The determination of turbulent skin friction by means of Pitot tubes. Journal Royal Aeronautical Society, Vol. 28, pp. 52-54 (1956)
- [2.2.13] Smith, K. G.; Gaudet, L. and Winter, K. G.: The use of surface Pitot tubes as skin friction meters at supersonic speeds. A.R.C. R & M, N° 3351 (1964)
- [2.2.14] McAllister, J. E.; Pierce, F. J. and Tennant, M. H.: Preston tube calibration and direct force floating element measurements in a two-dimensional turbulent boundary layer. Journal of Fluid Engineering, Vol. 104, pp. 156-160 (1982)
- [2.2.15] Tanner, L. H.: Skin friction measurements by viscosity balance in air and water flows. Journal of Physics E: Scientific Instruments, Vol. 12, N° 7, pp. 610-619 (1979)
- [2.2.16] Settles, G. S.: Recent skin friction techniques for compressible flows. AIAA Paper 86-1099 (May 1986)
- [2.2.17] Seto, J. and Hornung, H.: Two-directional skin friction measurement utilizing a compact internally-mounted thin-liquid film skin friction meter. AIAA Paper 93-0180 (Jan. 1993)
- [2.2.18] Monson, D. J. and Higuchi, H.: Skin friction measurements by a dual-laser-beam interferometer technique. AIAA Journal, Vol. 19, N° 6, pp. 739-744 (1981)
- [2.2.19] Kim, K. S.; Lee, Y.; Alvi, F. S.; Settles, G. S. and Horstman, C. C.: Laser skin friction measurements and CFD comparison of weak-to-strong swept shock/boundary layer interactions. AIAA Paper 90-0378 (Jan. 1990)
- [2.2.20] Monson, D. J.: A laser interferometer for measuring skin friction in three-dimensional flows. AIAA Paper 83-0385 (Jan. 1983)
- [2.2.21] Gaudet, L. and Gell, T. G.: Use of liquid crystals for qualitative and quantitative 2-D studies of transition and skin friction. RAE, Tech. Memo Aero 2159 (June 1989)
- [2.2.22] Consigny, H.; Mentré, V. and Bétremieux, A.: Méthodes de mesure de flux de convection dans les souffleries R2 et R3 de Chalais-Meudon. Mise en oeuvre actuelle et développements envisagés. Colloque d'Aérodynamique Appliquée de l'AAAF, Poitiers (France), Oct. 26-28, 1987
- [2.2.23] Consigny, H. and Le Sant, Y.: Détermination des échauffements cinétiques sur maquettes en souffleries par la méthode des températures superficielles. Journées d'études, Mesures de températures, Paris, June 19-20, 1990
- [2.2.24] Lee, Y.; Settles, G. S. and Horstman, C. C.: Heat transfer measurements and CFD comparison of swept shock wave/boundary layer interactions. AIAA Paper 92-3665 (July 1992)
- [2.2.25] Consigny, H.; Le Sant, Y.; Bouvier, F.; Baumann, P. and Merienne, M. C.: Heat transfer measurement techniques used or in development at ONERA Chalais-Meudon. NATO ARW New Trends in Instrumentation for Hypersonic Research, Le Fauga, France, April 27 - May 1, 1992
- [2.2.26] Parsley, M.: The use of thermochromatic crystals in heat transfer and flow visualization research. Second International Symposium on Fluid and Flow Visualization, Sheffield, England, Sept. 1988
- [2.2.27] Gartenberg, E. and Roberts, S., Jr.: Twenty-five years of aerodynamic research with infrared imaging. *Thermosense XIII*, SPIE Proc. Vol. 1467, pp. 338-353 (1991)
- [2.2.28] Bouchardy, A. M.; Durand, G. and Gauffre, G.: Processing of infrared thermal images for aerodynamic research. 1983 SPIE Int. Technical Conference, Geneva, April 18-22, 1983
- [2.2.29] Balageas, D.; Boscher, D.; Deom, A. and Gardette, G.: Heat transfer measurements in ONERA super and hypersonic wind tunnels using passive and active infrared thermography. First European Symposium on Aerothermodynamics for Space Vehicles ESA/ESTEC, Noordwijk (The Netherlands), May 28-30, 1991
- [2.2.30] Gauffre, G.: Détection de la transition laminaire-turbulent par thermographie infrarouge. La Recherche Aéronautique, N° 1988-2, pp. 11-22 (1988)
- [2.2.31] Legendre, R.: Lignes de courant d'un écoulement permanent. Décollement et séparation. La Recherche Aéronautique, N° 54 (Nov.-Dec. 1956)
- [2.2.32] Détery, J.: Physics of vortical flows. Journal of Aircraft, Vol. 29, N° 5, pp. 856-876 (May 1992)

- [2.2.33] Quélin, C. and Barberis, D.: Etalonnage et utilisation des sondes anémoclinométriques 3 trous. ONERA Rapport Technique N° 104/1865AN (Feb. 1988)
- [2.2.34] Gaillard, R.: Development of a calibration bench for small anemoclinometer probes. Symposium on "Measuring Techniques for Transonic and Supersonic Flow in Cascades and Turbomachines", Rhodes-Saint-Genèse (Belgium), Sept. 17-19, 1990
- [2.2.35] Gaillard, R.: Calibration and use of an ONERA miniature "five-hole" probe. 7th Symposium on Measuring Techniques for Transonic and Supersonic Flow in Cascades and Turbomachines, Aachen (Germany), Sept. 21-23, 1983
- [2.2.36] Taslim, M. E.; Kline, S. J. and Moffat, R. J.: Calibration of hot-wires and hot-films for velocity fluctuations. Report TMC-4, Stanford University, Department of Mechanical Engineering (Aug. 1978)
- [2.2.37] Kovaszny, L. S. G.: The hot-wire anemometer in supersonic flow. J. A. S., Vol. 17, N° 9, pp. 565-572 (Sept. 1950)
- [2.2.38] Horstman, C. C. and Rose, W. C.: Hot-wire anemometry in transonic flow. AIAA Journal, Vol. 15, N° 3, pp. 395-401 (March 1977)
- [2.2.39] Weinstein, L. M.: An improved large-field focusing schlieren system. AIAA Paper 91-0567 (Jan. 1991)
- [2.2.40] Alvi, F. S. and Settles, G. S.: Structure of swept shock wave-boundary layer interactions using conical shadowgraphy. AIAA Paper 90-1644 (June 1990)
- [2.2.41] Lu, F.K. and Settles, G. S.: Structure of fin shock/boundary layer interactions by laser light-screen visualization. AIAA Paper 88-3801 (July 1988)
- [2.2.42] Settles, G. S.: Swept shock-boundary layer interactions - Scaling laws, flowfield structure and experimental methods. AGARD-FDP-VKI Special Course on "Shock Wave/Boundary Layer Interactions in Supersonic and Hypersonic Flows", AGARD Report 792 (1993)
- [2.2.43] Adrian, R. J.: Particle-imaging techniques for experimental fluid mechanics. *Annual Review of Fluid Mechanics*, Vol. 23, pp. 261-304 (1991)
- [2.2.44] Surget, J.; Détery, J. and Lacharme, J.-P.: Holographic interferometry applied to the metrology of gaseous flows. First European Congress on "Optics Applied to Metrology", Strasbourg (France), Oct. 26-28, 1977
- [2.2.45] Détery, J.; Surget, J. and Lacharme, J.-P.: Interférométrie holographique quantitative en écoulement transsonique bidimensionnel. La Recherche Aérospatiale, N° 1977-2, pp. 89-101 (1977)
- [2.2.46] Solignac, J.-L.: Etude interférométrique de l'écoulement à Mach 5 autour d'une sphère. La Recherche Aérospatiale, N° 125 (1968)
- [2.2.47] Solignac, J.-L. and Détery, J.: Contribution à l'étude aérodynamique des systèmes propulsifs à double flux. *Israel Journal of Technology*, Vol. 10, N° 1-2, pp. 97-111 (1972)
- [2.2.48] Sirieix, M. and Solignac, J.-L.: Contribution à l'étude expérimentale de la couche de mélange turbulent isobare d'un écoulement supersonique. AGARD CP N°4, Part I (1966)
- [2.2.49] Vest, C. M.: *Holographic Interferometry*, Wiley-Interscience, New-York (1979)
- [2.2.50] Détery, J. and Marvin, J. G.: Shock wave / boundary layer interactions. AGARDograph N° 280 (1986)
- [2.2.51] Matulka, R. D. and Collins, D. J.: Determination of three-dimensional density fields from holographic interferometry. *Journal of Applied Physics*, Vol. 42, pp. 1109-1119 (1971)
- [2.2.52] Yu, Y. H. and Kittleson, J. K.: Reconstruction of a three-dimensional, transonic rotor flowfield from holographic interferograms. AIAA Journal, Vol. 25, N° 2, pp. 300-305 (Feb. 1987)
- [2.2.53] Hsu, J. C. and Settles, G. S.: Measurements of swept shock wave/turbulent boundary layer interactions by holographic interferometry. AIAA Paper 89-1849 (June 1989)
- [2.2.54] Goldstein, R. J.: Measurement of fluid velocity by laser doppler techniques. *Applied Mechanics Review*, Vol. 27, pp. 753-760 (June 1974)
- [2.2.55] Yanta, W. J.: Turbulence measurements with a laser doppler velocimeter. NOLTR 73-94 (1973)
- [2.2.56] Cline, V. A. and Bentley III, H. T.: Application of a dual beam laser velocimeter to turbulent flow measurements. AEDC-TR-74-56 (1974)
- [2.2.57] Modarress, D. and Johnson, D. A.: Investigation of turbulent boundary layer separation using laser velocimetry. AIAA Journal, Vol. 17, N° 7, pp. 747-752 (July 1979)
- [2.2.58] Détery, J.: Investigation of strong shock / turbulent boundary layer interactions in 2D transonic flows with emphasis on turbulence phenomena. AIAA Paper 81-1245; see also: AIAA Journal, Vol. 21; N° 2, pp. 180-185 (Feb. 1983)
- [2.2.59] Détery, J.: Contribution of LDV to the validation of advanced theoretical models. *Proceedings of the Fifth International Conference on Laser Anemometry, Advances and Applications*, 23-27 August 1993, Veldhoven (The Netherlands)
- [2.2.60] McLaughlin, D. K. and Tiederman, W. G.: Biasing correction for individual realization of laser anemometer measurements in turbulent flows. *The Physics of Fluids*, Vol. 16, N° 12, pp. 2082-2088 (Dec. 1973)

- [2.2.61] Buchave, P.: Biasing errors in individual particle measurements with LDA counter signal processor. Proc. of the LDA Symposium, Copenhagen, 1975, pp. 258-278
- [2.2.62] Ruck, B. and Pavlovski, B.: Limited accuracy of turbulence measurement in laser Doppler anemometry. Proceedings of the Fifth International Conference on *Laser Anemometry, Advances and Applications*, 23-27 August 1993, Veldhoven (The Netherlands).
- [2.2.63] Boutier, A.; d'Humières, C. and Soulevant, D.: Three-dimensional laser velocimetry: a review. Symposium on *Application of Laser Anemometry to Fluid Mechanics*, Lisbon, Portugal, 2-4 July 1984; see also: ONERA T.P. N° 1984-43
- [2.2.64] Blin, E.; Micheli, F. and Jacquin, L.: Sur l'analyse de la turbulence par vélocimétrie laser dans les écoulements supersoniques. 3ème Congrès Francophone de Vélocimétrie Laser, 21-24 Sept. 1992, Toulouse (France)
- [2.2.65] Lederman, S.: Experimental techniques applicable to turbulent flows. AIAA Paper 77-213 (Jan. 1977)
- [2.2.66] Trolinger, J. D.: Laser applications in flow diagnostics. AGARDograph N° 296 (1988)
- [2.2.67] McKenzie, R. L.: Progress in laser-spectroscopic techniques for aerodynamic measurements - An overview. AIAA Paper 91-0059 (Jan. 1991)
- [2.2.68] Grisch, F.; Bouchardy, P.; Péalat, M.; Chanez, B.; Pot., T. and Coët, M.-C.: Rotational temperature and density measurements in a hypersonic flow by dual-line CARS. *Applied Physics B* 56, pp. 14-20 (1993)
- [2.2.69] Gross, K. P.; McKenzie, R. L. and Logan, P.: Measurements of temperature, density, pressure, and their fluctuations in supersonic turbulence using laser-induced fluorescence. *Experiments in Fluids* 5, pp. 372-380 (1987)
- [2.2.70] Laufer, G. and McKenzie, R. L.: Temperature measurements in hypersonic air flows using laser-induced  $O_2$  fluorescence. AIAA Paper 88-4679-CP (Sept. 1988)
- [2.2.71] Hanson, R. K.: Combustion diagnostics: planar imaging techniques. Twenty-first Symposium (International) on Combustion, The Combustion Institute, pp. 1677-1691 (1986)
- [2.2.72] Hiller, B. and Hanson, R. K.: Simultaneous planar measurements of velocity and pressure fields in gas flows using laser-induced fluorescence. *Applied Optics*, Vol. 27, N° 1, pp. 33-48 (Jan. 1988)
- [2.2.73] Whitfield, J. D.: Support interference at supersonic speeds. AGARD Report N° 300 (March 1959)
- [2.2.74] Sivier, K. R. and Bogdonoff, S. M.: The effect of support interference on the base pressure of a body of revolution at high Reynolds numbers". Princeton University, Report N° 332 (Oct. 1955)
- [2.2.75] Carrière, P. and Sirieix, M.: Effets aérodynamiques de l'éclatement d'un jet de fusée. *La Recherche Aérospatiale*, N° 89, pp. 3-10 (July-Aug. 1962)
- [2.2.76] Moreau, R.: Use of magnetic suspension system in ONERA wind tunnels. Proceedings of the ARL Symposium on *Magnetic Wind Tunnel Model Suspension and Balance Systems*, pp. 199-245 (April 1966)
- [2.2.77] Bayden, R. P.: A review of magnetic suspension and balance systems. AIAA Paper 88-2009 (May 1988)
- [2.2.78] Sirieix, M.; Détery, J. and Monnerie, B.: Etude expérimentale du proche sillage de corps de révolution en écoulement supersonique. 19th International Congress of Astronomy, 13-19 Oct. 1968, New-York
- [2.2.79] Détery, J.: ONERA research on afterbody viscous/inviscid interaction with special emphasis on base flows. Proceedings of the Symposium on *Rocket / Plume Fluid Dynamics Interactions*, The University of Texas at Austin, Vol. 3 (1983)
- [2.2.80] Pindzola, M.: Jet simulation in ground test facilities. AGARDograph N° 79 (1963)
- [2.2.81] Korst, H. H.; White, R. A.; Nyberg, S.E. and Agrell, J.: Simulation and modelling of jet plumes in wind tunnel facilities. *Journal of Spacecraft*, Vol. 18, N° 5, pp. 427-434 (Sept.-Oct. 1981)

## 2.3 Application of CFD Techniques to Model 3-D Afterbody Flow Phenomena

### 2.3.1 Introduction

This chapter presents a review of the state of Computational Fluid Dynamics (CFD) for analysis of 3-D afterbodies in 1993-94. The current uses of CFD analysis will be reviewed, and the chief obstacles to fast and reliable prediction of 3-D afterbody flows will be discussed.

The products of CFD analysis and experimental investigation differ in one critical aspect: CFD analysis provides a complete 3-D description of the flowfield, while experimental investigation seldom provides a full explanation of the flow phenomena which produce the observed behavior. The chief use of CFD analysis at present is based on this point: CFD analysis is used to gain a qualitative understanding of the key elements of a complex flow field. The quality of CFD predictions is established by comparison with experimental data at a limited number of points, and the predictions are used to "fill in the gaps" in the measured data and provide a complete description of the flowfield.

The second chief application of CFD has been to provide data which cannot be obtained in the wind tunnel. This includes data free of wall and support interference, and data at conditions not amenable to ground test (e.g., hypersonic conditions).

Prediction of aircraft performance parameters (forces and moments) has been a more demanding application for CFD. Drag estimates to usable precision have proven especially difficult for CFD analysis methods. However, predictions of incremental effects - the differences in force and moment on two similar geometries - have been made with increasing confidence and precision in recent years. This ability to predict increments has allowed CFD to contribute substantially in the screening of similar, competing design concepts, and the optimization of a vehicle shape. CFD analysis is just beginning to be used for quantitative prediction of aircraft performance parameters, such as drag. Of course, drag predictions leading to optimization are the focus of the present study.

The remainder of this section focuses on the specific issues of CFD analysis of nozzle and afterbody flowfields. Immediately below (Section 2.3.2), the physical features of the flow are discussed, and the impact of those features is discussed in terms of requirements for the CFD analysis. Subsequently (Section 2.3.3), the state of the art in CFD practice is discussed in the context of these key flowfield features.

### 2.3.2 Pertinent Flow Physics Issues

Prediction of 3-D afterbody flows has been notoriously difficult for CFD analysis. The chief parameter of interest is

drag, which is especially difficult to predict. Several complicating issues are present for this application:

- The flows over the afterbody are dominated by thick turbulent boundary layers.
- The boundary layers are subjected to a sustained adverse pressure gradient, which often leads to flow separation in this application.
- The physical flows often exhibit large-scale unsteadiness, which is not taken into account in the CFD predictions. The impact of this unsteadiness on turbulence modeling assumptions is unknown.
- The boundary layers over a 3-D afterbody are subject to significant lateral pressure gradients, which induce strong secondary flows.
- Afterbody geometries often are quite complex, as they include single- and twin-engines, empennage (tails, booms, and fairings), gaps in the geometry, and variable (movable) geometry. All of these elements can be important, and should be modeled.
- The afterbody flows are significantly modified by the presence of a flowing propulsive jet (the plume), which has an impact both by its shape and by its entrainment.

As a result of these issues, the accurate prediction of afterbody flows remains a formidable challenge for CFD prediction methods. The major technical issues will be reviewed in somewhat more detail next.

#### 2.3.2.1 Geometry Issues

Realistic 3-D afterbodies have a very complex geometry. Many complicating features are present, including:

- Movable flaps.
- Empennage - horizontal and vertical tails.
- Gaps between nozzles to accommodate movable surfaces.
- Booms and other support structure.

These features place high demands on geometry modeling and grid generation capabilities for CFD analyses. The impact of these complications on the CFD analysis process is discussed in Sections 2.3.3.1 and 2.3.3.2.

#### 2.3.2.2 Boundary Layer Properties

The boundary layers are turbulent, relatively thick (having grown over the full length of the vehicle), and they are subject to a sustained adverse pressure gradient. This combination of factors means that important large-scale features of

the afterbody flowfield will be dominated by the behavior of the turbulent boundary layer. Thus, the quality of results for afterbody computations depends strongly on the fitness of the turbulence model. In most situations, the boundary layer can be assumed to be fully turbulent; transitional effects can be neglected.

The vehicle surfaces are curved in both the axial and lateral directions; the radii of curvature often are of the same length scale (or smaller) as the boundary layer thickness. Thus, wall curvature effects may be significant in these flows. Further, the boundary layer is subjected to significant lateral pressure gradients due to the effects of the empennage and variations in lateral curvature. These gradients induce significant secondary flows, which often cause complications in present turbulence models.

A simple afterbody-nozzle flowfield is illustrated in Figure 2.3-1. Approaching the afterbody and nozzle, the boundary layer is growing slowly (in the absence of other influences) in a nearly constant pressure simple flowfield. The shoulder at the beginning of the nozzle creates a locally minimum pressure. Therefore, the boundary layer approaching the shoulder experiences a favorable pressure gradient (diminishing pressure in the running direction of the boundary layer) and the boundary layer has a tendency to become thinner.

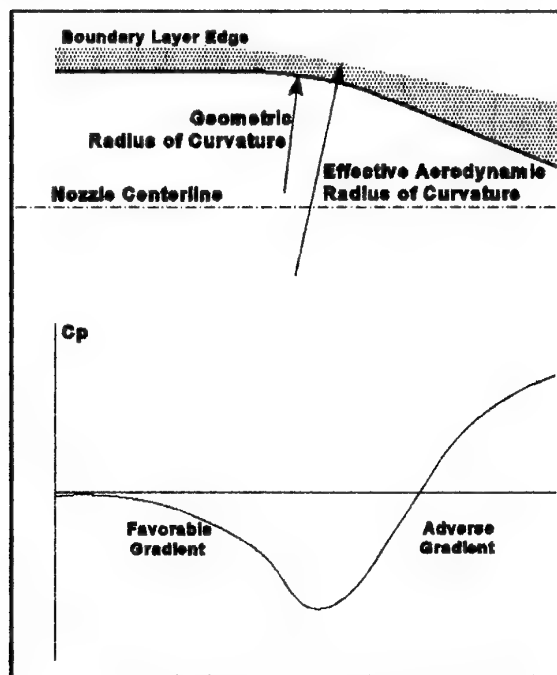


Figure 2.3-1. General Behavior of Turbulent Boundary Layer

Past the minimum pressure point, the gradient becomes adverse and the boundary layer begins thickening rapidly. This adverse pressure gradient continues unabated (in most

instances) until reaching the nozzle exit. The boundary layer continues thickening significantly, and flow reversal or separation will occur. This interaction in the final adverse pressure gradient region is recognized as (perhaps) the key problem in predicting afterbody flowfields accurately.

However, a second region also poses important issues: the shoulder region (i.e., near the minimum pressure point). The initial favorable pressure gradient causes the boundary layer to become thinner, and the following adverse pressure gradient causes the boundary layer to thicken. Both these influences tend to reduce the effective aerodynamic curvature of the afterbody and nozzle at the shoulder, thus reducing the depth of the pressure minimum. Modeling this interaction requires that the turbulence model provide accurate growth rates in both favorable and adverse pressure gradients. This issue, too, places high demands on the numerical method in general, and the turbulence model in particular.

The chief impact of viscous interactions is to modify the pressure distribution on the afterbody and nozzle. This modification, as previously discussed, is particularly apparent at the minimum pressure shoulder point, and in the last short distance before the nozzle trailing edge. At transonic speeds, a significant portion of the nozzle recompression may occur as a shock wave rather than as a distributed compression. In this event, the location and strength of the shock and its associated pressure rise also are strongly affected by interactions with the turbulent boundary layer.

Viscous effects also can be seen, of course, in the friction component of drag. This effect depends on the amount of wetted area, and therefore is more consequential on those drag components which span large amounts of surface area: the complete aftend, or the aftbody. Friction drag, due to a smaller wetted area, is not so significant on the nozzle drag alone.

### 2.3.2.3 Plume Issues

Optimum engine/nozzle performance, viewed in isolation, is almost always achieved by a fully expanded nozzle flow, for the conditions of operation of the engine. This term, "fully expanded," means the static pressure in the plume at nozzle exit is the same as that in the external stream. With the pressures in balance, the plume does not turn at the nozzle exit and no shock-expansion wave system is produced in the jet.

However, because of the interaction of the nozzle and freestream flow over the aftbody, a trade between maximum engine/nozzle performance and airframe drag is possible. A degradation in the nozzle exit flowfield may be useful, to achieve some more global optimum in the design. This, in fact, is the usual situation. CFD analysis has a valuable contribution to provide in optimizing this aspect of the vehicle design.

The plume(s) affect the flowfield in two important ways:

- The shape of the plume (dividing streamline) downstream of the nozzle exit acts as an effective body. At subsonic or transonic speeds this plume shape will modify the pressure distribution over the afterbody.
- The entrainment of the plume free shear layer will accelerate the air flow over the afterbody into the free shear layer, thus reducing afterbody pressure and increasing drag.

**Plume Shape** - The shape effect is essentially an inviscid phenomenon. The shape is governed by the expansion of the plume upon emerging from the nozzle, and by the subsequent wave patterns within the plume. For an increase in NPR, the plume tends to expand at a larger angle on emerging from the nozzle. This "billowing" effect causes a compression turning of the external flow at the nozzle exit, which increases with NPR. For subsonic and transonic cases, this increase in the external flow turning tends to elevate the pressure on the afterbody. Thus, the shape effect tends to reduce drag with increasing NPR.

However, this pressurization also increases the adverse pressure gradient on the aftbody and nozzle. As a result, the boundary layer will thicken rapidly and the recompression of the flow approaching the trailing edge will be degraded - which will tend, by itself, to increase drag. In this case, the relationship between drag and NPR becomes quite complex. Accurate resolution of shock and expansion wave systems within the plume is essential to predict these effects due to plume shape.

**Plume Entrainment** - The entrainment effect is essentially a viscous turbulent phenomenon. The key issue is the evolution of boundary layers from the external afterbody and interior nozzle, into the free shear layer between the plume and the free stream. Since the entrainment of flow over the afterbody is dominated by the shear layer very close to the nozzle and afterbody, models based on similarity assumptions have limited value. The nature of this turbulent flow, transitioning from dual boundary layers (external and internal) to a free shear layer in the presence of shock waves, places high demands on any turbulence model.

The elements of evolution of the turbulent boundary layers into the free shear layer are illustrated in Figure 2.3-2.

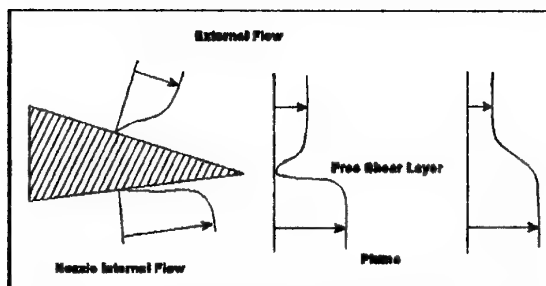


Figure 2.3-2. Evolution of Turbulent Boundary Layers into Plume Free Shear Layer

The boundary layer on the internal nozzle surfaces usually has been subjected to a sustained favorable pressure gradient as the exhaust flow is accelerated through the nozzle. As a result, this internal boundary layer is very thin, and it is producing high shear at the nozzle internal wall. The boundary layer on the external nozzle surface, on the other hand, has been subjected to a sustained adverse pressure gradient. As a result, the external boundary layer profile is that of low surface shear stress. Quite possibly, the external boundary layer is separated near the nozzle exit.

Once past the nozzle trailing edge, these two boundary layers interact immediately. The plume flow and the high-shear internal boundary layer begin entraining the low-shear external boundary layer. Modeling this interaction is very difficult, due to the high gradients in velocity, pressure, and shear stress which are present. Further, the issue of turbulence modeling is complicated by the diverse length scales in the merging flows: small turbulent length scales in the merging internal boundary layer, larger length scales in the external boundary layer. The near-field entrainment can have a significant impact on afterbody-nozzle drag, particularly if the external boundary layer is relatively thick and is in a low-shear state. Obtaining accurate predictions in this near-field region is both essential (at certain flight conditions) for an accurate drag prediction, and it is quite demanding.

Further downstream, the free shear layer (e.g., the mixing layer) evolves into a classical self-similar free shear layer. However, this evolution is further complicated by the probable presence of shock waves in the plume and perhaps in the surrounding external flow, and by three-dimensional effects in the flowfield. Further, these flows often exhibit significant unsteady or acoustic interactions, whose impact on the turbulent mixing and the model validity is unknown.

**Plume Vortices** - Streamwise vortices may be introduced in the plume mixing layer. These vortices may come from either the internal or external flows through/over the nozzle.

From the internal nozzle flow, these streamwise vortices most often arise from lateral pressure gradients (created by non-axisymmetric shape variations) acting on the boundary layer. These lateral gradients are produced by changes in the cross



section shape (e.g., transition from circular to rectangular shape), by local features in the internal nozzle geometry, or by turning the exhaust flow. They may arise from similar sources in external flow. In external flow, they also can be created by other interactions such as viscous flow about the root of protuberances (tail, antennae, etc.). Or, they may come from tip vortices from antennae, vortex generators, or forward aerodynamic control surfaces.

Whatever their origin, these streamwise vortices in the plume mixing layer can have a substantial effect on the shape and entrainment of the plume. These vortices travel downstream within the mixing layer, so their impact is cumulative. They can modify the plume extensively. However, due to the cumulative nature of this interaction their impact usually is not felt strongly in the immediate vicinity of the nozzle exit.

### 2.3.2.5 Tail Interactions

The presence of protruding tail surfaces, or other features, introduces significant added complications in the CFD modeling of the flowfield. A simplified representation of these issues is presented in Figure 2.3-3.

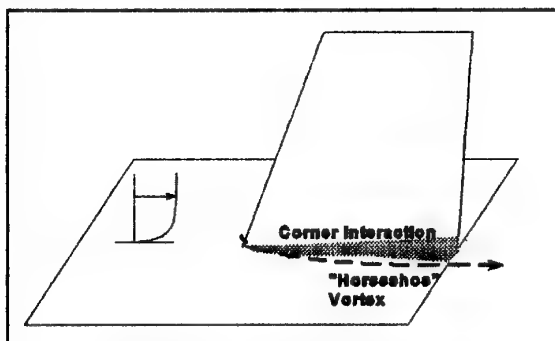


Figure 2.3-3. Interaction of Tail with Fuselage Boundary Layer

Geometric modeling and grid generation for this intersection geometry present some interesting challenges for certain methods. However, fundamental issues are seen in viscous and turbulent flow prediction.

Three important interactions occur in this type of flowfield:

- A complex three-dimensional pressure field results, in an inviscid sense, from the combined influences of the afterbody-nozzle (fuselage) shaping and the tail aerodynamic shaping (e.g., section and planform).
- A classical "horseshoe" vortex is produced by the tail's obstruction of the approaching fuselage boundary layer. This vortex streams aft along each side of the tail, in the root juncture region.
- A complex turbulent corner flow is produced in the tail-body intersection, as the boundary layer is subjected to complex shear stresses from the two intersecting walls.

The latter two interactions depend intimately on the interaction of the turbulent flow with the three-dimensional geometry and its pressure field. Accurate predictions of these phenomena, therefore, require sophisticated turbulence modeling. The absolute impact of these interactions depends (obviously) on specific vehicle integration details. Accurate drag prediction for complex (realistic) configurations will require a turbulence model which is effective in these areas.

### 2.3.3 Elements of CFD Analysis

Many technical elements must be integrated to produce a CFD prediction. The quality of the prediction will, of course, be controlled by the sum of the limitations of these elements.

Often, in engineering applications, the choice of analysis methods from the available spectrum is driven not only by technical capabilities applied to the needs at hand, but also by consideration of the cost and schedule required for the analyses.

For example, more complex turbulence models (e.g., "two equation" models) usually can be expected to give more accurate results in complex turbulent regions, compared with simpler models ("zero-equation" or "one-equation" models). However, the computing resources required for the technically-preferred two-equation models can range from twice to seven times that of the simpler models. Therefore, cost considerations are almost always inevitable in selecting the analysis approach.

#### 2.3.3.1 Geometry Definition

The geometries associated with 3-D afterbodies can be quite complex. The task of preparing these geometries for grid generation can be quite challenging. Often, it is necessary to simplify the geometry to obtain a shape which can be analyzed. The necessary modifications may include altering local shaping to eliminate gaps or discontinuities, blending sharp corners, or removing major elements such as tail surfaces. Some nozzle designs may allow flow to penetrate the surface in one place and emerge elsewhere, adding to the complexity of the CFD solution. Clearly, any of these alterations may have a significant impact on the predictions. In some cases, that impact may not be anticipated, leading to difficult interpretation of the results.

To simplify the problem of afterbody analysis to a practical degree, the forward portion of the model might be removed from the analysis. The engineer then must use his/her judgment to provide the essential elements of the flowfield from the missing geometry, at the point where the computations begin.



In this approach, the essential issue is to define the boundary layer entering the computational domain from the missing forebody. The boundary layer flowing onto the afterbody is affected by all the aircraft features located forward. The boundary layer will be generally distorted and non-uniform, as a generalized result of the forward flows. A wake may be present from the canopy (or, other forward components). Streamwise vortices from wing leading edges, strakes, forebody chines, and other features may have a continuing effect in modifying the boundary layer on the afterbody. Definition of other geometric features also may be important.

In some cases, various types of defects may be present in the geometry used for CFD analysis. Most Computer-Aided Design (CAD) systems generate geometry in local elements, often called "patches." For most CAD systems, no compatibility constraints are enforced between the patches. Several types of defects may be encountered. The geometric definition may simply be incorrect. Or, omissions (gaps) may be found between the patches. A more complex issue arises when the patches overlap. In the overlap region, the geometry is doubly defined. At intersecting surfaces, some patches may extend inside the body. These portions of the patches are recognized by the designer as being superfluous, but it can be a tedious process to remove them (this process is called "trimming" the patches). Therefore, often they remain in the geometric definition.

Each of these issues represents a defect in the geometry definition, in terms of its fitness for CFD analysis. These defects (if present) must be corrected during the geometry acquisition and grid generation phase of the CFD analysis process. Usually, this step requires the exercise of judgment by the CFD engineer: in determining (for example) how the gap should be filled, or which definition should be used in a multiply-defined region.

The impact of imprecision in this step depends on several factors. The sensitivity of the physical flowfield to local features of the geometry is affected by many elements (e.g., Mach number, boundary layer state) and often cannot be established easily, in advance.

The sensitivity of the numerical method, too, can be affected by localized details of the geometry. For example, small discontinuities in the surface geometry definition can be propagated into the off-body computational domain through kinks in the grid, which (depending on the solution method) can affect the predictions. Some methods for grid generation and flow solution may utilize data on the local geometry slope or curvature, in addition to spatial location data. Thus, local discontinuities in these properties may, depending on the method, have a material impact on the predictions.

The choice of numerical method may affect the sensitivity to small variations in geometry. Some early grid generation methods, for example, required analytically defined geometry definitions. This approach allowed analytic differentiation of the geometry, but at a high cost in versatility and the ability

to detect flaws in the geometric definition. Other methods used geometry specifications defined by point inputs, but they then differentiated the geometry once or twice to obtain slope or curvature data which then affected the process of grid generation. These methods often produced elegant results on suitable geometry definitions, but they exhibited high sensitivity to minor deviations in terms of geometry input point location or spacing. Some flow solver algorithms may also use second derivative data in the geometry or grid - as before, this approach tends to improve accuracy in suitable applications, at the cost of rapid degradations of results (i.e., sensitivity to minor changes in geometry/grid) if the application is not nominal.

### 2.3.3.2 Grid Generation

After the analysis geometry has been defined in a suitable format, the next task is grid generation. For geometries with the complex features of 3-D afterbodies, grid generation can be a challenging issue. The schemes which are popular can be considered in three categories:

- **Multi-Block Structured** - The computational domain is broken into a number of blocks, and grid is produced in each block. The blocks uniquely span the domain, with either marginal or zero overlap. Depending on the method, compatibility requirements may apply between adjacent grid blocks. Data are exchanged between blocks and imposed as boundary conditions on the adjacent blocks.
- **Multi-Block Overlapping (Chimera)** - The domain is broken into many blocks (as before), but the blocks always overlap significantly. Generally, data are transferred between blocks with relatively simple 3-D interpolation methods, and imposed as simple Dirichlet boundary conditions.
- **Unstructured** - Unstructured grids, often composed of tetrahedral elements, are constructed to fill the domain. The techniques to do this in the general case are extremely complex and sophisticated. However, once the grid has been produced the solution process is straightforward.

Some new CFD analysis systems combine several of these methods into a single capability. For example, structured grids may be used in combination with unstructured grids for a "hybrid" analysis.

The complexity of afterbody geometries, and the high sensitivity of the flows, combine to place high demands for versatile and accurate grid generation methods. As a result, ensuring acceptable quality in the grids is a key issue in afterbody flow prediction. Hidden defects, or poor practices, may produce grids which will degrade the solution.

Producing a high-quality grid about a complex geometry is very difficult. A high-quality grid should have the following characteristics to provide accurate results:

- It is (nearly) orthogonal everywhere.
- It provides a high density of grid points wherever a high gradient occurs in any flowfield property.
- It exhibits only a moderate stretching (i.e., variation in grid point spacing along any of the coordinate directions).
- It should not turn sharply (i.e., no "kinks" should be present), unless very near to a corner in the geometry.

For a simple geometry, suitable grids meeting all these criteria usually can be generated readily, by a variety of methods. However, for a complex geometry (including most realistic afterbodies when empennage or multiple nozzles are included) it can be difficult to avoid serious compromises. The thresholds of sensitivity to degradations in these areas vary with the flow solver algorithm and with different implementations. However, allowing for variations between methods, each of these four points can affect the quality of a CFD prediction.

Visual inspection is often inadequate for identifying grid defects. Automated inspection schemes, using a suitable set of grid quality metrics, are essential for first-time success on complex grids such as those required for afterbody flow prediction.

The distribution of the grid in relation to flow features can have a large impact on the quality of the predicted results. Thus, the experience of the engineer in anticipating the essential features of the flow (including their location and strength) can be very important. Alternatively, a sophisticated adaptive scheme may be used automatically during the flow solution to adjust the grid as the flow features develop. Some sample goals (these may vary significantly depending on the flow solution method) include:

- **Shear Layers** (boundary layers, free shear layers, wakes) - prefer at least 20 grid points across the shear layer. The complication is that the location of the shear layer may not be known a priori. For boundary layers, it also is important (in most methods) to place some grid points within the laminar sublayer, at (for example) a  $y^+$  of 2. This requirement varies, depending on the turbulence model that is used, and the type of data to be predicted. The information needed to meet this goal in a given application, too, is not usually known (or even estimated with confidence) a priori - particularly for a complex flowfield.
- **Shock Waves** - Depending on the algorithm, the variations in flow properties when passing through a shock waves may be distributed across two to five (or more) grid cells. Of course, in reality a shock wave is

(effectively) a discontinuity in the flow properties. Therefore, high local grid density is needed to limit the unrealistic spreading of the shock pressure rise. This can be difficult to provide, because the location of the shock may not be known with precision prior to the calculation. Further, most CFD flow solver algorithms in effect model the local variations with higher-order polynomials or similar nonlinear functions. Unrealistic oscillations ("ringing") in the flow properties can be obtained when the region of fitted functions spans this physical discontinuity. Ringing is avoided (or controlled) by adopting limiters such as TVD ("Total Variation Diminishing") which cause the algorithms to revert to first order modeling in high gradient regions.

- **Vortices** - Vortices can be resolved with general accuracy (trajectory, general impact on the flowfield) with around five grid points in each direction across the vortex. However, prediction of details of the vortex structure require a much higher number of grid points. As in previous examples, this is difficult to provide since the location of the vortex is not known a priori.

The obvious solution to these issues is simply to use a large number of grid points, thereby ensuring that adequate modeling will be provided. However, the cost (and often, the risk) in achieving a satisfactory solution grows at least in proportion to the number of grid points, and often at a faster rate (up to the square of the number of points). Thus, grid "overkill" usually is unaffordable.

The more desired solution is to utilize adaptive solution methods, whereby the grid is adjusted and (usually) points are added as needed to improve resolution of features as they form during the course of the solution. Adaptive methods usually are very complex, and there is some discussion regarding the appropriate control functions and technical approach to achieve stable adaptation. For structured grid analyses, adaptive methods have enjoyed little success except in simple applications. However, adaptive techniques are used with far greater benefits in unstructured grid applications. In this type of analysis, points can be added or moved locally without a far-reaching impact, thus greatly easing the burdens in applying the method.

### 2.3.3.3 Flow Solver Algorithms

Tremendous variation is seen in the algorithms used for numerical solution of the Euler and Navier-Stokes equations. No consensus has emerged regarding the desired attributes of a flow solver algorithm for this application, except for the familiar and obvious issues of accuracy, efficiency, robustness, and versatility.

The application of boundary conditions can pose significant difficulties. If the plume flow computation is initiated in supersonic flow (at the nozzle exit, for example), then the physical consistency of the boundary conditions at that point

must be considered carefully. Any inconsistency will produce a false shock-expansion wave system within the plume, which will persist throughout the region of interest.

The wide range of physical features present in these flows places high demands on the flow solver algorithm. Discontinuities such as shock and expansion waves and free shear layers must be resolved with precision, since these features dominate elements of the flows. One key requirement, of course, is that the flow solver algorithm must have the versatility to utilize the complex grids and boundary conditions needed for this application.

Due to the complexity and sensitivity of the physical flows, computations of transonic afterbody flowfields are very expensive, i.e., many iterations are required, on dense grids. Therefore, for engineering suitability this application places a particular premium on the efficiency of the algorithm.

In addition, the high gradients of static temperature within and at the edge of the plume(s) may pose a special difficulty to some analysis methods. These gradients produce rapid variations in the local speed of sound. Certain methods, which use characteristics-based strategies, may experience local instabilities in these regions.

#### 2.3.3.4 Turbulence Models

A large number of turbulence models have been developed, and are candidates for application to the problem of afterbody flow prediction. These generally are categorized according to the number of partial differential equations (PDEs) which are solved for each model.

Perhaps the most popular turbulence model is that of Baldwin and Lomax (Ref. 2.3-1). This is an algebraic, or zero-equation model - so-named because it employs no partial differential equations. Algebraic equations are used to define the effective eddy viscosity based only on local flow properties. This type of model is popular because it is simple, inexpensive to use, and it is qualitatively accurate for a range of flows.

However, for flows such as transonic afterbodies with complex pressure gradients, strong secondary flows, shock interactions, and free shear layers, algebraic models may become unreliable. The effective turbulent viscosity computed using simple models may exhibit locally unrealistic behavior, even reverting to laminar values at various points in the flowfield.

More complex models generally are needed in these applications. These models solve one or more partial differential equations (PDEs) to describe field properties such as turbulent kinetic energy. These field properties are then used to predict the effective turbulent viscosity.

No PDE-based model enjoys the popularity of the simpler Baldwin-Lomax model. A PDE-based model can be expected

to do at least as well as an algebraic model, and generally better. However, these benefits often come at the price of a significant increase in the total compute time of the analysis. An increase of as much as 100% or even 200% might be seen. Therefore, an engineering validation which does not take into account the cost of the solution will generally identify a higher-order turbulence model as the preferred choice.

In "one-equation" models, one PDE is solved for a turbulent Reynolds number (in effect, a velocity scale of the turbulent motion). A popular one-equation model has been developed by Baldwin and Barth (Ref. 2.3-2). This model has been used with good results in predicting a number of complex flowfields.

A large number of two-equation models have been developed and presented in the technical literature. These models are based on PDEs for  $k$  (local turbulent kinetic energy),  $\epsilon$  (local turbulent dissipation),  $\tau$  (local turbulent time scale), or other parameters.

These zero-, one-, and two-equation turbulence models all require an assumption that the turbulence is isotropic. Another family of turbulence models, not yet widely used for engineering computations, avoids this assumption. Reynolds stress transport models (RSTM) are based on an individual PDE for each of the six components of Reynolds stress. However, RSTM have yet to be used for many complex engineering applications, and they add considerably to the computational requirements.

Another approach is to apply an algebraic modification for non-isotropic Reynolds stresses to the predictions of a one- or two-equation model. These are referred to as "Algebraic Reynolds Stress Equation" models.

Solutions of PDEs for turbulence modeling can be very slow (i.e., expensive) if required on dense packed grids such as are found near viscous walls. Consequently, in some models the turbulence properties near a wall are estimated through simple algebraic modeling methods, called "wall functions." These methods are based on the assumption that the flows close to the wall are in turbulent equilibrium (and other assumptions). This approach greatly improves the cost of using advanced PDE-based turbulence models. However, the accuracy of these models will be degraded if the wall function assumptions are violated - for example, in separated flows.

In contrast to wall functions is the "low Reynolds number formulation," based on direct integration of the PDEs to the wall. Damping functions are used to blend the high Reynolds number (i.e., outer boundary layer) PDEs with the near-wall (low Reynolds number) flow. However, the finer grids required near the wall in this approach result in a more expensive solution.

Additional families of turbulence models include Large Eddy Simulation (LES) models combined with Sub-Grid Scale (SGS) turbulence models. These models are based on

recognizing different length and time scales in turbulence. Different techniques are used to model the large and small scales. The large scales are computed directly, and modeling assumptions are used only for the small scales using an SGS model such as the Smagorinski or dynamic model.

The ultimate step, of course, is to compute all length/time scales directly. This approach, called Direct Numerical Simulation (DNS) is at present an element of basic research into turbulence physics. These solutions are incredibly expensive, and consequently are not used in the engineering process.

Ultimately, all turbulence models rely upon the developers' success in reducing the complex underlying physics to simpler functional relationships. The elements of a turbulence model consist of generalized mathematical forms, and a variety of arbitrary factors (coefficients) to set the relative scales of the modeling elements. These scale factors must be evaluated empirically, through comparisons and adjustments using selected sets of experimental or DNS data. Generally, the more complex models have a larger number of arbitrary coefficients.

Therefore, the reader must be concerned with the generality that has been achieved in setting these coefficients. In the process of determining the proper values of the empirical coefficients, the turbulence model developer inevitably "tunes" the model to a specific class of flowfields. Thus, it can be risky to declare one turbulence model to be "the best" based on accuracy in predicting a set of flows with similar physics.

#### 2.3.3.5 Unsteady Flows

If the boundary layer about the afterbody is separated at transonic conditions, in all likelihood the flows will exhibit large-scale unsteadiness. In this condition, the usual assumptions in turbulence modeling regarding Reynolds averaging most probably are violated. However, the turbulence models usually are not modified for this eventuality.

Further, the plume(s) may exhibit high-amplitude acoustic resonances, called "screech." These issues, too, are generally ignored.

Thus, it must be recognized that the models used in the CFD community for unsteady afterbody flows suffer from several weaknesses in addition to the well-known issues in turbulence modeling.

Most CFD solution methods used in the engineering community have been developed to provide efficient solutions to steady-state problems. A variety of methods are used to achieve this end. These methods destroy the transient (time-domain) accuracy of the solution. The chief acceleration method, for example, is "local time stepping." In this technique, different time steps may be used at every grid point in each iteration step. Thus, the temporal relationships

between properties throughout the computational domain are not preserved.

There is some philosophical debate, within the CFD community, regarding the behavior of these methods when computing a flow that is physically unsteady in the larger length and time scales (i.e., larger scales than those of classical turbulence). There seem to have been cases of convergence to high precision, which implies the method found a steady solution where one does not exist physically. This situation is attributed to unrealism in the physical models, inadequate resolution in the grid to define the unsteady physical mechanisms, or numerical features such as excessive artificial viscosity.

The expected outcome in this situation of physical unsteady flow would be failure to achieve a meaningful level of convergence in the CFD solution. After all, a steady-state solution does not (should not) exist. The CFD iterations should go into a limit cycle. However, if local time stepping is being employed, the engineer should be careful in attaching quantitative significance to behavior in this limit cycle (e.g., frequency or amplitude of any oscillations). Even if uniform time stepping is employed, in which case the solution may be claimed to be time-accurate, the results should be viewed with skepticism due to many issues in both the physical modeling and the numerical algorithms.

To summarize, the computation of physically unsteady flowfields with most CFD algorithms raises particular uncertainties. Philosophically, the algorithm should not achieve a high degree of convergence. Limit cycle behavior would normally be expected. In either event, the solution may or may not represent in a time-mean sense the physical flowfield.

#### 2.3.3.6 Implementation

Implementation is the discriminating issue in evaluating a CFD code. For example, any number of CFD codes solve the Navier-Stokes equations using the Baldwin-Lomax turbulence model. Thus, the mathematical basis for these codes is identical. However, the results differ substantially.

This is seen, for example, in validation studies performed in 1989 by McDonnell Douglas (Ref. 2.3-3). The test case is the ONERA M6 wing (Ref. 2.3-4). All solutions were obtained on the same grid, using the same computer and compiler, with consistent standards for declaring convergence. However, the results varied widely. Since the mathematical bases for each code are the same (Navier-Stokes equations, Baldwin-Lomax turbulence model) and the input data are the same (same flow conditions, same grid), the differences are attributed to the implementations of the algorithms within each code.

These implementation effects can be seen most readily by examining simulations of surface oil flow patterns. The reader should bear in mind the codes being compared

(following) are all solving the same equations (Navier-Stokes equations with the Baldwin-Lomax turbulence model) on the same grid, using the same computer and compiler. These solutions all were generated by the same engineer, who had several years of experience in Navier-Stokes CFD analysis. However, the implementations (of course) differ. Results are presented for the CFL3D code (Ref. 2.3-5, Figure 2.3-4), the TNS code (Ref. 2.3-6, Figure 2.3-5), and the TLNS3D code (Ref. 2.3-7, Figure 2.3-6).

Each analysis captures, in a qualitative sense, the primary feature of the flowfield - the shock-induced separation on the wing as a result of the elevated angle of attack at transonic speed. However, the results vary greatly in the specific nature of the flowfield in the vicinity of the strong viscous interaction. It should be noted, the comparison with the surface pressure data (presented in Ref. 2.3-3) showed no clear "winner" among the three codes whose results are presented here. Each prediction was close to the experimental data in some regions, and departed from the data in other regions.

Thus, care must be taken in attaching meaning to validations performed for a different code than the one which the investigator intends to use. Validations of other codes can be useful in showing what can be achieved, and in identifying pitfalls and important issues. However, the reader should not conclude that a mathematical modeling approach is either superior or unfit based on validations from a single code.

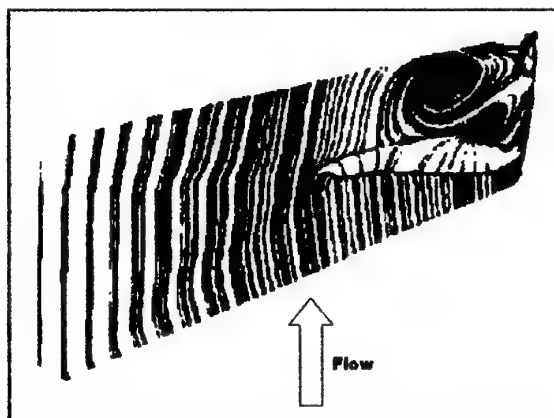


Figure 2.3-4. CFL3D Prediction of Surface Oil Flow for ONERA M6 Wing at Mach 0.837,  $\alpha=6.06^\circ$

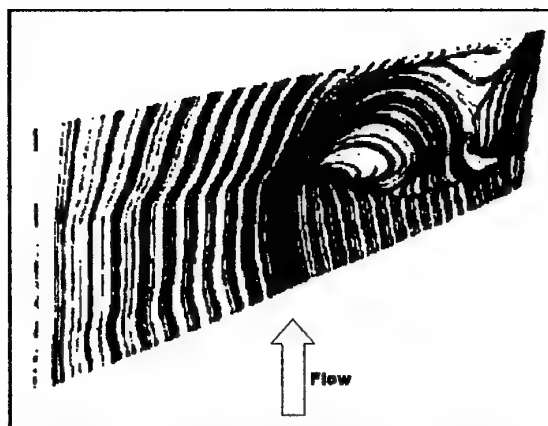


Figure 2.3-5. TNS Prediction of Surface Oil Flow for ONERA M6 Wing at Mach 0.837,  $\alpha=6.06^\circ$

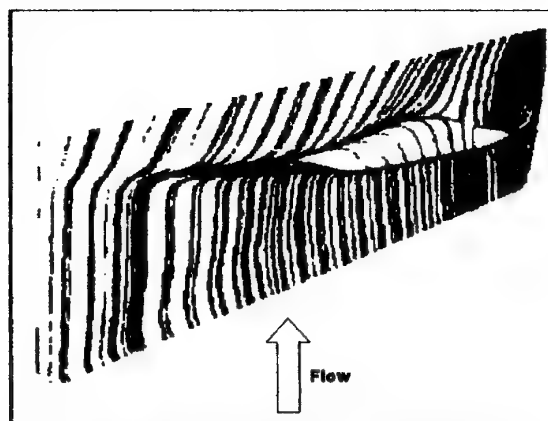


Figure 2.3-6. TLNS3D Prediction of Surface Oil Flow for ONERA M6 Wing at Mach 0.837,  $\alpha=6.06^\circ$

These solutions differ only in the implementation of their common mathematical basis, and (inevitably) in the usage practices (see following discussion). The implementation affects the results in many ways, in addition to the obvious case of an error by the programmer.

This situation can be illustrated by considering the implementation of the Baldwin-Lomax turbulence model. This model requires knowledge of the normal distance from the nearest wall to each grid point. The computation of the normal distance from a point to the nearest wall is simple if the wall is an infinite flat plate. In the general case, however, this computation requires an expensive search through all nearby wall cells. Special treatment may be needed if corners are present in the nearby walls. These computations can destroy the efficiency of an iterative Navier-Stokes solver, where perhaps a few million near-wall points must be treated for each iteration.

Expedient measures usually are taken, therefore, to obtain wall normal distances which can be obtained rapidly (without search procedures) and are usually fairly accurate. The most common approach is to take the distance along the grid coordinate line which passes from the wall through the point in question to the far field. If the grid is well constructed, this line is in fact normal to the wall and the procedure is quite accurate. However, in a relatively direct way the quantitative prediction of effective turbulent viscosity now depends on the orthogonality of the grid.

Due to these types of practical implementation issues, it is very difficult to compare CFD methods directly. In the example given above, the method can be expected to be in error if the grid is not orthogonal across the boundary layer. However, with an appropriate grid that method will be quite accurate, and (other issues ignored) it will be significantly faster than an alternative method.

### 2.3.3.7 Usage Practices

The state of the art in CFD analysis is such that agreement exists within the technical community on the most general aspects of usage practices. Further, variations in usage practices can have a large impact on the quality of results achieved. The usage practices vary in every respect. Some of the more critical issues are:

- Geometric fidelity.
- Placement of off-body boundaries.
- Grid topology and blocking strategy.
- Nominal grid density, stretching, and orthogonality.
- Grid quality - acceptable limits in orthogonality, stretching, skewness, etc.
- Computer word length employed - may affect numerical errors on dense grids..
- Boundary condition implementation.
- Flow solution initialization.
- Use of grid sequencing, multigrid, or other convergence acceleration techniques..
- Use of non-physical control parameters, e.g., numerical dissipation.
- Convergence criteria.

These factors are difficult to quantify. Each of them can affect the final quality of CFD predictions.

We have solicited usage data from the contributors who provided predictions for the recommended test cases. Due to the diversity of issues, no clear trends have emerged from a review of these data. The usage data are presented in Appendix C, for the readers' perusal.

### 2.3.3.8 Post-Processing

Several approximations also may be introduced in post-processing CFD predictions. For example, the computation of

streamlines and oil-flow simulations requires a stepwise integration through the velocity field. The oil flow simulation also requires a constraint, or a correction, to use only the component of velocity lying within the constrained surface. In the general case, with a non-orthogonal stretched grid, several approaches with varying degrees of rigor can be conceived.

A simple example is the order of the technique and the magnitude of the spatial step used for the stepwise integration of the streamlines. A first-order scheme with a one-cell step will produce plots that are visibly composed of piecewise line segments. A higher-order scheme with a small step size will produce results that show a wealth of detail, though that "detail" may be an artifact of integration algorithm and not of the solution. For example, if three-dimensional third-order interpolation is used to provide data for integration within a grid cell, then very complex patterns can be produced which do not represent the first- or second-order CFD solution. These streamline plots, therefore, should not be considered meaningful (i.e., representative of the flow prediction) on length scales less than one or two grid cell intervals. This issue can be difficult for the user to assess without detailed investigation.

Issues can arise in other aspects of post-processing. The pressure integration for drag can pose ambiguities. These issues are familiar to those who have developed similar procedures for computing pressure drag from wind tunnel data. One approach is to compute drag by summing the product of pressure times the rearward-facing area assigned to each point. Another approach is to fit a function to the surface pressure in each surface cell, and perform a mathematical integration of the data over that cell. This approach offers a higher-fidelity integration, but the results will be affected by the type of interpolating function which is fit to the data. These issues can alter the results by one to three aircraft drag counts (Ref. 2.3-8).

In comparing CFD drag data with experimental pressure-integrated drag data, this issue can become quite important. The wind tunnel data, for example, may be based on less than 100 surface data points, while the CFD data quite possibly can be based on over 100,000 surface data points. Furthermore, the algorithms used to process each data set may be quite different and inconsistent.

The most attractive approach, which was not possible in the present investigation, is to make the comparisons on a completely consistent basis by extracting CFD predicted pressures at the points where experimental measurements were taken, then computing drag using the same algorithm used in processing the experimental data. The pressure drag computed from the full CFD grid may vary by as much as five to eight aircraft drag counts from an integration of the same data by mapping to the wind tunnel measurement locations (Ref. 2.3-8).

Another area of significant ambiguity lies in determining the location of a three-dimensional flow separation point. In this area, ambiguity exists even on a conceptual basis. Computationally, the simplest approach is to declare separation when  $u < 0$  for any point in the boundary layer. However, this can be ambiguous if the flow is turned substantially from the original direction, or from the x-coordinate axis. Another approach is to determine whether a closed envelope of streamlines exists, isolating one region of flow, adjoining the surface of the body, from the remainder of the flowfield. However, this approach requires substantial post-processing to detect separation, and it is subject to the ambiguities in streamline tracing which were discussed earlier.

### 2.3.4 Summary

The analysis of transonic afterbody-plume flowfields is one of the most challenging topics in applied CFD. This analysis places high demands on both the geometry/grid capabilities, and on the turbulence model. The extreme physical sensitivity of the flows is reproduced in high numerical sensitivity, which leads to high compute times. Any weakness in the mathematical, physical, or numerical bases of the CFD method will degrade the quality of predictions in this application.

### References

- 2.3-1) Baldwin, B., and H. Lomax, "Thin Layer Approximation and Algebraic Model for Separated Turbulent Flows," AIAA Paper 78-257, 1978.
- 2.3-2) Baldwin, B., and T.J. Barth, "A One-Equation Turbulence Transport Model for High Reynolds Number Wall-Bounded Flows," AIAA Paper 91-0610, 1991.
- 2.3-3) Agrawal, S., and T.A. Kinard, "Evaluation of Three Navier-Stokes Solvers for Wing Flowfields," Proceedings of *First US National Congress on Computational Mechanics*, pg. 279, Chicago, July 21-24, 1991.
- 2.3-4) Schmitt, V., and F. Charpin, "Pressure Distributions on the ONERA-M6 Wing at Transonic Mach Numbers," AGARD-AR-138, May 1979, Chapter B-1.
- 2.3-5) Thomas, J.L., S.L. Taylor, and W.K. Anderson, "Navier-Stokes Computations of Vortical Flow Over Low Aspect Ratio Wings," AIAA Paper 87-0207, January 1987.
- 2.3-6) Holst, T.L., U. Kaynak, K.L. Gundy, S.D. Thomas, J. Flores, and N. Chaderjian, "Numerical Solution of Transonic Wing Flows Using an Euler/Navier-Stokes Zonal Approach," AIAA Paper 85-1640, July 1985. Also: *Journal of Aircraft*, Vol. 24, No. 1, pg. 17 (January 1987).
- 2.3-7) Vatsa, V.N., "Accurate Solutions for Transonic Flow Over Finite Wings," AIAA Paper No. 86-1052, May 1986.
- 2.3-8) Cosner, R.R., unpublished data from McDonnell Douglas, 1994.



## 2.4 Review of Computational Methods

The prediction methods presented here fall into two general classes:

- Engineering Methods, or Semi-Empirical Methods, exemplified by the Integral Mean Slope approach, and,
- CFD Methods for solving the Euler and Navier-Stokes Equations, using either structured or unstructured technology.

Since most Navier-Stokes codes also are capable of producing Euler solutions, both types of solutions are presented together. Further, the grid generation technology has a lot to do with the applicability of the Euler and Navier-Stokes solutions, and their quality. Therefore, special attention also is given to the grid generation tools.

The methods utilized in this investigation are described in this Section.

### 2.4.1 Semi-Empirical Methods

In this contribution, AERMACCHI has avoided methods that are not able to predict NPR and tail effect on afterbody drag, since these effects are the main topics of the selected test cases.

The method utilized by AERMACCHI can be defined as an engine-airframe integration method (see section 3.2.1.3). This semi-empirical method has been integrated in a complex scaling system and combined with other codes (related to inlet performance) which allows definition of the installed thrust and configuration trade-offs in the engine-airframe integration during preliminary design.

#### 2.4.1.1 Method Description

The methodology used is based on the method of Ref. 2.4-1, with some modifications related to the prediction of tail effects.

The method considers three flow regimes, defined as follows:

- subsonic, from  $M=0$  up to the drag divergence Mach number  $M_{DD}$ .
- transonic, from  $M_{DD}$  up to  $M<1.2$
- supersonic,  $M>1.2$

and for each flow regime define the following:

- aftend pressure drag
- tail pressure drag
- aftend friction drag
- tail friction drag

The drag divergence Mach number  $M_{DD}$ , that defines the boundary between the subsonic and transonic regimes, is determined as follows:

- using the code in Ref. 2.4-2 (RAXBOD, analysis of steady, inviscid, irrotational, transonic flow over axisymmetric afterbodies) the maximum local Mach number, over the equivalent body of revolution, is defined varying  $M$  at  $\alpha=0$ ;
- the  $M_{DD}$  is defined when the local Mach number over the afterbody reaches 1.02, in the equivalent shock-free flow computed using methodology similar to that of Ref. 2.4-2 (see Ref. 2.4-3).

Once the  $M_{DD}$  is defined, the pressure and friction drag for the aftend and tails can be computed. The subsonic aftend pressure drag for a single engine configuration is defined on the basis of the following empirical correlation (Ref. 2.4-1):

$$C_{DP} = \frac{K_1 \left( \frac{IMS}{M} \right)^{2/3} [A_{MB} - (A_s + A_b)] q + K_2 (A_s + A_b) q + K_3 * Fid}{q * A_{ref}}$$

For twin-engine configurations, the following equation is needed:

$$C_{DP} = \frac{K_1 \left( \frac{IMS}{M} \right)^{2/3} [A_{MB} - 2(A_s + A_b)] q + K_2 2(A_s + A_b) q + K_3 2Fid}{q A_{ref}}$$

Where  $K_1$ ,  $K_2$ , and  $K_3$  are defined in Figures 2.4-1, 2.4-2, and 2.4-3, relative to twin engine narrow spaced configurations with convergent-divergent nozzles.

The first term in the equations is the jet-off aftend drag. The second term is the aftend drag due to the variation from jet-off to design NPR. The third term represents the drag variation when going from design to higher NPR.

In the subsonic flow region, the tail pressure drag is assumed to be equal to zero.

The supersonic aftend pressure drag for a single engine comes from the following equation (Ref. 2.4-1):

$$C_{DP} = \frac{\left\{ \frac{K_4}{M^2 - 1} [A_{MAX} - (A_s + A_b)] q - K_5 (A_s + A_b) \left[ \frac{P_{s,ms} - P_{s,loc}}{P_{s,ms}} \right] \right\}}{(q A_{ref})}$$

For twin engines, the following equation applies:



$$C_{DP} = \frac{\left\{ \frac{K_4}{M^2-1} [A_{MAX} - 2(A_s + A_b)] q - K_5 2(A_s - A_b) \left[ \frac{P_{s,ent} - P_{s,loc}}{P_{s,e}} \right] \right\}}{(q A_{ref})}$$

where  $K_4$  and  $K_5$  are determined in Figures 2.4-4 and 2.4-5.

Similar to the subsonic flow regime, the first term in the equation is the aftend jet-off drag and the second is the drag variation when going from jet-off to jet-on condition.

The tail pressure drag increment at supersonic flow conditions is computed by means of a supersonic zero-lift wave drag code (Ref. 2.4-4) considering the difference in wave drag from tails-on to tails-off configurations.

In the transonic flow regime a transonic zero-lift drag function is adopted, with the aim to define the transonic pressure drag for tails off configurations and the tail pressure drag for configurations with tails. Entering Figure 2.4-6 with the value of  $[(M-M_{DD})/(1.2-M_{DD})]$  a ratio of  $[(C_{DP(M)} - C_{DP(MSUB)}) / (C_{DP(M=1.2)} - C_{DP(MSUB)})]$  is defined. Since the value of  $C_{DP(M=1.2)}$  and  $C_{DP(MSUB)}$  are known, the  $C_{DP}$  at transonic Mach number is easily defined.

To account for the skin friction drag, the method uses the Prandtl-Schlichting formula in order to define the skin friction coefficient in turbulent smooth flow:

$$C_f = \frac{0.455}{(\log Re)^{2.58}} (1 + 0.15 M^2)^{-0.38}$$

For  $Re > Re_{CUTOFF}$  the  $C_f$  is assumed to remain constant with the aim to consider the surface roughness.

When a partial body skin friction drag has to be computed (as in the present AGARD test cases) the  $C_{DF}$  from the metric break station to the end of the nozzle is equal to

$$C_{DF(AFTBODY)} = C_{DF(FULLBODY)} - C_{DF(METRICBREAK)}$$

A form factor is considered for tail components at subsonic flow.

## 2.4.2 CFD Methods (Euler and Navier-Stokes)

The Working Group has received CFD predictions using fifteen different methodologies. These contributions illustrate the broad and diverse nature of CFD methods currently used for aerospace applications. All of these are engineering codes, codes used for general purposes in the design and analysis of aerospace vehicles (as distinguished from research codes). Most of the methods are based on

multi-block structured grid solvers, though several contributions also were received using unstructured solvers. No contributions were provided, utilizing hybrid solvers (i.e., combining structured and unstructured methods in solving a single problem).

### 2.4.2.1 Grid Generation Impact

For complex geometries, grid generation is a labor-intensive activity. The process frequently relies on trial-and-error steps in producing a grid, then examining the grid and (perhaps) altering the product in some manner. For that reason, many grid generation programs have been implemented in an interactive environment, on modern color graphics workstations or X-Windows terminals.

The computational grid can have a significant impact on the quality of the resulting CFD solutions. Clearly, the grid must define the geometry and the flowfield features with sufficient resolution to provide accuracy. Equally clear, the grid must allow carrying the flow solution to a sufficient distance from the model, so that the far-field boundary conditions are adequate and accurate models of the equivalent flow in unconfined air, at that boundary location.

More subtle issues also can be identified, pertaining to grid generation. Depending on the characteristics of the individual flow solver, a loss of orthogonality in a structured grid can reduce the accuracy of the solutions, and increase the cost by causing a poor convergence rate. In unstructured grids, an analogous problem arises if the grid elements (often, tetrahedra) are flattened substantially, thereby departing from an ideal shape of a cell with nearly equal faces and included angles.

For higher-order solution schemes, errors also can be introduced if the grid is highly stretched in one (or more) of the coordinate directions. This issue can degrade accuracy or stability, with a clear impact on the quality and cost of the results.

### 2.4.2.2 Turbulence Model Impact

The physical models, embedded within the flow solver, also are a potential source of inaccuracies. Solutions of the Navier-Stokes equations, for example, are not performed with a resolution for direct prediction of small length and time scales of turbulence. Turbulence models are used, instead, to provide the gross effects of turbulence at larger scales of length and time (often, the only time scale represented in the model is steady-state).

Turbulence models are a notoriously weak element in obtaining accurate predictions of transonic flows in adverse pressure gradients. However, many advances have been produced over the recent years. Most of the turbulence models represented in the contributions to the present study,

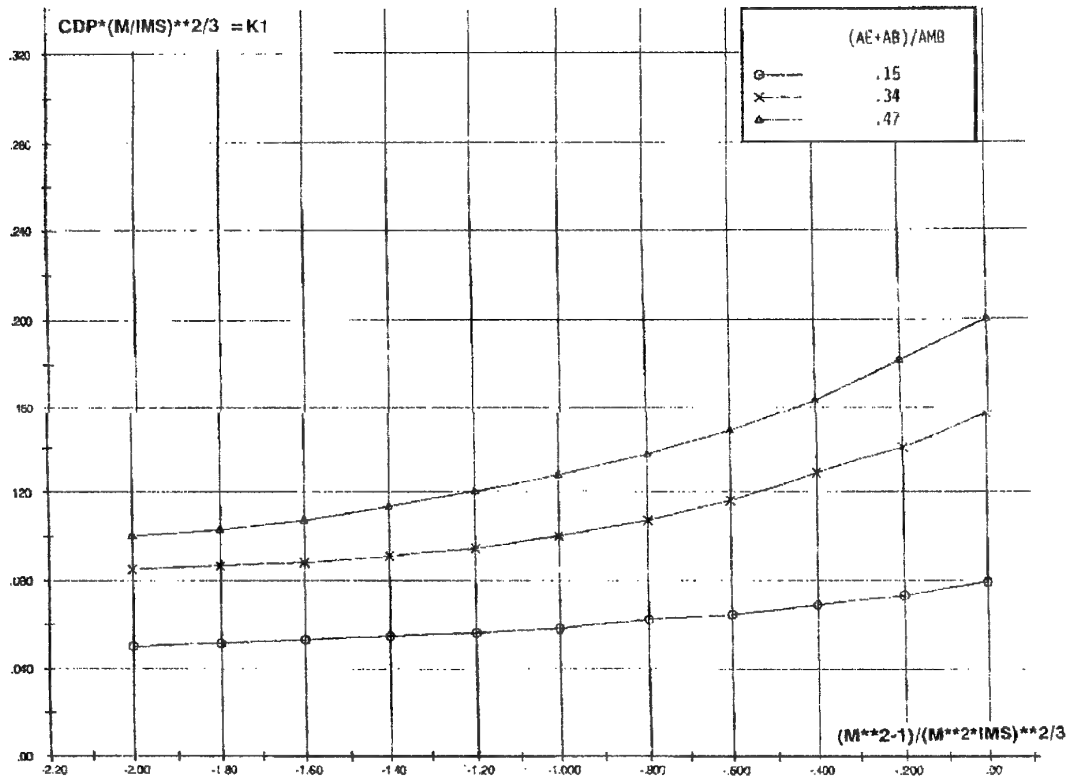


Figure 2.4-1. Jet-Off Aftend Pressure Drag Coefficient Parameter ( $K_1$ ) for Subsonic Flow (Twin Engine Narrow Spacing)

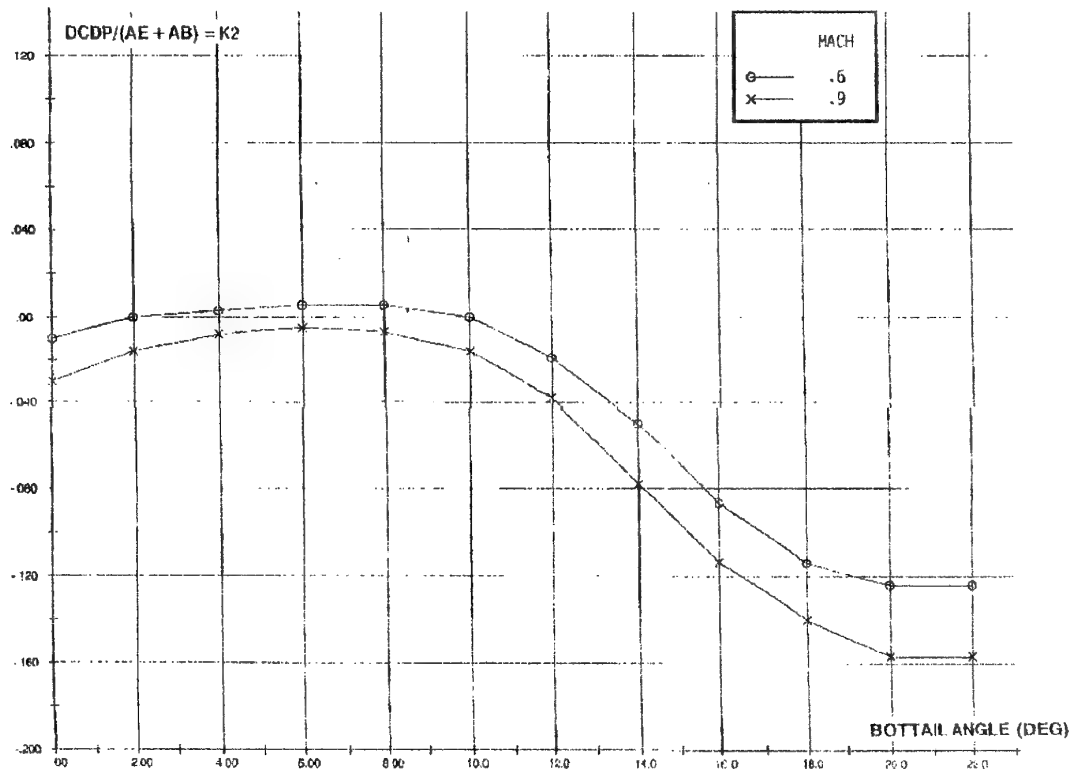


Figure 2.4-2. Aftend Pressure Drag Coefficient ( $K_2$ ) from Jet-Off to Design NPR for Subsonic Flow (Twin Engine Narrow Spacing)

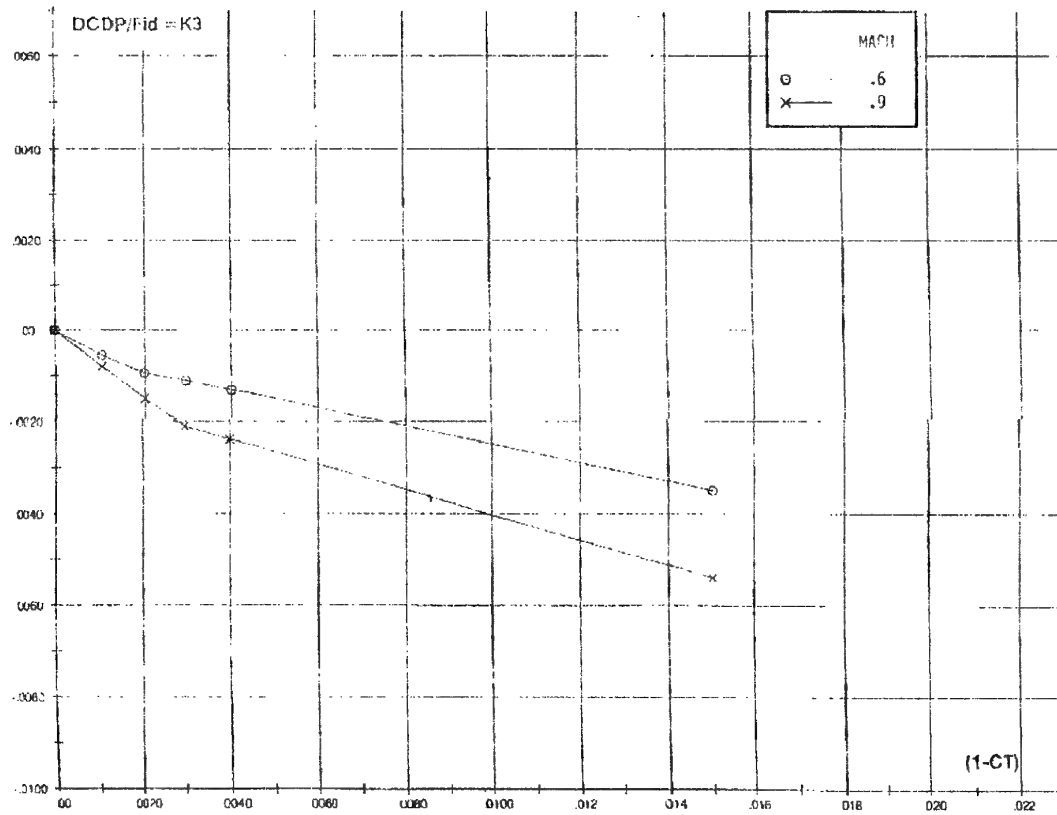


Figure 2.4-3. Aftend Pressure Drag Coefficient (K3) from Design to Operating NPR for Subsonic Flow (Convergent-Divergent Nozzle, Normal Power)

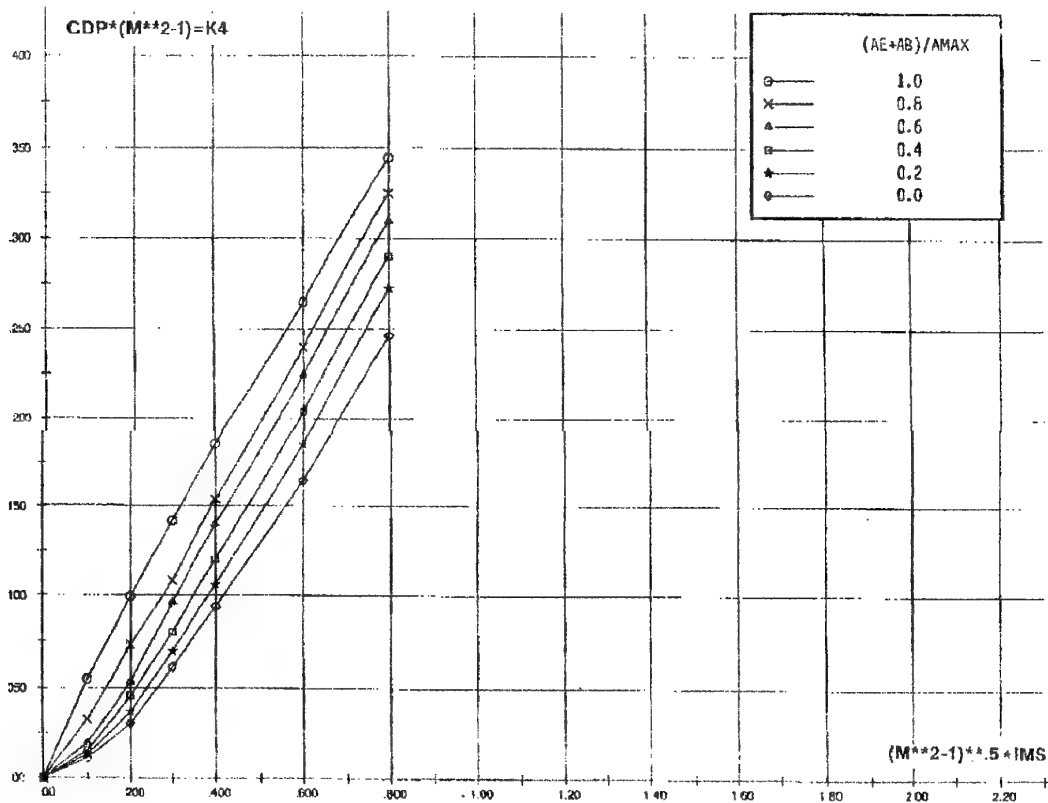


Figure 2.4-4. Jet-Off Aftend Pressure Drag Coefficient Parameter (K4) for Supersonic Flow (Twin Engine Configuration)

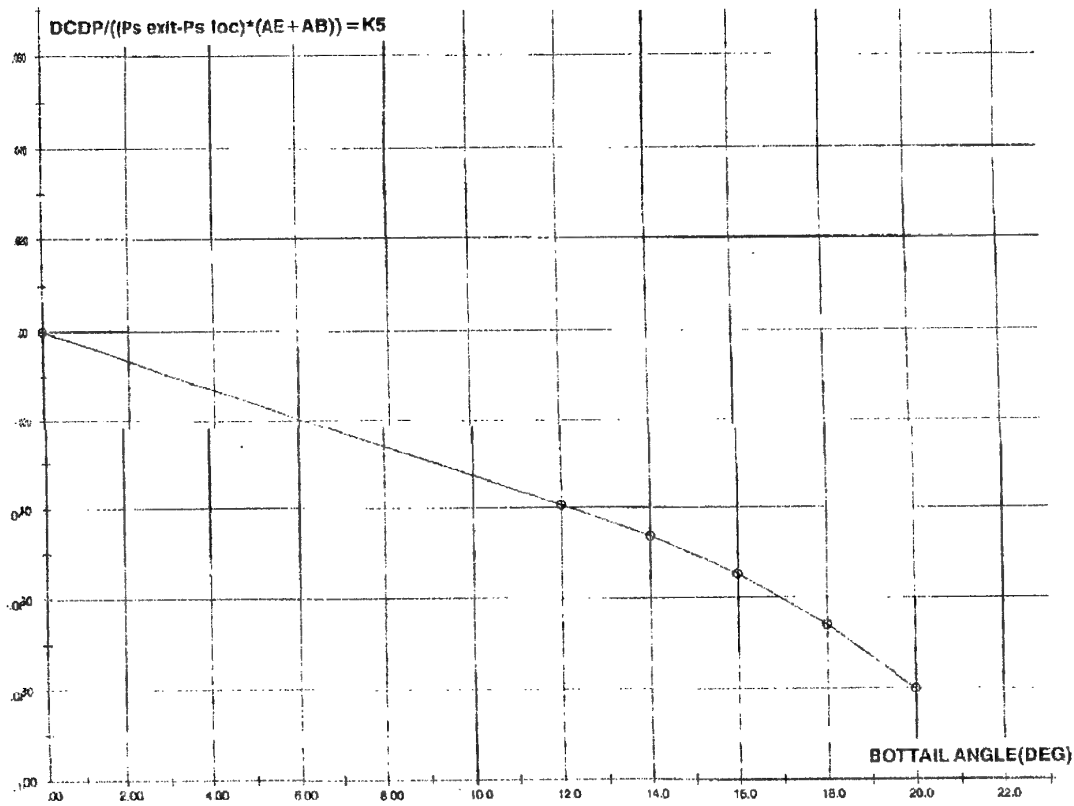


Figure 2.4-5. Aftend Pressure Drag Coefficient (K5) from Design to Operating NPR

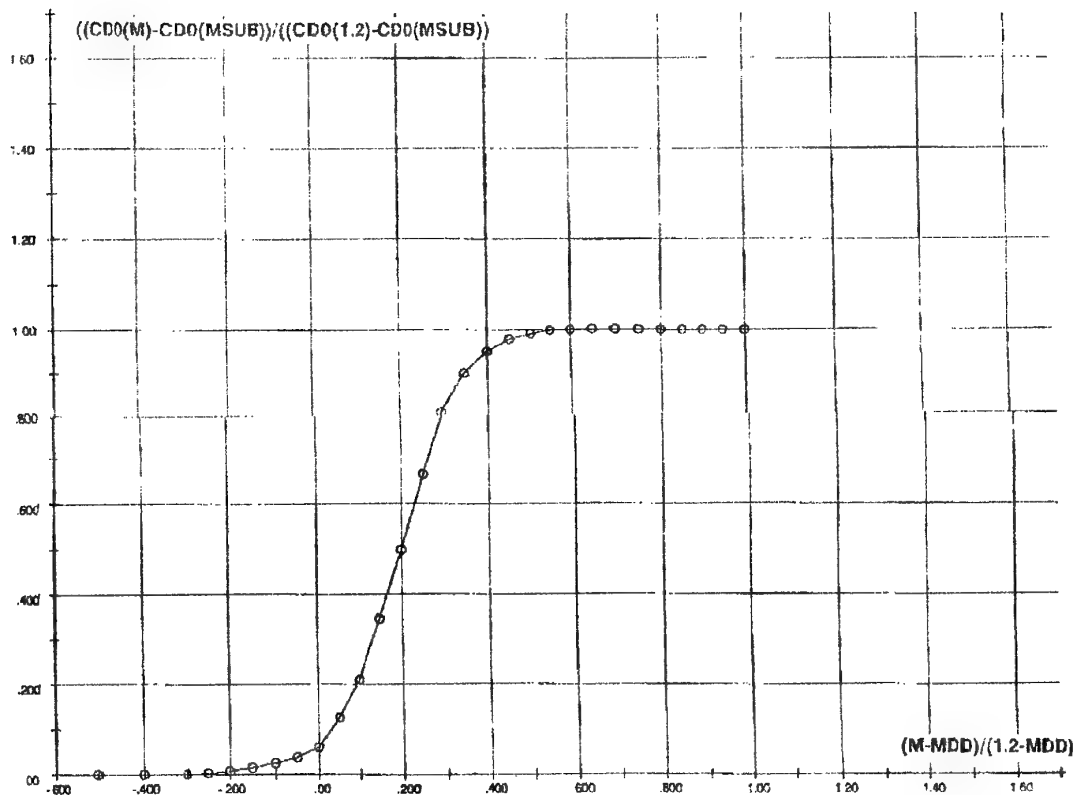


Figure 2.4-6. Transonic Zero Lift Drag Function

for example, were not available in the previous AGARD review of afterbody flow prediction (Ref. 2.4-5).

Assessing the fitness of turbulence models is a complex task, well beyond the scope of this Working Group activity. Therefore, in the discussion of contributed results (below) the comments relating to turbulence models should be regarded as preliminary in nature.

#### 2.4.2.3 Performance Issues

The Working Group solicited data from the contributors to enable an assessment of the performance of the CFD analysis process (time, cost, reliability, skill requirements). Several contributors provided information along this line; their data are presented in Appendix C. However, it quickly became apparent that a more systematic approach is needed to gain meaningful insight into these issues. Therefore, the data in Appendix C should be read as a general discussion of the barrier issues and the common techniques to overcome those issues. The Working Group does not believe that comparative significance should be attached to the specific quantitative data presented in Appendix C.

### 2.4.3 Contributed Predictions

#### 2.4.3.1 Grid Generators

Several grid generation systems were used to support the solutions which were contributed to the Working Group. These grid systems are described (briefly) in this section, presented in alphabetical order according to the name given to the system by the contributor(s).

In a few cases, different contributors used the same grid generation system. No attempt has been made to compare the grids which were produced by different groups using the same tools. In two cases, the grid produced by one contributor was used by another contributor, using a different flow solver code. These cases are noted in Section 3.5 and in Appendix C. However, no attempt has been made to draw a special conclusion regarding the results presented in these contributions.

#### Aermacchi System

The system consists of three separate programs: PREP (geometry acquisition and surface grid generation), AER-GRID (volume grid generator), and SPLITTER (domain block decomposition and grid editor)

Surface grid generation is based on cubic or B-spline methods. Volume grid generation is performed using transfinite interpolation methods (four different laws: Hermite, Lagrange, Hyperbolic Tangent, Exponential), normal control and normal smoothing. The complete system is workstation based with some graphical interfaces.

These codes are based on the methodology described in Ref. 2.4-6.

PREP is based on a subsonic panel program preprocessor. AERGRID and SPLITTER were developed by Aermacchi. These codes are property of Aermacchi S.P.A.

#### CUBE

CUBE is an interactive, structured and unstructured 2-D or 3-D grid generator based on a subdivision of the computational space. As a first step, the domain is divided into blocks fitted to the body. For the A.2 nozzle, six blocks have been used to represent the geometry. In a second step, a wide range of discretizations can be selected to treat each edge of the blocks. The distribution can be adapted to the problem, either constant size for the Euler code or a dense packing near the interface with a fixed height for the Navier-Stokes code. In a third step, a bilinear interpolation is used for the grid generator for 2-D grids while a Hermite interpolation is used for 3-D grids. Finally, a triangularization is applied for use by unstructured codes.

Grid generation requires on the order of one day. The CPU requirement is essentially zero for 2-D grids, and a few hours for 3-D grids. CUBE is a Dassault Aviation proprietary code.

#### Defence Research Agency (Tailored Grid Method)

Due to the simplicity of the B.4 configuration and the need to model only one-quarter of the flow field, a specific grid generation procedure not present in the SAUNA system has been used.

This procedure uses transfinite interpolation to create grids which are suitable for either viscous or inviscid flow computations. The resulting "tailor made" grids are compatible with the flow solver of SAUNA and provide grids with three levels of density, which can be used in subsequent grid sequencing and multigrid options of the flow code.

#### FLITE SD&VT

FLITE SD&VT (Finite Element Linear Tetrahedra Surface Definition & Volume Transformation) is a member of the FLITE suite, used for generation of unstructured grids made up of 4-noded linear tetrahedra, employing the Advancing Front method. This code was originally developed by Morgan et. al. (Ref. 2.4-7 and Ref. 2.4-8), and has been applied to transport aircraft powerplant installations (Ref. 2.4-9).

FLITE is a product of CDR of Swansea University.

#### GRIDGEN

GRIDGEN is a workstation-based interactive grid generation

code, consisting of four separate programs: GRIDBLOCK (domain decomposition, surface grids), GRIDGEN2D (refined surface grids), GRIDGEN3D (block volume grids in batch mode), and GRIDVUE3D (grid visualization). Uses both algebraic and elliptic methods. Includes volume and surface grid quality metrics. Except for the GRIDVUE3D program, this family of codes runs only on Silicon Graphics and IBM RS/6000 workstations. These codes are described more fully in Ref. 2.4-10 and Ref. 2.4-11.

The GRIDGEN system was developed by General Dynamics Fort Worth Division under contract to the US Air Force. Extensions have been added to GRIDGEN by MDA Engineering, under contract to various agencies of the US Government.

The GRIDGEN system is the property of the US Government; available to US citizens only. Requests should be made to the Aeromechanics Division, USAF Wright Laboratory, Wright-Patterson AFB, OH.

### I3G / PLUTO3D

The name I3G stands for "Interactive Graphical Grid Generation." I3G generally is used together with PLUTO3D. I3G performs surface grid generation.

I3G was developed by Lockheed, under contract to USAF Wright Laboratory. It is property of the US Government; available to US citizens only. Requests should be made to the Aeromechanics Division, USAF Wright Laboratory, Wright-Patterson AFB, OH.

PLUTO3D is a volume mesh generation code. It is based on transfinite interpolation with Laplacian smoothing invoked as required. This code was developed by USAF Wright Laboratory.

### ICEM

ICEM is a computer-aided design software package. It consists of three strongly integrated programs: DDN (a computer aided engineering and manufacturing system), MULCAD (a multi-domain topology generator), and PADAMM (a mesh generator).

ICEM is a workstation-based interactive software package, hosted on a Silicon Graphics Crimson VGX system. MULCAD and PADAMM provide clustering capabilities (geometric, hyperbolic tangential, exponential...), grid optimization (relaxation, interpolation) as well as a highly efficient visualization program. Grid capabilities are structured multi-block with point-match, non-point-match, or overlapping interfaces.

ICEM is a product of Control Data Corporation.

### JA 46

JA 46 is a 2-D or axisymmetric algebraic nozzle grid generator. It allows the computational domain to be split into arbitrary blocks for gridding. Multiple inflow and outflow boundaries can be defined. Geometric grid spacings are permissible in both directions. This code is Rolls-Royce proprietary.

### MACGS

MACGS (McDonnell Aircraft Computational Grid System) is a workstation-based grid generation system consisting of three elements: ZONI3G (geometry acquisition and domain decomposition), GMAN (volume grid generator), and GPRO (grid editor). It operates on three families of workstations (IBM, H-P, SGI) and in an X-window client-server environment.

ZONI3G is based on the panel method model generator, I3G, developed by Lockheed under contract to the US Air Force. Extensions to I3G/ZONI3G, and all work on GMAN and GPRO was carried out by McDonnell Douglas.

The MACGS system is the property of McDonnell Douglas Corporation. The U.S. Air Force has rights in certain portions of the MACGS code.

### MELISSA

MELISSA is an interactive, unstructured grid generator based on an advancing front technique. The front starts from a skin composed of the wall and the jet and proceeds towards infinity for the outer domain and towards the axis for the inner one. Every layer is controlled through its thickness and its level of condensation (in order to reduce the number of points away from the wall). This methodology is described more fully in Ref. 2.4-12.

MELISSA is a Dassault aviation proprietary code.

### STACKER

STACKER consists of a coupled algebraic 2-D grid generator and a 3-D stacking program. A clone of the 2-D algebraic grid generator JA46 is used to generate a grid at each circumferential station. These are stacked in constant  $\theta$  sections to produce the 3-D grid. A single block output grid is produced, with grid blanking used to restrict the flow solver. Topology input is manually added to define symmetry planes, repeats or centerline location. This code is Rolls-Royce proprietary.

#### 2.4.3.2 Flow Solvers

Each contributor for the test cases of this Working Group used a different flow solution code (as noted, in a few cases these codes were supported by the same grids, or the same

grid codes). A brief description of each flow solver is presented below (alphabetical order, based on the name of the code as given by the contributor).

#### ANSE

ANSE (Algorithm Navier-Stokes Explicit) is a single- or multi-block, structured grid, cell-centered, finite volume, 3-D explicit Reynolds-averaged Navier-Stokes code. It supports several turbulence models: a Cebeci-Smith type, a one-equation, and a  $k-\epsilon$  turbulence model. The algorithm uses a 2- or 4-step Runge-Kutta updating scheme. Further details are presented in Ref. 2.4-13. The present version is considerably enhanced from the version of ANSE developed by MIT. This code was developed for powerplant applications at Rolls-Royce Inc. The code is integrated into a suite of grid generators and other flow solvers known as CFDS. This code is Rolls-Royce proprietary.

#### CANARI

CANARI has both Euler and Navier-Stokes capabilities. It features a multi-domain approach for structured meshes. The numerical scheme is an implicit (residual smoothing), finite volume, cell-centered and time multi-step scheme (four-step Runge-Kutta). The Baldwin-Lomax algebraic turbulence model is implemented, and a two-equation  $k-\epsilon$  model is being validated. Further details of this method are presented in Ref. 2.4-14.

CANARI was developed at ONERA, and is available through them.

#### COBALT

COBALT is an unstructured Euler/Navier-Stokes code, able to treat general convex polyhedral cells. The numerical model is a finite volume upwind. Inviscid fluxes are found as a solution to the Riemann problem using Colella's approximate Riemann solver. COBALT features original solutions for anisotropic monotonicity. The Baldwin-Barth turbulence model is employed. This code features a wide variety of boundary conditions. A Runge-Kutta scheme used for time integration (1st, 2nd, or 3rd order accuracy).

COBALT is an original product of USAF Wright Laboratory. It is available from USAF Wright Laboratory to United States citizens.

#### EUGENIE (Euler)

EUGENIE is a multi-element unstructured code based on Galerkin finite volume method, with second-order upwind approximations. The default solution scheme is linearized implicit; the code also provides Runge-Kutta methods and unnested multigrids. Includes a large arsenal of boundary conditions and equilibrium / non-equilibrium high temperature models. EUGENIE is available in 2-D, axisymmetric, and 3-D versions. This method is described

more completely in Ref. 2.4-15 and Ref. 2.4-16.

EUGENIE was developed in collaboration with INRIA Sophia Antipolis, and it is a Dassault Aviation proprietary code.

#### FANSI

FANSI (Factored Algorithm Navier-Stokes Implicit) is a non-simply-connected finite volume 2-D or axisymmetric code for solving the Reynolds-averaged Navier-Stokes equations. This code can be run inviscid (Euler) or viscous (Navier-Stokes). It supports a Cebeci-Smith and Johnson-King turbulence model as well as an empirical transition model. The implicit procedure of Beam and Warming is used. This code was developed at Rolls-Royce, who retain all proprietary rights. It is loosely based on the code FANSI, developed at the Gas Turbine Laboratory at MIT. Further information can be obtained in Ref. 2.4-17 and Ref. 2.4-18.

#### FLITEFS

FLITEFS is a finite element solver for the compressible steady-state Euler equations. It is an edge-based scheme, using explicit time stepping with optional residual smoothing. This code was jointly developed by Swansea University and Imperial College. Further information can be obtained in Ref. 2.4-19.

#### FLO67P

FLO67P is a multi-block finite volume cell vertex Euler / Navier-Stokes code with central different discretization and blended 2<sup>ND</sup> - 4<sup>TH</sup> order numerical dissipation, multi-stage Runge-Kutta integration in time, and multigrid convergence acceleration technique. It supports the Baldwin-Lomax turbulence model. The code runs within PARAGRID, a domain decomposition environment developed by IBM ECSEC. This code is described more completely in Ref. 2.4-20 and Ref. 2.4-21.

This code is based on the code FLO67 developed by Intelligent Aerodynamics Inc. FLO67P is the result of cooperation of Aermacchi S.p.A., IBM ECSEC and Intelligent Aerodynamics Inc.

#### FLU3M

The FLU3M code provides solutions to either the Euler or Navier-Stokes equations. The Navier-Stokes solver represented either laminar or turbulent flow, using the Baldwin-Lomax and  $k-\epsilon$  turbulence models. The gas can be modeled as perfect, ideal, or bi-species. The code uses a 2<sup>ND</sup>-order MUSCL upwind scheme (Van Leer, Roe, or Osher) with a TVD limiter. This code runs on multi-block structured grids, which may be 2-D, axisymmetric, or 3-D. Both explicit and implicit (ADI) solvers are available, as well as a space-marching relaxation.

## NASCA

The NASCA (Navier-Stokes pour Corps Axisymétrique) code is a single-block axisymmetric Navier-Stokes code working on a general polygonal domain (a two-dimensional version also exists). The numerical scheme is optional (second order, centered or TVD upwind). A finite volume type of discretization is used, with an adaptation of the scheme to strongly non-uniform unstructured meshes. Both convection and diffusion terms are treated implicitly, the computation of a time step being entirely vectorized. The code supports two turbulence models: Baldwin-Lomax, and  $k-\epsilon$ .

The NASCA code is further described in Ref. 2.4-22.

The NASCA code was developed by the Fundamental Aerodynamics Branch of ONERA, and it is the property of ONERA.

## NASTD

NASTD is a multi-block structured grid code (patched and/or overlapping); versatile boundary conditions. It contains a variety of algorithms and turbulence models. For this study, it was used with the three-factor implicit scheme, block pentadiagonal solver of discretized second-order Roe upwind scheme with optional TVD limiters. Several turbulence models were used: Baldwin-Lomax (0-equation), Baldwin-Barth (1-equation), and Jones-Launder (2-equations). Convergence was established by monitoring pressure drag history.

NASTD is a McDonnell Douglas proprietary code. Certain elements of NASTD were developed under contract to the U.S. Navy.

## NPARC

NPARC solves the Reynolds averaged full Navier-Stokes equations in strong conservation form using the Beam-Warming approximate factorization algorithm. Second order central differencing is used for the spatial discretization and a Jameson-style artificial dissipation is used for stability. For the cases presented in this report, a two-equation Chien  $k-\epsilon$  turbulence model was used. In addition, the one-equation Baldwin-Barth turbulence model was used for one case. NPARC is primarily used to compute propulsion flows.

NPARC is a more recent version of the PARC3D code, which in turn is based on the ARC3D code. NPARC is developed and supported through a joint effort by the United States Air Force Arnold Engineering Development Center and the NASA Lewis Research Center. This code is available to United States citizens only.

## PAB3D (Version 10)

PAB3D is a finite volume multiblock code for solving the Navier-Stokes equations. The solver options are based on the upwind biased, Roe scheme and Van Leer scheme. The numerical algorithm in version 10 is a flux-splitting formulation with a third-order implicit operator in two directions and relaxation in the third direction. It contains a variety of boundary conditions and is capable of handling general patched grids. Several turbulence models, including the Baldwin-Lomax algebraic model and the Jones-Launder  $k-\epsilon$  with modifications by Hamid et. al. are available in PAB3D. Turbulence can be initialized by either a laminar or 0-equation computation. Freestream boundary conditions are set by Riemann inflow, and extrapolation outflow. Independent grid sequencing in each block in the I, J, and K directions can be specified. Conservative block interface patching capability is included. Forces and moments are computed in the code according to user instructions. Solution convergence is monitored by residue level and integrated aerodynamic performance such as mass flux, thrust, lift, and drag.

PAB3D is an original product of the NASA Langley Research Center. It is available from NASA Langley to United States organizations.

## SAUNA

SAUNA (Structured and Unstructured Numerical Analysis) is based on a vertex storage algorithm, using Jameson-style artificial dissipation and enhancements, explicit Runge-Kutta time marching and local time stepping. Multiple boundary condition types are provided, e.g., jet inflow and outflow, free-stream Riemann invariants, Rudy-Strikwerda characteristic outflow, reflection, etc. Grid sequencing and multigrid capabilities are included. Convergence is monitored by continuity equation residual or total forces.

## TEAM

TEAM provides steady-state solutions of the Euler, RANS, and Navier-Stokes equations using Jameson algorithms. The algorithm employs finite-volume spatial discretization augmented by numerical dissipation terms (either adaptive or characteristic-based schemes available); equations are integrated in time using a multi-stage time-stepping procedure. TEAM code can accommodate patched multiblock grids of arbitrary topologies. This code solves the RANS equations only where viscous effects dominate; Euler equations elsewhere. The Baldwin-Lomax turbulence model is used. The application of TEAM in this study is described in Ref. 2.4-23.



### VIRGINIE (Navier-Stokes)

VIRGINIE is an unstructured Navier-Stokes code. The numerical model is finite elements with Galerkin least squares approach, implicit with matrix free GMRES technique. This code is available in 2-D, axisymmetric, and 3-D versions. VIRGINIE supports several turbulence models including 0-, 1- and 2-equation forms. The supported turbulence models are Norris-Reynolds model for the one-equation, the k- $\epsilon$  and k- $\omega$  models for the 2-equation models. The methodology is presented in Ref. 2.4-24.

VIRGINIE was developed at Dassault Aviation, who retain all ownership

#### 2.4.4 Numbering System

In the remainder of this report, all contributions will be identified by a unique code. This code consists of a letter identifying the level of analysis, followed by a two-digit number indicating the specific methodology or CFD code. Three levels of analysis are presented: semi-empirical methods (code "S"), Euler or inviscid methods (Code "E"), and Navier-Stokes or viscous methods (Code "N").

Most of the Euler and Navier-Stokes codes used structured multi-block grids. Three of the codes, however, are based on unstructured grids - these codes are noted in the table of flow solvers. Where no such notation is provided, the reader should take the code to be based on structured multi-block grids.

The key to the prediction codes is presented in Table 2.4-1, and the key to the turbulence models is presented in Table 2.4-2.

No.	Organization	Grid Code	Flow Code	Turb. Models
S01	Aermacchi	--	--	--
E02 N02	Rolls-Royce	JA 48 STACKE R	ANSE	C-S 1-eq k- $\epsilon$
E03 N03	SNECMA	ICEM	CANARI	B-L k- $\epsilon$
E04 N04	USAF Wright Lab- oratory	GRID- GEN + conver- sion	COBALT (Unstruct.)	B-B
E05	Dassault	MELISSA	EUGENIE (Unstruct.)	--
E06 N06	Rolls-Royce	JA 48	FANSI	C-S J-K
E07	Rolls-Royce	FLITE SD&VT	FLITE.FS	(n/a)
E08 N08	Aermacchi	PREP AERGRID SPLIT- TER	FLO67P	B-L
N09	McDonnell Douglas	MACGS	NASTD	B-L B-B S-A J-L C
N10	NASA Lang- ley	GRID- GEN	PAB3D	B-L J-L*
E11 N11	DRA / ARA		SAUNA	B-L
N12	Lockheed		TEAM	B-L
N13	Dassault	CUBE MELISSA	VIRGINIE (Unstruct.)	B-L N-R k- $\epsilon$ k- $\omega$
N14	ONERA		NASCA	B-L k- $\epsilon$
N15	Aérospatiale	ICEM	FLU3M	B-L k- $\epsilon$
N16	NASA Lewis		NPARC	B-B C

Table 2.4-1  
Sources of Predictions Presented in This Report

Code	Turbulence Model	Type
C-S	Cebeci-Smith (Ref. 2.4-25)	Algebraic
B-L	Baldwin-Lomax (Ref. 2.4-26)	Algebraic
J-K	Johnson-King (Ref. 2.4-27)	
B-B	Baldwin-Barth (Ref. 2.4-28)	One Equation
S-A	Spalart-Allmaras (Ref. 2.4-29)	One Equation
N-R	Norris-Reynolds	One Equation
k- $\epsilon$	k- $\epsilon$ (a generalized name for a class of models) (Ref. 2.4-30)	Two Equations
k- $\omega$	k- $\omega$ (Ref. 2.4-31)	Two Equations
C	Chien (Ref. 2.4-32)	Two Equations
J-L	Jones-Launder (Ref. 2.4-33)	Two Equations
J-L*	Jones-Launder, mod- ified by Hamid et. al.	Two Equations

**Table 2.4-2**  
**Turbulence Models Used in This Report**

To illustrate: a Navier-Stokes solution provided by McDonnell Douglas Corporation, using the NASTD code with the Baldwin-Barth turbulence model, would be identified as "Contribution N09 (B-B)."

## References

- 2.4-1. Glasgow, E., D. Santman, L. Miller et al., "Experimental and Analytical Determination of Integrated Airframe Nozzle Performance," AFFDL-TR-72-101, Vol. I and II, 1972.
- 2.4-2. Keller, J.D., and J.C. South, "RAXBOD: A FORTRAN program for inviscid transonic flow over axisymmetric afterbodies," NASA TMX-72831, 1976.
- 2.4-3. —, "A Method for Estimating Drag-Rise Mach Number at Zero Incidence of Smooth or Bumpy Non-Ducted Axisymmetric Bodies With or Without Fins," ESDU 74013.
- 2.4-4. Craidon, C.B., "User's Guide for a Computer Program for Calculating the Zero-Lift Wave Drag of Complex Aircraft Configurations," NASA TM 85670, 1983.
- 2.4-5. —, "Report of the Working Group on Aerodynamics of Aircraft Afterbody," AGARD Advisory Report No. 226, June 1986.
- 2.4-6. Thompson, J.F., Z.U.A. Warsi, and C.W. Mastin, Numerical Grid Generation - Foundation and Application, Amsterdam: North Holland; New York: Elsevier.
- 2.4-7. Peraire, J., K. Morgan, and J. Peiró, "Unstructured Finite Element Mesh Generation and Adaptive Procedures for CFD," in *AGARD Conference Proceedings No. 464, Applications of Mesh Generation to Complex 3-D Configurations*, AGARD, Neuilly Sur Seine, pps. 18.1 to 18.12, 1990.
- 2.4-8. Morgan, K., J. Peraire and J. Peiró, "Unstructured Grid Methods for Compressible Flows," in *AGARD Report No. 787, Special Course on Unstructured Grid Methods for Advection Dominated Flows*, AGARD, Neuilly Sur Seine, pps. 5.1 to 5.39, 1992.
- 2.4-9. Peiró, J., J. Peraire, K. Morgan, O. Hassan, and N. Birch, "The Numerical Simulation of Flow about Installed Aero Engine Nacelle Using a Finite Element Euler Solver on Unstructured Meshes," The Aeronautical Journal of the Royal Aeronautical Society, June/July 1992, Paper 1845.
- 2.4-10. Steinbrenner, J.P., J.R. Chawner, and C.L. Fouts, "The GRIDGEN 3D Multiple Block Grid Generation System," WRDC-TR-90-3022, July 1990.
- 2.4-11. Steinbrenner, J.P., and J.R. Chawner, "The GRIDGEN Version 8 Multiple Block Grid Generation Software," MDA Engineering Report 92-01, December 1992.
- 2.4-12. Huet, F., "Génération de maillage automatique dans les configurations tridimensionnelles complexes," AGARD Conference, Loen, Norway, 24-25 May 1989.
- 2.4-13. Norton, R.J., and J.P. Kingsley, "Prediction of a High Bypass Flow Engine Nozzle Flowfield," AIAA Paper 92-3259.
- 2.4-14. Vuillot, A.-M., V. Couallier, and N. Liams, "3-D Turbomachinery Euler and Navier-Stokes Calculations with a Multi-Domain Cell-Centered Approach," AIAA/SAE/ASME/ASEE 29th Joint Propulsion Conference, Monterey, CA, 28-30 June 1993.
- 2.4-15. Fezoui, L., B. Stoufflet, "A Class of Implicit Upwind Schemes for Euler Simulations with Unstructured Meshes," *Journal of Computational Physics*, 84 (1), pp. 174-206, 1989.
- 2.4-16. Leclerc, M.P., B. Mantel, J. Périaux, P. Perrier, B. Stoufflet, "On Recent 3D Euler Computations around Complete Aircraft Using Adaptive Unstructured Mesh Refinements," *Proceedings of the Second World Congress on Computational Mechanics*, Stuttgart, Germany, 27-31 August 1990.
- 2.4-17. Norton, R.J., "Prediction of the Installed Performance of 2D Exhaust Nozzles," AIAA Paper 87-0245, January 1987.
- 2.4-18. Norton, R.J., W.T. Thompkins, Jr., and R. Haines, "Implicit Finite Difference Schemes with Non-Simply Connected Grids -- A Novel Approach," AIAA Paper 84-0003, January 1984.
- 2.4-19. Peraire, J., K. Morgan, and J. Peiró, "A Finite Element Multigrid Solver for the Euler Equations," AIAA Paper 92-0449, 1992.
- 2.4-20. Dellagiacoma, F., M. Vitaletti, A. Jameson, L. Martinelli, S. Sibilla, and L. Visintini, "FLO67P: A Multi-Block Version of FLO67 Running Within PARAGRID," *Proceedings of Parallel CFD '93*, Paris, May 1993.
- 2.4-21. Martinelli, L., and A. Jameson, "Validation of a Multigrid Method for Reynolds Averaged Equations," AIAA Aerospace Sciences Meeting, Reno, January 1988.
- 2.4-22. Benay, R., and P. Servel, "Applications d'un code Navier-Stokes à des écoulements d'arrière-corps d'avions et de missiles (Applications of a Navier-Stokes Code to Aircraft and Missile Afterbodies)," *La Recherche Aéronautique* (to be published).
- 2.4-23. Crose, M.R., "Computational Fluid Dynamics / Experimental Data Comparison of the AGARD Nozzle Test Case B.4.1," Lockheed Report LG94ER0030, January 1994.
- 2.4-24. Chalot, F., M. Mallet, and M. Ravachol, "A Comprehensive Finite Element Navier-Stokes Solver for Low and High-Speed Aircraft Design," AIAA Paper 94-0814, AIAA Aerospace Sciences Meeting, Reno, January

1994.

2.4-25. Cebeci, T., and A.M.O. Smith, "Analysis of Turbulent Boundary Layers," Applied Mathematics and Mechanics, Vol. 15, Academic Press, New York.

2.4-26. Baldwin, B.S., and H. Lomax, "Thin Layer Approximation and Algebraic Model for Separated Turbulent Flows," AIAA Paper 78-257, January 1978.

2.4-27. Johnson, D.A., and L.S. King, "A Mathematically Simple Turbulence Closure Model for Attached and Separated Boundary Layers," AIAA Journal, volume 23, number 11 (1985), pp. 1684-1692.

2.4-28. Baldwin, B.S., and T.J. Barth, "A One-Equation Turbulence Transport Model for High Reynolds Number Wall-Bounded Flows," AIAA Paper 91-0610.

2.4-29. Spalart, P.R., and S.R. Allmaras, "A One-Equation Turbulence Model for Aerodynamic Flows," AIAA Paper 92-0439, 1992.

2.4-30. Patel, V.C., W. Rodi, and G. Scheuerer, "Turbulence Models for Near-Wall and Low Reynolds Number Flows: A Review," *AIAA Journal*, Vol. 23, No. 9, pp. 1308-1319, (September 1985).

2.4-31. Wilcon, D.C., "Reassessment of the Scale-Determining Equation for Advanced Turbulence Models," *AIAA Journal*, Vol. 26, pps. 1299-1310 (1988).

2.4-32. Chien, K., "Prediction of Channel and Boundary Layer Flows with a Low Reynolds Number Turbulence Model," *AIAA Journal*, Vol. 26, No. 11 (November 1982).

2.4-33. Jones, W.P., and B.E. Launder, "The Calculation of Low-Reynolds-Number Phenomena with a Two-Equation Model of Turbulence," *International Journal of Heat and Mass Transfer*, Vol. 16, pp. 1119-1130 (1973).

-end-

## 2.5. Description of Test Cases A

### 2.5.1. Introductory Remarks

Test Cases A were collected to constitute a data bank allowing an in depth validation of advanced computer codes on basic configurations reproducing typical afterbody flow situations. These "basic" test cases were selected according to the following criteria:

- (i) The number of cases should be small in order to focus the validation effort on well chosen specific cases.
- (ii) Only three-dimensional configurations or cases with hot jet simulation should be considered, the cold jet case being only retained for reference purposes (axisymmetric cases with uniquely cold jet simulation are contained in other data banks [2.5.1]).
- (iii) A wide range of flow variables was not required, the aim being to proceed to in depth validations by considering detailed predictions of the flowfield.
- (iv) The selected cases should include flow field measurements which provide as complete a picture of the flow as possible, including its mean as well as its turbulent properties.
- (v) There should be no restriction on the publication of the data, so that the cases would be available for research workers to test their own codes in the future.

The chosen test cases are of varying complexity: the first one corresponds to the simplest three - dimensional effect achievable on an afterbody geometry, the second one introduces thermal effects on an axisymmetric afterbody and the third case is a twin-jet configuration with cold jets.

### 2.5.2. Accuracy of Test Results

No real estimate of the accuracy of the quoted results has been made. Surface pressure measurements have been executed with classical and well known techniques so that these measurements can be considered as accurate as a few percent in the most unfavorable cases. Obviously erroneous results, coming from defects in the measurements, have been excluded from the data bank. Accuracy of flow surveys with pressure and temperature probes is more difficult to assess, especially in the case of hot jet simulation, because of the many sources of error:

- Effects of concentrated pressure variations on the sensing element of the probe.
- Inaccuracy in the calibration of thermocouple probes, for the same reason.
- Poor response time of the temperature and static pressure probes.
- Deformation of probes and supports due to the loads which makes the exact location of the measurement point difficult to determine.

With the precautions taken (use of the forward scattering mode of operation and large differences in the

orientation of the fringe patterns), accuracy of the mean velocity measurements with the LDV systems can be considered good in most cases. Uncertainty is, in general, of the order of a few percent - 1% in regions of high speed flow, 5% in separated zones close to a base - and sufficient to properly validate computer codes. On the other hand, turbulence measurements have to be used cautiously due to the difficulty in making these measurements in three-dimensional flows. In the most favorable conditions, the accuracy on the normal stress components is about 5% and on the shear stress component about 10%. In addition, in some circumstances (regions close to a nozzle exit section), noticeable particle lag exists which causes an underprediction of the mean velocity by LDV. Also, low frequency fluctuations may affect the jet measurements by causing an overestimation of turbulence by the LDV system which cannot distinguish between these large scale unsteady motions and true turbulence.

### 2.5.3. Test Cases

#### 2.5.3.1. Test Case A.1.1 : Axisymmetric Body Without Jet at Incidence

##### I - Wind Tunnel

The present experiment was executed in a blow-down type wind tunnel with a free jet exhausting at a pressure close to the atmospheric pressure. The open test section is square in cross section and measures  $130 \times 130 \text{ mm}^2$ .

##### II - Model Configuration and Installation in Wind Tunnel

As shown in Fig. 2.5.1, the model consists of an upstream cylindrical body with a diameter  $D_{max} = 30 \text{ mm}$ , followed by a boattail of angle  $\beta = 6^\circ$  and a length  $L = 30 \text{ mm}$ . The locations of the pressure orifices are indicated in Fig. 2.5.1: 24 orifices are located along the afterbody at three circumferential positions ( $\varphi = 0^\circ, 90^\circ \text{ and } 180^\circ$ ) and 4 are on the base. As indicated in Fig. 2.5.2, the afterbody is mounted at the extremity of a sting installed in the test section and supported in the settling chamber by three shaped struts. The sting, whose diameter is  $30 \text{ mm}$ , is set at an incidence of  $5^\circ$ . Its end is held in the test section by two wires of  $0.3 \text{ mm}$  in diameter. Adjustable strut mounts allow the model to be aligned in the flow direction so that the sideslip angle is equal to zero.

##### III - Nominal Flow Conditions

The flow conditions were as follows:

Upstream Mach number:  $M_\infty = 0.54$

Stagnation pressure:  $P_{t\infty} = 10^5 \text{ Pa}$

Stagnation temperature:  $T_{t\infty} = 300 \text{ K}$

Reynolds number based on  $D_{max} = 30 \text{ mm}$  :  
 $Re_D = 3.56 \cdot 10^5$

Angle of incidence:  $\alpha = 5^\circ$

The velocity profiles of the incoming boundary layer at two axial (X) locations upstream of the base:

$$X/D_{max} = -1.2 \text{ and } X/D_{max} = -1.6$$

are given in tabular form in Annex A.1.1.1.1. For each X station, the boundary layer has been probed for three circumferential positions,  $0^\circ$  being on the lee-side and  $180^\circ$  on the windward side of the afterbody

#### IV - Data Available

The field measurements are presented in the coordinate system defined in Fig. 2.5.3:

- Its origin O is located at the centre of the base.
- The X-axis is horizontal and parallel to the undisturbed upstream velocity (zero incidence).

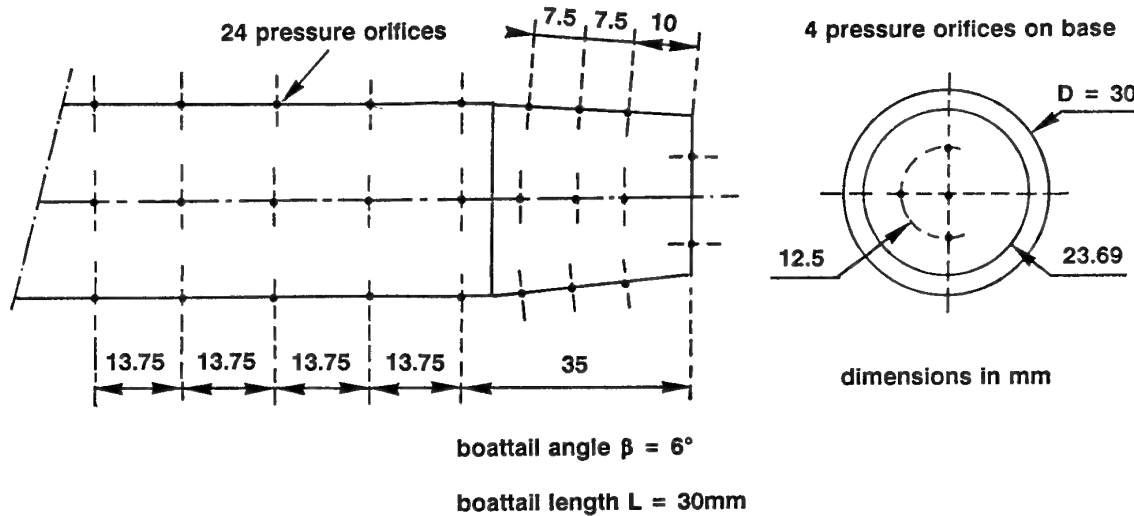


**Fig. 2.5.1 - Test Case A.1.1 : Afterbody definition and location of pressure orifices**

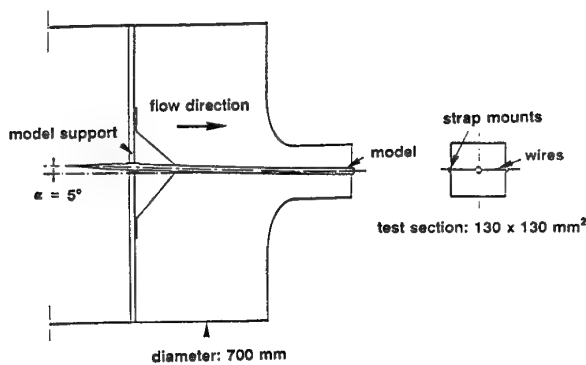


**Fig. 2.5.2 - Test Case A.1.1 : Model installation in the wind tunnel**

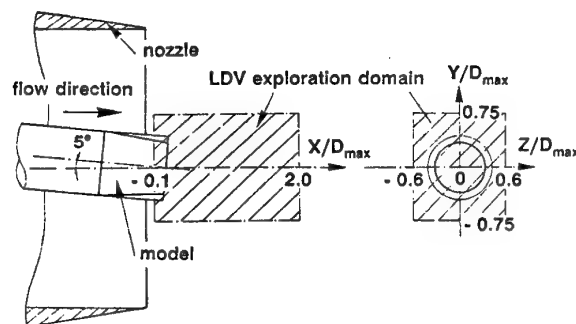


**Fig. 2.5.3 - Test Case A.1.1 : Domain explored with the LDV system**

- The transverse or radial axis Y is contained in the afterbody vertical plane of symmetry and makes an angle of  $5^\circ$  with the model axis.

- The spanwise axis Z is perpendicular to the X-Y plane.

The field measurements have been obtained by using a three-component LDV system. The mean and turbulent quantities were calculated from a sample of 4096 instantaneous measurements ( $U, V, W$ ).

Field properties were measured in the form of radial profiles (in the range:  $-0.75 \leq Y/D_{max} \leq 0.75$ ) for different stations downstream of the base (in the range:  $0.1 \leq X/D_{max} \leq 2.0$ ) and for different spanwise stations (in the range:  $0 \leq Z/D_{max} \leq 1.2$ ). A few profiles were taken between  $-1.2 \leq Z/D_{max} \leq 0$  to check the flow symmetry in the X-Y median plane.

The following data are available:

- Surface pressure on the afterbody.
- Base pressure distribution.
- Incoming boundary layer (see above).
- Mean flowfield properties:  $\bar{u}$ ,  $\bar{v}$ ,  $\bar{w}$
- Turbulent properties:  $\overline{u'^2}$ ,  $\overline{v'^2}$ ,  $\overline{w'^2}$ ,  $\overline{u'v'}$ ,  $\overline{u'w'}$ ,  $\overline{v'w'}$

and turbulence kinetic energy:

$$k = \frac{1}{2} \left( \overline{u'^2} + \overline{v'^2} + \overline{w'^2} \right)$$

V - References

2.5.2, 2.5.3, 2.5.4

VI - Point of Contact

Claude BERNER

I.S.L. Aerodynamics Department

B.P. 34

68301 SAINT LOUIS Cedex, France

### 2.5.3.2. Test Cases A.2.1 and A.2.2 : Axisymmetric Body with Jet Cold/Hot Flow

#### I - Wind Tunnel

The experiments have been executed in the S3Ch wind tunnel of the ONERA Chalais-Meudon establishment [2.5.5]. This is a continuous return wind tunnel working at atmospheric pressure. The flow Mach number can be adjusted in the range 0.3 - 1.2. The test section is nearly square in cross section, with a height of 764mm and a span of 803mm. An adjustable throat is placed at the test section outlet, first to fix the Mach number and secondly to isolate the flow under study from perturbations emanating from the downstream ducts. The test section can be equipped with perforated or adaptive walls when performing tests in the high subsonic or transonic range. The lateral doors of the test section have large windows allowing LDV measurements over a long distance. For the present experiment, the test section was equipped with perforated upper and lower walls, the porosity being equal to 20% and the divergence angle of the walls equal to zero.

The general shape of the model is defined in Fig. 2.5.4. It consists of an axisymmetric body, with a maximum diameter  $D_{max} = 105mm$ , fixed by a lateral strut to the floor of the wind tunnel. The meridional section of the forebody (model nose) is an elliptical arc with major axis 270mm. The forebody is followed by a cylindrical section having a length of 505mm.

The afterbody itself and the nozzle are defined in Fig. 2.5.5. The contour of the afterbody is made of rectilinear segments, the shape consisting of two successive conical surfaces with an angle  $7^\circ$  and  $13^\circ$ , respectively. The total length of the afterbody is 218mm.

The upstream part of the internal arrangement is made of a cylindrical duct having a diameter of 62mm. It is followed by a converging part made of a conical contour with an angle of  $13^\circ$ . The exit diameter of the nozzle is equal to 39.4mm and the diameter of the extremity of the afterbody is 42mm. As shown in Fig. 2.5.5 the nozzle contour has a radius over a distance of 3.27mm ensuring a smooth transition from the throat diameter to the diameter of the afterbody extremity.

The model was supplied with high pressure (max.  $5 \times 10^5 Pa$ ) and high temperature (max. 950K) air by means of a tubing system passing through the strut, as shown in Fig. 2.5.4. A perforated plate and a mixing device are placed upstream of the nozzle to insure a good thermal homogeneity of the jet. Stagnation conditions are measured by probes installed in the settling chamber preceding the nozzle.

The air is heated by a Joules effect electrical heater located outside the wind tunnel test section. The maximum achievable temperature with this heater

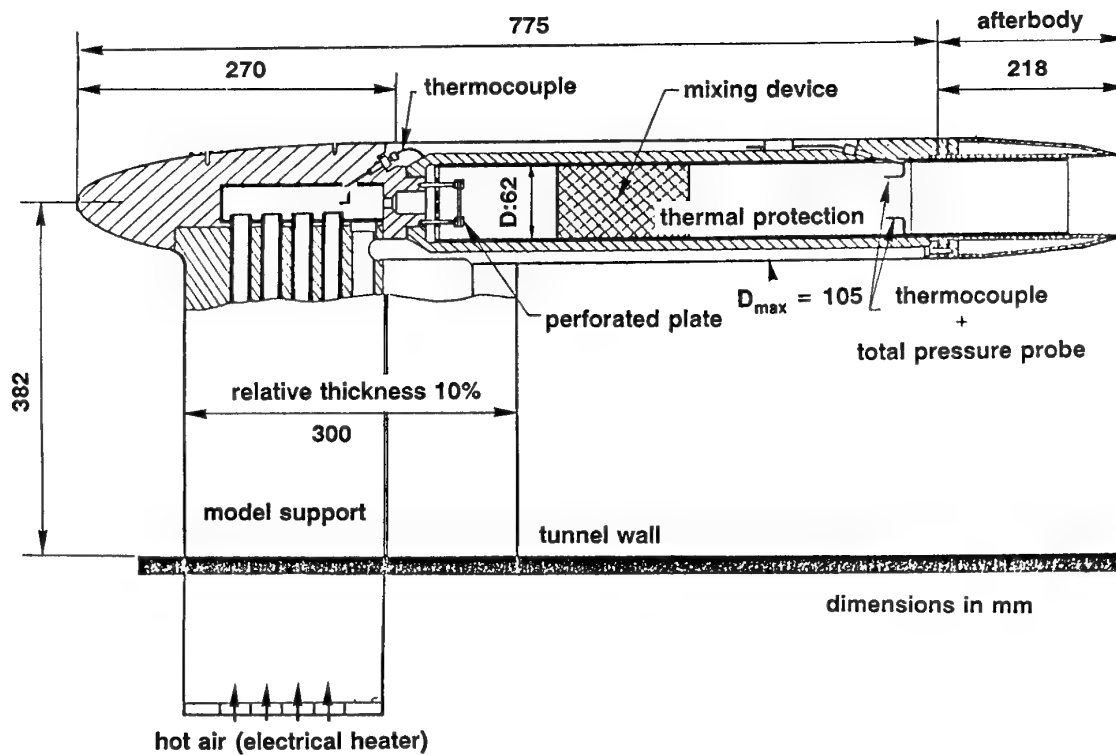
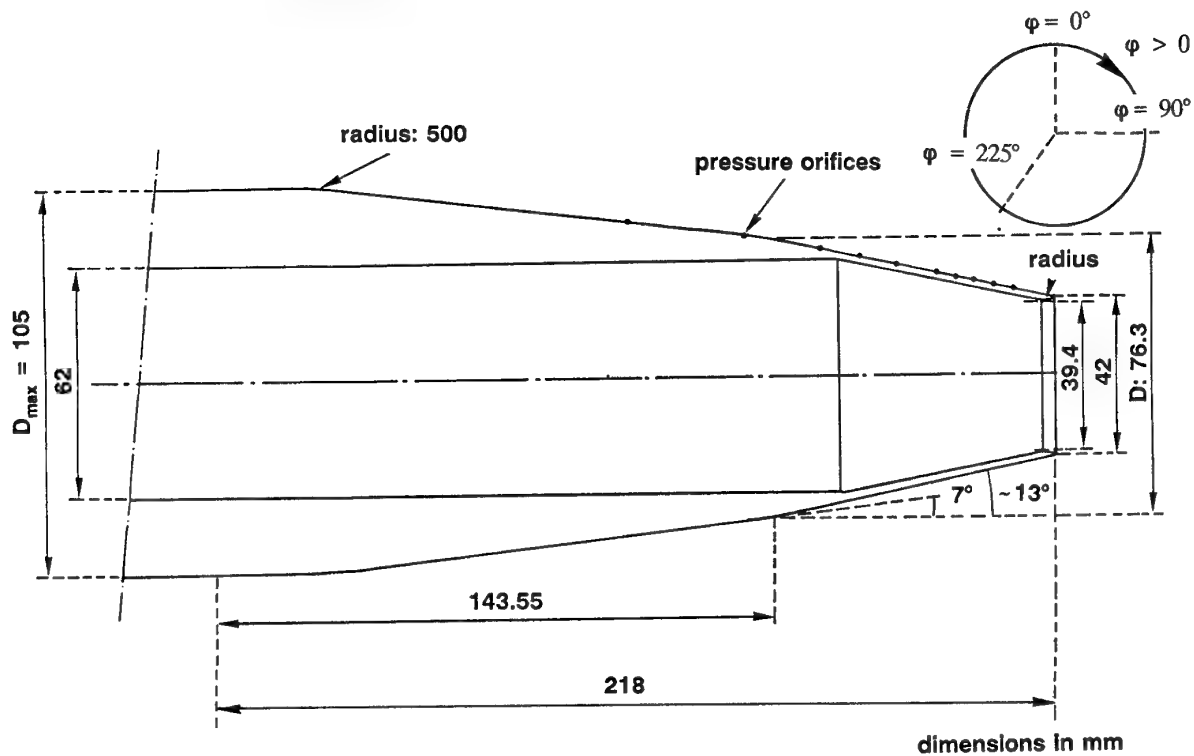


**Fig. 2.5.4 - Test Cases A.2.1 & A.2.2 : General arrangement of the model**





is close to 1200K for a mass flow rate of 0.5kg/s (the difference between this temperature and the jet stagnation temperature is due to heat losses in the ducts).

The afterbody is equipped with a total of 48 pressure orifices located as shown in Fig. 2.5.5. Four rows of 10 orifices were located on generators at the circumferential positions:  $\varphi = 0^\circ, 90^\circ, 225^\circ$  and  $315^\circ$ ; and eight orifices were located on the generator  $\varphi = 180^\circ$ . The abscissas of the pressure orifices with respect to the afterbody extremity are indicated in Table I.

### III - Nominal Flow Conditions

#### Test Case A.2.1: Cold Jet

Outer flow:

Upstream Mach number:  $M_\infty = 0.8$

Stagnation pressure:  $P_{t\infty} = 10^5 Pa$

Stagnation temperature:  $T_{t\infty} = 300K$

Jet flow:

Jet expansion ratio:  $P_{tj}/p_\infty = 4.8$

Stagnation pressure:  $P_{tj} = 3.149 \times 10^5 Pa$

Stagnation temperature:  $T_{tj} = 300K$

#### Test Case A.2.2 : Hot Jet

Outer flow:

Upstream Mach number:  $M_\infty = 0.8$

Stagnation pressure:  $P_{t\infty} = 10^5 Pa$

Stagnation temperature:  $T_{t\infty} = 300K$

Jet flow:

Jet expansion ratio:  $P_{tj}/p_\infty = 4.8$

Stagnation pressure:  $P_{tj} = 3.149 \times 10^5 Pa$

Stagnation temperature:  $T_{tj} = 935K$

The profile of the outer flow boundary layer at a station located 218mm upstream of the afterbody

extremity is given in Annex A.1.1.1.2. These measurements have been executed at two circumferential locations:  $\varphi = 0^\circ$  and  $30^\circ$ .

### IV - Data Available

The field measurements are presented in the coordinate system defined in Fig. 2.5.5:

- Its origin O is located at the centre of the nozzle exit section.

- The X-axis is along the axis of revolution, directed in the downstream direction.

- The Y-axis is along the radial direction.

The field measurements were obtained by using the LDV system described in Section 2.2. Due to the symmetry of the flow, the two-component version of the velocimeter was used, with the forward scattering mode of operation. The outer flow was seeded with incense smoke and the hot jet with magnesium oxide.

The flow was also probed by means of pressure (static and Pitot) and temperature probes. A wedge type probe was used to determine the static pressure and non ventilated chromel-alumel junctions to determine the stagnation temperature.

The field properties were measured in the form of radial profiles.

Tables II and III give the measurements made for each test case and the X location (in mm) of the radial profiles (indicated stagnation conditions are relative to the jet).

### V - References

2.5.6, 2.5.7

### VI - Point of Contact

Dominique REGARD

O.N.E.R.A. Aerodynamics Department

B.P. 72

92322 CHATILLON Cedex, France

Orifice N°	1	2	3	4	5	6	7	8	9	10
$-X(mm)$	109.14	79.19	59.1	49.25	39.01	29.16	24.03	18.91	14.18	9.06
$-X/D_{max}$	1.039	0.754	0.563	0.469	0.372	0.278	0.229	0.180	0.135	0.086
$\varphi = 0/90/225/315^\circ$	X	X	X	X	X	X	X	X	X	X
$\varphi = 180^\circ$			X	X	X	X	X	X	X	X

Table I : Locations of Pressure Orifices on the Axisymmetric Cold/Hot Jet Model

<i>TestCase</i>	$T_{st}(K)$	$P_{tj}/p_{\infty}$	<i>Wallpres.</i>	<i>Fieldpres.&amp;temp.</i>	<i>LDV</i>
A.2.1	300	4.8	<i>yes</i>	<i>yes</i>	<i>no</i>
A.2.2	935	4.8	<i>yes</i>	<i>no</i>	<i>yes</i>

**Table II** : Measurements Executed on the Axisymmetric Cold/Hot Jet Model

<i>TestCase</i>									
A.2.1									
$X(mm)$			25.5		51		75.5		135
$X/D_{max}$			0.243		0.484	0.719	0.719		1.287
<i>TestCase</i>									
A.2.2									
$X(mm)$	4.2	8.7	21	42	46	51	75.5	100	135
$X/D_{max}$	0.0413	0.0825	0.200	0.400	0.438	0.484	0.719	0.952	1.287

**Table III** : Location of Exploration Planes

### 2.5.3.3. Test Cases A.3.1 and A.3.2: Twin Jet Cold Flow

#### I - Wind Tunnel

These experiments have been conducted in the ONERA S3Ch wind tunnel already described in 2.5.3.3 and equipped with *solid walls* in the present case.

#### II - Model Configuration and Installation in Wind Tunnel

The general shape of the model is defined in Fig. 2.5.6. The afterbody is fixed to a forebody, equipped with a rounded nose, attached to the wind tunnel wall by a lateral strut swept at an angle of  $45^\circ$ . The overall length of the model is 927mm. The forebody has a maximum height of 110mm and a thickness of 55mm. In the normal arrangement, the model is fixed on the lower wall of the wind tunnel test section: this defines the "horizontal" and "vertical" planes (or sections) used for the model description.

The afterbody itself, the emerging part of the nozzles being excluded, has a total length of 165mm. This afterbody is terminated by a flat base from which the two nozzles emerge.

The cross section of the model nose is made of two rectilinear segments and two half circles, as shown in Fig. 2.5.6. The axial evolution of this section is defined by the contours of the nose in the horizontal and vertical planes. The definitions of these contours are given by considering a system of coordinates whose origin is placed at the nose, the X-axis being horizontal and directed in the downstream direction, the Y-axis contained in a horizontal plane and the Z-axis in a vertical plane (see Fig. 2.5.7).

The two contours are defined by strings of coordinate points (X,Y,Z) tabulated in Tables IV and V placed at the end of the Section. Considering first the vertical section (see Table IV), the contour is described by starting from a section located at  $X = 406.235mm$ , on the upper body, going towards the nose and continuing on the lower body to a station coincident with the leading edge of the strut. The contour in the horizontal plane is defined in the same way by starting from  $X = 451.809mm$  on one side, turning around the nose, and stopping at  $X = 451.839mm$  on the other side.

In fact, the contours are variable over a length  $L = 310mm$ . Downstream, the section of the model is constant over a length of 240mm. Then, there is a slight slope to insure continuity with the afterbody whose upstream maximum height is equal to 105mm.

The shape of the afterbody itself is defined by strings of coordinate points in a system defined in Fig. 2.5.8.

- The origin O is in the plane of the base.
- The longitudinal axis is along the model general axis, oriented from base to nose.
- The Y-axis is contained in the base plane and oriented from the "lee-side" to the "windward-side" of the model.
- The Z-axis is contained in the base plane and oriented in the transverse direction as shown in Fig. 2.5.8.

The plane  $Y = 0$  is a plane of symmetry for the afterbody.

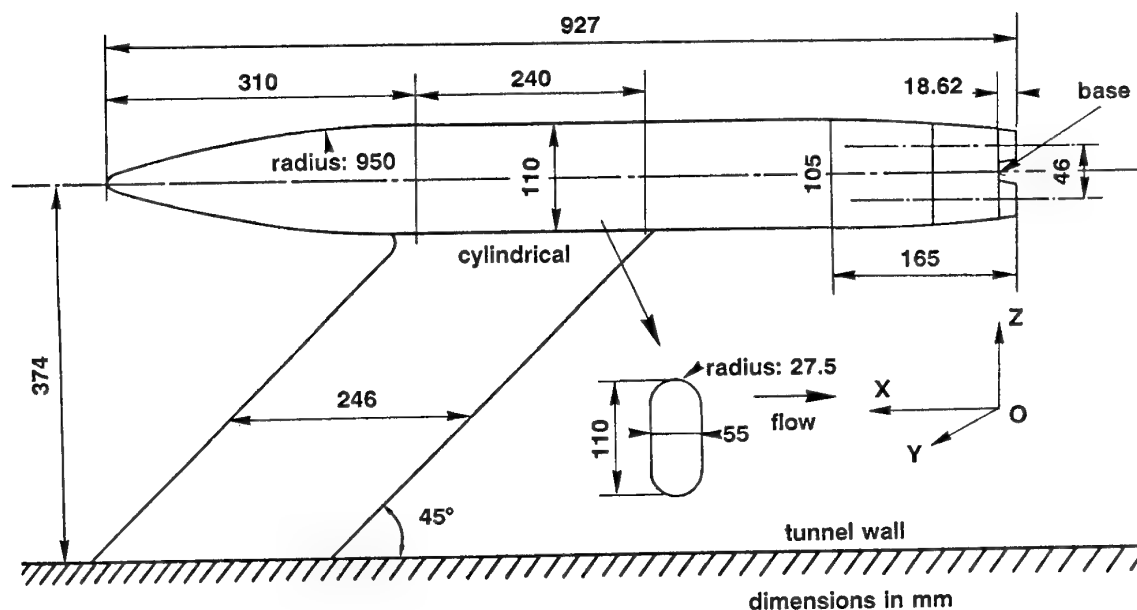


Fig. 2.5.6 - Test Cases A.3.1 & A.3.2 : General arrangement of the model

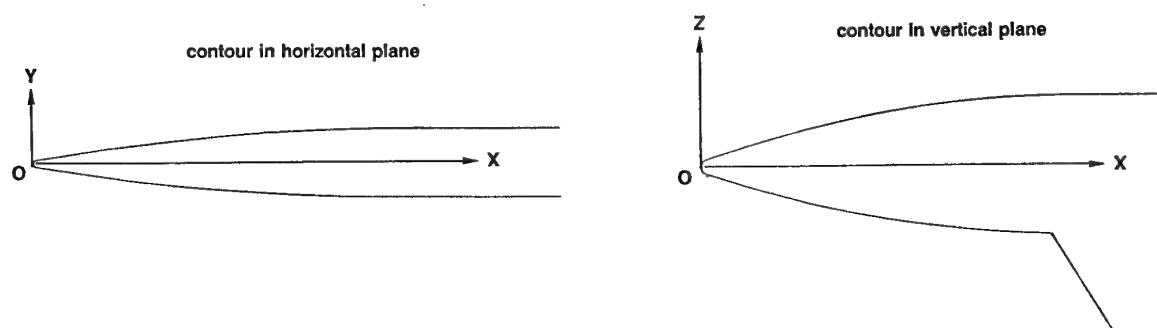


Fig. 2.5.7 - Test Cases A.3.1 & A.3.2 : System of coordinates used for the definition of the nose contour

The shape of the afterbody is defined by a set of about 40,000 points (X,Y,Z) contained in two 1.4 Mo, 3.5" disquettes. The first 165 values are the X coordinates of the line  $Z = 0$  in the afterbody upper surface. The following records define the afterbody contour in  $X = \text{constant}$  planes (from  $X = 0$  to  $X = 165\text{mm}$  with a step of 1mm). A CATIA definition of the afterbody is also available.

The two nozzles are axisymmetric and identical (see Fig. 2.5.9). In the "normal" position of the model, their axes are contained in a vertical plane and separated by a distance of 46mm. Their geometry is given in Fig. 2.5.10. The upstream settling chamber, containing a set of filters and grids, has a diameter of 36.2mm. This chamber is followed by two successive converging sections with convergence angles of  $10^\circ$

and  $54^\circ$ . The diameter of the throat is 20.9 mm. This "primary" nozzle is followed by a "secondary" nozzle made of a converging wall of angle  $5^\circ$ , with exit diameter of 29.22mm. In the experiments, the secondary flux was not simulated. The outer contour of the emerging part of the nozzle is rectilinear with a slope of  $15^\circ$ .

The emergence length of the nozzles, with respect to the base, is equal to 18.62mm.

In order to represent possible blockage effects, a precise definition of the test section, model location and support are given in Fig. 2.5.11.

In its entrance plane, the test section has a height of 764mm and a span of 803mm. The two side walls are rectilinear and parallel. The upper and lower walls are rectilinear and have a divergence angle of  $0.42^\circ$

for Test Case A.3.1 and of  $0.50^\circ$  for Test Case A.3.2, starting from the entrance section.

The model is located at a position such that the base is at 1324mm from the entrance plane of the test section. The model axis is at 378mm from the tunnel lower wall and at equal distance from the two side walls.

The shape of the strut supporting the model is defined in Fig. 2.5.12. The normal cross section of the strut is made of a modified NACA 64004 profile with a maximum thickness of 13.6mm, at 40% of the leading edge, and a total chordlength of 176mm. The shape in the leading edge region is made of a rectilinear part, over a distance of 0.025%, tangent to the NACA profile and to a radius of 0.2mm at the leading edge. The strut is swept at an angle of  $45^\circ$ . The junction between the strut and the model is at 314mm from the model nose (see Fig. 2.5.12), a radius of 10mm insuring a smooth transition between the strut and the model.

The stagnation conditions of the jets (pressure and temperature) were measured by probes installed in the settling chamber.

The upstream Mach number  $M_\infty$  is determined from the static pressure given by an orifice located in the middle of a side wall, 380mm downstream of the test section entrance plane.

The afterbody was equipped with 55 pressure orifices, their arrangement being given in Fig. 2.5.13. Seven orifices are on the base, in the inter-nozzle space, and the others are located on rows designated by: A, B, C, D, E and F, on the afterbody and by a, b, c, d and e on the nozzle. Lines c, b, d and e are in the continuation of lines A, F, B and C, respectively. The angular positions of these lines are given in Fig. 2.5.13. On each row, the orifices are at the same X locations which also coincide with the locations of the LDV exploration planes (see Table VI). The results given in Annex A.1.1.1.4 are plotted with a distance scaled to the nozzle length  $L_N = 18.62\text{mm}$ .

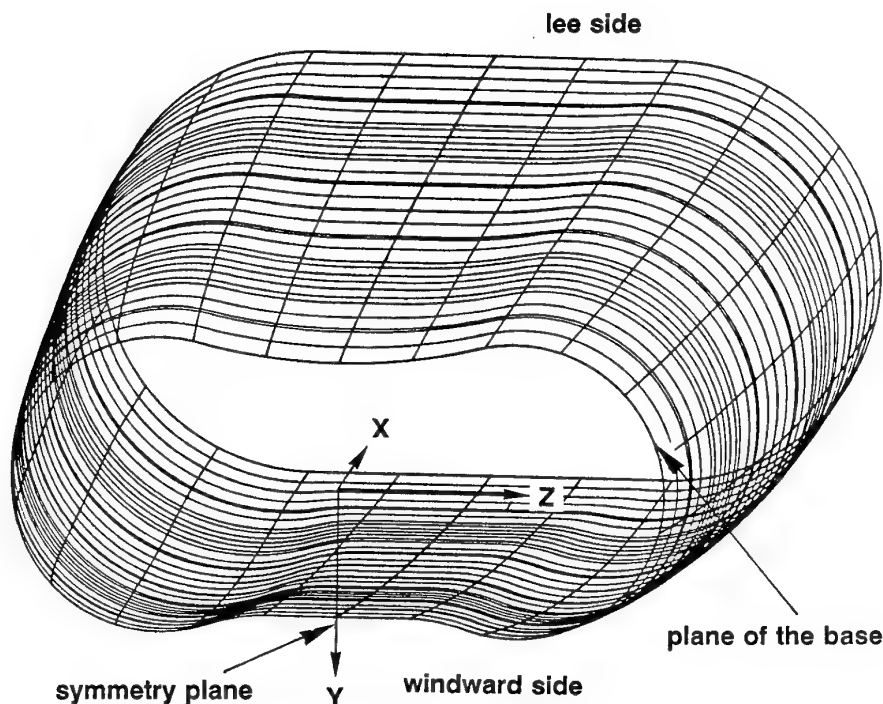


Fig. 2.5.8 - Test Cases A.3.1 & A.3.2 : Afterbody definition

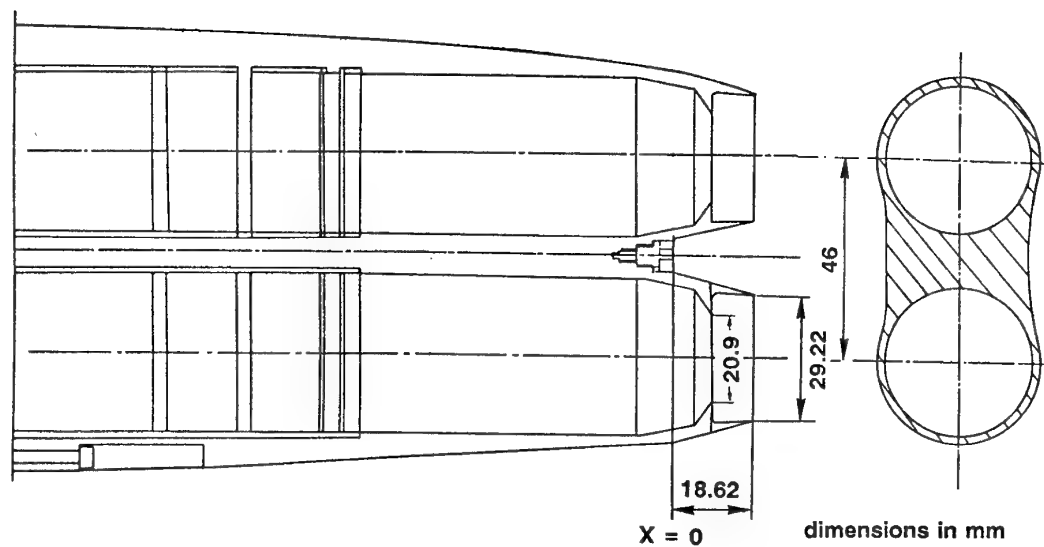


Fig. 2.5.9 - Test Cases A.3.1 & A.3.2 : Afterbody general arrangement

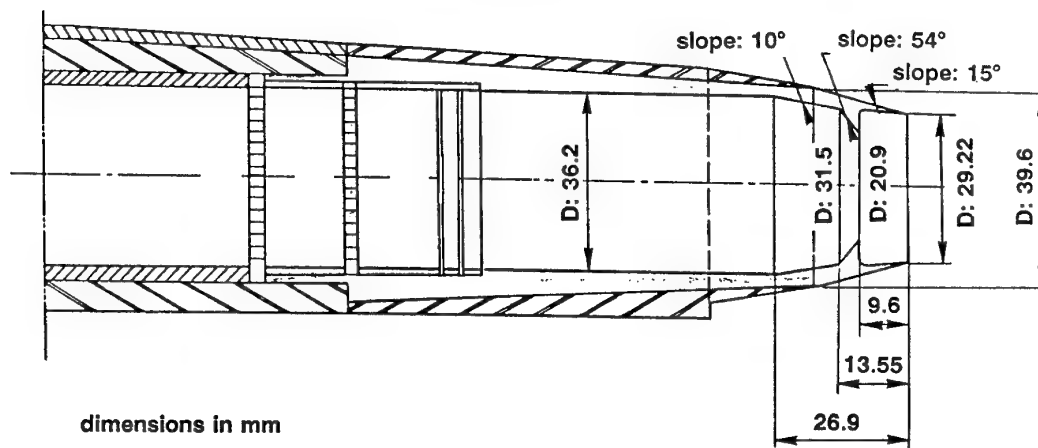


Fig. 2.5.10 - Test Cases A.3.1 & A.3.2 : Definition of the nozzles

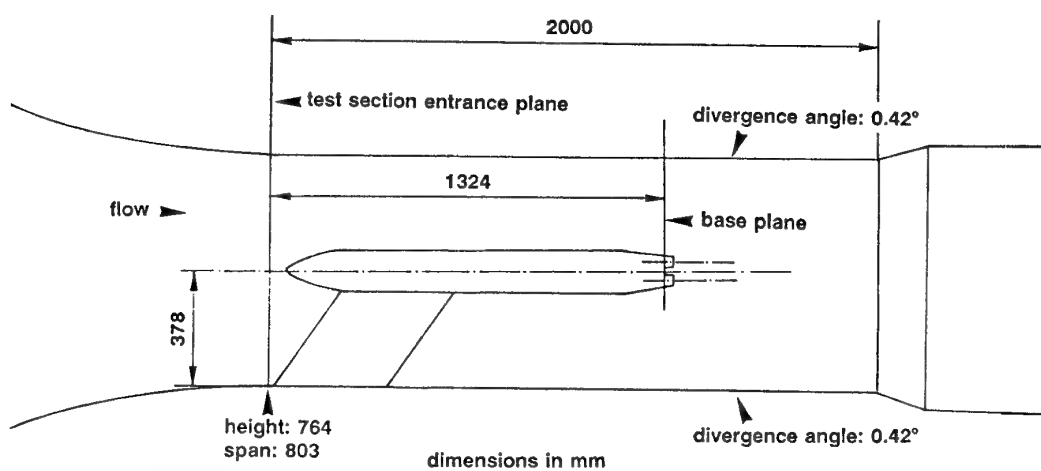


Fig. 2.5.11 - Test Cases A.3.1 & A.3.2 : Test section definition and model installation for the  $M_\infty = 0.85$  experiment

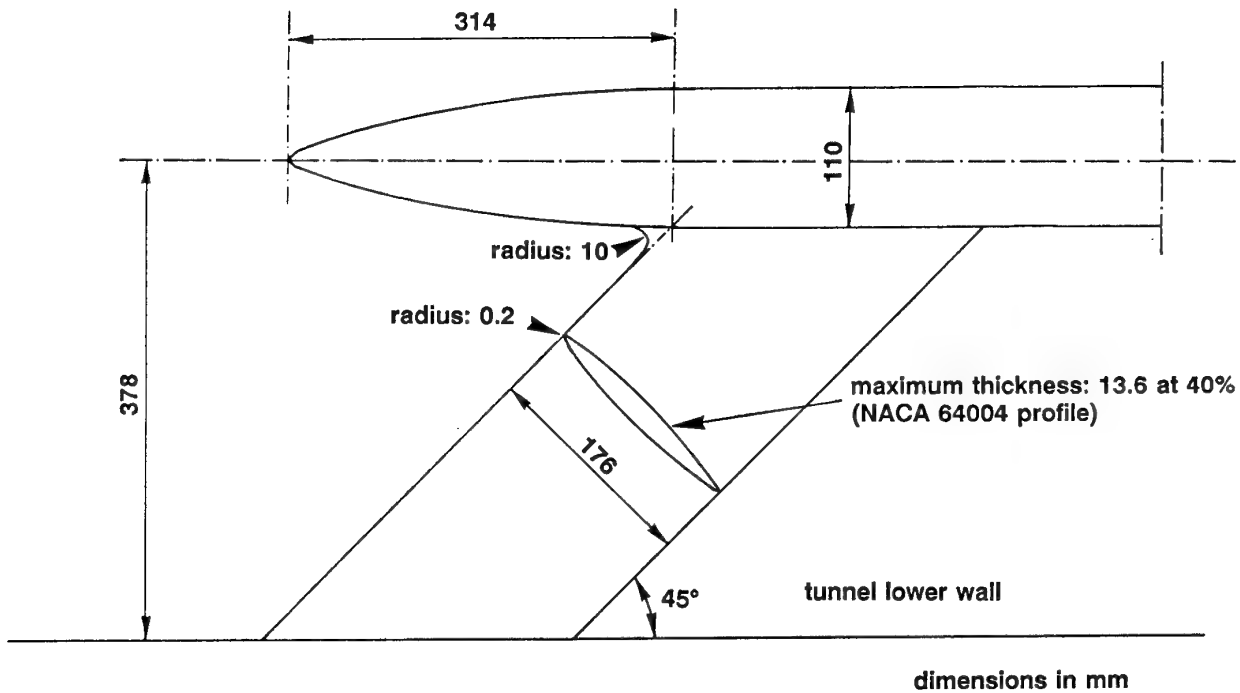


Fig. 2.5.12 - Test Cases A.3.1 & A.3.2 : Definition of the strut supporting the model

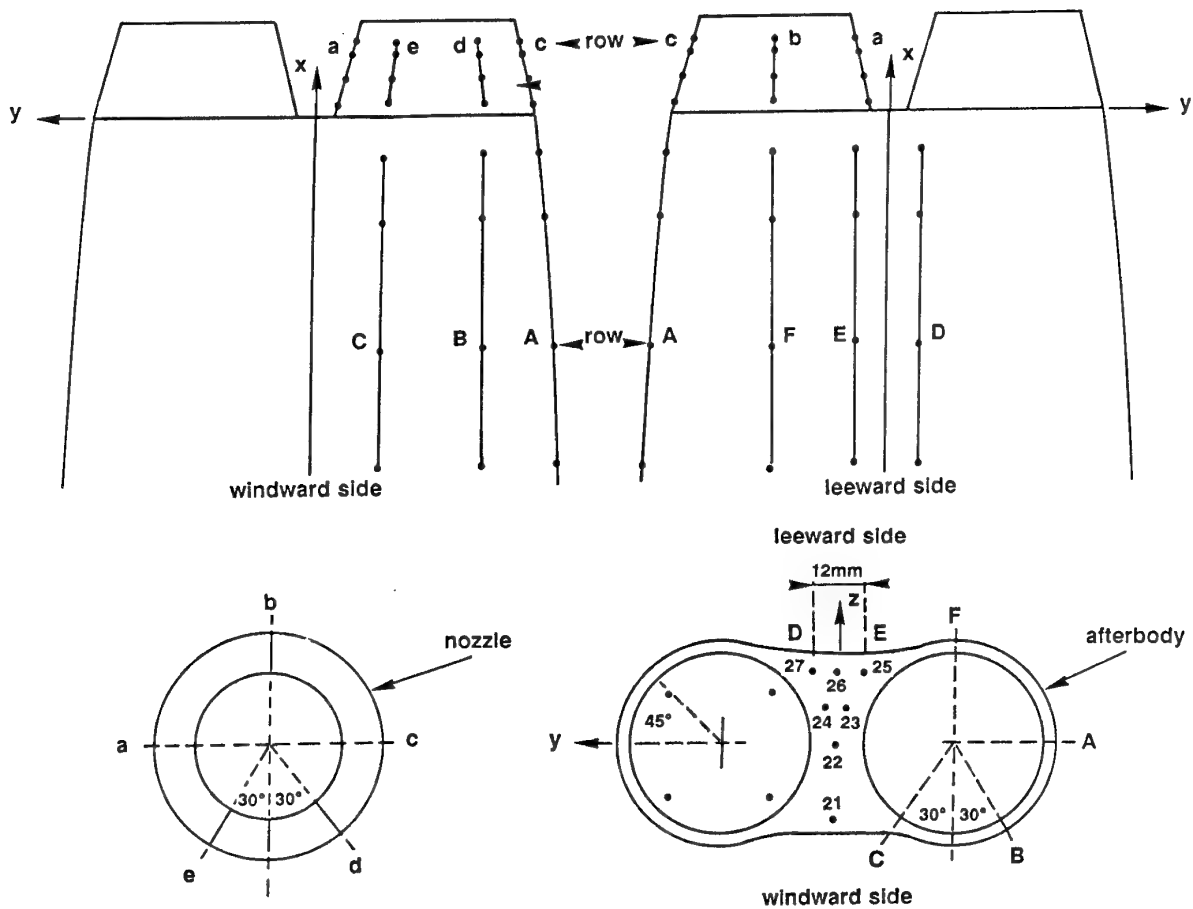


Fig. 2.5.13 - Test Cases A.3.1 & A.3.2 : Location of the pressure orifices

### III - Nominal Flow Conditions

#### Test Case A.3.1 (blockage effects):

##### Outer flow:

Upstream Mach number:  $M_\infty = 0.85$

Stagnation pressure:  $P_{t\infty} = 10^5 Pa$

Stagnation temperature:  $T_{t\infty} = 300K$

##### Jet flow:

Jet expansion ratio:  $P_{ij}/p_\infty = 5$

Stagnation pressure:  $P_{ij} = 3.118 \times 10^5 Pa$

Stagnation temperature:  $T_{st} = 300K$

#### Test Case A.3.2:

##### Outer flow:

Upstream Mach number:  $M_\infty = 0.80$

Stagnation pressure:  $P_{t\infty} = 10^5 Pa$

Stagnation temperature:  $T_{t\infty} = 300K$

##### Jet flow:

Jet expansion ratio:  $P_{ij}/p_\infty = 5$

Stagnation pressure:  $P_{ij} = 3.118 \times 10^5 Pa$

Stagnation temperature:  $T_{st} = 300K$

The properties of the incoming boundary layer at station  $X = -70mm$ , upstream of the base are as follows:

- Physical thickness:  $\delta = 7mm$
- Incompressible shape parameter:  $H_i = 1.3$

The LDV measurements were not fine enough to precisely define the velocity profile of this boundary layer. A distribution suitable for the calculations can be deduced from the given values of  $\delta$  and  $H_i$  by means of an analytical representation (e.g., Coles or Whitfield profiles). The properties of the boundary layer can be assumed constant around the afterbody at that location.

#### IV - Data Available

The flow field measurements were obtained by using the three-component version of the ONERA LDV system depicted in Section 2.2. Because of the high velocities to be measured, the forward scattering mode of operation was used. To allow measurements around the entire afterbody, a set of data was collected with the model strut mounted on the wind tunnel lower wall (the so-called "normal" position) and a second set was collected with the support fixed on one of the wind tunnel side walls (Test Case A.3.1 only). The outer flow was seeded with particles of incense smoke injected through an injector placed well upstream of the test section.

In a first series of experiments, the jets were not seeded because of difficulties then encountered in introducing particles in a high pressure flow.

The LDV measurements are presented in the coordinate system defined in Fig. 2.5.17:

- Its origin is located in the plane of the base at the intersection of the symmetry plane and the plane containing the nozzle axes.

- The X-axis is parallel to the nozzle axis and oriented in the upstream direction.

- The Z-axis goes through the centres of the nozzle traces in the plane of the base.

- The Y-axis completes the system and is oriented from the windward to the lee-side of the afterbody.

For Test Case A.3.1, the LDV measurements have been obtained in:

- 8 (Y,Z) planes, normal to the X-axis, located upstream of the nozzle exit sections and containing the surface pressure orifices and,

- 5 (Y,Z) planes passing downstream of the nozzle exit sections.

The X locations of these planes are given in Table VII:

The domain explored with the LDV system for Test Case A.3.1 is shown in Fig. 2.5.14. Each plane contained several hundred measurement points, the maximum being 600. At each point, the available quantities are the three mean velocity components and the six distinct components of the Reynolds tensor. Schlieren photographs and surface flow visualizations were recorded.

In order to have a more precise description of the flow in the vicinity of the afterbody, a second series of LDV measurements has been executed, for the two test cases along the exploration lines defined in Fig. 2.5.15.

- Nine exploration lines are contained in the plane  $Y = 0$ , extending from  $Z = -15mm$  ( $Z/L_N = -0.967$ ) to  $Z = 65mm$  ( $Z/L_N = 3.491$ ), their abscissas (with X axis oriented from nose to base) varying from  $X = -20mm$  to  $X = 60mm$  (or  $X/L_N = -1.074$  to  $X/L_N = 3.222$ ).

- The space between the nozzles has been probed along lines contained in the planes whose location is given in Table VIII:

In each of these planes, the explorations have been executed for Z varying between  $Z = -8mm$  to  $Z = 8mm$  ( $Z/L_N$  from  $-0.430$  to  $0.430$ ), by step of  $2mm$  ( $\Delta Z/L_N = 0.107$ ), and Y between  $Y = -25mm$  to  $Y = 25mm$  ( $Y/L_N$  from  $-0.806$  to  $1.343$ ) by step of  $5mm$  ( $\Delta Y/L_N = 0.269$ ).

The boundary layers above and below the afterbody have been probed in the plane  $Y = 0$  at  $X = -170mm$ .

#### V - References

2.5.8, 2.5.9

#### VI - Point of Contact

Jean DELERY

O.N.E.R.A.

Aerodynamics Department

92322 CHATILLON Cedex, France

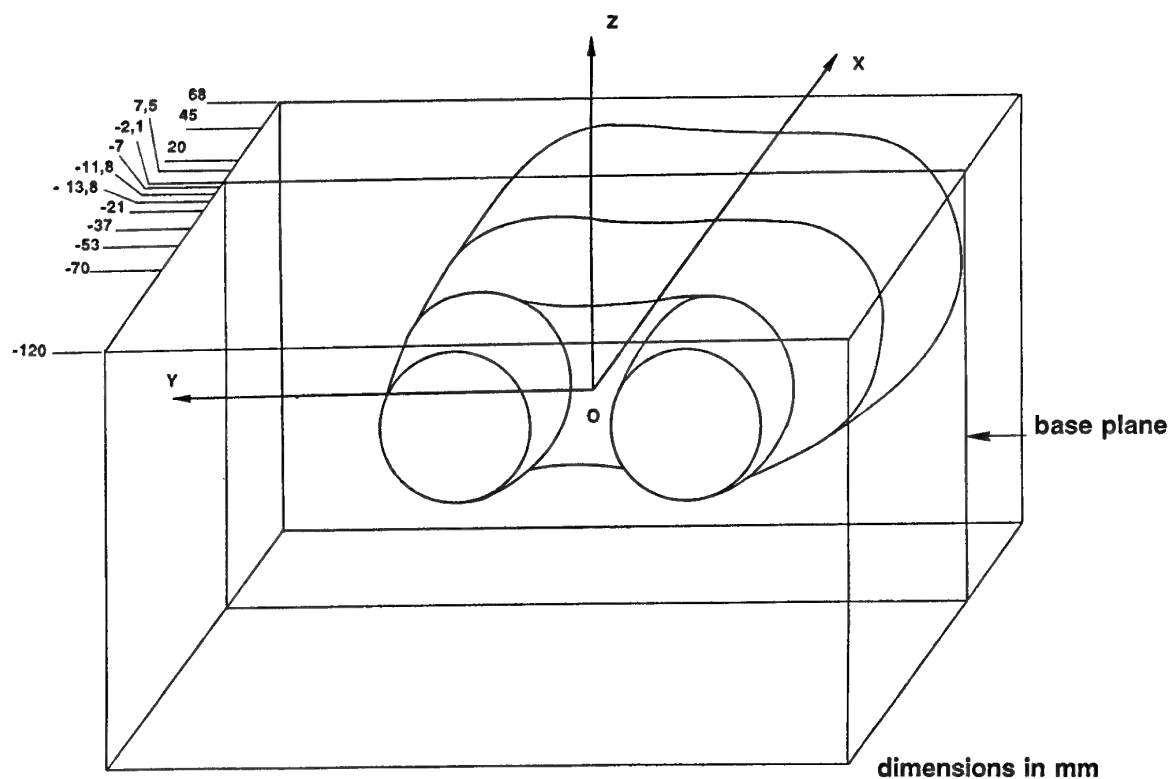


Fig. 2.5.14 - Test Cases A.3.1 : Domain explored with the LDV system

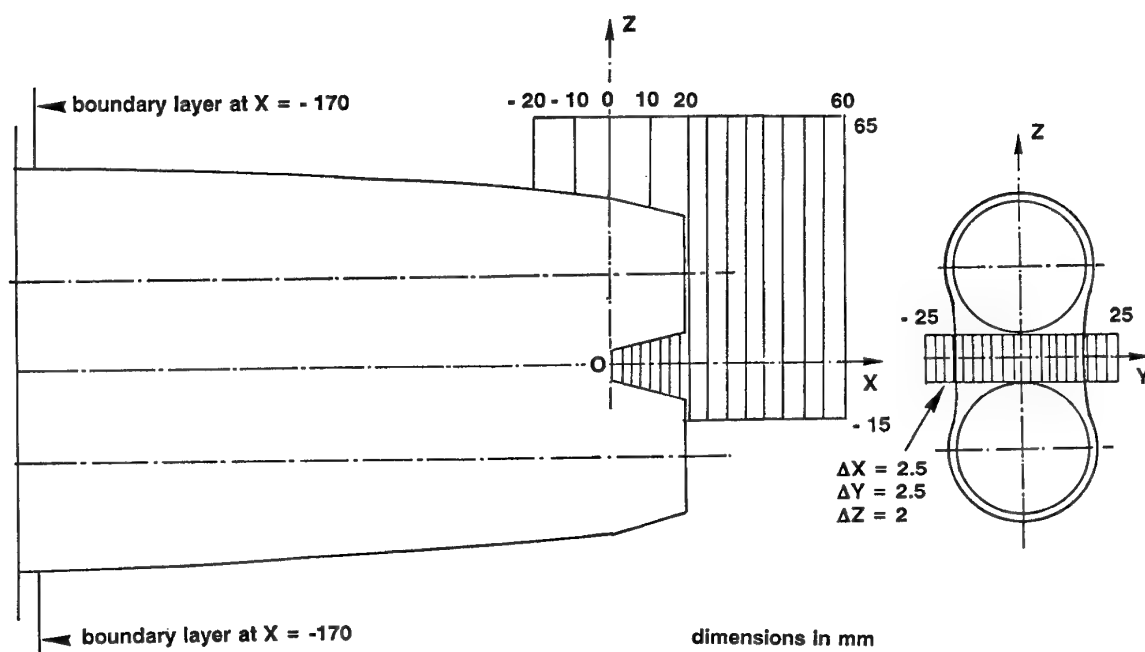
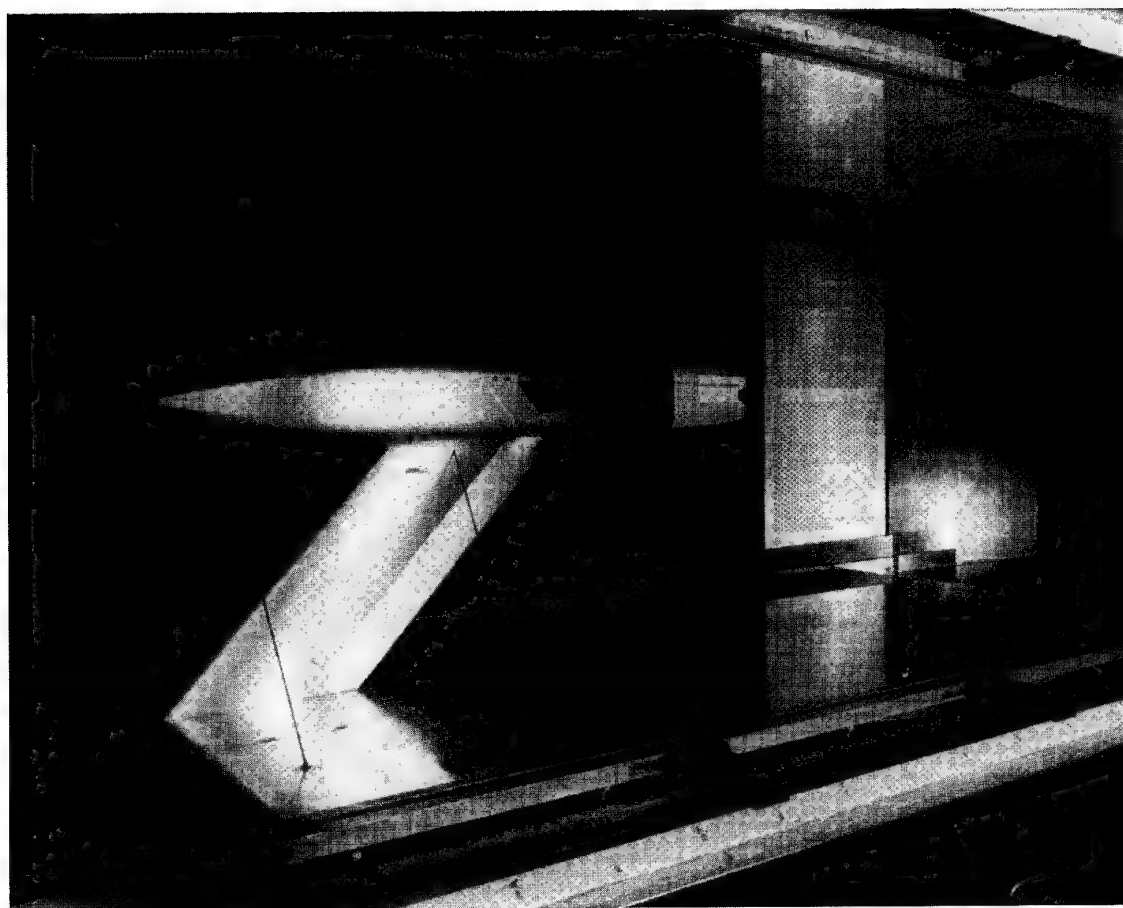


Fig. 2.5.15 - Test Cases A.3.1 & A.3.2 : Domain explored with the LDV system in the afterbody vicinity





Test Cases A.3 : Photograph of the model installed in the S3Ch wind tunnel

### 2.5.4. References

- [2.5.1] Report of the Working Group 08 on Aerodynamics of Aircraft Afterbody, AGARD AR N°226 (1986)
- [2.5.2] Berner, C.: Measurements and interpretations of 3-D high speed flows. Proceedings 3rd International Conference on Laser Anemometry, Advances and Applications, Swansea, Wales, Sept. 26-29, 1989
- [2.5.3] Berner, C. and Dupéroux, J. P.: Mesures simultanées des trois composantes du vecteur vitesse dans le sillage d'arrière-corps à symétrie de révolution en incidence. ISL-Report R 1/90
- [2.5.4] Berner, C. and Dupéroux, J. P.: Mesures simultanées des trois composantes du vecteur vitesse dans le sillage d'arrière-corps à symétrie de révolution en incidence - Annexe 1. ISL-Report S-CR 2/90
- [2.5.5] Pérouze, C.: Description de la soufflerie S3 renouvelée en 1987. ONERA-RT N° 117/1865AN (Feb. 1990)

[2.5.6] Bailly, D.; Regard D. and Pilon, J. A.: Opération MARCO: Essai de la tuyère de référence dans la soufflerie S3Ch et première qualification de la tuyère ventilée. ONERA-RSF N° 42/3482AY (Dec. 1991)

[2.5.7] Maury, P.: Opération MARCO. Tuyères de référence et ventilée alimentées en jet chaud. Soufflerie S3Ch. ONERA-PV N° 39/3482AY (Feb. 1993)

[2.5.8] Sémézis, Y. and Délery, J.: Arrière-corps bituyère. Synthèse des résultats obtenus à  $M_0 = 0.85$  dans la soufflerie S3Ch. Deuxième campagne d'essais. ONERA-RTS N° 13/4361AY (July 1991)

[2.5.9] Pérouze, C. and Soulevant, D.: Soufflerie S3Ch. Arrière-corps bituyère pour avion de combat. Exploration du champ aérodynamique par vélocimétrie laser (seconde série d'essais). ONERA-PV N° 12/4361AY (July 1990)

$X(mm)$	-68	-45	-20	-7.5	2.1	7	11.8	13.8
$X/L_N$	-3.651	-2.417	-1.074	-0.403	0.113	0.376	0.634	0.741

Table VI : Locations of the Sections Containing the Pressure Orifices for the Twin Jet Model (X axis oriented nose to base).

"Upstream" planes:

$X(mm)$	68	45	20	7.5	-2.1	-7	-11.8	-13.8
$X/L_N$	3.652	2.417	1.074	0.403	-0.113	-0.376	-0.634	-0.741

"Downstream" planes:

$X(mm)$	-21	-37	-53	-70	-120
$X/L_N$	-1.128	-1.987	-2.846	-3.759	-6.445

Table VII : Locations of Planes Explored with the LDV System for the Twin Jet Model. Test Case A.3.1 (X axis oriented base to nose)

$X(mm)$	2.5	5	7.5	10	12.5	15	17.5
$X/L_N$	0.134	0.269	0.403	0.537	0.671	0.806	0.940

Table VIII : Location of LDV Explorations Between the Nozzles

	X	Y
1	451.809	27.486
2	448.235	27.499
3	443.980	27.486
4	438.221	27.500
5	433.543	27.498
6	427.708	27.499
7	420.764	27.507
8	416.016	27.505
9	411.005	27.503
10	406.090	27.500
11	401.703	27.508
12	397.426	27.509
13	392.278	27.505
14	386.856	27.500
15	381.805	27.502
16	375.162	27.500
17	371.882	27.503
18	367.741	27.506
19	362.105	27.501
20	357.139	27.502
21	349.583	27.504
22	341.516	27.504
23	334.008	27.495
24	320.954	27.494
25	312.816	27.489
26	305.322	27.478
27	298.658	27.472
28	290.119	27.402
29	284.010	27.323
30	276.712	27.199
31	269.440	27.043
32	262.601	26.892
33	254.111	26.646
34	250.094	26.528
35	242.747	26.270
36	234.237	25.941
37	227.018	25.630
38	220.064	25.300
39	213.004	25.021
40	207.261	24.670
41	201.828	24.337
42	197.208	24.673
43	189.231	23.595
44	181.599	23.090
45	176.409	22.709
46	171.217	22.342
47	164.962	21.866
48	157.504	21.278
49	150.710	20.704
50	144.495	20.170
51	138.565	19.641
52	132.693	19.091
53	125.892	18.447
54	120.305	17.881
55	114.349	17.289
56	108.127	16.623
57	102.232	15.983
58	96.250	15.312
59	88.467	14.418
60	82.232	13.694
61	76.822	13.002
62	71.089	12.293
63	65.331	11.709
64	57.691	10.848
65	51.497	9.703
66	46.416	9.002
67	41.496	8.301
68	37.513	7.742
69	32.419	6.956
70	28.170	6.316
71	24.501	5.808
72	21.555	5.413
73	18.625	5.023
74	15.395	4.617
75	13.726	4.388
76	12.125	4.166
77	10.354	3.914
78	8.754	3.694
79	7.500	3.527
80	5.553	3.244
81	4.205	3.023
82	3.027	2.833
83	2.521	2.724
84	1.693	2.542
85	1.706	2.530
86	1.271	2.367
87	1.060	2.246
88	0.240	1.353
89	0.145	1.094
90	0.114	1.010
91	0.078	0.885

	X	Y
92	-0.007	0.315
93	-0.014	-0.116
94	0.039	-0.664
95	0.093	-0.876
96	0.239	-1.281
97	0.334	-1.467
98	0.488	-1.707
99	0.612	-1.867
100	1.235	-2.315
101	1.810	-2.536
102	2.504	-2.719
103	3.340	-2.899
104	4.597	-3.113
105	5.892	-3.320
106	7.488	-3.578
107	8.781	-3.762
108	10.507	-4.015
109	12.597	-4.303
110	14.657	-4.610
111	16.142	-4.802
112	18.355	-5.126
113	19.308	-5.231
114	21.009	-5.449
115	23.362	-5.742
116	25.164	-5.987
117	28.242	-6.439
118	31.401	-6.917
119	34.921	-7.443
120	37.761	-7.860
121	41.689	-8.431
122	46.273	-9.079
123	49.789	-9.562
124	52.295	-9.905
125	56.527	-10.483
126	60.706	-11.026
127	64.815	-11.565
128	69.785	-12.209
129	74.322	-12.783
130	80.630	-13.561
131	84.972	-14.072
132	90.592	-14.750
133	96.737	-15.444
134	100.551	-15.879
135	105.963	-16.453
136	110.404	-16.933
137	114.995	-17.413
138	121.725	-18.085
139	126.189	-18.538
140	131.183	-19.015
141	136.669	-19.516
142	142.688	-20.069
143	147.534	-20.488
144	154.177	-21.040
145	160.843	-21.575
146	166.449	-22.017
147	173.291	-22.521
148	180.687	-23.037
149	187.842	-23.527
150	195.256	-23.978
151	202.818	-24.432
152	210.615	-24.852
153	220.398	-25.353
154	229.332	-25.748
155	238.979	-26.108
156	246.083	-26.402
157	255.212	-26.683
158	264.194	-26.932
159	271.681	-27.095
160	280.272	-27.252
161	287.853	-27.352
162	295.282	-27.424
163	301.961	-27.470
164	310.306	-27.494
165	317.008	-27.492
166	324.149	-27.493
167	331.718	-27.493
168	339.965	-27.490
169	347.429	-27.489
170	355.308	-27.483
171	361.599	-27.486
172	369.653	-27.482
173	377.610	-27.481
174	385.358	-27.480
175	392.997	-27.478
176	402.067	-27.480
177	410.642	-27.472
178	419.872	-27.463
179	430.641	-27.471
180	440.134	-27.457
181	446.347	-27.456
182	451.839	-27.454

	X	Z
1	406.235	54.614
2	402.532	54.625
3	398.610	54.640
4	394.285	54.655
5	392.097	54.661
6	386.801	54.679
7	382.200	54.686
8	378.311	54.690
9	374.018	54.702
10	367.388	54.715
11	361.726	54.719
12	354.308	54.731
13	347.603	54.749
14	340.676	54.748
15	333.750	54.760
16	327.845	54.768
17	321.585	54.777
18	314.875	54.786
19	308.845	54.784
20	302.590	54.766
21	295.944	54.696
22	289.697	54.592
23	283.544	54.457
24	277.005	54.246
25	268.666	53.927
26	261.892	53.618
27	255.427	53.278
28	248.340	52.857
29	241.651	52.407
30	235.449	51.946
31	227.078	51.260
32	219.544	50.582
33	213.055	49.956
34	206.479	49.266
35	200.082	48.554
36	192.904	47.705
37	186.364	46.879
38	179.430	45.962
39	172.188	44.947
40	164.586	43.818
41	157.680	42.742
42	151.533	41.750
43	145.867	40.787
44	139.164	39.615
45	131.794	38.258
46	126.284	37.210
47	119.864	35.948
48	113.842	34.727
49	106.514	33.188
50	98.851	31.524
51	91.363	29.816
52	83.428	27.953
53	75.830	26.104
54	68.700	24.315
55	60.695	22.240
56	53.168	20.225
57	46.245	18.313
58	40.808	16.776
59	35.343	15.183
60	28.740	13.198
61	24.073	11.800
62	19.726	10.541
63	15.811	9.408
64	11.620	8.181
65	8.530	7.182
66	7.304	6.784
67	4.319	5.805
68	3.399	5.469
69	2.746	5.201
70	2.027	4.867
71	1.361	4.344
72	0.824	3.740
73	0.524	3.255
74	0.311	2.770
75	0.084	1.819
76	0.018	1.199
77	-0.010	0.560
78	-0.012	-0.544
79	0.017	-1.307
80	0.142	-2.261
81	0.308	-2.826
82	0.430	-3.134

	X	Z
83	0.560	-3.407
84	0.564	-3.580
85	0.861	-3.844
86	2.644	-5.018
87	3.821	-5.438
88	4.976	-5.813
89	6.289	-6.190
90	7.562	-6.560
91	8.941	-6.944
92	9.749	-7.173
93	11.419	-7.635
94	13.244	-8.134
95	15.517	-8.786
96	17.734	-9.416
97	19.884	-10.036
98	22.263	-10.726
99	25.153	-11.602
100	27.437	-12.300
101	29.599	-12.976
102	32.073	-13.755
103	35.014	-14.659
104	36.921	-15.228
105	39.381	-15.949
106	41.886	-16.677
107	44.480	-17.422
108	46.967	-18.122
109	49.388	-18.780
110	50.944	-19.191
111	52.447	-19.580
112	54.162	-20.009
113	56.161	-20.503
114	57.309	-20.796
115	65.379	-22.765
116	68.379	-23.563
117	71.978	-24.509
118	79.686	-26.555
119	81.811	-27.164
120	84.387	-27.860
121	86.018	-28.264
122	90.436	-29.338
123	95.918	-30.609
124	101.080	-31.792
125	107.541	-33.194
126	113.388	-34.475
127	117.707	-35.336
128	122.520	-36.309
129	127.792	-37.356
130	133.037	-38.352
131	137.996	-39.276
132	143.493	-40.281
133	148.271	-41.102
134	153.066	-41.918
135	158.037	-42.758
136	162.617	-43.475
137	167.396	-44.211
138	172.991	-45.045
139	177.771	-45.731
140	183.793	-46.559
141	189.250	-47.277
142	195.031	-47.996
143	200.066	-48.600
144	206.876	-49.372
145	212.335	-49.960
146	218.657	-50.600
147	224.942	-51.193
148	230.742	-51.696
149	235.513	-52.089
150	238.951	-52.353
151	243.585	-52.687
152	248.427	-53.020
153	252.830	-53.299
154	257.151	-53.561
155	261.921	-53.817
156	266.592	-54.044
157	270.146	-54.207
158	274.007	-54.363
159	278.088	-54.513
160	282.062	-54.647
161	285.635	-54.810
162	288.908	-54.956
163	292.164	-55.470

Table V : Nose Contour Definition. Vertical Plane

Table IV : Nose Contour Definition. Horizontal Plane



## 2.6 Computational Results and Evaluation

### 2.6.1 Preliminary remarks.

The cases in Series A were chosen to constitute a data base allowing an accurate validation of fundamental flows using CFD. The organizations involved in computing these fundamental test cases are listed in the following figure.

	Ref.	A.2.1	A.2.2
Aerospatiale	N15		
Dassault Aviation	N13		
Mc Donnell Douglas	N09		
NASA Langley	N10		
ONERA	N14		
Rolls-Royce	N05		
Snecma	N03		

Fig. 2.6-1

The different organizations have provided data mainly on test case A.2.2. There is no contribution for cases A.1 and A.3, and only a few on case A.2.1. This does not question either the choice of the fundamental cases or the quality or the accuracy of these experimental data. In fact, the main reasons why no entries have been delivered concerning A1 and A3 lie both in time constraints (the revised version of A3 has been available with a delay) as well as money constraints (manpower and CPU costs).

Nevertheless, experimental data for every Series A case presented in this report (see Appendix A), is without doubt, very helpful to validate present and future CFD codes.

The major features of the Series A cases have already been described in the previous chapter. On the one hand these relatively simple geometries highlight some important properties of the typical flowfield surrounding an afterbody (base flow in case A.1, thermal effects in case A.2, and twin jets in case A.3). On the other hand, the volume, variety and quality of measurements enable an accurate validation of codes.

The presentation of the comparison between experimental data and numerical results in the next section is structured according to the different physical properties and sorted along physical complexity ; the evaluation of the codes ability to simulate such flows goes from the classical validation based on wall pressure distributions to precise comparisons dealing with turbulent quantities.

The purpose of this work is not to establish a classification between the different contributors or even between the different numerical methods or turbulence models used. Drawing such a conclusion is

unfortunately a hard task, for some approaches may suit the simulation of a particular phenomenon, whereas some others are preferable to simulate another zone of the flowfield. Furthermore, the comparisons presented herein are only carried out on axisymmetric configurations, the extrapolation of the conclusions made to any kind of geometries and especially to 3D configurations is rather dangerous.

It seems more appropriate to consider these data as a mere snapshot of the present state of the art in the field of CFD, and try to determine some guidelines to improve methods.

### 2.6.2 Case A.2

#### 2.6.2.1 Description of the flow features

Unfortunately no entries were received for test cases A.1 and A.3. Therefore, the only test cases to be discussed in the following will be A.2.1 and A.2.2.

The test case A.2 is dedicated to the study of thermal effects. Two runs are considered : a cold jet (with  $T_{ij}=300K$ ) and a hot jet (with  $T_{ij}=935K$ ) issuing from the axisymmetric afterbody. These total temperatures of the jet, applied to otherwise identical flow, enable the extraction of thermal effects. The latter appear not only in the development of the jet but also in the pressure distribution of the afterbody.

A boundary layer develops around the body, starting from the stagnation point. A velocity profile at  $X/D_{max}=-2.076$  (end of the cylindrical part of the model) is shown in Fig. A5.1-19. Pressure distributions along longitudinal rows are shown in Fig. 2.5-5. A low pressure zone is found where the afterbody slope changes. It is followed by a recompression, peaking at the trailing edge of the nozzle.

Viscous effects can intervene if the pressure rise on the nozzle is too large to be sustained by the boundary layer, resulting in a separated zone. Should this happen, the downstream pressure distribution would be altered, and its level would exhibit a plateau. From the experimental pressure results, Fig. A5.1-20 to Fig. A5.1-30, a steady pressure rise is observed, with a slight drop in  $C_p$  slope near the nozzle exit. Hence, it can be claimed that the boundary layer remains grossly attached in the major part of the afterbody, regardless of the thermal effects. At the end of the nozzle, despite the  $C_p$  evolution, no evidence of separation can be found.

A weaker pressure rise is found for the heated jet (case A2.2) on the trailing edge of the nozzle. It should, however, be noticed that this portion is directly subject to heat conduction from the adjacent hot jet since the

insulating tube inside the model ends before the trailing edge of the nozzle at  $X/D_{\max} = -0.55$ , as can be seen on Fig.2.5.4 and Fig.2.5.5. This behaviour could be the result of the thickening of the boundary layer due to the heat release.

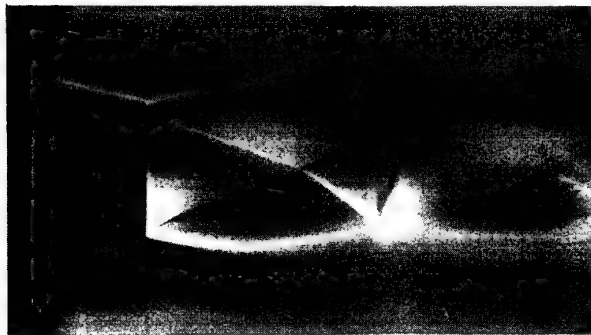


Fig.2.6-2 Flowfield Schlieren picture for Case A.2.1

The accuracy of the pressure distribution on the rear facing parts of the afterbody is crucial for drag predictions. Unfortunately, in this region, large discrepancies are often found and consequently lead to scattered drag predictions. Therefore, a great deal of attention has to be paid to this region.

Besides the classical pressure results, A2 test case provides information on field quantities thanks to a 2D Laser Doppler Velocimetry (LDV) survey. Both mean velocity and turbulence profiles have been surveyed at different locations : starting from  $X/D_{\max} = 0.0413$  to  $X/D_{\max} = 1.287$ . The first one stands just close to the nozzle exit. At this station, the trace of the boundary layer and the high shear at the lateral border of the jet can be observed on mean velocity profiles (see Fig. A5.1-31). The next stations exhibit some levelling of the profiles : the velocity defect of the wake is being filled and the shear is smeared.

Turbulence profiles reveal the high production region found in the shear layer. However, the absolute value of the experimental spikes at the two first locations seems to be grossly overestimated with a fluctuation of the order of the mean velocity!. This spurious level might be due to vibrations of the model, which would induce an additional signal, therefore spoiling the real fluctuating velocity measurements. Nevertheless, it should be noticed that the downstream locations give more realistic values.

The flow issuing from the converging nozzle has a higher pressure than the outer flow. Therefore, the jet is underexpanded and adapts itself to the environment through a train of Mach cells. The typical arrangement of these pressure waves can be observed on Schlieren pictures : see Fig. 2.6-2 for the A.2.1 cold test case and

Fig. 2.6.3 for the A.2.2 hot test case. Both exhibit the usual features of underexpanded axisymmetric jets : expansion, focalization of pressure waves into a Mach disk, and again expansion. No dramatic difference can be found due to the presence of thermal effects.



Fig.2.6-3 Flowfield Schlieren picture for Case A.2.2

#### 2.6.2.2 Presentation of different numerical approaches

The quality of a particular numerical simulation is not only a matter of numerical scheme or turbulence model efficiencies. In fact, the simulation process also takes into account pre and post-processing steps (including grid generation) which are likely to have a large influence on the final evaluation of the results.

#### Experimental simulation reliability.

The A.2 geometry is a single isolated axisymmetric nozzle tested at two different stagnation temperatures in the jet flow : a cold jet (case A.2.1) and a hot jet (case A.2.2). The external Mach number is 0.8. The main interest of these configurations lies in the amount and the accuracy of the available data for afterbody pressure distributions, mean velocity and turbulent quantities profiles in the jet. Such a test case is very useful for the validation of codes.

However, in order to perform any accurate code validation, it is essential to make sure that the computed test case is similar to the actual experimental test case. This problem, which seems quite obvious, is all the more crucial as the comparisons are based on turbulent quantities. For the latter parameters, any small difference in the geometry may cause large discrepancies between experimental and theoretical profiles.

The two major sources of differences are the uncertainties due to the experimental simulation (upstream conditions qualification, influence of wind tunnel wall on the flow surrounding the model, blockage

effects, in the present case tridimensional effects due to the strut supporting the model, and thermal deformation of the strut and the model...), and the uncertainties due to the numerical definition of the test case (geometry and grid discretization, choice of the boundary conditions, choice of the computational domain...). These two sides of the simulation reliability must be handled very carefully to correctly evaluate the performances of the numerical method itself.

The experimental arrangement of the model is presented in the following figure (a more extensive description of test case A.2 has been provided in chapter 2.5).

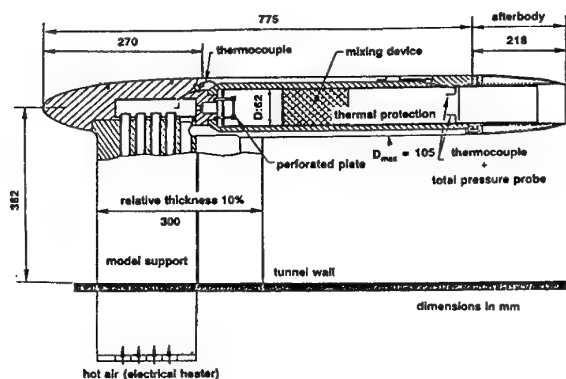


Fig. 2.6-4 Geometry for Case A.2

There are four main concerns about this experimental apparatus :

- (i) the evaluation and the homogeneity of upstream external conditions,
- (ii) the three dimensional effects due to the strut supporting the model,
- (iii) the reliability of the LDV measurements (seedings),
- (iv) and the thermal and mechanical resistance of the model.

With regards to the first two problems (i), (ii), in order to quantify the external incoming flowfield, a preliminary survey of the flowfield upstream of the afterbody (station  $X/D_{max} = -2.076$ ) was conducted during the experiments. The pitot pressure profiles measured at 12 different circumferential positions ( $\varphi = 0^\circ$  up to  $\varphi = 330^\circ$ ) show that the influence of the strut wake is restricted to a region of the flow no more than  $30^\circ$  either side of the strut ( $\varphi = 150^\circ$  to  $\varphi = 210^\circ$ ). The remaining region of the flow is quite homogeneous. and the axisymmetric hypothesis seems valid (which is confirmed by the measured afterbody pressure

distributions, and a posteriori by the computations performed). Furthermore, the use of perforated or adapted wall in the wind tunnel essentially eliminates flow perturbations due to the presence of walls in the vicinity of the model.

A third concern calls to LDV reliability (iii). It is important to realize that LDV results are given with two independent means of seeding : inside (hot jet) and outside (cold flow) with different particles. In this way, the actual profile lies somewhere between the two corresponding values. The discrepancy may be due to different response of the particles to the acceleration of the flow.

The last point (iv) is the most serious. Due to mechanical and thermal loads, the precise location of the model afterbody in the wind tunnel, may change during a survey, firstly with an overall movement (thermal effects), and secondly with vibrations around the mean position (mechanical effects). The overall displacement of the afterbody is not critical. A unique reference point on the model was used between two different runs so that the LDV grid was attached to the model. Moreover the displacement had a small magnitude. In the data, the consequences are evident on the mean radial velocity profiles where  $w$  is not equal to 0 along the axis of symmetry.

Vibrations have a strong influence on the turbulent quantities profiles just downstream of the afterbody trailing edge. Therefore the turbulent quantities profiles at  $X/D_{max} = 0.0413$  and  $X/D_{max} = 0.0825$  could be no longer reliable. Mean velocity profiles are less modified.

#### Computational domain extent.

One of the first issues in the numerical simulation of test case A.2 is the choice of the computational domain. The choice of the actual tridimensional geometry does not seem realistic. The cost of such a calculation is prohibitive. If fewer points are used, the calculation of the entire geometry may lack accuracy in the model vicinity, which represents the initial scope of this work.

In fact, all the calculations presented herein were performed on an axisymmetric geometry (i.e. without the strut). Nevertheless, two different computational domains were adopted.

The first approach (Contributions N09, N10 and N14) was to take into account the whole geometry (forebody, cylindrical section and afterbody) with the axisymmetric assumption (see figure 2.6-5). This choice simplifies the upstream boundary conditions (uniform subsonic flow), but on the other hand the mesh generation and the complete calculation are a bit more complex. However, for axisymmetric configurations such additional complexity is of minor importance.

Another problem with this specific domain decomposition is the necessity to formulate an hypothesis about the nature of the boundary layer, and more especially about the transition location. Without any further information, it is best to assume that the boundary layer remains turbulent from nose to tail.

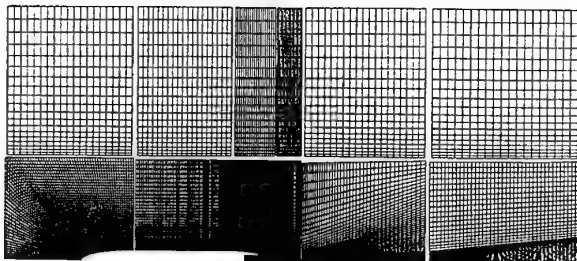


Fig. 2.6-5 Computational domain for Case A.2  
(Grid from Contribution N10)

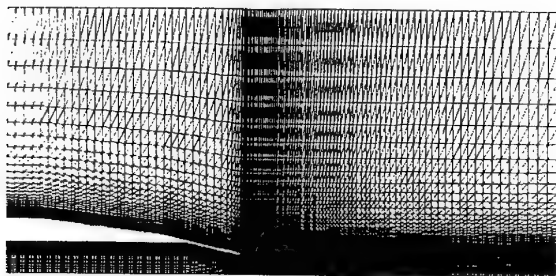


Fig. 2.6-6 Computational domain for Case A.2  
(Grid from Contribution N13)

The second possible choice of computational domain was to limit its extent, and begin the calculation in a section located in the cylindrical section of the model (see Fig. 2.6-6). This configuration has been favoured by Contributors N03, N06, N13 and N14. The problem is then to specify the right inflow conditions at the upstream face of the domain : both the outer flow since near the cylindrical section of the model the Mach number may be different from  $M_\infty$ , and the boundary layer which is very dependent on the history of the flow past the forebody. Some information are provided by the experimental data available at station  $X/D_{\max} = -2.076$  (pitot pressure profiles and wall static pressure), but there still remain some uncertainties about the temperature and turbulent quantities profiles.

#### Nozzle trailing edge.

The configuration tested in the A.2 cases has no base, and the throat shape is circular (see Fig. 2.6-7). This is for sure a theoretical geometry because during the experiments, due to thermal loads, some slight losses of shape may occur in this particular region. In that context, two of the contributors (N10, N14) have considered either a rearward-facing base area (see Fig. 2.6-8), or a nozzle trailing edge bluntness (see 2.6-9). In particular, contributor N10 has tried to assess the impact of the trailing edge shape for this A2 test case on the flow feature by simulating the flow surrounding different trailing edge shapes with the same numerical method. The comparison between the CFD predictions on the nominal and the blunt trailing edge geometries are presented and discussed in Section 2.6.2.3. As a preliminary conclusion, the influence of the trailing edge shape on the wall pressure distribution seems to be very small, whereas the plume immediately downstream of the nozzle trailing edge is largely affected (see the mean velocity profiles).

More information are available in Section 3.5 which contains some evaluations of the influence of the geometrical treatment of the trailing edge on CFD results.

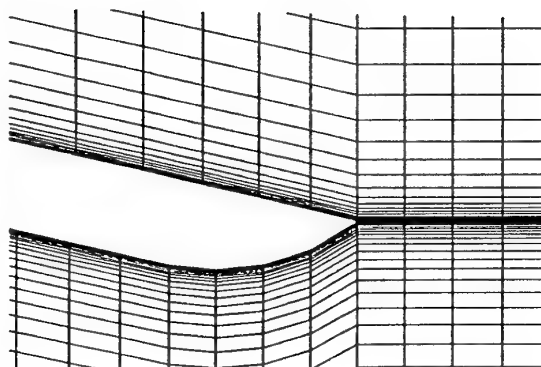


Fig. 2.6-7 Nominal geometry provided for Cases A.2  
(Grid from Contribution N03)

The trailing edge geometry had considerable impact on the initial expansion wave shape propagating from the trailing edge to the centreline. Downstream of  $X/D_{\max} \approx 0.1$ , the impact is more viscous and turbulence effects than geometry.



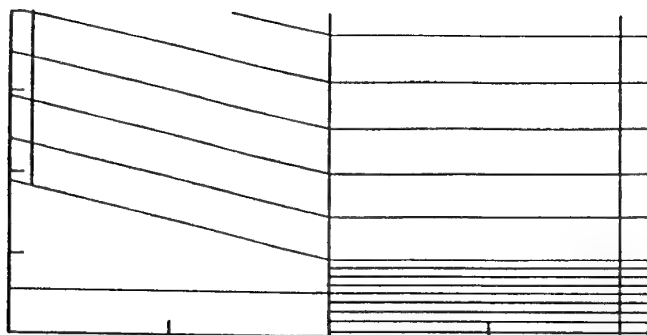


Fig. 2.6-8 Geometry with a rearward-facing base  
(Grid from Contribution N14)

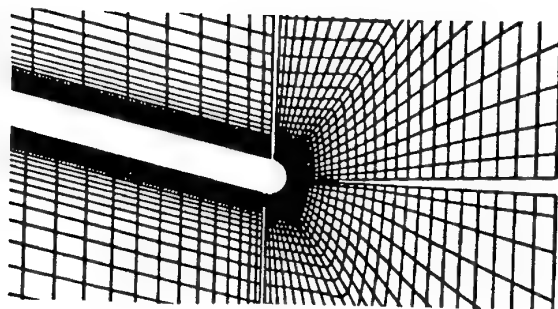


Fig. 2.6-9 Geometry with a blunt trailing edge  
(Grid from Contribution N10)

#### Turbulent quantities evaluation.

The final step of the validation process is obviously the comparison between the experimental data and the results provided by the numerical simulation. It generally requires post-processing of the numerical results calling for some classical laws. Concerning most of the quantities such as mean velocity components, Mach number or pressure distributions, this operation is straightforward. But as far as the turbulent quantities are concerned, the derivations may be ambiguous because they require some additional hypotheses, and from one contributor to another, these assumptions may change.

In order to clarify the comparisons presented in the following section, it seems important to formulate the hypotheses adopted to derive the turbulent quantities.

In the first place, from the experimental point of view, the data available by LDV measurements are the mean flowfield properties  $(\bar{u}, \bar{w})$ , and the turbulent properties

$(\overline{u'^2}, \overline{w'^2}, \overline{u'w'})$ . The turbulent energy  $k$  is derived with the assumption :

$$\overline{v'^2} = \frac{\overline{u'^2} + \overline{w'^2}}{2}$$

On the other hand, from the CFD point of view, the amount of data available depends on the turbulence model used for the simulation :

- the algebraic models generally provide the turbulent viscosity  $\mu_t$  (Baldwin-Lomax, Cebeci-Smith, Michel...),

- the models with one or two transport equations provide the values of the turbulent energy  $k$  and/or the turbulent dissipation  $\varepsilon$  and the turbulent viscosity  $\mu_t$  (Jones-Launder, Chien, Baldwin-Barth, Spalart-Allmaras...),

- and the second order closure models (or Reynolds stress models) provide the complete set of Reynolds stresses.

For the latter kind of turbulence models, the comparison between CFD and experimental data can be carried out without any ambiguity because it does not require any specific post-processing since the data available from both sides are the same.

Generally, the common way to derive the Reynolds stresses from the most widespread turbulence models, is to use the Boussinesq hypothesis :

$$-\rho \overline{u'_i u'_j} = \mu_t \left[ \frac{\partial \bar{u}_i}{\partial x_j} + \frac{\partial \bar{u}_j}{\partial x_i} - \frac{\partial \bar{u}_k}{\partial x_k} \delta_{ij} \right] - \frac{2}{3} \rho k \delta_{ij}$$

So, for the present application, the shear stress can be expressed as follows :

$$-\rho \overline{u'w'} = \mu_t \left[ \frac{\partial \bar{u}}{\partial z} + \frac{\partial \bar{w}}{\partial x} \right]$$

and the fluctuating longitudinal and axial velocity components :

$$-\rho \overline{u'^2} = \mu_t \left[ 2 \frac{\partial \bar{u}}{\partial x} - \frac{\partial \bar{w}}{\partial z} \right] - \frac{2}{3} \rho k$$

$$-\rho \overline{w'^2} = \mu_t \left[ 2 \frac{\partial \bar{w}}{\partial z} - \frac{\partial \bar{u}}{\partial x} \right] - \frac{2}{3} \rho k$$

In fact, these last two equations do not provide satisfactory results, and the classical approach to evaluate  $\overline{u'^2}$  and  $\overline{w'^2}$  is to set :

$$\overline{u'^2} \approx k$$

and

$$\overline{w'^2} \approx k/2$$

### 2.6.2.3 Evaluation of results

#### Flow feature description

Generally, most of the methods are able to predict, in a qualitative way, the overall structure of the flow surrounding the afterbody. This structure is mainly driven by the nozzle expansion rate ( $P_t/P_\infty$ ) and the external Mach number range (subsonic, transonic or supersonic).

In A.2 Cases where no large separation bubble is detected, the impact of the jet temperature and turbulence modelling on the Mach number contours is weak (see Contributions N03 and N10 on Fig. 2.6-10 and 2.6-11). The agreement between CFD results and experimental data (Schlieren pictures) is generally good but these comparisons do not represent a real challenge for the numerical methods.

One important point is the behaviour of the boundary layer near the nozzle exit. Discrepancies between the different Contributors are noticeable first due to the different throat shapes taken into account, and second due to the impact of the turbulence modelling in this region.

Most of the methods do not predict a boundary layer separation (Contributions N03 and N09 on Fig. 2.6-14). Contribution N10 experiences the impact of a blunt trailing edge (Fig. 2.6-12 and 2.6-13). The Mach number contours show a small separation bubble downstream of the trailing edge in the base lower part but no separation occurs on the afterbody surface upstream of the nozzle trailing edge.

Contributor N09 has noticed that the experimental pressure coefficient near the nozzle exit showed a drop in  $C_p$  slope which suggests that there may be a separation bubble in that region. Thus, he has performed a simulation with a combined laminar-turbulent technique (see Fig. 2.6-15). A preliminary laminar calculation predicts a separation bubble upstream of the trailing edge, then a turbulent calculation maintains this bubble, with a reduction of its extent. This result is very interesting because it clearly shows the influence of the initial flow conditions on the simulation results. The same method with the same turbulence model gives different results (Fig. 2.6-14 and 2.6-15) with a different initialization procedure. This could mean that the origin of the boundary layer separation is some turbulent

phenomena which are not taken into account by the models (anisotropy...).

In fact, neither Schlieren pictures nor pressure distributions show any boundary layer separation. Without any accurate measurement in the close vicinity of the nozzle trailing edge, there still remain some uncertainties about the presence of such a separation. In the following section, pressure distributions will give some further information about this particular point.

#### Pressure distribution

Surface pressures were measured in the wind tunnel at five rows of taps. These rows extend circumferentially along the whole nozzle external surface from  $\varphi=0^\circ$  (row 2) to  $\varphi=315^\circ$  (row 5). Except for row 3 which is located in the strut wake, the discrepancy between the measured pressure distributions along the different rows is small (see Contribution N13 on Fig. 2.6-16). This is the reason why the comparisons are only based on row 1 distribution.

As described in section 2.6.2.1, the flow structure is relatively simple : the external flow remains subsonic (no shock wave), there is no boundary layer separation and the afterbody shape is rather smooth. Such a configuration should be an interesting test case to study the behaviour of turbulence models in strong adverse pressure gradients.

The comparisons between the experimental and numerical data are presented in Figure 2.6-16. Downstream of the cylindrical section of the model, the afterbody shape consists of two successive shoulders. The first pressure tap is located between these two shoulders, and the last one just upstream of the nozzle trailing edge. The problem of the simulation is to handle the two flow expansions near the nozzle shoulders (up to station  $X/D_{\max}=-0.5$ ), and afterwards, the strong adverse pressure gradient.

From a general point of view, most of the simulations presented herein, give more or less the same trend : a rather good prediction of the pressure distribution in the upstream part of the afterbody, even if the some discrepancies may appear close to the shoulders, and an over-estimation of the pressure recovery along the downstream part of the nozzle (except for Contribution N06).

By looking more precisely at the numerical solutions, the first striking point is that only about half the methods predict the right pressure recovery between the afterbody shoulders at station  $X/D_{\max}=-1.039$  (N03, N09, N10 and N15) ; the other methods predict a too low pressure level (N06, N13 and N14).

Due to the simple shape of the afterbody, these discrepancies cannot be explained by the detailed accuracy of the shape discretization or the grid quality. Considering that the flow deflection at the first shoulder is weak, the impact on the downstream region of the nozzle should be smaller than the observed discrepancies. Moreover turbulence modelling does not seem to be involved here since, as Contributor N09 has shown (cf. Fig. 2.6-16), both 1- and 2- equation models give the same  $C_p$  level in this region. One explanation of this behaviour could come from the upstream boundary conditions. The upstream boundary of the computational domain of Contributions N06, N13 and N14 is located in the cylindrical section of the model. The only experimental data available in this region are a pitot pressure profile. Without any further information about temperature and turbulent quantities profiles in the incoming boundary layer, the quality of the upstream boundary condition is subject to the assumptions made to evaluate the missing quantities.

The predictions of Contributions N09, N10 and N15 are in good agreement with the experimental values at station  $X/D_{\max} = -1.039$ . This fact shows the benefit of a computation performed on the complete geometry including the model forebody ; there is no longer any problem concerning the upstream boundary conditions since the flow is uniform. Furthermore, the assumption of a fully turbulent boundary layer (from nose to tail) seems to be valid as far as the pressure distribution is concerned.

Concerning the flow expansion close to the second shoulder ( $X/D_{\max} \approx -0.7$ ), most of the methods predict a too low pressure level. In this area, the influence of turbulence on the boundary layer behaviour and therefore the wall pressure distribution, seems to be more significant.

One of the methods using the standard two-equation  $k-\epsilon$  with Jones-Launder near-wall model (Contribution N10) gives a good agreement with the experimental data on both sides of the shoulder. Due to the pressure taps location, the accuracy of the solution in the centre of the expansion flow area cannot be evaluated. The same qualitative behaviour is observed in Contribution N14 with the same turbulence model, but because of the uncertainties about the upstream conditions, there seem to be an overall gap between the predicted values and the actual ones.

The others solutions present more or less the same feature close to the shoulder with a very low static pressure at station  $X/D_{\max} \approx -0.7$ . Algebraic models (Baldwin-Lomax for Contribution N03 and N15, Cebeci-Smith for Contribution N06) predict the lower pressure. Then come the one-equation models (Spalart-Allmaras and Baldwin-Barth for Contribution N09), and finally, the two-equation models (Contributions N09 and N13).

The prediction of the strong pressure recovery along the downstream part of the afterbody is more critical. In this region, the boundary layer experiences the effects of nozzle converging shape, and "fluid obstruction" of the underexpanded jet issuing from the nozzle. Moreover, the ejector-like effect of the jet shear layer tends to counter the two previous effects by locally accelerating the flow.

It should be pointed out that without an accurate prediction of the pressure distribution in this particular region, any drag estimate is meaningless.

Generally, most of the methods overestimate this pressure recovery. Nevertheless, Contribution N06 with an algebraic turbulence model (Cebeci-Smith) gives a fairly good prediction with only a slight underestimate of the pressure level. So does Contribution N13, with a two-equation  $k-\epsilon$  model. By the very end of the afterbody, Contribution N13 predicts a pressure rise, and without any pressure tap in this region, this behaviour needs to be confirmed.

The solutions provided by Contribution N14 are a bit confusing : the global evolution of the pressure distribution and especially the slope of the curves seem correct, but there is a constant discrepancy between experimental and CFD data.

Results provided by the other simulations show the poor accuracy of the predicted pressure distribution. In spite of a large number of turbulence models : Baldwin-Lomax (N03, N14, N15), Spalart-Allmaras (N09), Baldwin-Barth (N09), standard  $k-\epsilon$  with Jones-Launder near-wall (N10), Chien  $k-\epsilon$  (N09, N14), the results are practically the same.

Some contributors have evaluated the influence of different parameters on the accuracy of their simulation : grid density, turbulence modelling, wall physical properties or trailing edge geometry.

As far as grid density is concerned, Contributor N10 has performed three calculations on the same geometry with the same numerical method and physical hypotheses (turbulence modelling...), but with three different grid densities (coarse, medium and fine). The results show that the agreement between CFD and experiment is better on the medium grid. This point does not however mean that the simulation performed on the medium grid is better than the others ; the agreement is only fortunate because a numerical solution should be grid-independent, and the finer the grid is, the more accurate the solution will be.

Contribution N10 has also tried to evaluate the impact of the trailing edge shape on the pressure distribution by taking into account two different shapes : the nominal geometry with a sharp trailing edge, and a modified one with a blunt trailing edge. The influence on the pressure

distribution is nearly negligible ; the discrepancies between the two numerical solutions are small compared to the differences between the CFD predictions and the experimental data in this region.

Additionally, the cooling effect of convection on the uninsulated nozzle was investigated by Contribution N10. One dimensional thermal heat balance was performed at three stations along the uninsulated portion of the nozzle using the local Reynolds number surveyed from the adiabatic wall solutions. The typical changes was 100 to 200 degrees Kelvin cooler along the internal surface, and 300 to 500 degrees Kelvin hotter externally depending on location. Only slight changes in the afterbody pressures were observed.

Contribution N09 has evaluated the influence of the turbulence model with three different one and two-equation models. The results show a slight improvement from the Baldwin-Barth to the Spalart-Allmaras model. But once more, the discrepancies between these three models remain lower than the discrepancies between the most accurate one and the experimental data.

All these observations tend to indicate that some phenomena are not taken into account by the simulations : flow separation, Reynolds stresses anisotropy or influence of the wall temperature. Concerning this last point, it is important to notice that this portion of the afterbody is subject to heat conduction from the internal hot jet since the insulating tube inside the model ends close to station  $X/D_{\max} = -0.55$ . The impact of the jet temperature on the external pressure distribution is shown on Fig. 2.6-17 (Case A.2.1 vs. Case A.2.2). The differences are noticeable in the downstream part of the afterbody ( $X/D_{\max} > -0.30$ ) where the pressure recovery in the cold jet case is higher. However, the discrepancies between cold jet and hot jet distributions are not only due to the external wall temperature because the "ejector-like" effect of the jet shear layer is much higher for a hot jet than for a cold jet. It is therefore difficult to separate the respective impact of these two phenomena.

All the previous calculations were performed using fully turbulent flows, and none of them predicts a flow separation. However the experimental surface pressure coefficient near the nozzle exit shows a drop in  $C_p$  slope which suggests there might be a separation bubble in that region. To simulate a separation bubble, Contribution N09 has tested a combined laminar-turbulent technique : the laminar solution predicts a boundary layer separation upstream of the nozzle trailing edge, and afterwards, the turbulent solution reduces the bubble extent, but maintains the separation. The results of this technique are in excellent agreement with the experimental data.

These results would indicate that the poor agreement between Contributions and experiments in the region

could come from the inability of the classical turbulence models to predict this separation.

Even though it seems ambiguous to extrapolate the comments made on a single test case to other configurations, the aerodynamic phenomena occurring in the flowfield surrounding Cases A.2 are typical enough to provide useful information about the efficiency of numerical methods for such simulations. These key issues can be summarized as follows :

- These comparisons clearly show the impact of the boundary conditions accuracy. Note that this point is not specific to afterbody flowfields. The predictions of some Contributions (N06, N13, N14) could have been improved with more appropriate upstream boundary conditions. This might be difficult as some uncertainties remain concerning the experimental wall temperature distribution along the downstream part of the afterbody.
- Turbulence modelling is obviously a key issue for this kind of simulations. As far as the pressure distribution is concerned, even though a large number of turbulence models has been used, and even though some solutions give better results than others, none of the classical approaches presented herein gives satisfactory results.
- The crucial physical parameter is the pressure recovery prediction. Most of the turbulence models overestimate the pressure distribution on the nozzle, and predict no boundary layer separation. Only the combined laminar-turbulent technique predicts the correct pressure distribution with a separation bubble near the nozzle exit.
- For the flow expansion close to the nozzle shoulders, the predictions provided by one or two-equation models seem to be in better agreement with the experimental data than zero-equation models predictions.

#### Boundary layer profiles

During the experiments, a pitot pressure survey provided data about the boundary layer at station  $X/D_{\max} = -2.078$  which is located in the cylindrical section of the model. The resulting mean axial velocity component profile are presented on Fig. A.5.1.1.19.

These profiles have been used to work out the upstream boundary conditions of several Contributions (N03, N06, N13 and N14), and so it is not worthwhile to perform any comparison of the boundary layer profiles for these contributions.

The other calculations are carried out on the complete model geometry from nose to tail (Contributions N09, N10 and N15). Since there is no information about transition, the boundary layer is assumed to be fully

turbulent. The results of these simulations are presented on Fig. 2.6-18.

The results of the Baldwin-Lomax model (N15) gives a marked underestimation of the boundary layer thickness. Nevertheless, the global shape of the velocity profile is consistent with the experimental one.

The Baldwin-Barth one-equation model (N09) gives a good prediction of the velocity profile in the internal part of the boundary layer ( $Z/\delta < 0.25$ ), but the agreement becomes very poor in the external part of the boundary layer. This surprising behaviour may probably come from the implementation of the model, or from the post-processing of the numerical results.

The other models experienced by Contributor N09, Spalart-Allmaras and Chien  $k-\epsilon$ , give results in very good agreement with the experimental data. Furthermore the results of the combined laminar-turbulent technique are quite the same as the fully turbulent calculations.

The boundary layer prediction in the upstream part of the model is not a difficult task. Some methods provide accurate simulations in this region. But, due to the small number of contributions presented here on this specific point, it is not possible to see the respective impact of the grid density, the numerical scheme, or the turbulence model and its implementation in the accuracy of the results, and thus to address a classification between the turbulence models. However, Baldwin-Lomax and Baldwin-Barth results should be better in regard to the known performances of these models.

#### Flow along the axis of symmetry

The evolution of the aerodynamic quantities along the plume axis of symmetry is an important feature of this kind of flowfield. Unfortunately, there are very few experimental data available in that region. Nevertheless it seems worthwhile to analyse the results provided by some Contributors.

The flow in the plume and therefore along the axis of symmetry is mainly driven by the expansion rate  $P_{ij}/P_\infty$ . However, the plume overall structure can be affected by physical or geometrical parameters either in CFD or in experiment.

Contributor N13 has compared the static pressure distribution along the axis for A.2.1 and A.2.2 Cases (Fig. 2.6-19). The jet temperature seems to have a great influence on cell lengths. This phenomenon may come from the different levels of turbulence intensity in the shear layer between hot jet and cold jet. In its simulations, Contributor N13 has used a  $k-\epsilon$  model. The comparison between the computed turbulent quantities and the experimental ones presented in the following,

shows a good agreement in A.2.2 Case. Nevertheless, it should be necessary to have the same comparison in A.2.1 Case to status on this issue.

Contributor N10 tried to see the impact of the trailing edge shape on the velocity and the turbulent energy distributions along the axis of symmetry (Fig. 2.6-20). The two geometries considered are a blunt trailing edge and the nominal one. It is clear that the shape of this part of the nozzle has a noticeable influence on the plume in the first cell. With the nominal trailing edge, the jet expansion is larger. This is surely due to its sharp geometry. Furthermore, afterbody convective cooling appears to have more influence further downstream than in the near flowfield.

#### Mean velocity profiles

The next step in the validation process is the comparison between CFD predictions and experimental data in the plume, and more especially in the shear layer which develops between the jet and the external flowfield.

During the experiments, LDV measurements were performed at four axial stations. The data available are mainly the mean axial and radial velocity components profiles, and the turbulent quantities profiles ( $\overline{u'^2}$ ,  $\overline{w'^2}$ ,  $\overline{u'w'}$ ). The experimental turbulent kinetic energy is derived from the previous quantities with the following assumption :

$$\overline{v'^2} = \frac{\overline{u'^2} + \overline{w'^2}}{2}$$

The first two stations are located just downstream of the nozzle trailing edge ( $X/D_{\max} = 0.0413, 0.0825$ ). In this portion of the plume, the profiles are mainly influenced by the incoming flows (external boundary layer and jet issuing from the nozzle). The impact of the mixing layer development is weaker.

The prediction of the profiles in the last two sections is more critical ( $X/D_{\max} = 0.4840, 1.2871$ ). At these locations, the flow feature results from the inviscid structure of the plume (compression/expansion zones), and the mixing layer evolution which is driven by turbulence. Moreover, these two aspects of the plume interact.

Once more, the key issue in this validation step is the turbulence modelling. But, because of the chosen configuration, the turbulence models performances are evaluated on a axisymmetric shear layer. Some models include corrections for axisymmetric flows, and so the extrapolations of trends observed on axisymmetric configurations to 3D configurations should be done carefully.

In the following, the comparisons between CFD results and experimental data are organized according to the physical quantities (mean velocity components then turbulent quantities). There are obviously some direct correlations between them, but the evaluation of the turbulence models is much clearer with this artificial separation.

The mean axial velocity component profiles are presented on Fig. 2.6-21 to 2.6-24.

The location of the first station is very close to the nozzle trailing edge. The velocity profile shape results from the flow profiles upstream of the nozzle exit ; the influence of the mixing layer between the plume and the external flow is quite negligible.

From the axis of symmetry to the external flow, the survey encounters the jet expansion, the thin mixing layer, and the afterbody boundary layer wake (see Fig. 2.6-21).

All the methods predict the overall shape of this profile, but there are some slight discrepancies in the jet centre, and in the boundary layer wake.

The discrepancies in the jet centreline are quite surprising. Some methods overestimate the velocity in the vicinity of the axis of symmetry (N03, N06, and N14). In this region, the flow issuing from the nozzle expands following an inviscid process which mainly depends on the nozzle throat shape and the internal boundary layer (for a large range of expansion rate). The influence of the internal boundary layer should be small because it becomes very thin close to the throat. So the explanation may come from one or more of the following :

- The uncertainties of the LDV measurements : the inner flow was seeded with magnesium oxide particles, and so the measured velocity may be lower than the actual one because of the size and the weight of these particles.
- The experimental estimation of the exact location of the nozzle exit station, due to the model displacement.
- The actual shape of the nozzle throat and trailing edge, and the accuracy of the numerical discretization of the throat.
- The grid density.

It is difficult to see what parameter is of major importance among this short list by comparing the results provided by the contributors : the three Contributions which are in good agreement with experimental data (N10, N13 and N15) have no obvious common feature as opposed to the others.

Nevertheless, the velocity profiles provided by Contribution N10 with two different throat shapes, clearly show that the throat shape plays an important part in the mean velocity flowfield in the downstream vicinity of the trailing edge (Fig. 2.6-21). In that case, the best results are obtained with a blunt trailing edge rather different from the nominal one. Contribution N14 also provides results in good agreement with experimental data with a blunt trailing edge. On the opposite, Contributions N13 and N15 provide good results with the nominal geometry. Further experimental and numerical investigations are needed to status on this point.

The throat shape has also a noticeable impact on the velocity profiles shape in the lower vicinity of the shear layer ( $Z/D_{\max} \approx 0.18$ ). All the Contributions but N10 and N14 provide irregular velocity profiles in this region. The fact is that Contributions N10 and N14 have taken into account a different nozzle trailing edge (blunt geometry), and the agreement seems better. This improvement of the solution by introducing an artificial base could indicate that there are some phenomena occurring at the nozzle trailing edge which are not correctly taken into account by the turbulence model (perhaps flow separation in the small nozzle cone as detailed in section 3.5).

The second feature of these profiles is the external boundary layer wake. Most of the solutions are in good agreement with the experimental data. The discrepancies are smaller for the velocity profiles than for the pressure distribution. The pressure distribution accuracy of Contribution N03 was rather poor, whereas the velocity profile matches quite well with the experimental data.

The differences in the boundary layer wake computed by Contribution N15 are related to the differences already observed in the boundary layer profiles in the cylindrical section of the model (see Fig. 2.6-18).

The same trends remain in the mean axial velocity profiles at the next station  $X/D_{\max} = 0.0825$  (see Fig. 2.6-22) :

- overestimation of the velocity near the axis of symmetry (N03, N06, N09, N14 and N15),
- irregular profiles in the internal side of the shear layer for the calculations performed on the nominal geometry (N03, N06, N09, N13 and N15), and a regular evolution for the others (N10, N14),
- and a rather good agreement in the boundary layer wake for most of the Contributions.

From this second axial station, the development of the mixing layer between the jet and the external flow begins to have a noticeable impact on the velocity

profiles shape, and thus, particular attention should be paid to turbulence modelling.

Contribution N03, with a Baldwin-Lomax model, predicts a too high level of mixing which results in an overestimation of the velocity recovery in the afterbody boundary layer wake, and a discrepancy in the profile slope near the shear layer centreline. In contrast, Contribution N15 predicts a too low level of mixing with the same turbulence model. The explanation comes from the model implementation. The Baldwin-Lomax model is a two-layer model developed for boundary layers with an inner and an outer formulation. In the shear layer, Contribution N03 has kept only the outer formulation, whereas Contribution N15 has maintained the two formulations which results in a too low turbulent viscosity near the shear layer centreline.

Contribution N14 has experienced a Baldwin-Lomax and a  $k-\epsilon$  model. The comparison between them shows that the algebraic model simulates a higher mixing level than the  $k-\epsilon$  model. However, the two simulations are in good agreement with the experimental data, with only a small overestimation of the plume width.

Contribution N06, with a Cebeci-Smith turbulence model, predicts with a good accuracy the flow behaviour in the shear layer, and more especially the evolution of the velocity profile from the previous station to the present one. The "overshoots" on both sides of the layer are due to the incoming flows but not to the turbulence modelling in the shear layer itself.

The one and two-equation models (N09, N10, N13 and N14) behave in the same way than the Cebeci-Smith model does : accurate prediction of the profile slope near the mixing layer centreline, profile evolution from station to station. It seems difficult to find trends between the various models :  $k-\epsilon$  for Contributions N10, N13 and N14, and Spalart-Allmaras for N09.

The improvement of the simulation accuracy due to the combined laminar-turbulent technique (N09) noticed on the afterbody pressure distribution, is still present in the plume at this location. Nevertheless, this improvement is more obvious in the boundary layer wake than in the mixing layer itself.

In the downstream stations  $X/D_{\max}=0.4840$  and  $X/D_{\max}=1.2871$  (see Fig. 2.6-23 and 2.6-24), the discrepancies underlined between the turbulence models behaviour are emphasized.

As far as the shear layer is concerned, the Baldwin-Lomax model still reproduces a too high mixing level (N03, N14) except for Contribution N15 because of the "boundary layer like" implementation of the model in the shear layer. Cebeci-Smith model is in good agreement with experimental data, particularly in the far flowfield (N06). The  $k-\epsilon$  solutions (N10, N13 and N14)

provide an accurate simulation of the velocity profile in the shear layer ; the predicted velocity curve slopes fit with the experimental one near the layer centreline.

In the middle of the plume ( $Z \approx 0$ ), the discrepancies between the predicted axial velocities and experimental data may be significant for some Contributions (N06, N09, N13, N14). This gap is due to slight differences in the numerical prediction of the overall plume structure which means that the velocity profiles comparisons are carried out at the same location with regard to the nozzle exit station, but at a different location with regard to plume structure with its expansion/compression waves. That is to say any small uncertainty in a profile location in the far flowfield may cause large discrepancies, especially close to an oblique shock.

The comparisons based on the mean radial velocity profiles are presented on Fig. 2.6-25 to 2.6-28. The prediction of this radial component of the velocity is more critical than the prediction of the axial component, and therefore the discrepancies are larger, even though their origin is due to the same phenomenon.

At the first station ( $X/D_{\max}=0.0413$ ), most of the methods predict the overall shape of the experimental profile, and especially the maximum value of  $W$ . This is particularly true for the simulations carried out on the nominal geometry (N03, N06, N13 and N15) ; the impact of the nozzle trailing edge shape is important on this maximum value (see N10, N14). However, all the solutions presented herein underestimate the radial location of this maximum in spite of the various geometries taken into account and the wide range of numerical methods and turbulence models considered. This result calls into question the measurements accuracy at this station.

The gap noticed on the axial velocity component near the plume axis of symmetry for some Contributions (N03, N06, N14), corresponds to the differences observed on the radial velocities near the axis.

At the next station ( $X/D_{\max}=0.0825$ ), some Contributions are in very good agreement with the experimental data (N10, N14). Contribution N09 gives a rather good prediction of the profile either with a turbulent calculation or with a combined laminar-turbulent technique, but the profile shape near the radial velocity component maximum is quite different with regard to the experimental profile. This last remark is true for all the contributions performed on the nominal geometry.

In fact, the accuracy of the turbulence modelling seems to have a smaller impact on the radial velocity profiles than on the axial velocity profiles. At station  $X/D_{\max}=0.4840$ , all the Contributions are qualitatively in good agreement with the experimental data. The



simulation of the mixing layer seems correct. The discrepancies in the core of the jet, are due to a bad prediction of the overall plume structure (location of the station with regard to the oblique shock).

The undershoot located close to  $Z/D_{\max}=0.25$  in the experimental profile, is predicted by none of the methods. This phenomenon does not appear at the other stations where LDV measurements are available, and is underlined by the only jet seeding (heavier particles). This probably comes from some inaccuracies in the LDV measurement due to particle drag.

At the last station ( $X/D_{\max}=1.2871$  on Fig. 2.6-26), some Contributions are still in good agreement with data (N10, N15), but for others, the accuracy fails in a significant way (N06, N14). In addition to the reasons previously expressed, the grid density may become insufficient far from the nozzle exit to correctly simulate the flow (N03).

It seems too ambitious to draw a final conclusion on the ability of numerical methods to simulate the mean flowfield surrounding an afterbody like A.2 Case. But due to the large number of methods, and moreover, due to the large number of turbulence models involved in this evaluation process, this work provides some reliable trends :

- All the methods presented here are able to simulate in a qualitative way the mean velocity field in the plume in the near flowfield ( $X/D_{\max}<2$ ). Some further experimental and numerical investigations are needed for the far flowfield.
- Close to the nozzle exit, the discrepancies between CFD and experimental data are mainly due to the accuracy of the flow simulations upstream of the trailing edge. The implementation of turbulence models in the shear layer is of minor importance.
- At the last stations, most of the differences observed come from slight differences in the prediction of the overall plume structure which results in erroneous estimations of the station location in regard to the expansion/compression waves in the plume.
- The Cebeci-Smith solution provides an accurate estimation of the mixing through the prediction of the velocity profile slope in the mixing layer. The other algebraic model (Baldwin-Lomax) tends to overestimate the mixing as far as velocity profiles are concerned.
- Accurate predictions are provided by the one or two-equation turbulence models. Such models are able to correctly reproduce the impact of turbulence on the mean velocity field : velocity recovery downstream of the afterbody boundary layer, evolution of the slope in the velocity component profiles...

### Turbulent quantities profiles

The comparisons between the measured and predicted turbulent quantities profiles are presented on Fig. 2.6-29 to 2.6-36 with the shear stress and the turbulent kinetic energy profiles. It is necessary to make some preliminary remarks before any evaluation of these results.

- The experimental data in the first two stations are not reliable probably because of the model vibrations.
- Only two turbulence models are involved in this comparison process : the Baldwin-Lomax model (N14), and the k- $\epsilon$  model (N10, N13 and N14). This is definitely not sufficient to draw a definitive conclusion on the ability of turbulence model to handle such a shear layer.

At the first two stations ( $X/D_{\max}=0.0413$  and  $X/D_{\max}=0.0825$ ) the comparisons are made from code to code without taking into account the experimental results.

Contributions N10 and N13 give almost the same maximum turbulent intensity level in the shear layer centreline ( $Z/D_{\max}\approx 0.20$ ). There are some discrepancies in the shear stress evaluations between these two solutions in the upper part of the shear layer (N10 provides  $u'w'>0$ , and N13  $u'w'<0$ ). The experiment also gives  $u'w'<0$  but there is doubt about the experimental values. In any case, the very low turbulent intensity in this region above the shear layer centreline should not have a great impact on the mean flowfield.

Contribution N14 predicts a low turbulent intensity even in the shear layer centreline with a k- $\epsilon$  model, whereas the Baldwin-Lomax simulation provides a maximum turbulent intensity consistent with N10 and N13 k- $\epsilon$  simulation. The Baldwin-Lomax solution predicts a shear stress peak too large.

The trailing edge shape does not seem to have an influence on the turbulence intensity in the shear layer (see Contribution N10 on Fig. 2.6-29).

It is hard to establish a relation between the turbulent quantities profiles and the mean velocity profiles in the upstream part of the plume. In this region, the velocity profiles are much more influenced by the incoming flows than turbulence in the shear layer. On the other hand, the differences observed in N14 Contributions between k- $\epsilon$  and Baldwin-Lomax (estimation of the shear stress peak width) result in the evolution of the mean axial velocity component (overestimation of mixing by the Baldwin-Lomax solution).



At the following stations, all the  $k-\epsilon$  methods give similar results. The agreement with experimental data becomes very good as the flow progresses downstream. This point is consistent with the prediction of the mean axial velocity profile, and especially with the correct prediction of the profile slope near the shear layer centreline. The Baldwin-Lomax solution (N14) keeps on overestimating the shear stress peak width ( $X/D_{\max}=0.4840$ ).

As a preliminary conclusion, these comparisons shows than for this particular configuration, the  $k-\epsilon$  turbulence models are clearly able to reproduce the level of turbulent intensity in the shear layer. There still remain one uncertainty about the behaviour of these models close to the nozzle trailing edge because of the poor accuracy of the experimental data.

### 2.6.3 Conclusions of A.2 Test Cases.

A general conclusion of the previous evaluation is the fair agreement of the different solutions of the review. However, the aim of the A.2 Test Case is rather ambitious since it focuses not only on classical quantities (pressure distribution) but also on the physical phenomena encountered in afterbody flows. From this respect, it is found that results are rather scattered and differ from each other and also from the available experimental data.

A recurrent list of problematic issues appear :

- the recompression on the downstream portion of the nozzle is systematically overpredicted.
- there still remain a doubt on the actual nature (separated, attached) of the boundary layer close to the trailing edge nozzle,
- the entrainment effects, and the mixing layer thickness is not always well predicted,
- and although the overall feature of the Mach cells are well represented, there are some discrepancies in the evaluation of their actual size.

These difficulties may be the result of factors of different kind :

- The initialisation procedure is crucial to impose the inflow conditions, especially the upstream boundary layer. The quantities involved are not only velocities, pressure and temperature but also turbulent quantities such as  $\mu_t$ ,  $k$  or  $\epsilon$ .
- The initial zone of the jet needs to be well represented. It will have an impact on the expansion of the jet, on development of the mixing layer and also on the size of the Mach cells.

- Turbulence models are found to perform very nicely in the jet. In particular, mixing (expressed in terms of velocity and turbulent quantities) is remarkably well predicted in this axisymmetric configuration.

- In the trailing edge zone of the afterbody, the turbulence model choice seems to have a small influence on the pressure distribution. In fact, the influence could have been much more pronounced if strong separation or shock interactions were present.

- However, turbulence modelling is not the only factor and the remaining discrepancies between experiment and CFD should be sought both in the grid (topology and density) and in the numerical scheme.

- Attention is drawn at this point on the importance of numerical viscosity. This quantity, although of major importance on results should received more attention. It may indeed happen that this viscosity is of the order of, or even higher than the modelled turbulent viscosity. In such a scenario, both the numerical scheme and the grid impose a leading value of viscosity which is wrong, regardless of the sophistication and of the representativity of the turbulence model.

- No experimental data on drag were available and therefore no CFD evaluation were provided by Contributors. However, it seems that CFD prediction would have revealed a large scatter in their prediction.

- It appears that the crucial issue for drag prediction is to manage the representation of a typical physical phenomenon. In particular a separation can be triggered either by the natural tendency of the flow on the actual geometry, or if the code is not sufficient, with the help of a modified geometry or with a special initialising procedure.

As a result, should one consider Computational Fluid Dynamics as black art? Surely not, but it should be stressed that the quality of the final result will depend on the way the CFD team will have handled the whole process :

- the way of treating the problem : extension of the computational domain (whole physical domain or only the rear part of the afterbody), what kind of physical phenomena should we expect, at what location ?

- the grid : structured vs. unstructured, higher density in "zones of interest",

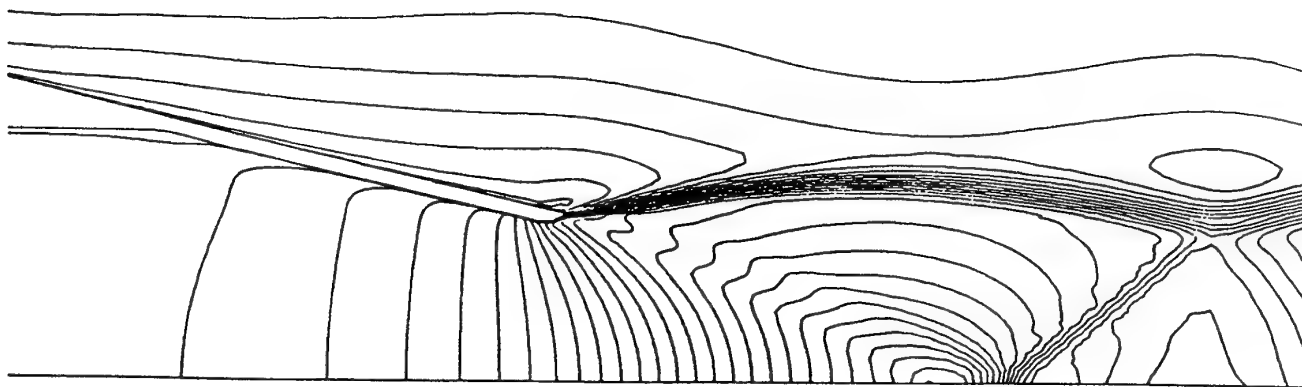
- initialising procedure : inflow conditions and also the initial field (uniform field, Euler solution, laminar vs. turbulent Navier-Stokes solution).

- choice of turbulence model,

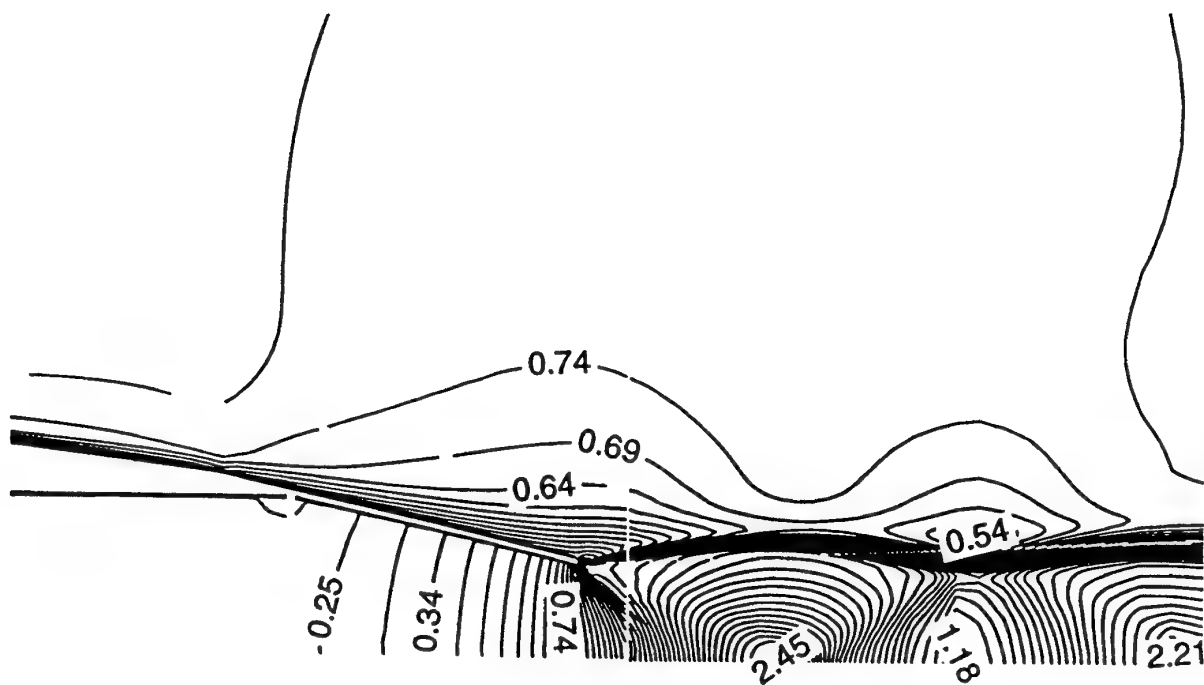
- converging procedure (use of restarts...),

- and post-processing.

As a final remark, one may acknowledge the importance of having a knowledge of the experimental data before sending out one's results. This kind of work is not, and was not intended to be a blind-test! Most of the contributors have all applied a trial and error way of progressing. The previous knowledge of the physical phenomena to be encountered is therefore crucial to adapt one's grid or convergence procedure.

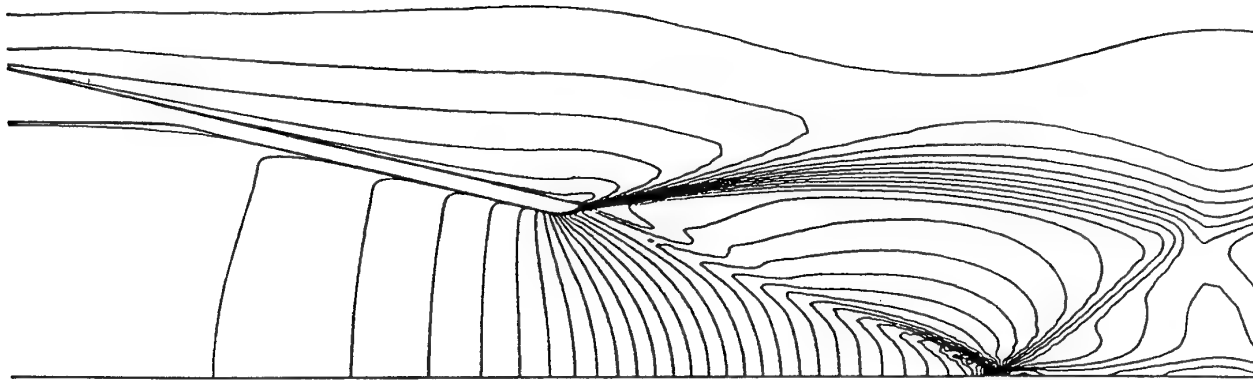


Contribution N03

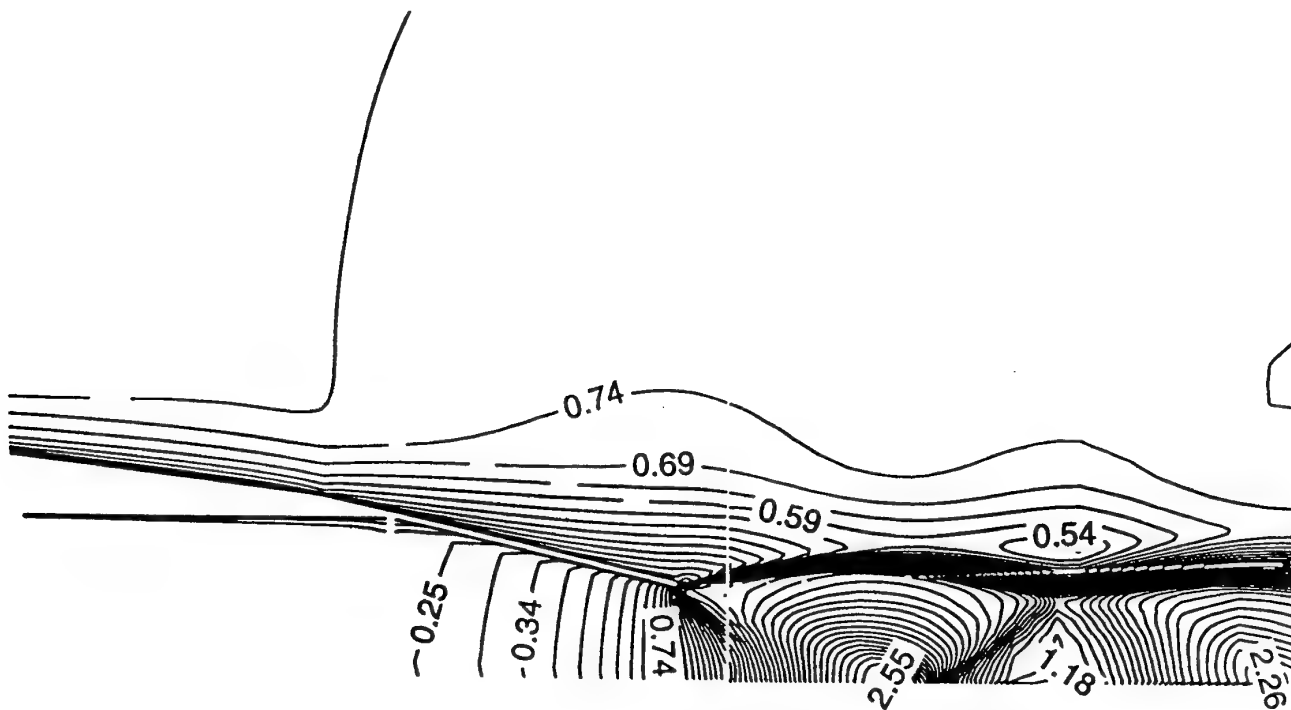


Contribution N10

Figure 2.6-10 Case A.2.1 (cold jet) Mach Number Contours



Contribution N03



Contribution N10

Figure 2.6-11 Case A.2.2 (hot jet) Mach Number Contours

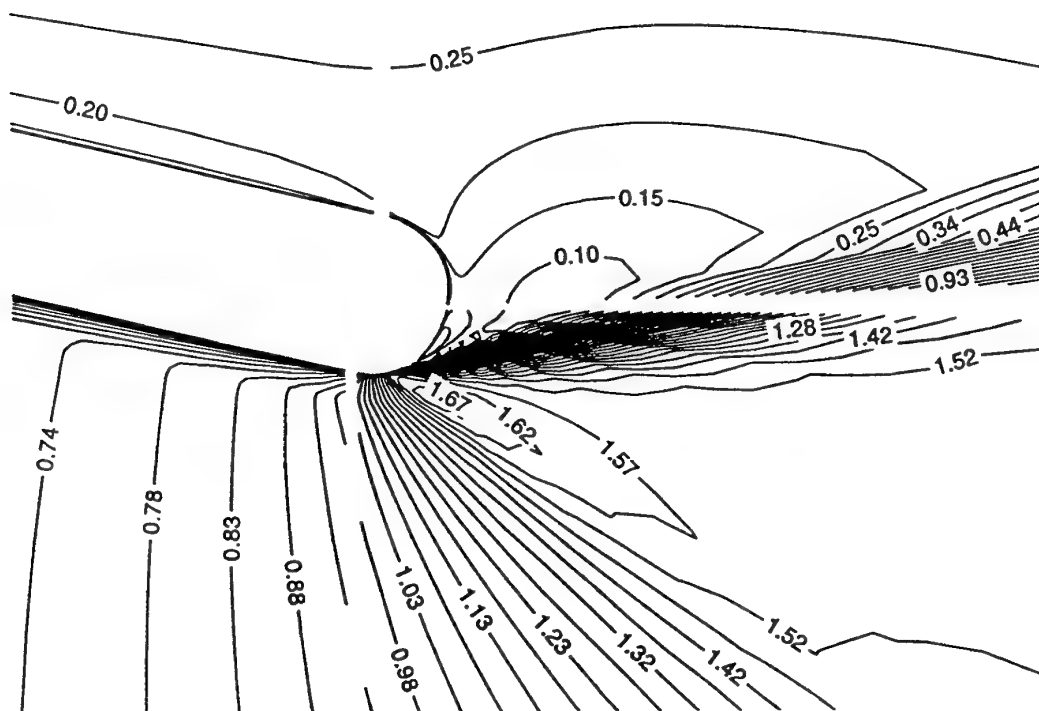


Figure 2.6-12 Case A.2.1 (cold jet) Mach Number Contours close the Nozzle Trailing Edge  
(from Contribution N10)

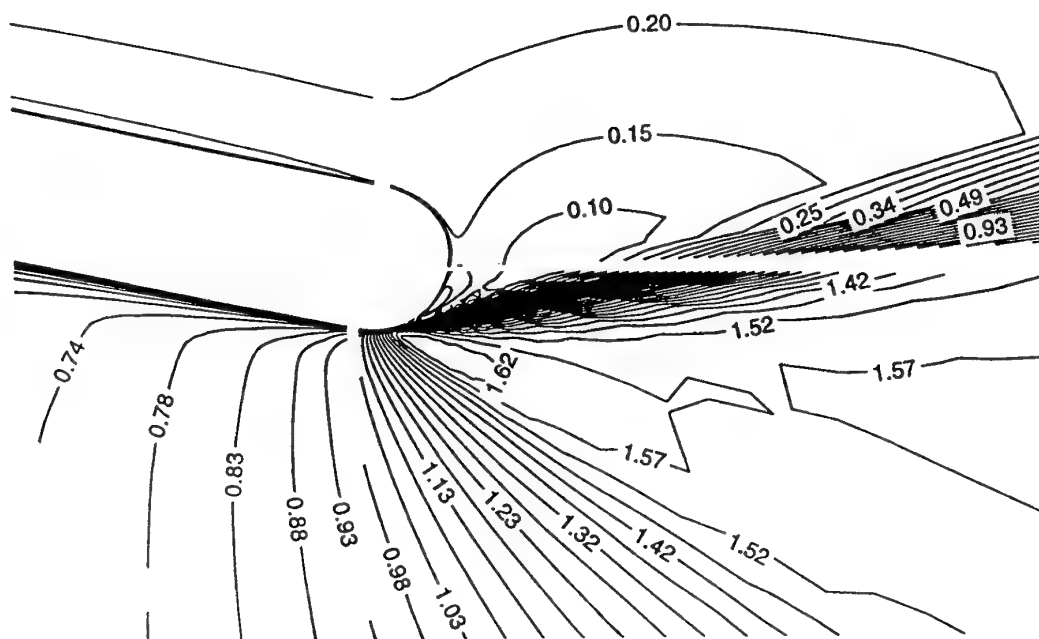
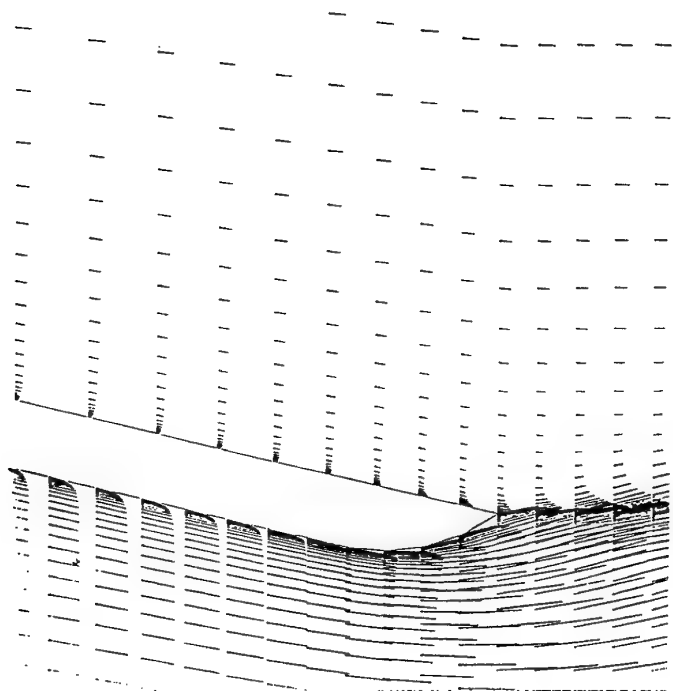
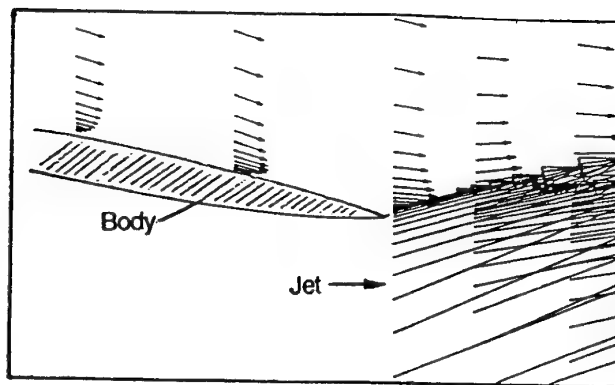


Figure 2.6-13 Case A.2.2 (hot jet) Mach Number Contours close the Nozzle Trailing Edge  
(from Contribution N10)

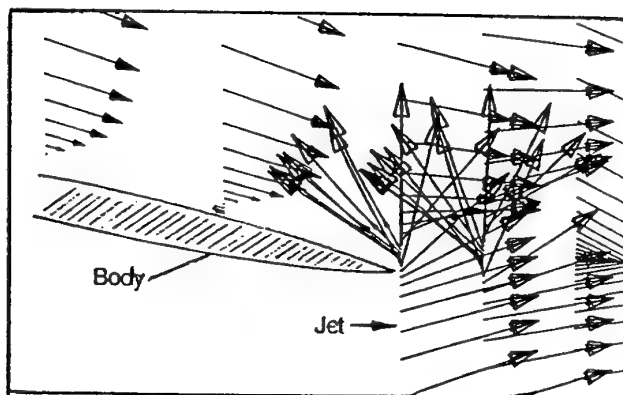


Contribution N03



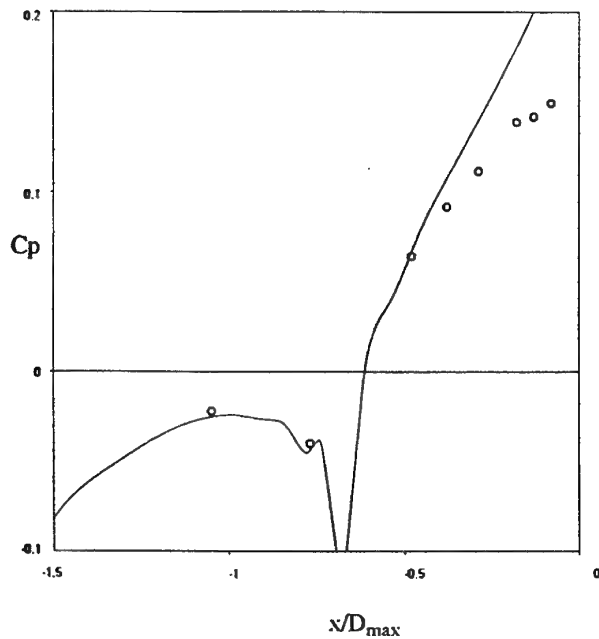
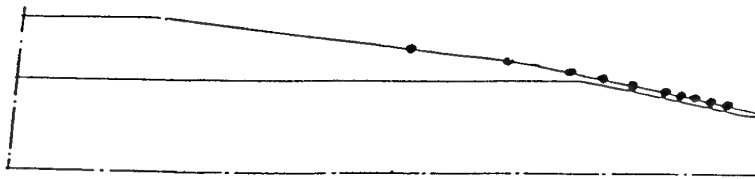
Contribution N09

Figure 2.6-14 Case A.2.2 (hot jet) Velocity Vector Plot without Separation

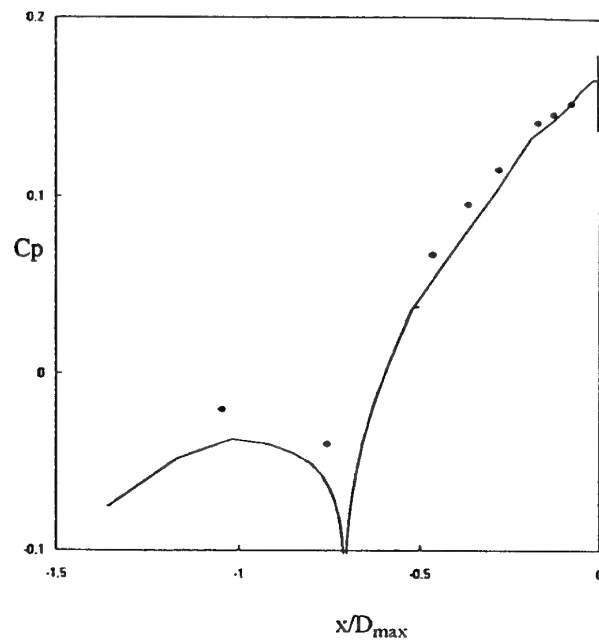


Contribution N09

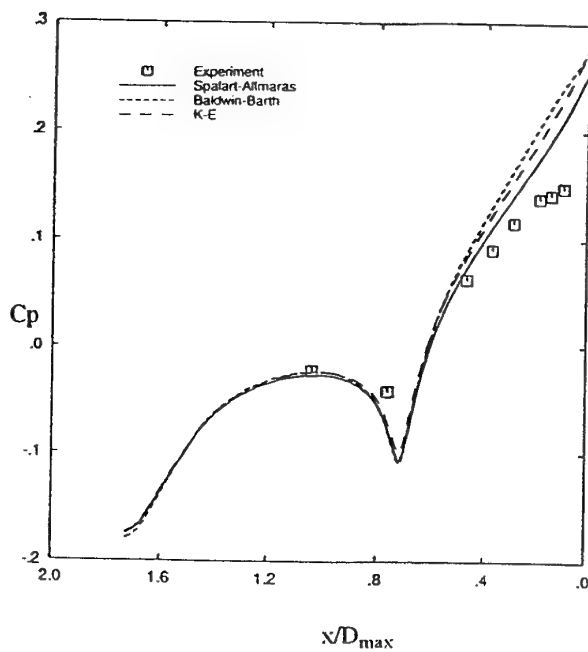
Figure 2.6-15 Case A.2.2 (hot jet) Velocity Vector Plot with Separation



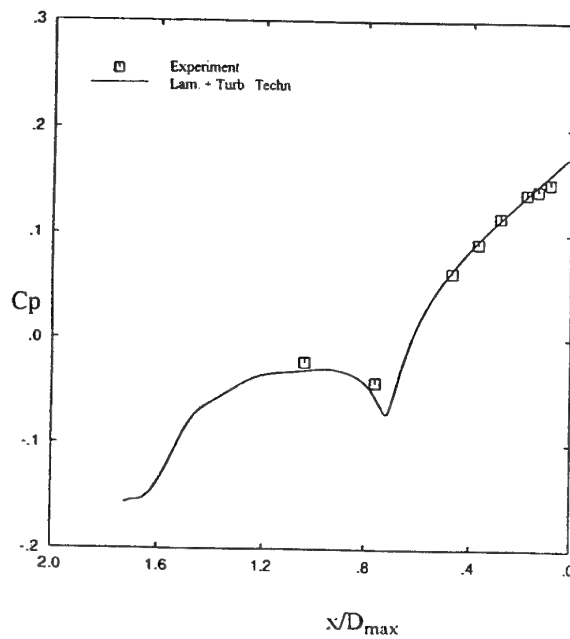
Contribution N03



Contribution N06

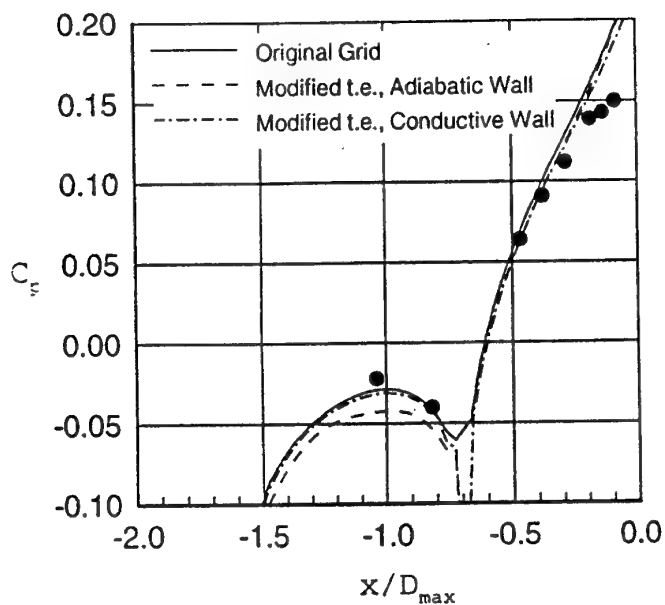
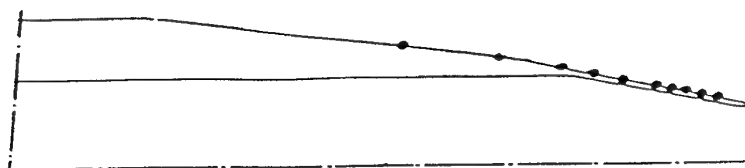


Contribution N09

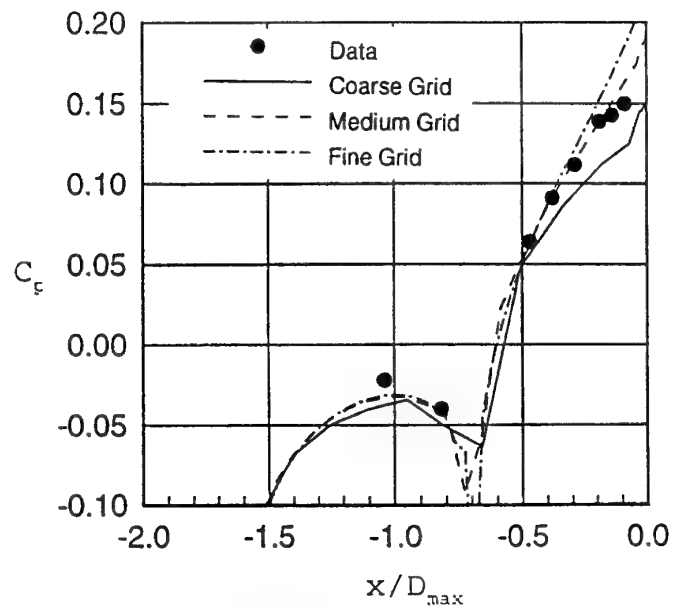


Contribution N09

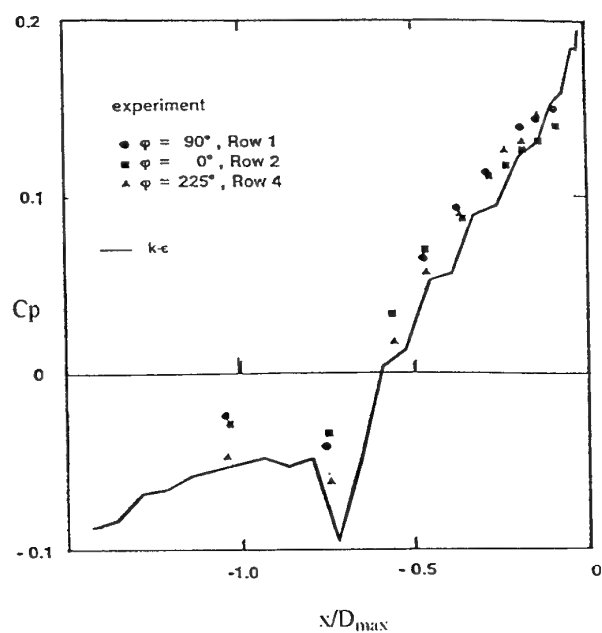
Figure 2.6-16 Case A.2.2 Static Pressure Coefficient on the Afterbody



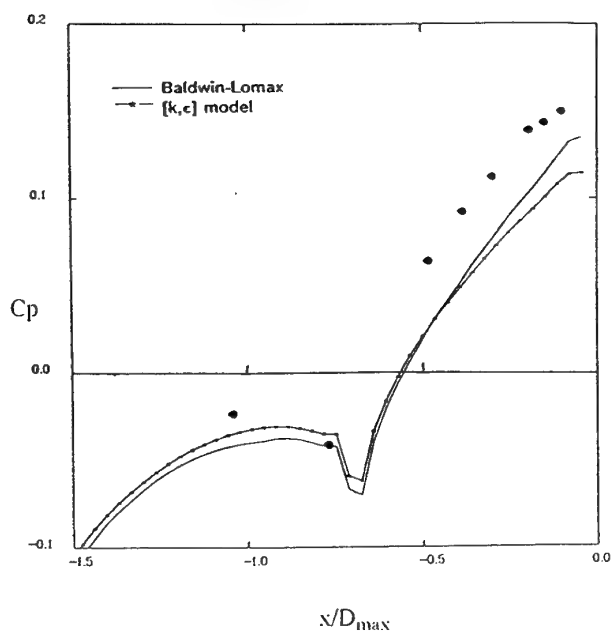
Contribution N10



Contribution N10



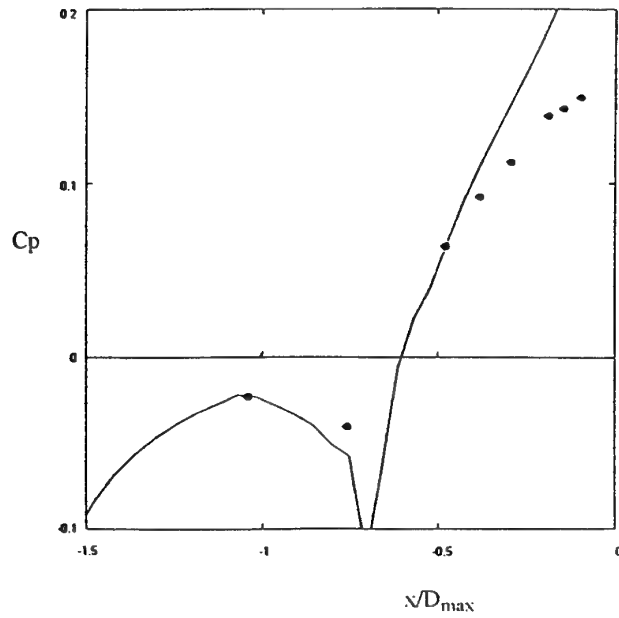
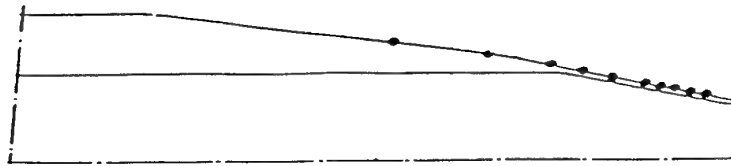
Contribution N13



Contribution N14

Figure 2.6-16 (continued) Case A.2.2 Static Pressure Coefficient on the Afterbody





Contribution N15

Figure 2.6-16 (continued) Case A.2.2 Static Pressure Coefficient on the Afterbody

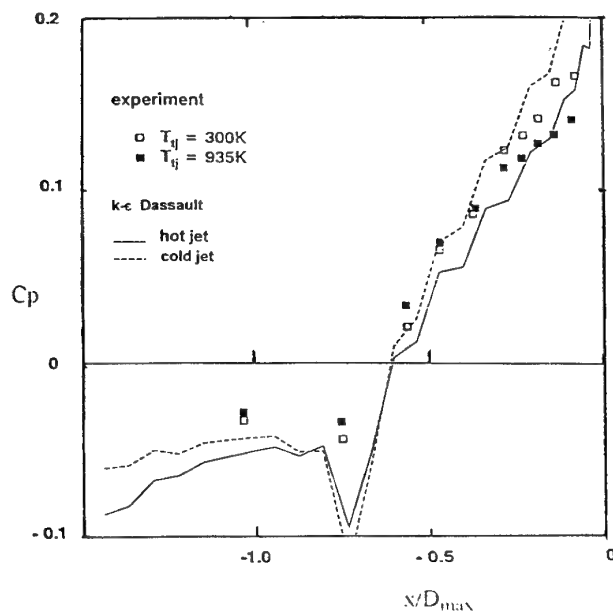
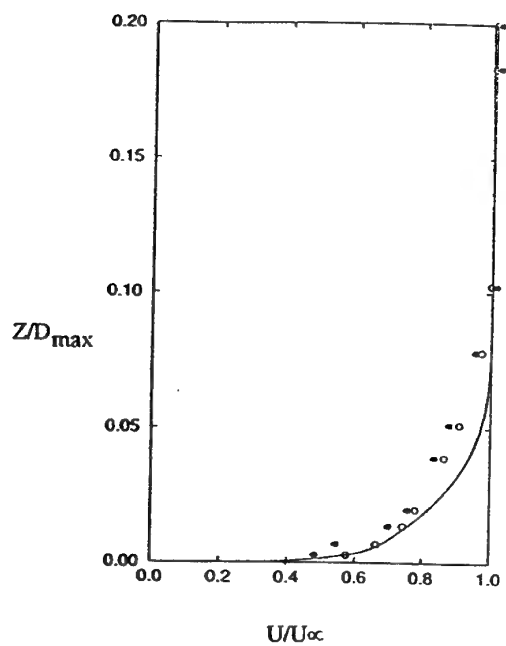
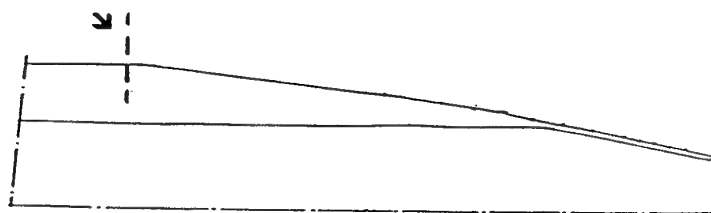
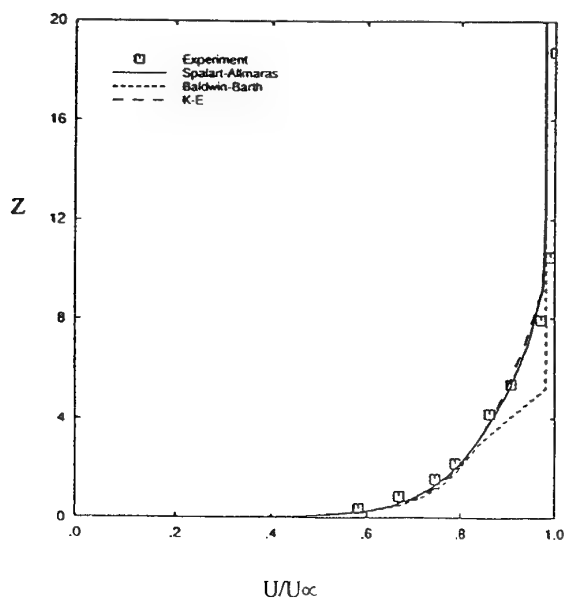


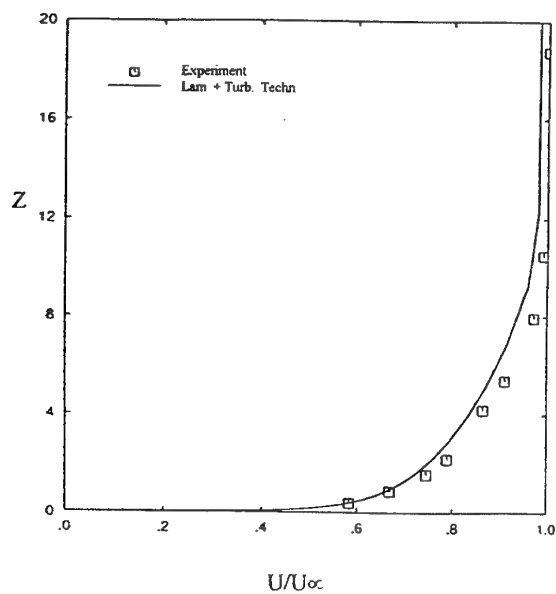
Figure 2.6-17 Influence of Jet Temperature on the Static Pressure Coefficient on the Afterbody  
(from Contribution N13)



Contribution N15



Contribution N09



Contribution N09

Figure 2.6-18 Case A.2.2 Boundary Layer Profiles at  $x/D_{max} = -2.076$

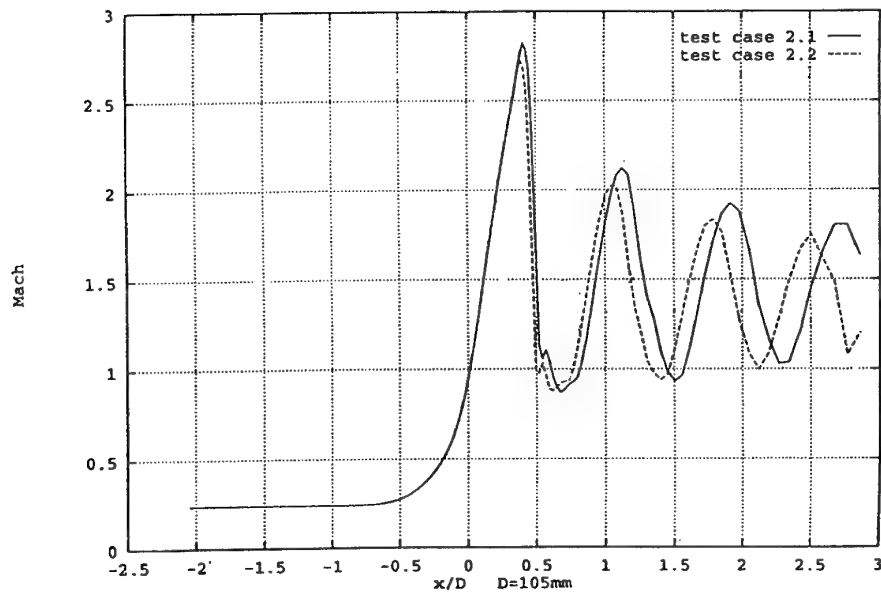


Figure 2.6-19 Case A.2.2 Static Pressure Distribution along the Axis of Symmetry  
(from Contribution N13)

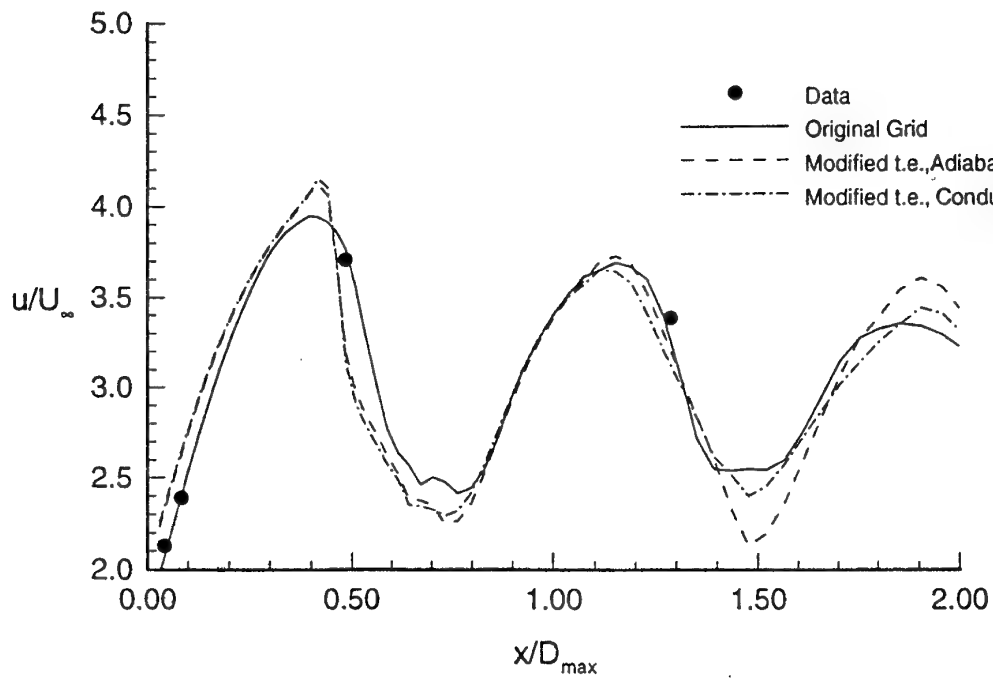
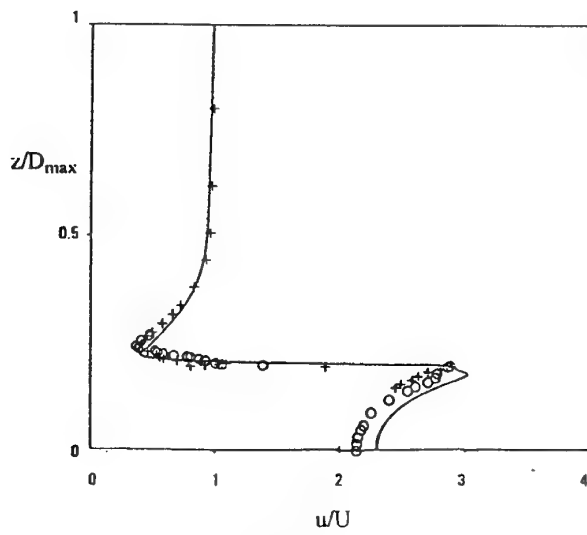
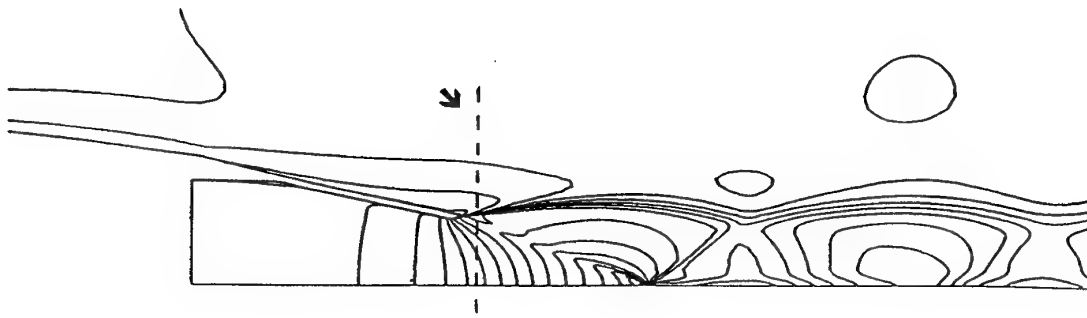
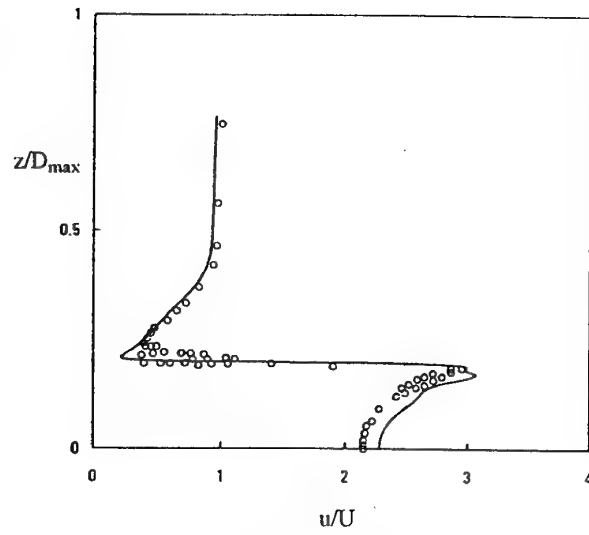


Figure 2.6-20 Mean Velocity Distribution along the Axis of Symmetry  
(from Contribution N10)

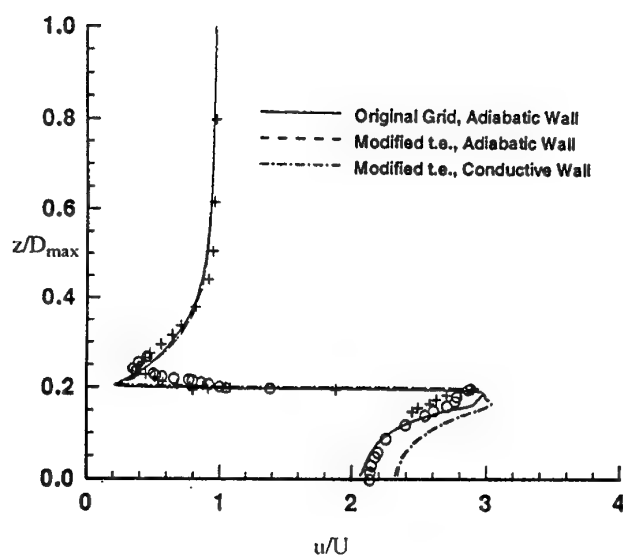
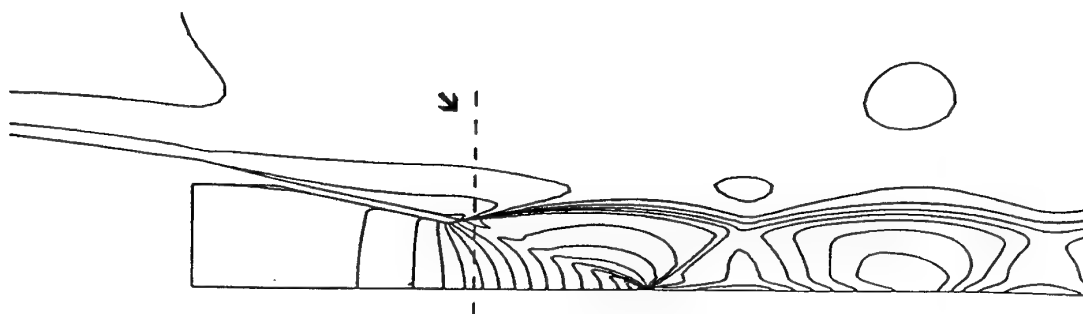


Contribution N03

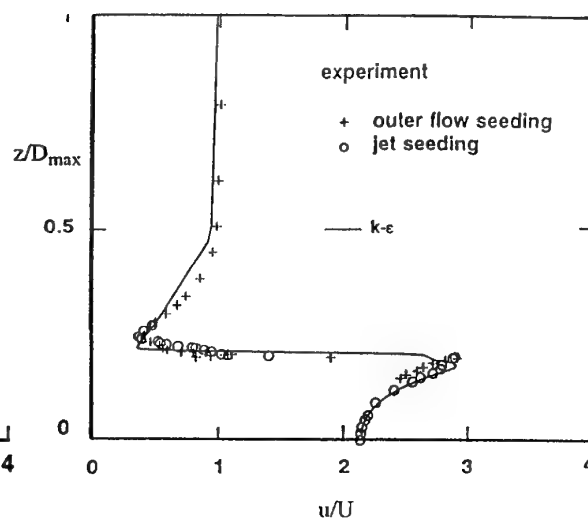


Contribution N06

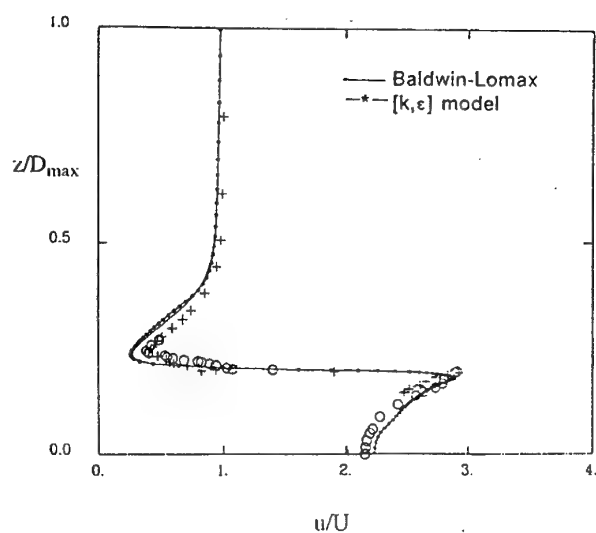
Figure 2.6-21 Case A.2.2 Profiles of Mean Axial Velocity Component at  $X/D_{\max} = 0.0413$



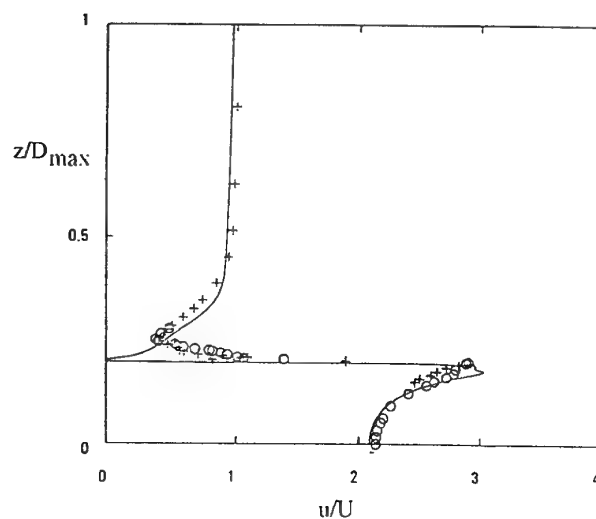
Contribution N10



Contribution N13

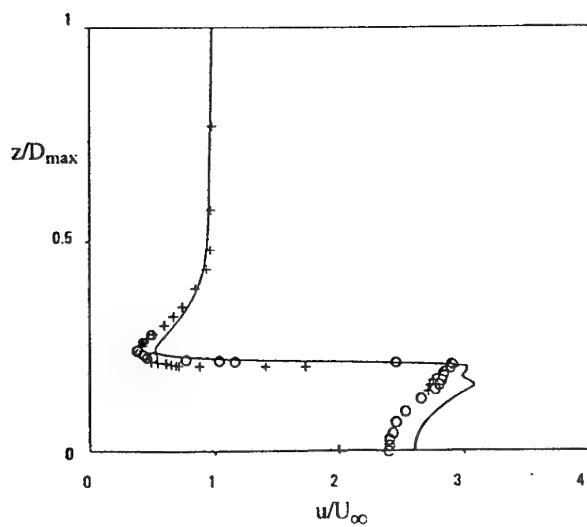
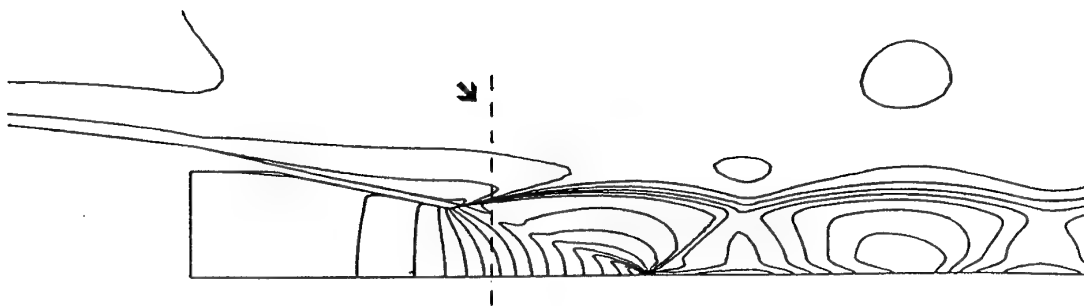
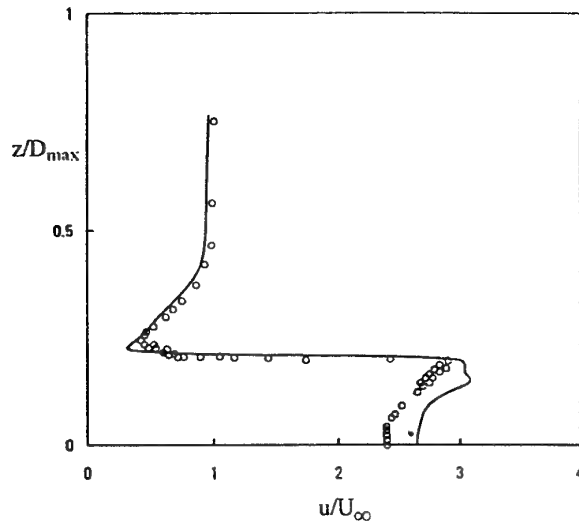
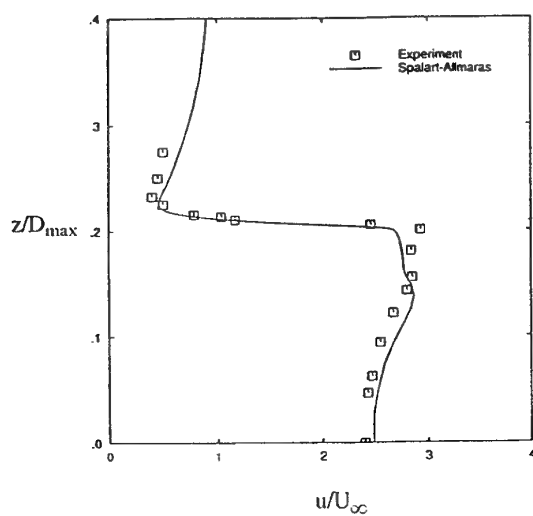
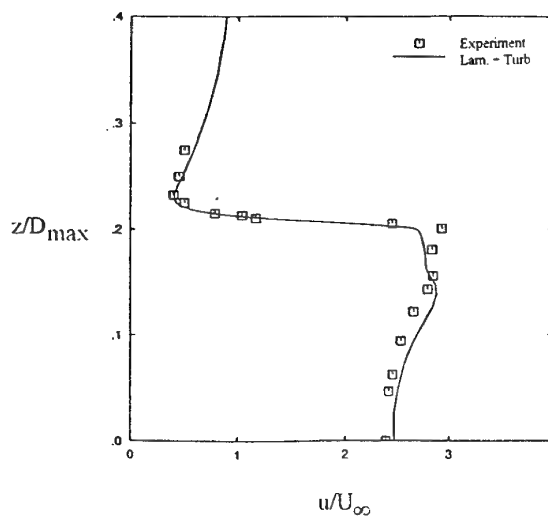


Contribution N14



Contribution N15

Figure 2.6-21 (continued) Case A.2.2 Profiles of Mean Axial Velocity Component at  $X/D_{\max} = 0.0413$

Contribution N03Contribution N06Contribution N09Contribution N09Figure 2.6-22 Case A.2.2 Profiles of Mean Axial Velocity Component at  $X/D_{\max} = 0.0825$

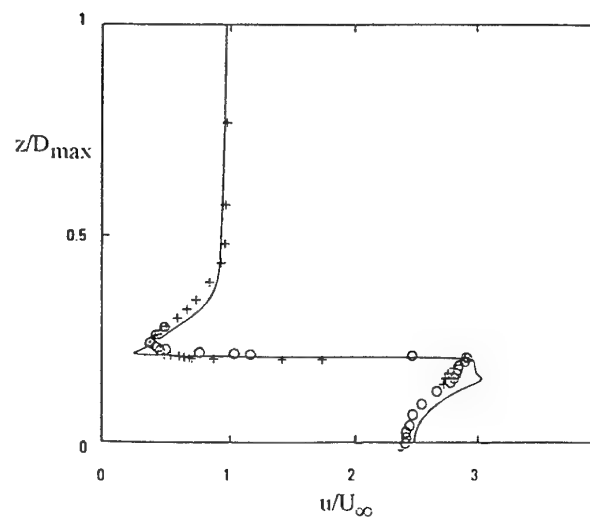
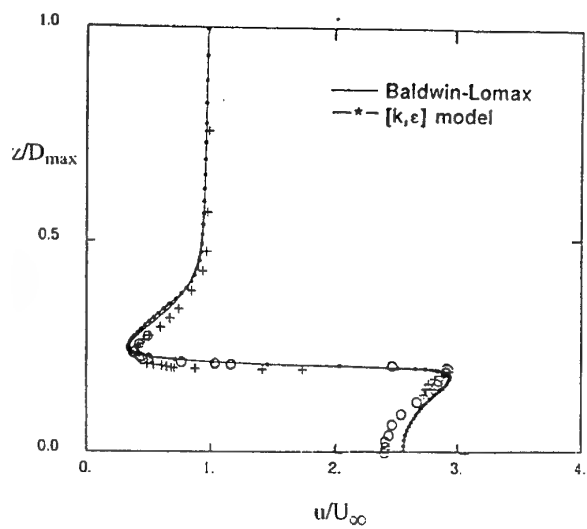
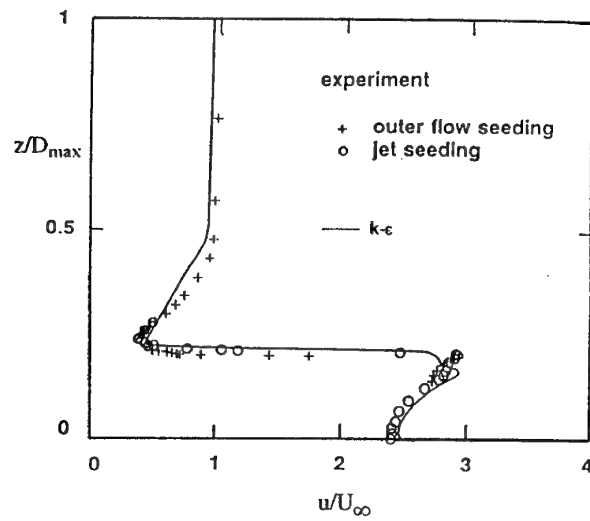
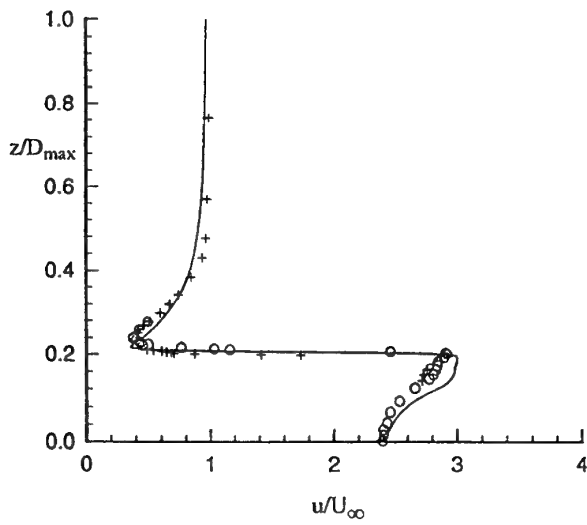
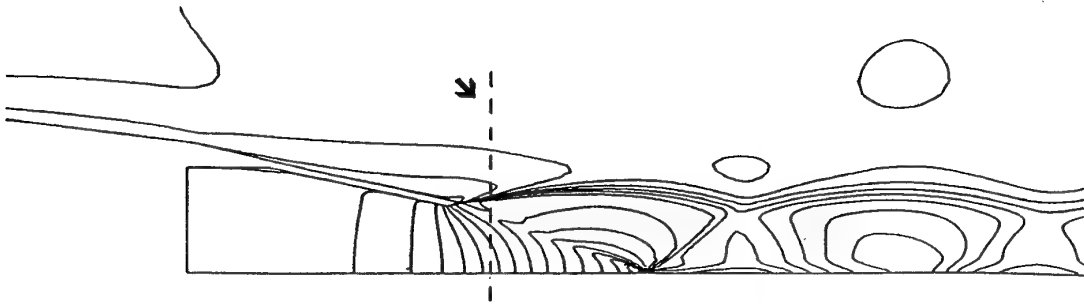
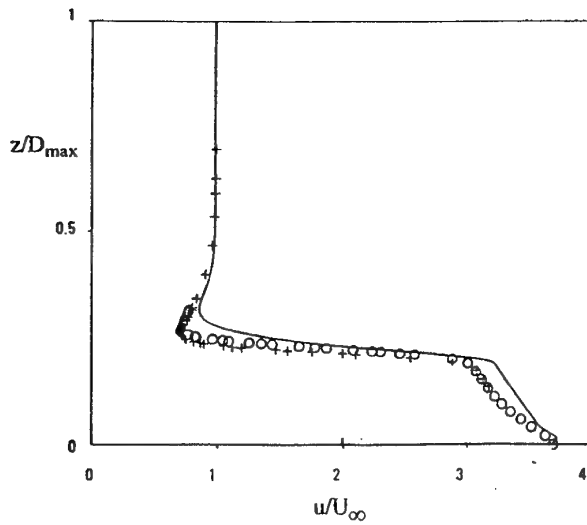
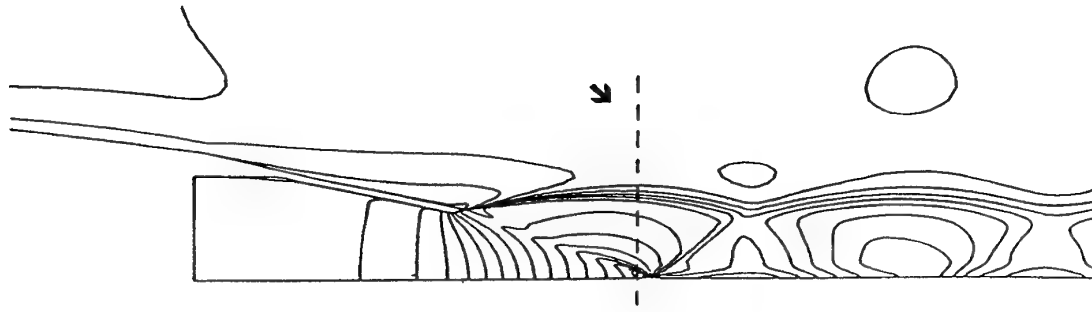
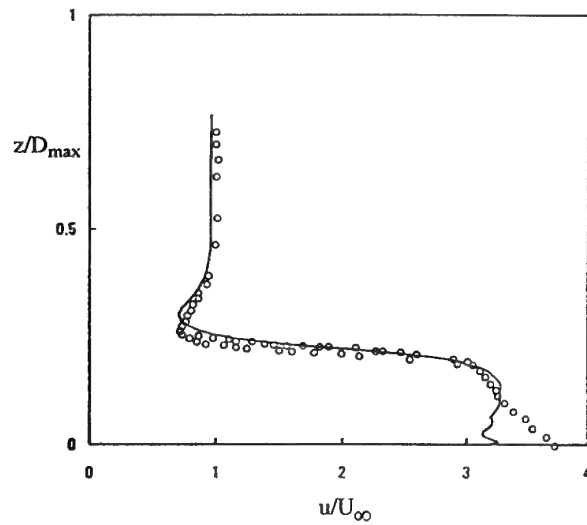


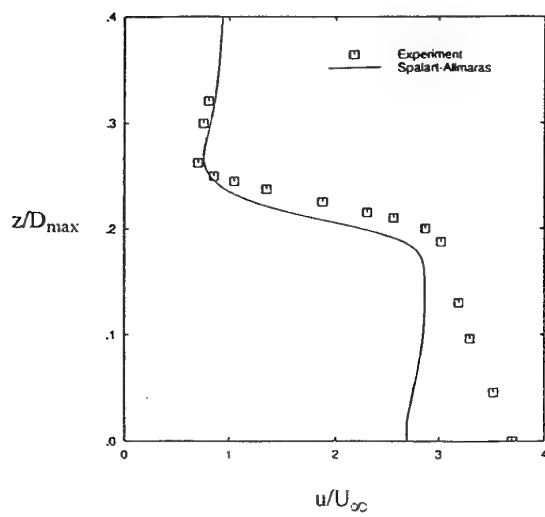
Figure 2.6-22 (continued) Case A.2.2 Profiles of Mean Axial Velocity Component at  $X/D_{\max} = 0.0825$



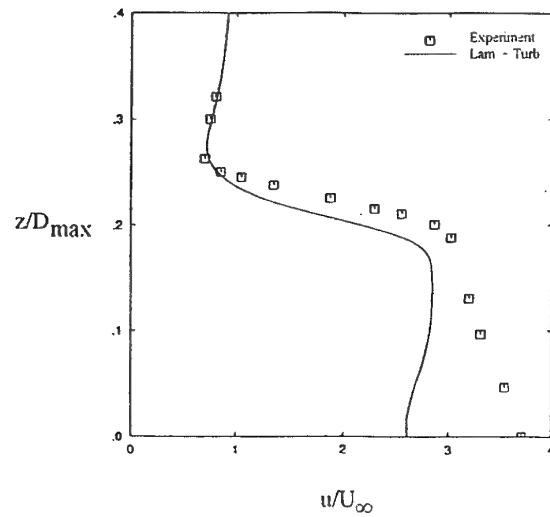
Contribution N03



Contribution N06



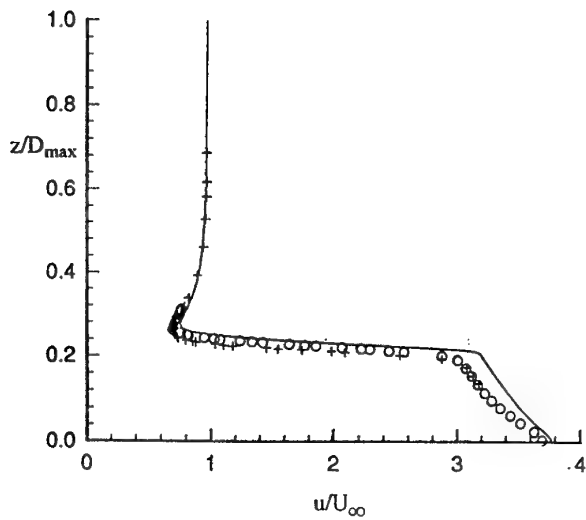
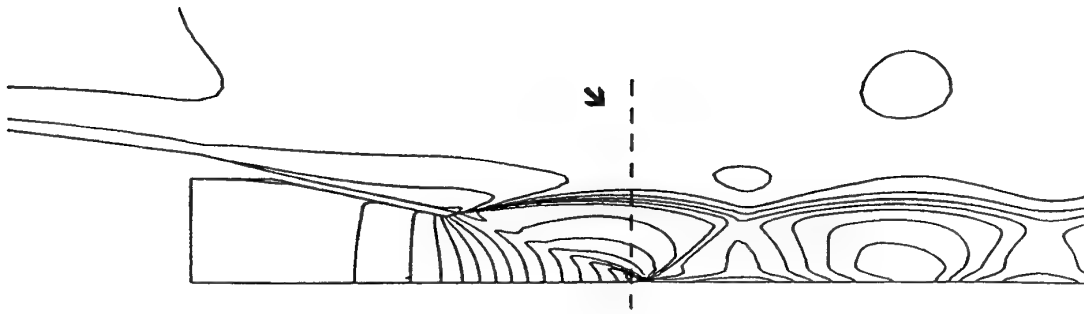
Contribution N09



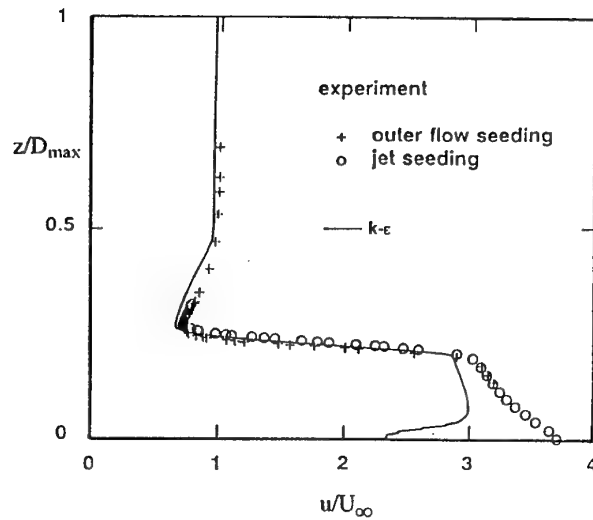
Contribution N09

Figure 2.6-23 Case A.2.2 Profiles of Mean Axial Velocity Component at  $X/D_{\max} = 0.4840$

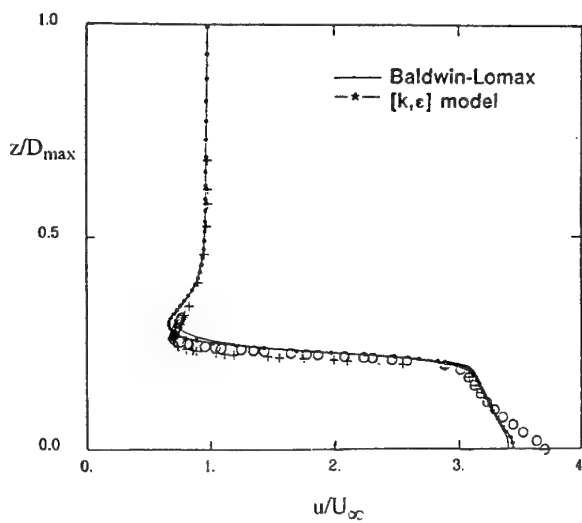




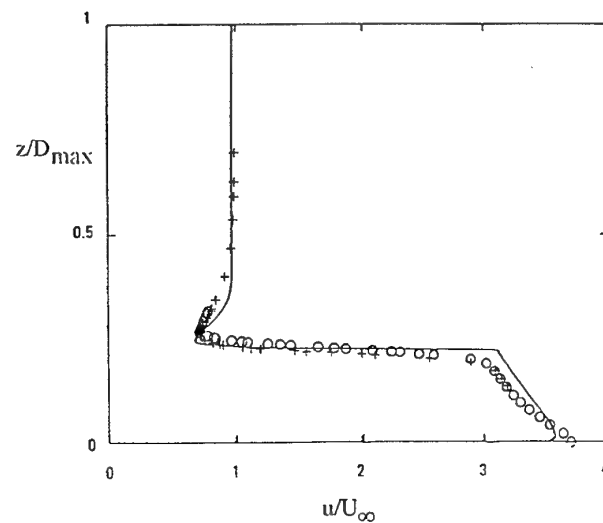
Contribution N10



Contribution N13

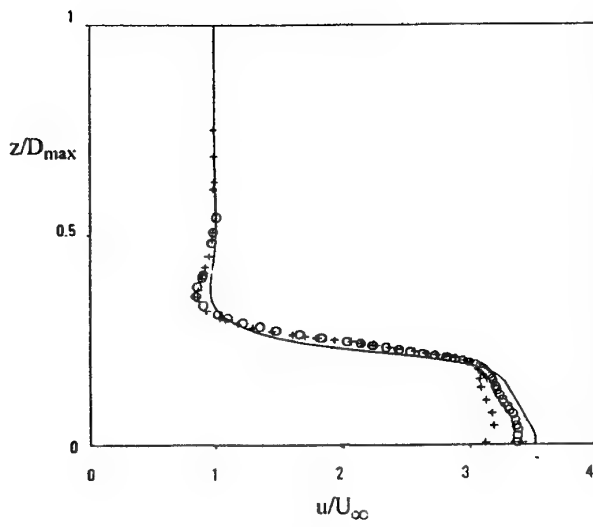
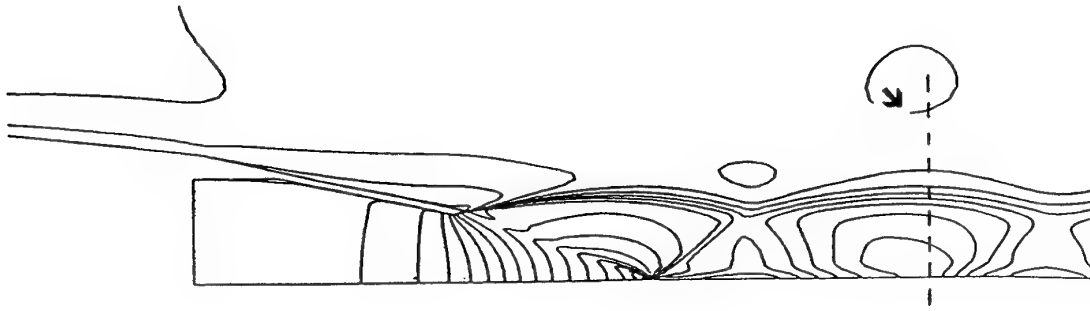


Contribution N14

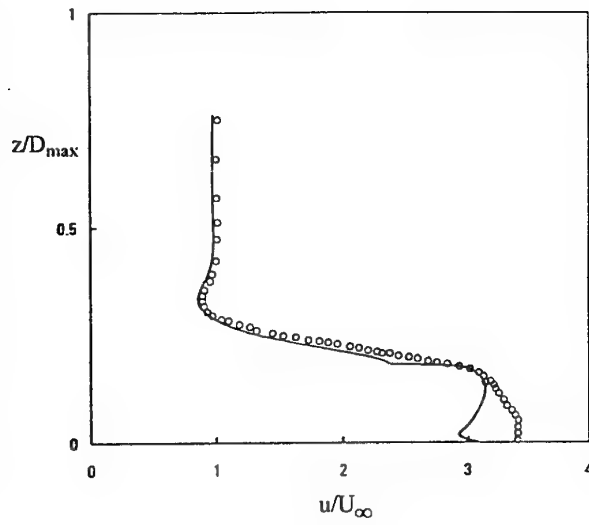


Contribution N15

Figure 2.6-23 (continued) Case A.2.2 Profiles of Mean Axial Velocity Component at  $X/D_{\max} = 0.4840$

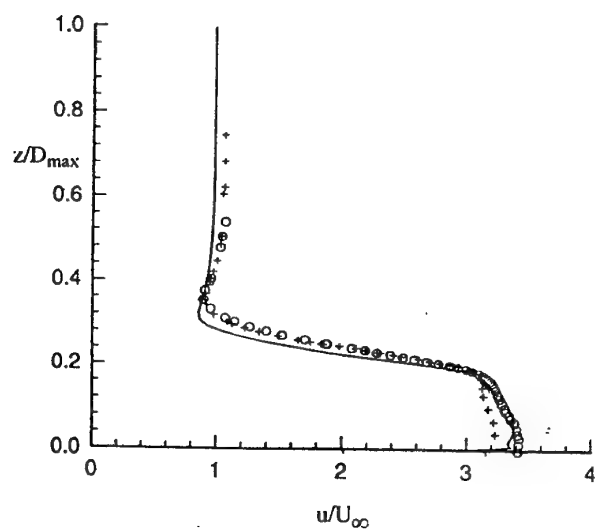
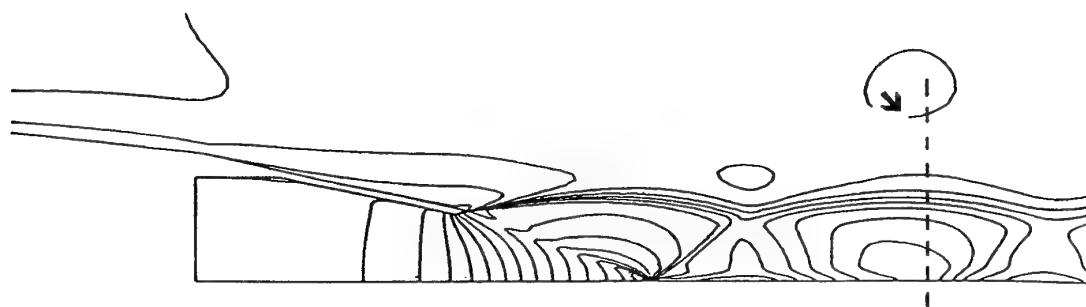


Contribution N03

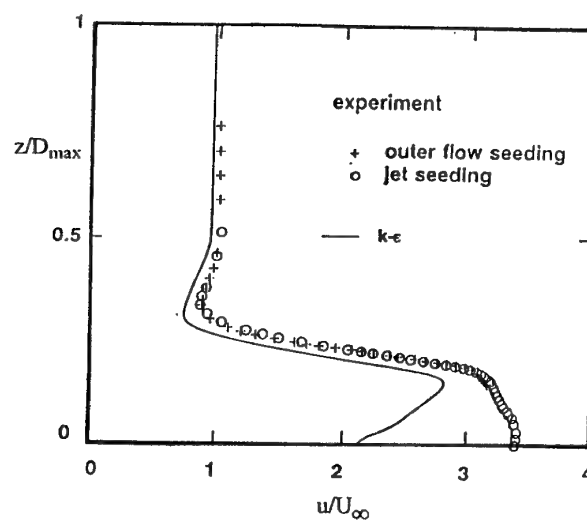


Contribution N06

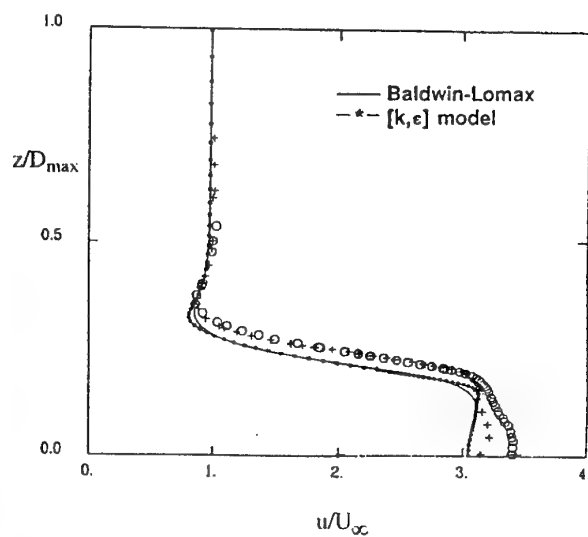
Figure 2.6-24 Case A.2.2 Profiles of Mean Axial Velocity Component at  $X/D_{\max} = 1.2871$



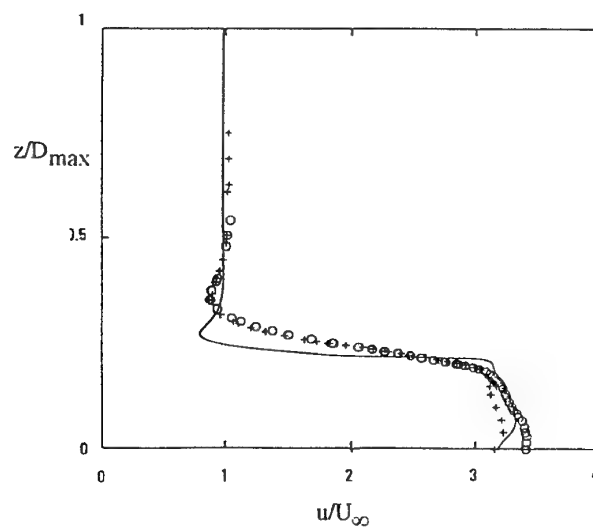
Contribution N10



Contribution N13

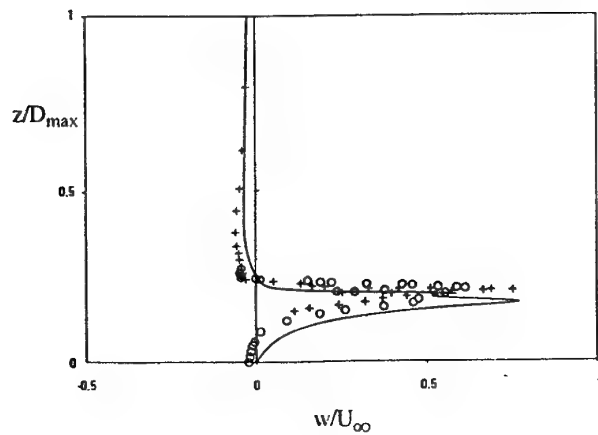
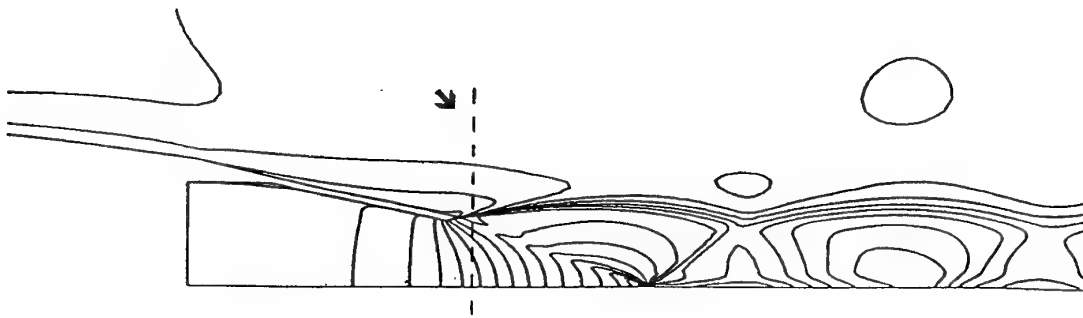


Contribution N14

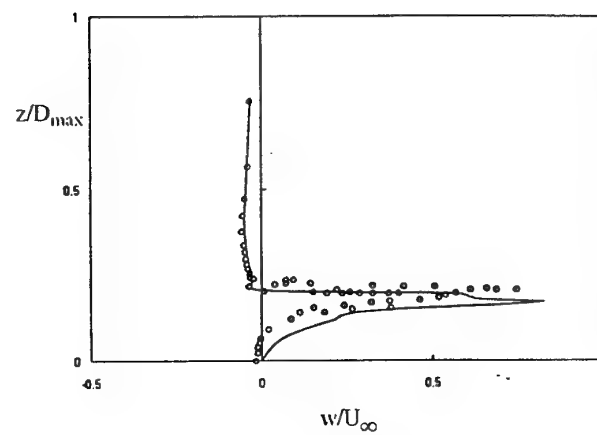


Contribution N15

Figure 2.6-24 (continued) Case A.2.2 Profiles of Mean Axial Velocity Component at  $X/D_{max} = 1.2871$

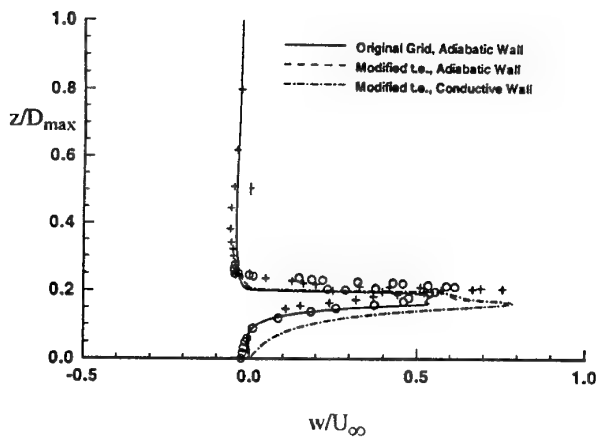
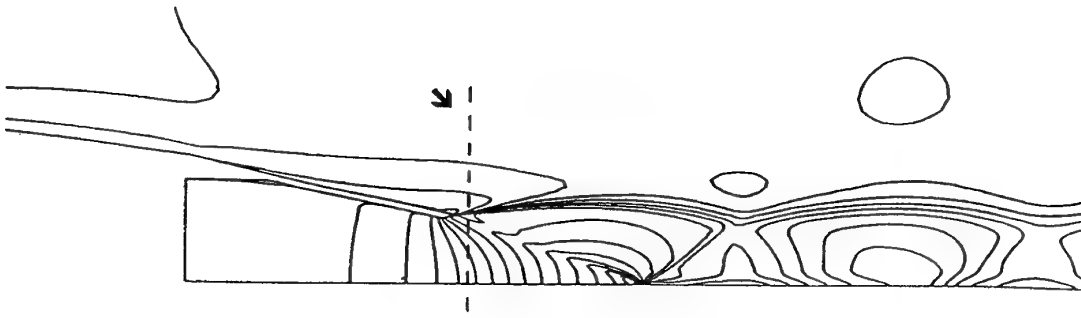


Contribution N03

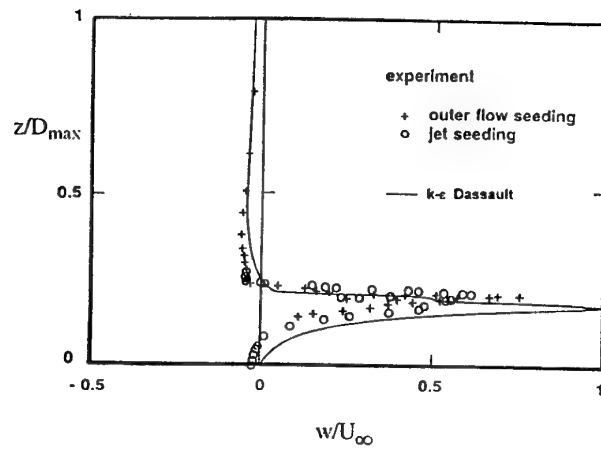


Contribution N06

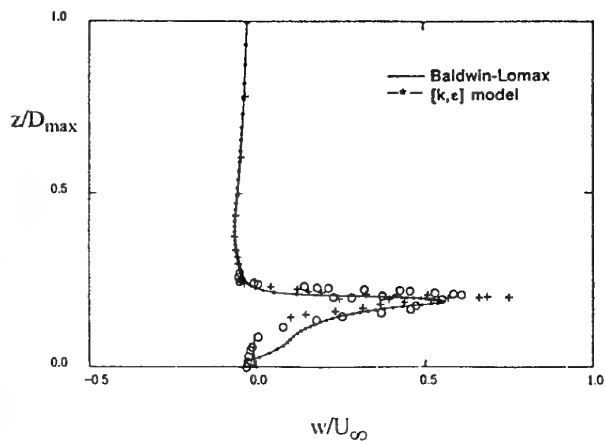
Figure 2.6-25 Case A.2.2 Profiles of Mean Radial Velocity Component at  $X/D_{\max} = 0.0413$



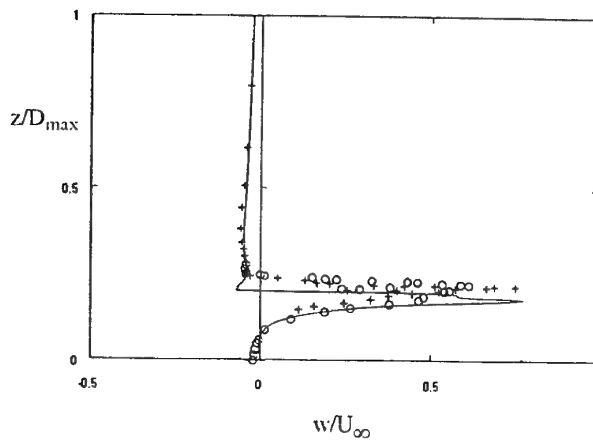
Contribution N10



Contribution N13

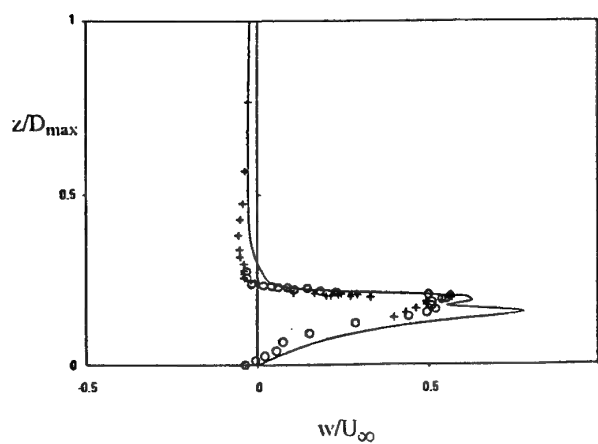
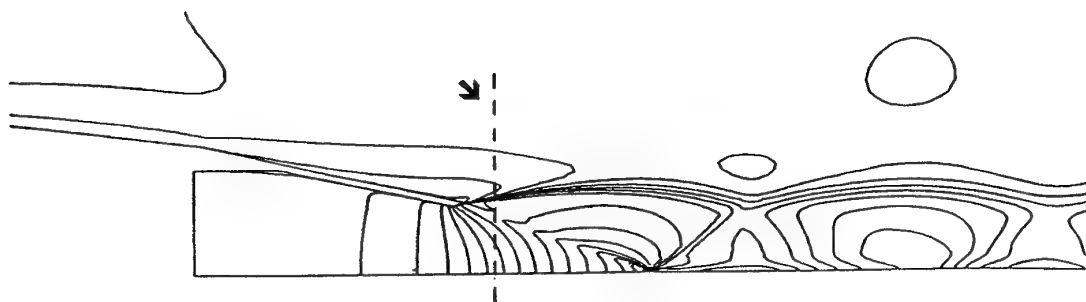
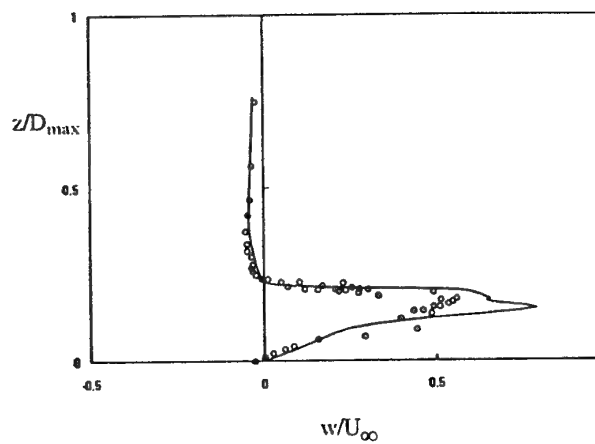
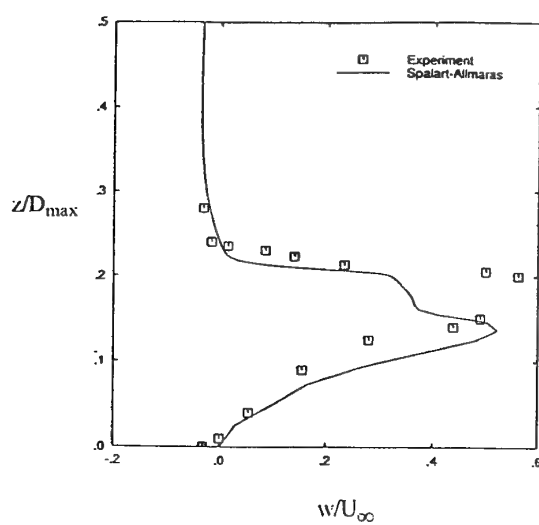
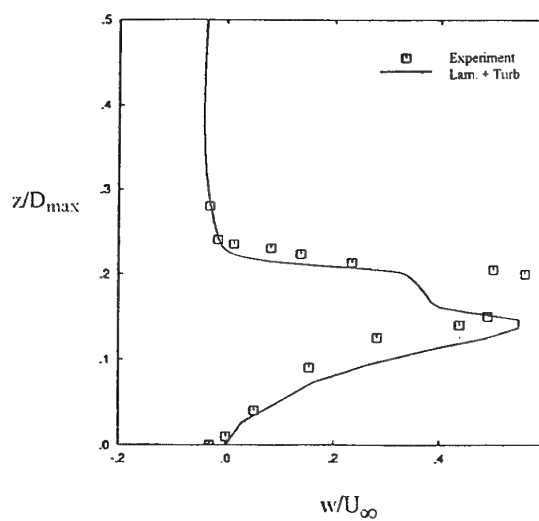


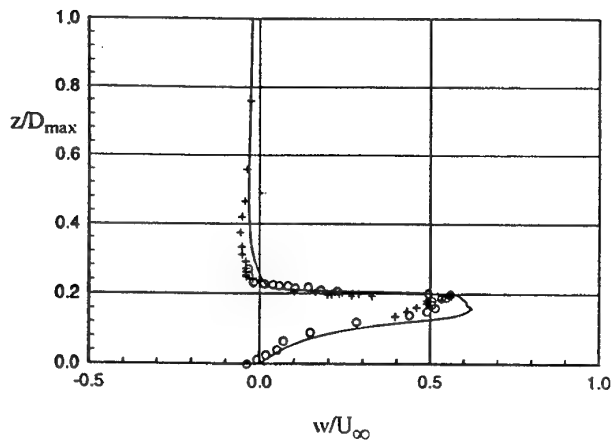
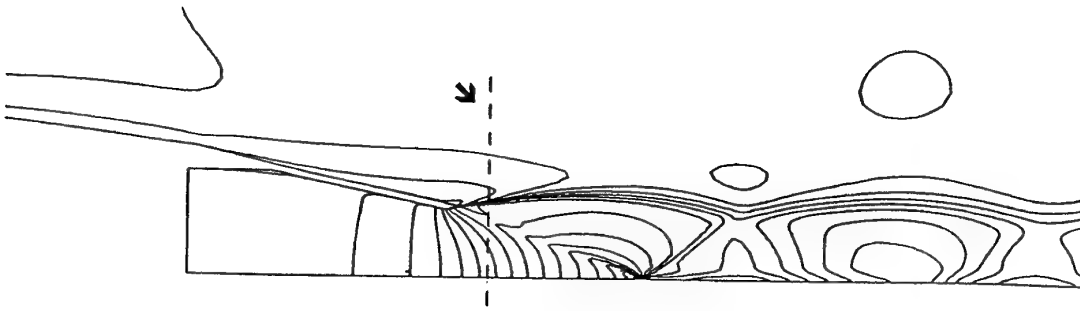
Contribution N14



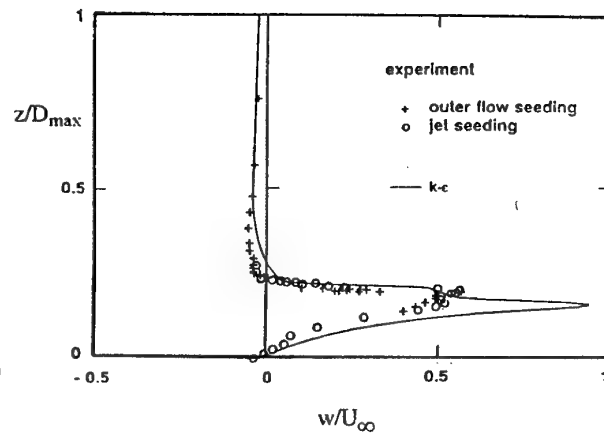
Contribution N15

Figure 2.6-25 (continued) Case A.2.2 Profiles of Mean Radial Velocity Component at  $X/D_{\max} = 0.0413$

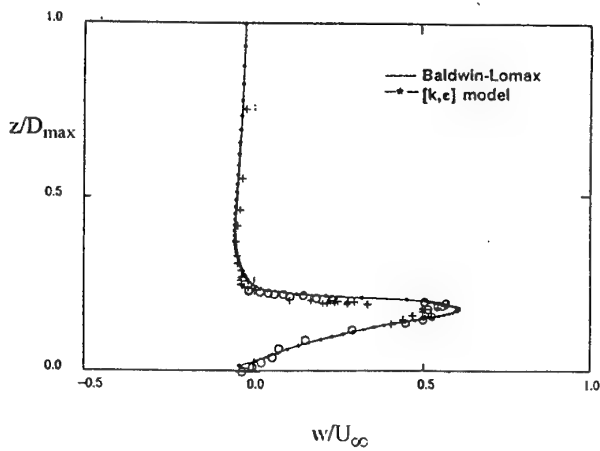
Contribution N03Contribution N06Contribution N09Contribution N09Figure 2.6-26 Case A.2.2 Profiles of Mean Radial Velocity Component at  $X/D_{max} = 0.0825$



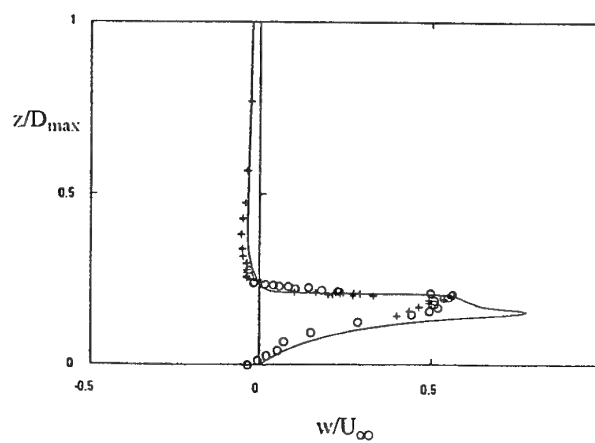
Contribution N10



Contribution N13

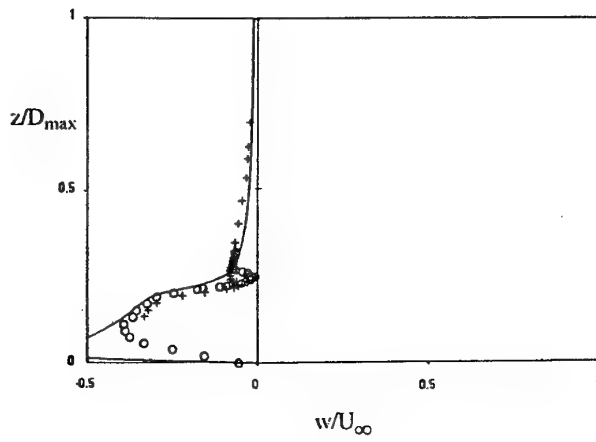
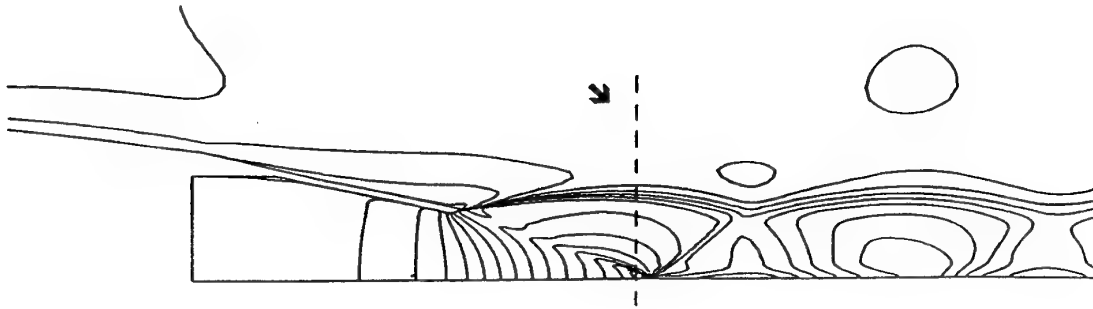
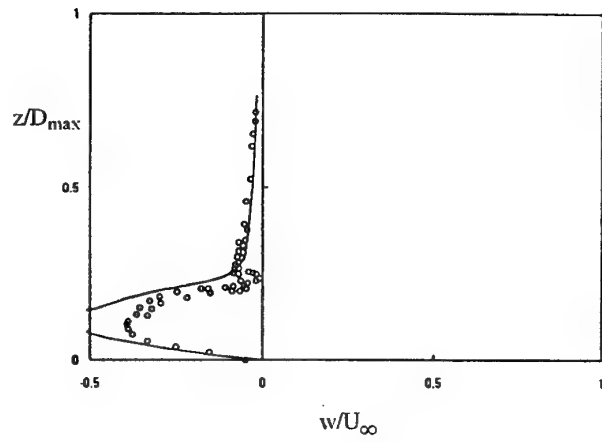


Contribution N14

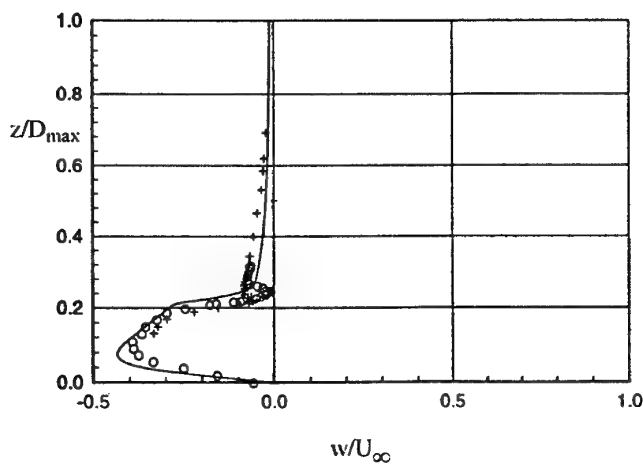
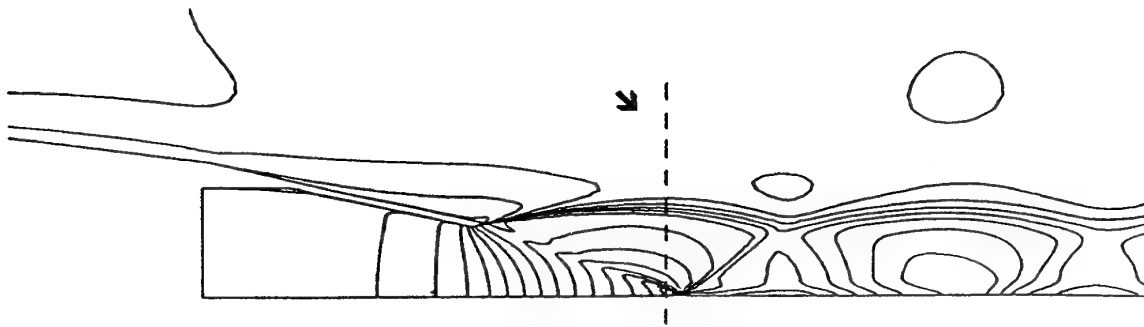


Contribution N15

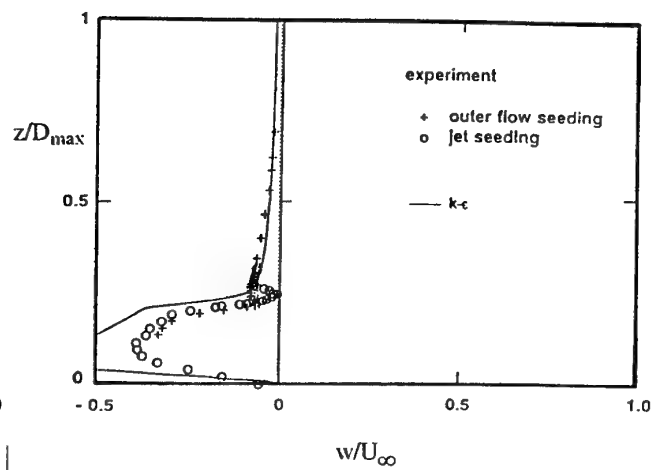
Figure 2.6-26 (continued) Case A.2.2 Profiles of Mean Radial Velocity Component at  $X/D_{max} = 0.0825$

Contribution N03Contribution N06Figure 2.6-27 Case A.2.2 Profiles of Mean Radial Velocity Component at  $X/D_{\max} = 0.4840$

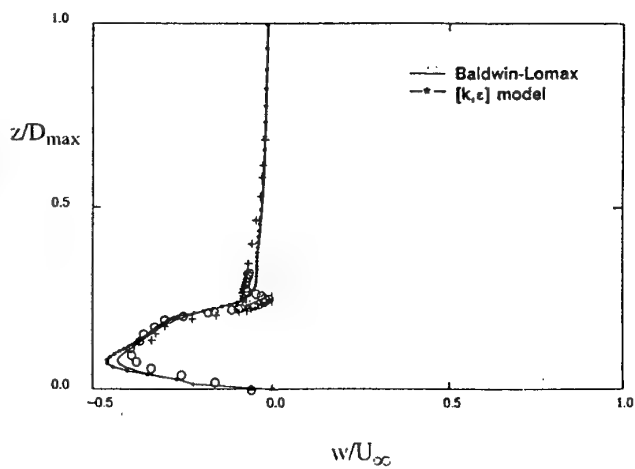




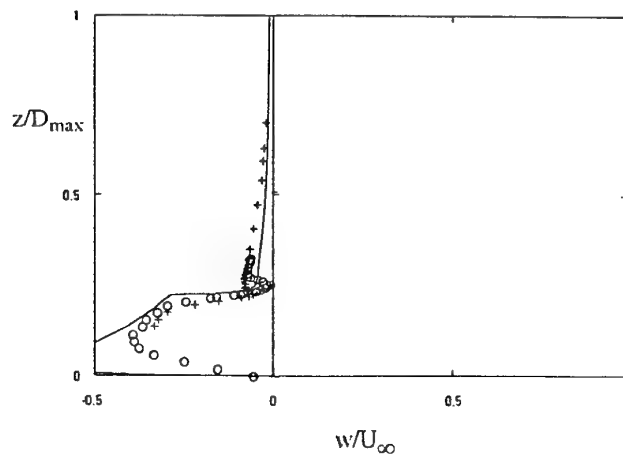
Contribution N10



Contribution N13

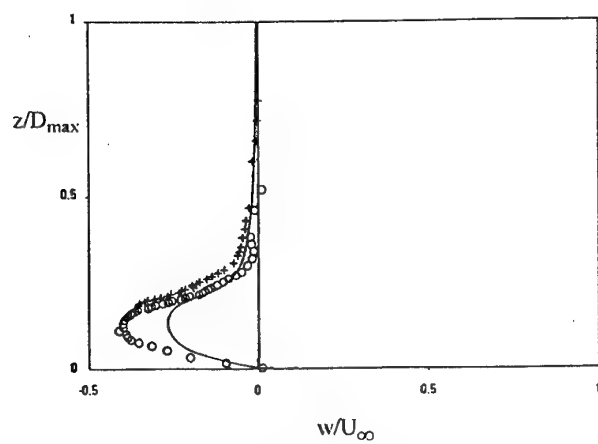
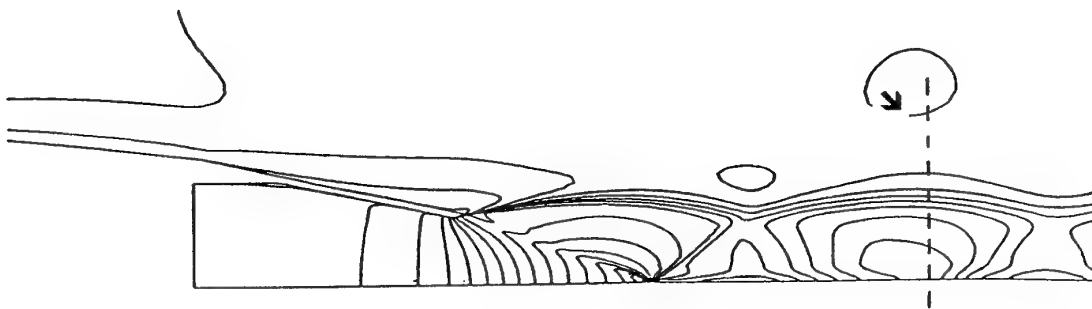


Contribution N14

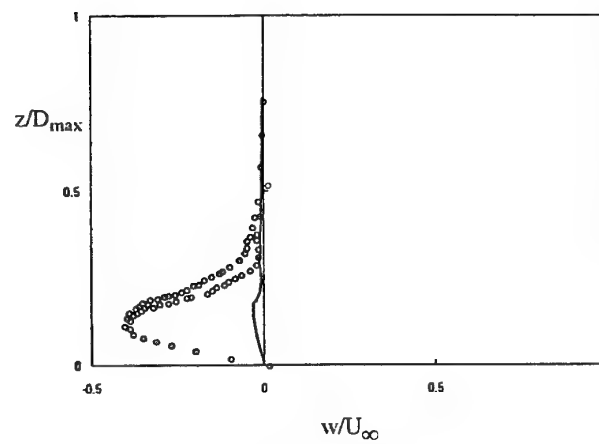


Contribution N15

Figure 2.6-27 (continued) Case A.2.2 Profiles of Mean Radial Velocity Component at  $X/D_{\max} = 0.4840$

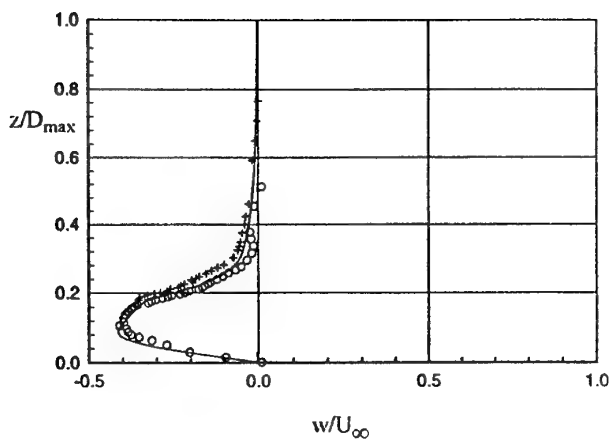
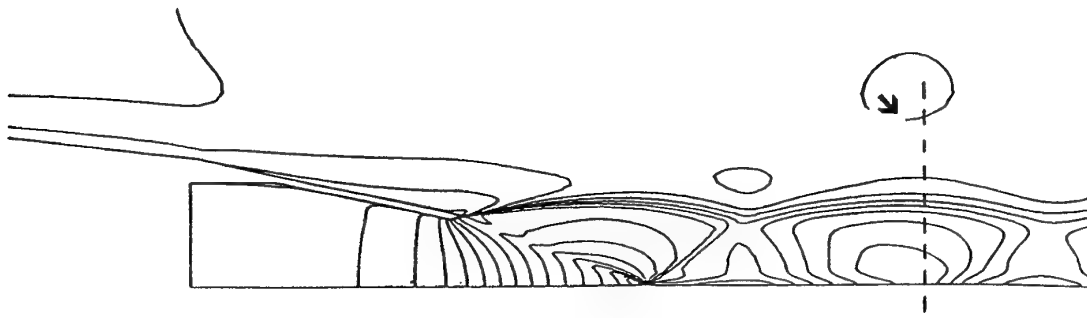


Contribution N03

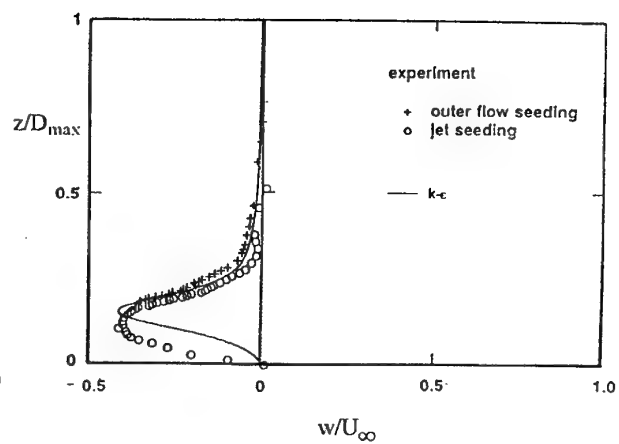


Contribution N06

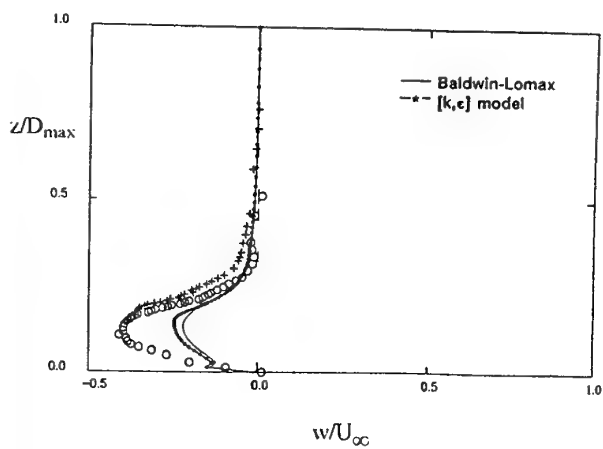
Figure 2.6-28 Case A.2.2 Profiles of Mean Radial Velocity Component at  $X/D_{\max} = 1.2871$



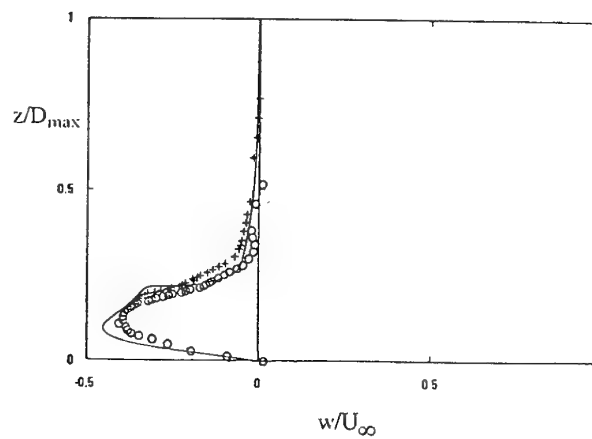
Contribution N10



Contribution N13

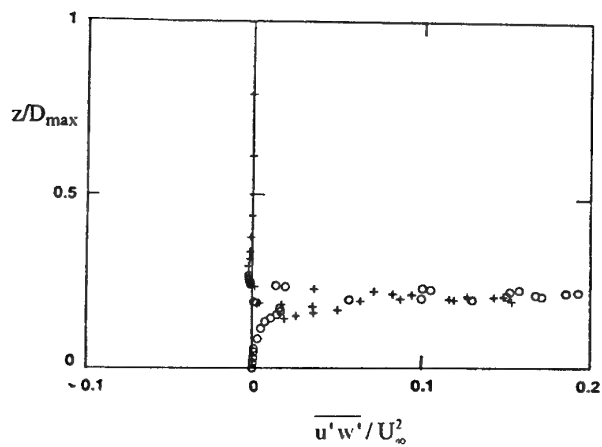
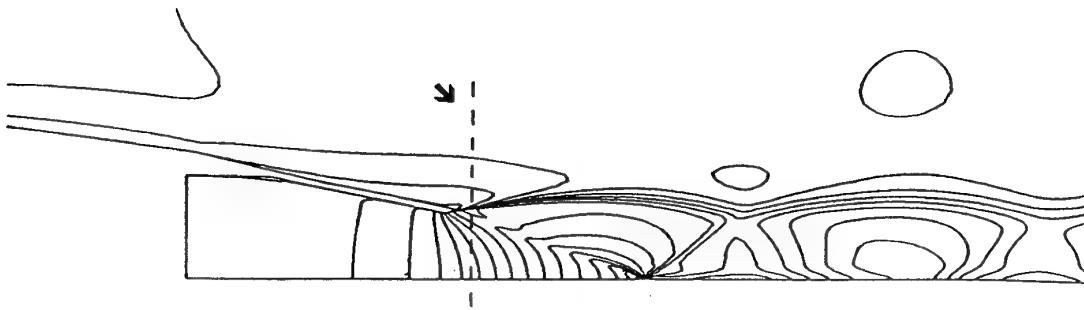


Contribution N14

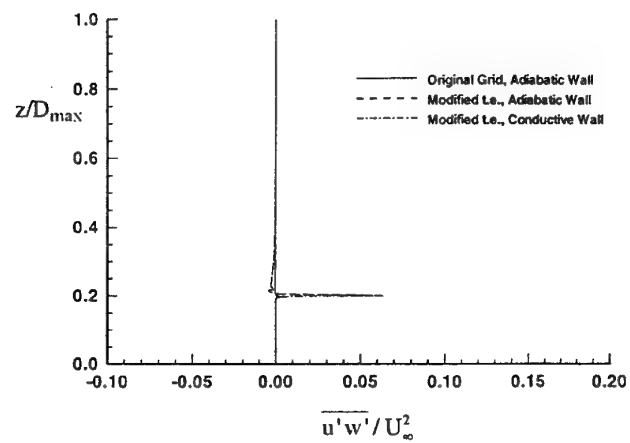


Contribution N15

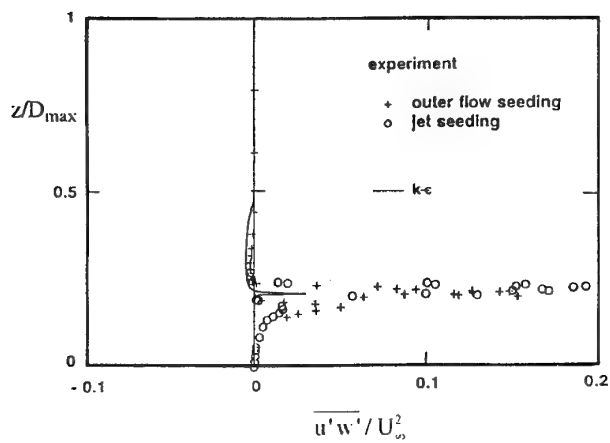
Figure 2.6-28 (continued) Case A.2.2 Profiles of Mean Radial Velocity Component at  $X/D_{\max} = 1.2871$



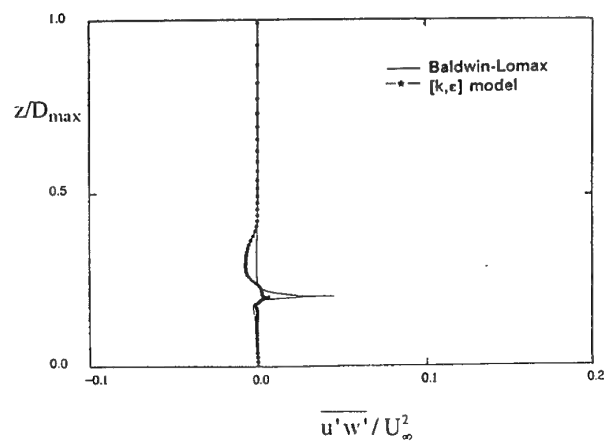
Experiment



Contribution N10

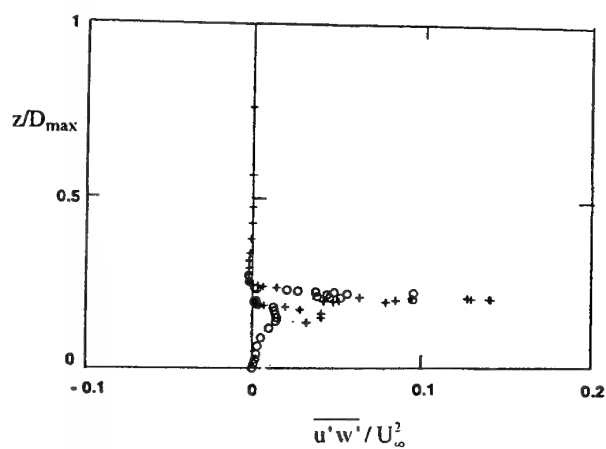
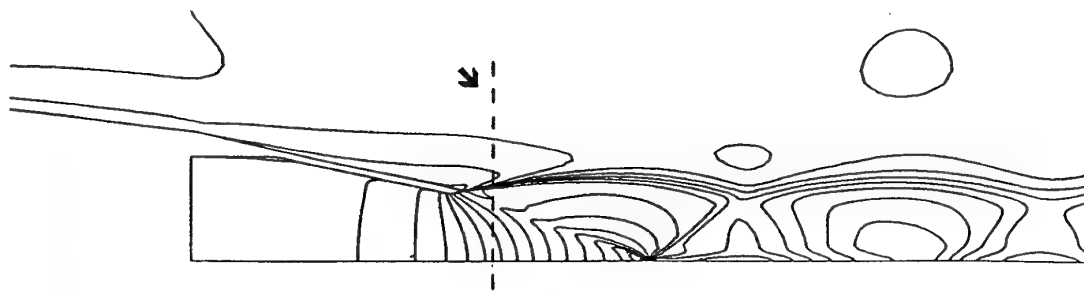


Contribution N13

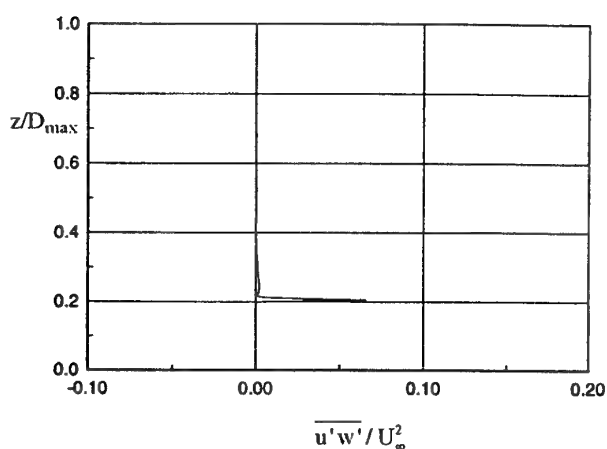


Contribution N14

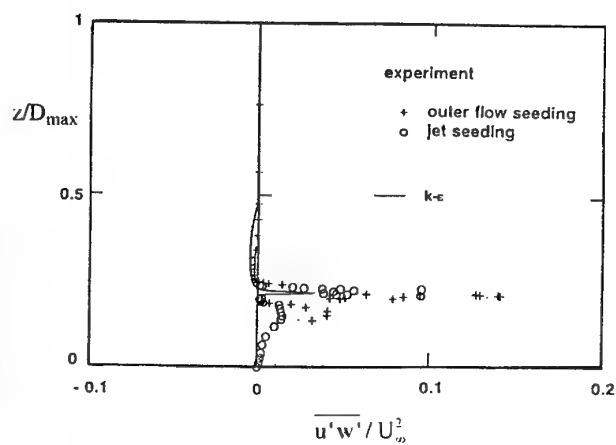
Figure 2.6-29 Case A.2.2 Profiles of Turbulent Shear Stress at  $X/D_{\max} = 0.0413$



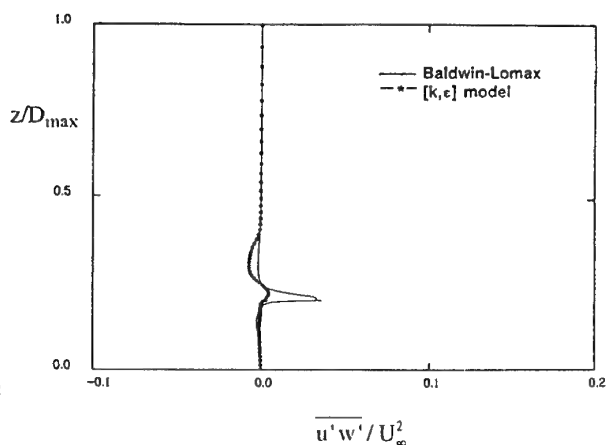
Experiment



Contribution N10

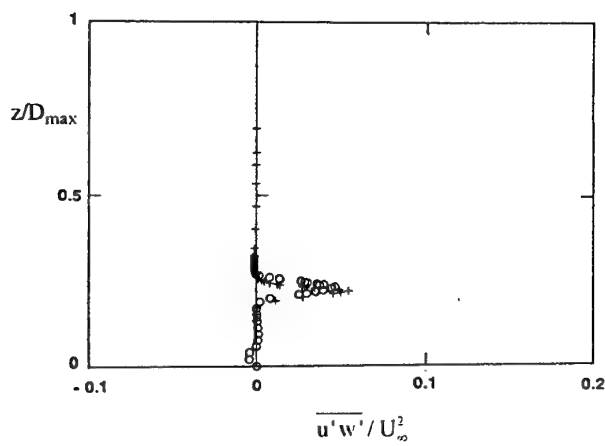
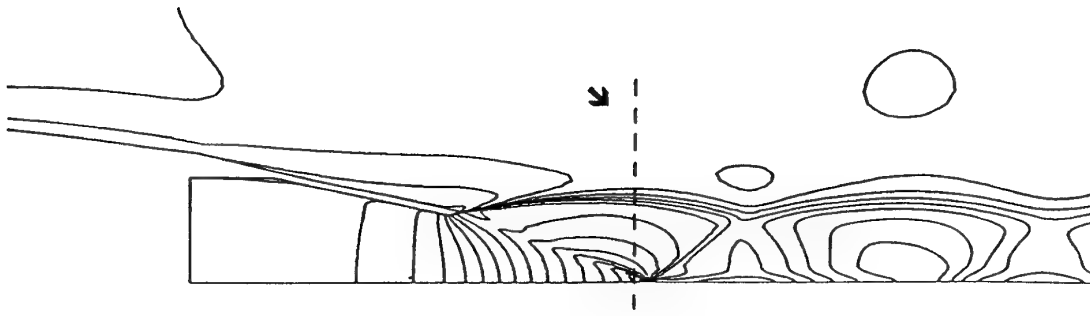


Contribution N13

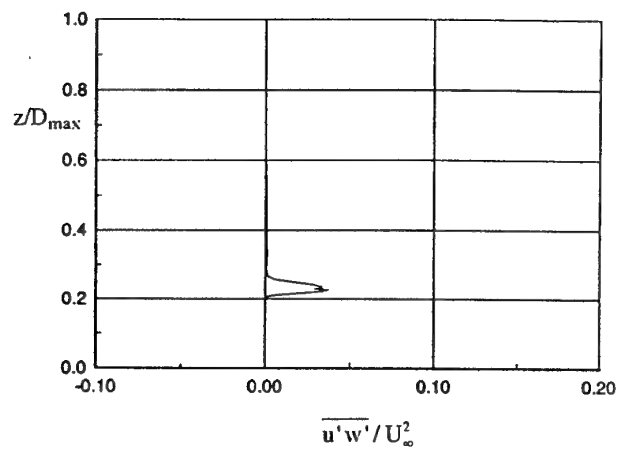


Contribution N14

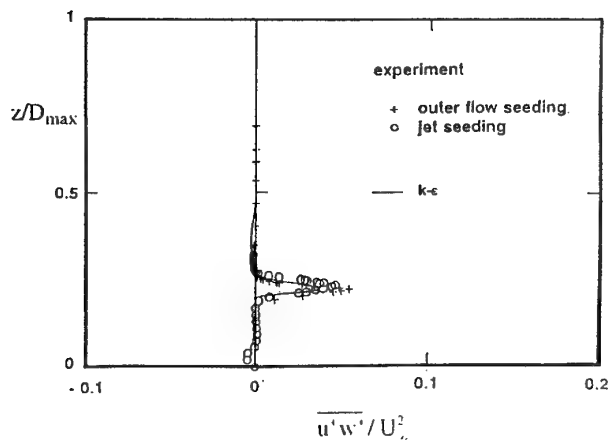
Figure 2.6-30 Case A.2.2 Profiles of Turbulent Shear Stress at  $X/D_{\max} = 0.0825$



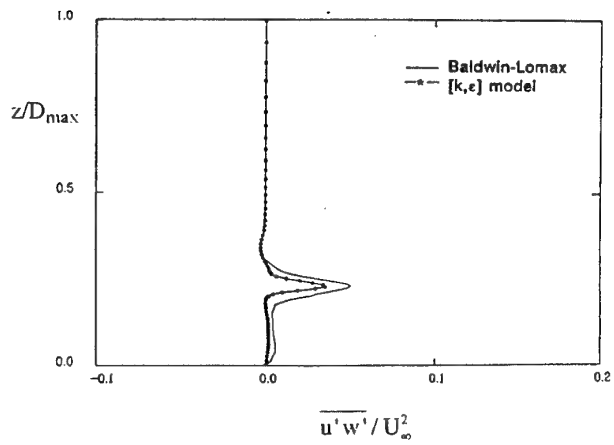
Experiment



Contribution N10



Contribution N13



Contribution N14

Figure 2.6-31 Case A.2.2 Profiles of Turbulent Shear Stress at  $X/D_{\max} = 0.4840$

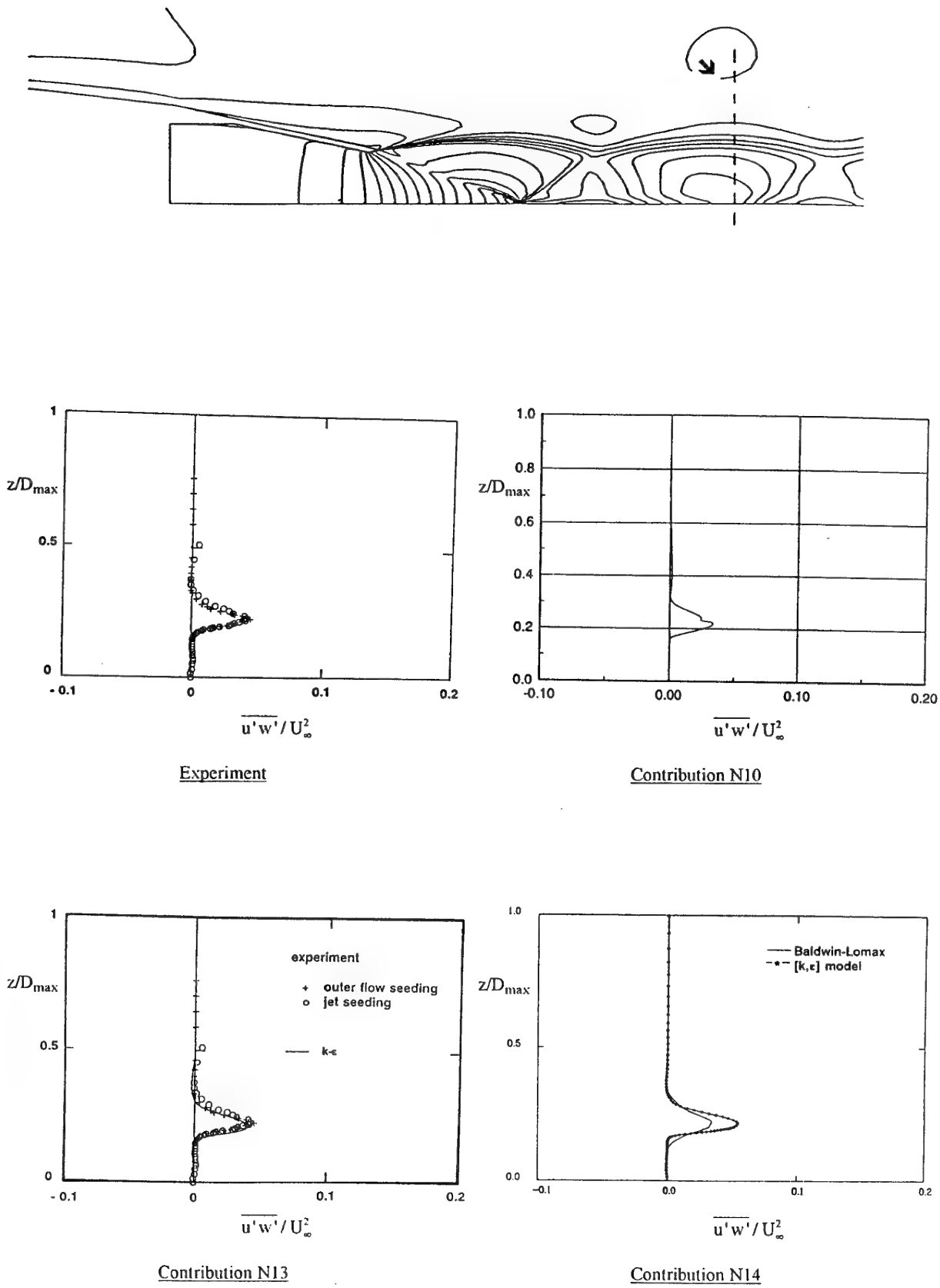


Figure 2.6-32 Case A.2.2 Profiles of Turbulent Shear Stress at  $X/D_{\max} = 1.2871$

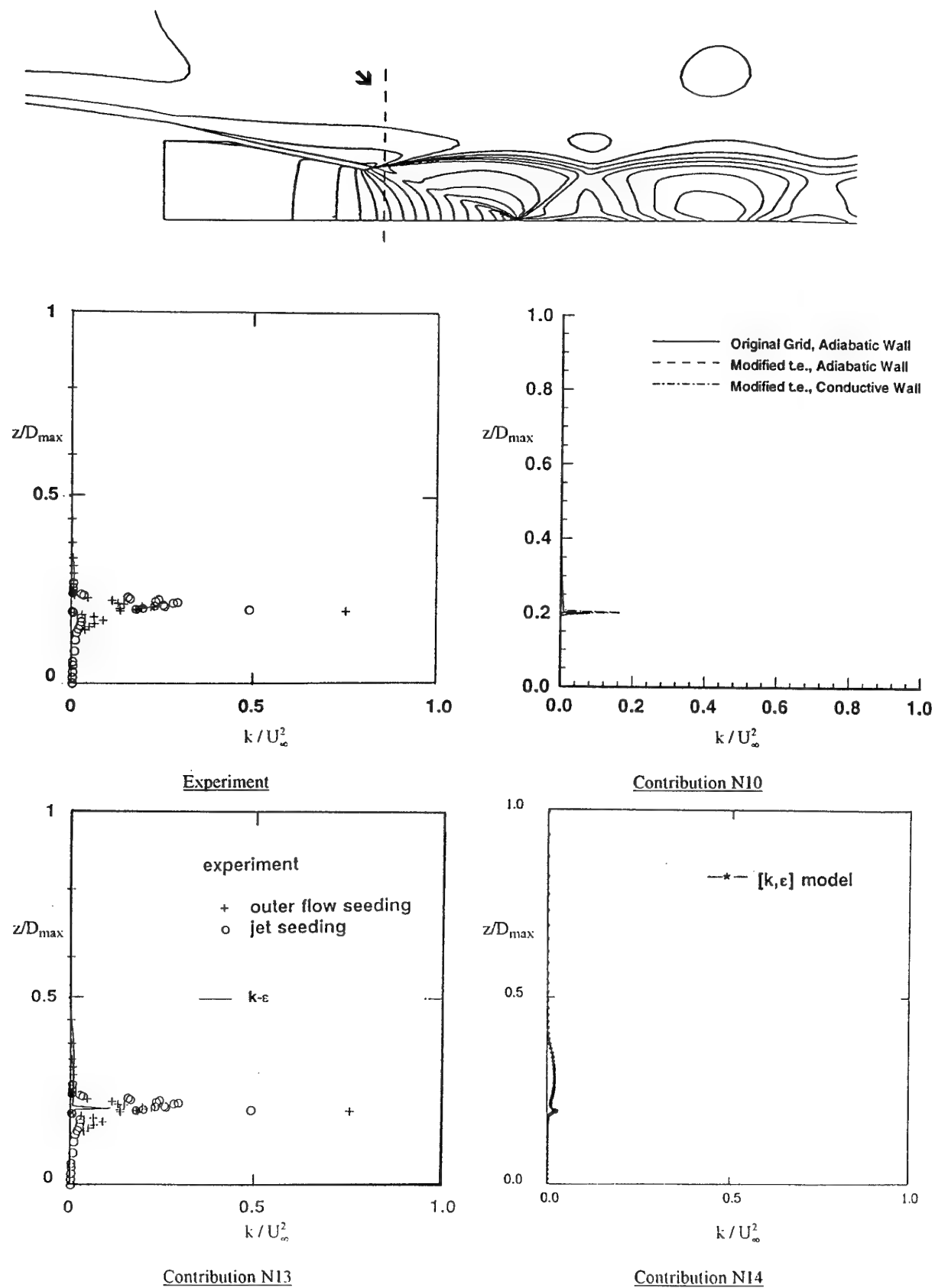
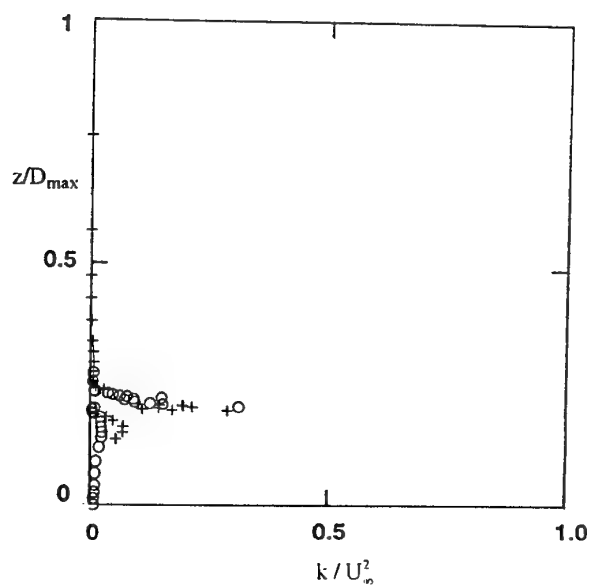
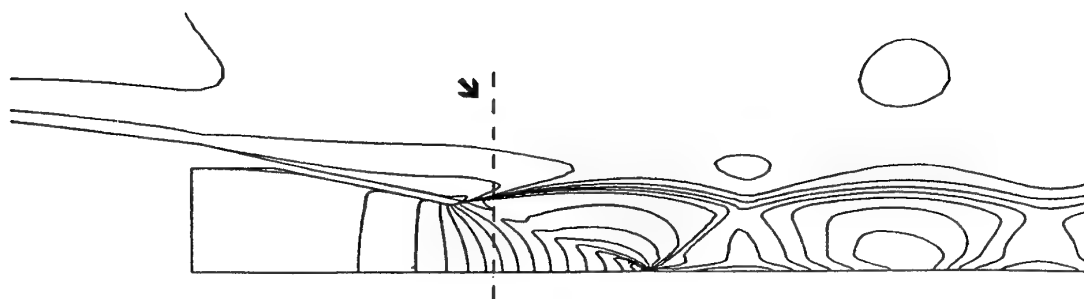
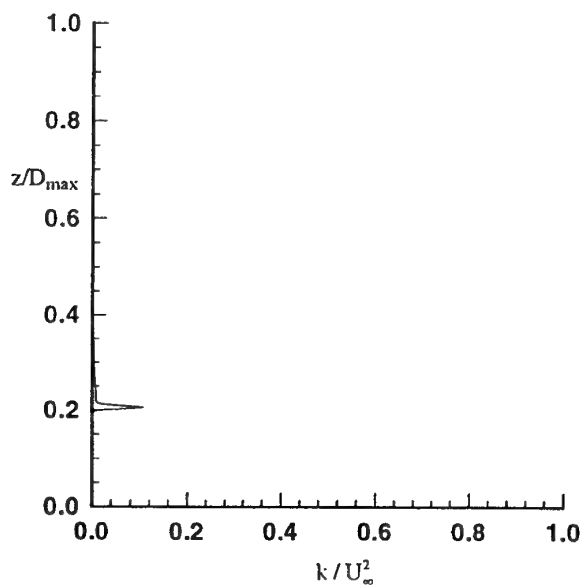


Figure 2.6-33 Case A.2.2 Profiles of Turbulent Kinetic Energy at  $X/D_{\max} = 0.0413$

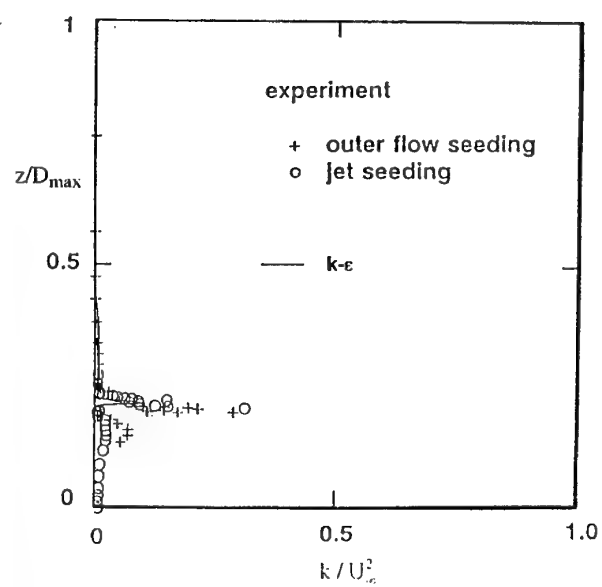




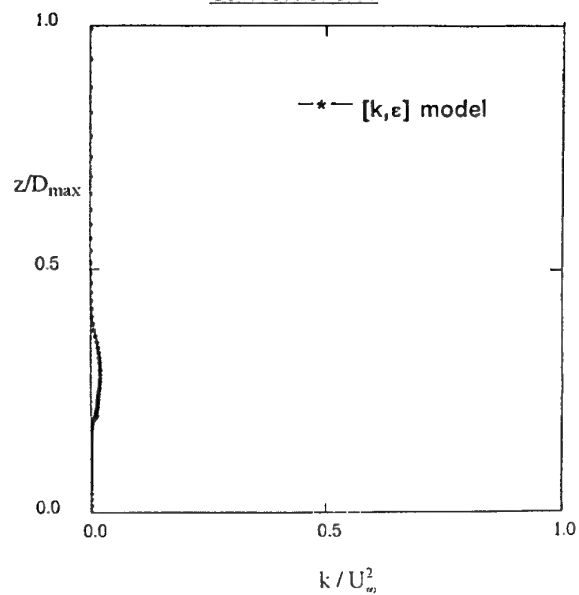
Experiment



Contribution N10



Contribution N13



Contribution N14

Figure 2.6-34 Case A.2.2 Profiles of Turbulent Kinetic Energy at  $X/D_{\max} = 0.0825$

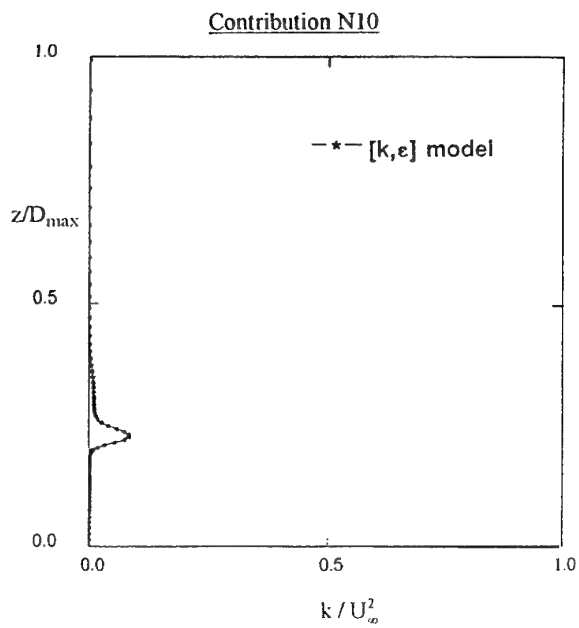
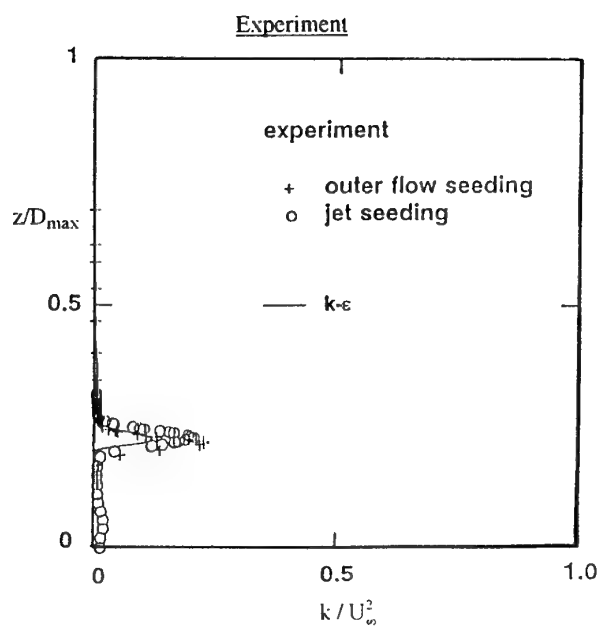
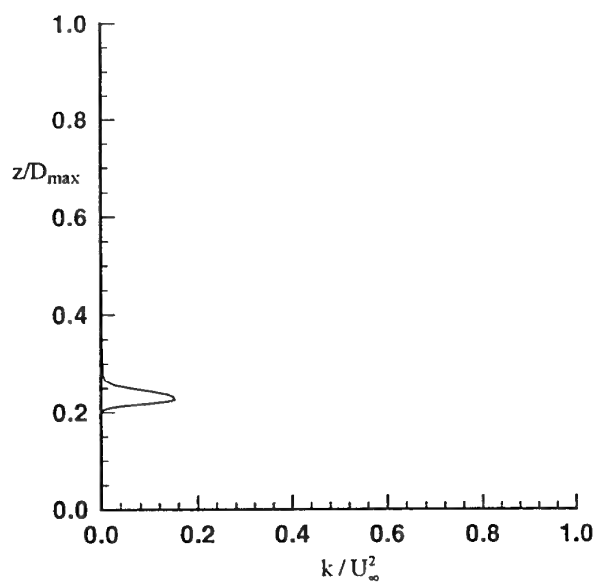
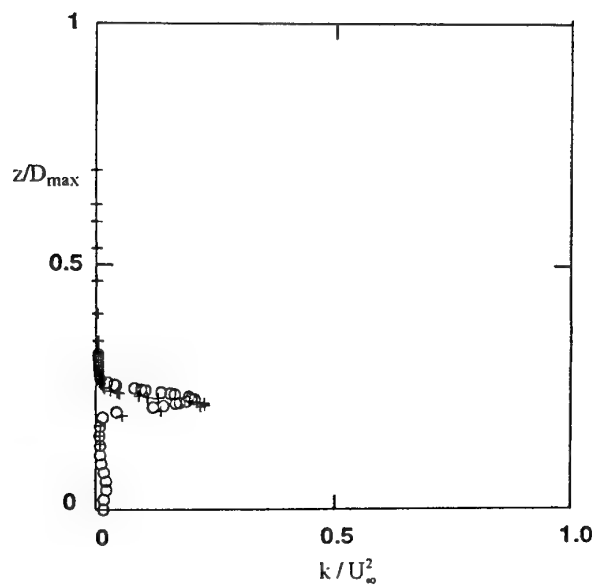
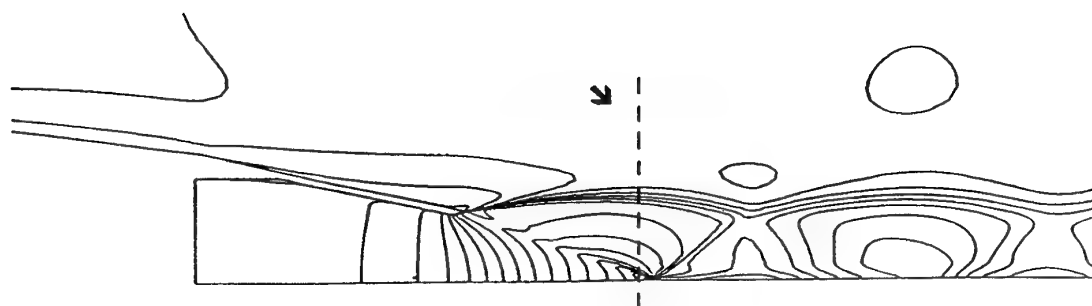
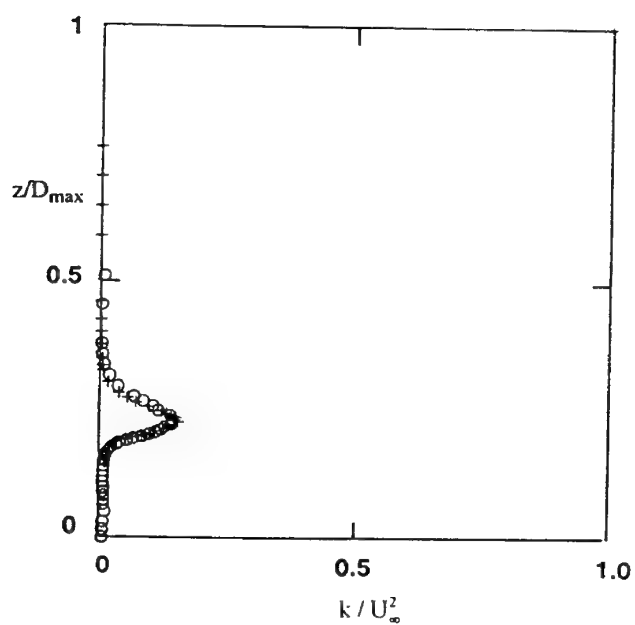
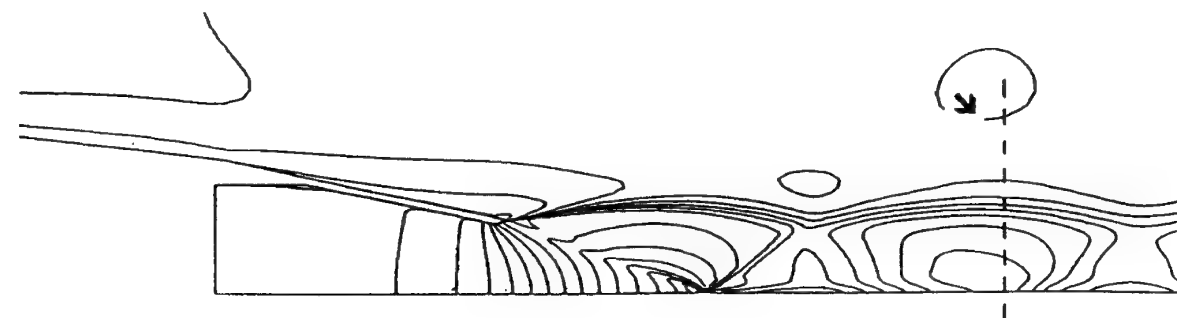
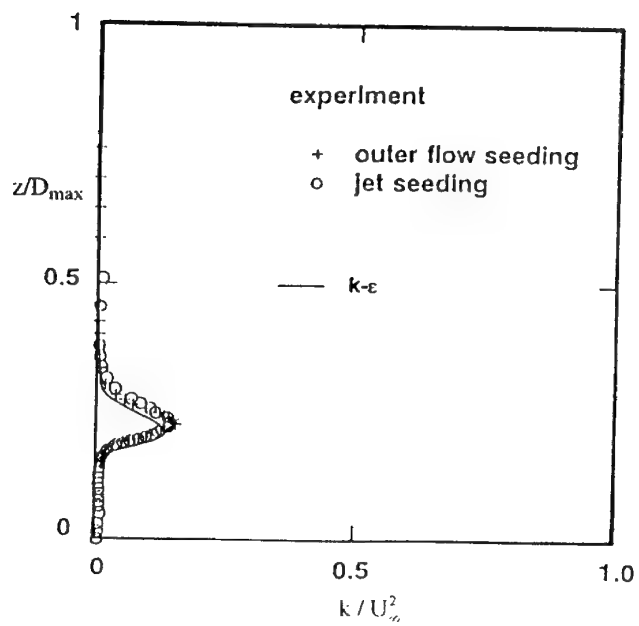


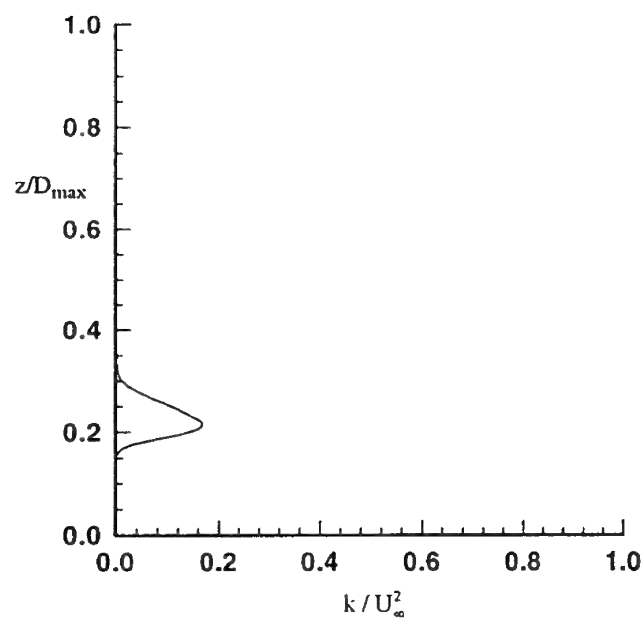
Figure 2.6-35 Case A.2.2 Profiles of Turbulent Kinetic Energy at  $X/D_{\max} = 0.4840$



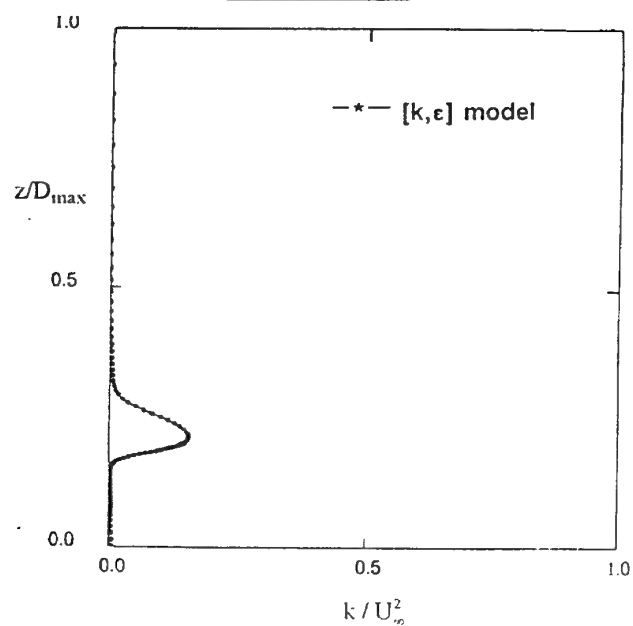
Experiment



Contribution N13



Contribution N10



Contribution N14

Figure 2.6-36 Case A.2.2 Profiles of Turbulent Kinetic Energy at  $X/D_{\max} = 1.2871$

## 2.7 Recommendation for future work

The aim of A test cases was to provide thorough data (mean pressure both at the wall and in the flow, mean velocities as well as turbulent quantities in the flow) on simple configurations. Due to the relative absence of geometrical complexities, and to the wealth of experimental data available, the level of expectation was quite high in terms of prediction quality.

The analysis of the different computational results has revealed that even inviscid flow features (as pressure upstream of an airbody shoulder) were not necessarily well predicted. Although this prediction seemed both basic and straightforward, it should not be overlooked. This relates of course to numerical issues (quantity conservation, form of initialisation, way of conducting the job, convergence...), but also to grid issues (minimum grid density, grid quality criteria...).

As expected turbulence has provided various level of agreement with experimental data. However, the test case A.2 may not have been too selective since no massive separation was expected. A doubt still remains on the turbulent quantities initial values to consider when the computational domain starts within the body.

In general, representativity of the global viscosity should be assessed in a more precise way. Since it is the sum of molecular viscosity, turbulent viscosity (referring to turbulence model) and numerical viscosity (referring to the combinaison of the numerical scheme and the grid discretisation), the final result is the blend of all these factors. It means that any of these points should not be overlooked. In particular, care has to be paid so that turbulent model effects are not buried in numerical viscosity.

Therefore, validation has still to be considered has a priority in the CFD world. Efforts should be pursued to provide experimental test cases for different geometrically simple configurations but very well documented. Use of an advanced and exhaustive metrology, able to deliver data with a high level of confidence both at the wall and in the flow has to be secured. Mean quantities as well as turbulent quantities are sought on an adequate (in terms of density and location) acquisition grid. This should reveal the presence of even minute recirculation zones.

These fundamental test cases will enable the required effort of assessment and validation of modelisations. The answer is required to give confidence in *prediction* of more complex flows which is the aim of CFD since engineers and designers are concerned primarily with *predictions* rather than *postdictions*.

### 3. DESIGN

#### 3.1 Design of Complex 3-D Aircraft Afterbodies - General Considerations

##### 3.1.1 Introduction

The report of the previous AGARD Working Group on afterbody aerodynamics (WG08, Reference 3.1-1) discussed at some length the modelling of axisymmetric afterbody flows, including the representation of jets and model support stings; wind tunnel experimental techniques; and the challenge of three-dimensionality in terms of drag and flow instability. The preceding sections of this report have recapitulated the fundamental flow phenomena and demonstrated the progress which has been made since the publication of Reference 1 in the Computational Fluid Dynamics (CFD) modelling of those phenomena. The following sections go on to discuss the practicability of applying recent CFD method developments to the solution of design engineering problems on complex, three-dimensional afterbodies typical of high performance combat aircraft.

In practice, three-dimensional (3-D) effects appear as soon as it is attempted to integrate an otherwise simple afterbody into an overall aircraft configuration. The task facing the afterbody aerodynamicist involved in project design is to understand how the fundamental flows interact about a complex configuration to produce typical 3-D flow characteristics and to apply that understanding to particular configurations.

The ultimate goal of afterbody design is to contribute to the successful design and release to service of project aircraft. The criteria for success, and therefore the approach to the aerodynamic design of a particular project afterbody, are determined by the role requirements and the relative significance of the various aspects of the project. Hence, the afterbody aerodynamicist must be aware of both the requirements of the project aircraft and the range of techniques which will allow those requirements to be met as accurately, quickly, and efficiently as possible.

Subordinate to the ultimate project goal, the twin objectives of afterbody aerodynamic design are to optimize performance and avoid adverse aerodynamic behaviour such as instability, buffet, or vibration. The former requires the achievement of low drag, the pursuit of which leads to the generation of steep adverse surface static pressure gradients and the deliberate production of high base static pressure coefficients. Both tend to provoke or exacerbate airflow separations, the effects of which can be made worse by energetic turbulence in the base region and in the mixing of the propulsive jet with the free stream. Thus, care is needed in balancing the aerodynamic objectives, whilst not losing sight of the refinement of the overall design (see, for example, Reference 3.1-2).

The following sections review the points at which the afterbody aerodynamicist is involved in a project, the factors influencing afterbody design, and the general tools and techniques available for the design of 3-D afterbodies for project aircraft.

##### 3.1.2 Afterbody Aerodynamics within the Overall Design Process

The life of a particular aircraft project can be described as consisting of a number of contiguous or overlapping phases in time. These phases themselves may be defined in different ways: for the purpose of this section, the following definitions will be used:

- Requirements Phase
- Concept Phase, including Feasibility Studies
- Development Phase, including Risk Reduction, Basic and Detailed Design, and Flight Clearance
- Production Phase, including Production Standard Flight Clearance and Release to Service
- Service, including subsequent modifications.

In addition to these project-specific phases, parallel programmes of supporting and enabling research are usually in progress, focused to a greater or lesser extent on particular project features.

##### 1) Requirements Phase

Afterbody aerodynamic design is not usually a key issue during the Requirements Phase, though advanced warning of the possible need to consider highly novel afterbody / nozzle concepts can be obtained.

##### 2) Concept Phase

During the Concept Phase the afterbody aerodynamicist is usually required to provide advice on choices of engine and nozzle and contribute to performance estimates and trade studies in support of concept and feasibility studies. Care needs to be exercised in ensuring the consistency of thrust and drag book-keeping during trade studies. At this stage any requirements for highly novel designs, for example for thrust vectoring or low observables, ought to be clearly identified.

### 3) Development Phase

The greatest involvement of afterbody aerodynamics usually takes place during the Development Phase. Basic design issues are resolved, the performance assessments made during the Concept Phase are refined, and appropriate activities carried out to identify and reduce the risk areas of the configuration prior to basic design ("lines") freeze.

Typically, project cost and timescale constraints limit the amount of dedicated test data which can be acquired during the early part of the Development Phase. Usually it would be much more useful to have a dedicated afterbody model tested before design freeze, but in practice, because of cost, this model is often one of the last to be manufactured. This limitation forces a reliance on data from generic and supporting research, theoretical and empirical methods, and information from published data.

Following the basic design freeze, detailed design activities are required to be supported. The design of the afterbody is refined and definitive performance information is generated. At this stage, a fully representative aircraft afterbody model is commonly tested, often in conjunction with a model build which is representative of the appropriate six-component forces and moments model used for overall configuration stability, control, and drag investigations. Inputs are generated to the aircraft drag datasets and throttle-dependent engine installation datasets.

The input to clearance for flight is mainly via such performance inputs to the aircraft Operating Data Manual (ODM), and does not usually involve safety-critical items. However, the increasing use of thrust vectoring for control purposes for configurations having either high airframe agility or deliberately reduced "traditional" aerodynamic control necessitates the generation of a detailed, comprehensive, and accurate description, including a numerical model, of jet effects on all forces and moments. In such circumstances the afterbody aerodynamicist is required to co-operate closely with specialists in flight mechanics and Integrated Flight and Powerplant Control Systems (IFPCS) as well as with powerplant manufacturers.

In addition, experience on recent high-performance aircraft has led to an increased emphasis on the prevention of adverse airflow behaviour in the afterbody region, which may take the form of airflow separation effects on stability and control,

buffet, vibration, or hostile acoustic environment. Not all such phenomena are yet identified in flight clearance requirements, but there is an increasing need to ensure their elimination from the design and to demonstrate their absence prior to flight.

Prototype or development test aircraft are usually constrained to a minimum of instrumentation, for which all of the various engineering specialisations must compete. It is therefore unusual for the afterbody aerodynamicist to play more than a monitoring role during development flight testing, possibly with some support to performance verification.

The identification and solution of aerodynamic problems during flight testing are costly, time consuming, highly visible, and hence extremely undesirable, emphasising the need for care and attention to detail during the preceding design stages.

### 4) Production Phase

During the Production Phase the afterbody aerodynamicist may be called on to provide advice and guidance on changes which may be made to configuration, surface finish, excrescence, or sealing details, particularly if the design is rationalized to expedite production. If such configuration changes are made or, for instance, additional sensors installed, revised performance datasets may be required for the production standard flight clearance and for release to service. Apart from these exceptions, the involvement of afterbody aerodynamics in the Production Phase is not usually significant.

### 5) Service

Following the initial release to service, a successful project aircraft will usually proceed through several marks, variants, and modification standards. Many of these may involve the addition of such items as rearward-facing sensors or countermeasures equipment, the installations and fairings of which may require careful integration with the basic design in order not to compromise its aerodynamic behaviour. In addition, it is likely that information will be required concerning thermal, acoustic, and vibration environments, as inputs to equipment requirements.

### 6) Supporting and Enabling Research

In order to ensure an adequate capability to carry out project design tasks when required, it is prudent to conduct a parallel programme of supporting and enabling

research. The minimum content of such a programme should consist of a regular survey of existing knowledge, for example via "open" published literature, to maintain awareness of the state of the art and compile suitable databases.

The development and regular use of theoretical and empirical methods enable their prompt and appropriate use when project tasks require them, secure the benefits from the investment in and use of CFD techniques, and assist in developing and maintaining understanding of the contributory flow phenomena.

Dedicated wind tunnel experiments are frequently considered to be expensive. Nevertheless, wind tunnel testing remains the only currently practical method to obtain information about novel afterbody/nozzle configurations. Care should therefore be exercised to ensure that generic wind tunnel tests produce information with the widest possible relevance and applicability.

In special circumstances dedicated research flight testing may be carried out, but it is the most expensive method of gathering data and its use is likely to be identified closely with larger research or demonstration programmes.

### 3.1.3 Factors Influencing 3-D Afterbody Design

Throughout the design process the afterbody aerodynamicist is required to interface with a number of other specialisations, whose requirements often conflict with those of purely aerodynamic design. The key issues determine the approach to the design and influence the tools and techniques employed to solve design problems.

#### 3.1.3.1 Performance

The fundamental purpose of afterbody aerodynamic design is to achieve the highest possible level of performance, which must remain uppermost in the objectives of the afterbody aerodynamicist, even when taking account of overall aircraft performance and manoeuvre requirements and practical constraints. The achievement of high performance requires in turn a trade-off between drag, weight, and engine thrust subject to installation effects, leading to the choice of nozzle type and propulsion system philosophy.

Having selected the nozzle type, the next task of the afterbody aerodynamicist is to influence the design in order to minimise the airframe drag. Somewhat different approaches to minimum drag design are needed for subsonic, transonic, and supersonic conditions.

Sub- and transonic drag depends primarily on the minimisation of effective base area (see Reference 3.1-1) and judicious choice of afterbody boat-tail curvature (see, for example, Reference 3.1-3). Supersonic afterbody drag is more dependent on interferences between the fuselage and flying surfaces and is more deeply integrated with the drag of the overall configuration.

References 3.1-4, -5, -6, -7 and -8 and subsequent sections of this report contain descriptions of jet and configuration effects, and outline methodologies for drag prediction.

Jet effects at supersonic conditions for fully-expanded convergent-divergent nozzle installations are relatively slight. However, for under-expanded convergent nozzles they become significant, are typically much more pronounced than at subsonic conditions (see Reference 3.1-6), and can be a significant mechanism within the overall aircraft supersonic zero-lift drag.

In addition to the overall guidelines for drag minimisation, some particular issues require careful attention. These include the avoidance of the "scrubbing" of the jet on any parts of the airframe downstream of the nozzle exit, which incurs a high drag penalty, and the design of the "highly matched" propulsion systems which were characteristic of earlier, "point design" aircraft, typically for continuous operation at high supersonic Mach numbers, for example the Lockheed SR-71 and supersonic transports (SST's) such as Concorde. In the case of Concorde, nozzle exit flow conditions were not only carefully controlled to optimise afterbody performance, but also closely integrated with the nozzle and intake secondary flows, providing shock system and intake spillage control (see, for example, Reference 3.1-9).

At the same time as providing guidance for design for optimum performance, it is also necessary to generate data for performance predictions. For this purpose, a knowledge is needed of the weight of the nozzle installation and how it varies for different possible installations.

At this stage it is also necessary to determine the method of thrust and drag accounting (or book-keeping) which is to be used. This leads in turn to a definition of the reference conditions for that part of the aircraft drag which is to be accounted as zero-lift drag of the airframe and that part which is accounted with the throttle-dependent drag term usually assigned to the engine performance dataset (often termed an "installation dataset").

The choice of accounting method is influenced by the role of the aircraft, the choice of engine, the typical operating conditions of the nozzle, and the custom and practice of both airframe and engine

manufacturer. It is therefore inappropriate to provide recommendations on accounting method, apart from the need to ensure consistency.

### 3.1.3.2 Flow Characteristics

It is an important part of the aerodynamic design of a project aircraft afterbody to develop an understanding of the characteristics of the airflow over (and possibly within) the afterbody, in terms of the dominant flow mechanisms, such as vortices and principal interferences, and details such as corners, gullies, and leakage paths, paying particular attention to gross or incipient airflow separations.

The interactions of the afterbody flow with the overall configuration play a significant part in supersonic drag; at subsonic conditions the presence of large aerodynamic interferences can also have a significant effect on drag, for example via strong negative pressure fields, which can also give "early warning" of possible transonic shock formations and the risk of shock-induced separation. Adjacent flying surfaces, such as the empennage or delta wings, are the main contributors to such effects, which are further affected by control surface movement. The tendency towards small, compact configurations also results in close coupling of aerodynamic phenomena and an increased likelihood that external stores will interfere with the afterbody flowfield.

Boundary layer development is of great importance in determining afterbody flow characteristics. It is easily possible for boundary layer thicknesses at the end of the afterbody of even a small military combat aircraft to exceed 0.15m (6ins.) in general, and twice that thickness in gullies or corners. The pursuit of low drag levels, and hence of minimum base areas, steep boat-tail angles, and high base and end-of-boat-tail surface static pressures, results in high adverse pressure gradients which can be sufficient to separate the boundary layer. This effect is more pronounced in corners, such as the junctions between fuselage and flying surfaces, where boundary layers are usually thicker, and in gullies where the three-dimensional divergence of the effective channel tends to increase the pressure gradients further.

Airflow separation, particularly if unpredicted or uncontrolled, is generally undesirable and its avoidance is therefore usually a design aim. It causes increased drag (by adding to the effective base area) and buffet. The separation of airflow on flying or control surfaces can degrade aircraft stability or reduce control power and effectiveness. Separation on the afterbody is further exacerbated by the local adverse pressure gradients, which cause any separations, once established, to spread and generally preclude the possibility of subsequent re-attachment.

Unavoidable separations ought to be controlled, for example by local relaxation of boat-tail angles

at the expense of increased base area or by deliberately fixing the separation by means of local surface discontinuities. In extreme circumstances, the effects of afterbody flow separations can be ameliorated by the use of standard palliatives such as vortex generators, although the local thickness of the boundary layer, together with possible requirements to minimise or avoid excrescences and achieve the smoothest possible external surface, militate against the use of conventional vortex generators.

The susceptibility of the boundary layer to separate can also be influenced by upstream features such as vents or outlets, particularly boundary layer bleed outlets, which may have the effect of introducing additional low-energy air and further thickening the afterbody boundary layer.

The buffet caused by separation on the afterbody is not only transmitted to the airframe as a random vibration, but can also couple with particular airframe vibration modes. Both types of vibration can have detrimental effects on aircrew ride comfort and aircrew and sensor performance (see References 3.1-1 and -2).

In addition to buffet caused by separation, the presence of energetic, large-scale turbulence in the base region and in the jet mixing layer can also result in airframe vibrations without apparent separation.

The need to incorporate moving parts, such as thrust reverser components, or to accommodate relative movement of engine and airframe under aircraft manoeuvre loads results in discrete joints and gaps in the afterbody external surface. If leakage paths exist between such joints and regions of high local pressure, such as the central base, separations can be provoked. Care is therefore needed to ensure adequate sealing in the afterbody region, and such features should be represented as closely as possible on appropriate wind tunnel models.

A good understanding of the local flow characteristics is also necessary in order to determine the best locations for any secondary inlets and outlets which may be required. For example, aircraft environmental control system (ECS) outlets are often located at or near to the rear of the aircraft: a suitable low-pressure region is essential in order to maintain adequate venting and ECS airflow throughout the aircraft. The effect of any auxiliary airflows on the overall afterbody flowfield also needs to be understood.

The adoption of any novel or exotic nozzle types or arrangements also influences the overall afterbody flowfield. Examples include any highly matched propulsion systems involving shock system control, or any configurations in which the nozzle exit is located upstream of the end of the afterbody or of flying surface trailing edges. In the latter cases, jet impingement, jet "scrubbing",



or Coanda Effect can be encountered - or, indeed, be deliberately introduced. The interaction of impinging, attached, or entrained jets with adjacent surfaces is highly configuration dependent and, if introduced, is likely to be one of the dominant flow features of the configuration. It is therefore beyond the scope of the general conclusions of this report and will not be discussed further.

### 3.1.3.3 Stability and Control

The degradation of stability and control characteristics by the onset of airflow separation and the possible use of palliatives to restore adequate margins have been outlined in the preceding section.

Stability and aerodynamic control requirements are the main drivers of the choice of empennage size and location, and need to be incorporated in the design process along with drag and other interference considerations. Thus, close co-operation is required between the afterbody aerodynamicist, who typically represents the interests of performance, and the stability and control specialists in order to ensure the optimum compromise.

Current emphasis on manoeuvrability, airframe agility, vertical/short take-off and landing (VSTOL), advanced short take-off and vertical landing (ASTOVL), and configurations with deliberately constrained control arrangements lead to an increased use of jets for force (e.g. lift) and moment generation. The use of thrust vectoring is of particular interest to the afterbody aerodynamicist. As well as axisymmetric or non-axisymmetric nozzles capable of vectoring in one or more axes, use is also made of novel or exotic nozzle locations, possibly resulting in or making use of jet impingement or Coanda Effect, which were briefly described in the preceding section.

### 3.1.3.4 Buffet, Vibration and Acoustics

Mention has already been made (Section 3.1.3.2) of buffet and vibration resulting from afterbody flow instabilities, both with and without actual airflow separation. Not only are suitable prediction, modelling, and analysis techniques required during the design process: some knowledge is also needed of the basic vibration modes of the complete airframe.

As well as large-scale buffet and vibration phenomena, the presence of the jet produces an acoustic environment which needs to be taken into account and which can be hostile or damaging. Particular examples from recent experience include twin jet plume resonance, sometimes called "screech", which is potentially damaging to structure and equipment, particularly nozzle components, and is therefore of interest to both

airframe and engine manufacturers (see, for example, Reference 3.1-10 and Section 2.1 of this report).

The acoustic environment is also of importance in the choice of sensor locations and the qualification of other equipments. For configurations with the jet exit upstream of the end of the airframe, acoustic fatigue is a significant structural design factor.

### 3.1.3.5 Configuration Integration

The interactions of afterbody aerodynamic characteristics with the overall configuration have been discussed in the preceding sections. The importance of nozzle location choice, supersonic drag, separations, and other interferences between the afterbody, empennage, other adjacent flying surfaces and stores indicate the necessity of the close integration of afterbody design with that of the total configuration.

### 3.1.3.6 Engine Installation Requirements

In addition to the engine/airframe interfaces identified in the preceding sections, certain features and requirements of the powerplant system impinge upon afterbody aerodynamic design.

For example, the adoption of exotic nozzle configurations may result in a requirement for particular geometries or the provision of secondary airflows.

The minimum girth of the afterbody is typically determined by the engine "space envelope", including an allowance for deflections relative to the airframe, which in turn leads to the need to decide on the proportion of aerodynamic load which can be carried on the engine jet pipe and that which must be carried on the airframe. As the rear fuselage structure also carries significant loads from vertical and horizontal tail surfaces, and sometimes wing attachments, the possible use of structurally load-bearing jet pipes should be seriously considered, the potential benefits being offset against issues of engine removal, hot/cold structure interfaces, and maintainability. The need to incorporate engine services such as cooling air inlets, air outlets, drains, and system purge outlets must also be taken into consideration.

Engine removal requirements dictate the size and position of engine bay doors, which require sealing and the definition and maintenance of acceptable surface steps and gaps.

If a particular nozzle is chosen and designed by the airframe - rather than the engine - manufacturer, it is necessary to ensure that the exit area and any area variation are fully compatible with engine operation.

### 3.1.3.7 Structural Considerations

The whole of a project aircraft design is strongly driven to achieve the lowest possible weight. This often results in the need to compromise the design away from a purely aerodynamic optimum, not least in the afterbody region. The afterbody aerodynamicist can help to ensure that the departure from that aerodynamic optimum is as small as possible by participating as closely as possible with the structural design process and providing the most timely and accurate information when required.

The key structural issues affecting afterbody aerodynamic design are likely to be structural space or volume requirements, cooling requirements for mechanical or material purposes, and the acoustic and thermal environments.

### 3.1.3.8 Equipment Installations

Much of the equipment installed in, on, or near the afterbody is usually associated with the powerplant and those systems which extract power from the engine, such as hydraulics and electrical generation. The gearboxes and other ancillary and auxiliary devices and services typically require space, cooling air, and adequate venting, which must not be neglected when making afterbody aerodynamic design assumptions.

Particular additional mechanical equipments frequently incorporated into the aircraft afterbody include a brake parachute and arrestor hook, both of which tend to violate the clean, unbroken external surface which is aerodynamically desirable.

The afterbody and empennage are also increasingly popular locations for rearward-facing sensors or countermeasures equipment, which usually require a space envelope significantly larger than their basic size, to incorporate protection from the thermal and acoustic environments.

### 3.1.3.9 Other Considerations

As well as the factors specifically referred to in the preceding sections, a number of other general design drivers can influence the ability to achieve an aerodynamically optimum design. These principally include manufacturing process requirements; cost; reliability; maintainability; and accessibility.

Afterbody design for low observables is a specialised discipline which is usually role- and configuration-specific and at this time frequently sensitive. Its requirements are sufficiently over-riding that they ought to be identified clearly at the outset of the design process.

### 3.1.4 Tools and Techniques

As in other aerodynamic specialisations, afterbody aerodynamics rests on a foundation of theory, experiment and experience and is subject to the usual advantages and disadvantages of each. The current state of the art in each area is described in some detail in the other sections of this report.

Theoretical methods encompass increasingly capable CFD codes used in isolation; combinations of simple CFD methods with correlations of experimental data; and empirical methods which often consist again of experimental data in conjunction with theoretical techniques such as the various types of area rule or area transfer rule applied in supersonic design optimisation.

The following sections of this report discuss the extent to which existing CFD methods are capable of accurately predicting the various aspects of afterbody aerodynamic behaviour. They can already be used judiciously to investigate particular flow features in detail and develop understanding of the flow mechanisms present on a given configuration, and to predict the gross interferences between main components. It is important to understand the limitations of the methods which are available, and to exploit their respective strengths creatively and effectively.

In addition to CFD methods themselves, the processing of experimental data from unsteady or high-response pressure measurements makes increasing use of the theoretical methods common in flutter or dynamic analysis.

Experimental afterbody aerodynamics is centred on wind tunnel testing of subscale models, usually at high speed. Standard measurement techniques of forces, moments, steady and unsteady pressures, and flow visualisation are employed, with some adaptation to enable measurement on the afterbody as a separate component. Particular attention is paid to the minimisation of support system interference and to the accurate extraction of balance measured force data (see, for example, Reference 3.1-11 and Section 3.3 of this report). Static rig tests may also be used, particularly to characterise nozzle flows.

Flight tests of afterbody aerodynamics are uncommon, and usually associated with the resolution of flight problems. However, the information which they yield can be of considerable value, particularly if comparisons are possible between flight and wind tunnel or theoretical results, and between different flight measured parameters which can assist in identifying the causes and effects of flow phenomena.

Flight also constitutes a significant part of experience, but one to which quantitative values can only infrequently be assigned. There is now a considerable body of experience in afterbody aerodynamics, and most of the phenomena of interest have been known of for a considerable time. The main challenge facing the afterbody aerodynamicist is to interpret the large amount of available information in order to derive design guidelines and develop design methodologies. Previous experience assists in developing a physical understanding of the flows both at and off the surface and in deriving correlations and approximations. Experience from other aerodynamic specialisations also contributes through the adaptation and application of results and guidelines.

### 3.1.5 Concluding Remarks

The design of aircraft is a process which frequently starts at the front and finishes at the back: thus, the afterbody is the region of the aircraft where all the upstream assumptions and approximations tend to be resolved. Similarly, afterbody aerodynamic characteristics are dominated by the effects of viscosity, compressibility, and turbulence and so the common simplifying assumptions of aerodynamic theory provide an incomplete - and at times quite misleading - solution to afterbody flow prediction.

Therefore, the methods employed in afterbody aerodynamic design are of necessity hybrid. Judicious and careful use must be made of a mixture of theoretical and experimental techniques, supplemented by experience which may be obtained either directly or from the published experience of those working in the field.

The process is further complicated by the highly three-dimensional nature of real aircraft afterbodies, the particular interactions characteristic of a specific configuration, and the large number of non-aerodynamic design drivers and influences in the region.

Sufficient knowledge and techniques do, however exist to enable the twin aerodynamic objectives of high performance and good airflow quality to be achieved. Current developments offer the prospects of reduced design timescales and costs; reduced risk; and continuing improvements in the range of configurations which can be confidently dealt with and the degree of performance which can be achieved.

Successful afterbody design relies on the careful integration of existing knowledge, proven techniques, and new developments into a coherent design process.

### 3.1.6 References

- 3.1-1 *Report of the Working Group on Aerodynamics of Aircraft Afterbody*  
AGARD Advisory Report 226  
June 1986
- 3.1-2 Leyland D.C.  
*Lessons from Tornado Afterbody Development*  
AGARD CP339 Paper 8  
1983
- 3.1-3 Shrewsbury, G.D.  
*Effect of Boattail Junction Shape on Pressure Drag Coefficients of Isolated Afterbodies*  
NASA TM-X 1517  
March 1968
- 3.1-4 Presz, W.Jr., Konarski, M., and Grund, E.  
*Prediction of Installed Nozzle Flowfields*  
J. Aircraft Vol. 8, No. 12  
December 1971
- 3.1-5 Bergman, D.  
*An Aerodynamic Drag Study of Jet Engine Nozzles*  
AGARD CP-91-71 Paper 22  
September 1971
- 3.1-6 Stoddart, J.A.P.  
*Jet Effects on Boattail Pressure Drag at Supersonic Speeds*  
AGARD CP-91-71 Paper 23  
September 1971
- 3.1-7 Glasgow, E.R. and Santman, D.M.  
*Aft-End Design Techniques for Twin-Engine Fighters*  
J.Aircraft Vol. 11 No. 1  
January 1974
- 3.1-8 Miller, E.H.  
*Methodology for Analysis of Afterbodies for Three-Dimensional Aircraft Configurations*  
J.Aircraft Vol. 25 No. 5  
May 1988
- 3.1-9 Rettie, I.H. and Lewis, W.G.E.  
*Design and Development of an Air Intake for a Supersonic Transport Aircraft*  
J.Aircraft Vol. 5 No. 6  
November-December 1968
- 3.1-10 Seiner, J.M. and Manning, J.C.  
*Dynamic Pressure Loads Associated with Twin Supersonic Plume Resonance*  
AIAA Paper 86-1539  
June 1986
- 3.1-11 Cassie, A.M.  
*Accurate Drag Estimation Using a Single Component Drag Model Technique*  
AGARD CP 429 Paper 10

### 3.2 The Role of Empirical, Analytical and CFD Methods in the Design Process

In a new fighter design, the airframe propulsion system integration has become significantly more important and complex with the advent of the multimission aircraft in the 70's and in the last decade, when new technologies like enhanced manoeuvrability, high angle of attack capability and stealth have been integrated into this type of aircraft. The mutual interaction that occurs between the nozzle exhaust and the external flow field can alter the pressure distribution on the afterbody region and can produce both internal and external flow separation. Such interactions can result in significant penalties in both aircraft drag and thrust, as experienced by some early twin engine designs (for example G91Y, Tornado, F15).

During a new fighter type aircraft development, different phases must be fulfilled by the design team and for each phase the proper design tools (able to predict the aforementioned penalties) must be used, with the aim to obtain an optimized final result at minimum time and cost. Usually this design process involves the use of the following methods (excluding the experimental tests):

- empirical/analytical methods can be applied in the early stages of the design process, contributing to the configuration trade studies and providing preliminary performance prediction
- computational fluid dynamics (CFD) can be useful in a subsequent design phase in order to obtain a better understanding of experimental test results and solution to enhance geometrical details.

#### 3.2.1 Description

As previously said, the most suitable methods for preliminary design are those based on empirical correlations of parametric wind tunnel tests whereas when a configuration is selected CFD methods are preferred.

The present chapter will describe the following semiempirical methods:

- Integral Mean Slope, IMS
- Integral Mean Slope Truncated, IMST
- Engine/Airframe Integration Methods
- Empirical Supercirculation Effect Correlations

and the latest advances in CFD analysis and design methods. The need for semiempirical methods had its origin in the 70's, with the advent of multimission aircraft, due to inefficiency in

afterbody drag prediction based on pure analytical methods like linearized theory for bodies of revolution or potential flow for three dimensional configurations. These methods were available and compatible with the computer speed and memory of those years. An example of analytical methods validation is given in [3.2-1], where some of these methods were evaluated for predicting the thrust and afterbody drag for a twin-nozzle aircraft configuration. A summary list of the analytical methods investigated in those years is presented in the following table.

APPLICATION	METHOD
SUBSONIC EXTERNAL FLOW	- EQUIVALENT BODY/POTENTIAL FLOW ANALYSIS - * 3-D POTENTIAL FLOW - * P&WA 3-D TRANSONIC ANALYSIS - SECTOR ANALYSIS/MOC - * CORRELATION
SUPERSONIC EXTERNAL FLOW	- EQUIVALENT BODY/MOC - WAVE DRAG ANALYSIS - SECTOR ANALYSIS/MOC - * CORRELATION
INTERNAL FLOW	- * AEDC-ETTF TIME DEPENDENT ANALYSIS - * MOC - SECTOR ANALYSIS/MOC - * CORRELATION
ANNULAR BASE	- KORST ANALYSIS - * MODIFIED BRAZZEL/HENDERSON EMPIRICAL

\* : Recommended Methods

[3.2-1] concluded that "of the analytical methods investigated, none are recommended for predicting afterbody drag". Thus, to understand the flow behaviour around a complex 3D aircraft afterbody and define design guidelines, a series of parametric wind tunnel tests were developed. This wind tunnel campaign, carried out both in USA and Europe [3.2-1 - 3.2-6], were focused on exploring the effects of the most important parameters affecting the afterbody drag like:

- Mach number, nozzle pressure ratio, Reynolds number, boundary layer displacement thickness, jet temperature
- Aft end area distribution, twin nozzle spacing ratio, boattail angle, interfairing type and length, presence of tails and position, base area
- Nozzle type, i.e. convergent, convergent-divergent with and without secondary flow, unshrouded and shrouded plug, single-expansion ramp nozzle (SERN), 2D nozzle etc.

In recent years the improvement in computer speed and memory has allowed efficient solutions of the Euler and Navier - Stokes equations. The use of CFD methods is still too expensive for an extensive application in preliminary design. However good advances have been made in the last years, to define efficient CFD analysis and design methods [3.2-7 - 3.2-10]. CFD analysis methods are very useful to understand flow physical phenomena in the propulsion integration area. These phenomena include 3-D/vortical flow, thick boundary layer with adverse pressure gradients, separated flow, boundary layer/shock interactions, shear layer mixing and internal flow interactions. These phenomena usually have very complicated structure and sometimes are seldom identified from experimental test results and visualizations, so CFD analysis methods help to locate afterbody zones affected by the described phenomena. Present CFD design methods can be categorized as follows:

- Design by analysis
- Inverse design
- Optimization

but the use of them has been limited up to now for several reasons. These reasons can be summarized by the following observation:

- in order to model the correct flow physics, higher order codes must be used
- use of higher order codes implies difficulty in code tuning, so that the validation phase of the code appears to continue endlessly and the design application never seems to start
- CFD design techniques can involve many iterations of CFD solutions, so this design process can become expensive very rapidly
- except for design by analysis, the design logic for more automated applications is still in an early stage of development.

### 3.2.1.1 Integral Mean Slope

As a result of the mentioned parametric wind tunnel tests (examples are in [3.2-1 - 3.2-6]), data banks were established which allowed the definition of a drag correlating parameter or shape factor, based on the fact that the pressure drag is significantly affected by cross sectional area distribution, especially in transonic and supersonic speed regimes, as proved by Whitcomb et al. with the area rule concept [3.2-11 - 3.2-13]. Swavely and Soileau [3.2-14], from area rule considerations, defined this shape factor, supposing that it was

related to the rate of progression of afterbody cross section. The relation which came out was the projected area weighted, non-dimensionalized slope of the cross sectional area distribution of the afterbody. This shape factor was named the Integral Mean Slope, IMS [fig. 3.2-1]

$$IMS = \frac{-\int_{A_9/A_{10}}^{1.0} \frac{d(A/A_{10})}{d(X/D_{eq})} d(A/A_{10})}{1 - (A_9/A_{10})}$$

When afterbody drag data for afterbodies of different geometrical characteristics were plotted as a function of the relative IMS parameter, a good correlation was found [fig. 3.2-2].

### 3.2.1.2 Integral Mean Slope Truncated, IMST

Data obtained from tests performed after the original correlation showed that IMS failed for certain configurations characterized by afterbody cross section distributions where regions with steep slopes caused flow separation. A correction of this problem was found [3.2-15] by defining a maximum slope of the non-dimensional area distribution which can be used in the IMS calculation [figs. 3.2-3, 3.2-4]. The defined maximum slope is substituted for the real slope at each step of the IMS calculation where the real slope exceeds the maximum. The best data correlation was obtained by defining an optimum maximum slope as a function of Mach number.

Further correlations demonstrated that the data considered, when corrected by a  $\Delta CD$  for tail type, varied almost exactly as the IMST parameter raised to the 2.77 power and so a drag parameter, function of Mach number only, was defined [fig. 3.2-5 and 3.2-6]. This drag parameter allows a first preliminary afterbody drag estimation. However it is not enough when a determination of integrated airframe-nozzle performance is required. For conducting mission analysis studies, during the preliminary design of a fighter type aircraft and in order to define a baseline configuration on which to perform initial wind tunnel tests, a better empirical method is required.

### 3.2.1.3 Engine/Airframe Integration Methods

Methods able to predict internal nozzle performance and aft-end drag have been developed [3.2-1, 3.2-16, 3.2-17]. These methods are based almost entirely on empirical correlation of parametric experimental data and they are capable of generating the installed thrust-minus-drag data, required for conducting mission analysis studies of fighter type aircraft. Usually, to predict the nozzle

thrust and discharge coefficients, semiempirical correlations are employed in conjunction with one-dimensional flow theory relationships. To estimate the aft-end pressure drag, correlations based on IMST coupled with relationships from analytical methods, are adopted to interpolate the cited experimental data base. The commonly used analytical methods relationships are those coming from:

- linearized theory for bodies of revolution
- potential flow for 3D configurations
- method of characteristics.

Depending on the flow regime on which the estimation has to be made. To predict annular base drag, other empirically based correlations are adopted in the engine/airframe integration methods, like that of Brazzel-Henderson [3.2-18], just to cite one of the most famous and useful. Analysing and correlating experimental data bases, other semiempirical corrections have been developed and integrated in these methods in order to account for the effect of :

- empennage presence and position [3.2-19-3.2-22] see fig. 3.2.7 and 3.2.8
- interfairing type and length [3.2-1, 3.2-2, 3.2-16] see fig. 3.2-9 and 3.2-10
- non-axisymmetric nozzle [3.2-19, 3.2-21 and 3.2-22], see fig. 3.2-7 and 3.2-11 - 3.2-14

on the afterbody drag.

Figures 3.2-15a, 3.2-15b and 3.2-16 shown examples of logical organization for the described methods.

#### 3.2.1.4 Empirical Supercirculation Effect Correlations

Non-axisymmetric nozzles are typically employed to enhance manoeuvrability, high angle of attack capability and stealth characteristics on new generation advanced fighters.

When nozzle exits are located near or at the trailing edge of a primary lifting surface, the vectoring of the jet induces a favourable external aerodynamic effect, by means of the so called "supercirculation effect", improving the lift to drag ratio at positive thrust vector angles [3.2-23 - 3.2-26]. Some dedicated wind-tunnel tests have been performed [3.2-27, 3.2-28] and from these results, correlations of the induced effects ( $CL_r$ ,  $CD_r$  and  $Cm_r$ ) have been formulated [3.2-29] in order to provide generalized design guidelines and performance prediction (see fig. 3.2-17 - 3.2-20). These correlations have been developed considering the similarities between the effects of a trailing edge

flap deflection and a vectored jet on a lifting surface. The jet deflection affects the wing circulation like a flap by means of its jet sheet. However, unlike the flap, the vectored jet has a variable penetration depth which is dependent upon the classical parameters:

- Mach number
- Nozzle Pressure Ratio
- Thrust vector angle
- Power setting

#### 3.2.1.5 CFD Design Methods

As previously stated present CFD design methods can be categorized as follows:

- Design by analysis
- Inverse design
- Optimization

The first design process implies:

- CFD analysis of a defined configuration
- Modify the configuration on the basis of CFD results
- CFD analysis of the modified configuration
- Iterating as necessary

Of course the success of this trial and error design method, depends on a lot of factors that can include experience, intelligence and, why not, luck of the team. An example of a design by analysis is in [3.2-30] (see fig. 3.2-21).

The inverse design process utilizes a CFD code with a design logic which will output the required configuration geometry to provide the input design pressure distributions. Of course this requires prior knowledge of the optimum or desired flow property on the part of the CFD analysts.

Configuration optimization by means of CFD design application implies computing the geometry required to optimize vehicle performance, for example lift, drag or thrust, rather than providing a geometry for some predetermined flow property (pressure distribution or velocity profile for example) which may or may not be an optimum.

The logic involved with this design process requires that a large matrix of geometry modifications must be computed, to define which geometry parameters to modify and how to modify them. Of course this procedure must be iterated until an optimum is reached. Because of cost most CFD design optimization to date have used lower order codes or simple geometry.

The last two design methods are still in an early stage of development and up to now it has not been possible to collect references with examples of



applications in the field of engine/airframe integration for complex 3D afterbodies.

In general terms CFD analysis offers a more rigorous approach to define afterbody performance during the design phase, with substantially increased complexity and cost, if compared with other methodology. The necessity for global assumptions regarding the flow is avoided, although localized assumptions (turbulence model) are required. CFD has, in general, three types of roles in the design process. These different roles are to provide :

Qualitative predictions describing the key features of the flowfield, to gain understanding (e.g., graphics identifying key boundary layer interactions).

Incremental predictions to quantify the differences in the flows due to variations in geometry or flow conditions (e.g., jet effects drag increments).

Quantitative predictions to produce absolute values of key performance parameters such as afterbody drag.

At present, the chief contribution of CFD probably is in the area of qualitative predictions, and some types of incremental predictions.

### **Qualitative Predictions**

Realistic 3-D afterbody flowfields feature very complex viscous interactions. These involve both boundary layer interactions and free shear layer/wake interactions. To improve the design, detailed information is needed on the behavior and the key contributors to these interactions. This information can be obtained through complex and expensive wind tunnel testing, through designers' insight, through correlations of existing data, or through CFD analysis.

In this role, either Euler or Navier-Stokes analyses can be valuable. The key interactions are all viscous dominated. However, important design guidance often can be obtained more rapidly through interpretation of inviscid (Euler) predictions. These inviscid predictions provide key information on pressure gradients, shock locations and strengths, and convergence or divergence of streamlines. Much information on boundary layer behavior can be inferred from these data by a knowledgeable engineer.

A more direct approach is to compute the viscous flow directly using a Navier-Stokes method. This application places high demands on the turbulence model (see previous discussion, Section 2.3).

A key to success is to understand any biases in the CFD tools that are employed. The CFD code need not be perfect, so long as the engineer understands

the limitations in its predictions.

For example, does the code tend to predict separation adequately, but predict reattachment too far downstream? With a good understanding of any systematic prediction errors, valuable and detailed insight into the physical flowfield can be gained .

### **Incremental Predictions**

CFD methods are being used increasingly to provide quantitative predictions of the incremental differences in performance quantities such as afterbody drag. These increments may be in either of two forms:

Geometry Increments - to quantify the impact of changes in the design, and

Flow Condition Increments - to compute the variations in drag (for example) due to changes in Mach number or nozzle pressure ratio.

Two key assumptions are embedded in this approach : (1) any errors in the CFD predictions, while they may be unknown, are of a bias rather than random nature, and (2) these errors depend (mainly) on parameters which are not varied. With maximum consistency, a systematic bias error ( though it may be unknown) can be eliminated from the incremental data.

An incremental prediction is untrustworthy if either solution in the increment involves flow physics for which the CFD method exhibits (apparently) random errors. A key example of this would be afterbody flows with extensive boundary layer separation.

Thus, incremental predictions usually find their highest value in evaluating modest changes of geometry changes which do not alter the main characteristics of the flow. Further, it is essential (at present) to maintain consistency in the grid, the operation of the turbulence model, and other elements of the solution.

### **Quantitative Predictions**

The goal of all flow analysis methods is to provide reliable quantitative predictions of key performance parameters (e.g., drag) to a meaningful level of precision. Portion of the Review of CFD Predictions (Section 3.5) is directed toward this issue.

However, it seems safe to say that the ability of CFD analysis to provide quantitative predictions of drag consistently to useful accuracy (say, within two drag counts) is not yet accepted. Exception can be found only in well-tested narrow classes of relatively simple configurations. Accurate

predictions of drag for complex 3-D afterbodies apparently will continue to be a challenge to the CFD community for several years.

### **3.2.2. Use**

The semiempirical methods described find their correct application in the conceptual/preliminary design phase of aircraft characterized by a complex 3D afterbody. During this phase, the design team must develop the most effective configuration which meets the defined requirements.

The final configuration is the result of a lot of system integration iterations. Therefore in this phase the designer needs tools that summarize experience and new technologies in each field.

A draft method like IMST is of course too simple to be used in complex trade studies, but a proper role can be found in conceptual activities aimed at first screening. Methods like those of [3.2-1, 3.2-16, 3.2-17 ] are very useful in the conceptual/preliminary design phase, because of their ability to drive the designer in trade studies of the engine/airframe integration concept and to give parametric trends on which to weigh the pros and cons of different solutions.

The use of CFD analysis and design methods, due to their complexity both in grid generation and methods definition, is recommended during final stage design phase with the aim to well understand physical flow phenomena to enhance the final configuration.

### **3.2.3. Needs**

To continue their effectiveness in the design application, the described methods need to be further developed, in order to enhance the quality of their results. The following needs are recognized :

- validation and upgrading of experimental data base, considering new advances in airframe and engine technology
- development of CFD methods, to obtain better experimental data correlations
- increased exchange among experimental and CFD specialists in order to enhance CFD design logic
- increased computer speed and memory in order to allow a real optimization design with higher order CFD codes.



### 3.2.4 Reference

- [3.2-1] Glasgow E., Santman D., Miller L. et al.  
"Experimental and analytical determination of integrated Airframe-Nozzle performance"  
AFFDL-TR-72-101, 1972 Vol. I et II
- [3.2-2] Aulehla F., Lotter K.  
"Nozzle/Airframe interference and integration"  
AGARD LS 53, paper 4, 1972
- [3.2-3] Price E.A.  
"Afterbody drag investigation of a twin-nozzle fighter type model at Mach numbers from .6 to 1.5"  
AEDC-TR-72-87
- [3.2-4] "Improved Nozzle testing techniques in transonic flow"  
AGARD-AG-208
- [3.2-5] Reubush D.E.  
"Effects of fineness and closure ratios on boattail drag of circular arc afterbody models with jet exhaust at Mach numbers up to 1.3"  
NASA TN D-7163, 1973
- [3.2-6] Pozniak O.M., Haines A.B.  
"Afterbody drag measurement at transonic speeds on a series of twin and single jet afterbodies terminating at the jet exit"  
ARC paper 1266, 1973
- [3.2-7] Leavitt L.D., Berrier B.L.  
"Transonic Propulsion Aerodynamic Research at NASA Langley Research Center"  
SAE 921937, 1992
- [3.2-8] Chen H.C., Su T.Y., Kao T.J.  
"A general multiblock Euler code for propulsion integration, Volume I: Theory document"  
NASA CR-187484, 1991
- [3.2-9] Abdol-Hamid, Khaled S.  
"Application of a multiblock/multizone code (PAB3D) for the three-dimensional Navier-Stokes equations"  
AIAA paper 91-2155, 1991
- [3.2-10] Balakrishnan L., Abdol-Hamid K.  
"A comparative study of two codes with an improved two-equation turbulence model for predicting jet plume"  
AIAA paper 92-2604, 1992
- [3.2-11] Whitcomb R.T.  
"A study of the Zero-Lift drag rise characteristics of wing body combinations near the speed of sound"  
NACA 1273, 1956 (Supersedes NACA RM L52H08, 1952)
- [3.2-12] Jones R.T.  
"Theory of wing-body drag at supersonic speeds"  
NACA 1284, 1956 (Supersedes NACA RM A53H18a)
- [3.2-13] Eminton E., Lord W.T.  
"Note on the numerical evaluation of the wave drag of smooth slender bodies using optimum area distribution for minimum wave drag"  
Journal of the Royal Aeronautical Society, Vol. 60, No. 541, 1956
- [3.2-14] Swavelly C.E., Soileau J.F.  
"Aircraft aft body/propulsion system integration for low drag"  
AIAA paper No. 72-1101
- [3.2-15] Brazier M.E., Ball W.H.  
"Accounting of aerodynamic forces on airframe/propulsion system"  
AGARD CP 150, paper 22, 1974
- [3.2-16] Boppe C.W.  
"Aircraft drag analysis methods"  
AGARD-R-783, paper 7, 1991
- [3.2-17] Miller E., Delaney F.J.  
"Level II nozzle/afterbody installed performance prediction program"  
AFWAL TR-88-3004, 1988
- [3.2-18] Brazzel C.E., Henderson J.H.  
"An empirical technique for estimating power-on base drag of bodies of revolution with a single jet exhaust"  
AGARD CP No. 10, 1966
- [3.2-19] Henderson W.P.  
"Propulsion integration for military aircraft"  
SAE 892234, 1989
- [3.2-20] Leavitt L.D.

"Effect of empennage location on twin-engine afterbody/nozzle aerodynamic characteristics at Mach numbers from .6 to 1.2"

NASA TR 2116, 1983

vectoring/reversing non-axisymmetric nozzle"

Journal of aircraft, Vol. 16, August 1979

[3.2-21] Capone F.J., Carson G.T.

"Effects of empennage surface location on aerodynamics of a twin engine afterbody model with non-axisymmetric nozzles"  
NASA TP 2392, 1985

[3.2-30] Jones W.T., Abdol-Hamid K.S.

"Computational analysis of drag reduction techniques for afterbody/ nozzle/ empennage configurations"  
SAE 912127, 1191 .

[3.2-22] Bangert L.S., Leavitt L.D., Reubush D.E.

"Effects of afterbody boattail design and empennage arrangement on aeropropulsive characteristics of a twin-engine fighter model at transonic speeds"  
NASA TP 2704, 1987

[3.2-23] Gal-Or B.

"Vectored propulsion, supermaneuverability and robot aircraft"  
Springer Verlag, 1990

[3.2-24] Capone F.J., Reubush D.E.

"Effects of varying podded nacelle-nozzle installations on transonic aeropropulsive characteristics of a supersonic fighter aircraft"  
NASA TP 2120, 1983

[3.2-25] Bowers D.L.

"Aerodynamic effects induced by a vectored high aspect ratio non-axisymmetric exhaust nozzle"  
Journal of Aircraft, Vol. 16, August 1979

[3.2-26] Capone F.J.

"Supercirculation effects induced by vectoring a partial span rectangular jet"  
Journal of Aircraft, Vol. 12, August 1975

[3.2-27] Capone F.J.

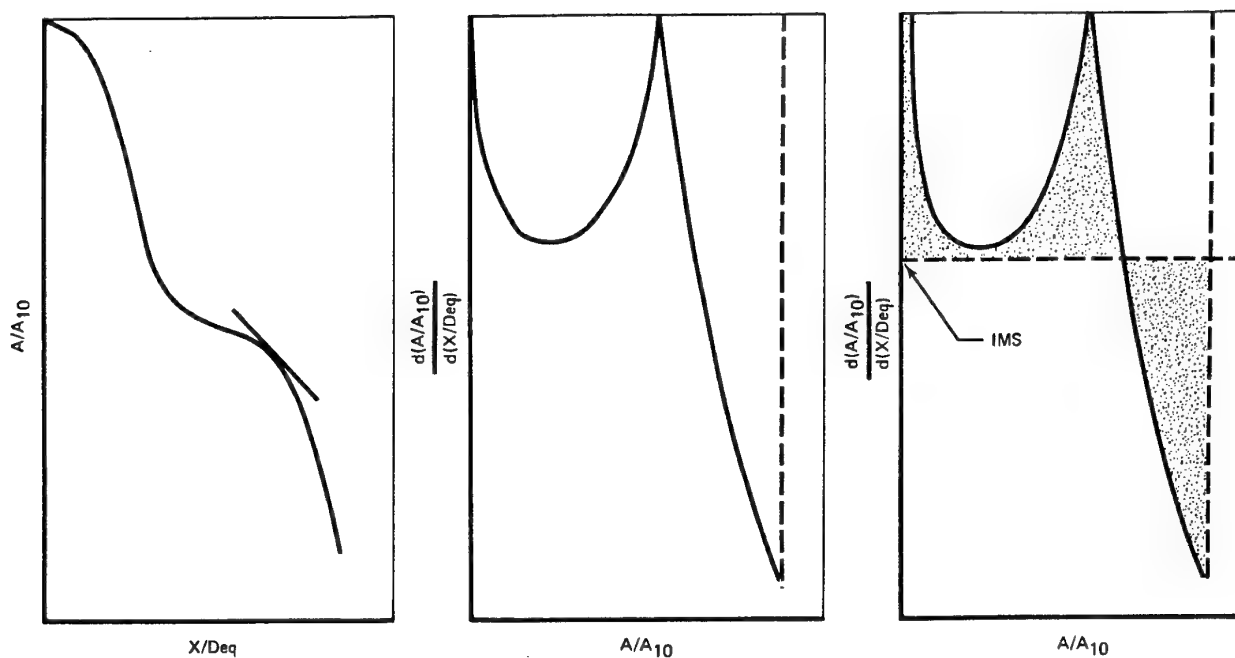
"A summary of experimental research on propulsive lift concepts in the Langley 16-ft transonic tunnel"  
Journal of Aircraft, Vol. 13, October 1978

[3.2-28] Hiley P.E., Kitzmiller D.E., Willard C.M.

"Experimental evaluation of non-axisymmetric exhaust nozzles"  
McDonnell Aircraft Co.  
AFFDL-TR-185, 1978

[3.2-29] Hiley P.E., Kitzmiller D.E., Willard C.M.

"Installed performance of



$$IMS = \frac{\int_{A_g/A_{10}}^{1.0} \frac{d(A/A_{10})}{d(X/Deq)} d(A/A_{10})}{1.0 - (A_g/A_{10})}$$

Fig. 3.2-1 Integral Mean Slope Concept from [3.2-14]

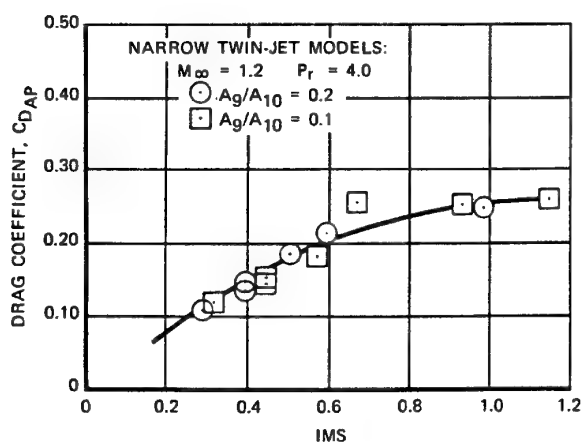


Fig. 3.2-2 Integral Mean Slope Correlation of Afterbody Data, from [3.2-14]

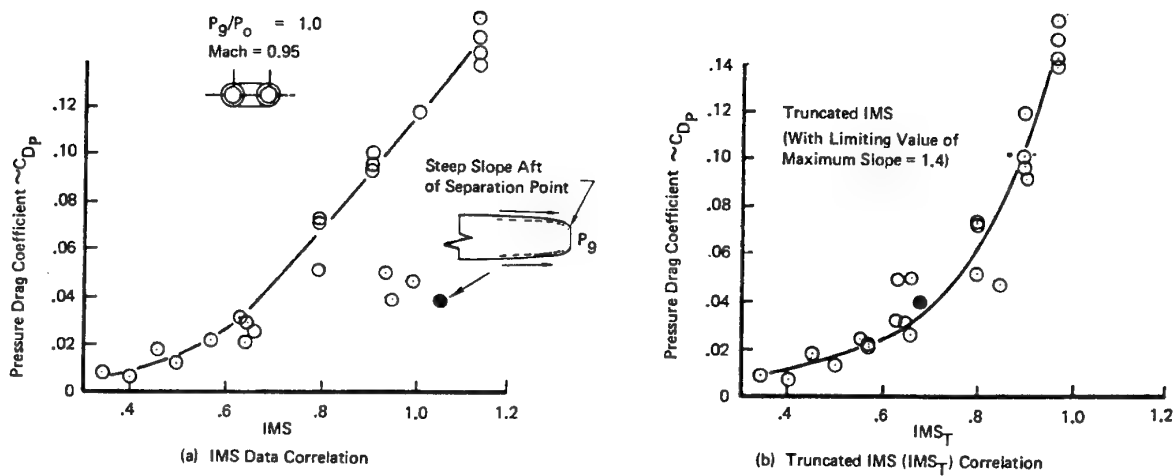


Fig. 3.2-3 IMS and IMST Data Correlation, from [3.2-15]

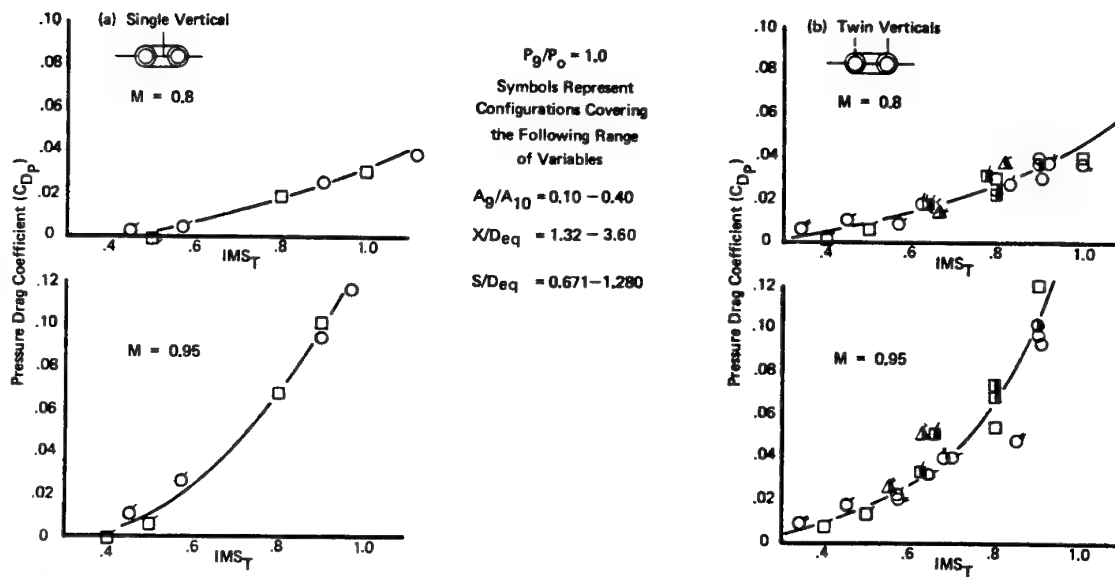


Fig. 3.2-4 Drag Correlation for Single and Twin Vertical Tail Configuration, from [3.2-15]

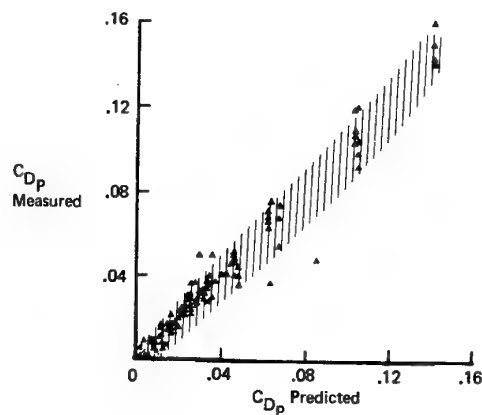


Fig. 3.2-5 Correlation Method Errors, from [3.2-15]

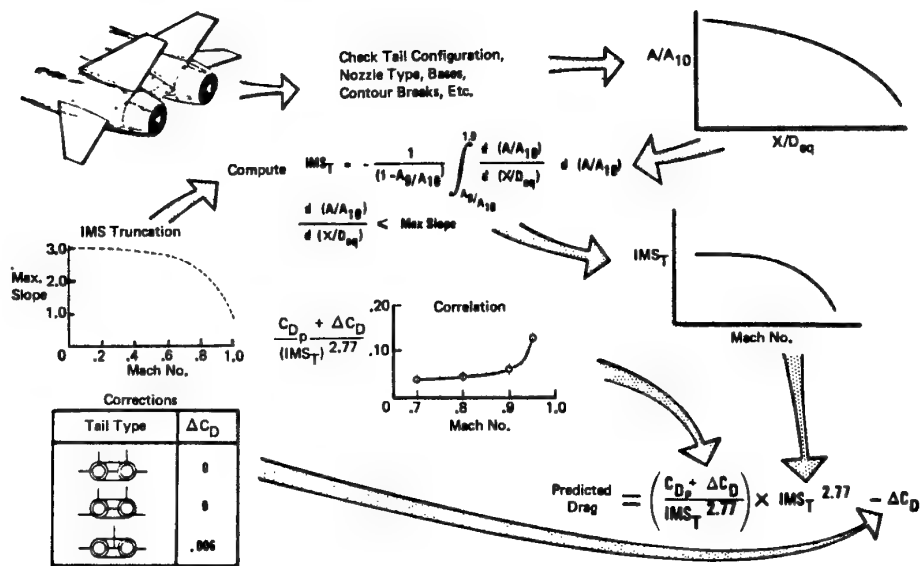
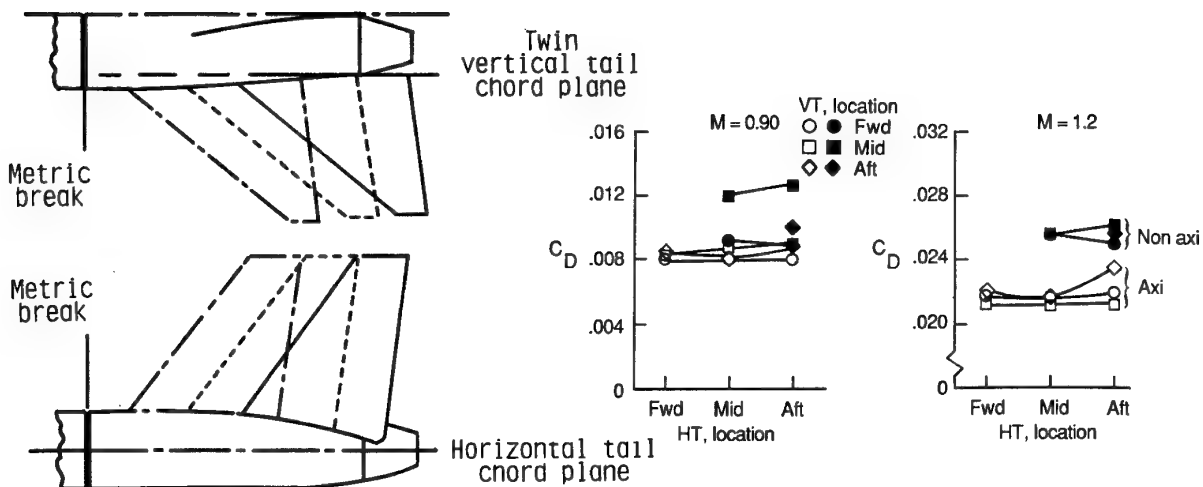


Fig. 3.2-6 Drag Prediction Procedure, from [3.2-15]

Fig. 3.2-7 Effect of horizontal and vertical tails on total nozzle/afterbody drag  $\alpha = 0^\circ$ , scheduled NPR, dry power, from [3.2-19]

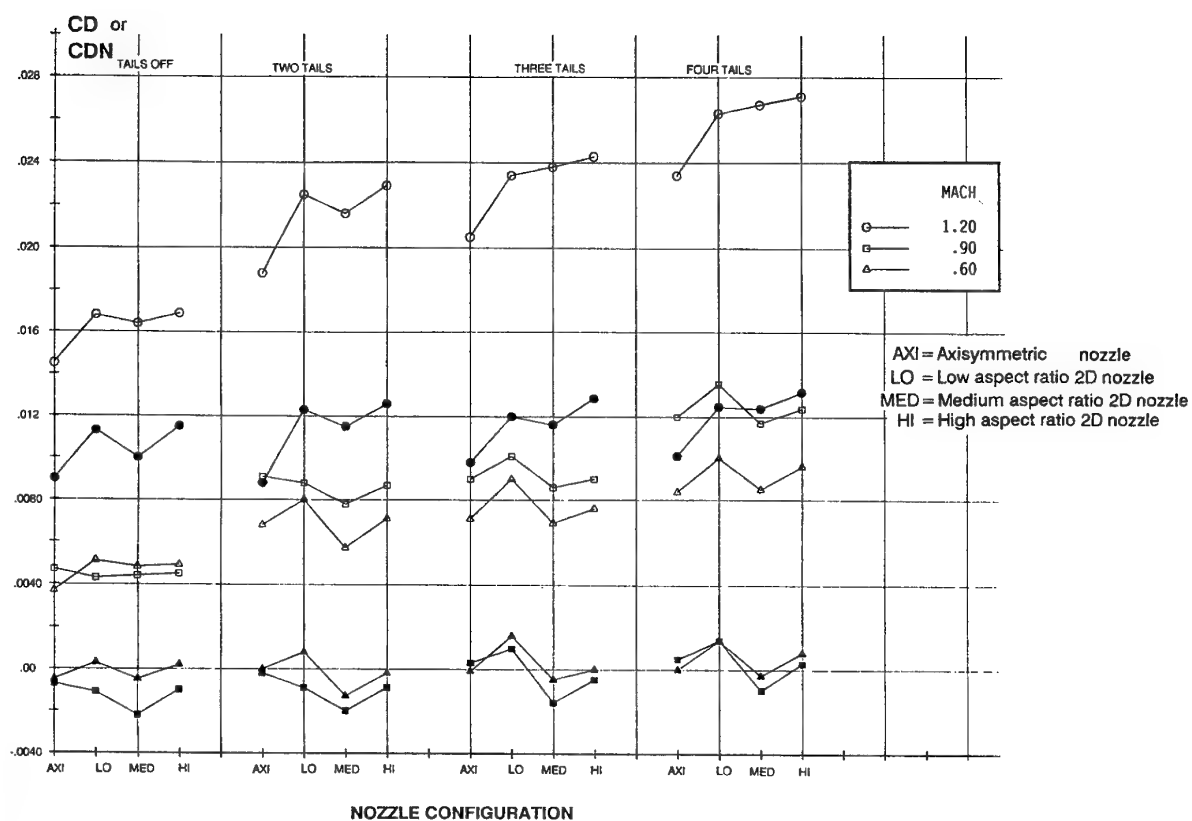


Fig. 3.2-8 Effect of nozzle-tail combination on drag coefficient of entire aft end and nozzle drag coefficient with  $\alpha = 0^\circ$  and  $\text{NPR} = 5.6$  at  $\theta_v = 0^\circ$ . Open symbols denote  $C_D$  solid symbols denote  $C_{Dn}$  from [3.2-22]

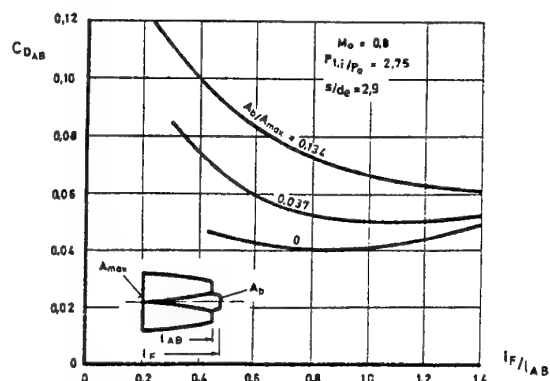


Fig. 3.2-9 Effect of interfering length on drag for constant base areas, from [3.2-2]

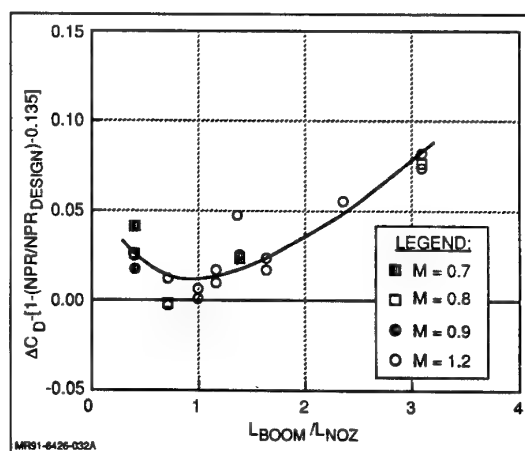


Fig. 3.2-10 Boom Correlation - Maximum A/B Nozzle, from [3.2-16]

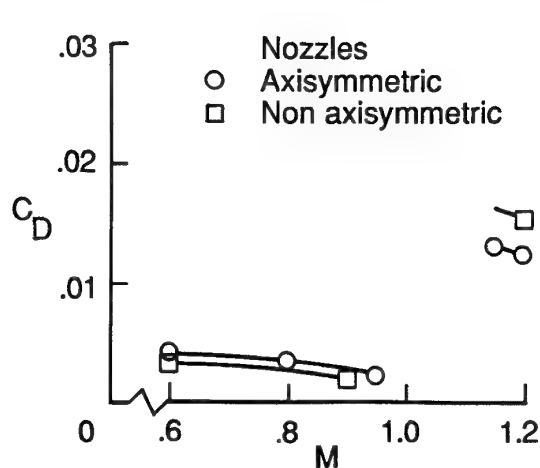


Fig. 3.2-11 Drag comparison for model with various nozzle types  $\alpha=0^\circ$ , scheduled NPR, dry power, and HT/VT-off, from [3.2-19]

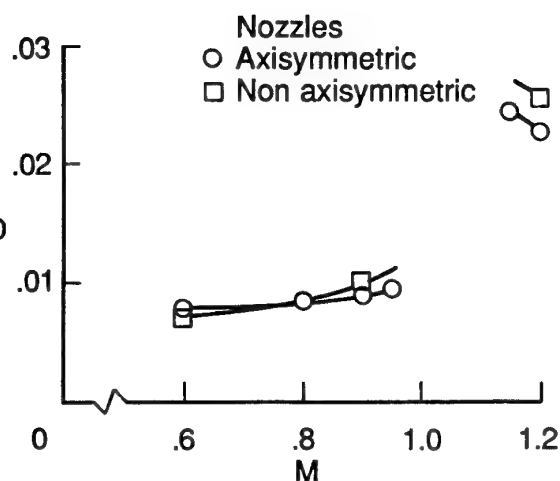


Fig. 3.2-12 Drag comparison for model with various nozzle types  $\alpha=0^\circ$ , scheduled NPR, dry power, and HT/VT-on (aft location), from [3.2-19]

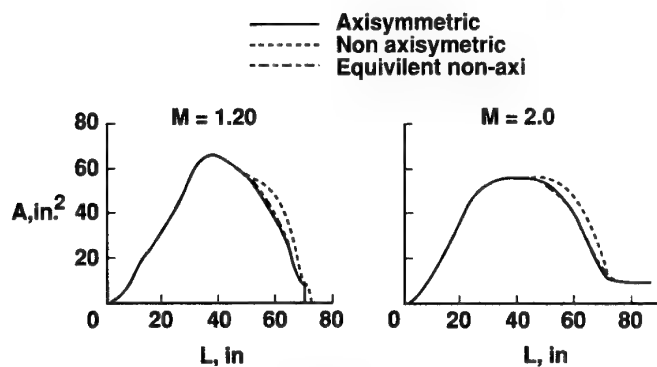


Fig. 3.2-13a Area distributions for the twin-engine configurations, from [3.2-19]

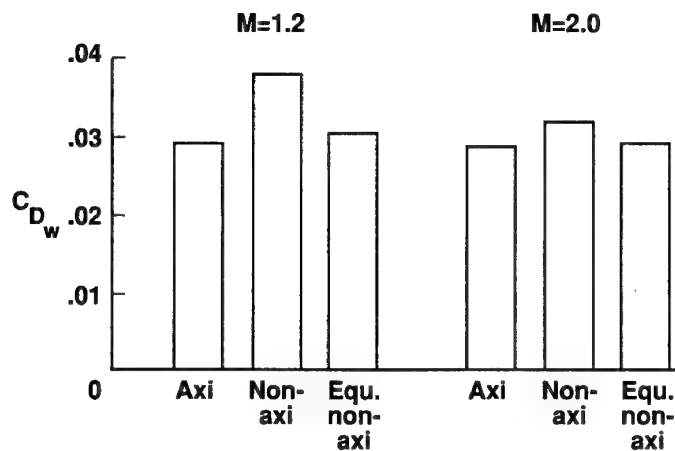


Fig. 3.2-13b Wave drag calculations for the twin-engine configurations, from [3.2-19]

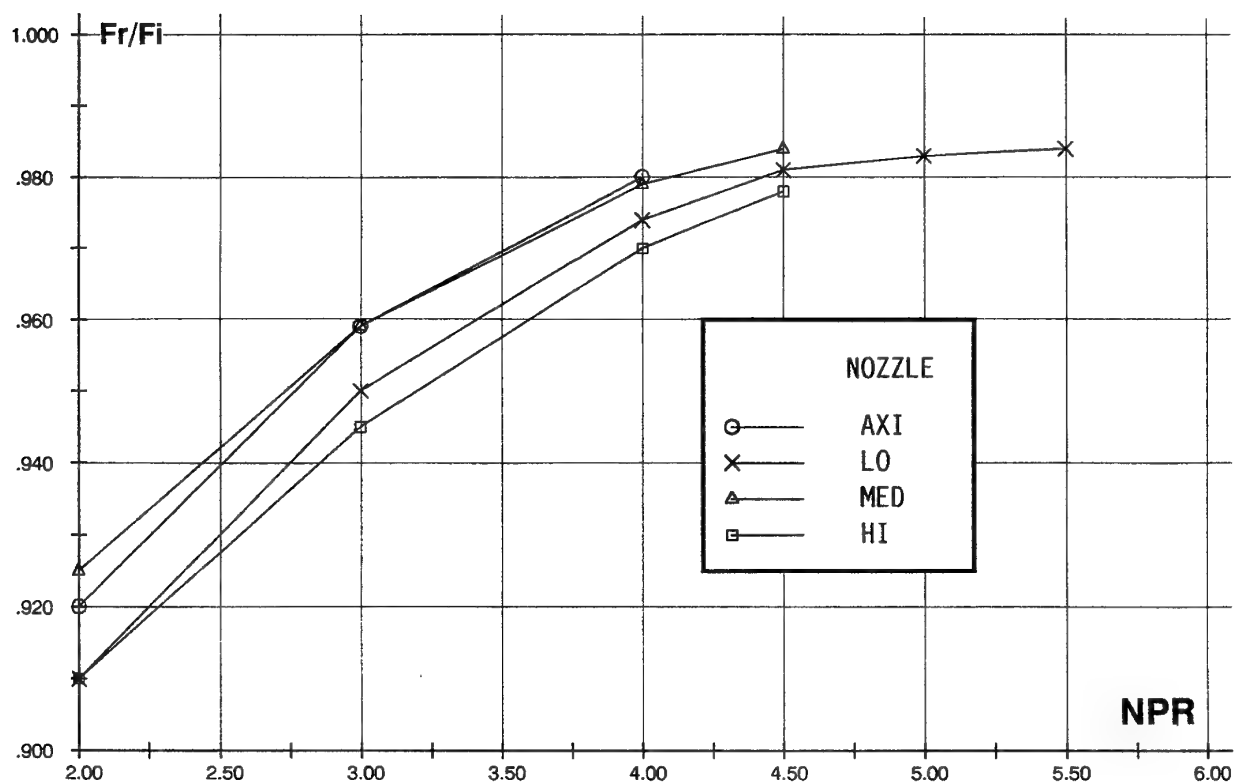


Fig. 3.2-14 Nozzle static internal performance, from [3.2-22]

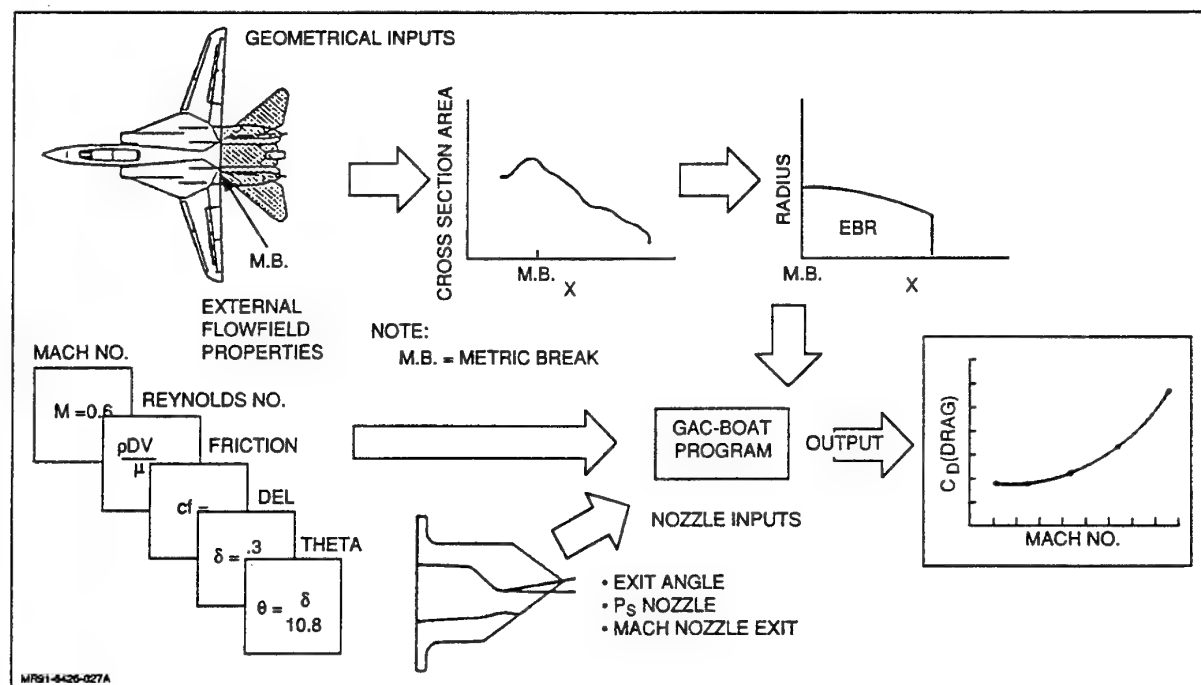
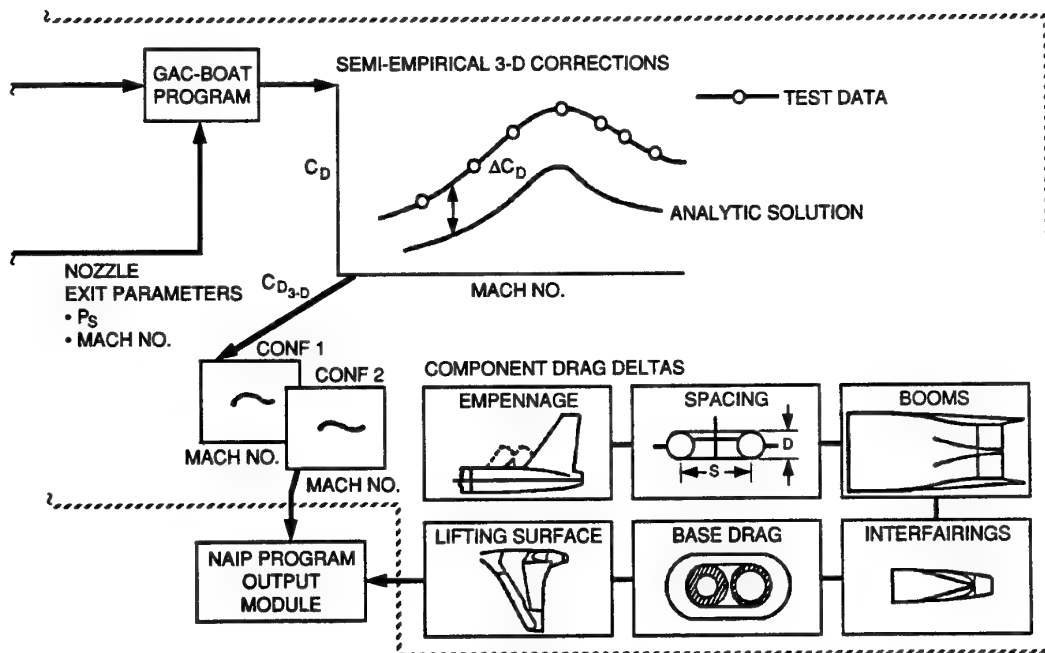
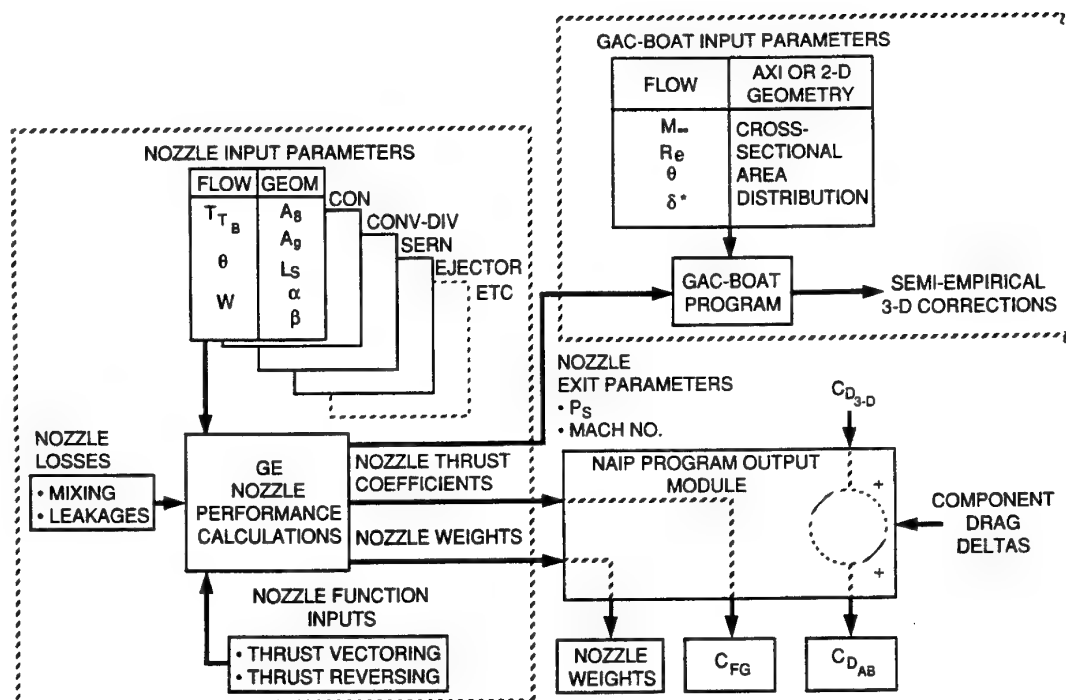


Fig. 3.2-15a Equivalent Body of Revolution Methodology Using GAC-BOAT Code, from [3.2-16]





MPN1-6428-028

Fig. 3.2-15b Level II Nozzle/Afterbody Installed Performance Prediction Program, ref. [3.2-16]

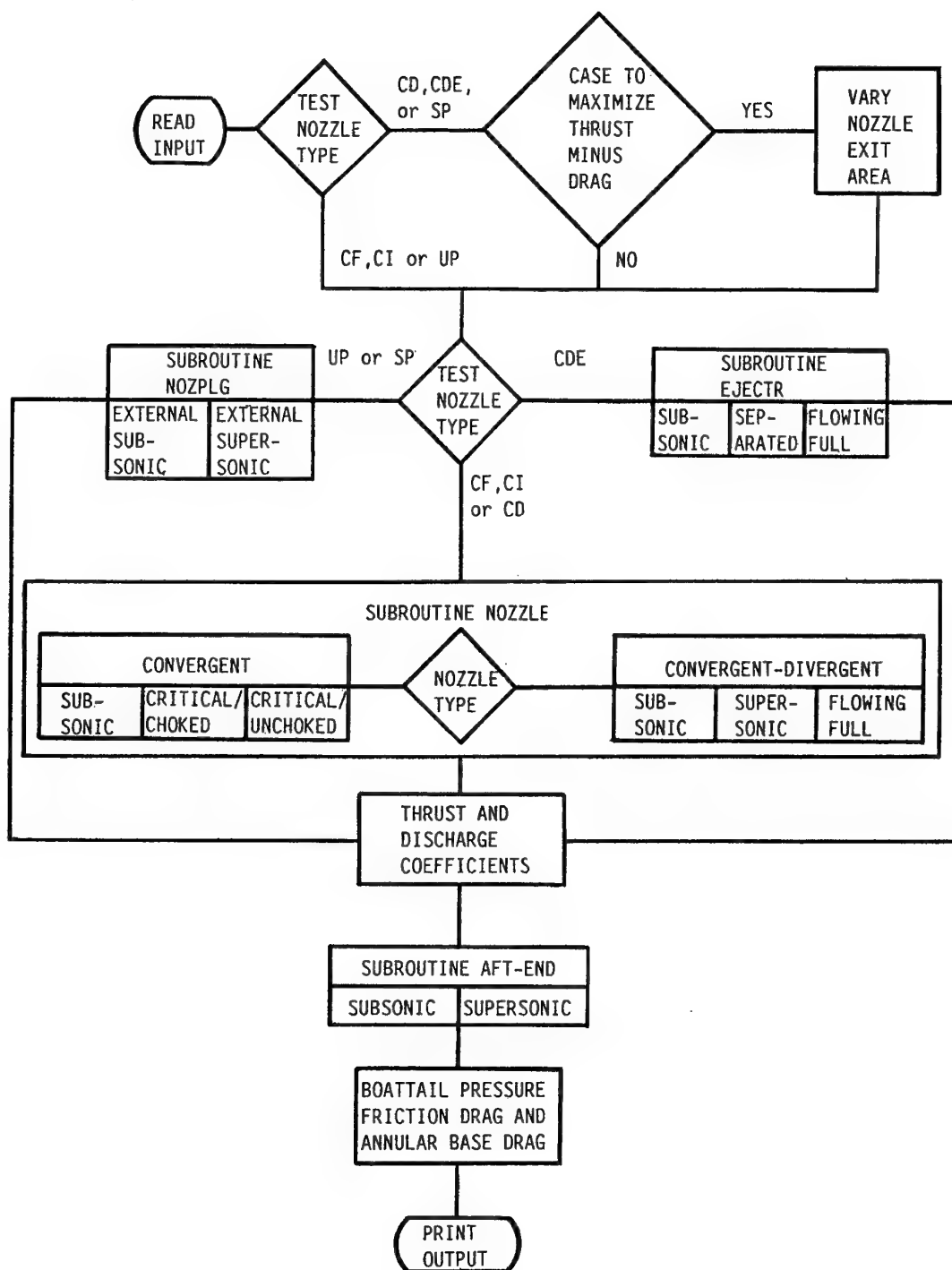


Fig. 3.2-16 Engine/Airframe Integration Method  
Computer code flow chart example,  
from [3.2-1]

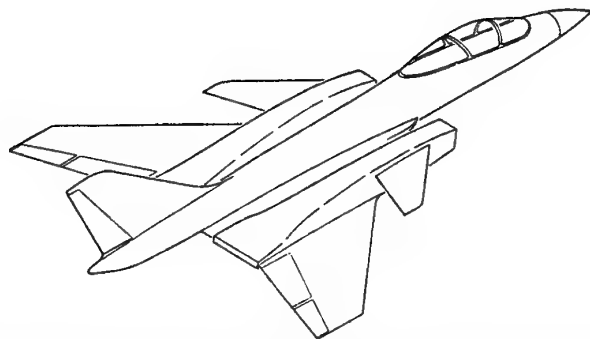
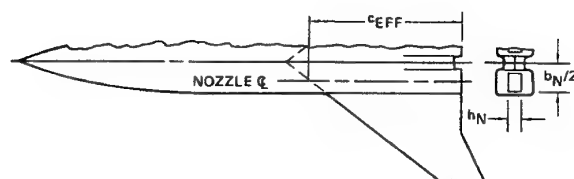
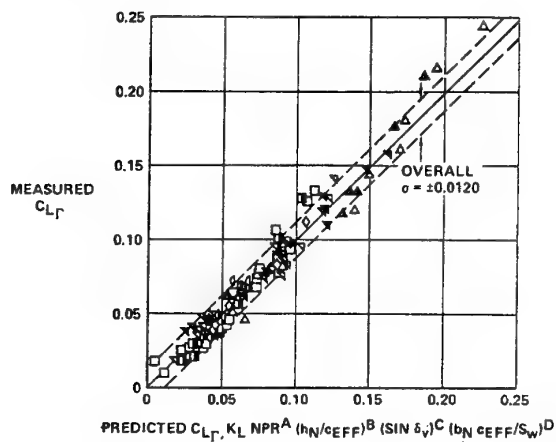


Fig. 3.2-17 Advanced aeropropulsion aircraft configuration, from [3.2-25]



SYM	NOZ
▽	ALBEN
▲	GE 2-D C-D
◊	P&WA 2-D C-D
□	VIP
◻	NASA PLUG

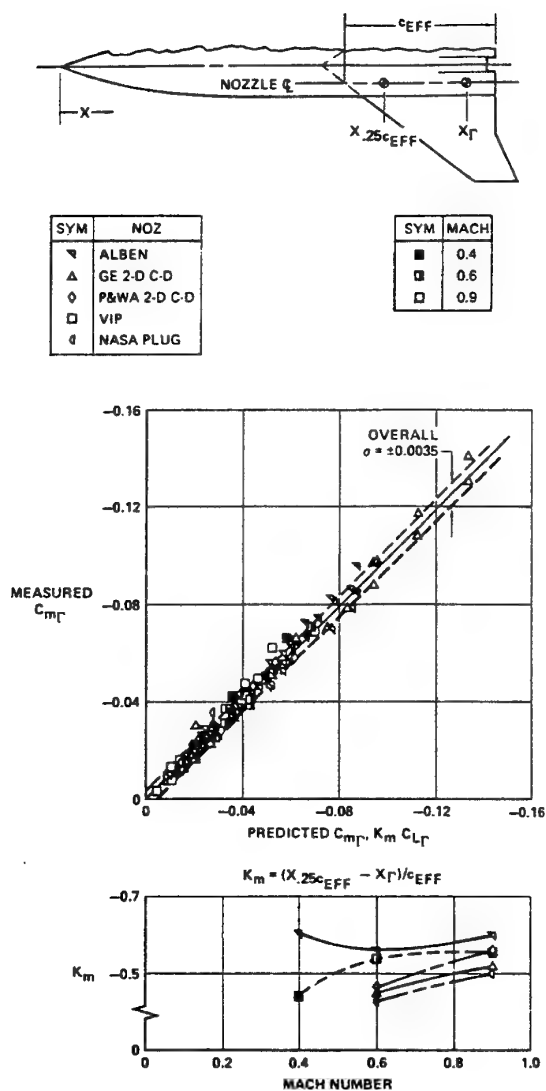
SYM	MACH
■	0.4
◼	0.6
◻	0.9



Summary of constants in thrust vector-induced lift correlation

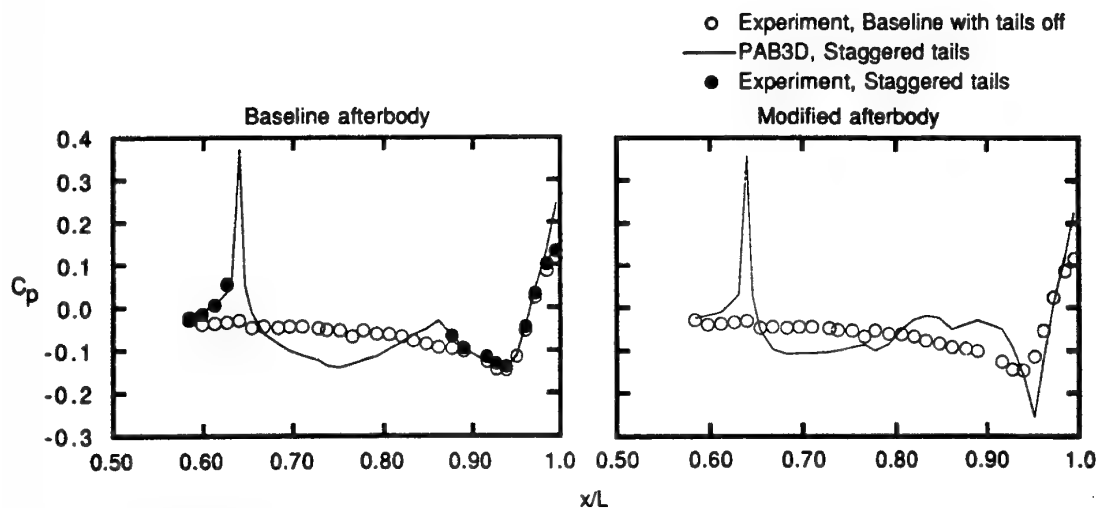
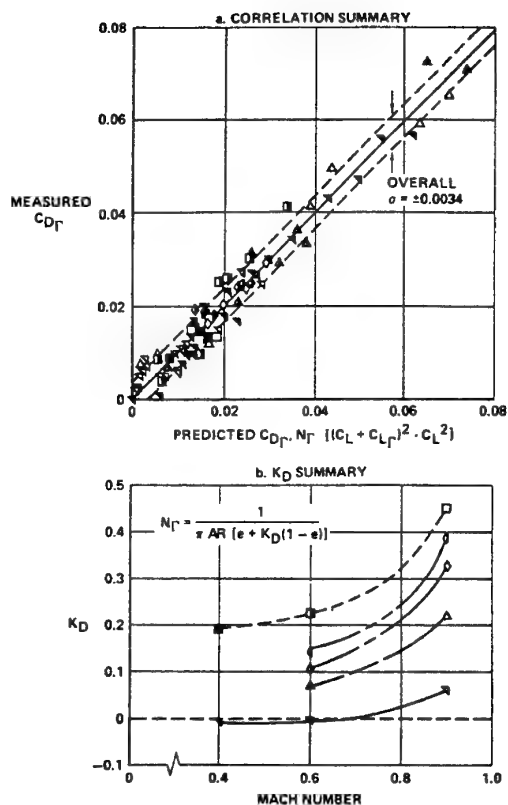
Nozzle	Exponent values				$K_L$ values		
	$A$	$B$	$C$	$D$	Mach 0.4	Mach 0.6	Mach 0.9
ALBEN	0.69	0.69	1.33	1.0	3.90	2.45	1.50
P&WA 2-D C-D	0.69	0.69	1.33	1.0		2.05	1.99
GE 2-D C-D	0.69	0.69	1.33	1.0		2.67	2.89
VIP	0.41	0	0	1.0	0.373	0.290	0.285
NASA plug	0.41	0	0.87	1.0		0.213	0.157

Fig. 3.2-18 Correlation of thrust vector-induced lift, from [3.2-28]



SYM	NOZ
▽	ALBEN
△	GE 2-D C-D
◇	P&WA 2-D C-D
□	VIP
◻	NASA PLUG

SYM	MACH
■	0.4
□	0.6
◻	0.9



### 3.3 State of the art assessment of testing techniques for aircraft afterbodies.

#### 3.3.1 Introduction.

The methods to obtain the effects of the exhaust on the aerodynamics of fighter aircraft afterbodies has not changed significantly over the last several years. The AGARD report of working group 08, Ref 1, outlines the model support methods, balances and inherent problems for obtaining the required jet effects data from force measurements. All of these basic techniques are currently employed with only subtle changes to improve particular aspects.

As the use of computational analysis improves, and its contribution to the understanding of afterbody flows expands, it is important to focus on the basic afterbody problem as it applies to actual development of fighter aircraft. For this reason the following synopsis is given of the testing method used to obtain the jet effects on the afterbody forces during the typical development of the modern day fighter. By understanding the requirements for the airplane configurator, the direction that Computational Fluid Dynamics needs to evolve to be of assistance to the airplane design process becomes clearer.

#### 3.3.2 Thrust-Drag Bookkeeping.

Figure 3.3.1 shows the components of a bookkeeping method to calculate airplane performance associated with a typical fighter airplane having either a single or twin axisymmetric or 2D nozzle arrangement.

All the elements for the provision of airplane performance are shown. Jet effects models determine the jet influence on all six components of force and moments. The following discussion deals with thrust-drag bookkeeping, this being the main parameter upon which aircraft cruise performance depends, however, the principals apply to the other components of force and moments.

Airplane development begins in the traditional manner with evaluation of the aerodynamics of the airplane. The models are called Force and Moment models (F & M). Empennage and wing positions are determined by stability and maneuverability requirements of the airplane. The aerodynamicist will conduct tests and adjust his base design configuration moving wings and tails to meet his stability and control (S&C) criteria. Drag is usually not a driver in this configuration search. These tests are conducted with "flow through" inlets. The inlets have the correct inlet lip geometry and are connected by a tube to simulated exhaust nozzles. Historically most models of this type are almost invariably mounted on an aft sting which ensures the least interference with the airplane aerodynamics. The whole model is on the balance in order that all aerodynamic forces in six components can be determined. The inlets on a "flow through" model experience ram pressure. The inlet flow passes through the model to convergent exhaust nozzles which, in order to pass mass flow with as little loss as possible, must be larger than those on the real airplane. Moreover, in order

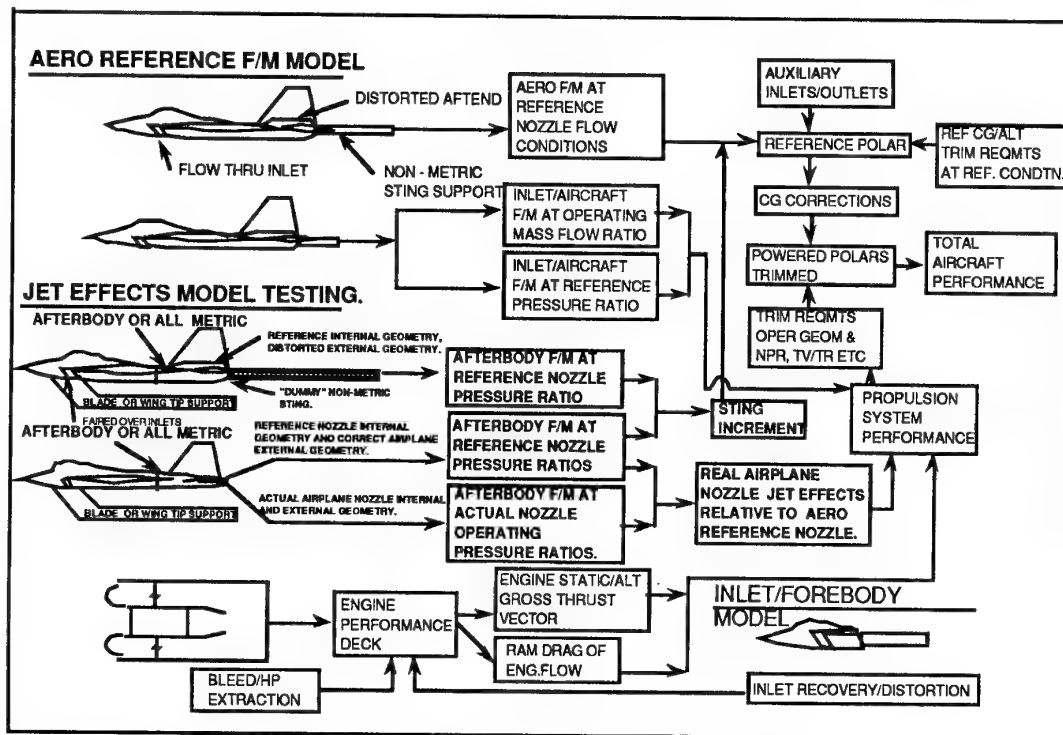


Figure 3.3.1 Thrust Drag Bookkeeping of Typical Fighter Aircraft.

to accommodate the rear sting support and the nozzle, or nozzles, the available real estate has to be increased. This almost always results in an aftend which does not have real airplane contours either for the nozzles or aftbody.

The definition of "jet effects", as defined in the bookkeeping system described, is relative to the flow through nozzle configurations. The "jet effects" of the flow through condition on all force and moments is automatically included by reason of the Aero model configuration. For this reason the reference condition is considered to have no jet effect. In actuality, relative to a nozzle with no flow, there is a jet effect but this is automatically incorporated in the reference drag polar. The no flow, or engine out condition, is dealt with separately as a propulsion increment. The aero models have the least drag afterbody configuration. It is important to appreciate that the bookkeeping system described is one of many that could be used and therefore the definition of "jet effects" as described herein is unique to the bookkeeping system used.

The aero F & M models generate six components of force (axial, normal and side forces and pitching, yawing and rolling moments) for the aircraft at all angles of attack and yawed flow conditions of the airplane. All these forces include the effects of the low drag afterbody. To generate the reference drag polar, the effects of the airplane model support sting and the associated aftbody must be determined. In addition, to complete the drag increments required to determine the airplane thrust-drag performance, the incremental effects of the jet on drag (and the other five force components for S & C) must be determined. These are determined by a "Jet effects" model which stresses afterbody configuration integrity.

The jet effects model is built with a different support system than the aero F & M model in order to determine the sting increment. This will usually be either a lower body strut, or wing tip support. The model is also built to accommodate three separate nozzle types:

1. Nozzles and afterbody identical to the F & M aero model used to determine the aero performance; flow through nozzles with the throat at the exit, distorted afterbody and a "dummy" sting. This non-metric sting is identical to that used for the aero testing except it is positioned close to, but detached from, the afterbody. (Since either the whole model or the afterbody is metric on the jet effects model, the influence of the sting on the afterbody can be determined without measuring the forces on the sting itself.)

2. The model is then tested with a nozzle having the correct external contours but with an "Aero reference" nozzle. This nozzle has the correct external contours, but like the F & M nozzle has a throat at the exit. This step is really an option in that it can be eliminated if the effects of the sting, distorted afterbody and the jet effects are combined for comparison with the aero F & M model. However, the understanding of the true "jet effects" is better determined by including this intermediate step, thereby isolating the sting and distorted aftbody effects from the true jet effect. The Aero Reference nozzle is run at flow through nozzle pressure ratios identical to those

used for the F & M model test. The difference between the results with the Aero reference and the F & M nozzle with dummy sting determines the effects of the distorted aftbody and the sting on afterbody drag and the other five components of force. This increment is added to the forces determined with the aero F & M model test to produce the reference drag polar and flow through S & C base. A typical axial force sting correction as a function of Mach number is shown in Figure 3.3.2.

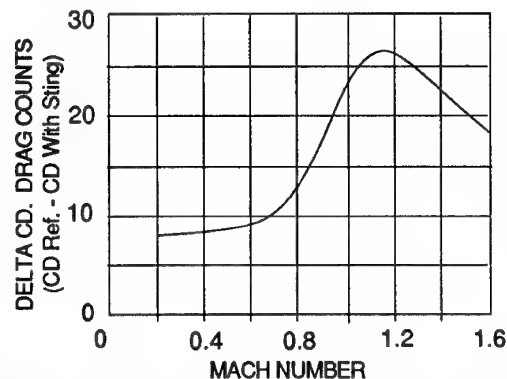


**Figure 3.3.2. Typical distorted afterbody and sting support drag increment. Aero Reference without sting - F & M Reference with sting.**

3. The "jet effects" increment for the real airplane nozzles is determined by testing the actual nozzle geometries, including thrust vectored nozzles, and subtracting the performance of the Aero Reference nozzle at the particular flow through pressure ratio for the test Mach number.

Each of the six force or moment parameters is plotted versus angle of attack (AOA) for various nozzle pressure ratios (NPR) at fixed Mach number conditions. The incremental difference between the real nozzle performance at operating pressure ratio and the Reference nozzle at flow through pressure ratio is obtained by differencing. A cross plot of the delta change in force as a function of NPR at constant AOA is then obtained.

These jet effects or throttle dependent force increments, including the effects of thrust vectoring, are used to modify the aero parameters as a function of the propulsion system thrust performance which is also defined as a function of NPR. The propulsion system performance is then used with the Reference drag polar to generate the airplane performance.

Modern day fighters do not necessarily have conventional axisymmetric or 2D-CD nozzles. Other nozzle types are treated in the same way as described above. Single expansion ramp nozzles (SERN) apply exactly the same techniques as above, the only difference being that the changes in scrubbing drag between the Aero Reference and the airplane nozzles becomes part of the "jet effects".

### 3.3.3 Current Test Methods.

Ref 2. gives an update of the state-of-the-art of testing techniques since the Ref 1. report. The paper concludes that the test techniques in use today are no different than

were employed ten years ago but the nozzle geometries now being considered or in use are more complex and the integration of these into aircraft afterbodies is becoming of correspondingly greater complexity. Highly integrated nozzle/afterbody designs and future designs which may move away from what is now the conventional single or twin nozzle exits will still need to respond to some form of the bookkeeping system outlined above. The techniques may be different but the end product will be the same.

Within the confines of the current testing techniques there is a fairly general consensus that no particular model support technique can be considered to have overwhelming advantage. Similarly the need for all metric or partially metric models is determined more by the aims of the experiment than one particular method being superior. It has become obvious that the different methods should be regarded as different approaches to try to satisfy the experimental aims within the restraints imposed by the test hardware and/or facility being used for the testing.

### 3.3.3.1 Support Methods:

Different experimenters have usually used several methods to obtain the "jet effects" data they require. However, it is important to understand that in the realm of jet effects testing all the final data is obtained in the form of increments. The question then becomes one of whether the support method has a greater or lesser affect on the increments measured and whether the effects are identical for the real nozzle configurations viz a viz the Reference to which it is related.

We have already seen that the aero configuration testing almost invariably involves a rear sting. For twin nozzle configurations this has generally been a sting connected to the rear of the aftend between the nozzles. Single nozzle configurations can conveniently employ a concentric sting or a tail support. This still results in a distorted afterbody or vertical tail in order to pass the required airplane nozzle flows and withstand the model loads. These support methods while protecting the forebody, midbody, wing and horizontal tail aerodynamic integrity, inevitably result in some part of the model being geometrically incorrect. The effects of these distortions of the real contours must be determined.

In order to obtain the aftend corrections it is essential to test the model supported in some other way and the most common forms are either wing tip support or lower body strut. Jet effects models are expensive and the body strut has the advantage of lesser cost and less risk in manufacture. Gun drilling of thin airfoil sections over considerable length is risky and the need to drill both wings for a wing tip support system doubles the possibility of manufacturing errors. The thin body strut causes little interference with the afterbody and until recently has been the preferable method because of the ability to yaw the model without yawing the strut.

Ref 3. states categorically that yaw testing should not be conducted with strut support systems. If, however, the strut remains within the butt line contours of the model

when the model is yawed, which may limit the yaw angle to quite small amounts (less than ten degrees), it has been surmised that the jet effect increments on rudder effectiveness in the yawed condition will be valid.

In the absence of a yaw requirement and provided the risk is acceptable, the wing tip support would undoubtedly be preferable. The advantage is that there is less argument about the effects of the outboard wing distortion required to adequately support the model than with the body strut support which inevitably must produce some wake interference.

The wing tip support adds more blockage with AOA unless the more complex method of wing tip gimbals is employed. This technique adds rather more complexity to the model support and air supply systems than providing a body strut capable of bottom or top mounting on the model for high AOA testing. A gimbled support system has the advantage of maintaining the model in the same place in the tunnel independent of AOA. This has advantages in both occupying the best position in the test section and better control of the interference due to wall reflections and/or stratified flow angularity within the tunnel flow.

A modification of the wing tip support has been developed by DRA and used by Rolls Royce, Ref 4. Figure 3.3.3 shows the use of a single sided wing tip support. The model is symmetrical about a center line with about one third of the wing in contour. The outer wing is clipped to match the part incorporated in the single strut support. The whole model and strut is metric. The model is of modular construction to permit easier changes of configuration.

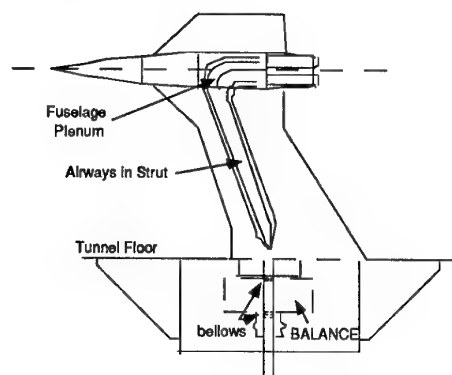


**Figure 3.3.3. Single sided wing tip support system (Ref 4)**

This method might appear to have an additional disadvantage to the all metric model in that the balance must also measure the forces on the strut support. However, the removal of the balance to a position where it is not restrained by the model geometry affords the luxury of being able to design the balance to be conditioned to the air feed arrangement. This results in a system where tare corrections are minimized and has been demonstrated as capable of resolving configuration change effects to two drag counts. The interference of the strut at

AOA is probably small and certainly no worse than the conventional wing tip support. If measurements were confined to the outer part of the model away from the strut the interference would be zero. The method does appear to limit the ability to yaw the model. However, as a tool to investigate the jet effects during early configuration development the configuration freedom offered would appear to have considerable merit.

### 3.3.3.2 Metric break.

#### a) All Metric Models.

There are three common designs of metric break. The all metric strut mounted model isolates the strut from the balance and measures all the body forces on the balance. The modified strut design described above includes what is essentially the strut forces as part of the modified wing through which the high pressure air for the nozzles passes. The balance in this case is external to the model relieving much needed space and permitting easier configuration changes, but it does include an unwanted part of the support system. Both of these complete metric model approaches have the problem of measuring small force changes in the axial direction by differencing large force measurements (thrust - drag) and thrust, to obtain drag. This leads to methods where the thrust is eliminated from the balance readings.

#### b) Afterbody Metric/Metric Thrust Models.

Both the strut and wing tip supported models can be used with a partially metric model. A partially metric model has the advantage of eliminating a large part of the model that is not influenced by the jet flow or where the jet effects are so small that they can be ignored. However, it may be difficult to determine where on the model the jet effects are small enough to be ignored. The forces being measured are still subject to the corrections of momentum tares in the balance and the elimination of the thrust to obtain drag increments. It is important that any distortion of the afterbody which will be tested with a partially metric model should be well behind the metric break.

When thrust is included in the force measured by the balance the thrust associated with the internal nozzle performance must be eliminated in order to acquire the "jet effects" data. The elimination of the thrust forces is normally accomplished by calibrating the nozzles for thrust either on a separate balance system or preferable using the model internal balance and conducting a wind-off calibration in the tunnel. These calibrations usually employ the technique of lowering the tunnel static pressure to levels commensurate with the operating conditions to be experienced with the wind-on. This enables the model to be designed to withstand only the internal pressures required to calibrate the nozzles to relatively low pressure ratios at ambient static pressure and obtain the higher nozzle pressure ratios by lowering the back pressure.

Calibration of nozzles installed in the model will include all the effects of the installation. Certain configurations may exhibit the effects of entrained flow over the aftbody by the nozzles especially on nozzles which are embedded in any channel formed by the vertical empennages.

Comparison of the results of the installed nozzles may well yield slightly different results than would be obtained in a static calibration of the nozzle in an isolated nozzle, Figure 3.3.4

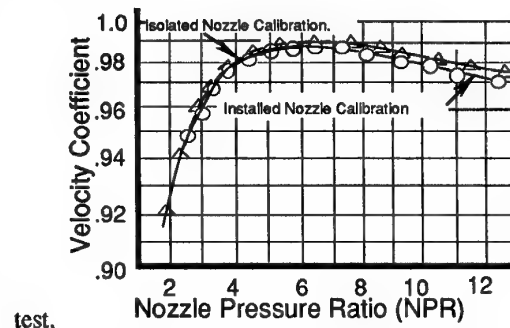


Figure 3.3.4 Comparison of Installed and uninstalled Nozzle velocity Coefficient.

The problem is how to deal with this drag increment. If the installed thrust level is used, then a portion of the "jet effect", namely that imposed by the jet statically, will be included in the thrust correction and not as a zero Mach number jet effect. This, however, is the easiest approach and has in the past been the most common. In most cases this may be the most reasonable approach but with increasingly integrated propulsion systems the effects of the installation cannot be ignored. The purist would desire to remove this force from the thrust calibration. Non-metric shields to prevent entrainment have been used successfully by engine manufacturers to ensure only internal nozzle performance is measured during full scale engine tests and a similar technique could be used on the model. A second method could use a separate calibration of the isolated nozzles to obtain the installation increment. The importance of using such data as an increment to be added to the installed calibrations should be emphasised because it is important to always determine the static thrust levels on the fully assembled model in the tunnel thereby ensuring that any bias errors are corrected when the static data is subtracted from the wind-on data. A decision must be made as to what portion of the nozzle constitutes the basis of the thrust to be extracted. If only internal thrust is required then methods to eliminate all external effects must be developed. If however, the nozzle mechanically cannot be built without including some part of the external surfaces then any forces generated on those surfaces legitimately belongs in the static thrust.

#### c) Afterbody Metric, Non-metric Thrust

There is an inherent attraction to measure the forces of interest directly rather than to measure forces one doesn't need and have the problem of extracting them from the required answer. This approach requires a clearance between the inner and outer nozzle contours and a freely supported shell for the afterbody in addition to the conventional metric break separating the metric afterbody from the non-metric forebody. This technique lends itself to conventional single flow axisymmetric or 2D-CD



nozzles. Ref 1 points out that for the highly integrated nozzles such as the single expansion ramp (SERN) type or blow-in door ejector nozzles, the design of the nozzle metric break becomes a real challenge. The need for physical clearances between the inner and outer nozzle contours results in some non-geometric similitude relative to the real nozzles and this problem is aggravated by smaller model scales. This clearance (usually about 0.050-0.070") is kept as small as possible to limit the geometric differences and allow sufficient movement for the balance deflections to prevent fouling over the angle of attack range required for the test.

Historically, such models are severely limited as to the maximum AOA they can accommodate and, if the empennages are also on the balance, the amount of tail deflection that can be obtained. Such models have the option of incorporating the empennages on the balance, on separate balances, or non-metric. Most known instances of this technique have included the empennages on the balance with or without separate balances to record empennage loadings.

There is no requirement to determine the thrust, but only to know the operating pressure ratio to which the increments can be related. Since the nozzle thrust is off balance the phenomenon of drag due to entrained external flow, which occurs on the all metric model, becomes part of the "jet effect" drag measurement, where it belongs, on the non-metric thrust model.

The balance in this model type measures drag directly and for this reason the balance force ranges are much less than in the fully metric or metric thrust configurations. Moreover, this allows the use of much smaller balances which can be placed well aft in the model and therefore further reduce the magnitude of the pitching moment forces they are required to measure. This affords the best potential to measure forces accurately. If carefully executed this method has the potential to be very accurate but there is also the potential for complete failure. The metric break corrections on such models are sometimes as big or bigger than the balance readings. These metric break corrections require the determination of the tare force on the afterbody due to pressure differentials across the metric break and also internally within the afterbody cavity correcting for the projected area of the afterbody minus the nozzle exit projected area. If differential pressures occur in the cavity due to extraneous leaks or differential pumping caused by the nozzle flow over an asymmetric aft metric break, the accuracy of this technique can very rapidly deteriorate. However, operated correctly the potential to measure drag differences of one or two drag counts can be achieved with this method.

### 3.3.3.3 Balances.

Balance selection has not changed since the AGARD report of 1986 (Ref. 1). Propulsive test balances for thrust metric models fall into two major categories, Flow through and force cancellation types. The former date from ten to fifteen years ago and work with a choked flow through the balance. Figure 3.3.5 shows a typical cross section of a flow through balance of this type.

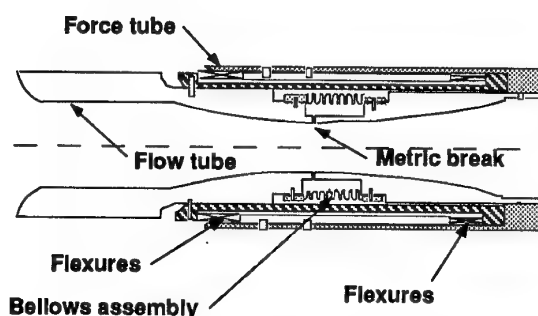


Figure 3.3.5 Flow through type balance.

The momentum and pressure tares are large. However, since the flow is choked through the balance the determination of an accurate momentum depends on the accuracy of determining mass flow. Residual momentum tares are determined by means of a zero thrust box or with calibration nozzles, such as ASME nozzles, with well defined thrust performance. Calibration is usually performed so as to relate the momentum tares to throat Reynolds number.

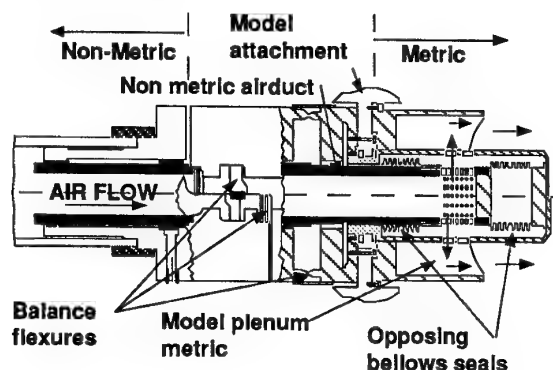


Figure 3.3.6 Force cancellation balance

Force cancellation balances are now in general use. Figure 3.3.6 shows the internal arrangement of the force cancellation type balance.

These balance systems considerably reduce the magnitude of the momentum correction by destroying the momentum as much as possible in the axial direction by two ninety degree flow passage direction changes. Momentum corrections for these balances are very small but bellows tares must still be determined. There appear to have been no major changes in flowing balance design since the AGARD 08 working group report (Ref. 1).

### 3.3.3.4 Surface pressures

Jet effects models generally contain a small number of surface pressure measurements. These are usually for diagnostic purposes. Models to determine loads are usually built without balances and use surface pressure integration. This technique is seldom used for jet effects testing in the development of an aircraft because the pressure integration does not lend itself well to obtaining

the components needed for S & C data but it is often applied to drag studies. It forms the major correlation method with CFD at this time. However, in order to adequately obtain accurate drags, a large number of pressure orifices are required. Whereas well behaved flows (e.g. afterbodies without empennages) often give good correlations with force data, the problem is compounded when empennages are added. The number of static pressures required to adequately define the surface pressure contours becomes prohibitive mechanically and increases cost. In addition the skin friction portion is not measured and must be calculated. This becomes particularly difficult where boundary layer build-up or separation occurs over parts of a complex geometry.

### 3.3.3.5 Pressure Indicating Paint (PIP)

Surface pressure measurement methods have the potential of being elevated to new possibilities with the development of Barometric or Pressure Sensitive Paint. Pressure indicating paints are coatings which contain

laser, favoured by the Russians, to the more common ultra violet light (either continuous or flash), and even normal artificial light (McDonnell Douglas), Ref 5. The change in luminescence is recorded by black and white video CCD cameras. Figure 3.3.7 is a schematic of the measurement system used in Ref. 5.

The grey scale image is correlated with either surface pressure measurements on the model or independent calibration using a pressure cell. An image is recorded prior to the wind on conditions. This image contains all the effects of paint thickness variation, surface curvature and shadows. A reference image is required at each of the conditions to be analyzed. This reference image is divided electronically into the recorded images taken with the wind and jet on. By selecting parts of the image where static pressures are recorded a calibration of the ratioed image grey scale to the local pressure can be obtained. Figure 3.3.8 shows such a correlation as presented in Ref. 5. The

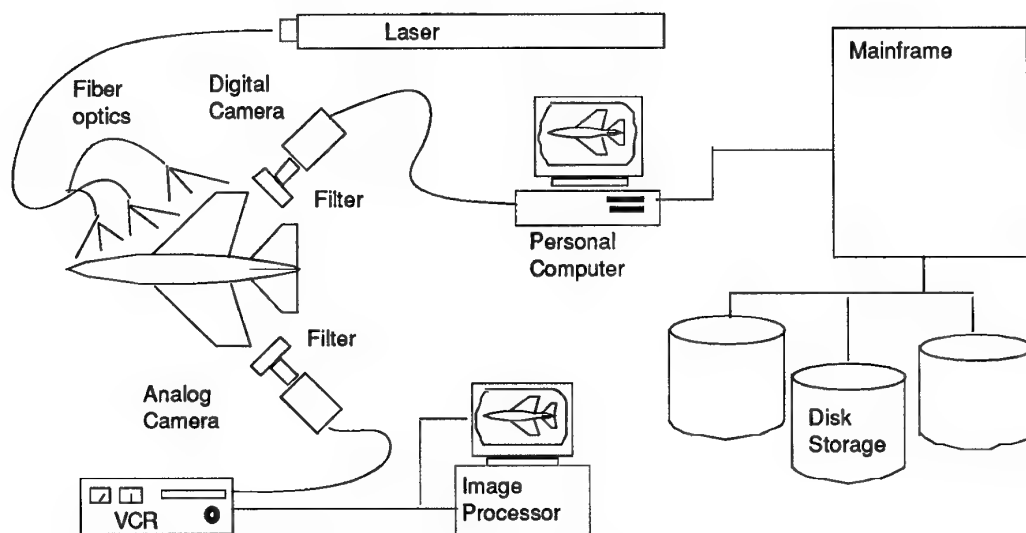


Figure 3.3.7 Schematic of measurement system based on pressure sensitive paint. Ref. 3.

photoluminescent materials in which the luminescence reaction is quenched by the presence of oxygen. When applied like conventional paint to the surface of the model, and illuminating the surface with light of appropriate wavelength, luminescence intensity distributions appear which can be directly correlated with the pressure adjacent to the surface. The intensity of the luminescence is inversely proportional to the partial pressure of oxygen which in turn is dependent on the pressure in contact with the treated surface. These paints have been developed more or less independently by various aerospace companies in the USA, NASA, and universities. Parallel developments have occurred in what was the Soviet Union by the Central Aero and Hydrodynamic Institute (TsAGI) and marketed through INTECO of Italy. Illumination techniques vary from

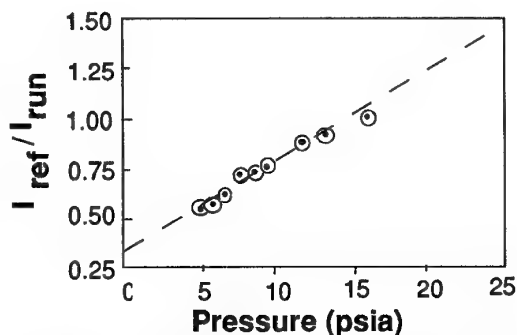
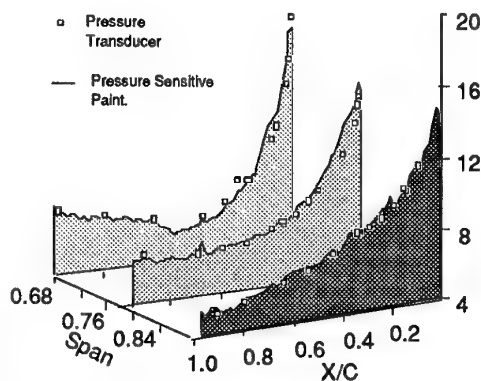


Figure 3.3.8. Linear least square fit of the calibration data. (Ref 5.)

black and white image can be color enhanced for better interpretation of the surface phenomena. Ref 5. gives a very clear synopsis of the method, the theory and the results that have been obtained for four different wind tunnel experiments. Data reduction equipment is very portable and does not require elaborate set-up.

Figure 3.3.9 illustrates a comparison of PIP with measurements of surface static pressures on a supersonic wing. The process is still relatively new and requires considerable development before it becomes a reliable and accurate pressure measurement tool. Several companies in the USA and Europe, either independently or in combination with Universities or Government facilities, such as NASA, are in the process of developing the techniques.



**Figure 3.3.9. A comparison of the pressure distributions on the wing of a high performance fighter model at Mach 1.2 and 0 deg. angle of attack, measured with pressure sensitive paint and wall taps.(Ref 5.)**

The process promises the eventual measurement of surface pressures at any point where paint can be applied and where a camera can view the illuminated surface. The lighting can be from almost any direction provided all the surface to be investigated is illuminated. Good results have been obtained for surfaces which include the surface irregularities associated with wing flaps or two dimensional nozzle flap discontinuities. Its major contribution will be the extrapolation of measured pressure data from surface pressure taps to areas where it is physically impossible to install pressure taps, and to interpolate between the static taps to map the entire surface. The number of surface pressures could be dramatically reduced by this method. Current paints are subject to deterioration by the light used to cause the phosphorescence. They are sensitive to paint thickness, temperature, mechanical handling, and their performance is impaired by an oily atmosphere. The current paints function best at high Mach number conditions but have been successful over a Mach range of 0.6 to 2.0.

### 3.3.4 Future Needs.

#### 3.3.4.1 Balance development

Traditionally, afterbody/nozzle integration has been a large contributor to the drag on fighter aircraft and the success of the aircraft may very well hinge on the ability to successfully integrate the propulsion system in the aircraft afterbody. The foregoing discussion of current techniques suggests that particular techniques may fit the requirements of a particular experiment better than others. For instance, for the determination of jet effects drag it is suggested that the use of the metric afterbody with non-metric (inner) nozzles provides the most direct measurements of the parameter being investigated. However, it has been commented that this technique is limited in AOA capability and the amount of tail angle which can be applied because of afterbody deflection on the balance. Studies of methods to maintain the required metric clearances under load could offer the best advance in balance technique permitting the non-metric thrust method to be extended to all airplane operating conditions. This may require the afterbody to become the balance itself.

The determination of S & C data will almost always require an all metric model for which any one of the all metric techniques discussed in this section, with their traditional balance approach, would provide an adequate platform

#### 3.3.4.2 Test Techniques.

There is an inherent problem with the current development methods used in industry. Aero testing of simple models is relatively inexpensive. Configuration development progresses with this type of model until a configuration is frozen. Jet effects models, which are always expensive, are then built of the configuration and tested to determine the throttle dependent drags.

The jet effects on the longitudinal and lateral stability of the aircraft can be either favorable or unfavorable depending mainly on Mach Number and the geometry of the operating nozzle. The majority of the S & C effects are favorable to the aerodynamics of the airplane and therefore their determination as an end item is at least an acceptable approach.

However, the jet effects on drag, which may determine the acceptability of a configuration, are highly configuration dependent. Jet effects at supersonic speeds are almost always favorable but at transonic speeds the design may well determine whether the jet effects are significant or not. For this reason the determination of at least the jet effects on drag should be accomplished during the development of the configuration.

It is not known with any precision at this time whether true optimum performance could be obtained for a fighter aircraft if an attempt were made to optimize the configuration with the power on. Since jet effects are very configuration dependent, the magnitude of the effect will be larger or smaller depending on the afterbody empennage arrangement and, much more importantly, the location of the jets relative to the vertical tails. Figure 3.3.10 shows the configurations investigated in Ref 6 which has conducted experiments along these lines.

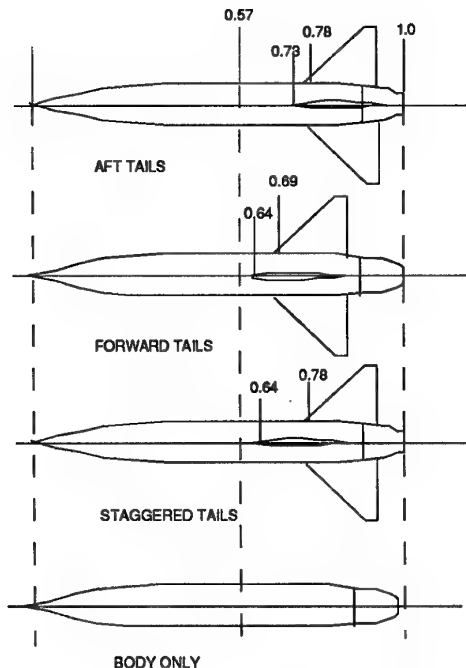


**Figure 3.3.10. Tail position variations tested by Ref 6**

Figure 3.3.11 shows these effects can be significant. The question remains, however, as to how to determine which configuration is optimum within the confines of the overall airplane stability and maneuverability requirements. The problem, certainly, is that the internal arrangement of the jet effect model with its high pressure flow passages, balance etc. does not lend itself to configuration modification nearly so easily as does the aero flow-through model. Moreover, the need to provide internal flow passages which will not choke when the Reference nozzles are being evaluated applies a considerable constraint to the model design. The flow passages have to be so large that the configuration mold lines for a tightly wrapped low drag fighter configuration almost always become the duct outer wall. This is a direct outcome of the bookkeeping system described herein. Were it possible to somehow eliminate the need for Reference nozzles with exit choking from the jet effects models then more generic models which could accommodate configuration changes of significance could be designed. Barring that as a solution the only remaining approach would be to have separate internal duct arrangements for the Reference configurations and smaller internal ducts for the real airplane nozzles thereby alleviating the difficulties of providing a generic afterbody development model. However, the cost would necessarily escalate.

Industry has been slowly realizing that there may be some potential benefit to determining what the influences of the afterbody configuration are on the overall aircraft

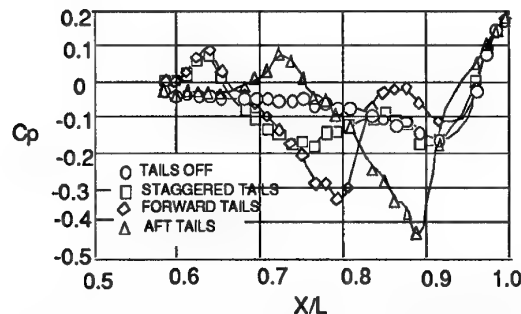


**Figure 3.3.11. Effect of tail arrangement on static pressures at 18 degrees from TDC at Mach = 0.9 and AOA = 0 Deg. (Ref 6.)**

performance during the early stages of configuration development. Ref 7. investigates the effects of boattail angle for isolated non-axisymmetric afterbodies on drag at transonic Mach numbers but without empennages. These data while providing excellent experimental data for the evaluation of CFD codes, and for that reason are very necessary, add very little to the real world problem other than reemphasizing the influence that nozzle boattail angle has on afterbody drag. Ref 8 contains a wealth of experimental data related to twin axisymmetric configurations. However, the experimentation limited itself to currently operational twin axisymmetric configurations where the exhaust nozzles were either level with, or protruded beyond, the trailing edges of the empennages. Thrust vectoring non-axisymmetric nozzles on fighter aircraft where maneuverability is enhanced has brought with it a more difficult integration challenge because the interference and interaction of empennages and nozzles is more severe.

Both Ref 3 and Ref 8 showed that vertical tail incidence can be used to create favorable flow effects on the jet/afterbody flow interactions. One aircraft has used differential rudder control to optimize the drag at subsonic conditions but the effect was over a very small Mach range and provided no advantage at other conditions. Experiments with vectored nozzles have shown that trim vectoring can improve the drag even when the jet induced lift must be counteracted by tweaking the aero surfaces. Might this suggest, however, that the configurations developed from aero testing alone may be deficient in optimizing the configuration for the presence of the jet and, therefore, has not provided the optimum jet-on configuration? It is obvious that this is an area of experimentation that should be investigated.

#### 3.3.4.3 Experimental Investigations Required.

The development of optimization factors for 3D afterbodies will probably require several experiments similar to those of Ref 8. to acquire enough generic data to support the airplane configurator.

Twin tail angle, spacing, toe-in/out, span and position relative to the jet are probably the most fundamental parameters to be studied. However, it would appear that the effect of different types of nozzle on jet effects has not been extensively examined, at least not to the point of

comparing types to determine whether type plays any part in afterbody optimization particularly with the highly integrated configurations.

It is apparent from the jet effects testing conducted to date that the jet effects in terms of drag increase are more pronounced on the upper afterbody surfaces than on the lower surfaces. This is undoubtedly associated with the effect of the jet flow on the interaction of the upper body flow and the vertical empennages. The lower surfaces without the empennages seem to be more tolerant of steeper boattail angles than the upper surface and of course the situation improves on the lower surface as AOA increases. The degree of "interference" is obviously associated with the relative positions of the nozzles and the vertical tails. However, there may be a case for reducing the upper body effects by designing the nozzles to have near optimum boattail angle on the upper surface and accommodate the majority of nozzle area change requirements on the lower side of the afterbody. This could really be considered as a type of the SERN nozzle concept but without the upper nozzle flaps being fixed or of unequal length. It would be important to try and maintain axial flow with such a geometry in order to reduce the introduction of vectored flow which would rapidly erode any afterbody drag improvement. The geometry of such nozzles might require the nozzle throat plane to digress from the traditional symmetry relative to the engine centerline and vary in waterline height. The geometry for independent operation of upper and lower flaps is already provided with the development of the vectoring nozzle. This concept does not, therefore, demand any major concept change but only the testing to investigate for possible advantages. This concept could benefit subsonic/transonic drag by transferring nozzle geometry changes to the more benign side of the afterbody.

Historically Jet effects models are very expensive. For that reason there is a tendency to refrain from jet effects testing until the configurations has at least established some kind of permanence. This tends to make the jet effects models some of the last in the development chain. One of the problems which jet effects tests inherit by being the last link in the chain of airplane aerodynamics development is that the model designs become very project orientated. This implies that they will only investigate the parameters associated with a particular design and since the design has been "frozen", only relatively small geometry modifications will be allowed. Moreover, because of the cost and number of variables associated with the testing, the instrumentation provided in the model will investigate only those phenomena directly associated with the required data.

Most jet effects testing does not include the flow interrogation required, such as Laser Doppler velocity evaluations (LDV) to understand flow phenomena or for CFD analysis validation. Moreover, because the tests are aimed at providing S&C data for the airplane envelope, they cover a large range of conditions and the time needed to conduct LDV surveys may be cost prohibitive in some tunnels. However, until such experiments are conducted,

the panaceas to aircraft afterbody problems will continue to be pragmatic and configuration dependent with seldom an understanding of exactly the cause of any problem.

Investigation of flow field phenomena requires more than the customary surface pressure instrumentation even though this is currently the information used to correlate with CFD analysis. It is important to determine why certain things improve or degrade performance and for this the flow in the free field is essential. There is a great need for such fundamental testing not only to determine the experimental effects but to assist in the development of the complex computer codes needed to evaluate and understand the flow phenomena to ensure that the code will not only reproduce the known flow phenomena of a particular afterbody configuration but that it may be relied upon to predict the flows for afterbodies not as yet experimentally tested. There still appears to be no concerted effort to determine the forcing functions that control the development of low drag afterbodies.

#### 3.3.4.4 Synergistic Optimization

Each system on an aircraft should perform a required major function. However, that system may have an ability to influence another system which if worked in combination will result in an improved overall efficiency. This technique is called synergism. A problem that works against synergism in the modern fighter aircraft is the unwritten rule that the aircraft must be recoverable from stall by the use of aerodynamic surfaces only. This almost always requires the aircraft to have larger horizontal control surfaces than would be required were the forces induced by the jet, either directly or by thrust vectoring, permitted in the stability equation. The reasoning behind this is that the power system cannot be relied upon to operate at all conditions and the loss of the airplane might occur if there is insufficient control with power off. Until this particular philosophy is modified or alternate emergency recovery systems can be devised which weigh less than the current methods, airplanes will continue to carry around more control power than is absolutely necessary.

#### 3.3.4.5 Data Manipulation Development.

Jet effects testing is aimed at acquiring incremental effects on control surfaces to determine the effect of the jet on longitudinal and lateral stability of the airplane. As fighter aircraft become more and more agile these effects become of more significance. Because there are at least four variables associated with the jet alone, throat area, nozzle area ratio ( $A_9/A_8$ ), vector angle and nozzle pressure ratio, the number of configurations to test, to ensure adequate coverage of all the possible effects, escalates. Add to these the combinations of angle of attack, yaw angle, horizontal and rudder angle and, of course Mach number, and the extent of the data matrix becomes dauntingly apparent.

There is a tendency to want to examine as many combinations of these variables as possible. If that approach is taken then in situations where cost is a significant player the amount of data acquired per run (An alpha sweep with a nozzle, at a NPR, at one horizontal or rudder angle, at one Mach number) is often limited to single runs. The problem is that in experimental data,

force and moment measurement repeatability is dependent on a combination of parameters which will far exceed those above. Increments based upon single run comparisons while permitting an answer to be obtained, could in fact be subject to considerable error and worse, have such inconsistency with say Mach Number, as to make the determination of trends almost impossible.

Most experimenters would desire to take several repeat runs of each configuration. If this were undertaken with the whole matrix the cost and time involved would be prohibitive and therefore token repeats are indulged to ensure no real anomalies exist. However, to obtain reliable data there is no substitute for run repeats and the experimentation should be designed to allow for this. *It is far better to limit the matrix and obtain reliable and more accurate data for a few conditions than unreliable and questionable data at many conditions.*

The design of the experiment should aim at a minimum of three runs per configuration. To deal wholly with all the possible variables these should preferably include at least one model rebuild of the configuration. That may be a secondary effect which the experimenter is reluctant to include. By taking three runs per configuration statistical analysis of variance could be applied to the data. It would enable the within run and run to run variance to be determined and an accurate determination by "F" test as to whether the increments between configurations, or the jet effects on one configuration, were significant or not at the 95% confidence level. This approach could be built into the data reduction equations which would need to combine runs and would determine which increments are significant and which are not.

Pre-test estimates of data accuracy are usually built upon the capabilities of the balance and associated pressure and temperature measurements. However, by far the more interesting data is that finally achieved in the test itself where all the parameters which affect the final result are active. Only by examining the overall scatter of the data, and that requires at least a run duplication for each configuration and preferably more, can the significance of the data being determined be evaluated. Tunnel operators should continuously monitor the capability of models tested in their facilities and apply statistical analysis of variance to the results with the purpose of determining experimental techniques which result in the highest quality data. Moreover, such analysis would considerably benefit the users who could evaluate before testing whether his experiment was capable of defining the particular data he is looking for and/or influence his testing technique to ensure he obtains reliable data. Some experiments might never be conducted were such information a part of designing the experiment!

#### 3.3.4.6 Model design challenge.

Jet effects testing aims to determine the S & C influences of the jet on the airplane aerodynamics. One major player in this equation is the nozzle geometry. Aircraft in which the nozzle is positioned well aft of the empennages have less effect on the aerodynamic control surfaces than nozzles which are situated between and often ahead of the trailing edge of the horizontal control surfaces. In these

cases the jet effects can be very significant. In order to investigate the effects of nozzle geometry, both throat and area ratio effects, a series of nozzles are built covering the expected nozzle operational characteristics. The problem is that for highly tuned systems the nozzle geometry varies considerably with power setting, Mach number and whether dry or afterburning power is being simulated. A fixed area throat and area ratio may, therefore, only simulate the "correct" conditions at one point in the envelope. Since jet effects testing aims to determine the effects over the whole envelope this necessitates building a multitude of nozzles and, to cover the operating envelope, testing with these nozzles at conditions where they would never operate with the designed in geometry in the real airplane. One answer is to build more fixed geometry nozzles. However, nozzle build and the changing necessary during testing are both expensive solutions. Much more efficient testing and exact representation of real life conditions would be provided by building a remotely actuated variable throat and area ratio nozzle into the model.

The small size of the test hardware, often 1/10th scale or less, makes this a real challenge to the designer. Mastery of such a design would lead to a substantial advance in jet effects testing. To date it is doubtful if any small scale powered nozzle has ever been successful.

#### 3.3.5 References..

1. "Report of Working Group on Aerodynamics of Aircraft Afterbody", AGARD-AR-226, June 1986
2. Bowers D.I. & Laughrey J.L. "Survey on Techniques Used in Aerodynamic Nozzle/Airframe Integration. Wright Patterson AFB, OH 45433. USA. AGARD Conference "Aerodynamic Engine/Airframe Integration" CP-498 OCT 1991. Ft-Wth Texas.
3. Bowers D. & Laughrey J. "A survey of an AGARD assessment of testing techniques for aircraft afterbody flow" Wright Patterson AFB. Oh. USA. AIAA-85-1465
4. Wood A.C.R. "Integration of Combat Aircraft Exhaust Nozzles". Paper #11 of the Proceedings of the RAeS/IMEchE conference on Engine Airframe Integration. Nottingham. U.K 15-16 Oct 1992.
5. Morris.M.J, Donovan. J.F,Kegelman. J.T, Schwab.S.D, Levy.R.L, McDonnell-Douglas Research Laboratories, and Crites.R.C, "Aerodynamic Applications of Pressure-Sensitive Paint" McDonnell Douglas Aircraft Company, St.Louis, Missouri 63166 AIAA 92-0264 Jan 6-9,1992 Reno,NV
6. Berrier.B NASA Langley Research Center, Hampton, Virginia 23665.
7. Bangert. Linda S.. "Effect of Afterbody Geometry on Aerodynamic Characteristics of Isolated Non-axisymmetric Afterbodies at Transonic Mach Numbers"

NASA Technical Paper 3236 Sept 1992

8. Leavitt, Lawrence J. "Effects of various empennage parameters on the aerodynamic characteristics of a twin-engine afterbody model." NASA Langley Research Center, Hampton, Virginia 23665.  
AIAA-83-0085 21st Aerospace Sciences Meeting.



### 3.4 Description of Group B Test Cases

#### 3.4.1 Introduction

Significant advancements have been made during the past decade on the use of computational fluid dynamics (CFD) for propulsion aerodynamic problems. Except for separated flow regimes, isolated 2-D afterbody/nozzle external and internal flow fields are routinely computed with reasonable accuracy. The internal performance of complex nozzles is computed with increasing confidence and the ability to handle ever increasing configuration complexity (twin engines, installed tail surfaces, 3-D nozzles, etc.) has improved. CFD applications have finally started to impact the aircraft design process.

A critical review of CFD codes available to the Working Group was undertaken, by applying them to selected experimental "design" test cases. These "design" test cases were selected to evaluate CFD codes which may be useful in the design process. Past experience has shown that this "test case" approach is a generally revealing and constructive activity. It clarifies the scope of the various codes and gives some indication of their current relative standing. It must be emphasized at the outset, however, that a limited review of the type undertaken here can never provide a full assessment of the present accuracy of predictions or of the relative merit of the different modelling or computational procedures for further development.

For (CFD) codes to be completely accepted as engineering tools for analysis and design of complex 3-D afterbodies, they must accurately predict the effects of geometric (tail position and deflection; nozzle type, shape and closure; engine spacing; etc.) and flight condition ( $M_\infty$ , NPR,  $\alpha$ , Re, etc.) variables. To adequately predict these effects, CFD codes must be capable of simulating the complex physical phenomena that are associated with the propulsion integration area. Some of these phenomena are 3-D/vortical flow, thick boundary layers with adverse pressure gradients, separated flow, boundary layer/shock interactions, shear layer mixing and internal/external flow interactions. During selection of the test cases, the Working Group considered both the variables and physical phenomena which must be simulated by CFD codes.

In addition to the effects of geometric and flow condition variables, the Working Group was also interested in evaluating the effects of code related variables such as code type, grid technique, grid density, turbulence model, etc. The evaluation of these effects could not be driven by test case selection and the Working Group relied on voluntary contributions to cover them.

#### 3.4.2 Group B Test Case Selection

The group B or "design" test cases were selected using the following criteria:

- (i) the number of cases should be small
- (ii) they should be confined to 3-D afterbody configurations
- (iii) they should cover the major variables involved:
  - free stream Mach number
  - nozzle pressure ratio
  - aftend shape
  - tail position
  - single and twin engines
- (iv) they should encompass cases in which boundary layer separation did and did not occur on the aftbody/nozzle
- (v) the experimental information should be as accurate and as comprehensive as possible, with emphasis on surface measurements
- (vi) there should be no restrictions on the publication of the data, so that the cases would be available for research workers to test their own codes in the future.

Table 3.4-1 shows the "design" test cases selected; it can be noted that each of the variables mentioned in (iii) is covered at least once. All "design" test cases were contributed by Mr. Bobby L. Berrier of NASA Langley Research Center, MS 280, Hampton, VA 23681-0001. Test cases were selected from experiments on an axisymmetric, single engine afterbody with and without tails; a twin engine afterbody (axisymmetric nozzles) with tails; and a nonaxisymmetric aftbody/nozzle. In each experiment, only two or three test points from the range of test conditions potentially available could be chosen. The test case geometry and experimental data were provided to all organizations that participated in this study.

#### 3.4.3 Accuracy of Test Results

No estimates have been made of the accuracy of the quoted results. In each of the experiments, there will have been quantifiable random inaccuracies resulting from normal instrumentation inaccuracies, but such errors in this type of test would not be significantly large in the context of the present comparisons with theory. However, the possibility of important bias errors in this type of test - especially affecting the net drag coefficient - is recognized. Such errors could arise from non-uniform entry flow, from model support interference, or from minor model defects. They cannot by their nature be quantified by the experimenter. However, the selected tests were conducted by teams with great experience in these and other experimental pitfalls. Furthermore, tests were chosen, as far as possible, to allow comparisons to be made of the effect of changing one parameter within a single test series, so as to minimize the importance of any bias errors. It should be noted that no attempt was made to apply wind tunnel blockage corrections to the quoted results since



all of the selected experiments were conducted in a very large wind tunnel which resulted in extremely low values of model blockage.

### 3.4.4 Test Cases

Brief details of the test cases follow. Their full experimental results are tabulated in Appendix B.

#### 3.4.4.1 Test Cases B.1 and B.2 - NASA Langley Single Engine Afterbody with (B.1) and without (B.2) tails

##### I. Model Configuration (see Figures 3.4-1 and 3.4-2)

- A. Forebody - Axisymmetric ogive, 24 in. in length with 14 deg. initial angle followed by a constant area cylinder (see Figure 3.4-1)
- B. Aftbody - Axisymmetric with closure representative of a typical single-engine fighter (see Figure 3.4-3)
- C. Nozzle - Axisymmetric convergent-divergent with expansion ratio of 1.02 (see Fig. 3.4-4)
- D. Tails (see Figure 3.4-5)
  - Test Case B.1 - None
  - Test Case B.2 (see Figure 3.4-6)
    - Vertical - NACA 64 series in a forward location
    - Horizontal - NACA 64 series in an aft location

##### II. Model Installation in Tunnel (see Figure 3.4-7)

0.148% blockage

##### III. Nominal Free Stream and Jet Conditions

- $M_\infty = 0.90$
- $P_{t\infty} = 14.7$  psi
- $q_\infty = 4.94$  psi
- $T_{t\infty} = 590$  °R
- $Re = 2.24 \times 10^7$  based on model length
- $\alpha = 0^\circ$
- NPR = 2.033 for case B.1.1
- = 4.991 for case B.1.2
- = 2.027 for case B.2.1
- = 2.997 for case B.2.2
- = 5.033 for case B.2.3
- $T_{tj} = 530$  °R

##### IV. Data Available

Following data are available on a 3.5" floppy disk in either MS-DOS or MAC-OS by contacting

Bobby L. Berrier  
Mail Stop 280  
NASA - Langley Research Center  
Hampton, Virginia 23681-0001  
USA

A. External surface pressures on aftbody, nozzle and tails

B. Drag coefficients

## V. References

3.4-1, 3.4-2, 3.4-3, 3.4-4, 3.4-5, 3.4-6

#### 3.4.4.2 Test Cases B.3 - NASA Langley Twin Engine Afterbody with tails

##### I. Model Configuration (see Figures 3.4-8 and 3.4-9)

- A. Forebody - Circular cross-section up to simulated, faired-over, side mounted, rectangular inlets attached to a constant area rectangular cross-section (10 in. x 5 in.) with rounded corners (1 in. radius) and high wing. (see Figure 3.4-8)
- B. Aftbody - Twin nacelles joined with engine interfairing which terminates with a horizontal knife edge at nozzle connect station. (see Figure 3.4-10)
- C. Nozzle - Twin axisymmetric convergent-divergent with expansion ratio of 1.15 (see Figure 3.4-11)
- D. Wing - Aspect ratio = 45; Taper ratio = 0.5; leading edge sweep = 45°; cranked trailing edge; thickness ratio = 0.067 at root; thickness ratio = 0.10 at tip (Wing doubles as part of model support system with tips being unrealistically thick to carry loads. Wing tip booms attach model to tunnel support system.) (see Figure 3.4-8)

##### E. Tails

- Horizontal - NACA 64 series in a mid location. (see Figures 3.4-12 and 3.4-13)
- Vertical - Twin NACA 64 series tails (see Figures 3.4-12 and 3.4-13)
  - Test case B.3.1 - Vertical tails in mid location
  - Test case B.3.2 - Vertical tails in aft location
  - Test case B.3.3 - Vertical tails in forward location

##### II. Model Installation in Tunnel (see Figure 3.4-14)

0.257% blockage

##### III. Nominal Free Stream and Jet Conditions

- $M_\infty = 0.90$
- $P_{t\infty} = 14.7$  psi
- $q_\infty = 4.94$  psi
- $T_{t\infty} = 590$  °R
- $Re = 5.61 \times 10^6$  based on wing mean aerodynamic chord
- $\alpha = 0^\circ$
- NPR = 3.4
- $T_{tj} = 530$  °R

##### IV. Data Available

Following data are available on a 3.5" floppy disk in either MS-DOS or MAC-OS by contacting

Bobby L. Berrier  
Mail Stop 280  
NASA - Langley Research Center  
Hampton, Virginia 23681-0001  
USA

- A. External surface pressures on aftbody, nozzle and tails
- B. Drag coefficients

#### V. References

3.4-7, 3.4-8

#### 3.4.4.3. Test Cases B.4 - NASA Langley 2-D C-D Single Isolated Nozzle

##### I. Model Configuration (see Figures 3.4-15 and 3.4-16)

- A. Forebody - Conical nose tip which transitions to a superelliptical cross section at  $x = 26.5$  in. that was nearly rectangular with large rounded corners. The cross-sectional area and external geometry remained constant from  $x = 26.5$  in. to  $x = 55.8$  in. at which point the nozzle external contour begins. (see Figure 3.4-15)

- B. Nozzle - Single 2-D C-D nozzle with a nozzle expansion ratio of 1.25 and a throat aspect ratio (ratio of nozzle throat width to nozzle throat height) of 2.38. (see Figure 3.4-17)

- E. Tails - None

##### II. Model Installation in Tunnel (see Figure 3.4-16) 0.144% blockage

##### III. Nominal Free Stream and Jet Conditions

- $M_\infty = 0.60$  for Case B.4.1  
 $= 0.94$  for Case B.4.2
- $p_{t\infty} = 14.7$  psi
- $q_\infty = 2.90$  psi for Case B.4.1  
 $= 5.13$  psi for Case B.4.2
- $T_{t\infty} = 600$  °R
- $Re = 1.73 \times 10^7$  for Case B.4.1  
 $= 2.10 \times 10^7$  for Case B.4.2  
based on model length
- $\alpha = 0^\circ$
- NPR = 4.00
- $T_{tj} = 545$  °R

#### IV. Data Available

- A. External surface pressures on nozzle
- B. Internal surface pressures on nozzle flaps
- C. Pitot pressure in jet exhaust, shear layer and free stream at and downstream of nozzle exit

#### V. References

3.4-9, 3.4-10, 3.4-11, 3.4-12, 3.4-13

#### 3.4.5 References

3.4-1

Berrier, Bobby L.: Effect of Nonlifting Empennage Surfaces on Single-Engine Afterbody/Nozzle Drag at Mach Numbers From 0.5 to 2.2. NASA TN D-8326, 1977.

3.4-2

Henderson, William P.; and Burley, James R., II: Effect of Empennage Arrangement on Single-Engine Nozzle/Afterbody Static Pressures at Transonic Speeds. NASA TP-2753, 1987.

3.4-3

Berrier, Bobby L.: Effect of Empennage Interference on Single-Engine Afterbody/Nozzle Drag. AIAA Paper No. 75-1296, 1975.

3.4-4

Burley, James R., II; and Berrier, Bobby L.: Effects of Tail Span and Empennage Arrangement on Drag of a Typical Single-Engine Aft End. NASA TP-2352, 1984.

3.4-5

Burley, James R., II; Carlson, John R.; and Henderson, William P.: Experimental and Numerical Results for a Generic Axisymmetric Single-Engine Afterbody With Horizontal and Vertical Tails at Transonic Speeds. NASA TM-87755, 1986.

3.4-6

Jones, William T.; and Abdol-Hamid, Khaled S.: Computational Analysis of Drag Reduction Techniques for Afterbody/Nozzle/Empennage Configurations. SAE Paper No. 912127, 1991.

3.4-7

Leavitt, Laurence D.: Effect of Empennage Location on Twin-Engine Afterbody/Nozzle Aerodynamic Characteristics at Mach Numbers From 0.6 to 1.2. NASA TP-2116, May 1983.

3.4-8

Leavitt, Laurence D.; and Bare, E. Ann: Effects of Twin-Vertical-Tail Parameters on Twin-Engine Afterbody/Nozzle Aerodynamic Characteristics. NASA TP-2158, May 1983.

3.4-9

Putnam, Lawrence E.; and Mercer, Charles E.: Pitot-Pressure Measurements in Flow Fields Behind a Rectangular Nozzle With Exhaust Jet for Free-Stream Mach Numbers of 0.00, 0.60, and 1.20. NASA TM-88990, November 1986.

3.4-10

Compton, William B., III; Thomas, James L.; Abeyounis, William K.; and Mason, Mary L.: Transonic Navier-Stokes Solutions of Three-Dimensional Afterbody Flows. NASA TM-4111, July 1989.

3.4-11

Compton, W.; and Abdol-Hamid, K.: Navier-Stokes Simulation of Transonic Afterbody Flows with Jet Exhaust. AIAA Paper No. 90-3057, August 1990.

- 3.4-12 Compton, William B., III; and Abdol-Hamid, Khaled S.: Navier-Stokes Simulation of Nozzle-Afterbody Flows With Jets at Off-Design Conditions. AIAA Paper No. 91-3207, September 1991.
- 3.4-13 Compton, W. B., III; Abdol-Hamid, K. S.; and Abeyounis, W. K.: Comparison of Algebraic Turbulence Models for Afterbody Flows with Jet Exhaust. AIAA Journal, Vol. 30, No. 11, pp. 2716-2722, November 1992.

IDENTIFICATION						FREE-STREAM CONDITIONS			JET FLOW CONDITION		POSITION
Case	Horiz. tail	Vert. tail	# of engines	nozzle shape	boattail separation	$M_{\infty}$	Nom. $q_{\infty}$ , psi	Nom. $T_{t\infty}$ , °R	NPR	Nom. $T_{ij}$ , °R	$\alpha$ , deg.
B.1.1	None	None	One	Axi.	Yes	0.901	4.94	590	2.033	530	0.010
B.1.2	None	None	One	Axi.	Yes	0.901	4.94	590	4.991	530	0.009
B.2.1	Aft	Fwd	One	Axi.	Yes	0.900	4.94	590	2.027	530	0.021
B.2.2	Aft	Fwd	One	Axi.	Yes	0.900	4.94	590	2.997	530	0.021
B.2.3	Aft	Fwd	One	Axi.	Yes	0.900	4.94	590	5.033	530	0.021
B.3.1	Mid	Mid	Two	Axi.	Yes	0.901	4.94	590	3.407	530	-0.004
B.3.2	Mid	Aft	Two	Axi.	Yes	0.899	4.94	590	3.400	530	-0.004
B.3.3	Mid	Fwd	Two	Axi.	Yes	0.899	4.94	590	3.402	530	0.031
B.4.1	None	None	One	Rect.	No	0.600	2.90	587.8	4.00	541.2	-0.02
B.4.2	None	None	One	Rect.	Yes	0.938	5.13	619.3	4.02	549.9	-0.02

Table 3.4-1: "Design" test cases. All from NASA experiments.

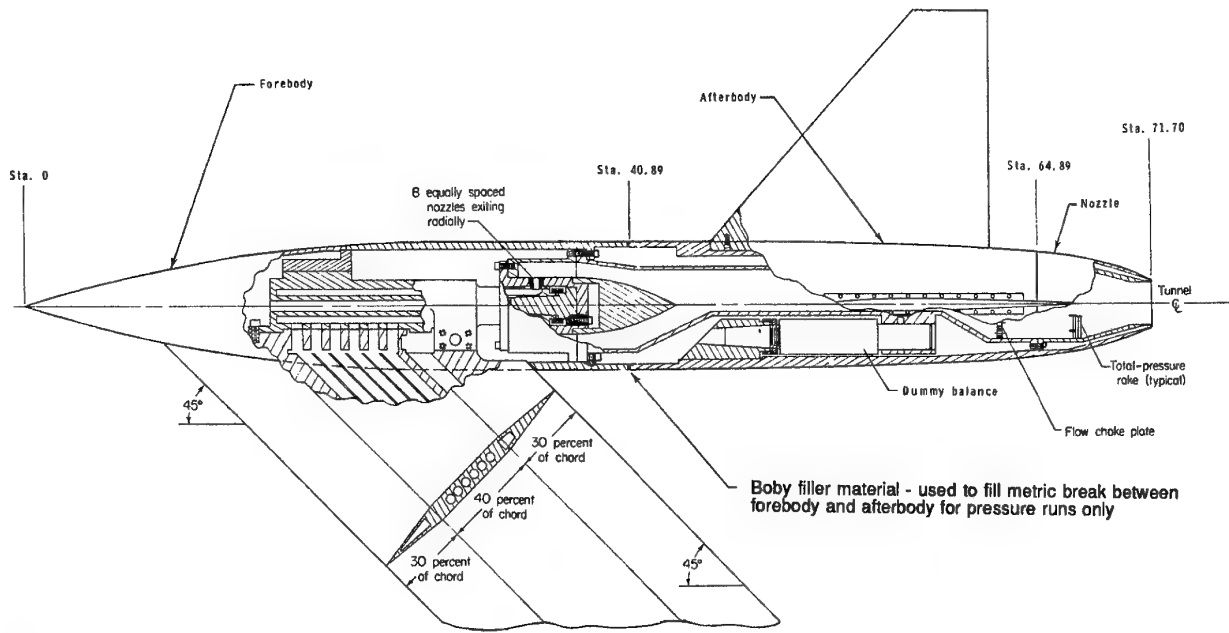


**Figure 3.4-1:** Sketch of NASA Langley Research Center single engine afterbody with tails. (All linear dimensions are in inches)

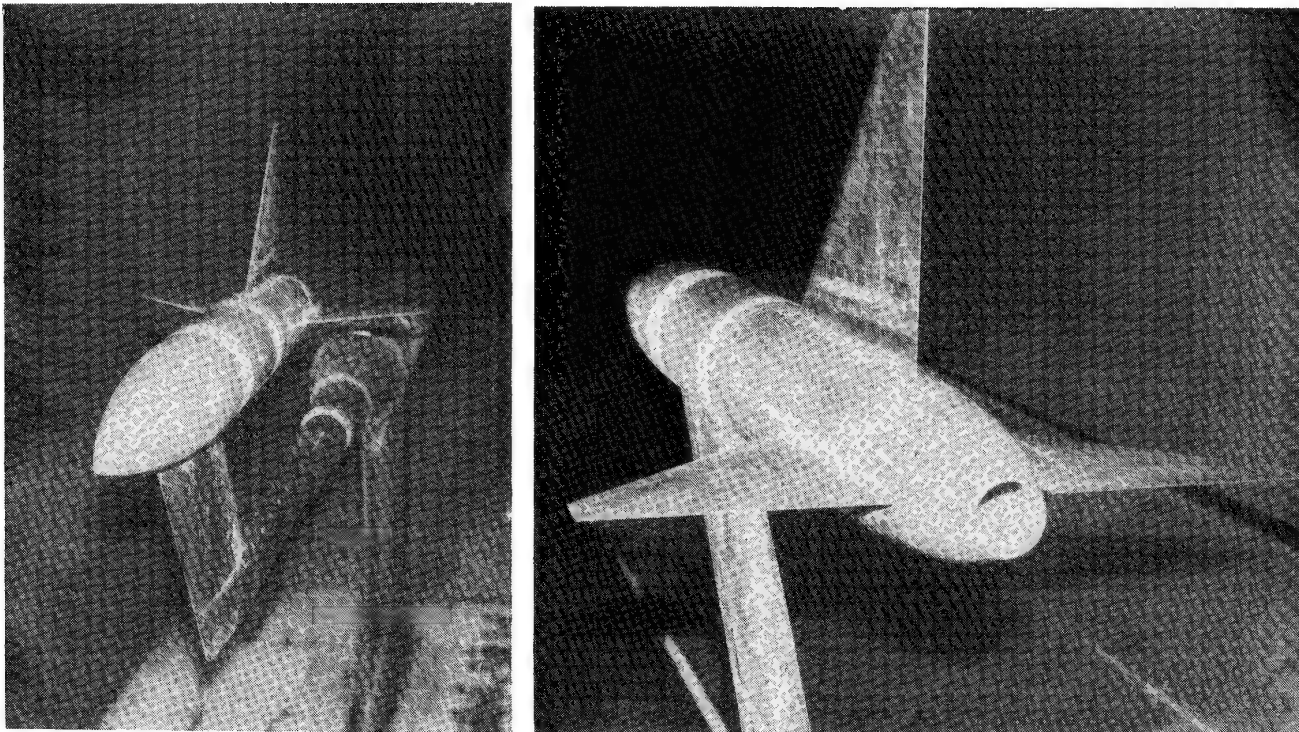
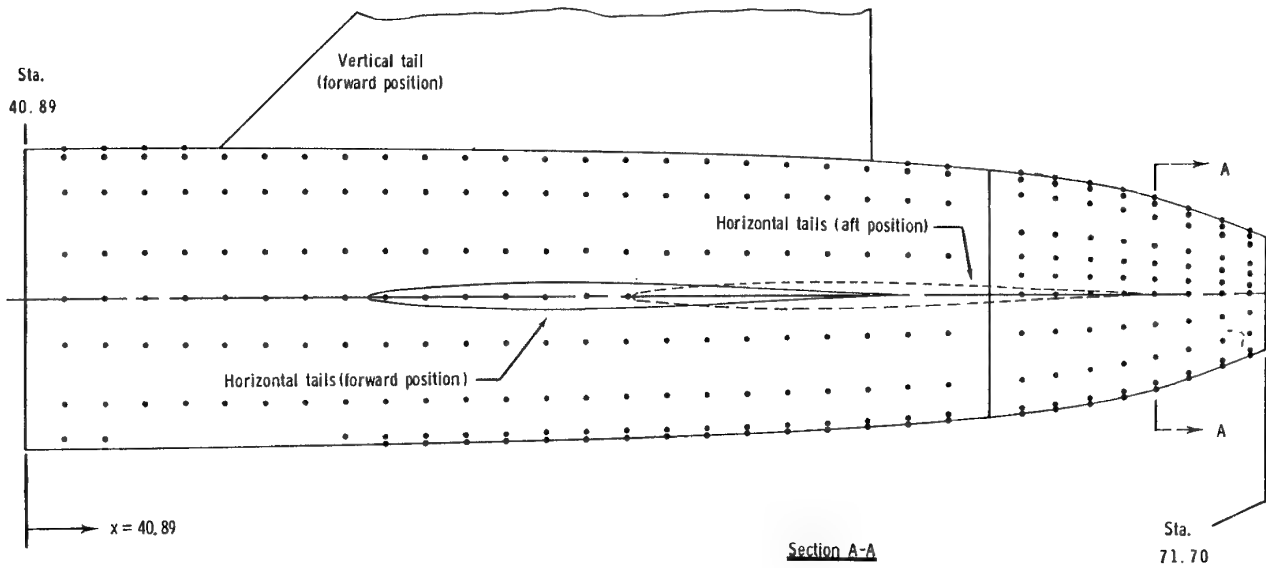


**Figure 3.4-2:** Photographs of model in the NASA Langley Research Center 16-Foot Transonic Tunnel.



Nozzle/afterbody external geometry

	x, in.	r, in.
1	40.888	3.670
2	41.700	3.670
3	43.700	3.665
4	45.700	3.654
5	47.700	3.636
6	49.700	3.612
7	51.700	3.580
8	53.700	3.539
9	55.700	3.488
10	57.700	3.425
11	58.700	3.389
12	59.700	3.348
13	60.700	3.302
14	61.700	3.248
15	62.312	3.217
16	62.700	3.184
17	63.200	3.147
18	63.700	3.108
19	64.300	3.056
20	64.888	3.000
21	65.700	2.919
22	67.181	2.726
23	67.700	2.635
24	68.700	2.400
25	69.700	2.098
26	70.700	1.750
27	71.700	1.374

x, in.	x/l	$\Phi$ , deg											
		0	18	36	45	54	72	81	90	108	135	162	180
41.813	.524	x	x		x		x		x	x	x	x	
42.838	.598	x	x		x		x		x	x	x	x	
43.808	.612	x	x		x		x		x	x	x	x	
44.728	.626	x	x		x		x		x	x	x	x	
45.587	.640		x		x		x		x	x	x	x	
46.588	.654		x		x		x		x	x	x	x	
47.588	.668		x		x		x		x	x	x	x	
48.588	.682		x		x		x		x	x	x	x	
49.588	.696		x		x		x		x	x	x	x	
50.588	.710		x		x		x		x	x	x	x	
51.588	.724		x		x		x		x	x	x	x	
52.588	.738		x		x		x		x	x	x	x	
53.588	.752		x		x		x		x	x	x	x	
54.588	.766		x		x		x		x	x	x	x	
55.588	.780		x		x		x		x	x	x	x	
56.588	.794		x		x		x		x	x	x	x	
57.588	.808		x		x		x		x	x	x	x	
58.588	.822		x		x		x		x	x	x	x	
59.588	.836		x		x		x		x	x	x	x	
60.588	.850		x		x		x		x	x	x	x	
61.588	.864		x		x		x		x	x	x	x	
62.588	.878		x		x		x		x	x	x	x	
63.588	.892		x		x		x		x	x	x	x	
64.588	.906		x		x		x		x	x	x	x	
65.588	.920		x		x		x		x	x	x	x	
66.588	.934		x		x		x		x	x	x	x	
67.588	.948		x		x		x		x	x	x	x	
68.588	.962		x		x		x		x	x	x	x	
69.588	.976		x		x		x		x	x	x	x	
70.588	.990		x		x		x		x	x	x	x	
71.588	.996		x		x		x		x	x	x	x	

Figure 3.4-3: Aftend pressure instrumentation and external geometry. (All linear dimensions are in inches)

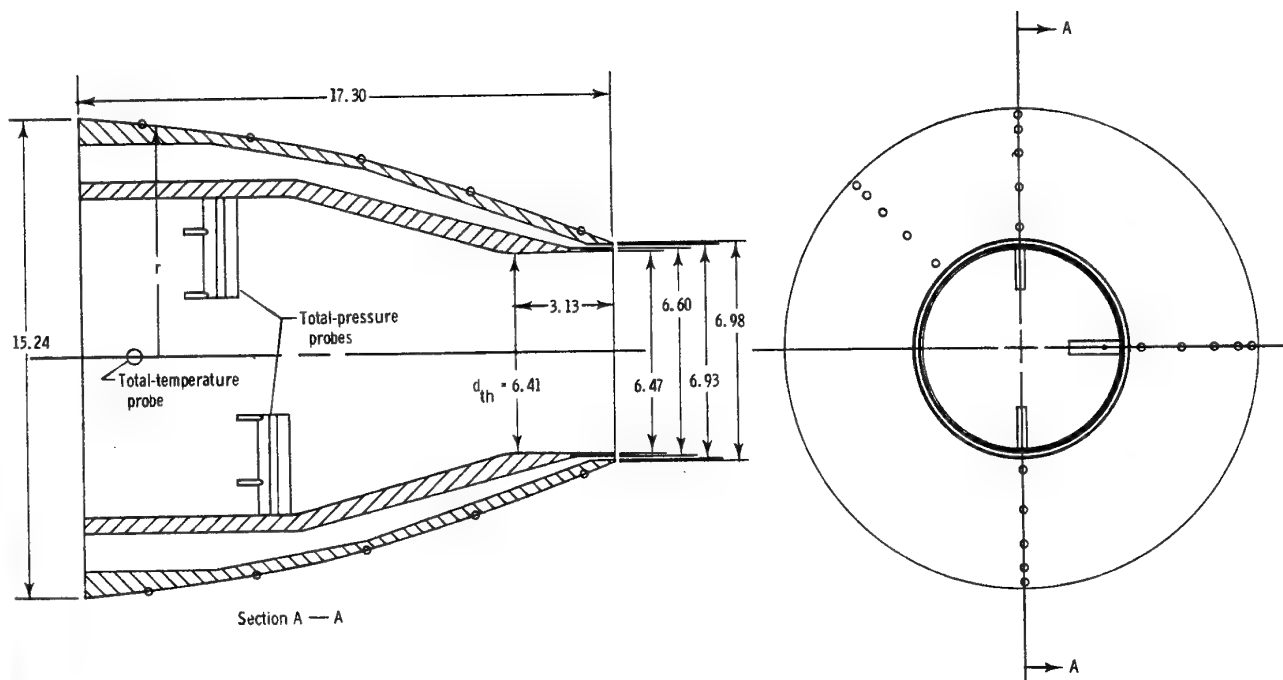


**Figure 3.4-4:** Sketch of nozzle showing important dimensions. (Linear dimensions are in centimeters)

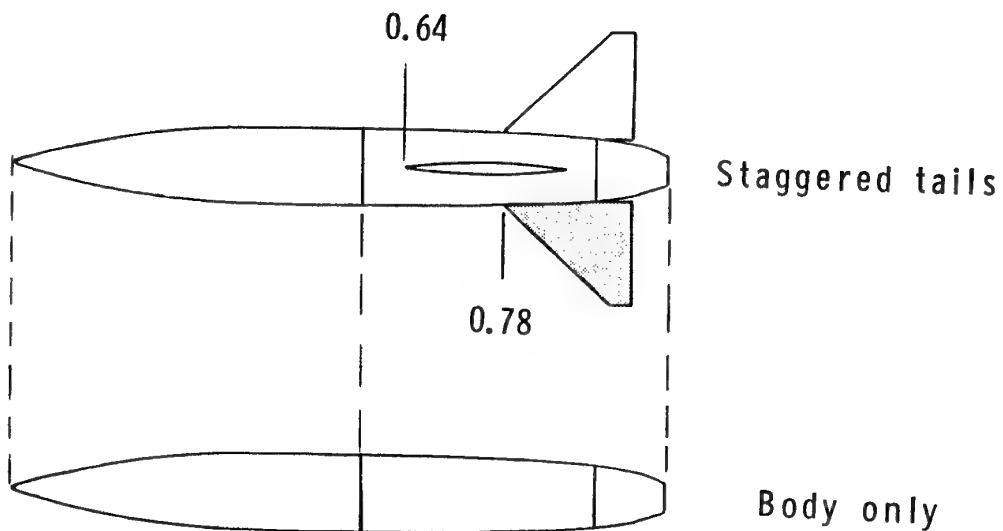


**Figure 3.4-5:** Planform view of test case tail arrangements. (Dimensions are in fractions of body length)

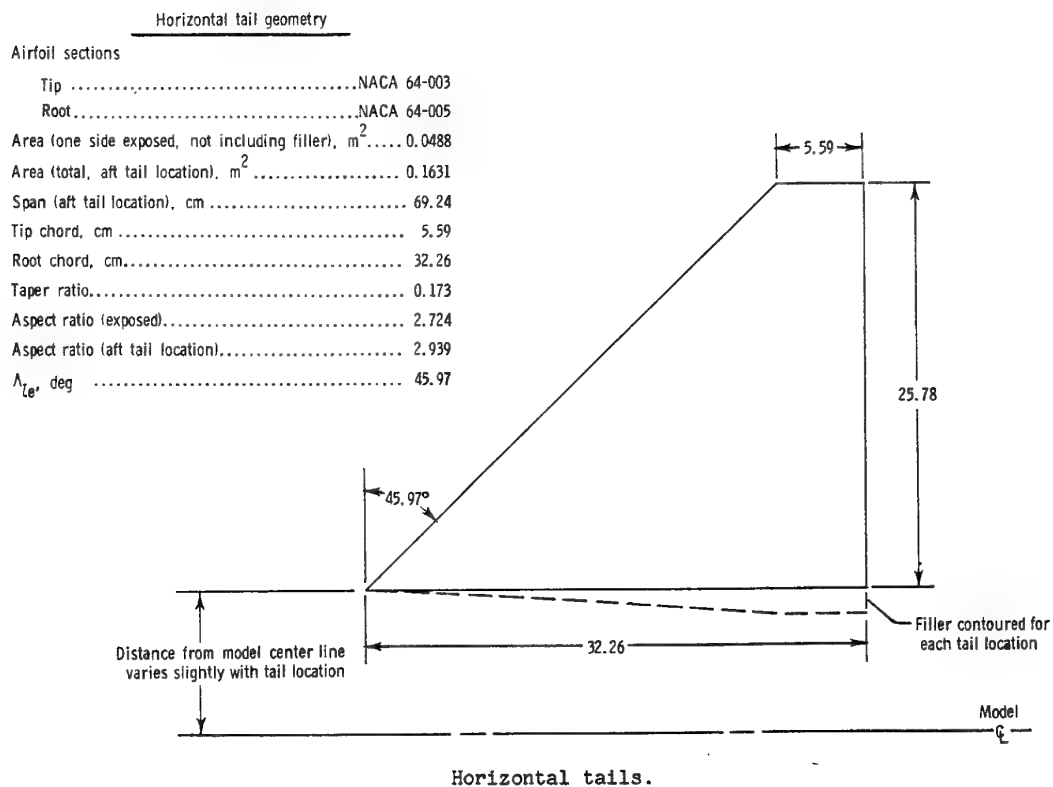
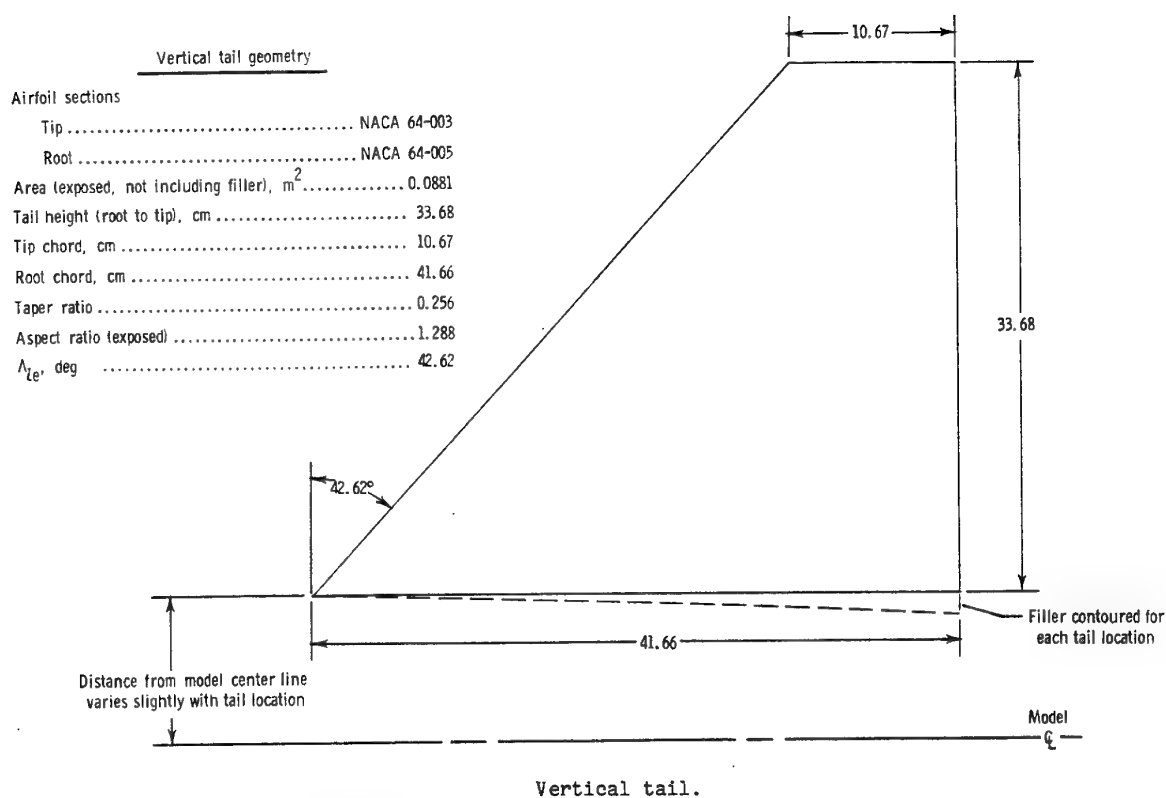


**Figure 3.4-6:** Sketches of empennage surfaces. (All dimensions are in centimeters)

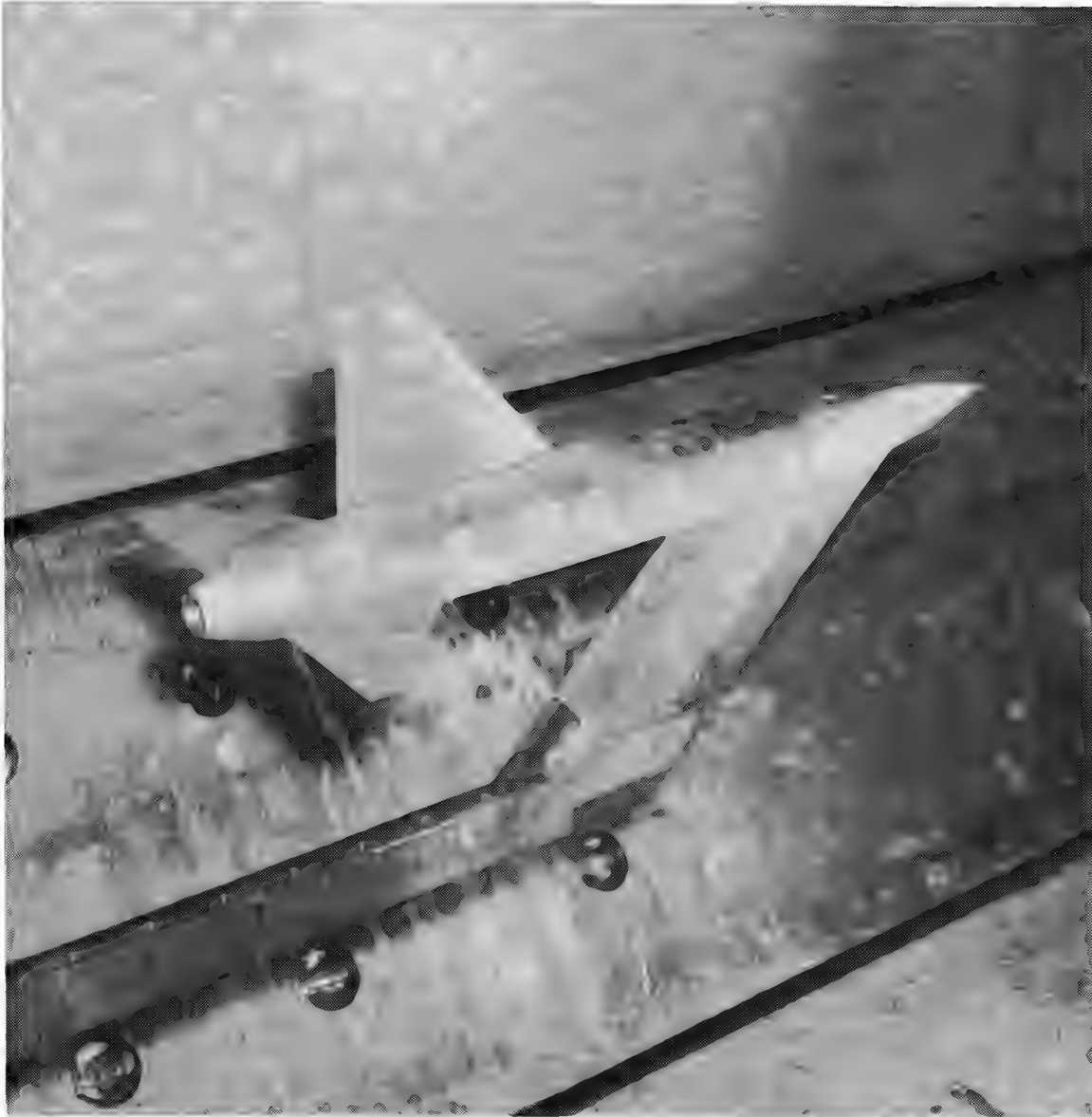


*Figure 3.4-7: Photograph of test case B.2 installed in the NASA Langley Research Center 16-Foot Transonic Tunnel.*



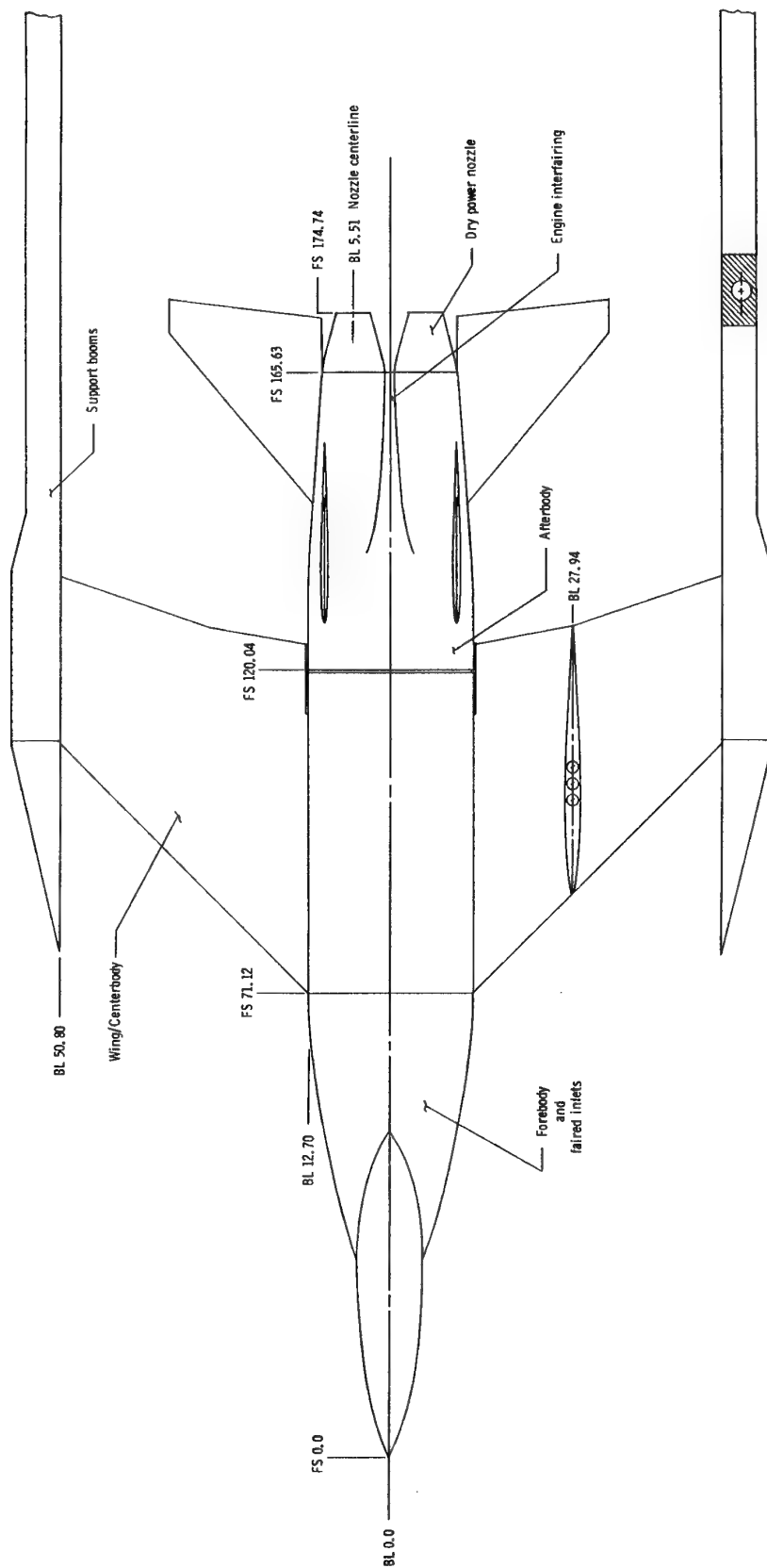


**Figure 3.4-8:** Sketch of NASA Langley Research Center twin-engine afterbody model with tails. (All linear dimensions are in centimeters)

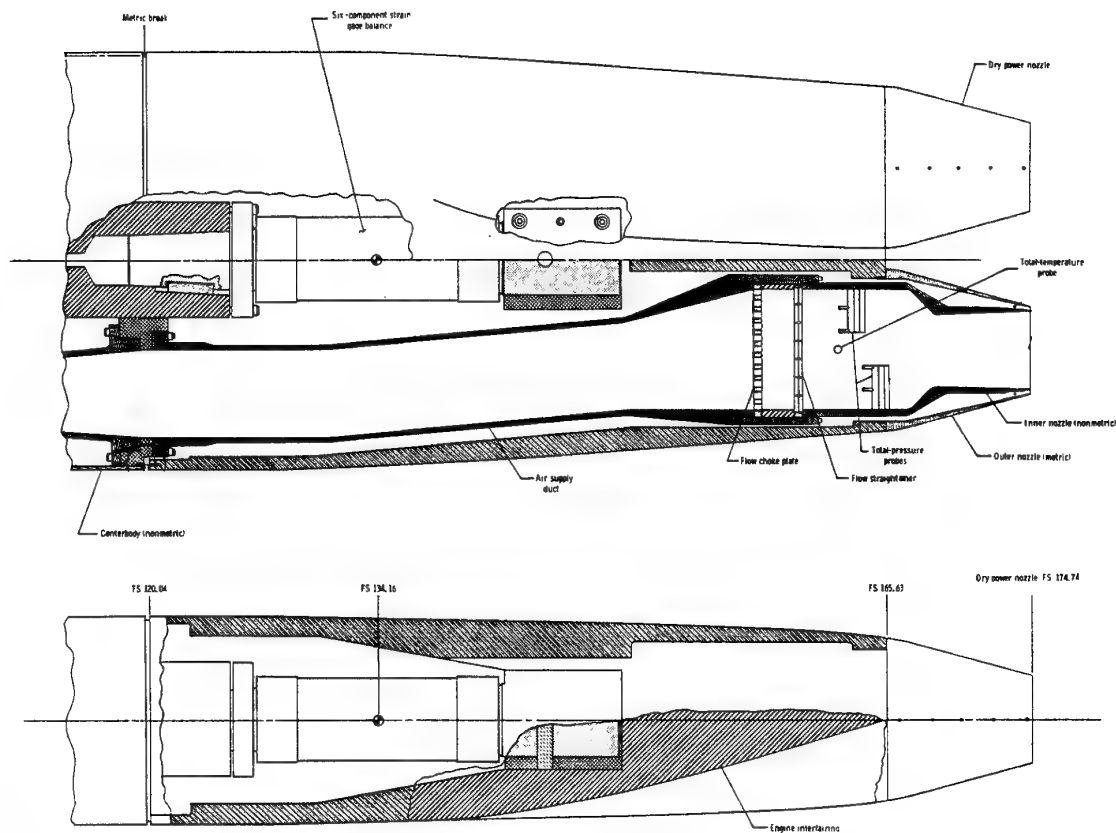


Figure 3.4-10: Sketch of twin-engine aftend. (Linear dimensions are in centimeters)

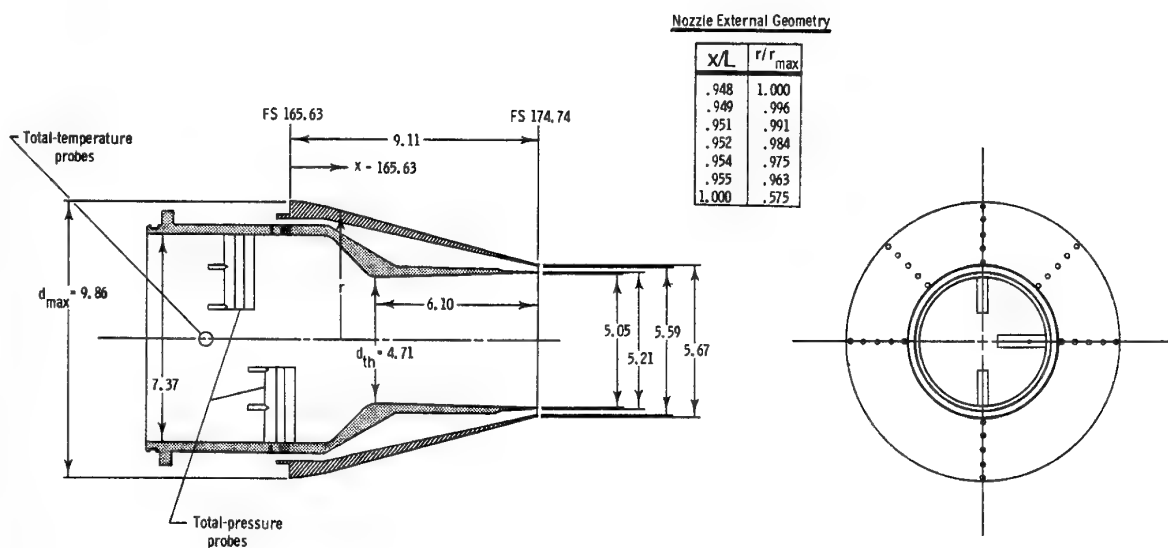
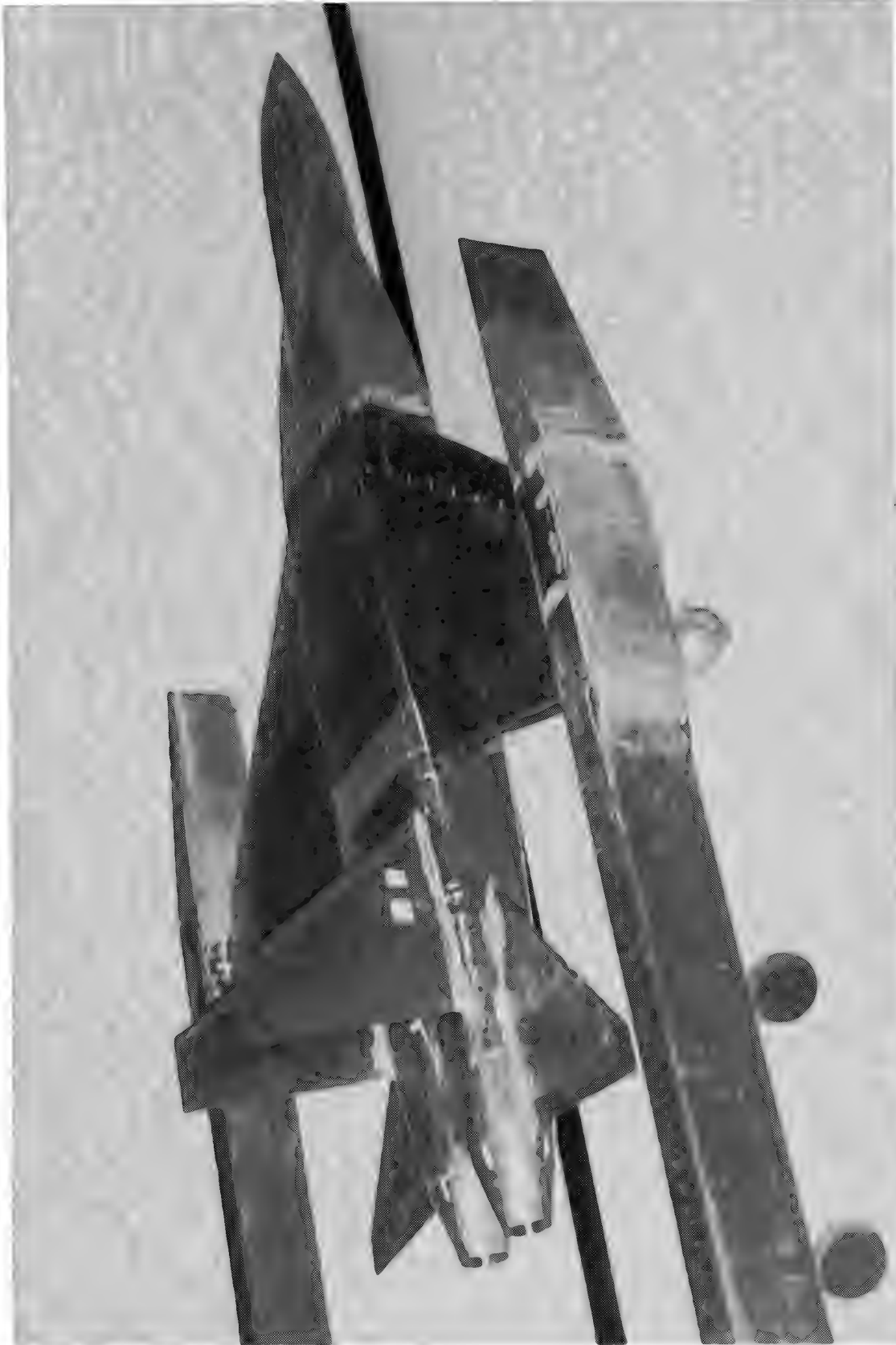
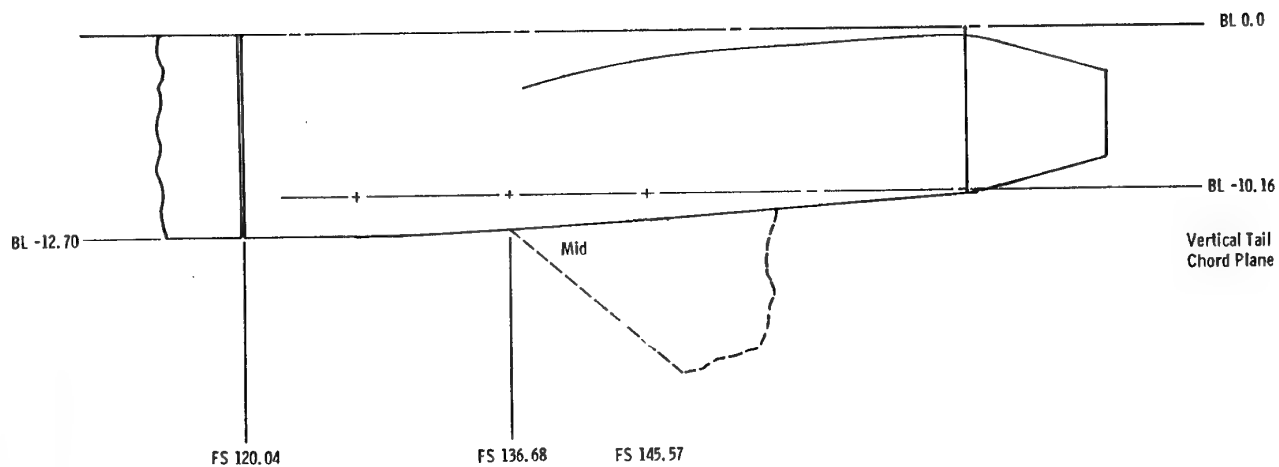


Figure 3.4-11: Sketch of nozzle. (Linear dimensions are in centimeters)



**Figure 3.4.9** Photograph of NASA Langley Research Center twin-engine afterbody model with tails.  
(Test case B.3.3)

## TOP VIEW



## SIDE VIEW

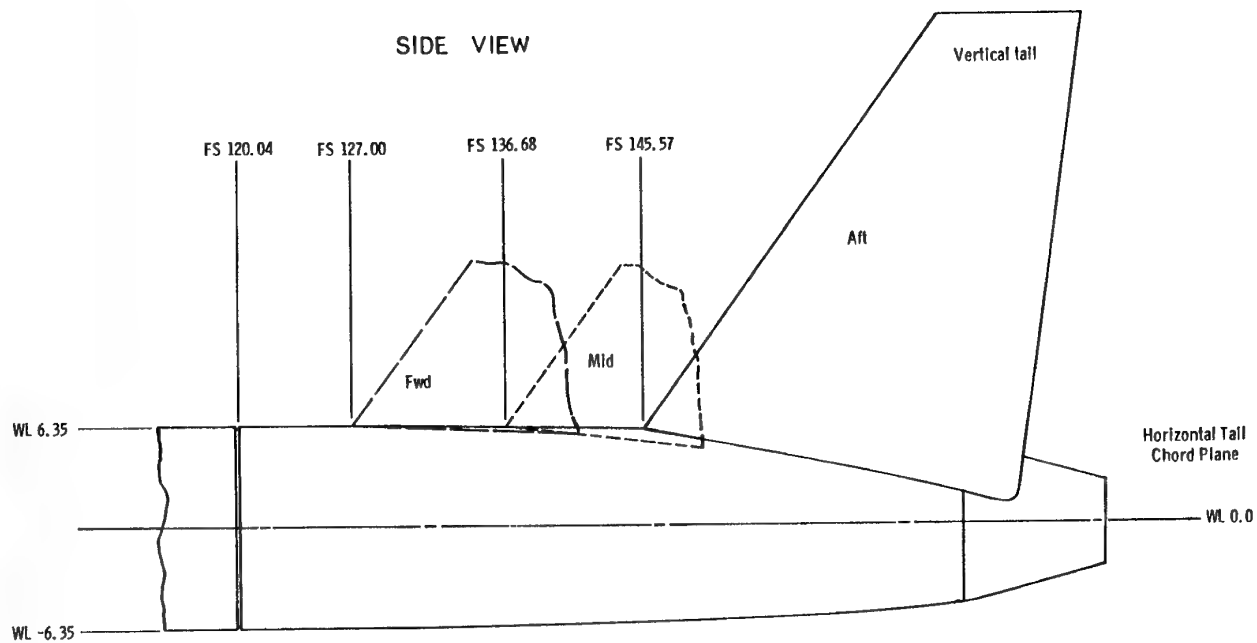


**Figure 3.4-12:** Sketch showing test case tail arrangements. (Linear dimensions are in centimeters)

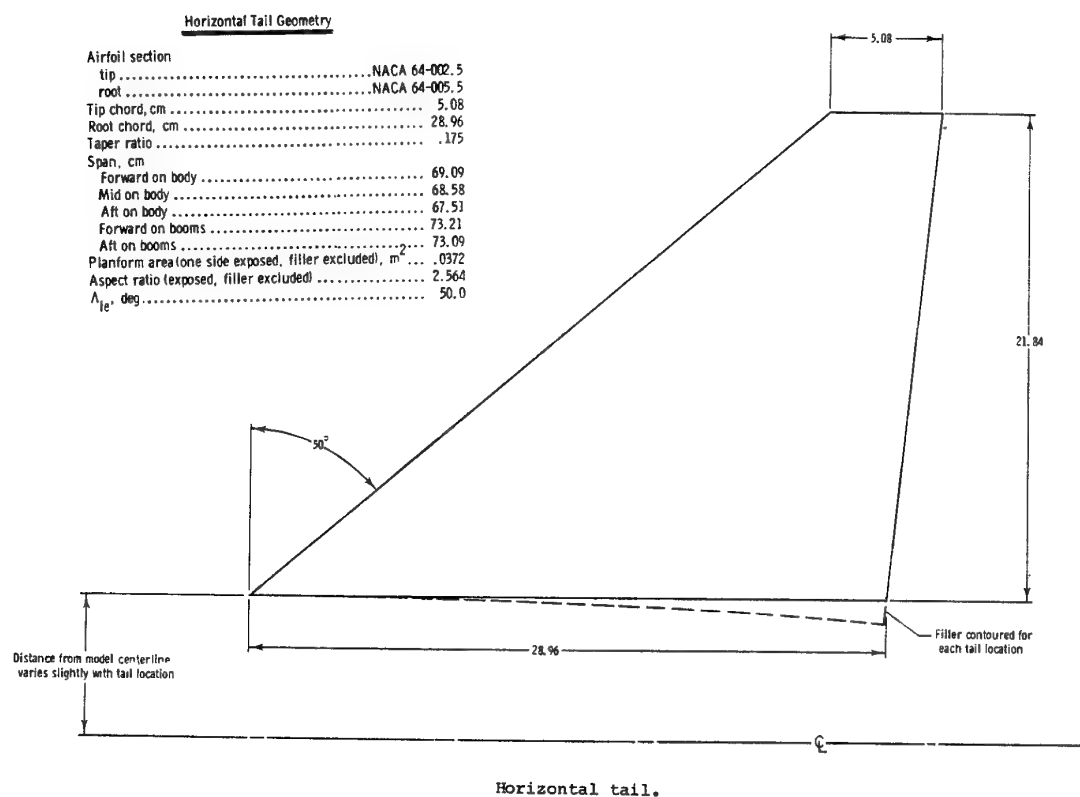
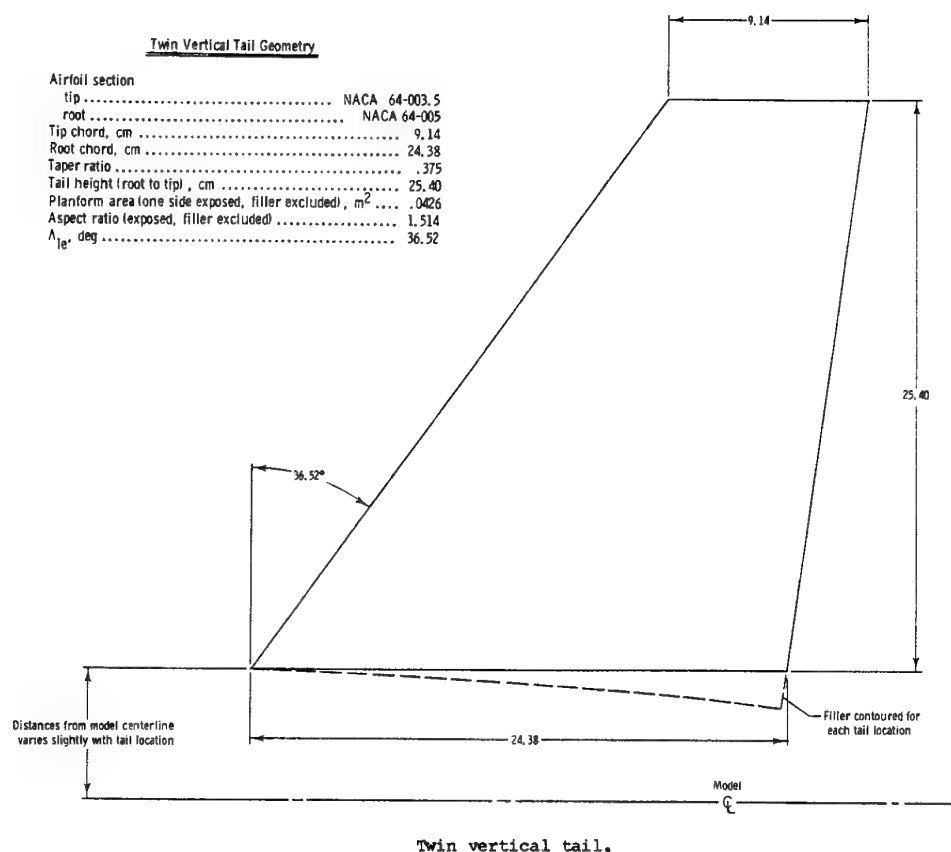


**Figure 3.4-13:** Sketches of empennage surfaces. (Linear dimensions are in centimeters)



**Figure 3.4-14:** Photograph of test case B.3 installed in the NASA Langley Research Center 16-Foot Transonic Tunnel on the wing-tip support system.

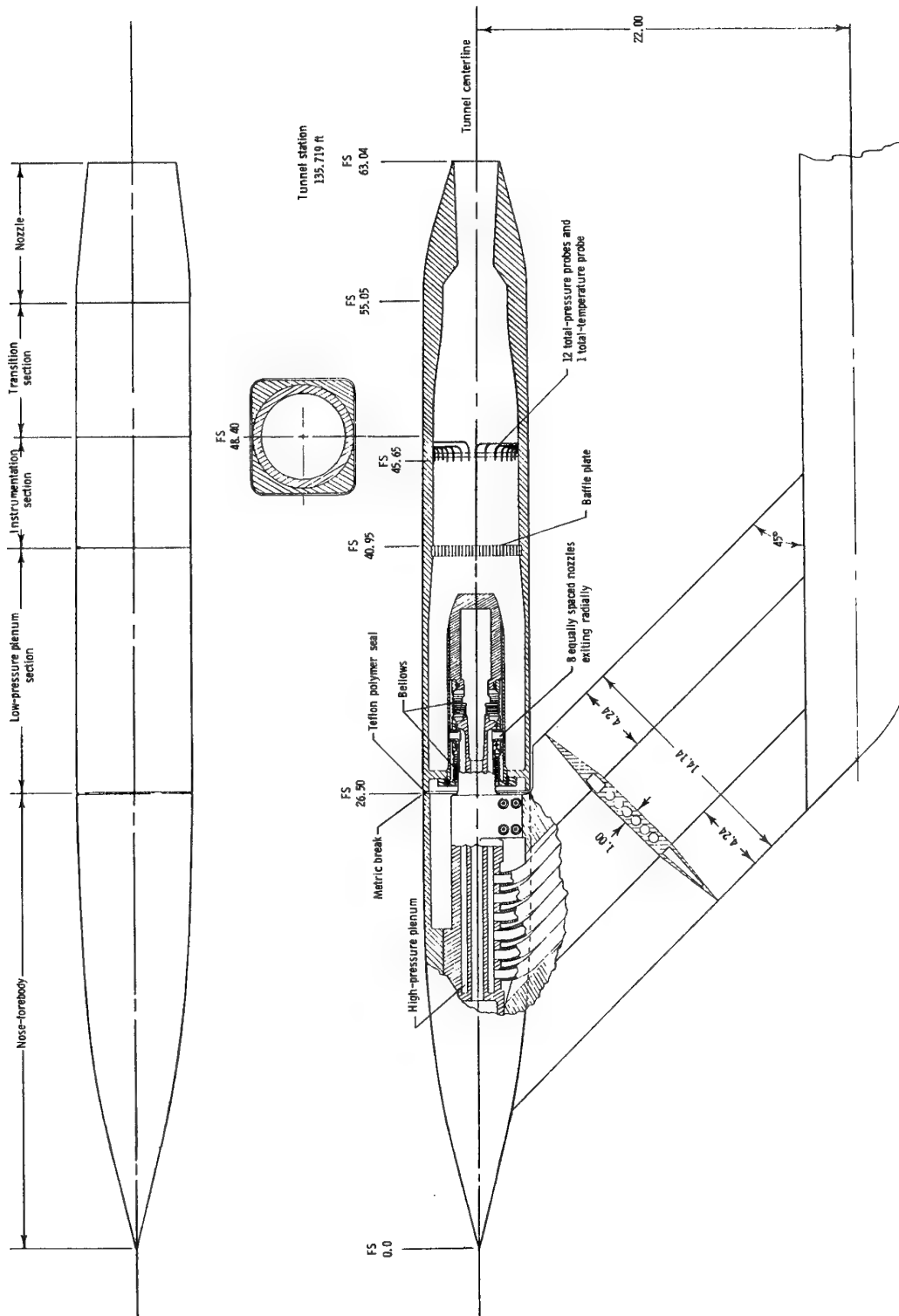


**Figure 3.4-15:** Sketch of NASA Langley Research Center single jet 2-D C-D model. (All linear dimensions are in inches.)

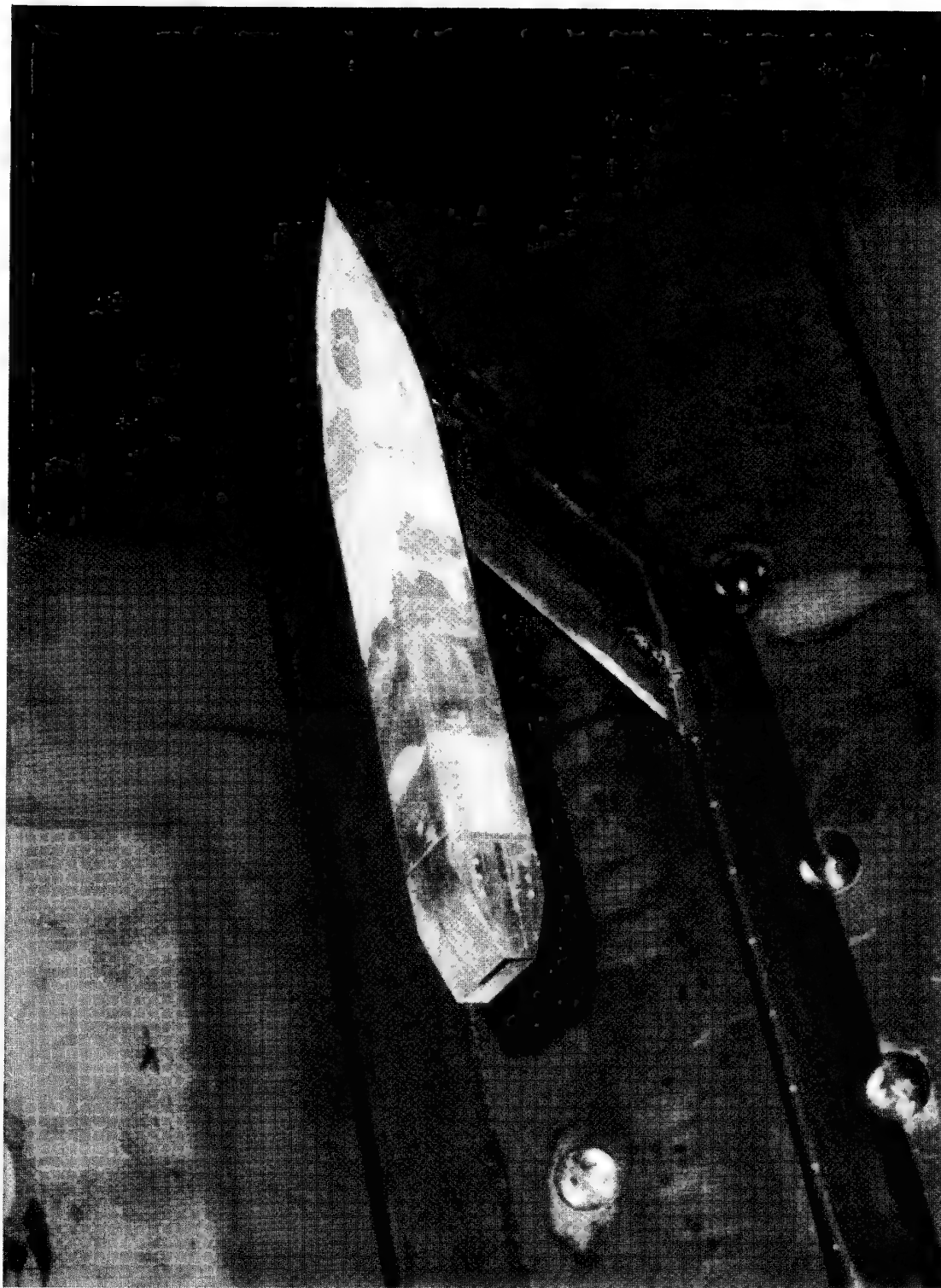


**Figure 3.4-16:** Photograph of test case B.4 installed in the NASA Langley Research Center 16-Foot Transonic Tunnel.



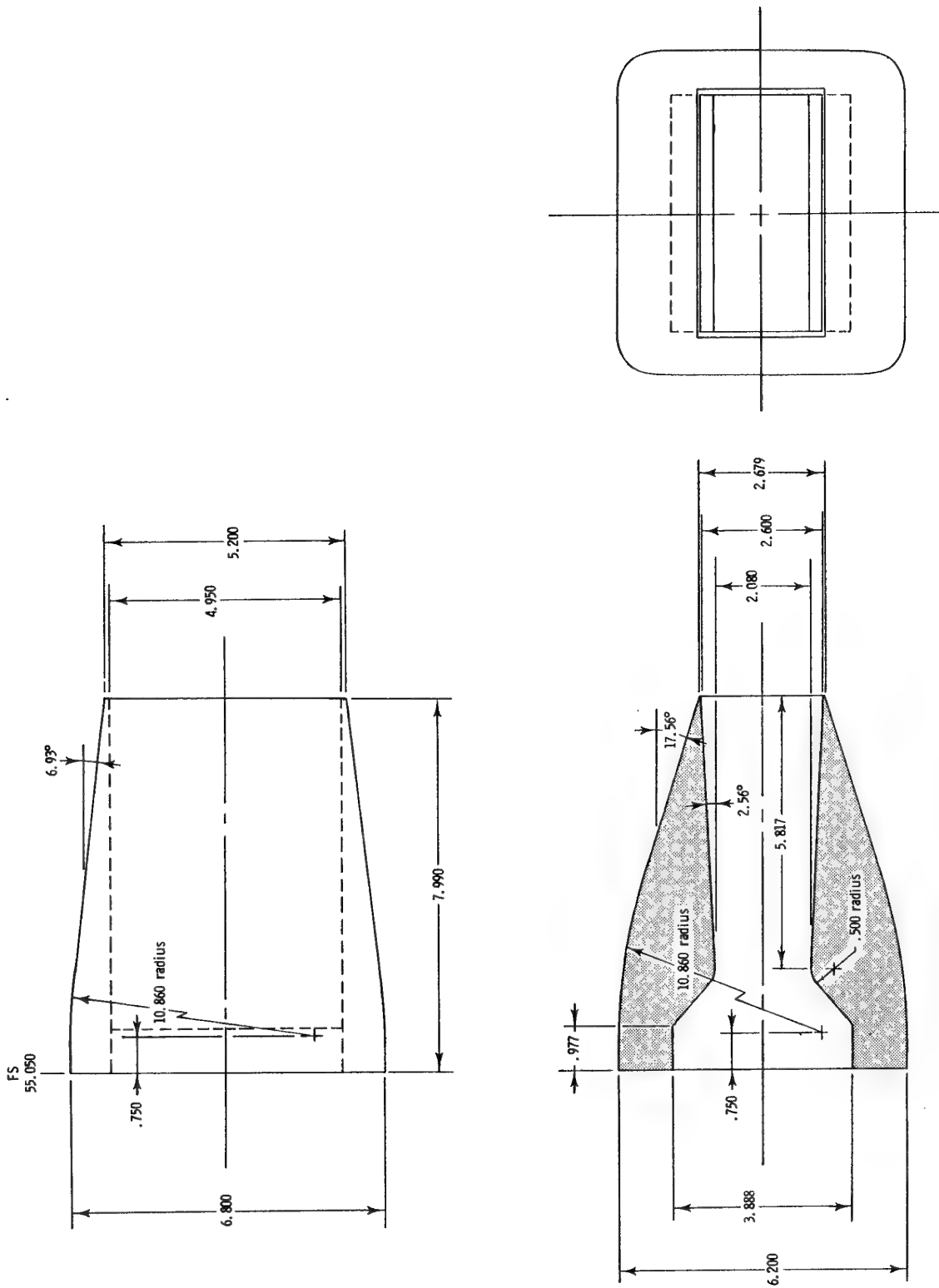


Figure 3.4-17: Sketch of 2-D C-D nozzle configuration showing important dimensions. (All linear dimensions are in inches.)

### 3.5 Computational Results for Engineering Cases

The cases in Series B were chosen for their resemblance to engineering requirements, while the preceding Series A cases were chosen for the availability of more fundamental data to assess prediction accuracy. The organizations contributing data to these comparisons are indicated in Figure 3.5-1, below.

	S01	E02	E03	E04	E05	E06	E07	E08	N09	N10	E11	N12	N13	N16
	Aermacchi (Beml-Emphical)	Rolls-Royce (ANBE)	SNECMA (CANARD)	USAF Wright Lab (COBALT)	Dassault (EUGENIE)	Rolls-Royce (FAN81)	Rolls-Royce (FLITE.FS)	Aermacchi (FLO87P)	McDonnell Douglas (NABTD)	NASA Langley (PAB3D)	DRA / ARA (BAUHA)	Lockheed (TEAM)	Dassault (VIRGINIE)	NASA Lewis (NPARC)
B.1.1														
B.1.2														
B.2.1														
B.2.2														
B.2.3														
B.3.1														
B.3.2														
B.3.3														
B.4.1														
B.4.2														

Figure 3.5-1 - Summary of Submitted Cases

The submitted data are presented in this Section, organized by test case. This presentation approach was chosen to facilitate comparisons between methods, for assessing the current state of the art. The reader should be aware, no clear winners or losers are revealed in these comparisons. Each method did particularly well on some cases, and poorly on others. These comparisons should be viewed as a sampling of the state of the art as it existed in 1993. Guidelines were given to the contributors regarding the geometry and flow conditions to be modeled, and the data plots to be provided. No guidance was given regarding key modeling issues such as grid density, or transition and turbulence modeling. Therefore, the results were not produced on a consistent basis.

Further, various organizations approached this process in different ways. One contributor, for example, used a code and personnel with a background emphasizing plume flow-field predictions. Naturally, their approach was well developed for that portion of the flowfields. Several

contributors applied recently-developed CFD codes to these test cases - codes with advanced technology but little operational experience. Some contributors assigned experienced staff to this task, while others viewed this effort as an opportunity to develop people, codes, and technology. Several contributors experienced instability and lack of continuity in staffing these tasks over the two-year duration of the study.

Therefore, the reader is urged to interpret these data as a summary of the current state (1993-94) with indication as to the challenges which remain before us. The authors have drawn certain conclusions based on comparisons among the various sets of data provided to the Working Group. The reader must bear in mind, however, that these comparisons lack a consistent approach. Therefore, any conclusions based on comparisons between different codes or different cases must be considered with caution.

Most of the comparisons with experimental data are made in terms of wall static pressure. Additional comparisons are made in terms of intrusive Pitot probe surveys, pressure-integrated drag, and total drag (measured by a force balance). Unfortunately, only limited comparisons are available for the direct predictions of CFD analysis: Off-body velocity, pressure, and temperature, and turbulence parameters such as turbulent kinetic energy or Reynolds stress. Additional numerical diagnostic data are presented in some cases, such as convergence histories. Other qualitative interpretive data also are presented for some cases: simulated oil flow visualizations, off-body plots of velocity vector fields, Mach number contours, etc.

**Experimental Uncertainty** - The test cases were chosen based on the evaluated high quality of their data. It is believed, for example, that wind tunnel wall corrections are not needed for these cases. No contributors performed any of these corrections. Also (and somewhat more debatedly) we have not asked contributors to consider the effects of the wind tunnel support system for the test models.

Estimated uncertainties in the experimental data have been provided by the organization contributing the B-series test cases. These estimated uncertainties are:

- Surface pressure coefficient ( $C_p$ )  $\pm 0.005$
- Drag coefficient as measured on a balance,  $\pm 0.0050$  in terms of maximum cross-section area of the forebody-aftbody-nozzle combination, and  $\pm 0.0005$  in terms of a representative aircraft wing area.
- Drag coefficient as obtained from integration of measured surface pressures,  $\pm 0.0100$  in terms of maximum cross-section area of the forebody-aftbody-

nozzle combination, and  $\pm 0.0010$  in terms of a representative aircraft wing area.

### 3.5.1 Case B.1

Case B.1 is a single axisymmetric nozzle, tested at zero angle of attack and sideslip. Due to the simplicity of this case, it is a fundamental test of basic capabilities for afterbody flowfield modeling. This geometry is illustrated in Figure 3.5-2.

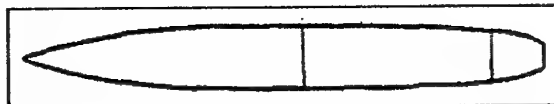


Figure 3.5-2 - Geometry for Cases B.1.x

All CFD contributions have included the internal nozzle flow upstream of the jet exit, in their analyses (see Figure 3.5-3). This approach avoids the necessity of prescribing flowfield boundary conditions at the exit plane, where the flow is not necessarily uniform. Preferably, the exhaust flow computation begins upstream of the throat, where the flow is subsonic. Any non-physical character in the assumed inflow boundary conditions will be dissipated quickly in the subsonic flow. A similar error in a supersonic flow region would persist indefinitely in the plume, in a shock-expansion wave system.

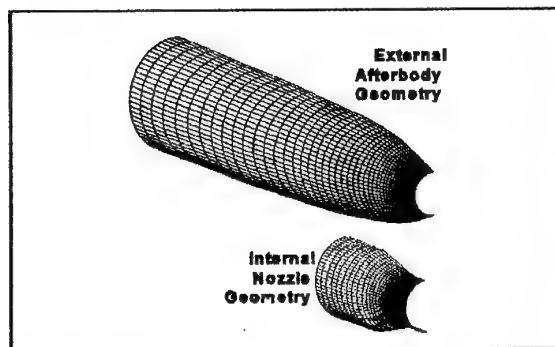


Figure 3.5-3 - Afterbody and Nozzle Geometry for Cases B.1.1 and B.1.2

This geometry features relatively gradual surface curvature, except in the corner at the nozzle lip. Therefore, grid density requirements are driven by naturally-occurring flowfield gradients, rather than by sharp variations in the surface geometry. This, actually, is a complication since the location of sharp flowfield gradients is not known in advance (e.g., boundary layer separation and reattachment points). Therefore, application of those codes which lack a solution-adaptive capability (i.e., most of the codes) must compensate

for this uncertainty by providing a high grid density over most of the afterbody.

The viscous interaction and (potential) boundary layer separation arises through a gradual evolution of the turbulent boundary layer. Thus, accurate prediction of this flowfield is a test mainly of the turbulence model. The two cases, B.1.1 and B.1.2, are both at Mach 0.9,  $\alpha=0^\circ$ . They differ only in the NPR which is at a value of 2.033 (Case B.1.1) and 4.991 (Case B.1.2).

**Nozzle Base Area** - The geometry as tested in the B.1 cases had a small blunt base area (See Figure 3.5-4). The reference geometry as provided to the contributors provided a somewhat idealized representation of the nozzle trailing edge. The inner and outer nozzle contours were represented in the analysis as coming to a sharp corner, without rearward-facing base area. This reference geometry is illustrated in Figure 3.5-5. One of the contributors (N09) analyzed the B.1.1 case to assess the impact of the actual vs. nominal trailing edge geometry, and concluded that this feature has negligible impact on the predictions (these results are presented below, in the discussion of predictions for Case B.1.1). Another contributor (N10) investigated this issue in a more comprehensive manner, and concluded the details of modeling the trailing edge can have a significant impact on the pressure distributions. This latter investigation is presented, in some detail, in Section 3.5.1.3 (below).

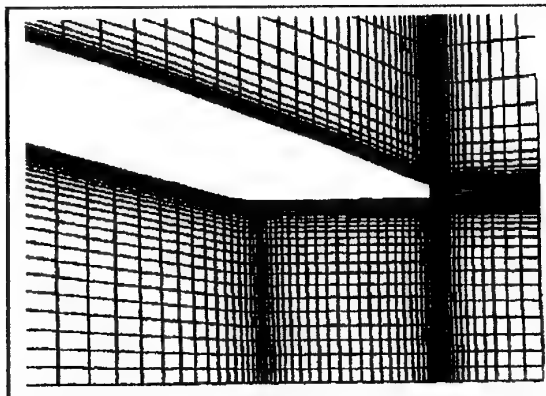


Figure 3.5-4. Blunt Trailing Edge Geometry for Cases B.1.1 and B.1.2 (Grid from Contribution N09)

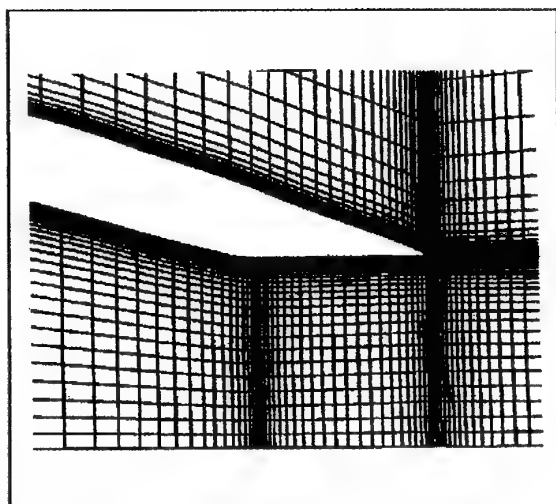


Figure 3.5-5 - Nominal Geometry Provided for Cases B.1.1 and B.1.2 (Grid from Contribution N09)

### 3.5.1.1 Case B.1.1

For case B.1.1, the freestream Mach number is 0.9 and the angle of attack is zero. The nozzle pressure ratio (NPR) is 2.033, producing a near-design exit flow condition. The flowfield is (nominally) axisymmetric.

The general nature of this flowfield is illustrated in Mach number contour plots which are presented in Figure 3.5-6. Two plots are presented, from an inviscid (Euler) solution, and a viscous (Navier-Stokes) solution. The obvious difference between the two solutions, of course, is the omission of viscous effects in the boundary layer and plume free shear layer, in the Euler solution. The boundary layer thickens significantly on the final portion of the external nozzle in the Navier-Stokes solution. Inside the nozzle, where the boundary layer has been subjected to a sustained favorable pressure gradient, the boundary layers are very thin.

Other differences can be noted, too. The Euler solution shows a modest subsonic expansion at the nozzle shoulder (say,  $x=65$  in the dimensional units of this Figure). A subsonic compression is present in the external flow, centered on the corner at the lip (i.e., trailing edge) of the nozzle. In the Euler solution, the plume internal flow remains subsonic past the geometric throat. This is due to the high pressure in the external stream at the nozzle exit. Due to the external stream compression at the exit, the external pressure at the nozzle exit is sufficiently high as to prevent the internal flow from expanding to supersonic speeds.

In the Navier-Stokes solution, strong viscous interactions in the external stream prevent the external pressure from rising

very strongly at the nozzle exit. Consequently, a lower ambient (exit) pressure is imposed on the internal jet flow, and a sufficient pressure ratio exists for the internal stream to expand to supersonic speeds inside the nozzle, downstream of the geometric throat.

About one plume diameter downstream of the nozzle exit, both the Euler and Navier-Stokes flow predictions again become comparable.

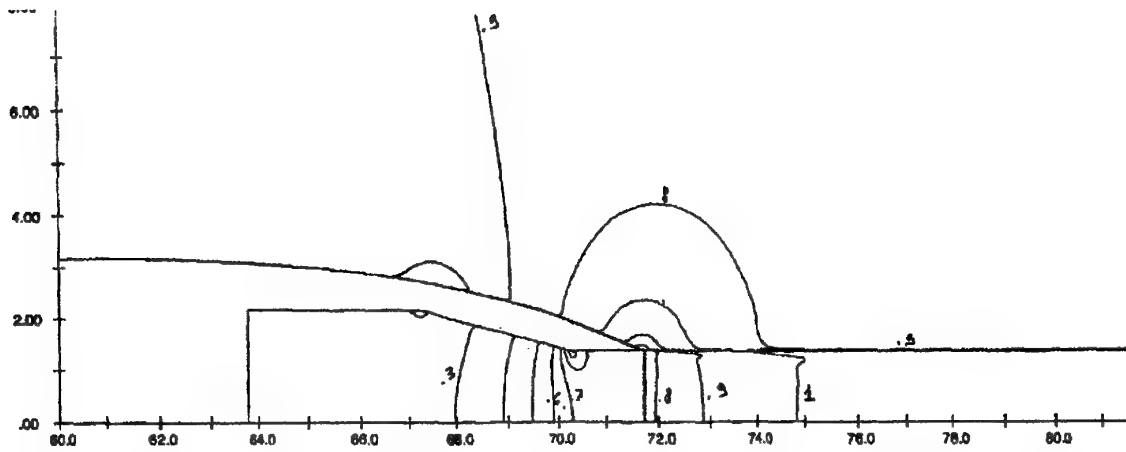
It seems that this interesting aspect of subsonic or supersonic flow in the internal nozzle, downstream of the throat, may depend on the manner in which the internal flow solution is initialized. In the present case, it appears the internal flow in the Euler solution was initialized to a subsonic condition, allowing a full pressure interaction between the external and internal streams at the nozzle exit. In other examples, where the internal flow downstream of the geometric throat is initialized to supersonic conditions (i.e., a simple flow approximation is used to initialize the solution), the supersonic domain of dependence in the internal stream would prevent an upward-running interaction, and the internal flow probably would remain supersonic.

**Surface Pressure Comparisons** - Comparisons of the predicted and measured surface pressures for this case are presented in Figure 3.5-7. These data show most of the CFD methods provided good accuracy in the relatively benign region approaching the shoulder of the nozzle (for  $X/L < 0.90$ ). However, the flow at the minimum pressure point on the nozzle (about  $X/L = 0.93$ ) is fairly sensitive to the turbulence modeling and the grid, and results at this point varied.

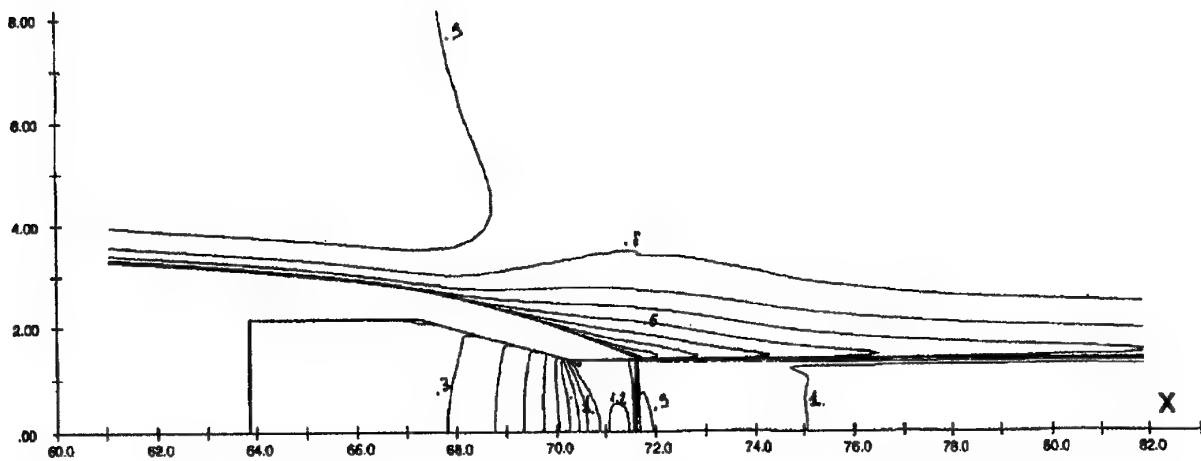
The recompression region approaching the nozzle trailing edge also is very sensitive to viscous modeling effects. Most methods did well in the initial portion of the recompression region ( $X/L = 0.94$  to  $0.98$ ), but difficulties were encountered in the final portion of the recompression region ( $X/L > 0.98$ ) where the viscous effects are the strongest. Each method over-predicted the pressure at the trailing edge. This suggests that either (1) the viscous interaction is modeled too weakly, or (2) the local effect of plume entrainment is under-predicted. Other possibilities, related to the details of the geometry and grid used in the analyses, are reviewed in Section 3.5.1.3.

Contribution N09 explored the impact of three different turbulence models, and the impact of the nominal vs actual test geometry (see Figures 3.5-4 and 3.5-5). Except for necessary differences due to the modeling of the blunt nozzle trailing edge, the grids in these comparisons were identical.

The three turbulence models used were the algebraic Baldwin-Lomax model (annotated as "B-L"), the one-equation (i.e., one partial differential equation or PDE) model

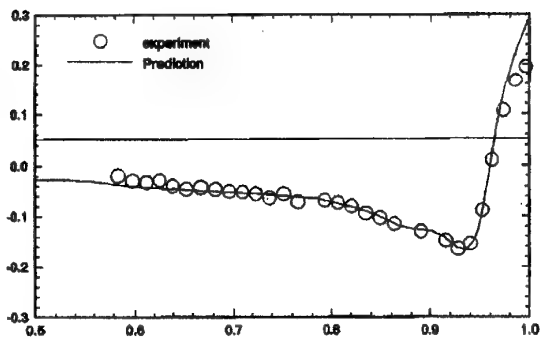


Euler Solution  
(Contribution E08)

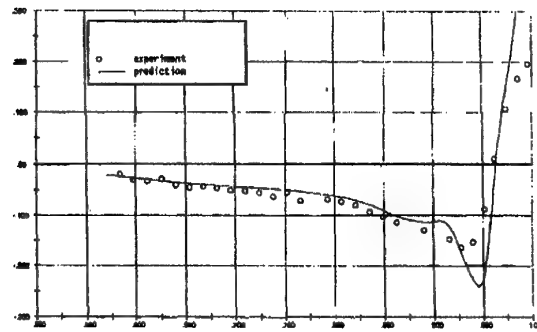


Navier-Stokes Solution  
(Contribution N08)

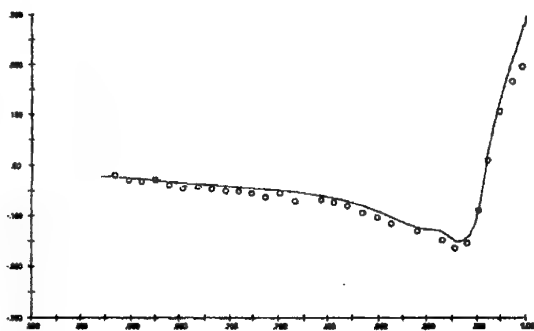
Figure 3.5-6. Predicted Mach Number Contours, Case B.1.1



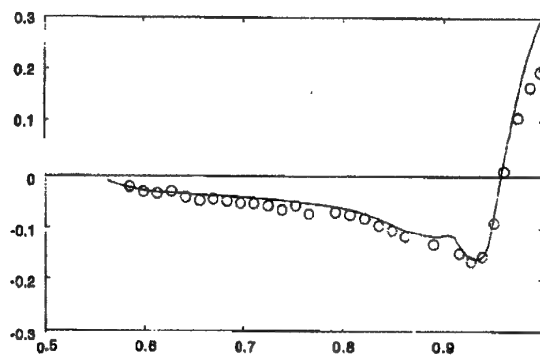
Contribution N04



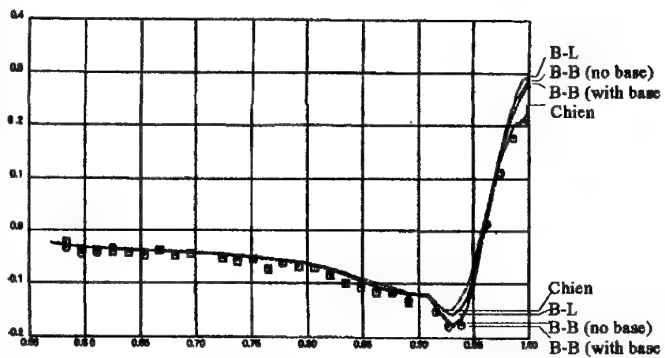
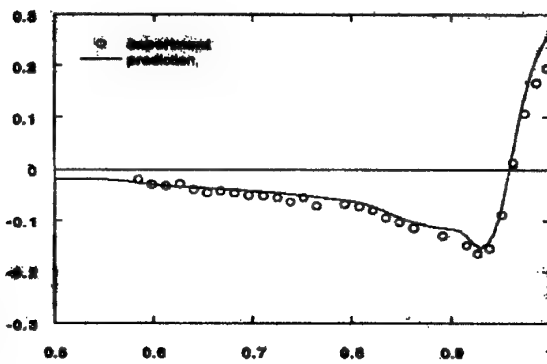
Contribution E08



Contribution N08



Contribution N10

Contribution N09  
(Several Turbulence Models)

Contribution N16

Figure 3.5-7. Comparison of Surface Pressures ( $C_p$  vs.  $X/L$ ), Case B.1.1

of Baldwin-Barth ("B-B"), and the two-equation  $k-\epsilon$  model of Chien ("Chien"). In addition, the Baldwin-Barth turbulence model was used in an assessment of the impact of the nominal vs. actual nozzle base geometry.

Significant differences were seen in the comparisons between the three turbulence models. Further, there was not a clear "winner" between the models tested. In the shoulder expansion region, the boundary layer is responding to first a favorable pressure gradient, then the onset of the adverse gradient. The Baldwin-Barth model gave the best results here, coming very close to the measured pressures. The other two models hinted at the shape of the pressure distribution here, but captured it with clearly less accuracy. Significantly, the other models all predicted pressure too high, i.e., a premature onset of the recompression. This outcome may result from a prediction of too-rapid boundary layer thickening in the adverse pressure gradient.

In the final recompression region, the boundary layer is thickening substantially. Generally speaking, the boundary layer is most likely to separate at this location, though it does not appear that separation was actually present in Case B.1.1. Here, the more sophisticated  $k-\epsilon$  model of Chien seems to have produced the best results, with the results of both Baldwin-Barth and Baldwin-Lomax underpredicting the strength of the viscous interaction. However, it is noted that the Chien model of Contribution N09 was less accurate than the other models in the expansion region (predicted pressure higher than the experimental data).

**Drag Predictions** - Three of the contributors provided complete drag predictions for this case. Two of the results were for Navier-Stokes CFD computations, and the third was for the semi-empirical method described previously.

The axial buildup of drag, from the beginning of the afterbody to the nozzle exit, is presented in Figure 3.5-8. This figure presents pressure drag, integrated from the model centerbody to a variable axial position.

$$C_D(X/L) = \int_{X/L=0.5}^{X/L} C_F I_{DRAG} d(A/A_{MAX})$$

where,  $I_{DRAG}$  is a unit vector in the drag direction, and  $A$  is a vector differential unit of area. As is seen in this equation, the drag in the B.1 series of test cases is normalized by  $A_{MAX}$ , the maximum cross-section area of the body.

The value of this integral at the nozzle exit ( $X/L=1.00$ ) is the net pressure drag of the aftbody-nozzle combination. This type of plot (Figure 3.5-8) is very useful in identifying the regions of the model where drag errors are encountered.

The comparison between test data (integrated experimental pressure data) and predictions indicate that Contribution N04

has generally done quite well. A slight error builds up steadily over the final recompression region (as was suggested in the surface pressure comparisons). The Euler method, Contribution E08, predicts excess drag (low pressure) the shoulder and then steadily under-predicts drag due to excess pressures in the recompression region. The Navier-Stokes version of this method (Contribution N08), however, underpredicts the drag in the shoulder expansion region, then sustains this error in the recompression region. Thus, it seems that the chief issue for the prediction of Contribution N08 lies in the expansion shoulder region. The same can be said for Contribution N10. The drag buildup integral is accurate up to about  $X/L=0.92$ , then a significant error builds up rapidly from  $X/L = 0.92$  to about 0.96 (i.e., the expansion shoulder region). This error seems to remain nearly constant over the final recompression region.

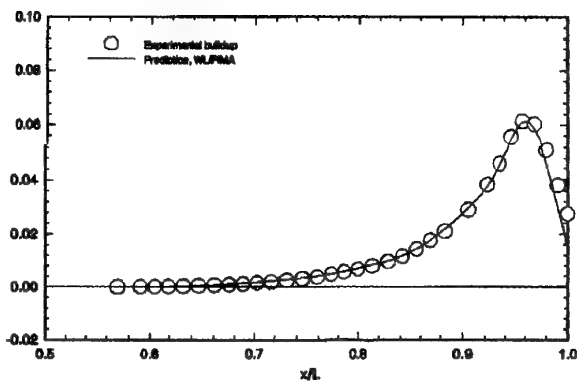
The net values of predicted drag are presented in Figure 3.5-9. Data for both pressure drag and total drag are presented. Both CFD contributors achieved good results for the aftbody pressure drag  $C_{DPA}$ . Nozzle pressure drag  $C_{DPN}$ , was measured as a negative value (i.e., thrust in this accounting system) and both contributors predicted a more negative value (i.e., predicted more thrust than was measured). This is consistent with the tendency of the codes to overpredict pressure in both the expansion shoulder and in the final recompression region. Both contributors did reasonably well (particularly well, in one case) on the total drag comparison ( $C_{DTP}$ ) with data measured by a force balance.

The semi-empirical methods produced extremely good results for the pressure component of drag, and good results for the total drag. The drag results are summarized below.

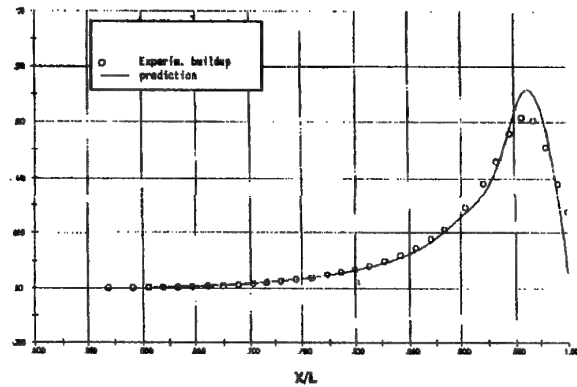
#### Pressure Drag

##### Drag Predictions:

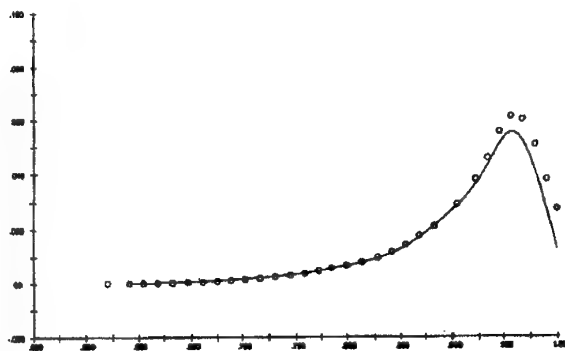
Contrib.	$C_{DPN}$	$C_{DPA}$	$C_{DTP}$
Exp.	-0.0015	0.0291	0.0276 ±0.0100
S01			0.0277
N04	-0.0145	0.0297	0.0152
E08			0.0054
N08			0.0129
N10	-0.0209	0.0260	0.0051



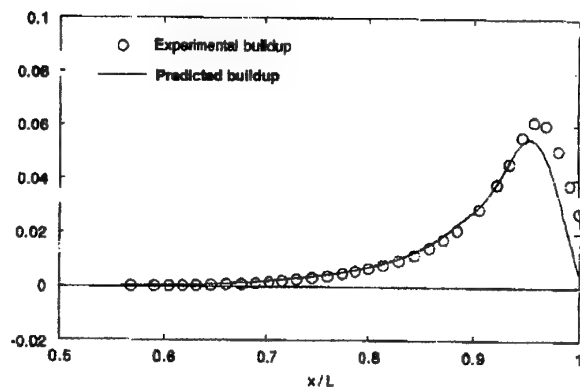
Contribution N04



Contribution E08



Contribution N08



Contribution N10

Figure 3.5-8. Comparison of Pressure Drag Buildup, Case B.1.1



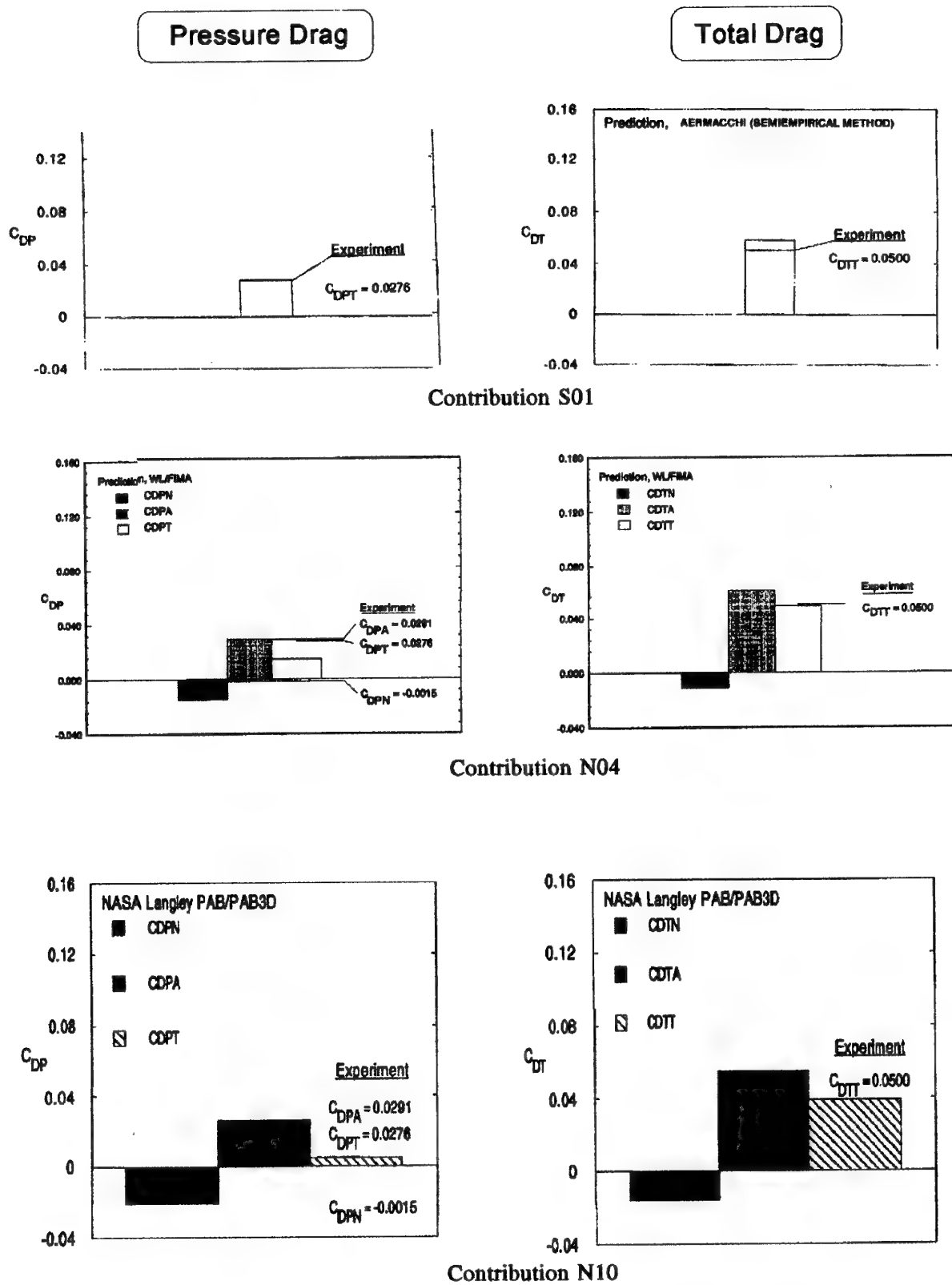


Figure 3.5-9. Comparison of Drag Predictions, Case B.1.1

Prediction Errors ( $C_{DPT}$ ):

Contrib.	$\Delta C_{DPT}$	% Error
Exp		Uncertainty $\pm 36.2\%$
S01	+0.0001	+0.0%
N04	-0.0124	-44.9%
E08	-0.0222	
N08	-0.0147	
N10	-0.0225	-81.5%

## Total Drag

## Drag Predictions:

Contrib.	$C_{DTN}$	$C_{DTA}$	$C_{DTT}$
Exp.			0.0500 $\pm 0.0050$
S01			0.0586
N04	-0.01094	0.05966	0.04872
N08			0.0332
N10	-0.0162	0.0551	0.0389

Prediction Errors ( $C_{DTT}$ ):

Contrib.	$\Delta C_{DTT}$	% Error
Exp	Uncertainty $\pm 0.0050$	Uncertainty $\pm 10.0\%$
S01	+0.0086	+17.2%
N04	-0.0013	-2.6%
N08	-0.0164	
N10	-0.0111	-22.2%

In these drag predictions, the semi-empirical method of Contribution S01 did quite well. The CFD methods also did a reasonable job with total drag. However, it is important to note that the CFD methods provided poor estimates of pressure drag, and did better on total drag. The under-prediction of pressure drag is consistent with the tendency to over-predict pressures at the nozzle trailing edge, and in some cases at the nozzle shoulder.

Because the CFD predictions of total drag were more accurate than the predictions of pressure drag, it appears that there were offsetting errors in the estimate of viscous (friction) contributions to the total drag. The friction forces probably were over-predicted, and this served to offset an under-prediction of pressure forces.

**Discussion** - Several factors could have influenced this situation. Any attempt to assess the key causes must be considered as speculation. Many Navier-Stokes CFD methods initialize solutions with zero boundary layer thickness and a no-slip wall condition. As the solution proceeds, the boundary layer begins to set up - first locally, in response to the wall no-slip condition, then in a more global manner as the velocity deficits from upstream regions are convected downstream.

This means that the usual pattern of skin friction predictions is to begin with a huge over-prediction of friction (the boundary layer is far too thin); the friction drops slowly as the solution evolves and the boundary layer grows. Thus, one speculative possibility is that the Navier-Stokes solutions may continue to evolve (if further iterations are performed), with a further reduction in friction drag and an increase in pressure drag.

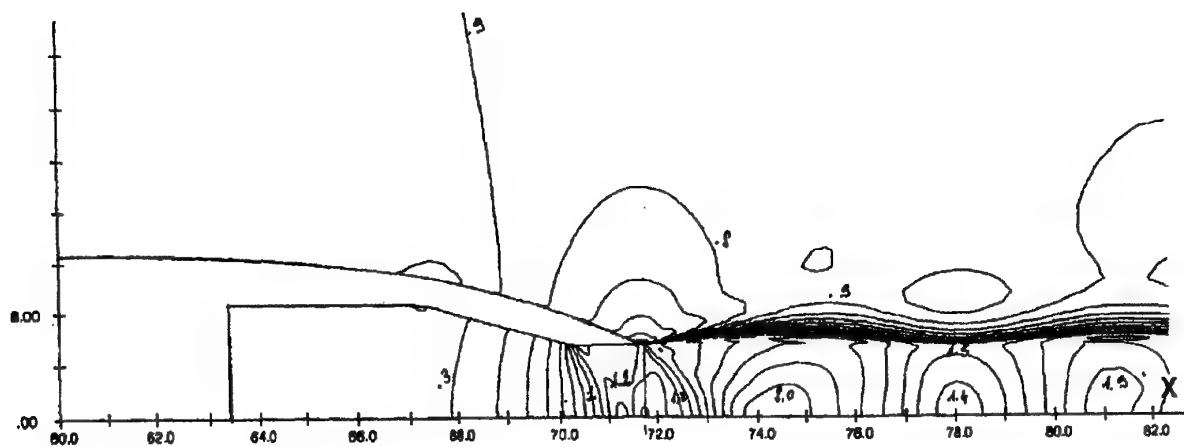
## 3.5.1.2 Case B.1.2

Case B.1.2 is identical to the previous case except the NPR is increased from 2.0 to 5.0. The off-body features of the flow are similar to those for Case B.1.1.

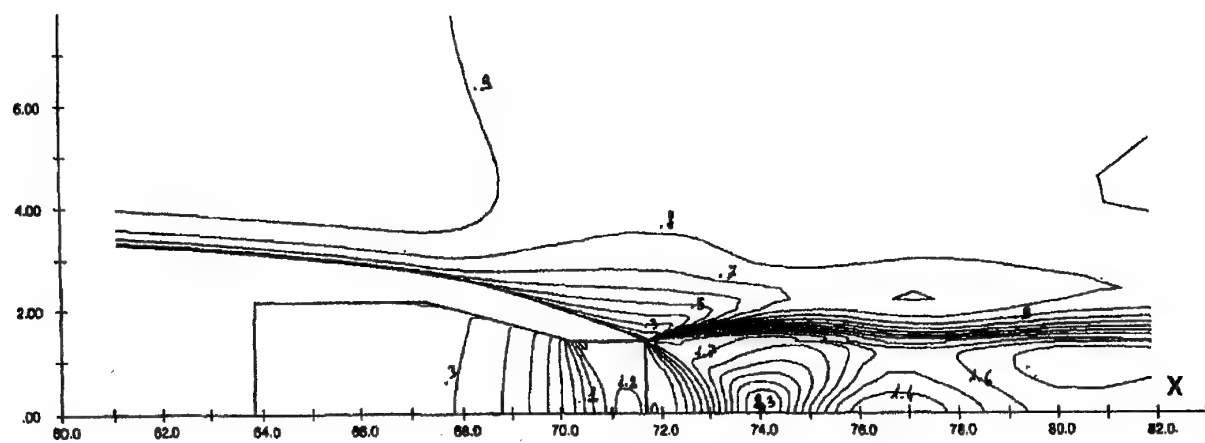
Contour plots of Mach Number are presented in Figure 3.5-10. For the external flow ahead of the nozzle exit, the Mach number distributions are quite similar to those in the previous case (see Figure 3.5-6). At this higher NPR, the internal flow has a sufficiently high pressure that it expands to supersonic speeds in both the Euler and Navier-Stokes predictions.

The free shear layer between the jet and the external flow is undulating in response to a shock/expansion wave system in the jet. The free shear layer is unexpectedly quite similar in both the Euler and Navier-Stokes solutions. This could indicate that the Euler solution is subject to high numerical dissipation.

**Surface Pressure Comparison** - The submitted comparisons of surface pressure predictions with experimental data for this case are presented in Figure 3.5-11. One contributor provided both Euler and Navier-Stokes solutions for this case. The Euler computation showed the expected behavior, producing too low a pressure at the nozzle shoulder, and re-compressing too high at the nozzle trailing edge. The Navier-Stokes analyses were clearly an improvement, though prediction problems persisted - particularly at the difficult

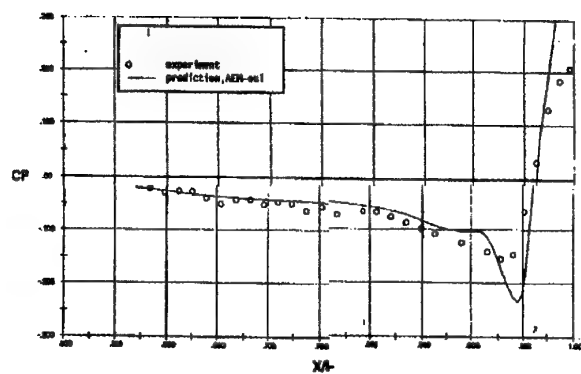


Euler Solution  
(Contribution E08)

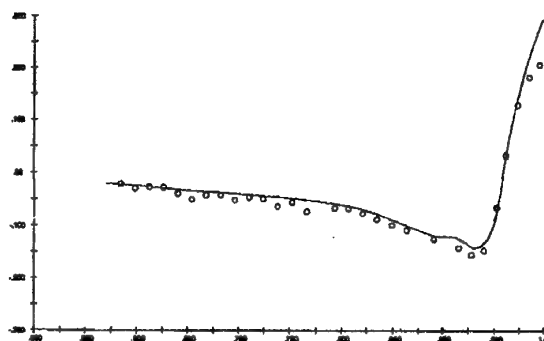


Navier-Stokes Solution  
(Contribution N08)

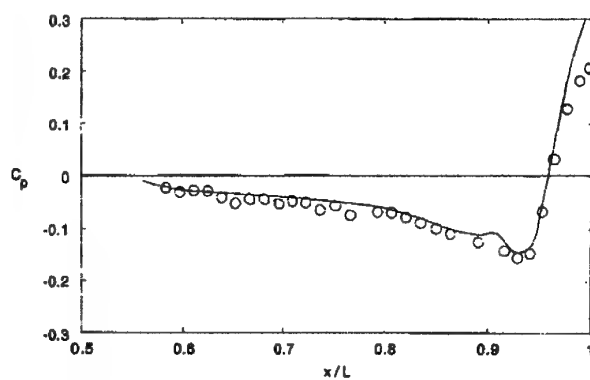
Figure 3.5-10. Predicted Mach Number Contours, Case B.1.2



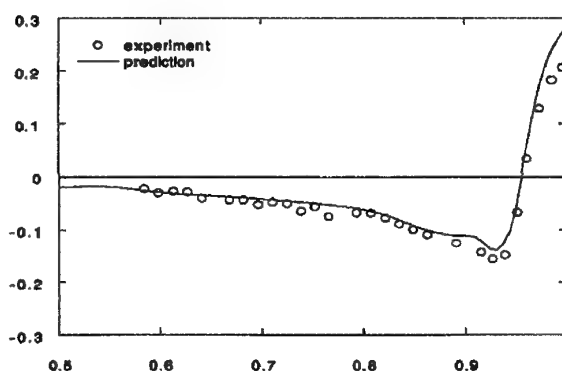
Contribution E08



Contribution N08



Contribution N10



Contribution N16

Figure 3.5-11. Comparison of Surface Pressures ( $C_p$  vs.  $X/L$ ), Case B.1.2 ( $\phi=108^\circ$ )

final recompression region where the viscous interactions are most important. Generally, the computed pressure distributions on the model are nearly identical to those from the previous case. The effect of the different NPR can only be seen, slightly, in the immediate vicinity of the nozzle exit - say,  $X/L > 0.98$ . In this region, all of the predictions show a slight increase in surface pressure (as would be expected) compared with the corresponding results from the previous case (see Figure 3.5-7).

**Drag Comparison** - The axial buildup of integrated drag is presented in Figure 3.5-12. These results are generally quite similar to those of Case B.1.1 (see Figure 3.5-8). Very close to the nozzle exit, the present results show slightly lower drag than was seen by the same Contributions for Case B.1.1.

Comparisons of the net pressure and total drag are presented in Figure 3.5-13. These comparisons present data from the semi-empirical method (Contribution S01) and one Navier-Stokes CFD methods (Contribution N10).

The outcome here is similar to that for Case B.1.1. The CFD analysis (Contribution N10) underpredicted the nozzle pressure drag,  $C_{DPN}$ . As before, this means the prediction was for too much nozzle aerodynamic thrust in the context of this accounting system. The aftbody pressure drag,  $C_{DPA}$ , shows better accuracy. The total pressure drag,  $C_{DPT}$ , is too low - producing a net thrust rather than drag. The semi-empirical method, however, has done quite well in predicting both the pressure drag and the total drag.

For total drag, Contribution N10 was somewhat more accurate. Since the method significantly underpredicted the pressure drag, one concludes that the friction drag is overestimated. This over-prediction of friction drag could arise from many causes - such as, weaknesses in the turbulence model, or inadequate convergence of the solution.

The semi-empirical method did very well for both the pressure drag, and the total drag, in this case. As was observed for the previous case (B.1.1), the accuracy was better for pressure drag than for total drag. These drag comparisons are summarized below.

### Pressure Drag

#### Drag Predictions:

Contrib.	$C_{DPN}$	$C_{DPA}$	$C_{DPT}$
Exp.	-0.0096	0.0296	0.0191 $\pm 0.0100$
S01			0.0218
E08			-0.0171
N08			-0.0065
N10	-0.0330	0.0253	-0.0077

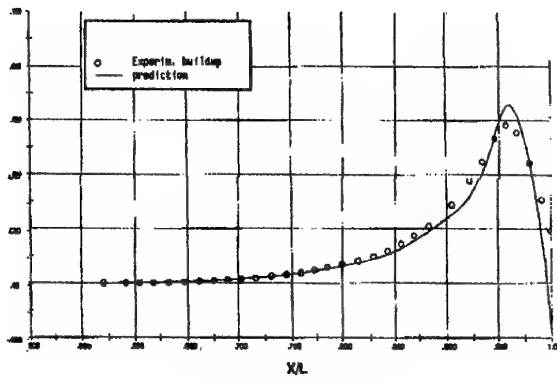
#### Prediction Errors ( $C_{DPT}$ ):

Contrib.	$\Delta C_{DPT}$	% Error
Exp	Uncertainty $\pm 0.0050$	Uncertainty $\pm 52.4\%$
S01	+0.0027	+14.1%
E08	-0.0362	
N08	-0.0256	
N10	-0.0268	-140.3%

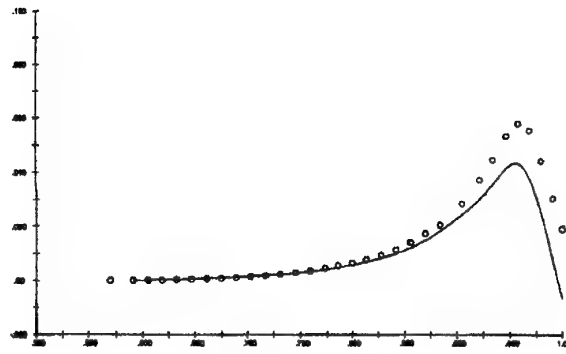
### Total Drag

#### Drag Predictions:

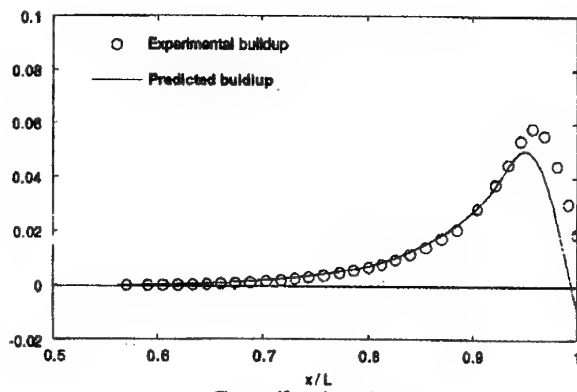
Contrib.	$C_{DTN}$	$C_{DTA}$	$C_{DTT}$
Exp.			0.0423 $\pm 0.0050$
S01			0.0527
N08			0.0302
N10	-0.0280	0.0543	0.0259



Contribution E08



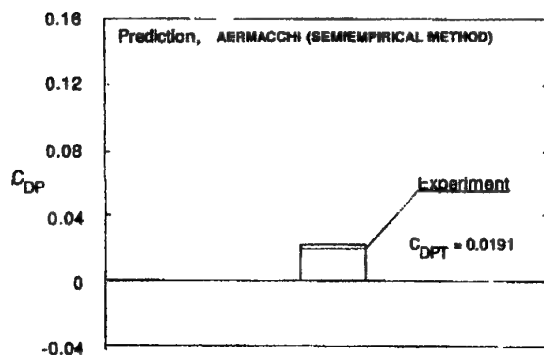
Contribution N08



Contribution N10

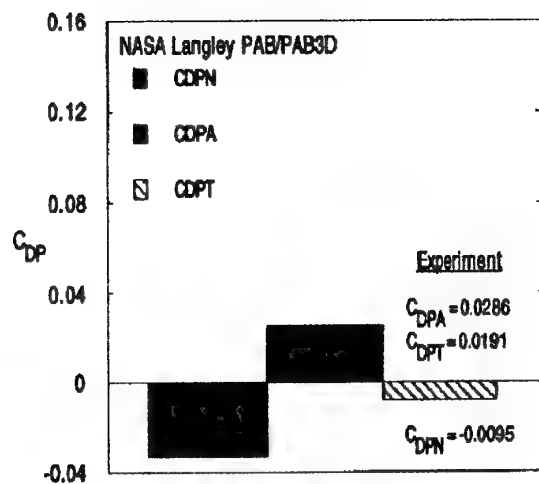
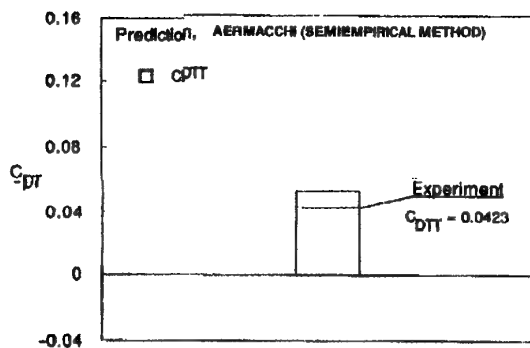
Figure 3.5-12. Comparison of Pressure Drag Buildup, Case B.1.2

### Pressure Drag



Contribution S01

### Total Drag



Contribution N10

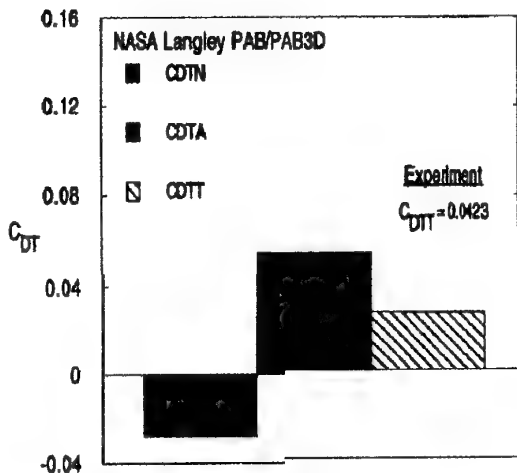


Figure 3.5-13. Comparison of Drag Predictions, Case B.1.2

Prediction Errors ( $C_{DTT}$ ):

Contrib.	$\Delta C_{DTT}$	% Error
Exp	Uncertainty $\pm 0.0050$	Uncertainty $\pm 11.8\%$
S01	+0.0104	+24.6%
N08	-0.0121	
N10	-0.0164	-38.8%

**Discussion** - This case proved more difficult, in terms of drag prediction accuracy. Each contribution (S01 and N10) produced over-predictions of the friction drag (i.e., total drag minus pressure drag). The semi-empirical method did rather well on pressure drag (not as well as it did on the previous case), while the CFD method gave quite poor results for pressure drag.

### 3.5.1.3 Sensitivity to Trailing Edge Modeling Technique

Toward the end of the activities coordinated by this Working Group, staff at the NASA Langley Research Center conducted an investigation of the various modeling techniques for the trailing edge. The B.1.1 test case was used for this study. In addition to the "standard" solution which was presented in Section 3.5.1.1, four additional solutions were executed. These additional solutions are presented here.

The test geometry has a small blunt base at the trailing edge of the nozzle. The rearward-facing base area, in turn, consists mainly an annular gap (a metric break) provided to isolate the non-metric internal nozzle duct from the metric aerodynamic shell of the forebody, aftbody, and nozzle. This geometry is illustrated in Figure 3.5-14.

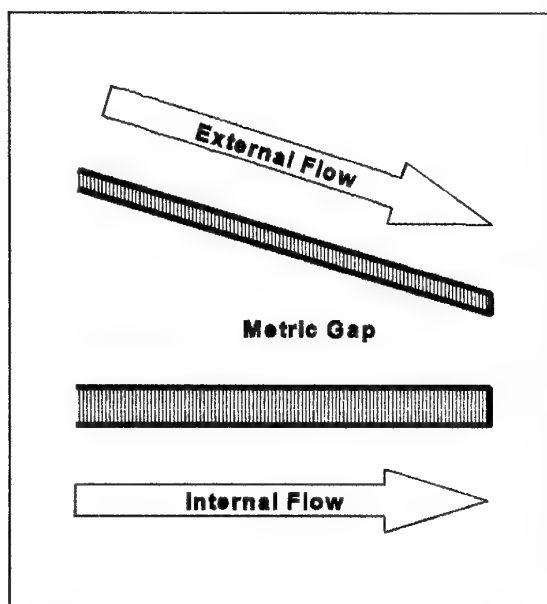


Figure 3.5-14 - Detail at Nozzle Trailing Edge

This trailing edge region poses two difficulties for fast CFD analysis. First, the blunt base area requires specialized modeling in constructing the grid. Second, the metric gap between the external and internal shells of the nozzle is very difficult to model accurately. Further, the argument is made that the flow is separated behind the blunt base, and therefore local details of the base geometry are inconsequential. One approximation is to ignore the metric gap, and to model the blunt base as being filled (solid wall).

A second approximation is to eliminate the blunt base in the CFD model, in the supposition that it is "small" compared to the thickness of the external boundary layer, and therefore the blunt base has negligible impact on the overall flowfield. In this latter approach, a modified geometry is created. Usually, the external nozzle aerodynamic surface is held fixed, and a revised internal aerodynamic surface is defined. The common approach is to maintain the internal nozzle wall flow angles, but increase the internal flow diameter slightly to eliminate the blunt base. It also is important to maintain the proper area ratio between the throat and the exit; therefore, the throat is slightly repositioned upstream.

The impact of these various modeling techniques was investigated by NASA Langley Research Center (Contribution N10). The "standard" solution was presented in Section 3.5.1.1, using the sharpened trailing edge approximation and a standard grid density. Their "standard" solution is generally comparable to the other contributions presented in Section 3.5.1.1.



As a first step in the CFD investigation, additional axial grid density was provided near the trailing edge of the nozzle. The underlying geometry came to a sharp trailing edge, using the same geometry definition as in the "standard" solution by these contributors (N10) and most of the other contributors. This technique produced a prediction of a well-behaved flowfield, as is seen in Figure 3.5-15. (In this and the subsequent figures, the multiple blocks of the grid have been slightly displaced for clarity. In fact, the blocks abutted each other without any gaps).

Next, the actual blunt base height of the nozzle trailing edge was modeled. However, the base area was modeled as a solid boundary, through which no flow could pass. This is the maximum degree of modeling fidelity used by any of the contributors in the solutions presented in Section 3.5.1.1. This level of modeling provided prediction of a clear recirculation region behind the base, as might be expected (see Figure 3.5-16). The downward curve of the external-flow streamlines as they pass over the nozzle trailing edge is clearly visible (compare with Figure 3.5-15). The curvature seen here is associated with a reduced pressure on the external surface very near the nozzle exit. This analysis level will be identified, below, as the "Blunt Base Model."

For the next level of enhanced modeling, the entire base area was opened to the flow. An open cavity was modeled in the annular gap of the metric break. The inner and outer walls of the annular gap were assumed to have zero thickness, and a computational grid was provided extending several gap heights forward into the model. This approach featured an established vortex standing inside the cavity, and it eliminated the recirculating vortex which had stood behind the blunt base in the previous example (the blunt base model). This result, called the "Cavity Model," is presented in Figure 3.5-17.

Next, the true thickness of the inner and outer walls was modeled, providing an accurate representation of the cavity and base region. This approach produced generally the same results as the previous case behind the base, but it presented a different forced vortex pattern inside the cavity. These results, which are called the "Cavity/Base Model (Grid 1)," are seen in Figure 3.5-18.

Finally, a variant of the previous case was analyzed, with additional grid provided in the axial direction near the trailing edge of the model (this is called "Cavity/Base Model, Grid 3"). These results are presented in Figure 3.5-19.

Among the approaches which included the cavity, an important issue was to include the real thickness of the walls. The shape of the dividing streamline off the upper (external) edge of the base, for the three cavity cases, is presented in Figure 3.5-20. The two cases which included modeling of the wall (base) thickness produced similar results, while the

cavity case (zero thickness walls) produced a different dividing streamline.

Each of these modeling techniques also produced a different pressure distribution on the aftbody and nozzle. The pressure distributions for the standard case (as presented previously in Figure 3.5-7) and four of the enhanced cases, are presented in Figure 3.5-21. The standard case is denoted by a series of "x" on the figure. It is noted that the first enhancement, increasing the grid density near the sharp trailing edge, eliminated about half the error in predicted pressure at the nozzle exit. The next enhancement, modeling the blunt base, produced some additional improvement. The cavity model (i.e., zero thickness base and walls) produced excellent agreement with the experimental data. However, the prediction agreement deteriorated when the actual thickness of the walls and the base was modeled. This latter outcome is unexpected, and an interpretation of this result has not yet been established.

#### 3.5.1.4 Discussion of Results

These CFD solutions experienced consistent difficulties in accuracy, in two regions:

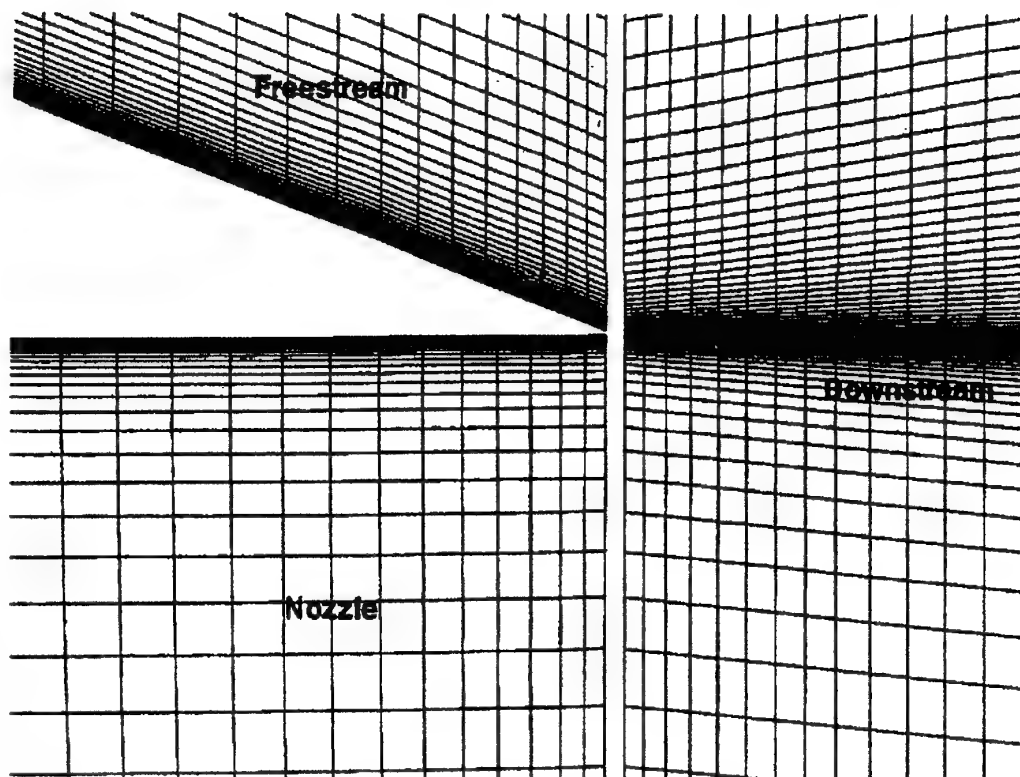
- Nozzle shoulder region, where the geometry is most highly curved in the longitudinal direction, and the pressure gradient is changing from a mild favorable gradient to a stronger adverse gradient ( $x/L = 0.85$  to  $0.95$ ), and,
- Nozzle trailing edge region, where the viscous effects and the interaction with the plume are the strongest ( $x/L = 0.98$  to  $1.00$ ).

To assess the relative importance of each region, the associated rearward-facing areas have been computed:

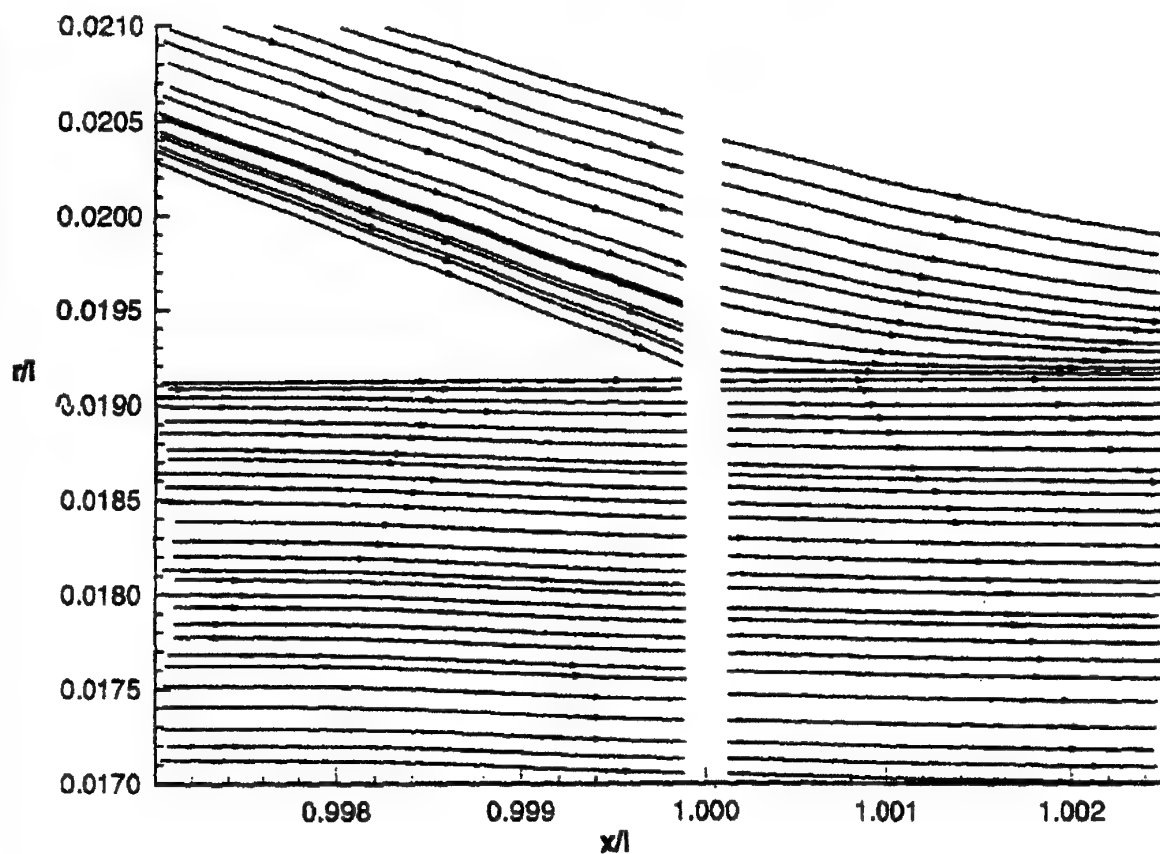
Region	Range ( $x/L$ )	Rearward-Facing Area as Fraction of $A_{MAX}$
Shoulder	0.85 to 0.95	0.324
Nozzle Trailing Edge	0.98 to 1.00	0.126

These data show that, for this geometry, more rearward-facing area is found in the expansion shoulder region than in the nozzle recompression region. Thus, accurate prediction of pressure in the aftbody-nozzle expansion shoulder region is of at least comparable importance as accuracy in the nozzle trailing edge region.

Based on the drag buildup data (Figure 3.5-8 and 3.5-12), it appears the drag errors mainly were produced at the nozzle

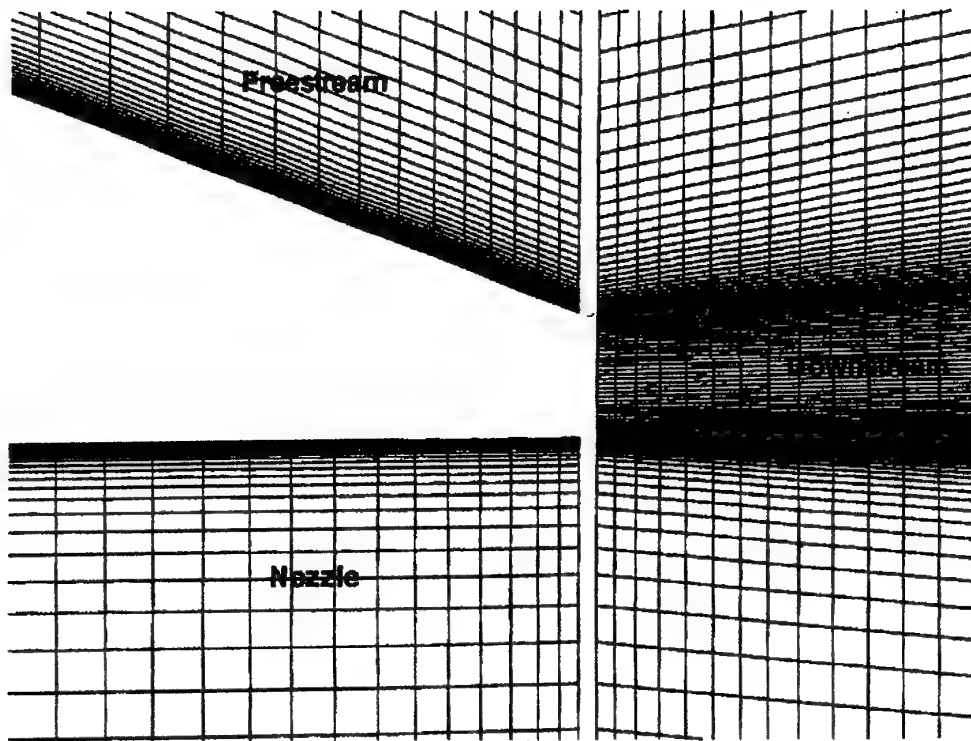


(a) Grid Detail Near Trailing Edge

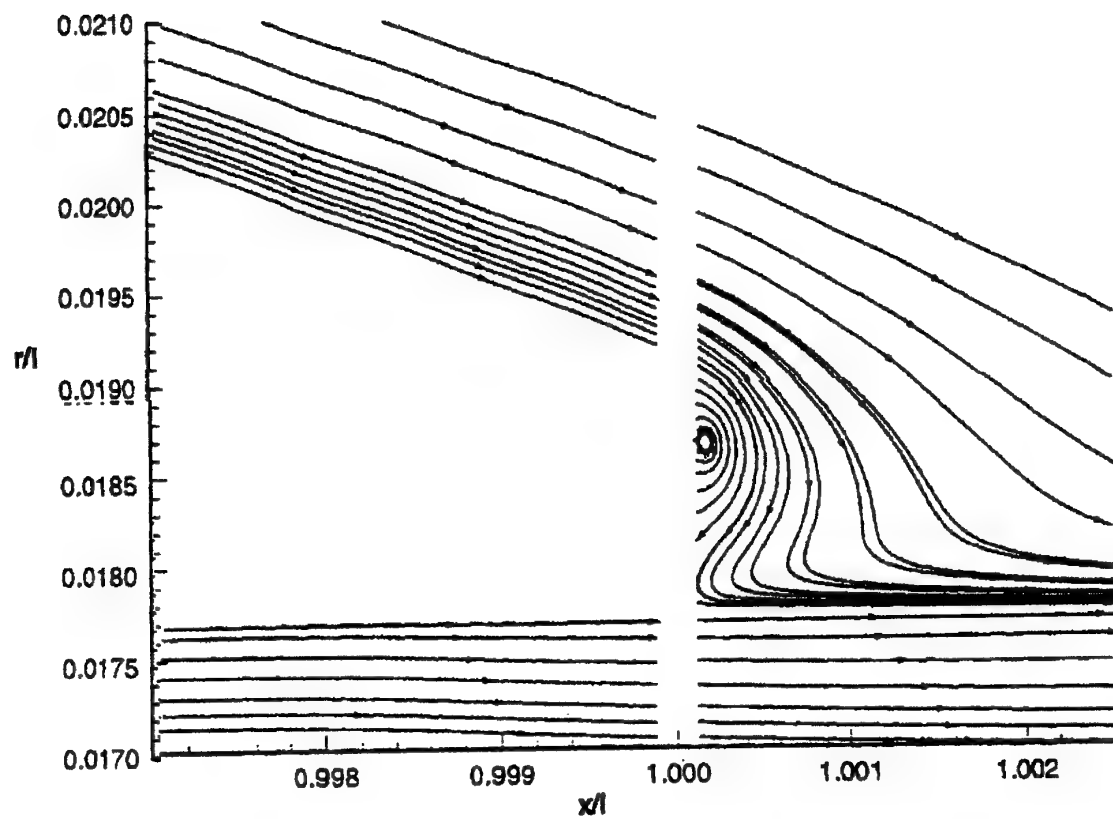


(b) Computed Streamlines Near Trailing Edge

Figure 3.5-15. Modified Grid, Sharp Trailing Edge Model, Case B.1.1  
(Contribution N10)

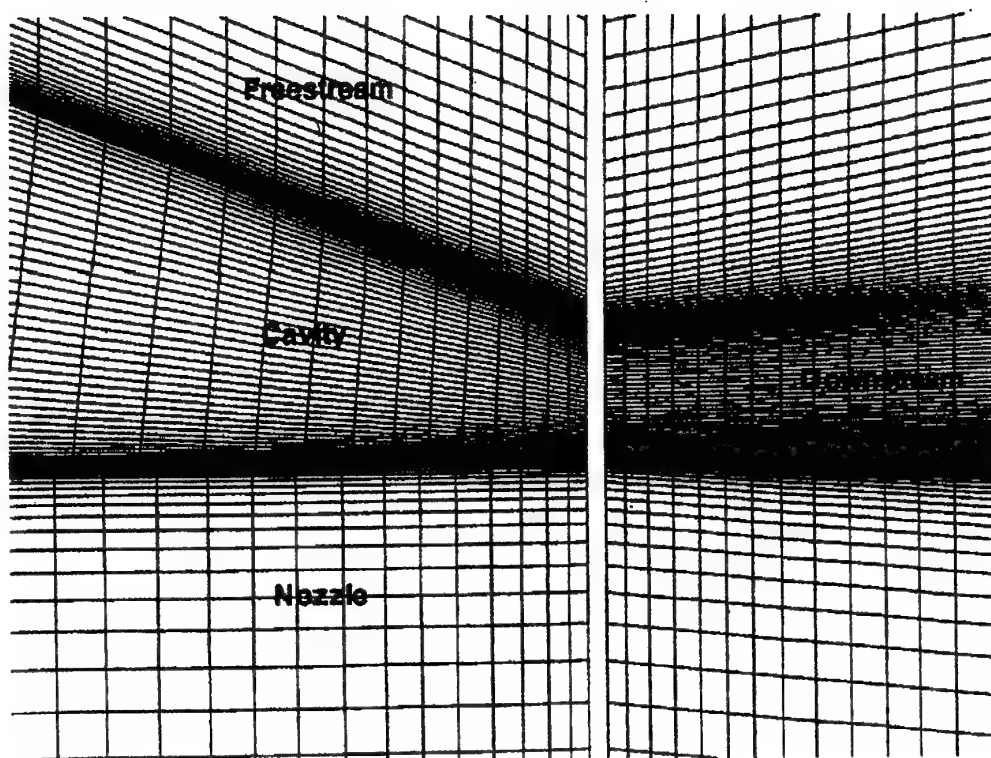


(a) Grid Detail Near Trailing Edge

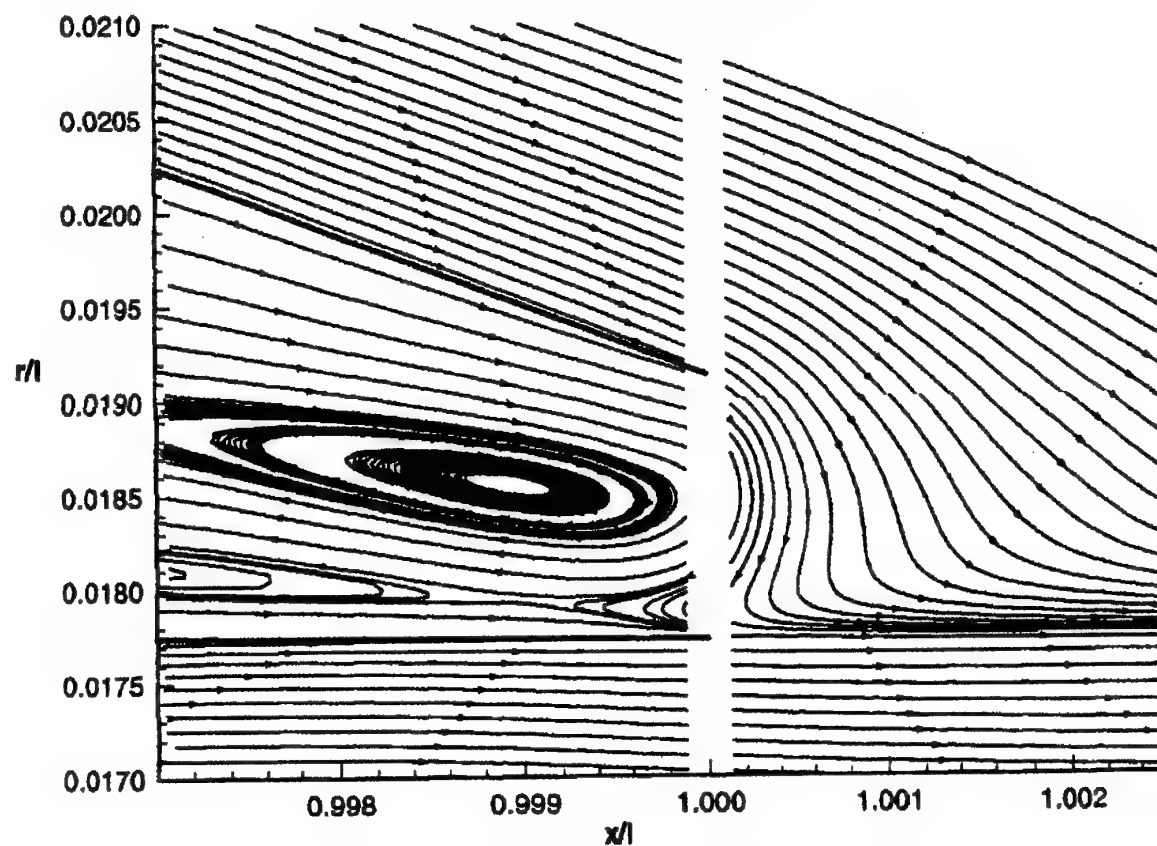


(b) Computed Streamlines Near Trailing Edge

Figure 3.5-16. Modified Grid, Blunt Base Model, Case B.1.1  
(Contribution N10)

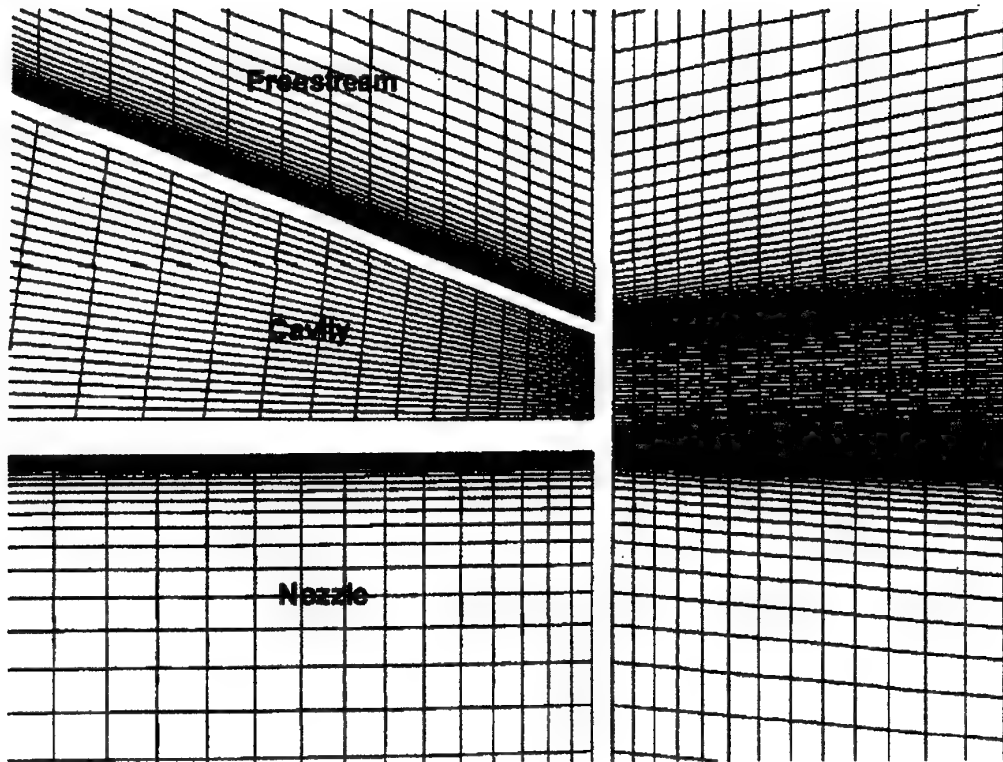


(a) Grid Detail Near Trailing Edge

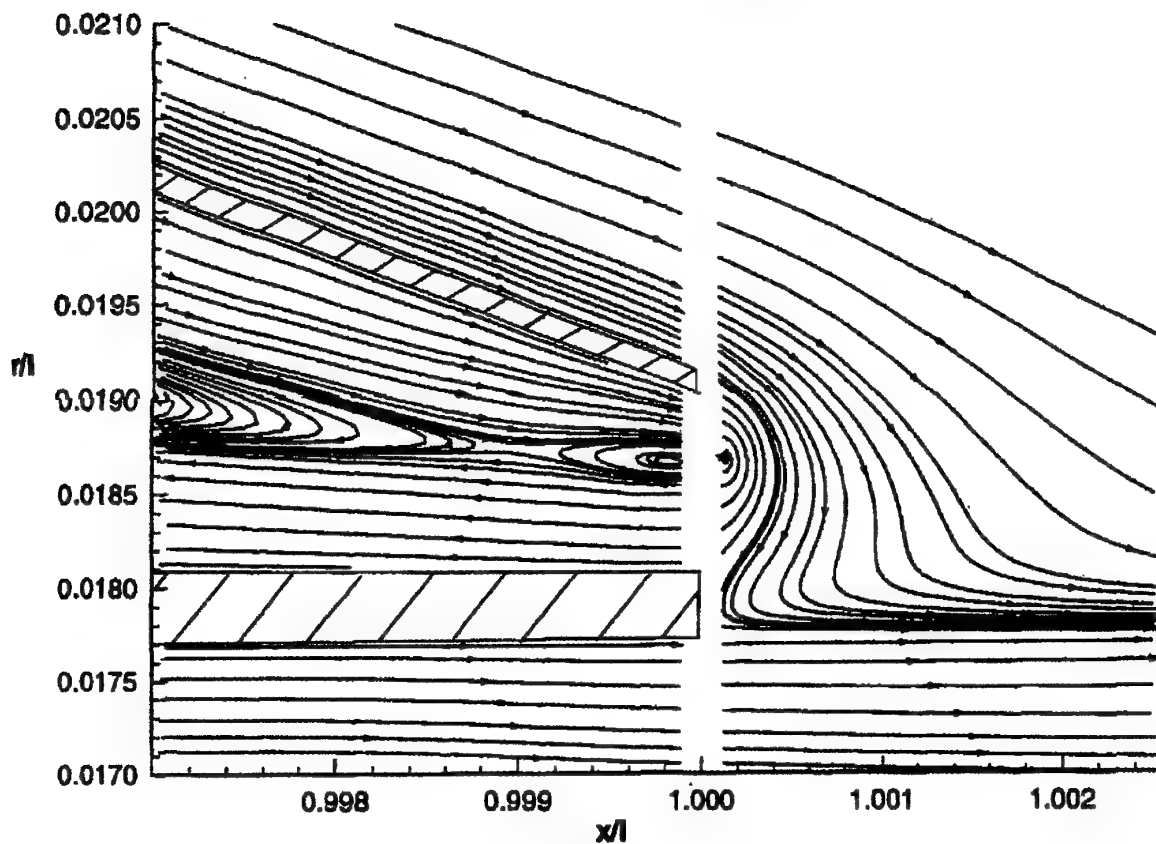


(b) Computed Streamlines Near Trailing Edge

Figure 3.5-17. Modified Grid, Cavity Model, Case B.1.1  
(Contribution N10)

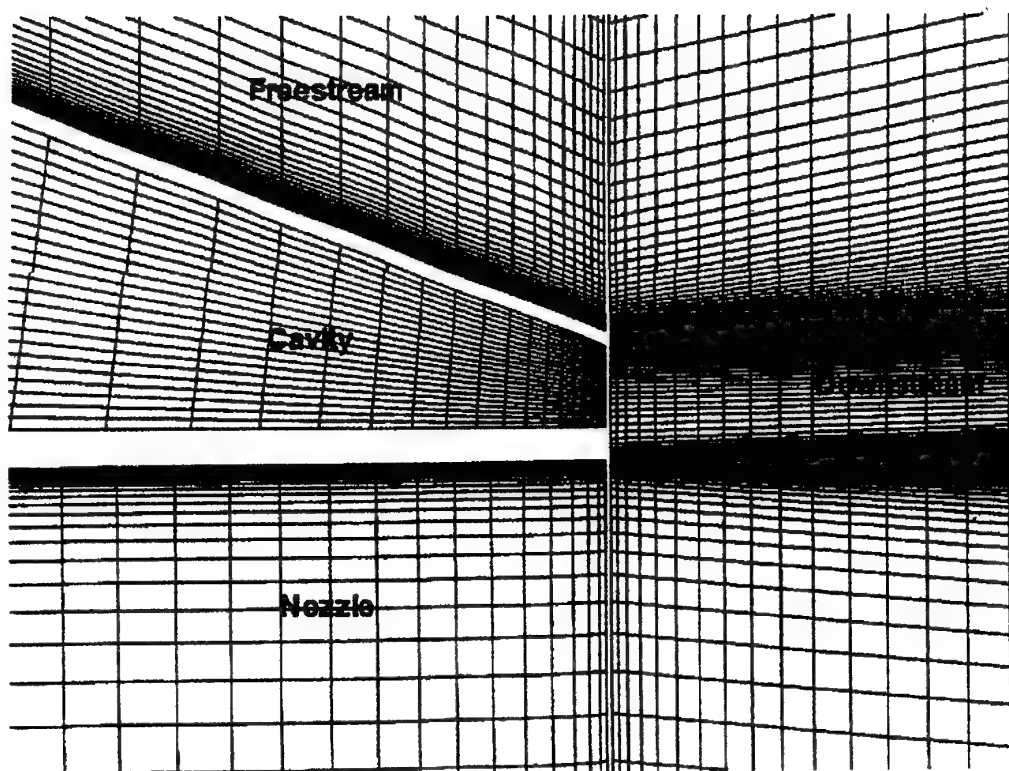


(a) Grid Detail Near Trailing Edge

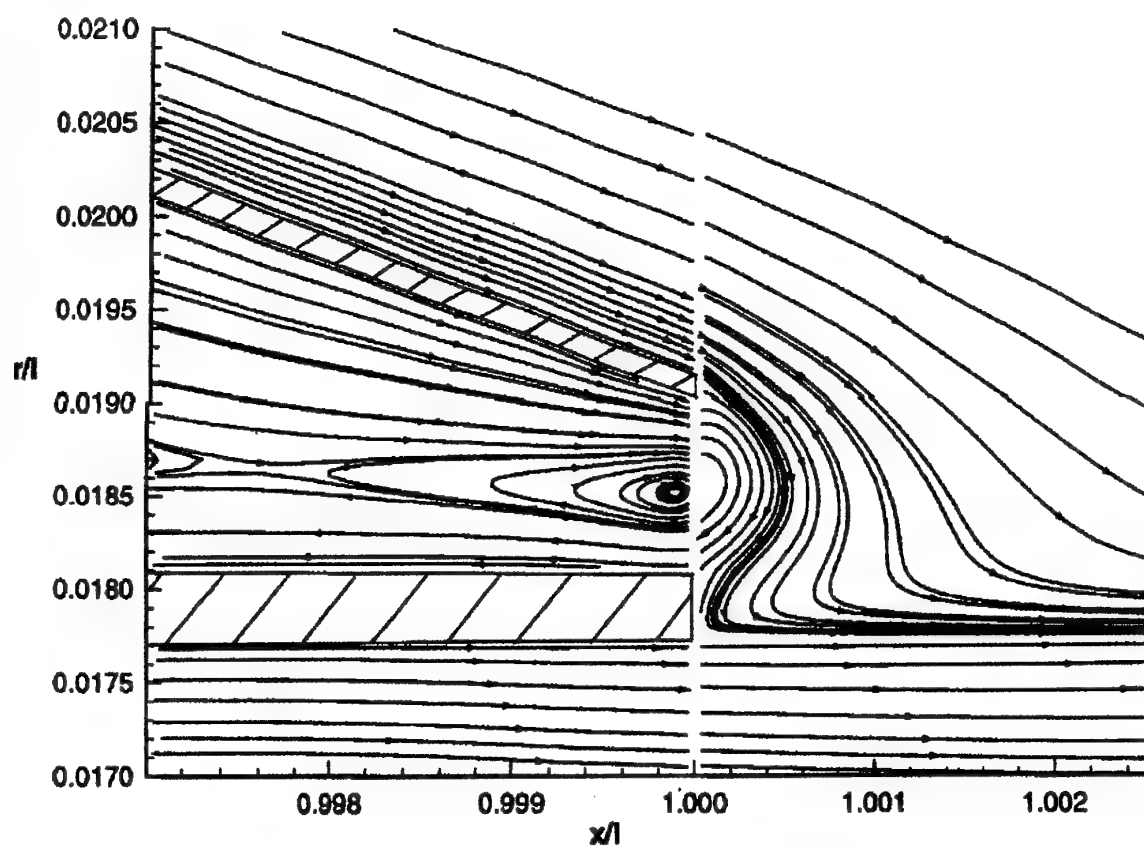


(b) Computed Streamlines Near Trailing Edge

Figure 3.5-18. Modified Grid, Cavity/Base Model ("Grid 1"), Case B.1.1  
(Contribution N10)



(a) Grid Detail Near Trailing Edge



(b) Computed Streamlines Near Trailing Edge

Figure 3.5-19. Modified Grid, Cavity/Base Model ("Grid 3"), Case B.1.1  
(Contribution N10)

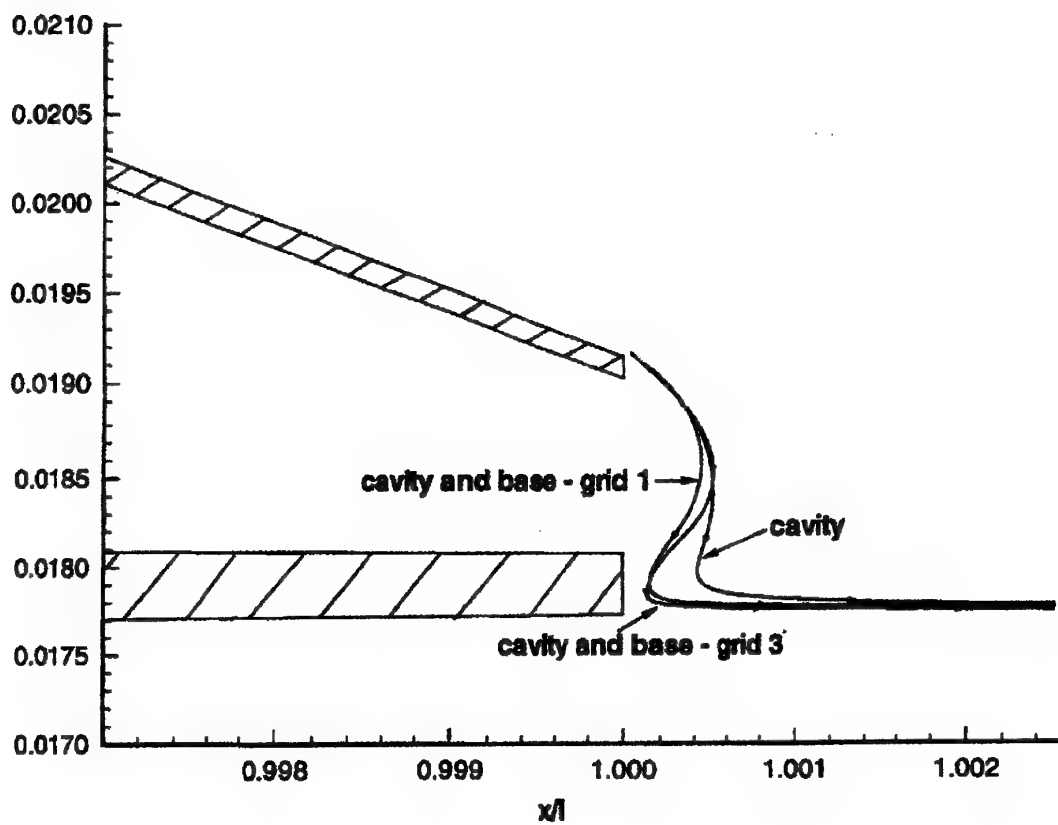
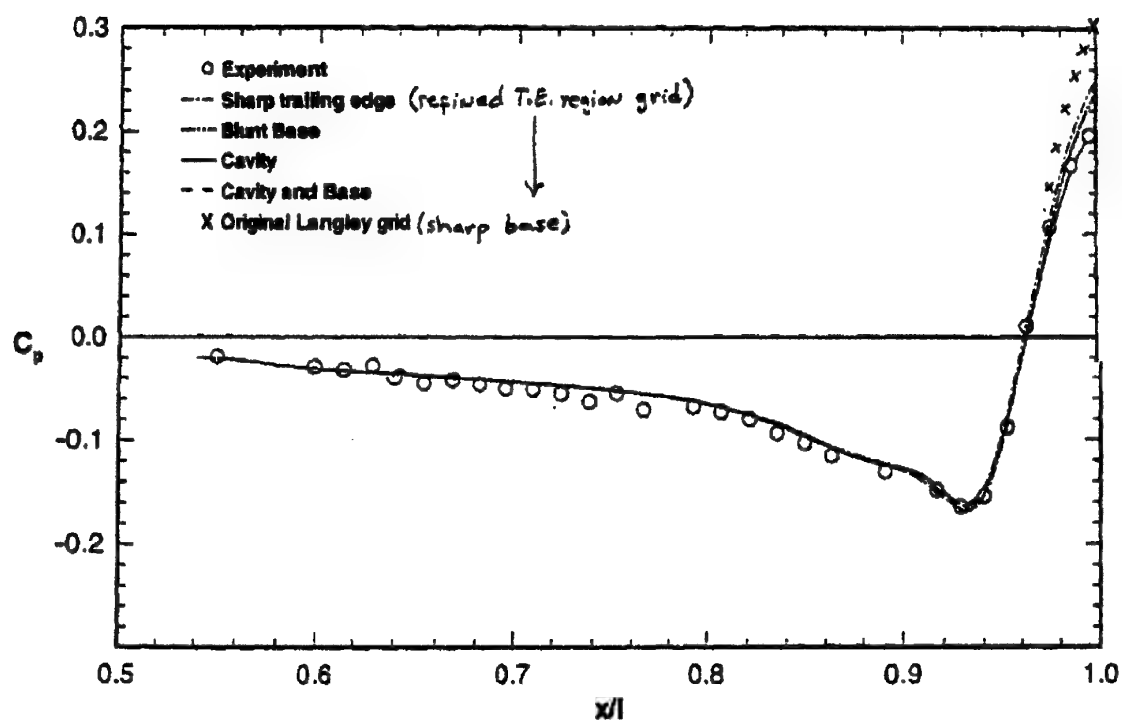
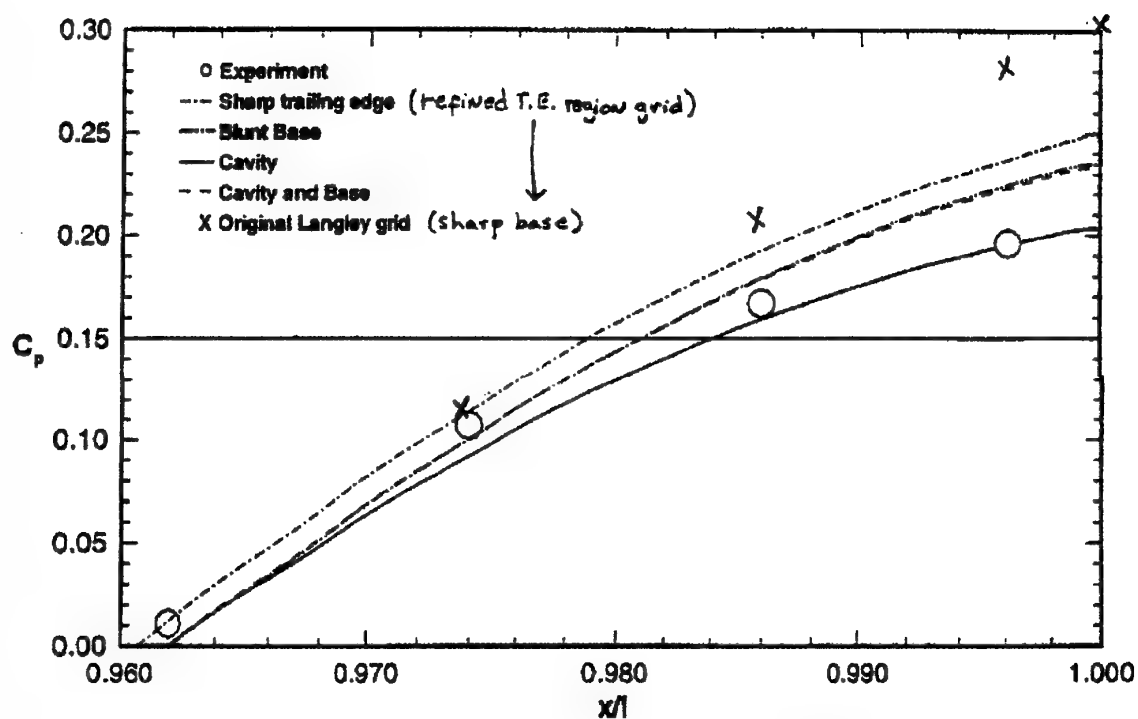


Figure 3.5-20. Comparison of Trailing Edge Streamlines, Case B.1.1  
(Contribution N10)



(a) Afterbody-Nozzle Surface Pressures



(b) Detailed View of Pressures Near Trailing Edge

Figure 3.5-21. Effect of Trailing Edge Modeling on Surface Pressure, Case B.1.1  
(Contribution N10)



shoulder, and the error grew somewhat larger in the final recompression region. Presumably, this situation is controlled mainly by grid density, turbulence modeling, and operational practices (convergence criteria).

**Drag Variation Due to NPR** - Drag prediction has proven to be very difficult. This has long been recognized as a deficiency in current aero-propulsion technology. As a partial response, engineering staff frequently use the predictive methods to assess the increment in drag due to certain changes. The operative assumption is that the methods will predict trends and differences accurately, even though the underlying individual data are not highly accurate. From another perspective, this approach rests on an assumption that the prediction errors, while they are not understood, are nevertheless consistent and generally repeatable among closely related solutions. Therefore, in computing a drag difference, the repeatable/consistent error is eliminated and a reliable estimate of drag variation is produced.

The data of Cases B.1.1 and B.1.2 were examined to assess the accuracy of the predicted drag increments due to the variation in NPR from 2 (Case B.1.1) to 5 (Case B.1.2). These data are presented below.

Contrib.	$C_{DTT}$ NPR=2 (B.1.1)	$C_{DTT}$ NPR=5 (B.1.2)	$\Delta C_{DTT}$ (NPR 5-2)
Exp.	0.0500	0.0423	-0.0077
S01	0.0586	0.0527	-0.0059
N10 ("standard" solution)	0.0389	0.0259	-0.0130

Both methods predicted the general trend of drag reduction with increased NPR. The semi-empirical method (S01) did quite well on this rather classical trend, while the CFD method (N10) over-predicted the NPR impact, significantly.

The study of the trailing edge modeling techniques, presented in Section 3.5.1.3, clearly showed that the choice of modeling approach can affect the results at the levels of precision which are sought today. This study considered only geometry and grid issues; the same turbulence model was employed in all the cases. However, it is yet unclear whether this outcome was influenced by additional variations such as changes in CFD code application practices, or perhaps by variations in grid quality factors such as stretching or orthogonality. Nevertheless, the study clearly shows that other issues in addition to turbulence modeling should be considered in seeking high accuracy for these flowfields.

A solution by the method of Contribution N10 was provided to the Working Group for the jet-off condition (same Mach

number and Reynolds number as test cases B.1.1 and B.1.2). Since this condition was not part of the established test cases, no other group analyzed this flow condition. The predicted surface pressures for this jet-off case are presented in Figure 3.5-21.

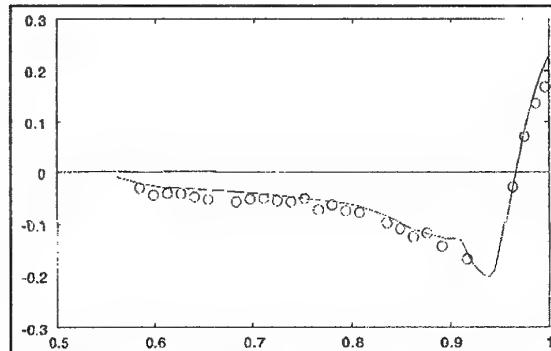


Figure 3.5-22 - Comparison of Surface Pressures ( $C_p$  vs  $X/L$ ) at Jet-Off Condition for the Geometry of Test Case B.1 (Contribution N10)

The jet-off condition was executed using the "standard grid" of Contribution N10, as employed for the solutions presented in Sections 3.5.1.1 and 3.5.1.2. This solution did not use the improved trailing edge modeling techniques which were discussed in Section 3.5.1.3. Therefore, wall pressures for the jet-off solution are properly compared with other solutions as were presented in Figures 3.5-7 and 3.5-11.

Comparison of the result in Figure 3.5-22 (jet-off) with the result in Figure 3.5-7 (NPR=2) shows that the solution accuracy near the nozzle trailing edge is noticeably better in the jet-off case.

The results for drag vs. NPR for Contribution N10 are presented in Figure 3.5-23. This figure includes pressure drag results for the jet-off condition (these data are plotted as NPR=1). This figure confirms the results presented earlier in this section, for the drag variations between NPR=2 and NPR=5. However, it is noted that the prediction of pressure drag is noticeably more accurate for the jet-off condition, than for either of the cases with the flowing jet. In reality, the accuracy of the predictions was worst at the highest NPR condition.

This outcome suggests that the presence of the jet leads to degraded accuracy in the predictions of trailing edge pressure and pressure drag. This outcome is not necessarily obvious, since the jet-off condition is likely to entail much higher curvature in the external streamlines at the nozzle exit, combined with an interaction with the low-energy flow behind the non-flowing nozzle exit. Thus, one might expect degraded accuracy in the jet-off analysis.

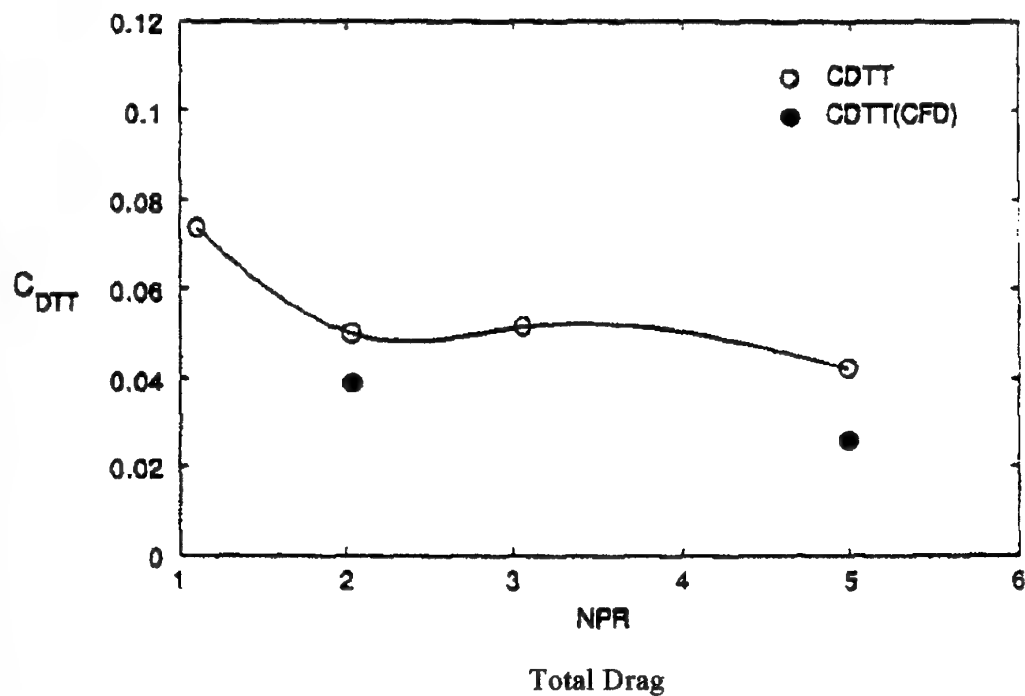
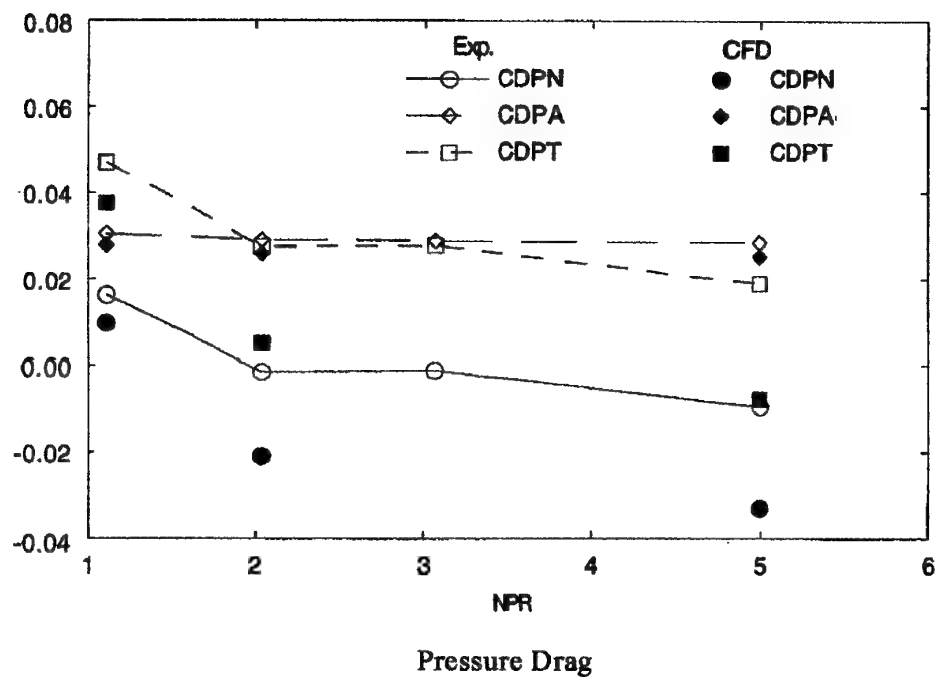


Figure 3.5-23. Comparison of Drag Variations Due to NPR,  
Cases B.1.1 and B.1.2  
(Contribution N10)

From this outcome, it seems possible to conclude that the presence of the jet introduces a significant modeling inaccuracy. Stated in another way, the jet effects do not seem to be modeled properly. These effects center on the freestream/jet mixing and entrainment processes. As the influence of the jet is enhanced at higher NPR, the modeling accuracy seems to become worse. Since Contribution N10 is based on a state-of-the-art two-equation turbulence model, which has done very well in many applications (as is shown throughout this Section), it seems this set of comparisons allows us to identify a fundamental limitation in current turbulence modeling.

### 3.5.2 Case B.2

The geometries for Cases B.2.1, B.2.2, and B.2.3 are identical; the cases differ only in the NPR value. The geometry consists of a single vertical fin and a pair of horizontal fins, placed on a simple axisymmetric body. The axisymmetric body is identical to that of the B.1 cases. Thus, the body length  $L$  which is used to normalize the spatial coordinate also is the same as in the B.1 test cases. This geometry is illustrated in Figure 3.5-24.

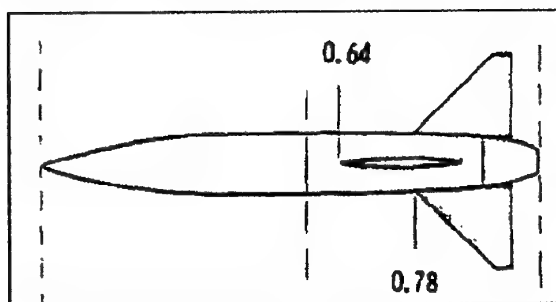


Figure 3.5-24 - Geometry for Test Cases B.2.x

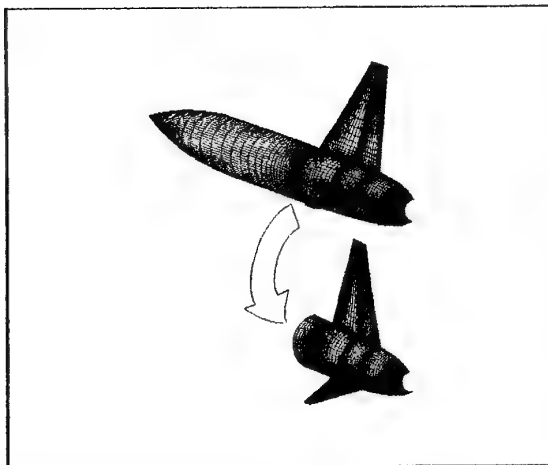


Figure 3.5-25 - Surface Grid, Cases B.2.x

Therefore, the chief interaction of interest, in comparison with the previous B.1 cases, is the flowfield impact of the horizontal and vertical tails. The pressure fields from these tails will interact with each other, and with the turbulent boundary layer on the axisymmetric body, in a complex manner.

The chief viscous interactions are those on the main body (where the boundary layer is thicker than on the tails), in the region alongside the tails where the boundary layer is subject to the pressure fields caused by the presence of the tails. A secondary viscous interaction will occur at the junction between the fuselage and the leading edge of a tail surface. Here, a classical horseshoe vortex forms in the fuselage boundary layer, immediately forward of the body-tail junction. This vortex will stream aft in the body-tail corner on either side of the tail, sweeping flow down the tail and away on the body.

Three cases are presented in the B.2 series. They differ only in the NPR. For each case, the horizontal tail is at an aft location and the vertical tail is (relatively speaking) forward. This arrangement is illustrated in Figure 3.5-25.

The B.2 series can be viewed as being a classical jet effects test case. Experience has shown that the effect of the jet on the flowfield is quite complex. The effect of the jet on induced stability and control parameters, drag, and other data of engineering interest is configuration dependent. Results from one configuration should not be interpreted as being typical, or representative of, any other configuration.

In each case, the freestream Mach number is 0.900 and the angle of attack is nominally zero (actually  $0.02^\circ$ ). A cold exhaust jet ( $T_{ij} = 530^\circ\text{R}$ ) was flowing in each case. The only

variable between cases is the Nozzle Pressure Ratio ( $NPR = P_{ij} / P_{\infty}$ ).

Case	NPR
B.2.1	2.027
B.2.2	2.997
B.2.3	5.033

Circumferential locations on the body are identified by their angular coordinate,  $\phi$ . The vehicle top centerline, which is in the plane of the vertical tail, is  $\phi = 0^\circ$ . The horizontal tails are mounted at a symmetrical position,  $\phi = 90^\circ$ . For this series of test cases, the drag coefficients are based on the maximum cross sectional area of the body ( $A_{MAX}$ ), which is the approach used as well in the B.1 series.

The "landmarks" of this geometry are:

Feature	Location (X/L)
Vertical Tail, leading edge at fuselage	0.64
Horizontal Tail, leading edge at fuselage	0.78
Vertical Tail, trailing edge	0.87
Aftbody/Nozzle Junction	0.91
Horizontal Tail, trailing edge	0.96

The horizontal and vertical tails have a significant impact on the surface pressures on the aftbody and nozzle. Generating a suitable grid, and obtaining an accurate solution, can be fairly difficult as grid generation for the tail surfaces entails different strategies from grid generation for the afterbody surfaces. Most of the CFD contributors focused their modeling efforts on the afterbody and plume. As a result, several contributors have commented that they do not expect the highest accuracy near the tails. This expectation is borne out by the comparisons of surface pressures on the horizontal and vertical tails (to be presented below). All of the CFD contributions over-predicted the pressures on the tails near the mid-chord (i.e., the predicted pressure did not drop as low as the pressure in the experimental data). Errors in CP of up to +0.05 (i.e., too high) were seen in many of the predictions for the tail surfaces, near the mid-chord location.

### 3.5.2.1 Case B.2.1

This case was computed by four of the CFD contributors. One contributor (E08) performed Euler analysis, and the others performed Navier-Stokes analysis. In addition, drag computations were presented based on the semi-empirical method, S01.

The contours of Mach number in the vertical symmetry plane (i.e., the plane of the vertical tail) are presented in Figure 3.5-26. These data were produced by an inviscid analysis (Contribution E08) and therefore they do not show the viscous wake from the vertical tail. These contours show a simple subsonic expansion over the shoulder of the model (X from about 64 to 68, in the dimensional units of this figure). This is followed by a subsonic compression, centered in the nozzle lip. A comparison of the results for Cases B.1.1 and B.2.1 suggests that a slightly higher compression at the nozzle was achieved for Case B.1.1 (body alone, no tails). The nozzle internal flow also is well behaved, with a localized compression seen in the corner at X=67, and an expansion at the throat.

It should be noted that, due to the modest NPR (about 2.0) and the elevated external pressure near the nozzle exit in this inviscid prediction, the nozzle internal flow remains subsonic. This was the case, too, in the corresponding inviscid solution for Case B.1.1 (see Figure 3.5-6). The comparable Navier-Stokes solution for Case B.1.1 (same Figure) achieved a much reduced external flow pressure at the nozzle lip. With the reduced external pressure, the internal nozzle flow became choked at the throat, and accelerated to Mach 1.2 to 1.3 at the nozzle exit. Presumably, the same is true for the present case. We may expect that the inviscid (Euler) solutions will be characterized by subsonic flow throughout the internal nozzle (due to higher external pressure), while the Navier-Stokes solutions will reach sonic speeds near the geometric throat, and accelerate to supersonic speeds in the final diverging portion of the internal nozzle. Both classes of solution produce similar plume flow predictions, starting about one jet diameter downstream of the nozzle exit.

**Surface Pressure Comparisons** - The impact of the tails on the body pressures can be seen by comparing the surface pressure distributions (following next) with the data for Case B.1.1, presented in Figure 3.5-7.

The first comparison, Figure 3.5-27, presents surface pressure at  $\phi = 0^\circ$ . This is the vertical symmetry plane and the mounting position for the vertical tail, thus the data have a gap at the location of the tail. The pressure field predicted by both Contributions N09 and N10, forward of the tail, shows good agreement with the test data, with the surface pressure rising sharply just before the leading edge of the tail.

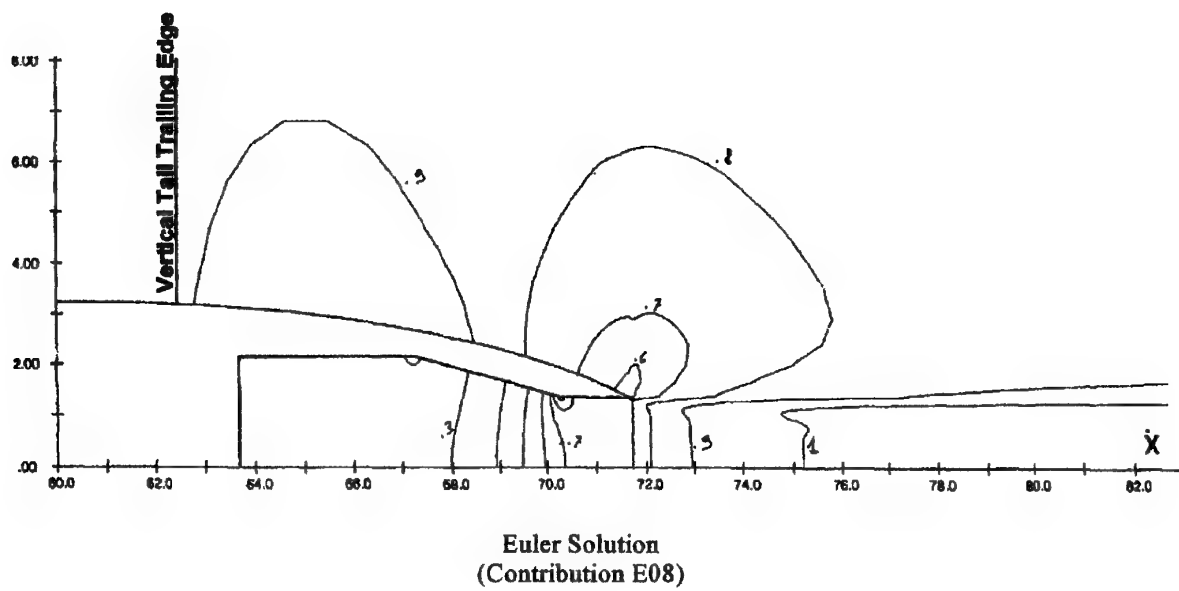
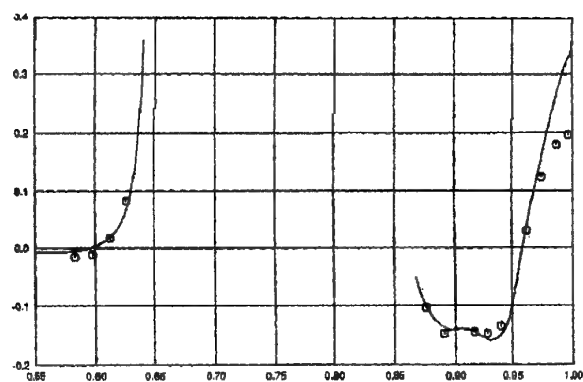
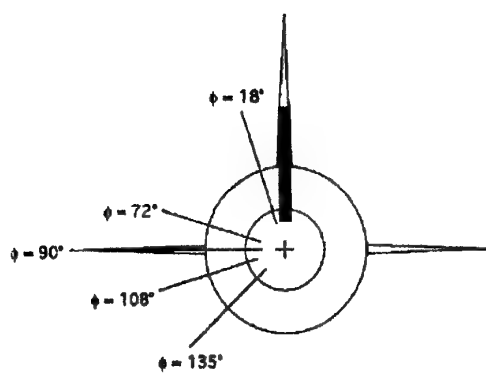
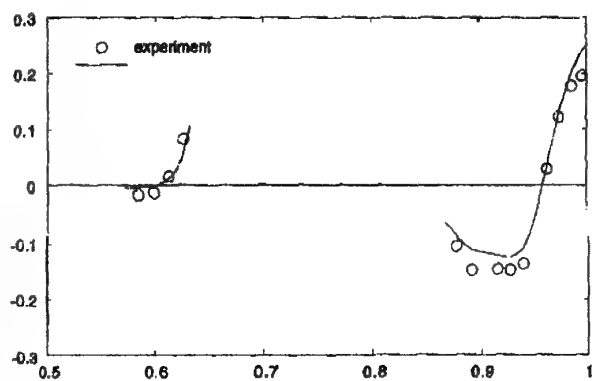


Figure 3.5-26. Predicted Mach Number Contours in Vertical Symmetry Plane, Case B.2.1



Contribution N09



Contribution N10

Figure 3.5-27. Comparison of Surface Pressures ( $C_p$  vs  $X/L$ ), Case B.2.1,  $\phi=0^\circ$

Aft of the tail, these pressure taps are in the viscous wake from the tail. Therefore, the boundary layer flow along this line of taps is modified by the tail wake interaction. The minimum pressure due to the body alone occurs around  $x/L=0.93$  (see, for example, Figure 3.5-7). For both cases (tails-on and tails-off) the minimum value is about  $C_p=-0.15$  (the flow becomes sonic at  $C_p^*=-0.188$ ). However, the body pressure is reduced to low values forward of  $X/L=0.93$  by the presence of the horizontal tails mid-chord expansion (say,  $x/L=0.88$  to  $0.92$ ). The shape of the pressure profile near the minimum is flattened and lengthened, thus adding pressure drag to the aftbody and nozzle. Both CFD predictions show this interaction, with Contribution N09 showing slightly better accuracy.

Since the flow in this region is in the viscous wake of the vertical tail, one would expect a slight reduction in the pressures achieved on the external surfaces in the final recompression approaching the nozzle exit. This is seen in the experimental data, which reach a  $C_p$  slightly below 0.2 in the present case (tails-on) and slightly above 0.2 in Case B.1.1 (tails-off). Both CFD predictions over-predict the pressure significantly, near the nozzle exit. However, Contribution N10 (using a  $k-\epsilon$  turbulence model) indeed shows a reduction in pressure at the nozzle trailing edge, compared with predictions by the same method in the equivalent tails-off case. For Contribution N09, using a one-equation model, a slight increase in pressure is noted near the nozzle trailing edge, compared with Case B.1.1.

The next row of pressure taps is at  $\phi=18^\circ$ , which is near the top centerline of the model (see Figure 3.5-28). This row of taps runs cleanly alongside the vertical tail, and a continuous comparison can be made. The three contributors' predictions are all in good agreement with the features of the flow at this location.

Approaching the leading edge of the vertical tail (with, of course, a small lateral displacement), the pressure rises. The pressure then drops to a local minimum in running past the mid-chord point of the vertical tail (about  $x/L = 0.75$ ), and shows some recompression as nearing the trailing edge of the vertical tail and the leading edge of the horizontal tail ( $X/L \sim 0.80$  to  $0.85$ ).

Downstream of this point, these pressure taps are affected by the wake of the tail, but they are not directly in the wake. The pressure drops again due to the expansion curvature of the nozzle (see body-alone case, Figure 3.5-7) to a minimum of roughly the same value as the body-alone case, B.1.1, at about  $X/L = 0.93$ . From this point, a continuous recompression occurs to the nozzle trailing edge, with an increasing viscous interaction setting in as the boundary layer continues growing rapidly.

Each method captures well the compression approaching the leading edge of the vertical tail ( $X/L = 0.60$  to  $0.65$ ). All

three methods provide pressure predictions which are slightly high in the favorable pressure gradient region along the forward portion of the vertical tail root ( $X/L = 0.65$  to  $0.75$ ). Quite possibly, this is due to the overprediction of pressures near the mid-chord of each tail surface (this issue will be further discussed, below).

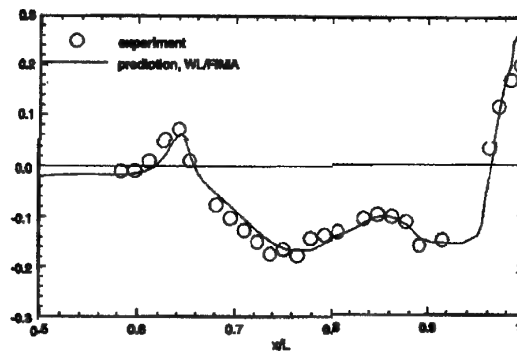
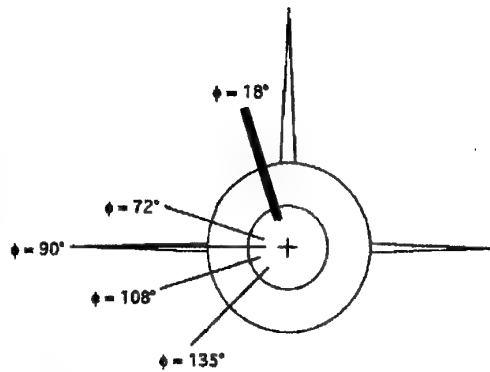
In the mild adverse recompression region ( $X/L = 0.76$  to  $0.86$ ), the methods are more accurate. Surprisingly, the Euler data from Contribution E08 appear to be somewhat more accurate in this region. In the shoulder region, the Euler method shows a low-pressure excursion which is not present in either Navier-Stokes solution. However, this excursion also was seen in the B.1.1 solution (no tails) by the same method (see Figure 3.5-7). Due to a gap in the experimental data at this point, the validity of this predicted feature cannot be verified. However, it does not seem physically plausible.

In the nozzle compression region ( $X/L > 0.9$ ), each method provides similar good accuracy for most of the points, up to the final recompression aft of the vertical tail trailing edge. The Euler method, as would be expected, predicts unrealistic high recompression. The two Navier-Stokes methods show reduced recompression (compared with the Euler prediction), though the trailing edge pressure by these methods also is higher than indicated by the experimental data.

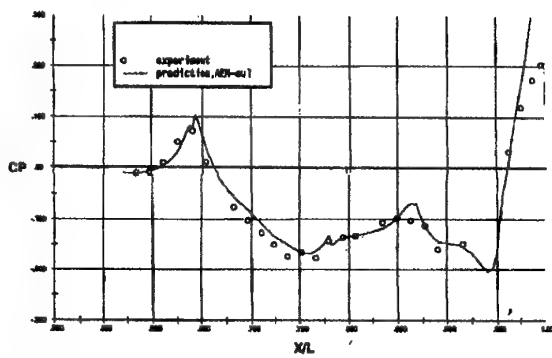
The next location,  $\phi=45^\circ$  (Figure 3.5-29), is equidistant from the vertical and horizontal tails. Due to increased lateral (circumferential) distance from the vertical tail leading edge, only a slight pressure rise is seen at  $X/L \sim 0.63$ . The minimum pressure from the vertical tail mid-chord is at about the axial location of the horizontal tail leading edge. These two perturbations nearly cancel at this location, producing only a modest wiggle in the pressure distribution. Sustained expansion then is noted, driven by first the thickness of the horizontal tail and then by the nozzle surface curvature. The pressure in this region is predicted too high, which may be due to problems with over-prediction on the tail surfaces.

Due to the effect of the slight compression of the horizontal tail trailing edge, the minimum pressure point is slightly forward of its body-alone location (Case B.1.1). However, the value of minimum pressure is roughly the same. The recompression to the nozzle trailing edge is quite mild at first, then it becomes severe. In this region, no experimental data are available.

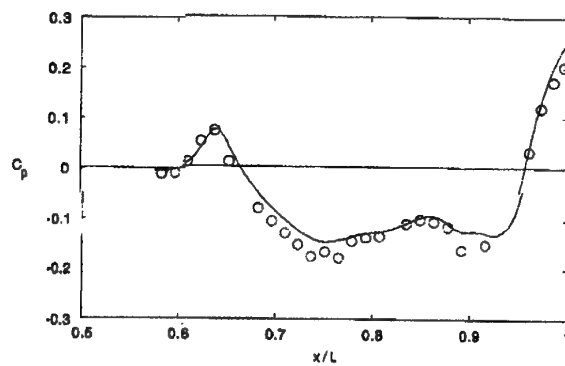
The two Navier-Stokes predictions are quite similar in this region of the data (which excludes the final recompression region). The predicted pressures are higher than the measured data in the region of  $X/L \sim 0.75$ , where the offsetting interactions from the two tail surfaces are present. The flow in this region, influenced by both tails, probably is very complex - placing high demands on the turbulence models. Contribution N09 provides slightly better agreement with data near the minimum pressure point (say,  $x/L = 0.90$ ).



Contribution N04



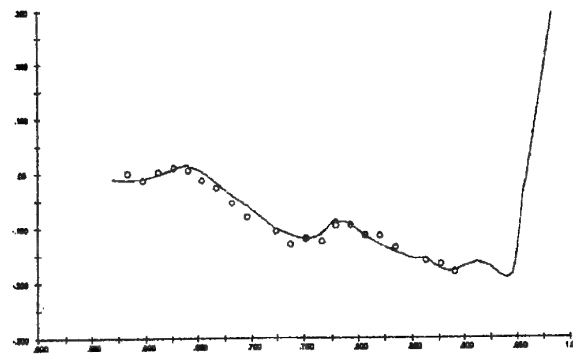
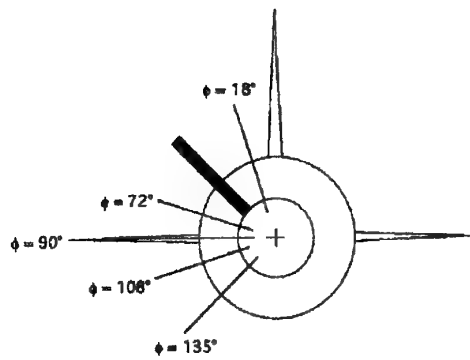
Contribution E08



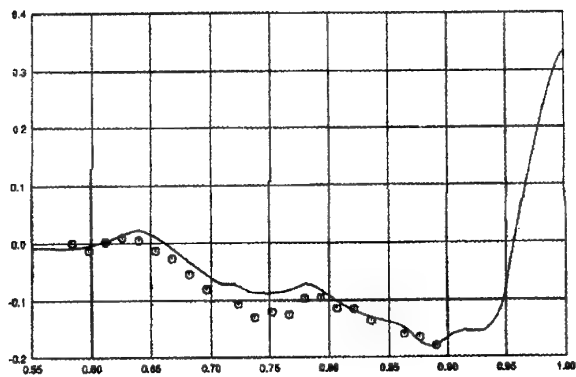
Contribution N10

Figure 3.5-28. Comparison of Surface Pressures, Case B.2.1,  $\phi=18^\circ$

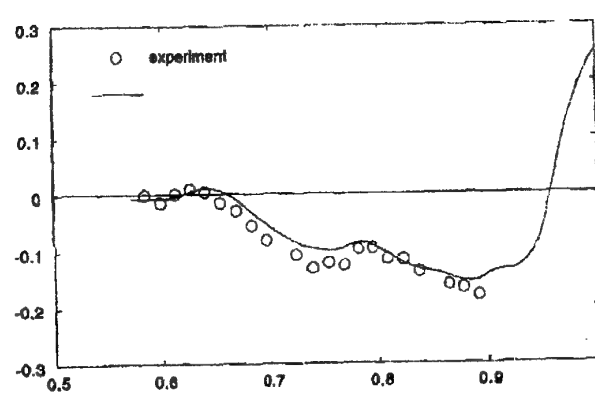




Contribution E08



Contribution N09



Contribution N10

Figure 3.5-29. Comparison of Surface Pressures ( $C_p$  vs.  $X/L$ ), Case B.2.1,  $\phi=45^\circ$

Contribution N09 predicts higher recompression at the nozzle trailing edge, compared with Contribution N10. No experimental data are available in this region, but based on other comparisons it seems safe to say that the experimental pressure at the trailing edge is lower than either prediction.

The next comparison (Figure 3.5-30) is for  $\phi=72^\circ$ . This comparison could be considered the counterpart of Figure 3.5-28, as this case is displaced  $18^\circ$  from the centerline of the horizontal tail. The flow expands gradually up to about  $X/L=0.74$  due to the longitudinal curvature of the aftbody. These pressures are very similar to those in the body-alone case, B.1.1 (see Figure 3.5-7). A sharp rise is then felt, caused by proximity to the leading edge of the horizontal tail.

The pressure next drops rather steeply from  $x/L = 0.80$  to  $0.87$  under the combined influences of the flow expansion over the aftbody and the horizontal tail. The minimum pressure is significantly further forward than in the body-alone case ( $X/L=0.88$  as compared with  $0.94$ ), as would be expected, and the minimum value of pressure is almost  $0.1$  lower (in terms of  $C_p$ ) than the minimum in the body-alone case. Since the minimum pressure occurs much further forward than in the body-alone case, the adverse pressure gradient to the nozzle trailing edge is in some sense less severe, since it occurs over a larger distance. An inflection is seen in the pressure distribution near  $x/L=0.92$  (contributions E08 and N10), where the body-alone minimum pressure point occurs. Each prediction is in good agreement up to the final minimum pressure point ( $X/L=0.88$ ). The good agreement of the Euler method (Contribution E08) demonstrates that viscous interactions are not critical in this region. Further, all the methods exhibit a similar inaccuracy close to the minimum pressure. This consistency indicates that viscous effects are not responsible for this error, and it raises the possibility that the geometry definition is inaccurate.

In the final recompression ( $X/L > 0.96$ ) the Euler method, as would be expected, predicts pressures too high. The two Navier-Stokes methods provide similar results in this final recompression region: one method (Contribution N04) seems slightly more accurate near the minimum pressure point, while the other method (Contribution N10) seems better near the nozzle trailing edge.

The circumferential location of the horizontal tail,  $\phi=90^\circ$ , was plotted by all four contributors (Figure 3.5-31). The comparisons at this location are interrupted between  $X/L \sim 0.78$  and  $0.92$ , where the line  $\phi=90^\circ$  lies buried inside the tail-body junction.

Forward of the horizontal tail leading edge, the pressure initially is dropping due to the gradual curvature of the aftbody surface (this is seen, too, in the body-alone data of Figure 3.5-7). Approaching the leading edge of the

horizontal tail, the pressure rises sharply. The Euler method does not capture the initial portion of this rise as well as the Navier-Stokes methods. This situation suggests that the precursor of the pressure rise is a viscous effect which passes forward more effectively through the boundary layer rather than the inviscid stream (where the local Mach number is somewhat above  $0.9$ ). All of the methods capture the final sharp pressure rise accurately, approaching the leading edge ( $X/L = 0.74$  to  $0.78$ ).

In the region aft of the trailing edge of the horizontal tail (i.e., after  $X/L \sim 0.92$ ), there is a steady adverse pressure gradient up to the nozzle exit. The pressure rise is about the same as in the body-alone case, but it occurs over a slightly longer axial distance and is therefore slightly less severe. However, at this circumferential location the wake from the horizontal tail is in continuous contact with the fuselage boundary layer.

Three of the comparisons are incomplete in the initial portion of the recompression region, though the data presented in previous Figures suggest that all the methods (both Euler and Navier-Stokes) are in reasonable agreement with test data until  $X/L > 0.96$ . In this final recompression region, the Euler method of course over-predicts the pressure. One Navier-Stokes method (N09) also over-predicts significantly, while the other two methods over-predict by a more modest amount. However, each viscous method underestimates the pressure modification of this final viscous interaction.

The final comparison on the body surface is presented for  $\phi=135^\circ$  (Figure 3.5-32). The pressure distribution shows the expected slow drop initially ( $X/L \sim 0.6$  to  $0.75$ ) due to the longitudinal curvature of the aftbody. A slight upward perturbation is seen near  $X/L = 0.78$  due to the leading edge of the horizontal tail. A steady drop in pressure then ensues under the influence of both the horizontal tail and the body longitudinal curvature. Throughout this region, both prediction methods show similar results.

The pressure reaches a minimum at about the same location as was seen at previous circumferential lines near the horizontal tail (i.e.,  $X/L \sim 0.88$ ) and about the same minimum value of pressure. The method of Contribution N04 captures this region fairly well, while Contribution N10 predicts slightly elevated pressures (compared with the experimental data) and an inflection point. This inflection point is a little forward of the body-alone minimum pressure point (Case B.1.1, see Figure 3.5-7) and therefore the source of this inflection is uncertain.

A sustained adverse pressure gradient is present from the minimum at  $X/L=0.90$  up to the nozzle exit. Both methods do quite well in the recompression pressure rise, and they are fairly close (but above) the final surface pressure ahead of the nozzle trailing edge. Each method shows lower

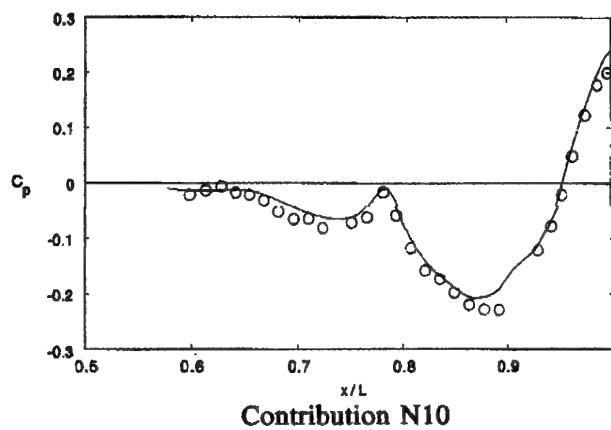
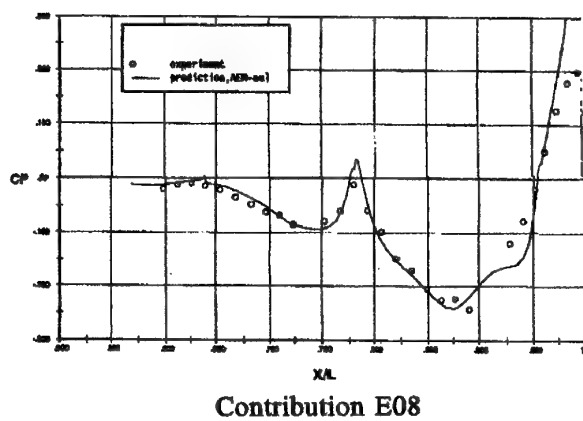
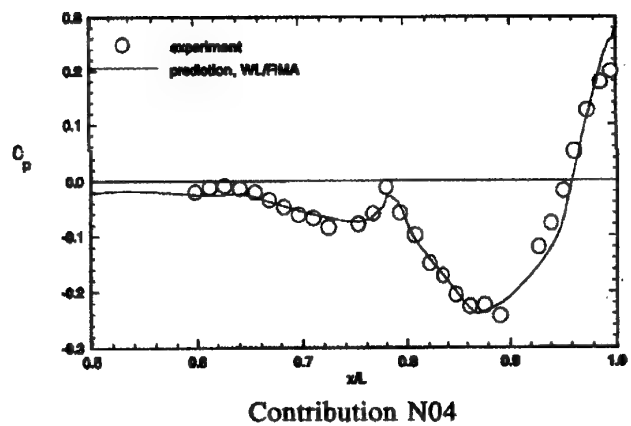
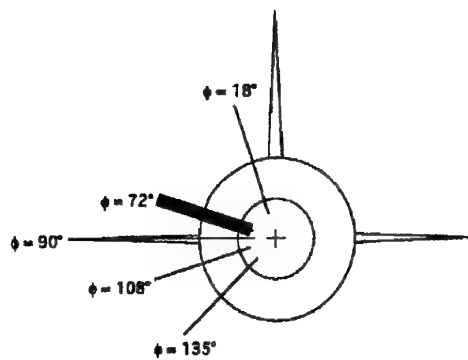
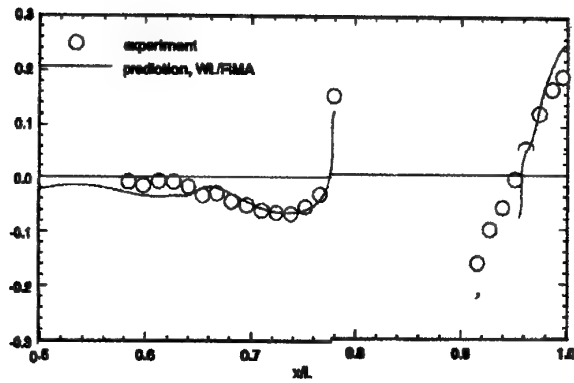
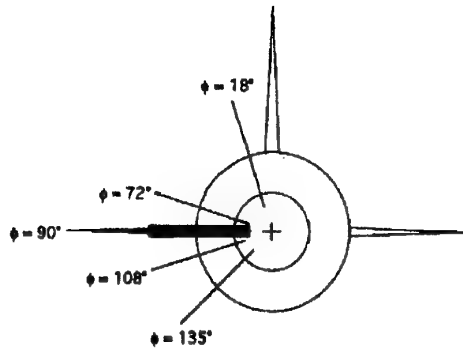
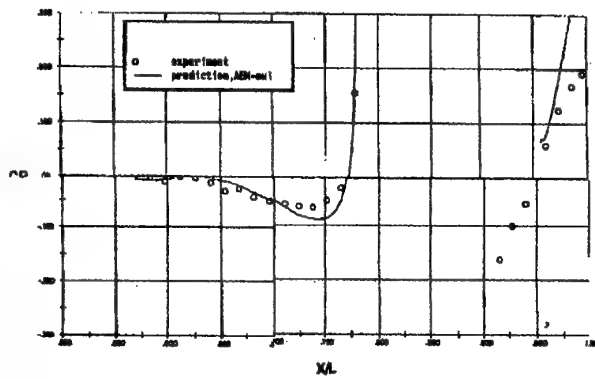


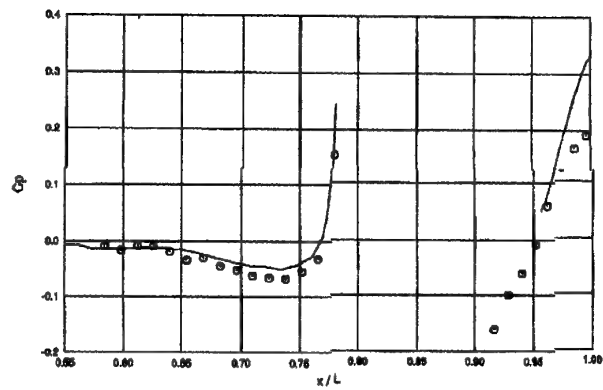
Figure 3.5-30. Comparison of Surface Pressures, Case B.2.1,  $\phi=72^\circ$



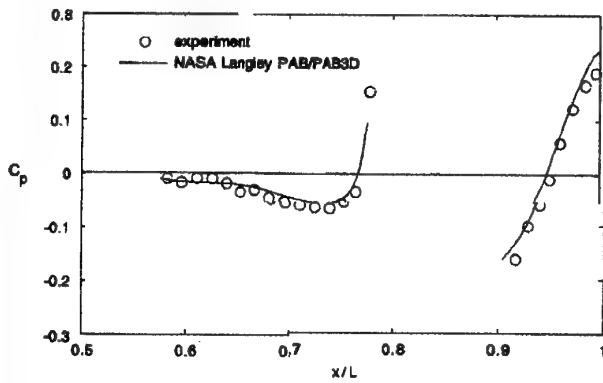
Contribution N04



Contribution E08



Contribution N09



Contribution N10

Figure 3.5-31. Comparison of Surface Pressures, Case B.2.1,  $\phi=90^\circ$

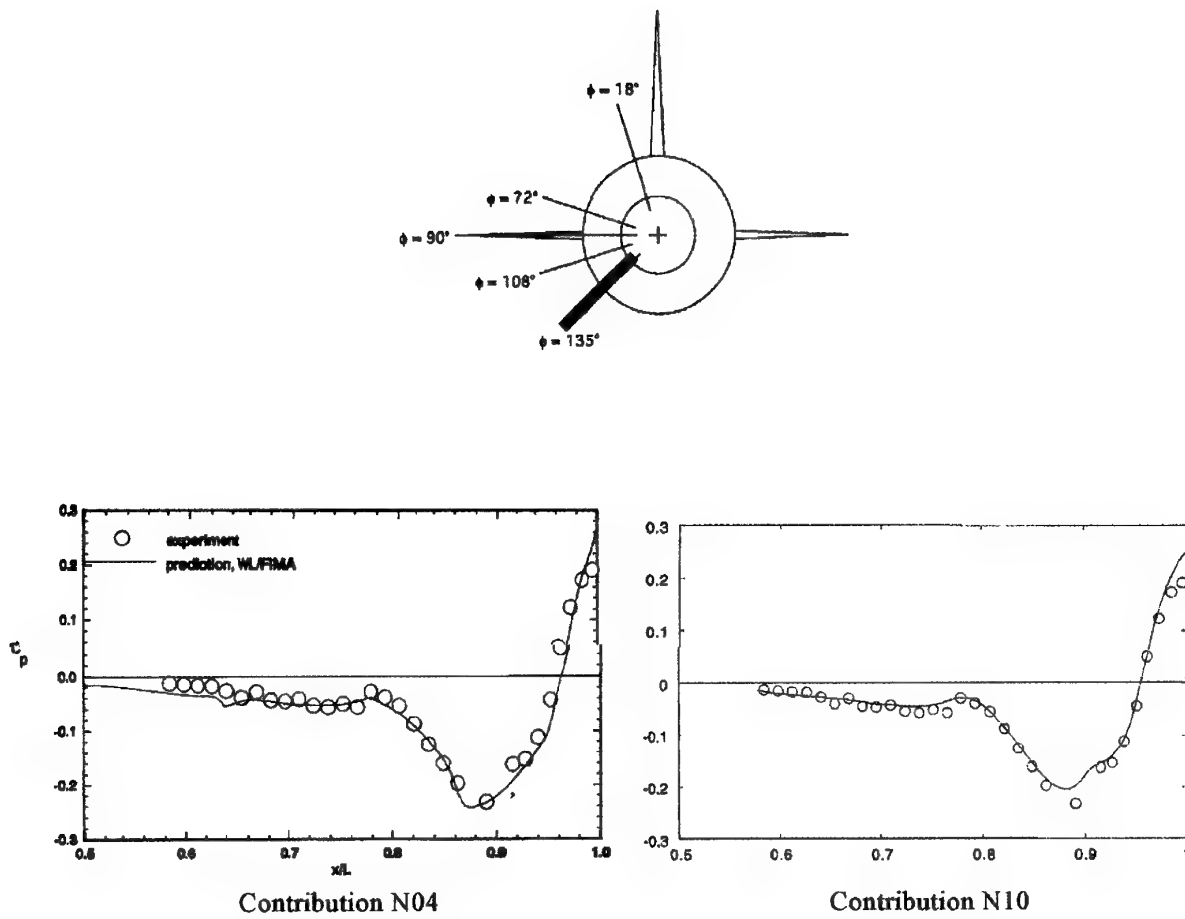


Figure 3.5-32. Comparison of Surface Pressures ( $C_p$  vs  $X/L$ ), Case B.2.1,  $\phi = 135^\circ$

recompression (i.e., better accuracy) for this case compared with the tails-off case (e.g., Figure 3.5-7).

Pressure data for a chordwise row of taps on the horizontal tail, near the root ( $y/b=0.1$ ), are presented in Figure 3.5-33. None of the prediction methods provide accurate data in this region. The reader is referred to Appendix C for data on the computational grids used in this region. Two contributors (N09 and N10) indicated their modeling techniques may have been relatively crude in this region, in their ability to model flows over the horizontal tail. Each method used an H-grid over the leading edge (except for Contribution N04, which used an unstructured grid). The grid over the main portion of the tail was coarse, compared with accepted practice for modeling a wing (tail) to high accuracy. The problem of grid generation for the horizontal tail may have been complicated by the axial (longitudinal) location of this surface, which is alongside the mid-chord portion of the vertical tail. This axial overlap of the two aerodynamic surfaces provides a complication in some grid generation methods, thus (potentially) degrading the solution accuracy.

Similar comparisons, for the vertical tail surface, are presented in Figure 3.5-34. As in the previous comparison, the chordwise pressure data are close to the root of the tail ( $z/b=0.1$ ). All four CFD methods again overpredict the pressures on the tail, though perhaps not by as wide a margin as was seen on the horizontal tail. This slight improvement in accuracy perhaps can be explained by the vertical tail leading edge being forward of the neighboring horizontal tail, thus simplifying somewhat the grid generation process. Interestingly, each method shows improved accuracy in the aft portion of the vertical tail, in a sustained adverse pressure gradient.

**Drag Comparisons** - A comparison of the measured pressures (just above) has shown that no CFD method is consistently more accurate than the other methods. Tabulated data on experimental and predicted drag for this case are presented immediately below.

#### Pressure Drag

##### Drag Predictions:

Contrib	CDPN	CDPA	CDPHT	CDPVT	CDPT
Exp.	-0.0130	0.0410			
S01					0.0494
N04	-0.0069	0.04111	0.01859	0.01908	0.07192
N10	-0.0304	0.0426	0.0054	0.0103	0.0279

#### Total Drag

##### Drag Predictions:

Contrib.	CDTN	CDTA	CDTHT	CDTVT	CDTT
Exp.					0.1055 $\pm 0.0050$
S01					0.1051
N04	-0.005601	0.05438	0.03781	0.03421	0.1208
N10	-0.0269	0.0698	0.0362	0.0371	0.1163

##### Prediction Errors:

Contrib.	$\Delta C_{DTT}$	% Error
Exp		Uncertainty $\pm 4.7\%$
S01	-0.0004	-0.4%
N04	+0.0153	+14.5%
N10	+0.0108	+10.2%

These drag data also are presented graphically in Figure 3.5-35.

**Discussion** - Each CFD method over-predicted the drag for this case. For the same body, same NPR, and no tails (Case B.1.1), the same CFD methods both under-predicted drag. The observed errors in pressure on the aftbody and nozzle at the external nozzle shoulder and the trailing edge would tend to under-predict drag. These errors are present with the body alone (Case B.1.1) and the body with tails (Case B.2.2).

The two CFD methods agree that the drag contributions are roughly equal from the aftbody-nozzle combination, the horizontal tail, and the vertical tail. Presumably, the effect of CFD prediction errors on the aftbody and nozzle is to under-predict drag. For both tail surfaces, the experimental data do not permit an assessment of CFD accuracy in the critical leading edge and trailing edge regions. Based on the available data, the predictions for the horizontal tail are fairly good on the forward section ( $x/c = 0.1$  to  $0.35$ ) and on the aft section ( $x/c = 0.7$  to  $0.9$ ). However, the predictions are quite poor in the mid-chord region for each method. For the vertical tail, all four CFD methods over-predicted pressure on the forward part of the tail ( $x/c = 0.1$  to  $0.5$ ) and they were more accurate on the aft part. This situation would lead to an over-prediction of drag.

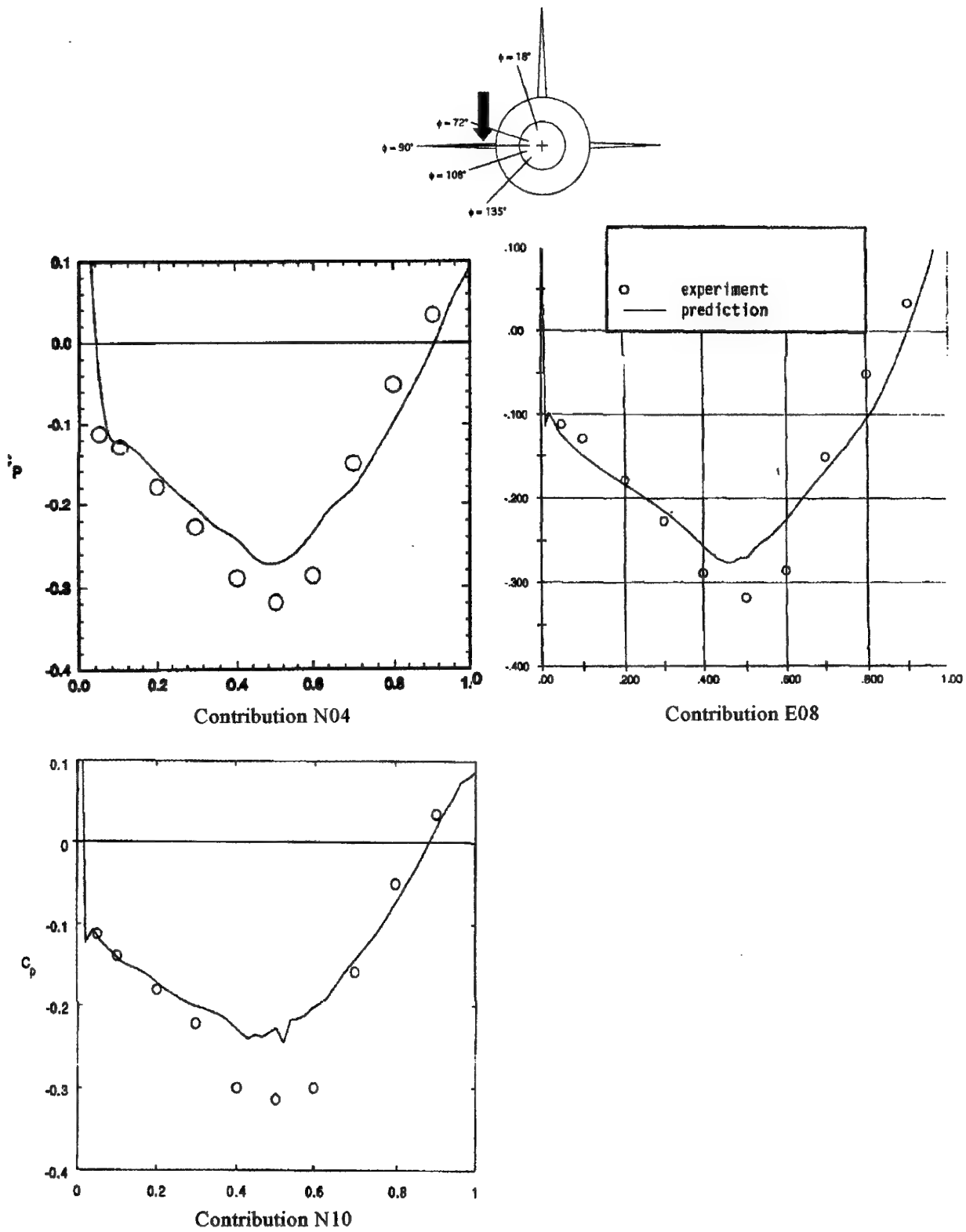


Figure 3.5-33. Comparison of Surface Pressures, Horizontal Tail Upper Surface, Case B.2.1

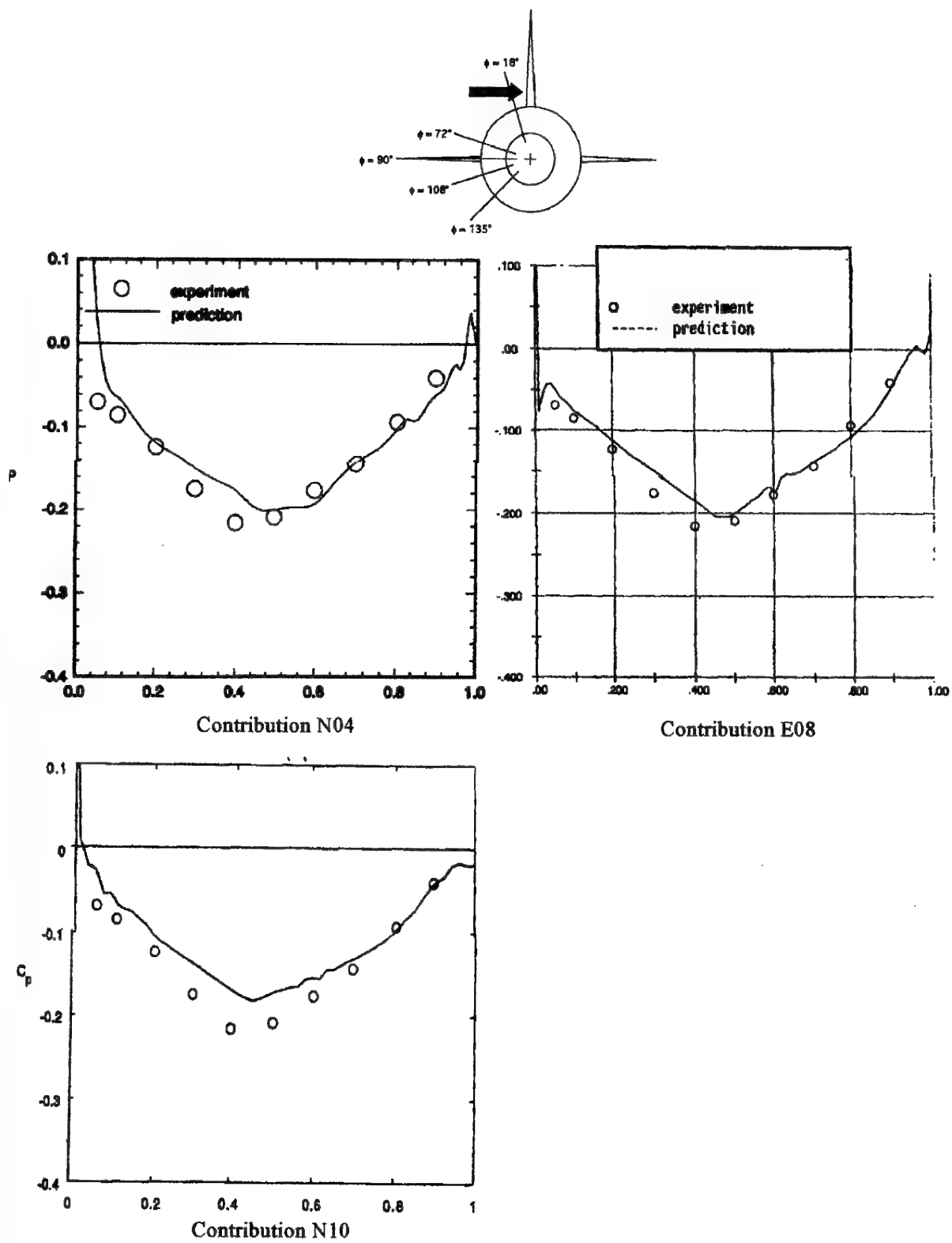
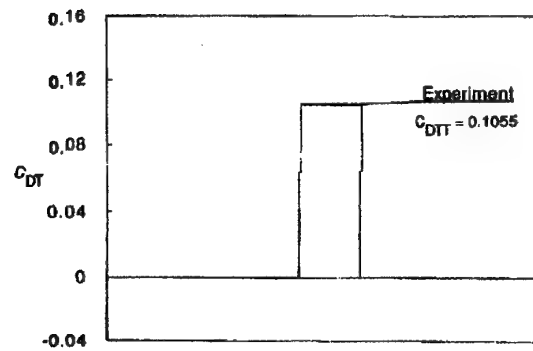


Figure 3.5-34. Comparison of Surface Pressures ( $C_p$  vs  $X/C$ ), Case B.2.1, Vertical Tail Surface

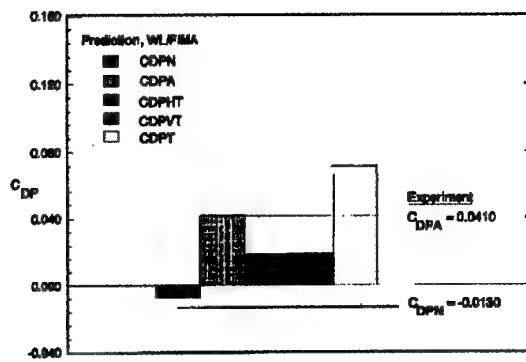


## Pressure Drag

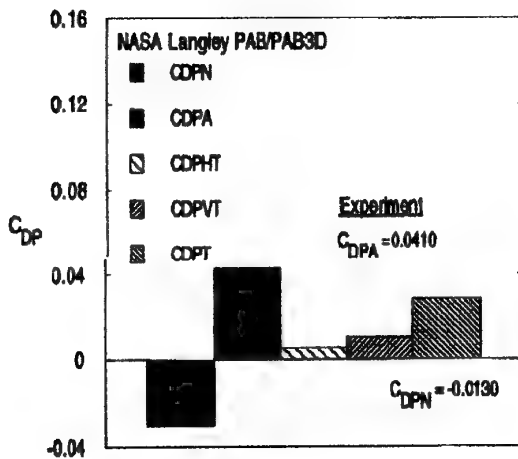
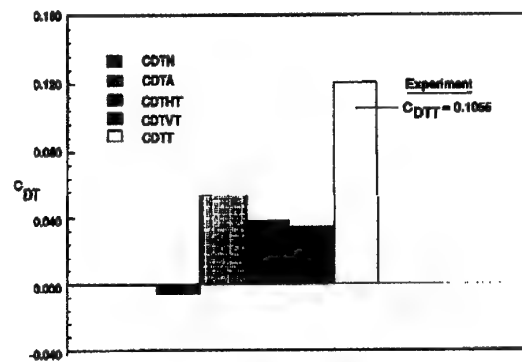
## Total Drag



## Contribution S01



## Contribution N04



## Contribution N10

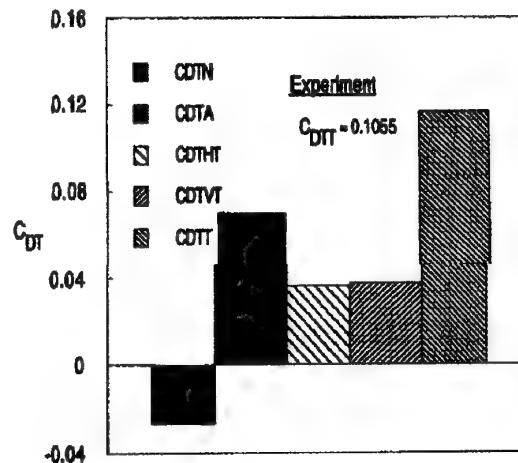


Figure 3.5-35. Comparison of Drag Predictions, Case B.2.1

It should be noted that only one row of pressure taps is available to support this assessment of drag prediction error sources. Pressure data are not available over the main portion of the tail surfaces. However, the limited data available to us strongly suggests that these errors in drag prediction are largely derived from the pressures on the tails.

### 3.5.2.2 Case B.2.2

Case B.2.2 features geometry which is identical to that of Case B.2.1 (previous case). The only difference is that the NPR is increased from 2 to 3. As a reminder, the body geometry also is identical to that of Cases B.1.x. However, a direct comparison with data from Cases B.1.x will not serve to identify tail effects in Case B.2.2, since the B.1 series does not include an NPR similar to the present case. A comparison with the data of Case B.2.1 (previous case) will highlight the effect of NPR in these data.

Contours of off-body Mach number in the vertical symmetry plane, as computed using an Euler method (Contribution E08), are presented in Figure 3.5-36. These data may be compared with similar data for Case B.2.1, which differ from the present case only in that the NPR is lower. Very little difference is seen in the external flow. Slight changes are noted in the external flow compression at the nozzle lip, but it is difficult to say whether the magnitude of the compression is different.

The internal flow, however, is changed substantially in the inviscid prediction. With the increased NPR (now 3, instead of 2 previously) the internal nozzle flow is supersonic from the throat to (and beyond) the nozzle exit. In the previous case (see Figure 3.5-26) the predicted internal flow was subsonic (but this was judged to be due to excessive external recompression in the inviscid solution, rather than being a physically realistic prediction).

**Surface Pressure Comparisons** - Comparisons of surface pressure data with CFD predictions for  $\phi=18^\circ$  are presented in Figure 3.5-37. The effects of the NPR variation can be gauged by comparing this Figure (NPR=3) with Figure 3.5-28 (NPR=2). The two methods presented in the present case were both applied to Case B.2.1, thus a direct comparison can be made. The results for the present case are virtually identical to those of B.2.1, for each method. It appears that an effect of NPR can be seen (only slightly) at the trailing edge in Contribution N04. Otherwise, these data serve mainly to show that the CFD results are repeatable in the two cases.

Similar conclusions can be drawn for  $\phi=45^\circ$  in Figure 3.5-38 (compare with Figure 3.5-29),  $\phi=72^\circ$  in Figure 3.5-39 (compare with Figure 3.5-30), for  $\phi=90^\circ$  in Figure 3.5-40 (compare with Figure 3.5-31), and for  $\phi=135^\circ$  in Figure 3.5-41 (compare with Figure 3.5-32). The NPR variation from

2 to 3 seems to have almost no visible impact, in terms of the surface pressure distributions.

This outcome also is seen in the results of empennage pressures. The horizontal tail pressures (Figure 3.5-42) and the vertical tail pressures (Figure 3.5-43) are virtually identical, in both the CFD predictions and the experimental data, with the results for the lower NPR (compare with Figures 3.5-33 and 3.5-34).

**Drag Comparisons** - The drag predictions for the semi-empirical method (Contribution S01) and one of the Navier-Stokes methods (Contribution N04) are presented graphically in Figure 3.5-44. The drag data also are tabulated below.

#### Pressure Drag

Drag Predictions:

Contrib.	CDPN	CDPA	CDPHT	CDPVT	CDPT
Exp.	-0.0121	0.0410			
S01					0.0482
N04	-0.0088	0.0410	0.0181	0.0191	0.0719

#### Total Drag

Drag Predictions:

Contrib.	CDTN	CDTA	CDTHT	CDTVT	CDTT
Exp.					0.1060 $\pm 0.0050$
S01					0.1039
N04	-0.0075	0.05424	0.03875	0.03428	0.1198

Prediction Errors ( $C_{DTT}$ ):

Contrib.	$\Delta C_{DTT}$	% Error
Exp		Uncertainty $\pm 4.7\%$
S01	-0.0021	-2.0%
N04	+0.0138	+13.0%

The drag data present the same conclusion as the pressure data. The effect of NPR (varying from 2 to 3) is negligible. In the experimental data, this variation produces a net drag

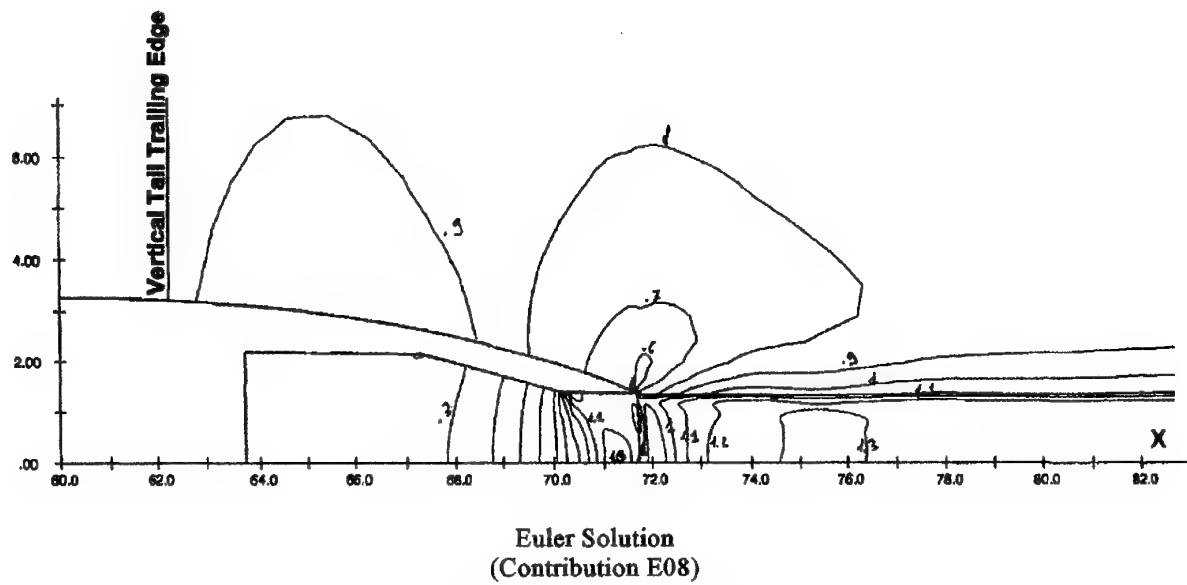


Figure 3.5-36. Predicted Mach Number Contours in Vertical Symmetry Plane, Case B.2.2

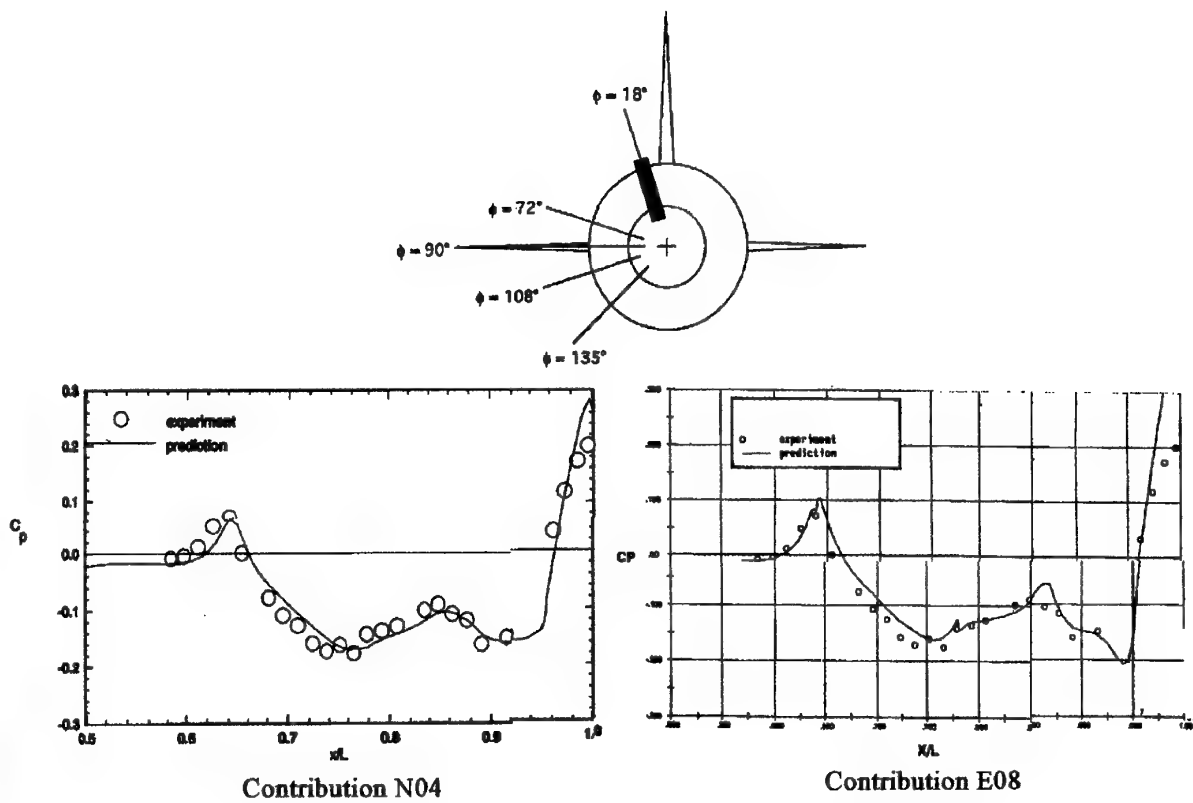


Figure 3.5-37. Comparison of Surface Pressures, Case B.2.2,  $\phi=18^\circ$

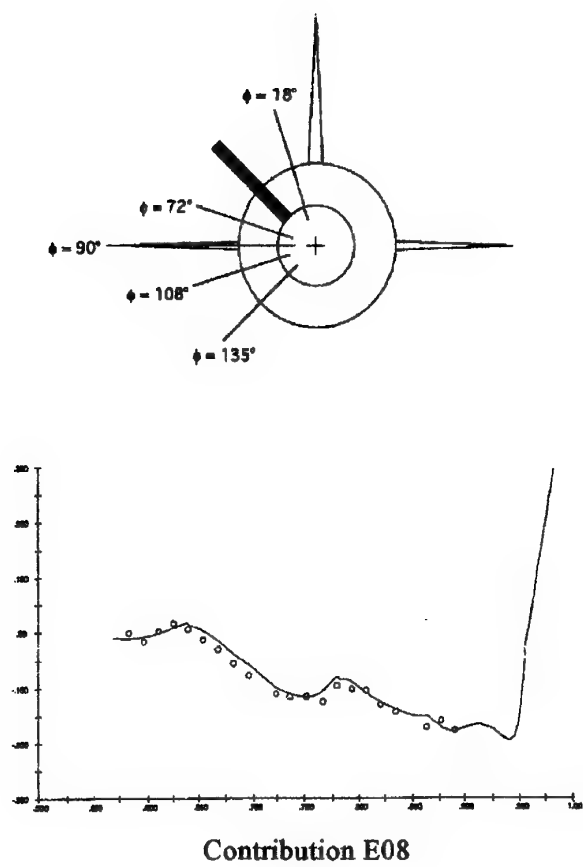


Figure 3.5-38. Comparison of Surface Pressures ( $C_p$  vs.  $X/L$ ), Case B.2.2,  $\phi=45^\circ$

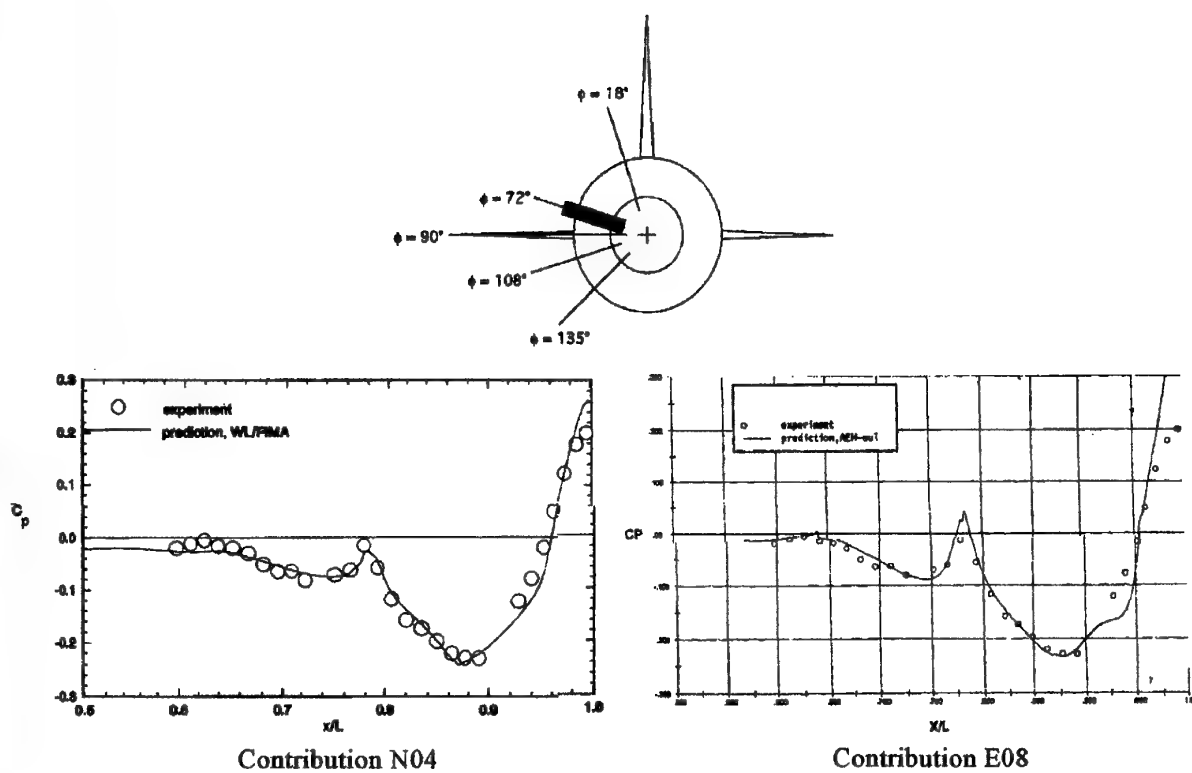


Figure 3.5-39. Comparison of Surface Pressures, Case B.2.2,  $\phi=72^\circ$

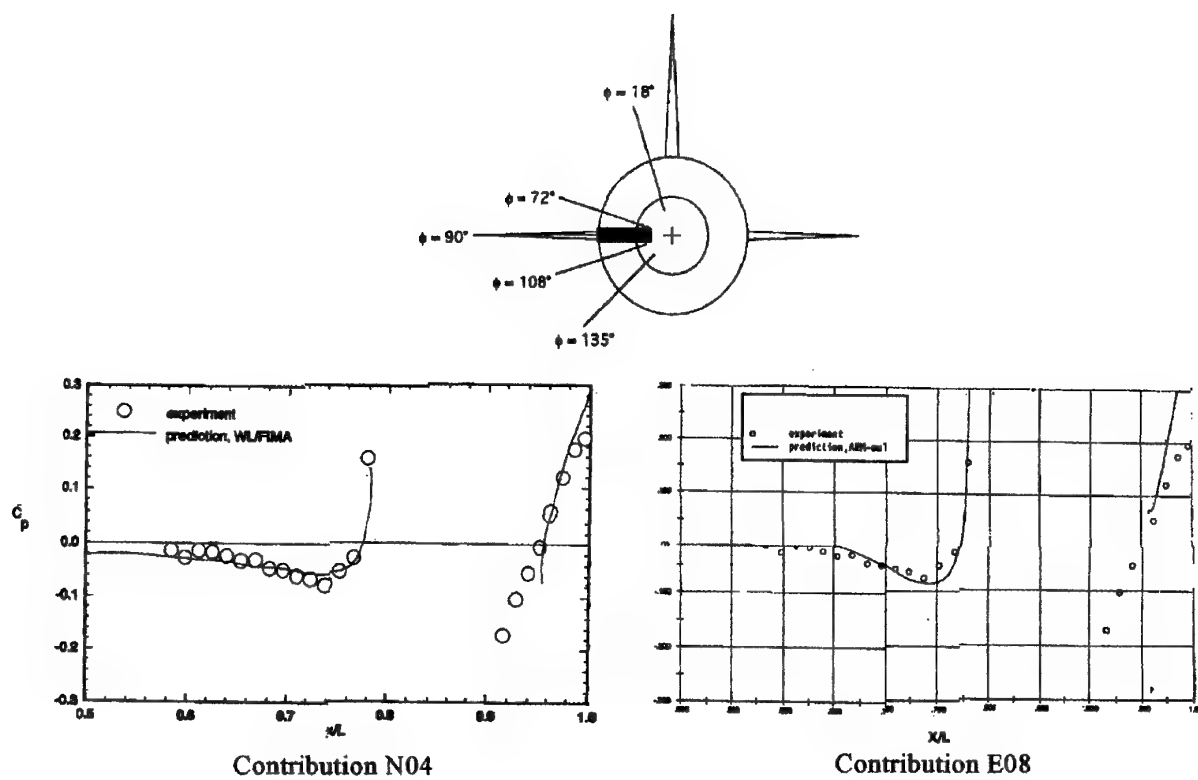


Figure 3.5-40. Comparison of Surface Pressures, Case B.2.2,  $\phi=90^\circ$

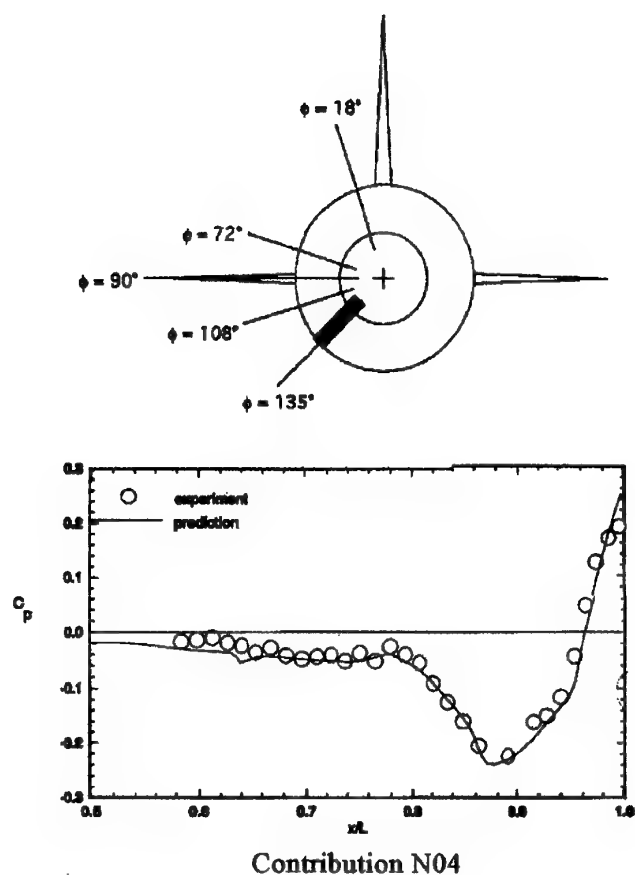


Figure 3.5-41. Comparison of Surface Pressures ( $C_p$  vs  $X/L$ ), Case B.2.2,  $\phi = 135^\circ$



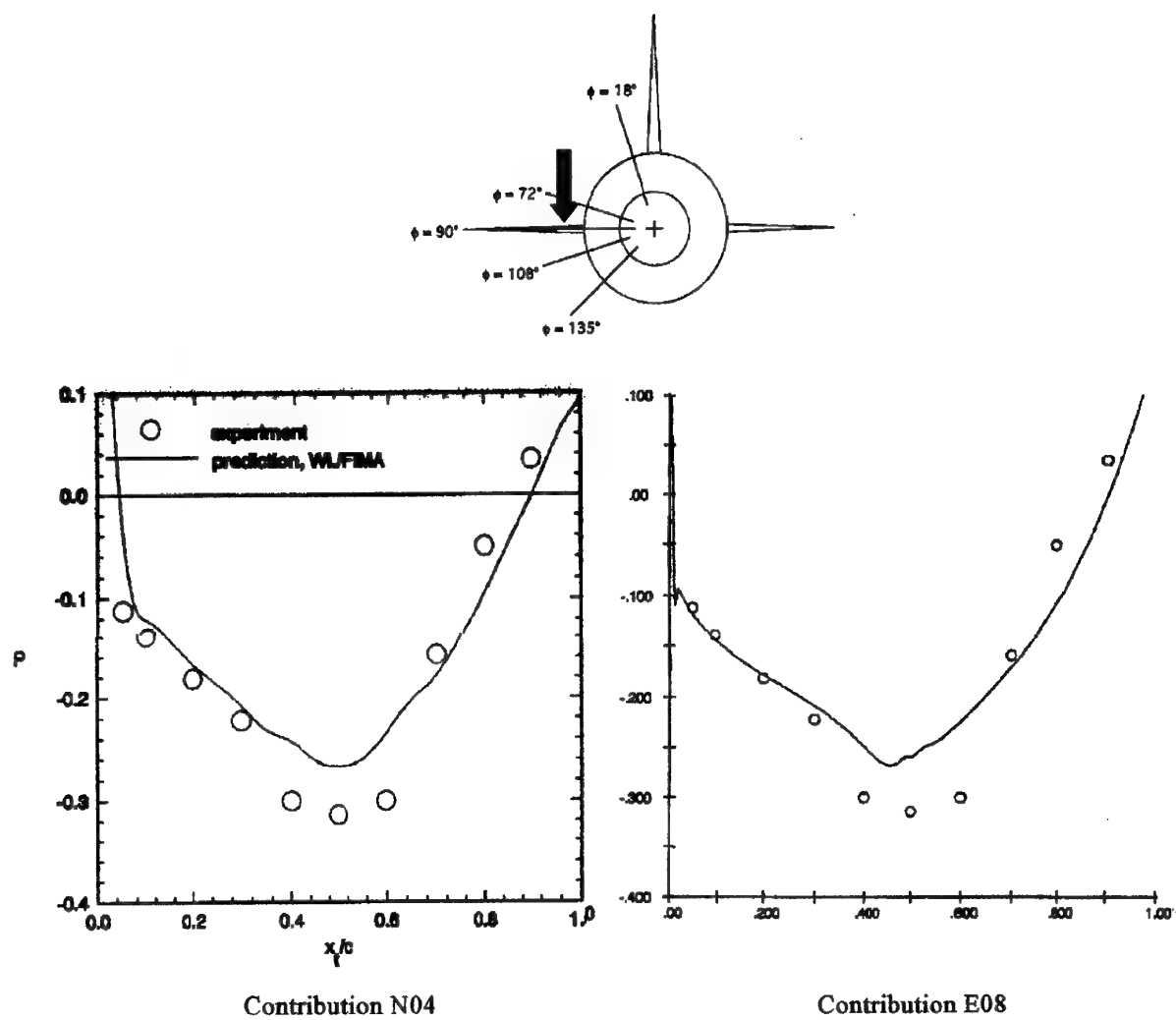


Figure 3.5-42. Comparison of Surface Pressures ( $C_p$  vs.  $Xt/C$ ), Case B.2.2, Horizontal Tail Upper Surface

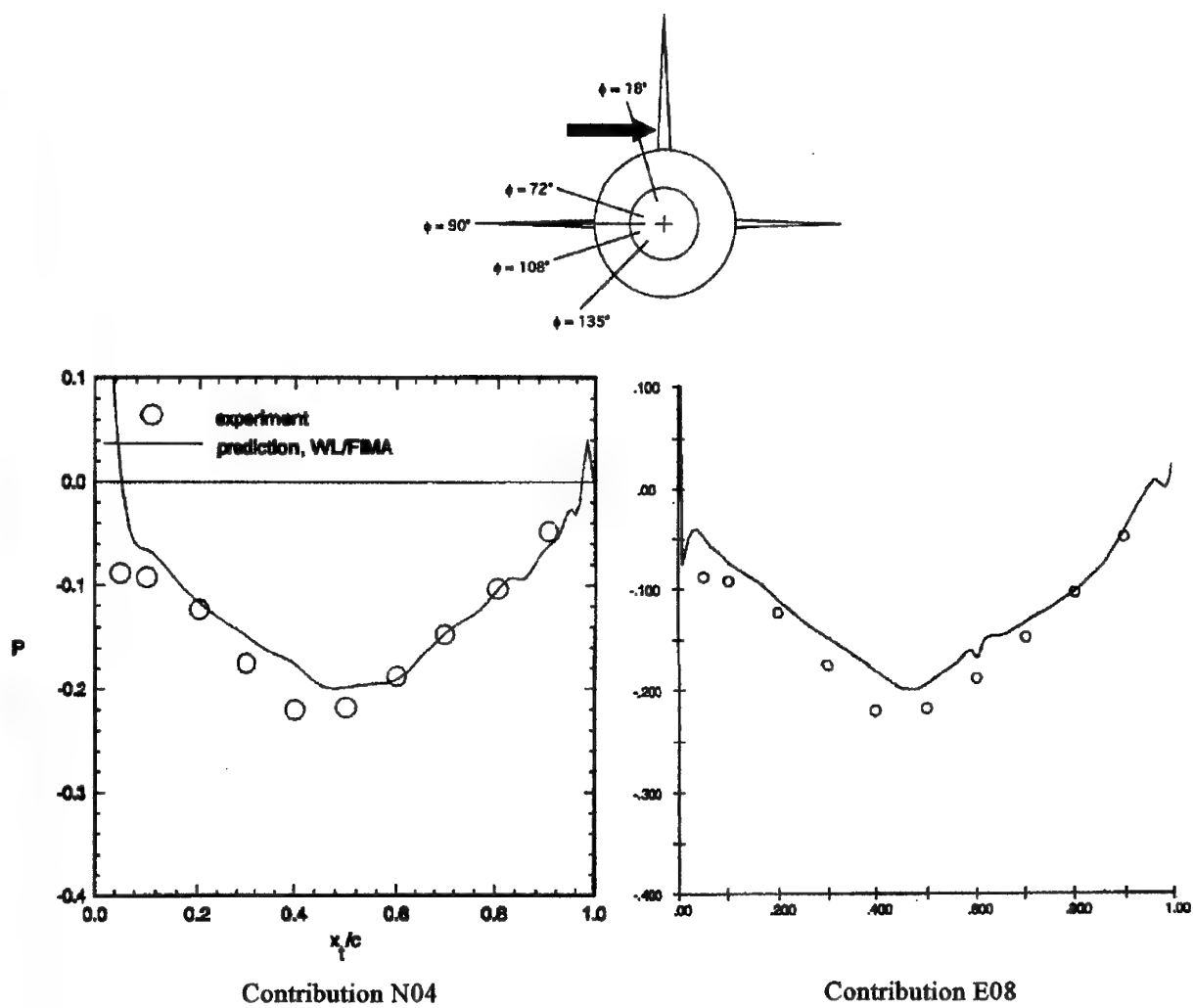
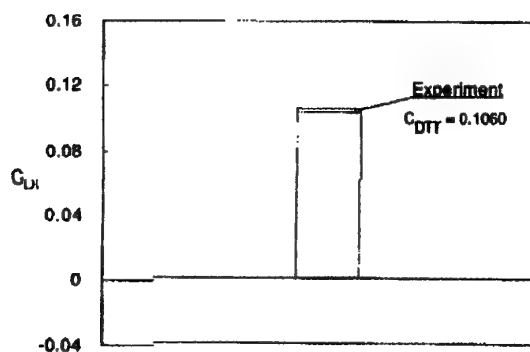


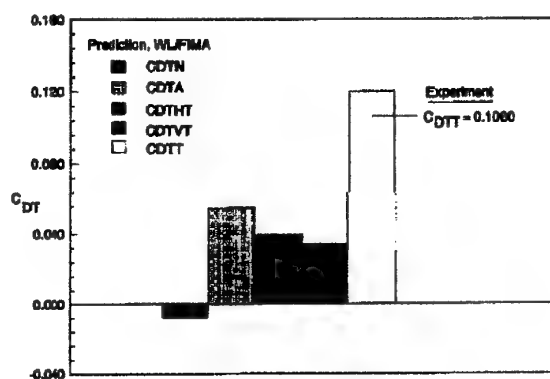
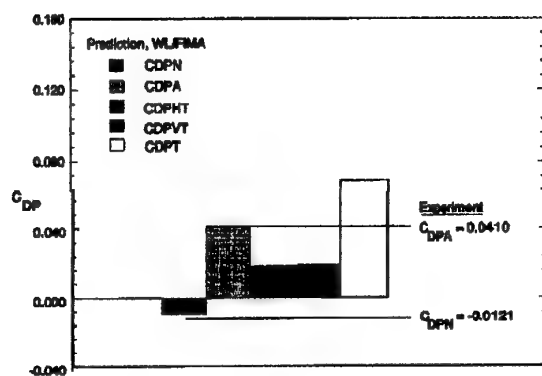
Figure 3.5-43. Comparison of Surface Pressures ( $C_p$  vs.  $X_t/C$ ), Case B.2.2, Vertical Tail

## Pressure Drag

## Total Drag



## Contribution S01



## Contribution N04

Figure 3.5-44 Comparison of Drag Predictions, Case B.2.2

increase of +0.0005 (say, 0.5%). This minor variation certainly falls within the range of experimental uncertainty. Method N04 predicts the afterbody pressure drag remarkably well, but is less accurate for the nozzle pressure drag. No data are available to assess the pressure drag accuracy on the tail surfaces. However, the errors in predicting total drag are not explained in terms of aftbody and nozzle pressure drag. As in the previous case, the drag on the tails probably exceeds the drag on the aftbody and nozzle. Presumably, therefore, the largest portion of the drag prediction error is due to overpredicting drag on the tails, and due to underpredicting friction forces on the aftbody and nozzle.

**Discussion** - Compared with Case B.2.1, the present Contribution S01 shows a drag change of -0.0012 (-1.1%), and Contribution N04 shows a change of -0.0010 (-1.0%). There is general agreement among all the data that the NPR variation from 2 to 3 has negligible impact. A comparison of these two cases illustrates mainly the level of repeatability in the data.

### 3.5.2.3 Case B.2.3

This case also features the same geometry as Cases B.2.1 and B.2.2. Again, the body for this geometry (i.e., excluding tails) is identical to the axisymmetric body of Case B.1.2. The only difference in the present case is that the NPR is increased to 5, from the previous values of 2 and 3 (Cases B.2.1 and B.2.2, respectively).

The contours of Mach number in the vertical symmetry plane ( $\phi=0^\circ$ ) are presented in Figure 3.5-45. These predictions by an Euler method (Contribution E08) naturally do not illustrate the boundary layer and wake flows. The external and internal flows forward of the nozzle exit are virtually identical with the previous case (see Figure 3.5-36).

Due to the higher NPR, the jet velocities downstream of the nozzle exit are much higher than in the previous case. Jet Mach numbers above 2.0 are predicted, compared with maximum values of about 1.3 in the previous case. Perhaps due to the increased magnitude of the velocity gradient between the jet and the external flow, a much thicker "mixing layer" is predicted in the present case. This, however, is (apparently) due to numerical diffusion, since the prediction of an Euler method should produce a contact discontinuity rather than a continuous gradient.

**Surface Pressure Comparisons** - Surface pressures for the vertical symmetry plane,  $\phi=0^\circ$ , are presented in Figure 3.5-46. These predictions may be compared with similar data, for lower NPR, in Figure 3.5-27. A gap is present in these data where this line falls inside the vertical tail.

Forward of the vertical tail, the CFD prediction and the experimental data show clearly the pressure rise up to the leading edge of the tail.

Aft of the tail, near the minimum pressure point, the predicted pressure is slightly elevated, compared with both the experimental data (Figure 3.5-46) and with the same prediction method at lower NPR (Figure 3.5-27). The increase in surface pressure with higher NPR is perhaps to be expected, though it is not seen in the corresponding experimental data. This combination of observations could suggest that the CFD methods captured the shape effect of the NPR variation (this would cause increased afterbody pressure) but perhaps they failed to capture the increased entrainment (which would cause decreased afterbody surface pressure).

In the recompression region, the experimental data are virtually unchanged from the case at lower NPR. However, the CFD prediction (Contribution N10) is considerably more accurate. At this NPR (now about 5 rather than the previous 2) the turbulence model is (apparently) much more accurate. Of course, the effect of increased NPR may be felt in either the inviscid shape effect or in viscous entrainment. Any impact of plume shape should be seen in the experimental surface pressures - but it is not there. Therefore, we might conclude that the improvement in accuracy is due to more accurate turbulence modeling in the plume entrainment region. Another possibility is that the turbulence model may have captured the wake of the vertical tail more accurately at this condition.

The next pressure comparison is for  $\phi=18^\circ$  (Figure 3.5-47). These data, for tails on at NPR=5, can be compared with similar data for the same geometry at lower NPR (Figures 3.5-28 and 3.5-37), and for the same body, without tails, at the same NPR (Figure 3.5-11).

The comparison in the present case is very similar to the data for the same geometry at the two lower NPR values. The pressure is over-predicted alongside the tails, as was seen in the previous two cases. A slight elevation in the trailing edge pressure can be seen in the Navier-Stokes data (Contribution N10) compared with Case B.2.1 (NPR=2). The pressure rise in the CFD prediction appears to be less than the rise in the experimental data due to the NPR variation. In other words, the usual CFD over-prediction of pressure at the trailing edge of the nozzle appears to have lessened (again) at the higher NPR. The overprediction of pressure by the Euler method remains quite large, as would be expected.

Comparisons of surface pressure for  $\phi=45^\circ$ , midway between the vertical and horizontal tails, are presented in Figure 3.5-48. In the region where experimental data are present, the comparison is essentially identical with the results from the two previous cases. Again, the CFD prediction rises to a lower final pressure at the nozzle exit, compared with

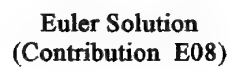


**Figure 3.5-45. Predicted Mach Number Contours in Vertical Symmetry Plane, Case B.2.3**

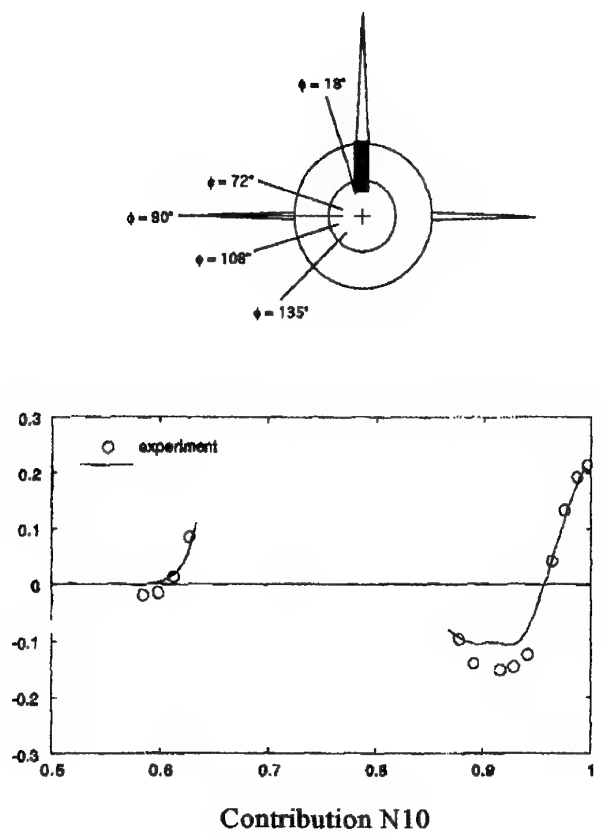


Figure 3.5-46. Comparison of Surface Pressures, Case B.2.3,  $\phi=0^\circ$

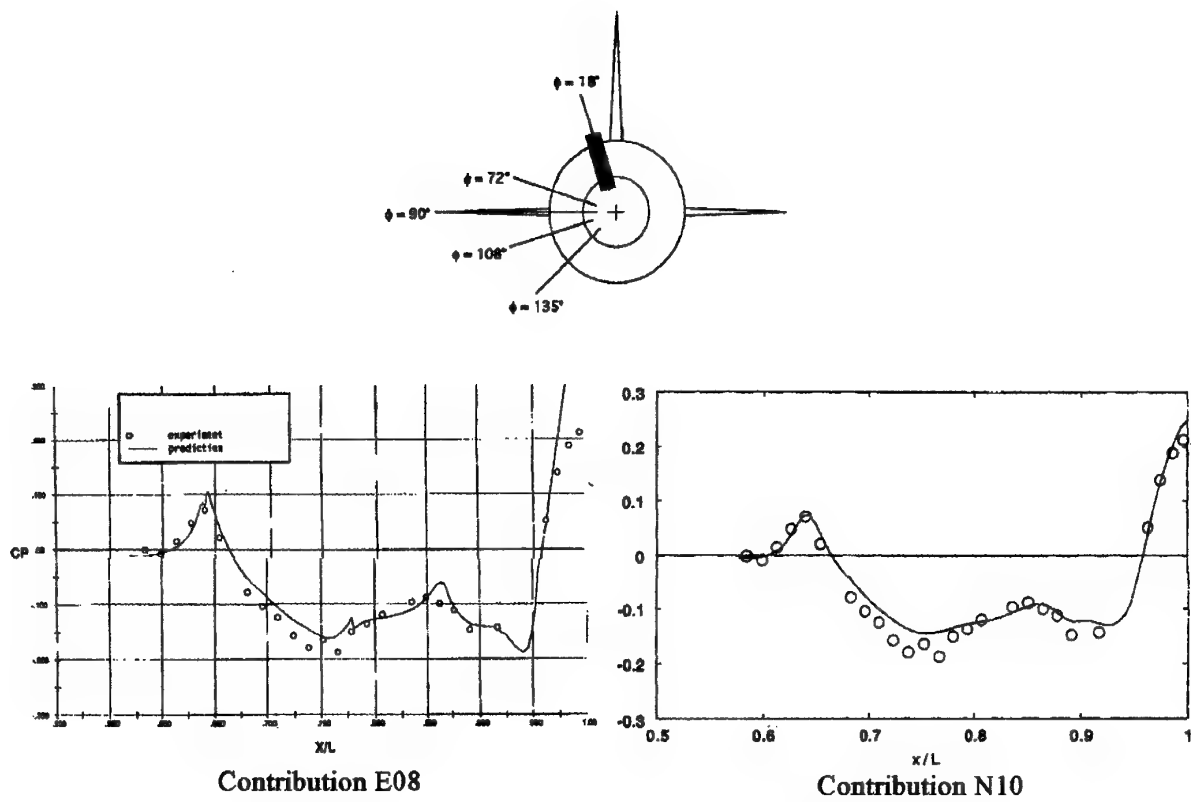


Figure 3.5-47. Comparison of Surface Pressures ( $C_p$  vs  $X/L$ ), Case B.2.3,  $\phi = 18^\circ$

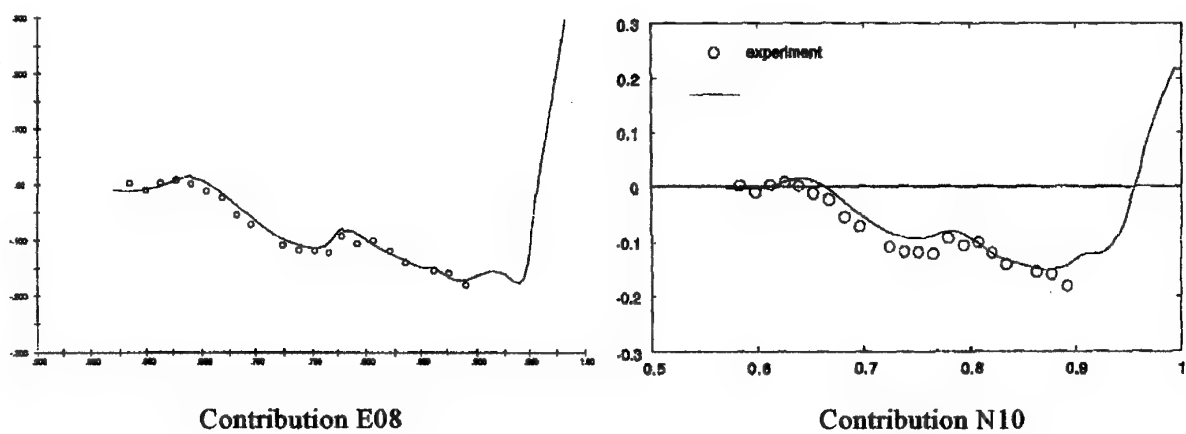
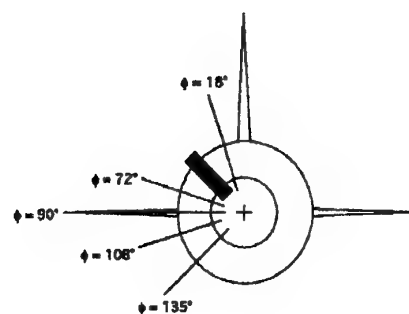


Figure 3.5-48. Comparison of Surface Pressures ( $C_p$  vs.  $X/L$ ), Case B.2.3,  $\phi=45^\circ$



previous cases at lower NPR. Based on other comparisons, this outcome may be more accurate but no experimental data are available for confirmation.

Similar results are seen at  $\phi=72^\circ$  (Figure 3.5-49, to compare with Figures 3.5-30 and 3.5-39). A variation in the predictions due to the change in NPR from 2 to 5 is only seen in the nozzle pressures (say,  $X/L > 0.97$ ). The Navier-Stokes prediction of Contribution N10 is somewhat more accurate (i.e., lower pressure) in this region at the higher NPR, compared with its performance at NPR=2. Interestingly, the experimental data indicate a slight increase in pressure at the nozzle exit due to increased NPR. These trends are sustained at the other two locations of body pressure comparisons,  $\phi=90^\circ$  and  $\phi=135^\circ$  (Figures 3.5-50 and 3.5-51).

The comparison in pressure on the horizontal tail (Figure 3.5-52) are essentially identical to those results achieved in the other two cases of this series. The agreement between predictions and test data on this tail surface is not good.

Surface pressure on the vertical tail, just above the juncture with the body ( $y/b=0.1$ ), are presented in Figure 3.5-53. The comparison with experimental pressure data shows the (expected) relatively poor agreement. Comparison with the data for NPR=2 (Figure 3.5-34) suggests little change in the Navier-Stokes results of Contribution N10, though the Euler results of Contribution E08 seem to have experienced a slight increase in pressure all along the vertical tail chord, in the present case at the higher NPR.

**Drag Comparisons** - Drag data are presented graphically in Figure 3.5-54, for a semi-empirical method (Contribution S01) and a Navier-Stokes CFD method (Contribution N10). These data also are tabulated below.

#### Pressure Drag

Drag Predictions:

Contrib.	CDPN	CDPA	CDPHT	CDPVT	CDPT
Exp.	-0.0196	0.0404			
S01					0.0435
N10	-0.0300	0.0409	0.0059	0.0113	0.0281

#### Total Drag

Drag Predictions:

Contrib.	CDTN	CDTA	CDTHT	CDTVT	CDTT
Exp.					0.0960 $\pm 0.0050$
S01					0.0992
N10	-0.0265	0.0684	0.0343	0.0414	0.1226

Prediction Errors ( $C_{DTT}$ ):

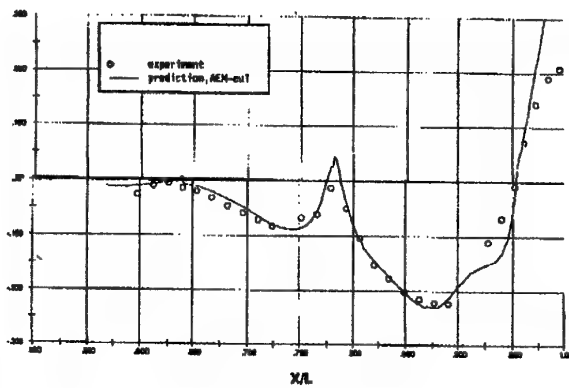
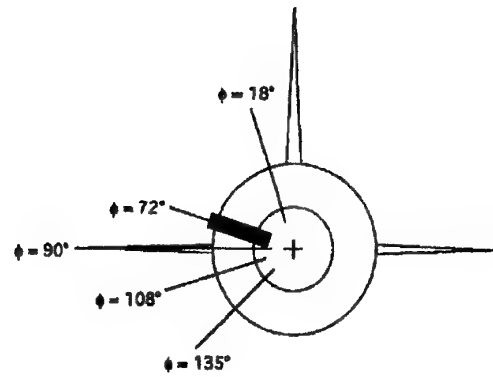
Contrib.	$\Delta C_{DTT}$	% Error
Exp		Uncertainty $\pm 5.2\%$
S01	+0.0032	+3.3%
N10	+0.0266	+27.7%

The semi-empirical method again produces very good agreement with the experimental data ( $\Delta C_{DTT}=+0.0032$ , or an error of 3.3%). This prediction, in fact, falls within the experimental uncertainty of  $\pm 5.2\%$ . The Navier-Stokes method of Contribution N10 experienced some anomalies compared with that method's solution for Base B.2.1 (see previous discussion of surface pressure comparisons). The reasons for this anomalous behavior are unknown.

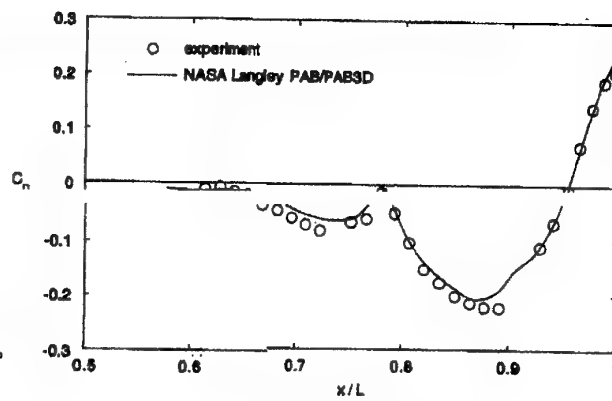
#### 3.5.2.4 Discussion of Results

A consistent pattern was noted of over-predicting the pressures on the horizontal and vertical tails, on the forward portion of the tails back to the mid-chord region. This overly-high pressure also is noted on the aftbody, alongside the tails. In the case where the tails were not present (Case B.1.1) this region of the afterbody was predicted much more accurately. While we cannot say why the predictions were poor in this region, it should be noted that more than one contributor stated that their grid generation techniques were not well-suited to providing accuracy over the tails in close proximity to the afterbody surface. One can easily question the turbulence modeling also, in the corner between the tails and the afterbody.

A common use of CFD analysis, today, is to predict the increment (or, the difference) in a figure such as drag, due to a simple variation among two or more flowfields. In this section, two types of incremental predictions will be reviewed based on these data: The ability to predict the drag increment due to adding tails, and the drag increment due to NPR variations.



Contribution E08



Contribution N10

Figure 3.5-49. Comparison of Surface Pressures ( $C_p$  vs  $X/L$ ), Case B.2.3,  $\phi=72^\circ$

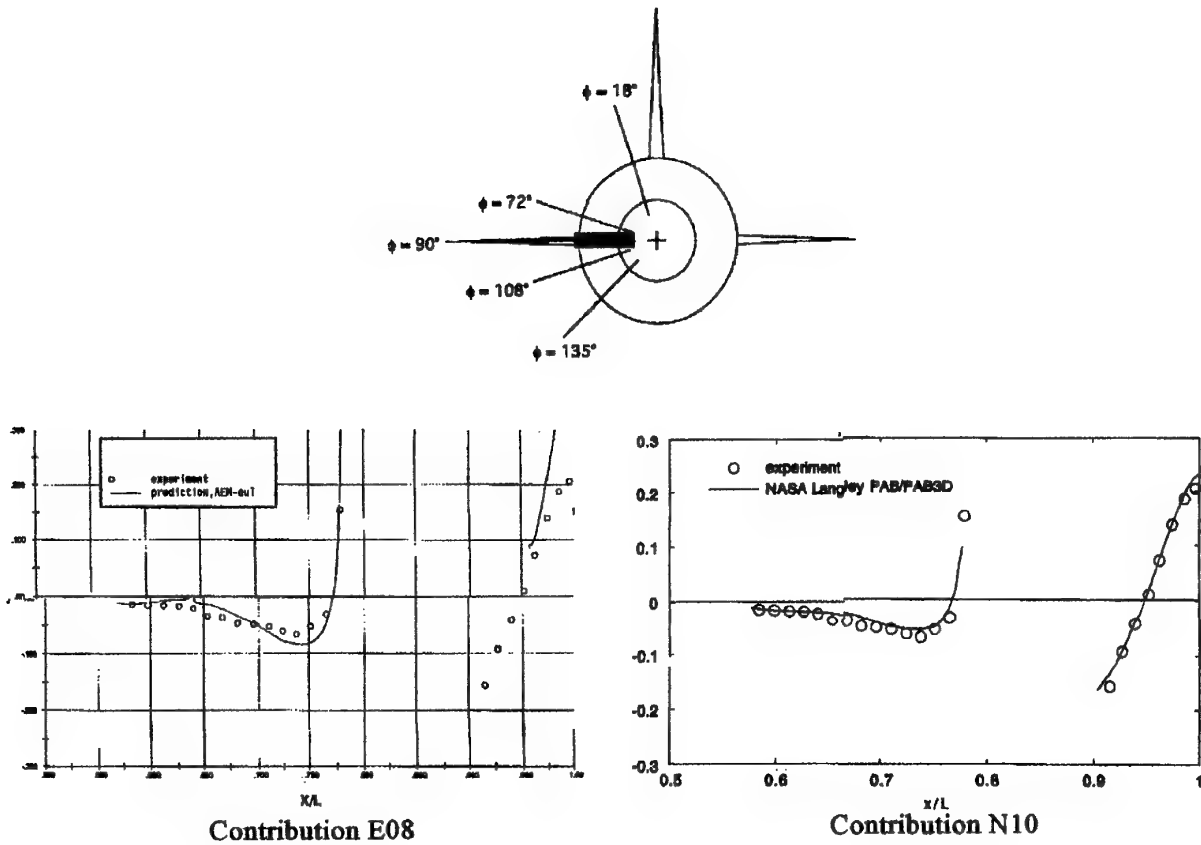


Figure 3.5-50. Comparison of Surface Pressures ( $C_p$  vs  $X/L$ ), Case B.2.3,  $\phi=90^\circ$

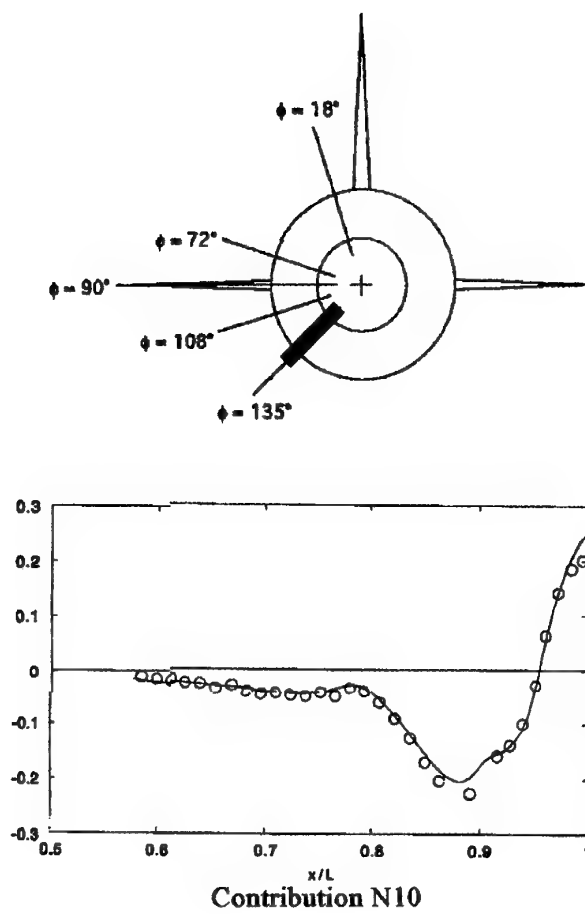


Figure 3.5-51. Comparison of Surface Pressures ( $C_p$  vs  $X/L$ ), Case B.2.3,  $\phi=135^\circ$

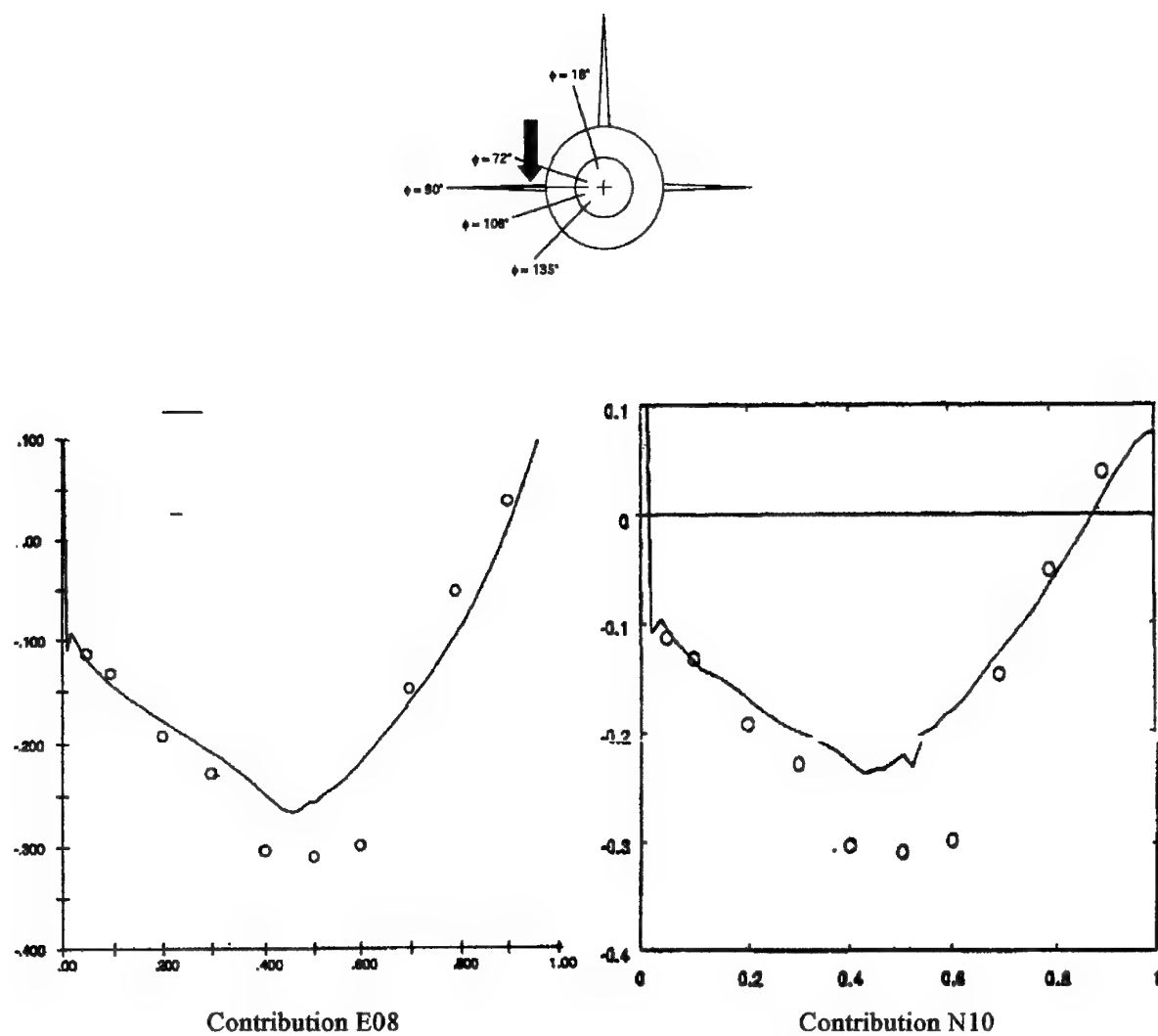


Figure 3.5-52. Comparison of Surface Pressures ( $C_p$  vs  $X/C$ ), Case B.2.3, Horizontal Tail Upper Surface

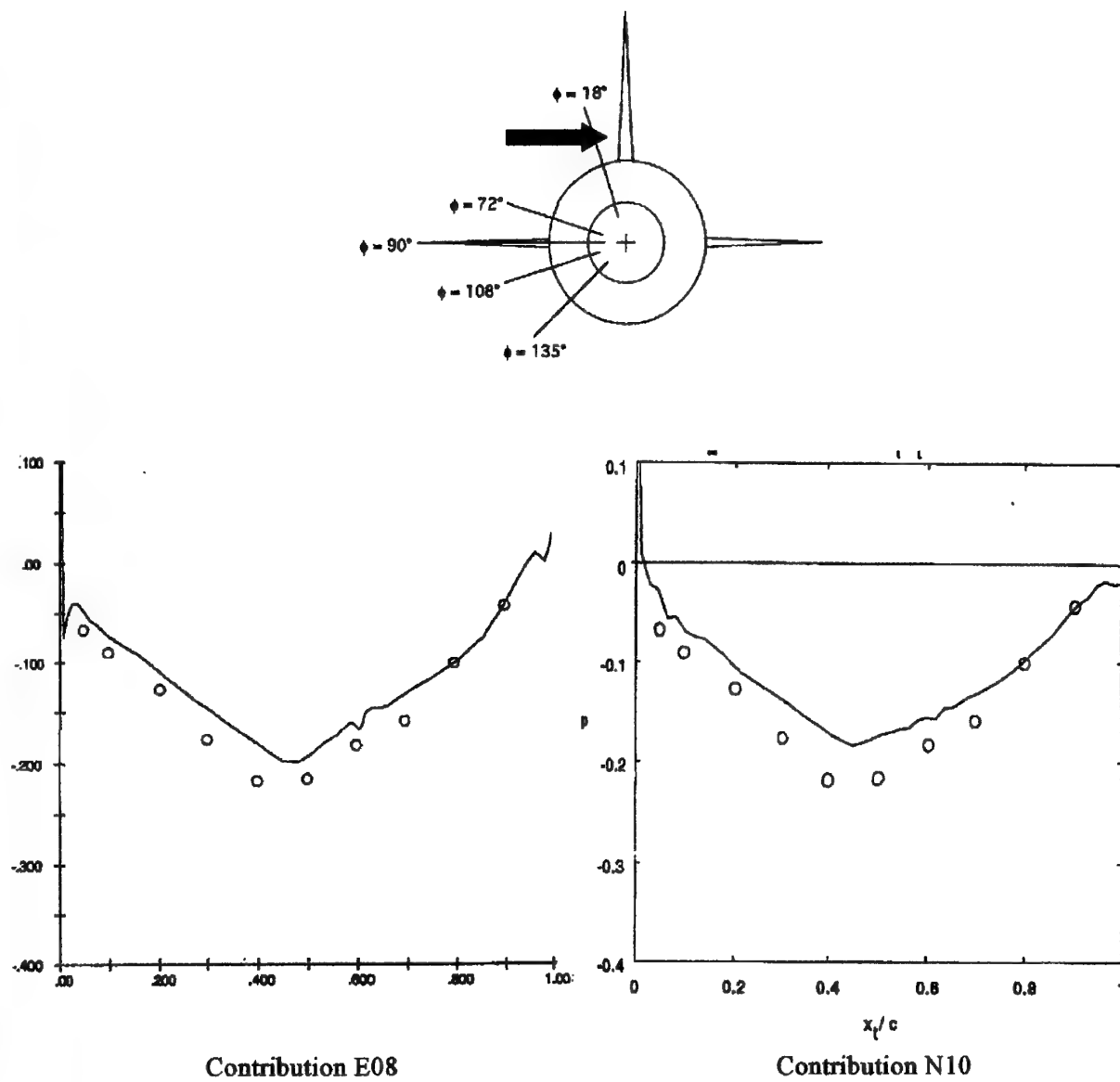


Figure 3.5-53. Comparison of Surface Pressures ( $C_p$  vs  $X/C$ ), Case B.2.3, Vertical Tail

## Pressure Drag

## Total Drag

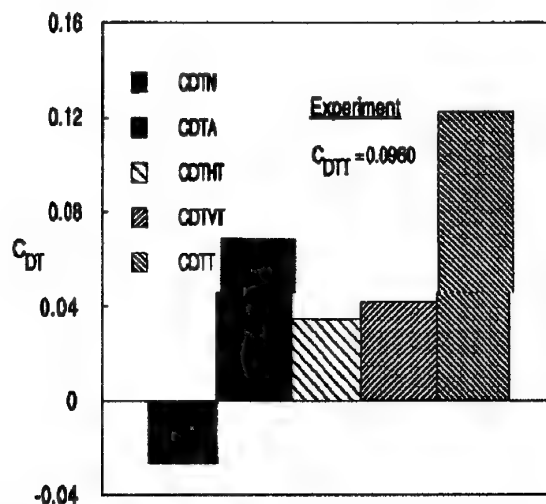
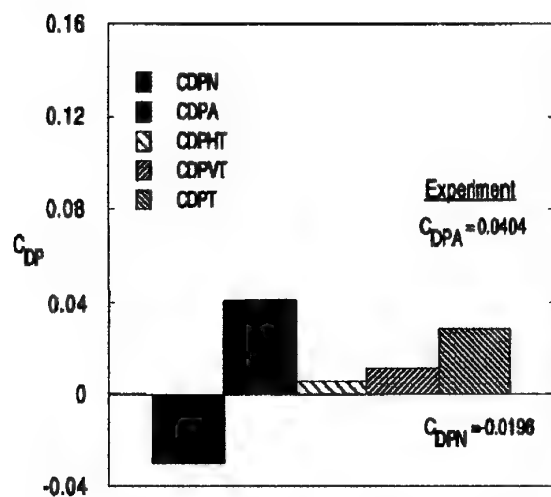
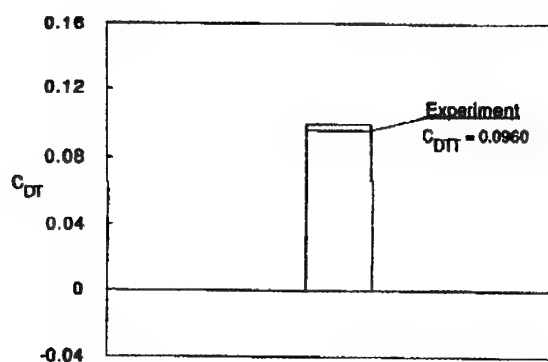


Figure 3.5-54. Comparison of Drag Predictions, Case B.2.3

A note of caution should be taken. The CFD community generally agrees that accurate drag increments can be obtained, provided that careful and consistent procedures are used in obtaining both solutions to be used in producing the drag increment. The solutions which were contributed to this working group, for the present report, were generated on a single-case basis. The contributors were not advised of a need to produce accurate drag increments, and therefore they may not have used appropriate consistent procedures. Therefore, it is possible that these results do not represent the current state of the art in computing drag increments for tail effects and NPR variations.

**Tail Drag Increments** - A comparison of data among Cases B.1.1, B.1.2, B.2.1, and B.2.3 allows an assessment of the ability to predict drag increments due to tail installation. These data are compared at two values of NPR (2 and 5). The numerical drag data are presented below:

Total Drag ( $C_{DTT}$ ), NPR=2:

Case	Tail Off (B.1.1)	Tail On (B.2.1)	Increment (On minus Off)
Exp	0.0500	0.1055	+0.0555
S01	0.0586	0.1051	+0.0465
N04	0.0487	0.1208	+0.0721
N10	0.0389	0.1163	+0.0774

Total Drag ( $C_{DTT}$ ), NPR=5:

Case	Tail Off (B.1.2)	Tail On (B.2.3)	Increment (On minus Off)
Exp	0.0423	0.0960	+0.0537
S01	0.0527	0.0992	+0.0465
N10	0.0259	0.1226	+0.0967

The semi-empirical method (S01) underpredicted the drag increment due to the tails, at both values of NPR. Interestingly, the method's increment due to tails was exactly the same at both NPR values.

The Navier-Stokes method drag increments could only be computed at the lower NPR value. Both methods (N04 and N10) predicted almost the same drag increment, and this value was about 60% larger than the experimental drag increment.

**NPR Drag Increments** - The drag increments due to NPR are tabulated below. Further, the data for one Navier-Stokes prediction (Contribution N10) are presented graphically in Figure 3.5-55.

Case	NPR=2 (B.2.1)	NPR=3 (B.2.2)	NPR=5 (B.2.3)	$\Delta C_{DTT}$ (NPR 3-2)	$\Delta C_{DTT}$ (NPR 5-2)
Exp	.1055	.1060	.0960	+.0005	-.0095
S01	.1051	.1039	.0992	-.0012	-.0059
N04	.1208	.1198		-.0010	
N10	.1163		.1226		+.0063

The experimental data show that the difference in drag between NPR of 2 vs 3 is negligible - about 0.5%. The prediction methods generally are consistent with this, though Contribution N10 shows a noticeably larger (positive) drag increment.

Over the larger range of NPR (from 2 to 5) a more significant drag increment was measured experimentally. The semi-empirical method S01 also predicted a significant increment, though not of comparable magnitude to that which was measured. The CFD method also showed a fairly large impact, but with the incorrect sign. The observations and speculations related to this issue were discussed in Section 3.5.2.3.

**Conclusions** - From the B.2 series of test cases, we can conclude that:

- CFD methods can be used to predict interference effects of tails on the afterbody.
- Within the range of their database, semi-empirical methods can perform very well at drag prediction including empennage.

### 3.5.3 Case B.3

The three test cases in the B.3 series feature a geometry similar to that of a twin-engine fighter. The geometry has two axisymmetric exhaust nozzles, and two vertical tails mounted toward the outboard side of each nozzle. The horizontal tails also are mounted on each nozzle. This geometry was illustrated previously, in Figures 3.4-12 and 3.4-13.



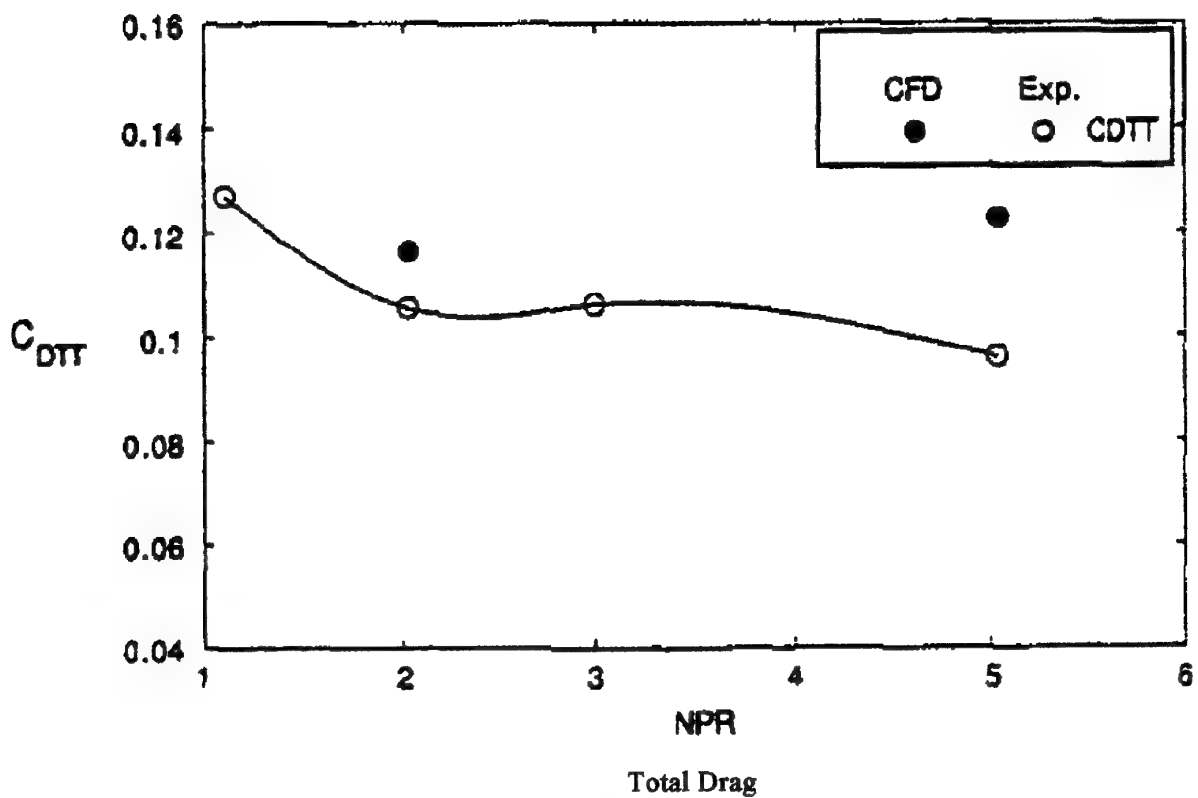
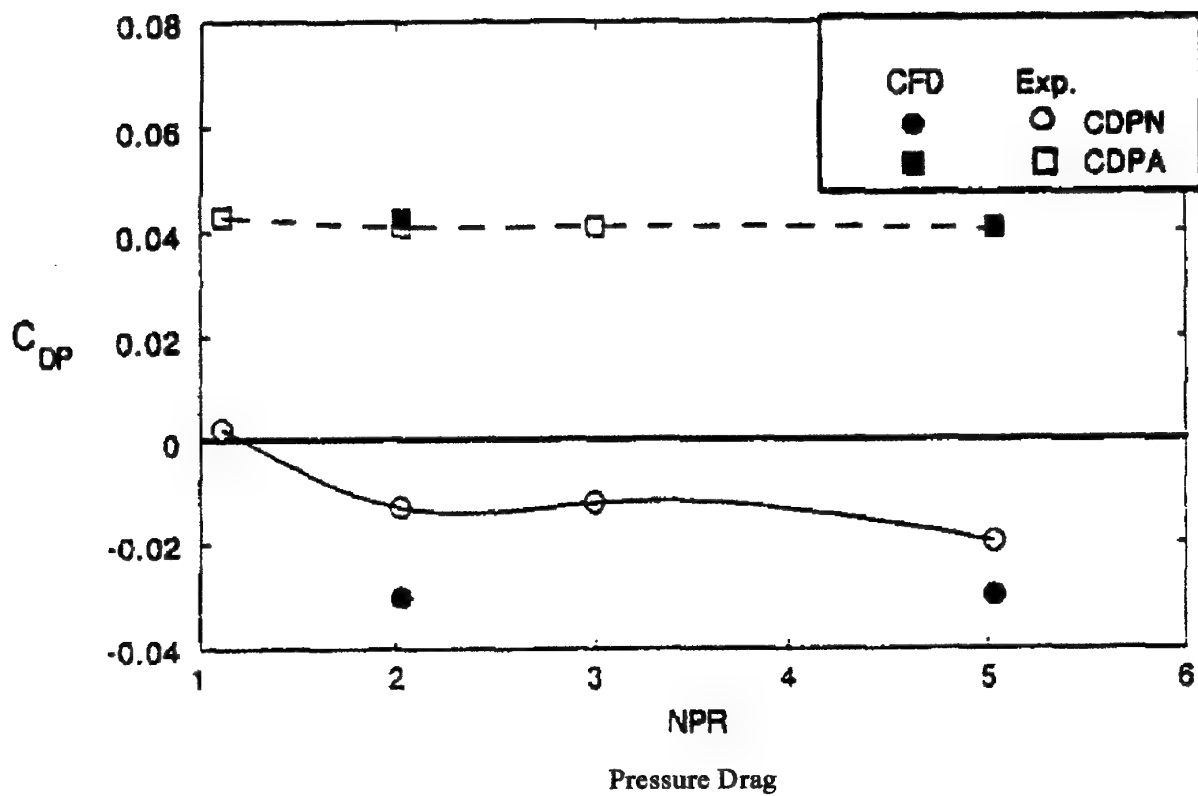


Figure 3.5-55. Comparison of Drag Variations Due to NPR,  
Cases B.2.1 and B.2.3  
(Contribution N10)

The three test cases differ only in the placement of the vertical tails. Therefore, the chief interaction of interest is the drag impact of the vertical tails, at various placements. The pressure fields from the vertical and horizontal tails will interact with each other, and with the turbulent boundary layer, in different manners depending on whether the horizontal and vertical tails are aligned with each other or staggered, and their placement with regard to the expansion and compression fields on the fuselage and body.

The flow conditions are identical for all three cases:

*Freestream Conditions:*

$$M_{\infty} = 0.90$$

$$\alpha = 0^\circ$$

$$P_{\infty} = 14.7 \text{ psia}$$

$$T_{\infty} = 590^\circ\text{R}$$

$$R_{e,c} = 5.61 \times 10^6$$

*Jet Exhaust Conditions:*

$$\text{NPR} = 3.4$$

$$T_{ij} = 530^\circ\text{R}$$

The horizontal tails are mounted (fore-and-aft) at the "mid" location (see Figures 3.4-12 and 3.4-13).

*Horizontal Tail Location:*

Leading Edge intersects fuselage at  $X/L=0.782$ .

Trailing Edge intersects fuselage at approximately  $X/L=0.950$ .

The only difference between the cases is the mounting location of the vertical tails, as shown below.

Case	Vertical Tail Location
B.3.1	Mid
B.3.2	Aft
B.3.3	Forward

The pressure data are presented along longitudinal lines, at various angles of  $\phi$ , the circumferential angle. This angle is measured from the top centerline of the nozzle ( $\phi = 0^\circ$ ) around the inboard side of the nozzle, to the bottom centerline, to the outboard side of the nozzle. For the B.3

test cases, the drag data are normalized by the reference wing area. Thus, the drag coefficient values should not be compared directly with data from the other series of test cases (B.1, B.2, and B.4).

*3.5.3.1 Case B.3.1*

The first case to be examined is Case B.3.1. This case has the vertical tails mounted at the mid location. At this configuration, the leading edges of both the vertical and horizontal tails intersect the fuselage at the same axial location.

The key locations for this case are:

$X/L=0.782$  Leading edge of horizontal and vertical tails.

$X/L=0.922$  Trailing edge of vertical tail.

$X/L=0.948$  Junction of aftbody and nozzle (slope discontinuity); trailing edge of nozzle inter-fairing.

$X/L=0.950$  Trailing edge of horizontal tail.



Figure 3.5-56. Geometry Model for Case B.3.1  
(Contribution N09)

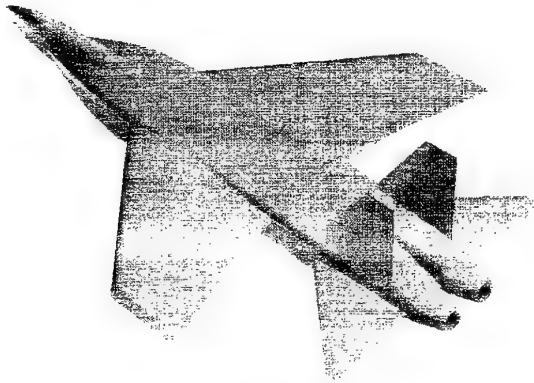


Figure 3.5-57. Geometry Model for Case B.3.1  
(Contribution N09)

Two contributors submitted Navier-Stokes solutions for this case, and one contributor provided a semi-empirical drag analysis for comparisons.

Oil flow simulations, as predicted in Contribution N09, are presented in Figures 3.5-58 and 3.5-59. These predictions indicate the viscous flow generally is well-behaved on the fuselage, wings and tails. However, substantial viscous interactions are occurring on the nozzle, particularly on the upper surface. There is clear evidence of wakes and vortices separating from the model surface in this region. Another strong viscous interaction is occurring along the inboard side of the junction between the vertical tail and the afterbody. This interaction is quite strong in the aft portion of this tail-body junction, and the flow is separated in this corner. Further, based on these oil flow simulations it seems a vortex is departing from the model surface just inboard of the trailing edge of the vertical tail.

**Surface Pressure Comparison** - The first comparison (Figure 3.5-60) is for the top centerline of the nozzle:  $\phi=0^\circ$ . Initially, the pressures rise slowly approaching the axial location of the leading edges of all the tail surfaces ( $X/L \sim 0.77$ ).

Downstream of this point, the data at this value of  $\phi$  lie inboard of the vertical tail and the pressures drop sharply as the flow passes alongside the tail. The flow accelerates to supersonic speeds, as indicated by the low surface pressure. The flow then compresses rapidly - the experimental data and one CFD solution (N10) suggest a fairly strong shock is present, while the second CFD solution suggests a slightly softer pressure rise (N09). This smearing of the shock in Contribution N09 may be due to a coarse grid density here. Recompression continues to the nozzle exit, with good accuracy provided by both CFD methods. An inflection is seen in the pressure data near  $X/L=0.95$ . This is in the vicinity of three geometry discontinuities: (1) the trailing

edges of the nozzle interfairing, (2) the trailing edge of the horizontal tail, and (3) the junction between the afterbody and the nozzle, which is the location of a slope discontinuity. Of these, the latter is probably most responsible for the pressure inflection in these results.

The second comparison ( $\phi=45^\circ$ ) is in the upper inboard sector of the nozzle. These comparisons are presented in Figure 3.5-61. At the point where the experimental data begin, the flow has expanded to supersonic speeds ( $C_p = -0.5$  corresponds to a local Mach number of about 1.18). The comparison begins with a sharp pressure rise in the range of  $X/L = 0.87$  to  $0.90$ . This rise is due to a shock standing between the nozzles on the upper surface of the interfairing (this shock will be seen at the same location,  $X/L=0.88$  on the upper surface, in other data as well).

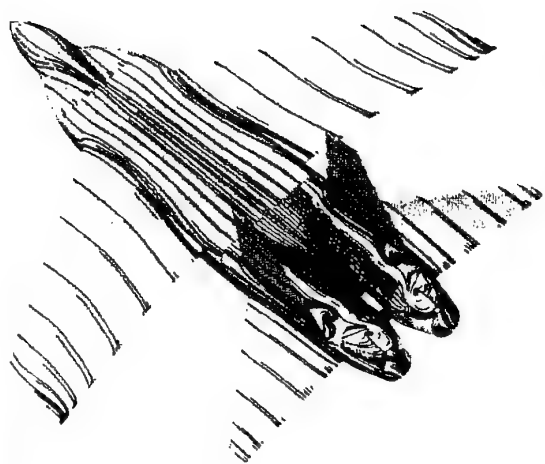
The experimental and predicted pressures show a modest plateau around  $X/L = 0.90$  to  $0.94$ , the region of the trailing edges of both the vertical tail and the interfairing between the nozzles. One CFD prediction (N09) shows a clear localized pressure drop on the nozzle surface, at the afterbody-nozzle junction. It seems this prediction has not modeled an adequate viscous interaction at this location on the interfairing, and the prediction has the flow following the interfairing curvature too closely. The other solution (N10) shows a plateau which is also seen in the experimental data. Both these features are often associated with a flow separation point. From this point, a sustained recompression is present to the nozzle exit.

Data comparisons for  $\phi=60^\circ$  are presented in Figure 3.5-62. The prediction of Contribution N09 displays generally the same features as in the previous circumferential location. These features include a local minimum pressure prediction at about  $x/L=0.95$  which is related to slope discontinuity between the afterbody and the nozzle. A more mild interaction is seen in the experimental data at this location.

The comparisons on the nozzle inboard surfaces, just above the interfairing, are presented in Figure 3.5-63 for  $\phi=75^\circ$ . At this angle of  $\phi$ , most of the nozzle external surface is buried in the interfairing except for the aft-most portion. The experimental and predicted data both show a gradual pressure rise to the trailing edge of the nozzle and interfairing.

The inboard-most portion of the nozzle surface ( $\phi=90^\circ$ ) is presented in Figure 3.5-64. These data fall in the small gap between the nozzle external flaps, and the interfairing. The CFD prediction (N09) shows the same slope as the data, but at a somewhat higher pressure. Both the experimental and predicted data suggest, by the low values of recompression achieved, that the boundary layer is very thick and dominating the flow properties in this region.

The next several comparisons are for the lower inboard quadrant of the afterbody and nozzle. Data for  $\phi=105^\circ$  are



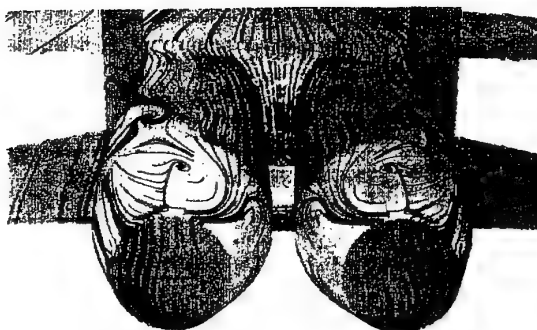
Aircraft Upper Surface



Close-Up View of Nozzle Upper Surface



Aircraft Lower Surface



Nozzle Upper Surface

Figure 3.5-58. Predicted Surface Oil Flow Patterns, Case B.3.1  
(Contribution N09)

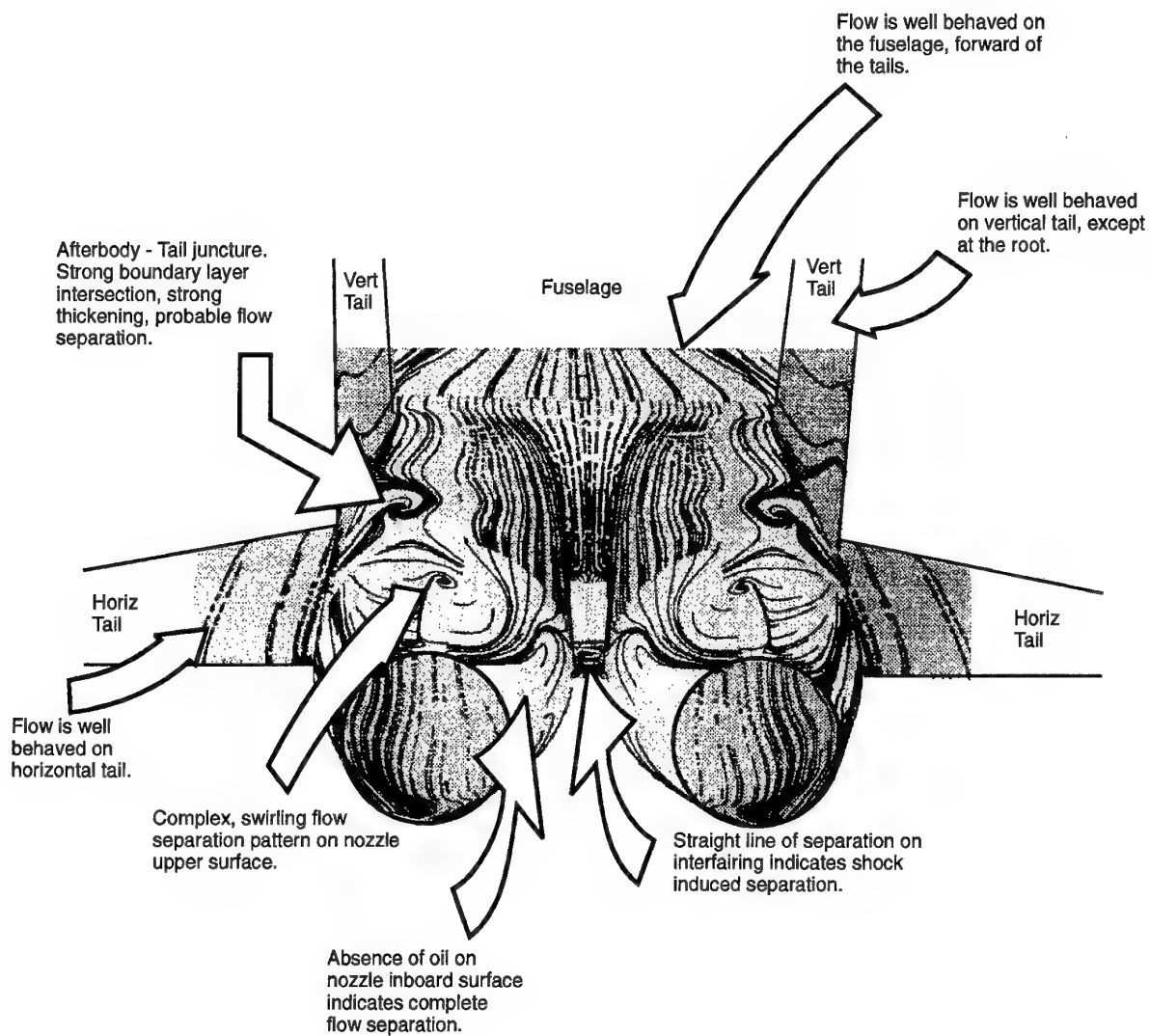
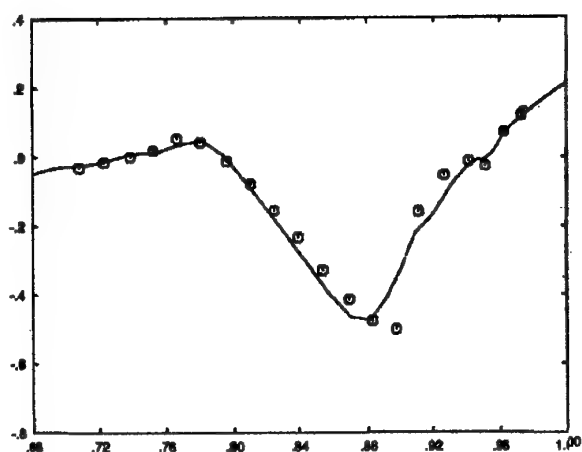
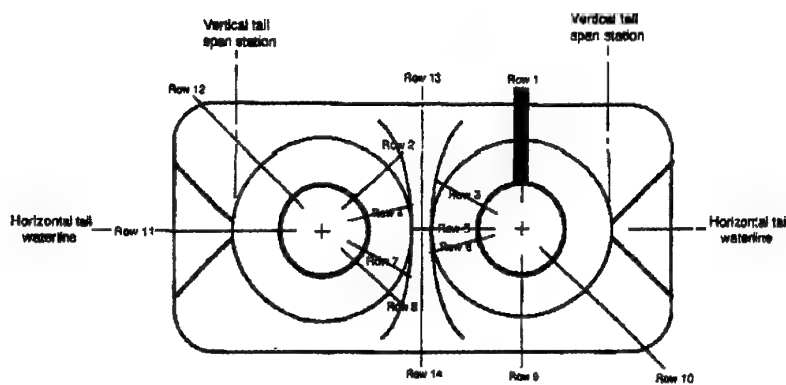
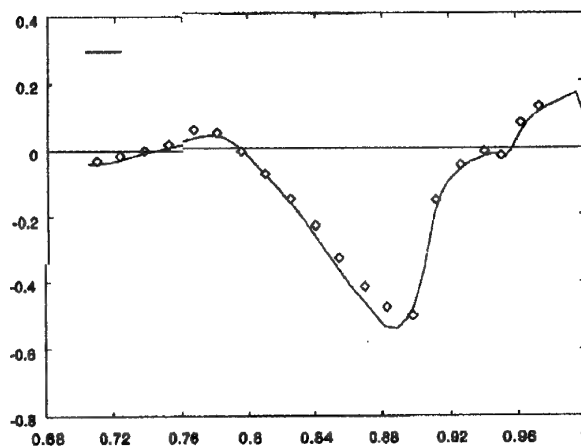


Figure 3.5 - 59. Predicted Surface Oil Flow Patterns with Annotations, Case B.3.1  
(Contribution N09)

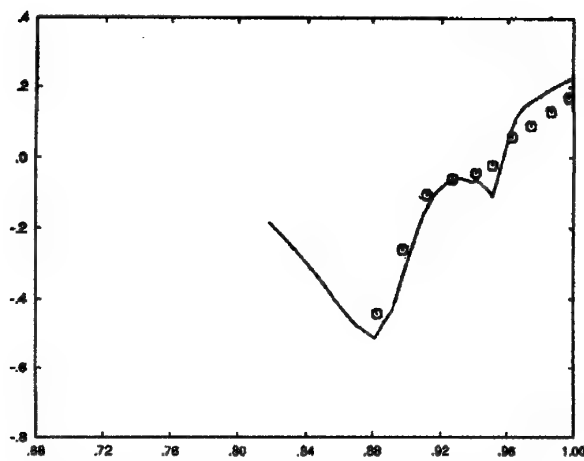
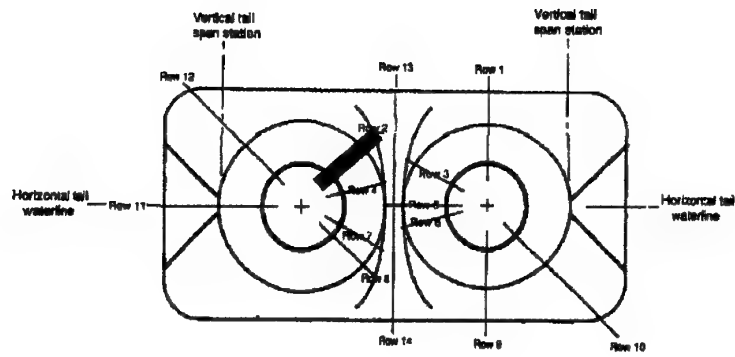


Contribution N09 (B-B turbulence model)

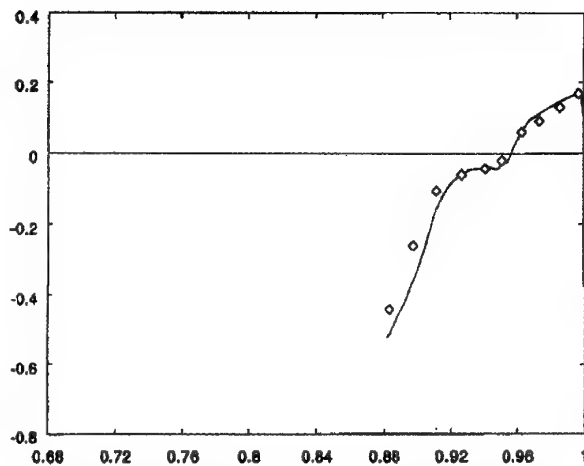


Contribution N10

Figure 3.5-60. Comparison of Surface Pressures ( $C_p$  vs  $X/L$ ), Case B.3.1,  $\phi=0^\circ$



Contribution N09 (B-B turbulence model)



Contribution N10

Figure 3.5-61. Comparison of Surface Pressures ( $C_p$  vs  $X/L$ ), Case B.3.1,  $\phi=45^\circ$

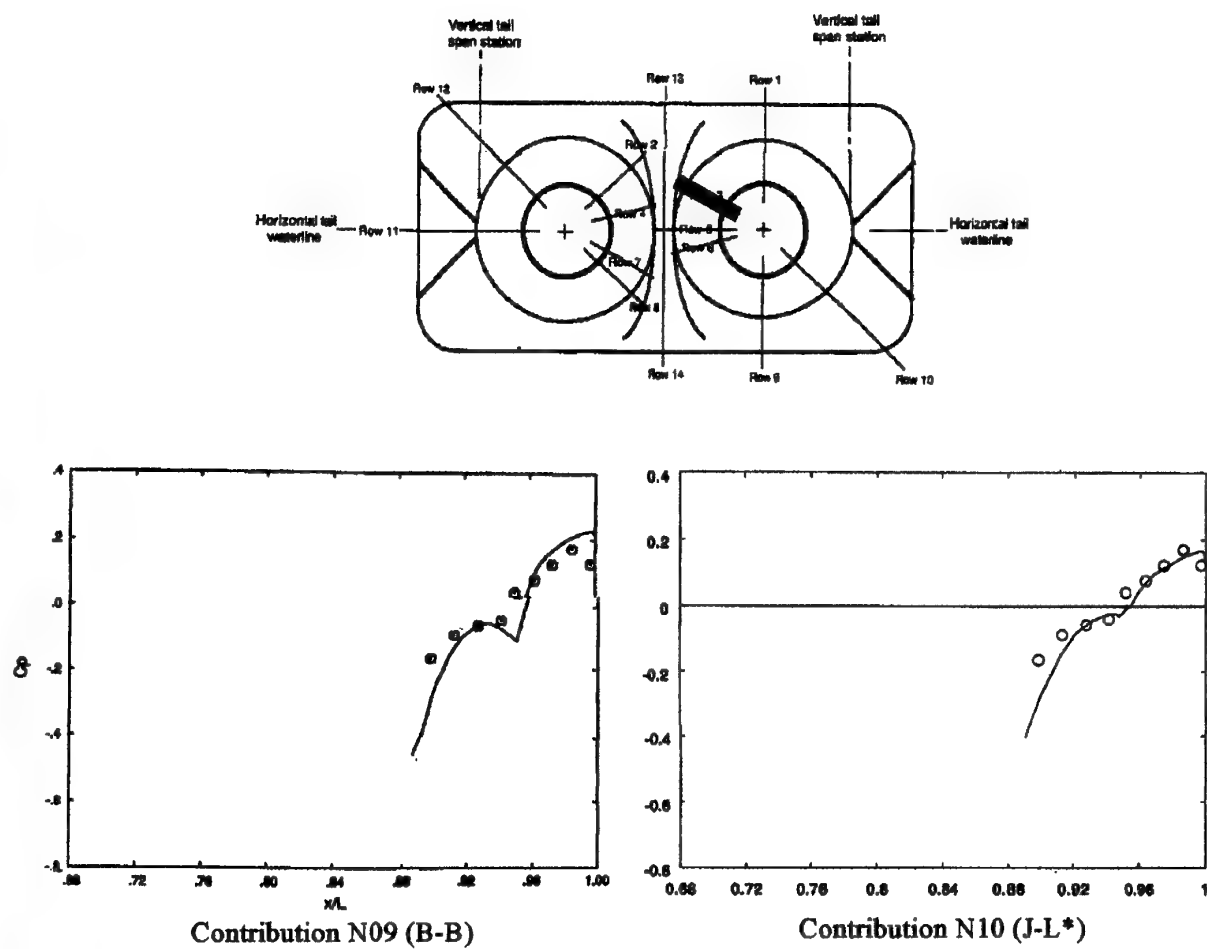


Figure 3.5-62. Comparison of Surface Pressures ( $C_p$  vs  $X/L$ ), Case B.3.1,  $\phi=60^\circ$



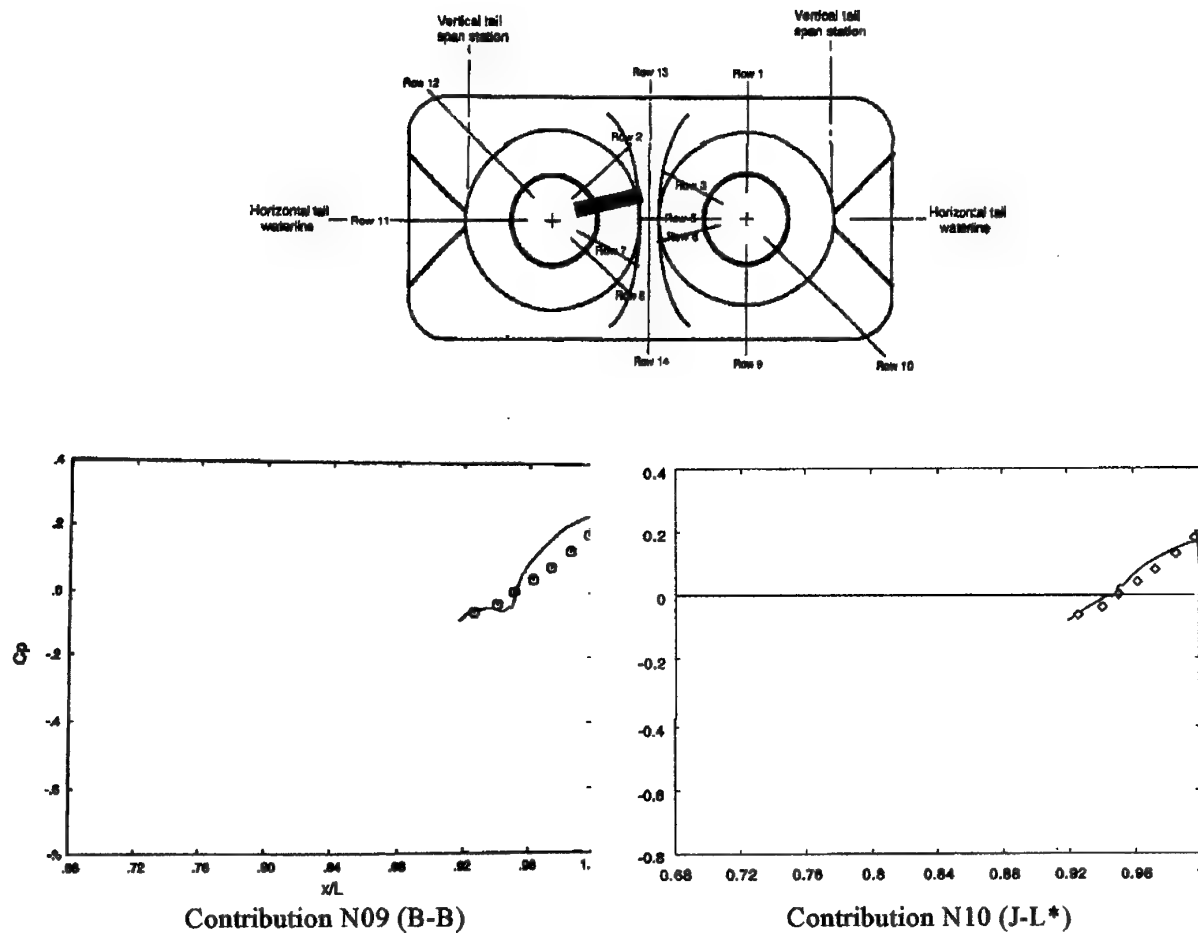


Figure 3.5-63. Comparison of Surface Pressures ( $C_p$  vs  $X/L$ ), Case B.3.1,  $\phi=75^\circ$

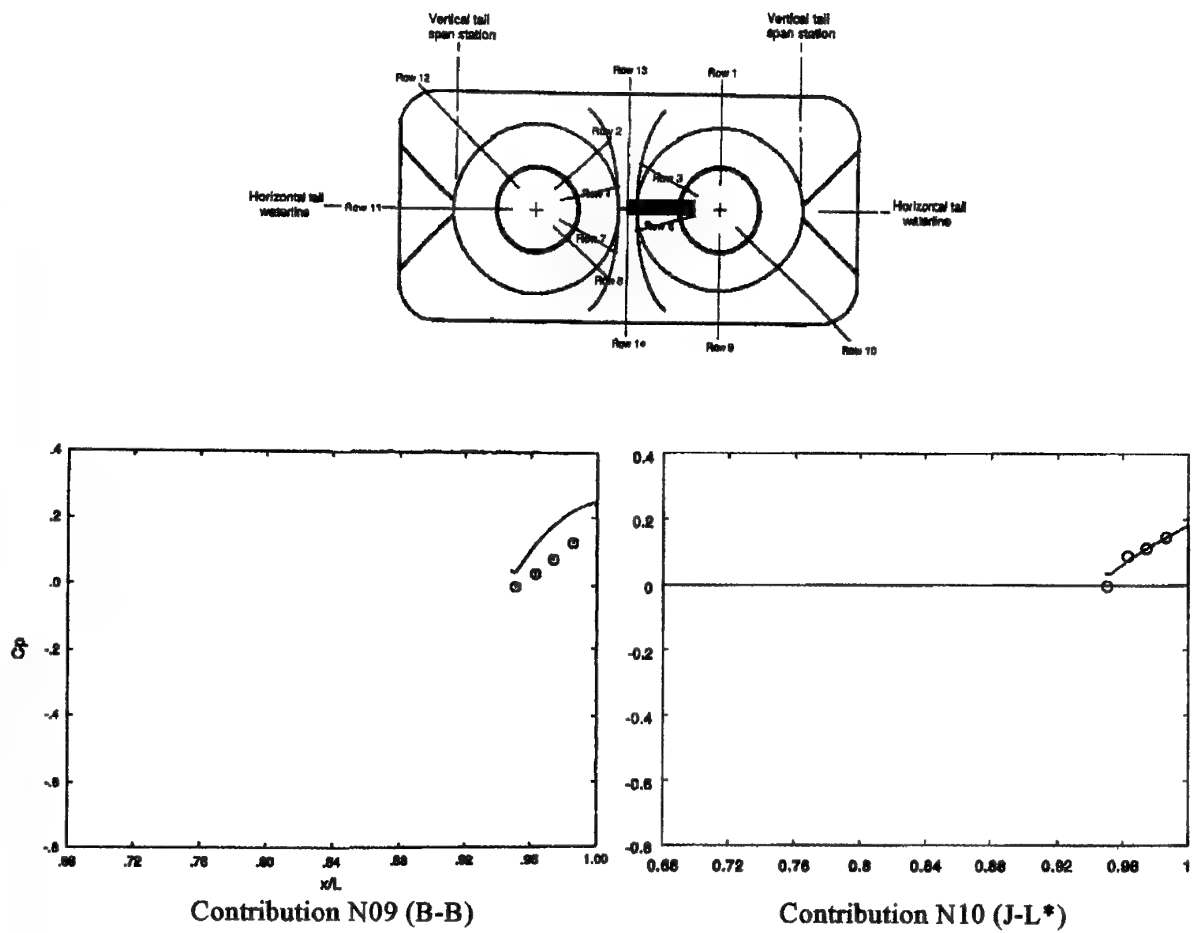


Figure 3.5-64. Comparison of Surface Pressures ( $C_p$  vs  $X/L$ ), Case B.3.1,  $\phi=90^\circ$

presented in Figure 3.5-65. These data, taken  $15^\circ$  below the horizontal symmetry plane of the model, show the same gradual pressure rise that was noted at a similar distance above the horizontal plane ( $\phi=75^\circ$ , Figure 3.5-63). The pressure minimum at about  $x/L=0.95$ , as seen previously, is associated with the slope break at the beginning of the nozzle.

Data further down around the nozzle are presented in Figure 3.5-66, for  $\phi=120^\circ$ . These comparisons show good accuracy in predicting the flow along the nozzle external surface, leading up to the expansion at the beginning of the nozzle at  $x/L=0.948$ . At this circumferential location, the experimental data reproduce the local pressure minimum which this solution contained at other circumferential locations. Downstream of this point, the prediction is qualitatively correct (gradual pressure rise) but an excess recovery of pressure is predicted leading up to the trailing edge of the nozzle ( $x/L=1.00$ ).

The same general features are seen also at the next circumferential station,  $\phi=135^\circ$  (Figure 3.5-67). Both solutions reproduce the features of the solution. Contribution N09 seems more accurate on the nozzle upstream of the interfairing ( $x/L < 0.948$ ) but exhibits an overprediction of pressure on the aft-most portion of the nozzle. Contribution N10, however, is very accurate on the aft nozzle and less accurate on the afterbody up to the end of the interfairing.

Pressures along the extended lower centerline of the nozzle ( $\phi=180^\circ$ , Figure 3.5-68) are quite benign up to the end of the interfairing and the beginning of the nozzle ( $x/L=0.95$ ). Downstream of this point, a steady compression occurs to the nozzle exit. Both predictions are in good agreement with the data throughout.

The next two comparisons are located along the lower outboard quadrant of the aftbody and nozzle. The first of these is at  $\phi=225^\circ$  (Figure 3.5-69). Both CFD predictions are in generally good agreement with the data throughout. Interestingly, both predictions show a slight and nearly identical over-estimate of the surface pressure in the region of  $x/L = 0.88$  through  $0.94$ , alongside the horizontal tail. This over-prediction is reminiscent of the results observed previously in the B.2 series of test cases. Contribution N09 contains a slight over-prediction of the pressure at the nozzle exit, while Contribution N10 does quite well here.

Figure 3.5-70 presents data at  $\phi=267^\circ$ . This location is essentially at the outboard-most point on the circumference of the aftbody and nozzle. Data are missing in the region  $x/L$  from  $0.795$  (approximately) through  $0.92$ , where the horizontal tails are attached to the vehicle. Both CFD contributions model the pressures approaching the tails ( $x/L < 0.795$ ) though N09 may do so with slightly better accuracy. Aft of the tails, N09 shows a small negative pressure excursion at the beginning of the nozzle which

seems credible, though it is not validated by the experimental data. Further downstream, this N09 prediction is quite close to the measured data up to the nozzle exit. Contribution N10 also shows a (smaller) negative excursion at the same point ( $x/L \approx 0.96$ ), and a slight under-prediction of the pressures on the nozzle.

Pressures on the upper outboard surface of the nozzle are presented in Figure 3.5-71, for the line of pressure taps at  $\phi=315^\circ$ . The gap in the data is the location of the vertical tail. The pressure taps forward of the tail are also outboard of the tail (due to the angle), and the taps aft of the tail are also inboard of the vertical tail. Contribution N09 agrees closely with the measured data on the afterbody, approaching the vertical tail ( $x/L < 0.82$ ). Contribution N10 in this region also exhibits the same behavior, though the local high pressure alongside the leading edge of the tail is not resolved as well.

Aft of the vertical tail ( $x/L > 0.88$ ) the solutions show some qualitative differences: N09 indicates a small region of nearly constant pressure is present (locally supersonic speeds), followed by a sharp pressure rise (a shock wave) and then a more gradual compression on the nozzle. Contribution N10 suggests a more distributed pressure rise, with only an indication of a precursor constant-pressure region. The resolution of the experimental data does not allow us to assess which prediction is more realistic. At the nozzle trailing edge, Contribution N09 overpredicts the pressure. Both CFD predictions, however, show a sustained pressure rise to the nozzle exit (i.e., attached flow) while the experimental data show a constant pressure plateau for  $x/L > 0.96$  which suggests the flow is separated.

Limited experimental data also are available on the top centerline (symmetry plane) of the model, as presented in Figure 3.5-72. Contributions N09 and N10 are in good agreement with the few data points. It should be noted: the model geometry on this plane terminates at  $x/L=0.948$ , the trailing edge of the interfairing. At this point, the CFD prediction shows a discontinuity. The CFD data presented downstream of this point are in free space, along an extended line in the plane of the nozzle axis (this is also the case in the next comparison).

A larger amount of experimental data are provided on the bottom centerline of the model (Figure 3.5-73). Again, Contributions N09 and N10 show good agreement with the full extent of these data.

A comparison of Figure 3.5-72 (model top centerline) with Figure 3.5-73 (model bottom centerline) reveals the main differences between the flow on the top and on the bottom of the boattail. The flow on the bottom is fully subsonic and smooth, whereas the flow on the top becomes supersonic due to the channeling and accelerating effects of the vertical tails. This supersonic pocket also can be recognized in other data

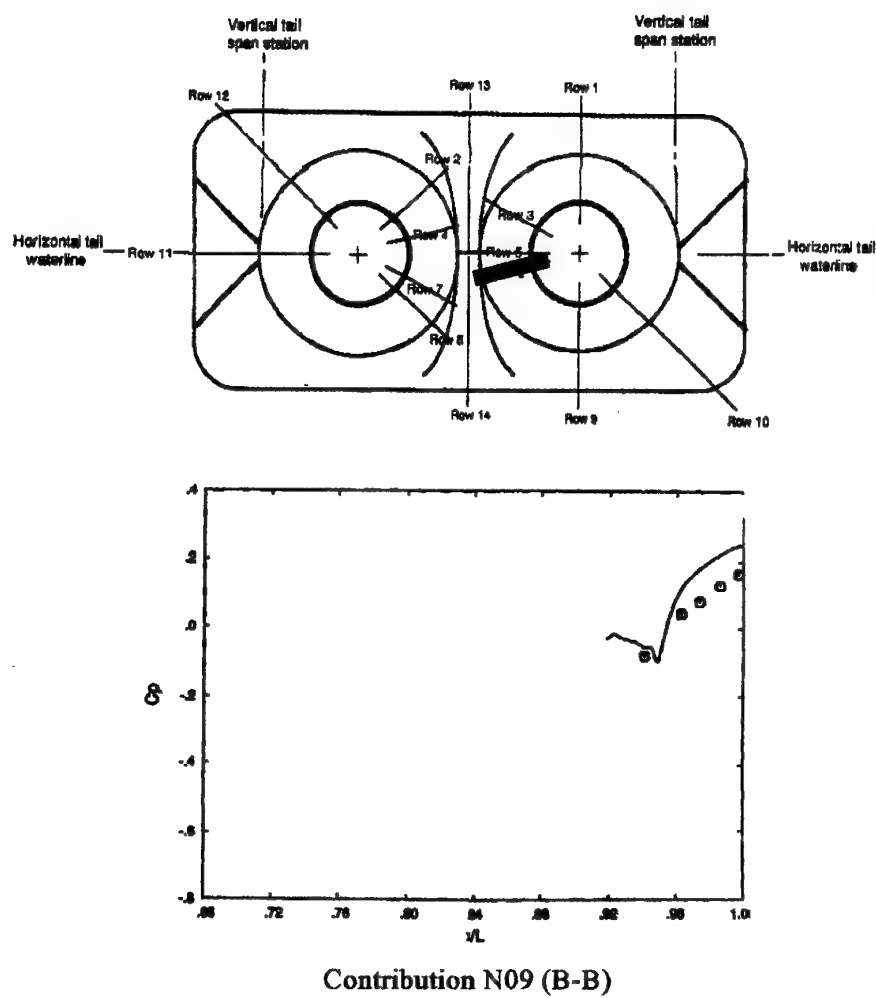


Figure 3.5-65. Comparison of Surface Pressures ( $C_p$  vs  $X/L$ ), Case B.3.1,  $\phi=105^\circ$

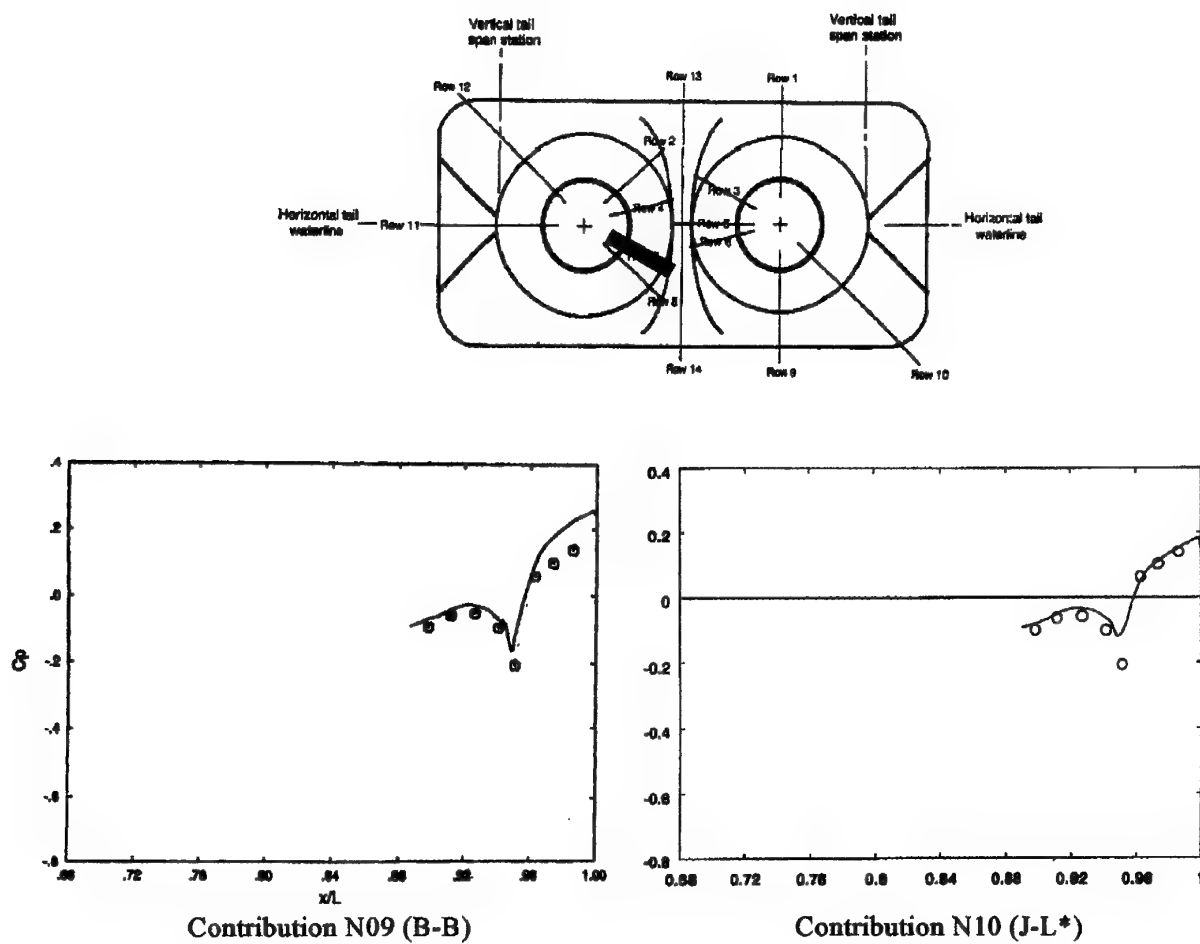


Figure 3.5-66. Comparison of Surface Pressures ( $C_p$  vs  $X/L$ ), Case B.3.1,  $\phi=120^\circ$

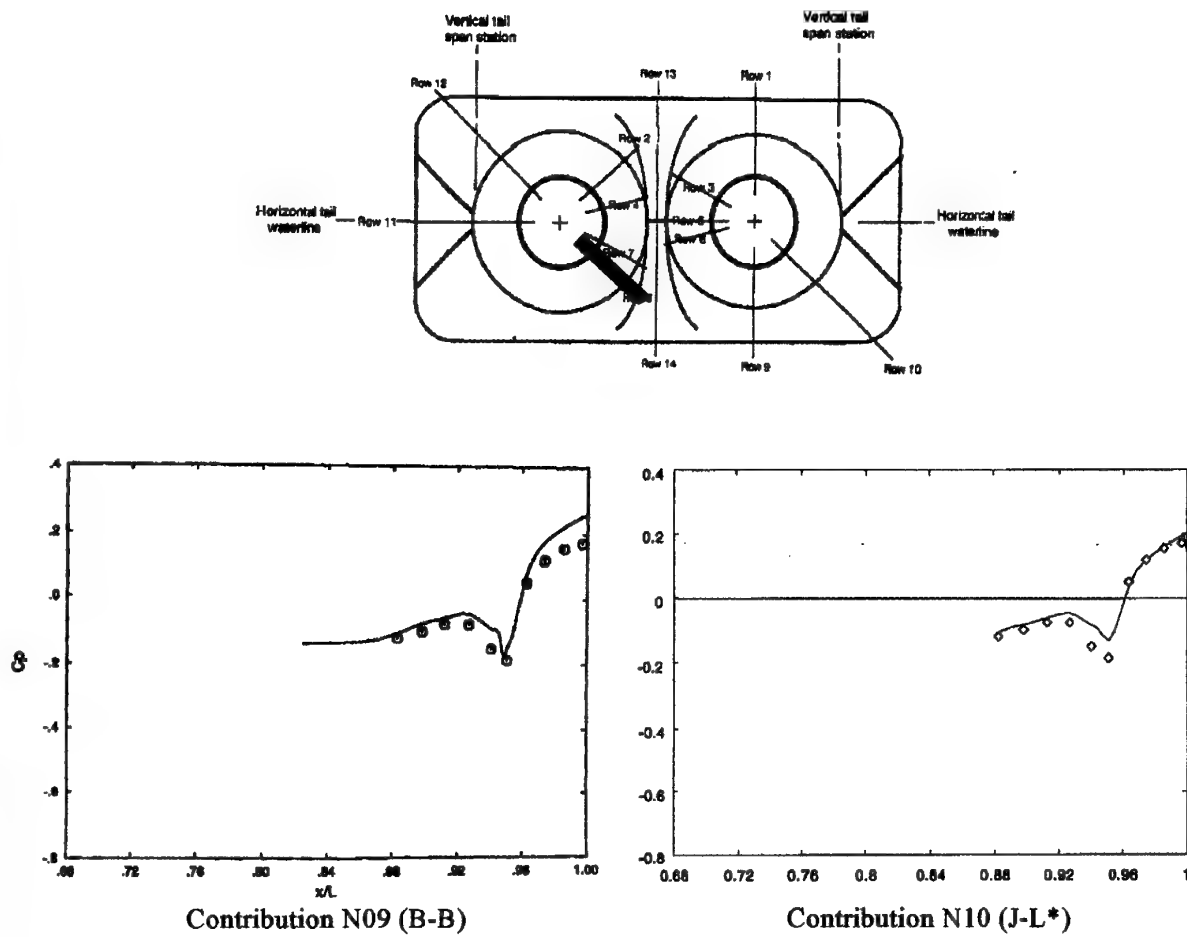


Figure 3.5-67. Comparison of Surface Pressures ( $C_p$  vs  $X/L$ ), Case B.3.1,  $\phi=135^\circ$

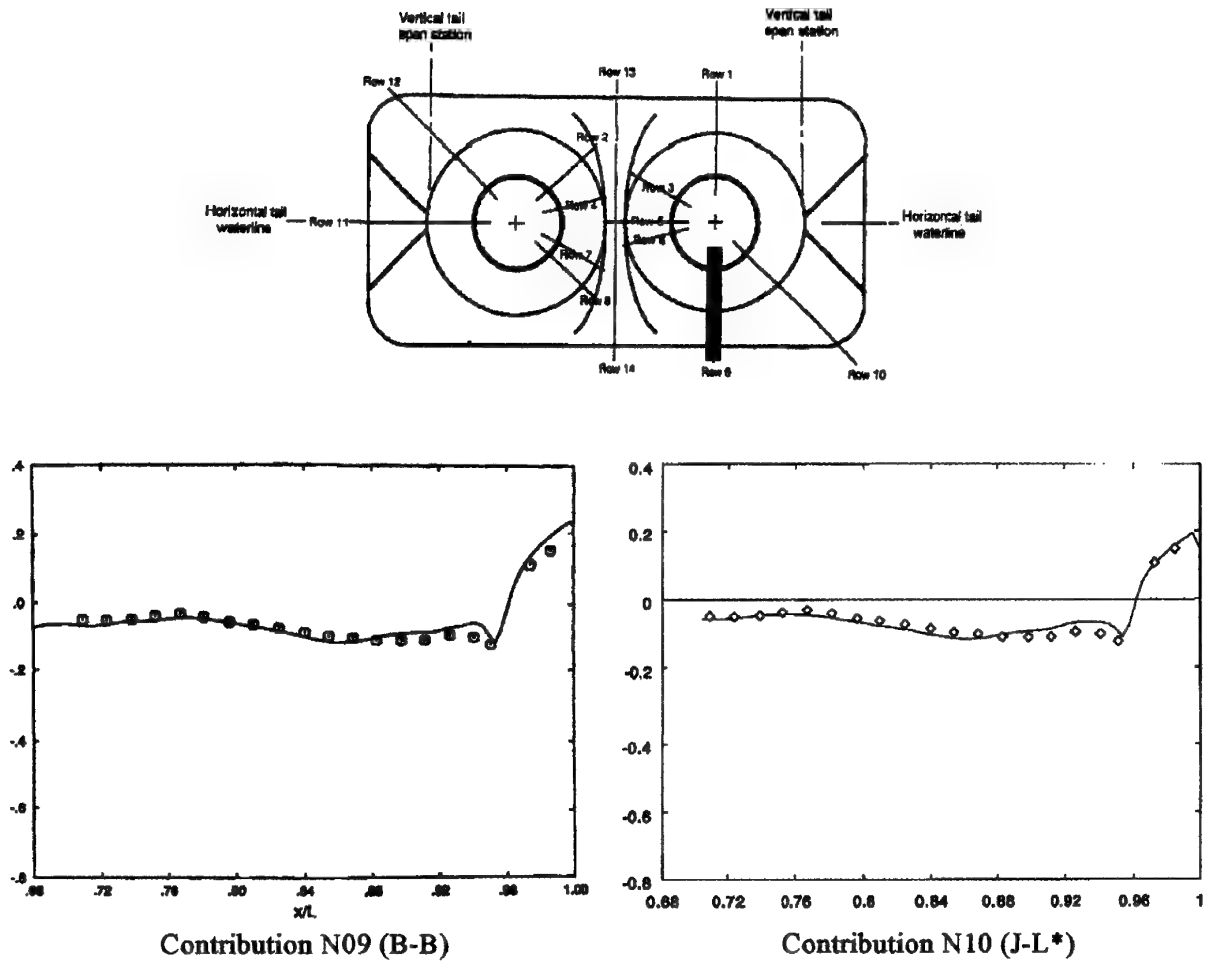


Figure 3.5-68. Comparison of Surface Pressures ( $C_p$  vs  $X/L$ ), Case B.3.1,  $\phi=180^\circ$

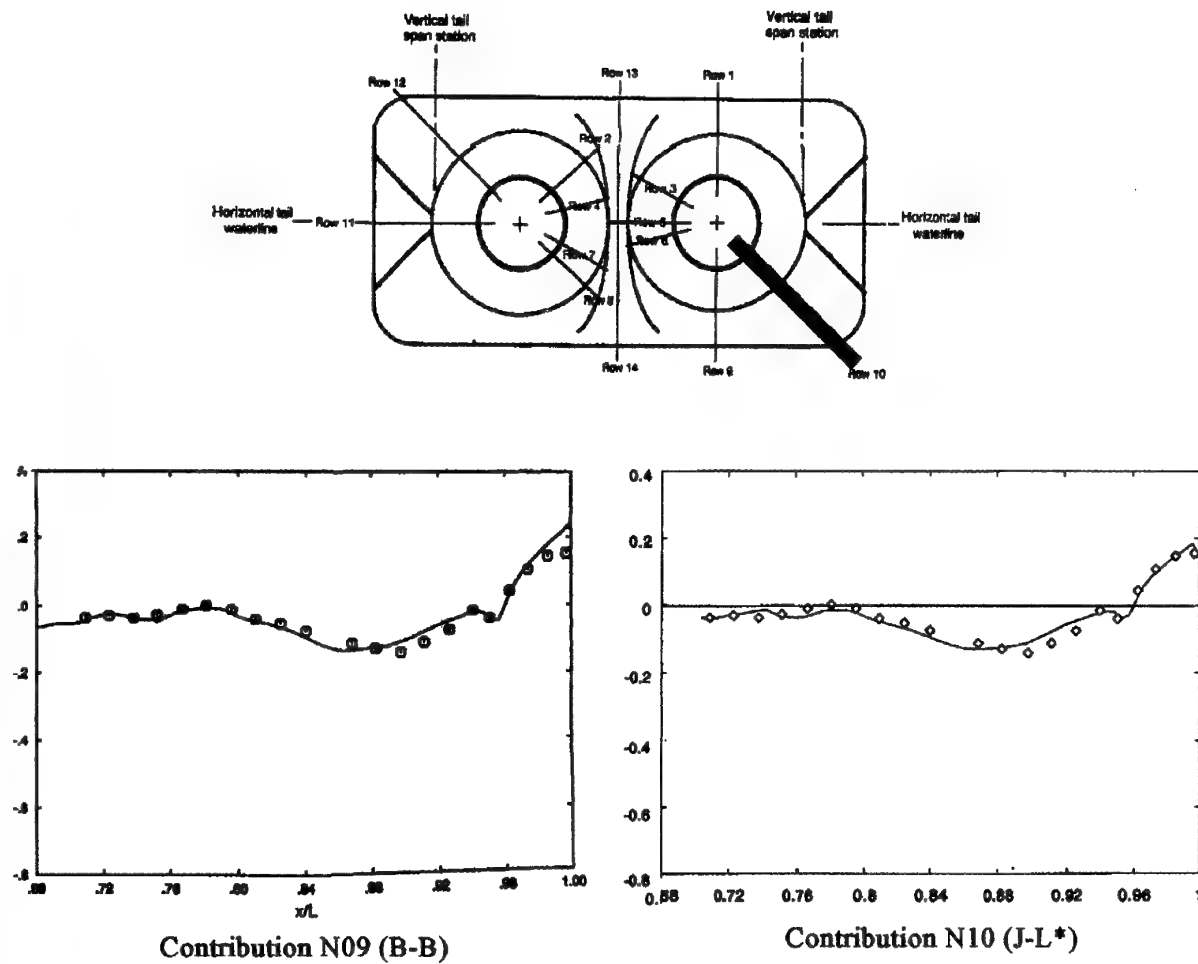
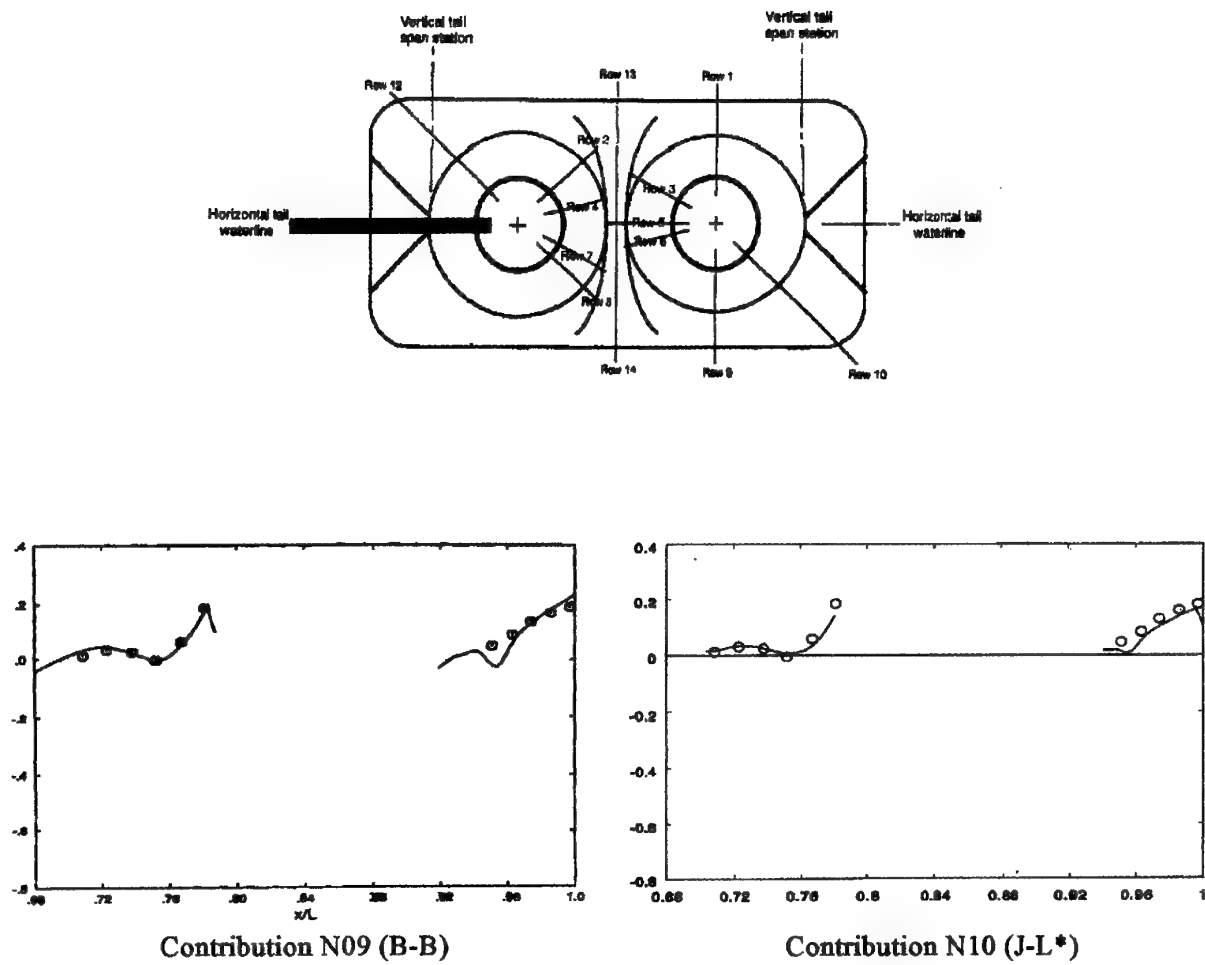


Figure 3.5-69. Comparison of Surface Pressures ( $C_p$  vs  $X/L$ ), Case B.3.1,  $\phi=225^\circ$





**Figure 3.5-70. Comparison of Surface Pressures ( $C_p$  vs  $X/L$ ), Case B.3.1,  $\phi=267^\circ$**

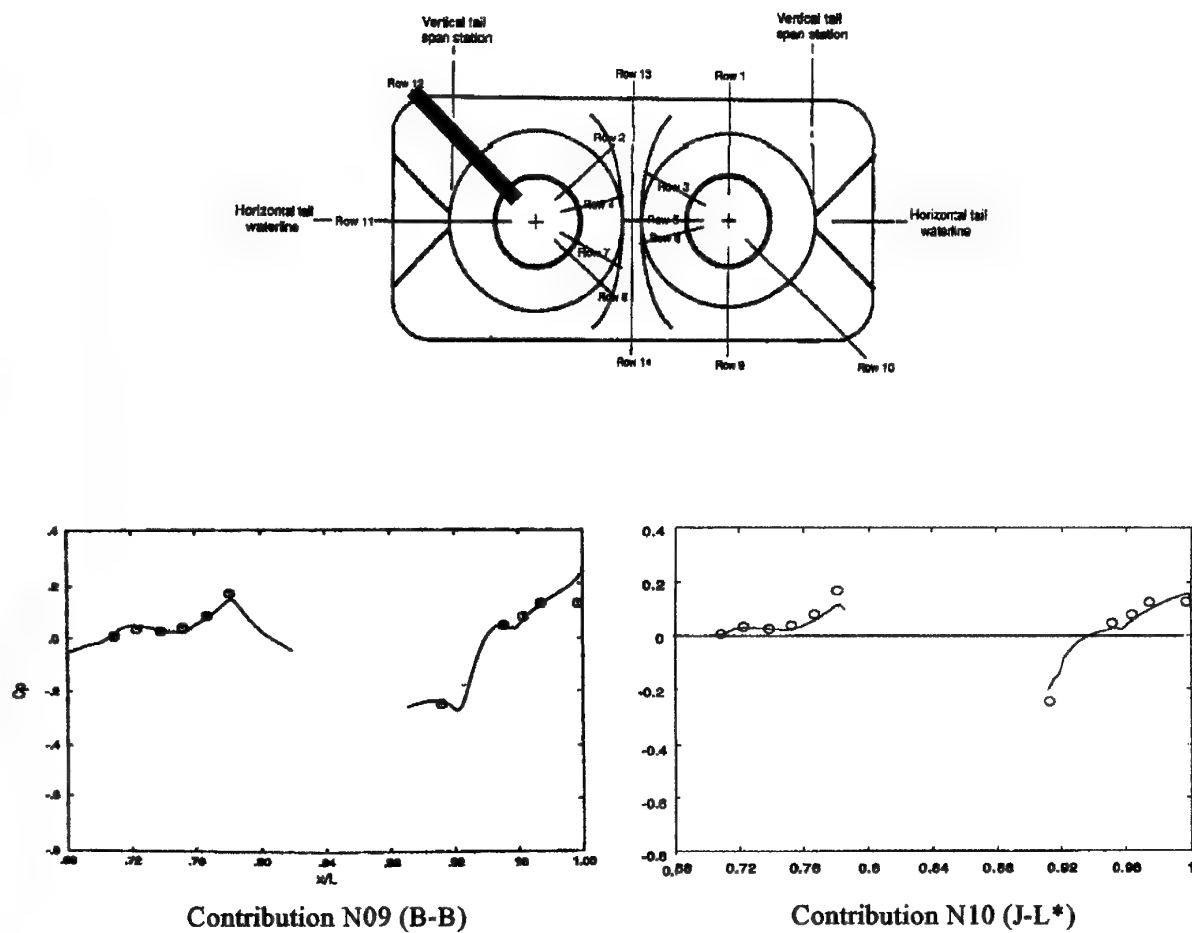


Figure 3.5-71. Comparison of Surface Pressures ( $C_p$  vs  $X/L$ ), Case B.3.1,  $\phi=315^\circ$

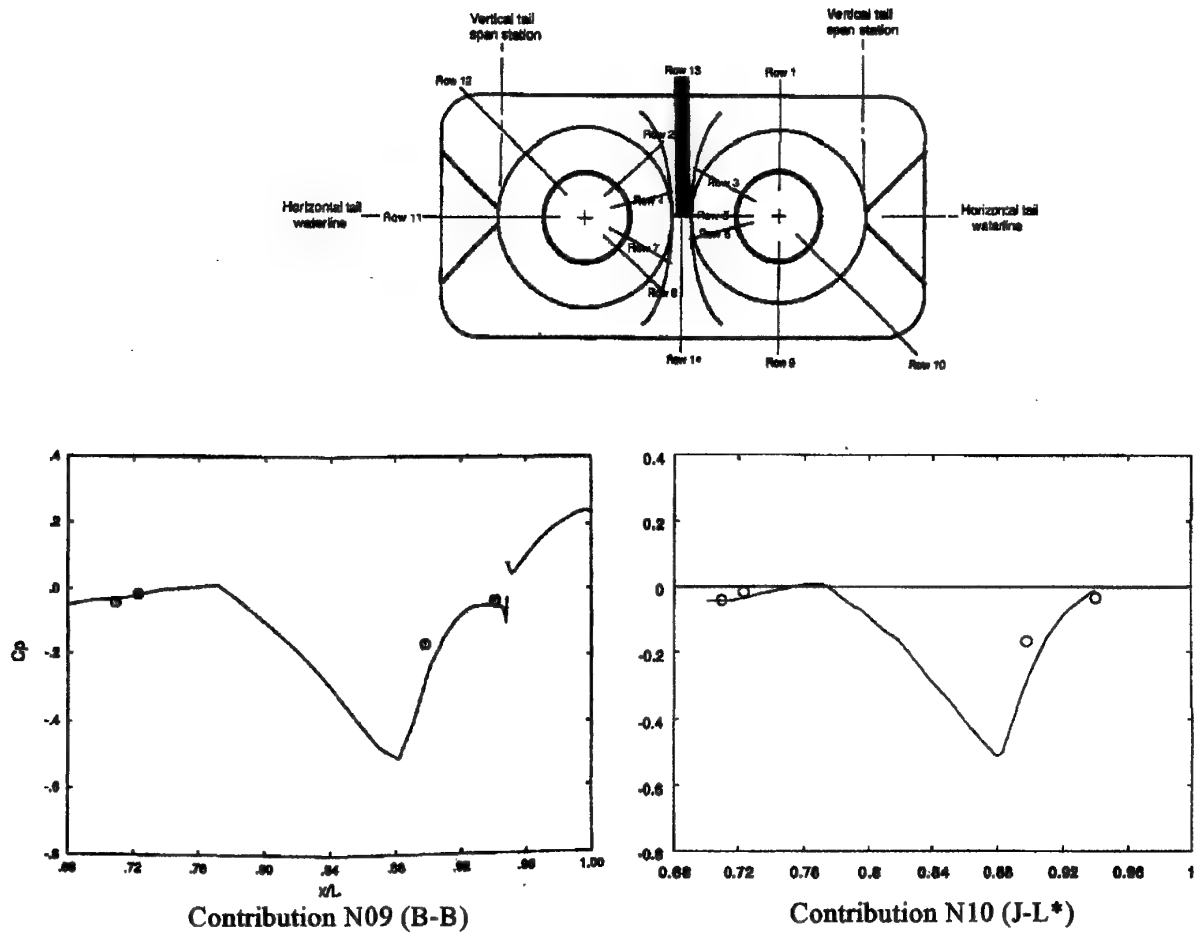


Figure 3.5-72. Comparison of Surface Pressures ( $C_p$  vs  $X/L$ ), Case B.3.1, Model Top Centerline

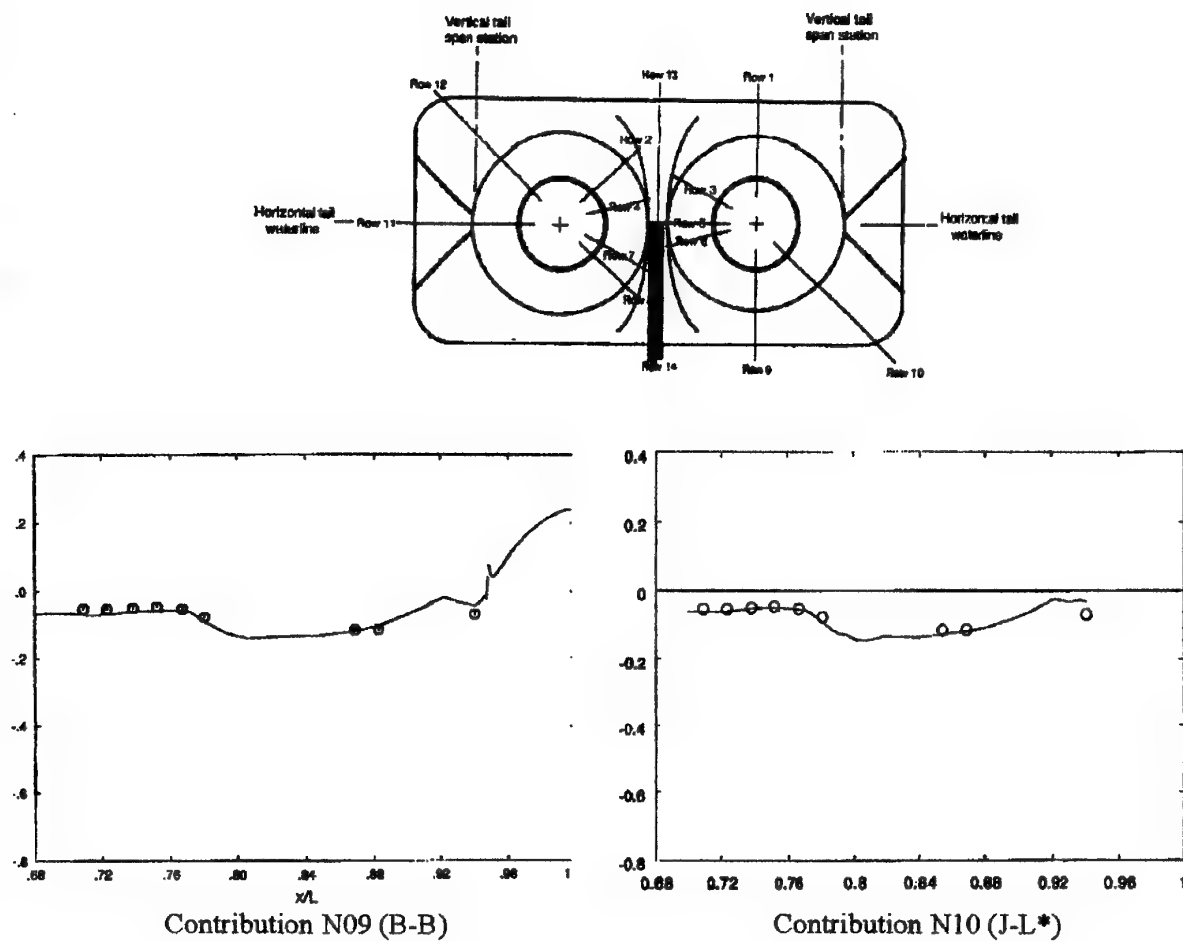


Figure 3.5-73. Comparison of Surface Pressures ( $C_p$  vs  $X/L$ ), Case B.3.1, Model Bottom Centerline

on the upper surface between the tails (c.f. Figures 3.5-60, -61, -62). It is thus of considerable lateral extent - fully spanning the distance between the vertical tails, based on all available data from experimental and CFD sources. This supersonic pocket is terminated by a shock somewhat upstream of the trailing edge of the interfairing.

**Drag Comparison** - Drag data for this case were provided from the semi-empirical method S01, and from the Navier-Stokes methods N09 and N10. These drag data are tabulated herein, and they are presented graphically in Figure 3.5-74 (excluding Contribution N09). The reader is reminded that these drag area are normalized by wing area, rather than the maximum forebody-afterbody cross-sectional area (as was done in previous cases).

#### Pressure Drag Predictions:

Contrib.	CDPN	CDPA	CDPHT	CDPVT	CDPT
Exp.	-0.0020				
S01					0.0044
N09 (B-B)	-0.0025	0.0042	0.0003	0.0018	0.0037
N10	-0.0020	0.0045	0.0006	0.0025	0.0055

#### Total Drag Predictions:

Contrib.	CDTN	CDTA	CDTHT	CDTVT	CDTT
Exp.					0.0084 ±0.0005
S01					0.0087
N09 (B-B)	-0.0025	0.0053	0.0015	0.0035	0.0078
N10	-0.0019	0.0061	0.0021	0.0043	0.0106

#### Total Drag Prediction Errors ( $C_{DTT}$ ):

Contrib.	Error ( $\Delta C_{DTT}$ )	% Error
Exp.		Uncertainty ±6.0%
S01	+0.0003	+3.6%
N09 (B-B)	-0.0006	-7.1%
N10	+0.0022	+26.2%

The most accurate results were produced by the semi-empirical method, S01. The two CFD methods differed widely in the total drag. Method N09 underpredicted drag, which might be expected since this method had a consistent tendency to overpredict pressures slightly on the nozzle. Surprisingly, Method N10, which generally was quite accurate on the nozzle, showed a larger drag discrepancy. Additional experimental drag data are not available to resolve this discrepancy. Method N09 produced drag estimates which were always lower than those of Method N10, on every vehicle component, by about the same amount: 0.0006 to 0.0008. The available experimental data do not allow an assessment as to whether this is more accurate, on a component basis.

**Discussion** - In this complex geometry, it is difficult to reach a meaningful conclusion in assessing the CFD results. The differences which were observed can easily be attributed to minor differences in grid generation, usage practices (e.g., convergence level) and other small factors. The approach of Method N09 perhaps did better on the aftbody and near the tails, while Method N10 gave better results on the nozzle. A solid explanation for the differences in predicted drag has not been established.

#### 3.5.3.2 Case B.3.2

In this case, the vertical tails are mounted at the aft location. The geometric points of interest are:

$X/L=0.782$  Leading edge of horizontal tail.

$X/L=0.833$  Leading edge of vertical tail.

$X/L=0.948$  Trailing edge of nozzle interfairing.

$X/L=0.950$  Trailing edge of horizontal tail.

$X/L=0.973$  Trailing edge of vertical tail.

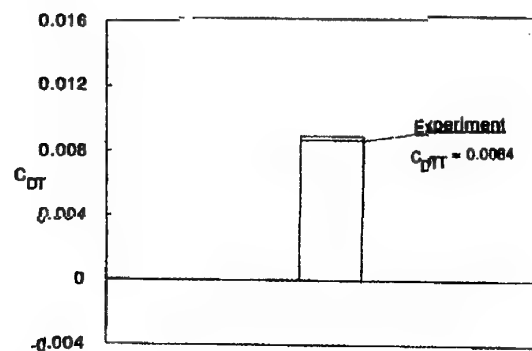
The only data submitted for this case were semi-empirical predictions of vehicle drag (Contribution S01).

**Surface Pressure Comparison** - The semi-empirical method of S01 does not produce a full description of the flowfield. Consequently, no comparisons of surface pressure predictions are available for this case.

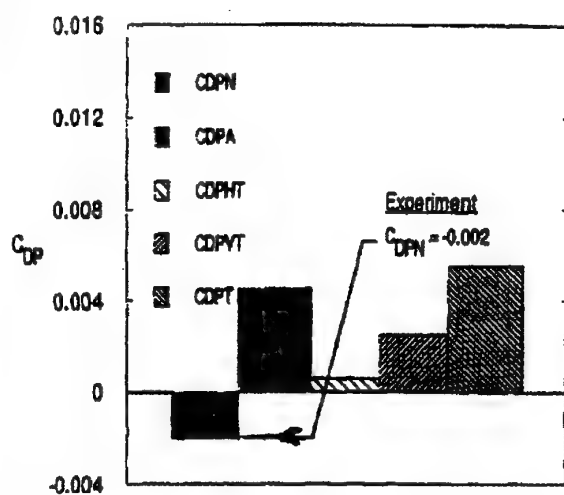
**Drag Comparison** - The drag predictions of the semi-empirical method S01 are presented below. These data are presented graphically in Figure 3.5-75 (normalized by reference wing area).

## Pressure Drag

## Total Drag



Contribution S01



Contribution N10

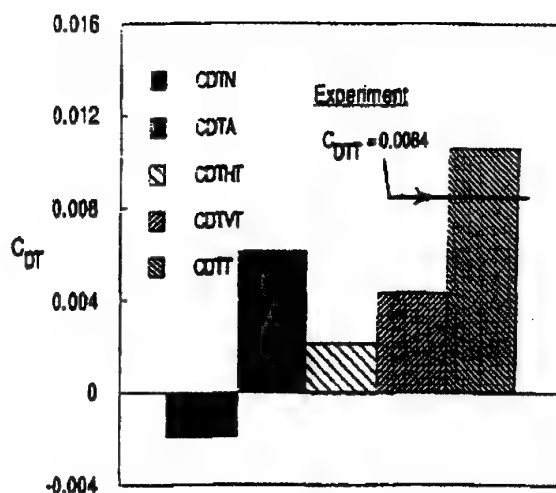
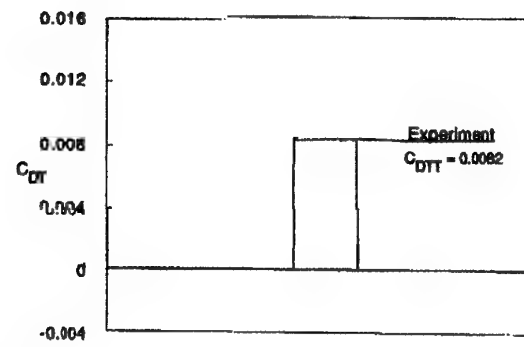


Figure 3.5-74. Comparison of Drag Data, Case B.3.1

**Pressure Drag****Total Drag****Contribution S01****Figure 3.5-75. Comparison of Drag Data, Case B.3.2**

## Pressure Drag Predictions:

Contrib.	CDPN	CDPA	CDPHT	CDPVT	CDPT
Exp.					
S01					0.0028

## Total Drag Predictions:

Contrib.	CDTN	CDTA	CDTHT	CDTVT	CDTT
Exp.					0.0082 $\pm 0.0005$
S01					0.0081

Total Drag Prediction Errors ( $C_{DTT}$ ):

Contrib.	Error ( $\Delta C_{DTT}$ )	% Error
Exp.		Uncertainty $\pm 6.1\%$
S01	-0.0001	-1.2%



Figure 3.5-76. Modeled Geometry for Case B.3.3  
(Contribution N10)

This case was performed by one contributor using a Navier-Stokes analysis, and by another contributor using a semi-empirical drag estimation method. These comparisons with the measured data are presented next.

The surface pressure distributions on the aftbody, nozzle, and tails are presented qualitatively in Figure 3.5-77 (predictions from Contribution N10). The most noticeable feature is a low pressure region running down the vertical tail from the tip at mid-chord. This minimum pressure region runs down to the root of the vertical tail, and across the afterbody. This pressure is sufficiently low that the local flow is reaching supersonic speeds in the partially enclosed channel between the vertical tails. Presumably, this type of behavior also was present in Cases B.3.1 and B.3.2.

Simulated local oil data (from Contribution N10) are presented in Figure 3.5-78. These data show that the boundary layer is well behaved on the inboard vertical tail and on the afterbody. The boundary layer also is very "clean" on most of the nozzle circumference, exhibiting strong viscous interactions only on the most inboard portion of the nozzle, aft of the termination of the interfairing. In this region, very localized in terms of circumference, a clear flow separation is noted.

**Surface Pressure Comparison** - The first comparison of surface pressure is on the top centerline of the nozzle,  $\phi=0^\circ$ . These data are presented in Figure 3.5-79.

The flow in the larger portion of this region, from  $X/L = 0.65$  to  $0.92$ , is dominated by the vertical tails. The pressure distribution in this case (forward tails) is the same as in case B.3.1 (mid tails) except the flow features occur further forward. The flow shows a gradual pressure rise as it comes alongside the leading edge of the vertical tail at  $X/L=0.727$ . From that point aft, a steady expansion is present along the chord of the vertical tail, reaching a very low pressure ( $C_p = -0.55$ , equivalent to Mach 1.21).

This low pressure is terminated by a shock wave at about  $X/L = 0.85$ , which raises the pressure to near-ambient values. The pressure then remains constant, at about ambient freestream pressure, over the range  $X/L$  from  $0.88$  to  $0.95$ .

For this case, method S01 produced an outstanding prediction of the total drag. This prediction is exact, within the experimental uncertainty of the test data.

**Discussion** - The semi-empirical method produced an amazing drag prediction for this case. This should not be viewed as fortuitous, since the prediction for the mid tail location (Case B.3.1) also was very good.

## 3.5.3.3 Case B.3.3

This case features the vertical tails at the forward location. The key geometric points of interest are:

$X/L=0.727$  Leading edge of vertical tail

$X/L=0.782$  Leading edge of horizontal tail.

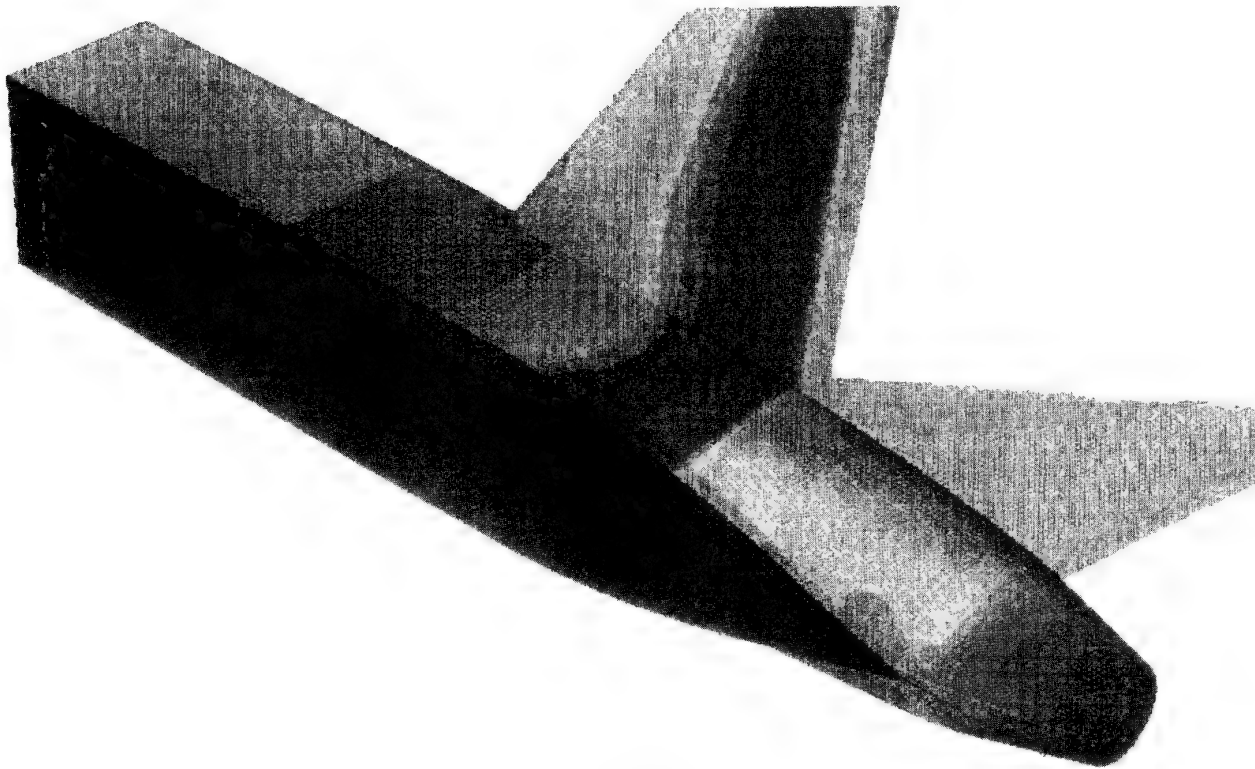
$X/L=0.867$  Trailing edge of vertical tail.

$X/L=0.948$  Junction of aftbody and nozzle (slope discontinuity); trailing edge of nozzle interfairing.

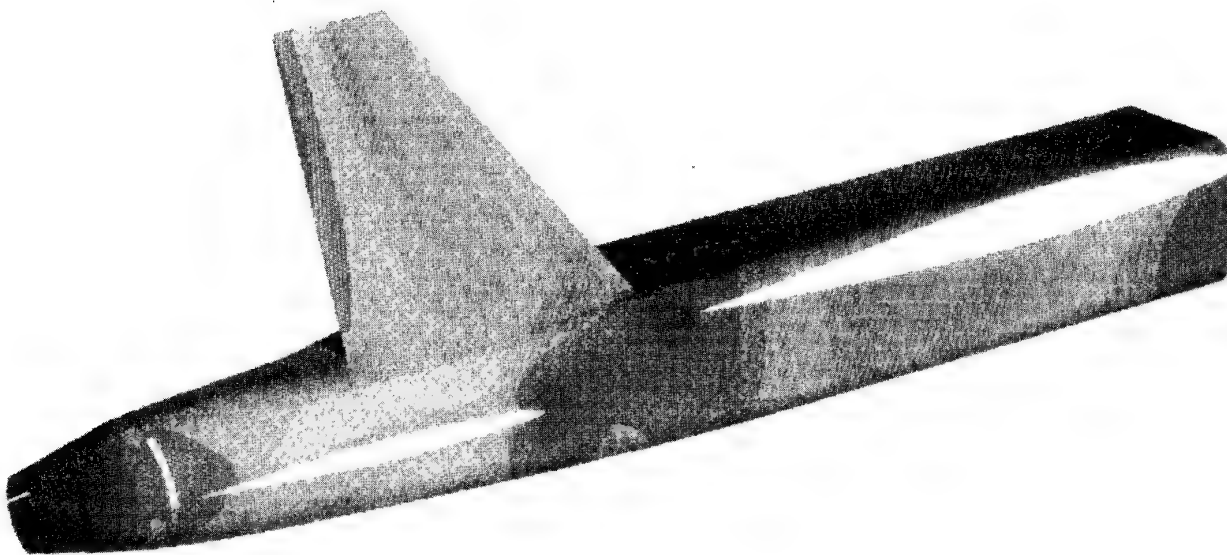
$X/L=0.950$  Trailing edge of horizontal tail.

The geometry for this case is presented in Figure 3.5-76.





Inboard View



Outboard View

Figure 3.5-77. Predicted Surface Pressures, Test Case B.3.3  
(Contribution N10)

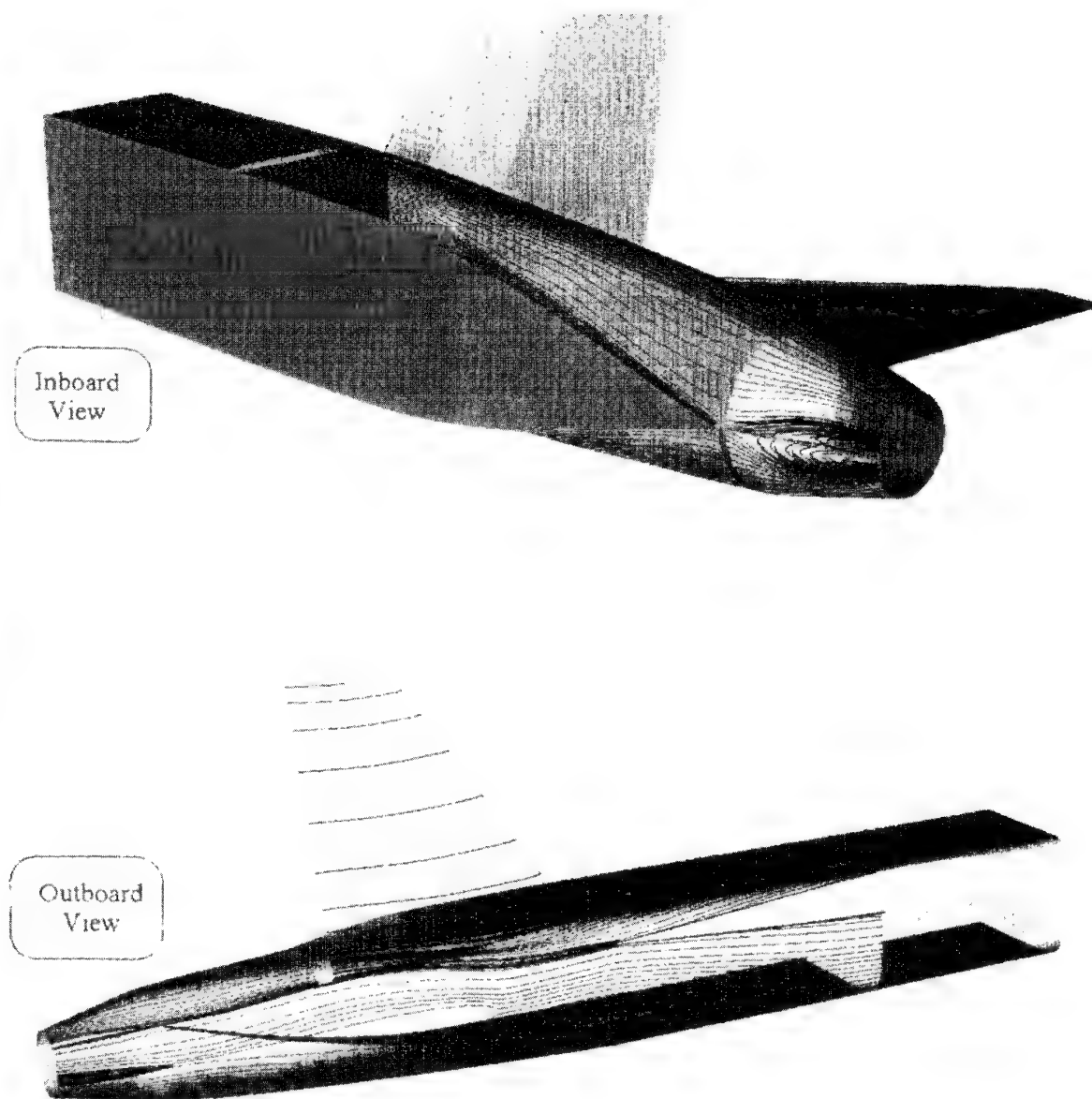


Figure 3.5-78. Computed Surface Oil Flow Patterns, Case B.3.3  
(Contribution N10)

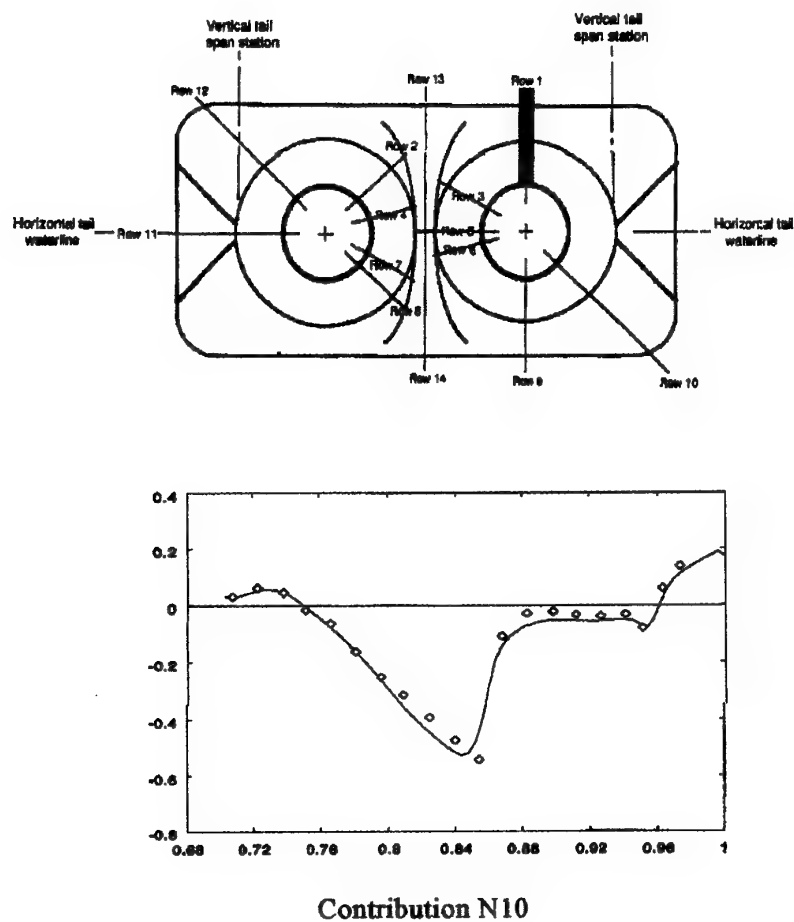


Figure 3.5-79. Comparison of Surface Pressures ( $C_p$  vs  $X/L$ ), Case B.3.3,  $\phi=0^\circ$

A strong pressure rise is seen on the nozzle ( $X/L$  from 0.96 to 1.00). The prediction (Contribution N10) is in good agreement with the test data nearly everywhere. Slight discrepancies are seen near the shock wave, at about  $X/L = 0.86$ . A slight downward "tick" is seen at about  $X/L=0.95$ , where the aftbody ends and the nozzle begins. This localized low pressure is due to the discontinuity in surface slope at this point.

The next comparisons, presented in Figure 3.5-80, are in the inboard quadrant of the nozzle, at  $\phi=45^\circ$ . Data only are available aft of  $X/L=0.88$ , where the nozzle at this circumferential angle emerges from the interfairing. The initial set of data are in the nearly-constant pressure region between the vertical tails, aft of the shock. Here the method is in generally good agreement with the test data, though the prediction is slightly low in pressure. The recompression on the nozzle is predicted very well. Similar results also are seen at the location  $\phi=60^\circ$ , presented in Figure 3.5-81.

Surface pressures are compared closer to the interfairing, at  $\phi=75^\circ$ , in Figure 3.5-82. At this angle, the nozzle is exposed only aft of  $X/L=0.93$ . The aft portion of the constant pressure region between the nozzles is captured, with (again) a slight underprediction of the pressure. The subsequent recompression on the nozzle is predicted with good accuracy.

Pressures at the inboard side of the nozzle,  $\phi=90^\circ$ , are presented in Figure 3.5-83. Only a small portion of the nozzle surface is exposed, in the region aft of the trailing edge of the interfairing. Good accuracy is seen in predicting the slow pressure rise to the nozzle exit location.

Pressures in the lower inboard quadrant of the nozzle are compared for  $\phi=120^\circ$  (Figure 3.5-84) and  $\phi=135^\circ$  (Figure 3.5-85). In this region, the flow is largely shielded from the influence of the vertical tails. The pressures (both test and prediction) show a gradually rising pressure up to about  $X/L=0.92$ , then a sharp drop approaching the trailing edge of the interfairing and the beginning of the nozzle at about  $X/L=0.95$ . The nozzle recompression to the exit plane begins at  $X/L=0.96$ . The predictions are in good agreement with the test data throughout.

Pressure along the bottom centerline of the nozzle ( $\phi=180^\circ$ ) are shown in Figure 3.5-86. Along this angle, the flow is quite benign up to the aftbody-nozzle junction at  $X/L=0.96$ . Slight variations in surface pressure were measured, and they were captured accurately by the predictions. The final recompression on the nozzle ( $X/L > 0.96$ ) also was captured well by Contribution N10, though for the first time in this test case, a noticeable overprediction of pressure occurs near/at the nozzle exit.

Surface pressure data in the lower outboard quadrant of the aftbody and nozzle,  $\phi=225^\circ$ , are presented in Figure 3.5-87.

Along this angle, the flow is influenced by the horizontal tails, which intersect the aftbody in the region of  $X/L$  from 0.78 to 0.95. The predictions generally capture the pressure variations alongside the horizontal tail, though the predicted oscillations seem to be leading the measured oscillations slightly. A minor low-pressure inflection is noted at  $X/L=0.95$ . This is the location of the junction between the aftbody and the nozzle, where a slope discontinuity occurs. Aft of this point, the recompression on the nozzle is predicted accurately, all the way to the nozzle exit.

The pressures at the outboard side of the aftbody and nozzle ( $\phi=267^\circ$ ) are presented in Figure 3.5-88. A large gap occurs in these data, where the locating angle falls inside of the horizontal tail.

Forward of the horizontal tail, the prediction (Contribution N10) captures quite well the pressure rise leading up to the leading edge of the tail. Aft of the trailing edge, the recompression is modeled well, though the prediction is consistently a little low compared with the test data.

Pressures on the upper outboard quadrant of the nozzle, at  $\phi=315^\circ$ , are presented in Figure 3.5-89. The gap in these data is at the location of the vertical tail. Forward of the data gap (i.e., the tail) this line of data lies outboard of the axis of the vertical tail. Aft of the data gap, these data lie inboard of the axis of the vertical tail. Pressures here are heavily influenced by the vertical tail and in the aft segment of the data these pressure data are shielded from any influence of the horizontal tail.

About  $X/L=0.73$  (at the left edge of the plotted data) the pressure reaches a local maximum. This point is alongside the leading edge of the vertical tail, and the prediction method shows good accuracy. Aft of the leading edge ( $X/L$  from 0.73 to 0.80) the pressure drops slowly under the influence of the expansion along the forward chord of the vertical tail, just above the afterbody surface.

From  $X/L = 0.80$  (approximately) to 0.87, the location of the trailing edge of the vertical tail, a gap is present in the data. Aft of the trailing edge of the vertical tail, where the data resume, the nearly-constant pressure region behind the tail-aftbody shock is noted. The prediction at this location is consistent with the predictions of pressure in the region, at other circumferential locations on the afterbody upper surface. However, the first experimental data point aft of the vertical tail trailing edge is slightly elevated compared with the next experimental point. This relative trend is not captured in the prediction. The recompression on the nozzle, from  $X/L = 0.96$  to 1.00, is captured accurately.

Data on the model top centerline, between the nozzles, are presented in Figure 3.5-90. The experimental data are quite sparse, but the CFD prediction of Contribution N10 is in good agreement with the few data points. The test data

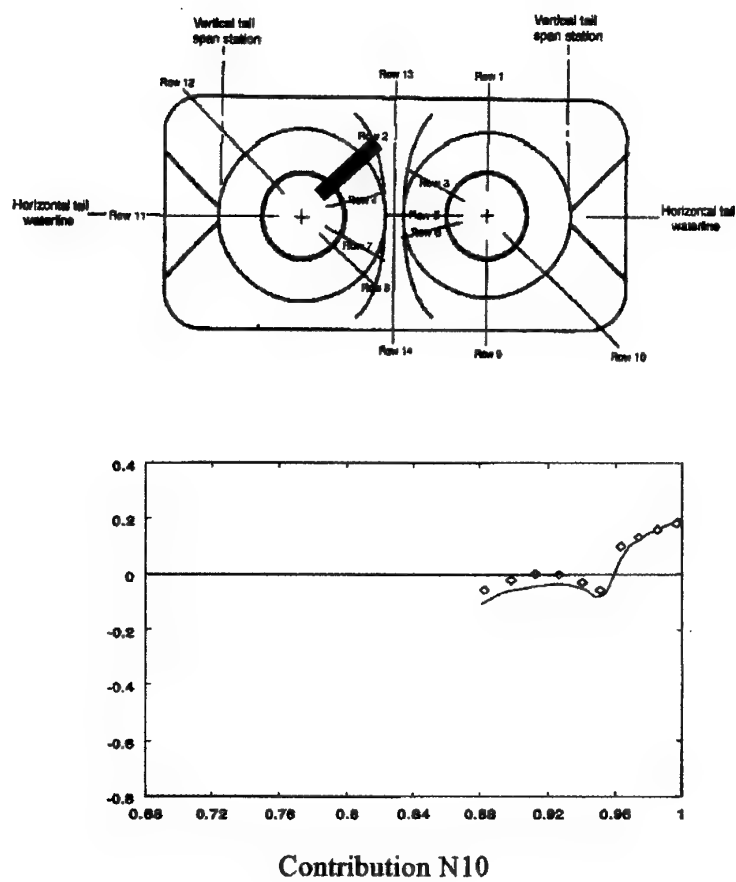
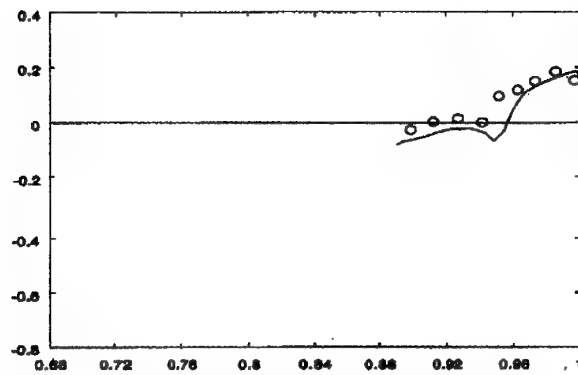
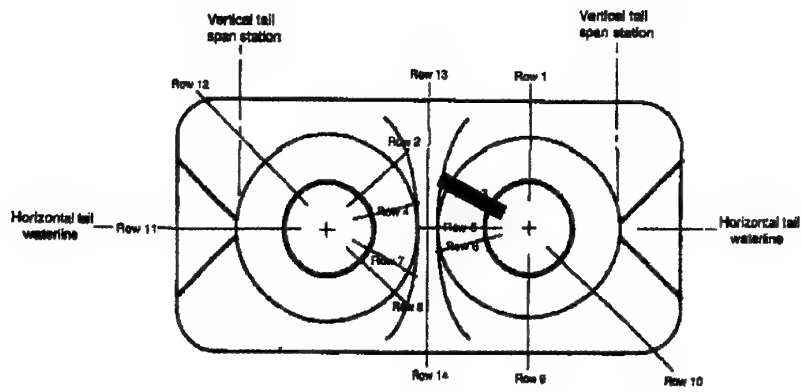


Figure 3.5-80. Comparison of Surface Pressures ( $C_p$  vs  $X/L$ ), Case B.3.3,  $\phi=45^\circ$



Contribution N10 (J-L\*)

Figure 3.5-81. Comparison of Surface Pressures ( $C_p$  vs  $X/L$ ), Case B.3.3,  $\phi=60^\circ$

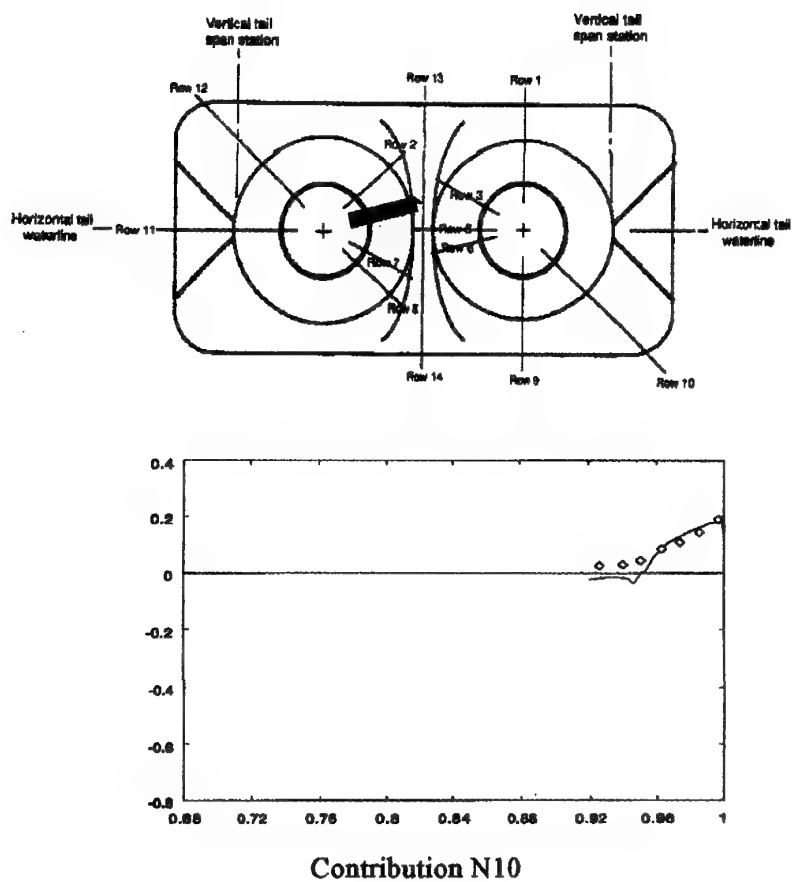


Figure 3.5-82. Comparison of Surface Pressures ( $C_p$  vs  $X/L$ ), Case B.3.3,  $\phi=75^\circ$

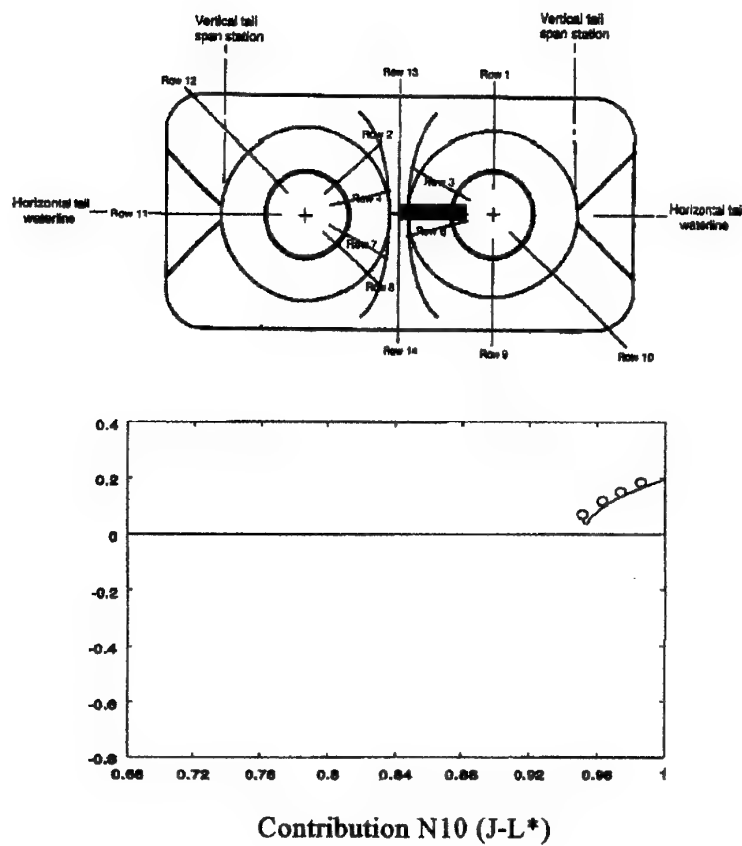


Figure 3.5-83. Comparison of Surface Pressures ( $C_p$  vs  $X/L$ ), Case B.3.3,  $\phi=90^\circ$



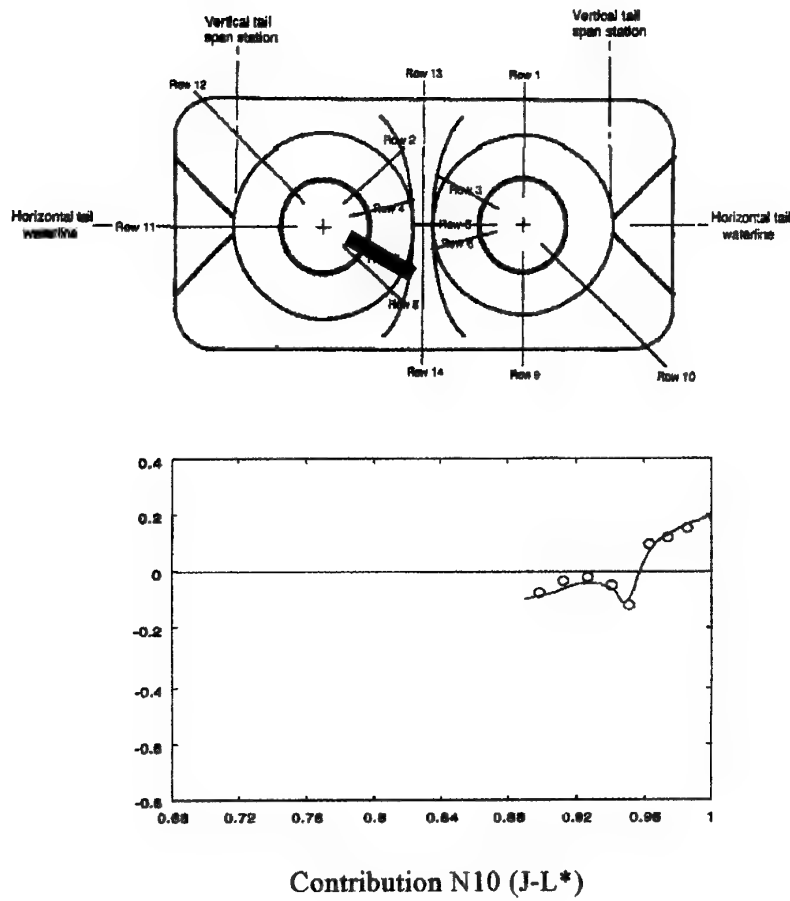
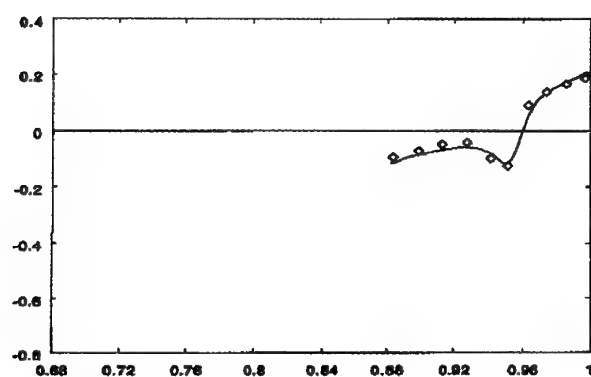
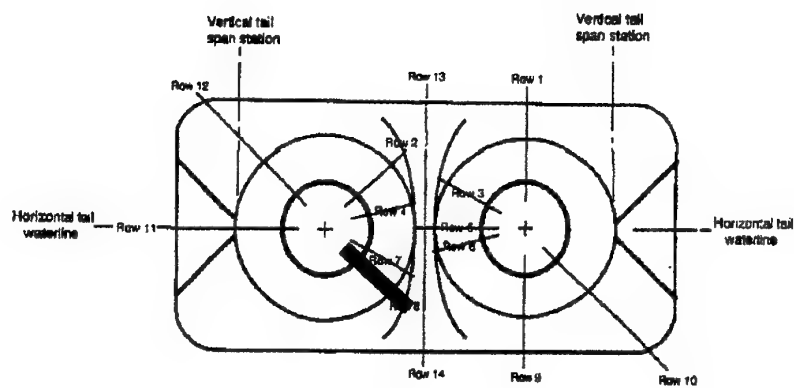


Figure 3.5-84. Comparison of Surface Pressures ( $C_p$  vs  $X/L$ ), Case B.3.3,  $\phi=120^\circ$



Contribution N10

Figure 3.5-85. Comparison of Surface Pressures ( $C_p$  vs  $X/L$ ), Case B.3.3,  $\phi=135^\circ$

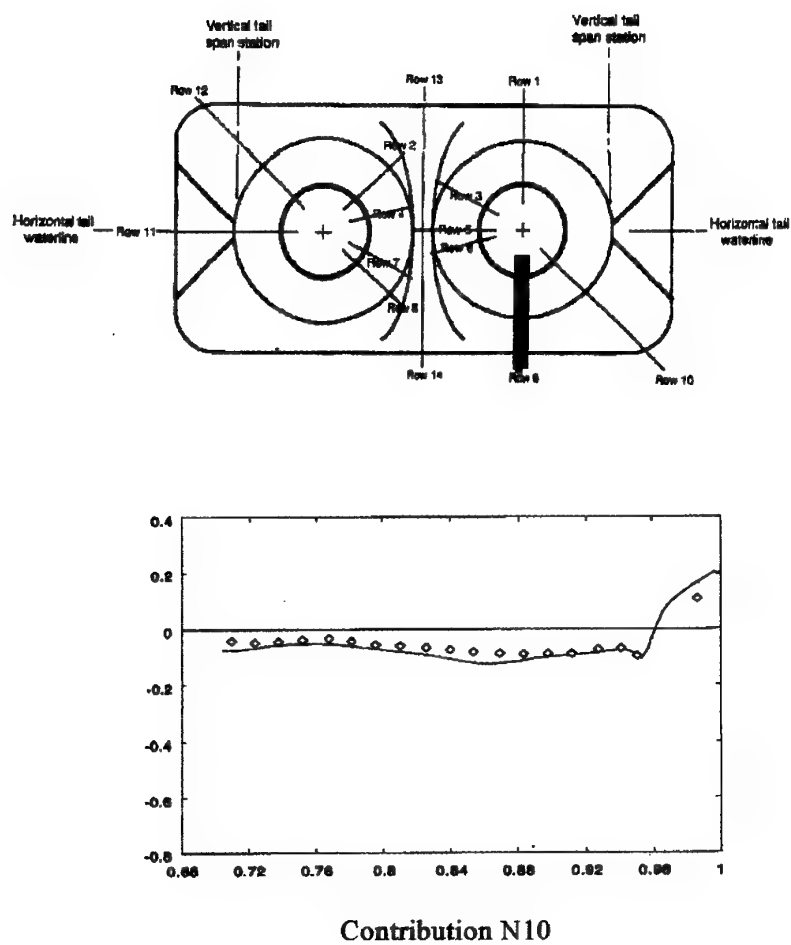


Figure 3.5-86. Comparison of Surface Pressures ( $C_p$  vs  $X/L$ ), Case B.3.3,  $\phi=180^\circ$

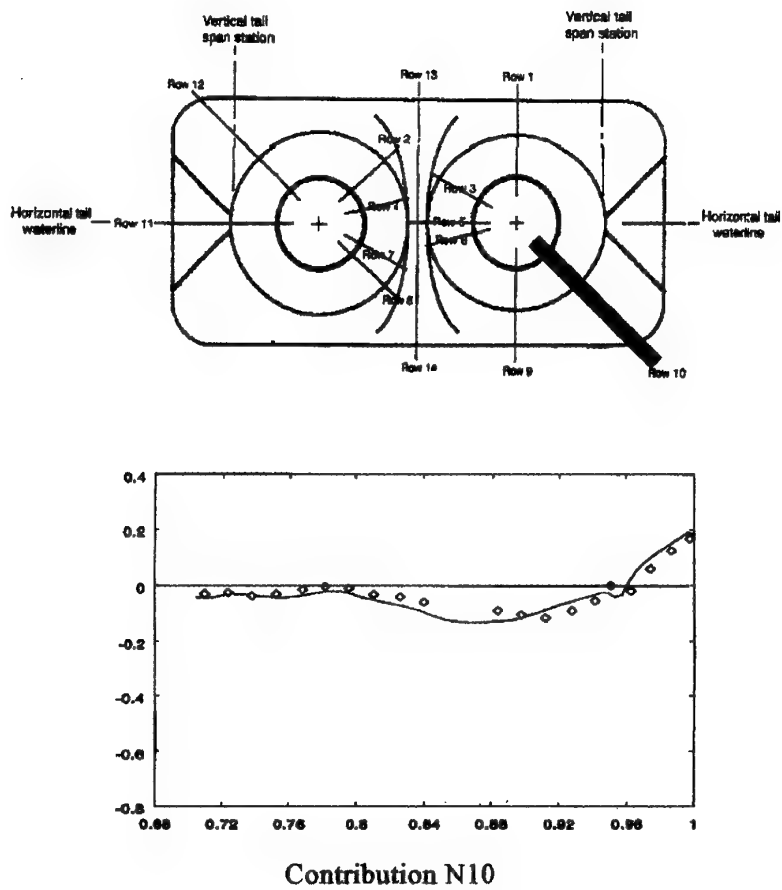
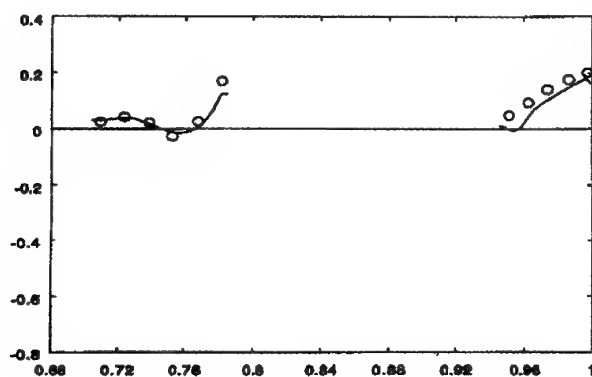
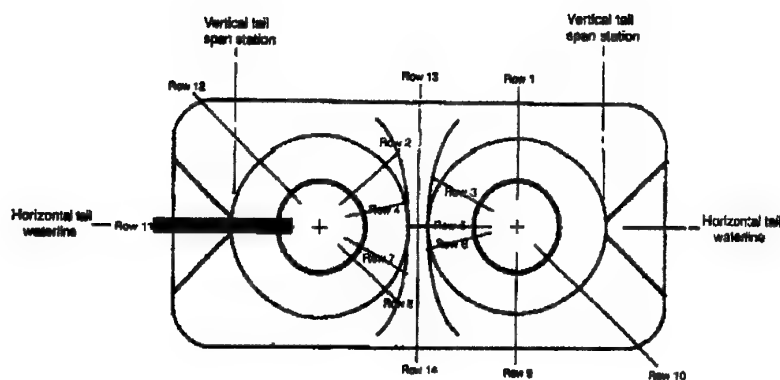


Figure 3.5-87. Comparison of Surface Pressures ( $C_p$  vs  $X/L$ ), Case B.3.3,  $\phi=225^\circ$



Contribution N10

Figure 3.5-88. Comparison of Surface Pressures ( $C_p$  vs  $X/L$ ), Case B.3.3,  $\phi=267^\circ$

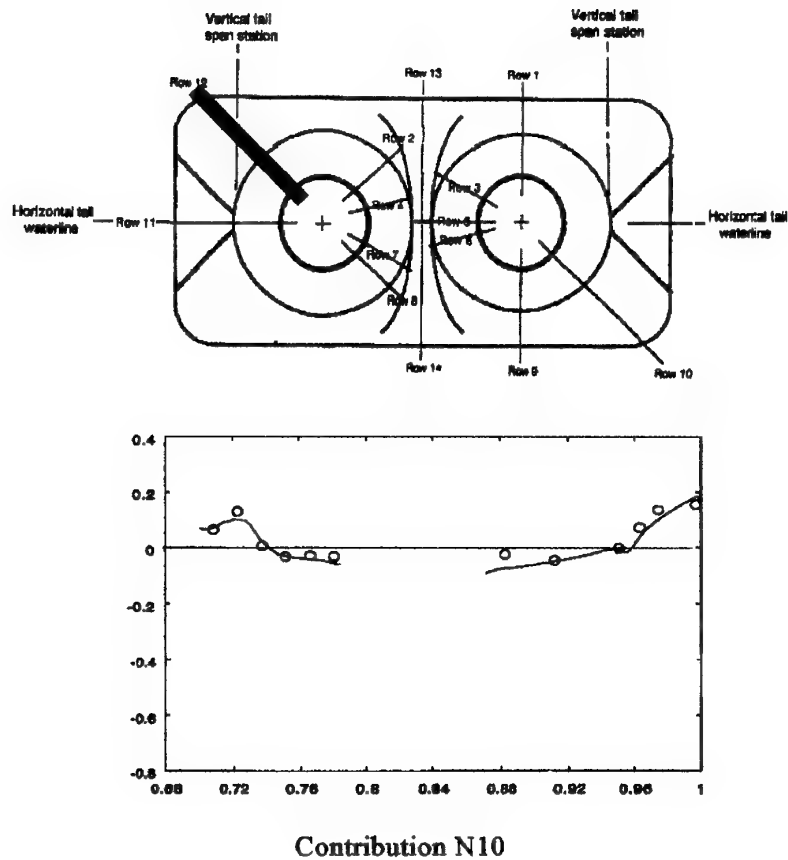
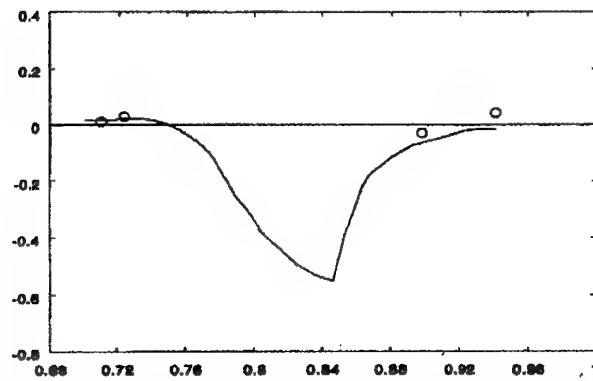
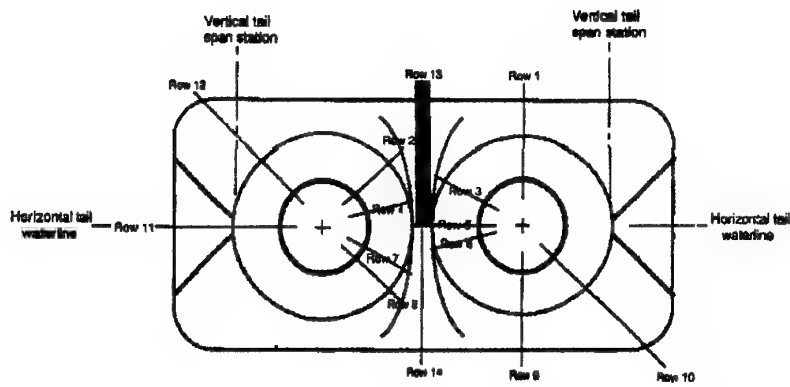


Figure 3.5-89. Comparison of Surface Pressures ( $C_p$  vs  $X/L$ ), Case B.3.3,  $\phi=315^\circ$



Contribution N10 (J-L\*)

Figure 3.5-90. Comparison of Surface Pressures ( $C_p$  vs  $X/L$ ), Case B.3.3, Model Top Centerline

suggest that the flowfield is benign along this line, but the CFD data and the test data from nearby points both show the sharp variations due to the shock which spans the region between the vertical tails.

Pressure comparisons along the bottom centerline of the model are presented in Figure 3.5-91. Both the test data and the predictions indicate that only minor pressure variations are occurring along this line of pressure taps.

**Drag Comparison** - The drag data from the experiment, the semi-empirical method, and the Navier-Stokes method are presented below, and in graphical form in Figure 3.5-92 (normalized by reference wing area).

#### Pressure Drag Predictions:

Contrib.	CDPN	CDPA	CDPHT	CDPVT	CDPT
Exp.	-0.0022				
S01					0.0022
N10	-0.0022	0.0042	0.0005	0.0029	0.0054

#### Total Drag Predictions:

Contrib.	CDTN	CDTA	CDTHT	CDTVT	CDTT
Exp.					0.0078 ±0.0005
S01					0.0064
N10	-0.0020	0.0058	0.0019	0.0045	0.0102

#### Total Drag Prediction Errors ( $C_{DTT}$ ):

Contrib.	Error $\Delta C_{DTT}$	% Error
Exp.		Uncertainty ±6.4%
S01	-0.0014	-17.9%
N10	+0.0024	+30.8%

The drag prediction of the semi-empirical method (S01) is significantly worse for this case (forward vertical tails), compared with the other two cases (mid and aft vertical tails). One can speculate that the tail location in the present case is outside the data base which was used to build Method S01.

The drag data from the CFD method (Contribution N10) are comparable to the results yielded by the same method in Case B.3.1. The prediction of pressure drag on the nozzle is

excellent, and the wetted area is quite small leading to the conclusion that the total drag on the nozzle also is quite good. Data are not available to support further conclusions. One might speculate, however, that the drag of the tails is difficult to predict with accuracy, and that frictional drag on the large wetted area of the afterbody also could have contributed to the discrepancy with the measured data.

#### 3.5.3.4 Discussion of Results

Geometrically, these are the most complex test cases in this study. It is very difficult to produce grids modeling a complete configuration with full fidelity. Under these circumstances, the predictions of the CFD methods probably represent a fair sample of the state of the art, excluding (perhaps) results from a major, focused study operating with large resources (people, time, and computers).

The most interesting result, however, was the very good predictions of the semi-empirical method in Cases B.3.1 and B.3.2.

**Drag Increment Due to Tail Location** - The data provided by Contributions S01 and N10 allow an assessment of the ability to predict the drag variation due to changes in the location of the vertical tails. These drag data are tabulated below.

#### Drag Increment Due to Tail Location

Contrib.	CDTT Mid Tail	CDTT Aft Tail	CDTT Fwd Tail	$\Delta C_{DTT}$ Aft minus Mid	$\Delta C_{DTT}$ Fwd minus Mid
	B.3.1	B.3.2	B.3.3		
Exp.	0.0084	0.0082	0.0078	-0.0002	-0.0006
S01	0.0087	0.0081	0.0064	-0.0006	-0.0023
N10	0.0106		0.0102		-0.0004

The experimental data, perhaps surprisingly, show little impact of vertical tail location on total drag. The semi-empirical method is in general agreement with the experimental increment in the variation between aft and mid tails, but it greatly overpredicts the increment between forward and mid tails. This situation reflects the single-case prediction accuracy demonstrated by this method (more particularly, the reduction in accuracy for Case B.3.3).

The result achieved by the Navier-Stokes method is more interesting, perhaps. This method showed significant errors in predicting  $C_{DTT}$  for both the forward and mid tail configuration (error in  $C_{DTT}$  > 0.0030 in both cases).



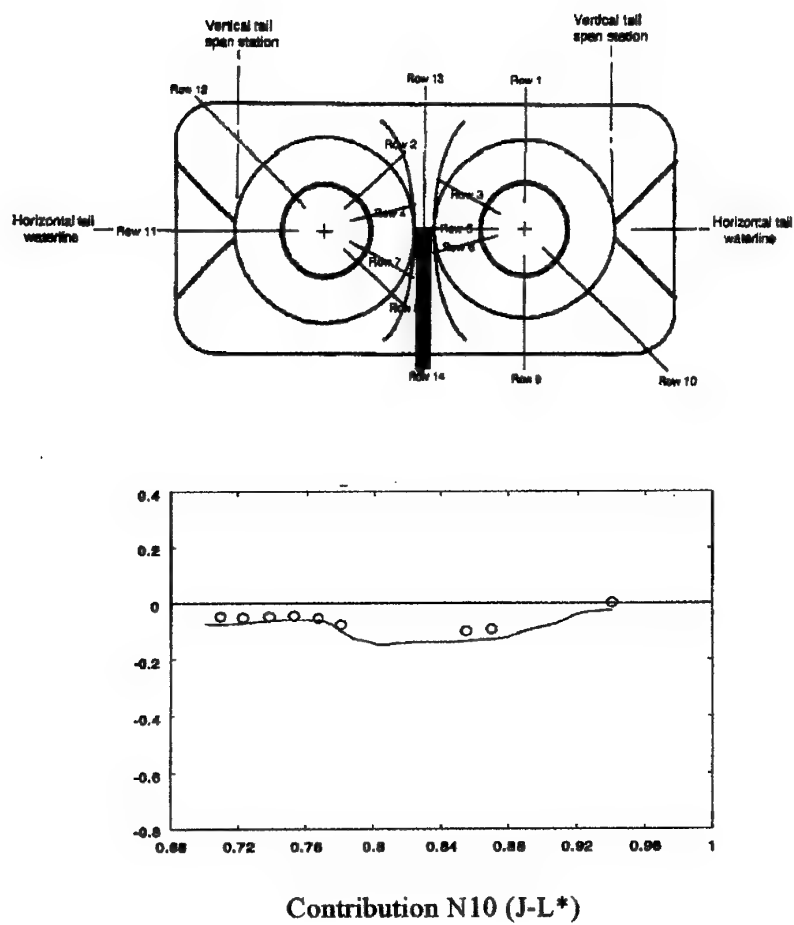


Figure 3.5-91. Comparison of Surface Pressures ( $C_p$  vs  $X/L$ ), Case B.3.3, Model Bottom Centerline

# Pressure Drag

# Total Drag

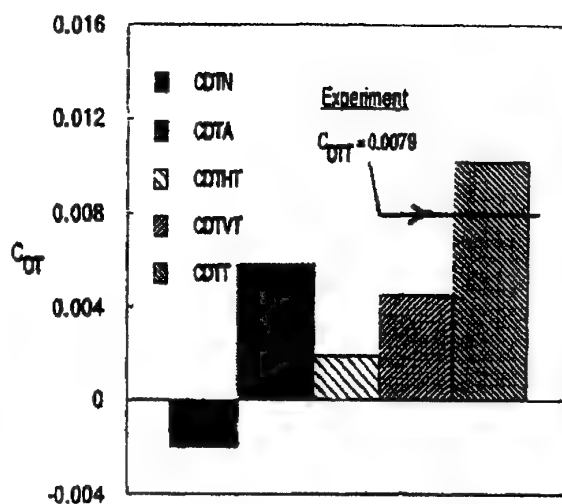
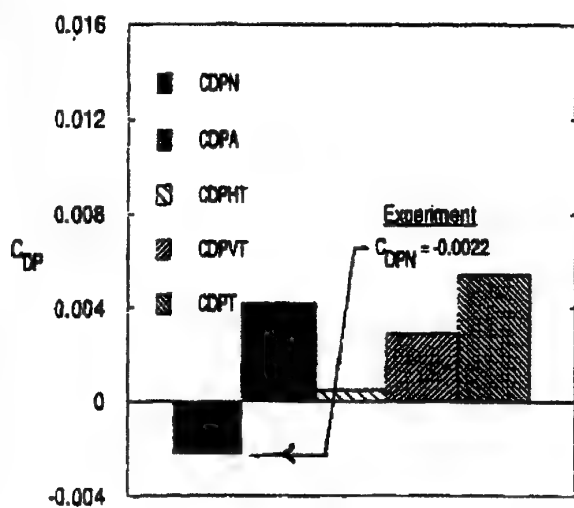
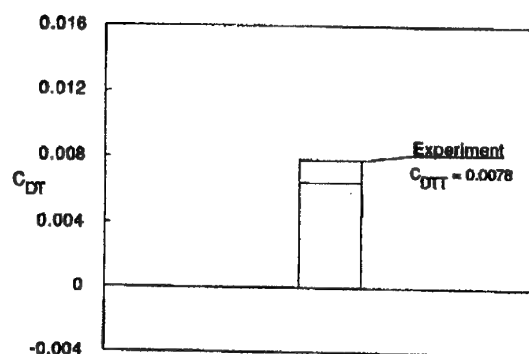


Figure 3.5-92. Comparison of Drag Data, Case B.3.3

However, the increment in drag is calculated with much better accuracy ( $C_{DTT}$  within 0.0002). This approach can be seen as supporting the use of CFD analysis for computing drag increments, even where the single-point value of the drag prediction is subject to significant error or uncertainty.

The B.3 series of test cases features a complex three-dimensional transonic flowfield, with substantial viscous interactions. In general, the prediction methods did quite well in modeling this complex flowfield. Regions of both attached and separated flow were predicted with good accuracy, even in the presence of several complicating geometric features (e.g., horizontal and vertical tails, gaps between nozzles, interfairing). These cases may be said to exemplify the progress which has occurred since the previous investigation of afterbody flows by AGARD, ten years ago.

### 3.5.4 Case B.4

The B.4 geometry is a single, isolated two-dimensional nozzle, tested at two Mach numbers. For the Mach 0.6 flowfield (Case B.4.1), the boundary layer is attached. For the Mach 0.94 flowfield (Case B.4.2), the boundary layer is extensively separated. This deceptive geometry poses interesting challenges for those who would predict its flowfield.

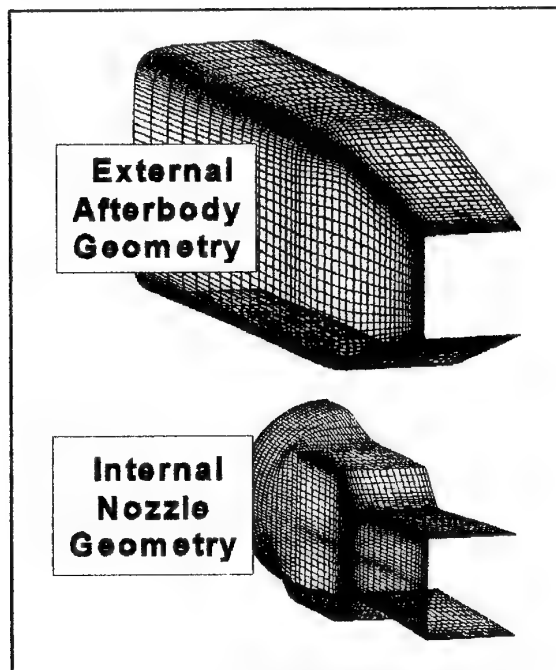


Figure 3.5-93. External and Internal Aerodynamic Geometry for Case B.4 (Contribution N09)

The external and internal surface geometry for this aftbody and nozzle is presented in Figure 3.5-93. The B.4 test geometry is nominally symmetric both left/right, and top/bottom. The figure, for example, shows only the left half of the model. Most of the CFD groups took advantage of the symmetry, and modeled only half of the geometry (a few groups used both symmetries, and modeled only a quarter of the geometry).

As was mentioned previously, CFD analysts frequently prefer to model the internal nozzle geometry, starting at a point upstream of the throat. This approach makes it easier to ensure that the computational flow properties are physically consistent. This geometry features a circular feed/plenum chamber, transitioning to a throat with a rectangular cross section, and a two-dimensional supersonic expansion passage.

The geometry is identical for both test cases. The only variation is the Mach number, which is 0.60 in Case B.4.1 and it is 0.94 in Case B.4.2. The NPR, for both cases, is nominally 4.00; the freestream total pressure is 14.7 psia, the freestream total temperature is 600°R, and the jet total temperature is 545°R.

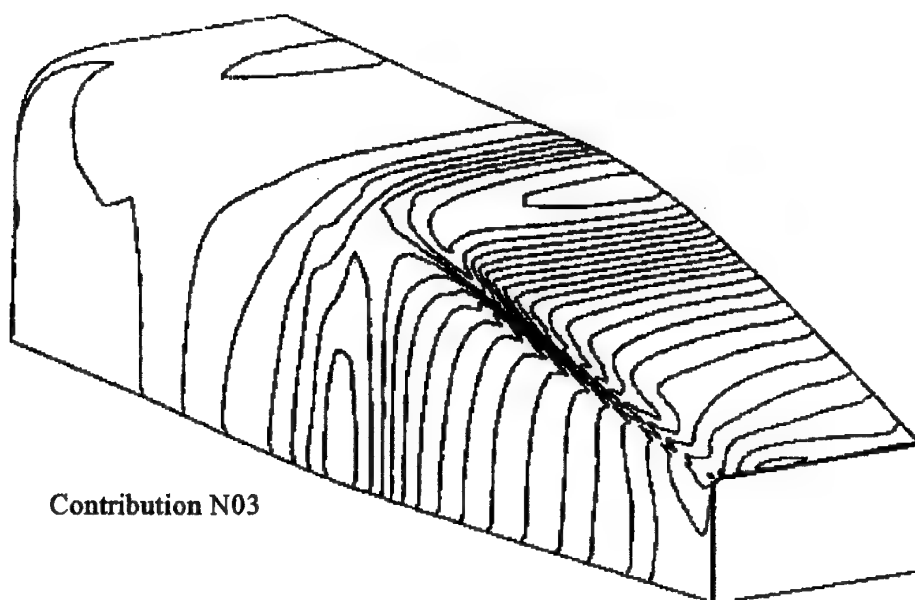
#### 3.5.4.1 Case B.4.1

This case, at a freestream Mach number of 0.6, does not feature extreme pressure gradients. This is seen, for example, in the mapping of predicted surface pressure that is presented in Figure 3.5-94.

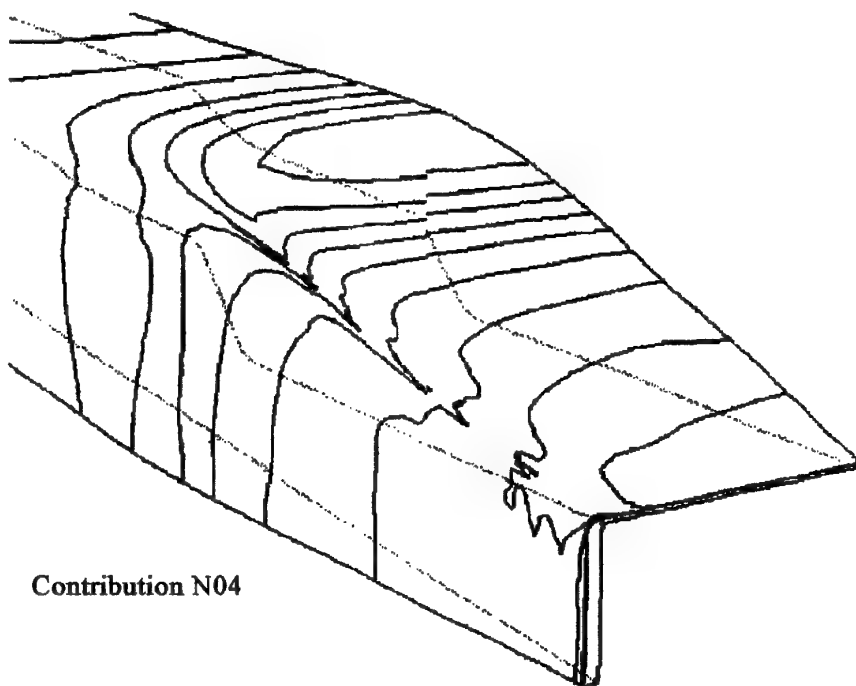
The boundary layer remains fairly well-behaved in this case. No evidence of separation is observed in these computations. The predicted velocity field (Contribution N10) shows a well-behaved boundary layer all the way to the trailing edge of the nozzle (Figure 3.5-95). The pressure field (static, Pitot, and total pressure) also shows clean attached flow in both the vertical symmetry plane (Figure 3.5-96) and the horizontal symmetry plane (Figure 3.5-97). The Mach number contours also are predicted to be quite benign (see Figure 3.5-98). A simulation of oil flow patterns was provided from Contribution N02. These data also show that the boundary layer is well behaved over the entire aftbody and nozzle (Figure 3.5-99).

The data which are presented, are organized according to physical location. In other words, all predictions at the same location (thus, results which are to be compared with the same set of experimental data) will be presented together.

The reader is cautioned that the solutions presented below are based on a wide range of methods. The solutions are consistent only in that they used the same geometry and flow conditions, and results were provided at set locations. No consistency is present in grid construction, flow solution



Contribution N03



Contribution N04

Figure 3.5-94. Predicted Surface Pressure Contours, Case B.4.1

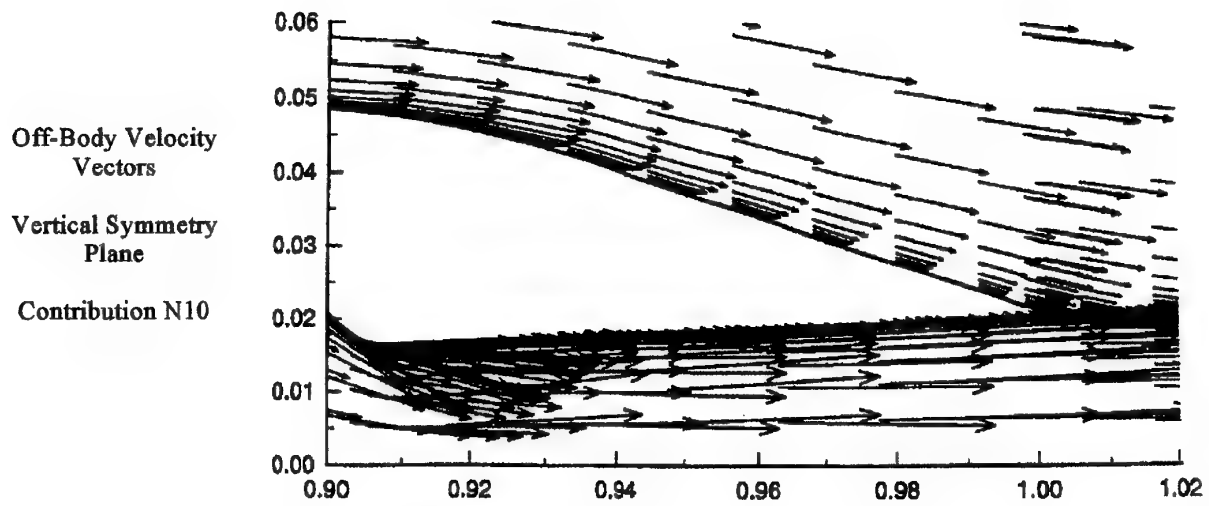


Figure 3.5-95. Predicted Off-Body Velocity Vectors, Case B.4.1, Vertical Symmetry Plane

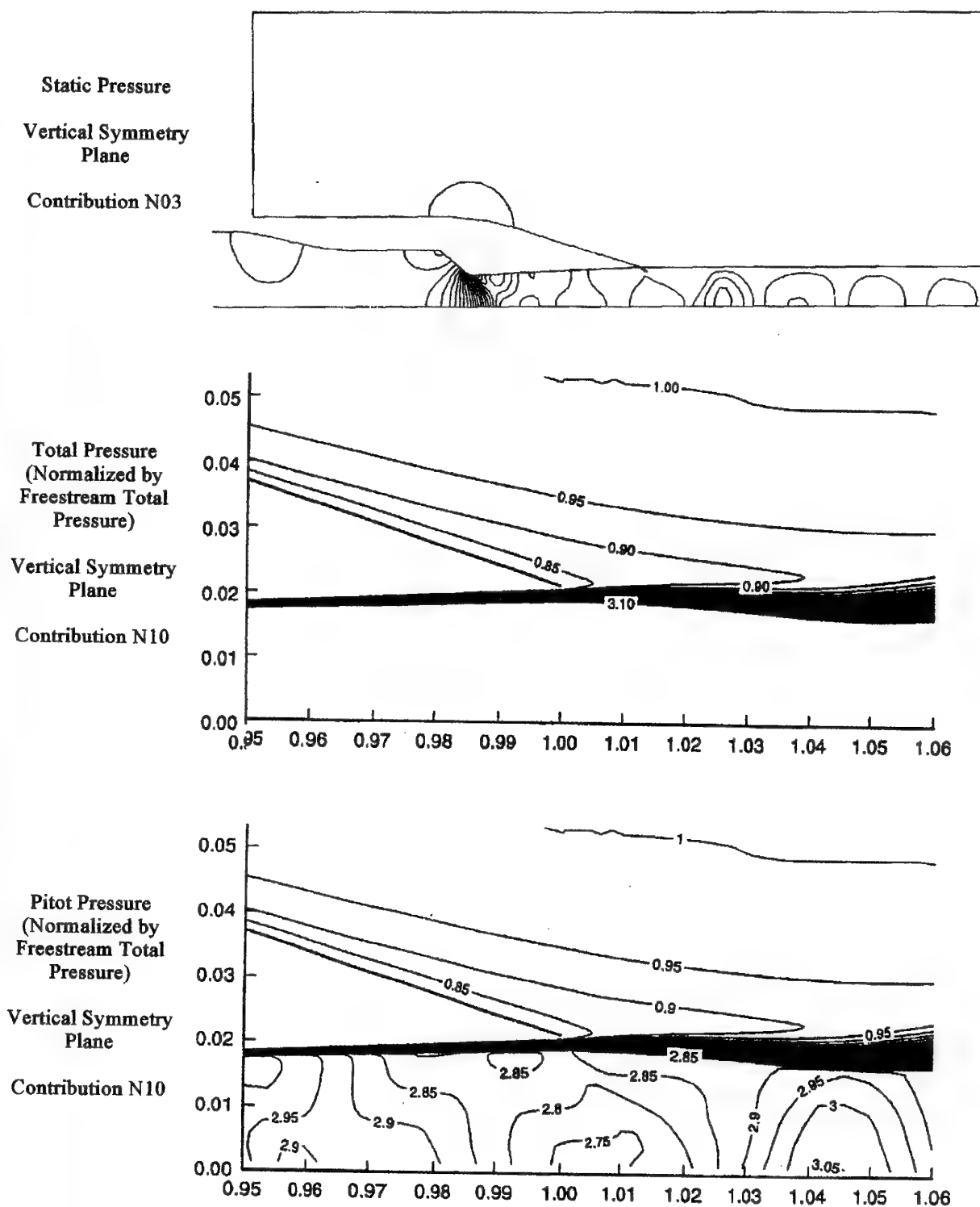


Figure 3.5-96. Predicted Off-Body Pressure Contours, Case B.4.1, Vertical Symmetry Plane

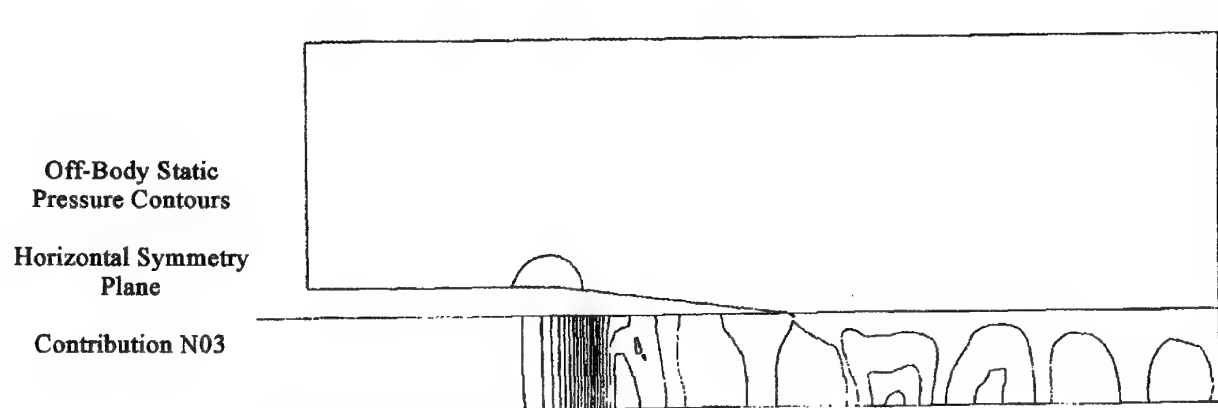
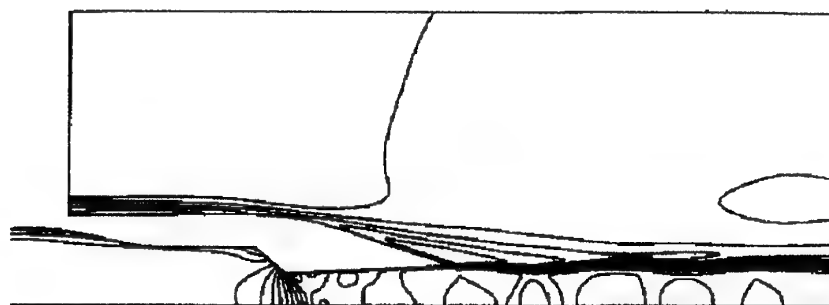
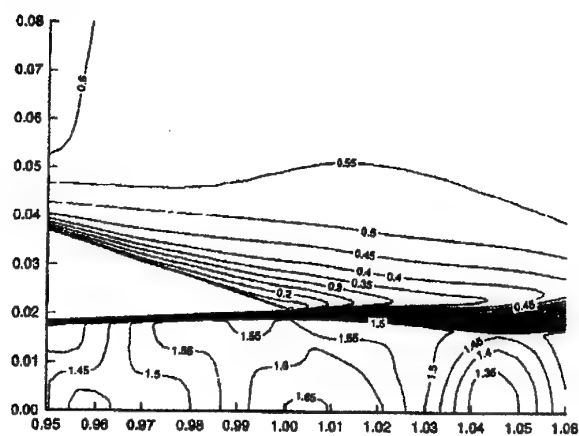


Figure 3.5-97. Predicted Off-Body Static Pressure Contours, Case B.4.1, Horizontal Symmetry Plane



Vertical  
Symmetry  
Plane

Contribution N03



Contribution N10

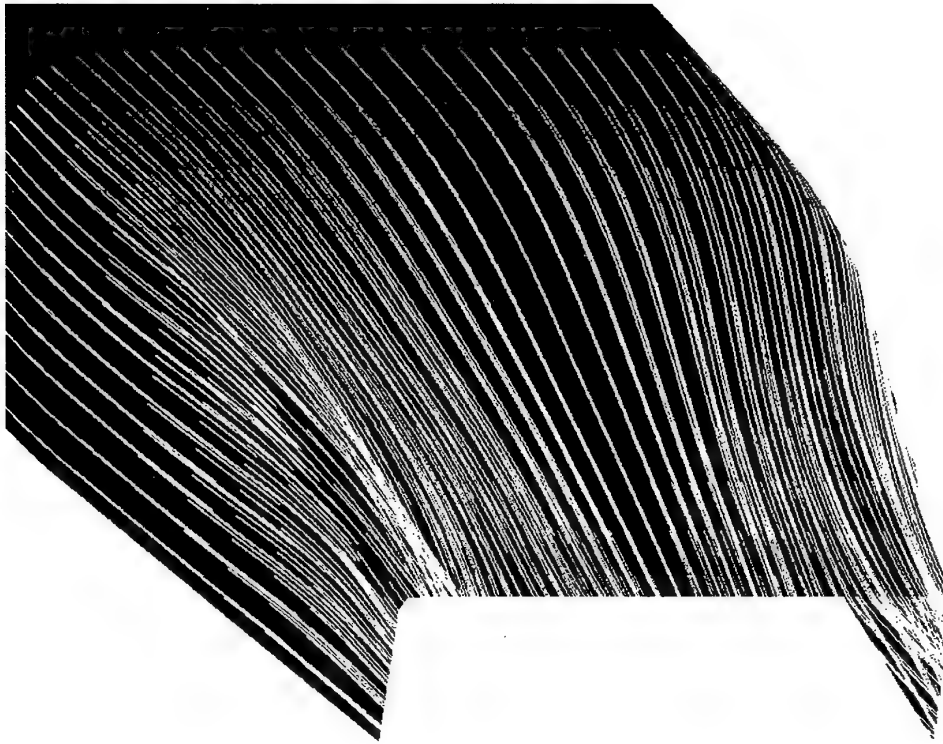
Horizontal  
Symmetry  
Plane



Contribution N03

Figure 3.5-98. Predicted Off-Body Mach Number Contours, Case B.4.1





Contribution N02  
(Cebeci-Smith Turbulence Model)

**Figure 3.5-99. Predicted Surface Flow Patterns, Case B.4.1**

algorithms, turbulence models, usage practices, or post-processing algorithms.

The authors will attempt to point out differences in results among the methods. However, it is inappropriate to draw larger conclusions, beyond the scope of this study, based on these results. These results should be viewed as a sampling of the state of the art in 1992-94, rather than as a systematic comparison of various methods. Further, a reader who is looking for a clear "winner" or a "best method" will be disappointed. Each method produces excellent results for some comparisons, and poor results in others.

**Surface Pressure Comparisons** - In this section, quantitative comparisons are presented between experimental data and various CFD predictions. As a sub-theme, comparisons also will be made between different levels of analysis (Euler vs. Navier-Stokes), between different grid densities, and between different turbulence models. Brief descriptive commentary will be offered in the following discussion, and summary observations and conclusions will be presented in Section 3.5.4.3.

For this case, the boundary layer remains attached. Secondary (lateral) flows are present, but by all available data they are not large. The turbulence modeling focus is on attached boundary layers in a sustained adverse pressure gradient. The flow is subcritical (i.e., the flow does not reach sonic speed anywhere), thus no shock waves are present. Further, the geometry is rather simple. For these reasons - simple geometry and no shock waves - the demands on the grid generation systems are not high.

Surface pressures were measured in the wind tunnel at five rows of taps. These rows extend circumferentially along one quadrant of the nozzle external surface, from Row 1 (top centerline) to Row 5 (sidewall centerline). The strongest viscous interaction is found on Row 1, and the most complex interaction (but not necessarily dominated by viscous effects) probably occurs in Rows 2 and 3.

Experimental and CFD data for the vertical symmetry plane ("Row 1") are presented in Figure 3.5-100. In general, each solution begins with accurate predictions at the most upstream point of the comparison region. However, most of the predictions experience difficulty at the nozzle expansion shoulder (around  $x/L = 0.91$ ) where the pressure field shifts from a favorable gradient to an adverse gradient in a region of longitudinal curvature. As seen in previous test cases, the pressure field is in a sensitive balance, and the prediction quality is strongly influenced by details in the CFD methodology.

The majority of the methods predict too low a pressure in this region, i.e., the flow expands too strongly. This behavior might be assumed to be due to an inadequate viscous interaction. Both the Euler methods (Contributions

E05 and E11) underpredict the pressure by similar degrees in this region.

For one of the methods, the zero-equation Cebeci-Smith turbulence model gave better results in this region than did a two-equation model (Contribution N02), and the Baldwin Lomax model (N11, N12) also did quite well. The two methods using the one-equation Baldwin-Barth model (N04 and N09) exhibited a similar tendency for delayed onset of the adverse pressure gradient.

Results for the two-equation turbulence models (N02, N03, N10, and N13) do not exhibit any consistent trend in this shoulder region. One method (N10) produced excellent results at the shoulder, while the other three methods predicted a pressure slightly too high (this might be associated with an early onset of the adverse pressure gradient and early boundary layer thickening) in the viscous flow interaction.

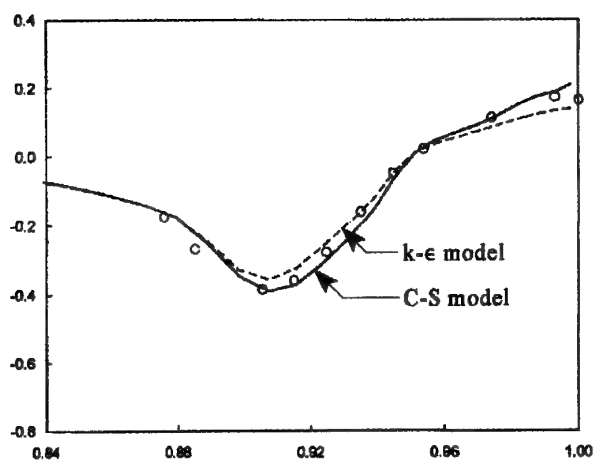
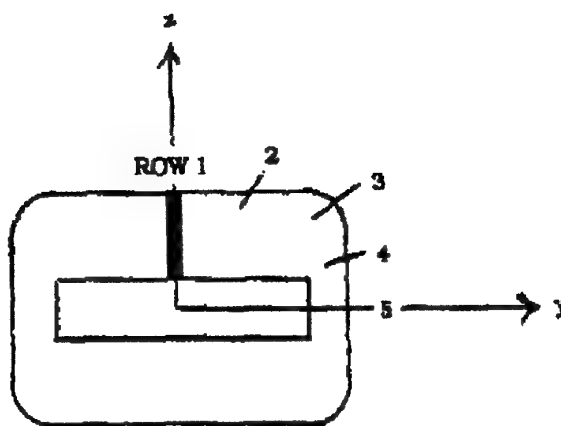
Predictions in the initial recompression region ( $x/L = 0.92$  to  $0.97$ ) are generally good. The accuracy here seems to depend largely on the accuracy achieved in the shoulder region. This is seen in several solutions (Contributions N04, E05, N09, N10, N11, and N12). Only two of the methods showed improved accuracy in the initial recompression region, compared with the accuracy at the shoulder (N03 and N13).

The two Euler solutions (E05 and E11) produced quite similar results. Both predicted an overly-strong expansion of the flow around the nozzle shoulder (say,  $X/L=0.89$  to  $0.93$ ). Most of the Navier-Stokes methods produced noticeably better accuracy here. This observation suggests that viscous interactions play an important role in the pressure distribution at the shoulder (the reader is reminded of a similar observation, for attached flow over the B.1 test cases geometries).

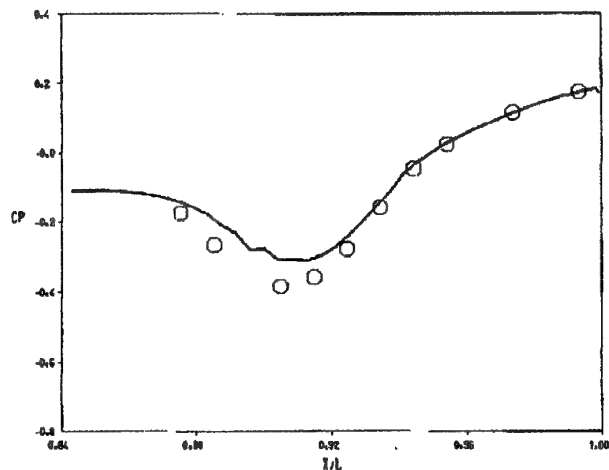
The final recompression region ( $x/L = 0.97$  to  $1.00$ ) features stronger viscous interactions, and the interaction with the plume. The plume is in an expanding state as it emerges from the nozzle, due to the internal nozzle expansion angle. Thus, the local effect of the plume is to present a compression corner at the nozzle exit.

The two Euler methods (Contributions E05 and E11) both over-predicted pressures in this region, by a wide margin. This result is to be expected, since this methodology does not represent the important viscous interaction near the nozzle trailing edge.

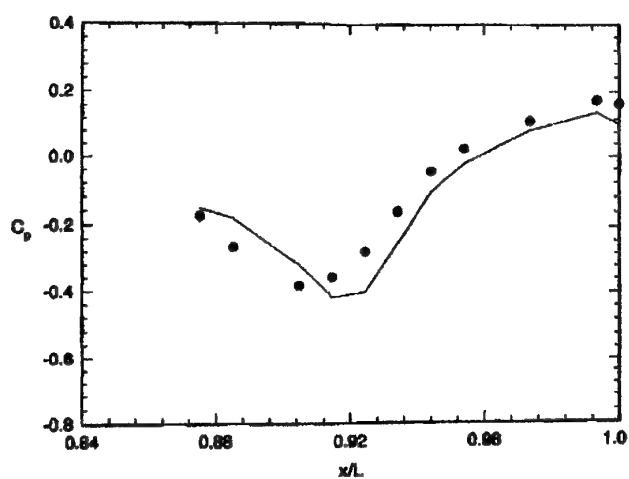
Most of the Navier-Stokes methods also exhibited the now-familiar tendency to over-predict pressures in this region: N02 (C-S), N10 (J-L\*), N11 (k- $\epsilon$ ), N12 (B-L), and N13 (k- $\epsilon$ ). Some of the methods did very well: N03 (k- $\epsilon$ ), N04 (B-B), and N02 (k- $\epsilon$ ). Contribution N09 (B-B) underpredicted the



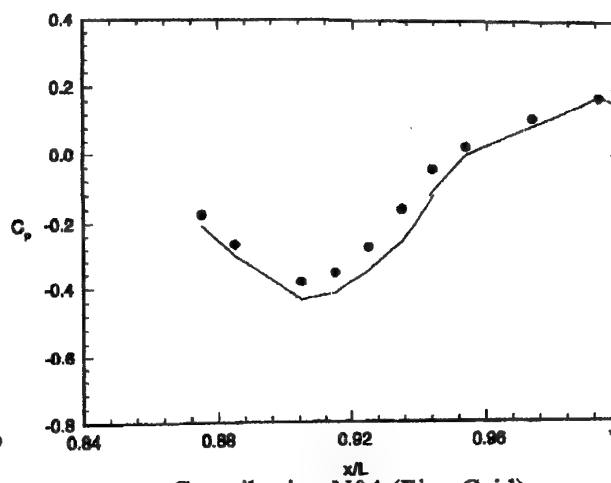
Contribution N02



Contribution N03



Contribution N04 (Coarse Grid)



Contribution N04 (Fine Grid)

Figure 3.5-100 (First Part). Comparison of Surface Pressures ( $C_p$  vs.  $x/L$ ), Case B.4.1, Row 1

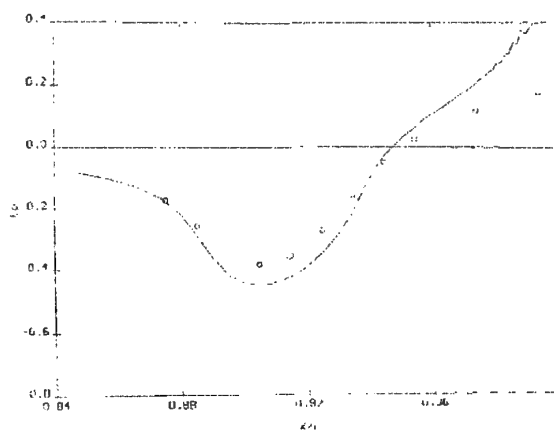
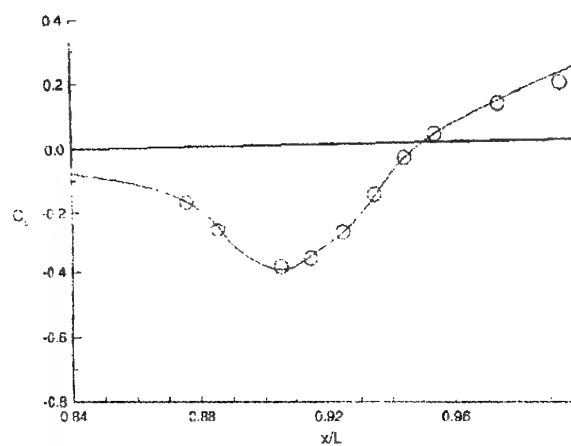
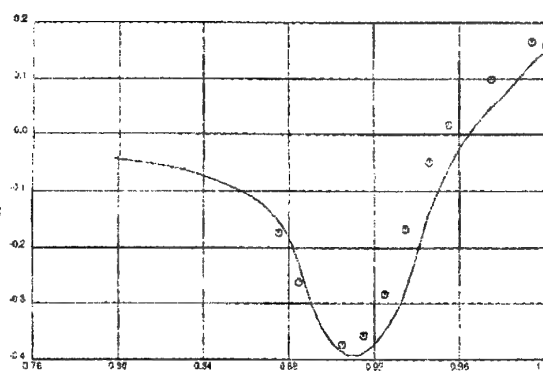
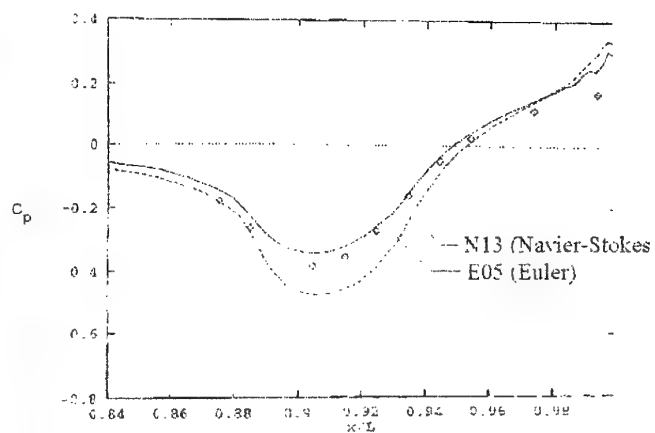
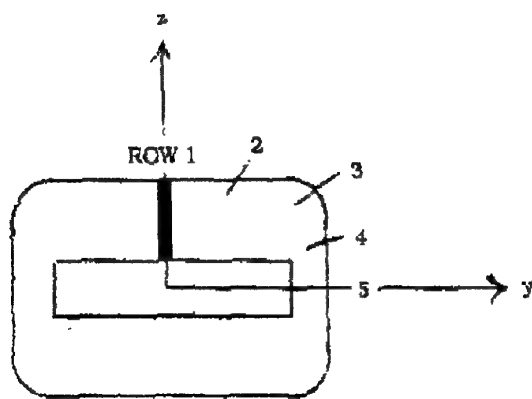
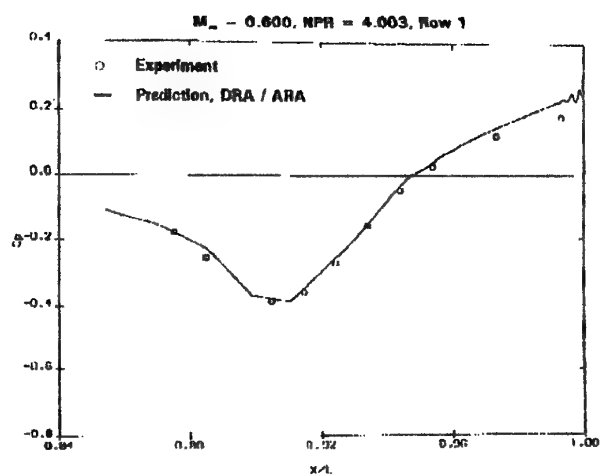
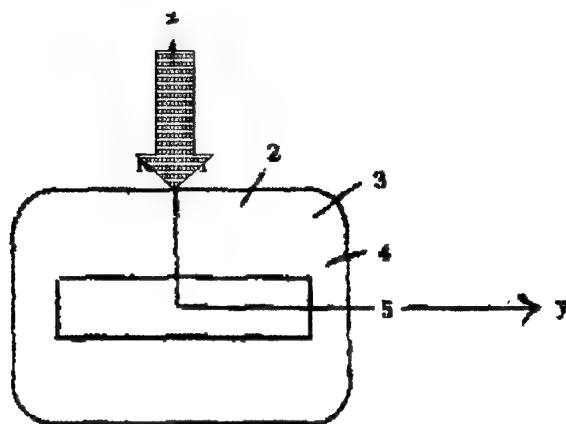
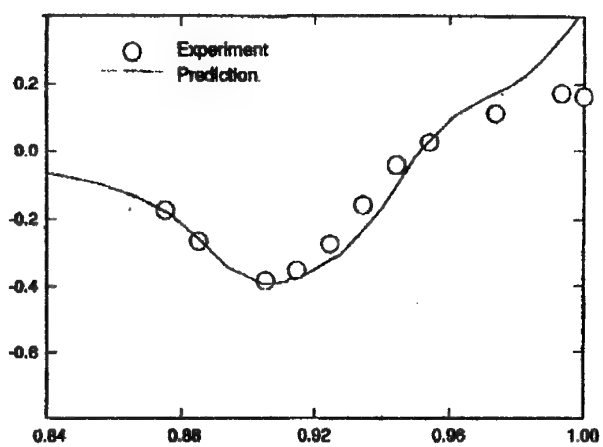


Figure 3.5-100 (Continued). Comparison of Surface Pressures ( $C_p$  vs.  $x/L$ ), Case B.4.1, Row 1



Contribution N11



Contribution N12

Figure 3.5-100 (Concluded). Comparison of Surface Pressures ( $C_p$  vs  $x/L$ ), Case B.4.1, Row 1

pressure in the final recompression region, by almost the same margin as in the shoulder and initial recompression regions.

It is difficult to draw any conclusions regarding tendencies of the Navier-Stokes methods based on these results. None of the algebraic or zero-equation turbulence models did well at the trailing edge, but the results were quite mixed for the one- and two-equation models.

It is impossible to separate the effects of adverse pressure gradient from the effects of plume entrainment in these data. However, these overprediction errors also could be consistent with an underestimation of the local entrainment of the plume close to the nozzle exit.

One comparison of the effect of grid density is presented in these results. Contribution N04 was computed using grid sequencing, that is, the solution first was driven to a partial state of convergence on a coarse grid. Those results were then used to initialize a finer grid by interpolation, and the solution was restarted and carried to convergence. The Contributors of N04 provided both solutions (coarse and fine) to the working group. These results are not a fully controlled grid density study, but they can be used to illustrate some points.

The solution on the coarse grid exhibited a slightly delayed recompression at the shoulder, with a subsequent under-prediction of pressure by a nearly-constant margin throughout the recompression region to the trailing edge. This behavior is similar to that of Contribution N09, though the grid density used in N09 seems more than adequate. The solution of N04 on the fine grid showed improved accuracy, though again there was a tendency for consistent under-prediction of pressure in the recompression region - by a smaller degree than was seen on the coarse grid.

These data show the expected trends. The grid with high density, the "fine grid," shows improved accuracy in all regions of the flowfield. However, one cannot determine from this Figure whether the "fine grid" density is adequate. The benefit from further increases in grid density is unknown. Another issue, not addressed in these data, is the topology of the grid, i.e., the orientation and structure of the grid.

Data for Row 2 are presented in Figure 3.5-101. This Row of taps is on the nozzle upper surface, part of the way to the side of the nozzle. The five contributions for this set of data produced results consistent with the previous group of comparisons. The experimental data are sparse for this case, but the Navier-Stokes CFD results showed good agreement with the data. The Euler result of Contribution E05 showed the (now) familiar over-prediction of the flow expansion near the nozzle shoulder. No pressure taps were provided close

to the nozzle exit in this row, so accuracy in the final recompression region cannot be assessed with confidence.

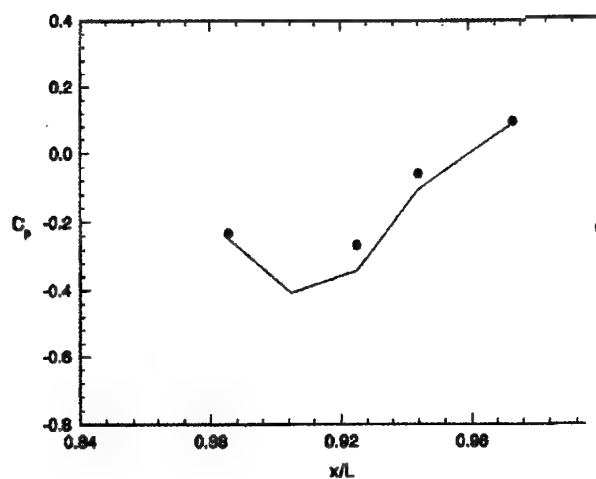
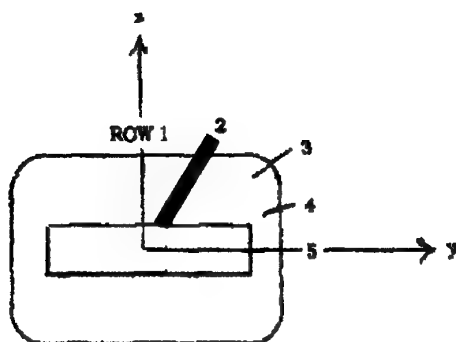
Row 3 is along the upper/outboard corner of this two-dimensional nozzle. The nozzle upper surface (e.g., Rows 1 and 2) experiences a strong expansion followed by a strong compression. The nozzle sidewall (Rows 4 and 5, not yet presented) has minimal expansion near the shoulder and a much smaller degree of recompression. The present location, Row 3, is in the transition between these two types of behavior. Since Row 3 also is a geometric transition between the upper and sidewall surfaces, this is the location where problems in grid generation would be most expected.

In this region, one might expect to find organized lateral flows in response to the pressure variations on the nozzle upper surface. In the shoulder region, the flow will tend to migrate from the sidewall up onto the nozzle, filling in the low-pressure expansion region. Farther aft, the reverse will occur: the elevated pressures in the nozzle recompression region will drive flow from the upper surface toward the sidewall. These lateral flows will be the strongest at the present location, Row 3. These flows also will tend to set up a system of streamwise vortices in the external flow, emanating from the corner location (Row 3). For further discussion of this phenomenon, the reader is referred to the discussion in Ref. 3.5-1 and Ref. 3.5-2.

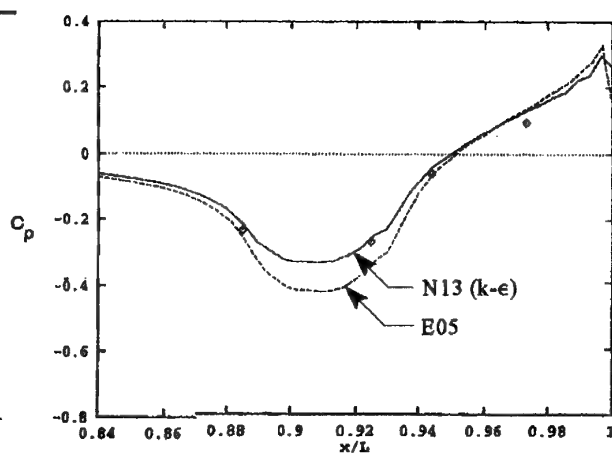
The pressure data comparisons for this Row are presented in Figure 3.5-102. Each prediction method does very well through the expansion region of the nozzle upper surface (around  $x/L = 0.91$ ). Differences in accuracy can be seen, however, in the initial recompression region. In this region, the lateral pressure gradients are reversing direction, shifting from flow onto the nozzle upper surface, in favor of flow off the nozzle upper surface. The secondary flow vortices which have been (presumably) created alongside the shoulder are now interacting with new vortices of opposite sign, created in response to the change in the direction of the lateral pressure gradients at the corner between the upper surface and the sidewall.

Several of the prediction methods do quite well in this complex flow region: N04 (B-B turbulence model), N02 (C-S and  $k-\epsilon$ ), N10 (J-L modified), E11, and N12 (B-L). The success of the Euler method E11 suggests that local features of viscosity modeling may not be critical here - by implication, the flows are locally inviscid depending more on viscous layers ahead of this region, and on the imposed pressure fields. Perhaps issues related to grid resolution are more important than turbulence modeling concerns, for this region.

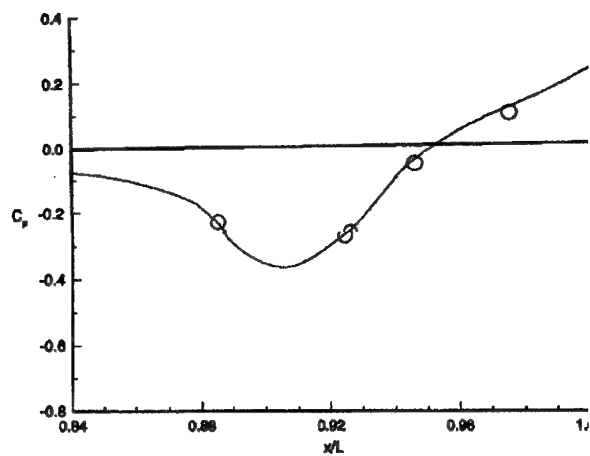
Methods E05, N12 (B-L), and N13 ( $k-\epsilon$ ) experience a localized instability, then they regain their accuracy. Contributions N03 ( $k-\epsilon$ ) and N11 (B-L) both overpredict pressure here. Interestingly, none of the methods under-



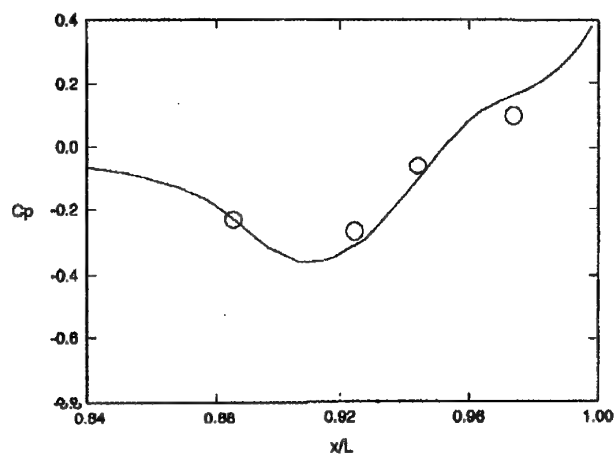
Contribution N04



Contributions E05 and N13

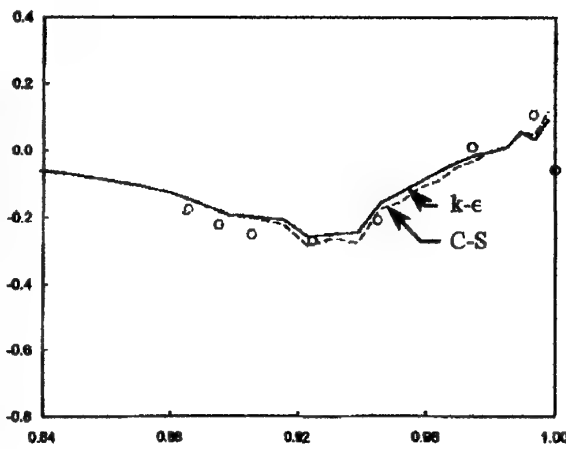
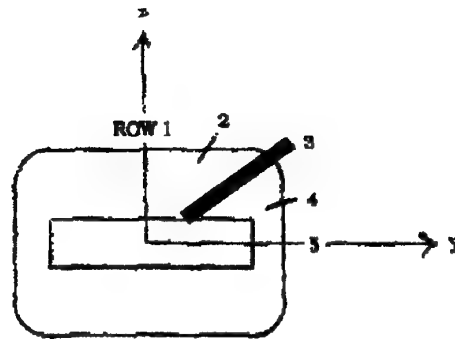


Contribution N10

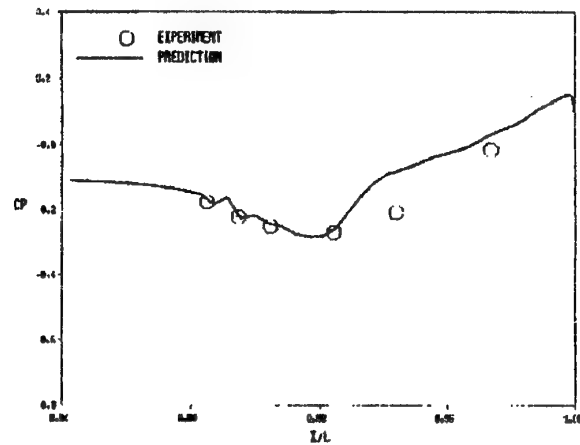


Contribution N12

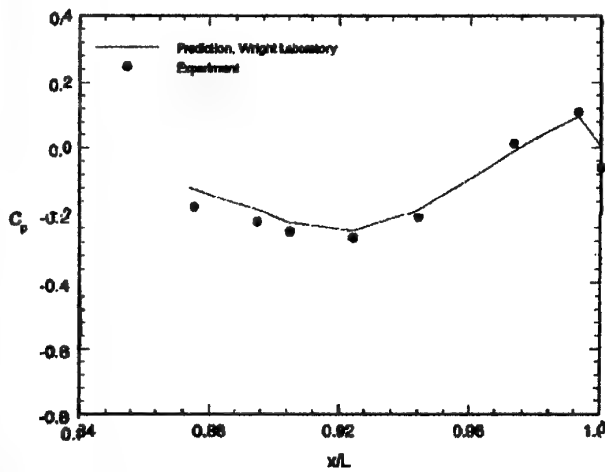
Figure 3.5-101. Comparison of Surface Pressures ( $C_p$  vs.  $X/L$ ), B.4.1, Row 2



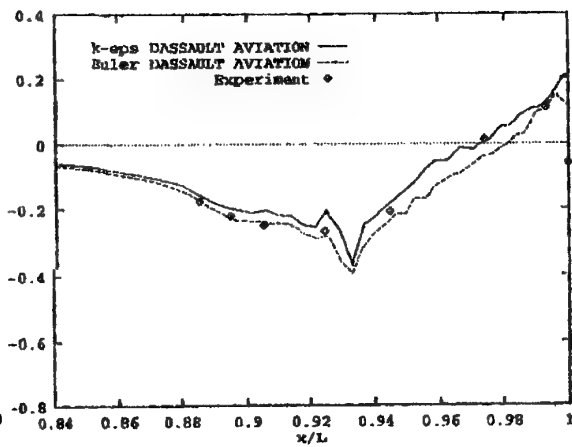
Contribution N02



Contribution N03



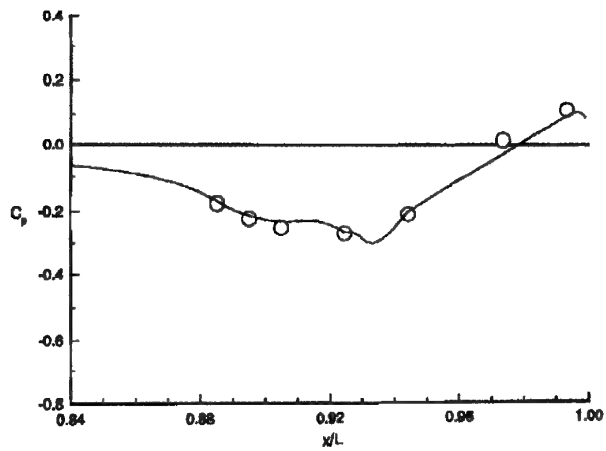
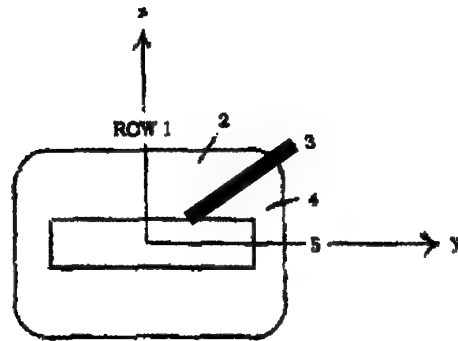
Contribution N04



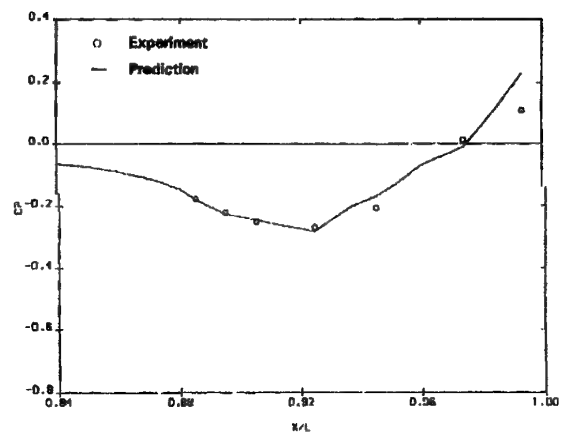
Contributions E05 and N13

Figure 3.5-102 (First Part). Comparison of Surface Pressures ( $C_p$  vs.  $x/L$ ), Case B.4.1, Row 3

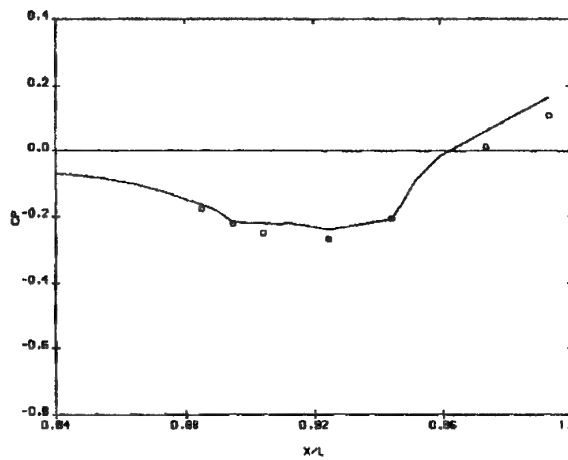




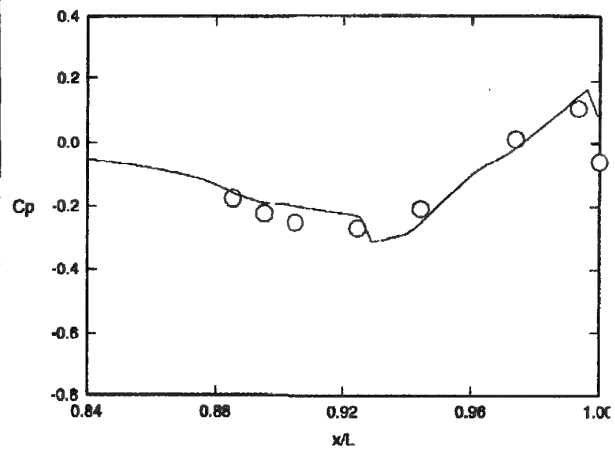
Contribution N10



Contribution E11



Contribution N11



Contribution N12

Figure 3.5-102 (Concluded). Comparison of Surface Pressures ( $C_p$  vs.  $x/L$ ), Case B.4.1, Row 3

predicted pressure in this region, even though several of them had underpredicted pressure in the adjacent shoulder region on the nozzle upper surface (e.g., Contributions N04, E11, N13).

Row 4 is on the nozzle sidewall, down part way to the lateral centerline. These comparisons are presented in Figure 3.5-103. As mentioned previously, the aftbody sidewall has very little contouring up to the final recompression region of the nozzle. A pressure minimum is seen around  $x/L = 0.91$  (alongside the shoulder on the nozzle upper surface) but the minimum pressure is much higher (closer to ambient) than was observed for Rows 1 and 2. The recompression, too, is fairly mild.

Ten solutions were contributed for this set of data. Each of them does fairly well, though none goes through the data. Interestingly, every method over-predicts pressure in the recompression region (to varying degrees).

The largest differences among the methods are seen close to the nozzle exit. Three of the predictions (N02 both turbulence models, and N12) show a pressure upturn here, while four of the predictions (N03, E05, and N10, N13) show a downturn. Experimental data are not available to assess these differing trends.

The pressure taps of Row 5 lie along the center of the aftbody and nozzle sidewall, i.e., the horizontal symmetry plane or sidewall centerline of the model. Eleven sets of solution data were provided. These surface pressure comparisons are presented in Figure 3.5-104.

The region near the nozzle shoulder expansion ( $x/L$  from 0.88 to 0.91) again caused difficulty for several of the predictions. The Euler methods (E05 and E11) predicted excessive expansion through this region. Their predictions are remarkably similar here. One Navier-Stokes solution (N09) showed a delayed pressure rise aft of the shoulder, consistent with its predictions at other rows of pressure taps. The other Navier-Stokes CFD methods, if they were in error here, all predicted pressures too high. This suggests the predicted boundary layer is thickening too rapidly over this curved surface, with a premature impact of the beginning adverse pressure gradient.

In the recompression region, all the predictions including the Euler methods matched the pressure gradient (i.e., the slope of the pressure curve). The data comparisons indicate the two Euler method predictions show accuracy similar to that of the Navier-Stokes methods for the initial recompression region (say,  $x/L$  from 0.92 to 0.97). This outcome suggests the pressure distribution is not strongly modified by viscous effects in this region.

Along the final recompression region, in the range of (say)  $x/L$  from 0.97 to 1.00, the experimental data are sparse. It

appears that this location also is not strongly affected by viscous interactions, as the Euler methods show accuracy similar to the Navier-Stokes methods (setting aside the instability in Contribution E11 at the nozzle trailing edge).

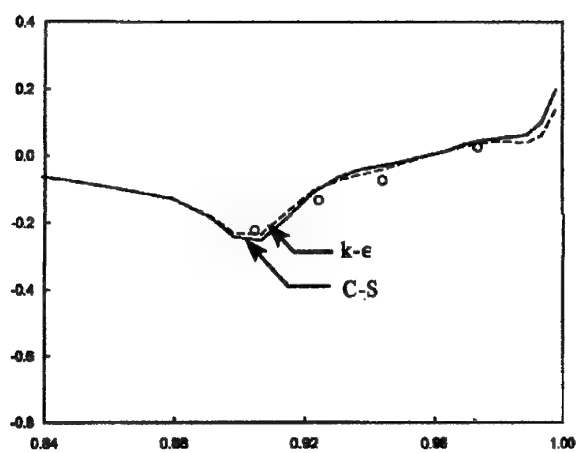
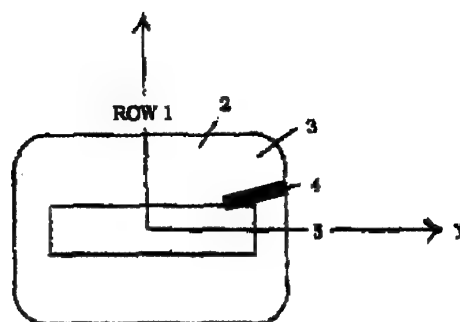
The experimental data show a strong downturn in pressure near the nozzle trailing edge. This feature was captured by most of the methods.

**Internal Surface Pressure Comparisons** - Experimental data were obtained for two rows of taps in the internal surfaces of the nozzle exit duct. In this region, the flow is subjected to a sustained favorable pressure gradient. Therefore, viscous modeling does not (presumably) contribute greatly to the achieved accuracy. However, the geometry is transitioning from a circular cross-section to a rectangular section at the throat and the nozzle exit (see 1). This type of transitional geometry poses some interesting problems in grid generation; which may have an impact in the predictions. Lateral (secondary) internal flows may be created in this transition region, giving rise to streamwise vortices. These vortices will convect downstream into the plume free shear layer, where they will have an impact on the shaping of that feature.

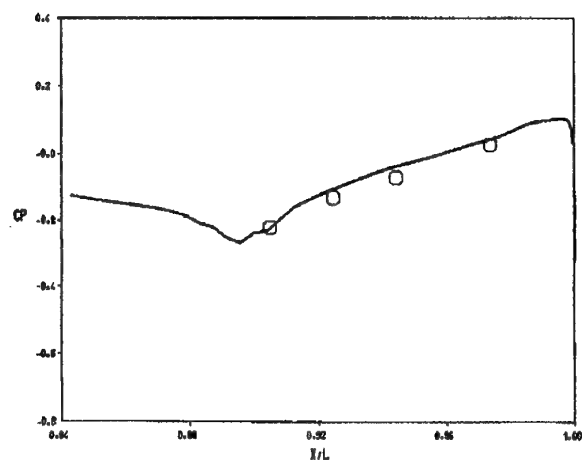
The internal duct features a throat, followed by an expansion region. The NPR is sufficiently high that the flow downstream of the throat remains supersonic. Therefore, this can be viewed as a problem in internal flow only. Since the exhaust flow is supersonic, the internal flow is effectively independent of the external flow.

Thus, to summarize:

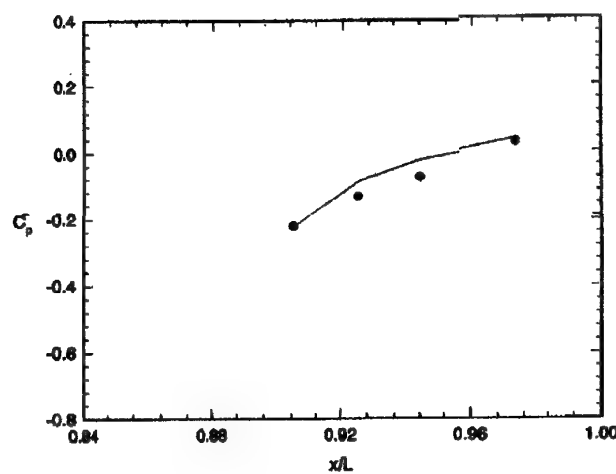
- The boundary layers are subjected to a strong favorable gradient throughout the nozzle. Further, the jet is exhausting into the external flow with a static pressure somewhat above the freestream static pressure (i.e., the boundary layer is not subjected to any adverse gradient at the nozzle exit, due to the external stream). Thus, viscous interactions should be minimal.
- The flow becomes supersonic before leaving the nozzle. Therefore, the internal flow is effectively decoupled from the external flow. This region can be viewed as an independent internal flow.
- The geometry transition from circular to rectangular duct cross-section with high aspect ratio may create problems in grid generation, whose impact possibly will be seen in the flow solutions.
- The sharp acceleration of the flow from subsonic to supersonic speeds, and the presence of high gradients due to wall curvature (particularly in the throat region), may lead to inaccuracies in the flow solutions.



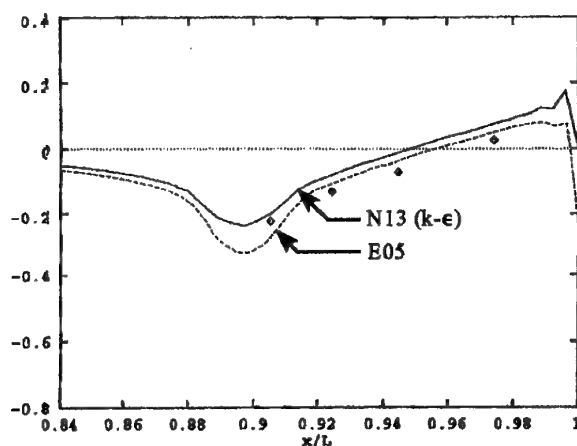
Contribution N02



Contribution N03

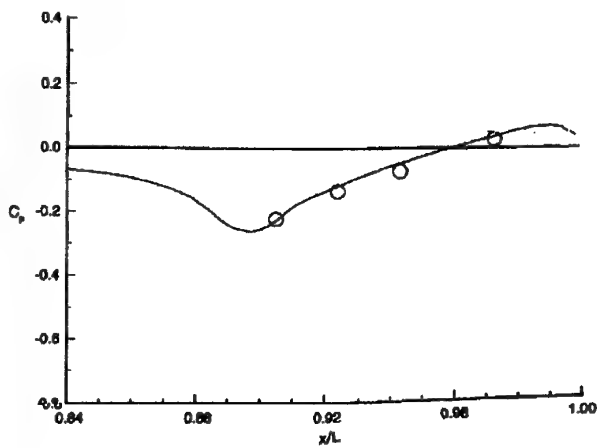
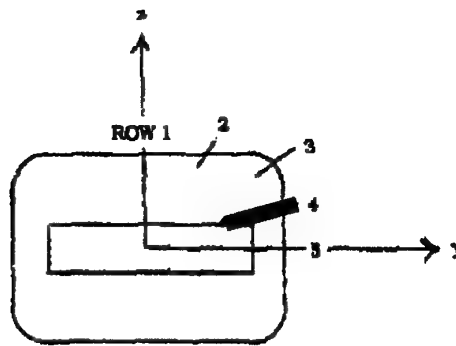


Contribution N04

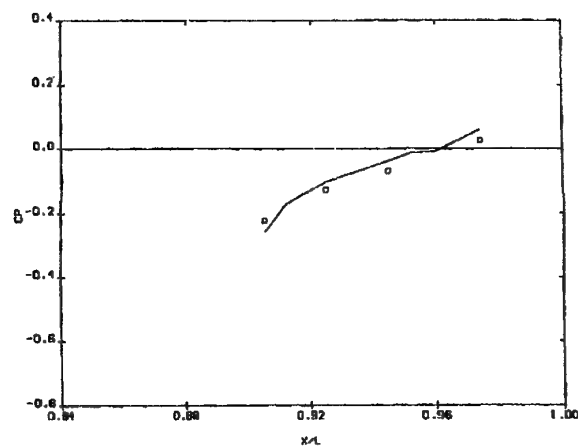


Contributions E05 and N13

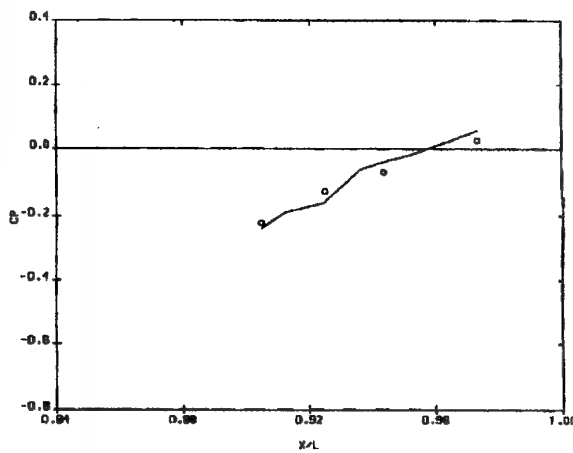
Figure 3.5-103 (First Part). Comparison of Surface Pressures ( $C_p$  vs.  $X/L$ ), Case B.4.1, Row 4



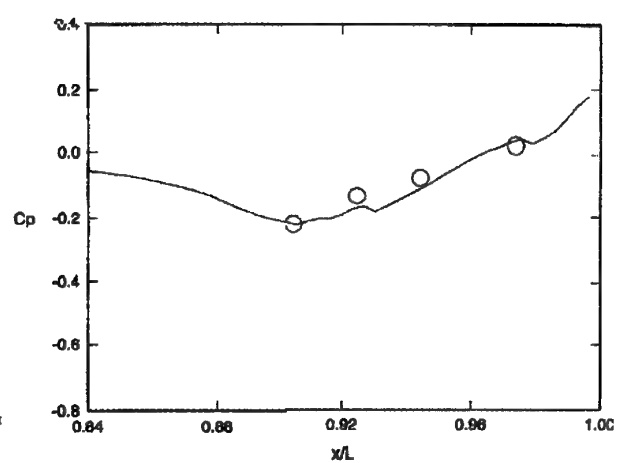
Contribution N10



Contribution E11



Contribution N11



Contribution N12

Figure 3.5-103 (Concluded). Comparison of Surface Pressures ( $C_p$  vs.  $x/L$ ), Case B.4.1, Row 4

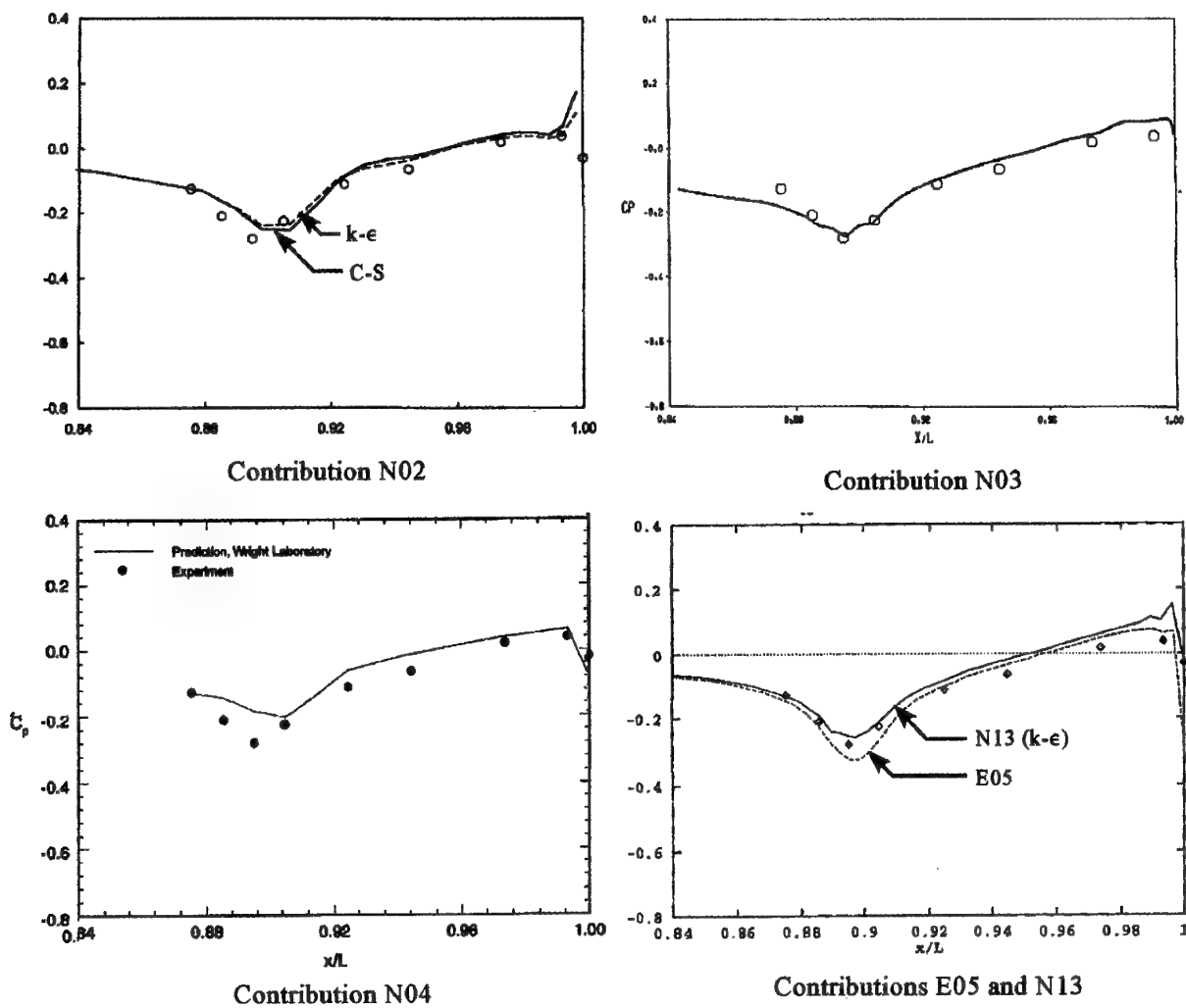
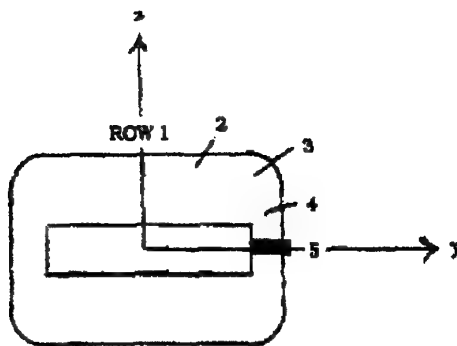
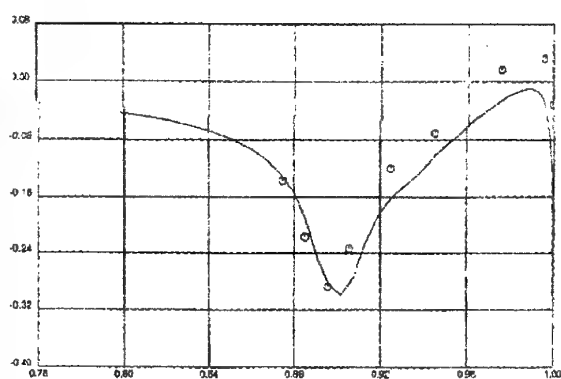
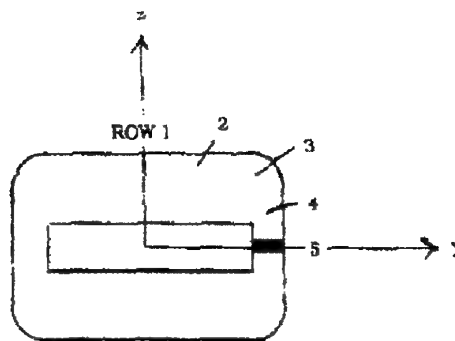
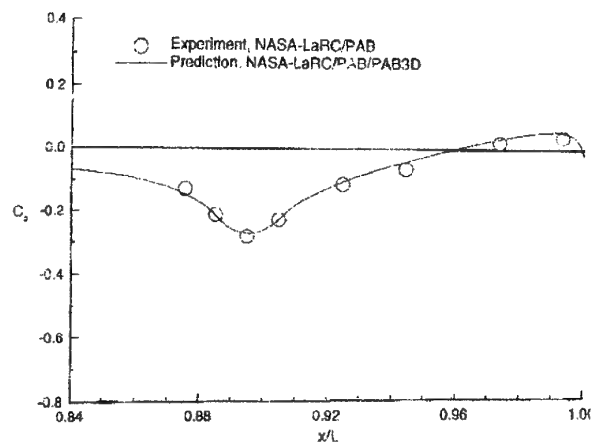


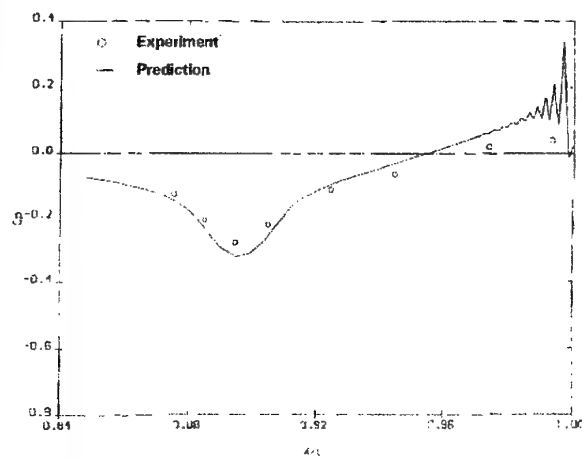
Figure 3.5-104 (First Part). Comparison of Surface Pressures ( $C_p$  vs.  $X/L$ ), Case B.4.1, Row 5



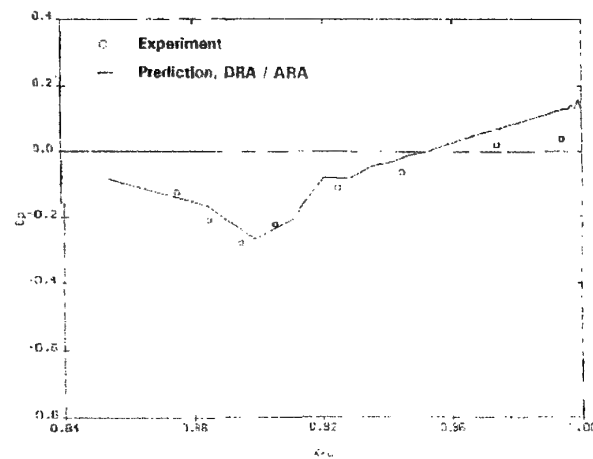
Contribution N09 (B-L turbulence model)



Contribution N10



Contribution E11



Contribution N11

Figure 3.5-104 (Continued). Comparison of Surface Pressures ( $C_p$  vs.  $X/L$ ), Case B.4.1, Row 5

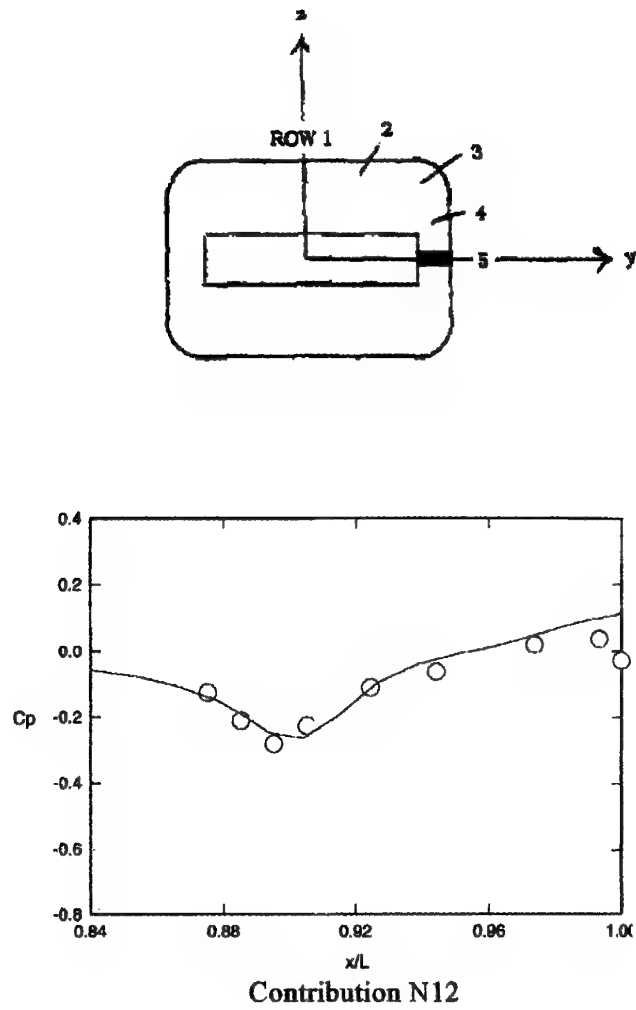


Figure 3.5-104 (Concluded). Comparison of Surface Pressures ( $C_p$  vs.  $X/L$ ), Case B.4.1, Row 5

- Several of the CFD solutions captured a shock-expansion wave structure in the nozzle, downstream of the throat. The experimental data are too sparse to confirm this wave structure, however it is believed the predictions are correct. This feature, too, may be difficult for some methods to resolve if the grid is sparse or the waves are resolved poorly in the numerical algorithm.
- Near a strong pressure gradient (i.e., throat region in this case) a numerical solution may exhibit "ringing", which is a spurious oscillation in the predictions. Or, the solution may smear the wave over a relatively wide region. Both of these are consequences of the numerical algorithm for modeling the underlying acoustic-convective scales of the flow.

The data for Row 6 (internal top centerline) are presented in Figure 3.5-105. Several of the predictions show the shock-expansion wave structure which was mentioned immediately above. This flow feature is seen in Contributions E05, N10, E11, and N11. Each of these predictions is in agreement with the sparse experimental data in the supersonic nozzle. The four predictions also exhibit a consistency among themselves. Therefore, it is believed that this structure does in fact exist, and should be resolved by the predictions.

Contribution N02 was focused on providing an economical solution for the external aftbody and nozzle plume flow-fields. The grid in the internal nozzle was recognized as being too sparse for accurate resolution of wave structures.

Contribution N04 shows good agreement with the experimental data, but provides no hint of the shock-expansion wave structure. Upon a query to the contributors, it was established that the post-processing procedure utilized CFD data only at the locations of the pressure taps. In between, a straight line was drawn. Therefore, the "missing" wave structure and apparent coarseness of the computation are quite possibly due to the post-processing scheme, and do not represent the underlying flow solution.

Contribution N03 resolves throat acceleration and hints at the presence of wave structures. However, the gradients are smeared over a significant distance, indicating that a high level of numerical dissipation may have been employed for this region.

Interestingly, the Euler solution E05 appears to resolve the throat expansion better than the companion Navier-Stokes solution, N13. This may indicate a high level of numerical dissipation in N13, or perhaps a lesser state of convergence due to the high computing requirements of the Navier-Stokes methodology. However, E05 shows a possible "ringing" upstream of the throat. Interestingly, E05 shows better accuracy at the first supersonic data point ( $x/L = 0.91$ ) but the Navier-Stokes solution N13 shows better agreement at other supersonic points. This is probably a fortuitous (non-

significant) outcome, which is dependent on the underlying supersonic wave system.

Contributions N10, E11, and N11 all do very well in this flowfield. Several of the solutions show a small upward deviation in pressure at  $X/L=0.89$  to  $0.90$ , before the sharp expansion begins. This positive "blip" is due to the inward turn of the nozzle internal wall, which was performed abruptly in the test article and in most of the CFD models. Thus, the positive deviation seems physically plausible, and should not be taken as an indication of a numerical oscillation.

Contribution N12 provides good accuracy at the throat. Downstream, the agreement with experimental data is fair and the wave structure is not captured. Perhaps this is due to using a coarse grid, or high numerical dissipation.

Row 7 is the nozzle sidewall (lateral) centerline. Along this line, the wall is essentially straight. The pressure variations are due to the curvature of the upper and lower walls.

The surface pressure comparisons for Row 7 are presented in Figure 3.5-106. These data are generally consistent with the data for Row 6, which were just discussed. The experimental data are quite sparse (four pressure taps). As before, some of the solutions consistently show a shock-expansion wave structure in the supersonic nozzle flow, which cannot be confirmed based on the sparse experimental data. However, for the reasons given above this feature (shock-expansion train in the nozzle) is believed to be present.

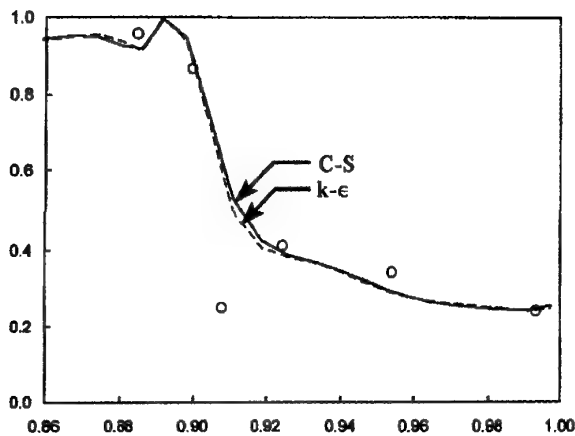
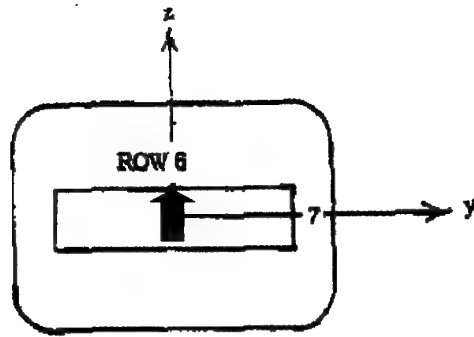
As was noted above, the grid for Contribution N02 is relatively coarse inside the nozzle, and yielded a low resolution solution. The post-processing method for Contribution N04 utilized CFD data only at the experimental pressure tap locations - good agreement is seen at those points, but the plots do not represent any features in the predictions in between the experimental data points.

Contribution N03 shows good agreement with the test data, and a relatively "soft" system of expansions and compressions inside the nozzle.

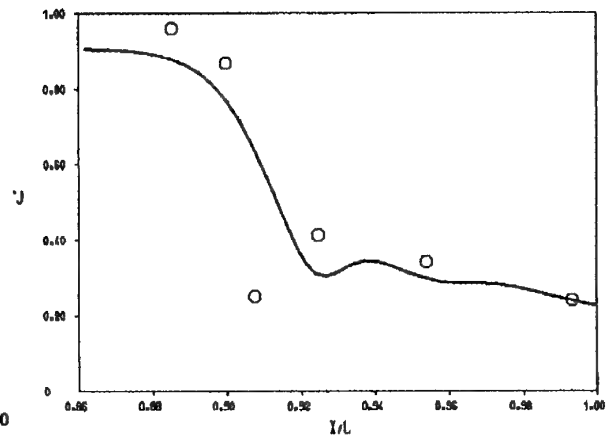
The Euler solution of Contribution E05 shows very good agreement with the data; noticeably better than the companion Navier-Stokes solution N13. One could speculate (as before) that the N13 solution is penalized by high numerical dissipation and/or a slow convergence rate compared with the Euler solution.

Two solutions (N10 and E11) are in agreement with the limited experimental data, and they clearly show the internal shock-expansion wave structure. Contribution N11 also suggests the presence of the wave structure, though not as strongly as in N10 and E11. Contribution N12 is in good

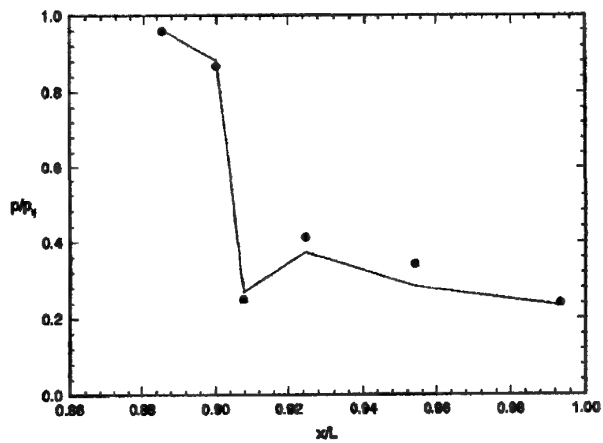




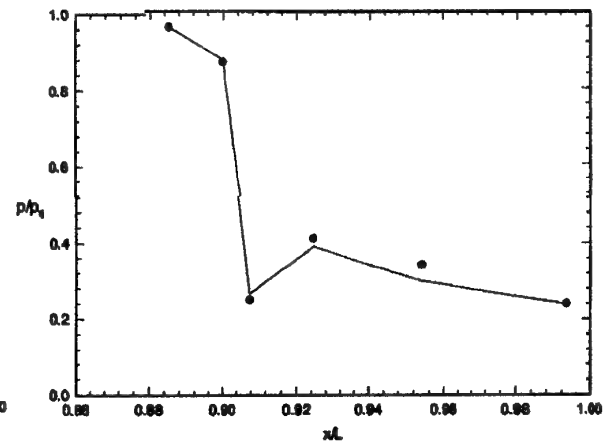
Contribution N02



Contribution N03



Contribution N04 (Coarse Grid)



Contribution N04 (Fine Grid)

Figure 3.5-105 (First Part). Comparison of Surface Pressures ( $P/P_t$  vs.  $X/L$ ), Case B.4.1, Row 6

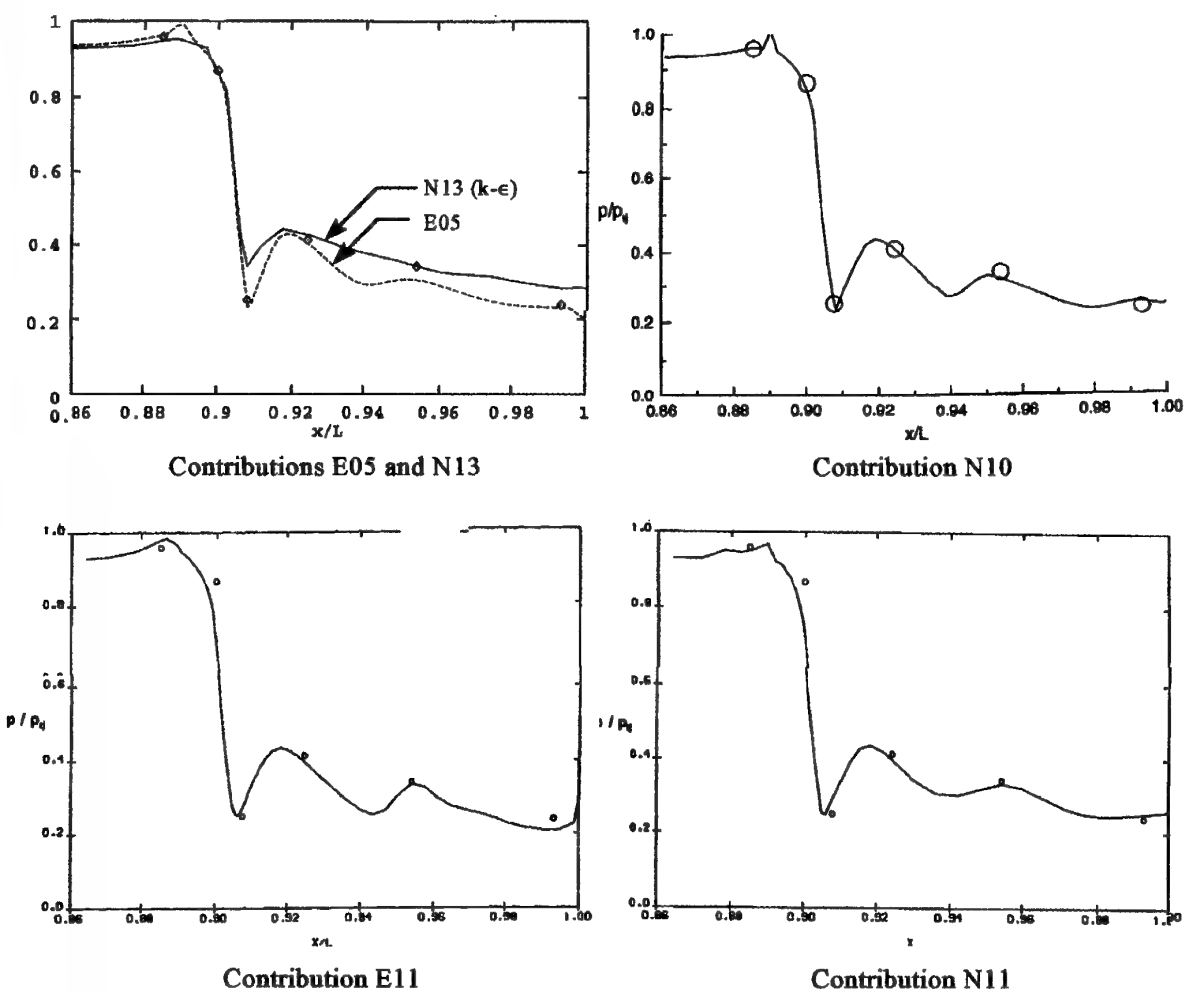
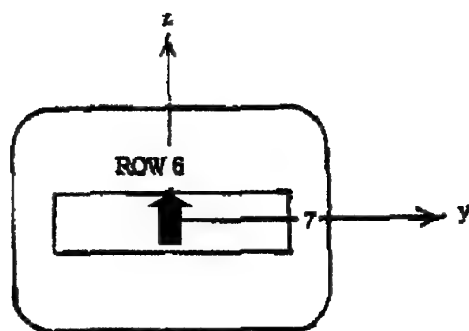


Figure 3.5-105 (Continued). Comparison of Surface Pressures ( $P/P_t$  vs.  $X/L$ ), Case B.4.1, Row 6

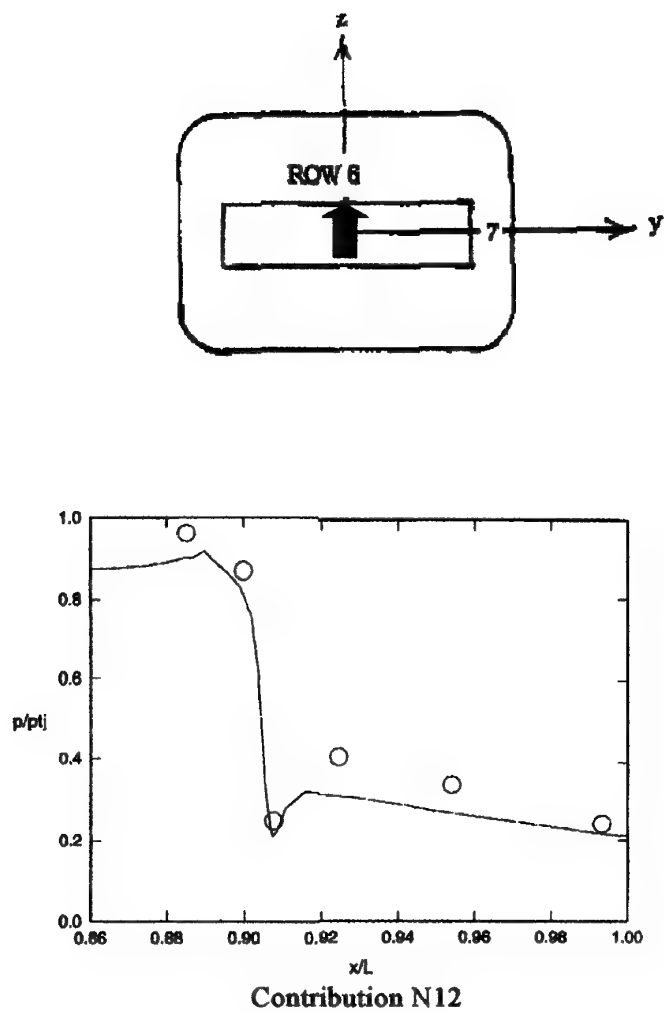
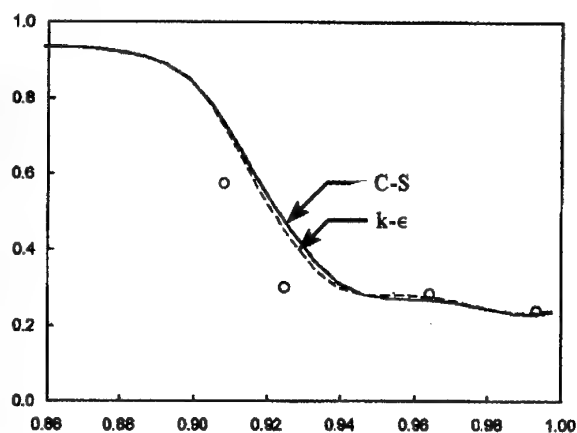
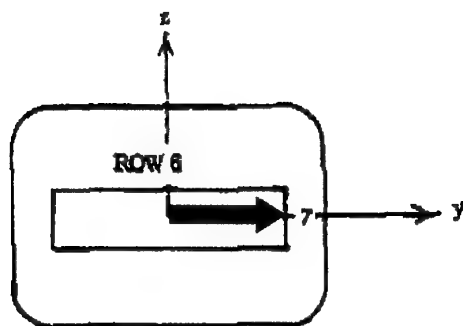
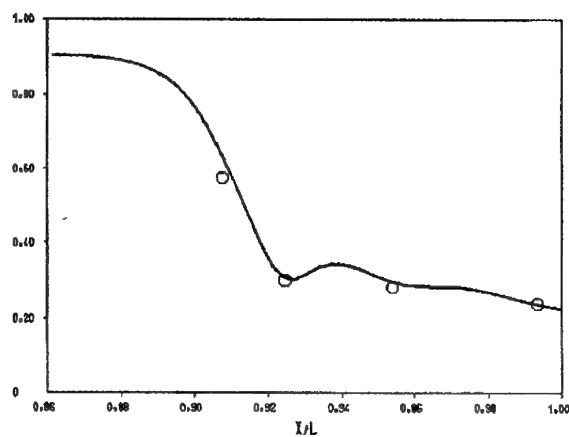


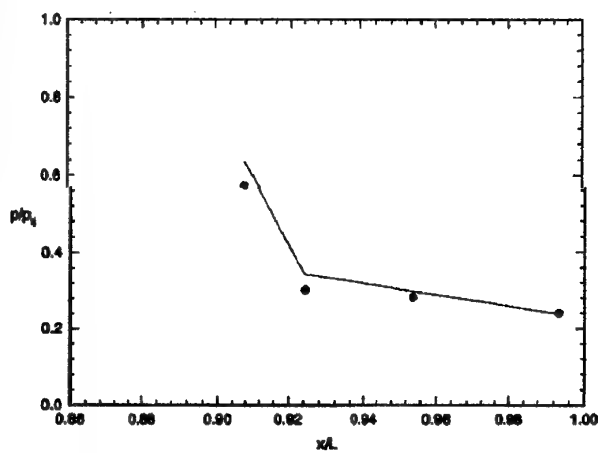
Figure 3.5-105 (Concluded). Comparison of Surface Pressures ( $P/P_t$  vs.  $X/L$ ), Case B.4.1, Row 6



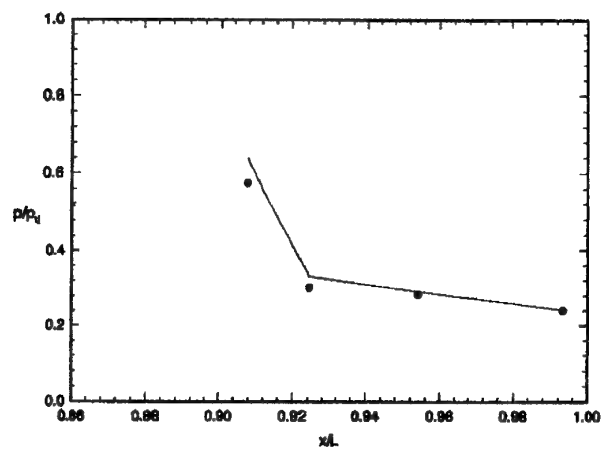
Contribution N02



Contribution N03

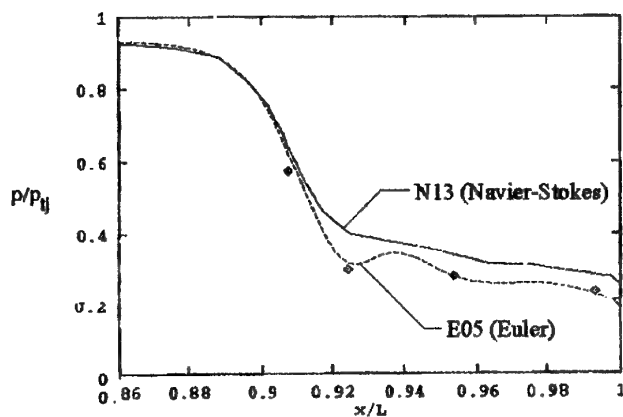
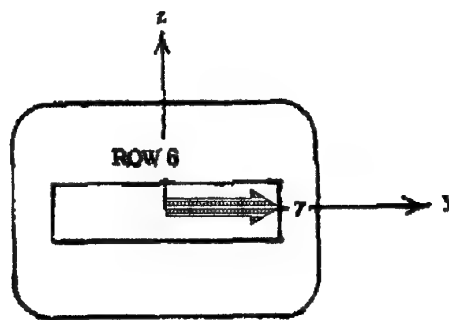


Contribution N04 (Coarse Grid)

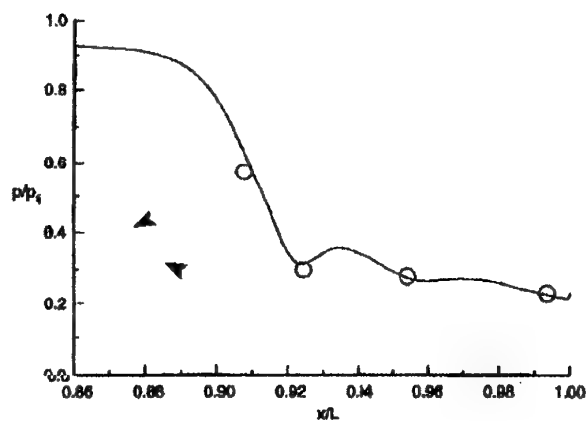


Contribution N04 (Fine Grid)

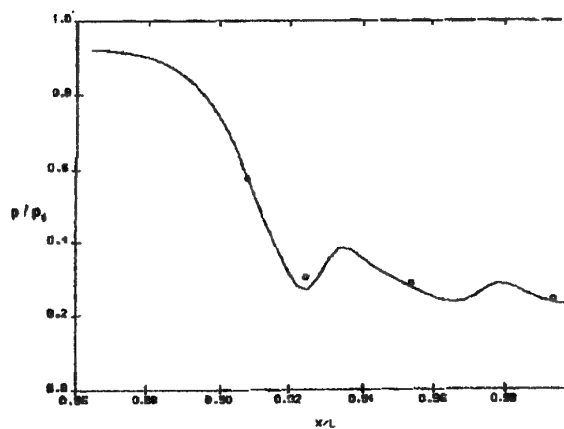
Figure 3.5-106 (First Part). Comparison of Surface Pressures ( $P/P_{tj}$  vs.  $X/L$ ), Case B.4.1, Row 7



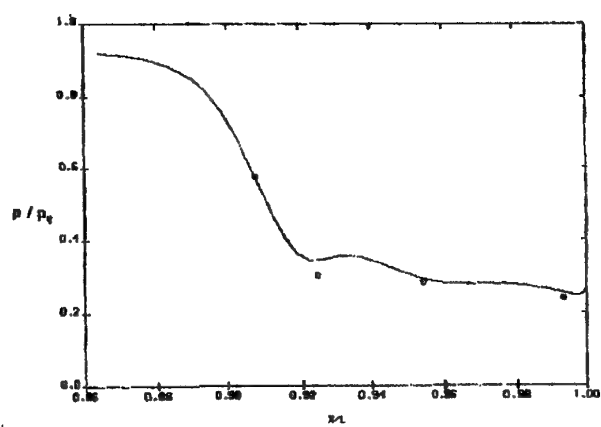
Contributions E05 and N13



Contribution N10



Contribution E11



Contribution N11

Figure 3.5-106 (Continued). Comparison of Surface Pressures ( $P/P_{tj}$  vs.  $X/L$ ), Case B.4.1, Row 7

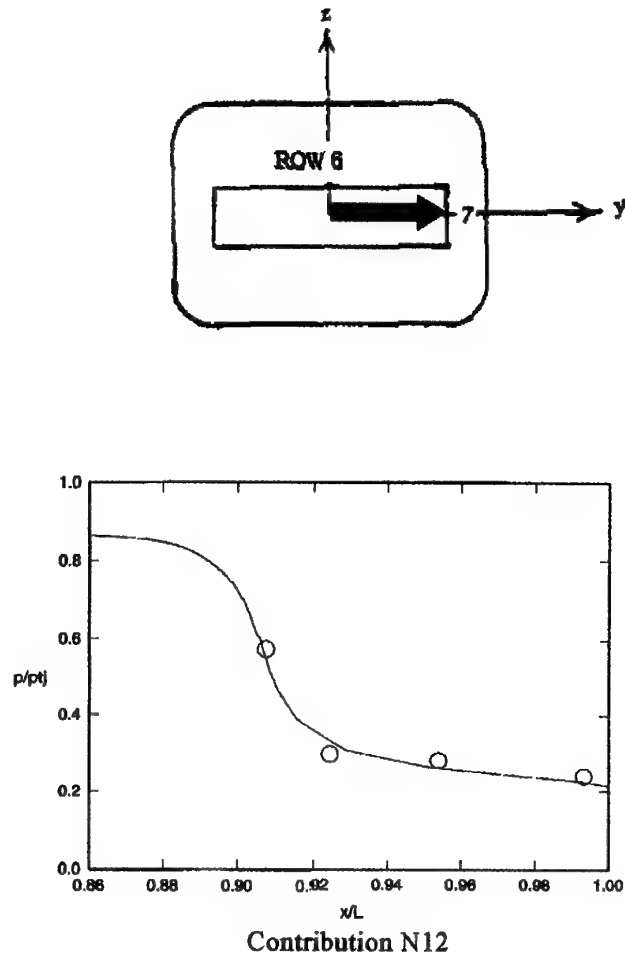


Figure 3.5-106 (Concluded). Comparison of Surface Pressures ( $P/P_t$  vs.  $X/L$ ), Case B.4.1, Row 7

agreement with the test data, though there is no hint of the (presumed) shock-expansion waves downstream of the throat.

In general, the internal flow predictions did not show the accuracy that might be expected in a flow with a sustained favorable pressure gradient, in a nozzle which is flowing full. Several of the contributors commented that they used only a coarse grid for the internal nozzle, thus enabling them to provide higher resolution in the external flow while minimizing the total cost of the CFD solutions. Based on the higher-resolution results, it appears that an internal structure of shock-expansion waves is present inside the nozzle. The need for resolving this wave system is unknown, in terms of impact on the flow predictions for the plume and the external nozzle.

**Plume Flowfield Comparisons** - The next portion of this discussion is directed toward the plume flowfields, in particular the free shear layer or mixing layer between the jet and the external stream. Experimental data were obtained by Pitot probe surveys at three axial locations: the nozzle exit ( $X/L = 1.00$ ), and at two downstream locations ( $X/L = 1.08$  and  $1.16$ ). The surveys at the nozzle exit could be viewed as establishing the flow properties at the beginning of the plume, where the viscous layer is mainly the aftbody-nozzle external boundary layer. Comparisons with the data at this location serve to confirm the accuracy of predicting the external flow and the jet exit flow approaching the nozzle exit.

The two downstream measurement locations serve to establish the ability to predict the plume mixing layer. This region is a difficult test of the turbulence models. Further, accuracy here is dependent on accuracy in predicting the upstream flows - in particular, the upstream turbulent boundary layer properties and the existence of any streamwise vortices in the free shear layer.

Several types of data are available to assess the modeling of this plume flowfield. First, a CFD prediction will be presented of the velocity vector field at the nozzle exit. Next, a qualitative (visual) comparison will be made of experimental surveys and CFD predictions defining the plume shape at the downstream measurement location ( $X/L = 1.16$ ). Finally, quantitative comparisons will be made between test data and predictions for two circumferential survey angles, at all three axial survey stations.

This can be viewed as a demanding prediction for the CFD methods. Clearly, the flows in the plume and the free shear layer depend on the accuracy of the upstream predictions. Several other complicating factors also are present:

- Turbulence models have uncertain accuracy for plumes and free shear layers, in general.

- Most turbulence models contain additional terms which differ between axisymmetric and planar free shear layers. The combination of planar flows and lateral curvature in the Case B.4 free shear layer thus poses a particular challenge.
- The free shear layers feature periodic interactions with the shock-expansion wave structure inside the supersonic jet. These interactions create internal pressure gradients in the mixing layer which additionally tax the turbulence models.
- The large gradients present in the plume, both axially and laterally, mean that high grid density must be provided for their resolution. If adequate grid is not provided, accuracy will be compromised. If a high density grid is used, the solution convergence rate will be penalized and (perhaps) numerical modeling deficiencies will come to the fore.

The crossflow velocity vectors in the nozzle exit plane, as predicted in Contribution N03, are presented in Figure 3.5-107. In the emerging jet flow (lower left portion of the Figure), the flow has a slight upward angle. This is due to the slope of the upper and lower walls of the internal nozzle.

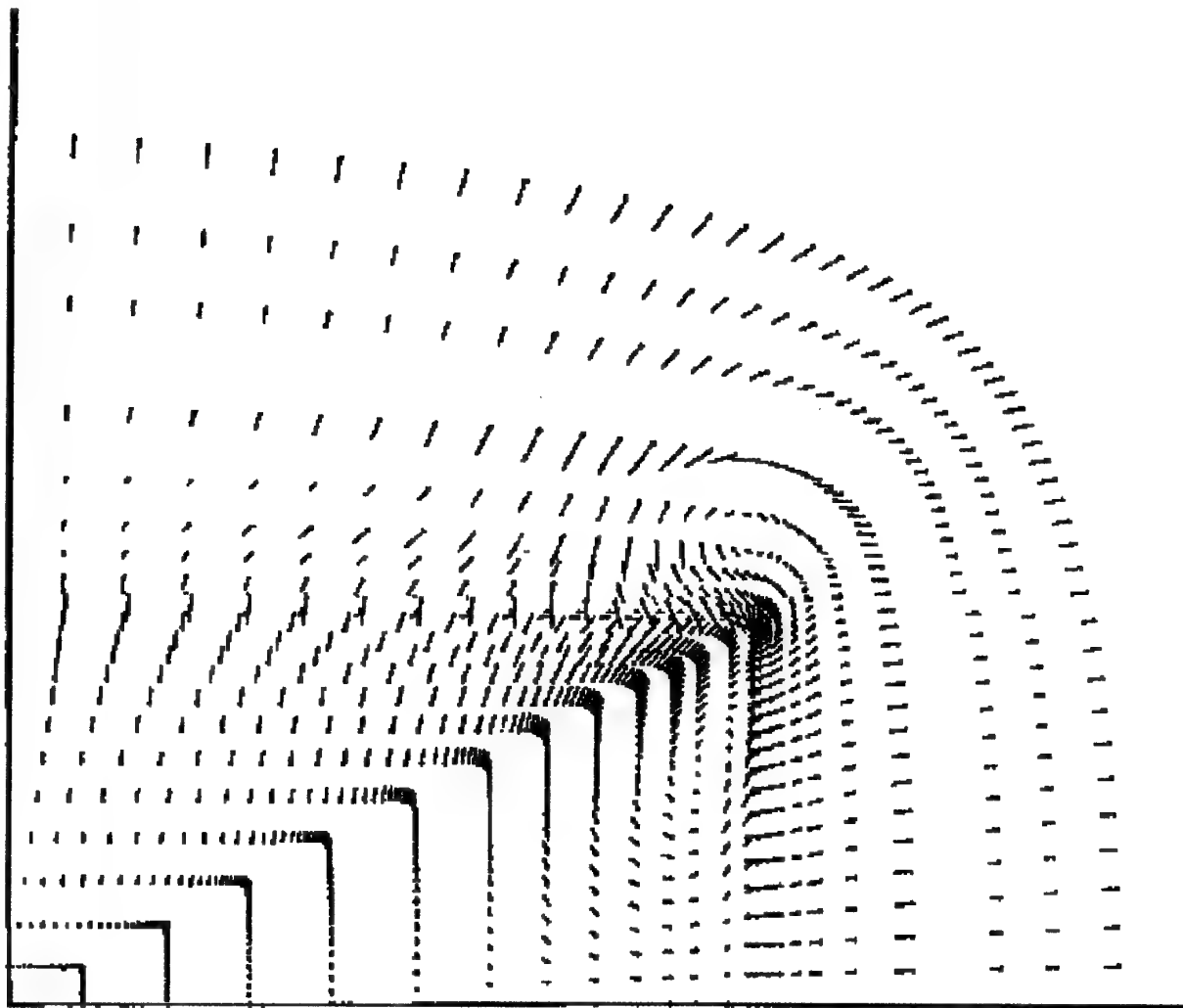
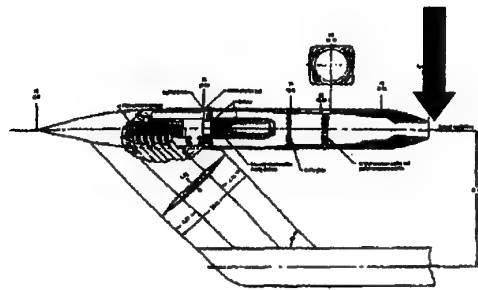
The internal flow also shows a clear counter-clockwise rotation along the internal nozzle sidewall, below the junction with the internal upper wall (lower center portion of the Figure). This is clear evidence of a predicted streamwise vortex, presumably arising due to lateral pressure gradients from the internal nozzle shape transition and the curvature of the internal upper and lower walls.

The external flow (center of the Figure) shows a significant clockwise-rotating vortex. This streamwise vortex, presumably, was created in the nozzle recompression region as the flow "spilled" over the sidewall from the more contoured upper wall.

The external flow takes a general trend away from the nozzle axis. This is taken to be a result of the general compression of the external flow which is occurring on the nozzle surface at this location.

The experimental plume free shear layer was extensively surveyed at the downstream location,  $X/L = 1.16$ . CFD predictions at this location were provided by seven contributors. These data are presented in Figure 3.5-108. For reference, the Pitot probe survey locations for the quantitative comparisons (following) also are noted on this Figure.

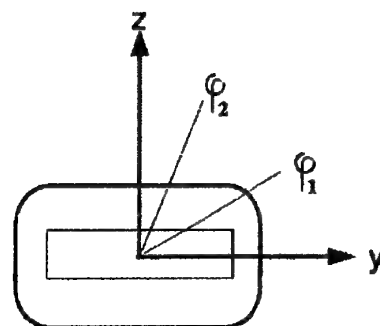
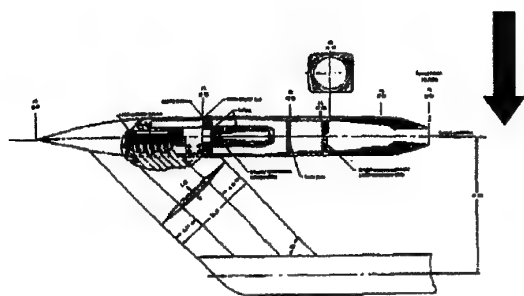
The experimental data show a fairly thick free shear layer has formed at this location. However, a clear inviscid core persists in the plume. The curvature of the vertical portion of the free shear layer (the portion which emerged from the



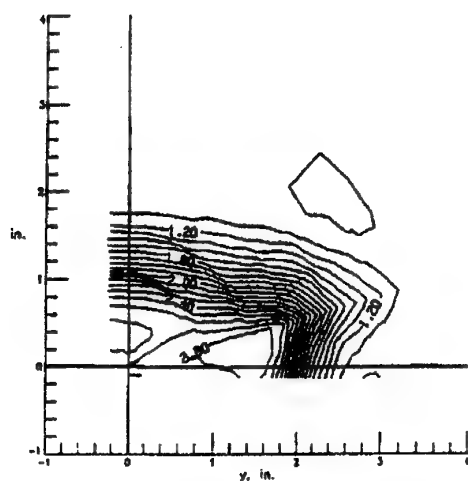
Contribution N03

Figure 3.5-107. Predicted Plume Velocity Vectors, Case B.4.1,  $X/L=1.00$  (Nozzle Exit Station)

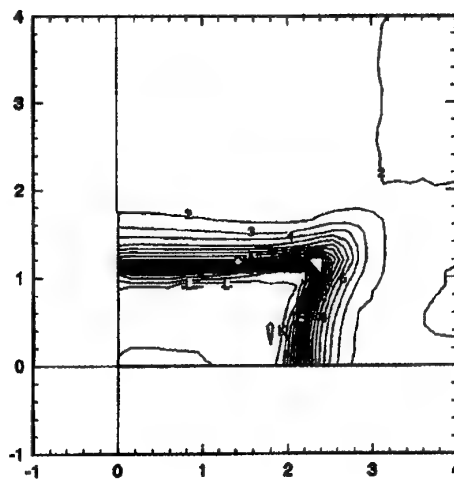




Pitot Probe  
Survey Locations

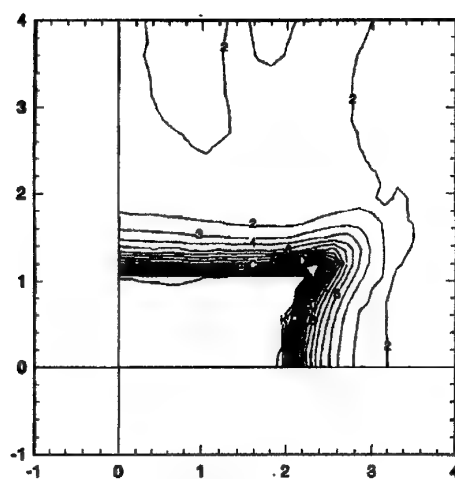


Experiment



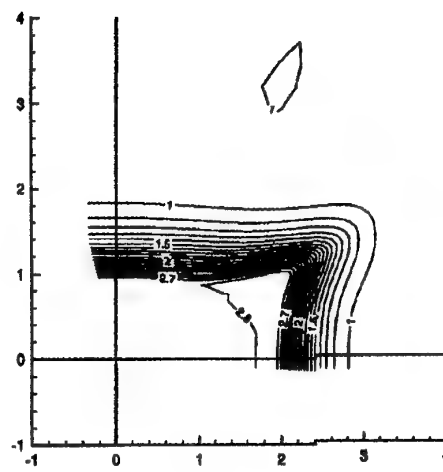
Contribution N04 (Coarse Grid)

Level	$p_0/p_\infty$
M	3
L	2.9
K	2.8
J	2.7
I	2.6
H	2.5
G	2.4
F	2.3
E	2.2
D	2.1
C	2
B	1.9
A	1.8
9	1.7
8	1.6
7	1.5
6	1.4
5	1.3
4	1.2
3	1.1
2	1
1	0.9



Contribution N04  
(Fine Grid)

Level	$p_0/p_\infty$
M	3
L	2.9
K	2.8
J	2.7
I	2.6
H	2.5
G	2.4
F	2.3
E	2.2
D	2.1
C	2
B	1.9
A	1.8
9	1.7
8	1.6
7	1.5
6	1.4
5	1.3
4	1.2
3	1.1
2	1
1	0.9



Contribution N10

Figure 3.5-108 (First Part). Predicted Plume Pitot Pressure Contours, Case B.4.1,  $X/L=1.16$

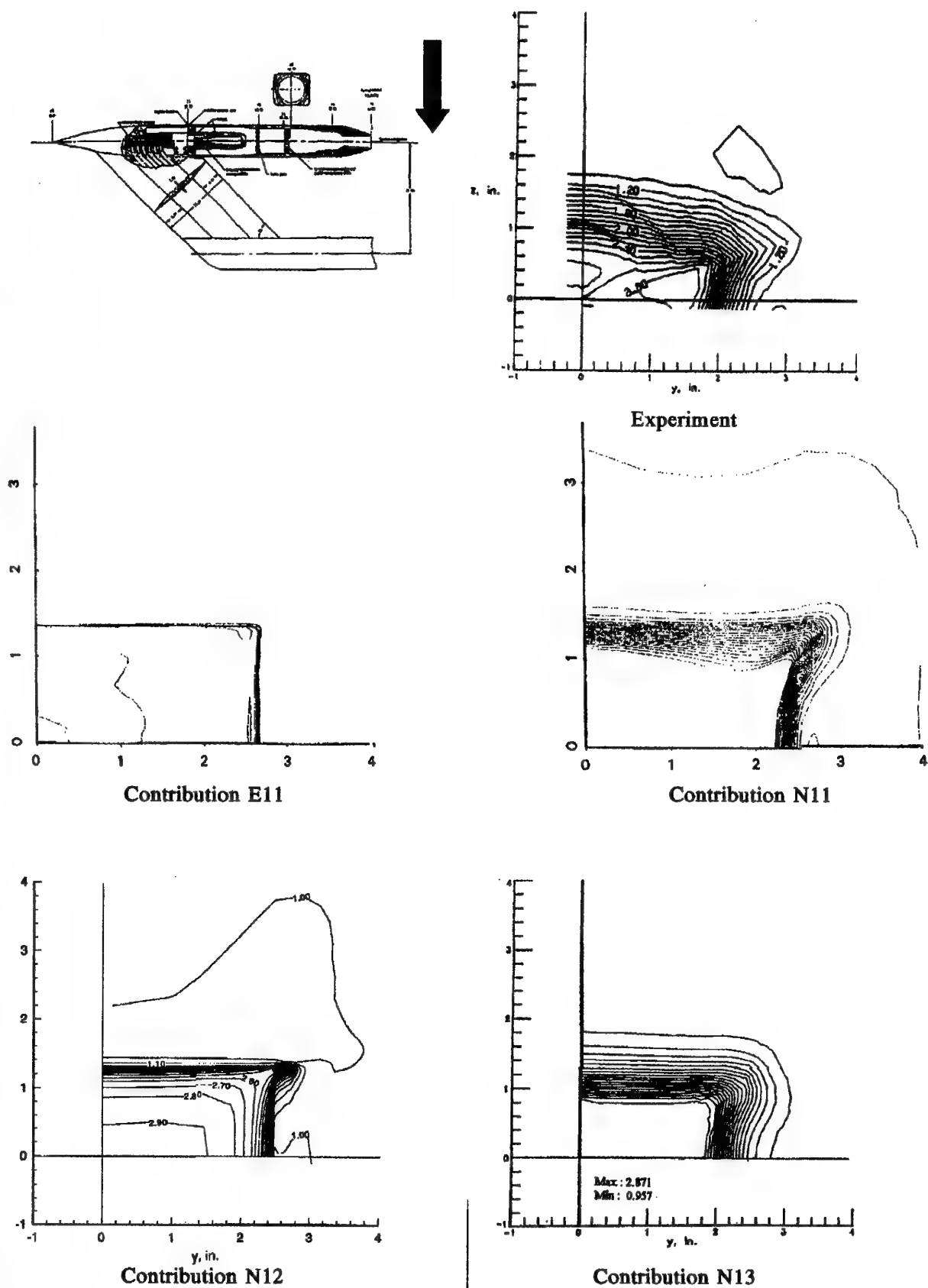


Figure 3.5-108 (Concluded). Predicted Plume Pitot Pressure Contours, Case B.4.1,  $X/L=1.16$

nozzle sidewall) suggests the shape is being modified by a clockwise-rotating vortex. This vortex (presumably) came from the spillage of flow from the nozzle upper (compression) surface over to the sidewall in the nozzle recompression region.

The CFD predictions all show a thinner free shear layer, compared with the experimental data. Generally, the outer extent of the free shear layer is predicted about right, but the inward spread of the mixing layer is significantly under-predicted. The influence of a clockwise vortex can be seen in these predictions.

Quantitative comparisons are presented next, based on the experimental Pitot probe surveys at two circumferential locations. The first location,  $\phi_1 = 24.3^\circ$ , passes through the plume corner interaction (see Figure 3.5-108 for location reference). This is a particularly complex portion of the flow, which poses several problems for CFD predictions. The second location,  $\phi_2 = 69.2^\circ$ , passes through the (generally) planar portion of the upper free shear layer.

These comparisons are made in terms of Pitot pressure, which is the measurement obtained by a simple measurement probe. At subsonic speeds, the Pitot pressure is the same as the total pressure. At supersonic speeds, the Pitot pressure and the total pressure differ because a normal shock stands immediately ahead of the (blunt) measurement probe. The total pressure in the flow (ahead of the probe and its associated normal shock) is reduced by flowing through the probe standoff shock. The probe measures the total pressure behind the standoff shock, called the Pitot pressure. However, in the absence of the probe, the flow at that location would be at the local total pressure, not the measured Pitot pressure. The Pitot pressure depends on the local total pressure, and the local Mach number (i.e., the strength of the normal standoff shock).

The first set of comparisons (Figure 3.5-109) are located at the nozzle exit plane,  $X/L = 1.00$ . These comparisons can be viewed as an assessment of accuracy in predicting the flows over the aft portion of the nozzle. The ability to predict the free shear layer is not assessed in these first comparisons.

The data at this location have the following characteristics, starting from the nozzle axis (the lower limit of each plot):

- a) The nearly uniform core of the jet flow.
- b) The outer edge of the internal boundary layer, seen as a gradual reduction of velocity over several of the closely-spaced data points.
- c) The large velocity jump due at the boundary between the internal and external streams.

- d) The velocity deficit of the external boundary layer, which gradually recovers to the uniform external free stream.

Most of the methods capture the Pitot pressure at the jet core. The experimental data clearly show that the Pitot pressure at the jet axis is slightly reduced; a short distance from the axis the Pitot pressure is higher. This is a consistent result in the experimental data, and it is seen in several of the predictions as well (N03, N04, N10, N11). This lower Pitot pressure means that either the total pressure is lower on/near the axis, or the Mach number is higher (leading to elevated losses as the flow passes through the normal shock ahead of the measuring probe).

Some of the CFD flow predictions indicated that a shock-expansion wave system may exist inside the nozzle (but this cannot be established with the available experimental data). In that event, it is possible that higher total pressure losses may have occurred along the axis of the jet due to repeated crossings of the shock waves in this presumed internal wave system. Further, it seems plausible that some of the shock intersection on the axis of the internal nozzle may have Mach-type reflections on the symmetry axis, producing a small normal shock rather than two crossing oblique shocks. While this discussion is based on limited evidence, such an interaction could account for a deficit in total pressure with a well-defined boundary in the experimental data, and in some of the CFD solutions.

The distance from the jet axis to the inner edge of the mixing layer (i.e., the high pressure plateau) is predicted accurately by all methods. This is only to be expected, since the location is immediately at the jet exit.

The mixing layer has minimal thickness at this location. The outer edge of the mixing layer clearly shows the velocity deficit of the external nozzle boundary layer. One of the Euler methods (E11) shows a clear example of "ringing" at both limits of the free shear layer.

Next, we will consider the velocity deficit from the external boundary layer (normalized distance  $y > 2.8$  for  $\phi_1$ ,  $y > 1.2$  for  $\phi_2$ ). Since the free shear layer only forms at this point, and therefore has not evolved at all, these comparisons in some sense pertain more to the accuracy of modeling the external nozzle wall boundary layer, rather than the free shear layer.

The Euler methods E05 and E11, as would be expected, are in poor agreement with the data. Most of the Navier-Stokes methods did well here (the reader is reminded that the boundary layer remains attached for this case).

Most of the methods produce the correct asymptotic value of uniform Pitot pressure (or total pressure, since the flow here is subsonic). It is puzzling to note that the data from con-

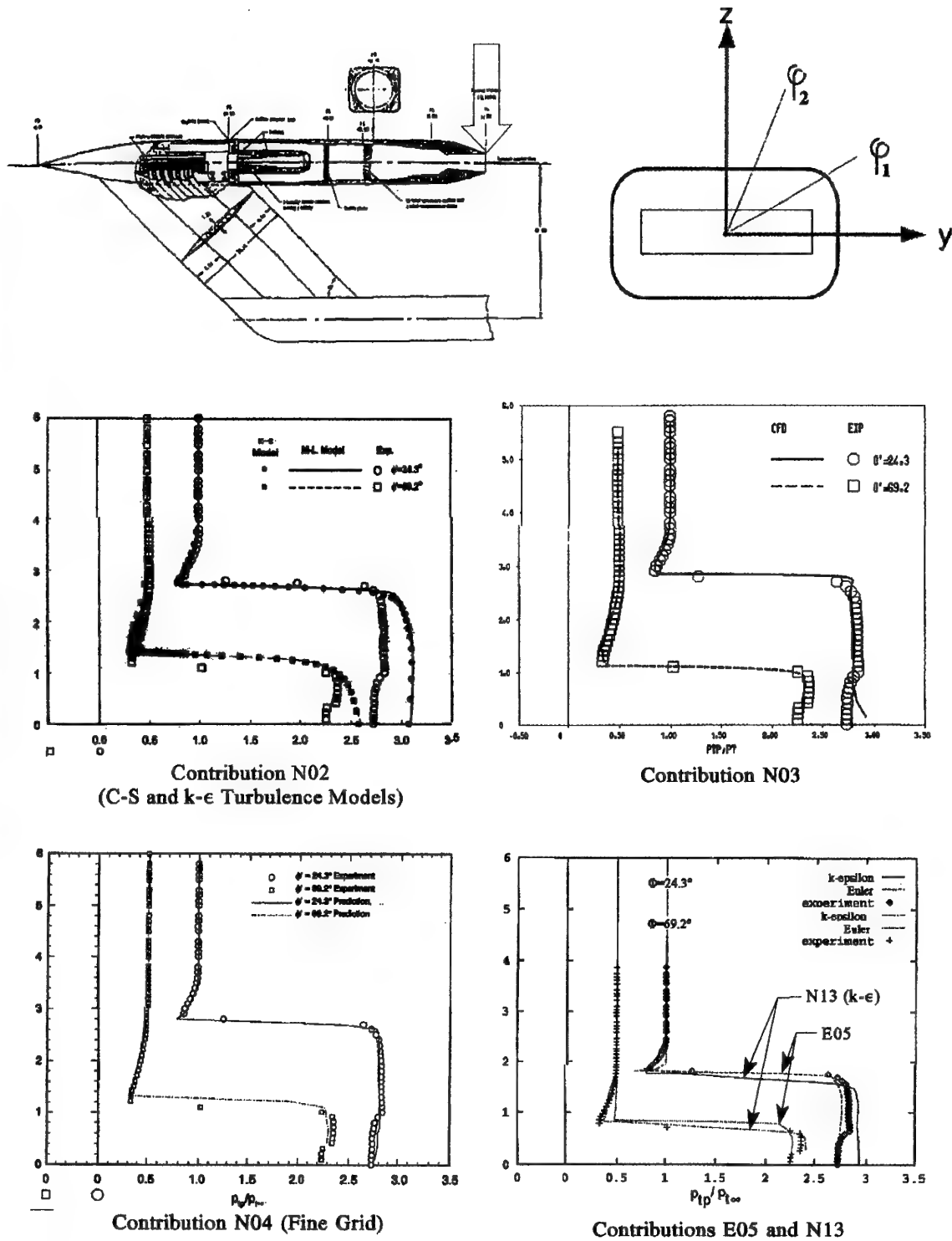


Figure 3.5-109 (First Part). Comparison of Plume Pitot Pressures, Case B.4.1,  $X/L=1.00$  (Nozzle Exit Station)

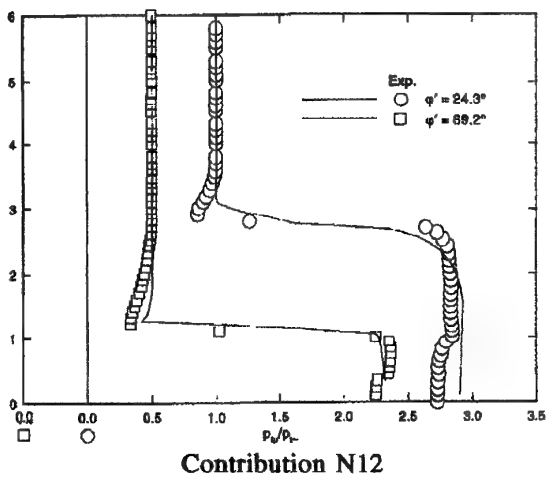
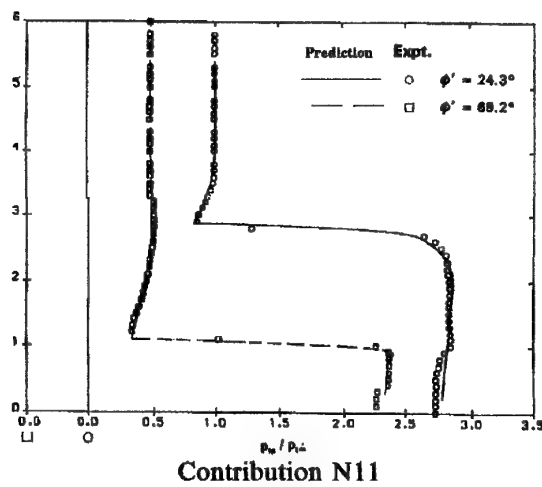
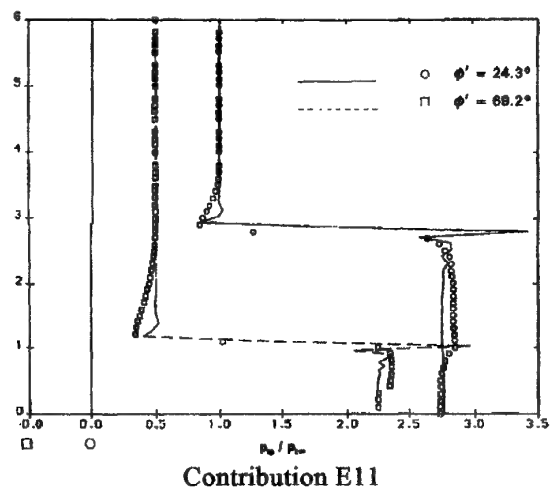
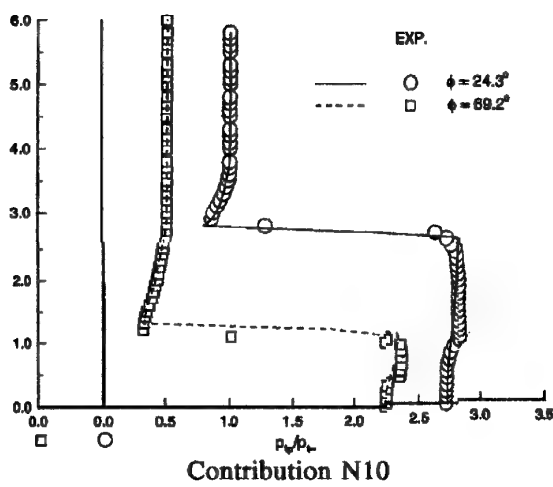
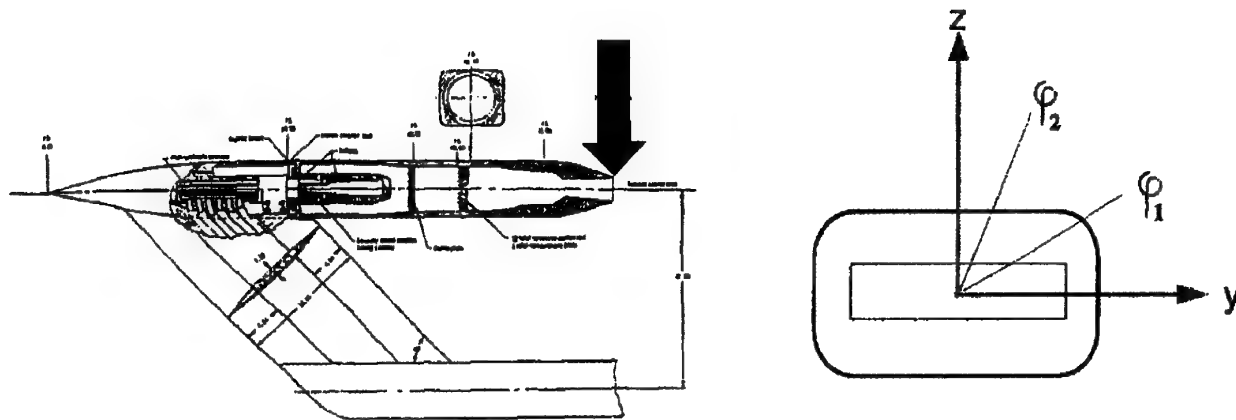


Figure 3.5-109 (Concluded). Comparison of Plume Pitot Pressures ( $P/P_{t,\infty}$  vs  $R$ ), Case B.4.1,  $X/L=1.00$  (Nozzle Exit Station)

tribution E11, however, arrive at a different value far from the jet.

At the next measurement station ( $x/L = 1.08$ ) the free shear layer evolution has begun. Pitot pressure comparisons at this station are presented in Figure 3.5-110. The features of the flowfield at this point include:

- The Pitot pressure at the jet axis is somewhat reduced from that at points surrounding the axis. This may be due to reduced total pressure on the axis, or elevated Mach number.
- A clearly defined free shear layer exists, between the jet inviscid core and the external freestream.
- A velocity deficit remnant of the external nozzle boundary layer remains at the outer edge of the free shear layer.

Both Euler methods under-predict the Pitot pressure in the core of the jet. If we can presume the flow to be inviscid here (i.e., no total pressure losses up to this point), then this discrepancy must be due to the predicted Mach number being too high, or therefore the static pressure is too low.

The Pitot pressure at the inviscid core of the jet is predicted accurately by most of the Navier-Stokes methods. Most of these contributions also show increasing Pitot pressure in the jet core, moving away from the axis.

None of the methods did particularly well at the free shear layer. Contribution E11 again shows classical "ringing" at both limits of the mixing layer. All of the Navier-Stokes methods placed the inner edge of the free shear layer too far from the jet axis - i.e., inadequate inward spreading. They did much better at locating the outer edge of the mixing layer.

One can only speculate at the reasons for this consistent bias among all the predictions. The results nevertheless are entirely consistent. This behavior, however, has been noted (indeed, it is a classical result) in comparing predictions for planar and axisymmetric jet mixing layers. In general, turbulence models which are accurate for planar free shear layers, predict an inadequate inward spreading rate for axisymmetric free shear layers. To compensate for this, additional terms may be added to the turbulence model. This observation leads to the suggestion that the present mixing layer, at least at its inner edge, "behaves" more like an axisymmetric layer rather than a planar layer. It also may be that the streamwise vortices present in the flow are enhancing the mixing rate preferentially in the inward direction.

The final set of comparisons is for the downstream station,  $x/L = 1.16$ . These comparisons are presented in Figure 3.5-111. The reader is reminded that contour plots of Pitot

pressure, in the crossflow plane, were presented previously (see Figure 3.5-108).

The experimental data indicate the following features in the flowfield at this station:

- The plume retains an inviscid core. The Pitot pressure is slightly lower on the jet axis, compared with nearby points in the inviscid portion of the jet.
- The free shear layer is being modified under the influence of streamwise vortices which were generated on the internal and external nozzle surfaces.
- The outer edge of the free shear layer shows no remaining trace of the velocity deficit from the external nozzle wall boundary layer.

The results at this location are consistent with the observations at the previous location. The distinguishing aspect of the comparisons is that the inward spreading rate of the free shear layer is predicted too low, by a significant degree. This deficiency is seen in every Navier-Stokes contribution, to varying degrees. Speculation as to the reasons for this behavior in the predictions was presented previously.

Several of the methods also underpredict the outward spreading rate, particularly at the circumferential location  $\phi_2$ . Five contributions, N02, N03, N04, N11, and N12, show a lingering velocity deficit at the outer edge of the free shear layer. This suggests that the turbulent mixing is under-predicted at the outer free shear layer, apart from any issue as to whether the inner mixing process is better represented by planar or axisymmetric turbulence model techniques.

**Pressure Drag** - Experimental data are not available, therefore a quantitative assessment of pressure drag cannot be provided. However, some interesting observations can be made based on the distribution of pressure drag buildup.

This pressure drag buildup is the integrated pressure force, in the drag direction, from a location forward of the nozzle up to any station in question. In mathematical terms, the quantity can be defined as:

$$C_{DP}(x/L) = \int_{x/L=0.88}^{x/L} C_p I_{DRAG} \cdot d(A/A_{MAX})$$

In this equation,  $I_{DRAG}$  is a unit vector in the drag direction,  $A$  is a vector differential of area, and  $A_{MAX}$  is the (scalar) value of the maximum forebody-afterbody cross-section area, used to normalize the drag coefficient. Thus, the integrated pressure drag to the nozzle exit,  $C_{DP}(X/L=1.00)$ , is the total pressure drag on the aftbody and nozzle. However, the

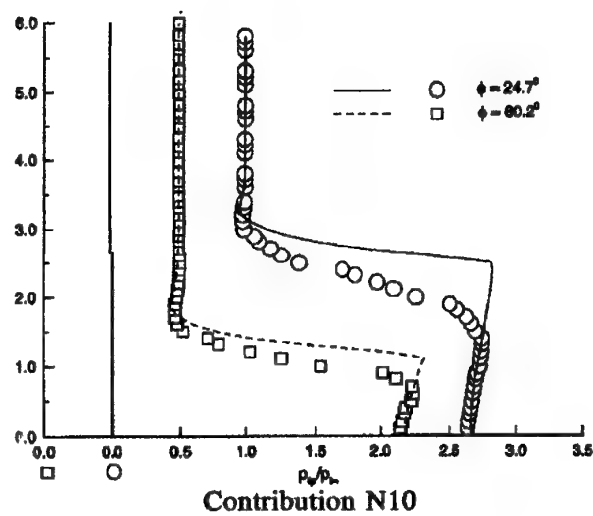
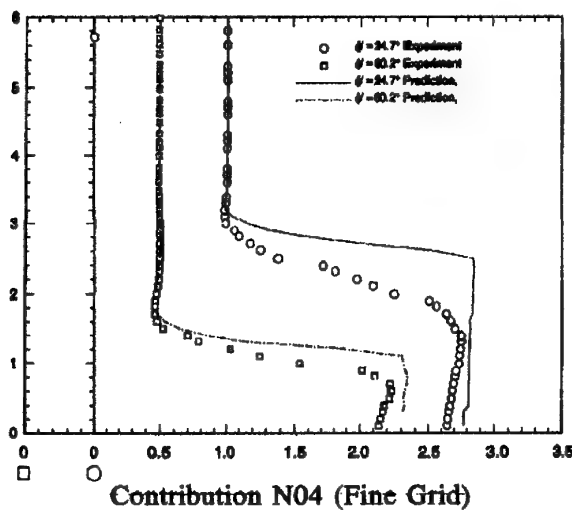
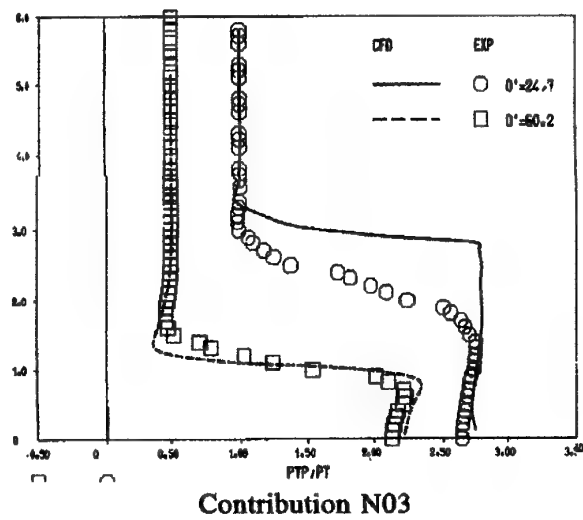
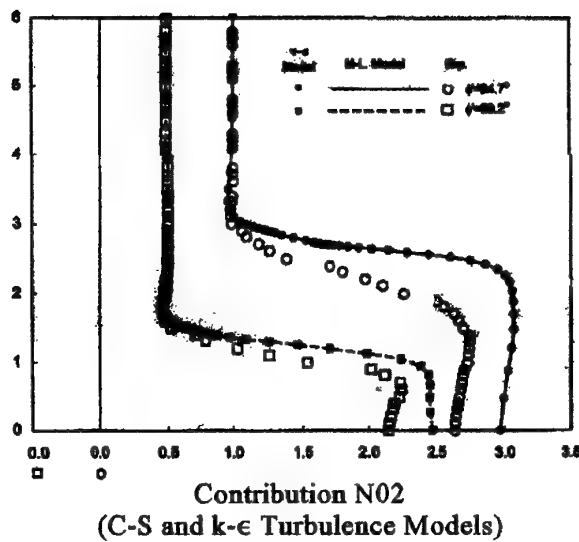
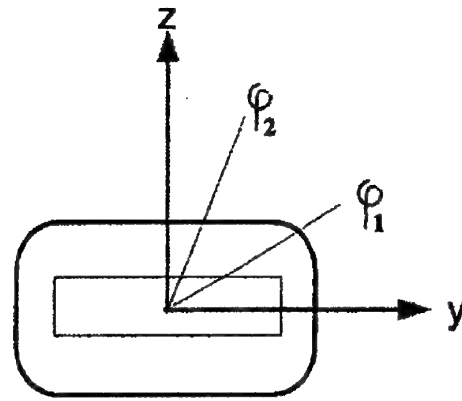
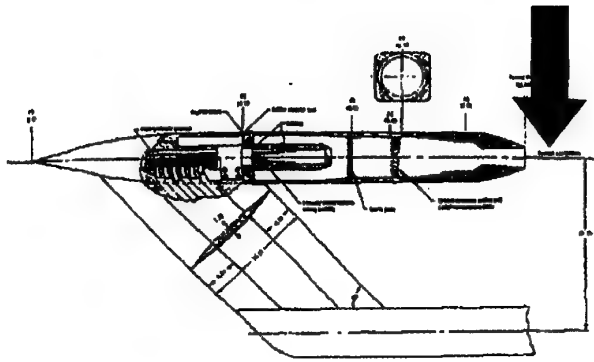
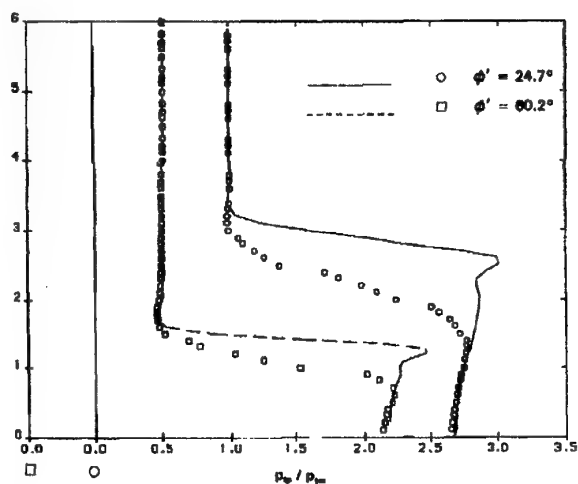
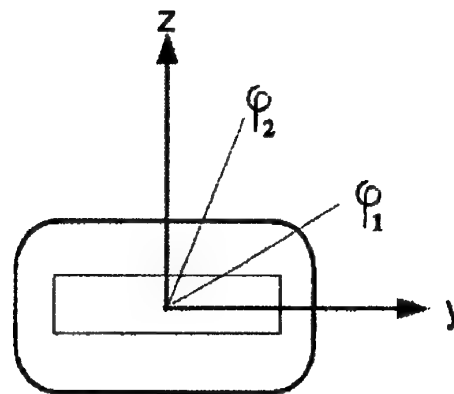
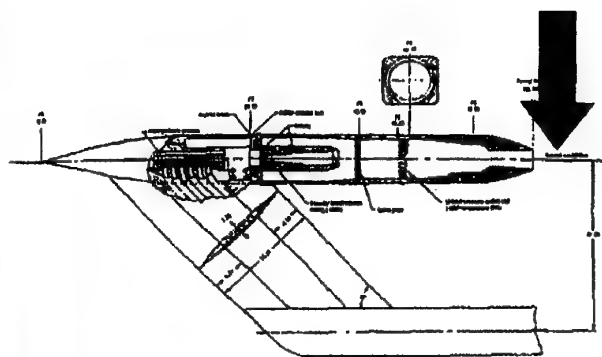
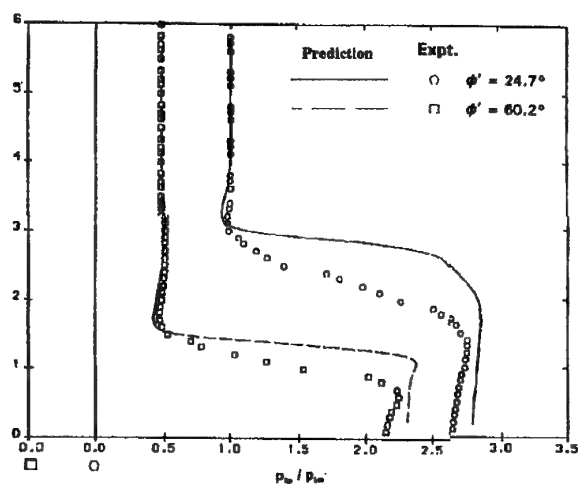


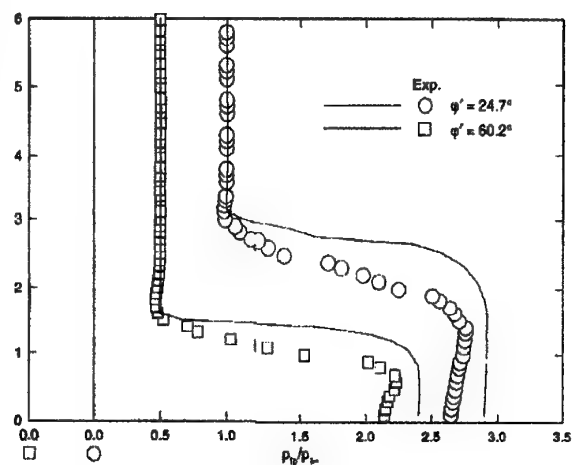
Figure 3.5-110 (First Part). Comparison of Plume Pitot Pressures, Case B.4.1,  $X/L=1.08$



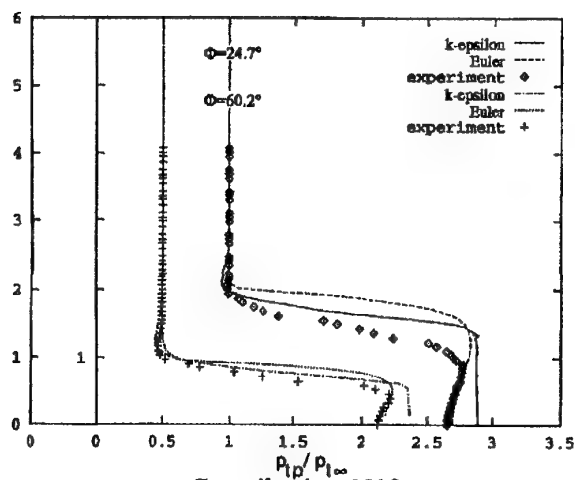
Contribution E11



Contribution N11



Contribution N12



Contribution N13

Figure 3.5-110 (Concluded). Comparison of Plume Pitot Pressures ( $P'/P_{t,inf}$  vs  $R$ ), Case B.4.1,



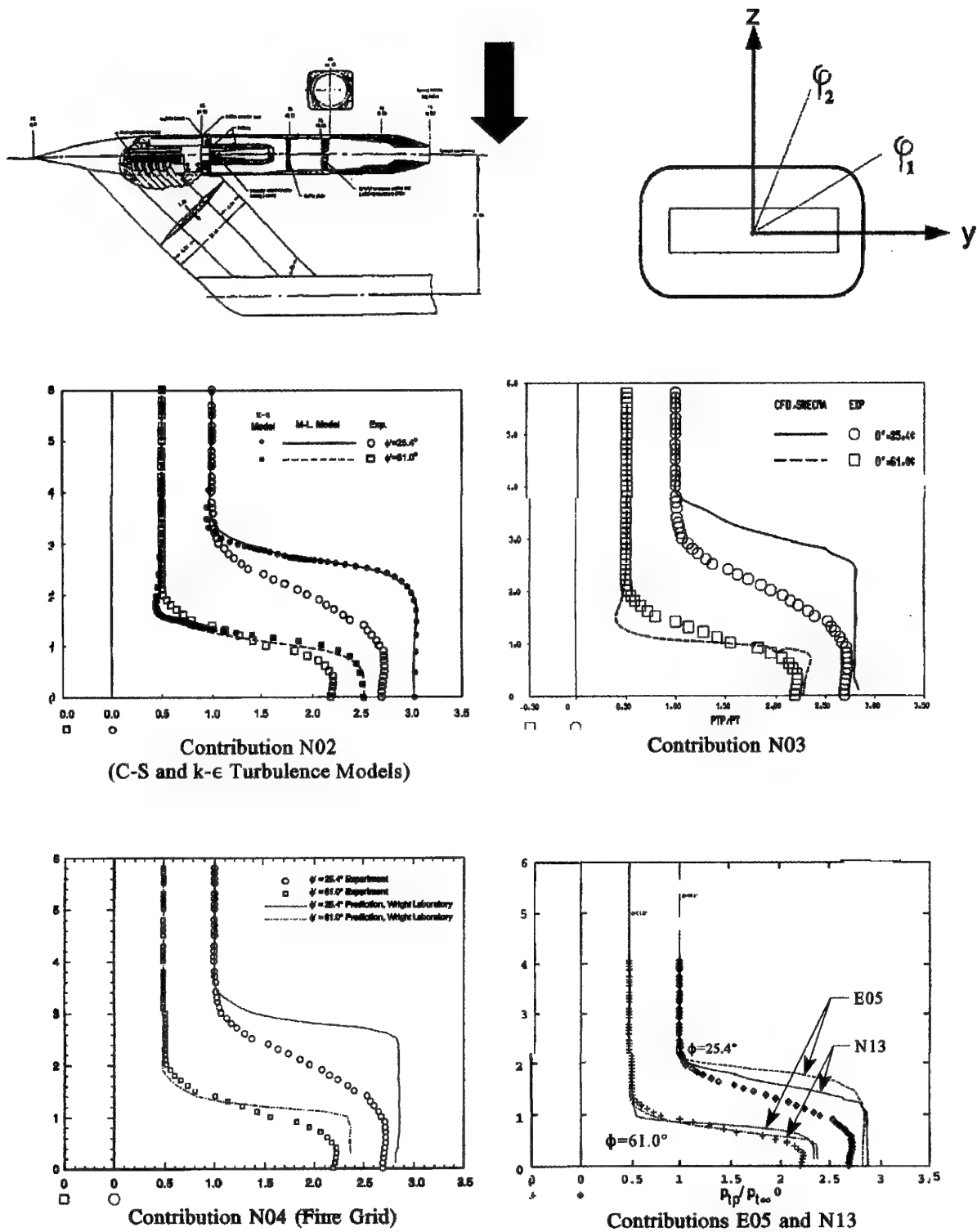


Figure 3.5-111 (First Part). Comparison of Plume Pitot Pressures ( $P'/P_{t,\infty}$  vs  $R$ ), Case B.4.1,  $X/L=1.16$

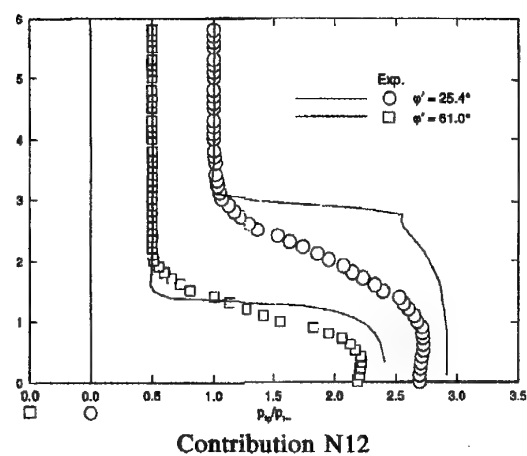
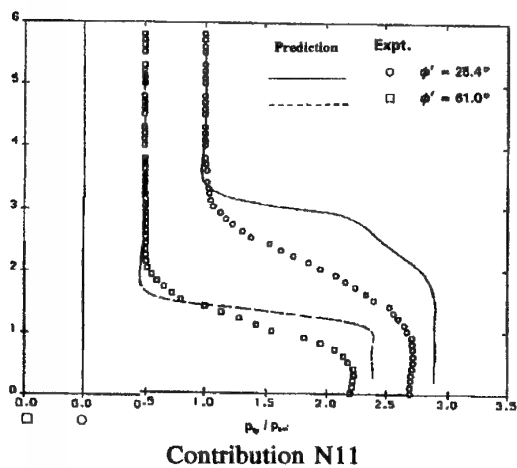
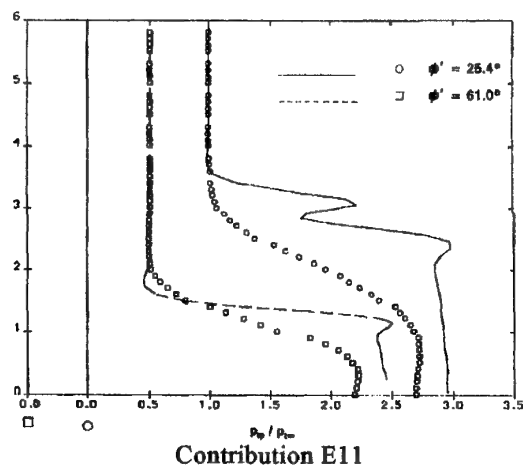
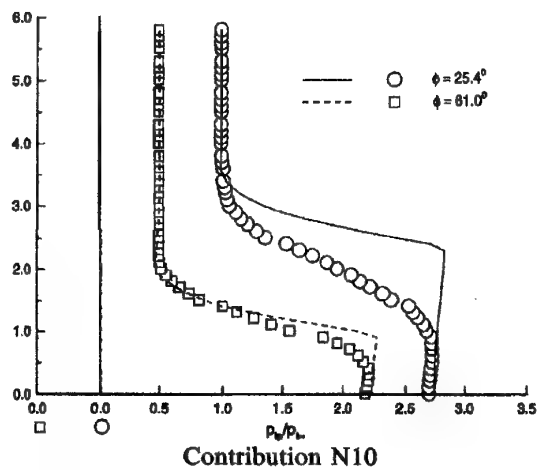
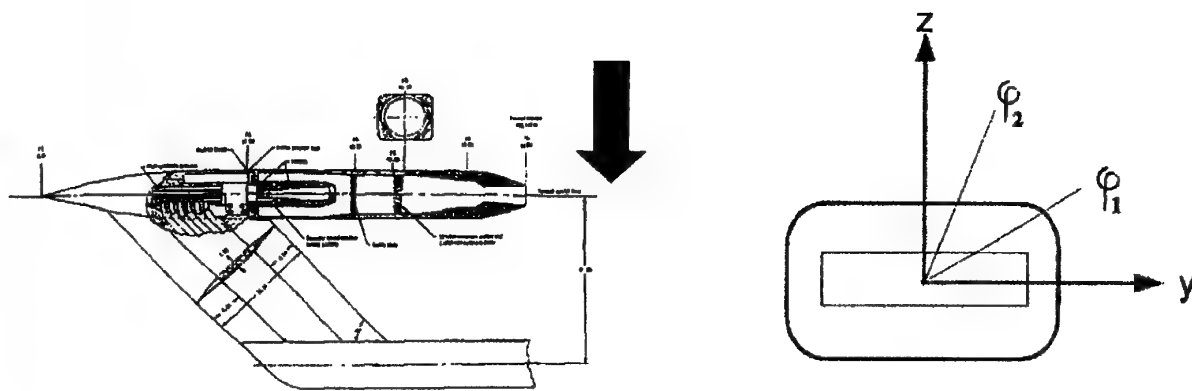


Figure 3.5-111 (Concluded). Comparison of Plume Pitot Pressures ( $P'/P_{t,\infty}$  vs  $R$ ), Case B.4.1,  $X/L=1.16$

distribution of drag at intermediate value of  $x/L$  can be instructive.

Three contributors provided plots of the buildup of pressure drag, for Case B.4.1. These data are presented in Figure 3.5-112. Of course, a similar plot (or total drag value) is not available from experimental sources to assess these predictions.

Each Contribution presents a similar trend: the pressure drag builds up rapidly over the initial portion of the afterbody, where the pressures are below ambient and the geometry presents rearward-facing surfaces. The drag drops in the recompression region, as the pressure begins to exceed the ambient value. The three contributions (four, counting the coarse/fine grid variations in Contribution N04) all have the same shape of the curve, but they each reach different maximum values before the integrated drag begins to drop.

Two of the contributions, N03 and N12, reach similar values of  $C_{DP} \approx 0.030$  at  $x/L = 1.00$  (i.e., the total pressure drag on the aftbody and nozzle). The third contribution, N04, reaches a significantly lower value of about 0.012. Interestingly, the net pressure drag from Contribution N04 on the coarse grid is significantly higher than the final value on the fine grid (about 0.020 vs 0.012).

#### 3.5.4.2 Case B.4.2

The geometry for Case B.4.2 is identical to the previous case, B.4.1. The jet conditions, too, are identical. The only difference is the Mach number, which is now 0.94 instead of 0.60.

For this case, the external flow accelerates to supersonic speeds as it flows over the shoulder onto the nozzle. The flow then shocks down to subsonic speeds, with a strong shock-boundary layer interaction. The surface pressure contours for this case are presented in Figure 3.5-113.

The Mach number field in the vertical symmetry plane is presented in Figure 3.5-114. The two CFD predictions for this Figure are in good agreement, showing a strong shock wave standing on the shoulder about  $x/L = 0.93$ . This shock is of sufficient strength to separate the boundary layer. The boundary layer then remains separated past the nozzle trailing edge.

These features in the vertical symmetry plane are also revealed in visualizations of the local velocity vectors and the static pressure field (Figure 3.5-115). Due to the extensive flow separation, the external flow aft of the shock wave does not follow the nozzle contour. The effective aerodynamic flow angle is substantially less than the geometric angle. Only a very weak recompression occurs. In this

nozzle region of separated flow, the pressure gradients are quite mild.

The nozzle sidewall has very little contouring. Only a slight expansion shoulder is present, and the geometry converges at a shallow angle to the nozzle trailing edge. Predicted off-body flow properties in this region (horizontal symmetry plane) are presented in Figure 3.5-116. A weak shock can be noted at the shoulder region. In the adverse pressure gradient region, from the shoulder shock to the nozzle trailing edge, the boundary layer thickens substantially. However, no extensive flow separation occurs (indeed, it may be there is no flow separation at all).

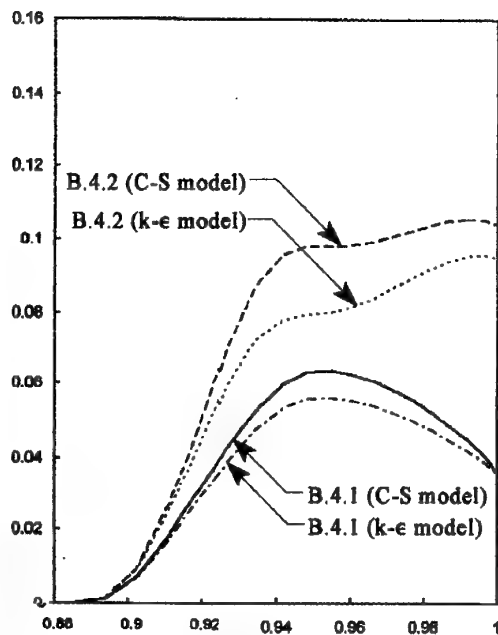
Graphics illustrating the flows on the nozzle surface are presented in Figure 3.5-117. The data from Contribution N03 show the region of predicted flow separation, illustrated by distinctive shading on the nozzle upper surface. Off-body flow properties in both symmetry planes also are presented. The data from Contribution N10 simulate a classical oil flow test. These data clearly show, based on the N10 results, that the boundary layer is separated laterally all along the nozzle upper surface, with a complex recirculation region noted afterward. However, the flow remains attached in these data along the sidewall.

The contouring on the sidewall of the nozzle is much less severe, consequently the pressure variations also are weaker. As a result of this disparity, the flow interactions are highly three dimensional along the corner between the nozzle upper/lower surfaces (significant pressure variations) and the sidewall (minimal pressure variations). This is particularly true in the region downstream of the shock-boundary layer interaction, where the boundary layer is separated.

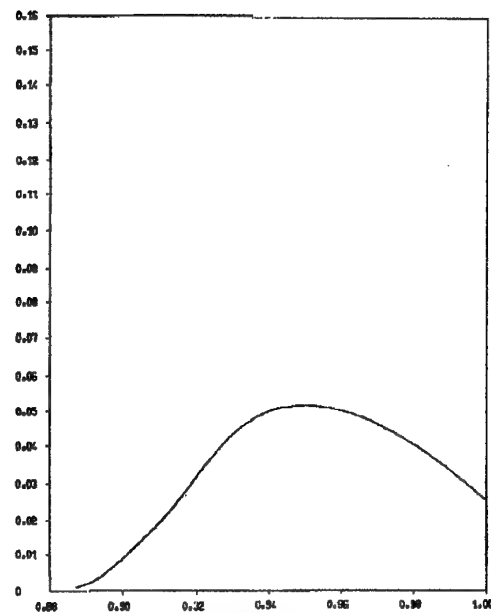
These data show that the flows in Case B.4.2 are substantially more complex than those in the preceding case. Supercritical flow is present with strong shock waves, and a strong three-dimensional shock-boundary layer interaction is present.

**Comparison of External Surface Pressures** - Data comparisons for Row 1, on the top centerline of the nozzle, are presented in Figure 3.5-118. Twelve CFD contributions were provided for this data set.

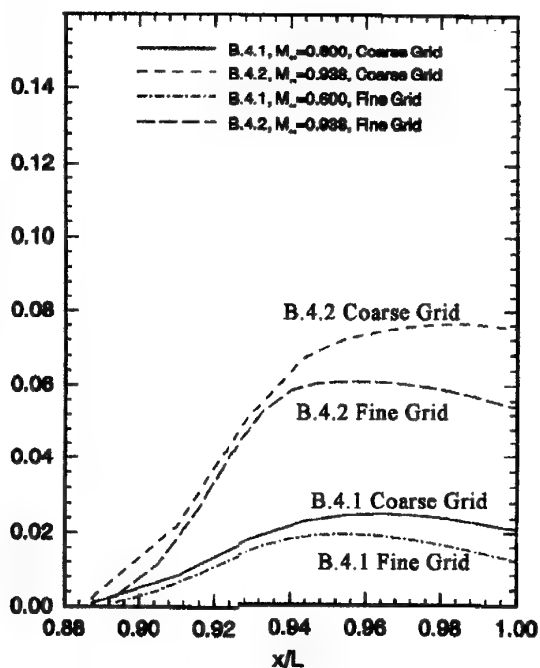
The flow along the top centerline features a strong expansion to a value of  $C_p \approx -0.55$ , terminated by a relatively strong shock which immediately raises the pressure coefficient to, say,  $-0.15$ . Based on both the experimental pressure data and the CFD predictions, this shock causes immediate and extensive separation of the boundary layer across most of the nozzle upper surface. The boundary layer remains separated past the end of the nozzle. In this region, only a weak added pressure rise occurs, reaching  $C_p \approx 0$  at the nozzle trailing edge.



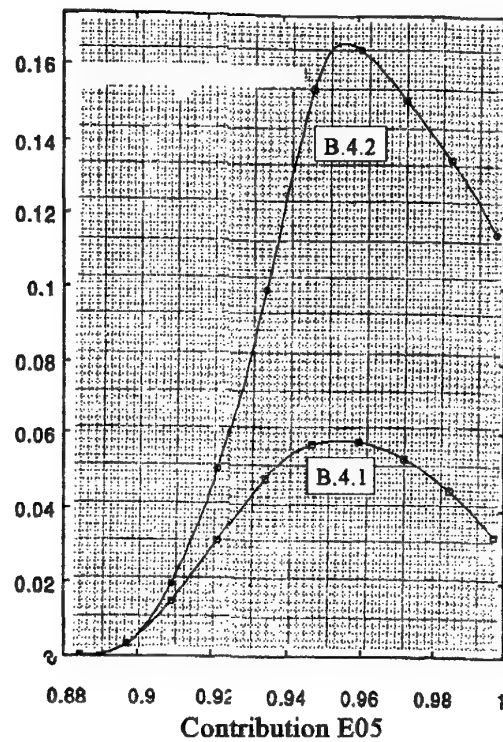
Contribution N02



Contribution N03

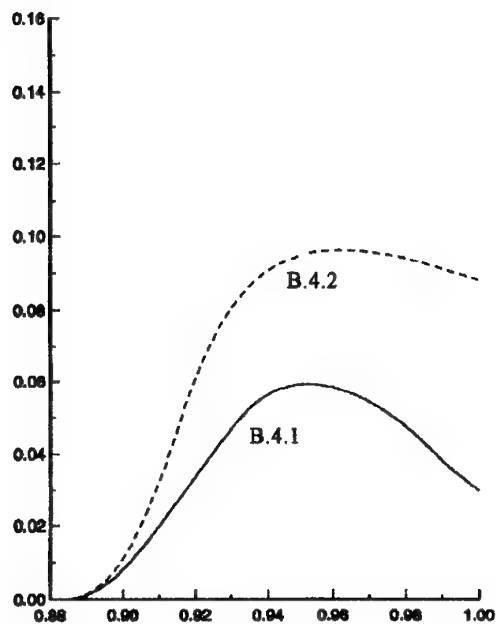


Contribution N04

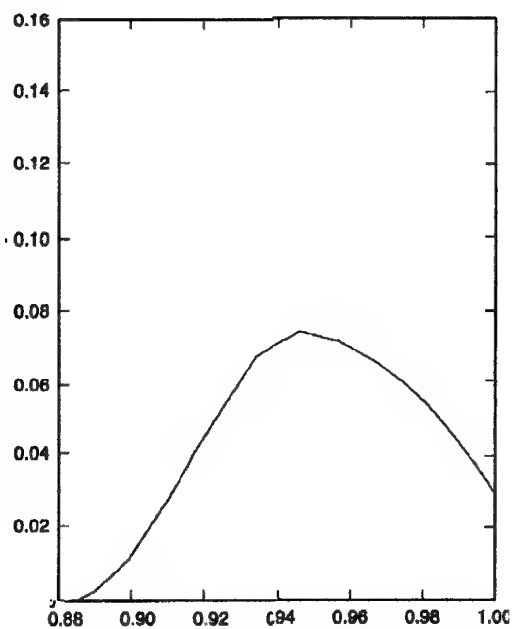


Contribution E05

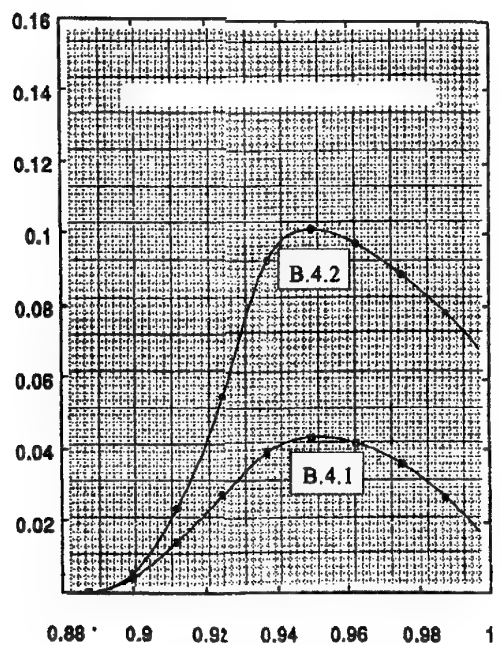
Figure 3.5-112 (First Part). Predicted Buildup of Pressure Drag, Case B.4.1



Contribution N10

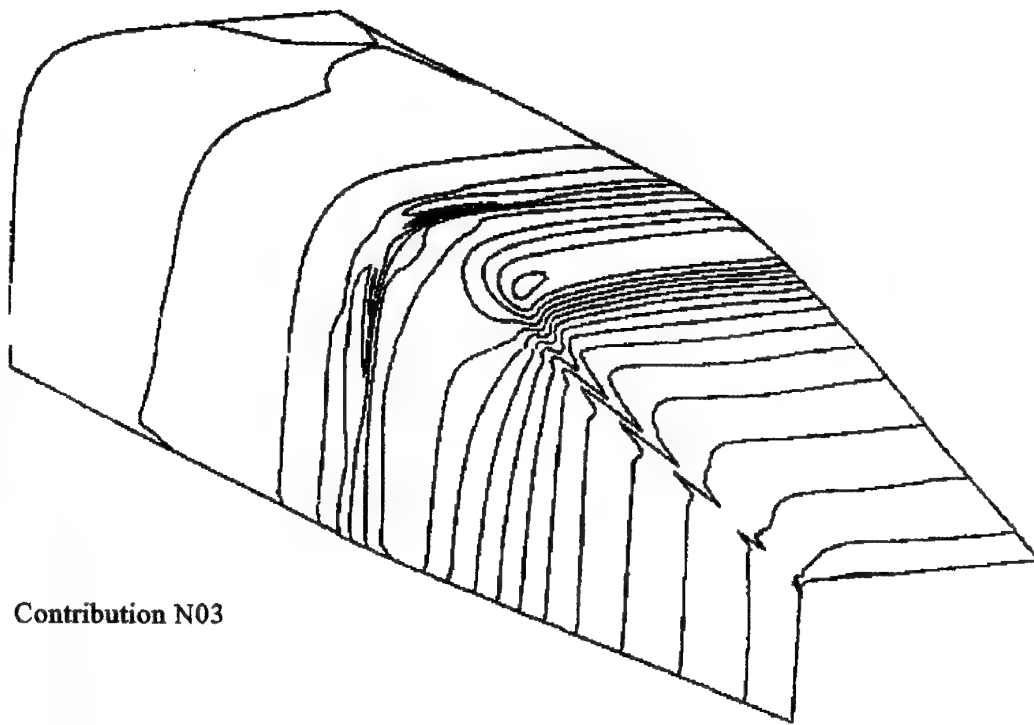


Contribution N12

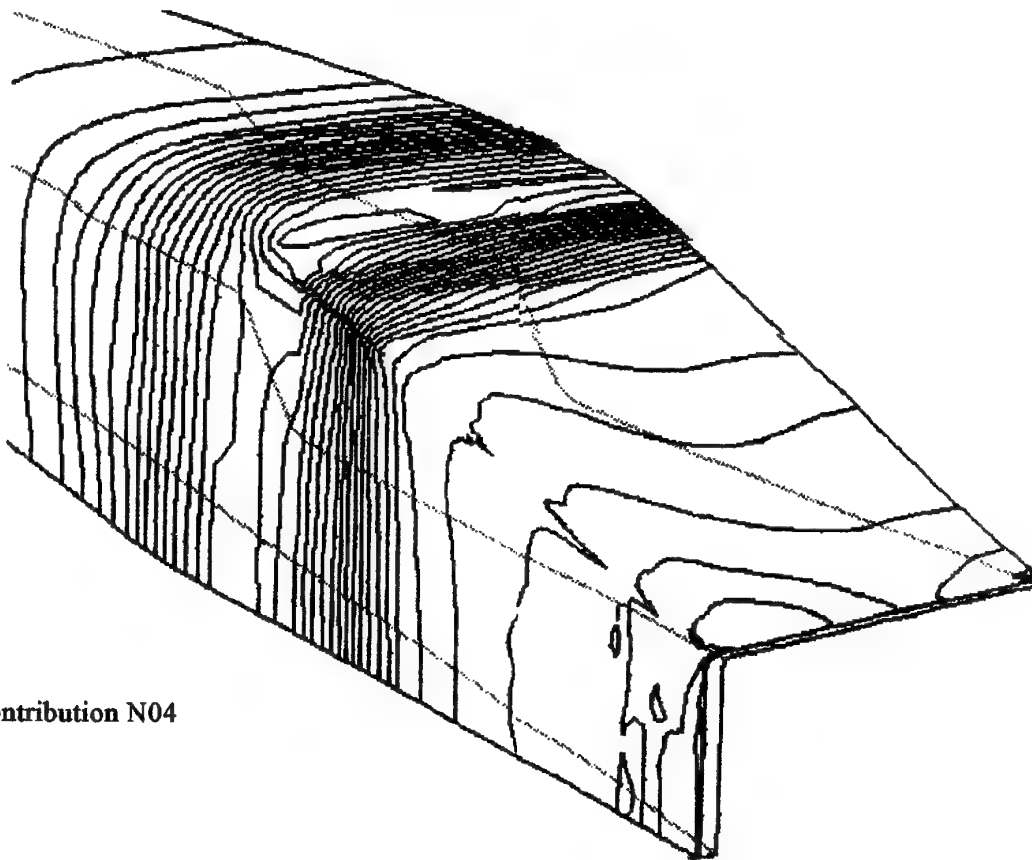


Contribution N13

Figure 3.5-112. Predicted Buildup of Pressure Drag, Case B.4.1



Contribution N03



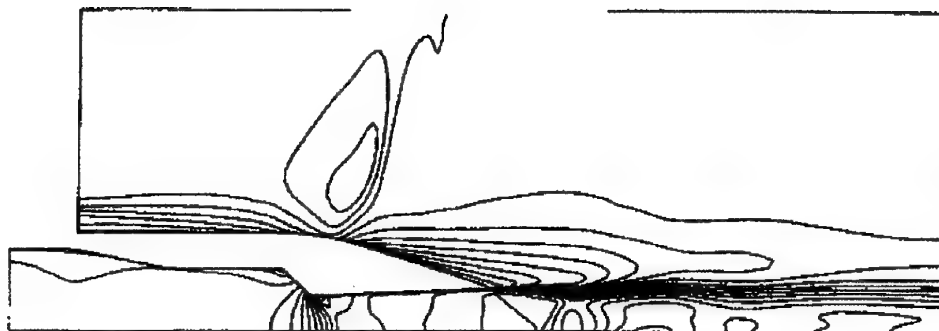
Contribution N04

Figure 3.5-113. Predicted Surface Pressure, Case B.4.2

Off-Body Mach  
Number Contours

Vertical Symmetry  
Plane

Contribution N03



Off-Body Mach  
Number Contours

Vertical Symmetry  
Plane

Contribution N10

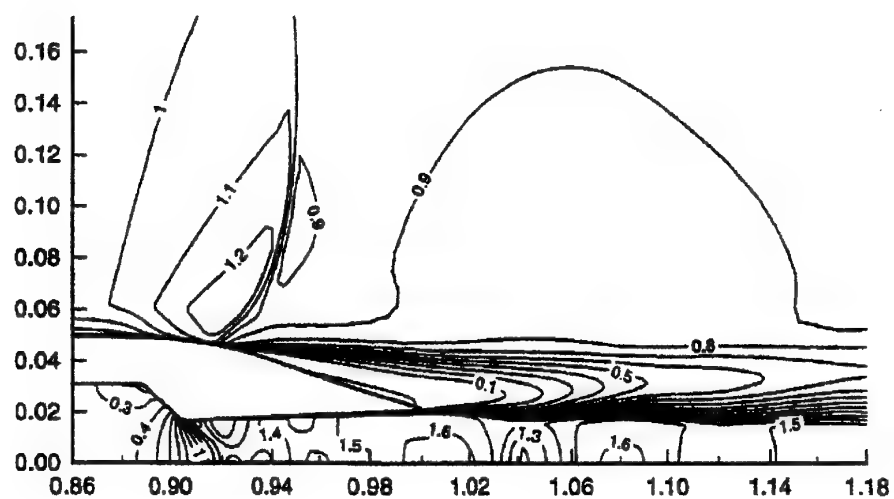
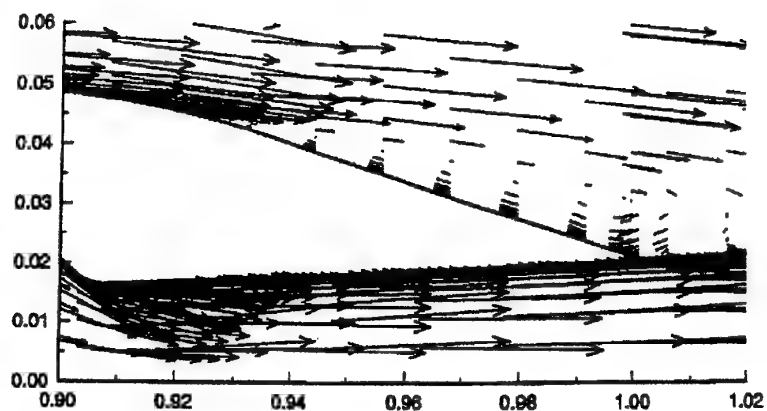


Figure 3.5-114. Predicted Off-Body Mach Number Contours, Case B.4.2, Vertical Symmetry Plane

Off-Body Velocity  
Vectors

Vertical Symmetry  
Plane

Contribution N10



Off-Body Static  
Pressure Contours

Vertical Symmetry  
Plane

Contribution N03

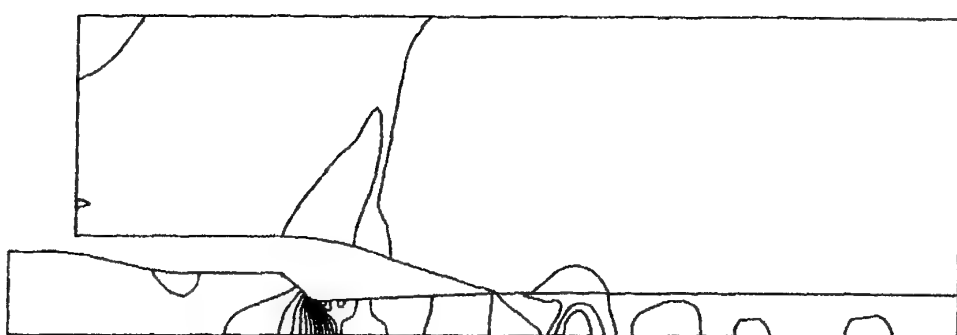


Figure 3.5-115. Predicted Off-Body Velocity and Static Pressure, Case B.4.2, Vertical Symmetry Plane



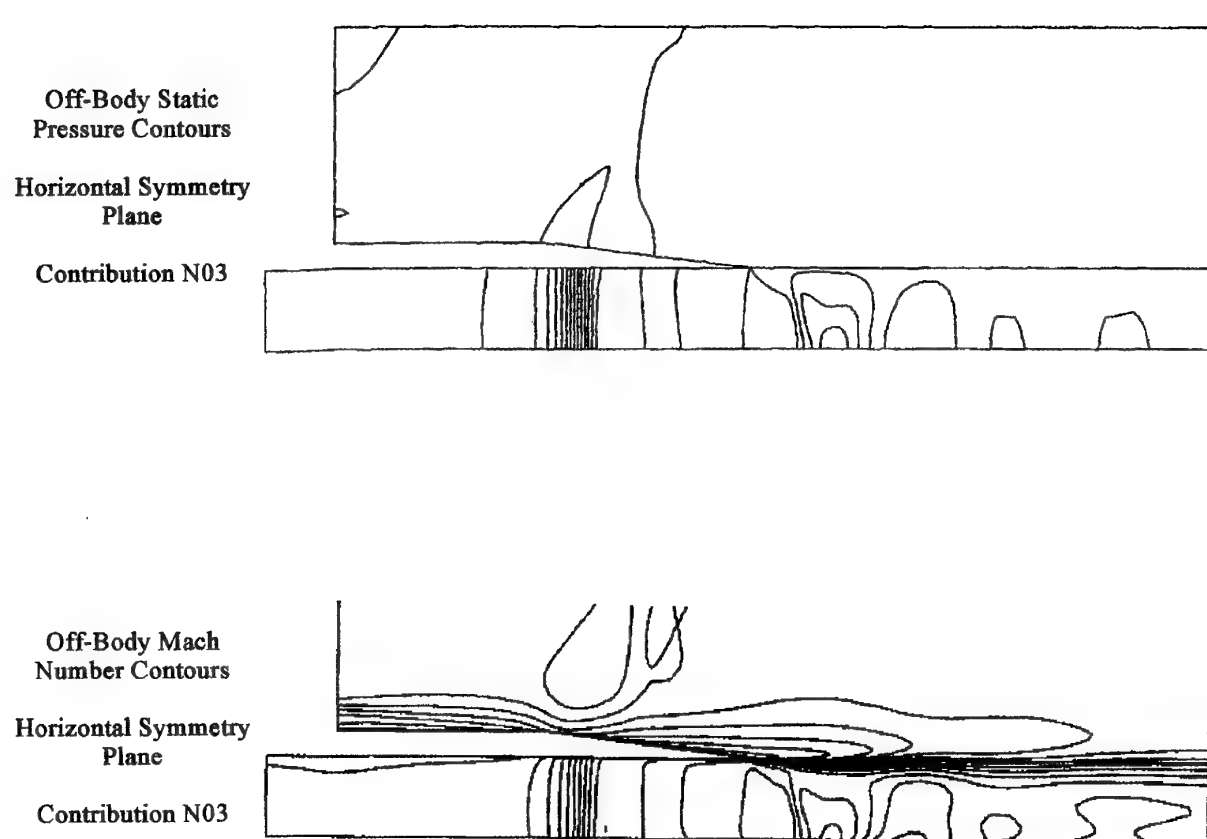


Figure 3.5-116. Predicted Off-Body Flow, Case B.4.2, Horizontal Symmetry Plane

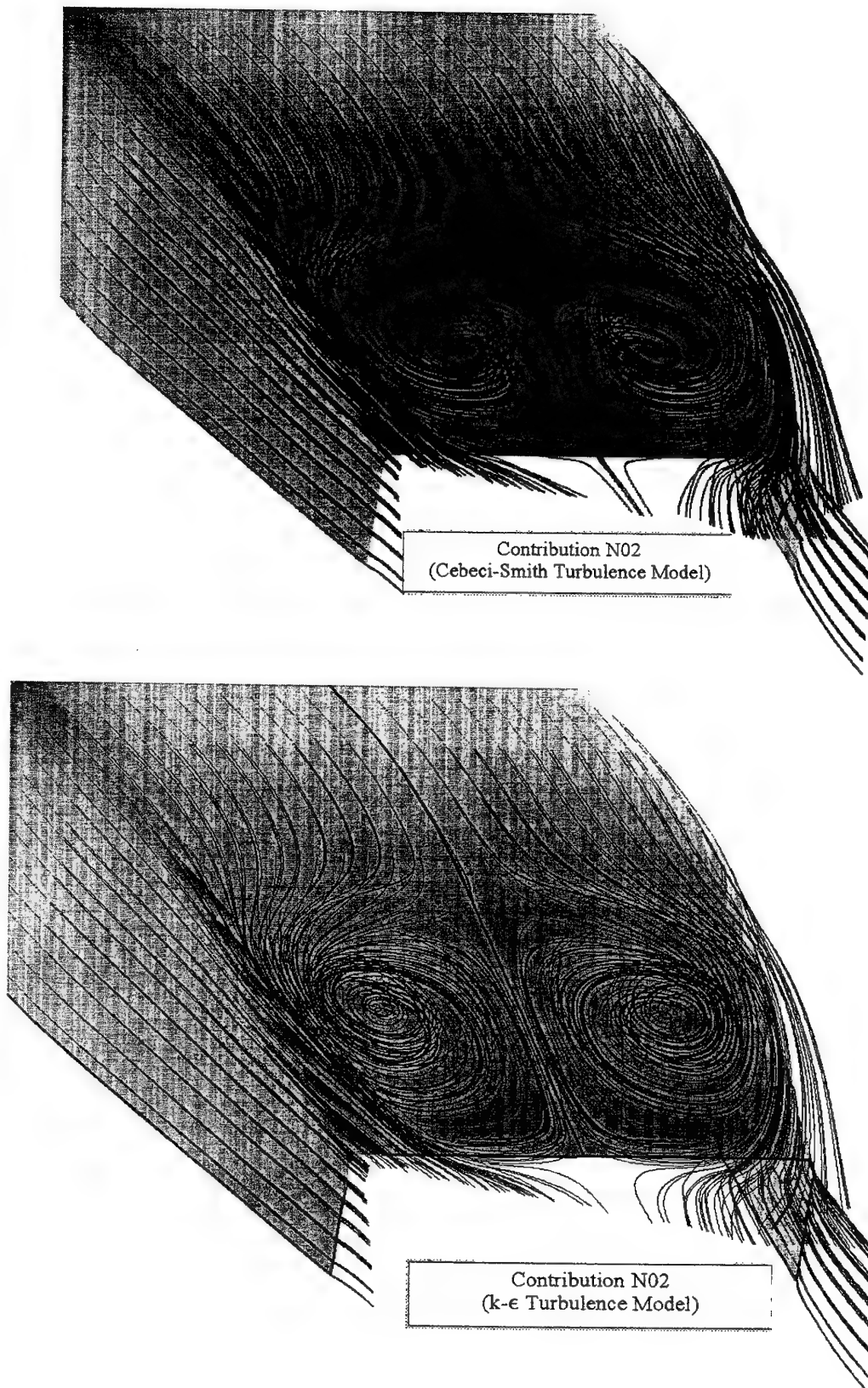
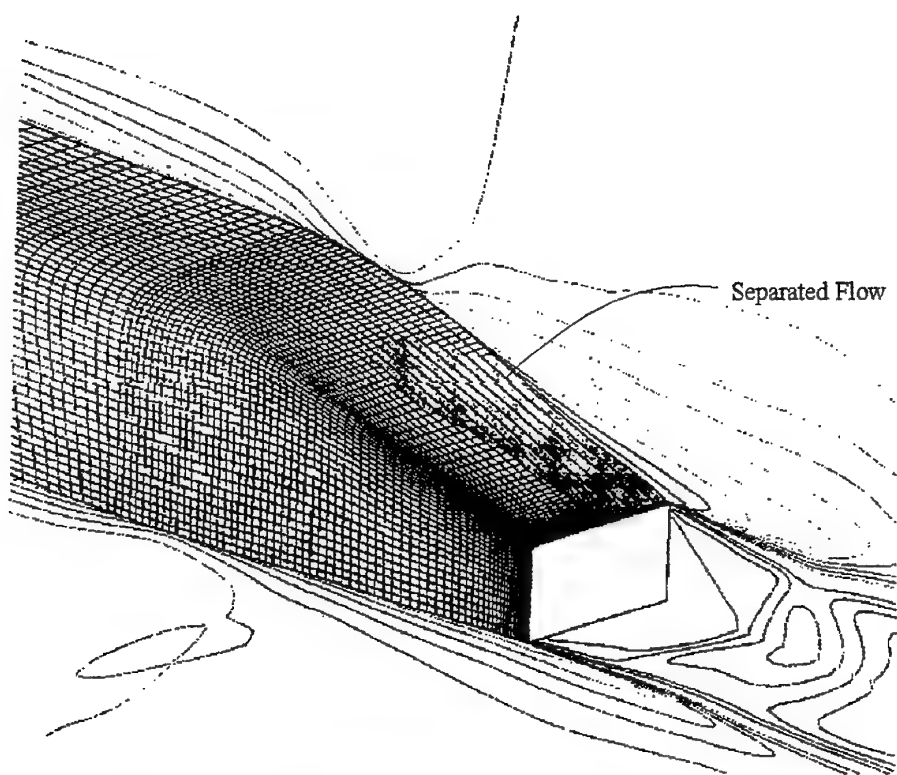
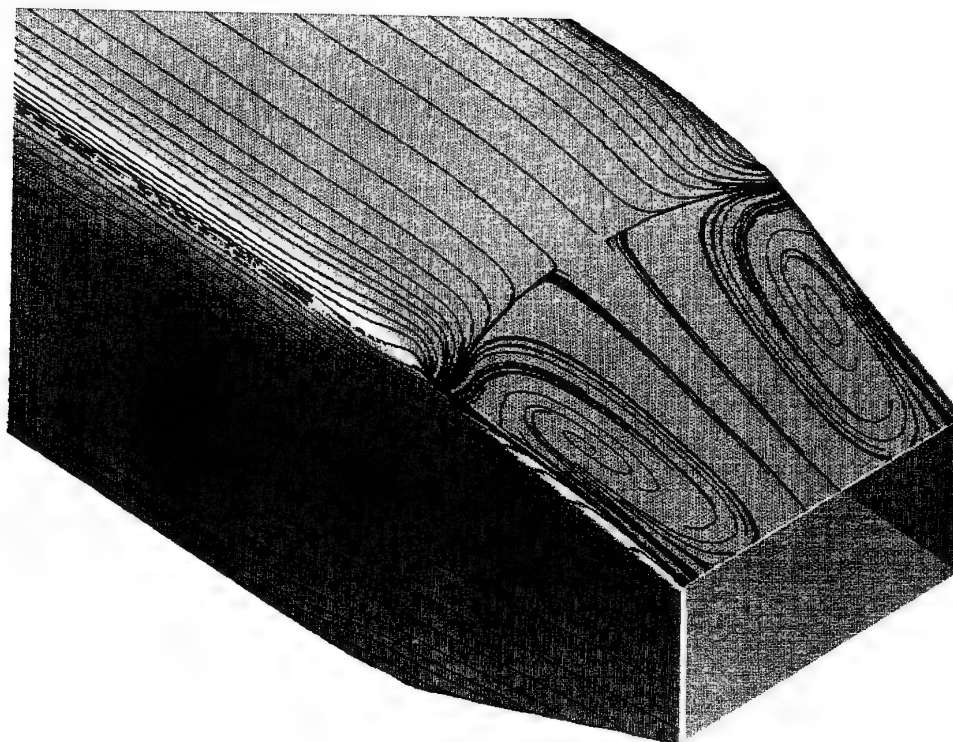


Figure 3.5-117 (First Part). Predicted Surface Flow Patterns, Case B.4.2

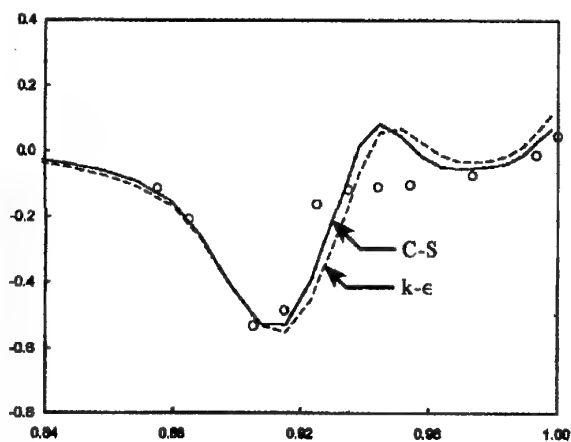
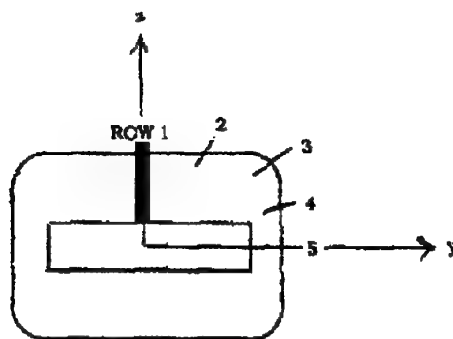


Contribution N03

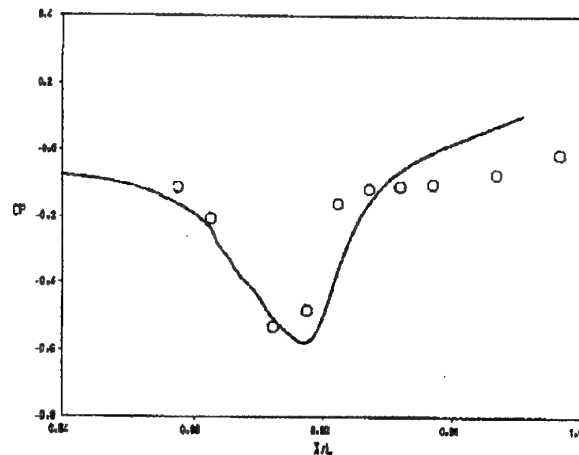


Contribution N10

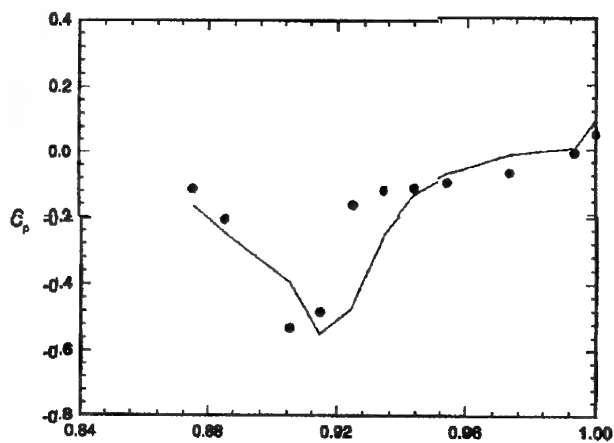
Figure 3.5-117 (Concluded). Predicted Surface Flow Patterns, Case B.4.2



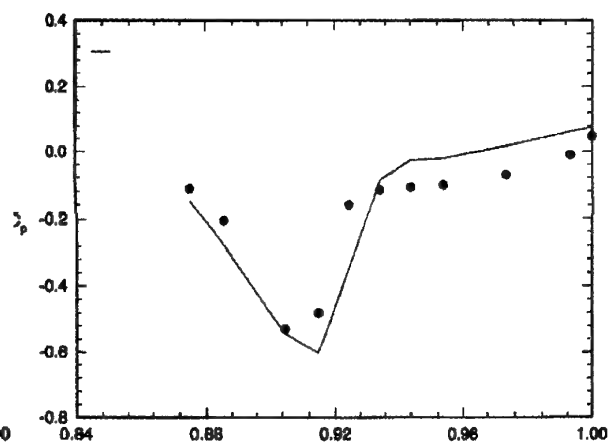
Contribution N02



Contribution E03



Contribution N04 (Coarse Grid)



Contribution N04 (Fine Grid)

Figure 3.5-118 (First Part). Comparison of Surface Pressures ( $C_p$  vs.  $X/L$ ), Case B.4.2, Row 1

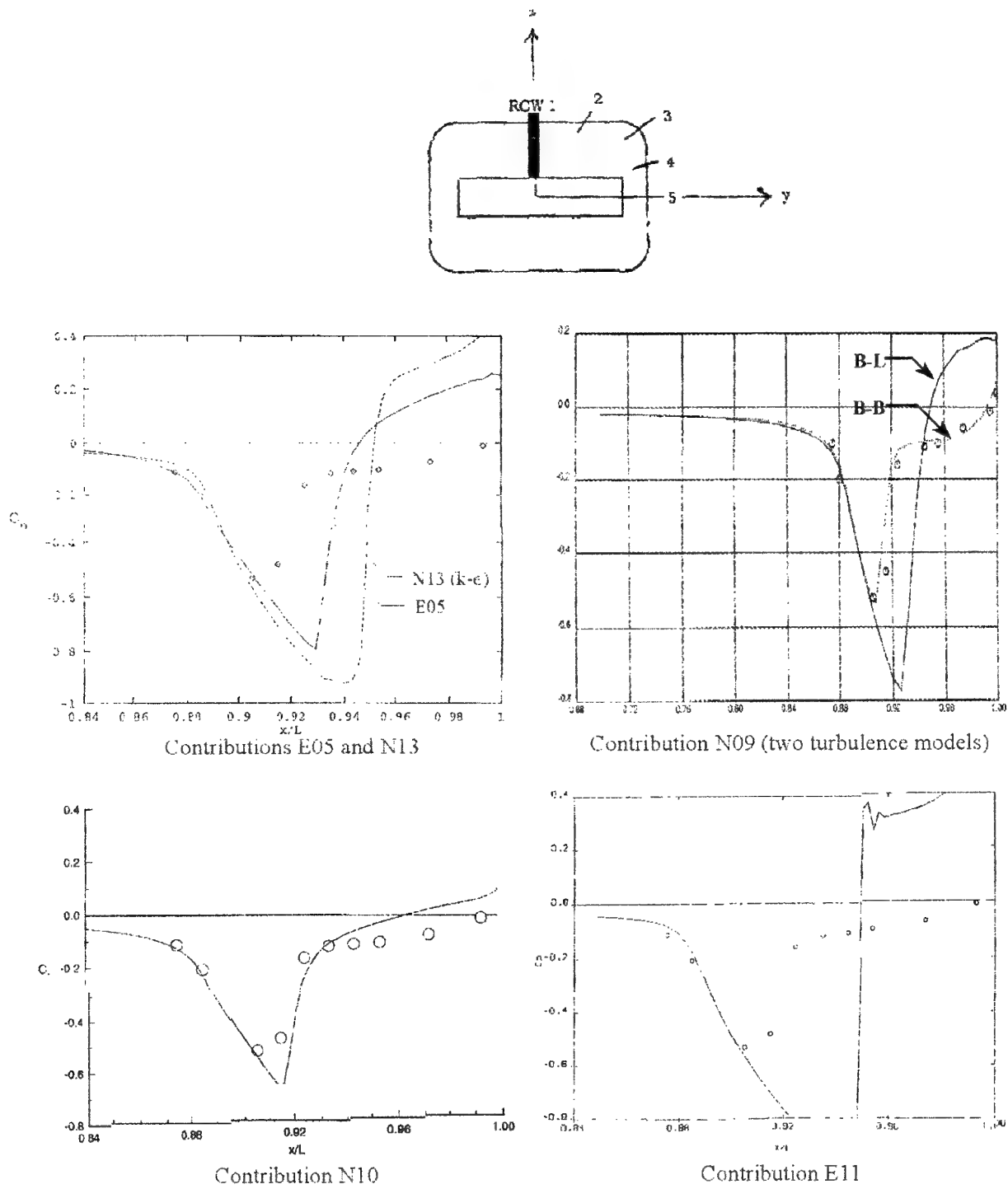
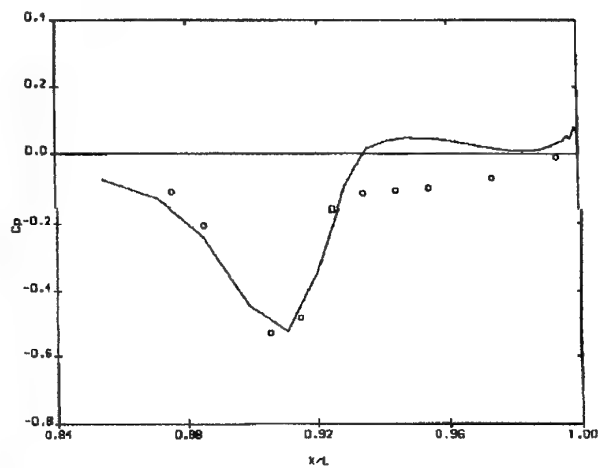
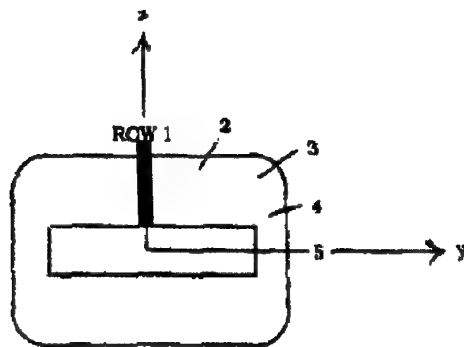
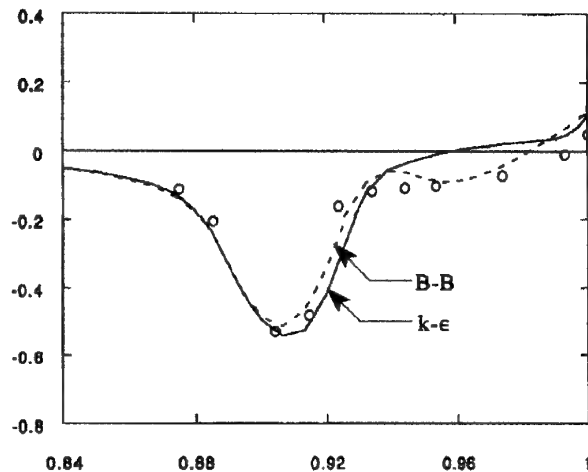


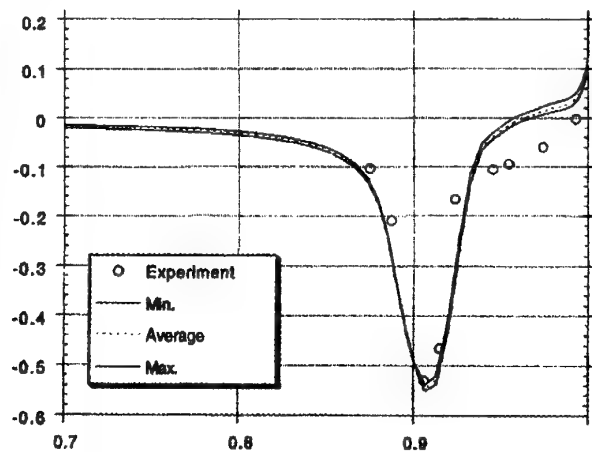
Figure 3.5-118 (Continued). Comparison of Surface Pressures ( $C_p$  vs.  $x/L$ ), Case B.4.2, Row 1



Contribution N11



Contribution N16

Contribution N16 ( $k-\epsilon$ )  
Envelope of Solution FluctuationsFigure 3.5-118 (Concluded). Comparison of Surface Pressures ( $C_p$  vs.  $X/L$ ), Case B.4.2, Row 1

The two Euler contributions, E05 and E11, both agree well with the experimental data through the initial expansion region, up to the shock location. However, they each place the shock too far downstream, and therefore the predicted flow continues to expand well past the point where the shock is standing. Both Euler methods place the shock at about  $x/L \approx 0.95$ , and the predicted shock is far too strong. Consequently, the pressure rises too high behind the shock, and continues to rise slowly to the nozzle exit plane. Contribution E11 exhibits numerical "ringing" behind the shock.

From these results, we can conclude that the viscous effects are not important in the initial expansion region. However, viscous effects play an important role in establishing the location of the shock and its strength.

The Navier-Stokes methods all experienced difficulty with this case. Several of them, for example, placed the shock too far downstream and consequently they over-predicted the shock strength (N03, N04, N09 B-L, and N13). Presumably, this occurred because the strength of the viscous flow modification behind the shock was underpredicted. Interestingly, Contribution N02 provided very good results through the expansion region, and it located the shock more accurately than several of the other methods, using the (simple) algebraic Cebeci-Smith (C-S) turbulence model. With the  $k-\epsilon$  model, the shock was placed too far aft and it was as a result too strong. Contribution N09 did very well indeed with the one-equation Baldwin-Barth (B-B) turbulence model; the same algorithm on the same grid, using the algebraic Baldwin-Lomax (B-L) model did quite poorly. Contribution N10, using a two-equation Jones-Launder (J-L) model, predicted the expansion and shock very well, and did a credible job in the separated flow region from the shock to the nozzle exit. The same comments also may be applied to Contribution N11, though it did not do quite as well as N10 in the separated region aft of the shock.

The outcome of these initial comparisons is confusing. No correlation can be made with the level of turbulence modeling. Very good results were achieved with algebraic models, one-equation models, and two-equation models. Each class of turbulence model also did poorly in other contributions.

The flow characteristics along Row 2 are similar to the previous results for Row 1. These latter results are presented in Figure 3.5-119. The experimental data are quite sparse, and they do not define very well the expansion region, or the shock location and strength. In general, the outcome is the same as the previous comparisons (Row 1).

This figure illustrates the manner in which CFD analysis complements experimentation. The test data for this row are sparse, but they depict (apparently) a relatively benign flowfield of nearly constant pressure. The CFD data show that in fact a shock of significant strength is present in this

row, and the experimental data suggesting benign conditions are misleading, based entirely on the tap locations.

Row 3 lies along the corner between the nozzle upper surface and the sidewall. This region features high lateral curvature, and lateral pressure gradients due to the relatively benign curvature of the sidewall in contrast with the high pressure variations due to curvature of the upper wall. Due to the presence of high curvature in the lateral direction, this region might pose difficulties in grid generation for some methods. These comparison data are presented in Figure 3.5-120.

The general features of the flow are similar to those discussed previously. The strong shock is in about the same location, with about the same strength. The flow appears to be separated from the shock to the nozzle exit, with its pressure over that region rising slowly to the freestream ambient pressure.

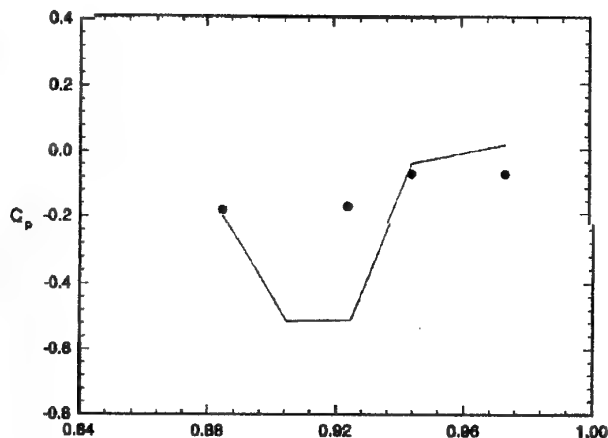
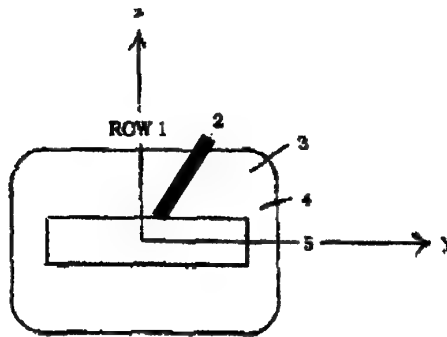
Eight CFD solutions were contributed for comparison with this set of data. All the contributions show accurate predictions in the initial expansion region, forward of the shock. The Euler contribution (E05) shows the expansion continuing too far (i.e., the shock is too far downstream) and the shock then is too strong when it occurs.

The six contributions of Navier-Stokes solutions generally place the shock more accurately than they did for the previous comparisons along Rows 1 and 2. In Contribution N02, the two turbulence models about straddle the shock location, with the Cebeci-Smith model placing the shock slightly too far upstream and the  $k-\epsilon$  model erring by about the same amount in the downstream direction. The best results in the separated region from the shock to the trailing edge might be attributed to Contribution N02 (both the C-S and J-L turbulence models seems to do equally well) and Contribution N10 (modified J-L model).

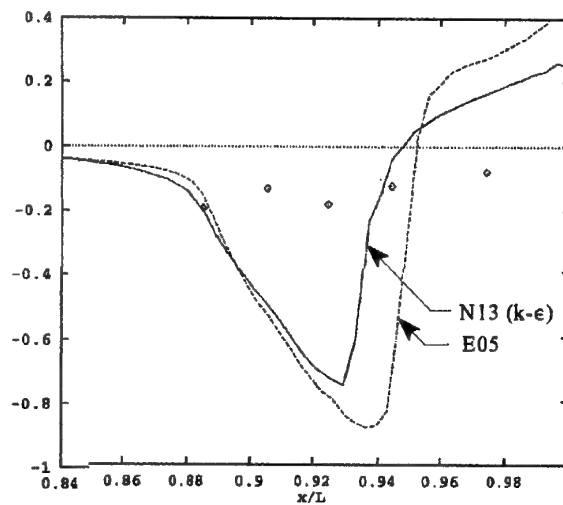
Row 4 runs along the upper portion of the nozzle sidewall. The pressure gradients are less severe here - also, the experimental data are sparse. The surface pressure comparisons for this row of taps are presented in Figure 3.5-121.

A distributed pressure rise is present at about the same axial location as the strong shock which dominated the flows over the nozzle upper surface. Based on the surface pressure ahead of this rise, the flow is clearly supersonic. However, both the experimental data and the CFD predictions suggest that the pressure rise is distributed, not sharp, and has not coalesced into a single shock wave.

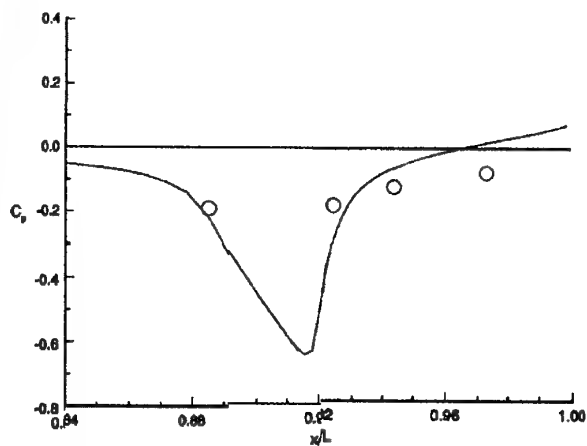
The experimental pressure data do not strongly indicate whether the boundary layer is attached or separated behind this pressure rise. The CFD predictions, too, are mixed on this point.



Contribution N04 (Fine Grid)



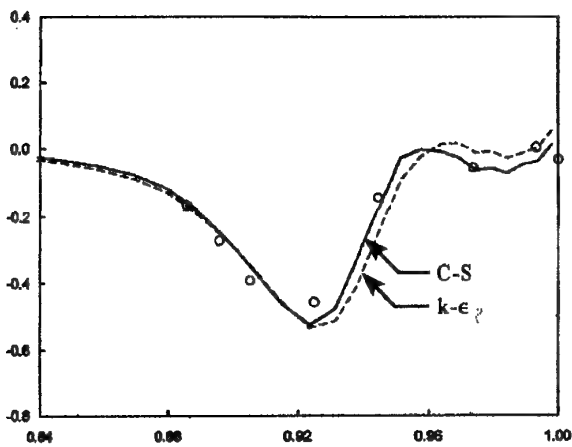
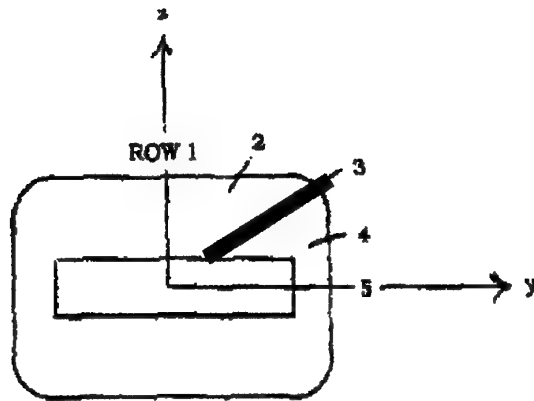
Contributions E05 and N13



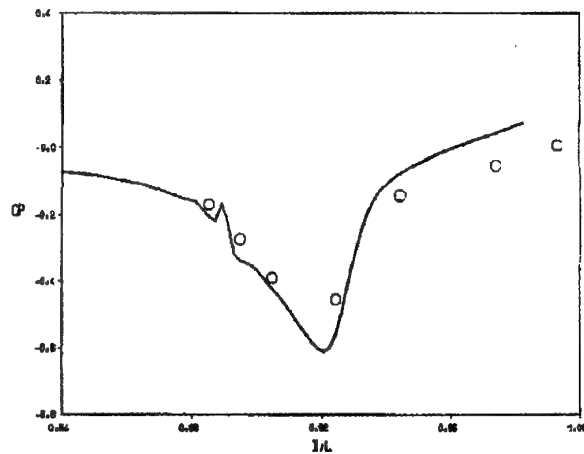
Contribution N10

Figure 3.5-119. Comparison of Surface Pressures ( $C_p$  vs.  $x/L$ ), Case B.4.2, Row 2

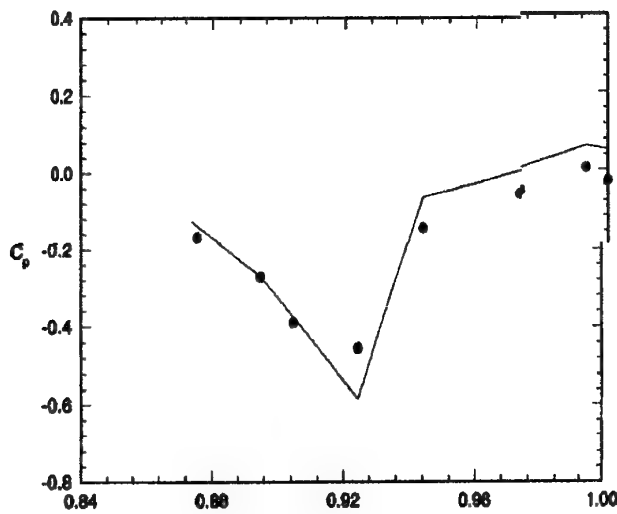




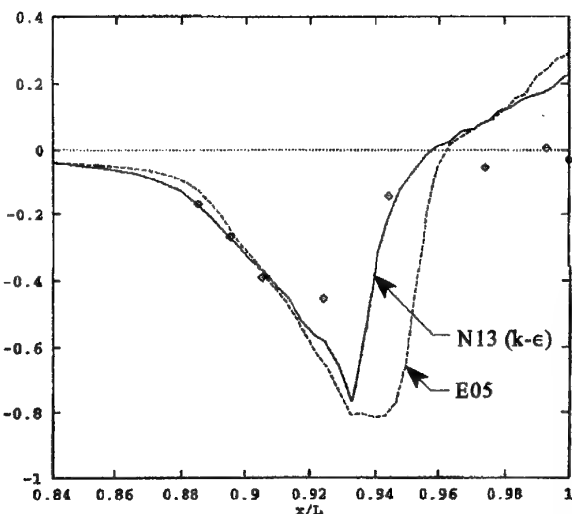
Contribution N02



Contribution N03



Contribution N04 (Fine Grid)



Contributions E05 and N13

Figure 3.5-120 (First Part). Comparison of Surface Pressures ( $C_p$  vs.  $x/L$ ), Case B.4.2, Row 3

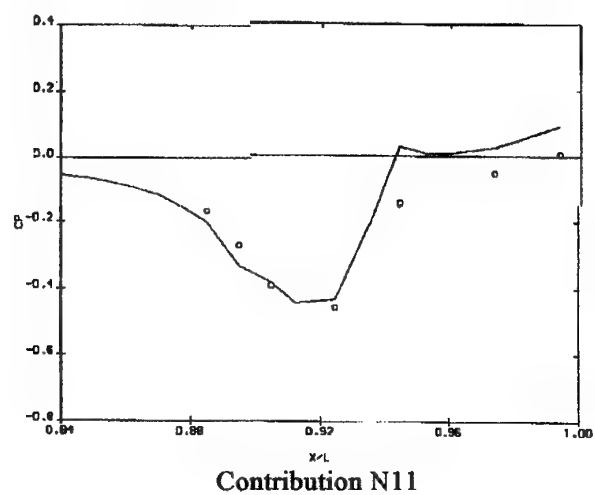
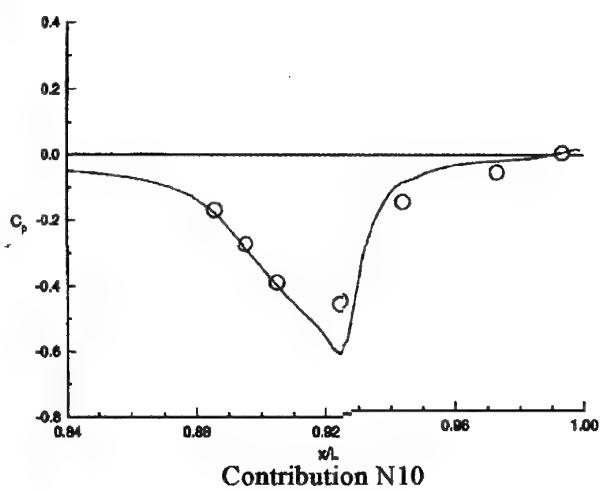
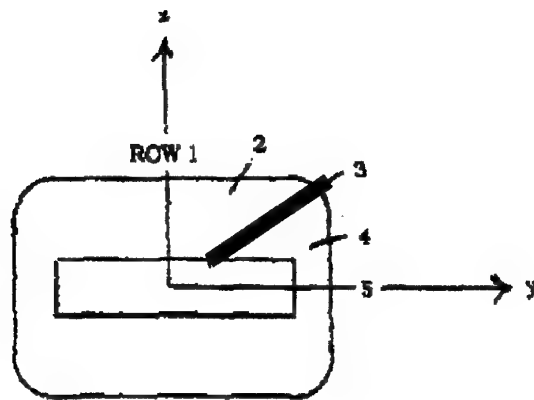


Figure 3.5-120 (Concluded). Comparison of Surface Pressures ( $C_p$  vs.  $X/L$ ), Case B.4.2, Row 3

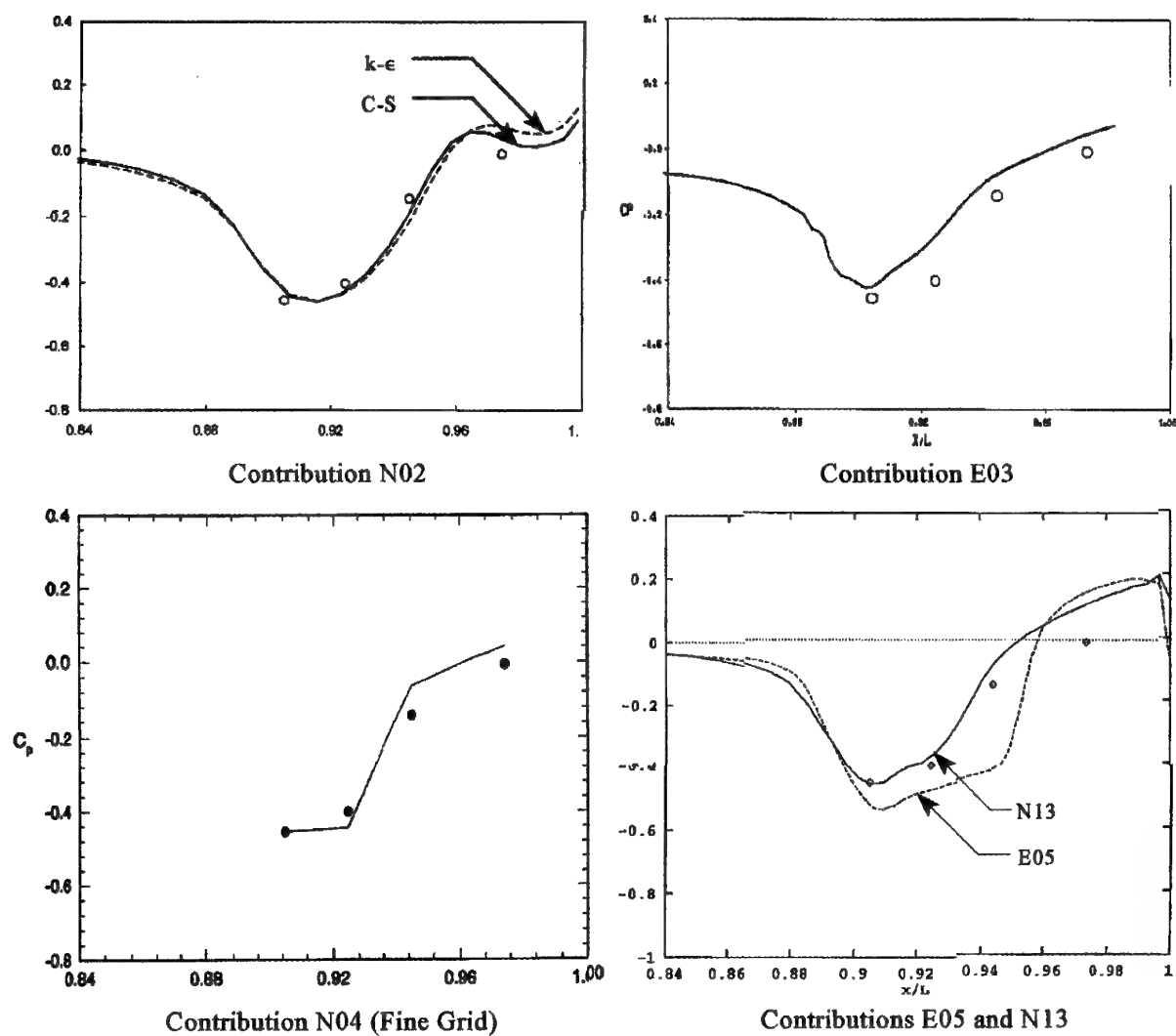
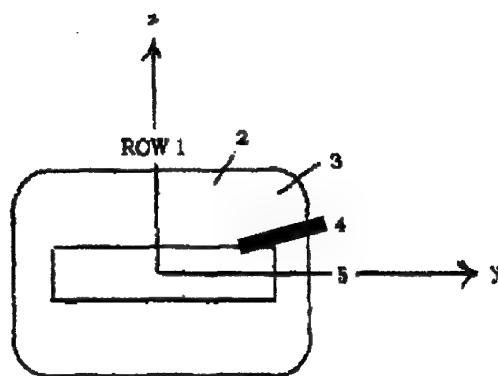
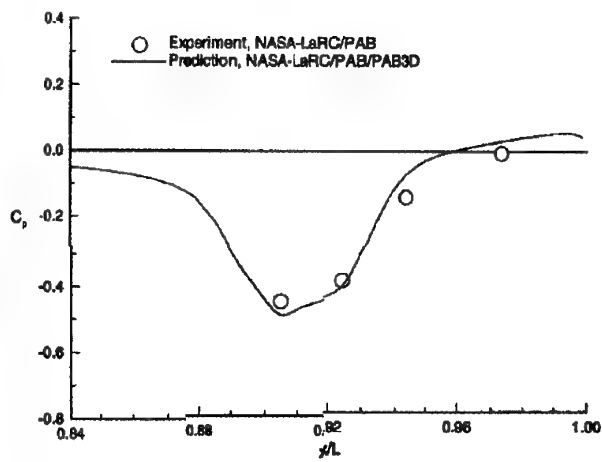
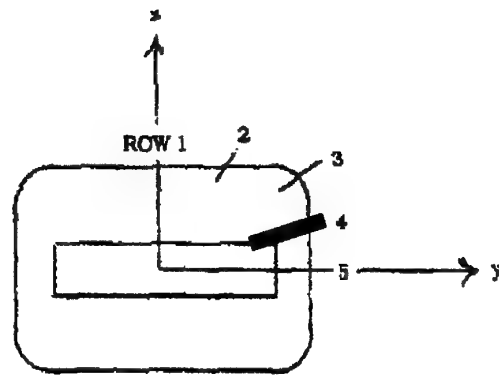
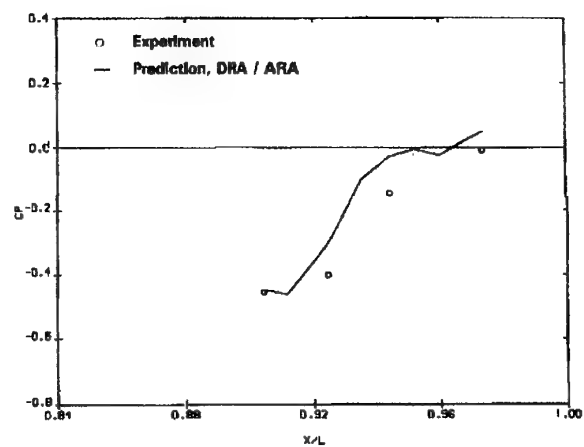


Figure 3.5-121 (First Part). Comparison of Surface Pressures ( $C_p$  vs.  $x/L$ ), Case B.4.2, Row 4



Contribution N10



Contribution N11

Figure 3.5-121 (Concluded). Comparison of Surface Pressures ( $C_p$  vs.  $X/L$ ), Case B.4.2, Row 4

The Euler contribution (E05) is surprisingly accurate for all these data. The initial expansion region is captured well. So is the pressure rise, though it is placed somewhat too far downstream and the shape of the pressure profile in this region is unusual. In general, the Euler comparison suggests that viscous interactions play an important role in the shock and post-shock regions, but not the overwhelming role that they played in the previous comparisons for this case.

The Navier-Stokes contributions all located the shock reasonably well - particularly Contributions N02 (both turbulence models), N04, N10, and N13. However, success in locating the shock did not correlate with success in modeling the post-shock region. For example, N13 did well at the shock but over-predicted the downstream pressures. Conversely, N03 placed the shock a little too far upstream, but did quite well behind the shock, to the nozzle exit.

Row 5 is located on the centerline of the nozzle sidewall. Comparisons of measured and predicted surface pressure for this location are presented in Figure 3.5-122. The general features are the same as in Row 4. The initial pressure rise occurs in supersonic flow, but it is distributed over some distance and is not coalesced into a single strong shock wave. Aft of this region (i.e.,  $x/L > 0.95$ ) the pressure continues to rise slowly, reaching freestream ambient pressure at the nozzle exit. The experimental data are somewhat ambiguous regarding the state of the boundary layer in this region. The slow pressure rise suggests that the boundary layer is not separated. However, the recompression only to the freestream ambient pressure could be an indication of flow separation.

Eleven CFD solutions were contributed for this set of data. The two Euler contributions (E05 and E11) again do well in the expansion region, and they locate the beginning of the pressure rise accurately. This suggests that in this region, up to about  $x/L=0.91$ , the pressures are not significantly influenced by viscous interactions. The initial pressure rise ( $x/L$  from 0.91 to about 0.94) is modeled smoothly, but with an unusual shape, by Contribution E05. Contribution E11 exhibits a peculiar oscillation with a low-pressure extreme, followed by a strong coalesced shock. These Euler results, compared with the experimental data, indicate that aft of  $x/L = 0.91$ , the pressure distribution depends significantly on turbulent or viscous interactions.

Several of the Navier-Stokes solutions show the expansion is weakened too much by the modeling of the viscous interactions. This suggests the predicted boundary layer is thickening too rapidly in response to the initial portion of the adverse pressure gradient.

The initial portion of the recompression region (say, from  $X/L = 0.93$  to 0.96) shows a continuous pressure rise, indicative of an attached boundary layer. The two Euler methods both show an inadequate pressure rise in the early

portion of this recompression region, followed by a shock near  $X/L = 0.95$ . The Navier-Stokes solutions, confirmed by the experimental data, indicate that the shock may or may not be present (i.e., coalesced); the pressure at the wall in any event is distributed over a significant distance.

The final portion of the recompression region,  $X/L > 0.96$ , proved to be (as expected) more difficult. The experimental data exhibit a poorly-defined plateau, suggesting that the flow possibly is separated. No experimental oil flow data are available, on this portion of the model, to establish whether the boundary layer is attached or separated.

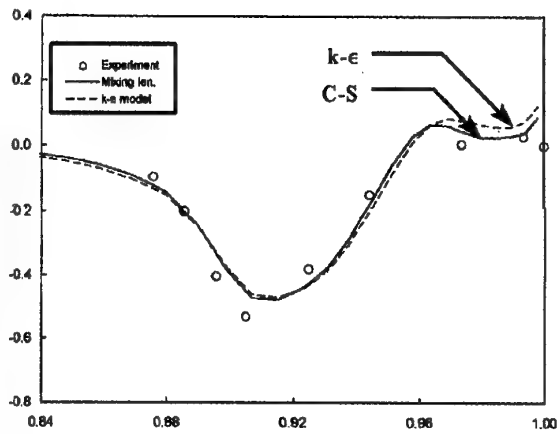
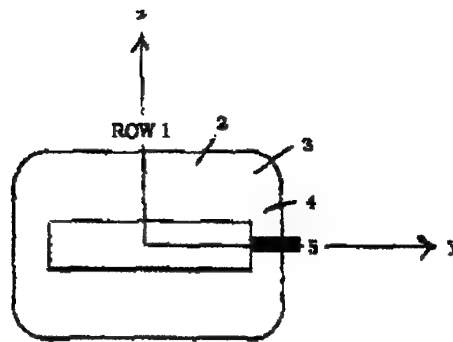
The Euler methods both over-predicted the pressure in this region, though they both captured the downturn in pressure immediately before the nozzle trailing edge.

Most of the Navier-Stokes methods matched the data fairly well - very well in two or three cases. This success was achieved without an apparent correlation with the class of turbulence model employed, suggesting that the local details of the turbulence field may not be as important as the overall state of the velocity deficit approaching the recompression, in achieving accuracy here

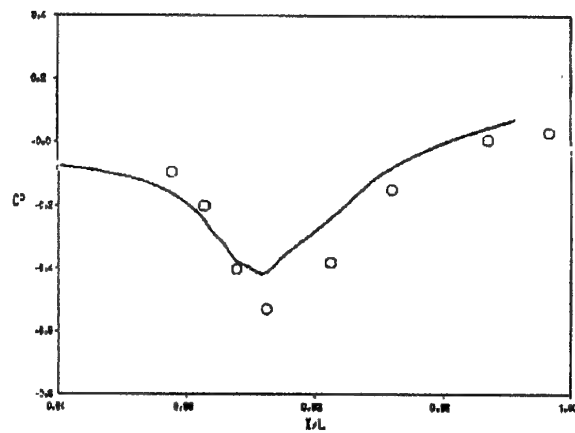
**Comparison of Internal Surface Pressures** - Rows 6 and 7 present wall pressure measurements for the internal nozzle flow (see Figure 3.5-93 for illustration of this geometry). As a reminder - the complication here is related to the change in cross-section of the flow passage, from circular to rectangular. The flow is accelerated through the exhaust duct, therefore the pressure gradients for the most part are favorable and the viscous interactions therefore are minimized.

The flow from the throat to the nozzle exit is supersonic. Further, the NPR for this case is the same as in the preceding case (B.4.1) and the duct geometry is the same. Therefore, one would expect the experimental data and the CFD data to be nearly identical as for Case B.4.1, Row 6 (Figure 3.5-105) and Row 7 (Figure 3.5-106).

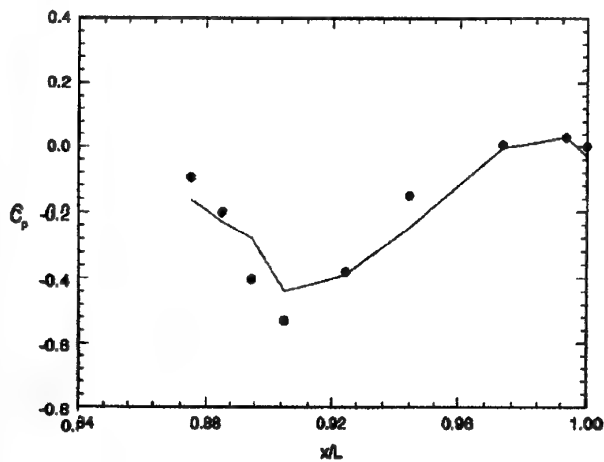
The data for Row 6 are presented in Figure 3.5-123. These data show the expected agreement with the data for Case B.4.1 (Figure 3.5-105). The chief feature is the sharp acceleration of the flow through the throat, around  $X/L=0.90$ . The flow continues to accelerate downstream of the throat, in the divergent 2-D passage. All the CFD methods capture these features. In comparing Contributions E05 and N13, the reader should note that the Navier-Stokes grid (N13) is much coarser than the Euler grid (E05), thus accounting for the unexpected result of more accurate predictions from the Euler method. Also, the internal nozzle grid in Contribution N02 is considered by the contributor to have been very coarse inside the nozzle.



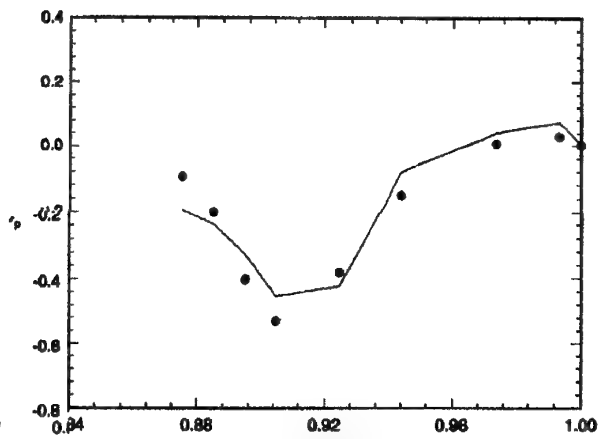
Contribution N02



Contribution N03

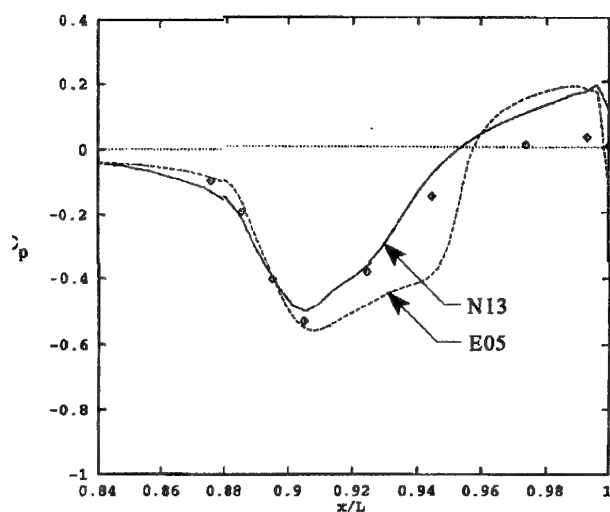
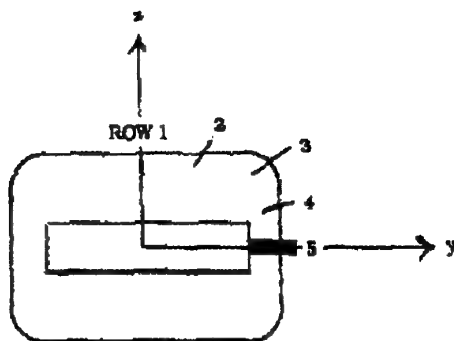


Contribution N04 (Coarse Grid)

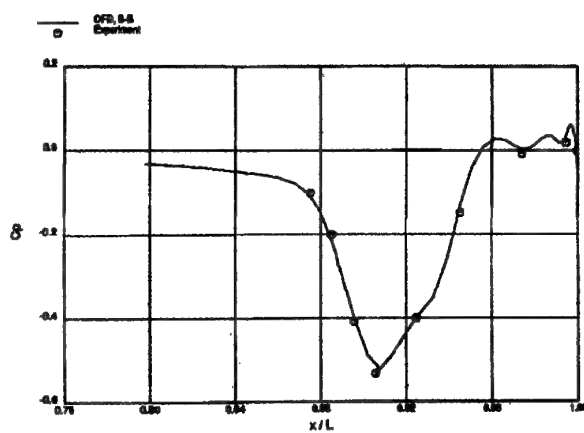


Contribution N04 (Fine Grid)

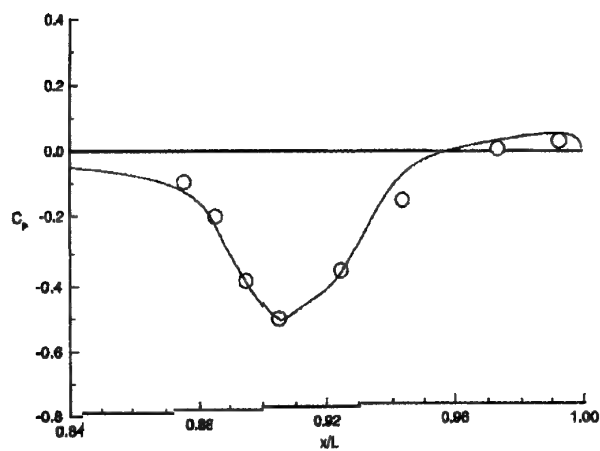
Figure 3.5-122 (First Part). Comparison of Surface Pressures ( $C_p$  vs.  $x/L$ ), Case B.4.2, Row 5



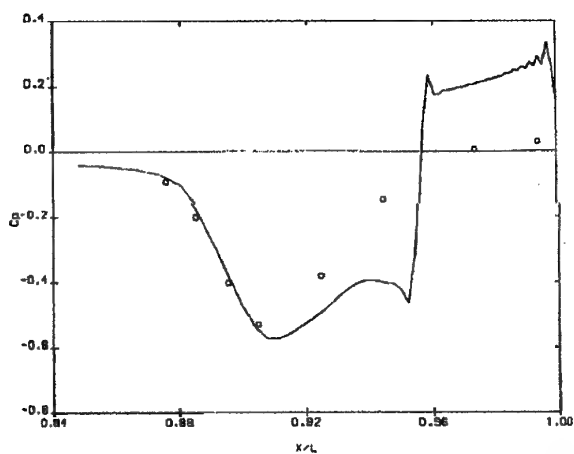
Contribution E05 and N13



Contribution N09 (B-B)



Contribution N10



Contribution E11

Figure 3.5-122 (Continued). Comparison of Surface Pressures ( $C_p$  vs.  $x/L$ ), Case B.4.2, Row 5

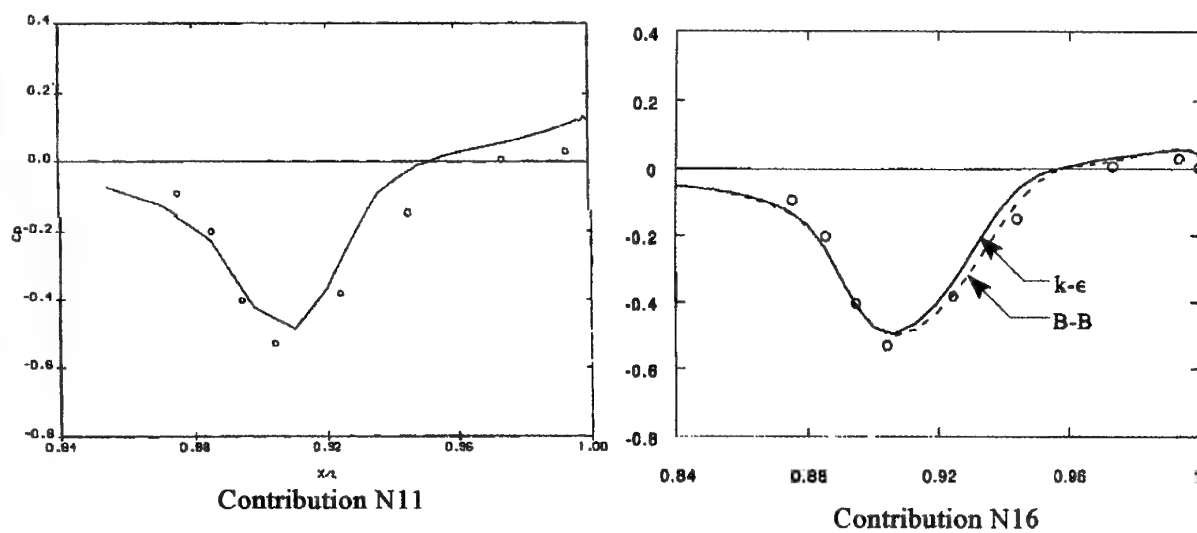
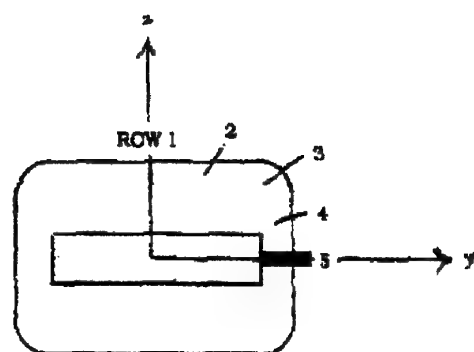
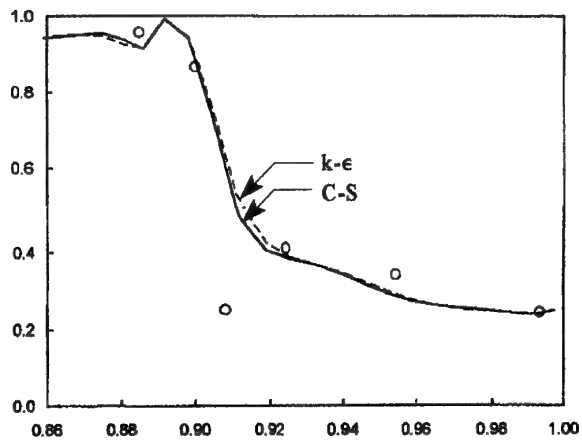
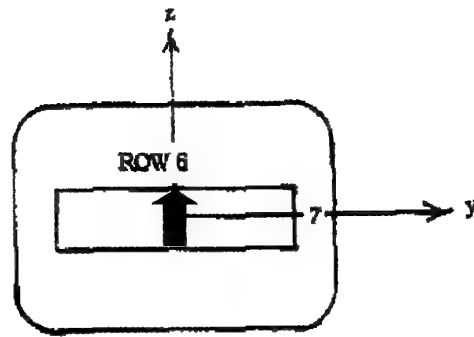
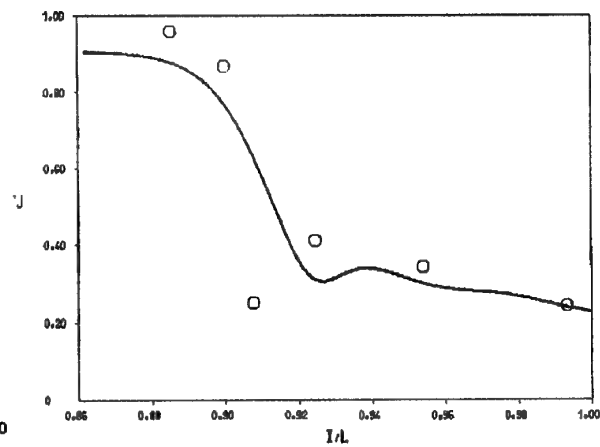


Figure 3.5-122 (Concluded). Comparison of Surface Pressures ( $C_p$  vs.  $X/L$ ), Case B.4.2, Row 5

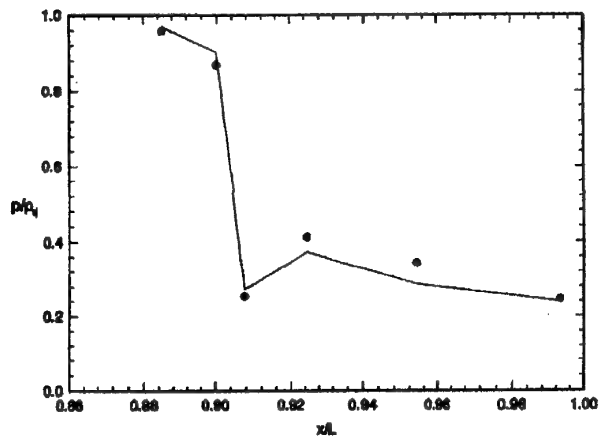




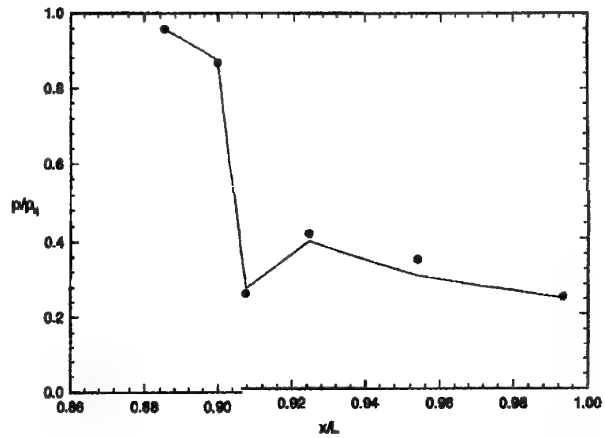
Contribution N02



Contribution N03

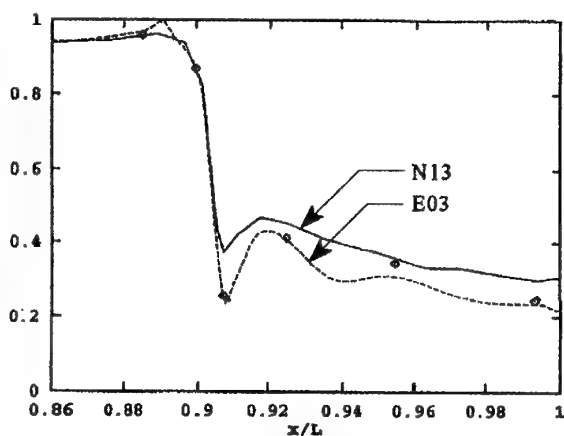
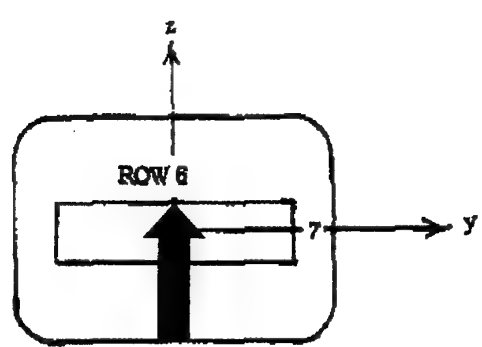


Contribution N04 (Coarse Grid)

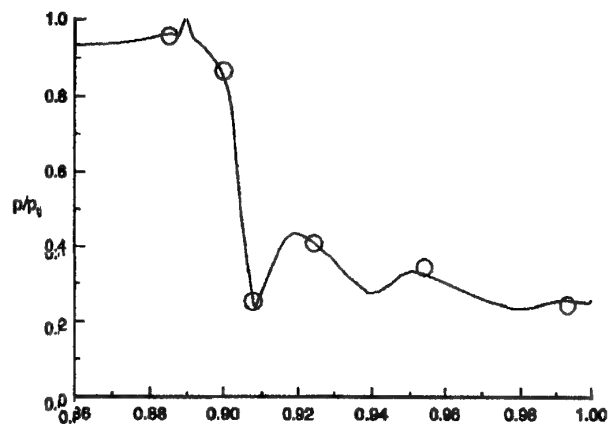


Contribution N04 (Fine Grid)

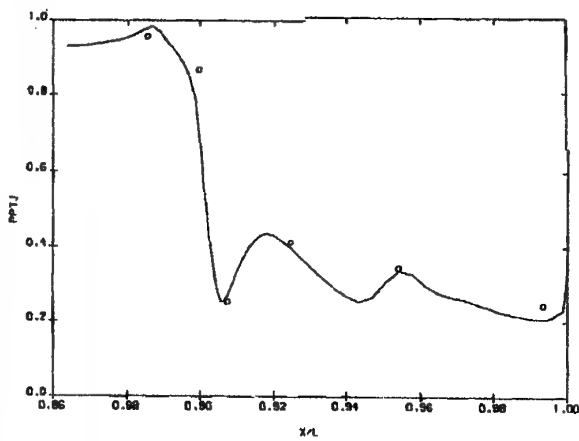
Figure 3.5-123 (First Part). Comparison of Surface Pressures ( $P/P_t$  vs.  $X/L$ ), Case B.4.2, Row 6



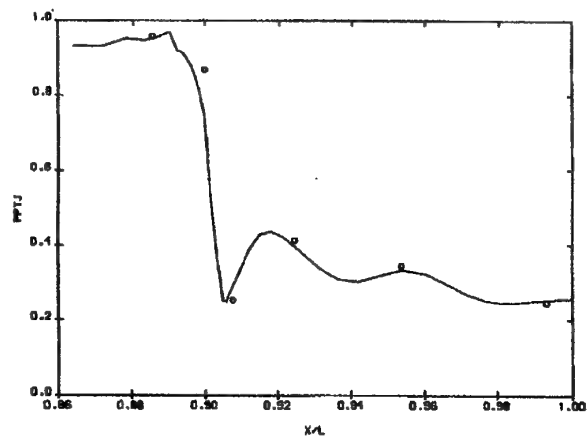
Contributions E05 and N13



Contribution N10



Contribution E11



Contribution N11

Figure 3.5-123 (Continued). Comparison of Surface Pressures ( $P/P_{tj}$  vs.  $X/L$ ), Case B.4.2, Row 6

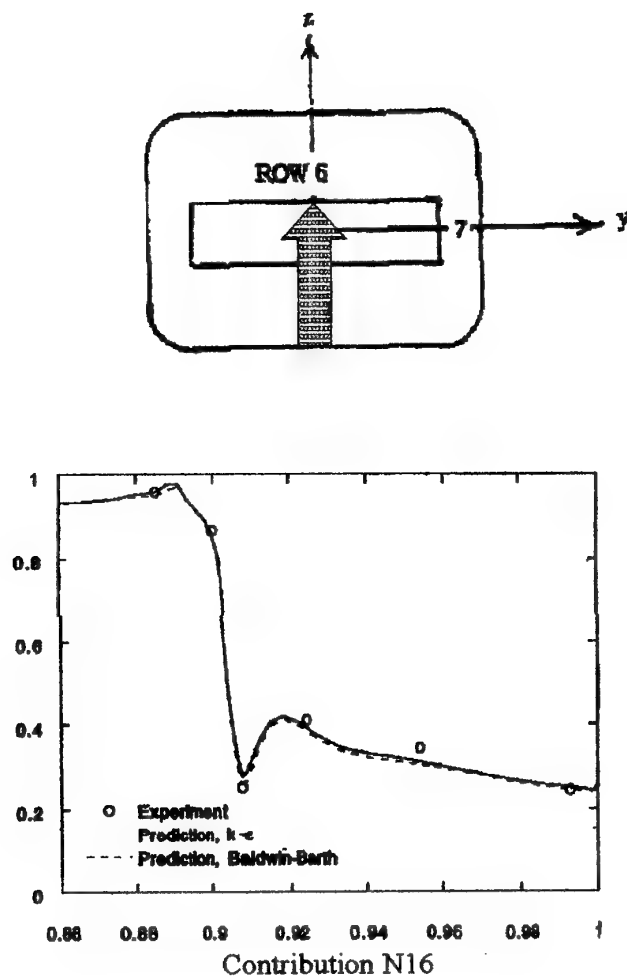


Figure 3.5-123 (Concluded). Comparison of Surface Pressures ( $P/P_t$  vs.  $X/L$ ), Case B.4.2, Row 6

The data for Row 7 are presented in Figure 3.5-124. These predictions, too, are consistent with those of Row 6 (previous figure) and with those of Case B.4.1 (Figure 3.5-106).

**Plume Flowfield Comparisons** - The next series of figures present CFD predictions for the plume flowfield. Unfortunately, no experimental data are available to assess the accuracy of these predictions. The discussion, therefore, will proceed on the basis of the qualitative features of the jet and the mixing layer.

The first set of data shows the predicted flowfield at the nozzle exit plane (Figure 3.5-125). This figure shows a simple, well-behaved flow of the jet at the exit.

The velocity vector field in the crossflow plane (i.e., the lateral plane) at the nozzle exit is presented in Figure 3.5-126. This figure shows several interesting features. Within the plume flow (lower left quadrant of the Figure) the flow is expanding at the exit, as would be expected. However, near the middle of the outboard wall (i.e., the bottom of the figure, near the center) the vectors show some circulation, indicating a vortex may be present in the jet flow at the exit.

The external flow shows a bulk motion upward and outward (left center of the Figure), which is due to the recompression (upward motion) and the spill of the fluid laterally over the side of the nozzle (outward motion). This lateral spill has created a strong vortex in the external flow, above the lateral corner of the nozzle (center of the Figure).

The final plume Figure shows the contours of Pitot pressure some distance downstream of the jet exit, at  $X/L = 1.16$  (Figure 3.5-127). This contribution shows a moderately-thick free shear layer. Based on the previous set of data, for Case B.4.1, it may be that the free shear layer is substantially thicker than is indicated in this Figure.

**Drag Buildup** - The axial buildup of pressure drag, for one Navier-Stokes contribution, is presented in Figure 3.5-128. These data are consistent with the results for the previous case, B.4.1. For these calculations, the drag is normalized using the maximum cross-section area of the model forebody and afterbody ( $A_{MAX}$ ). The results, firstly, show that the drag is over-predicted on the coarser grid. Secondly, the drag level is established in the region  $X/L$  from 0.88 to 0.94, i.e., the region of attached flow forward of the shock. Downstream of the shock, the boundary layer is separated and the wall pressure rises to near-ambient levels. As a result, almost no offsetting recompression is achieved to reduced the pressure drag.

### 3.5.4.3 Discussion of Results

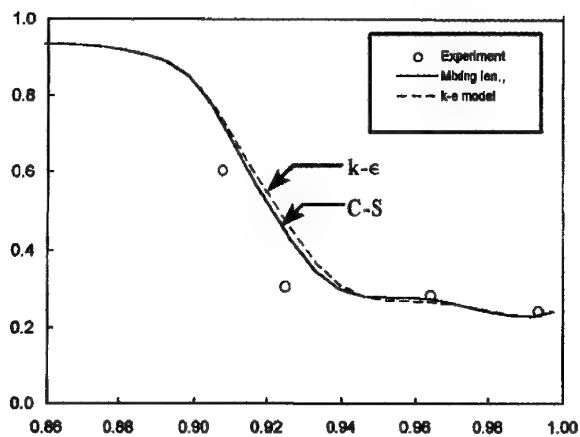
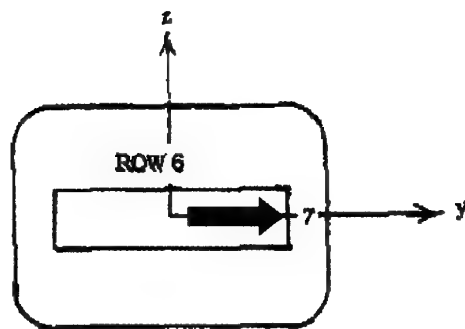
The B.4 test cases pose an interesting and unexpectedly difficult challenge to all aspects of the flow prediction. The flow at Mach 0.6 (test case B.4.1) remains attached, but the pressure field on the aftbody and nozzle is significantly modified by viscous interactions. The flow at Mach 0.94 (test case B.4.2) is dominated by a strong shock-boundary layer interaction, which causes extensive flow separation on the nozzle upper surface. Due to differing expansion and compression fields on the upper surface and the sidewalls, lateral pressure gradients are created which reverse sign in moving toward the exit (both test cases). These lateral pressure gradients produce a complex pattern of streamwise vortices, emanating from the nozzle lateral corner, which flow into the plume and the mixing layer. An impact of these vortices can be deduced from the shape of the mixing layer.

Further, some evidence based on CFD solutions was noted, that indicates a shock-expansion wave system may be present in the supersonic portion of the nozzle internal flow. This wave system (if it exists) was resolved to varying degrees, or not at all, by the various CFD methods. The impact of an accurate definition of this wave system on the plume flowfield predictions is not known.

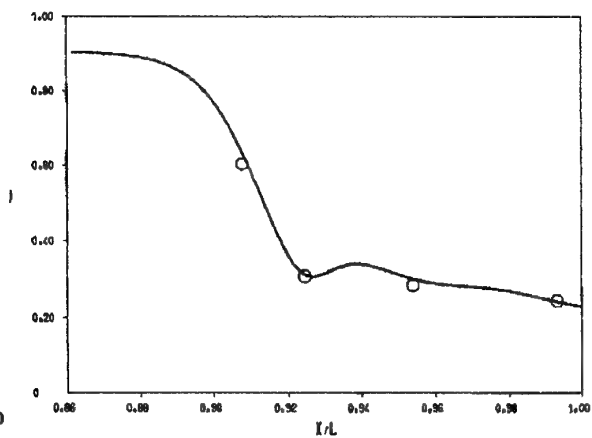
Each of these factors is a complication of the fluid dynamic models in most CFD codes. In general, prediction accuracy for the B.4 test cases was not comparable to that achieved in the other test cases. Further improvements in accuracy may await advances in turbulence modeling for shock-separated flows, strong secondary flows, and plumes interacting with streamwise vortices. The poor resolution of the (presumed) shock-expansion wave system inside the nozzle serves as a reminder that it may not be possible to compromise any element of a CFD solution, if the goal is high quantitative accuracy.

### References

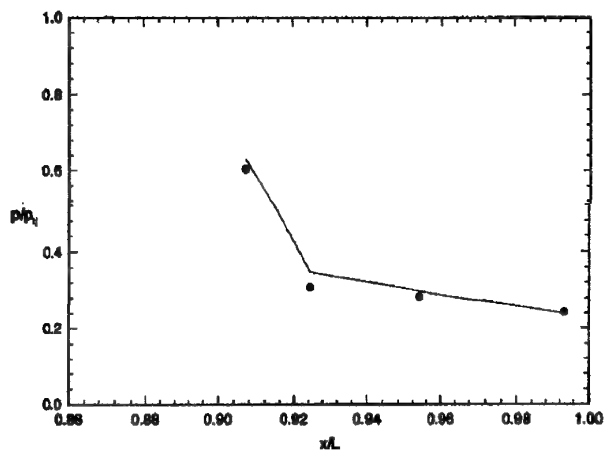
- 3.5-1. Compton, W.B., III, J.L. Thomas, W.K. Abeyounis, and M.L. Mason, "Transonic Navier-Stokes Solutions of Three-Dimensional Afterbody Flows," NASA TM-4111, July 1989.
- 3.5-2. Compton, W.B., III, K.S. Abdol-Hamid, and W.K. Abeyounis, "Comparison of Algebraic Turbulence Models for Afterbody Flows with Jet Exhaust," AIAA Journal, Vol. 30, No. 11, November 1992, pp. 2716-2722.



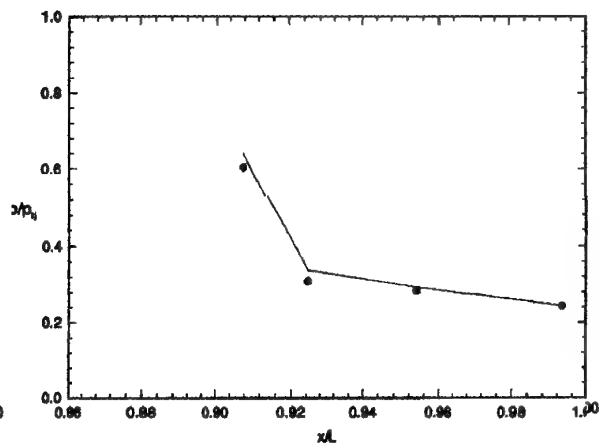
Contribution N02



Contribution N03

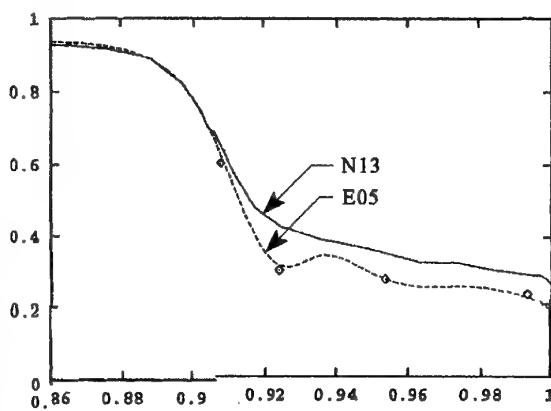
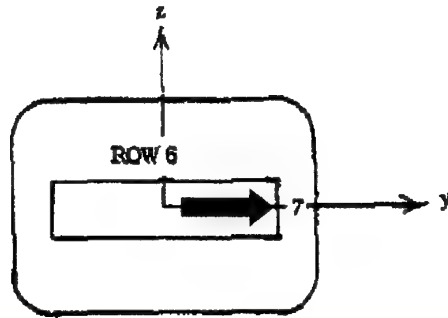


Contribution N04 (Coarse Grid)

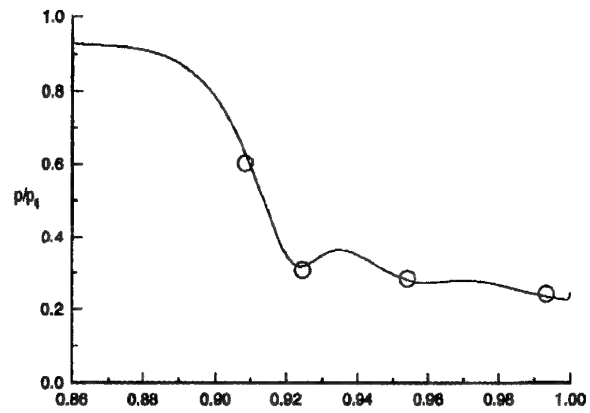


Contribution N04 (Fine Grid)

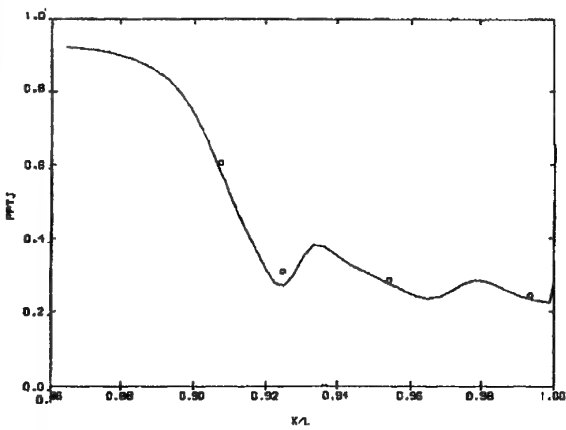
Figure 3.5-124 (First Part). Comparison of Surface Pressures ( $P/P_t$  vs.  $X/L$ ), Case B.4.2, Row 7



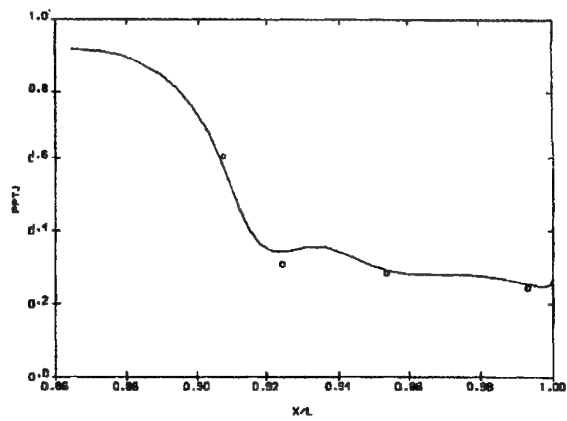
Contributions E05 and N13



Contribution N10



Contribution E11



Contribution N11

Figure 3.5-124 (Continued). Comparison of Surface Pressures ( $P/P_{tj}$  vs.  $X/L$ ), Case B.4.2, Row 7

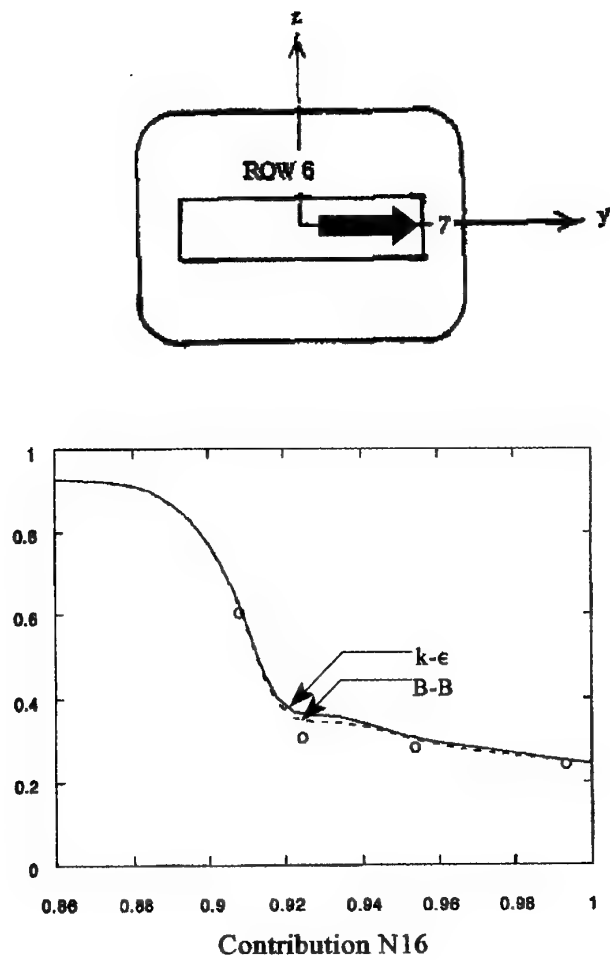


Figure 3.5-124 (Concluded). Comparison of Surface Pressures ( $P/P_{tj}$  vs.  $X/L$ ), Case B.4.2, Row 7

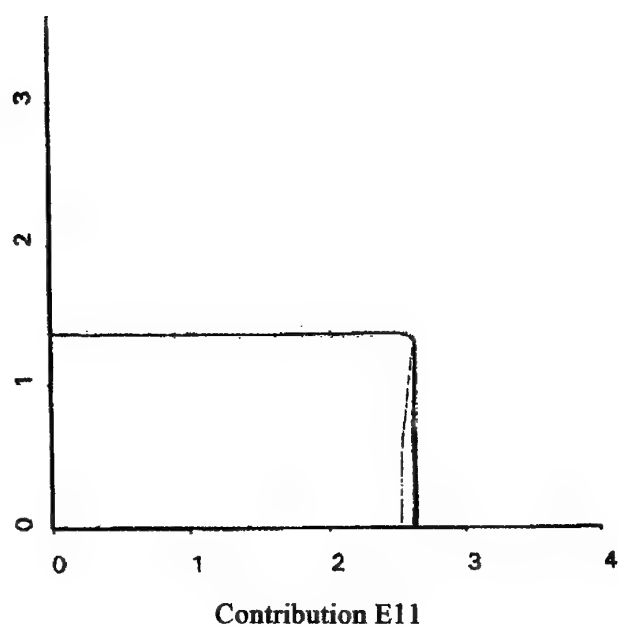
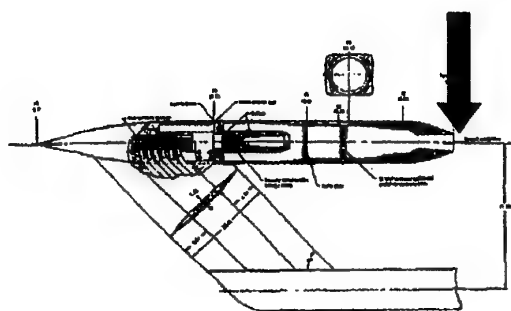
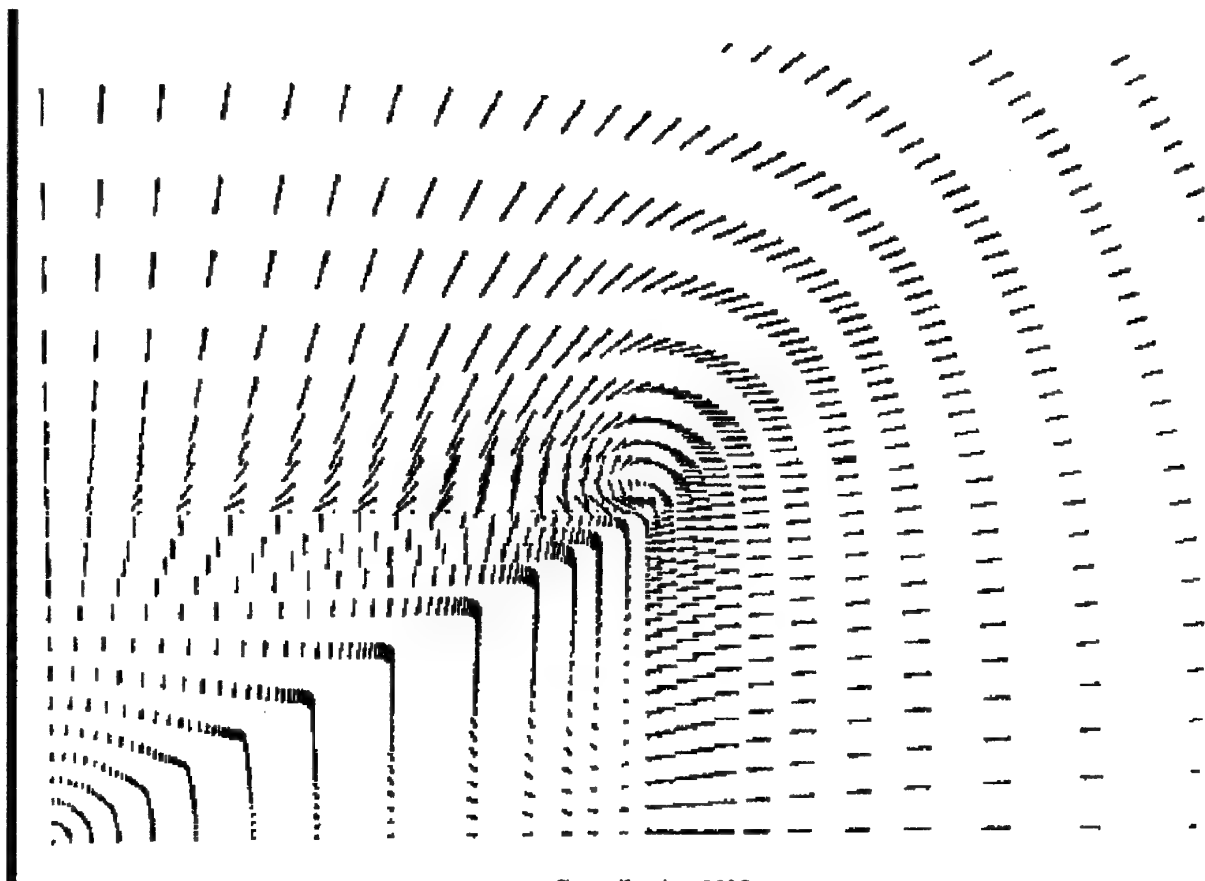
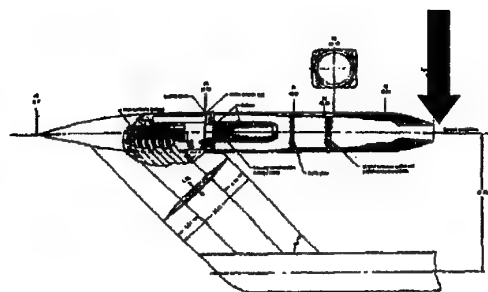


Figure 3.5-125. Predicted Plume Pitot Pressure Contours, Case B.4.2,  $X/L=1.00$  (Nozzle Exit Plane)





Contribution N03

Figure 3.5-126. Predicted Plume Velocity Vectors, Case B.4.2,  $X/L=1.00$  (Nozzle Exit Plane)

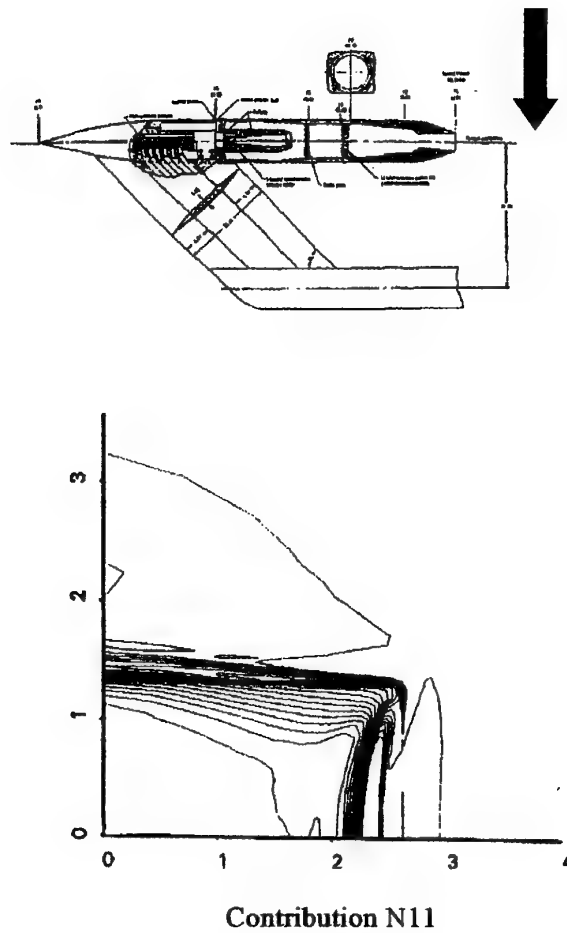
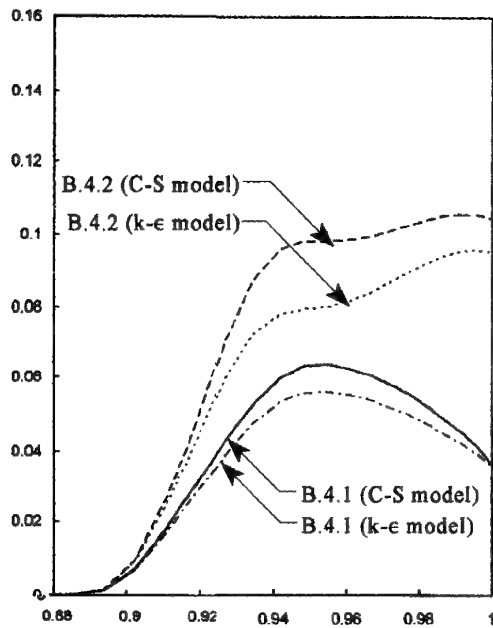
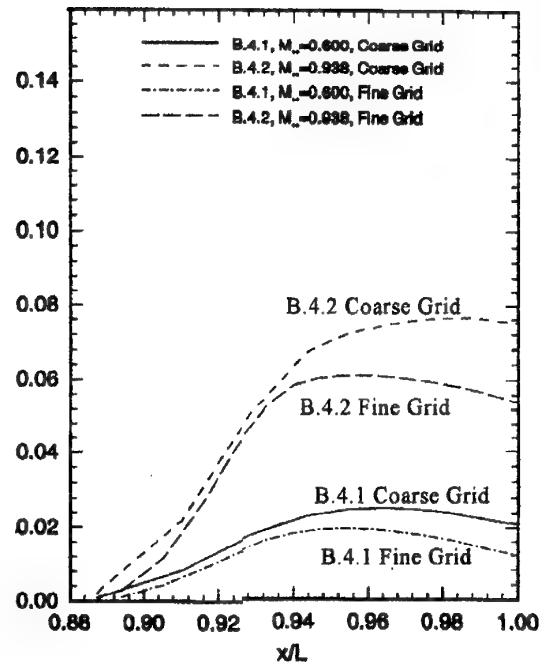


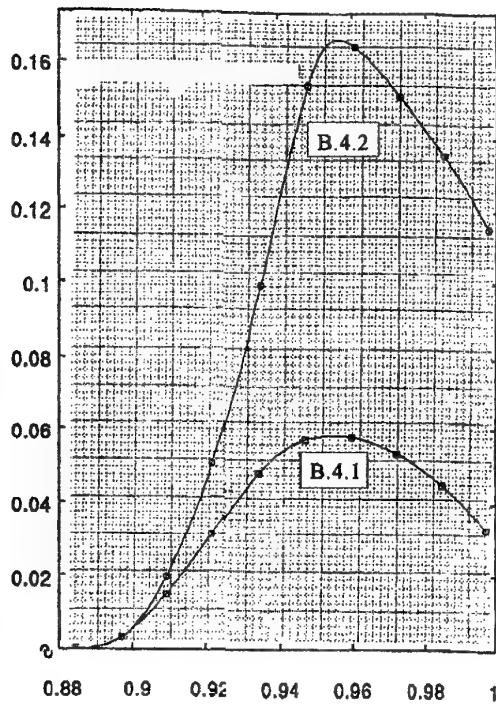
Figure 3.5-127. Predicted Plume Pitot Pressure Contours, Case B.4.2,  $X/L=1.16$



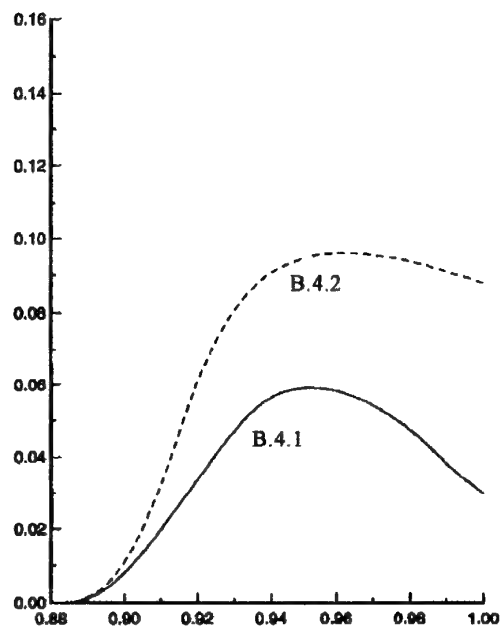
Contribution N02



Contribution N04



Contribution E05



Contribution N10

Figure 3.5-128 (First Part). Predicted Buildup of Pressure Drag, Case B.4.2

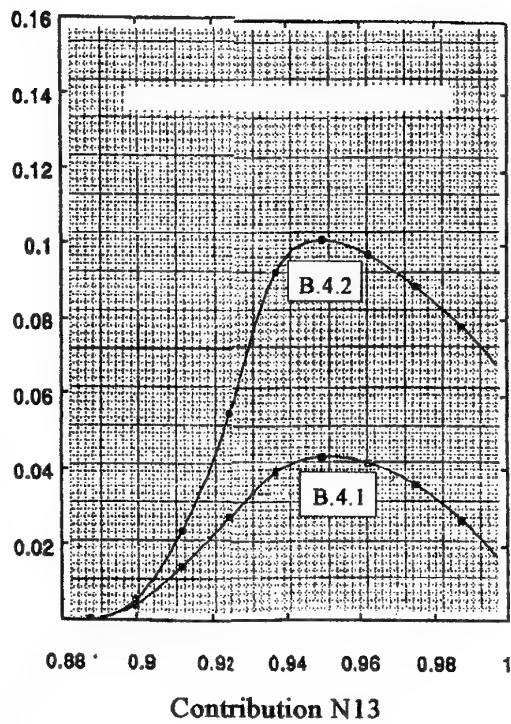


Figure 3.5-128 (Concluded). Predicted Buildup of Pressure Drag, Case B.4.2

### 3.6 Recommendation for Future Work

From the discussions of the results of the individual test cases the following major conclusions can be summarized:

- o The semi-empirical methods produced very good results for test cases within the range of their data bases. They neither offer flowfield data nor a drag breakdown.
- o The CFD methods showed the progress predicted by AGARD Working Group 08. All the methods are able to reasonably predict the flow about complex three-dimensional afterbodies depicting complex flow phenomena like massive separations, shock/boundary layer interactions, vortices and free shear layers. Some of the results must be considered as extremely good in comparison with experimental data.
- o However the CFD results presented open questions that still have to be answered:
  - These investigations could not determine the effects of local code instabilities and numerical viscosity on the results.
  - The same is true for the differences of modeling of vortices and their interaction with boundary layers, free shear layers and shocks.
  - In spite of the tremendous progress in turbulence models it is not clear why e.g. the same turbulence models in different codes produced different results and even trends. There is still the need for "better" turbulence models for boundary layers with adverse pressure gradients, separations, free shear layers (2D, axisymmetric or mixed, and 3D), and shock/boundary layer/vortex interactions.
  - How much can elements of the flow problem be compromised without impairing accuracy? E.g., can the geometry of nozzle trailing edges be modified or must it be modelled in every detail?
  - How large is the effect of consistency of CFD solutions, i.e. user experience, grid quality, numerical method, on the reliability and accuracy of the absolute and incremental drag predictions by CFD?
  - Is it necessary to consider the support and tunnel interference effects for improving quantitative accuracy?
  - Can CFD results be used for the scaling of the results of cold jet flow tests or calculations to real flight conditions?

From these conclusions the following recommendations can be made:

- o The application of semi-empirical models should be improved by extending their data base with the results of additional afterbody experiments.
- o For CFD, improvements of turbulence models and codes should still be pursued. However this work cannot be within the scope of an AGARD working group. This work should be and is on-going at different research institutions and Universities. For the consideration of local flow problems like separations, shock boundary layer interactions or even free shear layers, geometries, flow conditions and experimental data of the test cases considered by this working group should be used as a basis for these developments.  
Turbulence parameters off the model walls could be determined by simple, basic experiments.
- o After these improvements have sufficiently matured there seems to be the need for a major, focused study. This study should comprise both experimental and CFD work in a concerted action.

An afterbody model geometry should be selected by CFD and experimental people with regard to the flow problems to be expected. For this afterbody a model should be designed for testing in different wind tunnels. Candidates for this model could be one of the model geometries considered in this working group or any other geometry of interest at that time. CFD results presented in this report or newly performed CFD results could be used for the selection of test conditions and instrumentation for the model.

Careful experiments should produce not only surface but also free stream data. The data should also include measurements of friction and Reynold stresses for the validation of turbulence models. Testing at a range of Reynolds numbers will clarify the effects of this flow parameter on the results. Of extreme importance will be the determination of the flow and turbulence parameters at the inflow and outflow boundaries of the CFD solutions to be performed.

Tests should also be performed in wind tunnels with solid walls in order to produce results with unique flow boundary conditions. Measuring pressures on the wind tunnel walls will help to investigate the windtunnel wall effects and to validate the flow modelling of the CFD methods.

CFD calculations should be performed for the exact known test conditions without the knowledge of the

test data but with clearly defined goals like best absolute or incremental drag accuracy.

Differences between the nominal and the actual model geometry should be investigated by CFD.

Determination of accuracy of both the experimental and the numerical methods will be of utmost importance.

A thorough analysis of both the experimental and numerical results and the comparisons of the two will demonstrate the state of the art and the progress achieved compared with today.

The aim of the work during the years to come should be to develop CFD from a "diagnostic tool" (AGARD WG08) to a tool that can be used in a supplementary way with the wind tunnel for the production of design data.

- o Unsteady afterbody flows should be investigated experimentally and numerically.
- o Full scale test data at real flight conditions are needed to validate the CFD codes' ability to predict afterbody drag (forces) with sufficient accuracy for the aircraft designer.

## 4. CONCLUDING REMARKS

Nine years of progress in experimental and theoretical study of flows around aircraft afterbodies has significantly changed and improved the afterbody design process. WG08 predicted that future needs for a review of this subject would be centred around methods for the computation of 3-D viscous flows. This aspect has indeed grown to virtually dominate the research effort and seems set to continue to do so in the foreseeable future. The role of these methods in the design process is now both established and well understood. WG17 has focused on the effectiveness of current methods in modelling the fundamental features of afterbody flows and, equally, has endeavoured to assess their usefulness by applying them to a selection of design oriented test cases. The work to some extent provides a snapshot of current predictive capabilities.

Detailed conclusions and recommendations for future work are given in each of the main sections of the report. The purpose of the following paragraphs is to summarise the key findings and to deliver the main messages of WG17.

### 4.1 Fundamental Flow Phenomena

The majority of Navier-Stokes test case solutions were regarded as providing a reliable qualitative, physical description of the flowfield under consideration. Inadequacies in turbulence modelling were noted as the main contributor to poor modelling of the thickening boundary layer in the adverse pressure gradient region of the afterbody. Similarly, the free shear layer just downstream of the nozzle exit was generally not well modelled, evident usually from insufficient entrainment. It is in these regions that the largest drag discrepancies will generally be generated. No particular turbulence model gave consistently the best results, and no recommendation can be offered as to the best path to follow in this respect in the future. The foregoing remarks echo the findings of WG08 fairly closely, albeit in the context of 3-D rather than 2-D (axisymmetric) predictions. The recommendations of WG08 for code development do appear to have been largely followed in the transition to fully 3-D methods. Despite the considerable advances made in this period, turbulence modelling is still the critical technology for the prediction of afterbody flows.

The development of computational methods for the prediction of 3-D afterbody flows has so far been underpinned by a fairly limited amount of experimental data. A fundamental need exists for detailed experimental studies on complex flows around realistic, though preferably geometrically simple, 3-D configurations exploiting both classical intrusive techniques and where possible the latest advances in non-intrusive experimental techniques. Pressure sensitive paint, infra red thermography, LDV and laser spectroscopy techniques now offer the prospect of acquisition of a virtually complete description of a 3-D afterbody flowfield. The measurement of skin friction is highlighted as an area where further advances are needed and accelerated development of quantitative pressure sensitive paint techniques is recommended. Particular emphasis should be placed upon achievement of high data accuracy and appropriate spatial resolution in the measurement of quantities both on the body surface and in the flowfield.

### 4.2 Design

Semi-empirical methods can provide a highly effective way of interpolating and to some extent extrapolating existing afterbody drag data bases. Heavy reliance is placed upon the experience and insight of the user as to the applicability of the underlying correlation, but, where there is confidence in this respect, these methods can provide both good drag accuracy and unparalleled cost-effectiveness. They are therefore particularly suited to use in the initial stages of the design process where lack of insight into the flow mechanisms present and lack of drag breakdown information is not of primary importance. There is considerable scope and, it would appear, justification for the expansion of the existing experimental data base to widen the range of configurations to which such methods may be applied.

Reliable prediction of certain types of incremental drag has been shown to be possible using current CFD methods. This is the way that these methods are most commonly employed in the design process at the current time. With careful attention to consistency of approach, trends and to some extent sensitivity to particular changes will, in general, be indicated correctly. In addition, a valuable insight into the flow physics responsible for these incremental effects will be available. In the majority of situations, this information should fulfil most of the needs of the designer. The effect of geometric complexity on the viability of this process is best described in terms of the following simple observation: Calculation of a simple flow around a complex 3-D geometry is likely to be more successful than calculation of a complex flow around a simple geometry. A concerted effort is required to examine ways of further improving the reliability and accessibility of current methods to allow their potential to be fully realised. Mesh generation, robustness of flow solvers, efficiency of flow solvers and, in some instances, post-processing are particular areas where such effort could rapidly improve accessibility. Costs will be driven downwards at the same time, along with the risk in some instances, attached to the use of CFD in design. Additional, affordable, computing power should continue to become available and this will provide an underlying, additive, trend of improving accessibility. The need for continual focus on improvement of both the cost effectiveness and in particular the user-friendliness of these methods is nevertheless emphasised.

Whilst satisfactory prediction of absolute afterbody drag using current CFD methods may be achievable where a great deal of user experience has been accumulated on a particular configuration, prediction of completely arbitrary cases is likely to be problematic. Absolute afterbody drag prediction accuracy should now be one of the main focal points for the continuing development of CFD methods. However, the ultimate goal of acceptable afterbody drag prediction accuracy will not be reached at a single point in time. As we have seen over recent years, rapidly evolving design drivers such as observables and STOVL can lead to step-changes in nozzle and afterbody complexity, resulting in a moving target for design method development. A point should nevertheless be reached where the drag of a reasonably representative benchmark case can be reliably predicted by the majority of methods, at an appropriate level of cost.

The impact of the increasing use of CFD in the design process on the way in which wind tunnels will be used in the future is a particular point of interest. WG08 suggested that as numerical analysis matured it would increasingly supplement the wind tunnel. In the years since, this has certainly been the case and this is consistent with the view of the current WG regarding the ongoing relationship. The two are also broadly complementary in terms of their current cost effectiveness. This point is illustrated by the table below which presents the condensed view of the group on the cost of production of design data using CFD (where this is possible) compared to experiment:

	FEW DATA POINTS	FULL DATABASE
MONEY	CFD much less	CFD much greater
TIME	About the same	CFD much greater

### 4.3 General

A great deal remains to be understood regarding the effects of jet temperature and chemistry on drag and the flow mechanisms involved. Complete experimental investigation of these effects using the latest techniques is required.

Detailed study of Reynolds number effects is recommended in order to improve confidence in the use of CFD for the prediction of full scale flight cases.

The computation of unsteady afterbody flows and the acquisition of suitable experimental data for method validation is likely to be the next major challenge in the field of afterbody aerodynamics. Both numerical and experimental investigation of these flows is encouraged.

If the rate of development of CFD techniques seen over the last nine years is maintained, it may well be possible to include these aspects in a future review of the field.



# APPENDIX A: EXPERIMENTAL DATA FOR GROUP A TEST CASES

## A.1. Test Case A.1.1 (Axisymmetric Body Without Jet at Incidence)

### A.1.1. Surface Pressure Distribution

Row $\varphi = 0^\circ$		Row $\varphi = 90^\circ$		Row $\varphi = 180^\circ$	
$X/D_{max}$	$C_p$	$X/D_{max}$	$C_p$	$X/D_{max}$	$C_p$
-0.58	-0.0588	-0.33	-0.0441	-0.33	-0.0196
-0.83	-0.0931	-0.58	-0.0588	-0.58	-0.0343
-1.17	-0.0882	-0.83	-0.0980	-0.83	-0.0686
-1.63	-0.0294	-1.17	-0.0980	-1.17	-0.0784
-2.08	-0.0147	-1.63	-0.0588	-1.63	-0.0343
-2.54	-0.0098	-2.08	-0.0490	-2.54	-0.0196
-3.00	-0.0049	-2.54	-0.0392	-3.00	-0.0098
		-3.00	-0.0343		

Base pressure:  $C_{pB} = -0.0751$

### A.1.2. Boundary Layer Profiles

$$X/D_{max} = -1.2$$

Row $\varphi = 0^\circ$		Row $\varphi = 90^\circ$		Row $\varphi = 180^\circ$	
$Y/D_{max}$	$u/U_{max}$	$Y/D_{max}$	$u/U_{max}$	$Y/D_{max}$	$u/U_{max}$
0.607	0.000	0.500	0.000	0.397	0.000
0.627	0.435	0.517	0.589	0.413	0.764
0.630	0.450	0.520	0.623	0.417	0.812
0.633	0.481	0.523	0.666	0.420	0.853
0.637	0.505	0.527	0.705	0.423	0.889
0.643	0.543	0.530	0.743	0.427	0.917
0.650	0.576	0.533	0.777	0.430	0.941
0.657	0.598	0.537	0.805	0.433	0.958
0.667	0.629	0.540	0.852	0.437	0.972
0.683	0.671	0.553	0.922	0.440	0.982
0.700	0.697	0.560	0.967	0.447	0.993
0.767	0.770	0.600	0.999	0.453	0.997
0.867	0.850	0.633	1.000	0.460	0.999
0.967	0.932	0.667	0.999	0.477	1.000
1.067	0.989	0.700	0.999	0.493	1.000
1.167	0.998	0.743	0.998	0.527	1.000
1.267	1.000	0.767	0.998	0.560	1.000
1.467	0.998	0.833	0.997	0.627	1.000
1.000	0.997	0.693	0.999		
0.760	0.999				
0.827	0.999				
0.900	0.999				
1.000	0.999				

$$X/D_{max} = -1.6$$

Row  $\varphi = 0^\circ$ Row  $\varphi = 90^\circ$ Row  $\varphi = 180^\circ$ 

$Y/D_{max}$	$u/U_{max}$	$Y/D_{max}$	$u/U_{max}$	$Y/D_{max}$	$u/U_{max}$
0.643	0.000	0.500	0.000	0.363	0.000
0.663	0.415	0.517	0.580	0.377	0.837
0.667	0.421	0.520	0.604	0.380	0.868
0.673	0.469	0.523	0.647	0.383	0.898
0.687	0.527	0.527	0.686	0.387	0.925
0.690	0.552	0.530	0.721	0.390	0.947
0.700	0.591	0.537	0.797	0.393	0.963
0.733	0.672	0.547	0.884	0.397	0.976
0.800	0.760	0.553	0.927	0.400	0.984
0.867	0.824	0.560	0.960	0.403	0.991
0.933	0.883	0.567	0.979	0.407	0.994
1.000	0.994	0.570	0.986	0.413	0.997
1.067	0.986	0.580	0.992	0.420	0.999
1.100	0.994	0.590	0.998	0.428	0.999
1.117	0.996	0.600	0.999	0.433	0.999
1.200	1.000	0.633	0.999	0.443	1.000
1.300	1.000	0.667	1.000	0.460	1.000
1.400	1.000	0.733	0.999	0.493	0.999
1.500	1.000	0.800	0.999	0.527	0.999
1.667	1.000	0.900	0.999	0.560	0.999
0.627	0.999				
0.700	0.999				
0.800	0.998				
0.900	0.997				
1.000	0.997				

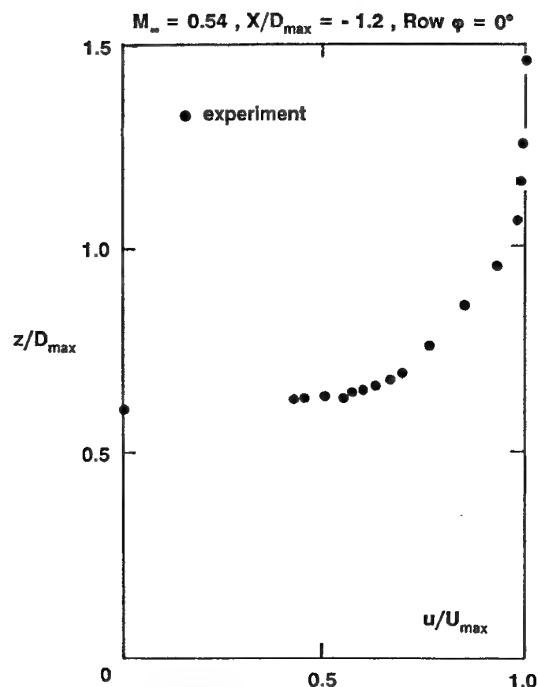


Fig. A.1.1 - Test Case A.1.1 : Boundary layer profile at  $X/D_{max} = -1.2$  and  $\varphi = 0^\circ$

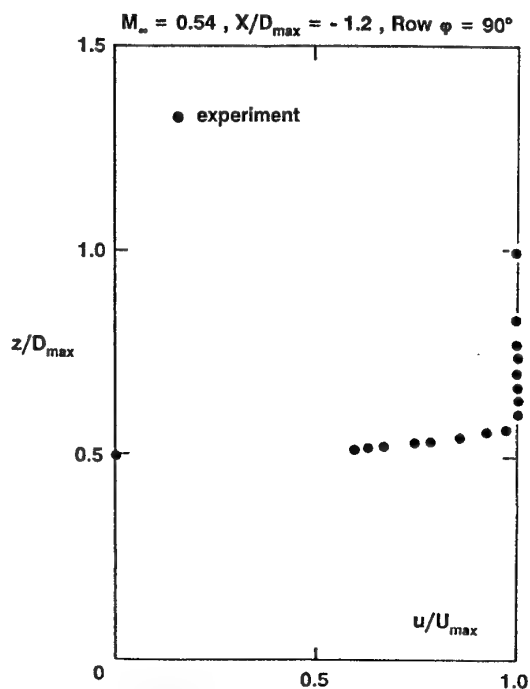


Fig. A.1.2 - Test Case A.1.1 : Boundary layer profile at  $X/D_{max} = -1.2$  and  $\varphi = 90^\circ$

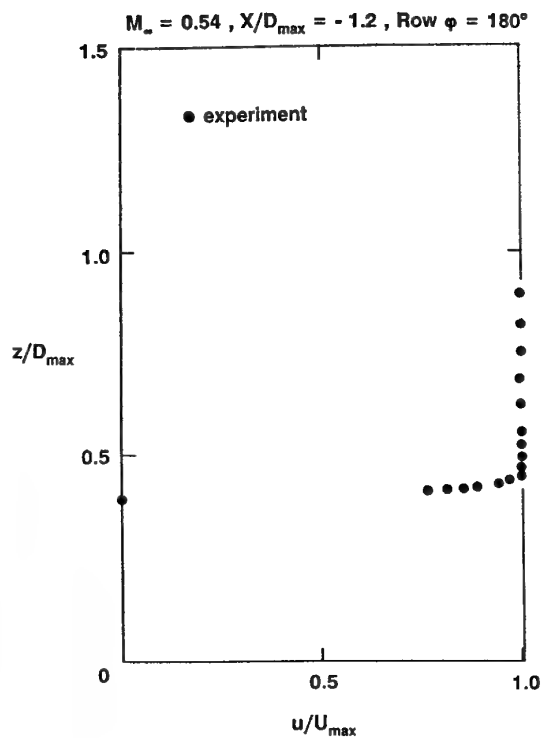


Fig. A.1.3 - Test Case A.1.1 : Boundary layer profile at  $X/D_{\max} = -1.2$  and  $\varphi = 180^\circ$

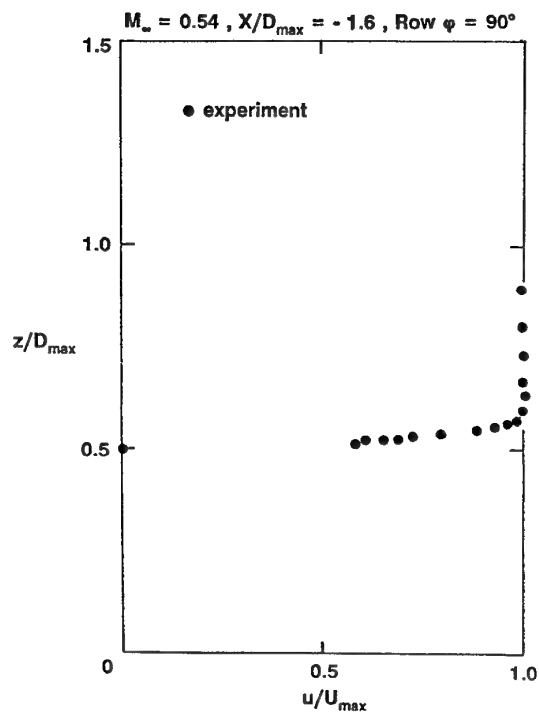


Fig. A.1.5 - Test Case A.1.1 : Boundary layer profile at  $X/D_{\max} = -1.6$  and  $\varphi = 90^\circ$

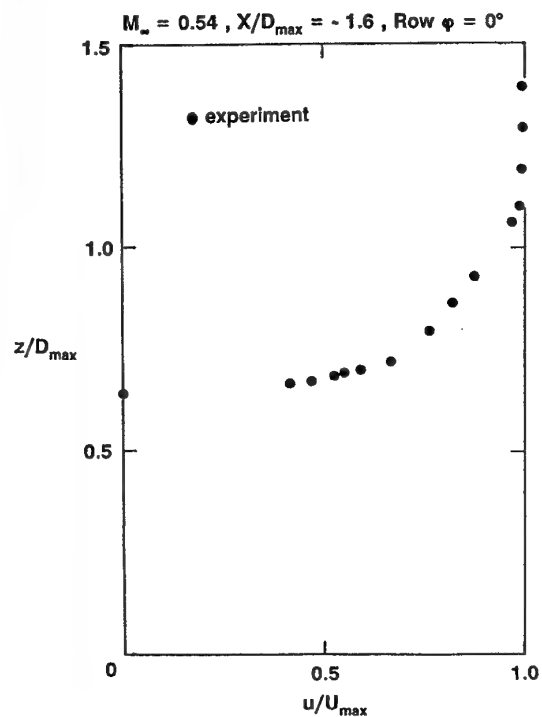


Fig. A.1.4 - Test Case A.1.1 : Boundary layer profile at  $X/D_{\max} = -1.6$  and  $\varphi = 0^\circ$

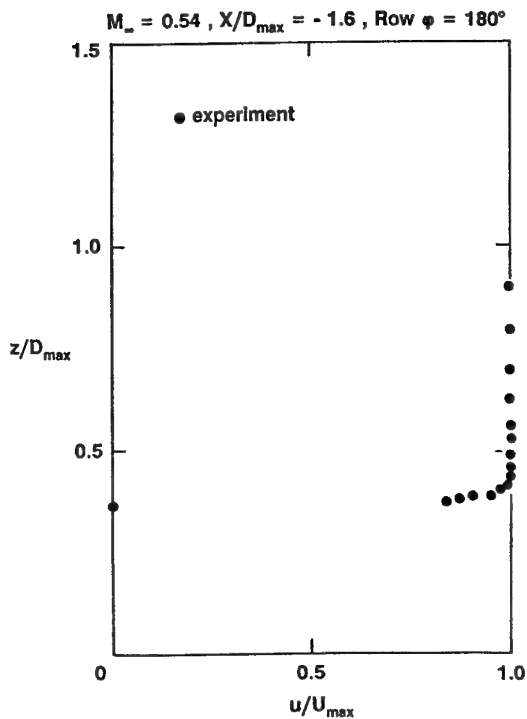


Fig. A.1.6 - Test Case A.1.1 : Boundary layer profile at  $X/D_{\max} = -1.6$  and  $\varphi = 180^\circ$

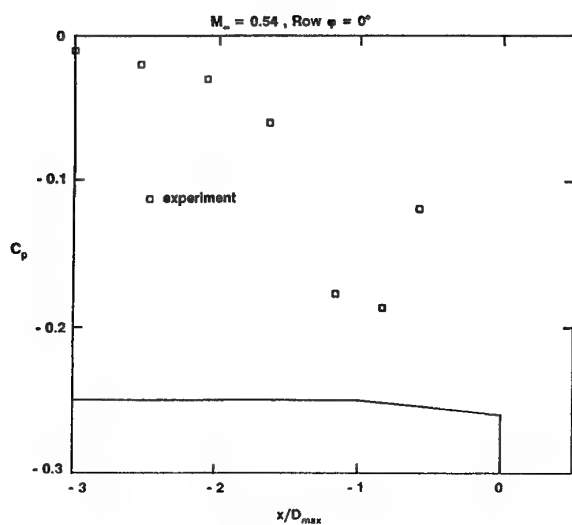


Fig. A.1.7 - Test Case A.1.1 : Static pressure coefficient on the afterbody on row  $\varphi = 0^\circ$

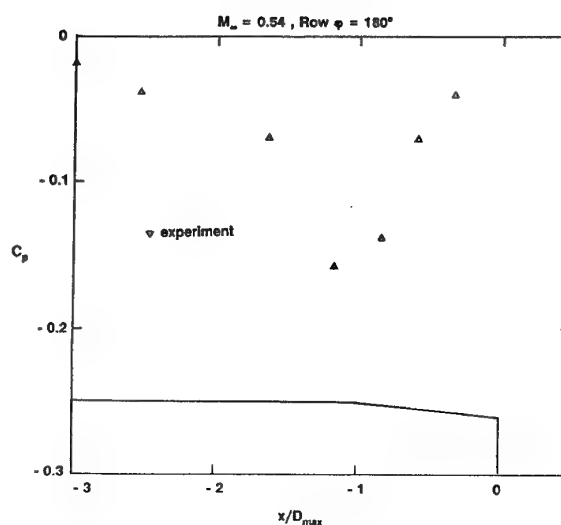


Fig. A.1.9 - Test Case A.1.1 : Static pressure coefficient on the afterbody on row  $\varphi = 180^\circ$

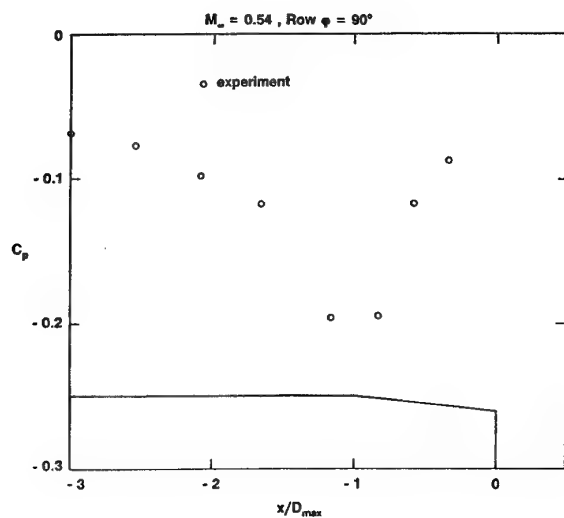
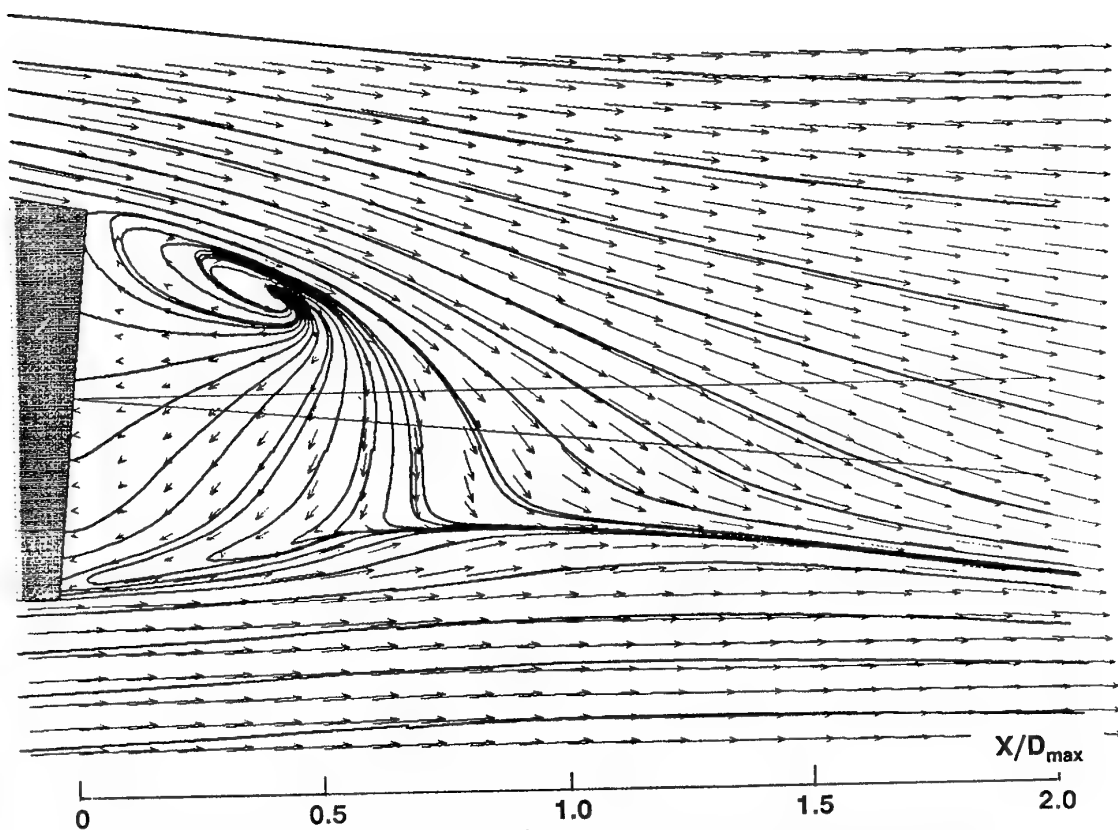
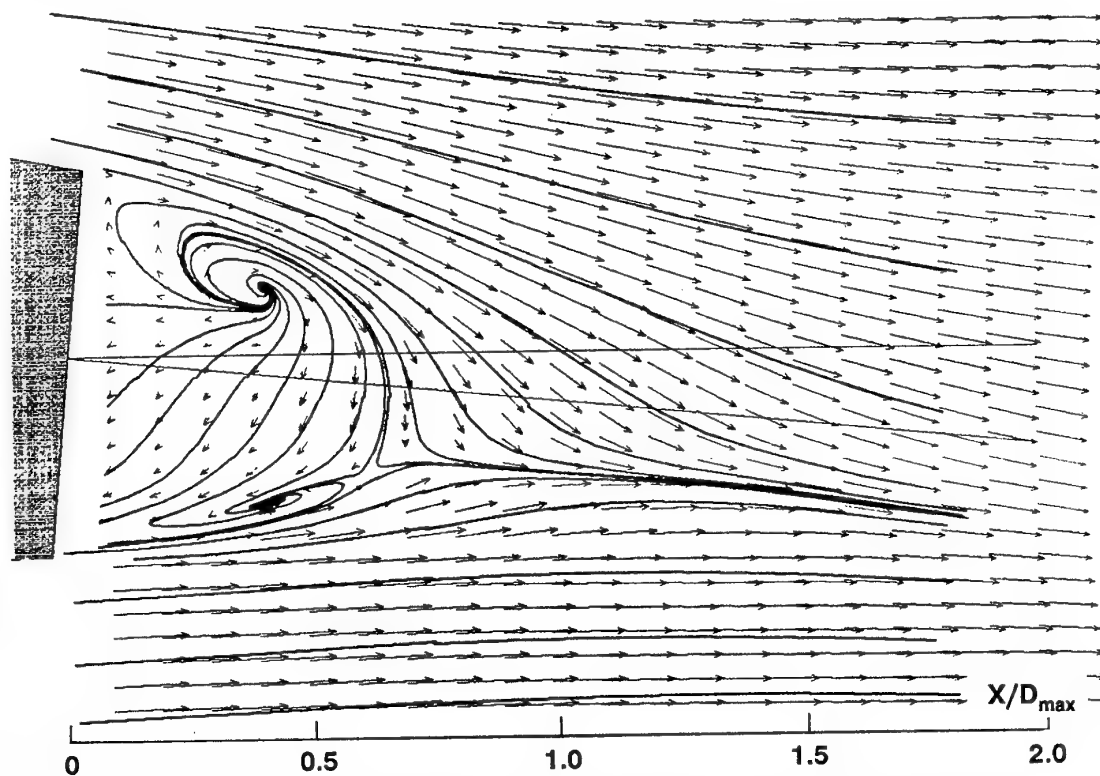


Fig. A.1.8 - Test Case A.1.1 : Static pressure coefficient on the afterbody on row  $\varphi = 90^\circ$



**Fig. A.1.10 - Test Case A.1.1 :** Mean velocity field in the longitudinal plane  $Z/D_{\max} = 0$   
(vector scale:  $1\text{cm} = 125\text{m/s}$  or  $u/U_{\infty} = 0.702$  for  $U_{\infty} = 178\text{m/s}$ )



**Fig. A.1.11 - Test Case A.1.1 :** Mean velocity field in the longitudinal plane  $Z/D_{\max} = 0.125$   
(vector scale:  $1\text{cm} = 125\text{m/s}$  or  $u/U_{\infty} = 0.702$  for  $U_{\infty} = 178\text{m/s}$ )

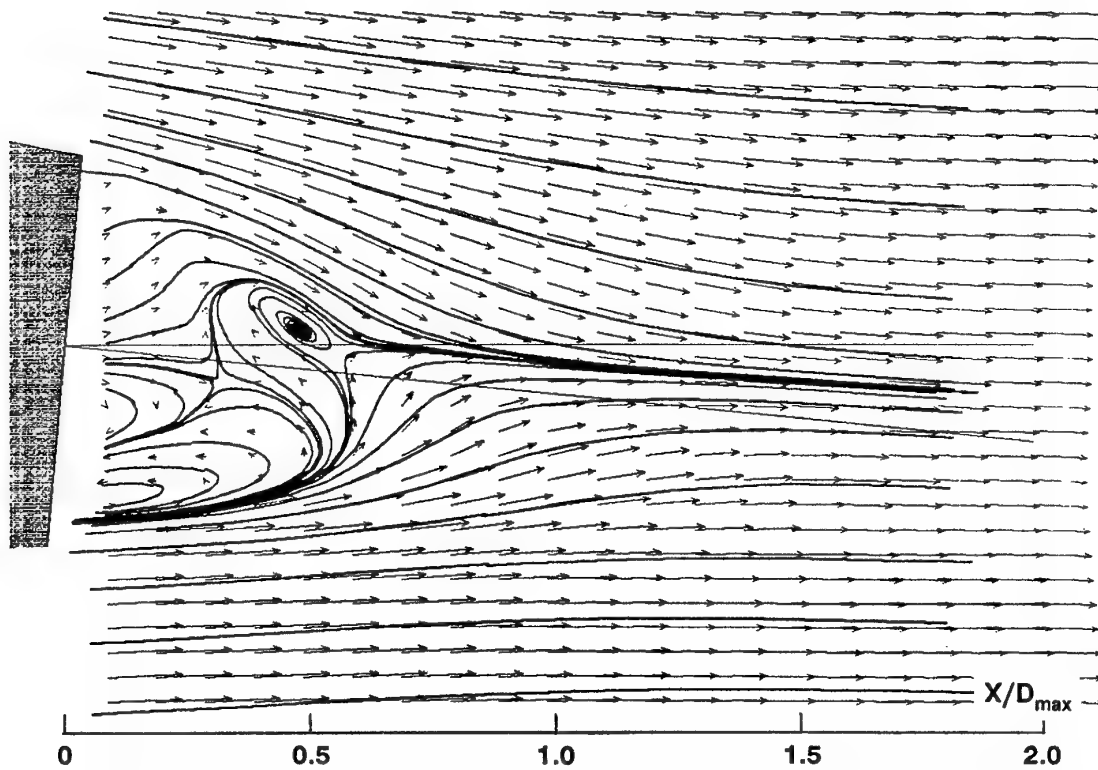


Fig. A.1.12 - Test Case A.1.1 : Mean velocity field in the longitudinal plane  $Z/D_{\max} = 0.250$   
(vector scale:  $1\text{cm} = 125\text{m/s}$  or  $u/U_{\infty} = 0.702$  for  $U_{\infty} = 178\text{m/s}$ )

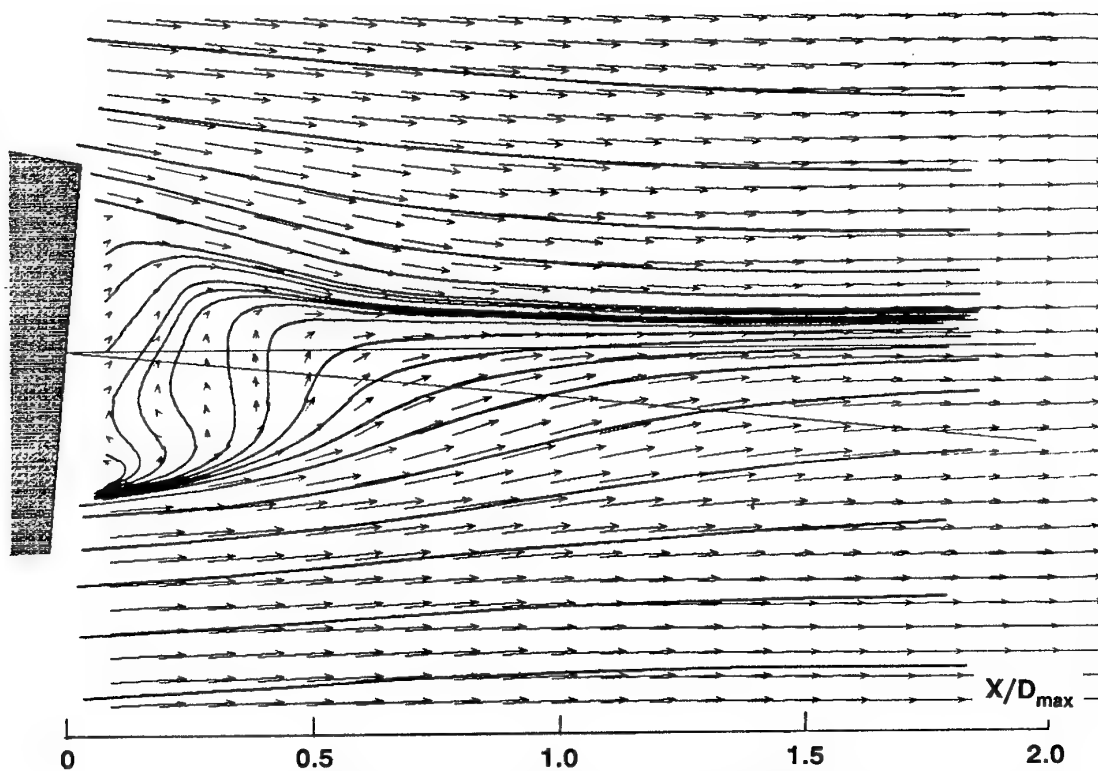


Fig. A.1.13 - Test Case A.1.1 : Mean velocity field in the longitudinal plane  $Z/D_{\max} = 0.375$   
(vector scale:  $1\text{cm} = 125\text{m/s}$  or  $u/U_{\infty} = 0.702$  for  $U_{\infty} = 178\text{m/s}$ )

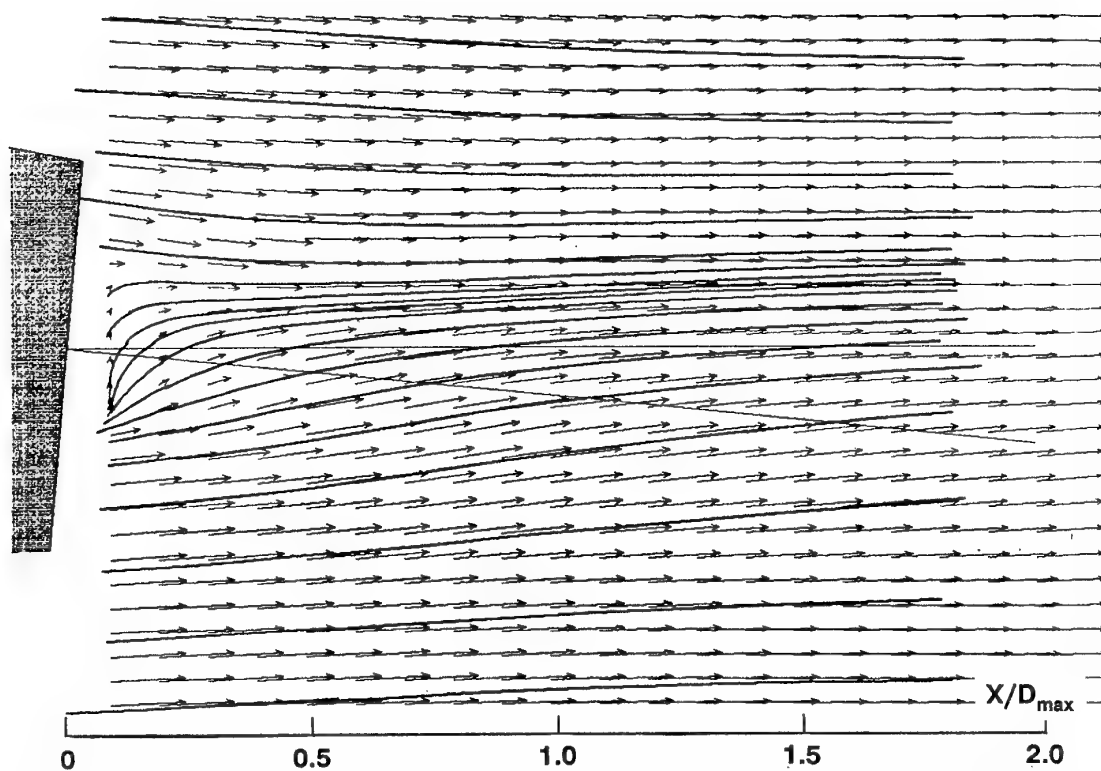


Fig. A.1.14 - Test Case A.1.1 : Mean velocity field in the longitudinal plane  $Z/D_{\max} = 0.50$   
(vector scale:  $1\text{cm} = 125\text{m/s}$  or  $u/U_{\infty} = 0.702$  for  $U_{\infty} = 178\text{m/s}$ )

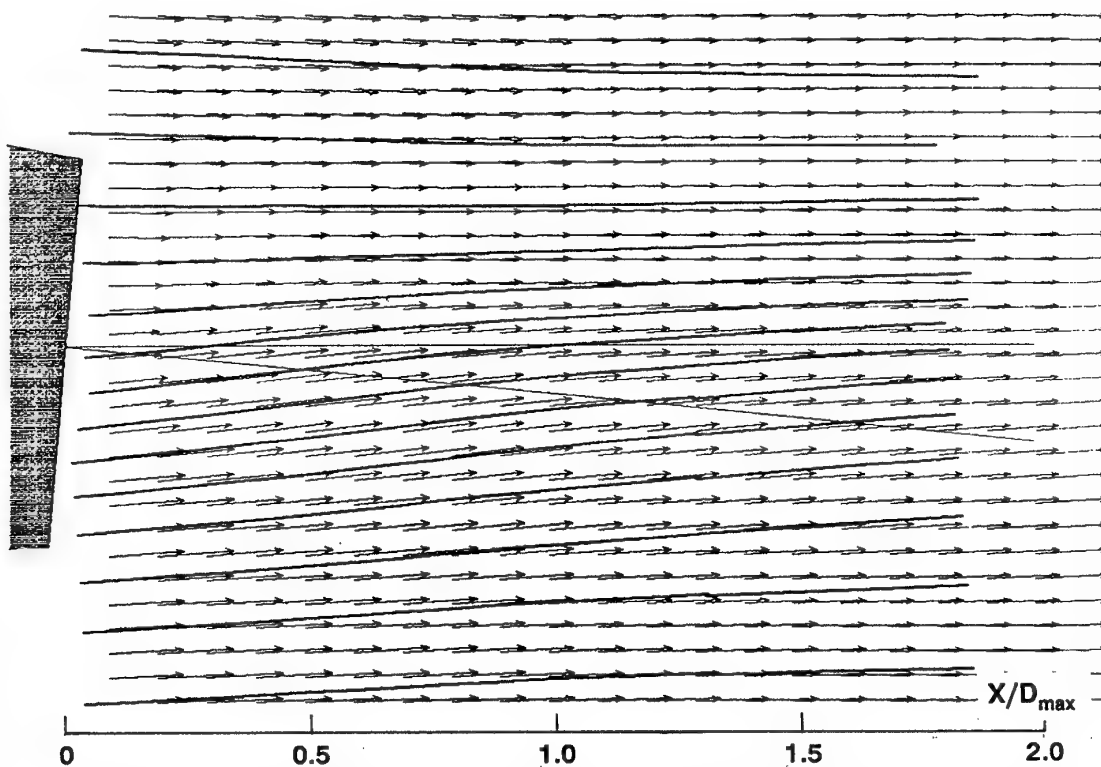


Fig. A.1.15 - Test Case A.1.1 : Mean velocity field in the longitudinal plane  $Z/D_{\max} = 0.625$   
(vector scale:  $1\text{cm} = 125\text{m/s}$  or  $u/U_{\infty} = 0.702$  for  $U_{\infty} = 178\text{m/s}$ )

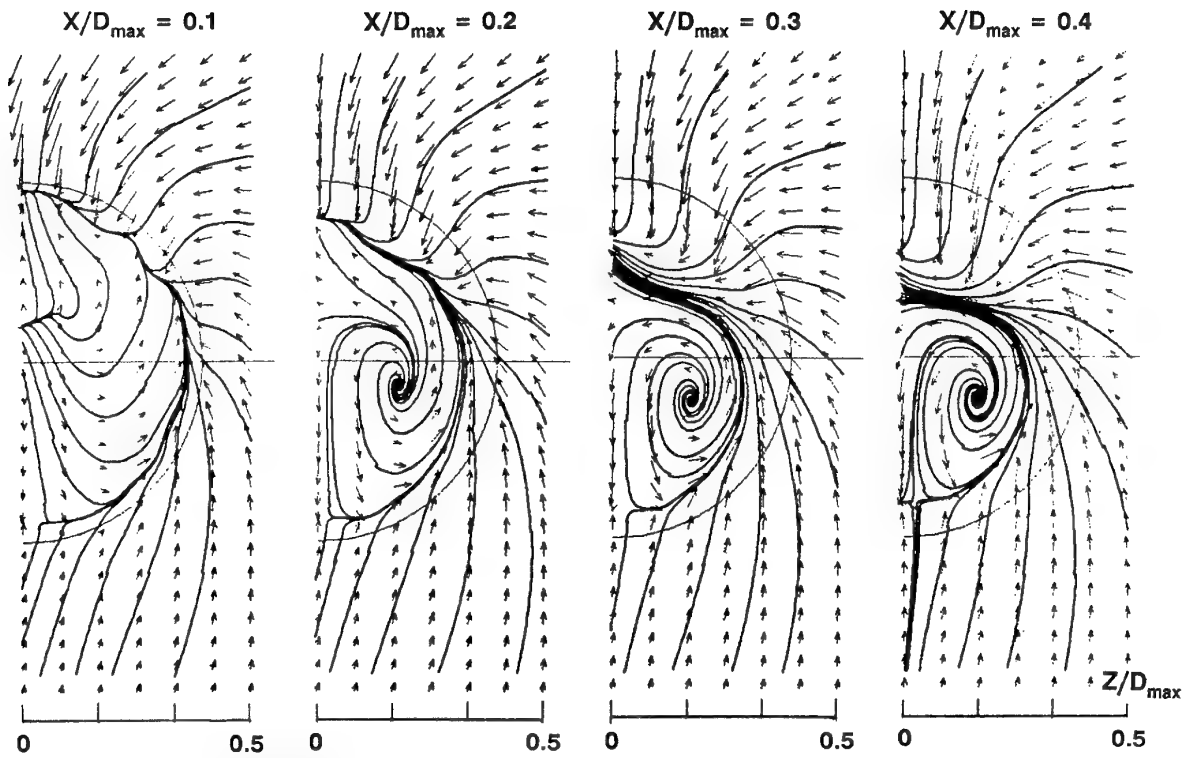


Fig. A.1.16 - **Test Case A.1.1** : Mean velocity field in the transverse planes  $X/D_{\max} = 0.1, 0.2, 0.3$  and  $0.4$  (vector scale:  $1\text{ cm} = 40\text{ m/s}$  or  $v/U_{\infty} = 0.225$  for  $U_{\infty} = 178\text{ m/s}$ )

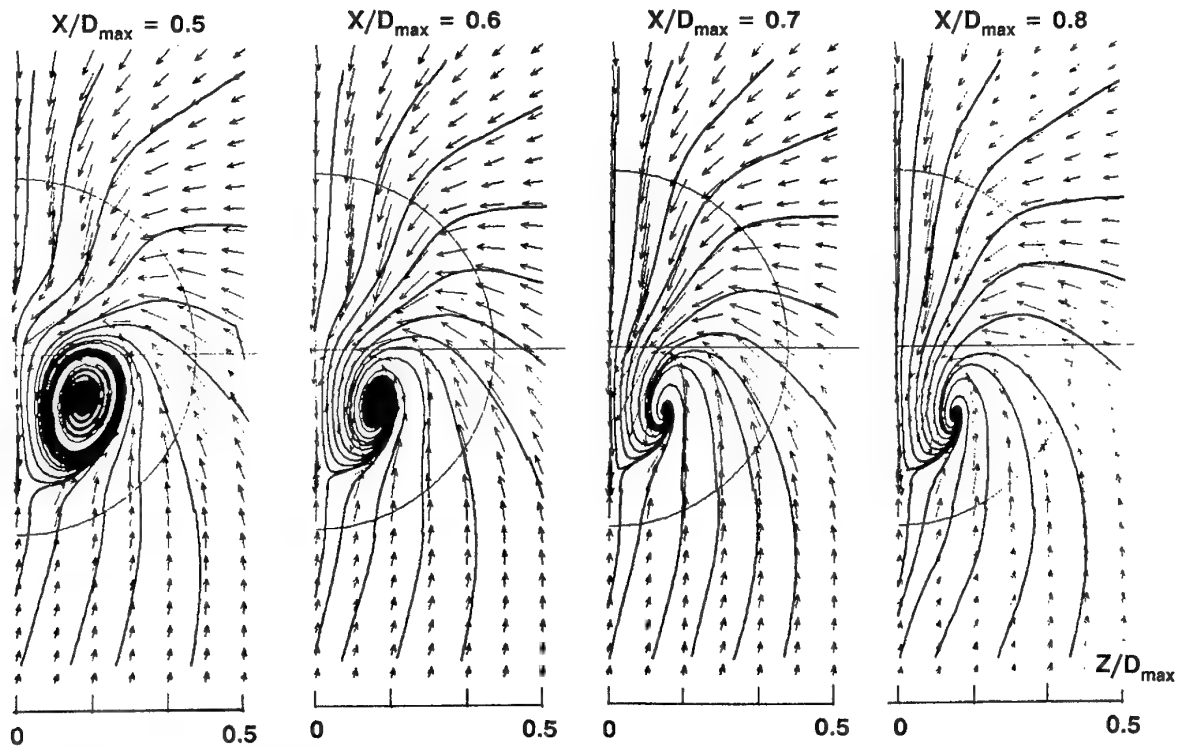


Fig. A.1.17 - **Test Case A.1.1** : Mean velocity field in the transverse planes  $X/D_{\max} = 0.5, 0.6, 0.7$  and  $0.8$  (vector scale:  $1\text{ cm} = 40\text{ m/s}$  or  $v/U_{\infty} = 0.225$  for  $U_{\infty} = 178\text{ m/s}$ )



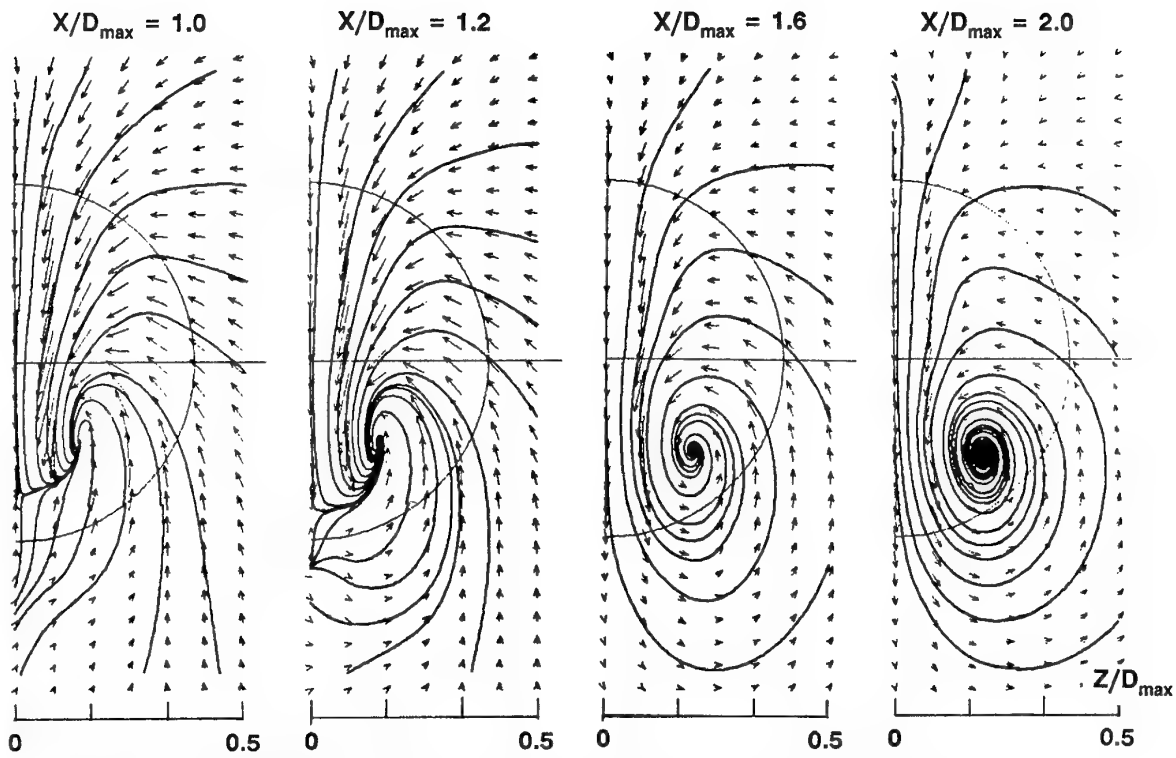


Fig. A.1.18 - Test Case A.1.1 : Mean velocity field in the transverse planes  $X/D_{\max} = 1.0, 1.2, 1.6$  and  $2.0$  (vector scale:  $1\text{cm} = 40\text{m/s}$  or  $v/U_{\infty} = 0.225$  for  $U_{\infty} = 178\text{m/s}$ )

**A.2. A2 Test Cases (Axisymmetric Body With Jet)****A.2.1. Test Case A.2.1 (Cold Jet Flow)***A.2.1.1. Surface Pressure Distribution*Row 1 -  $\varphi = 90^\circ$ 

$X/D_{max}$	$C_p$
-1.039	-0.028
-0.754	-0.057
-0.563	0.030
-0.469	0.073
-0.372	0.098
-0.278	0.132
-0.229	0.139
-0.180	
-0.135	0.168
-0.086	0.168

Row 2 -  $\varphi = 0^\circ$ 

$X/D_{max}$	$C_p$
-1.039	-0.032
-0.754	-0.041
-0.563	0.021
-0.469	0.066
-0.372	0.089
-0.278	0.125
-0.229	0.134
-0.180	0.143
-0.135	0.168
-0.086	0.168

Row 4 -  $\varphi = 225^\circ$ 

$X/D_{max}$	$C_p$
-1.039	-0.043
-0.754	-0.073
-0.563	0.011
-0.469	0.048
-0.372	0.089
-0.278	0.116
-0.229	0.125
-0.180	0.143
-0.135	0.161
-0.086	0.177

**A.2.2. Test Case A.2.2 (Hot Jet Flow)***A.2.2.1. Surface Pressure Distribution*Row 1 -  $\varphi = 90^\circ$ 

$X/D_{max}$	$C_p$
-1.039	-0.022
-0.754	-0.040
-0.563	
-0.469	0.064
-0.372	0.092
-0.278	0.114
-0.229	
-0.180	0.140
-0.135	0.144
-0.086	0.150

Row 2 -  $\varphi = 0^\circ$ 

$X/D_{max}$	$C_p$
-1.039	-0.028
-0.754	-0.036
-0.563	0.034
-0.469	0.068
-0.372	0.088
-0.278	0.112
-0.229	0.118
-0.180	0.126
-0.135	0.132
-0.086	0.140

Row 4 -  $\varphi = 225^\circ$ 

$X/D_{max}$	$C_p$
-1.039	-0.046
-0.754	-0.060
-0.563	0.016
-0.469	0.058
-0.372	0.088
-0.278	
-0.229	0.122
-0.180	0.128
-0.135	0.146
-0.086	0.176

## A.2.2.2. Boundary Layer Profile

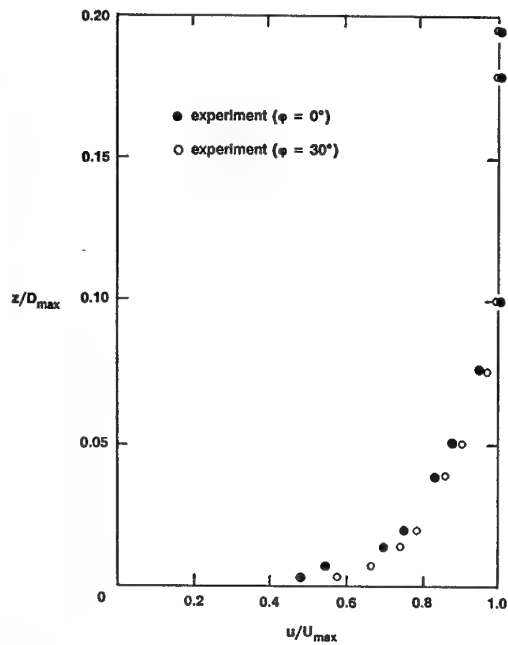


Fig. A.2.1 - Test Cases A.2.1 and A.2.2 : Boundary layer profile at  $X/D_{\max} = -2.076$

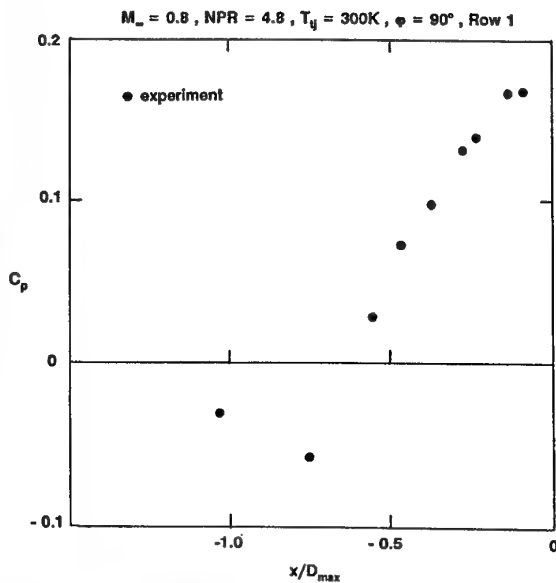


Fig. A.2.2 - Test Case A.2.1 : Cold jet. Static pressure coefficient on the afterbody. Row  $\phi = 90^\circ$

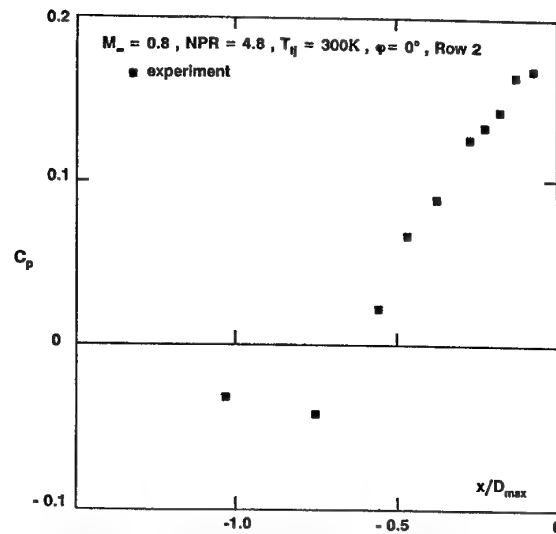


Fig. A.2.3 - Test Case A.2.2 : Cold jet. Static pressure coefficient on the afterbody. Row  $\phi = 0^\circ$

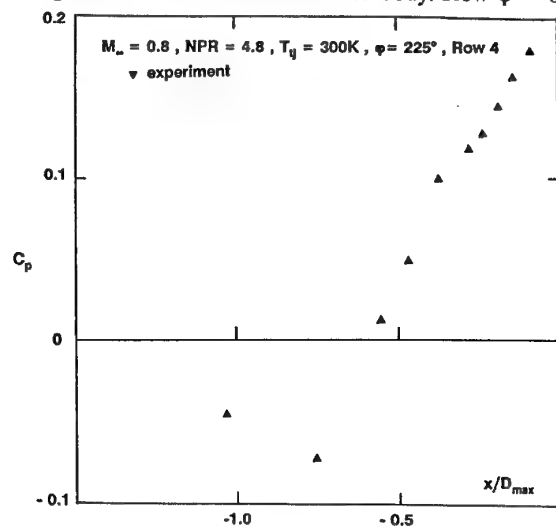


Fig. A.2.4 - Test Case A.2.1 : Cold jet. Static pressure coefficient on the afterbody. Row  $\phi = 225^\circ$

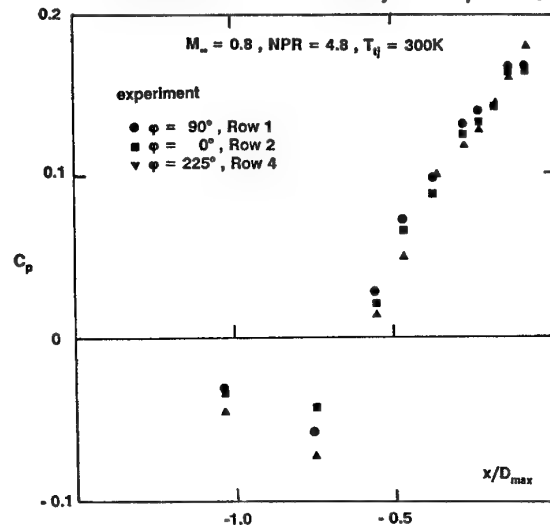


Fig. A.2.5 - Test Case A.2.1 : Cold jet. Static pressure coefficient on the afterbody. Rows  $\phi = 90^\circ$ ,  $0^\circ$  and  $225^\circ$

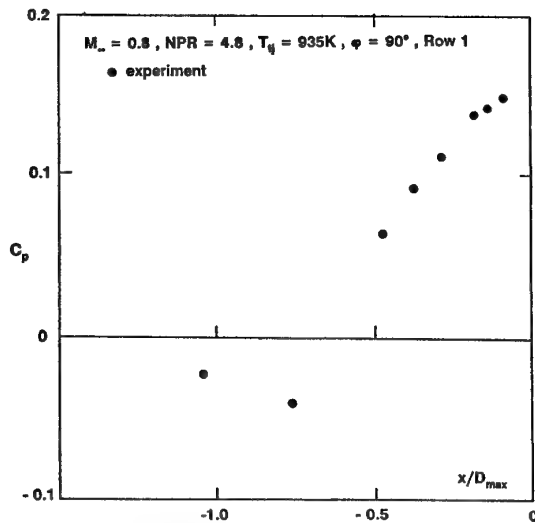


Fig. A.2.6 - Test Case A.2.2 : Hot jet. Static pressure coefficient on the afterbody. Row  $\phi = 90^\circ$

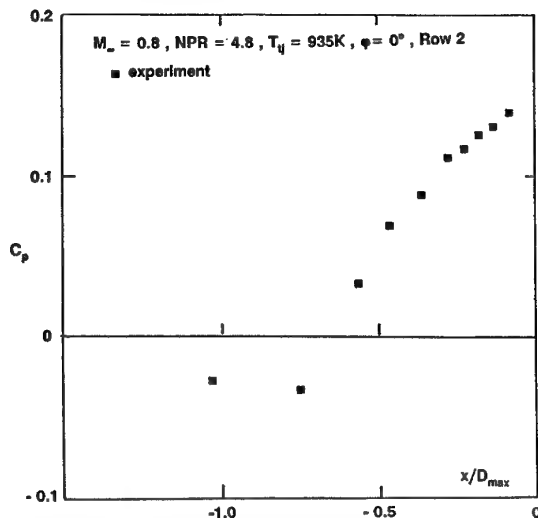


Fig. A.2.7 - Test Case A.2.2 : Hot jet. Static pressure coefficient on the afterbody. Row  $\phi = 0^\circ$

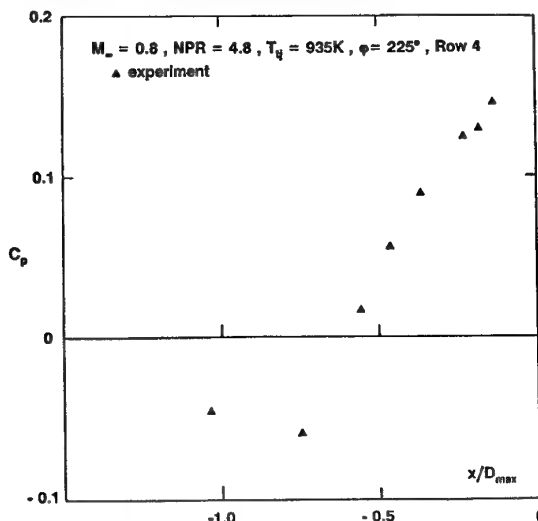


Fig. A.2.8 - Test Case A.2.2 : Hot jet. Static pressure coefficient on the afterbody. Row  $\phi = 225^\circ$

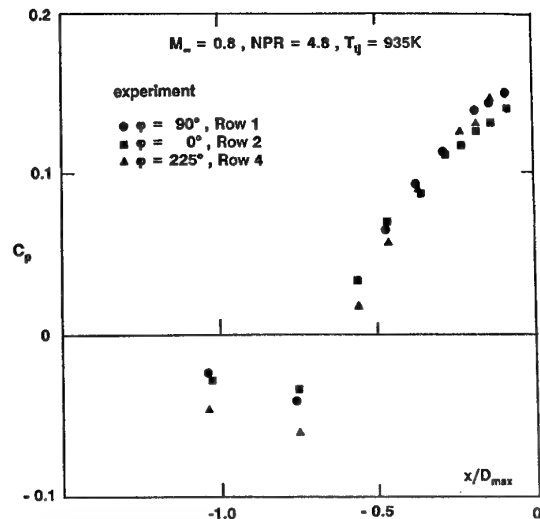


Fig. A.2.9 - Test Case A.2.2 : Hot jet. Static pressure coefficient on the afterbody. Rows  $\phi = 90^\circ, 0^\circ$  and  $225^\circ$

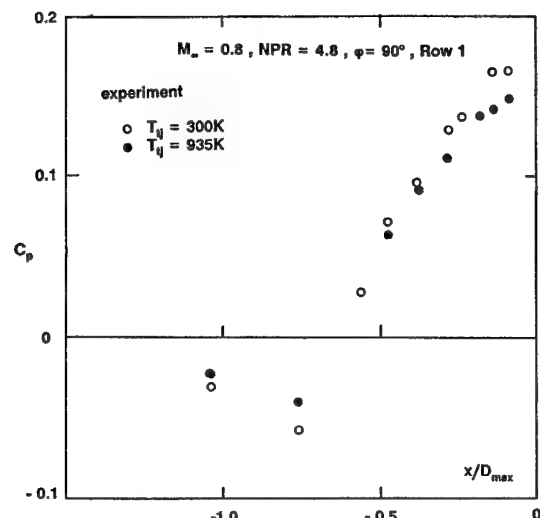


Fig. A.2.10 - Test Cases A.2.1 and A.2.2 : Cold and hot jets. Static pressure coefficient on the afterbody. Row  $\phi = 90^\circ$

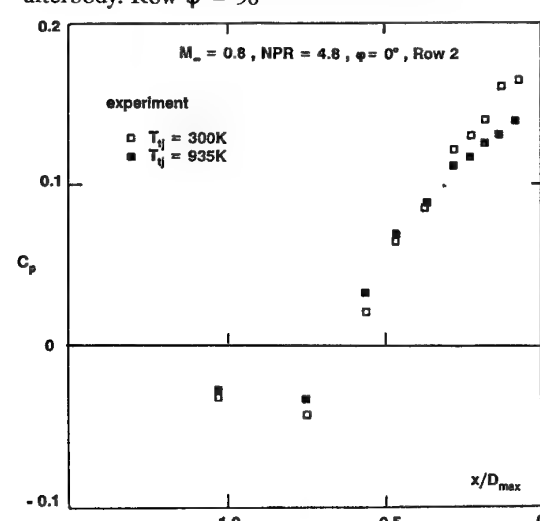


Fig. A.2.11 - Test Cases A.2.1 and A.2.2 : Cold and hot jets. Static pressure coefficient on the afterbody. Row  $\phi = 0^\circ$

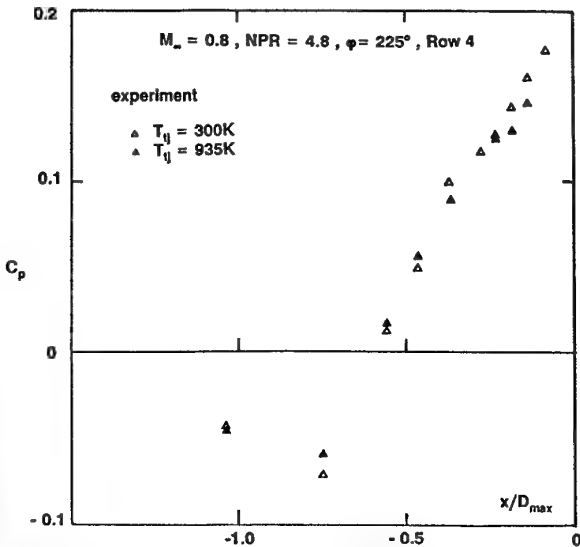


Fig. A.2.12 - Test Cases A.2.1 and A.2.2 : Cold and hot jets. Static pressure coefficient on the afterbody. Row  $\phi = 225^\circ$

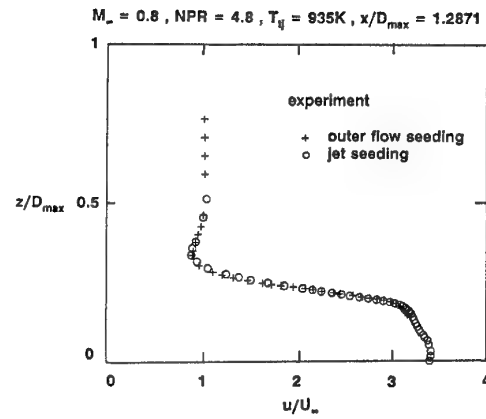


Fig. A.2.15 - Test Case A.2.2 : Hot jet. Profile of the mean longitudinal velocity component at  $X/D_{max} = 0.484$

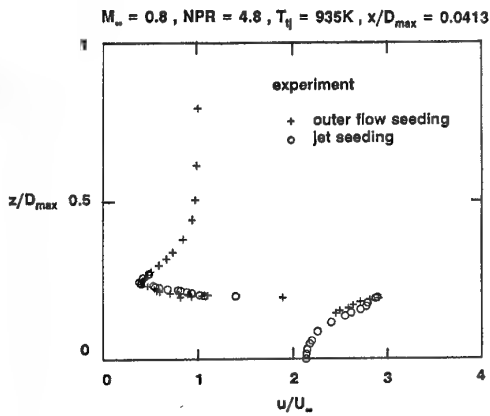


Fig. A.2.13 - Test Case A.2.2 : Hot jet. Profile of the mean longitudinal velocity component at  $X/D_{max} = 0.0413$

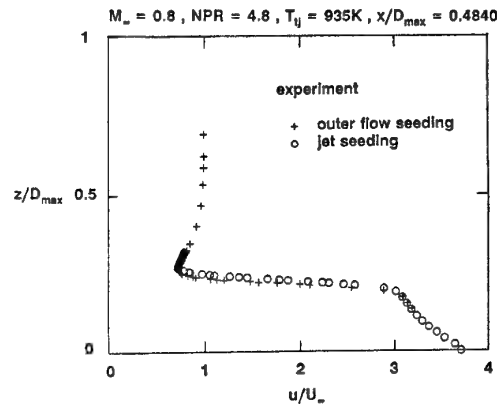


Fig. A.2.16 - Test Case A.2.2 : Hot jet. Profile of the mean longitudinal velocity component at  $X/D_{max} = 1.2871$

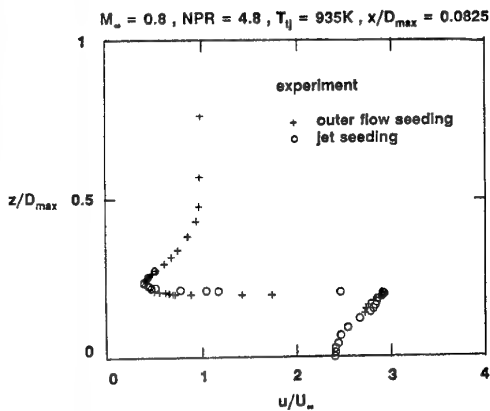


Fig. A.2.14 - Test Case A.2.2 : Hot jet. Profile of the mean longitudinal velocity component at  $X/D_{max} = 0.0825$

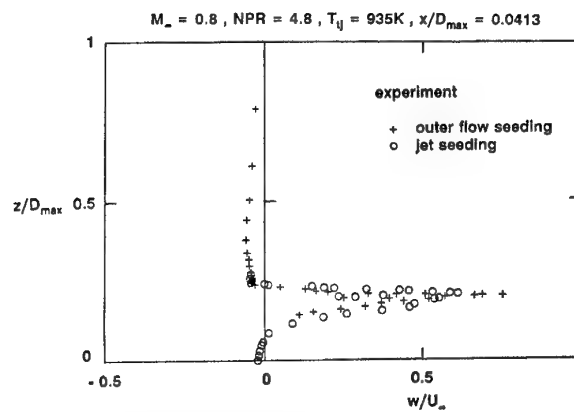


Fig. A.2.17 - Test Case A.2.2 : Hot jet. Profile of the mean radial velocity component at  $X/D_{max} = 0.0413$

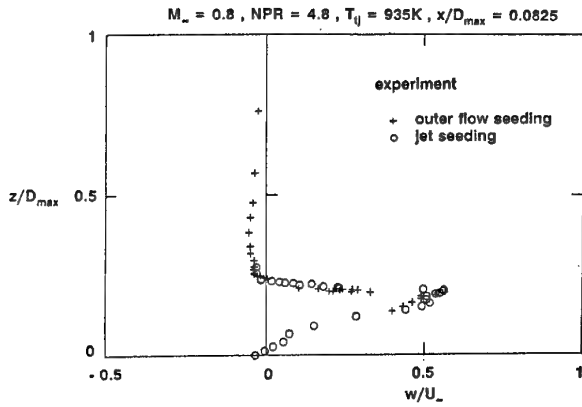


Fig. A.2.18 - Test Case A.2.2 : Hot jet. Profile of the mean radial velocity component at  $X/D_{\max} = 0.0825$

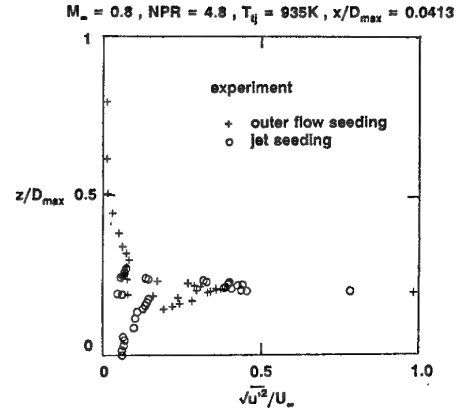


Fig. A.2.21 - Test Case A.2.2 : Hot jet. Profile of the fluctuating longitudinal velocity component at  $X/D_{\max} = 0.0413$

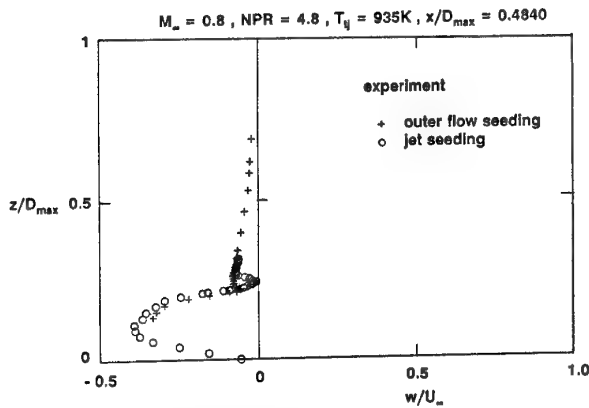


Fig. A.2.19 - Test Case A.2.2 : Hot jet. Profile of the mean radial velocity component at  $X/D_{\max} = 0.4840$

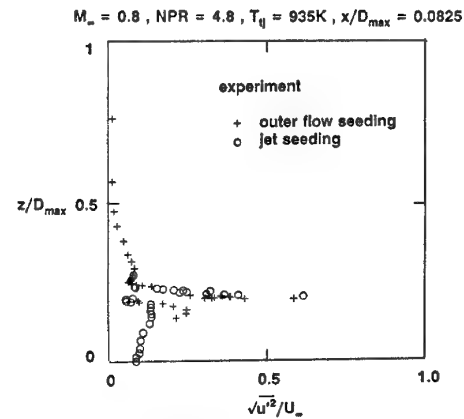


Fig. A.2.22 - Test Case A.2.2 : Hot jet. Profile of the fluctuating longitudinal velocity component at  $X/D_{\max} = 0.0825$

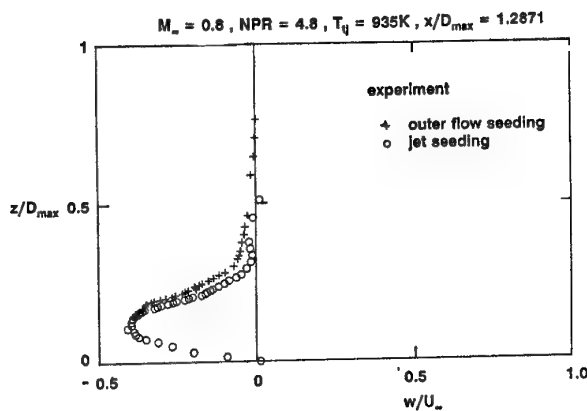


Fig. A.2.20 - Test Case A.2.2 : Hot jet. Profile of the mean radial velocity component at  $X/D_{\max} = 1.2871$

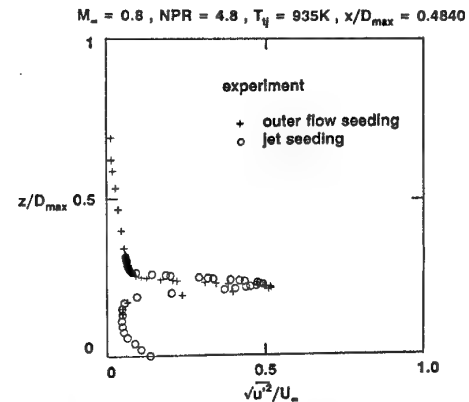


Fig. A.2.23 - Test Case A.2.2 : Hot jet. Profile of the fluctuating longitudinal velocity component at  $X/D_{\max} = 0.4840$

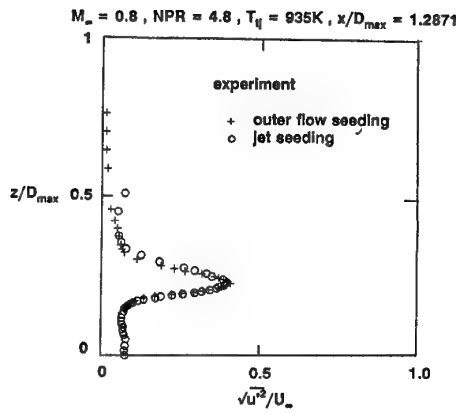


Fig. A.2.24 - Test Case A.2.2 : Hot jet. Profile of the fluctuating longitudinal velocity component at  $X/D_{max} = 1.2871$

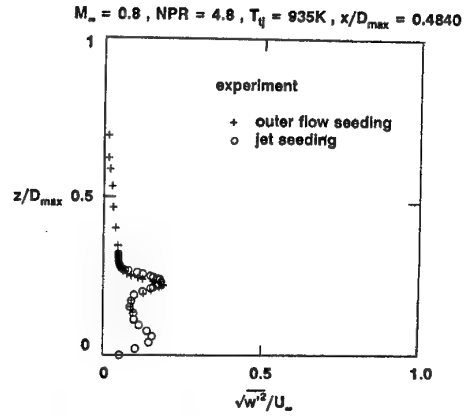


Fig. A.2.27 - Test Case A.2.2 : Hot jet. Profile of the fluctuating radial velocity component at  $X/D_{max} = 0.4840$

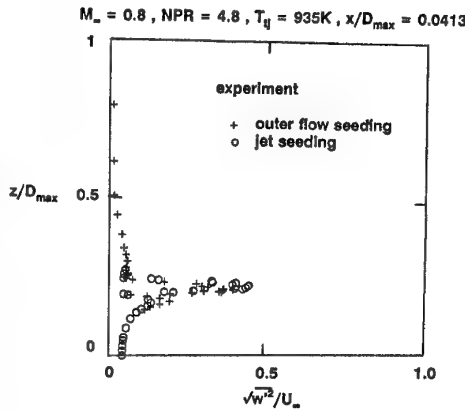


Fig. A.2.25 - Test Case A.2.2 : Hot jet. Profile of the fluctuating radial velocity component at  $X/D_{max} = 0.0413$

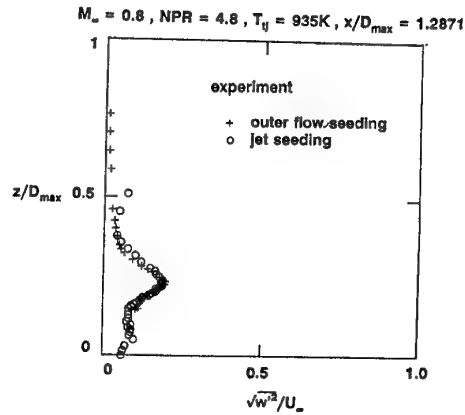


Fig. A.2.28 - Test Case A.2.2 : Hot jet. Profile of the fluctuating radial velocity component at  $X/D_{max} = 1.2871$

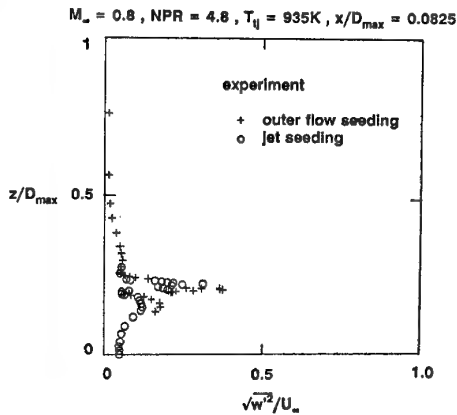


Fig. A.2.26 - Test Case A.2.2 : Hot jet. Profile of the fluctuating radial velocity component at  $X/D_{max} = 0.0825$

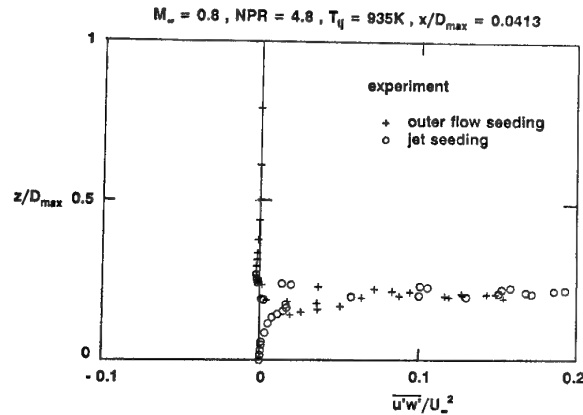


Fig. A.2.29 - Test Case A.2.2 : Hot jet. Profile of the turbulent shear stress at  $X/D_{max} = 0.0413$

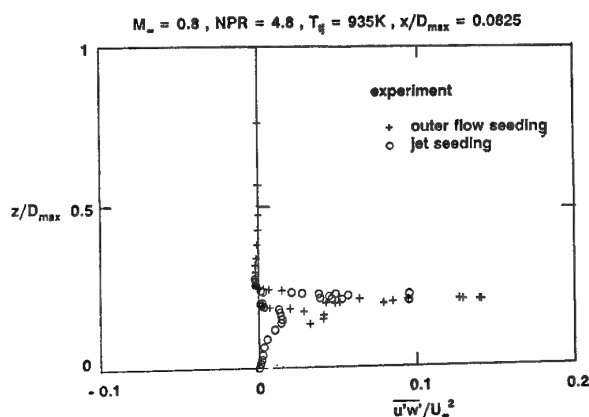


Fig. A.2.30 - Test Case A.2.2 : Hot jet. Profile of the turbulent shear stress at  $X/D_{max} = 0.0825$

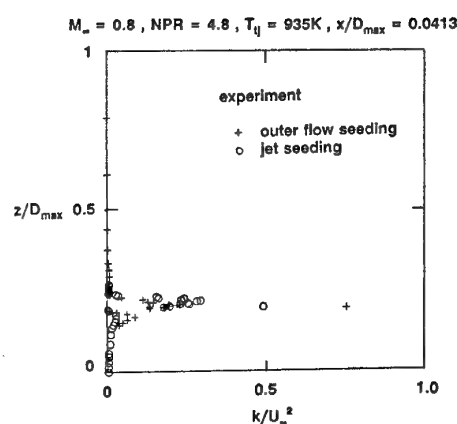


Fig. A.2.33 - Test Case A.2.2 : Hot jet. Profile of the turbulent kinetic energy at  $X/D_{max} = 0.0413$  (estimated value)

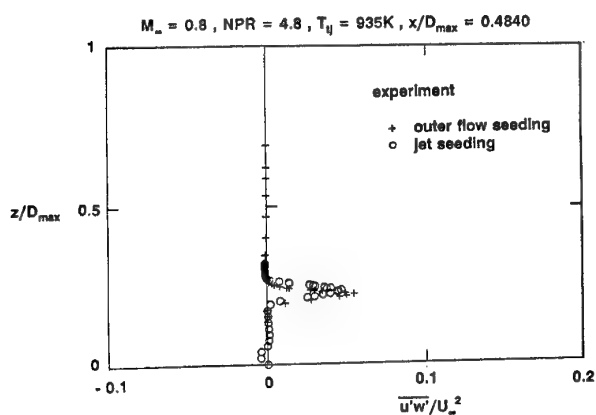


Fig. A.2.31 - Test Case A.2.2 : Hot jet. Profile of the turbulent shear stress at  $X/D_{max} = 0.4840$

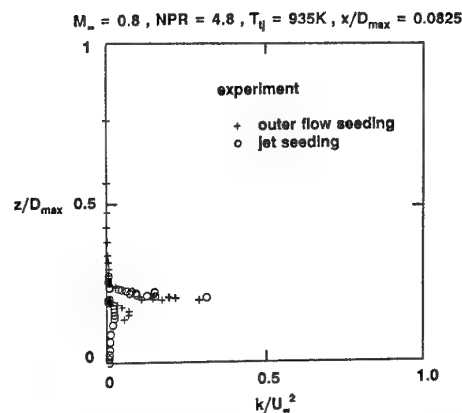


Fig. A.2.34 - Test Case A.2.2 : Hot jet. Profile of the turbulent kinetic energy at  $X/D_{max} = 0.0825$  (estimated value)

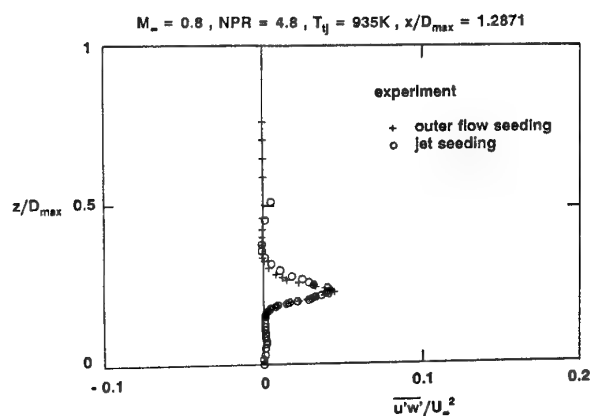


Fig. A.2.32 - Test Case A.2.2 : Hot jet. Profile of the turbulent shear stress at  $X/D_{max} = 1.2871$

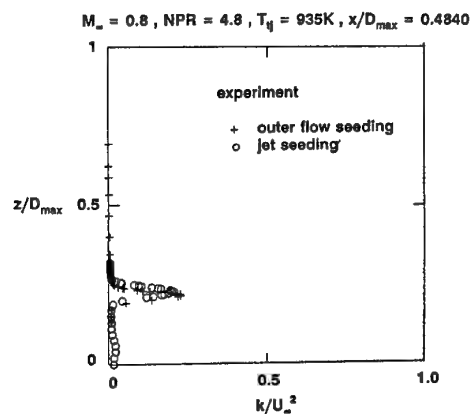


Fig. A.2.35 - Test Case A.2.2 : Hot jet. Profile of the turbulent kinetic energy at  $X/D_{max} = 0.4840$  (estimated value)



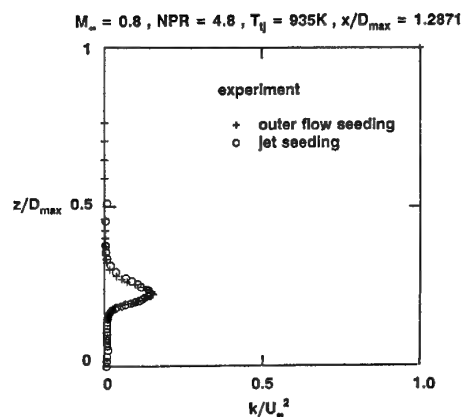


Fig. A.2.36 - Test Case A.2.2 : Hot jet. Profile of the turbulent kinetic energy at  $X/D_{max} = 1.2871$  (estimated value)

### A.3. A3 Test Cases (Twin Jet Afterbody)

#### A.3.1. Test Case A.3.1 ( $M_\infty = 0.85$ )

##### A.3.1.1. Surface Pressure Distribution

Rows A and c

Row A	$X/L_N$	$C_p$
35	-3.65	-0.271
34	-2.42	-0.270
33	-1.07	-0.307
32	-0.40	-0.328
Row c		
12	0.11	-0.290
11	0.38	-0.220
10	0.63	-0.186
9	0.74	-0.176

Rows B and d

Row B	$X/L_N$	$C_p$
39	-3.65	-0.288
38	-2.42	-0.285
37	-1.07	-0.283
36	-0.40	-0.310
Row d		
16	0.11	-0.268
15	0.38	-0.224
14	0.63	-0.193
13	0.74	-0.193

Rows C and e

Row C	$X/L_N$	$C_p$
43	-3.65	-0.314
42	-2.42	-0.292
41	-1.07	-0.267
40	-0.40	-0.235
Row e		
20	0.11	-0.235
19	0.38	-0.249
18	0.63	-0.273
17	0.74	-0.281

Row F and b

Row F	$X/L_N$	$C_p$
55	-3.65	-0.257
54	-2.42	-0.285
53	-1.07	-0.282
52	-0.40	
Row b		
8	0.11	-0.272
7	0.38	-0.216
6	0.63	-0.219
5	0.74	-0.233

Row D

Row D	$X/L_N$	$C_p$
47	-3.65	
46	-2.42	-0.289
45	-1.07	-0.284
44	-0.40	

Row E

Row E	$X/L_N$	$C_p$
51	-3.65	-0.260
50	-2.42	-0.292
49	-1.07	-0.272
48	-0.40	-0.250

Row a

Row a	$X/L_N$	$C_p$
4	0.11	-0.211
3	0.38	-0.234
2	0.63	-0.259
1	0.74	-0.264

Base region

	$Z/L_N$	$C_p$
21	-0.75	-0.218
22	0	-0.198
26	+0.75	-0.173
	$Y/L_N$	$C_p$
23	-0.12	-0.178
24	+0.12	-0.182
	$Y/L_N$	$C_p$
25	-0.27	-0.175
26	0	-0.173
27	+0.27	-0.185

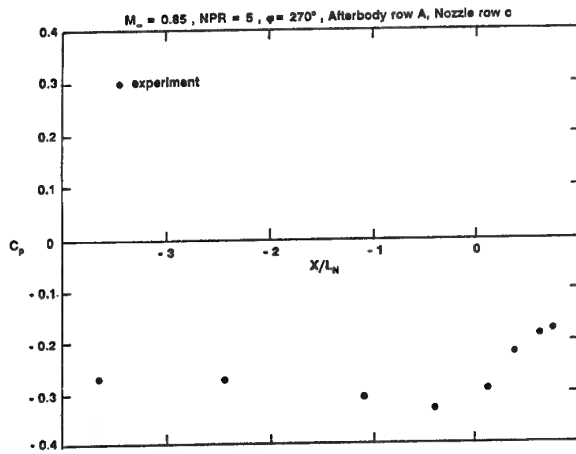


Fig. A.3.1 - Test Case A.3.1 : Mach number 0.85.  
Static pressure coefficient on the afterbody and nozzle.  
Rows A and c

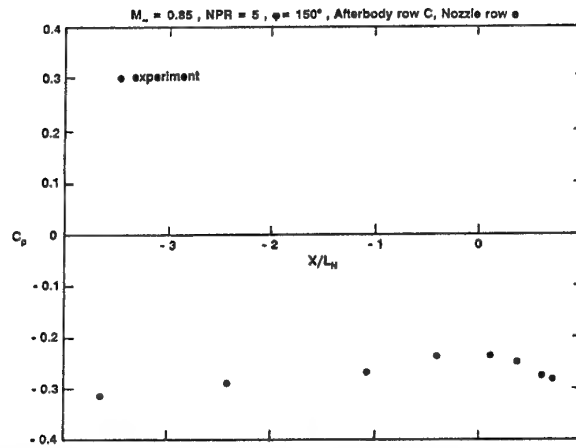


Fig. A.3.3 - Test Case A.3.1 : Mach number 0.85.  
Static pressure coefficient on the afterbody and nozzle.  
Rows C and e

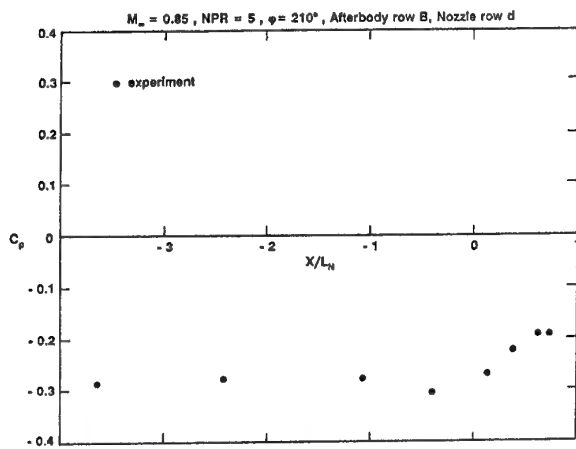


Fig. A.3.2 - Test Case A.3.1 : Mach number 0.85.  
Static pressure coefficient on the afterbody and nozzle.  
Rows B and d

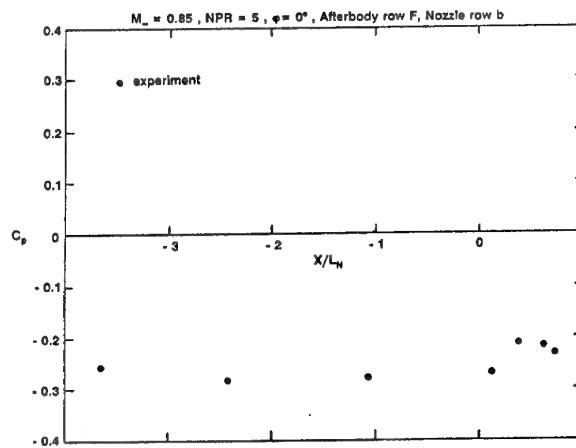


Fig. A.3.4 - Test Case A.3.1 : Mach number 0.85.  
Static pressure coefficient on the afterbody and nozzle.  
Rows F and b

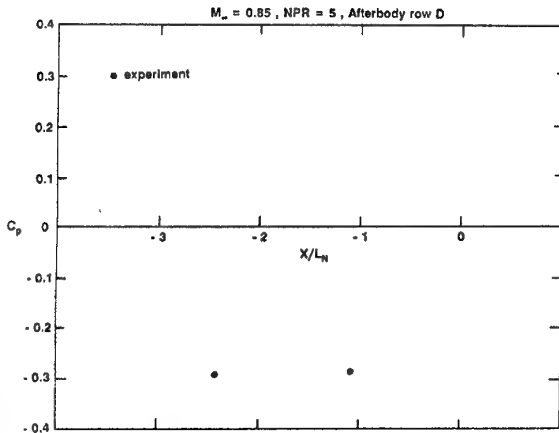


Fig. A.3.5 - Test Case A.3.1: Mach number 0.85. Static pressure coefficient on the afterbody. Row D

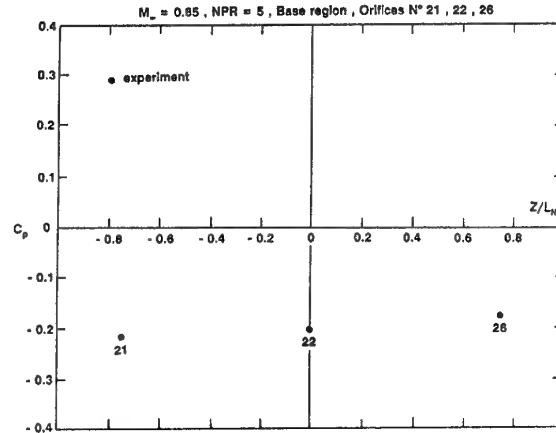


Fig. A.3.8 - Test Case A.3.1: Mach number 0.85. Static pressure coefficient on the base. Orifices N° 21, 22 and 26

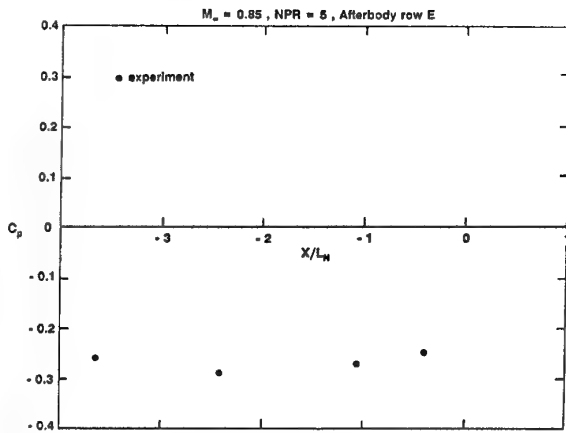


Fig. A.3.6 - Test Case A.3.1: Mach number 0.85. Static pressure coefficient on the afterbody. Row E

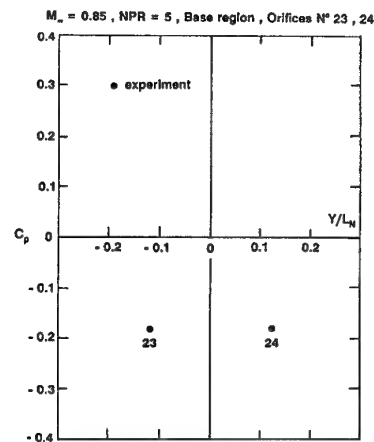


Fig. A.3.9 - Test Case A.3.1: Mach number 0.85. Static pressure coefficient on the base. Orifices N° 23 and 24

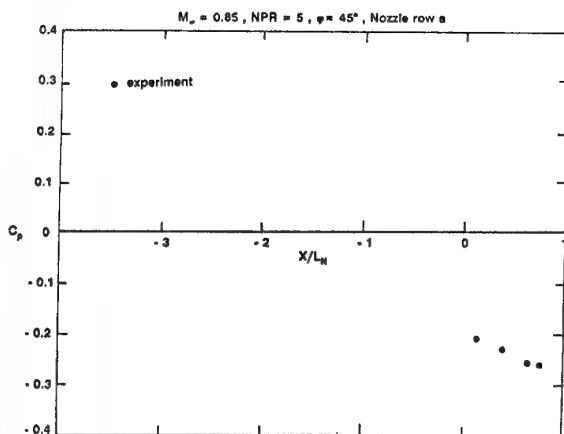


Fig. A.3.7 - Test Case A.3.1: Mach number 0.85. Static pressure coefficient on the nozzle. Row a

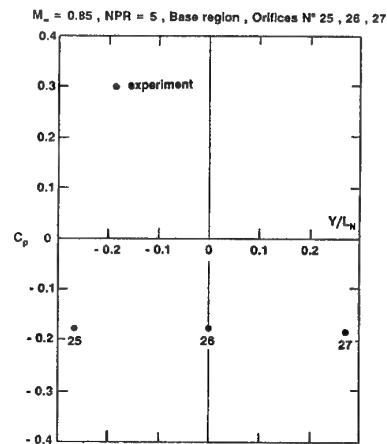
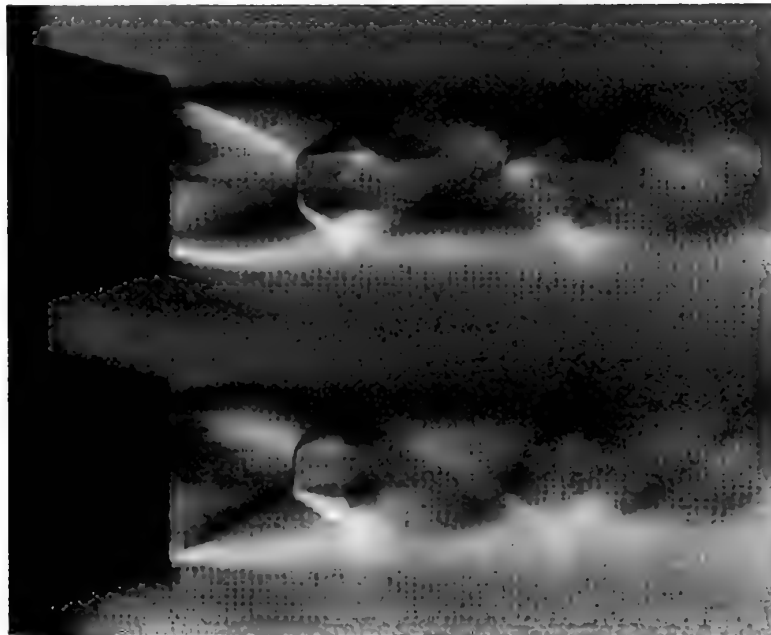


Fig. A.3.10 - Test Case A.3.1: Mach number 0.85. Static pressure coefficient on the base. Orifices N° 25, 26 and 27

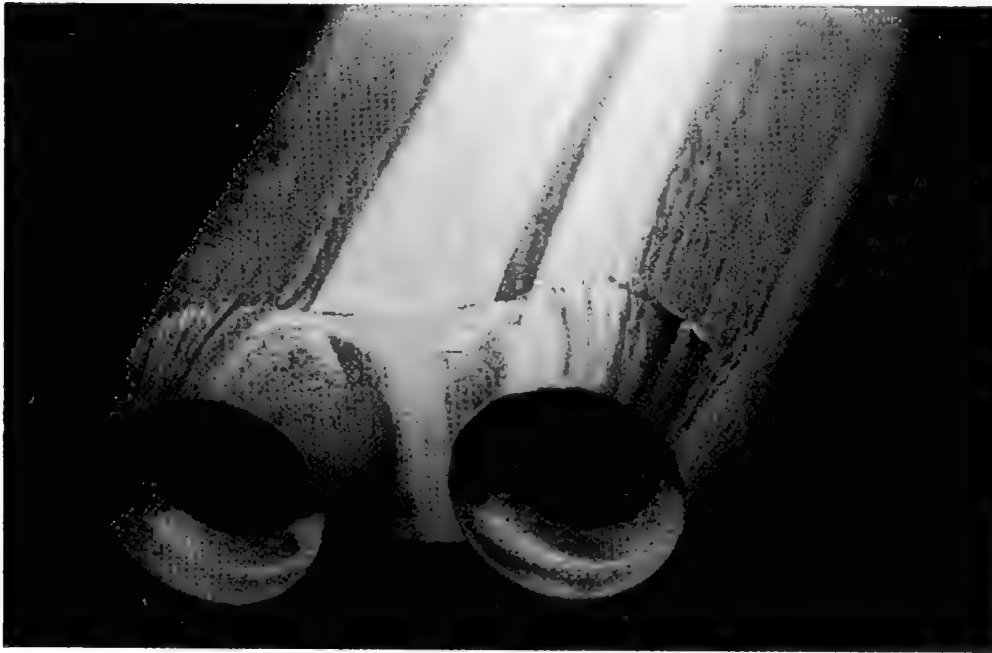
*A.3.1.2. Flow Visualizations*



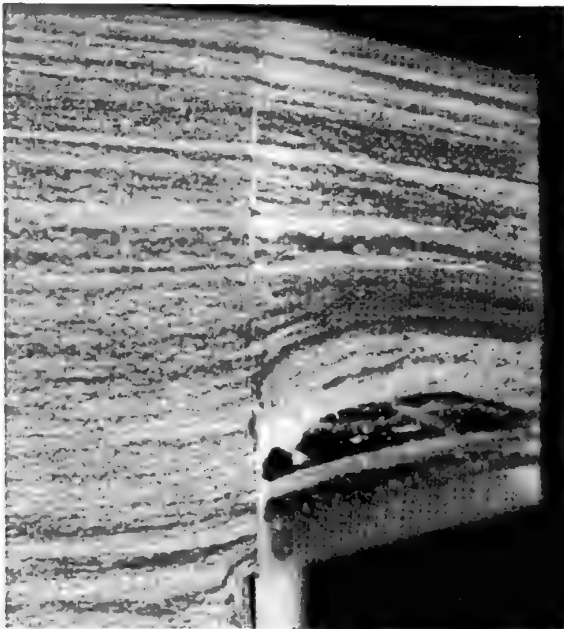
Test Case A.3.1 : Mach number 0.85. Schlieren photograph of the jets



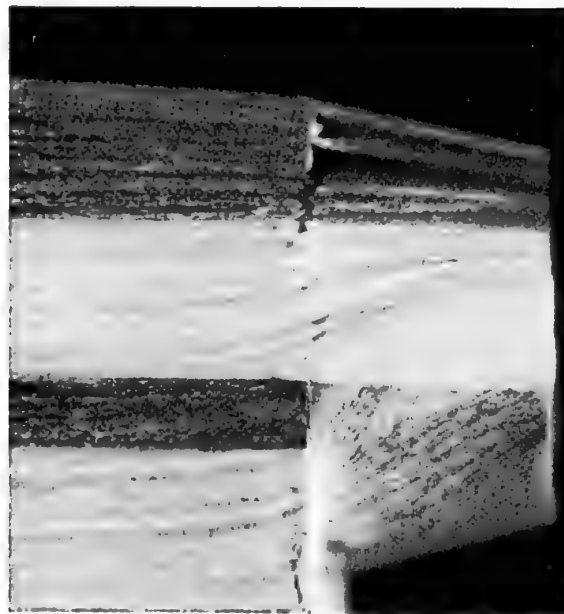
Test Case A.3.1 : Mach number 0.85. Surface flow pattern. Windward side



Test Case A.3.1 : Mach number 0.85. Surface flow pattern. Leeward side



Windward side



Leeward side

Test Case A.3.1 : Mach number 0.85. Surface flow pattern. Close-up of nozzle region.

**A.3.2. Test Case A.3.2 ( $M_\infty = 0.8$ )****A.3.2.1 Surface Pressure Distribution**

Rows A and c

Row A	$X/L_N$	$C_p$
35	-3.65	-0.114
34	-2.42	-0.124
33	-1.07	-0.157
32	-0.40	-0.173
Row c		
12	0.11	-0.146
11	0.38	-0.094
10	0.63	-0.066
9	0.74	-0.069

Rows B and d

Row B	$X/L_N$	$C_p$
39	-3.65	-0.140
38	-2.42	-0.139
37	-1.07	-0.135
36	-0.40	-0.158
Row d		
16	0.11	-0.127
15	0.38	-0.098
14	0.63	-0.082
13	0.74	-0.082

Rows C and e

Row C	$X/L_N$	$C_p$
43	-3.65	-0.159
42	-2.42	-0.138
41	-1.07	-0.119
40	-0.40	-0.127
Row e		
20	0.11	-0.114
19	0.38	-0.139
18	0.63	-0.165
17	0.74	-0.170

Row F and b

Row F	$X/L_N$	$C_p$
55	-3.65	-0.104
54	-2.42	-0.134
53	-1.07	-0.137
52	-0.40	
Row b		
8	0.11	-0.167
7	0.38	-0.104
6	0.63	-0.098
5	0.74	-0.112

Row D

Row D	$X/L_N$	$C_p$
47	-3.65	-0.132
46	-2.42	-0.127
45	-1.07	-0.135
44	-0.40	-0.126

Row E

Row E	$X/L_N$	$C_p$
51	-3.65	-0.109
50	-2.42	-0.132
49	-1.07	-0.134
48	-0.40	-0.125

Row a

Row a	$X/L_N$	$C_p$
4	0.11	-0.098
3	0.38	-0.122
2	0.63	-0.149
1	0.74	-0.153

Base region

	$Z/L_N$	$C_p$
21	-0.75	-0.098
22	0	-0.077
26	+0.75	-0.072
	$Y/L_N$	$C_p$
23	-0.12	-0.084
24	+0.12	-0.086
	$Y/L_N$	$C_p$
25	-0.27	-0.077
26	0	-0.072
27	+0.27	-0.081

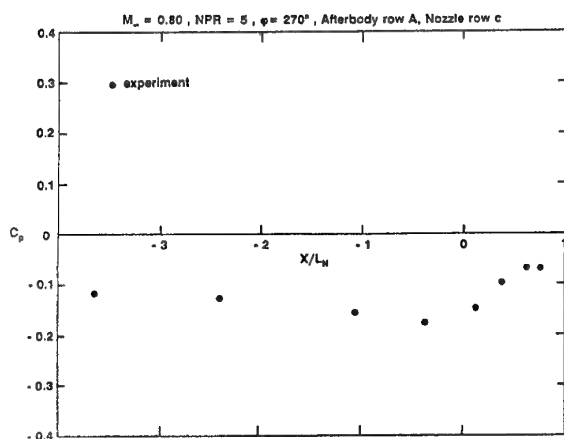


Fig. A.3.11 - Test Case A.3.2 : Mach number 0.80.  
Static pressure coefficient on the afterbody and nozzle.  
Rows A and c

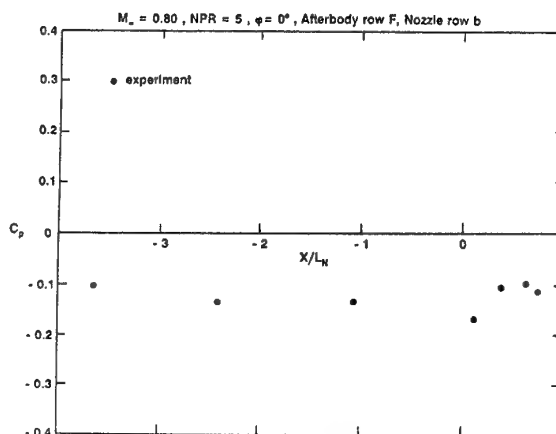


Fig. A.3.14 - Test Case A.3.2 : Mach number 0.80.  
Static pressure coefficient on the afterbody and nozzle.  
Rows F and b

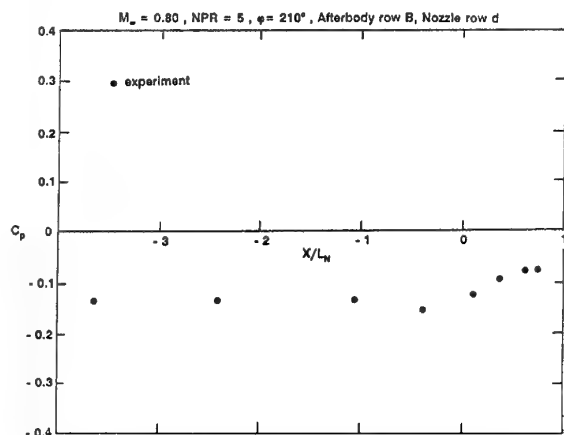


Fig. A.3.12 - Test Case A.3.2 : Mach number 0.80.  
Static pressure coefficient on the afterbody and nozzle.  
Rows B and d

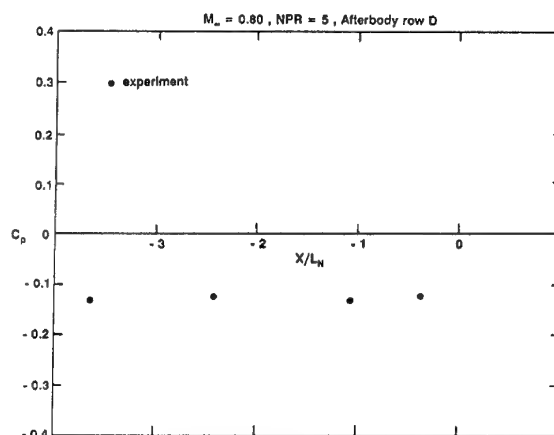


Fig. A.3.15 - Test Case A.3.2 : Mach number 0.80.  
Static pressure coefficient on the afterbody. Row D

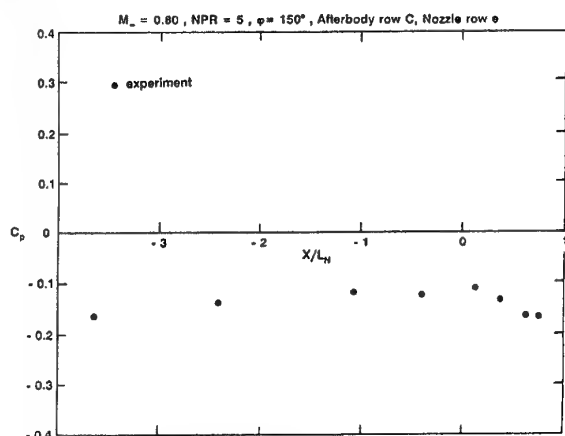


Fig. A.3.13 - Test Case A.3.2 : Mach number 0.80.  
Static pressure coefficient on the afterbody and nozzle.  
Rows C and e

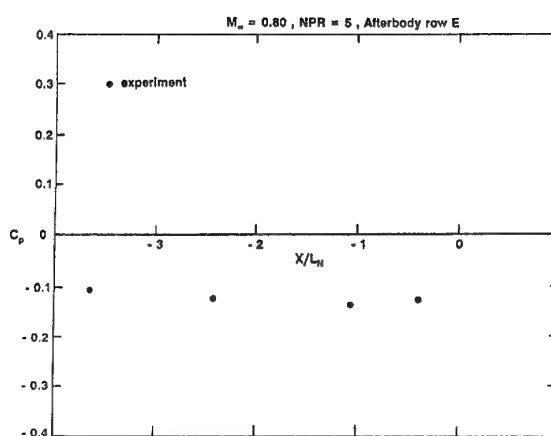


Fig. A.3.16 - Test Case A.3.2 : Mach number 0.80.  
Static pressure coefficient on the afterbody. Row E

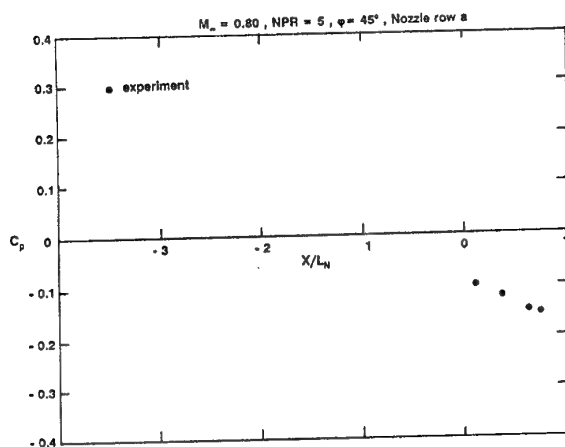


Fig. A.3.17 - Test Case A.3.2 : Mach number 0.80.  
Static pressure coefficient on the nozzle. Row a

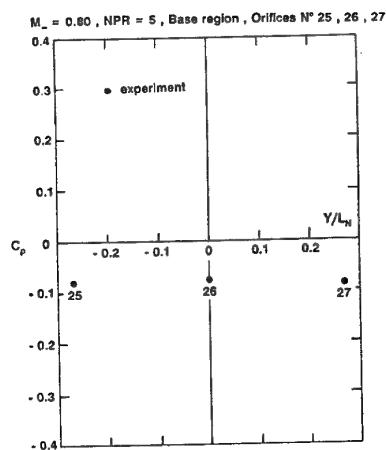


Fig. A.3.20 - Test Case A.3.2 : Mach number 0.80.  
Static pressure coefficient on the base. Orifices N° 25 ,  
26 and 27

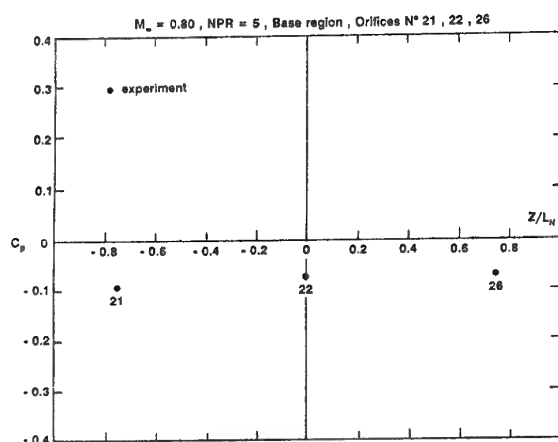


Fig. A.3.18 - Test Case A.3.2 : Mach number 0.80.  
Static pressure coefficient on the base. Orifices N° 21 ,  
22 and 26

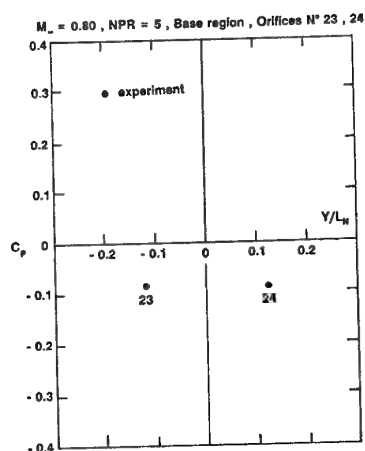


Fig. A.3.19 - Test Case A.3.2 : Mach number 0.80.  
Static pressure coefficient on the base. Orifices N° 23  
and 24



### A.3.2.2 Examples of LDV Velocity Field Measurements

(similar results are available for Test Case A.3.1)

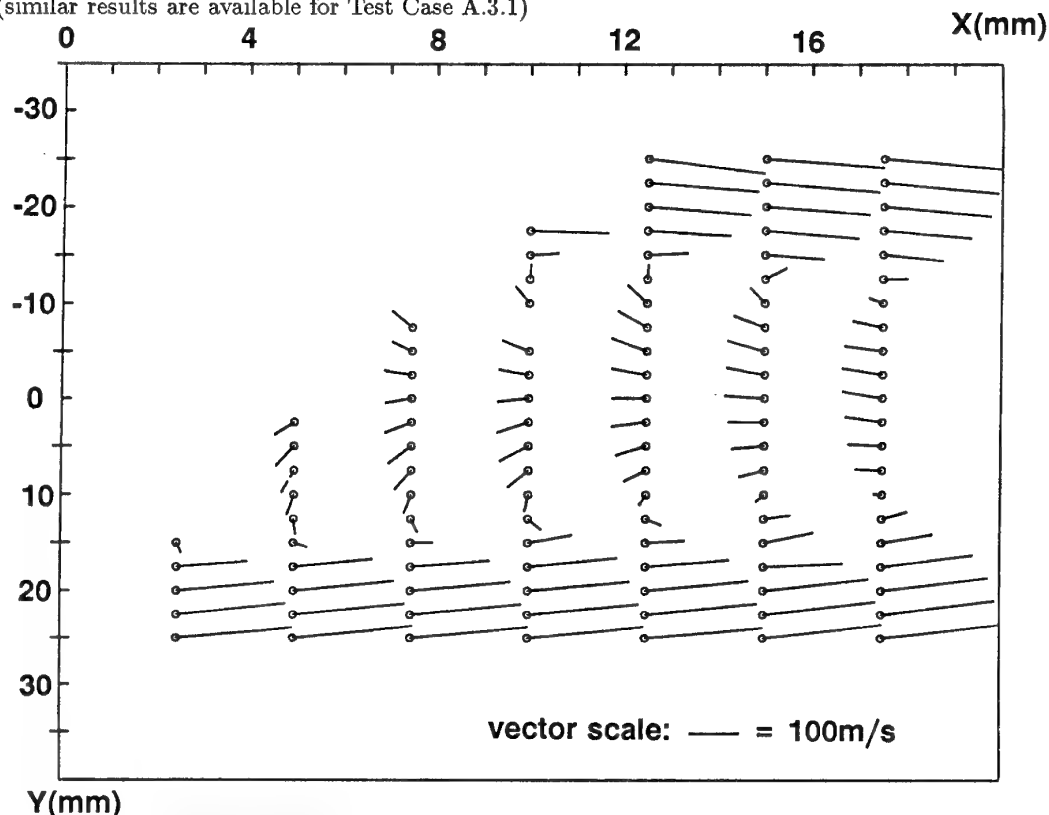


Fig. A.3.21 - Test Case A.3.2: Mach number 0.80. Mean velocity field in the backflow region. Component projected in the (X,Y) plane located at  $Z = -4\text{mm}$

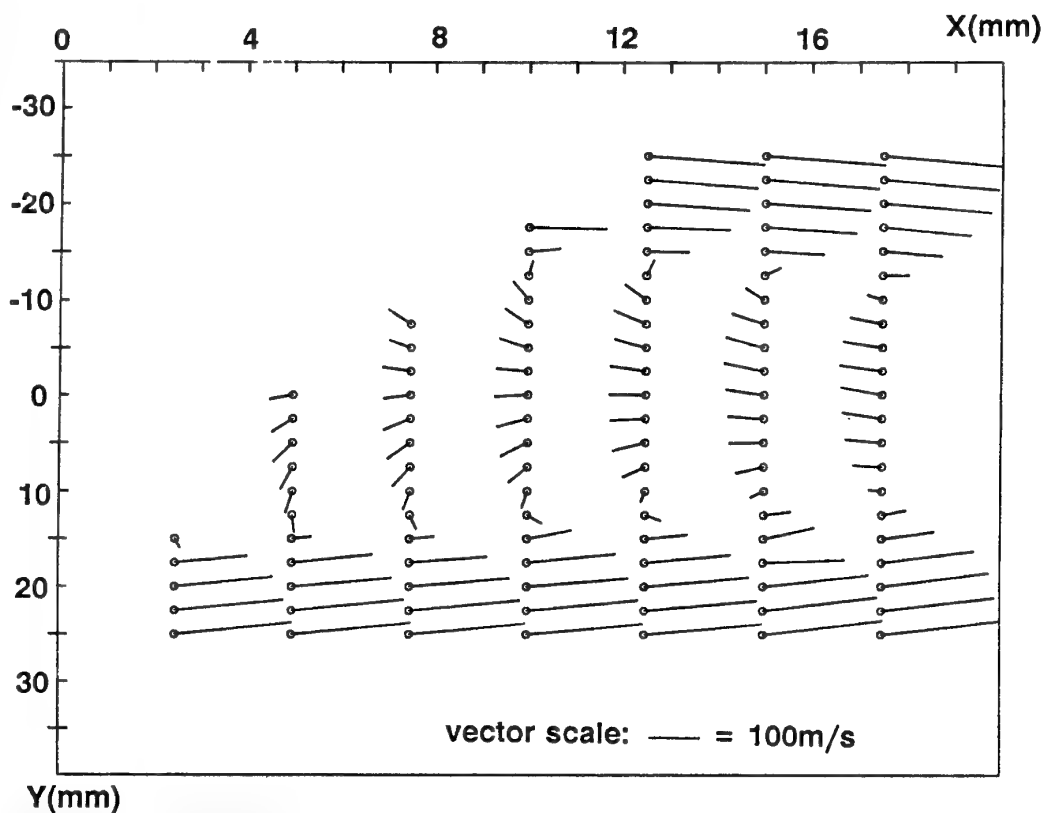


Fig. A.3.22 - Test Case A.3.2: Mach number 0.80. Mean velocity field in the backflow region. Component projected in the (X,Y) plane located at  $Z = -2\text{mm}$

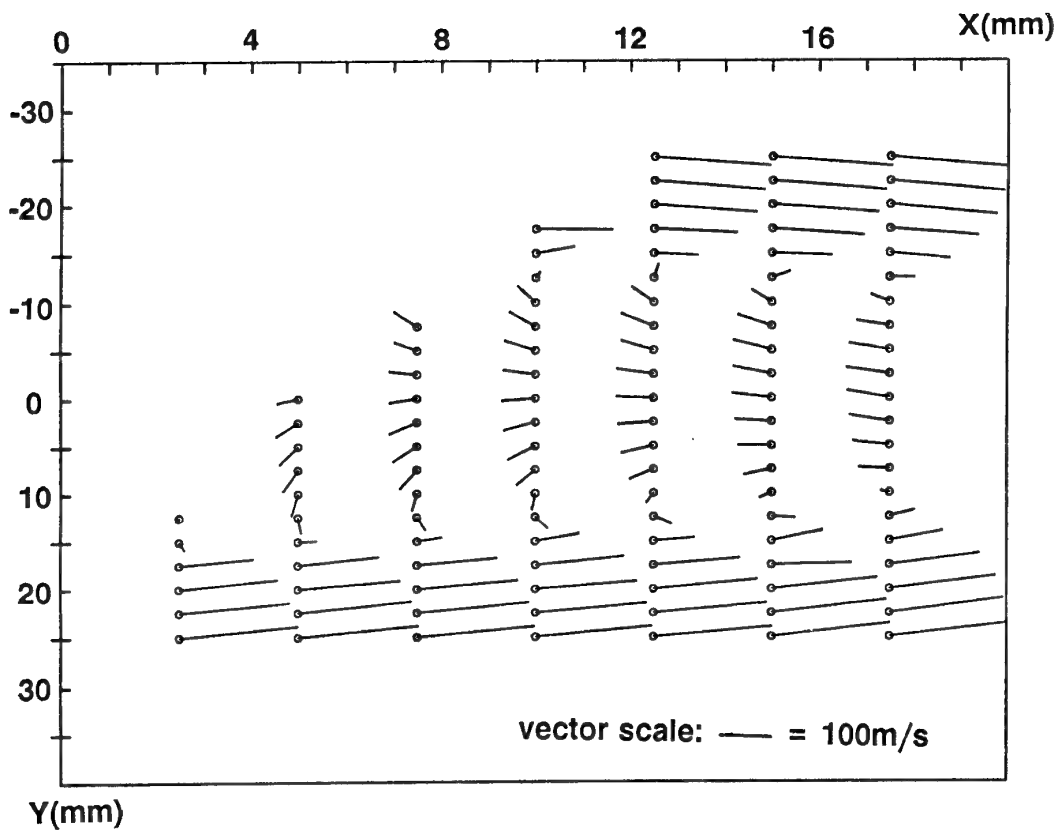


Fig. A.3.23 - Test Case A.3.2 : Mach number 0.80. Mean velocity field in the backflow region. Component projected in the (X,Y) plane located at  $Z = 0\text{mm}$

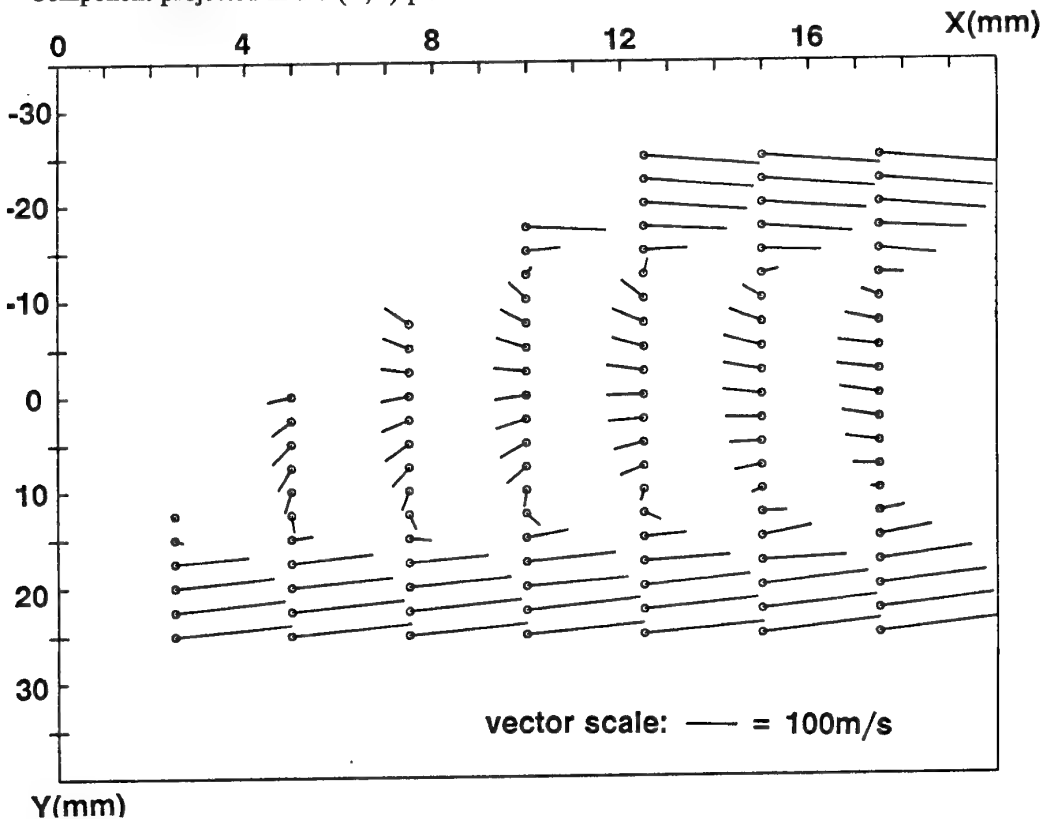


Fig. A.3.24 - Test Case A.3.2 : Mach number 0.80. Mean velocity field in the backflow region. Component projected in the (X,Y) plane located at  $Z = 2\text{mm}$

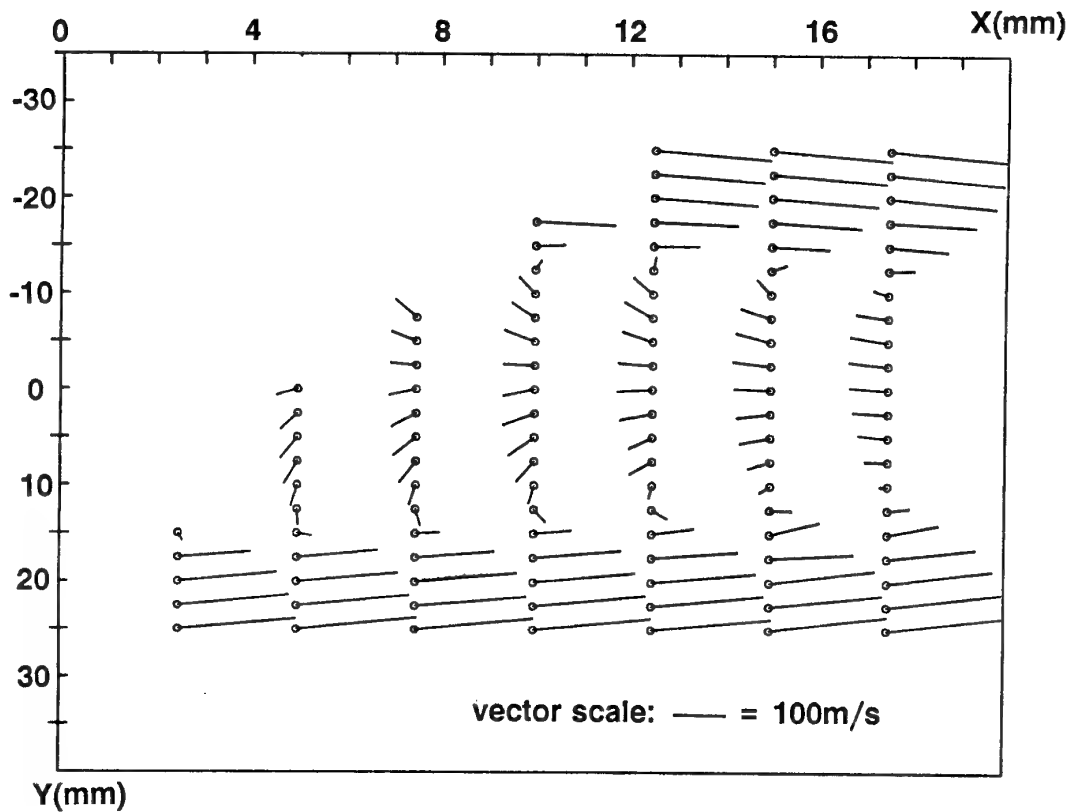


Fig. A.3.25 - Test Case A.3.2 : Mach number 0.80. Mean velocity field in the backflow region. Component projected in the (X,Y) plane located at  $Z = 4\text{mm}$

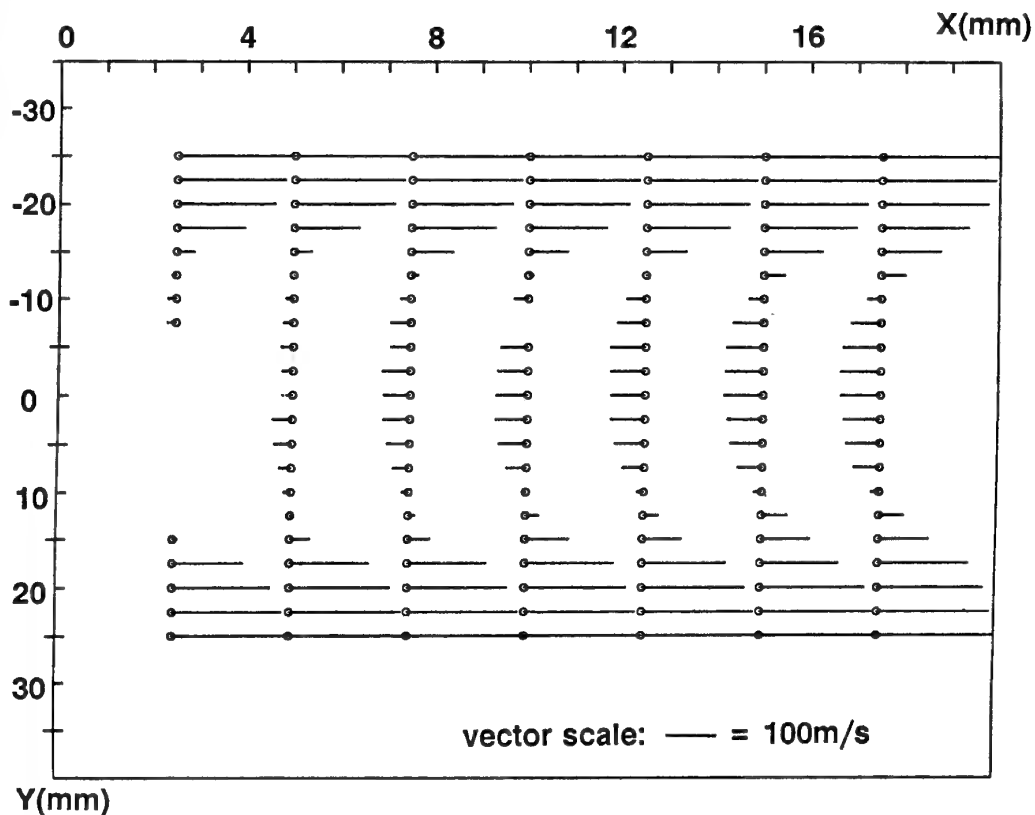


Fig. A.3.26 - Test Case A.3.2 : Mach number 0.80. Mean velocity field in the backflow region. X-wise component in the plane located at  $Z = -4\text{mm}$

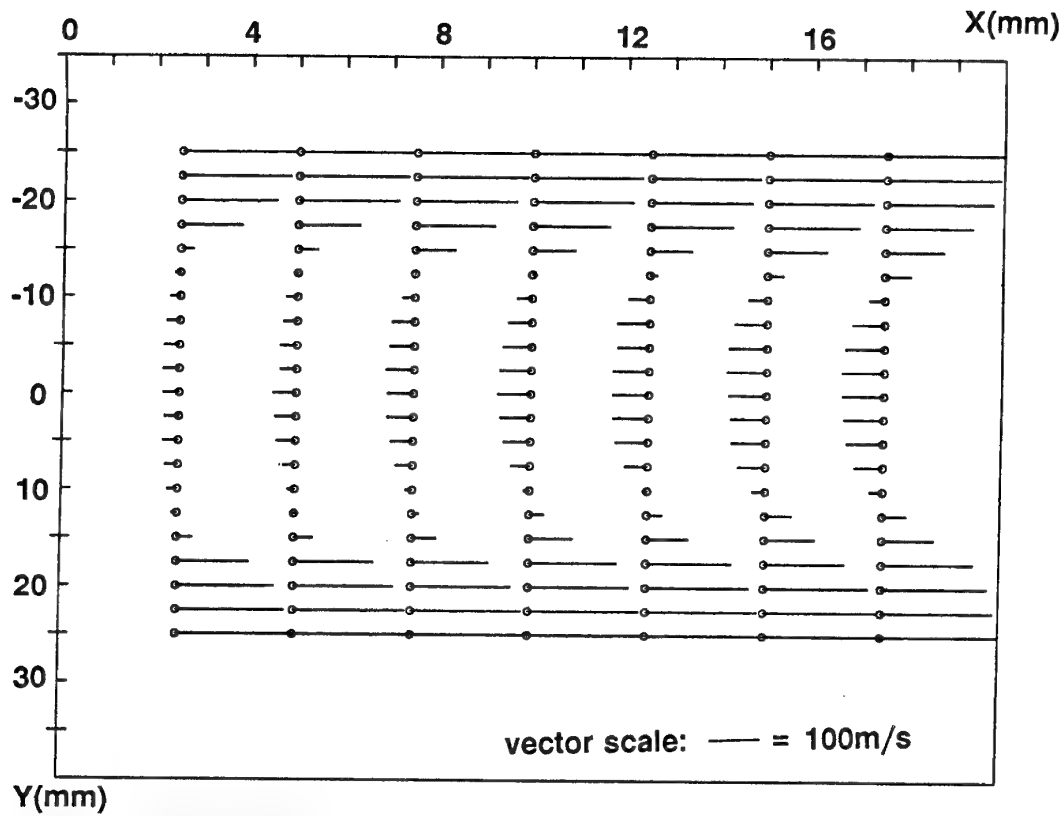


Fig. A.3.27 - Test Case A.3.2 : Mach number 0.80. Mean velocity field in the backflow region. X-wise component in the plane located at  $Z = -2\text{mm}$

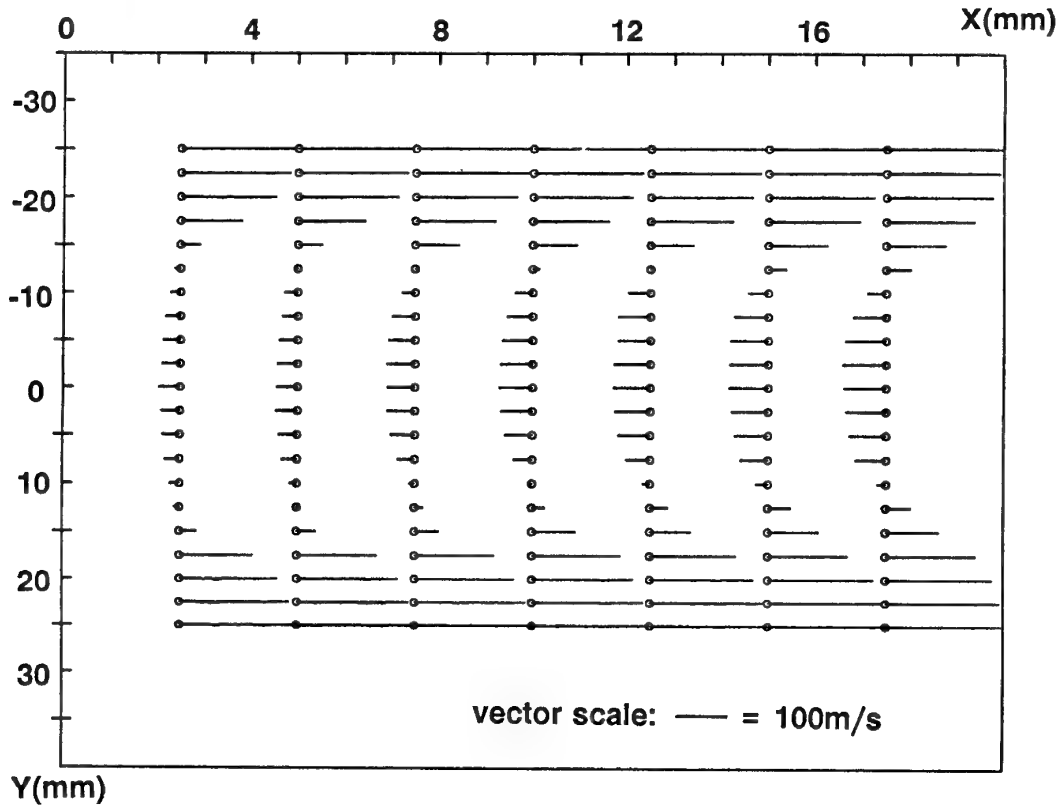


Fig. A.3.28 - Test Case A.3.2 : Mach number 0.80. Mean velocity field in the backflow region. X-wise component in the plane located at  $Z = 0\text{mm}$

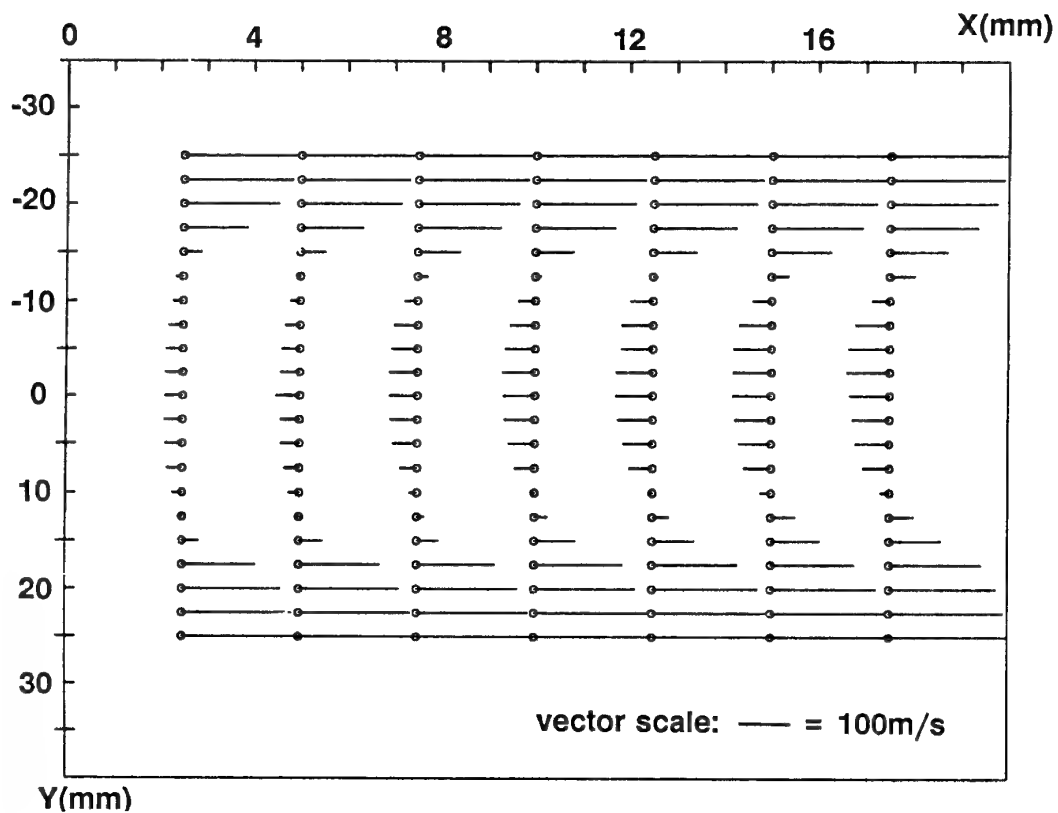


Fig. A.3.29 - Test Case A.3.2 : Mach number 0.80. Mean velocity field in the backflow region. X-wise component in the plane located at  $Z = 2\text{ mm}$

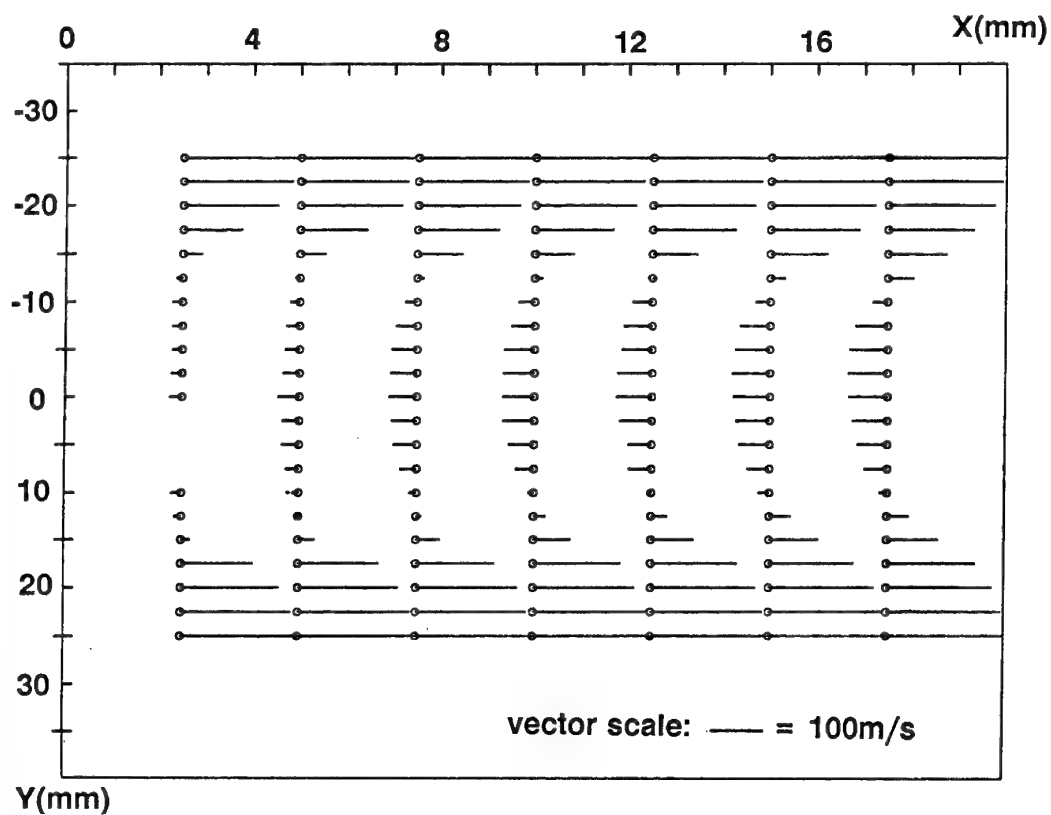


Fig. A.3.30 - Test Case A.3.2 : Mach number 0.80. Mean velocity field in the backflow region. X-wise component in the plane located at  $Z = 4\text{ mm}$

# B. APPENDIX B: EXPERIMENTAL DATA FOR GROUP B. TEST CASES

## B.1 B.1 Test Cases - Axisymmetric, Single-Engine Body with No Tails

### B.1.1 Test Case B.1.1 ( $M_\infty = 0.901$ , NPR = 2.033)

#### B.1.1.1 Surface Pressure Distribution

x/L	$C_p$	x/L	$C_p$	x/L	$C_p$
0.584	-0.019	0.724	-0.055	0.891	-0.130
0.598	-0.029	0.738	-0.063	0.916	-0.148
0.612	-0.032	0.752	-0.055	0.928	-0.164
0.626	-0.028	0.766	-0.071	0.940	-0.154
0.640	-0.039	0.793	-0.068	0.952	-0.088
0.654	-0.045	0.807	-0.073	0.962	0.011
0.668	-0.042	0.821	-0.080	0.974	0.107
0.682	-0.046	0.835	-0.094	0.986	0.167
0.696	-0.050	0.849	-0.103	0.996	0.196
0.710	-0.051	0.863	-0.115		

Table B.1-1: External pressure distributions for test case B.1.1 at  $\phi = 108^\circ$ .

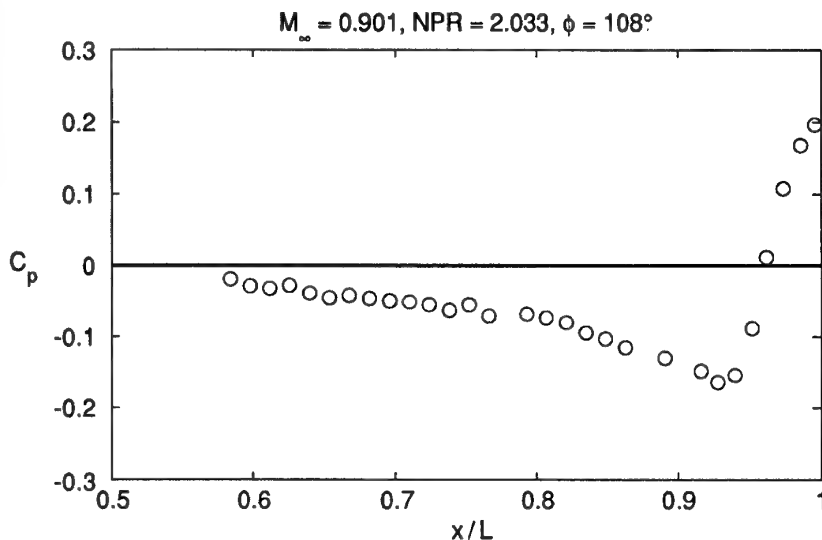


Figure B.1-1 - Static pressure distribution on single-jet test case B.1.1 at  $\phi = 108^\circ$ . Tails off.

#### B.1.1.2 Experimental Pressure Drag Coefficient Buildup

x/L	$C_{DP}$	x/L	$C_{DP}$	x/L	$C_{DP}$	x/L	$C_{DP}$
0.570	0	0.717	.001969	0.856	.014397	0.991	.038178
0.591	.000024	0.731	.002508	0.870	.017648	1.000	.027577
0.605	.000085	0.745	.003119	0.884	.021106		
0.619	.000145	0.759	.003737	0.905	.029093		
0.633	.000238	0.773	.004807	0.922	.038258		
0.647	.000450	0.786	.005727	0.934	.046009		
0.661	.000623	0.800	.006784	0.946	.055758		
0.675	.000827	0.814	.007978	0.957	.061536		
0.689	.001129	0.828	.009679	0.968	.060392		
0.703	.001559	0.842	.011729	0.980	.050918		

Table B.1-2: Experimental pressure drag coefficient buildup for test case B.1.1.

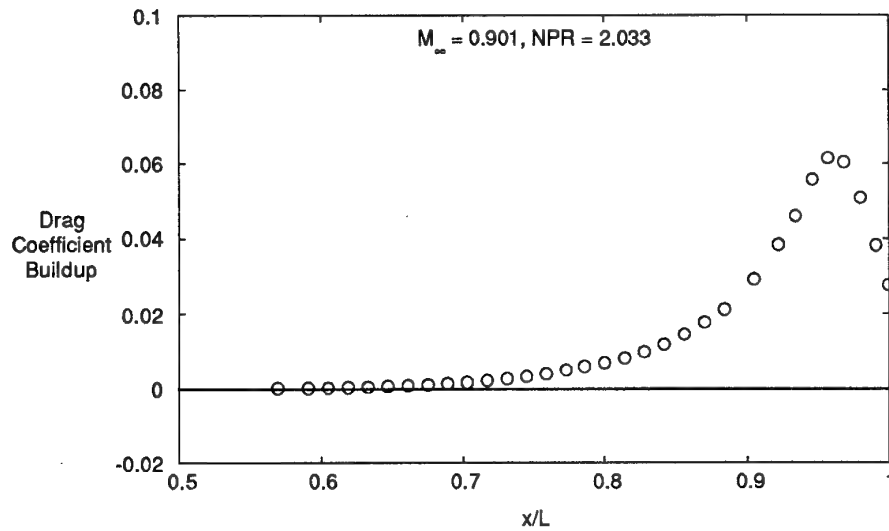


Figure B.1-2 - Drag coefficient buildup for test case B.1.1.

#### B.1.1.3 Experimental Pressure Drag Coefficients

NPR	$C_{DPN}$	$C_{DPA}$	$C_{DPT}$
1.111	0.0164	0.0306	0.0470
2.033	-0.0015	0.0291	0.0276 (B.1.1)
3.061	-0.0011	0.0289	0.0278
4.991	-0.0095	0.0286	0.0191 (B.1.2)

Table B.1-3: Experimental pressure drag coefficients for tail off (B.1) configurations.

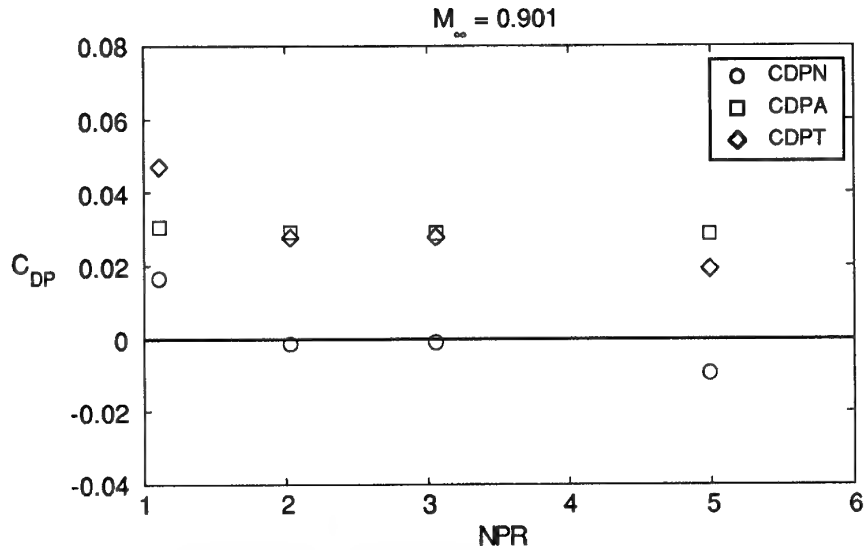
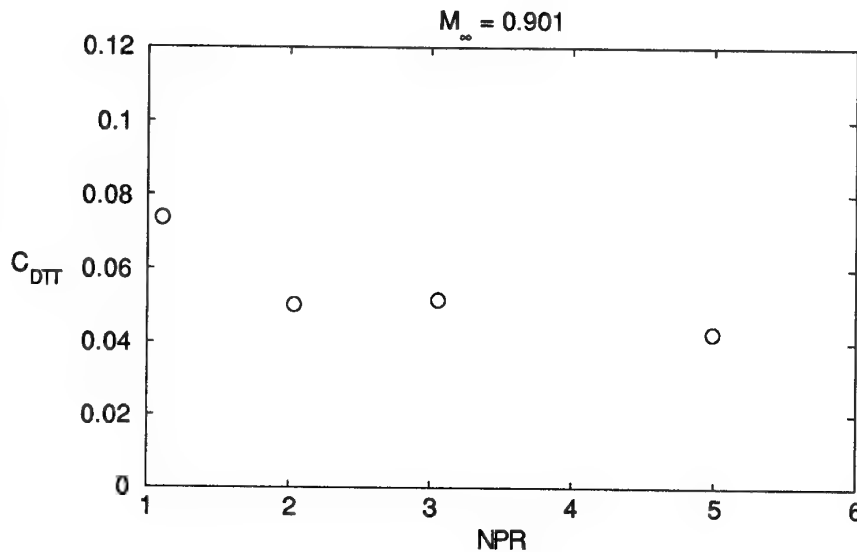


Figure B.1-3 - Variation of pressure drag coefficients with NPR.  
Tail off (B.1) configurations.

#### B.1.1.4 Experimental Total Drag Coefficients

NPR	$C_{DTT}$
1.111	0.0735
2.033	0.0500 (B.1.1)
3.061	0.0515
4.991	0.0423 (B.1.2)

**Table B.1-4:** Experimental total drag coefficients for tail off (B.1) configurations.



**Figure B.1-4 -** Variation of total drag coefficient with NPR.  
Tail off (B.1) configurations.

#### B.1.2 Test Case B.1.2 ( $M_{\infty} = 0.901$ , NPR = 4.991)

##### B.1.2.1 Surface Pressure Distribution

$x/L$	$C_p$	$x/L$	$C_p$	$x/L$	$C_p$
0.584	-0.022	0.724	-0.050	0.891	-0.125
0.598	-0.030	0.738	-0.064	0.916	-0.142
0.612	-0.027	0.752	-0.056	0.928	-0.155
0.626	-0.028	0.766	-0.074	0.940	-0.147
0.640	-0.040	0.793	-0.067	0.952	-0.066
0.654	-0.051	0.807	-0.068	0.962	0.033
0.668	-0.043	0.821	-0.077	0.974	0.129
0.682	-0.043	0.835	-0.088	0.986	0.183
0.696	-0.052	0.849	-0.099	0.996	0.207
0.710	-0.047	0.863	-0.109		

**Table B.1-5:** External pressure distributions for test case B.1.2 at  $\phi = 108^\circ$ .



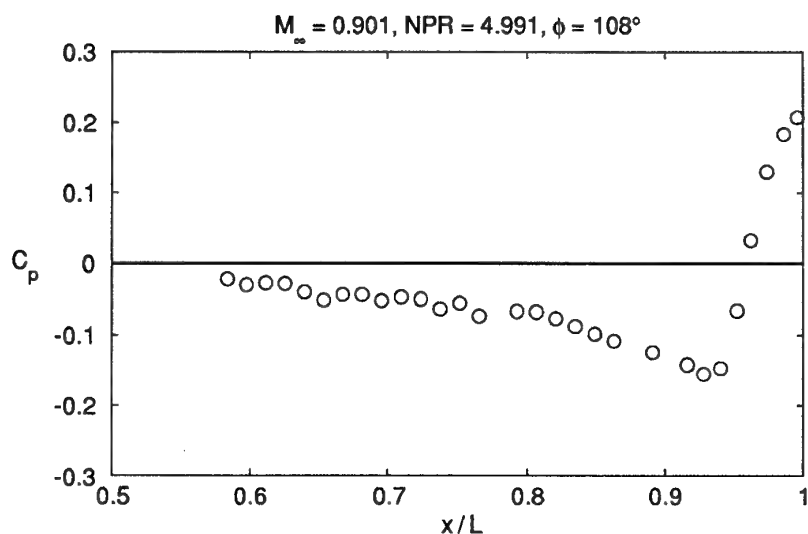


Figure B.1-5 - Static pressure distribution on single-jet test case B.1.2 at  $\phi = 108^\circ$ . Tails off.

#### B.1.2.2 Experimental Pressure Drag Coefficient Buildup

$x/L$	$C_{DP}$	$x/L$	$C_{DP}$	$x/L$	$C_{DP}$	$x/L$	$C_{DP}$
0.570	0	0.717	.001968	0.856	.014280	0.991	.030455
0.591	.000026	0.731	.002492	0.870	.017475	1.000	.019117
0.605	.000089	0.745	.003094	0.884	.020811		
0.619	.000145	0.759	.003729	0.905	.028571		
0.633	.000234	0.773	.004788	0.922	.037412		
0.647	.000447	0.786	.005672	0.934	.044828		
0.661	.000632	0.800	.006716	0.946	.053603		
0.675	.000842	0.814	.007906	0.957	.058269		
0.689	.001137	0.828	.009548	0.968	.055606		
0.703	.001561	0.842	.011573	0.980	.044438		

Table B.1-6: Experimental pressure drag coefficient buildup for test case B.1.2.

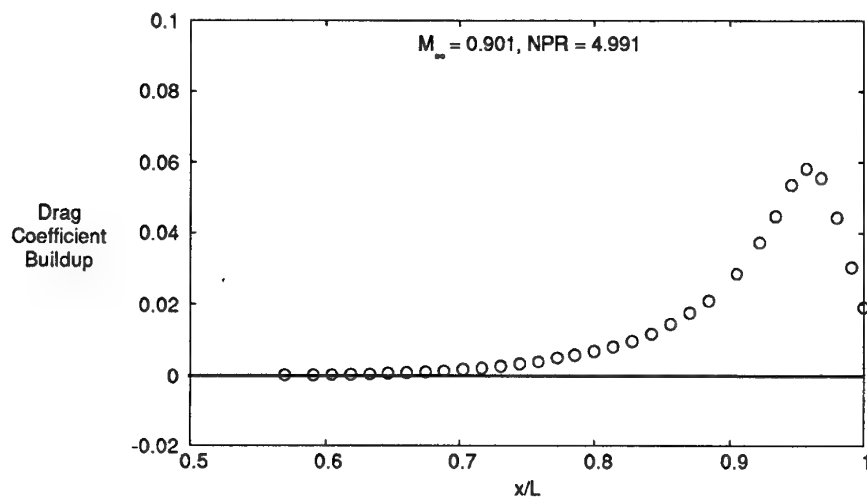


Figure B.1-6 - Pressure drag coefficient buildup for test case B.1.2.

#### B.1.2.3 Experimental Pressure Drag Coefficients

See Table B.1-3 and Figure B.1-3

#### B.1.2.4 Experimental Total Drag Coefficients

See Table B.1-4 and Figure B.1-4

## B.2 B.2 Test Cases - Axisymmetric, Single-Engine Body with Staggered Tails

### B.2.1 Test Case B.2.1 ( $M_\infty = 0.900$ , NPR = 2.027)

#### B.2.1.1 Surface Pressure Distribution

x/L	$C_p$	x/L	$C_p$	x/L	$C_p$	x/L	$C_p$
0.584	-0.010	0.724	-0.150	0.863	-0.103	0.996	0.203
0.598	-0.009	0.738	-0.174	0.877	-0.113		
0.612	0.010	0.752	-0.165	0.891	-0.160		
0.626	0.051	0.766	-0.177	0.916	-0.149		
0.640	0.072	0.779	-0.143	0.928	*****		
0.654	0.011	0.793	-0.136	0.940	*****		
0.668	*****	0.807	-0.133	0.952	*****		
0.682	-0.077	0.821	*****	0.962	0.033		
0.696	-0.103	0.835	-0.107	0.974	0.120		
0.710	-0.127	0.849	-0.099	0.986	0.173		

Table B.2-1: External pressure distributions for test case B.2.1 at  $\phi = 18^\circ$ .

x/L	$C_p$	x/L	$C_p$	x/L	$C_p$	x/L	$C_p$
0.584	*****	0.724	-0.085	0.863	-0.226	0.996	0.198
0.598	-0.020	0.738	*****	0.877	-0.224		
0.612	-0.012	0.752	-0.079	0.891	-0.243		
0.626	-0.009	0.766	-0.060	0.916	*****		
0.640	-0.014	0.779	-0.012	0.928	-0.120		
0.654	-0.021	0.793	-0.059	0.940	-0.078		
0.668	-0.035	0.807	-0.099	0.952	-0.019		
0.682	-0.048	0.821	-0.149	0.962	0.052		
0.696	-0.062	0.835	-0.171	0.974	0.126		
0.710	-0.068	0.849	-0.205	0.986	0.178		

Table B.2-2: External pressure distributions for test case B.2.1 at  $\phi = 72^\circ$ .

x/L	$C_p$	x/L	$C_p$	x/L	$C_p$	x/L	$C_p$
0.584	-0.009	0.724	-0.066	0.863	*****	0.996	0.191
0.598	-0.016	0.738	-0.068	0.877	*****		
0.612	-0.008	0.752	-0.055	0.891	*****		
0.626	-0.009	0.766	-0.032	0.916	-0.162		
0.640	-0.018	0.779	0.155	0.928	-0.100		
0.654	-0.034	0.793	*****	0.940	-0.060		
0.668	-0.030	0.807	*****	0.952	-0.008		
0.682	-0.045	0.821	*****	0.962	0.060		
0.696	-0.052	0.835	*****	0.974	0.124		
0.710	-0.062	0.849	*****	0.986	0.168		

Table B.2-3: External pressure distributions for test case B.2.1 at  $\phi = 90^\circ$ .

$x/L$	$C_p$	$x/L$	$C_p$	$x/L$	$C_p$	$x/L$	$C_p$
0.584	-0.012	0.724	-0.053	0.863	-0.197	0.996	0.191
0.598	-0.014	0.738	-0.056	0.877	*****		
0.612	-0.016	0.752	-0.050	0.891	-0.232		
0.626	-0.017	0.766	-0.056	0.916	-0.162		
0.640	-0.026	0.779	-0.028	0.928	-0.153		
0.654	-0.038	0.793	-0.038	0.940	-0.112		
0.668	-0.028	0.807	-0.054	0.952	-0.043		
0.682	-0.043	0.821	-0.087	0.962	0.051		
0.696	-0.045	0.835	-0.125	0.974	0.123		
0.710	-0.041	0.849	-0.160	0.986	0.173		

**Table B.2-4:** External pressure distributions for test case B.2.1 at  $\phi = 135^\circ$ .

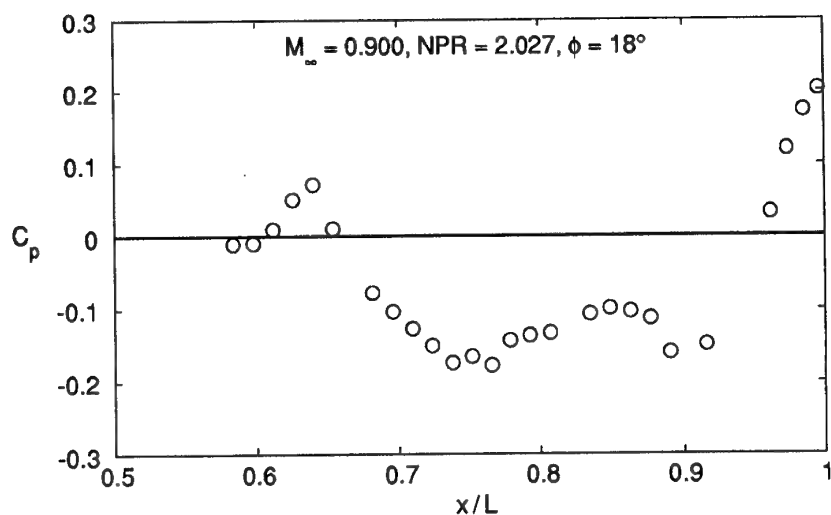


**Figure B.2-1** - Static pressure distribution on single-jet test case B.2.1 at  $\phi = 18^\circ$ . Staggered tails.

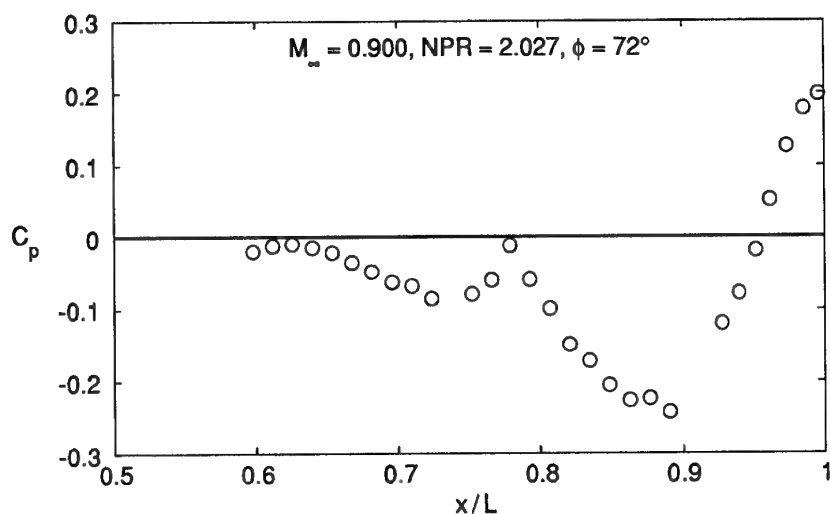


**Figure B.2-2** - Static pressure distribution on single-jet test case B.2.1 at  $\phi = 72^\circ$ . Staggered tails.

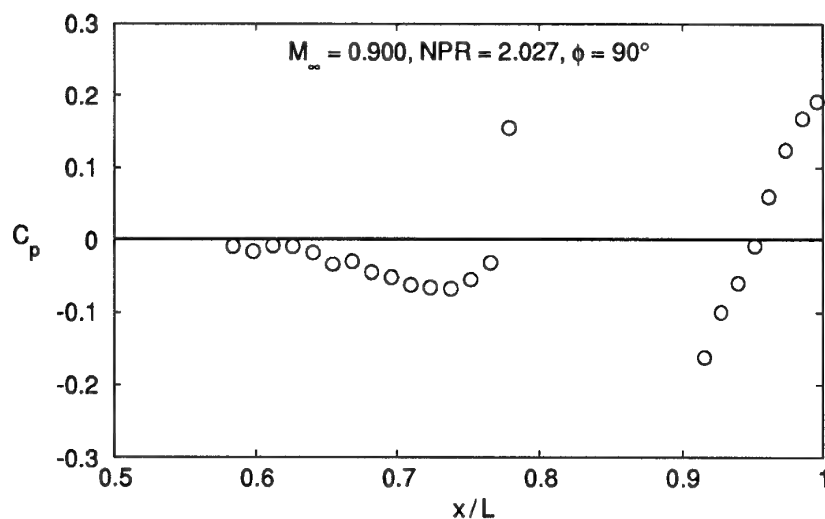


Figure B.2-3 - Static pressure distribution on single-jet test case B.2.1 at  $\phi = 90^\circ$ . Staggered tails.

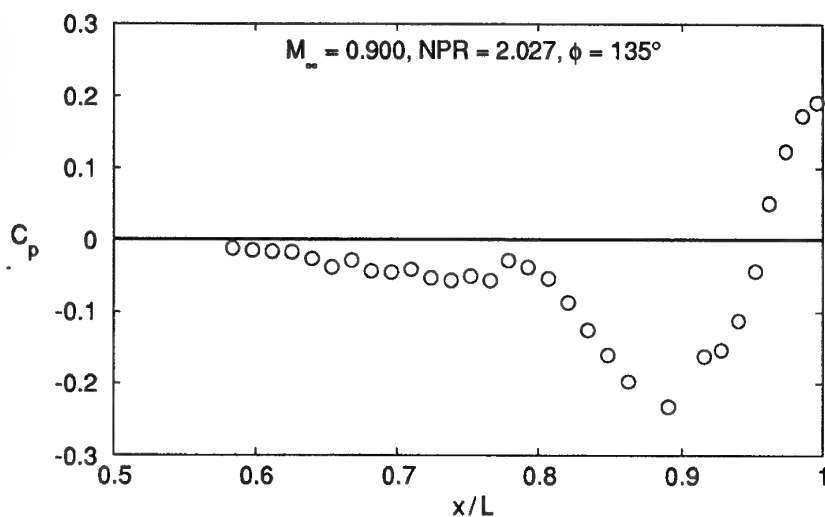


Figure B.2-4 - Static pressure distribution on single-jet test case B.2.1 at  $\phi = 135^\circ$ . Staggered tails.

#### B.2.1.2 Tail Pressure Distributions

$x_t/c$	Horizontal tail	Vertical tail
	Upper surface $y_t/b_t = 0.1$	$z_t/b_t = 0.1$
	$C_p$	$C_p$
0.05	-0.112	-0.069
0.10	-0.129	-0.085
0.20	-0.179	-0.124
0.30	-0.227	-0.175
0.40	-0.289	-0.216
0.50	-0.318	-0.209
0.60	-0.286	-0.177
0.70	-0.151	-0.144
0.80	-0.051	-0.093
0.90	0.034	-0.040

Table B.2-5: Tail pressure distributions for test case B.2.1.

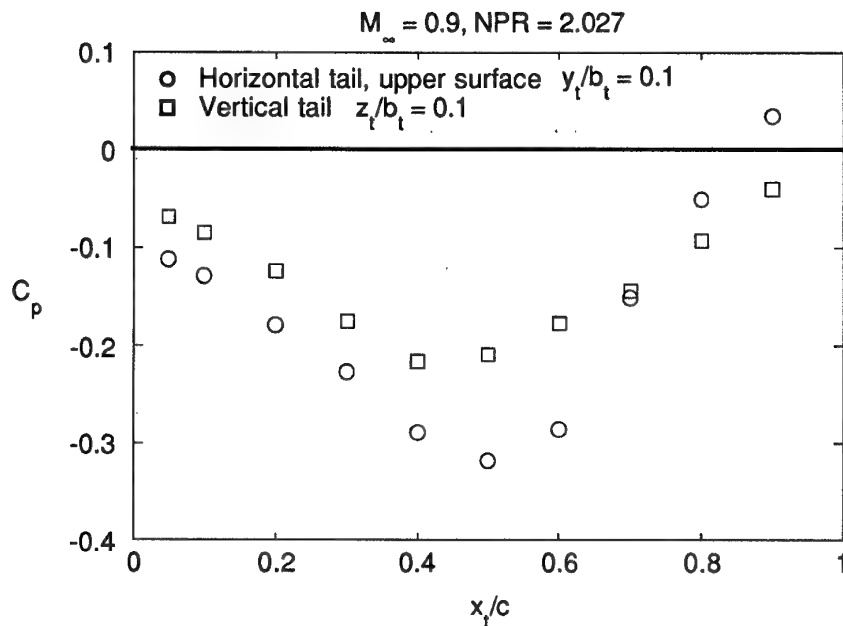


Figure B.2-5 - Tail pressure distributions for test case B.2.1. Staggered tails.

#### B.2.1.3 Experimental Pressure Drag Coefficients

NPR	$C_{DPN}$	$C_{DPA}$
1.113	0.0022	0.0428
2.027	-0.0130	0.0410 (B.2.1)
2.997	-0.0121	0.0410 (B.2.2)
5.033	-0.0196	0.0404 (B.2.3)

Table B.2-6: Experimental pressure drag coefficients for tail on (B.2) configurations.

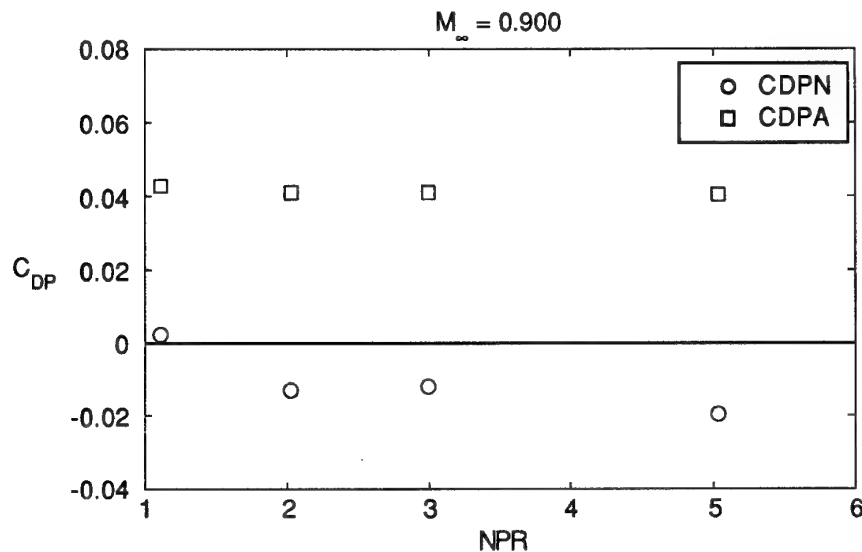


Figure B.2-6 - Variation of pressure drag coefficients with NPR. B.2 configurations.

### B.2.1.4 Experimental Total Drag Coefficients

NPR	$C_{DTT}$
1.113	0.1270
2.027	0.1055 (B.2.1)
2.997	0.1060 (B.2.2)
5.033	0.0960 (B.2.3)

Table B.2-7: Experimental total drag coefficients for tail on (B.2) configurations.

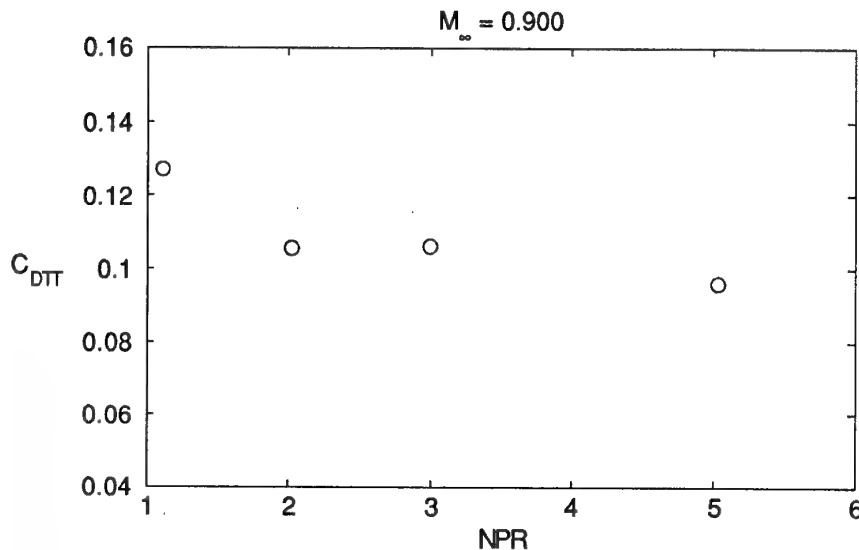


Figure B.2-7 - Variation of total drag coefficient with NPR. B.2 configurations.

### B.2.2 Test Case B.2.2 ( $M_\infty = 0.900$ , NPR = 2.997)

#### B.2.2.1 Surface Pressure Distribution

x/L	$C_p$	x/L	$C_p$	x/L	$C_p$	x/L	$C_p$
0.584	-0.008	0.724	-0.158	0.863	-0.106	0.996	0.200
0.598	-0.004	0.738	-0.172	0.877	-0.117		
0.612	0.012	0.752	-0.161	0.891	-0.160		
0.626	0.049	0.766	-0.176	0.916	-0.148		
0.640	0.072	0.779	-0.142	0.928	*****		
0.654	0.001	0.793	-0.136	0.940	*****		
0.668	*****	0.807	-0.127	0.952	*****		
0.682	-0.077	0.821	*****	0.962	0.034		
0.696	-0.108	0.835	-0.099	0.974	0.119		
0.710	-0.126	0.849	-0.089	0.986	0.173		

Table B.2-8: External pressure distributions for test case B.2.2 at  $\phi = 18^\circ$ .

x/L	C <sub>p</sub>	x/L	C <sub>p</sub>	x/L	C <sub>p</sub>	x/L	C <sub>p</sub>
0.584	*****	0.724	-0.081	0.863	-0.220	0.996	0.200
0.598	-0.020	0.738	*****	0.877	-0.228		
0.612	-0.012	0.752	-0.071	0.891	-0.229		
0.626	-0.005	0.766	-0.062	0.916	*****		
0.640	-0.016	0.779	-0.015	0.928	-0.121		
0.654	-0.020	0.793	-0.058	0.940	-0.078		
0.668	-0.030	0.807	-0.117	0.952	-0.019		
0.682	-0.051	0.821	-0.157	0.962	0.050		
0.696	-0.065	0.835	-0.173	0.974	0.123		
0.710	-0.064	0.849	-0.197	0.986	0.178		

**Table B.2-9:** External pressure distributions for test case B.2.2 at  $\phi = 72^\circ$ .

x/L	C <sub>p</sub>	x/L	C <sub>p</sub>	x/L	C <sub>p</sub>	x/L	C <sub>p</sub>
0.584	-0.013	0.724	-0.065	0.863	*****	0.996	0.195
0.598	-0.026	0.738	-0.076	0.877	*****		
0.612	-0.013	0.752	-0.053	0.891	*****		
0.626	-0.016	0.766	-0.027	0.916	-0.172		
0.640	-0.023	0.779	0.159	0.928	-0.103		
0.654	-0.032	0.793	*****	0.940	-0.054		
0.668	-0.030	0.807	*****	0.952	-0.005		
0.682	-0.046	0.821	*****	0.962	0.056		
0.696	-0.049	0.835	*****	0.974	0.120		
0.710	-0.060	0.849	*****	0.986	0.174		

**Table B.2-10:** External pressure distributions for test case B.2.2 at  $\phi = 90^\circ$ .

x/L	C <sub>p</sub>	x/L	C <sub>p</sub>	x/L	C <sub>p</sub>	x/L	C <sub>p</sub>
0.584	-0.017	0.724	-0.041	0.863	-0.205	0.996	0.190
0.598	-0.014	0.738	-0.052	0.877	*****		
0.612	-0.010	0.752	-0.037	0.891	-0.224		
0.626	-0.019	0.766	-0.052	0.916	-0.161		
0.640	-0.024	0.779	-0.026	0.928	-0.150		
0.654	-0.036	0.793	-0.040	0.940	-0.115		
0.668	-0.028	0.807	-0.055	0.952	-0.043		
0.682	-0.042	0.821	-0.091	0.962	0.048		
0.696	-0.048	0.835	-0.125	0.974	0.125		
0.710	-0.044	0.849	-0.160	0.986	0.169		

**Table B.2-11:** External pressure distributions for test case B.2.2 at  $\phi = 135^\circ$ .

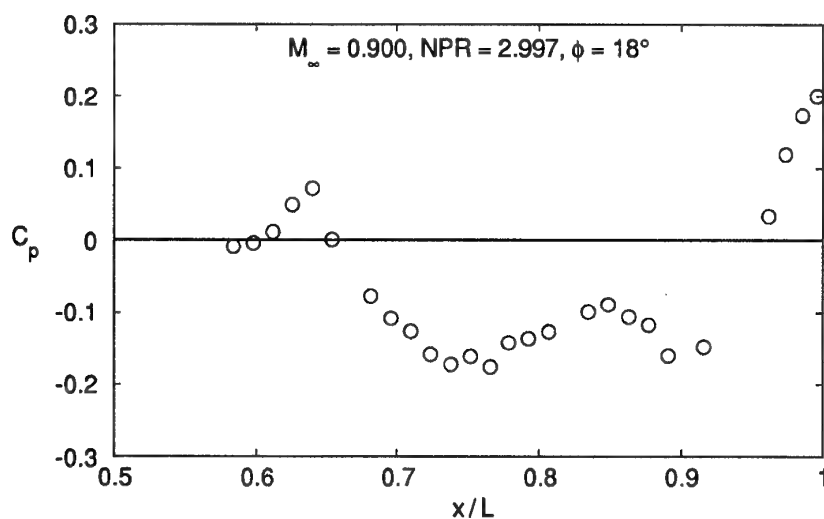


Figure B.2-8 - Static pressure distribution on single-jet test case B.2.2 at  $\phi = 18^\circ$ . Staggered tails.

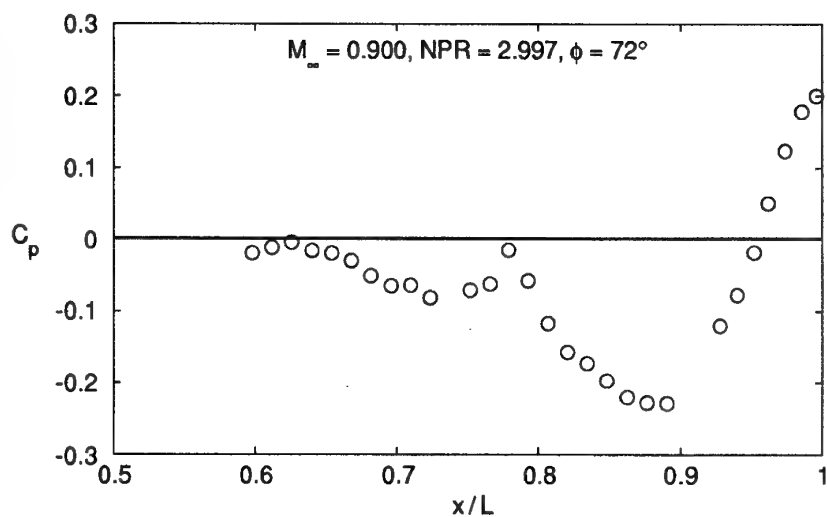


Figure B.2-9 - Static pressure distribution on single-jet test case B.2.2 at  $\phi = 72^\circ$ . Staggered tails.

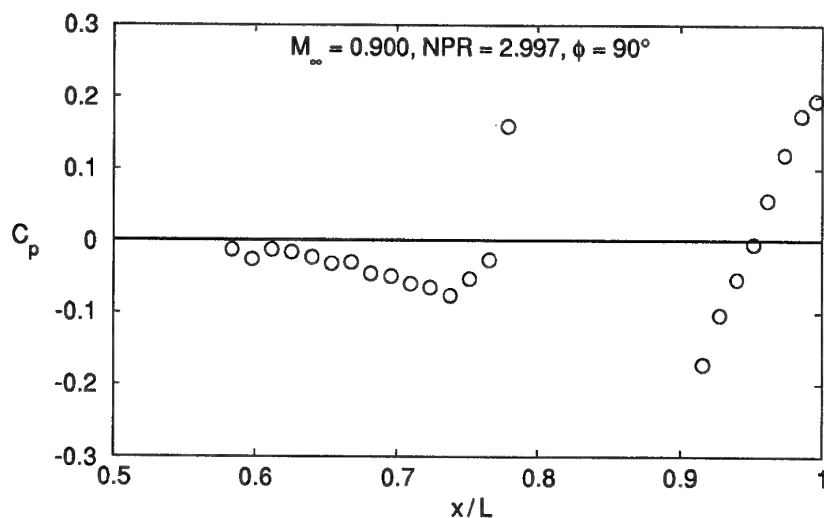


Figure B.2-10 - Static pressure distribution on single-jet test case B.2.2 at  $\phi = 90^\circ$ . Staggered tails.



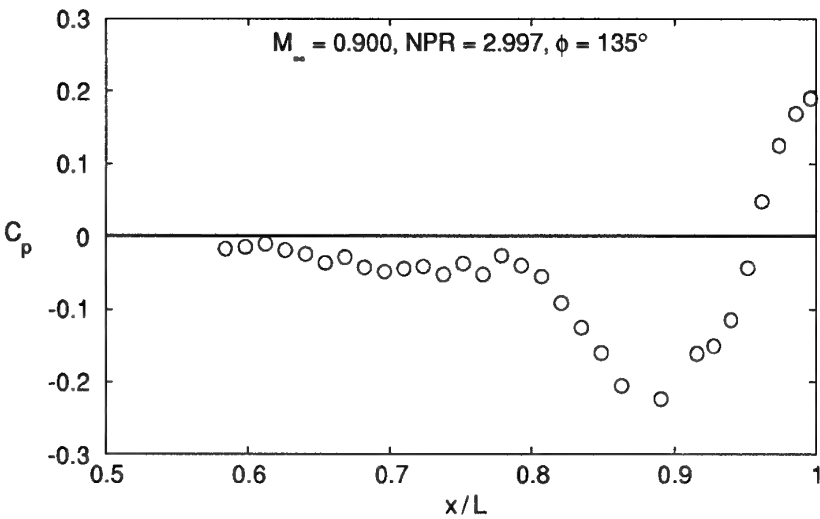


Figure B.2-11 - Static pressure distribution on single-jet test case B.2.2 at  $\phi = 135^\circ$ . Staggered tails.

B.2.2.2 Tail Pressure Distributions

$x_t/c$	Horizontal tail Upper surface $y_t/b_t = 0.1$	Vertical tail $z_t/b_t = 0.1$
	$C_p$	$C_p$
0.05	-0.112	-0.088
0.10	-0.139	-0.092
0.20	-0.181	-0.123
0.30	-0.222	-0.175
0.40	-0.300	-0.220
0.50	-0.314	-0.218
0.60	-0.300	-0.188
0.70	-0.158	-0.147
0.80	-0.050	-0.103
0.90	0.035	-0.048

Table B.2-12: Tail pressure distributions for test case B.2.2.

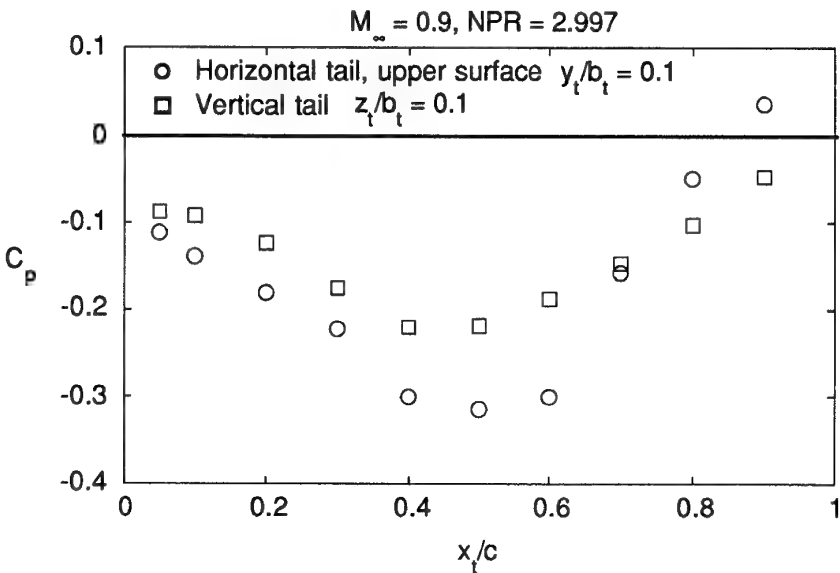


Figure B.2-12 - Tail pressure distributions for test case B.2.2. Staggered tails.

**B.2.2.3 Experimental Pressure Drag Coefficients**

See Table B.2-6 and Figure B.2-6

**B.2.2.4 Experimental Total Drag Coefficients**

See Table B.2-7 and Figure B.2-7

**B.2.3 Test Case B.2.3 ( $M_\infty = 0.900$ ,  
NPR = 5.033)****B.2.3.1 Surface Pressure Distribution**

x/L	$C_p$	x/L	$C_p$	x/L	$C_p$	x/L	$C_p$
0.584	-0.000	0.724	-0.157	0.863	-0.100	0.996	0.213
0.598	-0.007	0.738	-0.179	0.877	-0.112		
0.612	0.016	0.752	-0.164	0.891	-0.147		
0.626	0.049	0.766	-0.187	0.916	-0.143		
0.640	0.072	0.779	-0.150	0.928	*****		
0.654	0.022	0.793	-0.136	0.940	*****		
0.668	*****	0.807	-0.120	0.952	*****		
0.682	-0.079	0.821	*****	0.962	0.052		
0.696	-0.104	0.835	-0.097	0.974	0.139		
0.710	-0.124	0.849	-0.089	0.986	0.189		

Table B.2-13: External pressure distributions for test case B.2.3 at  $\phi = 18^\circ$ .

x/L	$C_p$	x/L	$C_p$	x/L	$C_p$	x/L	$C_p$
0.584	*****	0.724	-0.083	0.863	-0.215	0.996	0.208
0.598	-0.026	0.738	*****	0.877	-0.222		
0.612	-0.010	0.752	-0.068	0.891	-0.223		
0.626	-0.006	0.766	-0.062	0.916	*****		
0.640	-0.014	0.779	-0.013	0.928	-0.111		
0.654	-0.020	0.793	-0.051	0.940	-0.068		
0.668	-0.032	0.807	-0.104	0.952	-0.008		
0.682	-0.047	0.821	-0.153	0.962	0.072		
0.696	-0.060	0.835	-0.177	0.974	0.143		
0.710	-0.072	0.849	-0.202	0.986	0.190		

Table B.2-14: External pressure distributions for test case B.2.3 at  $\phi = 72^\circ$ .

x/L	$C_p$	x/L	$C_p$	x/L	$C_p$	x/L	$C_p$
0.584	-0.014	0.724	-0.061	0.863	*****	0.996	0.206
0.598	-0.015	0.738	-0.067	0.877	*****		
0.612	-0.016	0.752	-0.053	0.891	*****		
0.626	-0.017	0.766	-0.032	0.916	-0.156		
0.640	-0.021	0.779	0.153	0.928	-0.093		
0.654	-0.035	0.793	*****	0.940	-0.042		
0.668	-0.037	0.807	*****	0.952	0.011		
0.682	-0.047	0.821	*****	0.962	0.073		
0.696	-0.049	0.835	*****	0.974	0.138		
0.710	-0.053	0.849	*****	0.986	0.186		

Table B.2-15: External pressure distributions for test case B.2.3 at  $\phi = 90^\circ$ .

$x/L$	$C_p$	$x/L$	$C_p$	$x/L$	$C_p$	$x/L$	$C_p$
0.584	-0.009	0.724	-0.046	0.863	-0.203	0.996	0.201
0.598	-0.013	0.738	-0.048	0.877	*****		
0.612	-0.017	0.752	-0.041	0.891	-0.226		
0.626	-0.024	0.766	-0.048	0.916	-0.158		
0.640	-0.025	0.779	-0.033	0.928	-0.138		
0.654	-0.034	0.793	-0.039	0.940	-0.099		
0.668	-0.028	0.807	-0.060	0.952	-0.027		
0.682	-0.039	0.821	-0.090	0.962	0.064		
0.696	-0.044	0.835	-0.125	0.974	0.141		
0.710	-0.042	0.849	-0.169	0.986	0.185		

Table B.2-16: External pressure distributions for test case B.2.3 at  $\phi = 135^\circ$ .

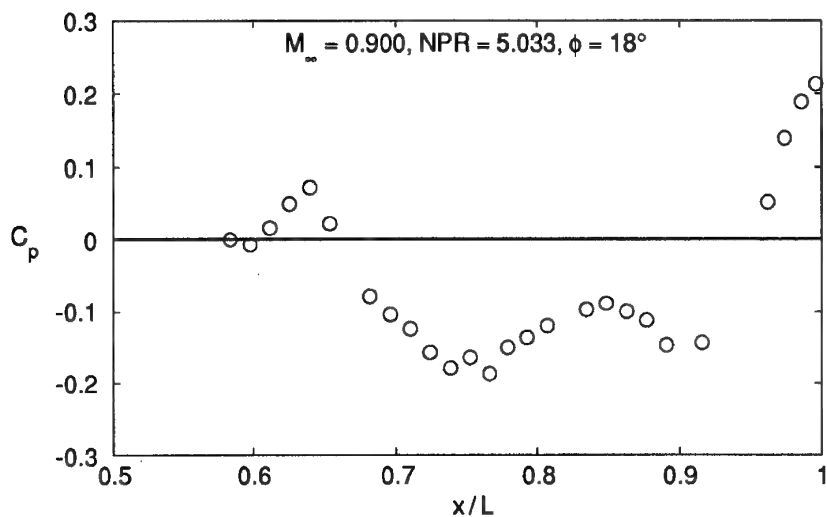


Figure B.2-13 - Static pressure distributions on single-jet test case B.2.3 at  $\phi = 18^\circ$ . Staggered tails.

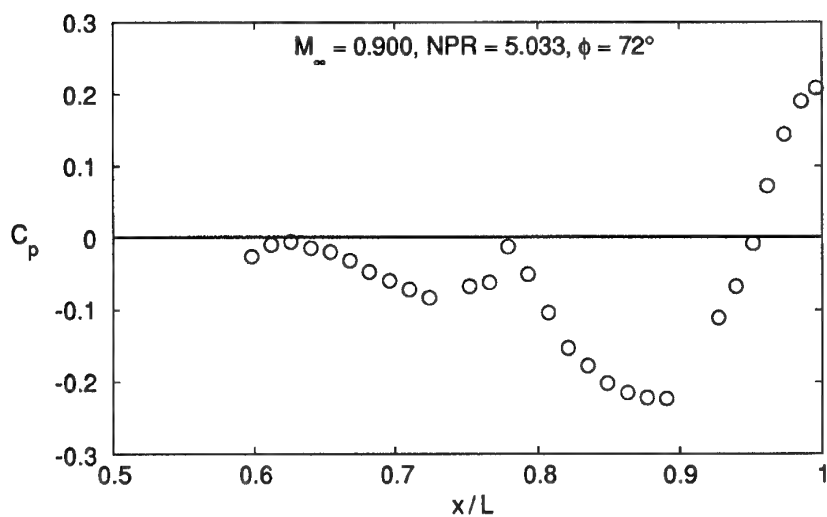


Figure B.2-14 - Static pressure distribution on single-jet test case B.2.3 at  $\phi = 72^\circ$ . Staggered tails.

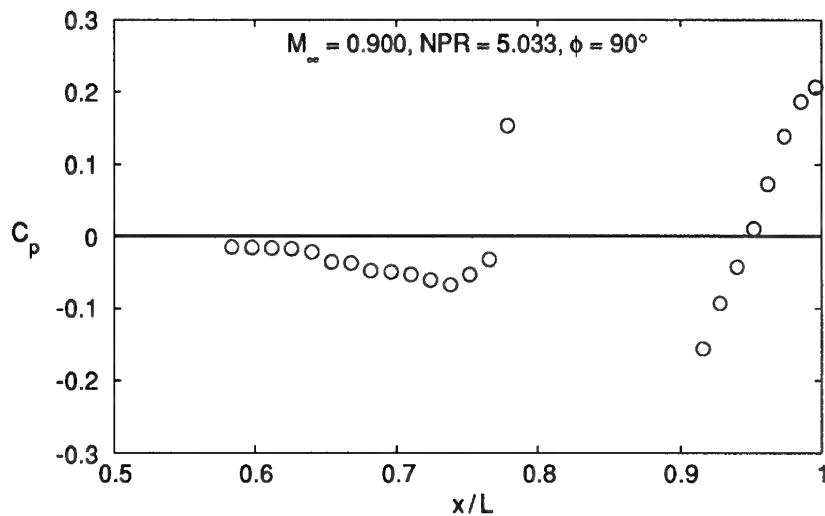


Figure B.2-15 - Static pressure distribution on single-jet test case B.2.3 at  $\phi = 90^\circ$ . Staggered tails.

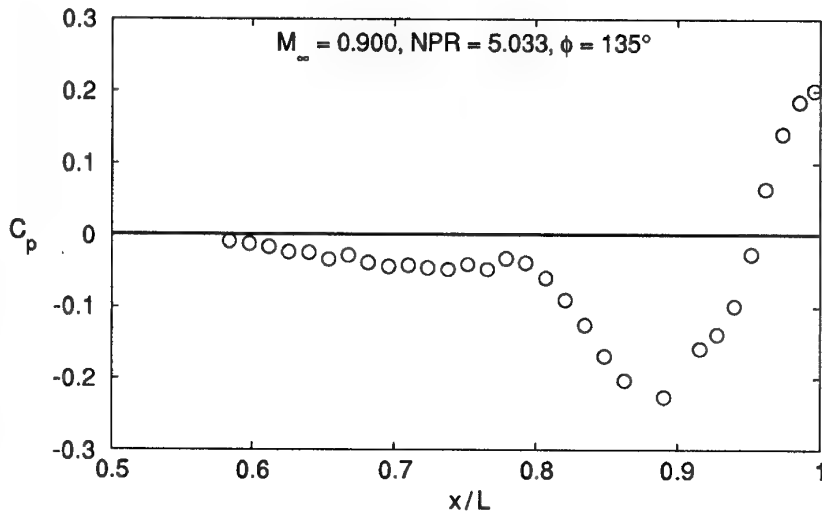


Figure B.2-16 - Static pressure distribution on single-jet test case B.2.3 at  $\phi = 135^\circ$ . Staggered tails.

#### B.2.3.2 Tail Pressure Distributions

$x_t/c$	Horizontal tail Upper surface $y_t/b_t = 0.1$	Vertical tail $z_t/b_t = 0.1$
	$C_p$	$C_p$
0.05	-0.113	-0.067
0.10	-0.132	-0.090
0.20	-0.192	-0.127
0.30	-0.228	-0.176
0.40	-0.303	-0.217
0.50	-0.309	-0.215
0.60	-0.298	-0.182
0.70	-0.147	-0.158
0.80	-0.051	-0.100
0.90	0.039	-0.042

Table B.2-17: Tail pressure distributions for test case B.2.3.

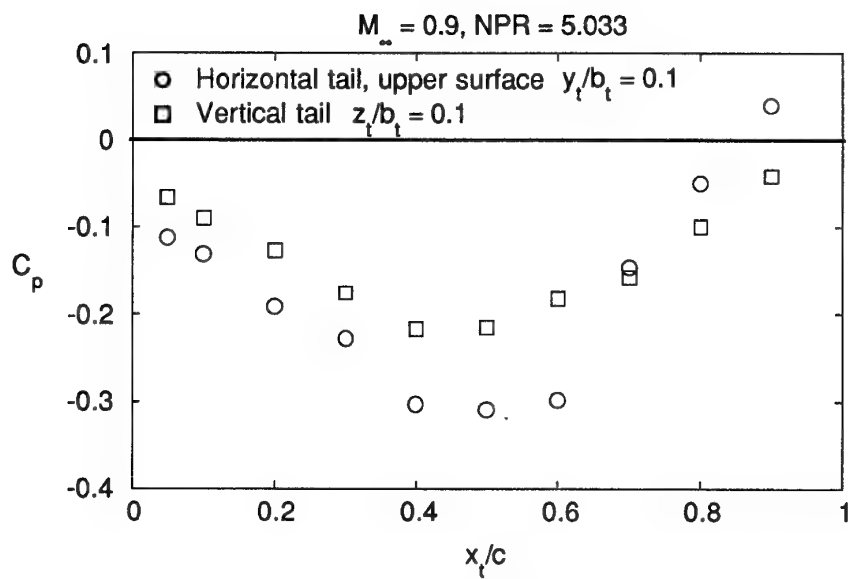


Figure B.2-17 - Tail pressure distributions for test case B.2.3. Staggered tails.

**B.2.3.3 Experimental Pressure Drag Coefficients**  
See Table B.2-6 and Figure B.2-6

**B.2.3.4 Experimental Total Drag Coefficients**  
See Table B.2-7 and Figure B.2-7

### B.3 B.3 Test Cases - Twin-Jet Body, $M_\infty = 0.90$ , $NPR = 3.4$

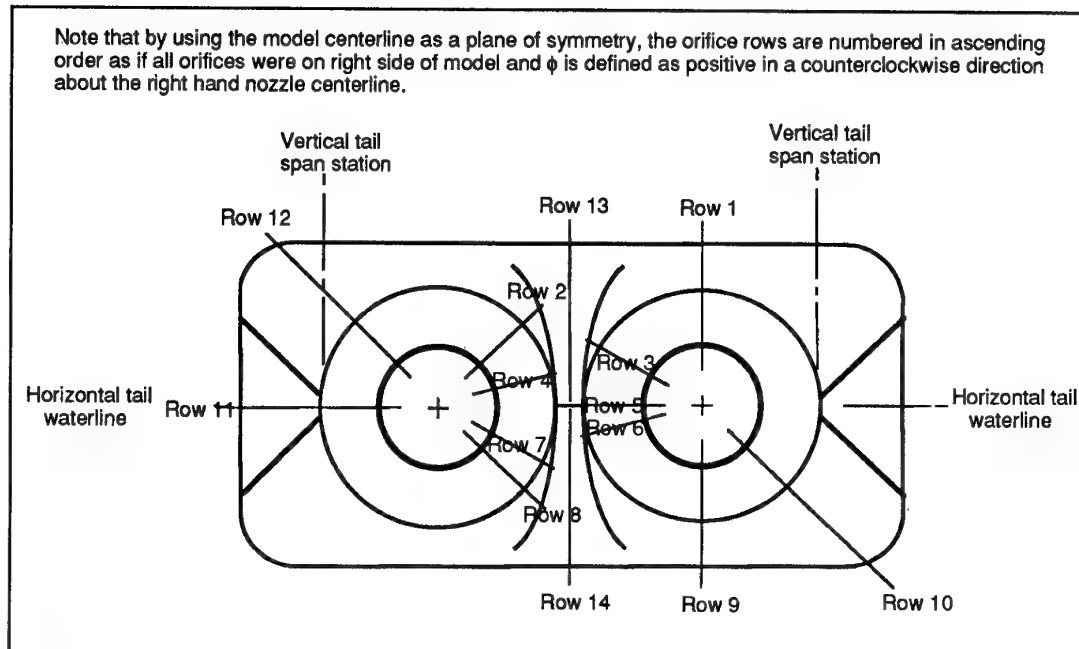


Figure B.3-1 - Definition of twin-jet test case B.3 external pressure orifice rows.

#### B.3.1 Test Case B.3.1 (Mid horizontal tails Mid vertical tails, $M_\infty = 0.901$ , $NPR = 3.407$ )

##### B.3.1.1 Surface Pressure Distribution See Table B.3-1

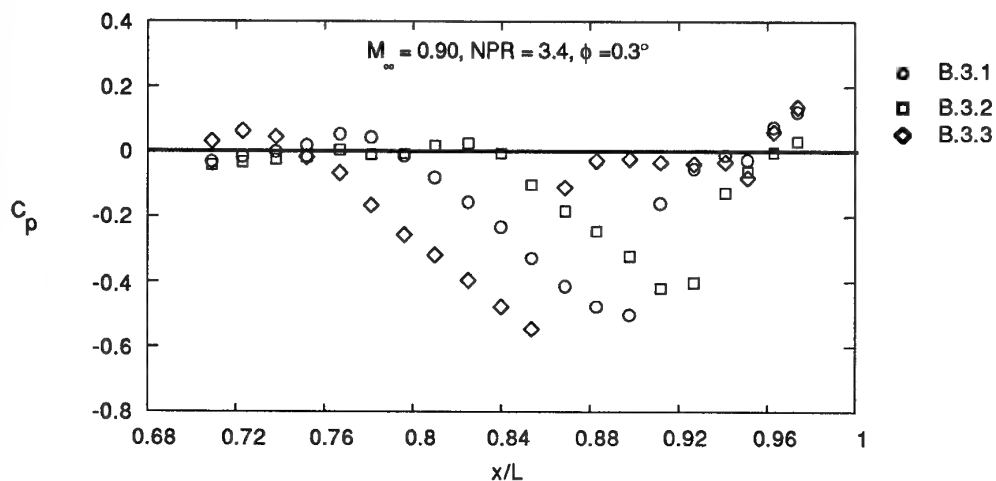


Figure B.3-1- Static pressure distributions on twin-jet test cases B.3 at  $\phi = 0.3^\circ$ , row 1.

Cp at  $\phi$  of

x/L	0.3°	44.5°	60.3°	74.5°	90.0°	105.1°	119.6°	134.7°	180.5°	225.4°	267.5°	314.5°	Top CL	Bottom CL
.709	-.031								-.050	-.037	.012	.007	-.042	-.054
.723	-.016								-.052	-.030	.031	.033	-.017	-.055
.738	0								-.049	-.037	.024	.026		-.051
.752	.019								-.039	-.026	-.005	.038		-.047
.767	.054								-.032	-.009	.059	.082		-.054
.781	.044								-.042	.003	.186	.170		-.078
.796	-.012								-.057	-.009				
.810	-.079								-.064	-.039				
.825	-.155								-.074	-.052				
.840	-.233								-.087	-.074				
.854	-.328								-.098					
.869	-.414								-.102	-.113				-.117
.883	-.476	-.441						-.118	-.111	-.129				-.115
.898	-.501	-.260	-.165					-.097	-.112	-.141				
.912	-.158	-.107	-.088					-.064	-.111	-.112			-.167	
.927	-.052	-.062	-.057	-.062				-.058	-.096	-.075		-.246		
.941	-.011	-.044	-.040	-.038				-.101	-.102	-.015				
.951	-.025	-.021	.041	.002	-.003	-.078		-.185	-.124	-.039	.046	.049	-.035	-.069
.963	.075	.059	.077	.041	.035	.041		.051	.045	.045	.084	.081		
.974	.123	.090	.123	.080	.077	.077		.118	.107	.109	.130	.127		
.986	.130	.130	.171	.130	.123	.125		.155	.148	.148	.162	.128		
.997	.169	.169	.124	.181	.161	.161		.171	.156	.156	.183			
Row #	1	2	3	4	5	6	7	8	9	10	11	12	13	14

Table B.3.1 - External static pressure coefficients on twin-jet test case B.3.1

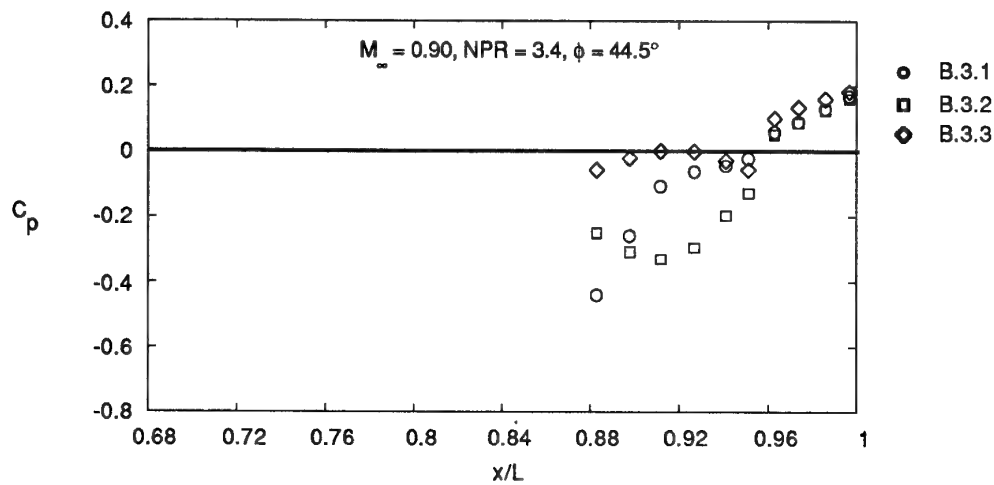


Figure B.3-2 - Static pressure distributions on twin-jet test cases B.3 at  $\phi = 44.5^\circ$ , row 2.

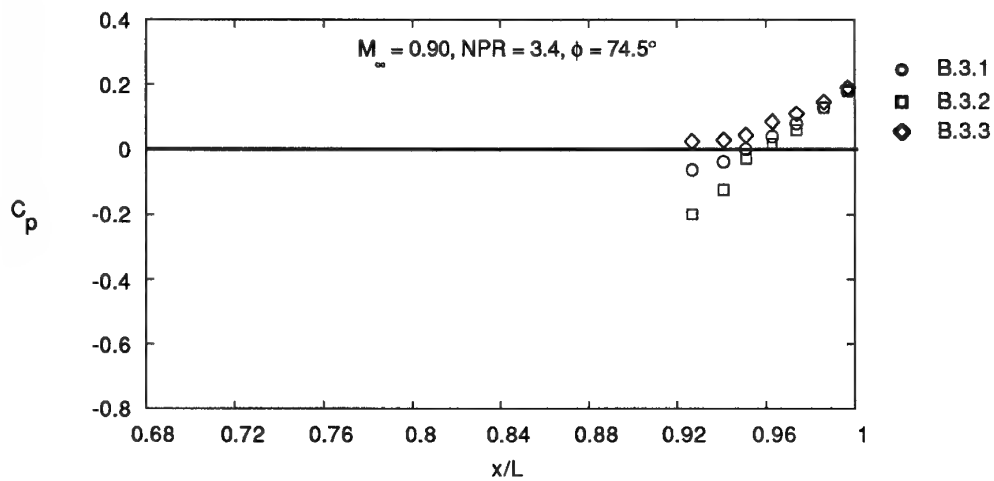


Figure B.3-3 - Static pressure distributions on twin-jet test cases B.3 at  $\phi = 74.5^\circ$ , row 4.

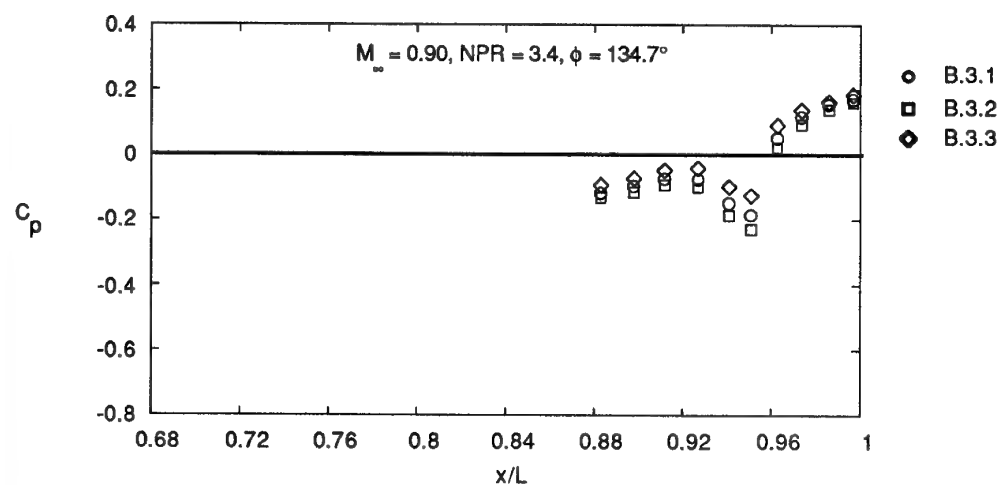


Figure B.3-4 - Static pressure distributions on twin-jet test cases B.3 at  $\phi = 134.7^\circ$ , row 8.



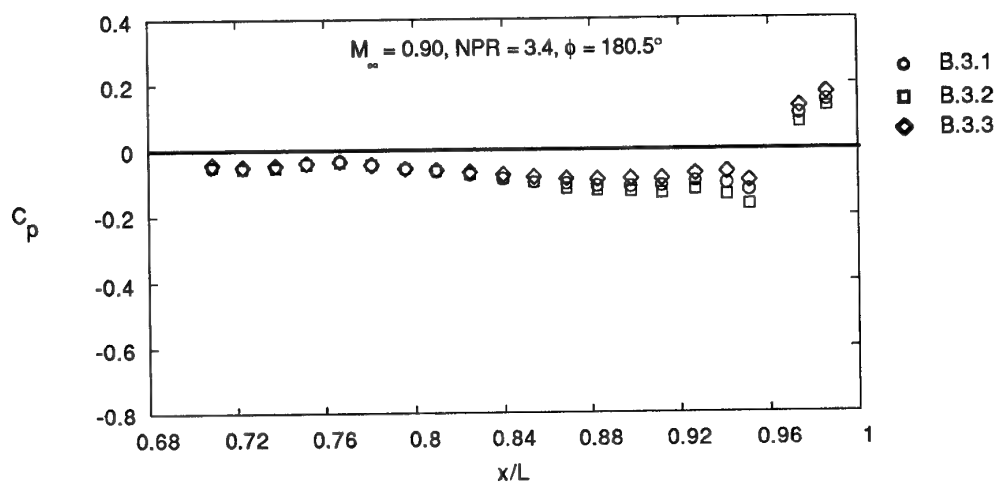


Figure B.3-5 - Static pressure distributions on twin-jet test cases B.3 at  $\phi = 180.5^\circ$ , row 9.

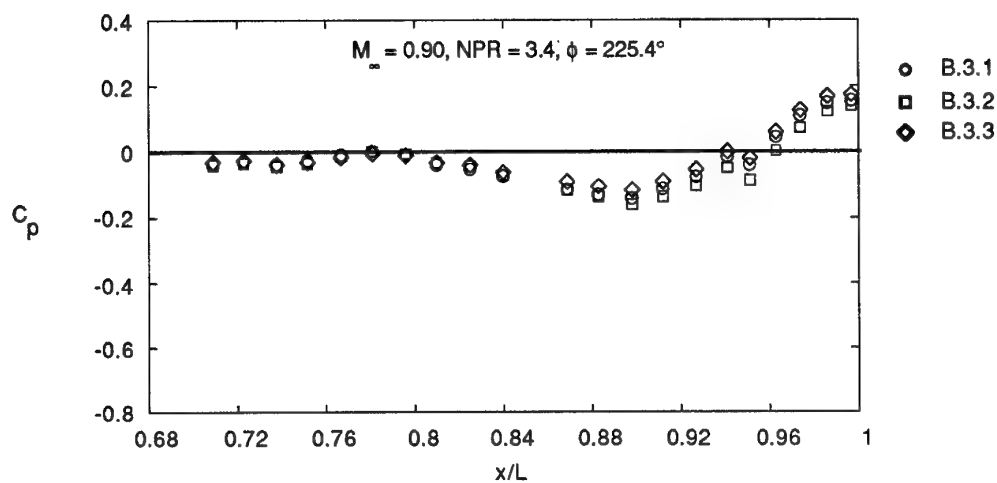


Figure B.3-6 - Static pressure distributions on twin-jet test cases B.3 at  $\phi = 225.4^\circ$ , row 10.

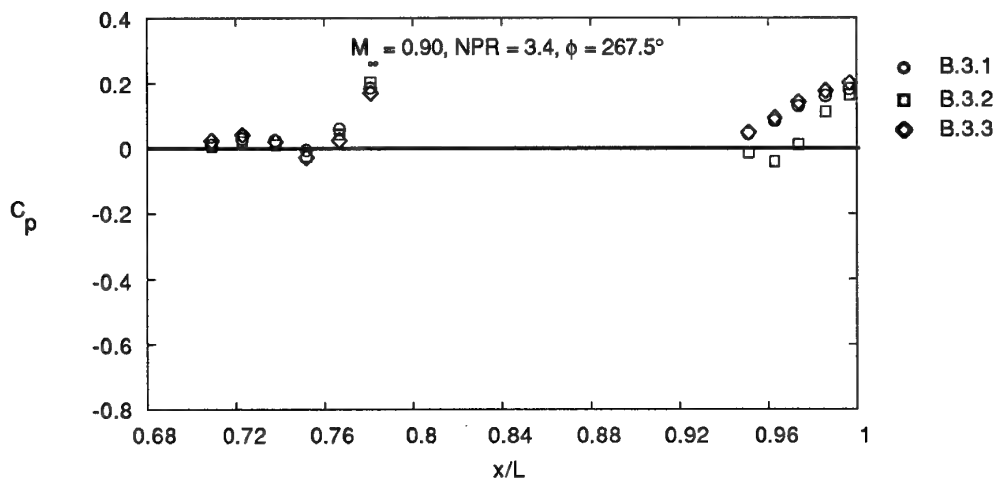


Figure B.3-7 - Static pressure distributions on twin-jet test cases B.3 at  $\phi = 267.5^\circ$ , row 11.

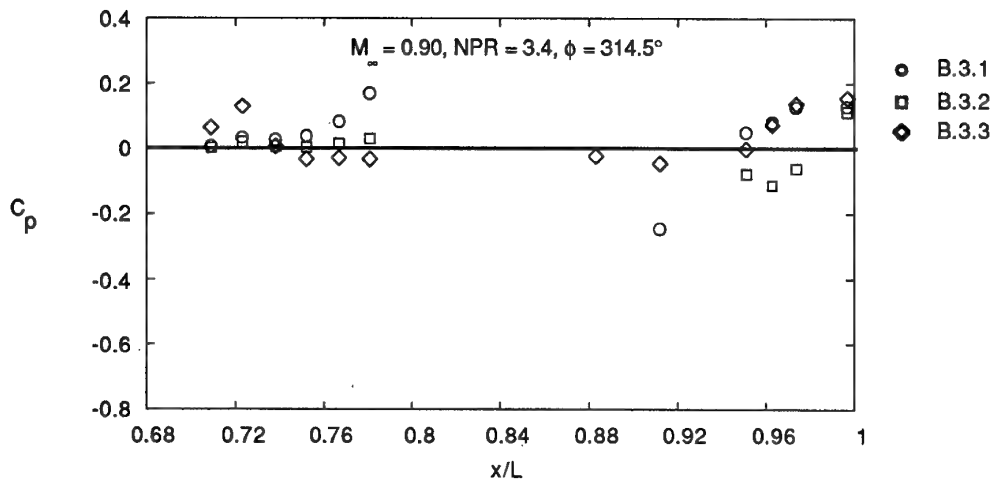


Figure B.3-8 - Static pressure distributions on twin-jet test cases B.3 at  $\phi = 314.5^\circ$ , row 12.

**B.3.1.2 Experimental Pressure Drag Coefficients on Nozzle and Total Drag Coefficients on Afterbody.**  
Reference area =  $A_{wing} = 664.4 \text{ in}^2$

Test Case	Horiz. tail	Vert. tail	Mach	NPR	$C_{DPN}$	$C_{DTT}$
B.3.1	Mid	Mid	0.901	3.407	-0.0020	0.0084
B.3.2	Mid	Aft	0.899	3.400	-0.0008	0.0082
B.3.3	Mid	Fwd.	0.899	3.402	-0.0022	0.0078

Table B.3-2: Experimental drag coefficients for test cases B.3.

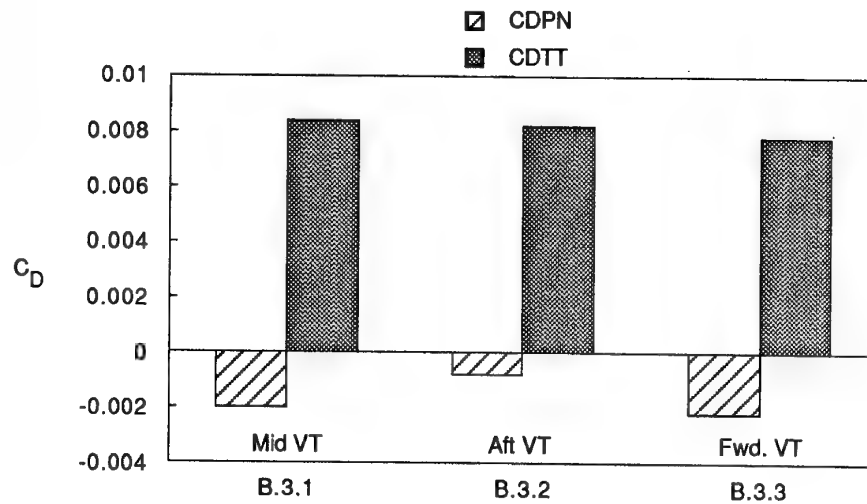


Figure B.3-9 - Experimental drag coefficients for test cases B.3.  $M_\infty = 0.90$ ,  $NPR = 3.4$ .

**B.3.2 Test Case B.3.2 (Mid horizontal tails,  
Aft vertical tails,  $M_\infty = 0.899$ ,  
 $NPR = 3.400$ )**

**B.3.2.1 Surface Pressure Distribution**

See Table B.3-3 and Figures B.3-2 to B.3-8

**B.3.2.2 Experimental Pressure Drag Coefficients on Nozzle and Total Drag Coefficients on Afterbody.**

Reference area =  $A_{wing} = 664.4 \text{ in}^2$

See Table B.3-2 and Figure B.3-9

**B.3.3 Test Case B.3.3 (Mid horizontal tails,  
Forward vertical tails,  $M_\infty = 0.899$ ,  
NPR = 3.402)**

**B.3.3.1 Surface Pressure Distribution**

See Table B.3-4 and Figures B.3-2 to B.3-8

**B.3.3.2 Experimental Pressure Drag Coefficients on Nozzle and Total Drag Coefficients on Afterbody.**

Reference area =  $A_{wing} = 664.4 \text{ in}^2$

See Table B.3-2 and Figure B.3-9

Cp at  $\phi$  of

x/L	0.3°	44.5°	60.3°	74.5°	90.0°	105.1°	119.6°	134.7°	180.5°	225.4°	267.5°	314.5°	Top CL	Bottom CL
.709	-.041								-.050	-.039	.006	.002	-.053	-.056
.723	-.032								-.055	-.034	.023	.021	-.033	-.058
.738	-.023								-.052	-.043	.013	.007		-.054
.752	-.016								-.041	-.034	-.022	.004		-.051
.767	.005								-.035	-.013	.044	.015		-.057
.781	-.009								-.043	.002	.204	.030		-.080
.796	-.006								-.055	-.005				
.810	.019								-.063	-.031				
.825	.027								-.072	-.044				
.840	-.004								-.086	-.069				
.854	-.101								-.098					
.869	-.182								-.117	-.114				-.126
.883	-.244	-.250						-.133	-.122	-.136				-.128
.898	-.321	-.308	-.338				-.117	-.114	-.127	-.159			-.324	
.912	-.419	-.330	-.303				-.085	-.094	-.132	-.136				
.927	-.402	-.295	-.243	-.197			-.083	-.100	-.121	-.103				
.941	-.126	-.195	-.165	-.123		-.109	-.134	-.186	-.138	-.048			-.082	-.098
.951	-.060	-.127	.053	-.027	-.031		-.247	-.228	-.167	-.086	-.012	-.077		
.963	-.002	.051	.093	.018	.036	.039	.038	.025		.004	-.039	-.112		
.974	.032	.088	.126	.060	.087	.088	.080	.094	.081	.073	.013	-.061		
.986		.126	.161	.129	.127	.130	.133	.140	.130	.123	.114			
.997		.162	.112	.179		.165	.162	.162		.141	.165	.113		
Row #	1	2	3	4	5	6	7	8	9	10	11	12	13	14

Table B.3-3 - External static pressure coefficients on twin-jet test case B.3.2

Cp at  $\phi$  of

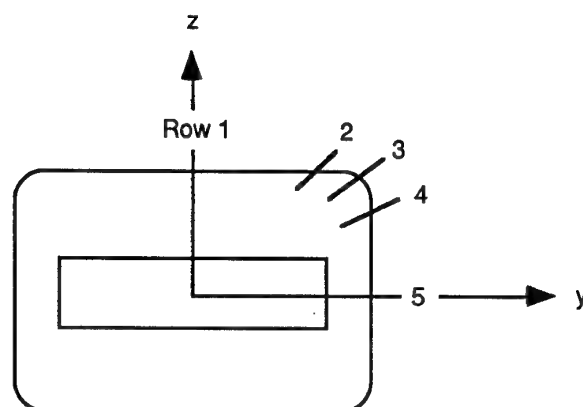
x/L	0.3°	44.5°	60.3°	74.5°	90.0°	105.1°	119.6°	134.7°	180.5°	225.4°	267.5°	314.5°	Top CL	Bottom CL
.709	.032								-.042	-.030	.025	.065	.010	-.048
.723	.062								-.049	-.025	.043	.130	.030	-.051
.738	.046								-.045	-.037	.022	.007		-.048
.752	-.016								-.038	-.030	-.027	-.032		-.045
.767	-.064								-.033	-.015	.027	-.028		-.054
.781	-.164								-.043	-.004	.171	-.031		-.077
.796	-.255								-.056	-.010				
.810	-.318								-.060	-.032				
.825	-.394								-.066	-.040				
.840	-.475								-.074	-.060				
.854	-.544								-.082					
.869	-.110								-.087	-.090				-.099
.883	-.028	-.057						-.094	-.090	-.104		-.023		-.092
.898	-.022	-.021	-.026				-.075	-.072	-.088	-.115			-.029	
.912	-.033	.001	.004				-.033	-.048	-.088	-.090		-.045		
.927	-.038	-.001	.015	.026			-.021	-.041	-.073	-.054				
.941	-.032	-.028	.001	.030			-.049	-.098	-.069	.001			.042	.003
.951	-.080	-.056	.097	.045	.071	-.013	-.119	-.125	-.096	-.018	.049	-.001		
.963	.061	.101	.119	.086	.088	.089	.097	.091		.061	.094	.073		
.974	.139	.135	.151	.110	.112	.112	.120	.138	.131	.126	.142	.137		
.986		.161	.185	.146	.147	.149	.154	.166	.173	.169	.177			
.997		.184	.154	.191		.185		.186		.174	.202	.155		
Row #	1	2	3	4	5	6	7	8	9	10	11	12	13	14

Table B.3.4 - External static pressure coefficients on twin-jet test case B.3.3

# B.4 B.4 Test Cases - Single jet, nonaxisymmetric 2-D C-D Nozzle with No Tails

## B.4.1 Test Case B.4.1 ( $M_\infty = 0.600$ , NPR = 4.00)

### B.4.1.1 External Surface Pressure Coefficient Distribution



View looking upstream from rear

Row	x, in.	y, in.	z, in.	x/L	Test Case B.4.1	Test Case B.4.2
					$M_\infty = 0.600$ NPR = 4.003 $C_p$	$M_\infty = 0.938$ NPR = 4.017 $C_p$
1	55.18	0.00000	3.10000	0.8753	-0.1744	-0.1127
1	55.80	0.00000	3.10000	0.8852	-0.2654	-0.2056
1	57.04	0.00000	3.02898	0.9048	-0.3833	-0.5296
1	57.66	0.00000	2.93953	0.9147	-0.3566	-0.4815
1	58.28	0.00000	2.81304	0.9245	-0.2762	-0.1606
1	58.90	0.00000	2.64815	0.9343	-0.1587	-0.1166
1	59.52	0.00000	2.45358	0.9442	-0.0466	-0.1081
1	60.14	0.00000	2.25736	0.9540	0.0244	-0.1014
1	61.38	0.00000	1.86491	0.9737	0.1143	-0.0719
1	62.62	0.00000	1.47246	0.9933	0.1747	-0.0101
1	BASE			1.0000	0.1653	0.0479
2	55.80	1.70000	3.09933	0.8852	-0.2333	-0.1901
2	58.28	1.58900	2.81304	0.9245	-0.2677	-0.1775
2	59.52	1.51400	2.45358	0.9442	-0.0580	-0.1201
2	61.38	1.40100	1.86491	0.9737	0.0947	-0.0768
3	55.80	3.18763	2.83000	0.8852	-0.1767	-0.1682
3	56.42	3.18233	2.82800	0.8950	-0.2215	-0.2715
3	57.04	3.16545	2.82200	0.9048	-0.2500	-0.3898
3	58.28	3.12765	2.73800	0.9245	-0.2683	-0.4545
3	59.52	3.00800	2.40700	0.9442	-0.2078	-0.1431
3	61.38	2.79131	1.81500	0.9737	0.0129	-0.0535
3	62.62	2.64577	1.42300	0.9933	0.1090	0.0063
3	BASE			1.0000	-0.0583	-0.0296

Table B.4-1 - External static pressure coefficients on single-jet, 2-D C-D nozzle test cases B.4.1 and B.4.2.

4	57.04	3.32897	1.51400	0.9048	-0.2225	-0.4547
4	58.28	3.17851	1.40700	0.9245	-0.1314	-0.4009
4	59.52	3.02780	1.22700	0.9442	-0.0716	-0.1416
4	61.38	2.80175	0.93200	0.9737	0.0267	-0.0072
5	55.18	3.40000	0.00000	0.8753	-0.1271	-0.0952
5	55.80	3.40000	0.00000	0.8852	-0.2104	-0.2005
5	56.42	3.38229	0.00000	0.8950	-0.2798	-0.4026
5	57.04	3.32898	0.00000	0.9048	-0.2256	-0.5292
5	58.28	3.17851	0.00000	0.9245	-0.1120	-0.3812
5	59.52	3.02780	0.00000	0.9442	-0.0640	-0.1498
5	61.38	2.80175	0.00000	0.9737	0.0201	0.0068
5	62.62	2.65104	0.00000	0.9933	0.0383	0.0300
5	BASE			1.0000	-0.0293	0.0023

Table B.4-1 - Concluded

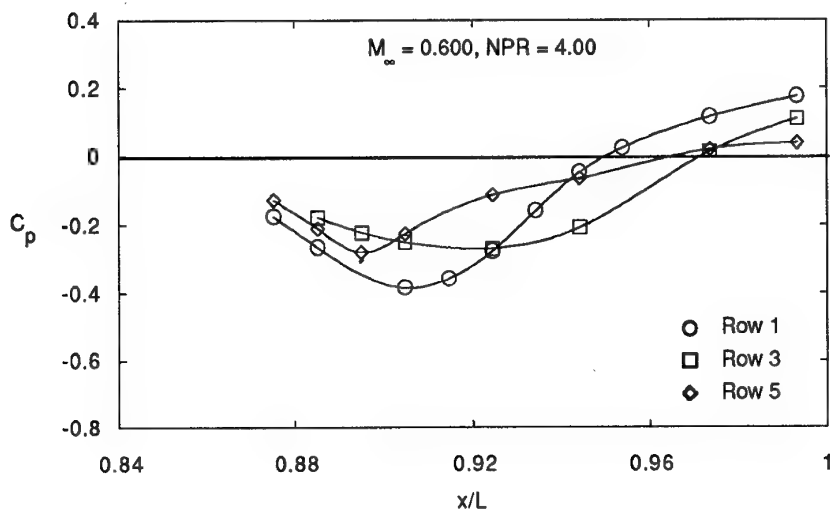
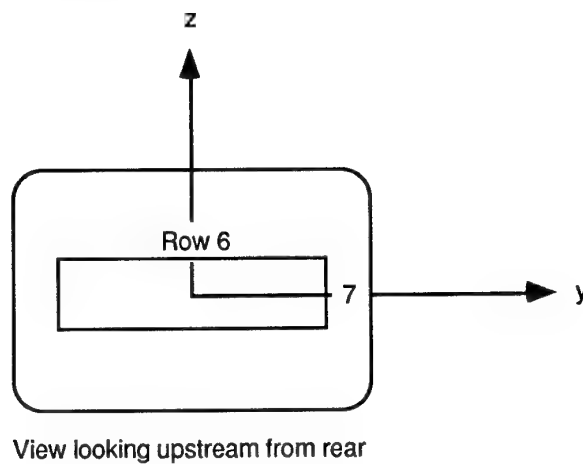


Figure B.4-1- External static pressure coefficient distributions for test case B.4.1.

## B.4.1.2 Internal Surface Pressure Ratio Distribution



Row	x, in.	y, in.	z, in.	x/L	Test Case B.4.1	Test Case B.4.2
					$M_\infty = 0.600$ NPR = 4.003 $p/p_{tj}$	$M_\infty = 0.938$ NPR = 4.017 $p/p_{tj}$
6	55.800	0.00000	1.94400	0.8852	0.959	0.958
6	56.730	0.00000	1.31107	0.8999	0.868	0.868
6	57.223	0.00000	1.04000	0.9077	0.251	0.253
6	58.280	0.00000	1.08683	0.9245	0.413	0.412
6	60.140	0.00000	1.17013	0.9540	0.343	0.344
6	62.620	0.00000	1.28119	0.9933	0.241	0.245
7	57.223	2.47500	0.00000	0.9077	0.575	0.604
7	58.280	2.47500	0.00000	0.9245	0.302	0.308
7	60.140	2.47500	0.00000	0.9540	0.284	0.284
7	62.620	2.47500	0.00000	0.9933	0.240	0.243

*Table B.4-2.- Internal static pressure ratios on single-jet, 2-D C-D nozzle test cases B.4.1 and B.4.2.*

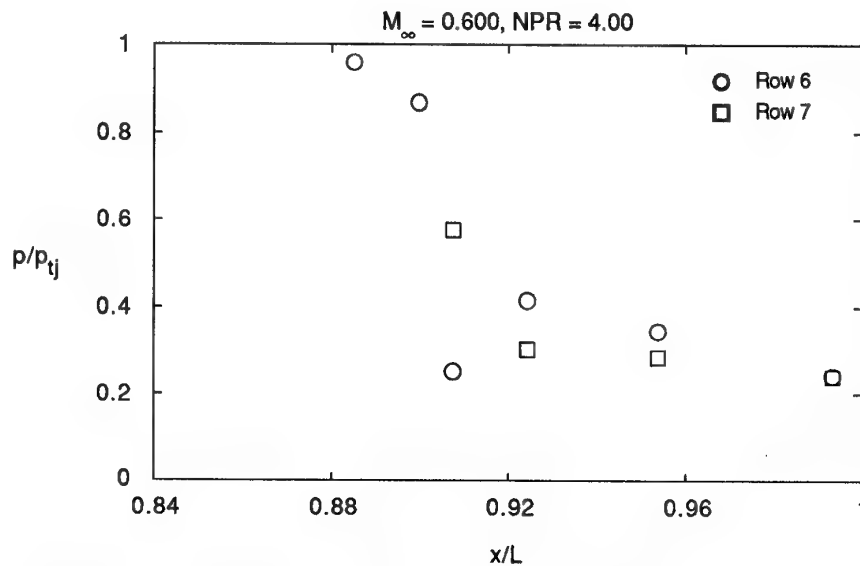


*Figure B.4-2 - Internal static pressure ratio distributions for test case B.4.1.*

#### *B.4.1.3 Pitot Pressure Ratio Distributions in Free-Stream and Jet Flow Field*

See Tables B.4-3, B.4-4 and B.4-5



y, in.	z, in.	$p_{t,p}/p_{t,\infty}$	r, in.	$\phi'$ , deg
--------	--------	------------------------	--------	---------------

-.112	.210	2.749	.102	69.2
-.063	.314	2.750	.216	68.1
-.035	.414	2.760	.319	69.2
.001	.508	2.848	.420	69.2
.031	.587	2.855	.505	69.2
.066	.678	2.861	.602	69.2
.124	.778	2.863	.716	68.1
.143	.881	2.862	.819	69.2
.179	.975	2.851	.920	69.2
.209	1.054	2.749	1.005	69.2
.243	1.145	1.521	1.102	69.2
.310	1.241	.831	1.216	68.1
.321	1.348	.835	1.319	69.2
.356	1.442	.846	1.420	69.2
.386	1.521	.864	1.505	69.2
.421	1.612	.879	1.602	69.2
.497	1.705	.900	1.716	68.1
.498	1.816	.915	1.819	69.2
.534	1.910	.926	1.920	69.2
.564	1.989	.940	2.005	69.2
.599	2.080	.950	2.102	69.2
.684	2.169	.960	2.216	68.1
.676	2.283	.968	2.319	69.2
.712	2.377	.978	2.420	69.2
.742	2.456	.986	2.505	69.2
.776	2.547	.991	2.602	69.2
.871	2.633	.994	2.716	68.1
.854	2.750	.996	2.819	69.2
.889	2.844	.996	2.920	69.2
.917	2.918	.995	2.998	69.2
.954	3.014	.995	3.102	69.2
.990	3.108	.994	3.202	69.2
1.031	3.218	.995	3.319	69.2
1.067	3.312	.994	3.420	69.2
1.095	3.385	.996	3.498	69.2
1.138	3.497	.996	3.619	69.2
1.167	3.575	.996	3.702	69.2
1.205	3.674	.996	3.808	69.2
1.273	3.852	.995	3.998	69.2
1.315	3.965	.995	4.119	69.2
1.345	4.043	.996	4.202	69.2

y, in.	z, in.	$p_{t,p}/p_{t,\infty}$	r, in.	$\phi'$ , deg
--------	--------	------------------------	--------	---------------

1.383	4.142	.995	4.308	69.2
1.450	4.320	.994	4.498	69.2
1.493	4.432	.994	4.619	69.2
1.523	4.510	.994	4.702	69.2
1.560	4.609	.998	4.808	69.2
1.628	4.787	.997	4.998	69.2
1.671	4.899	.996	5.119	69.2
1.700	4.977	.996	5.202	69.2
1.738	5.076	.997	5.308	69.2
1.806	5.254	.996	5.498	69.2
1.848	5.367	.996	5.619	69.2
1.878	5.445	.996	5.702	69.2
1.916	5.544	.996	5.808	69.2
1.983	5.722	.995	5.998	69.2
2.026	5.834	.994	6.119	69.2
2.056	5.912	.995	6.202	69.2
2.093	6.011	.995	6.308	69.2

Table B.4.1-3: Concluded.

y, in.	z, in.	$p_{t,p}/p_{t,\infty}$	r, in.	$\phi'$ , deg
1.262	.575	2.829	1.407	24.3
1.350	.615	2.828	1.505	24.3
1.447	.657	2.829	1.610	24.3
1.522	.693	2.829	1.693	24.3
1.619	.736	2.832	1.799	24.3
1.717	.781	2.831	1.907	24.3
1.806	.821	2.827	2.005	24.3
1.902	.863	2.820	2.110	24.3
1.978	.899	2.816	2.193	24.3
2.074	.942	2.814	2.299	24.3
2.173	.987	2.803	2.407	24.3
2.262	1.027	2.769	2.505	24.3
2.358	1.069	2.724	2.610	24.3
2.433	1.105	2.637	2.693	24.3
2.530	1.148	1.264	2.799	24.3
2.629	1.193	.852	2.907	24.3
2.717	1.233	.863	3.005	24.3
2.814	1.275	.898	3.110	24.3
2.889	1.311	.921	3.193	24.3
2.985	1.355	.948	3.299	24.3
3.084	1.399	.969	3.407	24.3
3.179	1.442	.985	3.512	24.3
3.259	1.473	.992	3.597	24.3
3.362	1.521	.996	3.711	24.3
3.446	1.557	.996	3.802	24.3
3.635	1.648	.998	4.012	24.3
3.715	1.679	.998	4.097	24.3
3.818	1.727	.998	4.211	24.3
3.901	1.763	.998	4.302	24.3
4.091	1.855	.997	4.512	24.3
4.171	1.884	.995	4.597	24.3
4.274	1.932	.998	4.711	24.3
4.357	1.968	.998	4.802	24.3
4.546	2.061	1.000	5.012	24.3
4.627	2.090	1.000	5.097	24.3
4.730	2.138	1.000	5.211	24.3
4.813	2.174	.999	5.302	24.3
5.002	2.267	.998	5.512	24.3
5.083	2.295	.998	5.597	24.3
5.185	2.344	.998	5.711	24.3
5.269	2.379	.998	5.802	24.3
5.457	2.473	.998	6.012	24.3
5.538	2.501	.998	6.097	24.3
5.641	2.549	.998	6.211	24.3
5.725	2.585	.998	6.302	24.3

y, in.	z, in.	$p_{t,p}/p_{t,\infty}$	r, in.	$\phi'$ , deg
-.016	-.003	2.726	.005	24.3
.080	.040	2.727	.110	24.3
.156	.074	2.728	.193	24.3
.252	.118	2.731	.299	24.3
.351	.163	2.736	.407	24.3
.439	.203	2.731	.505	24.3
.535	.246	2.739	.610	24.3
.611	.281	2.752	.693	24.3
.708	.324	2.762	.799	24.3
.806	.369	2.793	.907	24.3
.895	.409	2.841	1.005	24.3
.991	.451	2.839	1.110	24.3
1.067	.487	2.836	1.193	24.3
1.163	.530	2.831	1.299	24.3

**Table B.4.1-3:** Experimental pitot pressure ratio data for test case B.4.1 at  $x = 63.04$  in. and nominal values of  $\phi = 24.3^\circ$  and  $69.2^\circ$ .

y, in.	z, in.	$p_{t,p}/p_{t,\infty}$	r, in.	$\phi'$ , deg	y, in.	z, in.	$p_{t,p}/p_{t,\infty}$	r, in.	$\phi'$ , deg
-.026	-.006	2.642	-.005	24.7	4.737	2.135	.998	5.217	24.2
.082	.043	2.645	.113	24.7	4.832	2.133	.999	5.302	23.8
.168	.083	2.651	.208	24.7	5.082	2.315	.998	5.605	24.4
.266	.128	2.661	.316	24.7	5.193	2.340	.998	5.717	24.2
.337	.161	2.668	.394	24.7	5.289	2.335	.998	5.802	23.8
.428	.203	2.678	.495	24.7	5.537	2.522	.999	6.105	24.4
.536	.252	2.687	.613	24.7	5.649	2.545	.998	6.217	24.2
.622	.292	2.696	.708	24.7	5.747	2.536	.999	6.302	23.8
.720	.337	2.708	.816	24.7					
.791	.370	2.715	.894	24.7					
.883	.412	2.739	.995	24.7					
.990	.461	2.744	1.113	24.7					
1.077	.501	2.751	1.208	24.7					
1.174	.546	2.756	1.316	24.7					
1.245	.579	2.757	1.394	24.7					
1.337	.621	2.708	1.495	24.7					
1.444	.670	2.673	1.613	24.7					
1.531	.710	2.637	1.708	24.7					
1.628	.755	2.562	1.816	24.7					
1.700	.789	2.505	1.894	24.7					
1.791	.830	2.250	1.995	24.7					
1.899	.879	2.097	2.113	24.7					
1.985	.919	1.978	2.208	24.7					
2.082	.964	1.811	2.316	24.7					
2.154	.998	1.713	2.394	24.7					
2.245	1.039	1.382	2.495	24.7					
2.353	1.088	1.260	2.613	24.7					
2.439	1.128	1.184	2.708	24.7					
2.537	1.173	1.097	2.816	24.7					
2.608	1.207	1.063	2.894	24.7					
2.700	1.248	.988	2.995	24.7					
2.807	1.297	.980	3.113	24.7					
2.894	1.337	.979	3.208	24.7					
2.991	1.382	.988	3.316	24.7					
3.062	1.416	.993	3.394	24.7					
3.261	1.487	.999	3.605	24.4					
3.369	1.520	.997	3.717	24.2					
3.459	1.527	.997	3.802	23.8					
3.716	1.694	.998	4.105	24.4					
3.825	1.725	.999	4.217	24.2					
3.917	1.729	.998	4.302	23.8					
4.171	1.901	1.002	4.605	24.4					
4.281	1.930	1.001	4.717	24.2					
4.374	1.931	1.001	4.802	23.8					
4.627	2.108	1.000	5.105	24.4					

**Table B.4.1-4:** Experimental pitot pressure ratio data for test case B.4.1 at  $x = 68.176$  in. and nominal values of  $\phi' = 24.7^\circ$  and  $60.2^\circ$ .

y, in.	z, in.	$p_{t,p}/p_{t,\infty}$	r, in.	$\phi'$ , deg	y, in.	z, in.	$p_{t,p}/p_{t,\infty}$	r, in.	$\phi'$ , deg
					.981	2.013	.989	2.206	60.2
					1.037	2.111	.993	2.318	60.2
					1.078	2.181	.996	2.400	60.2
					1.128	2.268	.997	2.499	60.2
					1.181	2.359	.997	2.605	60.2
					1.230	2.447	.997	2.706	60.2
					1.286	2.545	.997	2.818	60.2
					1.327	2.615	.997	2.900	60.2
					1.377	2.701	.999	2.999	60.2
					1.429	2.793	1.000	3.105	60.2
					1.478	2.881	.999	3.206	60.2
					1.534	2.978	.999	3.318	60.2
					1.576	3.049	.999	3.400	60.2
					1.619	3.124	.997	3.487	60.2
					1.686	3.241	.997	3.621	60.2
					1.724	3.307	.997	3.697	60.2
					1.798	3.404	.997	3.818	59.9
					1.868	3.558	.998	3.987	60.2
					1.935	3.675	.998	4.121	60.2
					1.973	3.740	.998	4.197	60.2
					2.048	3.836	.998	4.318	59.9
					2.117	3.991	1.000	4.487	60.2
					2.184	4.108	1.000	4.621	60.2
					2.221	4.174	1.000	4.697	60.2
					2.298	4.269	1.000	4.818	59.9
					2.366	4.425	.999	4.987	60.2
					2.433	4.542	.998	5.121	60.2
					2.470	4.608	.999	5.197	60.2
					2.549	4.702	.999	5.318	59.9
					2.614	4.859	.997	5.487	60.2
					2.681	4.976	.997	5.621	60.2
					2.719	5.041	.997	5.697	60.2
					2.799	5.135	.997	5.818	59.9
					2.863	5.293	.999	5.987	60.2
					2.930	5.410	.999	6.121	60.2
					2.968	5.475	.999	6.197	60.2
					3.050	5.567	.999	6.318	59.9
-.116	.099	2.633	-.001	60.2					
-.063	.191	2.640	.105	60.2					
-.013	.278	2.652	.206	60.2					
.043	.376	2.668	.318	60.2					
.083	.446	2.679	.400	60.2					
.133	.533	2.717	.499	60.2					
.186	.624	2.733	.605	60.2					
.235	.712	2.722	.706	60.2					
.291	.809	2.610	.818	60.2					
.332	.880	2.517	.900	60.2					
.382	.966	2.035	.999	60.2					
.434	1.058	1.755	1.105	60.2					
.484	1.146	1.531	1.206	60.2					
.540	1.243	1.281	1.318	60.2					
.581	1.314	1.201	1.400	60.2					
.630	1.400	1.021	1.499	60.2					
.683	1.492	.980	1.605	60.2					
.733	1.579	.965	1.706	60.2					
.788	1.677	.963	1.818	60.2					
.830	1.747	.965	1.900	60.2					
.879	1.834	.975	1.999	60.2					
.932	1.926	.983	2.105	60.2					

Table B.4.1-4: Concluded.

y, in.	z, in.	$P_{t,p}/P_{t,\infty}$	r, in.	$\phi'$ , deg	y, in.	z, in.	$P_{t,p}/P_{t,\infty}$	r, in.	$\phi'$ , deg
.007	-.102	2.681	.007	-.5	4.623	-.150	.996	4.623	-.6
.108	-.103	2.694	.108	-.6	4.706	-.151	.997	4.706	-.6
.201	-.104	2.700	.201	-.6	4.813	-.152	.998	4.813	-.6
.305	-.106	2.707	.305	-.6	5.018	-.154	.999	5.018	-.6
.410	-.107	2.713	.410	-.6	5.123	-.155	.998	5.123	-.6
.507	-.106	2.699	.507	-.5	5.206	-.156	.998	5.206	-.6
.608	-.109	2.715	.608	-.6	5.313	-.157	.998	5.313	-.6
.701	-.110	2.724	.701	-.6	5.518	-.159	.998	5.518	-.6
.805	-.111	2.736	.805	-.6	5.623	-.160	.998	5.623	-.6
.910	-.112	2.747	.910	-.6	5.706	-.161	.997	5.706	-.6
1.007	-.111	2.747	1.007	-.5	5.813	-.162	.998	5.813	-.6
1.108	-.114	2.768	1.108	-.6	6.017	-.164	.999	6.018	-.6
1.201	-.115	2.784	1.201	-.6	6.123	-.165	.999	6.123	-.6
1.305	-.116	2.799	1.305	-.6	6.206	-.166	.998	6.206	-.6
1.410	-.117	2.813	1.410	-.6					
1.507	-.115	2.807	1.507	-.5	.008	-.068	2.764	.011	7.6
1.608	-.119	2.790	1.608	-.6	.113	-.054	2.765	.116	7.6
1.701	-.120	2.688	1.701	-.6	.217	-.040	2.766	.221	7.7
1.805	-.121	2.508	1.805	-.6	.300	-.029	2.762	.305	7.7
1.910	-.122	2.261	1.910	-.6	.404	-.015	2.768	.410	7.7
2.007	-.119	1.908	2.007	-.5	.504	-.002	2.781	.511	7.6
2.108	-.124	1.699	2.108	-.6	.609	.012	2.784	.616	7.6
2.201	-.125	1.496	2.201	-.6	.712	.027	2.789	.721	7.7
2.305	-.126	1.354	2.305	-.6	.796	.038	2.788	.805	7.7
2.410	-.127	1.231	2.410	-.6	.900	.052	2.798	.910	7.7
2.507	-.124	1.111	2.507	-.5	1.000	.064	2.821	1.011	7.6
2.608	-.129	1.054	2.608	-.6	1.104	.078	2.828	1.116	7.6
2.701	-.130	1.013	2.701	-.6	1.208	.094	2.836	1.221	7.7
2.805	-.131	.997	2.805	-.6	1.291	.105	2.838	1.305	7.7
2.910	-.132	.992	2.910	-.6	1.395	.119	2.849	1.410	7.7
3.007	-.128	.995	3.007	-.5	1.495	.131	2.867	1.511	7.6
3.108	-.134	.996	3.108	-.6	1.600	.145	2.854	1.616	7.6
3.201	-.135	.998	3.201	-.6	1.703	.160	2.795	1.721	7.7
3.305	-.136	.999	3.305	-.6	1.787	.172	2.707	1.805	7.7
3.410	-.137	.999	3.410	-.6	1.891	.186	2.516	1.910	7.7
3.518	-.139	.999	3.518	-.6	1.991	.197	2.181	2.011	7.6
3.623	-.140	.998	3.623	-.6	2.096	.211	1.916	2.116	7.6
3.706	-.141	.998	3.706	-.6	2.199	.227	1.720	2.221	7.7
3.813	-.142	.998	3.813	-.6	2.282	.238	1.579	2.305	7.7
4.018	-.144	.996	4.018	-.6	2.386	.252	1.416	2.410	7.7
4.123	-.145	.996	4.123	-.6	2.486	.263	1.266	2.511	7.6
4.206	-.146	.997	4.206	-.6	2.591	.277	1.178	2.616	7.6
4.313	-.147	.995	4.313	-.6	2.694	.294	1.147	2.721	7.7
4.518	-.149	.997	4.518	-.6	2.778	.305	1.114	2.805	7.7
					2.882	.319	1.080	2.910	7.7
					2.970	.346	1.052	3.001	7.9

**Table B.4.1-5:** Experimental pitot pressure ratio data for test case B.4.1 at  $x = 73.275$  in. and nominal values of  $\phi' = -0.6^\circ, 7.8^\circ, 15.9^\circ, 25.8^\circ, 28.4^\circ, 30.0^\circ, 38.4^\circ, 45.8^\circ, 61.0^\circ, 76.1^\circ$ , and  $90.6^\circ$ .

y, in.	z, in.	$p_{t,p}/p_{t,\infty}$	r, in.	$\phi'$ , deg	y, in.	z, in.	$p_{t,p}/p_{t,\infty}$	r, in.	$\phi'$ , deg
3.069	.365	1.035	3.102	8.0	1.544	.406	2.822	1.615	15.9
3.185	.378	1.019	3.218	8.0	1.626	.429	2.817	1.700	15.9
3.273	.372	1.013	3.305	7.7	1.742	.463	2.779	1.821	15.9
3.378	.386	1.004	3.410	7.7	1.828	.487	2.719	1.910	15.9
3.465	.415	1.000	3.501	7.9	1.925	.515	2.559	2.011	15.9
3.564	.435	.999	3.602	8.0	2.025	.544	2.400	2.115	15.9
3.680	.447	.998	3.718	8.0	2.107	.565	2.225	2.200	15.9
3.772	.476	.998	3.814	8.2	2.223	.600	2.026	2.321	15.9
3.960	.484	.995	4.001	7.9	2.309	.625	1.883	2.410	15.9
4.060	.504	.995	4.102	8.0	2.406	.652	1.719	2.511	15.9
4.175	.516	.996	4.218	8.0	2.506	.681	1.602	2.615	15.9
4.267	.547	.996	4.314	8.2	2.588	.702	1.499	2.700	15.9
4.456	.553	.995	4.501	7.9	2.704	.737	1.403	2.821	15.9
4.555	.574	.995	4.602	8.0	2.789	.762	1.339	2.910	15.9
4.671	.586	.995	4.718	8.0	2.887	.790	1.266	3.011	15.9
4.762	.618	.996	4.814	8.2	2.987	.818	1.208	3.115	15.9
4.951	.622	.998	5.001	7.9	3.069	.839	1.156	3.200	15.9
5.050	.644	.998	5.102	8.0	3.184	.875	1.102	3.321	15.9
5.166	.655	.998	5.218	8.0	3.270	.899	1.067	3.410	15.9
5.257	.689	.998	5.314	8.2	3.374	.929	1.045	3.518	15.9
5.446	.691	.998	5.501	7.9	3.476	.958	1.019	3.624	15.9
5.545	.714	.998	5.602	8.0	3.564	.983	1.007	3.716	15.9
5.661	.724	.998	5.718	8.0	3.657	1.010	1.000	3.812	15.9
5.752	.761	.998	5.814	8.2	3.855	1.066	.996	4.018	15.9
5.941	.759	.998	6.001	7.9	3.957	1.095	.996	4.124	15.9
6.040	.784	.998	6.102	8.0	4.045	1.120	.996	4.216	15.9
6.156	.794	.998	6.218	8.0	4.138	1.147	.996	4.312	15.9
6.247	.832	.998	6.314	8.2	4.335	1.203	.997	4.518	15.9
					4.438	1.232	.998	4.624	15.9
.002	-.034	2.768	.011	15.9	4.526	1.258	.998	4.716	15.9
.102	-.005	2.775	.115	15.9	4.619	1.284	.997	4.812	15.9
.183	.018	2.781	.200	15.9	4.816	1.340	.999	5.018	15.9
.300	.051	2.786	.321	15.9	4.919	1.370	.998	5.124	15.9
.386	.076	2.791	.410	15.9	5.006	1.395	.999	5.216	15.9
.483	.103	2.787	.511	15.9	5.099	1.421	.999	5.312	15.9
.583	.132	2.796	.615	15.9	5.297	1.478	.998	5.518	15.9
.664	.155	2.802	.700	15.9	5.399	1.507	.998	5.624	15.9
.780	.188	2.809	.821	15.9	5.487	1.532	.999	5.716	15.9
.866	.213	2.815	.910	15.9	5.580	1.559	.998	5.812	15.9
.963	.241	2.814	1.011	15.9	5.778	1.615	1.000	6.018	15.9
1.063	.269	2.821	1.115	15.9	5.880	1.644	.998	6.124	15.9
1.145	.292	2.828	1.200	15.9	5.968	1.669	.999	6.216	15.9
1.261	.326	2.831	1.321	15.9	6.061	1.696	.999	6.312	15.9
1.347	.350	2.835	1.410	15.9					
1.444	.378	2.821	1.511	15.9	-.013	.003	2.695	.011	25.4

Table B.4.1-5: Continued.

y, in.	z, in.	$p_{t,p}/p_{t,\infty}$	r, in.	$\phi'$ , deg	y, in.	z, in.	$p_{t,p}/p_{t,\infty}$	r, in.	$\phi'$ , deg
.078	.046	2.694	.110	25.4	4.507	2.160	.998	5.018	25.5
.177	.093	2.701	.221	25.4	4.576	2.210	.998	5.102	25.7
.255	.130	2.706	.307	25.4	4.640	2.326	.999	5.211	26.5
.349	.175	2.713	.411	25.4	4.742	2.349	.999	5.312	26.2
.439	.217	2.723	.511	25.4	4.958	2.375	.998	5.518	25.5
.529	.260	2.723	.610	25.4	5.026	2.426	.998	5.602	25.7
.629	.307	2.721	.721	25.4	5.088	2.549	.997	5.711	26.5
.707	.344	2.717	.807	25.4	5.190	2.570	.998	5.812	26.2
.801	.389	2.715	.911	25.4	5.410	2.590	.998	6.018	25.5
.891	.432	2.675	1.011	25.4	5.477	2.643	1.000	6.102	25.7
.981	.474	2.651	1.110	25.4	5.535	2.772	1.000	6.211	26.5
1.081	.522	2.603	1.221	25.4	5.639	2.791	1.000	6.312	26.2
1.159	.559	2.564	1.307	25.4					
1.252	.603	2.530	1.411	25.4	-.018	.016	2.692	.011	28.7
1.343	.646	2.395	1.511	25.4	.075	.063	2.701	.116	28.1
1.433	.689	2.327	1.610	25.4	.167	.114	2.705	.221	28.3
1.533	.736	2.229	1.721	25.4	.335	.202	2.720	.411	28.1
1.610	.773	2.146	1.807	25.4	.420	.256	2.720	.511	28.7
1.704	.817	2.072	1.911	25.4	.516	.299	2.723	.616	28.1
1.794	.860	1.951	2.011	25.4	.607	.351	2.717	.721	28.3
1.885	.903	1.859	2.110	25.4	.776	.437	2.699	.911	28.1
1.984	.950	1.738	2.221	25.4	.859	.496	2.629	1.011	28.7
2.062	.987	1.632	2.307	25.4	.957	.534	2.593	1.116	28.1
2.156	1.032	1.533	2.411	25.4	1.048	.588	2.529	1.221	28.3
2.246	1.074	1.368	2.511	25.4	1.217	.673	2.414	1.411	28.1
2.336	1.117	1.297	2.610	25.4	1.297	.736	2.234	1.511	28.7
2.436	1.164	1.218	2.721	25.4	1.398	.770	2.164	1.616	28.1
2.514	1.201	1.163	2.807	25.4	1.488	.824	2.054	1.721	28.3
2.608	1.246	1.119	2.911	25.4	1.658	.908	1.884	1.911	28.1
2.698	1.289	1.062	3.011	25.4	1.736	.976	1.746	2.011	28.7
2.788	1.331	1.046	3.110	25.4	1.839	1.006	1.670	2.116	28.1
2.888	1.379	1.030	3.221	25.4	1.928	1.061	1.560	2.221	28.3
2.966	1.416	1.024	3.307	25.4	2.099	1.144	1.393	2.411	28.1
3.060	1.460	1.012	3.411	25.4	2.175	1.216	1.252	2.511	28.7
3.224	1.560	1.011	3.602	25.7	2.280	1.241	1.189	2.616	28.1
3.298	1.657	1.004	3.711	26.5	2.368	1.298	1.122	2.721	28.3
3.396	1.686	1.000	3.812	26.2	2.540	1.379	1.054	2.911	28.1
3.605	1.729	.995	4.018	25.5	2.613	1.456	1.014	3.011	28.7
3.674	1.776	.996	4.102	25.7	2.721	1.477	1.006	3.116	28.1
3.745	1.880	.996	4.211	26.5	2.809	1.535	1.000	3.221	28.3
3.845	1.907	.996	4.312	26.2	2.982	1.615	1.000	3.411	28.1
4.056	1.944	.997	4.518	25.5	3.161	1.729	1.000	3.622	28.3
4.125	1.993	.997	4.602	25.7	3.233	1.774	.999	3.708	28.4
4.193	2.103	.997	4.711	26.5	3.322	1.840	.998	3.817	28.6
4.293	2.128	.996	4.812	26.2	3.502	1.929	.996	4.018	28.5
					3.601	1.966	.995	4.122	28.3

Table B.4.1-5: Continued.

y, in.	z, in.	$p_{t,p}/p_{t,\infty}$	r, in.	$\phi'$ , deg	y, in.	z, in.	$p_{t,p}/p_{t,\infty}$	r, in.	$\phi'$ , deg
3.673	2.012	.995	4.208	28.4	2.195	1.373	1.123	2.608	31.3
3.761	2.079	.996	4.317	28.6	2.274	1.421	1.082	2.699	31.3
3.941	2.167	.996	4.518	28.5	2.364	1.472	1.046	2.803	31.2
4.041	2.203	.996	4.622	28.3	2.470	1.503	1.019	2.910	30.7
4.113	2.250	.996	4.708	28.4	2.537	1.581	.994	3.007	31.3
4.200	2.319	.996	4.817	28.6	2.623	1.633	.992	3.108	31.3
4.381	2.406	.998	5.018	28.5	2.701	1.680	.990	3.199	31.3
4.481	2.441	.999	5.122	28.3	2.791	1.731	.993	3.303	31.2
4.553	2.488	.998	5.208	28.4	2.900	1.759	.997	3.410	30.7
4.639	2.559	.999	5.317	28.6	3.013	1.779	.999	3.518	30.1
4.820	2.645	.998	5.518	28.5	3.117	1.839	.997	3.638	30.1
4.921	2.678	.999	5.622	28.3	3.176	1.874	.997	3.707	30.1
4.992	2.726	.998	5.708	28.4	3.272	1.933	.997	3.819	30.1
5.078	2.798	.998	5.817	28.6	3.445	2.030	.996	4.018	30.1
5.259	2.884	.999	6.018	28.5	3.549	2.090	.996	4.138	30.1
5.361	2.916	.999	6.122	28.3	3.609	2.125	.995	4.207	30.1
5.432	2.963	.999	6.208	28.4	3.705	2.184	.996	4.319	30.1
5.517	3.038	.999	6.317	28.6	3.878	2.281	.996	4.518	30.1
					3.982	2.341	.996	4.638	30.1
-.027	.023	2.659	.007	31.3	4.042	2.375	.996	4.707	30.1
.059	.075	2.664	.108	31.3	4.137	2.435	.997	4.819	30.1
.137	.123	2.673	.199	31.3	4.310	2.531	.998	5.018	30.1
.226	.176	2.683	.303	31.2	4.415	2.592	.998	5.138	30.1
.320	.227	2.690	.410	30.7	4.474	2.626	.998	5.207	30.1
.400	.283	2.688	.507	31.3	4.570	2.686	.999	5.319	30.1
.486	.335	2.686	.608	31.3	4.743	2.782	.998	5.518	30.1
.564	.382	2.684	.699	31.3	4.847	2.842	.997	5.638	30.1
.653	.435	2.675	.803	31.2	4.907	2.877	.999	5.707	30.1
.750	.482	2.660	.910	30.7	5.002	2.937	.998	5.819	30.1
.827	.542	2.566	1.007	31.3	5.176	3.033	.999	6.018	30.1
.913	.594	2.508	1.108	31.3	5.280	3.093	.999	6.138	30.1
.991	.642	2.454	1.199	31.3	5.339	3.128	.999	6.207	30.1
1.081	.695	2.387	1.303	31.2	5.435	3.188	1.000	6.319	30.1
1.180	.737	2.316	1.410	30.7					
1.255	.802	2.101	1.507	31.3	-.043	.048	2.657	.009	38.3
1.341	.854	2.003	1.608	31.3	.030	.106	2.666	.101	38.4
1.419	.901	1.922	1.699	31.3	.107	.167	2.675	.200	38.4
1.509	.954	1.837	1.803	31.2	.189	.232	2.684	.305	38.4
1.610	.993	1.757	1.910	30.7	.276	.300	2.690	.415	38.3
1.682	1.061	1.609	2.007	31.3	.349	.358	2.680	.509	38.3
1.768	1.114	1.524	2.108	31.3	.422	.416	2.673	.601	38.4
1.846	1.161	1.457	2.199	31.3	.499	.477	2.658	.700	38.4
1.936	1.213	1.385	2.303	31.2	.582	.542	2.623	.805	38.4
2.040	1.248	1.312	2.410	30.7	.669	.610	2.571	.915	38.3
2.110	1.321	1.178	2.507	31.3	.742	.668	2.431	1.009	38.3

Table B.4.1-5: Continued.



y, in.	z, in.	$p_{t,p}/p_{t,\infty}$	r, in.	$\phi', \text{deg}$	y, in.	z, in.	$p_{t,p}/p_{t,\infty}$	r, in.	$\phi', \text{deg}$
.814	.726	2.343	1.101	38.4	4.735	3.829	.999	6.102	38.4
.891	.787	2.248	1.200	38.4	4.825	3.900	.999	6.216	38.4
.974	.852	2.117	1.305	38.4	4.902	3.956	1.000	6.312	38.3
1.061	.920	1.996	1.415	38.3					
1.134	.978	1.791	1.509	38.3	-.064	.075	2.691	.012	46.5
1.206	1.036	1.690	1.601	38.4	.010	.149	2.700	.116	46.0
1.283	1.097	1.603	1.700	38.4	.082	.226	2.707	.221	46.2
1.366	1.163	1.498	1.805	38.4	.140	.277	2.711	.298	45.5
1.454	1.230	1.414	1.915	38.3	.220	.357	2.714	.411	45.4
1.526	1.288	1.316	2.009	38.3	.281	.438	2.700	.512	46.5
1.598	1.347	1.258	2.101	38.4	.358	.508	2.684	.616	46.0
1.675	1.408	1.203	2.200	38.4	.428	.587	2.643	.721	46.2
1.758	1.473	1.144	2.305	38.4	.490	.634	2.601	.798	45.5
1.846	1.539	1.097	2.415	38.3	.571	.713	2.518	.911	45.4
1.919	1.598	1.039	2.509	38.3	.625	.801	2.299	1.012	46.5
1.990	1.657	1.017	2.601	38.4	.705	.868	2.194	1.116	46.0
2.068	1.718	1.002	2.700	38.4	.773	.948	2.053	1.221	46.2
2.150	1.783	.990	2.805	38.4	.841	.991	1.948	1.298	45.5
2.238	1.849	.988	2.915	38.3	.922	1.069	1.799	1.411	45.4
2.318	1.914	.984	3.018	38.3	.969	1.164	1.564	1.512	46.5
2.383	1.968	.986	3.102	38.4	1.052	1.227	1.476	1.616	46.0
2.472	2.038	.987	3.216	38.4	1.119	1.309	1.378	1.721	46.2
2.549	2.096	.991	3.312	38.3	1.191	1.347	1.312	1.798	45.5
2.631	2.159	.998	3.415	38.3	1.273	1.426	1.231	1.911	45.4
2.711	2.224	.996	3.518	38.3	1.313	1.526	1.139	2.012	46.5
2.775	2.278	.998	3.602	38.4	1.400	1.587	1.101	2.116	46.0
2.864	2.348	.997	3.716	38.4	1.465	1.670	1.063	2.221	46.2
2.941	2.406	.998	3.812	38.3	1.541	1.704	1.041	2.298	45.5
3.103	2.534	.995	4.018	38.3	1.624	1.782	1.018	2.411	45.4
3.167	2.588	.996	4.102	38.4	1.657	1.889	1.000	2.512	46.5
3.256	2.659	.997	4.216	38.4	1.747	1.947	.998	2.616	46.0
3.333	2.716	.996	4.312	38.3	1.811	2.031	.996	2.721	46.2
3.495	2.844	.996	4.518	38.3	1.892	2.061	.995	2.798	45.5
3.559	2.898	.997	4.602	38.4	1.974	2.138	.996	2.911	45.4
3.648	2.969	.997	4.716	38.4	2.058	2.223	.995	3.031	45.4
3.726	3.026	.997	4.812	38.3	2.123	2.289	.996	3.123	45.4
3.887	3.154	.999	5.018	38.3	2.183	2.350	.996	3.208	45.4
3.951	3.209	.998	5.102	38.4	2.254	2.424	.998	3.312	45.5
4.040	3.279	.998	5.216	38.4	2.325	2.494	.999	3.411	45.4
4.118	3.336	.999	5.312	38.3	2.409	2.579	.997	3.531	45.4
4.280	3.464	.999	5.518	38.3	2.474	2.645	.996	3.623	45.4
4.343	3.519	.998	5.602	38.4	2.534	2.706	.998	3.708	45.4
4.433	3.589	.997	5.716	38.4	2.605	2.780	.998	3.812	45.5
4.510	3.646	.998	5.812	38.3	2.760	2.936	.995	4.031	45.4
4.672	3.774	.999	6.018	38.3	2.825	3.001	.995	4.123	45.4

Table B.4.1-5: Continued.

y, in.	z, in.	$p_{t,p}/p_{t,\infty}$	r, in.	$\phi'$ , deg	y, in.	z, in.	$p_{t,p}/p_{t,\infty}$	r, in.	$\phi'$ , deg
2.885	3.062	.995	4.208	45.4	1.137	2.395	.998	2.615	61.3
2.956	3.137	.996	4.312	45.5	1.209	2.472	.998	2.718	60.8
3.111	3.292	.995	4.531	45.4	1.251	2.557	.999	2.812	60.9
3.175	3.357	.996	4.623	45.4	1.246	2.671	.999	2.910	62.0
3.235	3.418	.997	4.708	45.4	1.356	2.734	.997	3.018	60.8
3.307	3.493	.998	4.812	45.5	1.407	2.826	.997	3.123	60.8
3.462	3.648	.998	5.031	45.4	1.451	2.901	.998	3.210	60.7
3.526	3.714	.997	5.123	45.4	1.500	2.985	.997	3.306	60.7
3.586	3.775	.999	5.208	45.4	1.481	3.113	.999	3.410	62.0
3.657	3.849	.997	5.312	45.5	1.600	3.171	.999	3.518	60.8
3.813	4.004	.998	5.531	45.4	1.651	3.263	.998	3.623	60.8
3.877	4.070	.997	5.623	45.4	1.696	3.337	.998	3.710	60.7
3.937	4.131	.999	5.708	45.4	1.744	3.421	.998	3.806	60.7
4.008	4.206	.998	5.812	45.5	1.844	3.607	.995	4.018	60.8
4.163	4.361	.999	6.031	45.4	1.895	3.699	.995	4.123	60.8
4.228	4.426	.999	6.123	45.4	1.940	3.773	.995	4.210	60.7
4.288	4.487	.999	6.208	45.4	1.989	3.857	.995	4.306	60.7
4.359	4.562	.998	6.312	45.5	2.088	4.044	.996	4.518	60.8
					2.139	4.135	.996	4.623	60.8
-.114	.112	2.686	.012	61.4	2.184	4.209	.998	4.710	60.7
-.064	.203	2.702	.115	61.3	2.233	4.293	.995	4.806	60.7
-.012	.291	2.710	.218	60.8	2.332	4.480	.999	5.018	60.8
.034	.373	2.718	.312	60.9	2.383	4.572	.999	5.123	60.8
.071	.465	2.714	.410	62.0	2.429	4.646	.997	5.210	60.7
.125	.551	2.669	.512	61.4	2.478	4.729	.998	5.306	60.7
.176	.641	2.629	.615	61.3	2.576	4.916	.999	5.518	60.8
.233	.727	2.558	.718	60.8	2.628	5.008	.999	5.623	60.8
.277	.810	2.451	.812	60.9	2.673	5.082	.998	5.710	60.7
.306	.906	2.326	.910	62.0	2.722	5.165	.998	5.806	60.7
.364	.990	2.055	1.012	61.4	2.820	5.353	.999	6.018	60.8
.416	1.080	1.917	1.115	61.3	2.872	5.444	.999	6.123	60.8
.477	1.163	1.773	1.218	60.8	2.918	5.518	.997	6.210	60.7
.520	1.247	1.626	1.312	60.9	2.967	5.601	.998	6.306	60.7
.541	1.348	1.501	1.410	62.0					
.604	1.429	1.307	1.512	61.4	-.172	.134	2.693	.011	76.2
.656	1.518	1.227	1.615	61.3	-.150	.222	2.704	.102	76.1
.721	1.600	1.158	1.718	60.8	-.124	.327	2.712	.210	76.1
.764	1.683	1.096	1.812	60.9	-.102	.419	2.716	.305	76.1
.776	1.789	1.052	1.910	62.0	-.076	.521	2.704	.410	76.1
.843	1.868	1.013	2.012	61.4	-.053	.619	2.652	.511	76.2
.896	1.957	1.003	2.115	61.3	-.030	.708	2.589	.602	76.1
.965	2.036	.998	2.218	60.8	-.004	.813	2.478	.710	76.1
1.007	2.120	.997	2.312	60.9	.018	.905	2.342	.805	76.1
1.011	2.230	.999	2.410	62.0	.044	1.007	2.164	.910	76.1
1.082	2.307	.998	2.512	61.4	.067	1.104	1.897	1.011	76.2

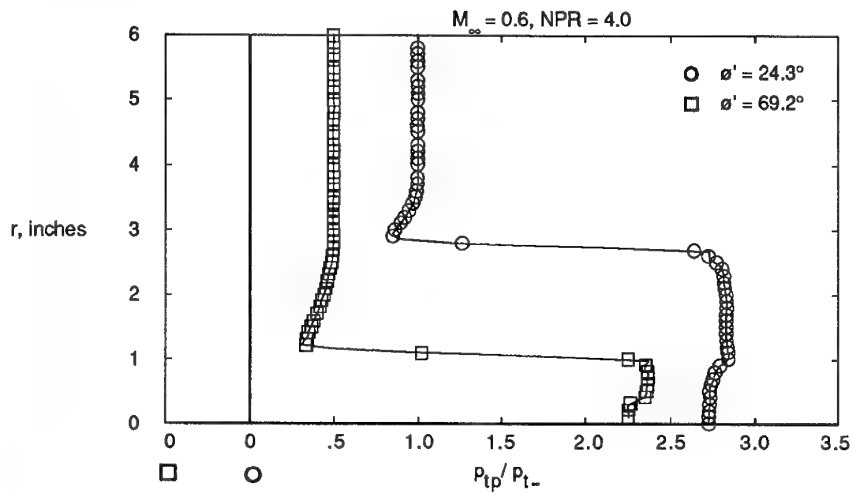
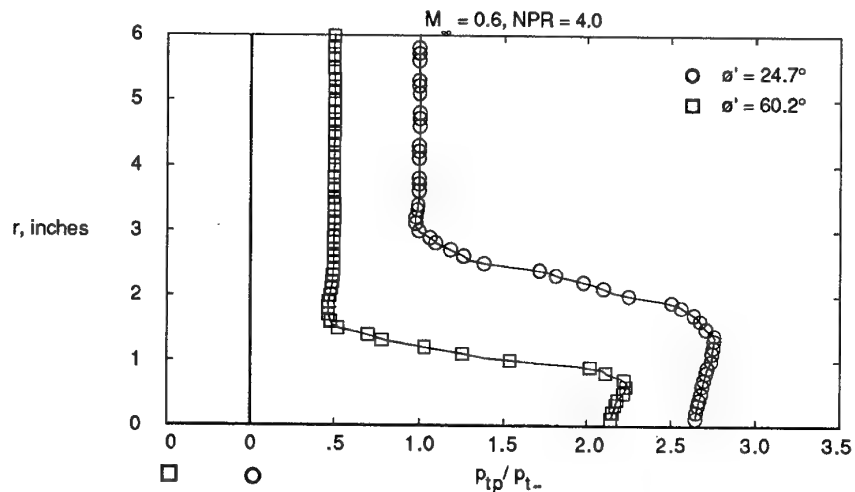
Table B.4.1-5: Continued.

y, in.	z, in.	$p_{t,p}/p_{t,\infty}$	r, in.	$\phi'$ , deg	y, in.	z, in.	$p_{t,p}/p_{t,\infty}$	r, in.	$\phi'$ , deg
.090	1.193	1.762	1.102	76.1	1.295	6.072	.999	6.128	76.1
.116	1.298	1.612	1.210	76.1	1.317	6.159	1.000	6.217	76.1
.138	1.390	1.481	1.305	76.1	1.333	6.234	1.000	6.294	76.1
.164	1.492	1.349	1.410	76.1					
.187	1.590	1.196	1.511	76.2	-.231	.142	2.695	.012	90.3
.210	1.678	1.134	1.602	76.1	-.232	.244	2.706	.114	90.3
.236	1.784	1.077	1.710	76.1	-.241	.330	2.717	.200	91.5
.258	1.875	1.039	1.805	76.1	-.243	.426	2.719	.296	91.5
.283	1.978	1.009	1.910	76.1	-.233	.539	2.706	.409	90.3
.306	2.075	.999	2.011	76.2	-.234	.642	2.641	.512	90.3
.329	2.164	.997	2.102	76.1	-.234	.744	2.565	.614	90.3
.356	2.269	.998	2.210	76.1	-.254	.829	2.459	.700	91.5
.378	2.361	.999	2.305	76.1	-.256	.925	2.302	.796	91.5
.403	2.463	.998	2.410	76.1	-.236	1.039	2.122	.909	90.3
.426	2.561	.999	2.511	76.2	-.236	1.142	1.846	1.012	90.3
.449	2.649	.999	2.602	76.1	-.237	1.244	1.700	1.114	90.3
.475	2.754	.998	2.710	76.1	-.266	1.329	1.566	1.200	91.5
.498	2.846	.999	2.805	76.1	-.269	1.425	1.430	1.296	91.5
.523	2.948	.998	2.910	76.1	-.238	1.539	1.306	1.409	90.3
.550	3.054	.997	3.019	76.1	-.238	1.642	1.155	1.512	90.3
.576	3.159	.997	3.128	76.1	-.239	1.744	1.099	1.614	90.3
.597	3.246	.997	3.217	76.1	-.279	1.829	1.055	1.700	91.5
.614	3.321	.997	3.294	76.1	-.282	1.925	1.023	1.796	91.5
.643	3.434	.998	3.410	76.1	-.240	2.039	1.003	1.909	90.3
.670	3.540	.997	3.519	76.1	-.241	2.142	.998	2.012	90.3
.696	3.645	.996	3.628	76.1	-.241	2.244	.998	2.114	90.3
.717	3.732	.997	3.717	76.1	-.292	2.329	.999	2.200	91.5
.734	3.807	.997	3.794	76.1	-.294	2.425	.999	2.296	91.5
.789	4.025	.996	4.019	76.1	-.243	2.539	.998	2.409	90.3
.816	4.130	.996	4.128	76.1	-.243	2.642	.999	2.512	90.3
.837	4.217	.996	4.217	76.1	-.244	2.744	.999	2.614	90.3
.854	4.292	.996	4.294	76.1	-.305	2.829	.999	2.700	91.5
.909	4.510	.997	4.519	76.1	-.307	2.925	.999	2.796	91.5
.935	4.616	.996	4.628	76.1	-.245	3.039	.998	2.909	90.3
.957	4.702	.997	4.717	76.1	-.237	3.127	.996	2.997	90.1
.974	4.777	.997	4.794	76.1	-.212	3.232	.998	3.102	89.7
1.029	4.996	.998	5.019	76.1	-.245	3.338	.998	3.208	90.2
1.055	5.101	.998	5.128	76.1	-.247	3.442	.998	3.312	90.3
1.077	5.188	.999	5.217	76.1	-.248	3.539	.999	3.409	90.3
1.094	5.263	.997	5.294	76.1	-.239	3.627	.998	3.497	90.1
1.149	5.481	.997	5.519	76.1	-.209	3.732	.998	3.602	89.7
1.175	5.586	.998	5.628	76.1	-.247	3.838	.998	3.708	90.2
1.197	5.673	.999	5.717	76.1	-.250	3.942	.998	3.812	90.3
1.213	5.748	.997	5.794	76.1	-.240	4.127	.995	3.997	90.1
1.269	5.967	1.000	6.019	76.1	-.206	4.232	.995	4.102	89.7

Table B.4.1-5: Continued.

y, in.	z, in.	$p_{t,p}/p_{t,\infty}$	r, in.	$\phi', \text{deg}$
-.249	4.338	.995	4.208	90.2
-.252	4.442	.995	4.312	90.3
-.241	4.627	.996	4.497	90.1
-.204	4.732	.997	4.602	89.7
-.251	4.838	.995	4.708	90.2
-.255	4.942	.998	4.812	90.3
-.242	5.127	.999	4.997	90.1
-.201	5.232	.998	5.102	89.7
-.253	5.338	.998	5.208	90.2
-.257	5.442	.998	5.312	90.3
-.243	5.627	.999	5.497	90.1
-.198	5.732	.998	5.602	89.7
-.255	5.838	.998	5.708	90.2
-.259	5.942	.998	5.812	90.3
-.244	6.127	.999	5.997	90.1
-.196	6.232	.998	6.102	89.7
-.257	6.338	.998	6.208	90.2
-.262	6.442	.998	6.312	90.3

Table B.4-5: - Concluded.

Figure B.4-3 - Pitot pressure ratio distributions at  $x = 63.04$  in. ( $x/L = 1.0$ ) for test case B.4.1Figure B.4-4 - Pitot pressure ratio distributions at  $x = 68.176$  in. ( $x/L = 1.08$ ) for test case B.4.1

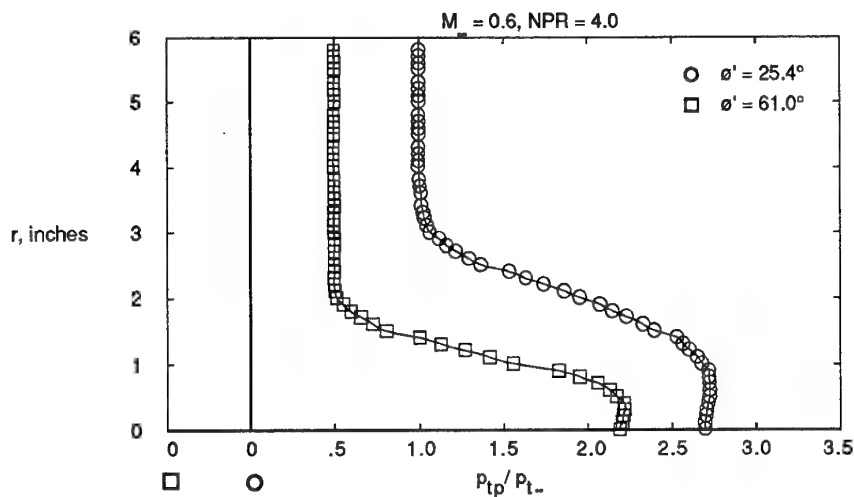


Figure B.4-5 - Pitot pressure ratio distributions at  $x = 73.275$  in. ( $x/L = 1.16$ ) for test case B.4.1

#### B.4.1.4 Pitot Pressure Ratio Contours in y-z Plane

See Table B.4-5

$M_{\infty} = 0.6, \text{NPR} = 4.0$   
 $x = 73.275$  in.,  $x/L = 1.1624$

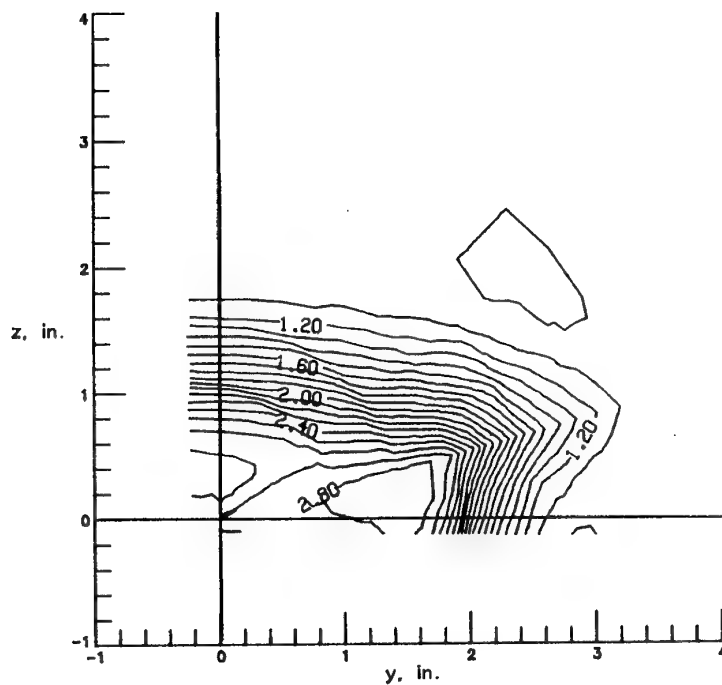


Figure B.4-5 - Contour plot in y-z plane of  $p_{tp}/p_{t\infty}$  at  $x = 73.275$  in. for test case B.4.1

#### B.4.2 Test Case B.4.2 ( $M_{\infty} = 0.938$ , NPR = 4.02)

##### B.4.2.1 External Surface Pressure Coefficient Distribution

See Table B.4-1

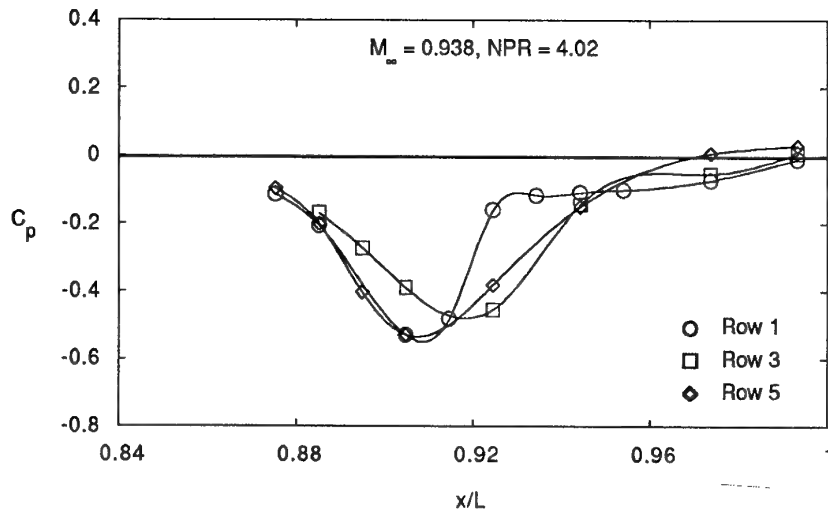


Figure B.4-7 - External static pressure coefficient distributions for test case B.4.2.

#### B.4.2.2 Internal Surface Pressure Ratio Distribution

See Table B.4-2

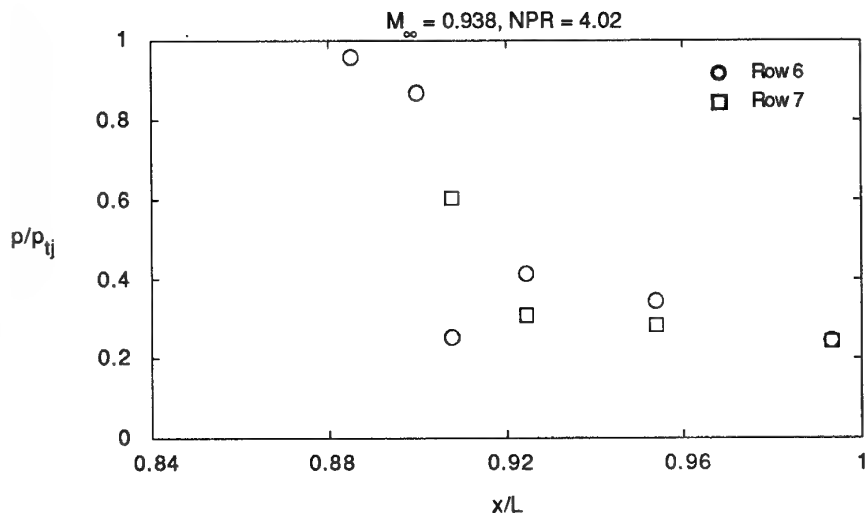


Figure B.4-8 - Internal static pressure ratio distributions for test case B.4.2.

## Appendix C - CFD Usage Notes

The organizations which contributed predictions for this assessment also were invited to provide comments on the generation of grids and the execution of the flowfield solutions. These comments are presented next.

The requested information included a discussion of the basic approach with particular attention to variations for particular aspects of these cases; discussion of operational issues such as convergence criteria and any anomalies noted during the course of the solution; and, an estimate of the time required by a skilled practitioner to produce the equivalent of these results (this, of course, requires an estimate by the contributor).

### C.1 Test Case Series A

#### C.1.1 Test Case Series A.2

##### C.1.1.1 Contribution N06 (Rolls-Royce FANSI)

**Grid Description** - The JA46 2-D/axisymmetric algebraic nozzle grid generator was used. The grid was generated in three blocks: core region 124x34, viscous region behind the blunt base 45x5, and external region 129x55. 85 axial points were used on the external wall and 80 axial points were used on the inside wall.

**Flow Solution Description** - Flow solutions were executed using FANSI with the Cebeci-Smith and  $k-\epsilon$  turbulence models. These cases were run on an Amdahl computer. Convergence was established by monitoring the maximum change and RMS error for the variables. When the RMS error appeared to level off or remain periodic the case was considered converged. No unusual events were noted in running these cases.

##### C.1.1.2 Contribution N09 (McDonnell Douglas NASTD)

**Grid Description** - The MACGS grid generation system was used. To reduce the computational cost, a 2-D (axisymmetric) grid was generated and run with the axisymmetric mode of the NASTD code. The grid consisted of four zones, with the sizes shown in the table, following.

Zone No.	I x J Dimension	Grid Points
1 - forebody	45 x 49	2,205
2 - afterbody	121 x 49	5,929
3 - internal nozzle and plume	49 x 79	3,871
4 - aft of the model	37 x 31	1,147
<b>TOTAL</b>		<b>13,152</b>

Zone 1 surrounds the forebody surface, Zones 2 and 3 cover the afterbody and downstream regions, which are the main areas of interest. Zone 4 represents the internal flow of the hot jet. The outer boundaries of Zones 1, 2, and 3 were extended outward away from the surface to an approximate distance of 20 times the body radius.

**Flow Solution** - A characteristic boundary condition was assumed for all the farfield boundaries. Zero-order extrapolation was used for the outflow boundary. An arbitrary inflow condition was specified for Zone 4 (the jet inflow, inside the nozzle), and this boundary was frozen at the specified conditions. The vehicle surface was set to a viscous wall. The boundaries were coupled with an option that communicates Roe left and right-states across the interface to the neighbor grids.

Axisymmetric viscous solutions were obtained using the NASTD code. Three different turbulence models were employed in this study: the one-equation Baldwin-Barth and Spalart-Allmaras, and the two-equation Chien  $k-\epsilon$ . Each solution was run using the thin shear layer Navier-Stokes equations, with the upwind Roe algorithm.

The total number of iterations in each solution is shown in the table, following. The number of iterations to obtain comparable levels of convergence varied significantly among the turbulence models. The solutions using the one-equation models (Spalart-Allmaras and Baldwin-Barth) typically required about 5 CPU hours on an H-P 755 computer. The  $k-\epsilon$  solution, however, took about 22 CPU hours.

Turbulence Model	No. of Iterations
Spalart-Allmaras	about 4,500
Baldwin-Barth	about 4,500
Chien $k-\epsilon$	about 14,000

Solutions were obtained in the standard mode, of running the code with one of the turbulence models applied throughout the flowfield, during the entire course of the solution. These solutions for the A.2.2 test case were presented in the main body of this report. Generally, the accuracy of these solutions was only fair, and poor near the nozzle exit. Too much recompression was predicted in these solutions, indicating that the boundary layer interaction with the freestream was predicted too weakly. All three turbulence models gave similar results.

With the advantage of having access to the experimental pressure data, we noted that there was a drop in the slope of the pressure coefficient with respect to the axial coordinate, near the nozzle exit. This circumstance suggested that there might be a separation bubble in that region. To trigger a separation in the CFD analyses, we executed first a laminar solution, then used that data as initialization for a Navier-Stokes solution (using the Spalart-Allmaras turbulence model). The laminar solution indeed produced a predicted separation bubble, which became smaller but was not eliminated in the subsequent turbulent Navier-Stokes solution. The second set of results, obtained through this two-stage approach, are in very good agreement with the experimental data.

#### C.1.1.3 Contribution N13 (Dassault MELISSA)

The solution was initialized by an Euler solution, using Method E05. Since the E05 solution was viewed as simply an intermediate position, no results from E05 were presented.

**Euler Initializing Solution** - The geometry was modeled as axisymmetric, using an unstructured grid of 7,400 points generated by CUBE. The flow solver (method E05) produced an axisymmetric Euler solution. Molecular vibrational effects were taken into account in the modeling of the hot jet.

This Euler solution was executed on an IBM RS/6000, in about 45 minutes of CPU time. Convergence was established by monitoring aerodynamic coefficients and residuals.

**Navier-Stokes Solution** - The Navier-Stokes solution, using Method N13, was started from the Euler solution with a boundary layer added. As before, the axisymmetry in the geometry was recognized and used to simplify the models. An unstructured grid of 13,500 points was generated by CUBE. The points are packed close to the wall and in the wake region. The first point off the wall is at a distance of 20  $\mu\text{m}$ .

This axisymmetric Navier-Stokes solution was executed with a two-layer k- $\epsilon$  turbulence model. Molecular vibra-

tional effects were taken into account, in modeling the hot jet.

This solution was executed on an IBM RS/6000, requiring about 12 hours of CPU time for each case in the A.2 series. Convergence was established by monitoring the evolution of aerodynamic coefficients and the residuals.

#### C.1.1.4 Contribution N14 (ONERA NASCA)

**Grid Description** - The axisymmetric grid was generated in one block with 120x140 points.

**Flow Solver Description** - The NASCA code was used for this case, with both the Baldwin-Lomax and the k- $\epsilon$  turbulence models. The case was executed on a Cray-Y/MP computer. The solution was initialized by running with the Baldwin-Lomax turbulence model, starting from a "rough" data field. This step required about 60 CPU minutes. From this intermediate result, the k- $\epsilon$  turbulence model was initialized and the solution was continued for about 120 CPU minutes. Convergence was established by the value of the implicit residual toward the corresponding value of  $10^{-6}$ .

#### C.1.1.5 Contribution N15 (Aerospatiale FLU3M)

**Grid Description** The grid is three blocks, axisymmetric, with a total of 40,000 points. Due to limitations from the turbulence model implementation, the grid surface  $J=1$  must lie in the walls, and in the jet free shear layer. Thus, the grid arrangement is as presented in Figure 1.

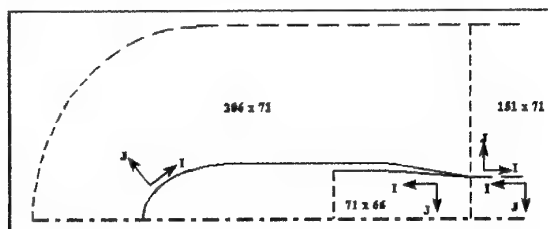


Figure C-1. Grid Layout for Case A.2.2, Contribution N15

(Illustration only, drawing not to scale)

**Flow Solution Description** - The Navier-Stokes equations were solved, using the Baldwin-Lomax turbulence model. The selected algorithm used Osher flux and the Van Leer limiter. These equations were solved in an axisymmetric implicit scheme.



## C.1.2 Test Case Series A.3

### C.1.2.1 Contribution N02 (Rolls-Royce ANSE)

**Grid Description** - The grid generator in this case was an unnamed, purpose-written FORTRAN routine. Subroutines were used from JA 46 and STACKER. Two inflow and outflow boundaries are defined. Geometric grid spacing can be adjusted in I J K direction and the final grid can be refined by application of in-house grid manipulation routines. Topologic input is manually added to define symmetry planes, repeats, or centerline locations.

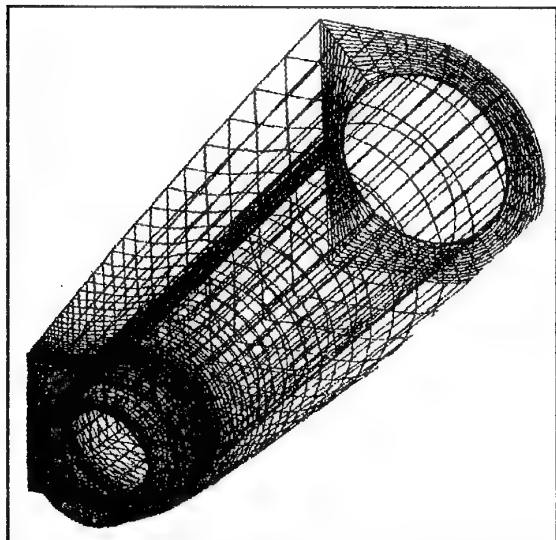


Figure C-2. Surface Grid for Configuration A.2  
(Contribution N02)

The resulting grid was one block of radial construction similar to that used on test case B.4. The principal distinguishing feature is the treatment of the inter-nozzle base region. Circumferentially running mesh lines on leaving the base were concentrated in a thin layer adjacent to the outer surface of the nozzle. This concentrated region was terminated at the plane of the base via a circumferentially-running point singularity with the then unsolved axially running mesh lines continuing forward within the solid model structure in common with those running through the base wall. Much effort went into varying the number of grid lines covering the base region and adjusting the radial expansion factors to minimize the grid cell size discontinuities caused by the large variations in circumferential grid topology. Axial grid spacings were adjusted to provide concentrations at both external and internal wall shape discontinuities. In the final grid, 61 radial points were used, 33 circumferential and 91 axial giving a total of 183,183 grid points.

**Flow Solution Description** - The ANSE Navier-Stokes flow solver was used, with the Cebeci-Smith turbulence model, to analyze the A.3.1 test case. The solution was executed on a Convex computer, using 131 hours for 4,300 iterations. A memory of 14 million words was employed. Convergence was established by monitoring the maximum change and the RMS error for the variables. When the RMS error appeared to level off, the case was considered converged.

**Assessment** - This analysis yielded plausible results which along many of the lines of surface pressureappings compare quite closely with those obtained by the Euler code **FLITEFS**. Both solutions, however, deviate markedly from the experimental data. The experimental  $C_p$ 's appear to be unreasonably low particularly at the start of the afterbody where value much closer to  $C_p=0$  would be expected. Unlike the Euler solution, there is also poor agreement with pressures in the base region where the computed values look too low.

### C.1.2.2 Contribution E07 (Rolls-Royce **FLITEFS**)

**Grid Description** - The grid in this case was a single completely unstructured finite element block constructed of 520,000 4-node tetrahedra, equivalent to 85,000 grid points.

**Flow Solution Description** - The flow solver **FLITEFS** was used. This code solves the compressible form of the steady-state Euler equations, using an edge-based finite element scheme with explicit time marching. Local time stepping is used for fast convergence, with the option of residual smoothing.

For the A.3.1 test case, probably as a result of the difficult flow conditions around the "cusped" nozzle throat, convergence proved difficult. Therefore, residual smoothing was not used and 1-stage explicit Runge-Kutta time stepping was invoked. The Courant number was reduced to around 0.3 compared with the more typical 2.0.

The solution was executed on the Silicon Graphics Indigo workstation (R4000) in 16 to 20 hours, using 11 million words of memory.

Normal practice is to judge convergence when the  $\log_{10}$  RMS residual in  $p$  has fallen by at least 4-5 orders of magnitude and become either level or periodic. In this test case, a reduction in residuals of only a little more than two orders of magnitude was achieved before the solution leveled out.

**Assessment** - This was generally judged to be a clean solution yielding plausible results which along many lines of surface pressureappings compare quite closely with

those obtained from use of the Navier-Stokes solver ANSE. Both solutions, however, deviate markedly from the experimental data. The experimental  $C_p$ 's appear to be unreasonably low particularly at the start of the afterbody where values much closer to  $C_p=0$  would normally be expected. The one region of the flow where there is good agreement is in the base.

## C.2 Test Case Series B

### C.2.1 Test Case Series B.1

#### C.2.1.1 Contribution N04 (USAF WL/FIM, COBALT Code)

**Grid Description** - The grid was a 2-D single-block, unstructured grid, created on a quadrilateral mesh of 14,318 grid points. The 2-D unstructured grid was constructed from a single plane of the original density 3-D multiblock grid used for cases B.2.1 and B.2.2.

**Flow Solver** - The COBALT code was used. These solutions were second-order in time and space. The second-order Baldwin-Barth turbulence model was used. Solutions were executed on a Cray-X/MP. The B.1.1 test case required 5.6 CPU hours, and used 2.1 M Words of memory.

The solution was run until the total axial force varied by less than 1% for 1,000 iterations. At this point, the average  $y^+=1.84$  and varied by 0.4% (over the final 200 iterations?). The number of supersonic cells varied by 1.8% (over the final 100 iterations?) at convergence.

#### C.2.1.2 Contribution E08 (Aermacchi, FLO67P)

**Grid Description** - The grid represents a 45 degree sector of the entire model, computed using symmetry boundary conditions. The grid consisted of five blocks with a total of 66,560 cells. Three of the blocks were for external flows with C-O topology, sized at 177x33x9 points. Two of the blocks were for the internal-external jet, using H-O topology, sized 113x25x9 points. The boundaries of the computational domain were placed as follows (L=model length, 71.7 inches):

Upstream - 0.89 L from the model

Downstream - 0.46 L

Upper far-field - 0.9 L

**Flow Solution Description** - Solutions were executed using the FLO67P code in its Euler mode. These cases were run on an IBM RS/6000-540. Convergence was

established by monitoring maximum and mean residuals, global aerodynamic coefficients, and the number of supersonic points. Generally, a two order of magnitude reduction in residual values allows flowfield stability and good communication between the blocks.

**Case B.1.1** - This Euler solution required 1,500 iterations with two levels of multigrid and CFL=2. The obtained convergence level is about a two order of magnitude reduction in absolute values of the mean residuals, while the drag coefficients oscillate  $\pm 2$  counts without any further damping. This solution required 7,562 CPU seconds on the IBM RS/6000-540.

The inviscid solution is representative up to  $X/L=0.9$  and then shows a negative pressure peak and a much higher base pressure. This leads to unrealistic drag coefficients; for this reason, we prefer to avoid the presentation of the global coefficients data which are strongly affected by this approximation. The drag coefficient buildup shows a good comparison with experimental data as far as  $X/L=0.95$ . The difference in pressure coefficients with experimental data in the region of  $X/L$  from 0.7 to 0.85 cannot be explained by viscous effects, and suggests a possible discrepancy in the geometry.

**Case B.1.2** - The identical grid from the B.1.1 case (immediately prior) was also used for this case. As before, the FLO67P code was used in its Euler mode, running on an IBM RS/6000-540 computer. This solution required 7,825 CPU seconds.

The computation strategy (multigrid levels, and CFL number) is the same as the B.1.1 case. The obtained convergence level is about two orders of magnitude in absolute values of mean residuals, while the drag coefficient oscillates  $\pm 4$  counts without any further damping.

The higher value of NPR generates near  $X/L=1$  a more positive pressure distribution and thus a more negative value of  $C_D$  than in the B.1.1 case. The computed data reveal the same trend as the experimental data, as the NPR changes from 2 to 5.

#### C.2.1.3 Contribution N08 (Aermacchi, FLO67P)

**Grid Description** - The grids for Navier-Stokes solutions are very similar to those used for Euler solutions (Contribution E08) with the addition of grid points in both the axial and normal directions.

The grid represents a 45 degree sector of the entire model, computed with appropriate symmetry boundary conditions. The grid consisted of five structured blocks with a total of 221,774 cells. Three blocks for external flow used a C-O topology and were sized 233x49x9. Two blocks for the

internal-external jet used H-O topology and were sized 249x49x9 points. The limits of the computational domain were the same as in Contribution E08.

**Flow Solution Description** - The FLO67P code was used, in its Navier-Stokes version. Solutions were executed on an IBM RS/6000-540.

Convergence was established by monitoring the maximum and mean residuals, global aerodynamic coefficients, and the number of supersonic points. An overall decrease of four orders of magnitude in the residuals allows flowfield stability and good communication between the blocks.

**Case B.1.1** - The solution was started with the flowfield obtained from 600 iterations on a coarse grid and 600 iterations on a medium grid. 1,500 iterations were run on the fine grid at CFL=2, without using the multigrid strategy. The obtained convergence level is about four orders of magnitude in absolute values of mean and maximum residuals. This solution required 261,411 CPU seconds on the IBM RS/6000-540 computer.

The negative pressure peak on the afterbody is under-predicted, while the maximum  $C_p$  on the trailing edge reaches the value of 0.3, higher than the corresponding experimental value. This effect could be explained with the excessive level of numerical dissipation introduced in the boundary layer region, which has been necessary to counteract the destabilizing effect of the contact discontinuity at the edge between the afterbody and the nozzle.

**Case B.1.2** - The same grid and flow solver were used as in the B.1.1 case (discussed immediately before this case). The FLO67P code was run in its Navier-Stokes mode, on an IBM RS/6000-540 computer, requiring 262,070 CPU seconds (72.8 CPU hours).

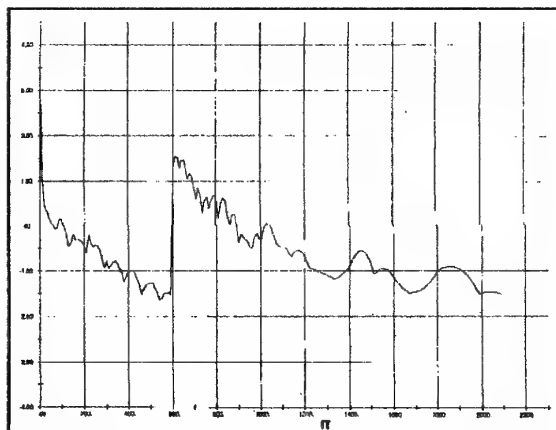


Figure C-3. Residual Convergence History  
Case B.1.2, Contribution N08

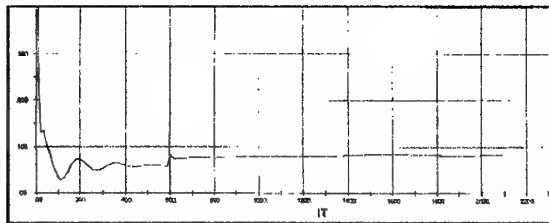


Figure C-4. Drag Convergence History  
Case B.1.2, Contribution N08

The obtained convergence level is about four orders of magnitude in absolute values of mean and maximum residuals. As in the B.1.1 case, the negative pressure peak on the afterbody is underestimated, while the maximum  $C_p$  on the trailing edge is higher than the corresponding experimental value. The same remarks on the high level of numerical dissipation made for the B.1.1 case can be repeated here; this could also explain the slight influence of different NPR on the pressure distribution on the afterbody.

#### C.2.1.4 Contribution N09 (McDonnell Douglas, NASTD)

The computational grid for cases B.1.1 and B.1.2, using Method N09, are presented in Figures C-5 and C-6.

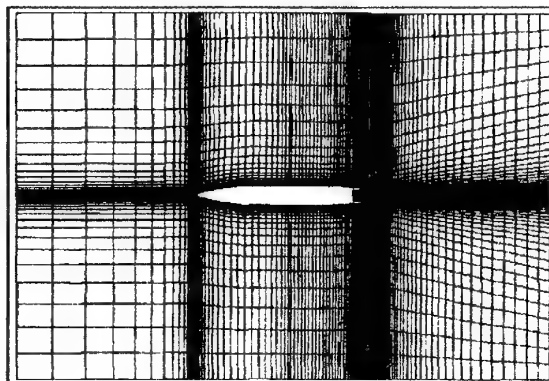


Figure C-5. Full Computational Grid  
Case B.1.x, Contribution N09

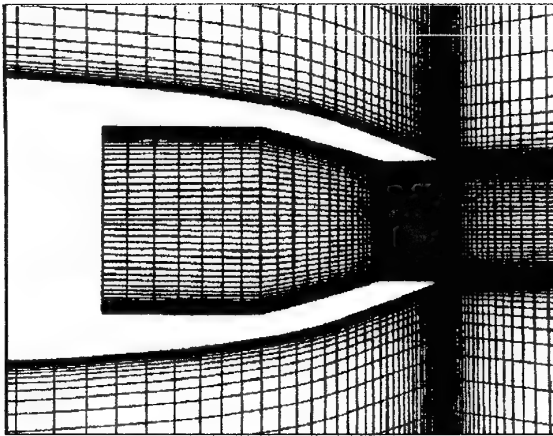


Figure C-6. Grid Cross-Section  
Case B.1.x, Contribution N09

#### C.2.1.5 Contribution N10 (NASA Langley Research Center)

**Grid Description** - GRIDGEN was used to generate a five-block axisymmetric grid to describe the axisymmetric single-jet afterbody configuration. The dimensions of the blocks are presented below:

Block	Circum. Grid	Axial Grid	Norm. Grid	Block Location
1	2	87	1	Upstream and nose
2	2	59	61	Afterbody
3	2	33	101	Initial block inside nozzle
4	2	5	41	Nozzle interior
5	2	55	41	Downstream and plume

The single-cell wedge grid was placed in the J,K-plane to take advantage of the implicit solver scheme in the same plane for the PAB3D code. Grid sequencing with a factor up to four in the J- and K-directions can be used for obtaining the solution.

In a two-dimensional grid oriented in the J,K-plane, the PAB3D code required separate blocks for different turbulence models. Laminar viscosity was used in Blocks 1 and 3, the low Reynolds number k- $\epsilon$  turbulence model was used in Blocks 2 and 5, and the high Reynolds number k- $\epsilon$  turbulence model was used in Block 5.

**Flow Solver Description** - A grid connectivity pre-processor was used for the PAB3D code. In this pre-processor, patched block interfaces, if any, were treated in the same manner as the block interfaces with one-to-one cell corre-

spondences. Cell-to-cell level interface data base tables were generated by the pre-processor. These data tables were read and used by the PAB3D code at code execution time. This approach made possible the implementation of a general grid sequencing method in PAB3D which allowed independent sequencing for each block in integral multiples in one or more of the I, J, and K directions. Hence, the grid sequencing scheme was tailored for accelerated convergence in different parts of this configuration. For example, grid sequencing of 2:1 in both directions was first used to establish quickly the inviscid properties of the flowfield. Next, fine grid was used in the boundary layer direction to develop the details of the viscous boundary layer and shear layers in the flow field. The full fine grid was then used to complete the solution.

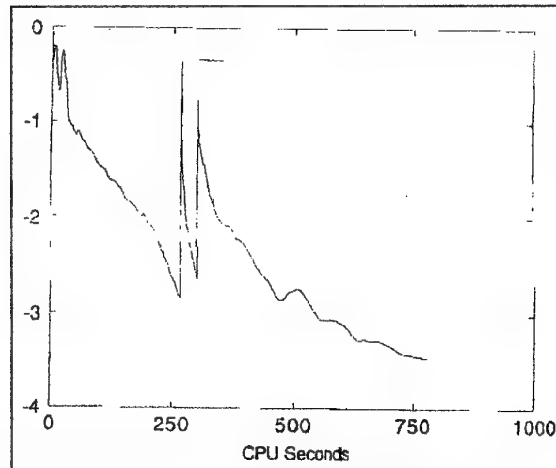


Figure C-7. Example of Residual Convergence for Test Case B.1 (Contribution N10)

The PAB3D version 10 code, developed in the Propulsion Aerodynamics Branch (NASA Langley Research Center), was used for this test case. The Roe scheme solver option in PAB3D was used. The k- $\epsilon$  turbulence variables were initialized by setting their values according to the vorticity in the upstream boundary layer which was computed by using a laminar viscosity or an algebraic turbulence model. For cases B.1.1 and B.1.2, laminar viscosity was used in blocks 1 and 3, and the k- $\epsilon$  two-equation turbulence model was used in blocks 2, 4, and 5. In the freestream, the Riemann inflow and free-stream boundary conditions were used. The extrapolation boundary condition was used at the outflow face. In the nozzle interior, the inflow total temperature and pressure were given at the inflow face. Finally, a generated symmetry boundary condition was used at the wedge faces of this single layer grid. A sample history of residual convergence for a case in this B.1 series is presented in Figure 2.

The aerodynamic performance computation is part of the PAB3D code. When the performance calculation option is

activated through the PAB3D input file, the force computations are directed by a small input file specifying integrated quantities to be computed and the control surfaces in the grid.

**Post-Processor Description** - Since the axisymmetric configuration was relatively simple, no post-processing steps were involved for the B.1.1 and B.1.2 cases. The drag components were computed within the PAB3D code. The PLOT3D software system was used for the presentation of color graphics.

As mentioned in the solver descriptions, a pre-processor was used to establish block interface connectivity. The pre-processor was developed by the Propulsion Aerodynamics Branch at NASA Langley Research Center for conservative patched interface applications. However, this pre-processor treated one-to-one block interfaces in the same manner as a patched interface. Hence, it was possible to establish a unified conservative block interconnect database for the entire grid. This unified block interface approach was incorporated in PAB3D as a standard feature. The general grid sequencing procedure in PAB3D was made possible by this unified conservative block interface database approach.

#### C.2.1.6 Contribution N16 (USAF/NASA Lewis, NPARC)

**Grid Description** - Computational grids were provided by McDonnell Douglas. Therefore, the grids were the same as were used in Contribution N09, except in the following elements. Because the NPARC code requires grid blocks that overlap at block interfaces, the grids were modified with the I3G interactive grid generator developed by the US Air Force at Wright-Patterson Air Force Base. I3G was used to add an additional grid plane at each interface to create the required overlaps. For the B.1 configuration, three overlap planes were added. The grid contained 11,647 grid points divided into four grid blocks. The largest concentration of grid points was located in the vicinity of the nozzle afterbody.

**Flow Solution Description** - The test cases were run with NPARC on the Cray-Y/MP at NASA Lewis Research Center. A total of 30,000 iterations were required for convergence in each case. For the B.1 cases, three CPU hours were required to obtain a converged solution from uniform initial conditions. The grid blocks containing the internal nozzle flow converged rapidly and were subsequently turned off to save CPU time. A solution was considered to be converged when the difference between the minimum and maximum pressure coefficient at each grid point was within one percent of the average pressure coefficient.

**Assessment** - For the B.1 cases, the pressure distributions

indicate relatively good agreement between the NPARC calculation and the experimental data. The minimum pressure predicted by the calculation was somewhat higher than the pressure obtained from the experiment.

### C.2.2 Test Case Series B.2

#### C.2.2.1 Contribution N04 (USAF WL/FIM, COBALT Code)

**Grid Description** - The grid was a single block, unstructured, hexahedral mesh with 134,952 grid points. The unstructured grid was constructed from a multiblock structured grid. Note - this grid was originally 2x more dense in each direction, but this size was reduced due to memory requirements of single block grid and the resulting difficulty in obtaining CPU time on currently available computer resources.

**Flow Solution Description** - The COBALT code was executed, second-order accurate in space and time, using the second-order Baldwin-Barth turbulence model.

Solutions were executed on the Cray C-90 computer. The B.2.1 case required 39 CPU hours, and the B.2.2 case required 33 CPU hours. For this latter case, an additional 25 hours were run to check the higher-order turbulence model. These solutions required 23.8 M Words of memory.

The solutions were run until the total axial force varied by less than 1% for 1,000 iterations. At this convergence point:

B.2.1: Average  $y^+ = 9.07$  and varied by less than 0.2%. The number of supersonic cells varied by 0.5%.

B.2.2: Average  $y^+ = 10.14$  and varied by less than 0.2%. The number of supersonic cells varied by 0.1%.

#### C.2.2.2 Contribution E08 (Aermacchi, FLO67P)

**Grid Description** - The grid represents a 90 degree sector of the entire model. The surface grid (body and vertical tail) was sent to Aermacchi by DEI (Dynamic Engineering Inc.). Then Aermacchi redistributed the points for multi-level and multi-grid computation. The total grid consisted of sixteen blocks with 206,592 cells in an H-O topology. Eight blocks defined the external outer flow with  $261 \times 17 \times 17$  points, and eight blocks defined the external inner flow with  $261 \times 21 \times 17$  points. Two additional blocks defined the internal/external jet with  $149 \times 25 \times 17$  points. The outer boundaries of the computational domain were placed as follows ( $L = 71.7$  inches, total model length):

Upstream - 0.558 L from the model.

Downstream - 0.56 L.

Upper farfield - 0.94 L to 1.32 L (conical shaped boundary)

**Flow Solution Description** - The FLO67P code, in its Euler mode, was used to obtain these solutions. The cases were run on an IBM RS/6000-540 computer.

Convergence was established by monitoring the maximum and mean residuals, the global aerodynamic coefficients, and the number of supersonic points. Generally, a two-order-of-magnitude reduction in residual values allows flowfield stability and good communication between the blocks.

**Case B.2.1** - The calculation strategy was based on using both multi-level and multi-grid techniques. 200 iterations were performed on a coarse grid, and 500 iterations on the fine grid with three levels of multigrid and CFL=3. The obtained convergence level is about two orders of magnitude in absolute values of mean residuals, while the drag coefficient oscillates  $\pm 4$  counts without any further damping. This solution required 26,214 CPU seconds (7.3 CPU hours) on the IBM RS/6000-540 computer.

The small irregularities in the surface pressure distributions are due to slightly imperfect communication between the blocks. The predictions for the vertical tail are in closer agreement with the experimental data than the predictions for the horizontal tail. For  $X/C > 0.5$  the horizontal tail experimental data show a change in curvature which is not detected by the solution. This could be caused by: (1) insufficient local grid refinement, (2) any problem in geometry definition, or (3) a problem in experimental data acquisition.

**Case B.2.2** - For this computation, the solution strategy was changed to achieve a CPU time reduction with the same solution quality as in Case B.2.1. 400 iterations were executed on the coarse grid, and 350 iterations on the fine grid. The obtained convergence level is about two orders of magnitude in the absolute values of the mean residuals, while the drag coefficient oscillates  $\pm 2$  counts without any further damping. This solution required 20,598 CPU seconds (5.7 CPU hours) on the IBM RS/6000-540 computer.

The computed pressure distributions over the afterbody have the same trend as the experimental data as NPR changes from 2 to 3, however the variations are very small. This is not true for the tails. As was seen in the previous case, better agreement between CFD predictions and experimental data is seen for the vertical tails, rather than the horizontal tails.

**Case B.2.3** - For this case, the same solution strategy was used as in Case B.2.2. The obtained convergence level is about two orders of magnitude in absolute values of mean residuals, while the drag coefficient oscillates  $\pm 2$  counts without any further damping. This solution required 19,860 CPU seconds (5.5 CPU hours) on the IBM RS/6000-540 computer.

The computed pressure distributions on the afterbody are essentially identical to those of the B.2.2 case, up to  $X/L=0.9$ . For  $X/L$  from 0.9 to 1.0, the trend of the computed NPR variation is the same as that in the experimental data. No significant NPR effect was seen over the tails.

#### C.2.2.3 Contribution N10 (NASA Langley Research Center)

GRIDGEN was used to generate a five-block grid for the single-engine afterbody with staggered tail surfaces. An H-O topology was used for this configuration, and one-to-one cell correspondence was used at all block interfaces. The block dimensions were chosen as follows:

Block	Circum. Grid	Axial Grid	Norm. Grid	Block Location
1	63	81	61	Upstream and nose
2	123	41	61	Above horizontal tail
3	123	41	61	Below horizontal tail
4	33	81	101	Downstream and plume
5	59	81	41	Engine interior

The total number of grid points was 1,400,000. The staggered tail surface locations were as follows:

Tail Surface	Block	I Range	J Range	K Range
Vertical	2	13-68	1	1-40
Horizontal Upper	2	43-98	61	1-40
Horizontal Lower	3	43-98	1	1-40

For the initial part of the computations, a coarse grid containing only one fourth of the total grid points was used to save time and computer memory during execution. Once a converged coarse grid solution was obtained, the restart file was expanded to the full grid size for final computations.

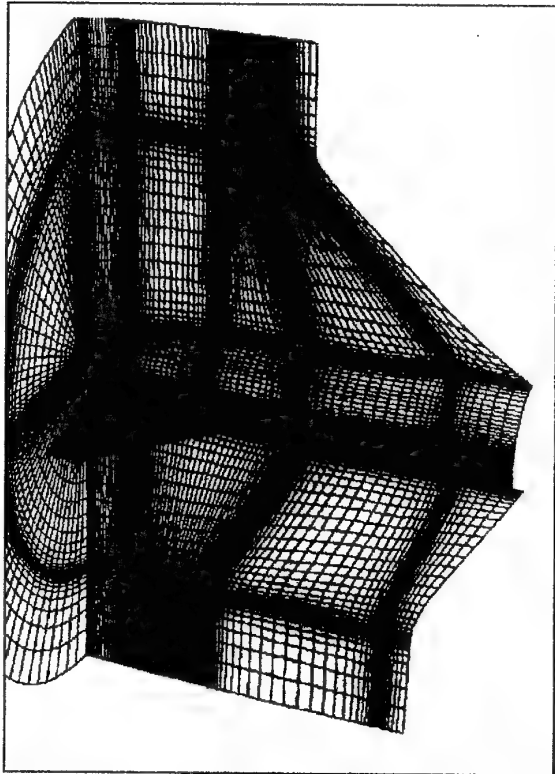


Figure C-8. Computational Grid for Cases B.2.x  
(Contribution N10)

**Flow Solver Description** - A grid connectivity pre-processor was used for the PAB3D code. In this pre-processor, patched block interfaces, if any, were treated in the same manner as the block interfaces with one-to-one cell correspondences. Cell-to-cell level interface data base tables were generated by the pre-processor. These data tables were read and used by the PAB3D code at code execution time.

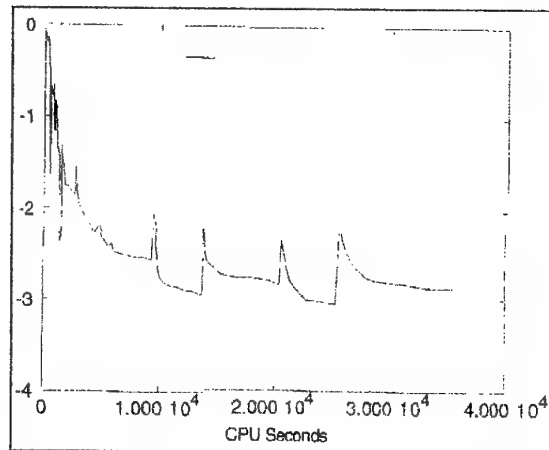


Figure C-9. Example of Residual History for Test Cases B.2 (Contribution N10)

The PAB3D version 10 code, developed in the Propulsion Aerodynamics Branch at NASA Langley Research Center, was used for these test cases. The Roe scheme solver option in PAB3D was used. The Baldwin-Lomax algebraic turbulence model was used in block 1, and the  $k-\epsilon$  turbulence model was used in the remaining four blocks. In addition, laminar viscosity was used in the first few grid planes in block 5 to initialize the  $k-\epsilon$  turbulence variables in the nozzle interior flow domain. At the freestream boundaries, the Riemann characteristics boundary condition was used. The extrapolation boundary condition was used at the outflow face. In the nozzle interior, the inflow total temperature and pressure were given at the inflow face. A typical history of residual convergence for the B.2 series of test cases is presented in Figure 3.

A multi-stage grid sequencing was used during the computation. The general grid sequencing method in PAB3D allows independent sequencing for each block in integral multiples in one or more of the I, J, and K directions. Hence, the grid sequencing scheme was tailored for accelerated convergence in different parts of this configuration.

For further enhancement of computational efficiency, the original grid was cut to one-fourth of its original size for the initial stages of grid sequencing. The interface connectivity database and the multi-block input files for PAB3D code execution were rewritten automatically for this smaller grid. Once a converged coarse-grid solution was obtained by using grid-sequencing in the smaller grid, the restart file was then expanded to the full grid size.

The computations were then continued to completion. The computations were conducted by using a single processor on the Cray-Y/MP supercomputer at the NASA Langley Research Center. The core memory requirements for the smaller and the full grid computations were 8,000,000 and

27,000,000 words, respectively. Approximately half the computational time was spent on the smaller grid.

The aerodynamic performance computation is part of the PAB3D code. When the performance calculation option is activated through the PAB3D input file, the force computations are directed by a small input file specifying integrated quantities to be computed and the control surfaces in the grid.

It should be noted that solutions were obtained only for cases B.2.1 and B.2.3. The flow field for case B.2.2 was similar to that for case B.2.3 as indicated by the given experimental data. Therefore, case B.2.2 was omitted from the NASA Langley computations.

**Post-Processor Description** - Two post-processing packages were used to examine the converged solutions B.2.1 and B.2.3.

A performance computation module, developed by the Propulsion Aerodynamics Branch at the NASA Langley Research Center, was incorporated in the PAB3D code as a standard option to compute quantities such as thrust, normal forces, moments, skin friction, lift, drag, and heat transfer. This module was designed to handle multi-stream propulsion system and multiple component aerodynamic configurations. The performance module was recently upgraded to be compatible with the grid sequencing procedure in the PAB3D version 10 code. If the performance calculations were activated in parallel to the solver iterations, a history of the performance calculations would be kept. It could be used as monitoring criteria for solution convergence. For the present set of calculations, the performance module was activated as a one-time event after the converged solutions were obtained. In either case, the performance calculations were directed by a small input file containing locations for the control surfaces in the grid and specifications of the integrated quantities to be computed.

A software package, "LOCATE," was used for selecting point-wise flow quantities from the CFD solution. This package was developed by the Propulsion Aerodynamics Branch at NASA Langley Research Center. It was designed to attain a high level of spatial resolution such that quantities such as boundary layer profiles above curved surfaces can be extracted from grid and solution files. Points can be located on either two-dimensional block faces or three-dimensional grid volumes. User input requirements were simple, flexible, and almost grid independent. Grid and solution files in PLOT3D format were required by the LOCATE code. The pressure coefficient comparisons between the experimental data and the computational solution for cases B.2.1 and B.2.3 were made using the LOCATE post-processor.

It should be mentioned that the grid block interconnect pre-

processor, as described under cases B.1.1 and B.1.2, was also used as a standard procedure for PAB3D version 10. In addition, two intermediate processing steps - namely, grid size reduction during the initial stages of the iterative solution process, and solution expansion from a coarse grid to a finer grid - were also written as standard software packages to support the PAB3D code system. These were important elements in the Propulsion Aerodynamics Branch CFD working environment which ensured a smooth and efficient process for CFD applications to complex geometries.

### C.2.3 Test Case Series B.3

#### C.2.3.1 Contribution N10 (NASA Langley)

**Grid Description** - Grids were generated for only the B.3.1 (mid vertical tail) and the B.3.3 (forward vertical tail) configurations, using GRIDGEN. H-O topologies were used, and the grid block interfaces were one-to-one. A total of 11 blocks were used to describe either of the B.3.1 or the B.3.3 geometries. The block dimensions and relative positions were:

Block	Circum. Grid	Axial Grid	Norm. Grid	Block Location
1	23	65	5	Upstream and nose
2	23	161	57	Upstream and nose
3	15	161	61	Forebody before wing root
4	21	73	61	Above the wing
5	21	89	61	Below the wing
6	23	49	61	Between vertical tails
7	53	49	61	Above horizontal tail
8	53	65	61	Below horizontal tail
9	29	145	33	Nozzle interior
10	17	145	33	Plume
11	17	161	61	Downstream

The grid contained approximately 1,500,000 points. All blocks except 6, 7, and 8 were identical for both the B.3.1 and the B.3.3 grids. The wing surface positions in these grids were.



Wing Surface	Block	I Range	J Range	K Range
Wing Upper	4	1-20	73	1-50
Wing Lower	5	1-20	1	1-50

The tail surface positions for the B.3.1 case (mid-location of the vertical tail) were:

Tail Surface	Block	I Range	J Range	K Range
Vertical Inboard	6	13-32	49	1-40
Vertical Outboard	7	13-32	1	1-40
Horizontal Upper	7	13-38	49	1-40
Horizontal Lower	8	13-38	1	1-40

The tail surface positions for the B.3.3 case (forward location of the vertical tail) were:

Tail Surface	Block	I Range	J Range	K Range
Vertical Inboard	6	5-29	49	1-40
Vertical Outboard	7	5-29	1	1-40
Horizontal Upper	7	13-38	49	1-40
Horizontal Lower	8	13-38	1	1-40

For the initial part of computations, a coarse grid containing only one-fourth of the total grid points was used to save computer time and memory during execution. Once a converged coarse-grid solution was obtained, the restart file was expanded to the full grid size for final computations.

**Flow Solver Description** - A grid connectivity pre-processor was used for the PAB3D code. In this pre-processor, patched block interfaces, if any, were treated in the same manner as the block interfaces with one-to-one cell correspondences. Cell-to-cell level interface data base tables were generated by the pre-processor. These data tables were read and used by the PAB3D code at code execution time.

The PAB3D version 10 code, developed in the Propulsion Aerodynamics Branch at NASA Langley Research Center, was used for these test cases. The Roe scheme solver option in PAB3D was used. The Baldwin-Lomax algebraic turbulence model was used in blocks 1 and 3, and the  $k-\epsilon$  turbulence model was used in the remaining nine blocks. In addition, laminar viscosity was used in the first few grid planes in block 9 to initialize the  $k-\epsilon$  turbulence variables in the nozzle interior flow domain. At the freestream

boundaries, the Riemann characteristics boundary condition was used. The extrapolation boundary condition was used at the outflow face. In the nozzle interior, the inflow total temperature and pressure were given at the inflow face.

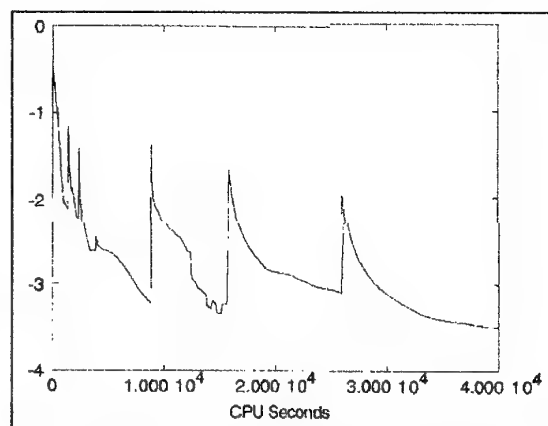


Figure C-10. Representative Residual Convergence History for Test Cases B.3 (Contribution N10)

A multi-stage grid sequencing was used during the computation. The general grid sequencing method in PAB3D allows independent sequencing for each block in integral multiples in one or more of the I, J, and K directions. Hence, the grid sequencing scheme was tailored for accelerated convergence in different parts of this configuration.

For further enhancement of computational efficiency, the original grid was cut to one-fourth of its original size for the initial stages of grid sequencing. The interface connectivity database and the multi-block input files for PAB3D code execution were rewritten automatically for this smaller grid. Once a converged coarse-grid solution was obtained by using grid-sequencing in the smaller grid, the restart file was then expanded to the full grid size. The computations were then continued to completion. The computations were conducted by using a single processor on the Cray-Y/MP supercomputer at the NASA Langley Research Center. The core memory requirements for the smaller and the full grid computations were 8,000,000 and 32,000,000 words, respectively. Approximately half the computational time was spent on the smaller grid. A representative history of residual convergence for this series of test cases is presented in Figure 4.

The aerodynamic performance computation is part of the PAB3D code. When the performance calculation option is activated through the PAB3D input file, the force computations were directed by a small input file specifying integrated quantities to be computed and the control surfaces in the grid. It should be mentioned also that a grid study

for the CFD solution was implicit in the NASA Langley computations as a result of using grid sequencing. It was noted that both grid resolution and grid quality had effects on the accuracy of the solutions.

**Post-Processor Description** - Two separate post-processing packages were used to examine the converged solutions B.3.1 and B.3.3.

A performance computation module, developed by the Propulsion Aerodynamics Branch at the NASA Langley Research Center, was incorporated in the PAB3D code as a standard option to compute quantities such as thrust, normal forces, moments, skin friction, lift, drag, and heat transfer. This module was designed to handle multi-stream propulsion system and multiple component aerodynamic configurations. The performance module was recently upgraded to be compatible with the grid sequencing procedure in the PAB3D version 10 code. If the performance calculations were activated in parallel to the solver iterations, a history of the performance calculations would be kept. It could be used as monitoring criteria for solution convergence. For the present set of calculations, the performance module was activated as a one-time event after the converged solutions were obtained. In either case, the performance calculations were directed by a small input file containing locations for the control surfaces in the grid and specifications of the integrated quantities to be computed.

A software package, "LOCATE," was used for selecting point-wise flow quantities from the CFD solution. This package was developed by the Propulsion Aerodynamics Branch at NASA Langley Research Center. It was designed to attain a high level of spatial resolution such that quantities such as boundary layer profiles above curved surfaces can be extracted from grid and solution files. Points can be located on either two-dimensional block faces or three-dimensional grid volumes. User input requirements were simple, flexible, and almost grid independent. Grid and solution files in PLOT3D format were required by the LOCATE code. The pressure coefficient comparisons between the experimental data and the computational solution for cases B.3.1 and B.3.3 were made using the LOCATE post-processor. Since the pressure tap positions and the grid topologies were the same for these two configurations, only one set of user input files was needed for both the B.3.1 and B.3.3 cases.

It should be mentioned that the grid block interconnect pre-processor, as described under cases B.1.1 and B.1.2, was also used as a standard procedure for PAB3D version 10. In addition, two intermediate processing steps - namely, grid size reduction during the initial stages of the iterative solution process, and solution expansion from a coarse grid to a finer grid - were also written as standard software packages to support the PAB3D code system. These were important elements in the Propulsion Aerodynamics Branch

CFD working environment which ensured a smooth and efficient process for CFD applications to complex geometries.

## C.2.4 Test Case Series B.4

### C.2.4.1 Contribution N02 (Rolls-Royce ANSE)

One grid block 68x29x63 was used. 30 radial points were used in both the core and external regions. 39 axial points were used on the external wall and 30 axial points were used on the inside wall. The surface grid for the external and internal nozzle surfaces is illustrated in Figure 5; the full-domain external grid is seen in Figure 6.

Axial region grid spacing was tailored to match the external flow with clustering around the external wall shape discontinuities. This gave rise to sparse grid spacing in the core region adjacent to the nozzle throat. With such a grid it was not expected to model the internal nozzle flow well. The extent to which this affects the ability to model the external flow to any useful level of accuracy is a contentious point which may be illuminated by comparison of the results of this solution with others where larger grids have been used to fully resolve the internal and external flow features.

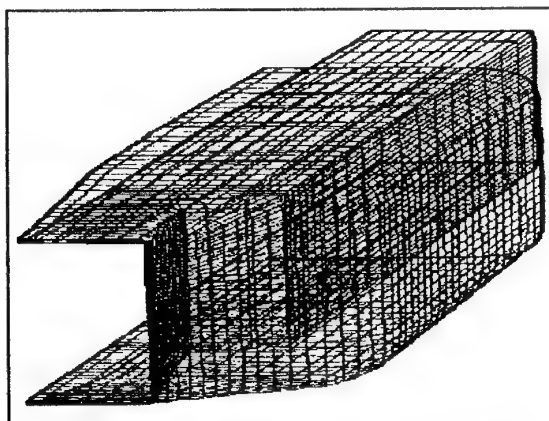


Figure C-11. External and Internal Surface Grids for Case B.4 (Contribution N02)

The ANSE flow solver was used, with the Cebeci-Smith and  $k-\epsilon$  turbulence models. Solutions were executed on the Cray-Y/MP in 9 hours, and on the Silicon Graphics Indigo workstation in 6 days. Solutions were run for 12,000 iterations, but they were converged in 8,000 iterations. Eleven million words of memory were used. Convergence was established by monitoring the maximum change and the RMS error for the variables. When the RMS change appeared to level off, the case was considered converged.

Little difference is seen between the pressure distributions produced by the  $k-\epsilon$  and Cebeci-Smith turbulence models for either of the two test cases (B.4.1 and B.4.2). What difference there is translates into a pressure drag delta approaching 10% in the case of the higher Mach number, partially separated flow. However, in the case of the lower Mach number, fully attached case (B.4.1), differences along the body compensate, to yield exactly the same drag.

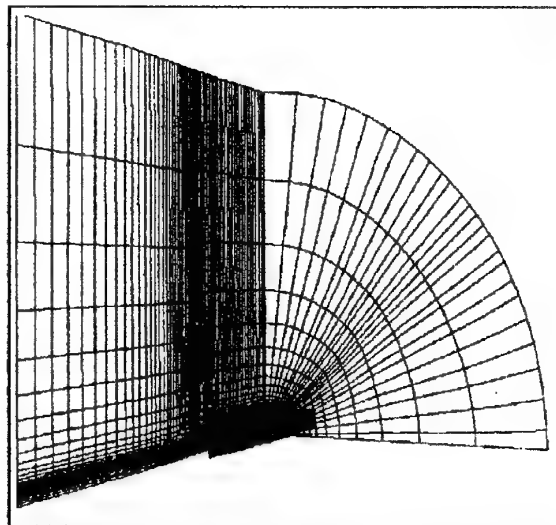


Figure C-12. External Computational Domain for Case B.4 (Contribution N02)

Unfortunately, no experimental force data are available for comparison.

#### C.2.4.2 Contribution N03 (SNECMA, CANARI)

**Grid Description** - The grid was generated in three blocks:

Block 1 - interior of the nozzle and the plume, sized 200x30x49 with 90x30x49 for the plume,

Block 2 - exterior of the nozzle and the plume, sized 186x40x49, with 90x40x49 for the plume, and,

Block 3 - large outer domain, 20x10x15.

A point-match interface was used between blocks 1 and 2, and a non-point-match interface was employed between blocks 2 and 3. Mesh orthogonality has been imposed on the walls.

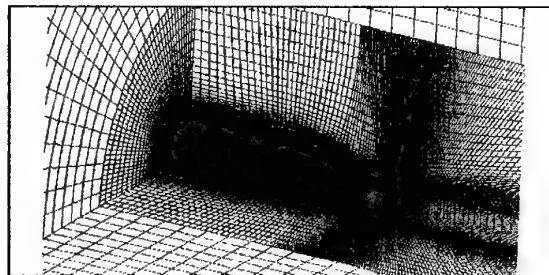


Figure C-13. Computational Grid Case B.4.x, Contribution N03

**Flow Solution Description** - The code CANARI was used, with the Baldwin-Lomax turbulence model. Solutions were executed on a Cray-Y/MP. These solutions required 40 hours for case B.4.1, and 60 hours for case B.4.2.

**Evaluation** - An Euler/thin-layer calculation on the forebody has been carried out for the B.4.2 case, to predict the shape of the thin-layer in the entry plane of the after-body Navier-Stokes calculation.

#### C.2.4.3 Contributions E04 and N04 (USAF WL/FIM, COBALT)

**Grid Description** - This contribution is based on the unstructured grid code, COBALT. The grid is a single-block, unstructured, hexahedral mesh with 764,187 grid points (fine grid) and 99,783 points (coarse grid). The grid was constructed from a multi block structured grid. The coarse grid consisted of every other point in all three directions deleted from the fine grid.

**Flow Solution Description** - The COBALT code was run with the Baldwin-Barth turbulence model. Solutions were executed on a Cray-Y/MP, and a Cray C-90. On the C-90 computer, the coarse grid required 20 CPU hours, and the fine grid required an additional 25 CPU hours. The fine grid solutions were started from interpolated coarse grid solutions.

The procedure for coarse grid solutions was as follows:

- 1) Run first-order Euler for 25,000 iterations.
- 2) Run turbulent first-order Navier-Stokes for 25,000 iterations.
- 3) Run turbulent second-order Navier-Stokes until conver-

gence (approximately 15,000 iterations).

These converged solutions were then interpolated to the fine grid and used as a starting point for the fine grid solutions. Fine grid solutions were then run turbulent second-order Navier-Stokes until convergence. The computer memory requirement was 18.5 M Words on the coarse grid, and 134.6 M Words on the fine grid.

Convergence was established by monitoring the average  $y^+$  for wall cells, drag on the afterbody, and number of cells with supersonic flow. The computation was stopped when the average  $y^+$  had been constant to four decimal places for 200 iterations, drag had been constant within 2 counts for 100 iterations, and the number of supersonic cells had been constant within 0.01% for 200 iterations.

By the nature of this approach (converge on a coarse grid, then interpolate and converge again on a fine grid), a comparison of solutions on two grid densities was a by-product of every solution. The fine grid solutions, in general, more closely matched experimental data than did corresponding coarse grid solutions.

Values of average  $y^+$  for all solutions are presented in the table below. The average  $y^+$  values for both the coarse and fine grid solutions exceed the desired threshold values. For both of the test cases the increased accuracy for the fine grid solutions can be attributed to the increase in axial grid density.

Test Case	Threshold Average $y^+$	Coarse Grid Average $y^+$	Fine Grid Average $y^+$
B.4.1	6.0	21.85	12.16
B.4.2	6.0	18.25	9.95

From the plots of Pitot pressure in the freestream/jet flowfield, it can be seen that the jet plume is not accurately modeled except in the region at the nozzle exit ( $x/L=1.0$ ). It was the objective of this organization to accurately predict the model surface pressure and drag characteristics, and therefore resources (grid points and therefore computer memory) were concentrated to accurately model the nozzle and aftbody geometry.

#### C.2.4.4 Contribution E05 (Dassault, EUGENIE)

Unstructured grids used in the solution of Cases B.4.1 and B.4.2, based on Method E05, are presented in Figure C-14, C-15, and C-16.

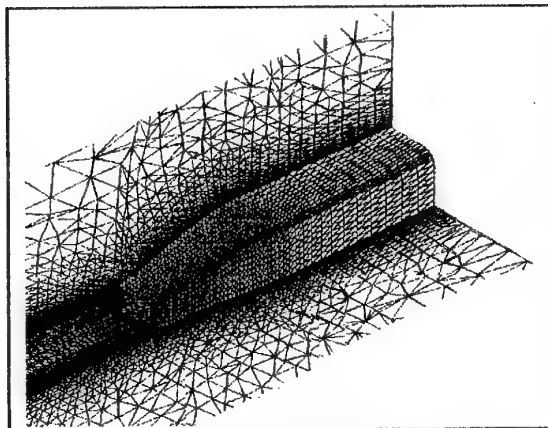


Figure C-14. Unstructured Grid for Cases B.4.1 and B.4.1 (Contribution E05)

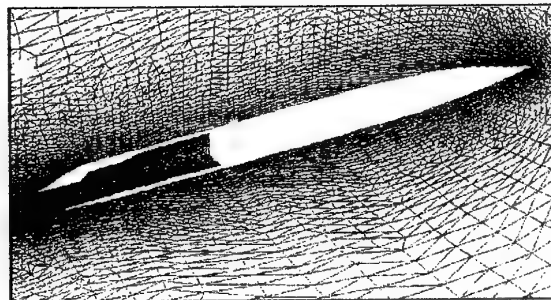


Figure C-15. Unstructured Grid for Cases B.4.1 and B.4.2 (Contribution E05)

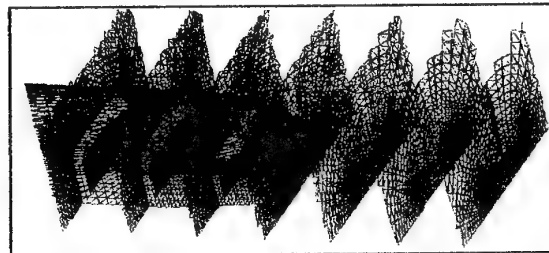


Figure C-16. Unstructured Grid for Cases B.4.1 and B.4.2 (Contribution E05)

#### C.2.4.5 Contribution N10 (NASA Langley Research Center)

**Grid Generation Description** - NASA Langley Research Center used a cylindrical grid whose axis coincided with the model axis to compute test cases B.4.1 and B.4.2. To minimize computer resources, symmetrical flow was

assumed about the vertical plane containing the model axis; hence, the computational domain is composed of only one half of the cylinder. The inflow boundary is one model length (approximately 20 model radii) upstream from the model nose, while the outflow boundary is approximately 30 model radii from the model surface.

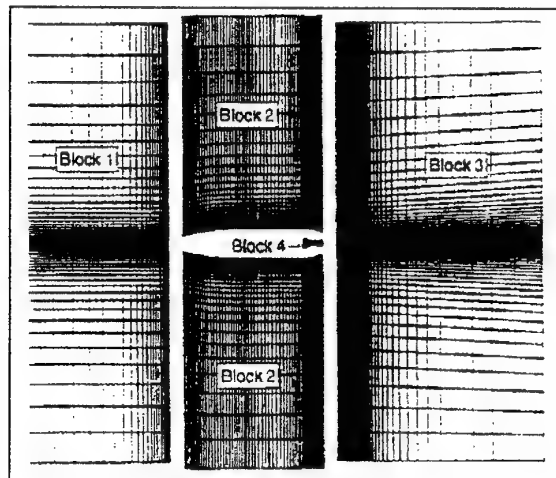


Figure C-17. Grid Layout for Cases B.4.1 and B.4.2  
(Contribution N10)  
*Grid blocks are separated for clarity*

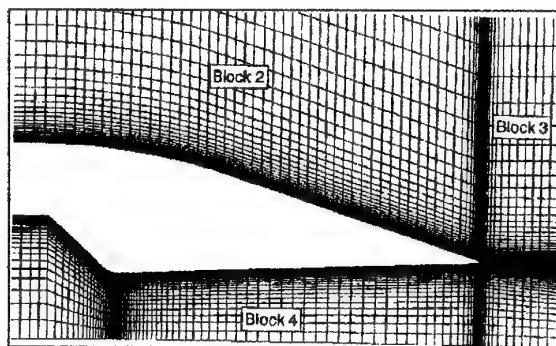


Figure C-18. Afterbody and Nozzle Grid for Cases B.4.1 and B.4.2 (Contribution N10)

The computational grid was generated using GRIDGEN (version 8). The grid is body-fitted (grid lines coincide with the model surface and other boundaries) to facilitate implementation of boundary conditions. The grid is composed of four blocks with point-to-point connectivity between the blocks. Each block used an H-O topology. The mesh density for each block is given in the following table:

Block	Location	I Dim.	J Dim.	K Dim.
1	Upstream	25	53	77
2	Model External	113	53	77
3	Downstream	57	53	153
3(a)	Downstream	81	53	153
4	Nozzle Internal	89	53	49

Where,

I is the streamwise direction;  
J is the circumferential direction, and,  
K is the radial direction.

Block 3(a) is a substitute for block 3 with a modified grid distribution and density. Block 3(a) was tested in order to improve the agreement between the computations and the data in the downstream part of the jet plume. However, it had a negligible effect on the results. The results presented at  $M_\infty = 0.60$  were computed with block 3(a) substituted for block 3. In order for the grid spacing to vary smoothly at the block interfaces, the cell dimensions normal to the block interfaces were equal for opposing cells on each side of the interface.

Grid lines are clustered near the body surface, on the afterbody, near the nozzle exit, and at the nozzle throat. They are also clustered in the circumferential direction near the corners of the afterbody. The small base at the nozzle exit is modeled. It has 29 grid points distributed along its height. The axial spacing of the grid at the nozzle exit is 20% of the base height. Grid cells next to the model surface had a dimension normal to the surface of 0.000300 inches on the external surface, and 0.000225 inches on the internal nozzle surface.

**Flow Solution Description** - The NASA Langley solutions were obtained with the multiple-block version of the Navier-Stokes code PAB3D (Ref. C-1). In PAB3D, the three-dimensional, time-dependent, Reynolds-averaged Navier-Stokes equations are normalized and written in strong conservation form for a Cartesian coordinate system ( $x, y, z$ ). Body forces are neglected. The relations between the energy, pressure, and enthalpy for an ideal gas complete the system of equations. The code allows for laminar viscous dissipation in all three directions. Turbulent viscous dissipation can be modeled in two directions, however the two turbulent terms cannot be coupled at the present time.

PAB3D employs the finite volume principle where the spatial derivatives in the equations are evaluated as conservative flux balances across the grid cells. The fluxes at the cell interfaces are determined with Roe's upwind-

biased flux-difference splitting combined with the min-mod gradient limiting procedure to ensure monotonicity across discontinuities such as shock waves. The scheme is spatially third-order accurate.

The time-difference algorithm used in the computational procedure is an approximately-factored alternating-direction implicit scheme in delta form. The approximate factorization is applied in the two cross-flow directions, while the terms in the axial, or main flow, direction are split and added to the two resulting factors.

**Turbulence Model** - Turbulence viscosity is modeled by several formulations in the code. The present solutions used the standard Jones-Launder turbulence model (Ref. C-2) as modified by Hamid et. al (Ref. C-3). The modifications consist of extending the turbulence model to its fully three-dimensional form and also writing it in generalized coordinates and in a conservative form similar to the governing equations.

**Boundary Conditions** - Since the free stream is subsonic, Riemann invariants for a one-dimensional flow were used to calculate the primitive flow variables  $\rho$ ,  $u$ ,  $v$ ,  $w$ , and  $p$  at the computational domain inflow and far-field boundaries.

Reflection boundary conditions were imposed at the symmetry boundaries of the computational domain and on its centerline. At the outflow boundary, where the flow is a mixture of the jet exhaust and the free stream, all gradients were set to zero regardless of the free stream conditions.

At the jet inflow boundary, jet total pressure, jet total temperature, and flow angle were specified. Finally, a no-slip and an adiabatic wall boundary condition were imposed on the body surface.

Boundary conditions for the turbulence model consisted of setting the turbulent kinetic energy ( $k$ ) and the turbulent dissipation ( $\epsilon$ ) equal to zero at the wall boundaries. At the symmetry and outflow boundaries, the gradients of these two terms were set equal to zero.

At the far-field boundary, a characteristic boundary condition for  $k$  and  $\epsilon$  was used, similar to the Riemann-invariant boundary condition for the Navier-Stokes equations. However, the turbulent characteristic condition contains only one eigenvector.

Transition from laminar to turbulent flow for the computations was fixed at the third grid plane downstream of the model nose (or the nozzle inflow station for the internal flow). The boundary conditions for the turbulent quantities at this transition plane were obtained in the following manner. First, the vorticity was computed in the two

preceding laminar planes, and the turbulent kinetic energy ( $k$ ) was scaled to the shape of the vorticity profiles. The maximum value of  $k$  was set to 1% of the square of the maximum velocity in the plane. The turbulent dissipation was then computed from the relation  $\epsilon = f(k, \epsilon, u, v, w)$ .

**Computer Resources Required** - The present computations were run on the NASA Langley Research Center Cray-Y/MP supercomputer. On that machine, PAB3D required the following resources:

Mode	Memory (Note 1)	CPU Time (Note 2)
Laminar	15	33 $\mu$ s
k- $\epsilon$ Turbulence Model	20	44 $\mu$ s

Note 1 - Words of memory per grid point

Note 2 - CPU time, per grid point, per time step.

**Solution Strategy** - Although Roe's flux-difference scheme is used to compute fluxes for the explicit side of the equations, van Leer's flux splitting scheme is used for the implicit side. This procedure enhances the robustness of the code while accurately capturing discontinuities with the fewest number of grid points.

The inflow grid block (block 1) was run as a laminar block with the viscous dissipation imposed only in the radial direction. Blocks 2, 3, and 4 were run as turbulent blocks with turbulent dissipation modeled by the modified Jones-Launder k- $\epsilon$  turbulence model. For blocks 2 and 4, the thin-layer assumption, which only retains the viscous terms normal to the surface of the model (the  $K$  direction) was made. In the plume (block 3), in addition to imposing the viscous terms only in the radial direction, a computation was made in which viscosity was calculated in both the radial and circumferential directions (the  $K$  and  $J$  directions). The two computations gave essentially the same results.

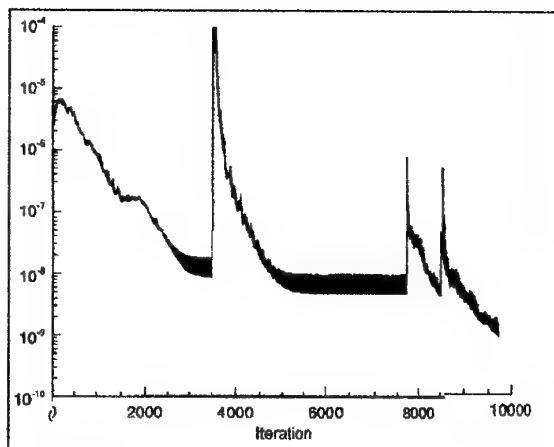


Figure C-19. - Residual Convergence History for Case B.4.2 (Contribution N10)

In the present computations, a grid sequencing strategy was followed to further enhance the convergence. The solution was run on the coarsest grids almost 8,000 time steps for the turbulence to develop before proceeding to the finer grids. The complete solution for test case B.4.2 took a total of 37 hours on the NASA Langley Research Center Cray-Y/MP supercomputer.

**Post-Processing Description** - In post-processing the solutions, a utility code was written to integrate the pressure-area terms for afterbody drag. When comparing the solutions to the experimental data, the solutions were interpolated to the geometrical coordinates of the experimental data. The interpolation was done with an unpublished code written by Jamshid S. Abolhassani of the GEOLAB at NASA Langley Research Center. Plotting was done with TECPLOT Version 6 and FAST Version 1.1.

#### C.2.4.6 Contribution E11 and N11 (DRA/ARA, SAUNA Code)

The case of the rectangular jet geometry (test case B.4) has been studied for the two freestream Mach numbers of 0.60 and 0.938 (cases B.4.1 and B.4.2 respectively). The Structured and Unstructured Numerical Analysis (SAUNA) package has been used for this study. SAUNA has been under development at ARA for several years under funding from the Defence Research Agency who are currently the main users of the facility. It is an extension of the 3-D structured grid multi-block approach pioneered at ARA in the early 1980's. At present the SAUNA package is primarily used for modeling complex configurations with the Euler equations on mixed structured and unstructured "hybrid" grids. A further facility (to be released in April 1994) allows for the zonal solution of the Navier-Stokes equations within selected structured grid blocks. A pre-

release version of this latter procedure has been used in this study using wholly structured grids. Both inviscid and viscous flow solutions have been contributed, on appropriate grids.

**Geometry Modeling** - The two test cases B.4.1 and B.4.2 have the body set at nominally zero incidence and yaw. Therefore the CFD representation of the problem has used the fact that two symmetry planes exist at  $Y=0$  and  $Z=0$  to model just the starboard upper quarter of the geometry, allowing more efficient computer storage and solution times. The complete body has been modeled including the nose and the entirety of the nozzle so that realistic boundary layers are present upstream of the critical flow regions. The base area could not be modeled so the trailing edge has been reduced to zero thickness by slight modifications to the nozzle geometry. The nozzle effectively has 8% more cross-sectional area but all internal angles and nozzle area ratios remain unchanged. The throat was moved upstream, away from the exit plane by 0.17 model inches to achieve this.

**Grid Generation** - Due to the simplicity of the configuration and the need to model only one-quarter of the flow-field, a specific grid generation procedure not present in the SAUNA system has been used. This procedure uses the algebraic technique transfinite interpolation to create grids which are suitable for either viscous or inviscid flow computations. The resulting "tailor made" grids are compatible with the flow solver of SAUNA and provide grids with three levels of density, which can be used in subsequent grid sequencing and multigrid options of the flow code. The grids are globally polar and fill the upper starboard quarter of the flowfield. Within the nozzle and jet a strictly polar topology does not exist because an extra series of Cartesian blocks have been included at the model axis. This type of block arrangement has been found to be more robust for jet flow solutions. Each grid is initially generated with 33 blocks but these are combined to form "macro-blocks" for more efficient use of vectorization in the flow solver. The number of points in the finest Euler grid is 220,000 and in the finest Navier-Stokes grid it is 340,000. In the Navier-Stokes grid the first points from the solid boundaries are set at a constant 0.000830 model inches from the surface.

**Flow Solution** - The following code features are common to both the Euler and Navier-Stokes capabilities of the SAUNA flow solver and have been used here.

- Vertex storage.
- Jameson style artificial dissipation and enhancements.
- Explicit Runge-Kutta time marching and local time stepping.



- Multiple boundary condition types, e.g., jet inflow and outflow, freestream Riemann invariants, Rudy-Strikwerda characteristic outflow, reflection, etc.
- Grid sequencing and multigrid.
- Convergence monitoring by continuity equation residual or total forces.

**Euler Solutions** - The blocks were combined into three macro-blocks (one for the external flow and two for the nozzle and jet flow) for the solution of the Euler equations. All three grid levels were used in the multigrid facility and the number of time steps completed were 100, 200, and 300 on the coarse, medium, and fine grid levels respectively. Enthalpy damping was switched off (due to the slight difference between the nozzle and the external flow total enthalpy) but all other run parameters were kept to their default values. Each flow run took 7300 seconds of CPU time on a Cray-2 computer and convergence was achieved in each case.

**Navier-Stokes Solutions** - The Navier-Stokes equations were only solved within regions next to solid surfaces and downstream of the trailing edge. Eight macro-blocks were required, three of which define the zones for the solution of the viscous equations. The Baldwin-Lomax turbulence model has been used with modifications from the established procedure for the macro-block containing the wake region. The procedure for getting convergence was more complicated than for the Euler equations alone and was arrived at through numerical experiment. The coarsest grid level was not used and the solution started with the calculation of laminar flow on the medium grid level (300 steps). A few time steps were then completed on the finest grid level, again calculating just for laminar flow. The procedure was completed on the finest grid by running with the Baldwin-Lomax turbulence model and using two multigrid levels (700 steps for  $M=0.6$  and 1,050 steps for  $M=0.938$ ). Convergence was judged to have been achieved once a drop in the density residual of three orders of magnitude on the finest grid level had been reached. Enthalpy damping was used in the initial stages of convergence to achieve stability. Run times were in the order of 30 seconds per step on the finest grid level, using the Cray-2, yielding total run times of about 10 hours. The maximum computer storage necessary when running the flow solver was 17.5 MWords.

#### C.2.4.7 Contribution N12 (Lockheed, TEAM)

**Grid Description** - The surface grids were developed using the Interactive Graphical Grid Generation (I3G) program (Ref. C-4). Within I3G, the domain was split into three separate zones. The six faces of each hexahedral zone were generated in I3G and output for volume mesh genera-

tion. Volume mesh generation was completed using the PLUTO3D code. The initial volume mesh was calculated using trans-finite interpolation (TFI) with Laplacian smoothing invoked as required. Due to geometric symmetry, only a single quadrant of the nozzle was modeled. The final CFD grid contained 194,695 nodal points.

To minimize computer resources, the computational grid did not include the entire 63.04-inch model. The external computational grid began at fuselage station 26.50 inches. This is the beginning of the constant cross-sectional area extending to the nozzle connect station. The internal computational grid began at fuselage station 52.87 inches. This is the beginning of the rectangular cross section.

The grid block structure is presented in Figure 10 at the vertical plane of symmetry. The flowfield domain contains three blocks. Block 1 is the internal region of the nozzle. It is an H-grid that also extends downstream for the full length of the flowfield. Block 2 is the external region of the nozzle. It is an O-grid that also extends downstream for the full length of the flowfield. Block 3 begins at the nozzle aft end and joins blocks 1 and 2. It is an O-grid and is referred to as the "lip zone."

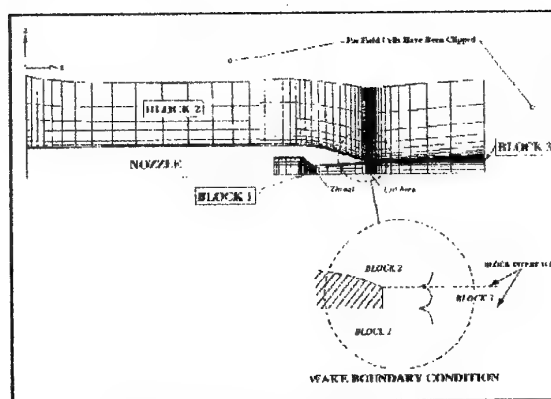


Figure C-20. Grid Block Structure  
(Contribution N12)

The grid dimensions, about one-quarter of the model, are:

Block	Axial Size	Circum. Size	Radial Size
1	122	31	31
2	122	16	16
3	71	31	21

The nozzle geometry is defined by the first 52 axial planes of Blocks 1 and 2. All block interfaces used point-to-point matching to eliminate interpolation as a potential source of



error in the flow solution. The flowfield points were clustered toward the nozzle surface and the surface grid points were clustered toward the nozzle exit plane. The grid density near the surface normal were appropriately clustered to keep the non-dimensional wall coordinate  $y^+$  near 0.3.

**Flow Solution Description** - Flowfield analyses were performed using the TEAM code to calculate the viscous flowfield about the nozzle boattail. Flowfield calculations were performed for Case B.4.1 (freestream Mach number 0.6). The nozzle entrance plane was modeled with a boundary condition imposing an NPR of 4.0, an exhaust temperature ratio of 0.987, and Mach number of 0.35.

The calculations were performed on Lockheed's Cray Y-MP/81 supercomputer. The solution converged after 30,000 iterations utilizing 16.4 hours of Cray CPU time, and requiring 9.8 M Words of memory. Criteria used to determine convergence included the relative change in time of the number of supersonic points, the values of integrated force and moment quantities, the average residual of the calculation, and the local pressure distribution. Figure 11 presents the convergence history for both the average residual and the number of supersonic points.

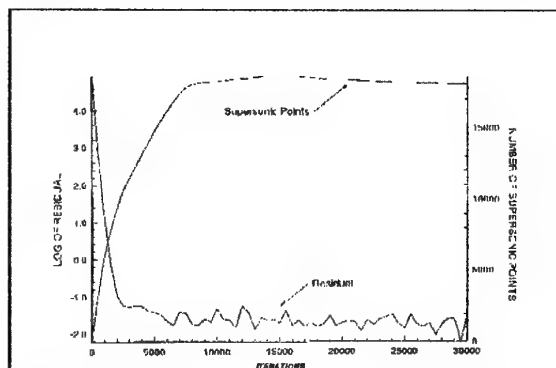


Figure C-21. Convergence History  
(Contribution N12)

For the present computations, the four-stage time-stepping scheme was invoked with a modified adaptive dissipation scheme. The Reynolds number was  $17.3 \times 10^6$  (based on model length from the nose to the nozzle exit) and the turbulent Prandtl number was 0.90. No initial external nozzle boundary layer thickness was specified. Therefore, boundary layer growth from the nose to fuselage station 26.50 inches was not included.

The application of the TEAM code to this B.4.1 test case has reinforced prior studies on the inadequacy of the Baldwin-Lomax algebraic turbulence model to properly predict jet wake/mixing entrainment phenomena. Improved turbulence models are required for exhaust flowfields.

Recent studies have shown significant improvements in plume predictions using two-equation  $k-\epsilon$  models with compressibility corrections. Additionally, Lakshmanan (Ref. C-5).

Efforts are currently underway at LASC to incorporate a two equation turbulence model into the TEAM code. The Chien low Reynolds number model has been incorporated, and gives good results in wall-bounded flows. It will next be extended to wake flowfields, after which this case will be revisited. The lack of wake spreading across the wake block interface will also be investigated, beginning with a new grid topology.

Additional modeling of the internal nozzle is required to accurately capture the flowfield immediately downstream of the nozzle exit. The non-uniformity of the experimental total pressure field indicates a disturbance has been caused in the internal nozzle due to either geometry or the quality of air delivered to the nozzle entrance. If the cause of this disturbance was known prior to grid generation, more attention could have been paid to how the air was delivered to the nozzle, internal shapes (model hardware versus the provided definition), and corner radii.

Properly predicting the aftbody boundary layer characteristics is required to match the pressure distributions and entrainment of the problem. Modeling the entire boattail problem from nose to nozzle exit with the proper transition location is necessary to obtain a good solution.

#### C.2.4.8 Contribution N16 (USAF/NASA Lewis, NPARC)

**Grid Description** - Computational grids were provided by McDonnell Douglas. Therefore, the grids were the same as were used in Contribution N09, except in the following elements. Because the NPARC code requires grid blocks that overlap at block interfaces, the grids were modified with the I3G interactive grid generator developed by the US Air Force at Wright-Patterson Air Force Base. I3G was used to add an additional grid plane at each interface to create the required overlaps. For the B.4 configuration, six overlap planes were added. The grid contained 831,105 grid points divided into seven grid blocks. The largest concentration of grid points was located in the vicinity of the nozzle afterbody.

**Flow Solution Description** - The test cases were run with NPARC on the Cray-Y/MP at NASA Lewis Research Center. A total of 30,000 iterations were required for convergence in each case. For the B.4.2 case, approximately 180 CPU hours were required to obtain a converged solution from uniform initial conditions. The grid blocks containing the internal nozzle flow converged rapidly and were subsequently turned off to save CPU time. An oscillatory behavior was observed in the pressure coeffi-

cient of Row 1 on the boattail near the separated flow region. The magnitude of the oscillation slowly damped out. Internal nozzle mass flow and L2 residual were monitored to determine convergence. A solution was considered to be converged when the difference between the minimum and maximum pressure coefficient at each grid point was within one percent of the average pressure coefficient.

**Assessment** - For the B.4 cases, the location of the minimum pressure obtained with the Chien  $k-\epsilon$  and the Baldwin-Barth turbulence models agree well with the experimental data. In the separated flow region, neither model agrees very well with the experimental pressure distribution, with the Baldwin-Barth model providing somewhat closer agreement. The internal pressure distributions calculated with the Chien  $k-\epsilon$  and the Baldwin-Barth models are very similar, and provide relatively good agreement with the experimental data along the boattail just before the afterbody shock.

### C.3 Post-Processing Techniques

#### C.3.1 Contribution N04 (USAF WL, COBALT)

**Pressure Drag** - The pressure acting on any given boundary cell face centroid is known. This face centroid pressure is taken to be the average pressure acting over the boundary cell face. Pressure drag is then determined by multiplying the cell face area normal to the drag direction by the average face pressure and summing over the cell faces on the boundary of interest.

**Skin Friction Drag** - The normal derivative of velocity at each boundary face centroid is known to second order accuracy. As with pressure, the velocity derivative at the face centroid is taken to be the average value for the cell face. Friction force for the cell is then determined by multiplying the cell face surface area by the average velocity derivative times the coefficient of viscosity. Friction drag is determined by taking the component of friction force in the drag direction for each cell face and summing over the cell faces of the boundary of interest.

#### C.3.2 Contribution N10 (NASA Langley Research Center, PAB3D)

A performance computation module, developed by the Propulsion Aerodynamics Branch at the Langley Research Center, was incorporated in the PAB3D code as a standard option to compute quantities such as thrust, normal and side forces, three components of moments, skin friction, and heat transfer. High level capabilities for specialized applications such as multi-stream nozzle and internal mixer configurations were included as part of the performance

module. Mass flux is computed by integrations over one or more cross sections in the flow path.

Force and moment calculations are conducted through a combination of integration of pressure and skin friction forces over solid surfaces, and the integration of momentum flux and pressure over the flow through surface of the control volume. In cases of skin friction calculations, the gradients of the local velocity in a direction normal to the wall and the local viscosity are used. Heat transfer is computed in a similar manner by using the local temperature gradient and conductivity.

These calculations can be performed at intermediate steps throughout the solution procedure to provide an integrated flow quantity convergence history in addition to monitoring the computational residuals in the flow solution algorithm. For the present set of flow analyses, the performance module was activated as a one-time process after the numerically converged solutions were obtained. The performance calculation was directed by a small input file containing locations of the control surfaces in the grid and specifications for the integrated quantities to be computed.

## References

- C-1. Abdol-Hamid, Khaled S., "Application of a Multi-block/Multizone Code (PAB3D) for the Three-Dimensional Navier-Stokes Equations," AIAA Paper 91-2115.
- C-2. Jones, W.P., and B.E. Launder, "The Calculation of Low-Reynolds-Number Phenomena with a Two-Equation Model of Turbulence," International Journal of Heat and Mass Transfer, Vol. 15, 1972.
- C-3. Abdol-Hamid, K.S., K. Uenishi, and W.M. Turner, "Three-Dimensional Upwinding Navier-Stokes Code with  $k-\epsilon$  Model for Supersonic Flows," AIAA Paper 91-1669, June 1991.
- C-4. Emsley, H.T., "Interactive Graphics for Geometry Generation," (USAF) WL/FIMM, Wright-Patterson AFB, WL-TM-91-316, June 1991.
- C-5. Lakshmanan, B., "Investigation of Supersonic Secondary Flows Using Nonlinear  $k-\epsilon$  Model," Old Dominion University, RTR 505-59-30-04, 1993.

-end-

## REPORT DOCUMENTATION PAGE

1. Recipient's Reference	2. Originator's Reference AGARD-AR-318	3. Further Reference ISBN 92-836-1023-7	4. Security Classification of Document UNCLASSIFIED/ UNLIMITED												
5. Originator	Advisory Group for Aerospace Research and Development North Atlantic Treaty Organization 7 rue Ancelle, 92200 Neuilly-sur-Seine, France														
6. Title	Aerodynamics of 3-D Aircraft Afterbodies														
7. Presented at/sponsored by	Fluid Dynamics Panel of AGARD														
8. Author(s)/Editor(s) Multiple	9. Date September 1995														
10. Author's/Editor's Address Multiple	11. Pages 496														
12. Distribution Statement	There are no restrictions on the distribution of this document. Information about the availability of this and other AGARD unclassified publications is given on the back cover.														
13. Keywords/Descriptors	<table><tr><td>Computational fluid dynamics</td><td>Aerodynamic configurations</td></tr><tr><td>Aerodynamics</td><td>Three dimensional flow</td></tr><tr><td>Aircraft</td><td>Drag</td></tr><tr><td>Afterbodies</td><td>Fuselages</td></tr><tr><td>Unsteady flow</td><td>Turbulent boundary layer</td></tr><tr><td>Aerodynamic characteristics</td><td>Turbulent flow</td></tr></table>			Computational fluid dynamics	Aerodynamic configurations	Aerodynamics	Three dimensional flow	Aircraft	Drag	Afterbodies	Fuselages	Unsteady flow	Turbulent boundary layer	Aerodynamic characteristics	Turbulent flow
Computational fluid dynamics	Aerodynamic configurations														
Aerodynamics	Three dimensional flow														
Aircraft	Drag														
Afterbodies	Fuselages														
Unsteady flow	Turbulent boundary layer														
Aerodynamic characteristics	Turbulent flow														
14. Abstract	<p>A state-of-the-art update has been performed into the aerodynamics of 3-D Aircraft Afterbodies. Particular attention has been paid to developments made in the computation techniques available to solve the complex flow physics generated at the nozzle/afterbody interface on geometries of realistic 3-D complexity. Results of computations performed on two selected sets of test cases are presented. Developments of experimental methods and empirical prediction techniques are also reviewed. Progress made since the last AGARD update (1986) are noted and recommendations made as to the required direction of future development efforts.</p>														

Aucun stock de publications n'a existé à AGARD. A partir de 1993, AGARD détiendra un stock limité des publications associées aux cycles de conférences et cours spéciaux ainsi que les AGARDographies et les rapports des groupes de travail, organisés et publiés à partir de 1993 inclus. Les demandes de renseignements doivent être adressées à AGARD par lettre ou par fax à l'adresse indiquée ci-dessus. *Veuillez ne pas téléphoner.* La diffusion initiale de toutes les publications de l'AGARD est effectuée auprès des pays membres de l'OTAN par l'intermédiaire des centres de distribution nationaux indiqués ci-dessous. Des exemplaires supplémentaires peuvent parfois être obtenus auprès de ces centres (à l'exception des Etats-Unis). Si vous souhaitez recevoir toutes les publications de l'AGARD, ou simplement celles qui concernent certains Panels, vous pouvez demander à être inclu sur la liste d'envoi de l'un de ces centres. Les publications de l'AGARD sont en vente auprès des agences indiquées ci-dessous, sous forme de photocopie ou de microfiche.

CENTRES DE DIFFUSION NATIONAUX

## ALLEMAGNE

Fachinformationszentrum,  
Karlsruhe  
D-76344 Eggenstein-Leopoldshafen 2

## BELGIQUE

Coordonnateur AGARD-VSL  
Etat-major de la Force aérienne  
Quartier Reine Elisabeth  
Rue d'Evere, 1140 Bruxelles

## CANADA

Directeur, Services d'information scientifique  
Ministère de la Défense nationale  
Ottawa, Ontario K1A 0K2

## DANEMARK

Danish Defence Research Establishment  
Ryvangs Allé 1  
P.O. Box 2715  
DK-2100 Copenhagen Ø

## ESPAGNE

INTA (AGARD Publications)  
Pintor Rosales 34  
28008 Madrid

## ETATS-UNIS

NASA Headquarters  
Code JOB-1  
Washington, D.C. 20546

## FRANCE

O.N.E.R.A. (Direction)  
29, Avenue de la Division Leclerc  
92322 Châtillon Cedex

## GRECE

Hellenic Air Force  
Air War College  
Scientific and Technical Library  
Dekelia Air Force Base  
Dekelia, Athens TGA 1010

## ISLANDE

Director of Aviation  
c/o Flugrad  
Reykjavik

## ITALIE

Aeronautica Militare  
Ufficio del Delegato Nazionale all'AGARD  
Aeroporto Pratica di Mare  
00040 Pomezia (Roma)

## LUXEMBOURG

Voir Belgique

## NORVEGE

Norwegian Defence Research Establishment  
Attn: Biblioteket  
P.O. Box 25  
N-2007 Kjeller

## PAYS-BAS

Netherlands Delegation to AGARD  
National Aerospace Laboratory NLR  
P.O. Box 90502  
1006 BM Amsterdam

## PORTUGAL

Força Aérea Portuguesa  
Centro de Documentação e Informação  
Alfragide  
2700 Amadora

## ROYAUME-UNI

Defence Research Information Centre  
Kentigern House  
65 Brown Street  
Glasgow G2 8EX

## TURQUIE

Millî Savunma Başkanlığı (MSB)  
ARGE Dairesi Başkanlığı (MSB)  
06650 Bakanlıklar-Ankara

**Le centre de distribution national des Etats-Unis ne détient PAS de stocks des publications de l'AGARD.**

D'éventuelles demandes de photocopies doivent être formulées directement auprès du NASA Center for Aerospace Information (CASI) à l'adresse ci-dessous. Toute notification de changement d'adresse doit être fait également auprès de CASI.

AGENCES DE VENTE

NASA Center for  
AeroSpace Information (CASI)  
800 Elkridge Landing Road  
Linthicum Heights, MD 21090-2934  
Etats-Unis

ESA/Information Retrieval Service  
European Space Agency  
10, rue Mario Nikis  
75015 Paris  
France

The British Library  
Document Supply Division  
Boston Spa, Wetherby  
West Yorkshire LS23 7BQ  
Royaume-Uni

Les demandes de microfiches ou de photocopies de documents AGARD (y compris les demandes faites auprès du CASI) doivent comporter la dénomination AGARD, ainsi que le numéro de série d'AGARD (par exemple AGARD-AG-315). Des informations analogues, telles que le titre et la date de publication sont souhaitables. Veuillez noter qu'il y a lieu de spécifier AGARD-R-nnn et AGARD-AR-nnn lors de la commande des rapports AGARD et des rapports consultatifs AGARD respectivement. Des références bibliographiques complètes ainsi que des résumés des publications AGARD figurent dans les journaux suivants:

Scientific and Technical Aerospace Reports (STAR)  
publié par la NASA Scientific and Technical  
Information Division  
NASA Headquarters (JTT)  
Washington D.C. 20546  
Etats-Unis

Government Reports Announcements and Index (GRA&I)  
publié par le National Technical Information Service  
Springfield  
Virginia 22161  
Etats-Unis

(accessible également en mode interactif dans la base de données bibliographiques en ligne du NTIS, et sur CD-ROM)



AGARD holds limited quantities of the publications that accompanied Lecture Series and Special Courses held in 1993 or later, and of AGARDographs and Working Group reports published from 1993 onward. For details, write or send a telefax to the address given above. *Please do not telephone.*

AGARD does not hold stocks of publications that accompanied earlier Lecture Series or Courses or of any other publications. Initial distribution of all AGARD publications is made to NATO nations through the National Distribution Centres listed below. Further copies are sometimes available from these centres (except in the United States). If you have a need to receive all AGARD publications, or just those relating to one or more specific AGARD Panels, they may be willing to include you (or your organisation) on their distribution list. AGARD publications may be purchased from the Sales Agencies listed below, in photocopy or microfiche form.

NATIONAL DISTRIBUTION CENTRES**BELGIUM**

Coordonnateur AGARD — VSL  
Etat-major de la Force aérienne  
Quartier Reine Elisabeth  
Rue d'Evere, 1140 Bruxelles

**CANADA**

Director Scientific Information Services  
Dept of National Defence  
Ottawa, Ontario K1A 0K2

**DENMARK**

Danish Defence Research Establishment  
Ryvangs Allé 1  
P.O. Box 2715  
DK-2100 Copenhagen Ø

**FRANCE**

O.N.E.R.A. (Direction)  
29 Avenue de la Division Leclerc  
92322 Châtillon Cedex

**GERMANY**

Fachinformationszentrum  
Karlsruhe  
D-76344 Eggenstein-Leopoldshafen 2

**GREECE**

Hellenic Air Force  
Air War College  
Scientific and Technical Library  
Dekelia Air Force Base  
Dekelia, Athens TGA 1010

**ICELAND**

Director of Aviation  
c/o Flugrad  
Reykjavik

**ITALY**

Aeronautica Militare  
Ufficio del Delegato Nazionale all'AGARD  
Aeroporto Pratica di Mare  
00040 Pomezia (Roma)

**LUXEMBOURG**

*See Belgium*

**NETHERLANDS**

Netherlands Delegation to AGARD  
National Aerospace Laboratory, NLR  
P.O. Box 90502  
1006 BM Amsterdam

**NORWAY**

Norwegian Defence Research Establishment  
Attn: Biblioteket  
P.O. Box 25  
N-2007 Kjeller

**PORTUGAL**

Força Aérea Portuguesa  
Centro de Documentação e Informação  
Alfragide  
2700 Amadora

**SPAIN**

INTA (AGARD Publications)  
Pintor Rosales 34  
28008 Madrid

**TURKEY**

Millî Savunma Başkanlığı (MSB)  
ARGE Dairesi Başkanlığı (MSB)  
06650 Bakanlıklar-Ankara

**UNITED KINGDOM**

Defence Research Information Centre  
Kentigern House  
65 Brown Street  
Glasgow G2 8EX

**UNITED STATES**

NASA Headquarters  
Code JOB-1  
Washington, D.C. 20546

**The United States National Distribution Centre does NOT hold stocks of AGARD publications.**

Applications for copies should be made direct to the NASA Center for AeroSpace Information (CASI) at the address below.

Change of address requests should also go to CASI.

SALES AGENCIES**NASA Center for**

AeroSpace Information (CASI)  
800 Elkridge Landing Road  
Linthicum Heights, MD 21090-2934  
United States

ESA/Information Retrieval Service  
European Space Agency  
10, rue Mario Nikis  
75015 Paris  
France

The British Library  
Document Supply Centre  
Boston Spa, Wetherby  
West Yorkshire LS23 7BQ  
United Kingdom

Requests for microfiches or photocopies of AGARD documents (including requests to CASI) should include the word 'AGARD' and the AGARD serial number (for example AGARD-AG-315). Collateral information such as title and publication date is desirable. Note that AGARD Reports and Advisory Reports should be specified as AGARD-R-nnn and AGARD-AR-nnn, respectively. Full bibliographical references and abstracts of AGARD publications are given in the following journals:

Scientific and Technical Aerospace Reports (STAR)  
published by NASA Scientific and Technical  
Information Division  
NASA Headquarters (JTT)  
Washington D.C. 20546  
United States

Government Reports Announcements and Index (GRA&I)  
published by the National Technical Information Service  
Springfield  
Virginia 22161  
United States  
(also available online in the NTIS Bibliographic  
Database or on CD-ROM)

